

ELECTRON DIFFRACTION OF COPPER PHTHALOCYANINE ON THE HVEM

W. F. Tivol, J. N. Turner, M. P. McCourt,* D. L. Dorset *

Wadsworth Center for Laboratories and Research, Albany NY 12201-0509 and School of Public Health, the University at Albany, Albany NY 12201-0509, USA

* Electron Diffraction Department, Medical Foundation of Buffalo, Inc., Buffalo NY 14203-1196, USA

The use of high-energy (1200 kV) electrons has been shown to be advantageous in the *ab initio* structure analysis from electron diffraction of organic compounds.^{1,2,3} Previous studies showed that *ab initio* analysis of copper perchlorophthalocyanine could be accomplished at accelerating voltages at or above 1000 kV, but not at 400 kV for crystals which are about 10 nm thick.^{1,2} Copper perbromophthalocyanine could also be analyzed *ab initio* at 1200 kV, but the presence of severe dynamical scattering precluded such analysis at lower voltages.³ A study of copper perchlorophthalocyanine at accelerating voltages from 200 kV to 1200 kV showed that dynamical scattering accounted for the differences among the diffraction patterns which lead to the failure of *ab initio* analysis at the lower voltages.²

The series of phthalocyanines offers a good model for the study of dynamical scattering and direct phasing methods, since it consists of relatively radiation-resistant compounds for which high-resolution diffraction patterns can be obtained. Furthermore, the symmetry of the molecule and the flatness of the unit cell simplify both the analysis and the multi-slice calculations used to investigate the effects of dynamical scattering. This allows studies at both the high voltages and the intermediate voltages (300 to 400 kV) used in modern electron microscopes.

Copper phthalocyanine was grown epitaxially from the vapor phase onto a clean KCl crystal face.⁴ Electron diffraction patterns were obtained from crystals of the metastable α -form tilted at 32° and oriented so that the electron beam was parallel to the c-axis.⁴

Electron doses were kept to a minimum by the use of a 30 μ m condenser aperture and a highly excited first condenser lens. The newly-installed video system allows scanning the specimen to find a crystal suitable for the correct orientation of the grid by rotating it within its own plane (See Fig. 1a.), following the crystal as the grid is rotated (See Fig. 1b.) and focusing the objective lens all at an illumination level below that necessary to distinguish anything by eye on the HVEM's phosphor screen.

The AEI EM7 high-voltage electron microscope was used at a voltage of 1000 kV in diffraction mode with a 10 μ m selected area aperture. The data were recorded on DuPont Lo-dose Mammography film. Diffraction spots are seen out to a resolution of 0.07 nm (See Fig. 2). Intensities were measured on a Perkin-Elmer 1010A flat bed microdensitometer and processed on a VAX 6210 computer and a 3100 workstation using the diffraction-analysis package⁵ of the SPIDER image processing software.⁶

The pattern obtained corresponds to a unit cell with lattice constants half those usually quoted, since in this projection the space group C2/c reduces to plane group p2.⁴ Analysis of the data is in progress.^{7,8}

References

1. Dorset, D.L., et al., *Ultramicroscopy* 38 (1991) 41.

2. Tivol, W.F., et al., *MSA Bulletin* 23 (1993) 91.
3. Dorset, D.L., et al., *Acta Cryst. A* 48 (1992) 562.
4. Murata, Y., et al., *J. Microsc.* 108 (1976) 261.
5. Tivol, W.F., et al., *Ultramicroscopy* 9 (1982) 117-130.
6. Frank, J., et al., *Ultramicroscopy* 6 (1981) 343-358.
7. Work was supported by Biotechnological Resource grant RR01219, awarded by the National Center for Research Resources, Department of Health and Human Services/Public Health Service and NSF grant CHE 9113899.
8. The authors wish to thank Dr. J. R. Fryer for the gift of the compound used and A. Leith for his help with the diffraction analysis software.

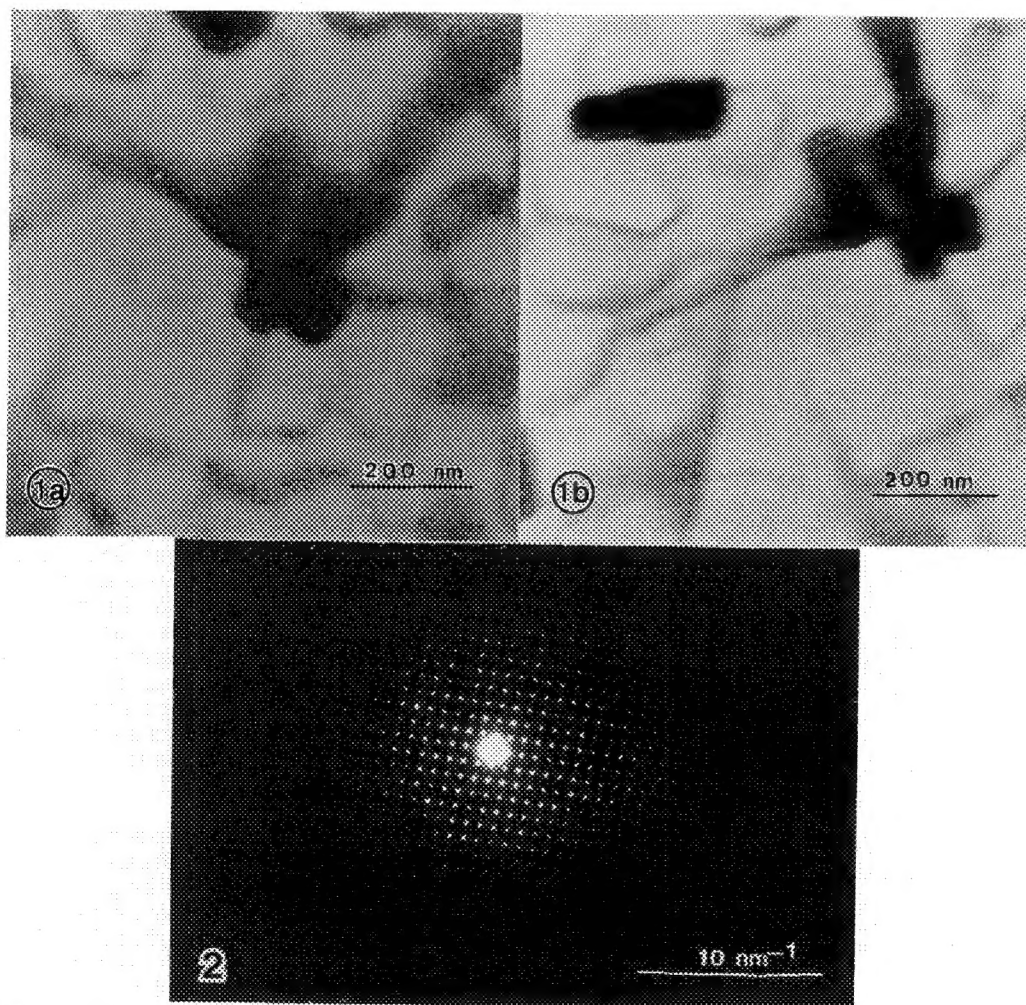


FIG. 1.--Images of copper phthalocyanine crystals. a) before stage rotation in grid plane, b) after rotation to obtain zone-axis orientation. Note contrast increase upon correct orientation.
 FIG. 2.--Electron diffraction pattern of copper phthalocyanine obtained at 1,000 kV accelerating voltage. Spots extend to a resolution of 0.07 nm.

ON THE EXPERIMENTAL DETERMINATION OF LOW-ORDER STRUCTURE FACTORS IN TiAl BY ENERGY-FILTERED CONVERGENT-BEAM ELECTRON DIFFRACTION

S. Swaminathan, I. P. Jones*, N. J. Zaluzec**, D. M. Maher*** and H. L. Fraser

Dept. of Materials Science and Engineering, The Ohio State University, Columbus, OH 43210

*School of Metallurgy and Materials, University of Birmingham, Birmingham, UK

**Center for Electron Microscopy, Argonne National Laboratory, Argonne, IL

***Dept. of Materials Science and Engineering, North Carolina State University, Raleigh, NC

It has been claimed that the effective Peierls stresses and mobilities of certain dislocations in TiAl are influenced by the anisotropy of bonding charge densities [1, 2]. This claim is based on the angular variation of electron charge density calculated by theory [e.g. 3,4]. It is important to verify the results of these calculations experimentally, and the present paper describes a series of such experiments. A description of the bonding charge density distribution in materials can be obtained by utilizing the charge deformation density ($\Delta\rho(r)$) defined by (1)

$$\Delta\rho(r) = \frac{1}{V} \sum (F_{\text{obs}} - F_{\text{calc}}) \exp(-2\pi i \mathbf{H} \cdot \mathbf{r}) \quad (1)$$

where V is the volume of the unit cell, F_{obs} is the experimentally determined low order structure factor and F_{calc} is the structure factor calculated using the Hartree-Fock neutral atom model [5]. To determine the experimental low order structure factors, a technique involving a combination of convergent beam electron diffraction (CBED) and electron energy loss spectroscopy (EELS) [6] has been used. Apart from the intrinsic accuracy of this technique for low order structure factors compared to measurements made using x-ray diffraction, it is our experience that measurements made using x-rays are also subject to error because of the large linear absorption coefficient ($\approx 64 \text{ cm}^{-1}$) and heavy defect population introduced during specimen preparation. In contrast, the CBED technique permits the diffracted intensities to be obtained on a small spatial scale from a defect free region of a crystal.

The experimental technique involved recording CBED patterns obtained from a number of reflections, with the sample oriented in each case at the Bragg condition. A Philips EM420 transmission/scanning transmission electron microscope (TEM/STEM) interfaced to a combination of commercial and custom built ancillary equipment in the Electron Microscopy Center of Argonne National Laboratory was used. Digital scans were produced using customized software and hardware with the data acquisition computer interface which allowed variable size and orientation of two dimensional rasters to be directed to the post-specimen double deflection coils of the TEM. The electron intensity was directed through the electron spectrometer to a photomultiplier tube (PMT) where upon it was processed using analog and digital signal processing equipment. The energy resolution limit of the spectrometer employed during these measurements was less than 0.75 eV. The angular resolution at a camera length of 600 mm and the 200 μm size entrance aperture was $\approx 0.3 \text{ mRad}$.

A thin foil of Ti52at%Al, prepared by electrochemical techniques, was used in the experiments. An example of a two dimensional energy filtered CBED pattern containing only the (200) dark field disk in TiAl is shown in Fig 1a. A rocking curve shown in Fig 1b, has been obtained by plotting the intensity profile through the center of the disk along line AB. The crystal orientation was chosen such that there is minimal interaction from higher order laue zone (HOLZ) lines on the bright-field and the dark-field disks. In the cases where there was a HOLZ line in the intensity profile AB, that part of the rocking curve affected by the HOLZ line was replaced by data unaffected by HOLZ lines taken from above or below the line. Removing these HOLZ effects permitted simulations to be performed while neglecting non-systematic reflections, which resulted in a considerable reduction of computation time. To establish confidence in this experimental technique, including the adjustment described above, it has been applied to the determination of the Si (220) structure factor at two different temperatures. The deduced structure factor is in excellent agreement with those measured using other methods. A

total of nine low order rocking curves have been determined in TiAl experimentally using the technique described.

These rocking curves have been matched using the three dimensional bloch wave formulation of the dynamical theory; the thickness t , the extinction distance ξ_g and absorption coefficient of the extinction ξ_g , was fitted for each reflection. The quantity $\chi^2 = (I_{calc} - I_{exp})^2$ was minimized by a quasi-Newton method with a finite difference gradient using the subroutine BCONF from the IMSL mathematical library [7]. The fitted values of the extinction distance and absorption coefficient were verified by repeating the experiments and calculations for various crystal thicknesses. The χ^2 minimization was also performed for different normalizing data points so that the extinction distance ξ_g and absorption coefficient of the extinction ξ_g were returned within one percent accuracy. A planar section of the deformation electron charge density distribution taken perpendicular to [001] (through the origin of the TiAl unit cell) is shown in Fig. 2. This deformation map is in good agreement with that produced by theory [e.g. 3,4].

References

1. B.A. Greenberg et al., Scripta Metall., (1988)22, 859.
2. S.A. Court et.al., Phil. Mag., (1990)A61, 141.
3. V.I. Anisimov et al., Fiz. Met. i Metall., (1987)63, 414.
4. T. Hong and A.J. Freeman, to be published in Phys. Rev. B, (1990).
5. P.A. Doyle and P.S. Turner, Acta Cryst., (1968)A24, 390.
6. J.M. Zuo, et al., Phys. Rev. Letts., (1988)61, 353.
7. J.E Dennis and R.B Schnabel, Numerical Methods for Unconstrained Optimization and Nonlinear Equations, Prentice-Hall, (1983) Englewood Cliffs, NJ.
8. This work has been supported in part by Wright Laboratories, Wright-Patterson Air Force Base, Dr. Dennis Dimiduk as Technical Advisor, the Office of Naval Research, Dr. George Yoder as Program Manager, and most recently the National Science Foundation, Dr. Bruce MacDonald, Program Manager.

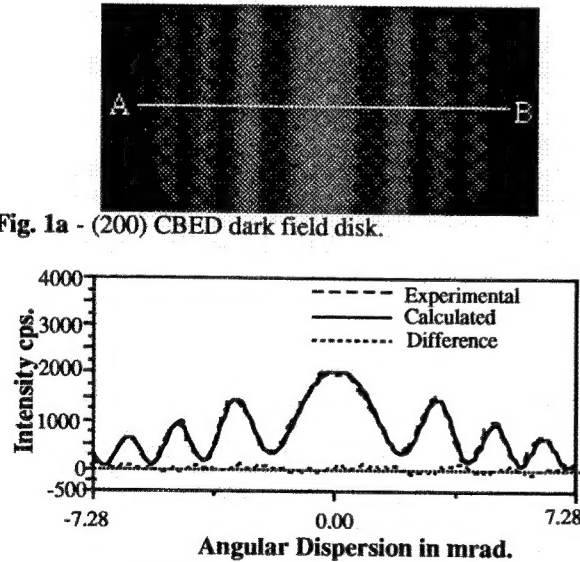


Fig. 1a - (200) CBED dark field disk.

Fig. 1b - Rocking curve from profile AB with the theoretically calculated fit.

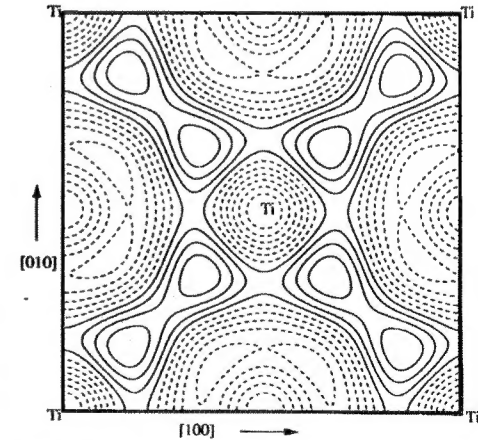


Fig. 2- Electron charge density deformation map for the (001) section in TiAl: Contour level = 0.025 electrons/Å³

ACCURATE METHODS FOR CRYSTAL STRUCTURE DETERMINATION USING ASPECTS OF DYNAMICAL DIFFRACTION THEORY

J W Steeds and R Vincent

Physics Department, University of Bristol, Bristol, BS8 1TL, UK

INTRODUCTION

An approach to the solution of crystal structures has been developed over the past ten years which is based on the intensities of high order Laue zone (HOLZ) fine structure lines present in zone axis patterns. It is a common observation that when the individual reflections in a HOLZ ring are studied in detail, several individual excess lines are observed. These individual lines are directly related to the excited branches of the dispersion surface, created by the two dimensional dynamical diffraction which occurs in the zero order Laue zone (ZOLZ)¹. They may either directly correspond to a single branch of the dispersion surface (a unique Bloch state) or else to a cluster of close branches (a small number of distinct Bloch states). It is often the case that the intensities of these lines may be derived from a pseudo-kinematical theory, which greatly simplifies the process of deducing atomic positions from the experimental data². The innermost lines (closest to the centre of the pattern) in a particular HOLZ ring generally correspond to Bloch states where the electrons are strongly bound to atomic strings, created by projecting the crystal structure along the zone axis direction. Different HOLZ fine structure lines often correspond to different sub-structural units of the complete crystal structure and when this is the case information about the different sub-lattices may be obtained independently by concentrating on one or other of the sets of lines. Because the reflections are at large diffraction angles, the observed intensities give very precise information about the sub-lattice locations and accuracies of about .01Å can be achieved without difficulty. In order to improve the data set, patterns may be recorded over a wide range of voltages sweeping out a large number of symmetry independent reflections (one hundred or so) in a chosen HOLZ plane. In order to obtain x, y and z components of atomic positions it may be necessary to combine the information obtained from more than one zone axis.

The first phase analysed in this way was the unknown structure of AuGeAs which turned out to have 12 atoms in the unit cell³. The second was a low temperature, commensurately modulated form, of 2HTaSe₂ with 108 atoms in the unit cell. Later analyses of Al-Ge metastable phases relied on Patterson functions based on the HOLZ data, and direct methods for phasing reflections^{5,6,7}. It was shown that each of the different HOLZ fine structure lines could be used to obtain a different Patterson map relating to a separate sub-lattice of the structure. These methods have also been used to solve an unknown structure in the LaCuO system that was found in a study of high temperature superconductors⁸.

Until recently, the patterns were recorded on film and had to be digitised afterwards for the extraction of quantitative data. Now that an energy-selecting filter has been fitted to one of our transmission electron microscopes (Hitachi HF2000) with a slow scan CCD system (Gatan imaging PEELS) it is possible to record the diffraction patterns digitally and to concentrate on the elastically scattered data. This development not only facilitates the acquisition of quantitative data and allows us to work with thicker specimens but it also means that we are able to extend our studies to charge distributions associated with bonding effects using the methods which have been pioneered by Bird and Saunders⁹ and Zuo and Spence¹⁰.

References

1. J. W. Steeds, J. R. Baker and R. Vincent, Vol. 1, Proceedings of 10th International

4. D. M. Bird, S. McKernan and J. W. Steeds, *J. of Phys. C: Solid State Phys.*, 18(1985)481
5. D. R. Exelby and R. Vincent, *EMAG - Micro 89*, *Inst. of Physics Conf. Sci. No. 98*, Vol. 1, (1990)127.
6. D. R. Exelby and R. Vincent, *Proceeding 12th International Congress for Electron Microscopy (Seattle 1990)*510.
7. R. Vincent and D. R. Exelby, *Phil. Mag. Let.* 63(1991)31.
8. P. A. Midgley and R. Vincent, *EMAG91*, *Inst. of Physics Conf. Sci. No. 119*(1991)413.
9. D. M. Bird and M. Saunders, *Ultramicroscopy*, 45(1992)241.
10. J. M. Zuo and J. Spence, *Ultramicroscopy*, 35(1991)185.

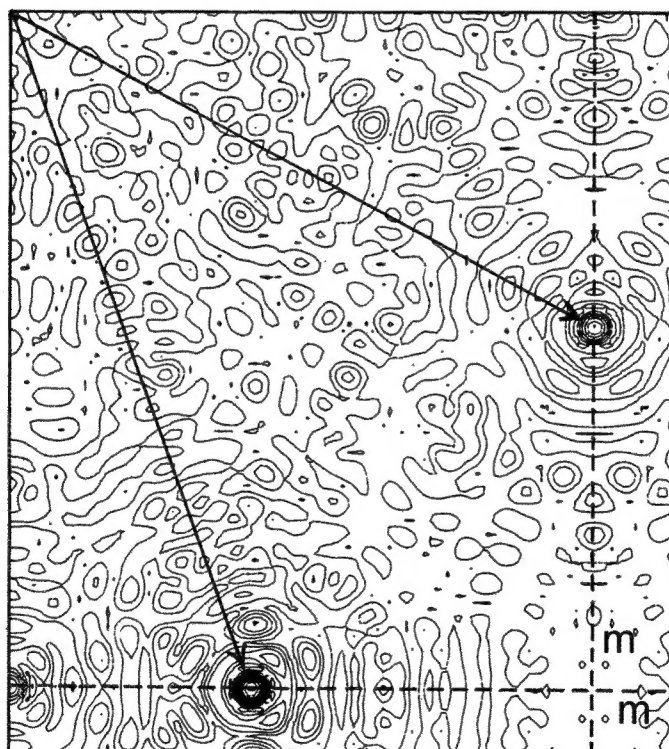


FIG. 1.--Modulus of the Patterson transform for the intensities of inner excess lines within FOLZ reflections around the [101] axis of the monoclinic Al-Ge phase. Self-correlation peaks at vertices of the contour map were removed by use of a modified data set, E^2-1 , where the E represented a normalised amplitude.

IMPROVEMENTS IN ELECTRON DIFFRACTION OF FROZEN HYDRATED CRYSTALS BY ENERGY FILTERING AND LARGE-AREA SINGLE-ELECTRON DETECTION

Rasmus R. Schröder and Christoph Burmester

Department of Biophysics, Max-Planck-Institute for Medical Research, P.O. Box 103820,
W-6900 Heidelberg, Germany

Diffraction patterns of 3D protein crystals embedded in vitreous ice are critical to record. Inelastically scattered electrons almost completely superimpose the diffraction pattern of crystals if the thickness of the crystal is higher than the mean free path of electrons in the specimen.¹ Figure 1 shows such an example of an unfiltered electron diffraction pattern from a frozen hydrated 3D catalase crystal. However, for thin 2D crystals electron diffraction has been the state of the art method to determine the Fourier amplitudes for reconstructions to atomic level, and in one case the possibility of obtaining Fourier phases from diffraction patterns has been studied.² One of the main problems could be the background in the diffraction pattern due to inelastic scattering and the recording characteristics for electrons of conventional negative material.

It was pointed out before,³ that the use of an energy filtered TEM (EFTEM) and of the Image Plate as a large area electron detector gives considerable improvement for detection of diffraction patterns. The Image Plate was used instead of other devices (CCD, negative material) since it combines large area detection, linear recording characteristics over a wide dynamic range, and - depending on the Image Plate Scanner system - almost ideal detection efficiency.^{4,5} However, results obtained so far suffered from technical limitations of the used EFTEM like the low electron energy (80keV), the limited range of diffraction lengths and the electron optics of the Castaign-Henry filter.

Figures 2 and 3 now show diffraction patterns of catalase crystals recorded with the new magnetic Omega filter EFTEM Zeiss EM912. Electron energy was 120keV, electron dose 260-520 electrons/nm² on the crystal, zero-loss electron diffraction ($\delta E=0$ eV energy loss) at an filter acceptance $\Delta E=5-10$ eV. The specimen temperature was at -167°C using an Oxford cryotransfer system CT3500. The Image Plate was scanned in a new design scanner⁴ with high spatial resolution and high detection efficiency.

The diffraction pattern in Figure 3 shows the [010] diffraction with almost all spots clearly visible above background. In the centre some inelastic electrons are not filtered out. These electrons probably have an energy loss of 4.8eV, the dissociation energy of H₂O to the radicals HO• and H•. However, using the Image Plate as detector it is possible to detect the full dynamic range by reading out the plate for a second time.⁵ Then the first order reflections appear clearly detectable above background (Figure 4). The diffraction pattern expands to a resolution of ca 2.8Å (arrowheads to Friedel pairs in Figure 4). With the technique described above it is now possible to record high resolution and low resolution part of a diffraction pattern in one single exposure of the crystal at a low electron dose. Thus it will now be possible to record more diffraction patterns from one crystal. With the Image Plate as large area detector it is then possible to study spot profiles in the diffraction patterns and their changes by crystal tilt or other manipulations.

References

1. R.R. Schröder, J. Microsc. (1992)166, 389.
2. T.A. Ceska and R. Henderson, J. Mol. Biol. (1990)213, 539.
3. R.R. Schröder and C. Burmester, Electron Microsc. (1992), Vol.I, EUREM 92, Granada, p393.
4. C. Burmester and R.R. Schröder, Electron Microsc. (1992), Vol.I, EUREM 92, Granada, p95.
5. C. Burmester and R.R. Schröder, manuscript in preperation.

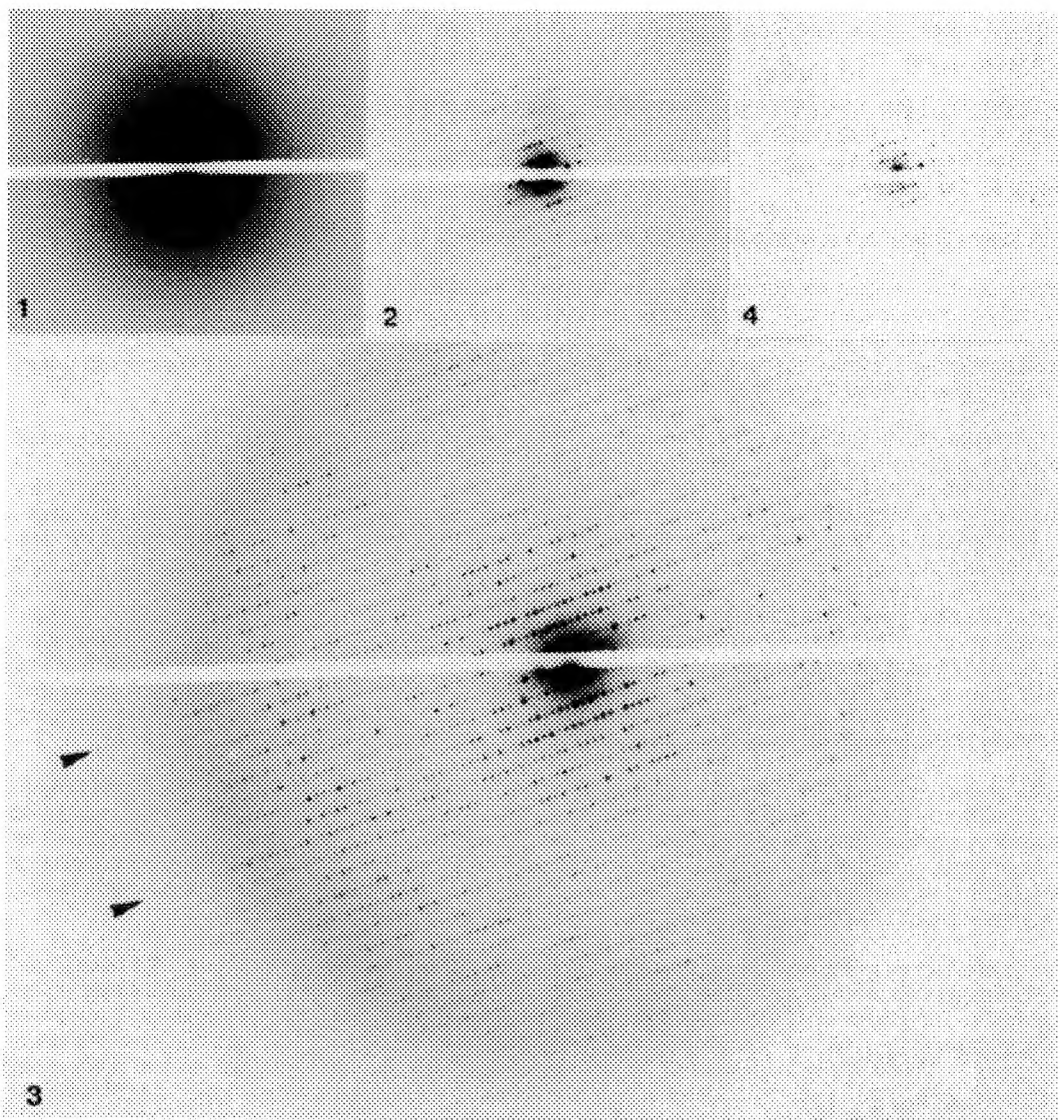


FIG. 1.--Conventional unfiltered electron diffraction pattern of a thick catalase crystal embedded in vitrified ice. Arrowheads mark the positions of visible reflections at medium resolution. Spots at lower or higher resolution are not detectable above the inelastic background.

FIG. 2.--Filtered Diffraction pattern of the crystal of Figure 1, recorded after Figure 1. Now reflections are visible.

FIG. 3.--[010] electron diffraction pattern of a thick catalase crystal on carbon film embedded in vitrified ice. Electron energy 120kV, zero-loss filtering $\delta E=0\text{eV}$, energy width ΔE ca 5eV, electron dose 520 electrons/nm². Note that almost all, the low resolution and atomic resolution reflections are visible. The highest resolution reflections (Friedel pair) clearly detectable are marked with arrowheads, they correspond to ca 2.8Å resolution and are outside the strong scattering ring of amorphous ice.

FIG. 4.--Expanded dynamic range image of the centre of the diffraction pattern shown in Figure 3. Now also the lowest order reflections can be resolved from background.

STRATEGIES FOR STRUCTURE DETERMINATION BY ELECTRON CRYSTALLOGRAPHY: APPLICATION TO TUBULIN

Kenneth H. Downing

Life Sciences Division, Lawrence Berkeley Laboratory, Berkeley CA 94720

Determination of protein structures at the atomic level by electron microscopy has long been a goal, and has finally become a reality. Progress on several protein structures has been steady, but the rapid flow of structures that was anticipated to follow the initial atomic model of bacteriorhodopsin (bR) has not yet appeared. We will discuss here some of the effects that have led to this slow rate of progress and things that still need to be done to speed up the process.

The first requirement for doing crystallographic work is the availability of crystals. To date only a small number of proteins have been crystallized to give high-resolution data. Many of the principles of 2-D crystal formation are clear, and the limitations are in the nature of the amounts of protein available for crystallization experiments. With more experience, crystal availability should no longer be a limitation. This will be useful because we envision the day when structures can be solved, at least through the data collection and processing stages, in a matter of days rather than the present years. What are the problems that make the process so long at present? The answer is primarily in the low success rate of collecting images (and electron diffraction patterns) of sufficient quality. The first cause of this problem is often imperfect specimen preparation; specimens are often denatured and disordered, wrinkled, torn by surface tension, dehydrated or embedded in too thick a layer to give adequate resolution. Although one can usually learn to identify by morphology those crystals that are most likely to be good, and sometimes preview the quality by peeking at electron diffraction patterns, data collection will be greatly advanced when most of the crystals are as well preserved as the best in present preparations.

Images of even the 'good' crystals too often suffer from severe degradation. At best, the signal at high resolution is only a few percent of what an ideal image would contain, mainly as a result of beam-induced damage and motion, charging and perhaps other effects. Although such technological developments as spot-scan imaging and higher accelerating voltages have done much to reduce these problems, a greater understanding of the causes of this signal loss will make extraction of high-resolution data much easier. Ultimately it should be possible for all images to be as good as the present best ones.

A question arises as to the number of images required to reliably determine the structure. We have found that 3-5 images can produce a reliable projection map at a resolution near 3.5Å. More than a single image is required to fill in gaps in the contrast transfer function. In addition, the signal is so weak in all images at high resolution that several measurements must be combined to provide a significant estimate of the structure factors. This is really a question of the number of unit cells that are combined, so that if we could increase the area of an image by a factor of 3-5 we would be able to extract statistically significant data from a single projection. In this we are limited sometimes by the size of available crystals, and by recording on photographic film. Obtaining larger crystals is always a subject of attention, and with images recorded on a CCD using spot-scan illumination, the size of images would be limited only by computer power and storage. Again, technical developments promise to solve some of the significant, rate-limiting problems.

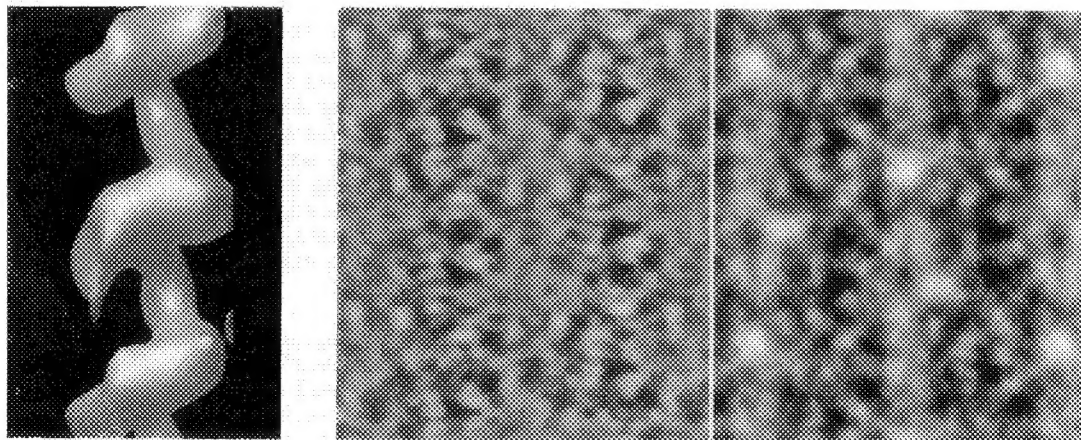
The course of structure determination often follows several rather distinct stages or milestones. Once crystals can be obtained, a projection map and 3-D reconstruction of negatively stained specimens are often generated, with a resolution around 20Å. Data for such a 3-D map could consist of a few tilt series of images, with perhaps some low-dose images for improved resolution, and could be collected in a single session on the microscope, with several days for image processing and interpretation. The low-resolution 3-D map provides a view of basic domain structure and orientation. When techniques have been derived to preserve the specimen without stain, a high-resolution projection is often produced. Again all the images could be collected in a single microscope session, and then processed in a matter of days. This

projection is not always easily interpretable and informative, but demonstrates the feasibility of further work. At this stage issues of contrast mechanisms often arise, which can be especially important in interpreting the low-resolution features. For example the contributions of amplitude contrast or contrast matching by the embedding medium can confuse the image.

The 3-D map is generated from data collected from tilted specimens. All the problems that appear to afflict untilted specimens seem to be worse with highly tilted specimens, and the success rate for obtaining good images decreases with increasing tilt angle. In addition there is the problem of the defocus ramp across the image, which can either be compensated by image processing or largely avoided in recording the image. For these reasons, and also because a number of parameters are refined iteratively in zones of increasing resolution, a moderate-resolution (6-10Å) 3-D map is usually produced. This map can provide much useful information about secondary structure organization. The number of images finally required for the high-resolution 3-D map, and the present low success rate in collecting these images, make the data collection still a daunting task, but offer much room for improvement in techniques.

Recent work on the structure of tubulin in our lab illustrates several of the points discussed. Figure 1 is a 3-D reconstruction of the negatively-stained tubulin protofilament, which is a primary structure in the sheets as well as microtubules and other tubulin assemblies (Downing, Wolf, Carlsson, Mosser, in preparation). Evidence has been found from other structural studies that there are at least three flexibly-connected domains, and this image gives an impression of the domain organization. Conformational changes observed under different polymerizing conditions can be observed at this resolution (Wolf, Mosser, Downing, in preparation).

We have found that these crystals are well preserved in glucose, and have calculated a projection with data to better than 4Å resolution, in fig. 2a. Although this map is rich in detail, the glucose masks much of the low-resolution contrast, making the protofilament outline difficult to discern. Specimens rinsed in uranyl acetate before glucose embedding retain the high-resolution order, but provide contrast that outlines the molecular envelope and the gap between protofilaments, as in fig. 2b. Improvement of the low resolution contrast is not at all a necessary step toward the atomic resolution structure, since at high resolution the boundaries will be unambiguously clear. However, including the low-resolution component allows merging the high resolution data from tilted specimens to the low-resolution 3-D data set. Collection of data from tilted specimens is currently under way. So far, solution of the tubulin structure is proceeding at a rate that reflects the accumulated knowledge of the learning curve, but it is clear that many factors conspire to make progress much slower than it could potentially be.



1. Three-dimensional reconstruction of tubulin protofilament in uranyl acetate. Protofilament contains alternating α and β subunits whose domain structure is seen at a resolution around 20Å.
2. Projection maps of tubulin sheets at around 4Å resolution. (a) embedded in glucose, high resolution structure is clearly resolved, but molecular outline is unclear. (b) a small amount of stain more clearly contrasts low-resolution features.

QUANTITATIVE ANALYSIS OF LOW-DOSE HIGH-RESOLUTION IMAGES AND DIFFRACTION PATTERNS FROM ZEOLITES USING A SLOW-SCAN CCD CAMERA

M. Pan and P.A. Crozier

Center for Solid State Science, Arizona State University, Tempe, AZ 85287-1704

Zeolites are an important class of low-density aluminosilicates framework structures with applications to the field of catalysis and molecular sieves¹. In order to understand the origin of the unique properties of these materials and hence optimize their performance, it is essential to have a detailed description of their structures. Zeolite structure is often described in terms of the secondary building unit (SBU) which is a specific configuration of the SiO₄ tetrahedrons¹. Structure determination of zeolites is then reduced to determine the types of SBUs and their connectivities when forming the 3-D framework structure.

It has been recognized that zeolites undergo rapid structural damage under electron beam irradiation. The use of a slow-scan CCD camera to record low-dose high resolution electron microscope (HREM) images from zeolites with the combination with real-space averaging techniques has been shown to be successful in obtaining the averaged unit cell with high signal-to-noise ratio (SNR). Since slow-scan CCD cameras have a linear response, a large dynamic range (e.g. 4×10^3) and record data in digital form, they are well suited to performing quantitative intensity measurements in electron microscopy. We will show that the CCD camera can be used to make meaningful and quantitative intensity measurements of images and diffraction patterns from zeolites. A Gatan 679 slow-scan CCD camera was attached to a JEM-4000EX microscope operating at 400 kV with a point resolution of 1.7 Å. ZSM-5 powders were used in our experiment. The details of the experimental procedures have been reported elsewhere^{2,3}.

Dynamical calculations show that, for thickness under ~ 100 Å, the weak-phase object approximation (WPOA) is valid for zeolites which allows HREM image intensity recorded at Scherzer defocus to be related to the projected potential of the structure³. As a result, there is a linear relation between the integrated potential in a SBU and the number of Si atoms in that unit. This is shown as follows:

$$\int V_1(r)dr / \int V_2(r)dr \equiv n_1 / n_2$$

where $V_1(r)$ and $V_2(r)$ are projected potentials corresponding to SBUs 1 and 2 respectively and r is a 2-D vector; n_1 and n_2 are the number of Si atoms in that unit. Fig. 1a shows a [010] projected potential map of a ZSM-5 crystal obtained from the real-space averaged image² by inverting and stretching the contrast. It is known that the ZSM-5 structure contains rings of atoms of 10, 6 and 5 as indicated in fig. 1a. To quantify the image data, circles of different sizes have been drawn to include the corresponding rings of atoms. The intensity for each ring is obtained by integrating the intensities within the circle. To plot the integrated intensities and determine the number of Si atoms within a ring, one needs to use the following boundary condition, the number of Si atoms forming the largest ring is usually known from, for example, sorption experiment and the straight line must go through the origin as a ring containing no atoms will have zero intensity. With this condition, the integrated intensities versus the number of Si atoms in the ring are plotted in fig. 1b. The data points are seen to lie on a straight line and the 5-member ring can be unambiguously distinguished from the 6-member ring.

Quantitative measurement of diffraction intensities and comparison with dynamical calculations have also been carried out for ZSM-5. Fig. 2a is a [010] electron diffraction pattern of ZSM-5 recorded using 1 s exposure. It is clear that both strong and weak diffraction spots are well recorded. The background associated with each spot and its shape can be studied in detail. The intensity for each spot was measured using the peak height and the averaged background in a 1-D intensity plot. This approximation is good if all diffraction spots have the same shape. Fig. 2b is the comparison of measured diffraction intensities with the dynamical simulations for 9 different spots. The intensity of (hkl) reflection is averaged over its equivalent reflections in the pattern. A good quantitative match is found for sample thickness of ~ 200 Å for all the spots except the (101). Using measured diffraction intensities to perform the structure determination will be discussed⁴.

References

1. D.W. Breck, Zeolite Molecular Sieves, John Wiley & Sons, New York, 1974.
2. M. Pan et al., Ultramicroscopy (1993) in press.
3. M. Pan et al., Ultramicroscopy (submitted).
4. Mobil R&D Corp. and Texaco Inc. are acknowledged for providing the zeolite samples. This work was supported by the HREM Industrial Associates Program at ASU and made use of the CHREM at ASU supported by NSF grant DMR-9115680.

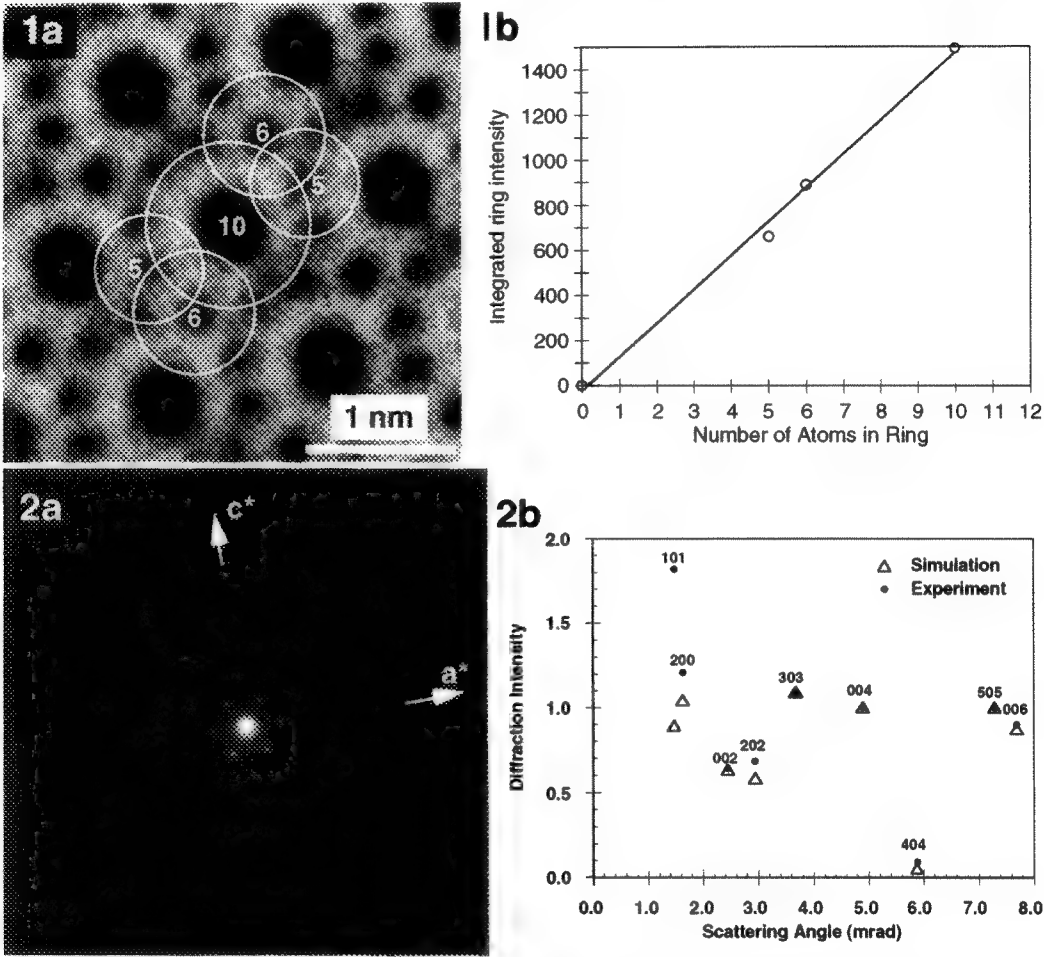


Fig.1(a) [010] projected potential map of a ZSM-5 crystal obtained by using real-space averaging method; (b) Plot of the integrated intensity versus the number of Si atoms in the ring. The straight line indicates the linear contributions from the number of Si atoms in the ring to the image intensity. Fig.2 (a) [010] electron diffraction pattern from a ZSM-5 crystal; (b) Comparison of diffraction intensities between experimental and theoretical values.

ELECTRON CRYSTALLOGRAPHY OF HELICAL PROTEIN ASSEMBLIES

D.L.D. Caspar, D.J. DeRosier, R. Diaz, D.G. Morgan, L.A. Melanson, C. Owen, J-L. Ranck and T. Ruiz

Rosenstiel Basic Medical Sciences Research Center, Brandeis University, Waltham MA 02254

Electron cryomicroscopy provides structural information on two dimensional crystals. Several membrane proteins have been solved to better than 4Å resolution^{1,2}. This class of structure has been difficult to attack by x-ray diffraction. Another class of structures that is difficult to solve by x-ray diffraction but may be amenable to electron microscopy is the helical protein assembly. Most of our knowledge of this class has come from electron microscopy although generally the work has revealed detail to a modest resolution of about 20 Å and in two special cases^{3,4} to about 10Å resolution. We have been trying to extend the methods for all helical structures in a manner analogous to those used for two dimensional crystals. The difference is that the scattered electron beams from helices are much weaker than those from two-dimensional crystals and the signal-to-noise ratio is poorer. We have developed methods for automatically processing large numbers of particles to extract signal from noise⁵. We are developing ways to detect the signal within single helical particles in regimes where the noise is much larger than the signal and we have been developing methods to obtain electron diffraction data from rafts of helical particles.

The automatic processing uses helical cross-correlation to detect and measure curvature, determine the precise positions of layer lines, determine the polarity of the particle, produce an estimate of the angular and axial disorder, and determine the out-of-plane tilt of the helix axis. The programs use this information to straighten particles and to extract layer line data to a preset resolution (9Å in our case). They then carry out several rounds of alignment and averaging to produce an average and a standard deviation for every independent Fourier coefficient along each layer line and from these data determine which coefficients are significantly above background (i.e., are different from zero). We applied these programs to electron micrographs of the bacterial flagellar filament. In transforms of individual images, layer lines to about 25 Å are seen but higher resolution layer lines are hidden in noise. As a result of averaging about 100 filaments we can extract significant data to 10 Å resolution.

Do all images within the set contribute equally to the averaged data set? To find out we developed a program that can detect signal hidden by noise. The program calculates the phase differences between the average and an individual image's transform. An individual reflection on a layer line has too much noise to make this a meaningful

measure but by combining a number of these, we obtain a reliable measure of the amount of signal. Theoretical analysis suggests that with as few as 10 data points from a single image, we should be able to detect significant signal when the signal to noise ratio is 0.2. Analysis of our set of filament images confirms this expectation. We then asked whether there was any significant correlation of the detected signal between a pair of layer lines, for example, the 25 Å layer line and the 10 Å layer line? The correlation was just at the 95% confidence limit and indicated that less than 5% of the variance in the 10 Å layer line data was accounted for by the variance of signal in the 25 Å layer line. Thus the signal present on a low resolution layer line was not an especially good predictor of the signal on a high resolution layer line. It appears that images whose 25 Å layer line data are most similar to that of the average are not the same images whose 10 Å data are most similar to the average.

The processing of images suggests that the phases obtained are reliable but due to factors such as the contrast transfer function and beam induced specimen movement, the corresponding amplitudes determined from images are not accurate. We undertook to obtain more reliable estimates of amplitude data using electron diffraction from ordered arrays of three helical assemblies: flagellar filaments, tobacco mosaic virus (TMV), and the stacked disk form of tobacco mosaic virus protein. The patterns in the case of TMV and the stacked disk form of TMV protein, for example extend to 3.8Å. The patterns are not as striking as those from two dimensional crystals because helices diffract weakly and the background scattering predominates. The development of programs to process the images is therefore more difficult. Because the layer lines are thin streaks, it is easy to locate the position of the equator but difficult to locate the meridian. We developed an algorithm that uses the background scattering to locate the meridian. The intersection of the meridian and equator define the center of the diffraction pattern. From the center we analyze radial annuli to determine the background scattering. To subtract the background scatter correctly, we had to develop an algorithm to eliminate the genuine layer line scattering from our estimate of the background scattering since the weaker layer lines often lay hidden in the background. Once the background is subtracted, the diffraction patterns reveal a wealth of layer line detail not readily visible in the original patterns.

References

1. R. Henderson, J.M. Baldwin, T.A. Ceska, F. Zemlin, E. Beckmann and K. Downing, *J. Mol. Biol.* (1990)213, 899.
2. B.K. Jap, P.J. Walian and K. Gehring, *Nature* (1991)350, 167.
3. T.-W. Jeng, R.A. Crowther, G. Stubbs, and W. Chiu, *J. Mol. Biol.* (1989)205, 251.
4. P.N.T. Unwin, *J. Mol. Biol.* (1993) in press.
5. D.G. Morgan and D.J. DeRosier, *Ultramicroscopy* (1992)46, 263.

FAST CALIBRATION OF CBED PATTERNS FOR QUANTITATIVE ANALYSIS

M.A.Gribelyuk, M.Rühle

Max-Planck-Institut fuer Metallforschung, Seestrasse 92 W-7000 Stuttgart 1 Germany

A new method is suggested for the accurate determination of the incident beam direction \mathbf{K} , crystal thickness t and the coordinates of the basic reciprocal lattice vectors \mathbf{V}_1 and \mathbf{V}_2 (Fig.1) of the ZOLZ plane in pixels of the digitized 2-D CBED pattern. For a given structure model and some estimated values \mathbf{V}_{est} and \mathbf{K}_{est} of some point O in the CBED pattern a set of line scans $A_k B_k$ is chosen so that all the scans are located within CBED disks. The points on line scans $A_k B_k$ are conjugate to those on $A_0 B_0$ since they are shifted by the reciprocal vector \mathbf{g}_k with respect to each other. As many conjugate scans are considered as CBED disks fall into the energy filtered region of the experimental pattern. Electron intensities of the transmitted beam I_0 and diffracted beams $I_{\mathbf{g}_k}$ for all points on conjugate scans are found as a function of crystal thickness t on the basis of the full dynamical calculation¹. The crystal thickness values t_i are considered at the nodes of the equidistant mesh in the guessed interval (t_{\min}, t_{\max}) . The respective coordinates of the line scans in the experimental CBED pattern are found which correspond to a given set of calculated line scans $A_k B_k$ for some trial coordinates of the incident beam direction \mathbf{K}_{Oest} and basic reciprocal lattice vectors \mathbf{V}_{est} . The experimental and calculated intensities are compared and the objective function

$$\chi^2(t, \mathbf{K}_{\text{est}}) = \frac{1}{M} \sum_{k=1}^M \frac{\sum_{i=1}^n \left| I_{\text{exp}}^{(i)}(k, \mathbf{K}_{\text{est}}) - c_k I_{\text{theo}}^{(i)}(k, t) \right|^2}{n I_{\text{theo}}^{2(\text{ref})}(k, t)}$$

is evaluated. In the procedure the objective function is minimized by the simplex method with respect to the coordinates of the basic reciprocal lattice vectors \mathbf{V} . Here M is the number of conjugate scans, n is the number of sampling points on each scan, $I_{\text{theo}}^{(i)}(k, t)$ and $I_{\text{exp}}^{(i)}(k)$ are the calculated and experimental intensities for the i -th sampling point in the line scan located in the CBED disk \mathbf{g}_k , c_k is the normalization constant, $I_{\text{theo}}^{(\text{ref})}(k, t)$ is the intensity at some reference point in the k -th calculated line scan. The variation of coordinates of the basic reciprocal lattice vectors \mathbf{V} leads to the change of the coordinates of the line scans in the experimental CBED pattern which correspond to the given set of calculated line scans. Fitting the experimental line scans to the calculated ones (rather than vice versa !) in the simplex optimization allows one to decrease drastically the number of complex matrix diagonalizations which are performed in the dynamical calculations. These have been found the most time consuming in the quantitative processing of CBED patterns. For a given total number of sampling points the further decrease is realized by a factor of M by considering a set of conjugate line scans $A_k B_k$ instead of an arbitrary line scan². For the optimized coordinates \mathbf{V}_{opt} and a given incident beam direction \mathbf{K}_{Oest} the objective function is found as a function of crystal thickness values t_i . The variation of the incident beam direction \mathbf{K}_{Oest} considered at the nodes of the equidistant mesh also involves the relative shift of experimental line scans to fit the Miller indices of the points in the calculated line scans. Therefore no additional complex matrix diagonalizations are required for evaluation of the objective function at any of the nodes \mathbf{K}_{Oest} . If for some of these values the coordinates of experimental scans are not located within CBED disks an alternative set of calculated scans should be taken. The analysis of the series of 2-D maps of the objective function $\chi^2(\mathbf{K}_{\text{Oest}})$ considered as a function of the crystal thickness t allows one to directly locate its absolute minimum which corresponds to the sought incident beam direction \mathbf{K} and the crystal thickness t .

The optimum strategy for the choice of the nodes of the crystal thickness and incident beam direction has been worked out by computer analysis and will be presented at the Meeting. The effect of the uncertainty in the structure factors $F(g)$ on the accuracy of calibration parameters is analyzed. One needs less than 15min. to achieve the accuracy $\Delta K < 10^{-3} \text{\AA}^{-1}$, $\Delta t < 0.1 \text{\AA}$ and $\Delta V < 1.5 \times 10^{-4} \text{\AA}^{-1}$ provided that a rough estimates $\Delta K = \pm 2 \text{\AA}^{-1}$, $\Delta t = \pm 500 \text{\AA}$ and $\Delta V/V = 10\%$ are known in advance. This makes the suggested method very practical and allows one to incorporate it in any procedure which involves quantification of CBED patterns (refinement of electron structure factors, determination of lattice parameters etc.). Some examples of the computer analysis are shown in Figs.2-7. In particular for GaAs (110) (Figs.2-4) several closely located local minima have been found in the maps $\chi^2(K_{0est})$ even if true calibration parameters are used (Fig.5). For this reason the simplex optimization of the incident beam direction might lead to spurious results. Figs.6 and 7 illustrate that the location of minima is highly dependent on the estimations of the crystal thickness and the coordinates of the basic reciprocal lattice vectors V in pixels of the digitized CBED pattern³.

References

1. J.M.Zuo, K.Gjonnes & J.C.H.Spence. J.Electr.Microsc.Tech. 12 (1989) 29
2. J.M.Zuo & J.C.H.Spence. Ultramicroscopy 35 (1991) 185
3. Dr.J.M.Zuo is acknowledged for providing the source code of the "TCBED" programm¹. One of the authors (M.A.G.) acknowledges the support of the Alexander von Humboldt Foundation.

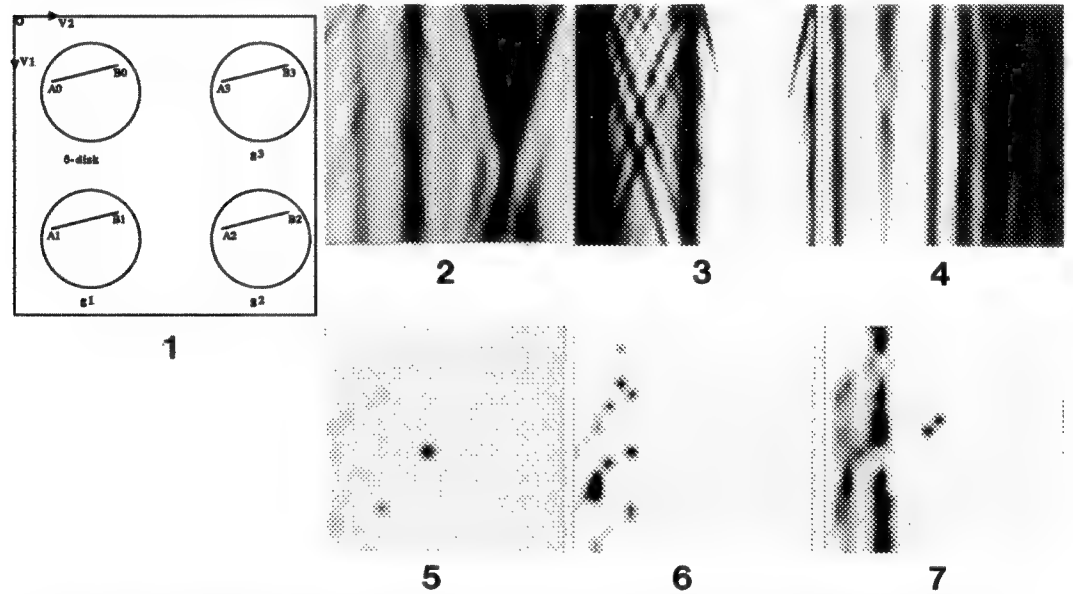


FIG.1- Choice of conjugate scans in CBED disks. Point O is upper left corner of digitized pattern. Basic reciprocal lattice vectors V_1 and V_2 are shown. FIGS.2-4 - Simulated 251x251pix CBED intensity distribution in 000 (2) 002 (3) and 004 (4) reflections for $t=1000 \text{\AA}$ thick GaAs. Centers of disks correspond to $K = [91.2 \ 108.8 \ -1.5]$. Sampling step 0.008\AA^{-1} . FIG.5 - 21x21pix. $\chi^2(K_{0est})$ map for model values of crystal thickness and basic vectors V . FIGS.6,7 - 21x21pix. $\chi^2(K_{0est})$ maps for model values of basic vectors V and $t=1100 \text{\AA}$ (6) and for model $t=1000 \text{\AA}$ and $V_1 = 1.05 V_{1mod}$. Sampling step in FIGS.5-7 is 0.1\AA^{-1} .

KINEMATICAL STRUCTURE FACTORS FROM DYNAMICAL DIFFRACTION?

Alwyn Eades

Center for Microanalysis of Materials, Materials Research Laboratory,
University of Illinois, Urbana, Illinois, 61801

In convergent-beam diffraction it is a common observation that kinematically forbidden reflections show "dynamical extinctions", also known as Gjønnes-Moodie lines, G-M lines, black crosses or dark bars. These zeros of intensity can be understood as resulting from the pairing of multiple diffraction routes so that each pair cancels¹. If the multiple diffraction routes for a reflection that is not kinematically forbidden could be paired in the same way, we could locate a position in the convergent-beam disc where the intensity would depend only on the structure factor for that one reflection. This would be extremely valuable because it would provide electron diffraction with a greatly simplified method of solving crystal structures.

It turns out that no such condition can be found. Here, an outline of the argument is given. A full account will be given elsewhere.

The pairing of the multiple diffraction routes depends on the existence of symmetry relations between different reflections. In order for the pair of routes to cancel, each individual reflection in one route must have a structure factor with the same magnitude as that for a reflection in the other route. At least one reflection must have a structure factor that is the negative of the paired reflection. The sign reversal is produced only by a two-fold screw axis or by a glide plane.

To meet these conditions, the multiple diffraction routes can be paired in one of three ways - depending on which symmetry elements are present. The three different ways of pairing the routes are indicated schematically in figure 1. For each kind of pairing, the rule to find the routes to be paired is a simple symmetry operation that should be clear from the diagram.

In each of these cases, however, there are some diffraction routes that cannot be paired. When the operation that generates the pair is applied to these routes they are transformed into themselves. Examples of such routes are given in figure 2.

When the observed reflection (that is, the end-point of all the multiple diffraction routes) is kinematically forbidden, it is easy to see that the unpaired routes must themselves include a reflection that is kinematically forbidden. Thus the unpaired routes contribute zero intensity and the Gjønnes and Moodie rules are preserved. Suppose now that we can find a reflection which is not kinematically forbidden and for which the diffraction routes can be paired so the each pair cancels, this would seem to be what we are looking for. However, in such a case, the unpaired routes will not (in general)

have zero intensity. Therefore the intensity in the observed reflection would depend not only on the structure factor for that reflection but also on the sum of the contributions of all the unpaired routes. This would seem to be the death knell of the hope for determining kinematic structure factors in such a simple way².

1. J. Gjønnes and A. F. Moodie, *Acta Cryst.* (1965) **19**, 65-67
2. Supported by the Department of Energy: DEFG02-91ER45439.

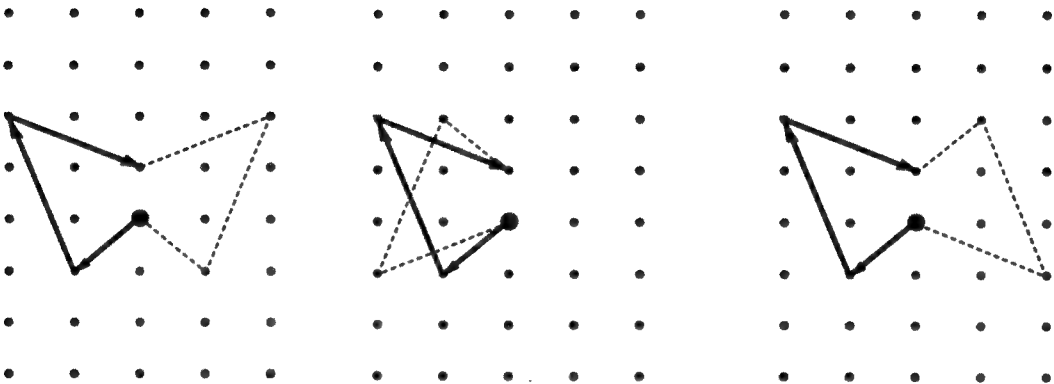


Figure 1. Diagrams to illustrate the pairing of multiple diffraction routes. The pairings are those used in the case of a glide parallel, a screw perpendicular and a glide perpendicular to the beam, respectively.

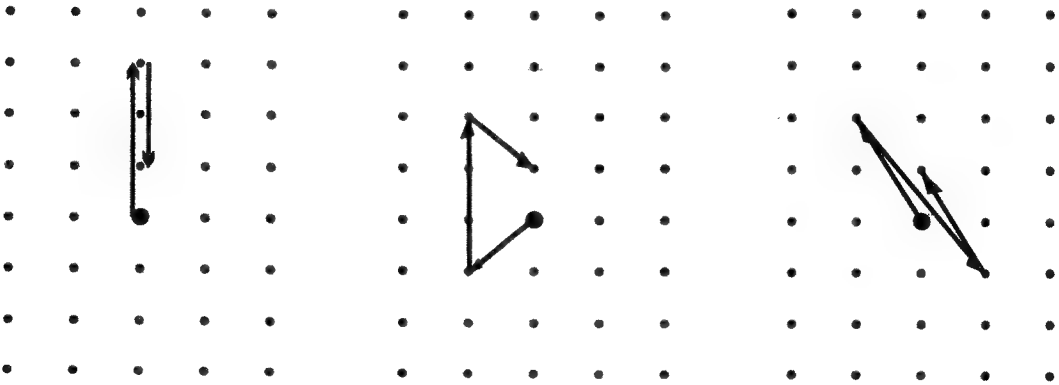


Figure 2. Examples to show that, for each case in figure 1, there are routes that cannot be paired.

Bravais Lattice Determination from A Single CBED Pattern*

J. M. Zuo

Physcis Department, Arizona State University, Tempe, AZ 85287

Traditional methods for Bravais lattice determination of unknown materials using electron diffraction involve symmetry determination from several low index zone axis diffraction patterns, measuring the distances between spots or disks and indexing them by trial and error method[1]. Such methods are often repetitive, error prone and difficult, if not impossible, for low-symmetry crystals. Thus a simpler, accurate, and automated method for lattice determination is highly desirable in electron diffraction. Here, a new method of Bravais lattice determination using an arbitrary single convergent beam diffraction (CBED) pattern is summarized. A full description of the method has been submitted for elsewhere [2]. The method uses the deficiency lines of high order and high order Laue zone (HOLZ) reflections to measure the primitive cell of the zone axis, and use the standard Krivy and Gruber procedure to reduce this arbitrary primitive cell to a unique Niggli cell, and thus the Bravais cell [3]. The method requires only a single CBED pattern taken slightly off zone axis center in the so-called kinematic orientation, similar to the one shown in figure 1 and 2, and assumes that both camera length and high voltage are known with reasonable accuracy. In figure 2, the HOLZ line g in the central disk is given by [4]

$$K_y = -g_x K_x / g_y + g_z K_z / g_y - g^2 / 2g_y \quad 1$$

in the kinematic approximation. Here K is the incident wavevector, and x, y , and z denote its component in the zone axis coordinate shown in figure 3. For each reflection, an arbitrary index (h, k, l) can be assigned based on the three shortest independent g vectors of the zone axis. Thus

$$g = ha^* + kb^* + lc^* = (h + kb_x + lc_x)x + (kb_y + lc_y)y + lc_zz \quad 2$$

Here, a^* , b^* and c^* form a primitive cell of the zone. The experimental HOLZ lines of figure 2 may be measured in two-dimensional film coordinates (x, y) . It is assumed that x is oriented along a^* . The relation between the film coordinate and the zone axis center coordinate may be described generally as

$$\begin{pmatrix} K_x \\ K_y \end{pmatrix} = \alpha \begin{pmatrix} 1 & 0 \\ 0 & 1 \end{pmatrix} \begin{pmatrix} x \\ y \end{pmatrix} + \alpha \begin{pmatrix} x_0 \\ y_0 \end{pmatrix} \quad 3$$

Here α is a scaling constant, and $\alpha = K/la^*l$ with L as the camera length. x_0 and y_0 are the center of the Laue circle on the film, which are treated as unknown although they may be visible as the center of Kikuchi bands. A HOLZ line on the film is measured to be

$$y = (m \pm \sigma_m)x + b \pm \sigma_b \quad 4$$

This may be transformed into the zone axis coordinate via the equation 3

$$K_y = mK_x + \alpha b - \alpha mx_0 + \alpha y_0 \quad 5$$

Comparing 5 to 1 and using equation 2, two equations can be obtained

$$kb_x + mkb_y + lc_x + mlc_y + h = 0 \quad 6$$

$$g_x x_0 + g_y y_0 + (g_x^2 + g_y^2)/2\alpha - lK_z c_z/la^*l\alpha + l^2 c_z^2/2\alpha + g_y b = 0 \quad 7$$

From equation 6, b_x , b_y , c_x and c_y may be obtained from 4 experimental lines with at least two of them in HOLZ, while from equation 7, x_0 , y_0 , $1/a$, c_z/la^*l , and c_z^2/a may be obtained, provided the solutions from equation 6 are used and there are total five experimental lines with at least 2 lines in HOLZ. From parameters c_z/la^*l and c_z^2/a , la^*l and c_z are obtained. Equations 6 and 7 proves that the crystal unit cell can be uniquely determined from sufficient number of HOLZ and ZOLZ lines with only wavenumber as the external parameter. In practice, however, the small residual dynamic effects and error in the measurement of HOLZ lines may leads to large error in determination of parameter c_z^2/α in equation 7. It is better to combine parameters ac_z/α and $\alpha = K/la^*l$ to obtain la^*l and c_z and solve equation 7 recursively with trial value of c_z^2/α , this requires the additional external parameter of camera length. Once the primitive cell, $a^* = la^*l(1,0,0)$, $b^* = la^*l(b_x, b_y, 0)$ and $c^* = la^*l(c_x, c_y, c_z)$, are found from the above

procedures, it may be reduced to the unique Niggli cell using the Krivy and Gruber procedure[3], which starts from a metric tensor of the primitive cell

$$\begin{pmatrix} \mathbf{a^* \cdot a^*} & \mathbf{b^* \cdot b^*} & \mathbf{c^* \cdot c^*} \\ \mathbf{b^* \cdot c^* / 2} & \mathbf{a^* \cdot c^* / 2} & \mathbf{a^* \cdot b^* / 2} \end{pmatrix} = |\mathbf{a^*}|^2 \begin{pmatrix} 1 & \mathbf{b_x^2 + b_y^2} & \mathbf{c_x^2 + c_y^2 + c_z^2} \\ (\mathbf{b_x c_x + b_y c_y}) / 2 & \mathbf{c_x / 2} & \mathbf{b_x / 2} \end{pmatrix} \quad 8$$

The error in each element of this metric tensor may be estimated from the error in each individual parameter. Once the Niggli cell is determined, the corresponding Bravais cell may be found from table 9.3.1 in the international table for crystallography, which list all 44 Niggli cells and their unique relation to the Bravais cell. The process for indentifying the right Niggli cell once the experiment metric tensor is obtained can be automated, for details, see [2]. For figure 1 and 2, the measured primitive cell is listed in table 1. From this primitive cell, a Niggli cell of type No 5 is found, which corresponds to body-center cubic. Figure 1 was take from Silicon, which has an fcc cell in real space and bcc in reciprocal lattice. The real space lattice constant was found to be 5.436, the lattice constant of Silicon is 5.4307. Once the lattice type was determined, the lattice constant may be refined to higher accuracy using the same set of experimenat HOLZ lines, for details, see [4].

*Supported by NSF grant DMR 9015867 and facilities of the ASU-NSF national center for HREM.
 [1] J. W. Edington, Practical Electron Microscopy In Materials Science, vol. 2, Van Nostrand Reinhold, New York, 1976
 [2] J. M. Zuo, Ultramicroscopy, submitted (J. M. Cowley "Festschrift")
 [3] I. Krivy and B. Gruber, Acta Cryst., A 32 (1976), 297-298
 [4] J. M. Zuo, Ultramicroscopy, 41 (1992), 211-223

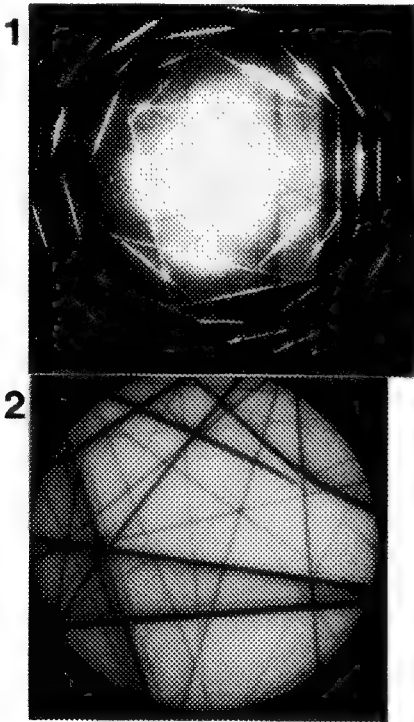


Table 1. Determined primitive cell parameters from figure 2. The theoretical values are calculated with Silicon lattice constant 5.4307 Å.

	exp	theory
la*l	0.5230±0.003	0.52082
bx	-0.0099±0.0008	0.0
by	1.83795±0.0023	1.83712
cx	-0.5003±0.0017	-0.5
cy	-0.34091±0.0012	-0.34021
cz	0.09668±0.00006	0.096225

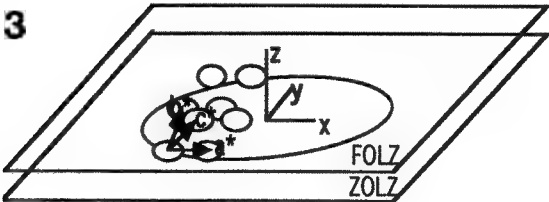


Fig. 1 and 2. Experimental CBED pattern from single crystal Silicon at 100 kV: 1) low camera length and 2) high camera length with zero disk only.
 Fig. 3. Schematic diagram of the zone axis coordinate and the primitive cell of the zone axis.

HIGH-RESOLUTION ELECTRON DIFFRACTION ANALYSIS OF STRUCTURAL CHANGES ASSOCIATED WITH THE PHOTOCYCLE OF BACTERIORHODOPSIN

Bong-Gyoon Han

Graduate Group in Biophysics, University of California, Berkeley, CA 94720

Bacteriorhodopsin (bR) is a membrane protein from *Halobacterium halobium* which acts as a light-driven proton pump. This protein is a single polypeptide and contains a single prosthetic group, retinal. When light illuminates bR, protons are pumped from inside to outside to generate an electrochemical potential gradient. The light activated retinal drives a sequential photocycle. Intermediates of the photocycle can be distinguished by visible absorption spectroscopy. The intermediates are named bR, J, K, L, M, N and O. In the L to M step, a proton is released from bR to the outside of the cell, to generate a proton concentration gradient. This proton gradient can be used later by ATP synthase for ATP synthesis. Recently, two M substates linked by one irreversible step have been detected and named M1 and M2 [1,2,3]. FTIR data has shown that these two M1 and M2 substates can be trapped by illuminating with green light at -33 °C and -13 °C respectively [1,2]. To understand the proton pumping mechanism of bR, high resolution difference electron density projection maps of M1 and M2 have been constructed in the present work, using electron diffraction techniques.

Purple membranes were purified from *Halobacterium halobium* strain ET1001 and fused to produce membrane patches with diameters larger than 4 µm. Fused membranes were mixed with a glucose solution in pH 6.5, 10 mM MOPS buffer and loaded on a carbon film supported by a copper grid. The specimen grid with mixed solution was blotted with filter paper and incubated for 10 minutes under humid air, which was previously equilibrated at 80 % relative humidity by bubbling the air through a saturated ammonium sulfate solution. The grid was then rapidly plunged into liquid nitrogen to trap the condensed water. The sample was exposed to previously focused, filtered green light for 30 seconds at -33 °C or -13°C to trap the M1 or M2 substate respectively. Liquid nitrogen was then poured on to the grid to trap the conformational changes induced by the formation of each M substate. Electron diffraction data were collected at a temperature lower than -160 °C. The bR data set needed for each substate was prepared using exactly the same protocol used to trap each substate, but omitting the illumination of green light. These "reference" data sets are named as bR1 and bR2, corresponding to M1 and M2 respectively. Electron diffraction data were recorded using a JEOL 4000 electron microscope at an accelerating voltage of 400 kV. Electron diffraction patterns were digitized and background subtracted spot intensities were measured. The final refined amplitude data were combined with phase data from Henderson et al [4] to produce difference Fourier projection electron density maps at 3.8 Å.

The difference electron density maps are shown in figures 1-4. Every map was contoured at the same level. Figure 2 represents a noise map constructed by subtracting two M1 sub-data sets. In this map, each sub-data set was constructed from 6 films. Other noise maps from bR1, bR2 and M2 showed similar amounts of noise. Figure 1 represents the M1-bR1 difference Fourier map from 12 films of M1 and 14 films of bR1. Figure 3 represents the M2-bR2 difference map from 13 films of M2 and 14 films of bR2. These M1-bR1 and M2-bR2 maps show statistically significant structural changes between light adapted bR and the two M1 and M2 substates. Figure 4 represents the (M2-bR2)-(M1-bR1) difference map constructed by subtracting Figure 1 from Figure 3. The prominent structural changes between M2 and M1 are detected near helix G, the Schiff base and aspartate 96. The 2-dimensional nature of projection maps limits the extent to which they can be interpreted in terms of changes in molecular structure at high resolution. For the moment, however, we can clearly state that there are distinct structural changes that occur during formation of the M1 intermediate, as has been implied in the infrared spectra, and that there are additional structural changes that occur when the protein advances into the M2 intermediate state. The high signal to noise levels obtained in visualizing these structural changes would seem to indicate that it is justified to continue these measurements in three dimensions.

References

1. P. Ormos et al., *Proc. Natl. Acad. Sci. USA* (1991)**88**, 473.
2. G. Perkins et al., *J. Structural Biol.* (1992)**109**, 142.
3. G. Varo et al., *Biochemistry* (1991)**30**, 5008.
4. R. Henderson et al., *J. Molecular Biology* (1990)**213**, 899.

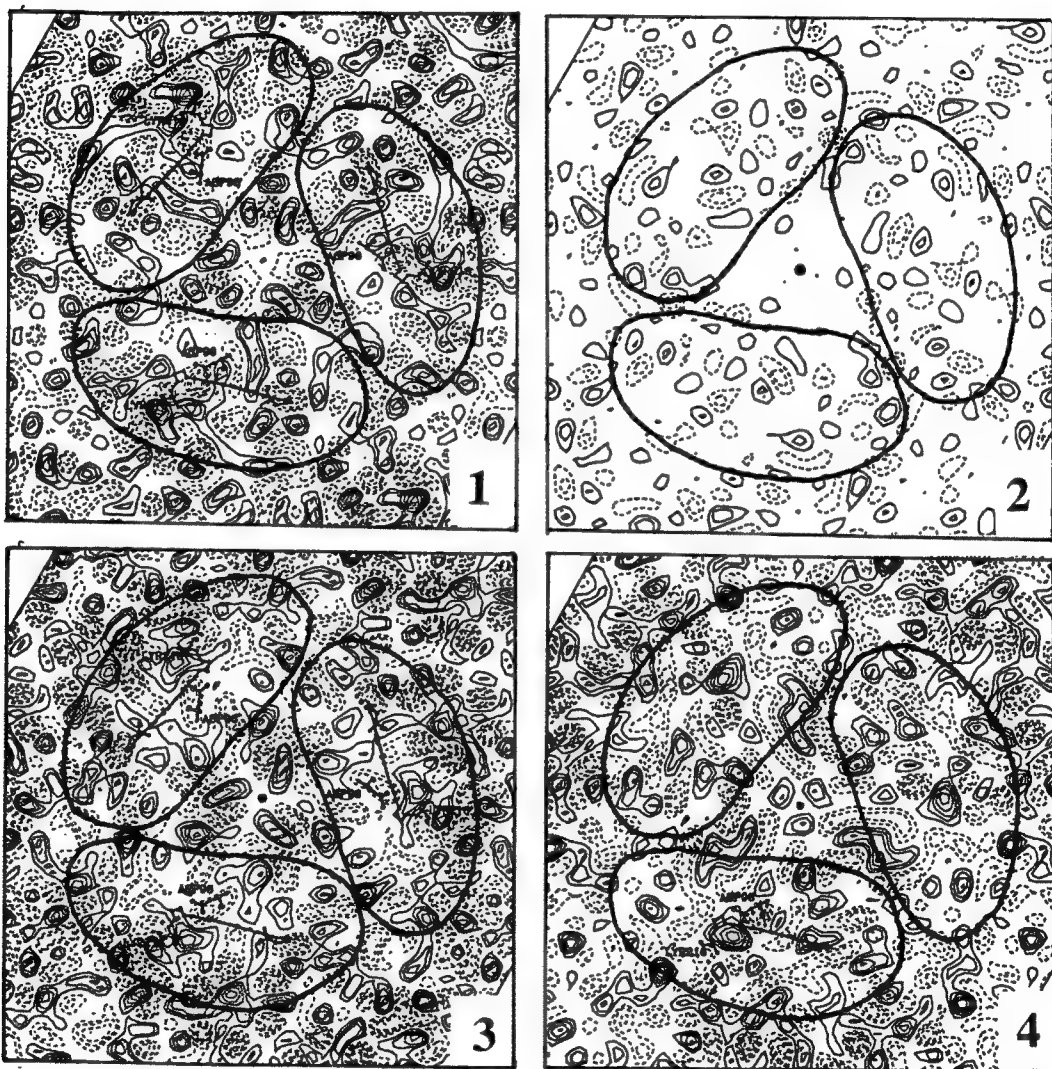


FIG. 1. --M1-bR1 difference Fourier electron density projection map at 3.8 Å.
 FIG. 2. --M1-M1 difference Fourier electron density projection noise map at 3.8 Å.
 FIG. 3. --M2-bR2 difference Fourier electron density projection map at 3.8 Å.
 FIG. 4. --(M2-bR2)-(M1-bR1) difference Fourier electron density projection map at 3.8 Å.

STRUCTURE FACTOR REFINEMENT BY LEAST-SQUARES INVERSION OF TWO-DIMENSIONAL CONVERGENT-BEAM PATTERNS

K. Marthinsen, R. Holmestad* and R. Høier*

SINTEF Applied Physics, N-7034 Trondheim, Norway and *Dept. of Physics
and Mathematics, Univ. of Trondheim-NTH, N-7034 Trondheim, Norway

While electron microscopy and diffraction for decades mainly have been a qualitative tool, there has been an increasing trend over the last years for more quantitative work. This trend applies in particular to convergent beam electron diffraction (CBED) where different methods for the retrieval of quantitative structure information from CBED intensities have been proposed.¹ In our group we have aimed at developing a general and automatic method based on the strong parameter dependencies that govern the complicated two-dimensional (2-D) intensity variations in the CBED-disks particularly in the non-systematic many-beam case.² The method is based on least squares fitting between digitized experimental and computed patterns. The advantage of this method as compared with alternative methods^{3,4} is many turning points in the intensity variations, which should give a high parameter sensitivity, and the fact that non-systematic many-beam effects are particularly sensitive to structure factor phases, which should make the method especially suitable to non-centric crystals.

The accuracy of the method is limited by the diffuse background which appears in experimental patterns, due to phonon, plasmon and single-electron excitations. This background is difficult to include properly in the simulations and can only be removed rather qualitatively and crudely from unfiltered data. This fact emphasizes the need for elastic energy filtered intensities. In our laboratory 2-D energy filtered CBED patterns may be obtained by a modified standard PEELS system attached to a Philips CM30 TEM, which enables energy filtering in the 0-300 keV range.⁵ This is an alternative to the new Gatan imaging sector filter⁶ or the Zeiss Omega filter⁷ attached to the Zeiss 912 TEM instrument. Our Gatan PEELS 666 is modified such that besides normal operation the whole detector assembly can be rotated 90° about a horizontal axis. In this mode the diode array records a one-dimensional energy filtered line profile of 1024 pixels across the CBED disk. A 2-D energy filtered image is obtained by deflecting the CBED pattern across the spectrometer entrance slit, acquiring one line at a time.

The present work reports on the first example of structure factor refinement from 2-D energy filtered CBED patterns obtained with this method. An energy filtered image of the 7,1,-5 disk corresponding to the 0,0,0; 7,1,-3; 7,1,-5; 0,0,8 four-beam case of InP was obtained at 150 keV with an energy window of 6 eV. To minimize the contribution of phonon scattering which is of course not removed by this energy window, the specimen is cooled to liquid nitrogen temperature. 7 parameters are included in the refinement, i.e. the elastic and absorptive part of U_{002} , the specimen thickness, the relative position (x and y), relative rotation and magnification of the theoretical with respect to the experimental pattern. A region, 50x16 pixels large, around the exact four-beam condition in the 7,1,-5 disk is used for the refinement. Before comparison with the computed pattern the digitized energy filtered pattern is subtracted a common background. Calculation of the theoretical pattern is based on full Bloch wave calculations with 53 beams and the least squares minimalization is carried out by the conjugate gradient method.² Absorptive scattering factors are calculated by the subroutine ATOM.⁸

In an initial refinement including only the thickness (starting at 1400 Å) and the 4 geometric parameters

the thickness was determined to approximately 1440 Å. The final refinement was then started at this value together with the small corrections obtained for the relative position, rotation and magnification, respectively. The final results for the thickness and the structure factors are shown in Table 1 where also results from a previous refinement based on unfiltered film-data are included for comparison.² In both cases subsequent calculations have confirmed that with the input data used these are true global minima.

In both cases we see that the refinement have given an increase in $|U_{002}|$ and $|U_{002}'|$ with respect to the tabulated values⁸, especially for the energy filtered data. The inconsistency in the results may be due to both unreliable input data and systematic errors in the refinement. For the unfiltered data it is of course a question whether the treatment of the diffuse background is good enough. For the energy filtered intensities this problem should in principle be eliminated, but there are still a contribution from inelastic phonon scattering left. Another problem with the filtered data is the so-called cross-talk problem, i.e. leakage of counts in one channel of the PEELS diode array to neighbouring channels, which gives a smearing out of the intensities along one line-scan. This problem can to a certain extent be handled by deconvolution, but this is so far not done with the present data. Systematic errors in the refinement may also be introduced by the fact that too few parameters are included in the refinement. Of special importance in that respect may be the Debye-Waller factors, and the amplitude and phase of the structure factors (e.g. U_{713} and U_{715}) of the other main reflections. Work are in progress to analyze these problems.

TABLE 1 Seven parameter refinement from the central part of the 7,1,-5 disk (50 x 16 pixels) of InP. Nominal voltage 150 keV.

	Unfiltered	Unfiltered	Filtered	Filtered	
	Start	Stop	Start	Stop	Tabulated ⁸
Thickness [Å]	1680.0	1680.2	1440.0	1439.9	
$ U_{002} $ [Å ⁻²]	0.02400	0.02468	0.02300	0.02526	0.02440
Φ_{002} [rad]	-	-	-	-	
$ U'_{002} $ [Å ⁻²]	0.00200	0.00218	0.00200	0.00322	0.00209
Φ'_{002} [rad]	-	-	-	-	
R-factor	4.560 10 ⁻³	4.400 10 ⁻³	7.790 10 ⁻³	5.705 10 ⁻³	

References

1. J.C.H. Spence and J.M. Zuo, in Electron Microdiffraction, New York: Plenum Press (1992).
2. R. Høier et al., Ultramicroscopy, in press.
3. J.M. Zuo and J.C.H. Spence, Ultramicroscopy (1991)35, 185.
4. D.M. Bird and M. Saunders, Acta Cryst. (1992)A48, 555.
5. R. Holmestad et al., Ultramicroscopy, in press.
6. A.J. Gubbens and O.L. Krivanek, Ultramicroscopy, in press.
7. J. Mayer, J.C.H. Spence and G. Mobus, Proc. Ann. MSA 49(1992)786.
8. D.M. Bird and Q.A. King, Acta Cryst. (1990)A46, 202.
9. R. Holmestad is supported by the Royal Norwegian Council for Scientific and Industrial Research.

DIRECT PHASE DETERMINATION AND REFINEMENT IN THE ELECTRON CRYSTALLOGRAPHY OF SMALL STRUCTURES

Douglas L. Dorset and Mary P. McCourt

Electron Diffraction Department, Medical Foundation of Buffalo, Inc., 73 High Street, Buffalo, NY 14203

The use of electron diffraction intensity data for quantitative determination of crystal structures was largely pioneered by Vainshtein, Pinsker and their co-workers, as recently reviewed¹, and was shown to produce results consistent with more typical X-ray structure analyses. Despite these encouraging results for a number of representative inorganic and organic materials, it is accurate to say that the technique has not been widely accepted by the crystallographic community. This is probably because, in several of the early analyses, contemporary X-ray structure results were used to provide heavy atom positions, thus providing much of the crystallographic phase information. Since it is also known² that correct phases, combined with even scrambled structure factor amplitudes, will lead to a Fourier map that appears to be 'correct', it is commonly (but incorrectly) thought that no *ab initio* electron diffraction determinations have been carried out for previously unsolved structures. In addition, the very complexity of n-beam dynamical scattering theory compared to 'primary extinction' corrections has dampened enthusiasm to continue this work.

Nevertheless there are many types of materials where such efforts, if possible, would provide the only possible hope of a single crystal determination, given that the sample limitation of thin microcrystals means that electron diffraction is the only way to obtain an undistorted representation of reciprocal space. Polymer physicists have known this for years and represent the major group using quantitative electron diffraction structure analyses^{3,4}. Even in this application, use of two figures of merit, i.e. the combined minimization of a crystallographic R-factor and an atom-atom nonbonded potential energy, implies a basic mistrust of the diffraction data as representing a simple Fourier transform of the underlying crystal structure. The only way to prove the utility of this approach would be to demonstrate that *ab initio* determinations, where no assumptions about the structure from other sources are imposed on the analysis, are indeed possible. Such a proof has come from the application of probabilistic estimates of phase invariant sums as they are commonly employed in X-ray crystallography⁵.

Two approaches to direct phasing have been taken. One is to evaluate individual three- and four-phase structure invariants for new phase values after the limited number of phases permitted for origin definition are assigned. This is particularly useful for the analysis of centrosymmetric structures, as demonstrated with several examples: diketopiperazine⁶, urea⁷, paraelectric thiourea⁷, several projections of linear polymers⁸, three-dimensional polymer structures⁷, (including polyethylene⁹), copper perchlorophthalocyanine¹⁰ and inorganic structures (including celadonite, muscovite, and phlogopite-biotite¹¹), boric acid¹², basic cuprous chloride and the lambda phase of alumina¹³. It is also possible to combine phase information from electron microscope images as shown for several alkane structures¹⁴⁻¹⁶. It has also been possible to determine phases for noncentrosymmetric structures such as mannan⁷ and poly(ϵ -caprolactone)¹⁷, but such structures are better approached by multisolution techniques using the tangent formula¹⁸, as shown for the ferroelectric thiourea structure¹⁹ and form III of poly(butene-1)²⁰. Other laboratories have combined electron microscope image phases with the tangent formula²¹, the Sayre equation²² and maximum entropy²³ to find new phase values. In all cases, the direct methods are remarkably 'robust', despite data perturbations from dynamical scattering, especially when the Σ_2 triple phase invariant is the major relationship used in these determinations.

As in X-ray crystallography, the initial atomic resolution model can be refined by a number of techniques. In our initial work, Fourier refinement has been found to be very effective for finding missing atomic positions or moving atoms to better sites, although it is clear that when dynamical scattering is important²⁴, the desired local minimum representing a geometrically more reasonable molecular architecture may be different from the 'true' global minimum where distorted intensities are allowed to produce a chemically meaningless model. Least-squares refinement has also been successfully applied to the structures of polyethylene and diketopiperazine²⁵ but requires that sufficient data are available per refineable parameter and that dampening parameters must be used to limit the size of atomic shifts. Fitting a model to a potential map has been shown to be useful, especially for cases, e.g. mannan²⁵, where the undersampling of diffraction data along the fiber axis (due to goniometer tilt limitations for solution-crystallized samples) does not allow one to localize individual atomic positions⁷.

To summarize, traditional phasing and refinement procedures can be applied to observed electron diffraction intensity data to yield structures agreeing favorably to earlier X-ray analyses, when a comparison is possible, or producing a geometrically reasonable model in the case of new structures. If care is taken to collect these intensities within the constraints of a quasi-kinematical scattering limit, there is no reason why any stigma should be attached to electron crystallographic analyses.

References

1. B. K. Vainshtein, B. B. Zvyagin, and A. S. Avilov, in *Electron Diffraction Techniques*, Vol. 1 (J. M. Cowley, ed.), Oxford Univ. Press, Oxford, 1992, pp. 216-312.
2. G. N. Ramachandran and R. Srinivasan, *Fourier Methods in Crystallography*, Wiley, NY 1970, pp. 62-67.
3. F. Brisse, *J. Electron Microsc. Techn.* (1989) 11, 272.
4. S. Perez and H. Chanzy, *J. Electron Microsc. Techn.* (1989) 11, 280.
5. H. A. Hauptman, *Crystal Structure Determination. The Role of the Cosine Seminvariants*, Plenum, NY, 1972.
6. D. L. Dorset, *Acta Cryst.* (1991) A47, 510.
7. D. L. Dorset, *Ultramicroscopy* (1991) 38, 23.
8. D. L. Dorset, *Macromolecules* (1992) 25, 4425.
9. D. L. Dorset, *Macromolecules* (1991) 24, 1175.
10. D. L. Dorset, W. F. Tivol, and J. N. Turner, *Ultramicroscopy* (1991) 38, 41.
11. D. L. Dorset, *Ultramicroscopy* (1992) 45, 5.
12. D. L. Dorset, *Acta Cryst.* (1992) A48, 568.
13. D. L. Dorset, unpublished results.
14. D. L. Dorset and F. Zemlin, *Ultramicroscopy* (1990) 33, 227.
15. D. L. Dorset, *Proc. Natl. Acad. Sci. USA* (1990) 87, 8541.
16. D. L. Dorset and W. P. Zhang, *J. Electron Microsc. Techn.* (1991) 18, 142.
17. D. L. Dorset, *Proc. Natl. Acad. Sci. USA* (1991) 88, 5499.
18. J. Karle and H. Hauptman, *Acta Cryst.* (1956) 45, 357.
19. D. L. Dorset, *Ultramicroscopy* (1992) 45, 357.
20. D. L. Dorset, M. P. McCourt, S. Kopp, J. C. Wittmann, and B. Lotz, *Acta Cryst.*, submitted.
21. H. F. Fan, S. B. Xiang, F. H. Li, Q. Pan, N. Uyeda, and Y. Fujiyoshi, *Ultramicroscopy* (1991) 35, 361.
22. Y. D. Mo, T. Z. Cheng, H. F. Fan, J. Q. Li, B. D. Sha, C. D. Zheng, F. H. Li, and Z. X. Zhao, *Supercond. Sci. Technol.* (1992) 5, 69.
23. W. Dong, T. Baird, J. R. Fryer, C. J. Gilmore, D. D. MacNicol, G. Bricogne, D. J. Smith, M. A. O'Keefe, *Nature* (1992) 355, 605.
24. D. L. Dorset, W. F. Tivol, and J. N. Turner, *Acta Cryst.* (1992) A48, 562.
25. M. P. McCourt and D. L. Dorset, unpublished results.
26. Research was funded in part by grants from the NSF (CHE91-13899) and the NIH (GM-46733).

THICKNESS MEASUREMENT OF GLUCOSE-EMBEDDED CROTOXIN COMPLEX CRYSTALS BY EELS

R.D. Leapman, J. Brink* and W. Chiu*

Biomedical Engineering and Instrumentation Program, NCRR, National Institutes of Health, Bethesda, MD 20892; *Verna and Marrs McLean Dept. of Biochemistry and W.M. Keck Center for Computational Biology, Baylor College of Medicine, Houston, TX 77030

In three-dimensional structure determination of macromolecules by electron crystallography it is necessary to combine diffraction patterns and images recorded at various tilt angles from different crystals.¹ In order to merge these data sets successfully all the crystals should have the same thickness. It has been proposed that parallel electron energy loss spectroscopy (EELS) might provide a useful means of assessing the thickness of a beam-sensitive organic crystal prior to recording the high-resolution structural data.² This can be achieved by measuring the fraction of the total transmitted electrons that do not lose energy, i.e., the zero-loss intensity. If I_z is the integrated zero-loss intensity and I_{tot} is the total integrated intensity in the energy loss spectrum, then the specimen thickness, t , is given in terms of the total inelastic mean free path, λ_i , by, $t/\lambda_i = \ln(I_{tot}/I_z)$. Results recently obtained from *n*-paraffin crystals have shown that it is feasible to determine the number of unit cell layers under low electron dose conditions.² Our aim here is to investigate the EELS approach further by applying it to glucose-embedded crotoxin complex crystals typically used for the electron crystallographic analysis.³ The crotoxin complex has a molecular weight of 24,000 Da and forms tetragonal crystals containing eight molecules per unit cell. The unit cell parameters are $a = b = 3.88$ nm, and $c = 25.6$ nm, giving a dry protein density of 0.828 g/cm³. If we assume that the embedded crotoxin complex crystals contain 40% glucose by weight, then the crystal has a total density of ~ 1.38 g/cm³. Taking previous estimates of the cross section per unit mass for protein and glucose,⁴ we obtain a value of $\lambda_i = 109 \pm 10$ nm for the inelastic mean free path of glucose-embedded crotoxin complex crystals at 100 keV beam energy. It has been shown that the crotoxin complex crystal may be formed in different thicknesses, the thinnest being 6.4 nm, which is a quarter of the full unit cell.³ One can therefore predict the possible values of t/λ_i as integral multiples of 0.06 (equivalent to 6.4 nm thick crystals) if no additional thickness is contributed due to the presence of glucose on the crystal surfaces.

The specimens of glucose-embedded crotoxin complex were analyzed with a VG Microscopes HB501 STEM equipped with a Gatan model 666 electron spectrometer.⁵⁻⁷ Suitable areas containing thin crystals were searched under low dose conditions (0.1 e/nm²/s) by means of the annular dark-field signal and micrographs were recorded digitally as shown in Fig. 1. Specimens were cooled to -160°C in order to minimize beam damage. The EELS data were collected from 0.5 μm diameter regions of the crotoxin complex crystals at a dose of <100 e/nm². Values of t/λ_i from 97 regions contained in twenty-eight separate crystals gave the histogram shown in Fig. 2, after a correction had been applied for subtracting the thickness of the thin carbon support film. It is seen from the histogram that 60% of the crystals have thicknesses less than or equal to one unit cell with the data falling into two main peaks. This may reflect a tendency for formation of crystals with thicknesses at half unit cell increments. The remaining values of t/λ_i corresponded to crystals with thicknesses in the range $3/2$ to $5/2$ unit cells. The observation that the peaks are not all distributed distinctly at integral multiples of t/λ_i can be explained by the variable amount of embedding glucose coating the crystals. In Fig. 3 the smallest observed t/λ_i value is 0.12 suggesting a glucose coating thickness of approximately 6 nm if the thinnest crystal had a thickness of one quarter unit cell. Alternatively, these measured values can be interpreted as corresponding to crystals of half unit cell thickness with a negligible glucose surface coating. Evidence for a layer of glucose coating the crystals is also indicated by the finite widths, $\Delta(t/\lambda_i) \sim 0.05$, of the peaks in

the histogram. Therefore, although we cannot precisely assign the crystal thickness to the nearest 1/4 unit cell, we can confidently determine it to a 1/2 unit cell.

Although our current study on the feasibility of using EELS to determine protein crystal thickness was performed with the dedicated STEM, such measurements could also be made with the conventional TEM. Quantitative on-line diffraction, that has recently been demonstrated for electron crystallography,⁸ and the EELS method discussed here can in fact now be combined through the availability of energy-filtering spectrometers equipped with slow scan CCD cameras.⁹ Such an approach could greatly increase the efficiency of data collection for electron crystallography.¹⁰

References:

1. L.A. Amos, R. Henderson and P.N.T. Unwin, *Prog. Biophys. Mol. Biol.* 39 (1982) 183.
2. P. Rez, W. Chiu, J.K. Weiss and J. Brink, *J. Microsc. Res. and Tech.* 21 (1992) 166.
3. T.W. Jeng and W. Chiu, *J. Mol. Biol.* 164 (1983) 329.
4. R.D. Leapman, C.E. Fiori and C.R. Swyt, *J. Microsc.* 133 (1984) 239.
5. O.L. Krivanek, A. C.C. and R.B. Keeney, *Ultramicroscopy* 22 (1987) 103.
6. R.D. Leapman and S.B. Andrews, *J. Microsc.* 161 (1991) 3.
7. J. A. Hunt and D.B. Williams, *Ultramicroscopy* 38 (1991) 47.
8. J. Brink and W. Chiu, *Proc. 10th Europ. Cong. Elect. Microsc., Grenada, 1992*, p. 15.
9. O.L. Krivanek et al., *Proc. 50th Annual EMSA Meet., 1992*, p. 1192.
10. This research was supported in part by grants from the NIH (RR02250) and the W.M. Keck Foundation.

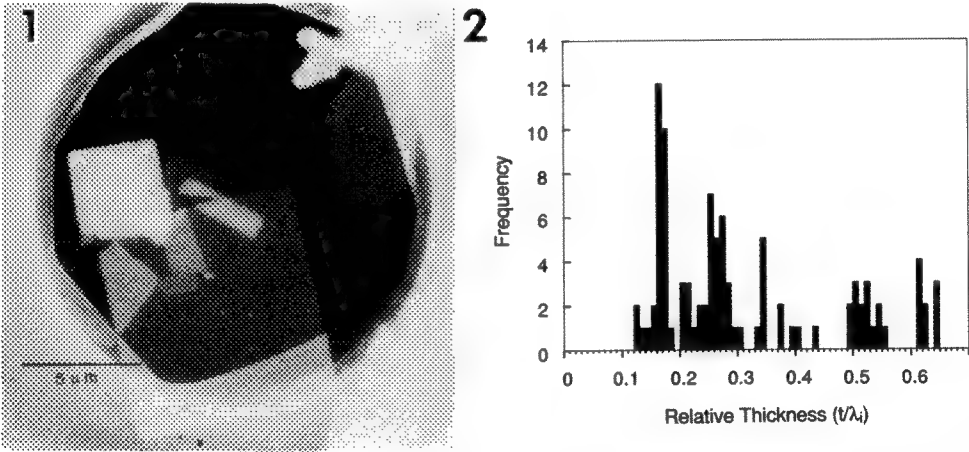


Fig. 1. -- Dark-field STEM micrograph of glucose-embedded crotoxin complex crystals recorded at 100 keV beam energy with an electron dose of $\sim 10^2$ e/nm².

Fig. 2. -- Histogram of ninety-seven t/λ_i measurements showing main peaks at values corresponding to thicknesses around 1/2 unit cell (12.8 nm) and 1 unit cell (25.6 nm).

DETERMINATION OF STRUCTURE FACTORS OF COPPER BY CONVERGENT-BEAM ELECTRON DIFFRACTION

John Mansfield*, Martin Saunders**, George Burgess***, David Bird** & Nestor Zaluzec****

*Electron Microbeam Analysis Laboratory, University of Michigan, Ann Arbor MI 48109-2143, USA

**School of Physics, University of Bath, Claverton Down, Bath, UK

***Dept. of Materials Science & Metallurgy, Cambridge University, Pembroke Street, Cambridge, UK

****Electron Microscopy Center, Materials Science Division, Argonne National Laboratory, Argonne, IL 60439, USA

There has been considerable recent interest in the determination of structure factors from convergent beam electron diffraction (CBED) patterns and the ultimate goal is the ability to retrieve the crystal structure of an unknown crystal by inversion of a CBED pattern. There are a number of different methods that have been used to extract structure factor information¹⁻². The zone-axis pattern fitting technique of Bird and Saunders¹ has recently been used to obtain structure factors for silicon that compare well with those obtained by X-ray methods³. This work extends the techniques to f.c.c. metals, specifically copper.

CBED patterns were recorded from [110] zone axes of electropolished foils of pure copper (99.999% purity) in the Philips EM420T at Argonne National Laboratory. The patterns were energy-filtered by scanning the whole pattern across the entrance aperture of a Gatan #607 serial energy loss spectrometer and collecting the zero loss intensity only (energy window ~5eV). An EDAX PV990 computer was used to control the scans and digitize the patterns into 512 by 512 pixel data arrays with an intensity range of 12bits (4096 counts). The patterns were recorded such that the direct disc and the six lowest order reflections filled the field of view. An example diffraction pattern is shown in figure 1.

The data was processed at the University of Cambridge, using SEMPER running on a Silicon Graphics workstation, to extract 25x25 pixels regions from the centers of the seven low order discs. The intensities from these regions were then matched to calculated patterns at the University of Michigan on Hewlett Packard HP9000/710 workstations. The fitting process is a quasi-Newton method that is described in reference 1 and it proceeds by varying a set of parameters to minimize of the difference between a theoretical pattern and the experimental pattern. The fitting parameters include: a set of low order structure factors (both elastic and absorptive), the specimen thickness, a normalization coefficient and a number of background intensity values. For copper [110] the fit solves for 77 beams exactly and another 74 beams are added by perturbation theory. The initial starting estimate for the structure factors included real part elastic values of Doyle and Turner⁴ and the imaginary absorptive values from Bird and King⁵. At the start of the fitting process only the 002 and 111 structure factors were varied, to limit the possibility of the fit being trapped in a local minimum, and then, as the fit began to converge, the higher order structure factors were varied. Fine tuning of the fit was accomplished by variation of the Debye-Waller factor. Structure factors as fitted from patterns from two different sample thicknesses are shown in table 1. The {111} and {002} structure factors differ appreciably from the neutral atom values, while the differences for {220} and {113} are of the order of the estimated error. Figure 2, however, compares the experimental data from a 111 reflection with the computer generated fit and shows the high quality of the fit..

References

1. D.M. Bird and M. Saunders, *Acta Cryst.* (1992) A46, p555.
2. J.M. Zuo and J.C.H. Spence, *Ultramicroscopy* (1992), p211.
3. M. Saunders, D.M. Bird, W.G. Burgess, A.R. Preston, and N.J. Zaluzec, "Determination of Bonding Charge Densities in Silicon", in *AEM '93, Proc. 27th Annual Meeting of MAS*, in press.
4. P.A. Doyle and P.S. Turner, *Acta Cryst.* (1968) A24, p390.
5. D.M. Bird and Q.A. King, *Acta Cryst.* (1990) A46, p202.

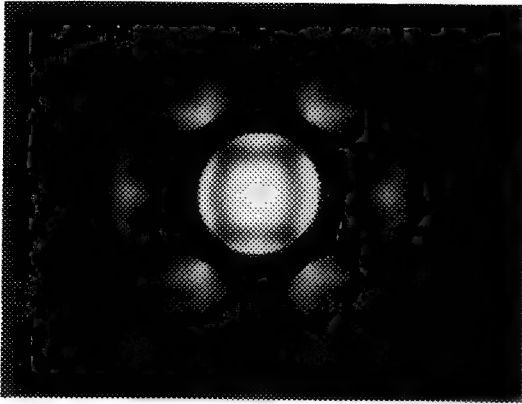
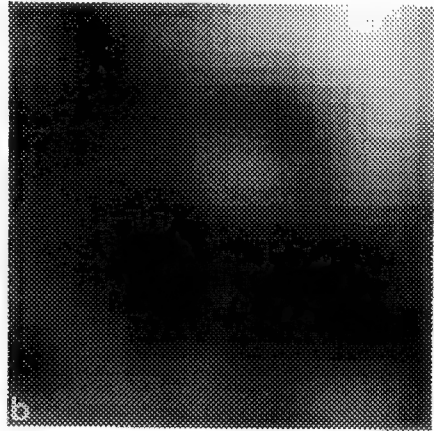
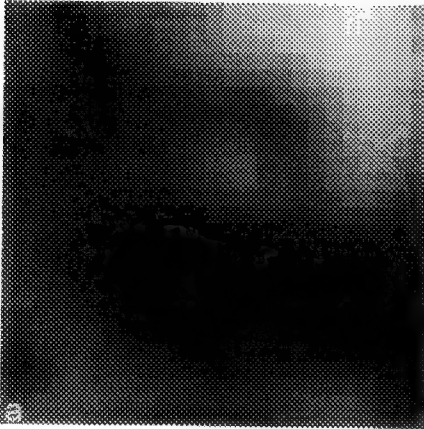


Figure 1. Energy Filtered (zero loss only, ~5eV window) Cu [110] Zone Axis CBED pattern. Recorded at 120kV, sample held at liquid nitrogen temperature.

Figure 2 (a) 25x25 pixel area extracted from the lower left 111 reflection in figure 1. (b) 25x25 pixel area of fitted 111 reflection



Parameter	Data Set 1 U_g values	Data Set 2 U_g values	Data Set 1 f_x values	Data Set 2 f_x values	Neutral Atom f_x values
{111}	3.898(3)	3.888(6)	21.50(1)	21.52(1)	21.78
{002}	3.435(4)	3.419(7)	20.13(1)	20.17(2)	20.35
{220}	2.436(11)	2.393(18)	16.14(5)	16.35(5)	16.21
{113}	2.044(10)	2.025(19)	13.96(5)	14.09(12)	14.09
t (in Å)	1052(1)	652(1)	-	-	-

Table 1. The U_g values are in units of \AA^{-2} and are fitted at liquid nitrogen temperature. The Cu lattice parameter is 3.61\AA and the accelerating voltage was 118kV. The estimated 2σ values are shown in parentheses. The authors believe that the results from the thicker pattern are more reliable as the sum of squares is smaller than for the thinner pattern and the residual map shows very little structure. The f_x values are the X-ray structure factors at liquid nitrogen temperature derived from the fitted U_g s using the Mott formula. The neutral atom structure factors are derived from Doyle and Turner⁴. It can be seen that the {111} and {002} structure factors differ appreciably from the neutral atom values, while the differences for {220} and {113} are of the order of the estimated error.

MEASUREMENT OF LATTICE PARAMETER AT THE NANOMETER SCALE USING CONVERGENT-BEAM MICRODIFFRACTION FROM A THERMAL EMISSION SOURCE

W. T. Pike

Jet Propulsion Laboratory, 4800 Oak Grove Drive, Pasadena CA 91109

With the advent of crystal growth techniques which enable device structure control at the atomic level has arrived a need to determine the crystal structure at a commensurate scale. In particular, in epitaxial lattice mismatched multilayers, it is of prime importance to know the lattice parameter, and hence strain, in individual layers in order to explain the novel electronic behavior of such structures. In this work higher order Laue zone (holz) lines in the convergent beam microdiffraction patterns from a thermal emission transmission electron microscope (TEM) have been used to measure lattice parameters to an accuracy of a few parts in a thousand from nanometer areas of material.

Although the use of CBM to measure strain using a dedicated field emission scanning transmission electron microscope has already been demonstrated¹, the recording of the diffraction pattern at the required resolution involves specialized instrumentation. In this work, a Topcon 002B TEM with a thermal emission source with condenser-objective (CO) electron optics is used. As many TEM manufacturers have adopted the CO mode as standard for high resolution electron microscopy, the technique described here should be practical in dozens of laboratories across the world without the need for additional specialized equipment or a more expensive field emission TEM.

By demagnifying the electron source using the condensor lenses, the beam can be made coherent and a convergent probe down to 0.5nm in diameter can be formed at the sample. Figure 1 shows a density trace across such a probe. By recording the deficit holz lines in the transmitted beam, the lattice parameter of the material through which the beam has passed can be determined². Although the electron intensity of such a pattern is much lower than the intensity from a field emission source, the inherently very large signal-to-noise ratio enables real time observation of the pattern via an image intensifier. The exposure time is typically a few seconds, short enough to avoid specimen drift under the probe. An added advantage of the demagnification of the source is the avoidance of probe wobble which is observed with field emission due to instabilities in the source.

Figure 2 shows a cross-section of a III-V quantum well (QW), together with diffraction patterns and matching holz line simulations with the probe positioned on the GaAs substrate and $\text{In}_x\text{Ga}_{1-x}\text{As}$ QW. The substrate pattern is used to determine the accelerating voltage of the microscope (which in general is not known with sufficient accuracy) by using the known lattice parameter of GaAs. This accelerating voltage, with suitable small dynamical corrections to account for the difference in the electron scattering between the two layers³, is then used in the simulation of the $\text{In}_x\text{Ga}_{1-x}\text{As}$ CBM pattern. It is assumed in the simulation that the QW is epitaxial on the substrate (as evidenced by the lack of misfit dislocations at the interface) and that therefore x , the In content, is the only free parameter. A good match is obtained for an In content of 0.26 ± 0.01 , which corresponds to an absolute accuracy in the lattice parameter measurement of 8 parts in 10,000.⁴

References

1. W. T. Pike *et al.*, J. Cryst. Growth (1991) **111**, 925
2. e.g. D. M. Maher *et al.*, Appl. Phys. Lett. (1987) **50** 574
3. Y. P. Lin *et al.*, Ultramicroscopy (1989) **27** 233
4. The work described in this paper was performed by the Center for Space Microelectronics Technology, Jet Propulsion Laboratory, California Institute of Technology and was sponsored by the Strategic Defense Initiative Organization, Innovative Science and Technology Office through an agreement with the National Aeronautics and Space Administration.

Fig. 1: Intensity profile of probe. Full-width-half-maximum is 0.5nm

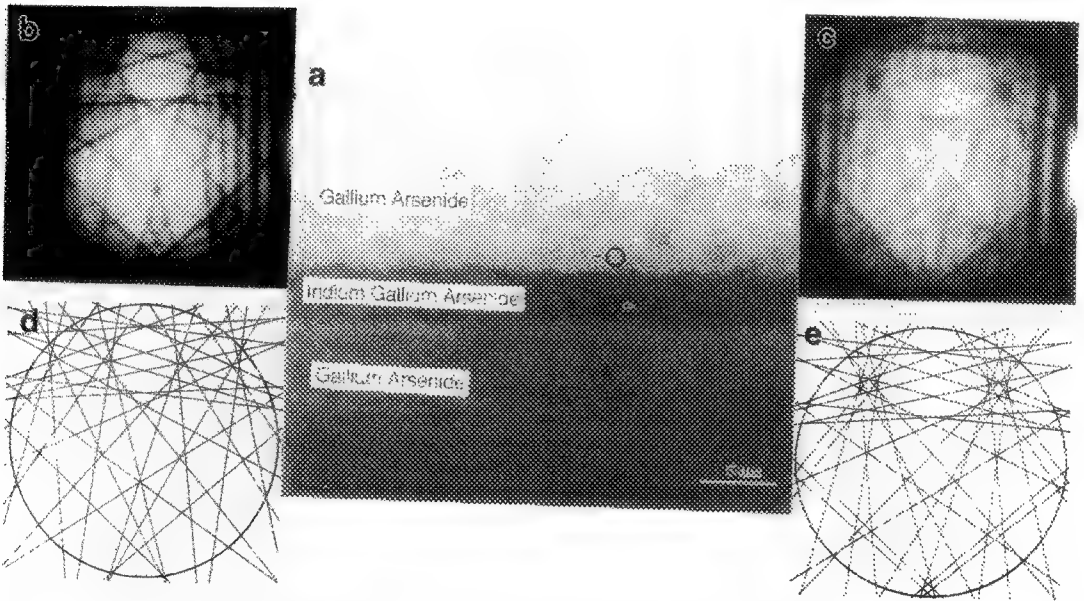


Fig. 2: (a) Cross-section of QW structure showing schematically position of probe for acquiring CBM patterns from (b) GaAs and (c) In_xGa_{1-x}As with dynamically corrected kinematical simulations (d) and (e).

ARE HOLZ LINES KINEMATIC IN OFF-ZONE-AXIS ORIENTATIONS?

J. M. Zuo*, A. L. Weickenmeier**¹, R. Holmestad*² and J. C. H. Spence*

Physics Dept., Arizona State University, Tempe, AZ 85287

The application of high order reflections in a weak diffraction condition off the zone axis center, including those in high order laue zones (HOLZ), holds great promise for structure determination using convergent beam electron diffraction (CBED)^{1,2}. It is believed that in this case the intensities of high order reflections are kinematic or two-beam like. Hence, the measured intensity can be related to the structure factor amplitude. Then the standard procedure of structure determination in crystallography may be used for solving unknown structures. The dynamic effect on HOLZ line position and intensity in a strongly diffracting zone axis is well known³. In a weak diffraction condition, the HOLZ line position may be approximated by the kinematic position⁴, however, it is not clear whether this is also true for HOLZ intensities. The HOLZ lines, as they appear in CBED patterns, do show strong intensity variations along the line especially near the crossing of two lines, rather than constant intensity along the Bragg condition as predicted by kinematic or two beam theory. The structure of the intensity variation contains information on the phase of the structure factors^{5,6} involved. Such intensity variations are often large as the example in figure 1 shows. Previous work has either ignored this variation by using a qualitative intensity scale² or has tried to measure the intensity in a relatively constant region⁷. If, however, these intensities are to be used quantitatively for structure determination, the intensity variation in the experimental pattern must not be ignored. Here we show that the intensity of high order reflection in weakly diffraction conditions is best approximated by a two-beam intensity expression with an effective Bethe interaction potential. This relatively simple analytic approximation may be used to predict the region of most two-beam like behavior and to estimate deviations from the ideal two-beam intensity.

In a weakly diffracting or so-called kinematic condition, the strong excitation of low order reflections near their Bragg conditions are carefully avoided. Only high order reflections showing significant intensity along narrow lines (close to the Bragg condition) are seen. In this case, near the line of a high order reflection g and away from intersections with other lines, we may consider this beam and the incident beam as two strong beams, while other beams are weak. Then the two-beam Bethe approximation can be applied, which gives the intensity of reflection g at the Bragg condition as

$$I_g = \sin^2 \left(\frac{\pi t}{K} |U_g^{\text{eff}}| \right) \quad 1); \quad \text{where} \quad |U_g^{\text{eff}}| = |U_g| \left| 1 - \sum_{h \neq 0, g} \frac{U_h U_{gh}}{2KS_h U_g} \right| \quad 2)$$

is the effective Bethe interaction potential, and U_g and S_g are the interaction potential of the crystal and the excitation error, respectively. Absorption is neglected here, the effects of absorption are under further study. Weak beam effects may also cause the maximum intensity along the line to deviate from the Bragg condition⁴. This small shift is assumed to be constant and ignored here. In contrast, in ideal two-beam conditions the intensity at the Bragg condition is

$$I_g = \sin^2 \left(\frac{\pi t}{K} |U_g| \right) \quad 3) \quad \text{and} \quad I_g = \left(\pi t |U_g| / K \right)^2 \quad 4)$$

in the kinematic approximation. To test the above approximations, we have simulated the intensity of the (6,-2,2) reflection in TiAl from point A to B in figure 2 at a thickness of 800 Å using many-beam Bloch wave calculations and equations 1, 3 and 4. The results are shown in figure 3. From figure 3, the intensity simulated by the Bloch wave calculation deviates significantly from the ideal two-beam intensity, and the deviations are remarkably well approximated by equation 1, while the kinematic approximation fails in this case. To see whether the same conclusion holds for a different thickness, we also simulated the variation with thickness at orientation C marked in figure 2, as shown in figure 4. Again, the two-beam Bethe approximation (eqn. 1) is closest to the full dynamic simulation, while both the kinematic and two-beam approximation give a 20% error at thickness 50 Å. An interesting question also arises at very small thickness, where the kinematic approximation should hold. However, the two-beam Bethe approximation predicts that the intensity should be proportional to the effective potential instead of the real potential. Obviously the Bethe approximation fails at small thickness. To see where it fails, we replotted figure 4 over a smaller thickness range in figure 5. Obviously, for a thickness below 20 Å the intensity is

closer to the kinematic approximation than to the Bethe approximation, while the opposite is true at a thickness above 50 Å. But most CBED patterns are obtained from much thicker crystals (about 800 Å) to see HOLZ lines.

In conclusion, the two-beam approximation with an effective Bethe potential is a better approximation for the intensity of high order reflections in weakly diffracting conditions (it is misleading to call these kinematic conditions). The interpretability of high order reflections using simple approximations makes them useful for structure parameter refinement, such as atomic positions and Debye-Waller factors.

*Supported by NSF grant 9015867 and ASU-NSF National Center for HREM; #Supported by Alexander von Humboldt Stiftung; @Supported by Royal Norwegian Council for Scientific and Industrial Research.

Reference

1. J. Taftø and T. H. Metzger, *J. Appl. Cryst.*, 1985, **18**, 110
2. R. Vincent and D. R. Exelby, *Phil. Mag. Lett.*, 1991, **29**
3. B. F. Buxton, *Proc. R. Soc. Lond.*, 1976, **A350**, 335
4. J. M. Zuo, *Ultramicroscopy*, 1992, **41**, 211
5. J. M. Zuo, R. Høier and J. C. H. Spence, *Acta. Cryst.*, 1989, **A45**, 839
6. D. Bird, R. James and Q. King, *Phys. Rev. Lett.*, 1987, **63**, 1118
7. Y. Ma, C. Rømming, B. Lebech, J. Gjønnes and J. Taftø, *Acta Cryst.*, 1992, **B48**, 11

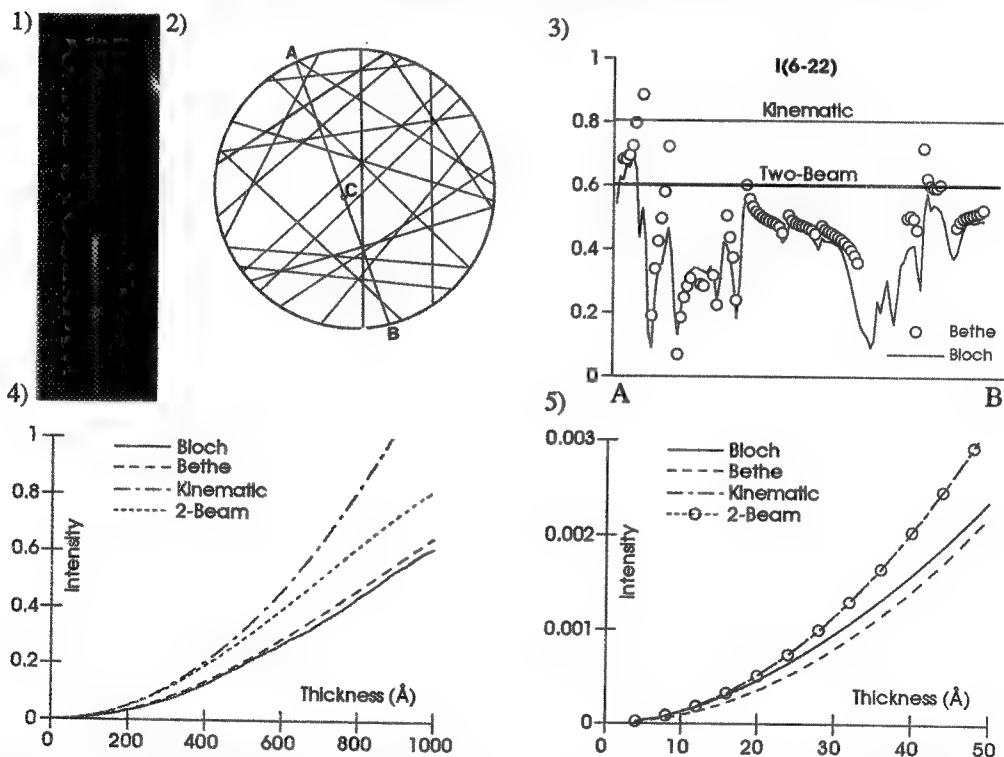


Fig. 1. A zero-loss experimental excess HOLZ line of TiAl at 120 kV from Zeiss 912 microscope.

Fig. 2. Simulated HOLZ pattern in zero disk near [5,3,-10] zone axis at 120 kV. The incident beam direction at center of the zero disk is $K_t=(2.25,-1.25,0.75)$ and the disk radius is 1.0 Å^{-1} .

Fig. 3. Intensities of (6,-2,2) reflection from A to B of figure 2. Both Bloch wave and Bethe calculations include the same 38 beams.

Fig. 4 and 5. Thickness dependence of $I(6-22)$ for beam direction at C (see figure 2).

DISLOCATION CONTRAST IN HIGH-ANGLE HOLLOW-CONE DARK-FIELD TEM

Z. L. WANG

Metals and Ceramics Division, Oak Ridge National Laboratory, P.O. Box 2008, Oak Ridge, TN, 37831-6376; and Department of Materials Science and Engineering, The University of Tennessee, Knoxville, TN, 37996-2200, USA

Dislocations were imaged using the high-angle hollow-cone dark-field transmission electron microscopy (HADF-TEM) technique.¹ Experiments were performed using a Philips CM30 TEM at 300 kV. Dislocations and grain boundaries show bright contrast in HADF-TEM images and there are no contrast reversals with thickness or defocus. The dislocation contrast shows no dramatic variation when the average semi-conical angle θ was increased from 40 to 110 mrad, but does show strong dependence on the diffracting conditions that are set up for the corresponding on-axis bright-field (BF) TEM image (Fig. 1). Under the "one-beam" (random orientation without strong diffraction) reflection condition (Figs. 1a and 1a'), the visibility of the dislocations is poor in either the BF-TEM or the HADF-TEM image. Under the two-beam diffracting condition (Figs. 1b and 1b') both BF-TEM and HADF-TEM images show optimized contrast. The features appearing in the HADF-TEM images have a good one-to-one correspondence with the features shown in the corresponding BF-TEM images; the dislocation contrast disappears in the HADF-TEM images if the condition $\mathbf{g} \cdot \mathbf{b} = 0$ is satisfied in the BF-TEM images, where \mathbf{b} is the Burgers vector (Fig. 2). Experimental observations have demonstrated that the conical scan HADF-TEM imaging has many characteristics that are analogous to those of conventional diffraction contrast imaging in TEM.

Due to differences in scattering geometries, strong incident beam channelling effects can be generated in high-angle annular dark-field scanning transmission electron microscopy (HAADF-STEM) but not in HADF-TEM, because the incident beam travels along the crystal zone axis in the former instead of at a large angle with respect to the zone axis in the latter. This difference greatly reduces the contribution of dechannelling contrast² in HADF-TEM imaging. On the other hand, the channelling of high-angle diffusely scattered electrons could occur in HADF-TEM but not in HAADF-STEM.³ The diffuse scattering contrast, in which the high-angle scattered electrons are generated from the diffuse scattering of the distorted crystal lattices around the dislocation cores, is not sufficient to interpret the dependence of the HADF-TEM image contrast on diffracting conditions (Figs. 1 and 2).

For specimens thicker than about 30 - 50 nm, the dislocation contrast in HADF-TEM is generated by a two-step mechanism: 1) the creation of diffuse scattering due to lattice distortion around the dislocation cores or defects; and 2) the subsequent, parallel to optic axis, channelling of the diffusely scattered electrons under the dynamic diffracting conditions that is set up initially for the corresponding BF-TEM image. The first step is analogous to the Huang scattering contrast, in which the regions containing point defects show bright contrast in HADF-TEM and HAADF-STEM images. It is the last step that makes HADF-TEM imaging to be analogous to conventional diffraction contrast imaging in many aspects. The subsequent diffraction process depends also on the distance of the dislocation from the crystal bottom surface. The diffusely scattered electrons from a dislocation located at the top surface would be strongly channelled (or diffracted), but those from a dislocation located at the bottom surface would not undergo any diffraction. Hence, different contrast could be produced at the two ends of the same dislocation line, in agreement with experimental observations.⁴

In conclusion, Huang scattering contrast and channelling (or diffraction) contrast have been found to be dominant mechanisms in the images, obtained with high-angle hollow-cone dark-field TEM, of dislocations and grain boundaries.⁵

1. J. Bentley, K.B. Alexander and Z.L. Wang, Proc. XIIth Intern. Cong. for Electron Microsc., L.D. Peachey and D.B. Williams eds., San Francisco Press, 2, 400.

2. J.M. Cowley and Y. Huang, Ultramicroscopy 40 (1992) 171.

3. J. Bentley and K.B. Alexander, private communication (1990).

4. Z.L. Wang, Ultramicroscopy, submitted (1993).

5. This research was sponsored by the Division of Materials Sciences, U.S. Department of Energy, under contract DE-AC05-84OR21400 with Martin Marietta Energy Systems, Inc.

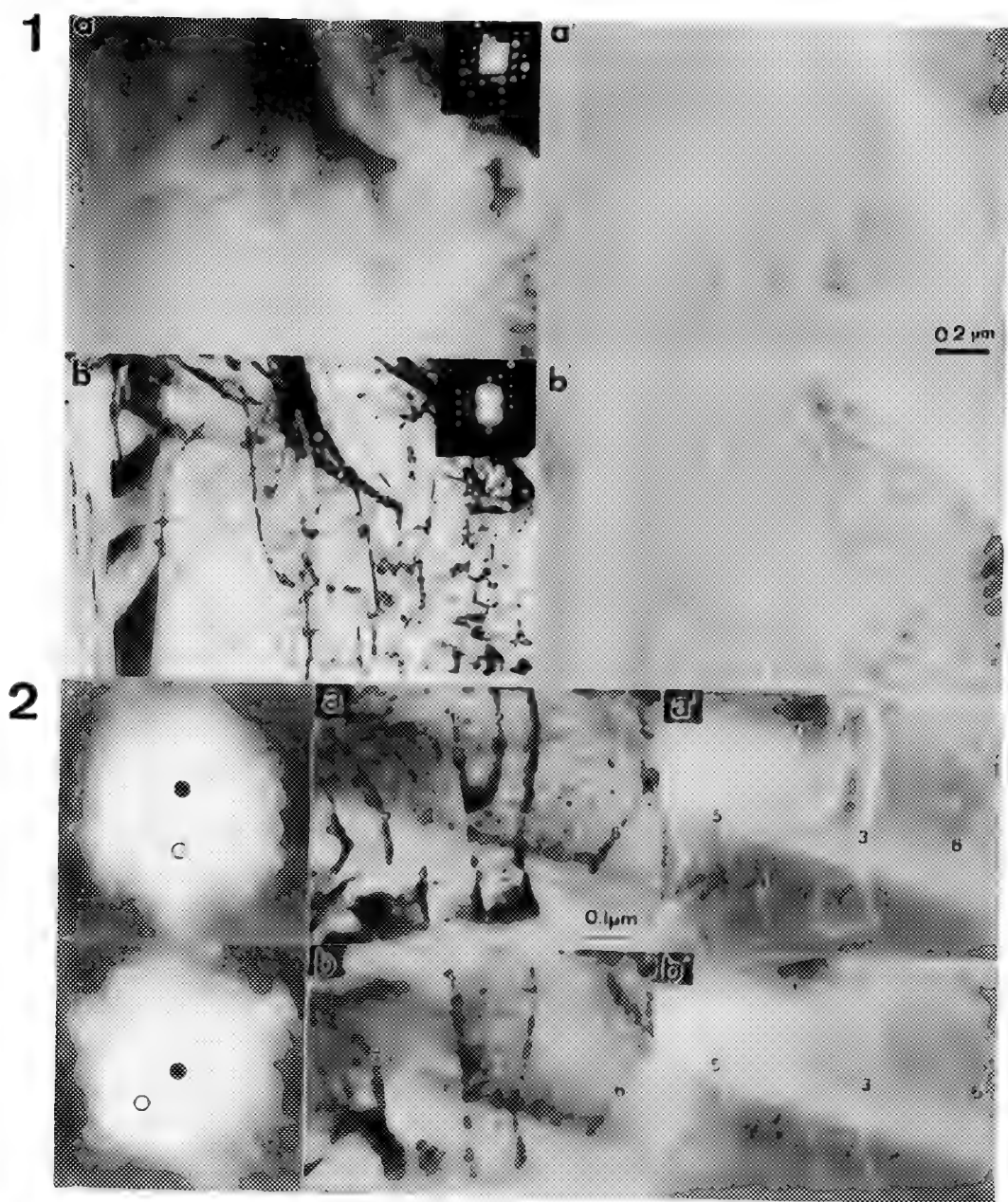


FIG.1.-- (a) and (b) are BF-TEM images and (a') and (b') are corresponding HADF-TEM images of Ag foil recorded under one-beam and two-beam diffracting conditions, respectively. $52 < \theta < 58$ mrad.

FIG.2.-- Comparisons of BF-TEM images (a, b) and HADF-TEM images (a', b') of Ag foil recorded under (a, a') $g = [440]$ and (b, b') $g = [400]$, two-beam diffracting conditions (left-hand side), showing dependence of HADF-TEM images on diffracting conditions that are set up for on-axis BF-TEM imaging. $63 < \theta < 69$ mrad. Solid circles and open circles indicate (000) and diffracted beams, respectively. Numbers indicate dislocations in BF-TEM image and their correspondences in HADF-TEM image.

THEORY OF TRANSMISSION LOW-ENERGY ELECTRON DIFFRACTION

W. Qian and J.C.H. Spence

Department of Physics, Arizona State University, Tempe, AZ 85287

Interpretation of the images from a point source electron microscope^{1,2} requires a detailed analysis of transmission low energy electron diffraction³. Here we present a general approach for solutions to the mixed Bragg-Laue case in transmission LEED (100-1000eV), based on the dynamical diffraction theory of Bethe⁴. However, the validity of the dynamical diffraction theory to low energy electrons can be justified by its connection to the band theory for low energy crystal electrons⁵.

Assume that the incident beam forms a plane wave and the crystal is a thin slab. According to Bethe, the total electron wavefield within crystal can be written as a linear combination of Bloch waves (equation 1). The Bloch wave excitation coefficients $b(\mathbf{j})$ can be determined by matching the boundary conditions, the wave amplitudes $C_g(\mathbf{j})$ and the wave vectors $\mathbf{k}(\mathbf{j})$ for each Bloch wave can be obtained by solving the time independent Schrodinger equations (equation 2).

$$\Psi(\mathbf{r}) = \sum_j b_j \sum_g c_g^{(j)} \exp\left(2\pi i [\mathbf{k}^{(j)} + \mathbf{g}] \cdot \mathbf{r}\right) \quad 1); \quad \left\{ K^2 - (\mathbf{k}^{(j)} + \mathbf{g})^2 \right\} C_g^{(j)} + \sum_{h \neq 0} U_h C_{g-h}^{(j)} = 0 \quad 2)$$

Therefore, the transmitted beam intensities can be evaluated for a given crystal potential. In the mixed Bragg-Laue case for transmission LEED (without high energy approximation), equation 2 yields $2n$ plane-wave components within crystal with wavevectors $\mathbf{k}(\mathbf{j})$. Which includes all of the forward and back-scattered beams, as well as the multiple scattering effects.

For low energy electrons diffraction (100 ~ 1000 eV) the main work is thus to determine the effective crystal potential. As for the case of kilovolt electrons, we write $V_{\text{eff}}(\mathbf{r})$ as

$$V_{\text{eff}}(\mathbf{r}) = V(\mathbf{r}) + V^{\text{ex}}(\mathbf{r}) + V^{\text{vir}}(\mathbf{r}) + iV'(\mathbf{r}) \quad 3).$$

Here, $V(\mathbf{r})$ is the elastic potential, $V^{\text{ex}}(\mathbf{r})$ presents the exchange effects between the incident and crystal electrons, $V^{\text{vir}}(\mathbf{r})$ is the real contribution to the crystal potential due to virtual inelastic scattering and $iV'(\mathbf{r})$ is the imaginary part of the potential which takes account of depletion of the elastic wavefield by inelastic processes ("absorption"). The elastic potential $V(\mathbf{r})$ can be obtained from X-ray scattering factors through the Mott-Bethe relation. The accurate determination of the exchange potential requires a full solution of the Hartree-Fock equation, using self consistent methods. However, as been commonly used in LEED, we evaluate $V^{\text{ex}}(\mathbf{r})$ through Slater potential based on the local approximation $V^{\text{ex}}(\mathbf{r}) = \text{const} \cdot \rho^{1/3}(\mathbf{r})$. The local electron density $\rho(\mathbf{r})$ was generated for our calculations using x-ray atomic scattering factors. For the virtual inelastic potential, it has been pointed out by Rez⁶ that there is no contribution from phonon scattering because phonon energies are too small. Plasmon scattering also gives no contribution to $V_g^{\text{vir}} (g \neq 0)$ because plasmon scattering is delocalized. The only contribution to $V_g^{\text{vir}} (g \neq 0)$ comes from inner shell single electron excitations, which is small due to the small excitation probabilities for low energy incident electrons (beam energy becomes comparable with the ionization threshold). We thus ignore $V_g^{\text{vir}} (g \neq 0)$. The contribution of virtual inelastic scattering to the mean inner potential V_0^{vir} can be estimated⁷ based on second order perturbation theory. Which gives $V_0^{\text{vir}} \sim 3$ eV in Aluminum for 250 eV incident beam electrons. The mean absorption potential V'_0 at different beam energies can be estimated using a model dielectric function⁸. However, the "anomalous" absorption coefficients (V'_g/V_g) of low energy incident electrons were converted for our calculations from the existing experimental values of the intensity absorption coefficients.

Many beam dynamical calculations have been performed based on equation 2 for thin Au films under plane wave illumination with energies in the range of 100 to 1000 eV. Figure 1 shows the total transmitted intensity versus film thickness for normal incidence on Au(110) at 250 eV. The intensity variations along film thickness for different beams are given in figure 2, for Au(110) at 260 eV. Which also shows the importance of multiple scattering effects for low energy electrons at thickness of larger than atomic dimensions. Figure 3 gives the corresponding reflected beam intensities versus crystal thickness. The intensities approach constant values when the crystal thickness is larger than about 50 Å, suggesting that this approach may also be used to calculate LEED intensities reflected from bulk crystals. Figure 4 shows the energy dependence of the transmitted beam intensities for a given thickness. Since the Ewald sphere is small, the electron intensity distribution is sensitive to beam energies. This work was supported by NSF Grant No. DMR91-12550. We are grateful to J.M. Zuo for useful discussions.

References

1. H.W. Fink et al., Phys. Rev. Lett. (1991) 67, 1543.
2. J.C.H. Spence et al., Proc. 51th Ann. MSA Meeting, Cincinnati (1993), submitted.
3. J.C.H. Spence and W. Qian, Phys. Rev. B (1992) 45, 10271.
4. H.A. Bethe, Ann. Phys. (Leipzig) (1928) 87, 55.
5. R.M. Stern et al., Reviews of Modern Physics (1969) 41, 275.
6. P. Rez, Acta Cryst. (1978) A34, 48.
7. W. Ichikawa and Y.H. Ohtsuki, J. Phys. Soc. Japan (1968) 27, 953.
8. D.R. Penn, Phys. Rev. B (1987) 35, 482.

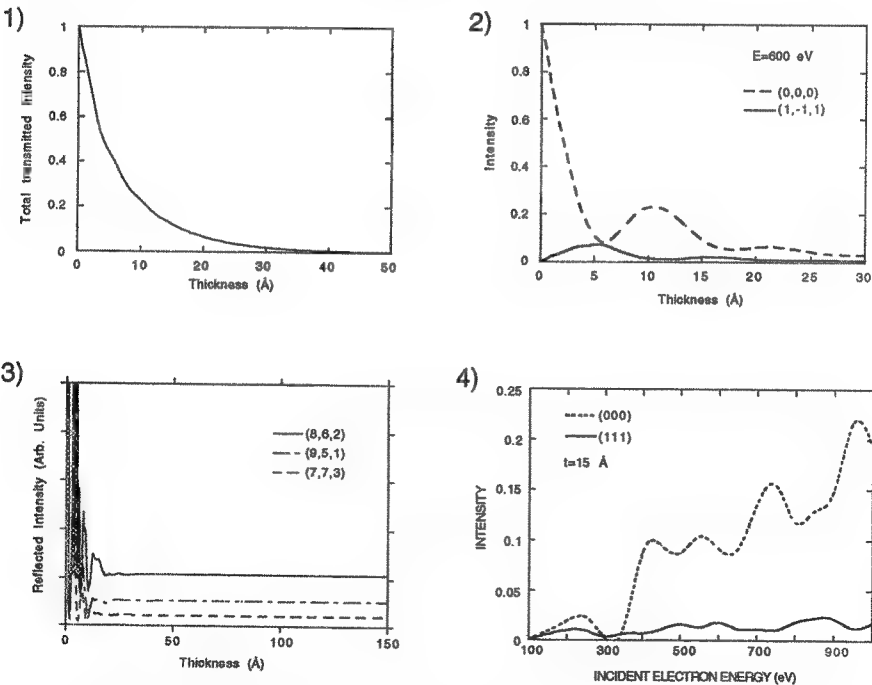


Fig.1. The total transmitted intensity versus crystal thickness at 250 eV along Au(110).
 Fig.2. Intensity variations of (000) and (111) beams along Au(110) for 600 eV incident electrons .
 Fig.3. The reflected beam intensities for 250 eV electrons on Au(110).
 Fig.4. Variation of transmitted beam intensities with beam energies for Au(110).

MEASUREMENTS OF DEBYE-WALLER FACTORS IN TiAl FROM ENERGY-FILTERED HOLZ LINE INTENSITIES

R. Holmestad, A. L. Weickenmeier, J. M. Zuo, J. C. H. Spence, and Z. Horita*

Dept. of Physics, Arizona State University, Tempe, AZ 85287, USA

*Dept. of Materials Science and Engineering, Kyushu University, Fukuoka, 812 Japan

This paper reports a new method to measure Debye Waller factors. The measurements are required for subsequent structure factor refinement in TiAl. The procedure is to obtain a large angle CBED pattern near a sparse zone axis, extract line scans *along* HOLZ lines from this pattern and use two beam intensity calculations to fit experiment and simulation by varying the Debye Waller factors. Unlike earlier work^{1,2}, we have used non-systematic reflections. The material studied is γ -TiAl (50-50), made from 25g ingots produced by arc-melting in an argon atmosphere, and homogenized for 1 day at 1473 K. Specimens were thinned by twin-jet electropolishing.

Elastic energy filtered patterns are required for accurate quantitative comparisons between experiment and theory. A Zeiss 912 Omega TEM/STEM electron microscope was used to obtain energy filtered CBED patterns, fitted with an Omega imaging energy filter, which forms images or diffraction patterns within any desired energy loss range. The Omega filter (and microscope command set) may be controlled by the same Macintosh computer which supports the Gatan model 679 CCD-camera used to acquire the CBED patterns. The smallest convenient energy window is about 10 eV, thus all the plasmon loss electrons are removed from the image if the window is set about the elastic peak. The energy loss due to phonon scattering is too small, so it is important to use a cold stage holder to reduce thermal scattering and reduce contamination. Mixed phonon-plasmon scattering, however, is removed, and this constitutes the bulk of the inelastic scattering. The Debye Waller factors thus refer to the cold stage temperature of -154°C.

A problem with the CCD-camera is the long tail in the point spread function³. This may be corrected to some extent by deconvolution. However, it is impossible to acquire a complete diffraction pattern on the CCD camera (pending the arrival of free lens control software), so that some film data was also used for indexing patterns. Figure 1 shows the energy filtered CBED pattern which was analyzed. The beam direction is near the $[-5\ 1\ 2]$ zone. The thickness was found from the $(1\ -3\ -1)$ rocking curve to be 964 Å.

Line scans along each HOLZ line were extracted, and the intensity variations were compared with simulations. Due to dynamical interactions the line profiles are not constant, as shown for the $(1\ 5\ 0)$ line in figure 2a. Figure 2b shows the simulation using Bloch wave calculations. In regions with only slight variations, the intensity is almost two-beam like. Here two-beam theory might successfully be applied to determine Debye Waller factors. To do so, a fitting program based on two beam theory has been set up to adjust theoretical intensities to the experimental counts using a χ^2 -criterion. Absorption due to phonon scattering has been taken into account employing the Einstein model⁴.

Table 1 shows the lines used and the fitted two-beam theoretical and experimental intensities, respectively. The value of χ^2 was found to be 20 for a mean square thermal displacement $\langle u^2 \rangle$ of 0.0036Å^2 (Ti) and 0.0077Å^2 (Al), respectively. These correspond to the Debye Waller factors $B=8\pi^2\langle u^2 \rangle$ of 0.28Å^2 and 0.61Å^2 , which are close to earlier results⁵. The Debye Waller factors were found to be insensitive to absorption. The large deviations from the experimental intensities are due to multi-beam interactions, which may be accounted for using a Bethe type effective potential rather than a pure two beam potential⁶.

R. H. is supported by Royal Norwegian Council for Scientific and Industrial Research. A.L.W. thanks the Alexander von Humboldt Stiftung for financial support. This project is supported by NSF grant DMR 9015867 and facilities of the ASU-NSF National Center for HREM.

References

1. Y. Ma, C. Rømming, B. Lebech, J. Gjønnes and J. Taftø, *Acta Cryst.* B48 (1992), 11.
2. For review, see J. Spence and J.M. Zuo, *Electron Microdiffraction*, Plenum, 1992.
3. W.J. de Ruijter and J.K. Weiss, *Rev. of Sci. Instr.* (1992) 63, 4314.
4. A. Weickenmeier and H. Kohl, *Acta Cryst.* A47 (1991), 590.
5. A. G. Fox, T.A. Stoner and S.C. Cade, *Scripta Met.*, 27 (1992), 1765.
6. Zuo et al., these proc.

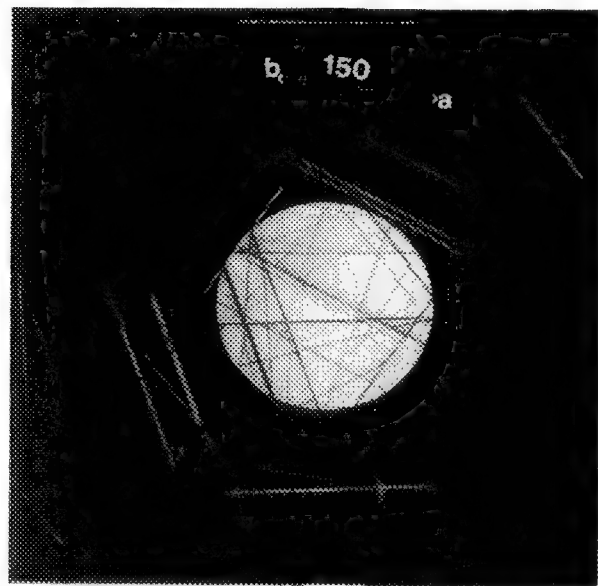


FIG. 1. Energy filtered CBED pattern from TiAl, 120 kV, T= -154°C, thickness 964 Å, near [-5 1 2] zone axis.

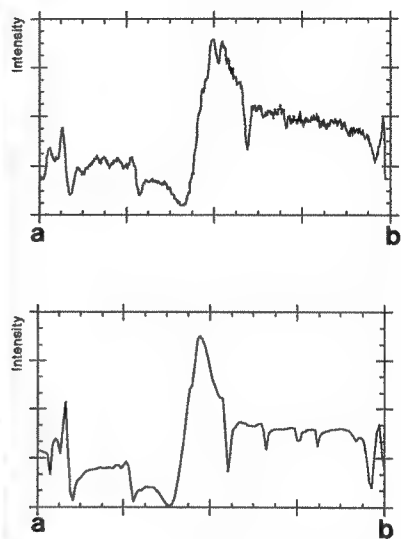


FIG. 2. Line profiles along the (1 5 0) disc.
a) Experimental
b) Simulated, using Bloch wave calculations

TABLE 1. Indices of the reflections used to fit the Debye Waller factors, experimental and fitted counts, deviation between fit and experiment in %.

h k l	experimental (counts)	fit (counts)	deviation (%)
1 5 0	510	511	0
2 -2 8	629	592	-5
2 6 2	1400	1510	8
-1 -5 1	2830	2660	-5
-3 -5 -5	1070	892	-16
3 1 9	375	328	-12
-3 -7 -3	491	661	34
-1 3 -5	2090	2150	3
0 6 4	1360	1140	-16
2 4 4	1930	2060	6

A STREAMLINED PROCEDURE FOR ACQUISITION AND MEASUREMENT OF ELECTRON-DIFFRACTION PATTERNS

D.C. Dufner and J.M. Ehrman

Electron Microscopy Center, Texas A&M University, College Station, Texas 77843

Electron diffraction is one of the most widely used techniques in the characterization of materials in the TEM. There are a number of computer programs used for measuring, indexing, and simulating electron diffraction patterns (EDP's), but many are stand-alone programs and require significant user interaction. For example, EDP's obtained on the JEOL 2010 in the Texas A&M Electron Microscopy Center can be measured with the Electron Diffraction Pattern Analysis¹ software provided with the Oxford Instruments eXL system. A separate program is used to acquire the pattern from the TV camera output, while the EDP Analysis program requires the user to select the transmitted and diffracted beams for measurement. Only two values of d-spacings are calculated by this program, which places an additional burden on the user to select other spots in order to get a more complete measurement of the pattern.

In this work, we propose a more streamlined approach in acquiring, saving, and measuring EDP's on a PC-based computer system. A schematic of the hardware/software configuration is shown in Figure 1. On the JEOL 2010, a Gatan Model 622 Mark II TV camera is used to collect the EDP's in the form of either live images or images recorded on videocassette tape. The Oxford Instruments eXL system utilizes a PC computer with a video frame averager to acquire and save images in MS-DOS format. When a pattern is saved, the macro sequence calls up Image-Pro Plus² to measure the pattern. Image-Pro Plus is used to determine the centroid positions of the transmitted and diffracted beam spots as shown in Figure 2, and a set of d-spacings is calculated from the measured distances between the spots (Figure 3). In the noninteractive user mode, a fixed window is used to limit the number of spots to be measured, while an interactive mode allows the user to specify the area of interest for analysis. When an EDP is selected, a macro sequence is initiated to perform all the operations, thus allowing the user to either interactively or noninteractively obtain a set of calculated d-spacings for that pattern.

This procedure was developed during the current investigation of chemical reactions in the Pt-Sn thin film system.³ In this study, numerous reaction products were found throughout the specimen grid. EDP's of these products were obtained by translating the grid with the TEM in the "diffraction" mode and recording these patterns on videotape. Due to the large number of different EDP's obtained in this study, the use of this on-line acquisition and measurement procedure represented a significant increase in time savings. This procedure would be very useful for analyzing a large number of EDP's obtained from well-populated sample grids such as those used for analysis of asbestos and other dispersed particulate materials.⁴

References

1. Electron Diffraction Pattern Analysis, v. 1.01, is a registered product of Oxford Instruments Ltd., Eynsham, Oxford, United Kingdom.

2. Image-Pro Plus, v.2.00.06, is a registered product of Media Cybernetics, Silver Spring, MD, U.S.A.

3. D.C. Dufner, Proc. Ann. EMSA Meeting 50(1992)52.

4. Partial support of this research was provided by the Center for Energy and Mineral Resources, Texas A&M University, College Station, Texas 77843. The use of instrumentation in the Texas A&M Electron Microscopy Center is gratefully acknowledged.

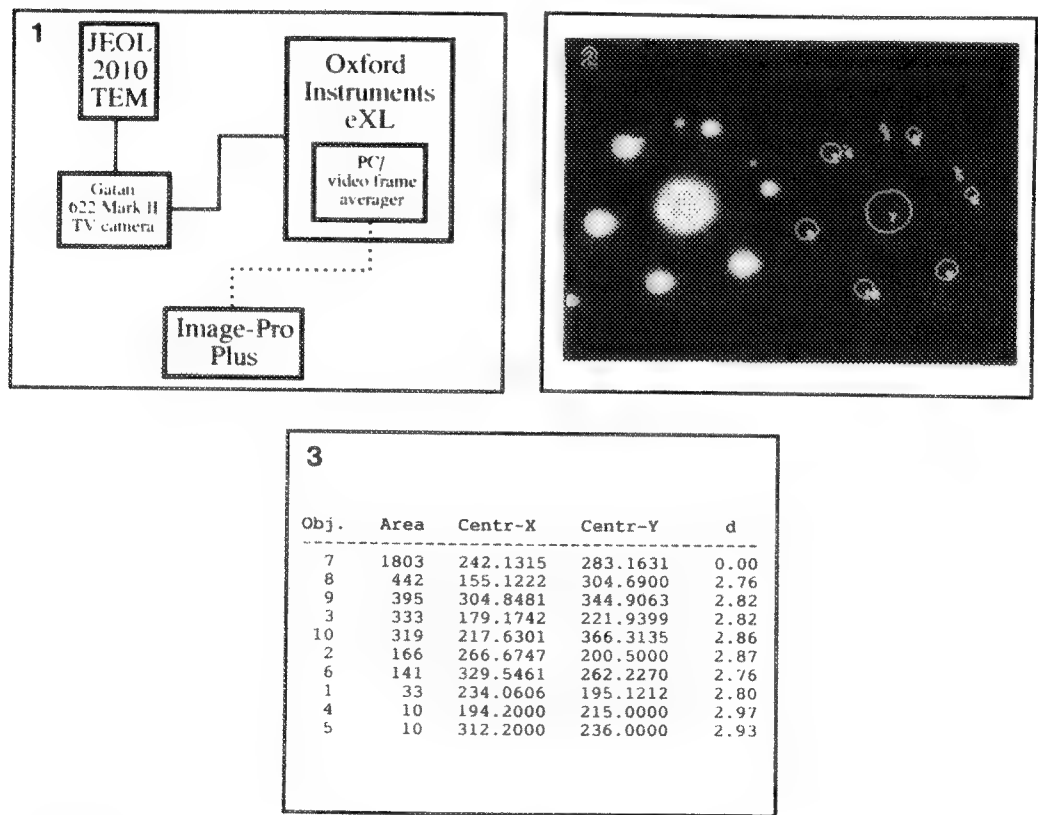


FIG. 1. -- Schematic drawing of hardware/software configuration used for acquisition and measurement of EDP's.

FIG. 2. -- [100] zone pattern of beta-Sn showing outline of spots by Image-Pro Plus. Normally, the outline is superimposed on the diffraction pattern, but it is shifted to the right for clarity.

FIG. 3. -- Printout of measurement results from diffraction pattern in Fig. 2. Image-Pro Plus determines the area of each spot and sorts the spots in descending order. Centroid positions of each spot are then determined, and d-spacings are calculated from distances between transmitted spot (#7) and diffracted spots.

BICRYSTALLOGRAPHY AND ELECTRON DIFFRACTION

Vinayak P. Dravid

Dept. of Materials Science & Engineering, Northwestern University, Evanston, IL 60208

Traditionally grain (or phase) boundaries have been modelled using coincidence site lattice (CLS)-type geometrical treatments¹. However, CSL utilizes only the lattice-translational symmetry of the crystals and is not applicable to nonsymmorphic crystals or in cases where the point group symmetry elements are important. Pond and coworkers², in an elegant series of papers proposed a complete geometric description of bicrystal containing an interface, i.e. bicrystallography. The use and application of bicrystallography has important implications for interface/surface structure, thin film growth and small particle studies.

Theoretical development of bicrystallography (or tricrystallography..etc.) is rather complete. However, same is not the case for experimental bicrystallography. There two important methods for bicrystal diffraction experiments: one is the plan-view technique, while the other involves edge-on interface parallel to the electron beam. Plan-view CBED can determine loss of symmetry due to RBT as demonstrated by Eaglesham et al.³ Dravid et al.⁴ used plan-view CBED to probe the symmetry of NiO-ZrO₂(CaO) eutectic interfaces. Figure 1 shows the expected symmetries in BF/WP and ZOLZ in the absence of an in-plane RBT. Figure 2a shows that the ZOLZ and WP symmetry conform to the absence of in-plane RBT. The survival of the sole mirror is confirmed by tilting along the mirror plane, as in Figure 2b.

We have also utilized the edge-on geometry of interfaces in nanodiffraction experiments for symmetrical tilt-grain boundaries in SrTiO₃. Symmetrical tilt grain boundaries contain well-defined and periodically arranged structural units. These structural units, to an approximation, define the atomic structure of interfaces. Figure 3 is an empirical model of a $\Sigma = 5$ (310) tilt-grain boundary in SrTiO₃, containing well-defined structural units at the boundary core. An in-plane rigid body translation (RBT) of $1/2[130]$ was identified using CTEM and HRTEM. As a first step, the structural model in Figure 3 was used as an input for diffraction simulations. Gaussian probes of various sizes, from 0.60 nm - 1.6 nm (FWHM), which are experimentally attainable probes in our HF-2000 200 keV cFEG TEM, were employed in multislice simulations. Simulations for probe size of 1.6 nm are shown in Figure 4, for three locations within the grain boundary core: on Sr site (a), on Ti site (b) and within a structural unit (c). The presence of RBT is well reflected in the lack of mirror symmetry, especially when the probe is located on Ti sites and within the structural units. One experimental nanodiffraction pattern which closely matches the probe size of 1.6 nm (Figure 4a) is shown in Figure 4d. Asymmetric streaking normal to the interface plane is clearly present in the experimental pattern. Additional experimental and theoretical results will be presented at the meeting. It will be argued that plan-view CBED and nanodiffraction are viable complementary quantitative technique for determination of the core structure of defects and interfaces.⁵

References:

- 1) W. Bollman, Crystal Defects and Crystalline Interfaces (springer-Berlin, 1970).
- 2) R.C. Pond & D. Vlachavas, Proc. Roy. Soc. Lond., 386A, p. 95 (1983).
- 3) D. Eaglesham et al., Phil. Mag., A60, p. 161 (1989).
- 4) V.P. Dravid et al., Proc. MRS, Vol. 159, p. 95 (1990).
- 5) This research is supported by the U.S. Dept. of Energy-DE-FG02-92ER45475 and NSF-DMR 9203722. The author acknowledges Mr. V. Ravikumar and X. Lin for assistance and useful discussions.

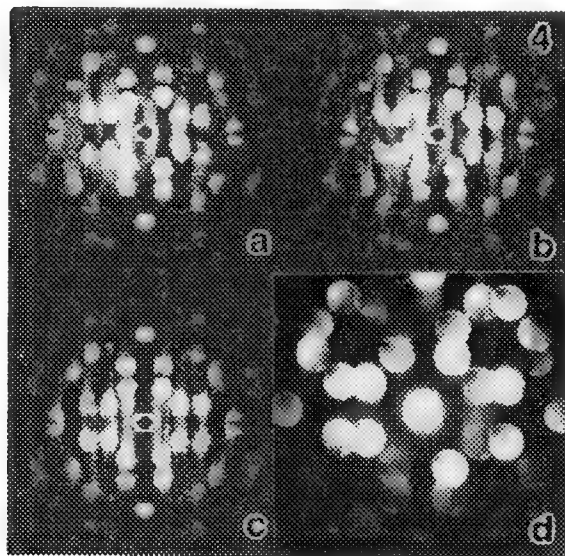
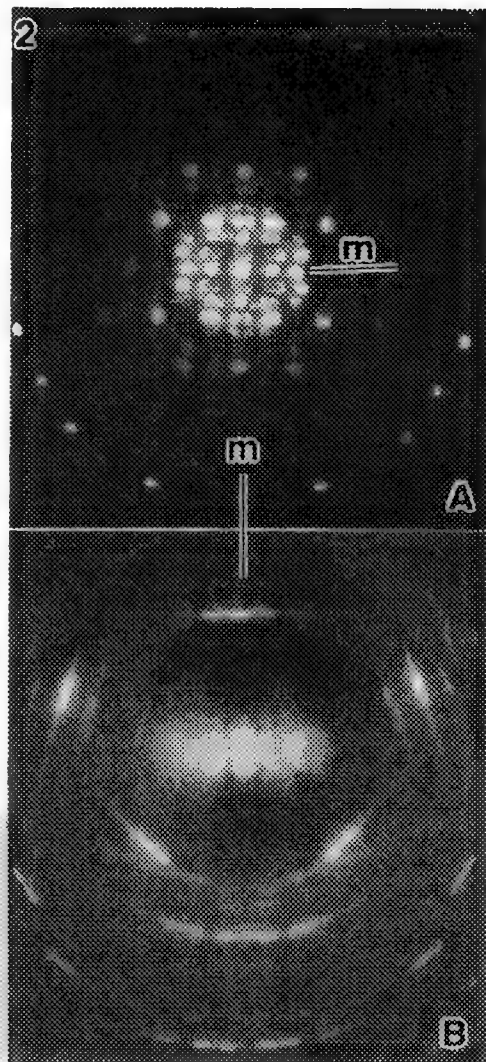
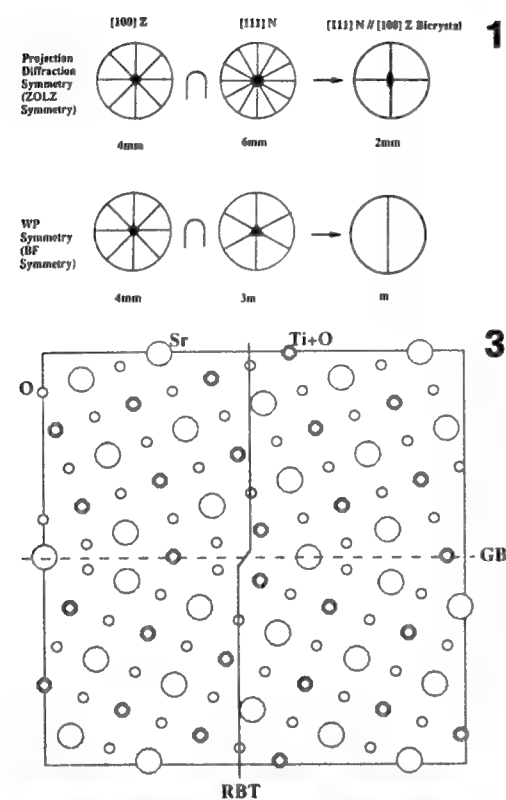


Figure 4: Nanodiffraction pattern with a 1.6 nm probe on (a) Sr site, (b) Ti site, (c) within a structural unit of the grain boundary, and (d) an experimental nanodiffraction pattern from the grain boundary.

Figure 1: Stereographic representation of expected symmetry in ZOLZ and BF/WP for NiO-ZrO₂(CaO) plan-view CBED. **Figure 2:** Plan-view CBED patterns (A): ZOLZ (2mm symmetry), WP (m symmetry), and (B) Confirmation of BF mirror after tilting along "m". **Figure 3:** An empirical structural model of the $\Sigma=5$ SrTiO₃ boundary incorporating the observed RBT.

THE ATOMIC-FORCE MICROSCOPE AND ITS FUTURE IN BIOLOGY

Jean-Paul Revel

Division of Biology, California Institute of Technology, Pasadena CA 91125 USA

The last few years have been marked by a series of remarkable developments in microscopy. Perhaps the most amazing of these is the growth of microscopies which use devices where the place of the lens has been taken by probes, which record information about the sample and display it in a spatial from the point of view of the context. From the point of view of the biologist one of the most promising of these microscopies without lenses is the scanned force microscope, aka atomic force microscope.

This instrument was invented by Binnig, Quate and Gerber and is a close relative of the scanning tunneling microscope.¹ Today's AFMs consist of a cantilever which bears a sharp point at its end.² Often this is a silicon nitride pyramid, but there are many variations, the object of which is to make the tip sharper. A laser beam is directed at the back of the cantilever and is reflected into a split, or quadrant photodiode. Either the cantilever or the sample is mounted on a piezo crystal which moves in X, Y and Z. At the beginning of a series of observations the cantilever is made to approach the sample until contact is made. As the cantilever 'touches' the sample it flexes slightly causing the reflected laser beam to move on the photodiode. The ratio of the currents put out by the different segments of the photodiode changes as the position of the reflected laser beam shifts. When the sample and cantilever are made to move relative to each other by scanning in X and Y, the resultant changes in signal from the photodiode can be used to form an image of what as a first approximation represents the sample topography. This detection system is so sensitive that it can register motions of less than an 0.1 nm in X and Y and a tenth of that in Z.

Contrary to what is the case in STM there need be no current flow between tip and sample. The sample can be an insulator or a conductor and it can also be immersed in fluid such as aqueous solutions. Thus, a priori, the AFM is ideally suited to work with biological samples, which are often insulators and need to be hydrated to be in natural state. Resolution is determined not only by the sensitivity of the detection system but by other factors as well, some instrumental and others, specimen dependent. A major instrumental factor is the shape of the tip. A coarse tip will make objects appear thicker (but not taller) than they are, and can also "skate" over closely placed objects showing one where there are two or more. In order to increase resolution and to allow probing of deep narrow structures, thin long tips are being designed. One approach to their fabrication, a twist on a major problem in electron microscopy, is to deposit contamination by focusing an electron beam on a "dirty" cantilever (or in a dirty microscope). The contamination which builds up takes the shape of a long thin needle which can be further sharpened by ion beam etching. Thus the bane of one microscopy becomes the height of technology of another. Scanned force microscopes can be used to study hard specimen at high resolution. It is more difficult to image biological molecules because they are much more compliant, so that the force applied by the tip has to be adjusted to a sufficiently low level so that it does not distort the sample rather than following its contour. In spite of this the AFM has already been used to study bacteriorhodopsin in purple membranes³ and components of the cell walls of bacteria^{4,5} as well as a number of other types of specimens which would a priori be expected to be soft. The ability of the AFM to distort the sample has been put to good advantage in the study of gap junctions⁶. At low forces (<2 nN) isolated gap junction plaques can be scanned continuously without any apparent change in structure. As the force is raised above 10nN however the uppermost of the two apposed membranes which form the gap junction becomes scraped off. This reveals the usually inaccessible extracellular face of gap junctions and permits a detailed study of the structure of the part of connexons which protrudes out of the membrane. Imaging connexons in this way shows that they are cylinders which protrude from the membrane about 1.4+/-4nm.⁷ The central pore has a diameter of 3.8nm on the extracellular side, and the probes can penetrate the pore up to 0.7nm. The wall is not uniform but shows a series of 5 or 6 crenations, suggesting that each represents one molecule of connexin. We and

others⁸ have also successfully begun an examination of both native and reconstituted collagen by AFM. The detail visible demonstrates a resolution equal to that achieved in replicas examined by electron microscopy. Study of hydrated collagen suggest that in vivo the outline of the collagen fibrils may be much smoother. The characteristic period seen in EM specimen may be due to collapse of regions of the fibrils where the tropocollagen subunits are not so tightly packed.

While results up to now suggest that the AFM may allow study of the topography of hydrated biological samples at resolutions even now close to those achievable by electron microscopy, I believe that it may become even more significant a tool for the study of live cells at high resolution.^{see 9} For years one of the dreams of cell biologists was to observe the behavior of cells and membrane components at high resolution. There were a number of attempts at fabricating environmental chambers which would allow cells to survive while being thin enough, not to degrade the quality of the images to too large a degree. The AFM may well present us with the opportunity to study the behavior of molecules in or near the cell membrane. A major hurdle will be to learn to use the AFM as something other than a tool for topographic analysis. In fact it is already clear that the signals are rarely just topographic. Inflection of the cantilever result from tip sample interactions which include attraction and repulsion by charges on tip and sample as well as bond formation between the two. It is possible to imagine that a systematic investigation will permit the use of tips to which specific probes will have been attached and which therefore may become useful in tracking cell surface molecules with which these probes would interact.

References

1. G. Binnig et al. *Phys.Rev.Lett.* (1986)56, 930.
2. T.R. Albrecht et al. *J.Vac.Sci. Technol.* (1990) A8, 3386.
3. H.-J.Butt *Biophys. J.* (1990)58, 1473.
4. F. Schabert et al. *Ultramicroscopy* (1992) 42-44, 1118.
5. G. Devaud et al. *Biophys. J.* (1992) 63, 630.
6. J.H.Hoh et al. *Science* (1991) 253, 1405.
7. J.H.Hoh et al. *Biophys. J.* in press
8. D.R. Baselt et al. (in preparation).
9. E.A.G. Chernoff and D.A. Chernoff (1992) *J.Vac. Sci. Technol.* A10, 596.
10. J.H.Hoh and P.K. Hansma (1992) *Trends Cell Biol.* (1992)

PREPARATION OF PLAN VIEW AND CROSS-SECTIONAL SPECIMENS FOR TEM

Peter J Goodhew

Department of Materials Science & Engineering, University of Liverpool, Liverpool L69 3BX, UK

The preparation of thin specimens remains one of the most important aspects of electron microscopy. Over the forty years in which materials TEM has been practised the rate of introduction of radically new techniques has been very low^{1,2,3}. In the 1960s microscopists were using electropolishing, chemical polishing, mechanical polishing, ion beam thinning and ultramicrotomy, many of which are also covered in this symposium thirty years later. The last three decades have seen a process of refinement and automation so that success rates and areas of thin sample are both much higher in the 1990s than they were in the 1960s. However the preparation of good specimens still requires skill and an element of "art" remains. The increase in electron energy which helped microscopists to overcome limitations of specimen preparation in the 1970s has now (for very good reasons) stopped, so the basic specimen thickness requirements for standard microscopy are now stable.

A simple flow diagram (Figure 1) indicates the methods most frequently used for many common sample geometries. The development of a huge variety of TEM-based imaging and analysis techniques has, however, meant that the requirements of a good specimen are now extremely stringent. The microscope technique to be used often dictates the critical features of the specimen, which must be delivered by the chosen preparation technique. Thus the list of key requirements now looks like this:

For EDX and EELS, including PEELS: No elemental segregation or re-deposition.

For HREM: Very thin regions supported by very stable areas.

For large angle CBED (LACBED): Fairly flat specimens without buckling or bending.

For quantitative hyleography: Parallel-sided specimens whose thickness is easily measured.

The range of techniques which are readily considered by the Materials Scientist has increased - there is now a willingness to consider ultramicrotomy (which was actually being used in the 1960s by V A Phillips and is now enjoying a resurgence) and the preparation of cross-sections is no longer considered impossibly daunting. Some types of specimen still present huge difficulties, and these difficulties are not likely to be resolved very quickly: There is a fundamental problem associated with the thinning of any pair of materials with very different properties. This situation arises in most structural composite materials, in which the fibre/matrix or particle/matrix interfaces are of particular interest, and in metal/semiconductor combinations where again the interfaces are of concern. It is never going to be easy to thin such specimens uniformly, since all methods of erosion tend to act differentially on materials with radically different mechanical and chemical properties. Nevertheless some successful examples will be discussed.

One entirely new technique has been developed in the last five years: The cleavage of small blocks of semiconductors so that they contain two perfectly orthogonal faces is not difficult (and is very rapid). If such a sample is examined in transmission through the 90° "wedge" then a unique sample can be studied in which the exact thickness is known at any point in the image. This then makes quantitative image interpretation uniquely possible.

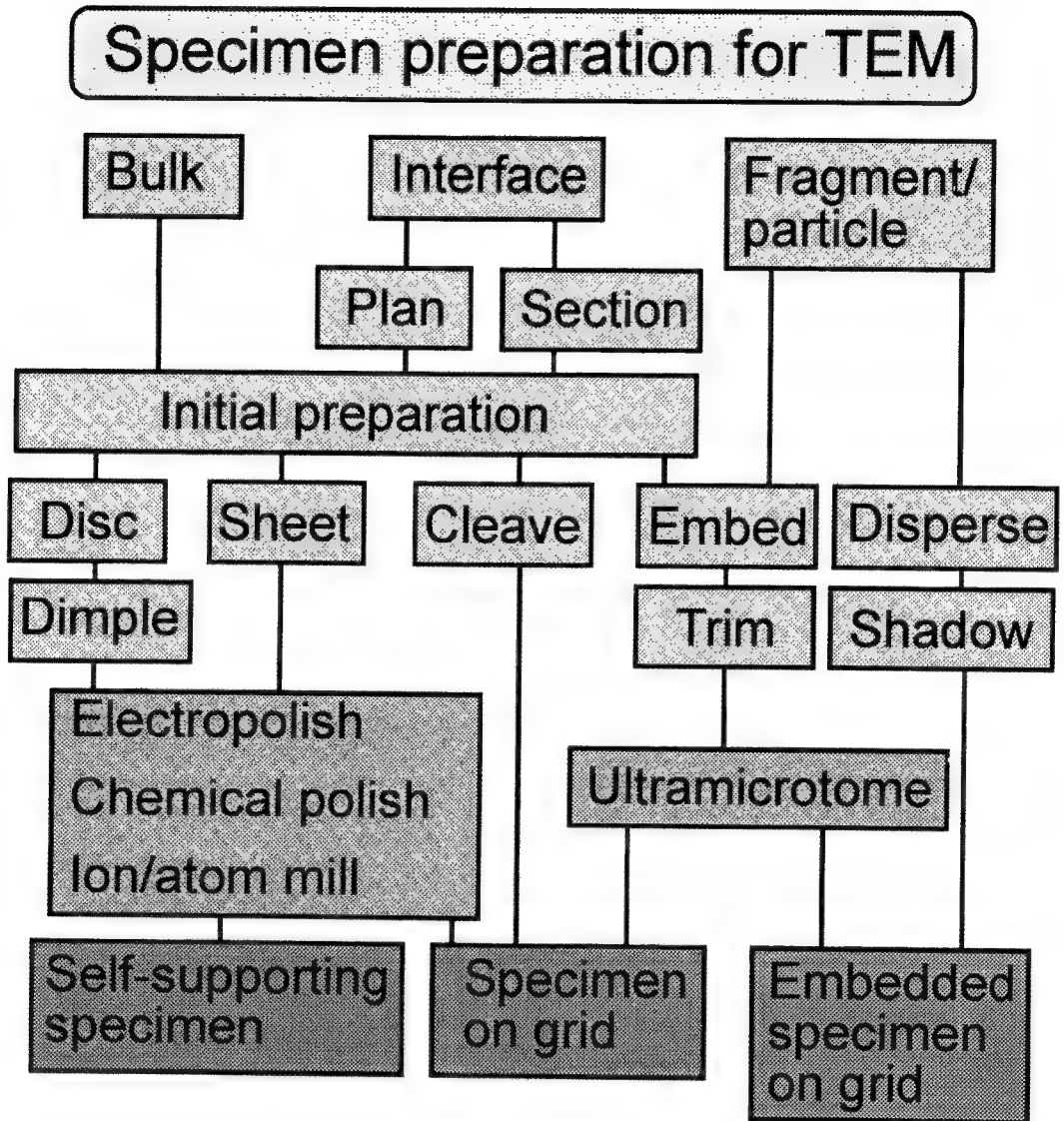


Figure 1. The major routes to thin specimens in materials science.

References

1. P J Goodhew "Thin Foil Preparation for Electron Microscopy" Vol 11 of Practical Methods in Electron Microscopy (Ed A M Glauret), Elsevier (1985)
2. P J Goodhew, Specimen preparation for transmission electron microscopy, RMS Handbook No. 3 Oxf Univ Press (1984)
3. P J Goodhew in "Specimen Preparation for Transmission Electron Microscopy of Materials" Ed J C Bravman, R M Anderson & M L McDonald MRS Symposium Proceedings Vol 115 (1988) 51-62

Rapid Preparation of Semiconductor Cross Sections for TEM Analysis

John Benedict, Ron Anderson and Stanley J. Klepeis

IBM, Department 13W, Building 630-E40, East Fishkill Facility, Hopewell Junction NY 12533-0999
USA

Semiconductor manufacturers examine cross sections of their semiconductor devices to check the quality and integrity of their product. The growing complexity and diminishing size of these devices has caused manufacturers to increasingly rely on the resolving and analytical capabilities of TEM. The manufacturers' requirements for TEM analysis are: high specimen preparation spatial resolution (preparation of a specific area, usually less than 0.5 microns in size), a large sample area (at least 0.5 mm) available for examination, and a short sample preparation time (e.g. several hours). To meet these needs we have developed a technique for rapid preparation of cross sections for TEM analysis.¹

The specific area to be cross sectioned on the sample is identified by marking it with a laser or Focused Ion Beam (FIB) tool. The sample is then cut down to a 3 × 6 mm rectangle with the area of interest in the center. This rectangle is mounted using wax onto a Tripod polisher with the area of interest protruding over the edge of the polisher. The sample is then wet polished down to the area of interest using a series of progressively finer grit diamond lapping films (30, 15, 6, 3, 1, 0.5, 0.1 micron) and water. A final polish of Syton HT-50 on a cloth cover wheel is used to polish into the area of interest and remove any scratches from the polished surface. This polished surface is then carefully wiped with a soapy cotton swab and rinsed with running water to remove any Syton HT-50 residues. The wax holding the sample to the Tripod polisher is dissolved using acetone and the sample is cleaned off in an ethanol rinse. The polished surface is attached to the polisher using Ross Ultra Super Glue with the remaining portion of the sample protruding past the end of the polisher. The sample is then wet polished down to the area of interest using the same series of diamond lapping films (30, 15, 6, 3, 1, 0.5, 0.1 micron) and water. The diamond lapping films are used to polish the sample down to optical transparency, and, in the case of silicon, until the sample appears light orange under transmitted light. Syton HT-50 on a cloth wheel is used to polish into the area of interest and remove any scratches from this surface. The sample is polished with Syton until multicolored fringes appear. The sample is then removed from the polisher using acetone and rinsed in ethanol. The aperture of a 2 × 1 mm slotted grid is centered over the area of interest and the sample is glued to the grid using M-Bond 610 adhesive. The adhesive is cured at 70°C for 15 minutes, after which the sample is ready to be examined in the TEM.

The process outlined above usually takes less than 4 hours from start to finish. The TEM specimen has a large area (usually >0.5 mm) available for analysis. Associated techniques such as ion milling may be used on the sample, especially for the case when the specimen contains tungsten components.

References:

- 1.) S. J. Klepeis, et al., in Specimen Preparation for Transmission Electron Microscopy of Materials, ed. Bravman, et al., Mater. Res. Soc. Proc. **115**, Pittsburgh, PA USA p. 179 (1987). R. M. Anderson et al., Microscopy of Semiconducting Materials 1989, Proceedings of the Physics Conference held at Oxford University, 10-13 April 1989, ed. by Cullis, A. G. and Hutchison J. L., Institute of Physics Conference Series Number 100, Bristol and New York, 1989. Benedict, J.P. et al., *EMSA Bulletin*, **19**, 2, p. 74, 1989. Klepeis, S. J., et al., *EMSA Proceedings*, ed. by Bailey, G.W., San Francisco Press, p. 712, 1989. Benedict, J.P. et al., in International Symposium on Electron Microscopy, ed. by Kuo, K. and Yao, J., World Scientific, p. 450, 1990. Benedict, J. et al., in Specimen Preparation for Transmission Electron Microscopy of Materials-II, ed. Anderson, R., Mater. Res. Soc. Proc. **199**, Pittsburgh, PA USA p. 189 (1990). Benedict, J. et al., in Specimen Preparation for Transmission Electron Microscopy of Materials-III, ed. Anderson et al., Mater. Res. Soc. Proc. **254**, Pittsburgh, PA USA p. 121 (1992). Anderson, R. in Specimen Preparation for Transmission Electron Microscopy of Materials-III, ed. Anderson et al., Mater. Res. Soc. Proc. **254**, Pittsburgh, PA USA p. 141 (1992).

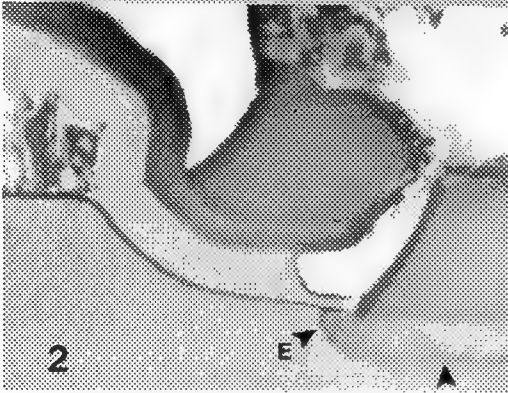
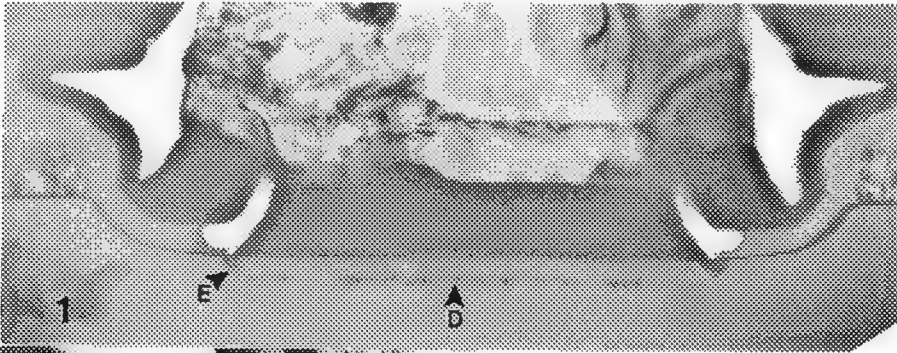


Figure 1. Low-magnification TEM micrograph showing etch pits (E) and dislocations (D) under contact.
 Figure 2. Higher magnification of the same contact showing etch pits and dislocations.
 Figure 3. Drawing of Tripod polisher showing specimen placement on polisher.

ADVANCES IN ULTRAMICROTOMY FOR PHYSICAL SCIENCES APPLICATIONS

G. McMahon* and T. Malis**

*Inst. for New Materials, Bau 43, Univ. Saarbrücken, D-6600, Germany

**Metals Technology Laboratories, CANMET, 568 Booth St., Ottawa, Canada K1A 0G1

As with all techniques which are relatively new and therefore underutilized, diamond knife sectioning in the physical sciences continues to see both developments of the technique and novel applications.

Technique Developments Development of specific orientation/embedding procedures for small pieces of awkward shape is exemplified by the work of Bradley et al on large, rather fragile particles of nuclear waste glass¹. At the same time, the frequent problem of pullout with large particles can be reduced by roughening of the particle surface, and a proven methodology using a commercial coupling agent developed for glasses has been utilized with good results on large zeolite catalysts². The same principle (using acid etches) should work for ceramic fibres or metal wires which may only partially pull out but result in unacceptably thick sections. Researchers from the life sciences continue to develop aspects of embedding media which may be applicable to certain cases in the physical sciences. Mascorro and co-workers³ have studied alterations to the standard mixtures for embedding resins with a view to lower viscosity and more rapid hardening, while Giamarra et al⁴ have examined the effects of microwave radiation for faster polymerization of the popular LR White resin. It would be useful to check if such radiation has any influence on the unfortunate tendency of embedding resins (along with most grid support films) to break down under the electron beam and redeposit on the surrounding portion of the section⁵, a problem for C-analysis or, if severe, for EEL analysis or elemental mapping.

Commercial developments have been both minor - countering the annoying reactivity of LR White with standard BEEM capsules by producing covered PTFE molds for flat embedding - and major, namely significant redesigns of ultramicrotomes for reduced vibrations, more accurate feed and increased 'operator friendliness'. Although usage of 35° and 55° diamond knives continues to grow, one of the more surprising developments has been the performance of the 45° histo or thick-sectioning knife with regard to ultrathin sectioning⁶. Extensive usage of two of these less costly knives (from different suppliers) has shown that they consistently produce flatter sections which are closer to the set thickness and that they are as good as 55° knives for sectioning hard particles and composites. On the minus side, it is not yet clear if resharpening will maintain the histo cutting performance, and the high frequency of knife marks from the (apparently) 'serrated' edge tends to pull apart weakly-bonded interfaces and can lead to virtual 'shredding' of the section below 20nm set thickness. However, it was amongst such shreds, cut by a state-of-the-art ultramicrotome, that the thinnest section fragments in the authors' experience have been found recently - of the order of 8-9nm thick (in Al) over regions suitable for extensive HREM. Such thicknesses may be crucial to the study of nanocrystalline materials (below).

Applications As materials applications and combinations grow ever more diverse, it becomes more difficult to differentiate them from some life science applications. Thus, studies of Ti implants in tooth/tissue material⁷, or cross-sections of avian eggshells⁸ (the latter winning the EMSA/Diatome Award for creative microtoming in 1992) may provide useful information for physical scientists regarding the methodologies used. More conventional physical science applications include the study of large (80-250 micron) Ni sulfide inclusions which shatter tempered glass when they undergo phase transformations⁹, or the study of segregation in irradiated stainless steel since the low mass of the microtomed section greatly reduces the X-ray count rate caused by the irradiation¹⁰. Limited success has been achieved with the sectioning of semiconductors for HREM of interfaces, eg HgCdTe on GaAs or ZnCdTe, Si epilayers on Si, and actual device gates¹¹. Finally, recent applications in the CANMET laboratories include a growing number of cases (metal matrix composites, corrosion products or protective layers) where interfaces or thin coatings are the areas of prime interest.¹²

Nanocrystalline materials are the focus of growing interest due to many unusual properties caused by an ultrafine (5-20nm) grain size and a boundary structure more 'open' than in conventional boundaries. HREM of such materials is difficult because wedge-shaped TEM specimens usually will contain overlapping grains and ion damage or electropolishing effects can be severe at the specimen edges, the only regions sufficiently thin for HREM. Specimens of pure Co, Y-12Fe and W-30Ga with an average grain diameter of approximately 10nm were embedded in LR White and sectioned in a Reichart Ultracut E. Sectioning proceeded without difficulty and both the Co and Y-Fe sections were of good quality as regards section integrity and size, and were very similar in appearance to homogeneous ductile metals (Fig. 1). An advantage of the uniform thickness obtained was the ready detection of differences due to average atomic number differences (Fig. 2). The W-Ga was both harder and more brittle, necessitating smaller sections which were often curled or torn. Nonetheless useable areas were obtainable, especially at the edges of the tears. The Co sections showed a most interesting development of texture (in diffraction patterns) but only after the first sections were cut, possibly implying actual rotation of surface grains under the shear force of a somewhat dulled knife edge, especially with no solute atoms in the grain boundaries to hinder the rotation. (No such texture developed in the other two nanoalloys). Further work is in progress with regard to this phenomenon and to production of even thinner sections.

References

1. C.R. Bradley et al, Spec. Prep. for TEM of Materials III, Mat. Res. Soc. Proc., 254 (1992) 279.
2. J.G. Ulan et al, Spec. Prep. for TEM of Materials II, Mat. Res. Soc. Proc., 199 (1990) 153.
3. J.A. Mascorro & G.S. Kirby, Proc. 50th EMSA Meeting (San Francisco Press, 1992) 746.
4. B.L. Giammara et al, Proc. 49th EMSA Meeting (San Francisco Press, 1991) 294.
5. T. Malis & D. Steele, Spec. Prep. for TEM of Materials III, Mat. Res. Soc. Symp., 254 (1992) 257.
6. T. Malis, Proc. 50th EMSA Meeting (San Francisco Press, 1992) 390.
7. D.E. Stefluk et al, 49th EMSA Meeting (San Francisco Press, 1991) 36.
8. S.Q. Xiao et al, Proc. 50th EMSA Meeting (San Francisco Press, 1992) 1102.
9. O.O Popoola et al, Spec. Prep. for TEM of Materials III, Mat. Res. Soc. Symp., 254 (1992) 271.
10. E.A. Kenik & M.G. Burke, Proc. 50th EMSA Meeting (San Francisco Press, 1992) 1218.
11. S.R. Glanvill, Proc. 12th Int. Congr. EM, 4 (1990) 28. Also, private communication.
12. G. Williams and T. Malis, these Proceedings.

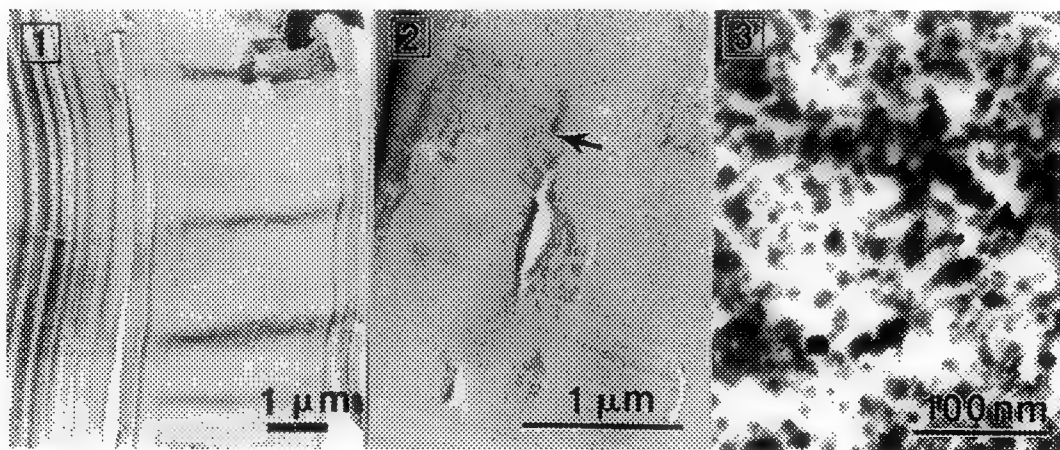


Fig. 1 Y-12Fe nanocrystalline alloy produced by inert gas condensation and in-situ cold compaction. Estimated thickness ~ 20-30nm with set thickness of 10nm (complicated by a contamination layer).
 Fig. 2 Section detail in Y-12Fe showing near-amorphous area (arrowed) with higher Y/Fe ratio.
 Fig. 3 W-30Ga section (~20nm) showing individual nanograins at thinner region near tear in section.

RAPID PRESERVATION OF BIOLOGICAL SPECIMENS FOR LIGHT AND ELECTRON MICROSCOPY AND FOR IMMUNOHISTOCHEMICAL AND IMMUNOCYTOCHEMICAL STUDIES USING MICROWAVE FIXATION

Gary R. Login* and Ann M. Dvorak**

Departments of Pathology at the Harvard School of Dental Medicine*, Harvard Medical School*,**, and the Beth Israel Hospital*,** and the Charles A. Dana Research Institute*,**, Boston, MA 02215

The use of microwave fixation for biological specimens is very promising and may provide unique biological insights and methodological advantages over standard chemical and physical fixation approaches. Microwave fixation methods are fast (e.g., completed in seconds or less)¹⁻⁴ and they make analysis of fast cellular events such as vesicle formation^{5,6} and fast reorganization of vitamin D receptors⁷ possible or more precise. This newly developed, rapidly emerging technology is playing an increasingly important role in providing new insights into cell biology.⁸

Microwave fixation is used by many investigators as an all encompassing description of a variety of methods where microwave irradiation is used in the fixation process. Certain limitations and possible advantages are associated with different microwave fixation methods. For example, the use of aldehydes during irradiation may influence the preservation of antigenicity of cellular macromolecules.⁹⁻¹¹ Therefore, it is useful to classify microwave fixation methods according to the following criteria: a) chemical environment around the specimen during irradiation, b) duration of microwave exposure, and c) the temporal relationship between the use of microwave irradiation and the use of other chemical or physical fixation modalities.

Using this classification system, we describe five approaches to microwave fixation⁸ 1) microwave stabilization¹² refers to the preservation of structure by microwave irradiation, without the superimposed effects of chemical fixatives; 2) ultrafast and fast primary microwave-chemical fixation define primary fixation processes in which specimens are irradiated by microwave energy in a chemical environment for milliseconds or for seconds to minutes; 3) microwave irradiation followed by chemical fixation involve immersion of specimens in a chemical environment (e.g., aldehyde mixtures) for minutes to hours *after* microwave irradiation in an effort to improve the uniformity of fixation; 4) primary chemical fixation followed by microwave irradiation defines a process by which microwave energy is used to augment primary fixation by chemicals; and 5) microwave irradiation is used in combination with freeze fixation to limit freezing artifacts.

A recommended method of microwave fixation in a large cavity (i.e., household) microwave oven is shown diagrammatically (Figure 1).¹³ The microwave oven is prewarmed for 2 minutes by irradiating a 300 ml distilled water load. Following the warmup procedure, the heated water load is replaced with room temperature water. Cells in suspension or blocks of tissue (<1 cm³) in a physiologically balanced solution are placed in containers with at least 1 dimension ~1 cm. Within 2 minutes of completing the warmup procedure, the specimen container (with samples and fresh chemical fixative) is placed on the floor of the microwave oven in a location predetermined to yield maximum irradiation of the sample (open arrow head). The sample is irradiated for seconds to a final solution temperature (Tf) <55 C. The specimen is transferred as quickly as possible to room temperature storage buffer.

Several studies show that biological specimens fixed by any of the microwave methods described are well preserved for light microscopy. Biological specimens fixed by microwave-chemical methods are well preserved for electron microscopy (Figure 2). Importantly, microwave-chemical methods preserve a variety of antigens better than conventional aldehyde and alcohol immersion fixation methods (Table 1).²³

References

1. G. R. Login and A. M. Dvorak, Am J Pathol 120(1985)230.

2. G. R. Login, et al., J Histochem Cytochem 34(1986)381.
3. G. R. Login, et al., J Histochem Cytochem 38(1990)755.
4. G. R. Login, et al., in Microwave Processing of Materials II, Materials Research Society, Pittsburgh, 189(1991)329.
5. P. S. Eggli, et al., Anat Rec 231(1991)156.
6. V. Mizuhira and H. Hasegawa, Proc Intl Congr Electron Micros 12(1990)182.
7. J. Barsony and S. J. Marx, Proc Natl Acad Sci, USA 87(1990)1188.
8. G. R. Login and A. M. Dvorak, Methods of microwave fixation for microscopy. A review of research and clinical applications: 1970-1992, Prog Histochem Cytochem, in press(1993).
9. A. S.-Y. Leong, et al., J Pathol 156(1988)275.
10. G. R. Login, et al., Lab Invest 57(1987)592.
11. G. R. Login, et al., Lab Invest 57(1987)585.
12. E. Marani, et al., Histochem J 20(1988)397.
13. G. R. Login and A. M. Dvorak, Scanning, in press(1993).
14. G. R. Login, et al., J Dent Res 71(1992)304.
15. S. Yamashina, et al., Acta Histochem Cytochem 23(1990)553.
16. K. Yasuda, et al., Acta Histochem Cytochem 22(1989)91.
17. P. S. Eggli, et al., Neuroscience 48(1992)737.
18. N. Azumi, et al., Mod Pathol 3(1990)368.
19. N. Benhamou, et al., J Electron Microsc Tech 17(1991)81.
20. Y. Kawasaki, et al., Am J Clin Pathol 97(1992)244.
21. H. Ohtani, et al., Acta Histochem Cytochem 23(1990)585.
22. Z. Kang, et al., Protoplasma 162(1991)27.
23. Supported by USPHS grants DE 10059 and AI 33372, and the Wm. F. Milton Fund, Harvard U.

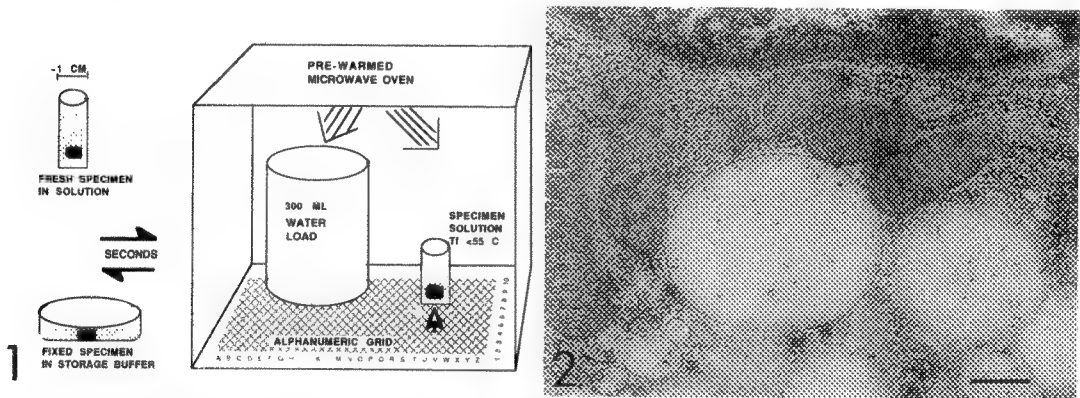


Fig. 1. Microwave fixation method (reprinted with permission¹³).
 Fig. 2. TEM of a rat parotid acinar cell fixed by fast, primary microwave-aldehyde fixation in 5 sec to 45 C and localization of amylase using a post-embedding, immunogold method.¹⁴ Bar = 0.3µm.

Table 1. *Superior* immunohistochemical and immunocytochemical staining of antigens in specimens fixed by microwave-chemical methods compared to conventional fixation in aldehyde or in alcohol.

Fast, Primary Microwave-Chemical Fixation vs. Aldehyde Fixation: Amylase^{14,15}, Chymotrypsin¹⁵, Collagen IV^{15,18}, Desmin¹⁸, Factor VIII¹⁸, γ-Glutamyl Transpeptidase¹⁶, Hyaluronin¹⁷, Keratin AE1/3¹¹, Keratin AE-1¹⁸, Laminin¹⁵, Pathogenesis-Related Protein¹⁹, Leu-18, Ln-2¹⁸, Ln-38
 Fast, Primary Microwave-Chemical Fixation Vs. Immersion Fixation In Alcohol: Ln-2¹⁸, P-53
 Tumor Suppressor Gene Product²⁰
 Microwave Irradiation Followed By Chemical Fixation Vs. Aldehyde Fixation: Carcinoembryonic Antigen²¹, Cytokeratins:40,46,50,52,56.5,58,65-67 kd²¹, Ln-1,3²¹, Rust Fungus Surface-Associated Proteins²², Vimentin²¹, von Willebrand Factor²¹

PREPARATION OF THIN-FILM-METAL/6H-SiC TEM SPECIMENS BY RPR ION MILLING

J.S.Bow, F.Shaapur, M.J.Kim, and R.W.Carpenter

Center for Solid State Science, Arizona State University, Tempe, AZ 85287-1704

HRTEM has proven to be the best method to study the interface structure of heterogeneous materials at the atomic level. One of the critical steps in these experiments is preparation of sufficiently thin cross section TEM (XTEM) specimens with different materials on both sides of the interface in good condition for HRTEM, especially when metal/ceramic materials are of interest. For the material system of a thin metal film on 6H-SiC substrate, the conventional ion milling method did not produce satisfactory XTEM specimens, because of the large difference in ion milling rates between metals and SiC. Most of the metal was ion milled away before a thin area of SiC was obtained. Two very important parameters, the thickness of the metal thin film normal to the interface and the atomic bonding structure across the interface were usually lost¹. Fig.1 shows an example. The original thickness of the metal was 100 nm, and most of that has been removed. An amorphous layer of 1 to 1.5 nm thickness apparently due to ion milling formed at the metal/SiC interface.

A modified ion milling method known as the reversing partial rotation^{2,3} (RPR) method, based on a preferential orientation ion milling scheme^{4,5}, was developed in our laboratory to mitigate the differential thinning effect. The specimens were rotated in a "rocking" rotation mode with a rocking angle sector centered around the normal to the edge-on interface at a constant (reversible) speed of 2 rpm. Typical range of the rocking angle (ω) used was 40 to 80 degrees. We found that smaller ω seemed to reduce the ion milling time, but increased the frequency of local thickness variation along the direction normal to the incident ion beam. Fig.2(a) and Fig.3(a) show low magnification TEM images for different ω angles. The time of ion milling for both specimens was less than two hours. Large thin areas were obtained, and the original width of metal films was preserved at thin regions in both cases. HREM images of the interfaces did not exhibit ion beam damage, Fig.2(b) and Fig.3(b). There were several elliptical holes with long axis approximately along the incident ion beam direction in the SiC substrate for the specimen with 40° rocking, even though it had more thin areas than the $\omega = 80^\circ$ specimen (Fig.3). Compared to an HREM image, a composition profile across an interface determined by position resolved nanospectroscopy requires a larger uniform thin area, because quantitative analysis suffers greatly from irregular local thickness variations.

The RPR ion milling method was found to be the most efficient method to obtain a satisfactory specimen for HRTEM in thin-film-metal/SiC materials to date. To obtain other reliable information such as composition profiles, further improvement in this process is required. We suggest that combined RPR rocking with interval continuous rotation may be a useful next step; we are investigating that procedure now.

References

1. J.S.Bow et al. in Proc.50th EMSA Ann. Meeting ed. by G.W.Bailey, J.Bentley, and J.A.Small (1992) p.252
2. F.Shaapur *ibid.* p.1426
3. F.Shaapur et al. *Mat. Res. Soc. Symp. Proc.* Vol 254 (1992) 153.
4. U.Helmersson et al. *J. Elec. Micr. Tech* 4 (1986) 361
5. P.H.Chang et al. *Mat. Res. Soc. Symp. Proc.* Vol 115 (1988) 93.
6. This research was supported by USDOE grant DE-FG02-87ER-45305. The microscopy was performed at ASU HREM Facility supported by Arizona State University and NSF-DMR-9115680. The specimens were supplied by Mrs. Potter and Dr. Davis from North Carolina State University.

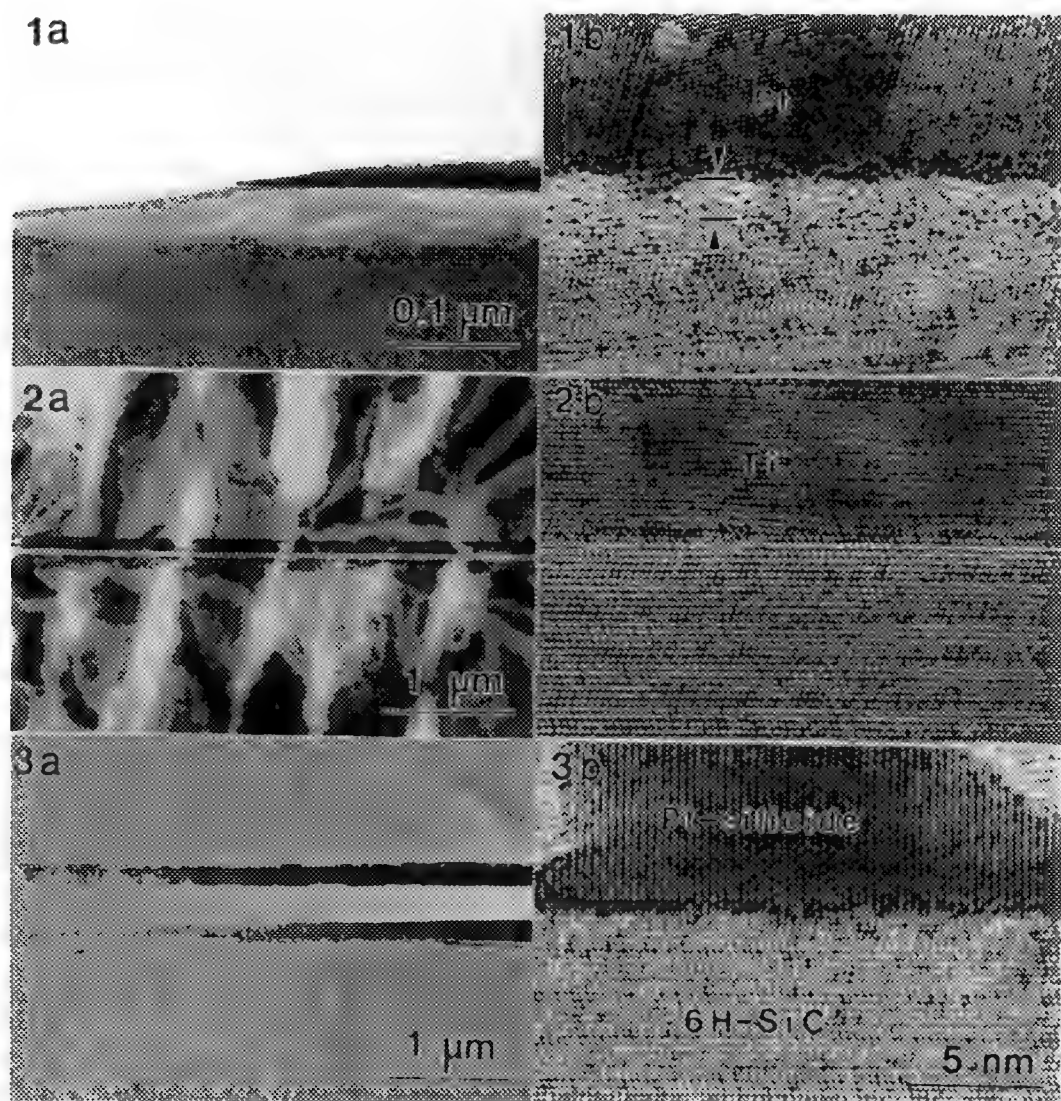


Fig.1 As-deposited Pt/6H-SiC, by conventional ion milling. (a) TEM micrograph, (b) HREM image.

Fig.2 As-deposited Ti/6H-SiC, by $\omega = 40^\circ$ RPR ion milling. (a) TEM micrograph, (b) HREM image.

Fig.3 750°C/20 min. annealed Pt/6H-SiC, by $\omega = 80^\circ$ RPR ion milling. (a) TEM micrograph, (b) HREM image.

TACKY DOT ARRAYS FOR ORDERED PARTICLE MOUNTING

Allan Cairncross*, David M. Flaherty*, Ulrich Klabunde**

* Du Pont Science and Engineering, ** Du Pont Chemicals, Du Pont Company, Experimental Station, Wilmington, Delaware, 19880

We describe for the first time a rapid way to mount particles on regularly spaced centers for microscopic examination. This innovative method mounts particles in ordered arrays rather than the random chaos of usual methods and therefore simplifies particle examination, identification and analysis. Advantages include the ability to easily mount single particles in controlled patterns and known locations, to mount tight clusters of 2 or more particles per center (Fig. 3); to repeatedly mount the same pattern/number of particles; to mount particles in unusual orientations (Fig. 5, 6) and to easily get the average weight of single particles. Examples of applications include mounting and examination of ores (Fig. 1), pollens (Fig. 2, 3), milled products, seeds (Fig. 4) and crystalline products (Fig. 5, 6).

The mounting medium consists of a pattern of fine adhesive centers typically on 1 by 3 inch glass slides or on clear plastic film that is easily cut to any size or shape. Many other substrates are possible and the size and shape of the adhesive centers and their spacing are adjustable. Dots as small as 13 μm have been produced. To facilitate mounting, holders have been designed that hold the slides and contain the particle sample as it is applied to the medium. The process is as simple as dusting the particles on the medium, rocking the particles back and forth briefly, and tapping off the excess.

The method is well suited for 25 to 1000 μm particles. Mounting thousands of nontouching particles one-to-a-center in a regular array on a slide greatly facilitates particle counting, automated image analysis, preparation of standards and analysis for quality assurance and control. For singular attachment the ratio of the largest particle to smallest should be three or less and the particles should be larger than the dot diameter. For round particles, ratios of particle to dot diameters of 1/1 to 4/1 give greater than 90% singular attachment. For crushed, rough particles the ratio should be 3.0 or greater for singular attachment. For mixtures of similar particles the mounting process is not critical. For mixtures of particles with different properties, the sample should be split to obtain representative samples and attached under kinetic control where all particles attach upon initial contact and no exchange occurs. Low attachment velocity and increasing tackiness of the centers favor kinetic control.

By mounting in an ordered pattern, each particle can be identified by coordinates and examined by multiple techniques. By weighing slides before and after mounting particles and easily counting the number of particles in the regular array an average weight per particle is determined. By turning the tacky dot slide and the mounting holder upside down and shaking up and down so the particles hit the inverted slide vertically, a high number of edge and corner mounts are obtained (Fig. 5, 6). Tacky dot patterns can be prepared by a variety of methods. Du Pont has several technologies and products for making tacky patterns by photoimaging that we find convenient.^{1,2}

References:

1. U. S. Patents no. 3,649,268; 4,174,216; 4,282,308.
2. F. A. Raymond and W. R. Hertler, J. of Imaging Science and Technology, 36 (1992) 243.

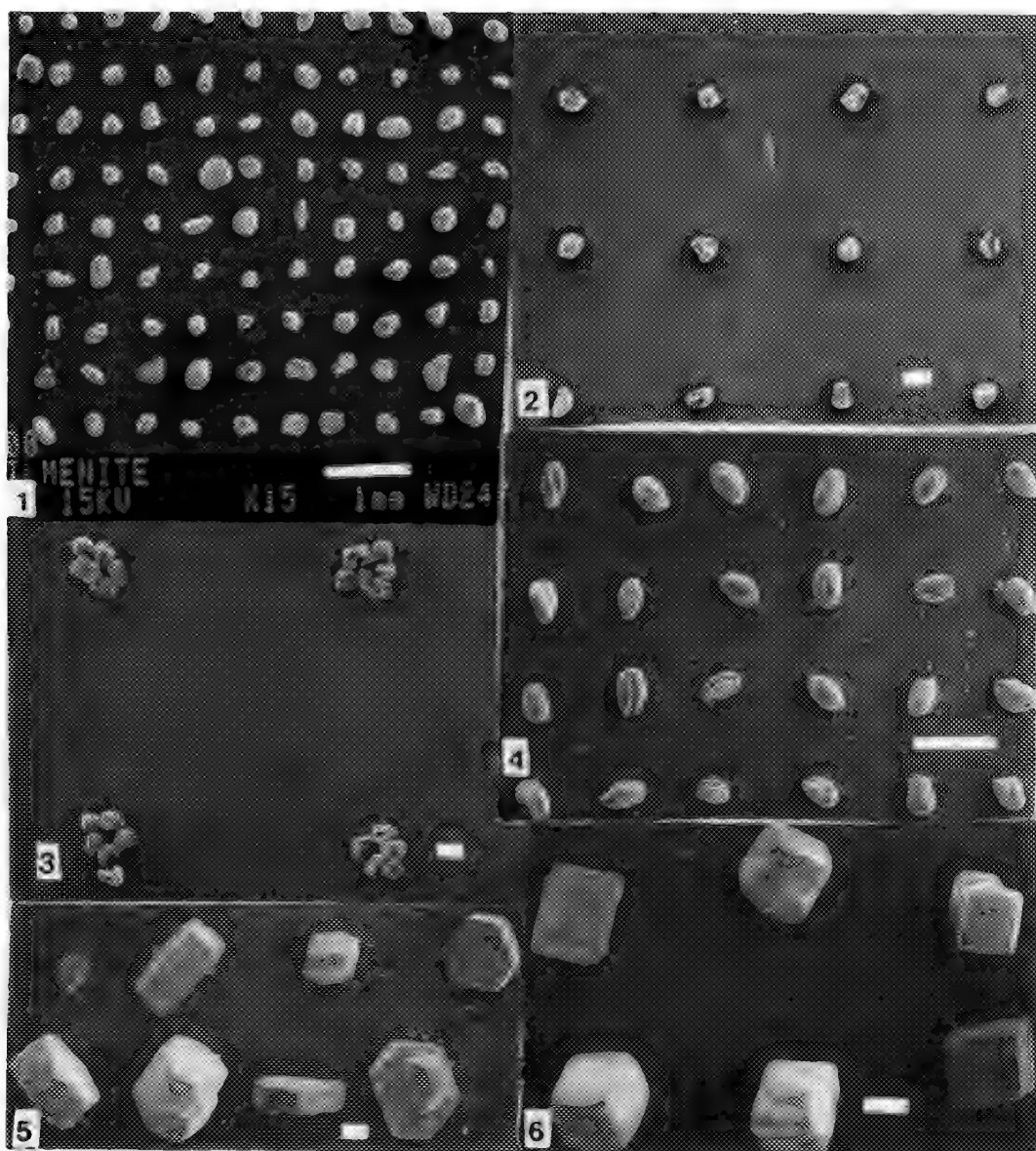


FIG 1 --SEM of ilmenite ore on 75 μm tacky dots/ 500 μm spacing. Bar = 1 mm

FIG 2 --SEM of 90 μm corn pollen on 40 μm tacky dots/ 500 μm spacing. Bar = 1 mm.

FIG 3 --SEM of clusters of 90 μm corn pollen on 150 μm tacky dots/ 1000 μm spacing. Bar = 100 μm

FIG 4 --SEM of arabidopsis seeds on 150 μm tacky dots/ 1000 μm spacing. Bar = 1 mm.

FIG 5 --SEM of sodium sulfite on 75 μm tacky dots/ 500 μm spacing, corner, edge, face mounting. Bar = 100 μm .

FIG 6 --SEM of sodium chloride on 75 μm tacky dots/ 500 μm spacing, corner and face mounted cubes, Bar = 100 μm .

CHEMICALLY ASSISTED ION-BEAM ETCHING (CAIBE) IN A LOW-ANGLE ION MILL

R. Alani and P.R. Swann

Gatan Research and Development, 6678 Owens Drive, Pleasanton, CA 94588, USA

In conventional ion mills, chemically assisted ion beam etching (CAIBE) has become an established method for TEM specimen preparation of certain materials.^{1,2} CAIBE employs a reactive gas which is brought in contact with the specimen through a jet assembly, while an inert gas ion beam is directed onto the same area. Therefore, thinning occurs by the combination of chemical reaction and physical sputtering, which leads to enhanced thinning rates. The reactive gas used in the CAIBE technique can be generated from a solid source which sublimates e.g. iodine or it can be injected directly from a pressurized gas bottle e.g. nitrous oxide. Nitrous oxide in combination with a xenon ion beam has been used for cross sectioning TEM specimens of diamond films on silicon³.

It is well known that indium-containing compound semiconductors develop indium islands on the surface when thinned with an argon ion beam. It is believed that preferential sputtering enriches the surface with indium and that heating by the ion beam melts the indium which then agglomerates to form small globules on the surface. Several workers have shown that the agglomeration of indium can be prevented by milling the specimen on a liquid nitrogen cold stage. The same result can be achieved more easily by improving the thermal contact between the specimen and the specimen platform so that the specimen is maintained close to room temperature during the milling process⁴. Specimen heating and island formation can also be suppressed by milling at low angles which reduces the amount of thermal energy transferred to the specimen. However, perhaps the best approach to reducing indium island formation is to avoid surface enrichment of indium in the first place by using the CAIBE technique.

In this paper we have investigated the effects of combining high-speed, low angle milling with CAIBE using a room temperature specimen stage. For this work we used a Precision Ion Polishing System (PIPS) equipped with a miniaturized version of the iodine CAIBE system used in a conventional ion mill¹. The vacuum system of the PIPS was also upgraded to handle corrosive gases. To test the capability of the new CAIBE, a plan view specimen of InP was dimpled to a thickness of 10 μ m and thinned in the PIPS. The iodine jet was set by opening the CAIBE valve. Before loading the specimen and beginning milling, the iodine valve was opened fully and run for a few minutes to get a steady state flow. Then the iodine flow was adjusted until the specimen chamber pressure reached $\approx 8 \times 10^{-5}$ Torr. The milling angle was 4° and only one gun was used at 5 keV to gain better control over the thinning rate. Fig. 1 shows a typical bright field TEM image of the InP specimen after the CAIBE milling. It can be seen that the specimen is free from indium islands. The features seen on the micrograph are dislocations produced by a scratch on the dimpled specimen surface. The total milling time was about 10 minutes which corresponds to a single gun thinning rate of 1 μ m/min. Milling was monitored using the PIPS optical microscope to observe interference fringes. The ion gun voltage was switched off when perforation occurred and immediately the iodine jet was turned off. The specimen had a large electron transparent area.

After establishing the milling condition for bulk InP specimens, it was decided to mill a cross sectional TEM specimen of an InP wafer. An InP(100) single crystal was coated with gold-palladium as a surface marker, in the Gatan Model 681 high resolution ion beam coater, cross sectioned¹, dimpled and ion polished using the CAIBE technique. Other than using the PIPS's ion beam modulation system which facilitates the thinning of cross sectional type specimens, the CAIBE milling condition were the same as used to produce the plan view InP specimens. Fig. 2 is a high resolution [110] micrograph of the specimen taken with the TEM operating at 120keV. It is seen that the microstructure of all the layers across the interface has been preserved even though the layers differ in chemistry and sputtering rates. The layers include the epoxy used for cross sectioning, the amorphous gold-palladium marker, the InP oxide and the InP substrate, all of which are labeled in the micrograph.

References

1. R. Alani, J.S. Jones and P.R. Swann, MRS Symposium Proceedings Vol. 119, 85, (1990)
2. A CAIBE system for the preparation of TEM specimens. USA patent, 5,009,743, (1989)
3. A.J. Mardinly, private communication, (1990)
4. R. Alani and P.R. Swann, accepted for publication in Journal of Computer Assisted Microscopy

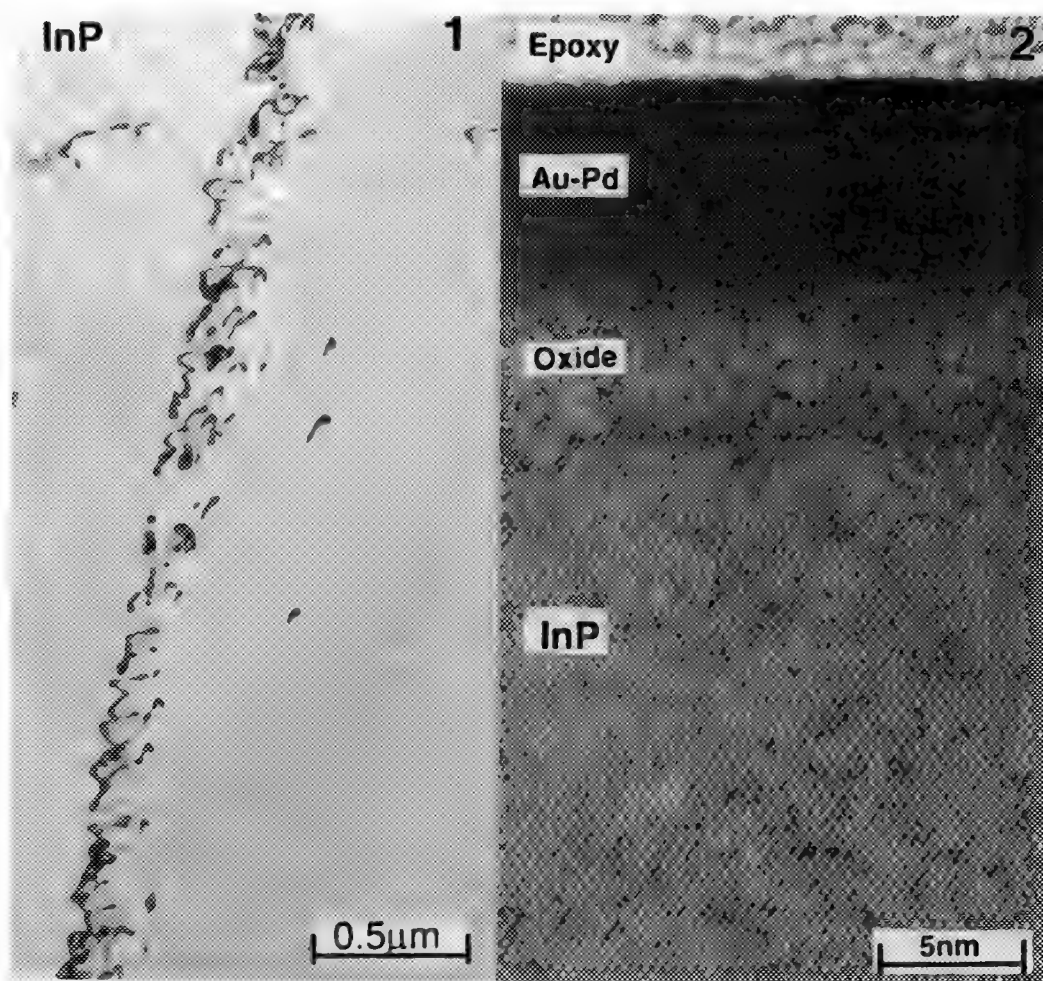


Fig. 1 Typical bright field TEM micrograph of the InP specimen after the CAIBE milling in the PIPS. Note, the specimen is free from indium islands. The features seen on the image are dislocations produced by a scratch on the dimpled specimen surface.

Fig. 2 HRTEM [110] image of a multilayered InP based wafer after the CAIBE thinning in the PIPS. The layers include the epoxy used for cross sectioning, the amorphous Au-Pd marker, the InP oxide and the InP substrate.

NANOMETER-RESOLUTION AUGER ELECTRON SPECTROSCOPY AND MICROSCOPY OF SMALL PARTICLES

JINGYUE LIU

Center for Solid State Science, Arizona State University, Tempe, AZ 85287

Small metal particles have peculiar physical and chemical properties and they are especially important in catalysis. A detailed understanding of catalytic processes requires knowledge of both the microstructure and the microchemistry of the catalyst system. Although nanometer scale surface topography of supported catalysts can be studied with secondary electron (SE) signals,¹ a chemically specific and surface sensitive signal such as Auger electrons must be used to extract compositional information about the surface species. Auger electron (AE) spectroscopy (AES) and scanning Auger microscopy (SAM) have been widely used for surface and catalyst characterization. In order to observe the active phases (small particles) of supported catalysts, it is necessary, however, to have nanometer scale resolution in SAM images.

With significant improvement in detection efficiency of low energy secondary electrons by employing magnetic parallelizers in our UHV scanning transmission electron microscope (STEM),² known as MIDAS (a Microscope for Imaging, Diffraction and Analysis of Surfaces),³ a spatial resolution of approximately 3 nm in SAM images has been achieved on bulk samples.⁴ A higher spatial resolution of about 1 nm has been obtained on thin specimens.^{5,6} Fig. 1 shows O KLL Auger peak and the background signal (20 eV above the O KLL Auger peak) intensity line scans across a straight edge of a small MgO cube. The edge resolution is approximately 1 nm for both the AE and the background signals. Information about the attenuation lengths of Auger electrons has been extracted from SAM images.⁶ Small metal particles deposited onto oxide carriers have been analyzed with Auger electrons.^{5,6} Ag clusters containing as few as 15 atoms, supported on α -alumina carrier, have been observed in SAM images with high contrast.⁵ Fig. 2 shows a Ag MNN AES spectrum obtained from small Ag particles deposited, in situ, onto a pre-cleaned thin carbon film.^{5,6} The peak-to-background ratio in this AES spectrum is very high ((P-B)/B ~ 1.6) because of the use of thin film and high energy (100 keV) probe.

Surface chemical information about the Ag/carbon system has been obtained by taking four images, at and above the carbon and silver Auger peak energies, as shown in Fig. 3. The contrast mechanisms of small particles in nanometer resolution SAM images have been investigated.^{5,6} Silver particles as small as 2 nm in diameter are clearly visible in Fig. 3a. The nano-scale pore structure of the carbon film is clearly shown in the C KLL Auger peak image (Fig. 3c). The high intensity of the Ag particles in the C KLL Auger peak image could occur for either chemical and/or electron scattering effects.^{5,6} Elemental maps have been obtained by off-line processing these energy selected images to yield true compositional information about the sample. Quantitative information about the Auger peak height and the SE background intensity from both the Ag particles and the supporting carbon film can be extracted from intensity line scans obtained by off-line processing the digitally stored SAM images. For example, Fig. 4 shows several intensity line scans of different signals across the two small Ag particles framed in Fig. 3c. Further particle analysis can be performed on these data set to yield information about the particle size distribution and the intensity variations of Auger signals with the change of the particle size.

The emission of Auger electrons from small particles is very different to that from flat surfaces. Electrons generated inside small particles will all escape provided that the radius of the particle is much smaller than the inelastic mean free path, λ , of the emitted electrons. In this limit the distinction between 'bulk' and 'surface' signals is no longer valid and the total number of the collected Auger electrons will be proportional to the volume of the particle. Fig. 5 shows calculated volume fraction of emitted Auger electrons as a function of the radius of Ag particles ($\lambda \sim 0.82$ nm). By using an intensity ratio method we will demonstrate that Ag particles containing as few as 10 atoms can be detected in nanometer resolution SAM images.⁷

References

1. J. Liu and G. E. Spinnler, Proc. 49th Annu. Meeting of EMSA (1991) 502; J. Liu et al., Proc. 50th Annu. Meeting of EMSA (1992) 1288; J. Liu and G. E. Spinnler, these proceedings.
2. P. Kruit and J. A. Venables, Ultramicroscopy 25 (1988) 183.
3. G. G. Hembree et al., Ultramicroscopy 31 (1989) 111.
4. G. G. Hembree and J. A. Venables, Ultramicroscopy 47 (1992) 109.
5. J. Liu et al., Surface Sci. 262 (1992) L111; J. Liu et al., Catal. Lett. 15 (1992) 133.

6. J. Liu et al., Ultramicroscopy, in press.
7. The author thanks Drs. G. E. Spinnler, G. G. Hembree, J. A. Venables and J. M. Cowley for helpful discussions. This research was supported by Shell Development Company and made use of the ASU CHREM supported by NSF grant DMR-9115680.

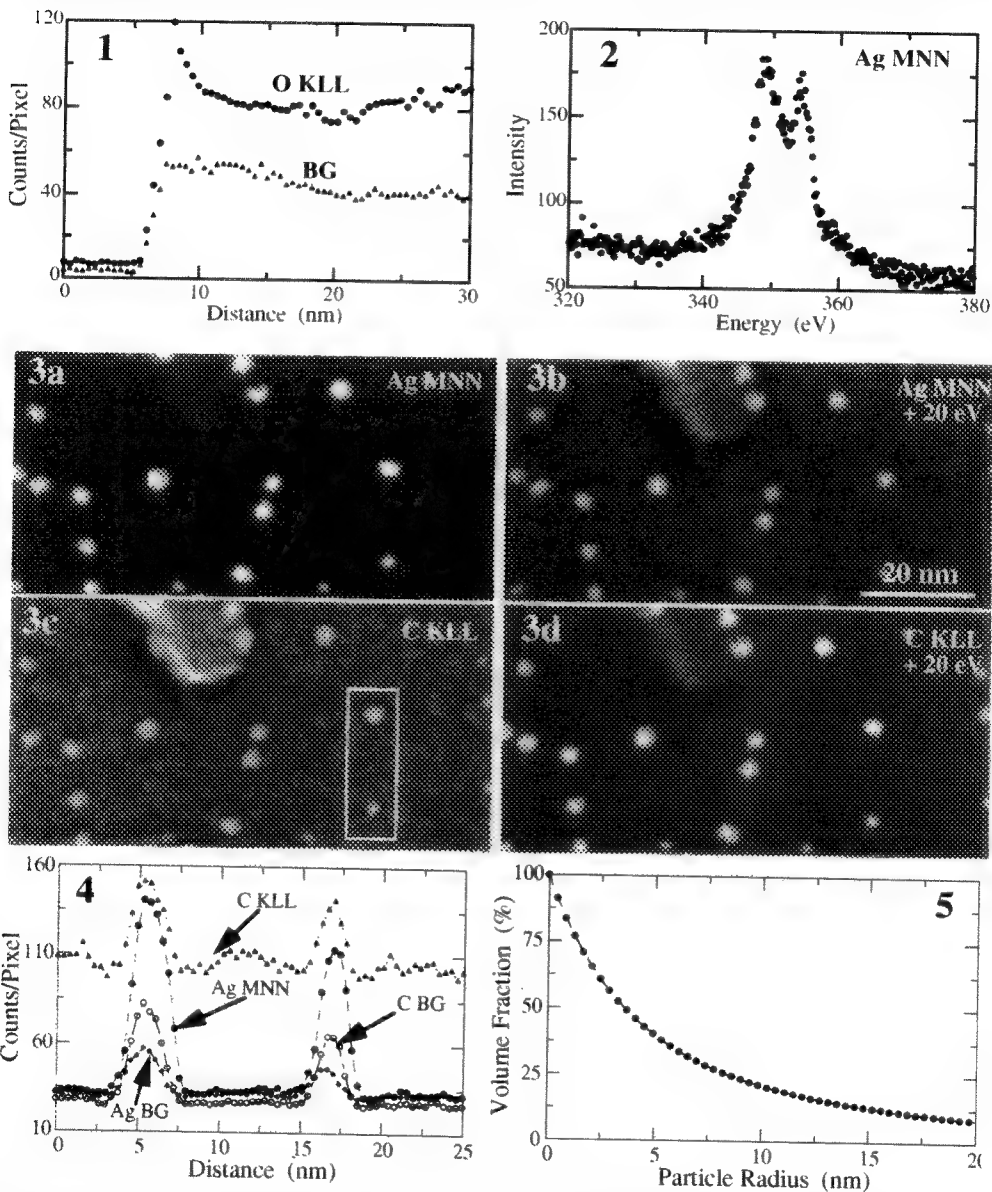


Fig.1--Oxygen KLL Auger and background signal intensity line scans across edge of small MgO cube.
 Fig.2--High energy resolution Ag MNN Auger electron spectrum obtained from Ag/carbon sample.
 Fig.3--Energy selected SE images obtained at (a) Ag MNN Auger peak, (b) Ag MNN+20 eV, (c) C KLL Auger peak and (d) C KLL+20 eV.
 Fig.4--Intensity line scans of different signals across small Ag particles framed in Fig. 3c.
 Fig.5--Calculated volume fraction of emitted Auger electrons as function of Ag particle size.

ANALYTICAL ELECTRON MICROSCOPY OF BIMETALLIC Pt-Rh ALLOY CATALYSTS

Rollin E. Lakis

Department of Materials Science and Engineering, Lehigh University, Bethlehem PA 18015

The goal of this investigation is to correlate the catalyst preparation procedure and the resulting particle microstructures with catalytic performance. The Pt-Rh system was selected because it is widely utilized in pollution control and for its potential application in the low temperature reduction of nitric oxide.¹

Two bimetallic catalysts were prepared for this study. They were both made by the aqueous impregnation of the respective metal chlorides into γ -alumina and contain approximately 0.5 wt% Pt and 0.5 wt% Rh. Catalyst A was prepared by a method which is designed to promote intimate mixing of the two metals after reduction. PtCl_4 was impregnated in the support material and air dried at room temperature for 24 hours. This material was then oxidized at 500°C in flowing O_2 for 15 hours. Following oxidation, the Rh was deposited, air dried, and reduced at 300°C for 15 hours. in flowing H_2 . Catalyst B was made by first impregnating the Rh, and after drying, oxidizing the material at 500°C in flowing O_2 for 15 hours. The Pt was then impregnated and dried. The catalyst was then reduced at 300°C for 15 hours. in flowing H_2 . This preparation was designed to minimize mixing of the two metals following preparation.

The compositions of individual particles, which were measured through their center by analytical electron microscopy using a VG-HB501 dedicated STEM, are presented in Figures 1 and 3. The Pt $M_{\alpha+\beta}$ and Rh $L_{\alpha+\beta}$ x rays were measured and processed using the software and library standards of the Link Systems AN10000 x-ray analyzer. Quantification was performed by the Cliff-Lorimer ratio method, assuming the effects of absorption and fluorescence were negligible.² An experimental $k_{\text{Pt,Rh}}$ -factor of 1.067 was measured on microtomed sections of Pt-13%Rh thermocouple wire. The error bars on Figures 1 and 3 represent $\pm 1\sigma$. These figures suggest that two substantially different particle populations were developed by the described processing. Catalyst A displays a bimodal concentration distribution (Figure 2), while catalyst B (Figure 3) appears to contain only Pt-rich particles in the catalytically active size regime (<10 nm). This distribution leads to an apparent Rh deficit if only this size regime is considered. However, Rh-rich particles 100 nm and larger were observed, but are not shown in Figure 3. These particles were likely formed during the oxidation step as Rh_2O_3 . The lack of particles which contain the expected bulk alloy composition (50% Pt), and the large number of particles which contain 15% Pt or 85% Pt, may upon thorough investigation provide the first microstructural evidence of a miscibility gap in the Pt/Rh system.³

Figure 4 shows preliminary results of catalytic testing using the reduction of nitric oxide as a probe reaction. This reaction was used to observe changes in the chemical and microstructural properties of the reactive particle surfaces. Reactivity at lower temperatures is desirable and is a property of an active catalyst. The behavior of both catalysts lies between the extremes defined by the activity of pure Pt and Rh which convert 50% of the NO at 67°C and 200°C respectively. Catalyst B was found to be more reactive than catalyst A. This suggests that if both catalysts contain the same amount of Pt and Rh, and if the catalytic activity of Pt-Rh alloys are linear with composition, more Pt is present on particle surfaces in catalyst B.

Surface compositional analysis by XPS provides an average analysis of all particle surfaces, and the bulk analysis of particles smaller than the photoelectron escape depth (~2 nm). Catalysts A and B were found to contain 21% Pt and 89% Pt respectively. This suggests that the particle surfaces of catalyst A are enriched with Rh, or that the Rh which is present is contained in proportionally more small particles. The value of 89% Pt for catalyst B, which is similar to the average composition that might be inferred from Figure 3, suggests that most of the Rh is isolated in large particles. These large particles possess a very low surface area-to-volume ratio, and are therefore underestimated by the surface sensitive XPS technique.^{4,5}

REFERENCES

1. H. G. Stenger, and J. S. Hepburn, *J. Energy & Fuels* (1987) 1, 412.
2. C. E. Lyman, J. S. Hepburn, and H. G. Stenger, *Ultramicroscopy* (1990) 34, 73.
3. E. Raub, *JLCM* (1959) 1, 3
4. This research is supported by the US Department of Energy under contract DE-FG0286ER45269.
5. The author is grateful to W. Furdanowicz and the Bethlehem Steel Corporation for the use of the dedicated STEM, and to A. C. Miller and the Scienta ESCA Laboratory at Lehigh University.

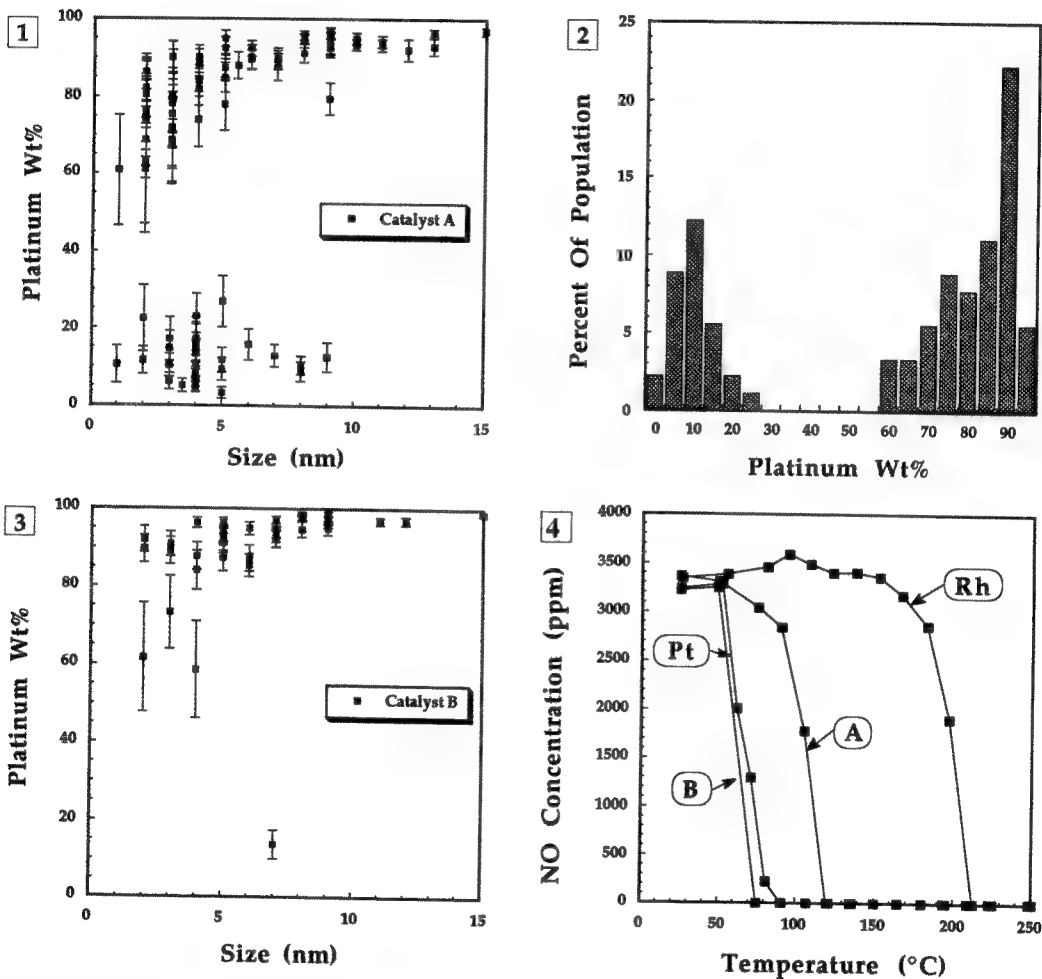


Fig. 1 Particle size vs. Pt composition for Catalyst A.
Fig. 2 Pt concentration histogram for Catalyst A.
Fig. 3 Particle size vs. Pt composition for Catalyst B
Fig. 4 Reaction temperature vs. nitric oxide concentration for pure Pt and Rh, and catalysts A and B. The disappearance of NO at lower temperatures indicates a more active catalyst.

APPLICATION OF ENERGY-FILTERED IMAGING TO THE CHARACTERIZATION OF HETEROGENEOUS CATALYSTS

P.A. Crozier and M. R. McCartney

Center for Solid State Science, Arizona State University, Tempe, AZ 85287-1704

Heterogeneous metal catalysts often consist of one or more metal species distributed over a highly porous oxide support. In many cases, there is not a clear understanding of the relationship between the microstructure of such systems and their catalytic properties. Indeed, the systems often possess complex morphologies with domains containing many different phases. To build up a clear picture of the microstructure of these materials it is essential to have an accurate representation of the distribution of elements over reasonably large areas of the sample. Here we employed a Zeiss EM 912 fitted with an omega filter to determine elemental distributions over large areas in amination catalysts¹.

The microscope, which operates at 120 kV, is interfaced to a Gatan slow-scan CCD camera (1024² pixels) which can be used to acquire images, diffraction patterns and energy-loss spectra from regions of the sample. At present our machine is fitted with a W filament as an electron source which gives high beam current but limits the usable energy resolution to about 2 eV.

The experiments were carried out on NiCuCr amination catalysts which essentially consist of particles containing a combination of Ni, Cu and Cr and possibly their oxides dispersed on an alumina substrate. TEM specimens were prepared by ultramicrotomy which gives large areas of reasonably uniform thickness which are suitable for performing energy-loss mapping.

Fig 1 shows the bright field image obtained from the sample. The image shows clusters of metal particles of variable size embedded in the Al₂O₃ substrate. Parallel energy-loss spectra acquired with the CCD camera from this entire region is shown in Fig 2. Each point in the spectrum was obtained by summing rows of pixels in the non-dispersive direction. The Ni L₂₃ and Al K edges are clearly visible above the background and were acquired in 1 and 10 s, respectively.

Images can be formed using inner-shell edges by acquiring two images at pre-edge energies for background calculation and one image at post-edge energy. The calculated background is subtracted from the post-edge image to obtain an image which represents only the inner-shell distribution.

Fig 3a and b shows 1024² pixel Ni and Al distributions obtained by this procedure. A dwell time of 10 s and an energy window of 25 eV was employed to acquire the pre-edge and post-edge images. A simple linear form was assumed for the background extrapolation. The elemental maps show the complimentary nature of the Ni and Al distribution as expected in a thin microtomed sample of this material.

The simple approach employed here can be carried out rapidly at the microscope providing the analyst with important information during the experiment. More sophisticated processing methods will also be described.

References

1. J. Mayer, Proc. EMSA 1992, 1198
2. R.F Egerton (1986), Electron Energy-Loss Spectroscopy in the Electron Microscope, Plenum Press, New York.
3. This work was supported by the HREM Industrial Associates Program and was performed in the Center for HREM at ASU (supported by NSF Grant DMR-8913384).

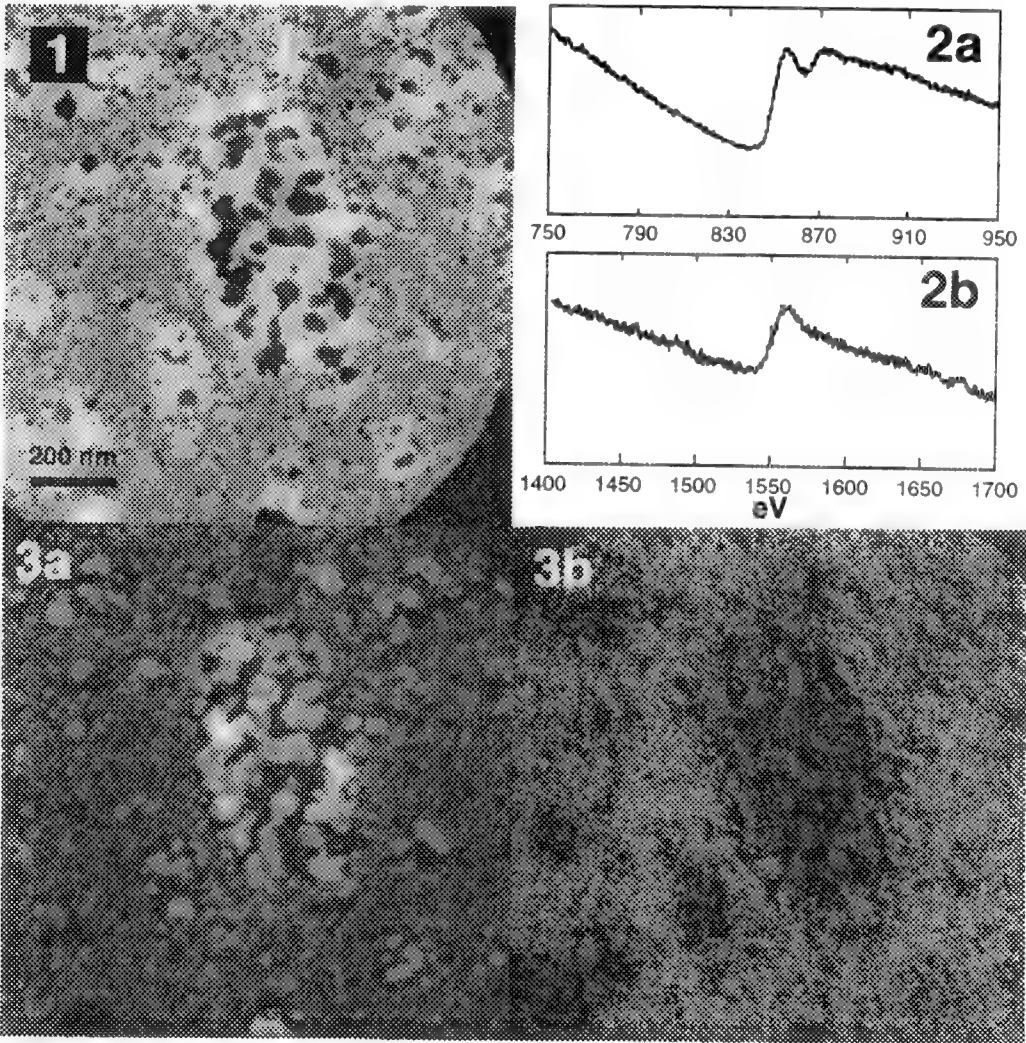


Fig 1: Bright field image of CuNiCr catalysts sample
Fig 2: a) Ni L₂₃ edge and b) Al K edge obtained from region shown in Fig 1.
Fig 3: a) Ni and b) Al distributions obtained using procedure outlined in text.

STRUCTURAL STUDY OF DEACTIVATION OF GALLOSILICATE CATALYSTS

C. Choi-Feng, J. B. Hall, B. J. Huggins, D. Li, J. A. Kaduk, L. M. Green, B. D. Alexander, W. J. Reagan

Amoco Research Center, P. O. Box 3011, Naperville, Illinois 60566, USA

Gallosilicate molecular sieves with an MFI structure are very promising catalysts for upgrading light olefins and paraffins to aromatics. Gallosilicate catalysts are quite stable at low reaction temperature, however, when subjected to high temperature, gallosilicate catalysts deactivate rapidly. The activity and selectivity of these catalysts are greatly influenced by both framework and non-framework gallium.¹ Although the framework gallium imparts acidity to the sieve, the nature of the non-framework gallium is unclear. In the present study, combined techniques of analytical electron microscopy (AEM), high resolution transmission electron microscopy (HREM) and X-ray diffraction (XRD) have been applied to study the fate of framework and non-framework gallium in progressively deactivated gallosilicate molecular sieve catalysts. To study this progressive process, fresh gallosilicate molecular sieve and the gallosilicate catalysts (with 40% Cab-O-Sil matrix) subjected to steaming treatments at different temperatures and durations were characterized.²

The microstructure of fresh gallosilicate catalysts consists of highly crystalline molecular sieve which is uniformly distributed in the amorphous supporting matrix (Fig. 1). As shown in Figure 2, gallosilicate sieve exhibits a typical MFI structure.³ The dimensions of the primitive monoclinic unit cell of the fresh sieve containing 2.4% Ga, as determined by XRD, are: $a = 20.110(9)$, $b = 19.946(8)$, $c = 13.379(5)$ Å, and $\alpha = 90.54(4)^\circ$. The unit cell volume is $5366(4)$ Å³. Based on a correlation between cell volume and framework Ga concentration, which is similar to the well-established correlations for B and Al substitution in the MFI framework, the measured unit cell volume for a MFI-gallosilicate molecular sieve indicates that most, if not all, of the Ga present is incorporated into the framework.⁴ Energy dispersive x-ray spectrometry (EDXS) analysis of the fresh catalysts indicates that all of the Ga is confined to the sieve particles, however, the distribution of the Ga is inhomogeneous among the sieve particles and within a single sieve particle.

There is little or no crystallinity loss in the catalysts which have been steamed at 1000 °F. EDXS analysis indicated that even after high temperature steaming, Ga was still confined to or associated with the sieve particles and did not migrate into the supporting matrix. After steaming the gallosilicate catalyst at 1000 °F for 3 hours, some gallium ions are ejected from the framework and migrate to the surfaces of gallosilicate particles to form Ga-rich nodules of 10-20 nm. This migration of Ga appears to be the cause for the catalyst deactivation. These surface nodules are identified by electron diffraction (ED) and XRD as either stable β -Ga₂O₃ or metastable α -Ga₂O₃ or its polytypes (Fig. 3). The sieve particles with the Ga₂O₃ nodules tend to be concentrated in localized areas. At initial stages of Ga migration and Ga₂O₃ nodule formation, there is still a low concentration of Ga remaining in the gallosilicate sieve. Eventually, as the steam deactivation process progresses, all the Ga ions migrate out of the sieve and form Ga₂O₃ nodules of larger sizes (30-60 nm after 48 hour steaming), as shown in Figure 4. However, the number of Ga₂O₃ surface nodules does not appear to increase.

The deactivation process for the catalyst steamed at 1400 °F appears to be more catastrophic than the catalyst steamed at 1000 °F. This is represented by crystalline structure destruction and by associated formation of internal Ga-rich particles. As expected, the deactivation process of this catalyst shows a further departure from equilibrium, as indicated by the much broader size distribution of the Ga₂O₃ surface nodules (5-60 nm) along with the different residual Ga concentrations among the nodule-free sieve particles.

References

1. L. Petit and J. P. Bournonville, in J. P. Jacobs et al. Ed., *Zeolites: Facts, Figures, Future*, Amsterdam: Elsevier (1989)1163.
2. Patent EP 107,875.
3. W. M. Meier and D. H. Olson, *Atlas of Zeolite Structure Types*, London: Butterworth-Heinemann (1992)138.
4. B.L.Meyers, et al., *J. Catal.* 91(1985)352.

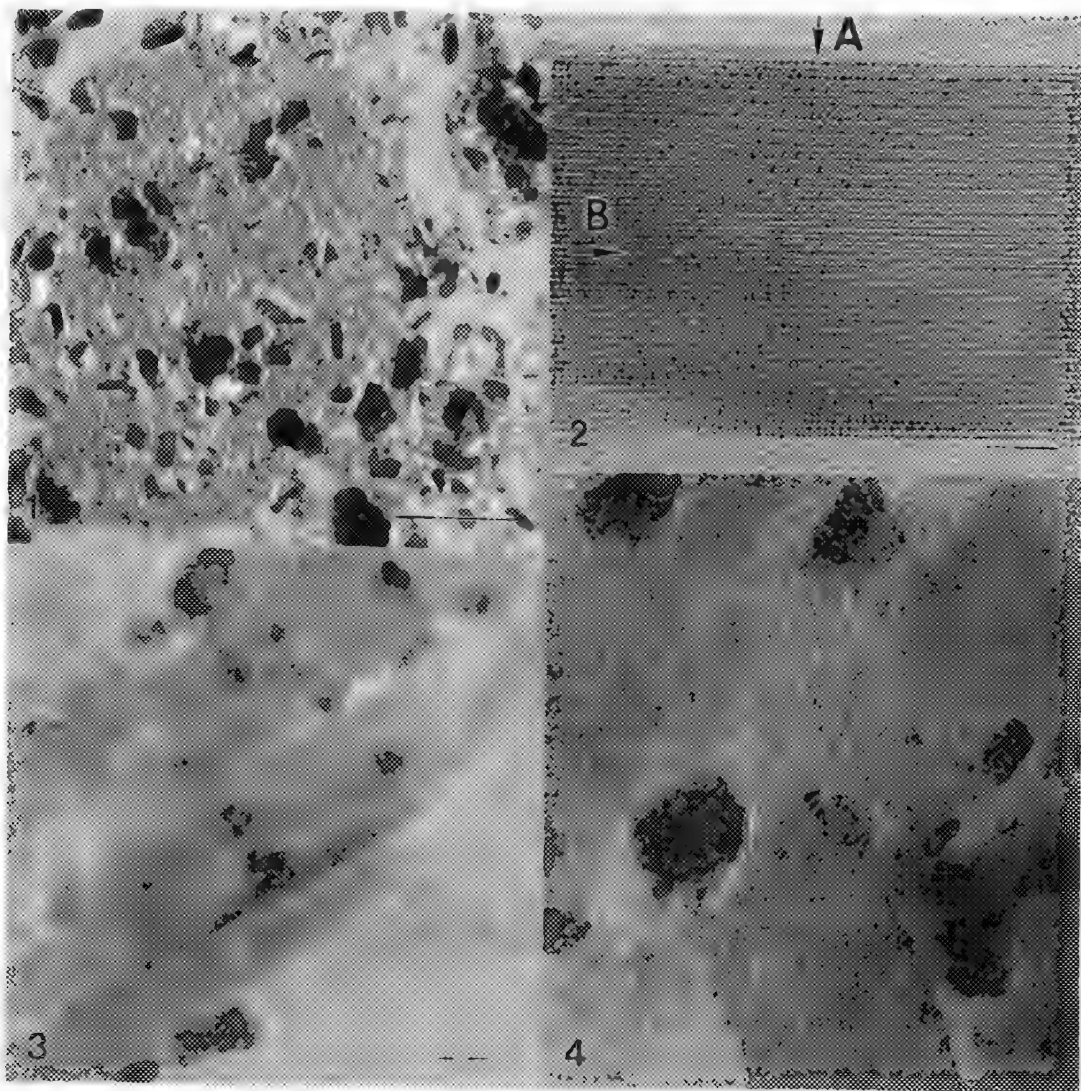


Fig. 1.--TEM of a fresh catalyst shows uniform dispersion of the sieve particles. Bar = 1 μ m.

Fig. 2.--HREM of a sieve crystal shows two dimensional channel structure (A & B). Bar = 10 nm.

Fig. 3.--HREM of the catalyst steamed at 1000 °F for 3 h. Ga₂O₃ surface nodules are formed. Bar = 20 nm.

Fig. 4.--HREM of the catalyst steamed at 1000 °F for 48 h. Ga₂O₃ surface nodules have grown larger. Bar = 20 nm.

CHARACTERIZATION OF COLLOIDAL MATERIALS BY CRYO-TEM

J. R. Minter

Eastman Kodak Company, Analytical Technology Division, Rochester, NY 14652-3712

Many researchers develop products and processes that depend upon colloidal materials. Rheological and other important material parameters are influenced by the morphology of the colloid.¹ The photographic industry uses many such colloids including silver halide sols, photographic coupler sols and emulsions, surfactants, and gelatin solutions and gels. High-resolution direct electron images of these systems in their native states permit photographic scientists to understand how changes in formulation produce changes in microstructure and, ultimately, to understand the photographic performance of the system.

We prepare thin biconcave liquid films spanning the holes in a perforated carbon film supported by an electron microscope grid (see Fig 1). To prevent changes in composition of the colloid caused by evaporation, the films are prepared in an environmental chamber and are propelled through a trap door into a container of liquid ethane.² The specimen is cooled at a rate sufficient to prevent crystallization of water. When maintained below -150 °C, these specimens are stable and compatible with the high vacuum of the electron microscope. Quenching of reacting systems at selected stages of reaction ("on-the-grid processing") permits study of dynamic processes.³ This procedure permits successful low-dose imaging of many practical colloids with minimal or no dilution and is preferable to the traditional approach of chemical fixation, staining, and drying. It complements scattering methods that frequently require significant dilution of the colloid.

For example, a lyophobic sol of Compound **1** (Fig 2) was prepared by neutralization of a basic solution in propanol/water/Aerosol OT.⁴ The propanol was removed by dialysis yielding a dispersion of about 2 wt% Compound **1**. A similar sol was stabilized by the addition of polyvinylpyrrolidone (PVP). With time, the unstabilized sol exhibited Ostwald ripening of metastable spheroidal particles (Fig 3 A&B) and transformation to a stable ribbon-like form (Fig 3B) accompanied by gelation as the ribbons formed an entangled network. The sol stabilized with PVP (Fig 4A&B) was much more stable upon aging.

This presentation also reports results of direct imaging of a double-jet precipitation of AgBr, the benefits of stabilizing AgX colloids with tetraazaindene, and the results of imaging the polymerization of a microemulsion of tetrahydrofurfural methacrylate, water, and Aerosol OT.^{5,6}

References

1. T. M. Clausen et al., *J. Phys. Chem.*, 96, 474 (1992).
2. J. R. Bellare et al., *J. Electron Microsc. Tech.*, 10, 87-111 (1988).
3. Y. Talmon et al., *J. Electron Microsc. Tech.*, 14, 6-12 (1990).
4. K. Chari et al., *J. Phys. Chem.*, to appear (1993).
5. A. P. Full et al., *Macromolecules*, to appear (1993).
6. The aid of Drs. K. Chari, M. Lin, J. Texter (Eastman Kodak Company) and Prof. Y. Talmon (Technion) is gratefully acknowledged.

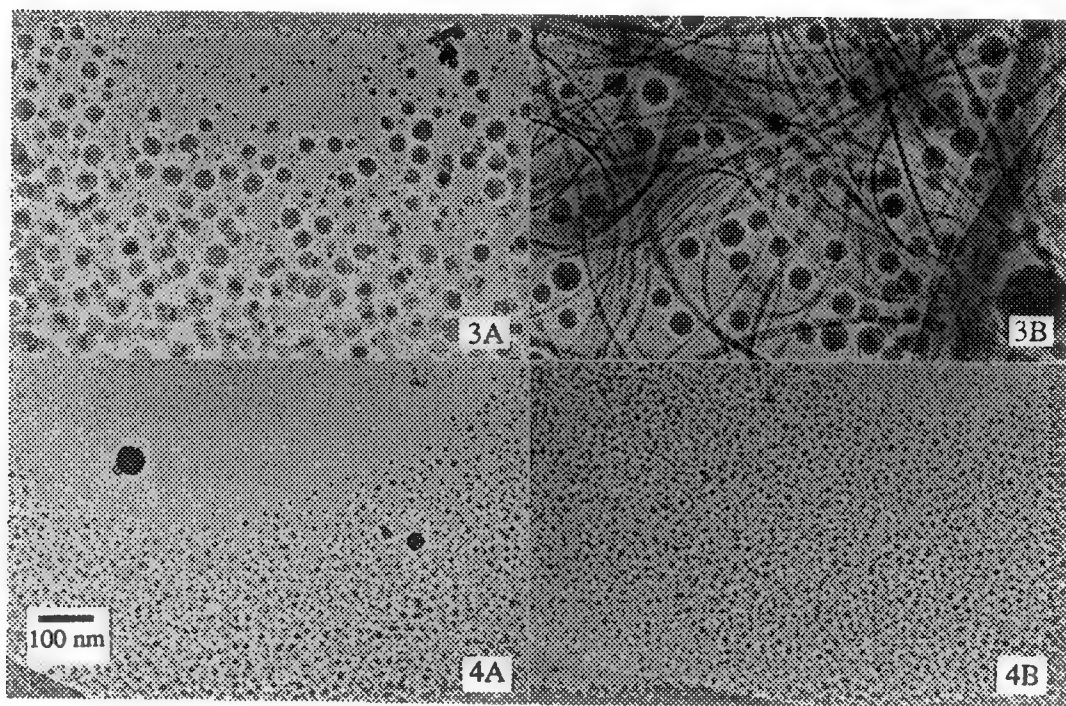
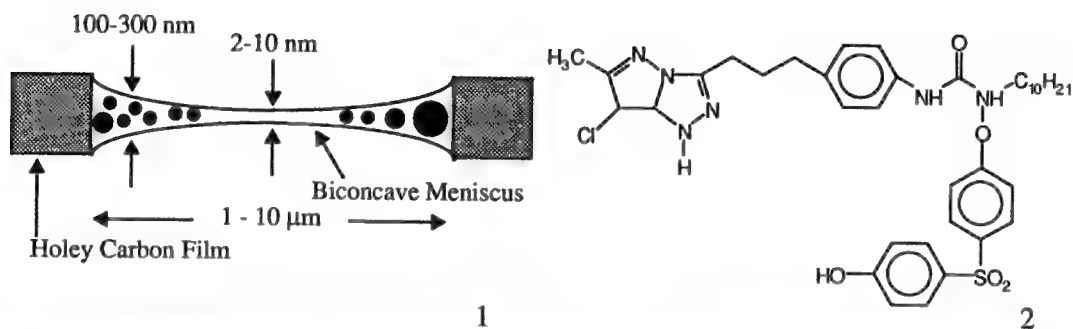


Fig 1. Cross-sectional schematic of a vitrified liquid specimen spanning one hole (1 to 10 μm in diameter) in a holey carbon film. Note the segregation by size of the particles.

Fig. 2 Structure of Compound 1.

Fig. 3 Low dose (10 electrons / \AA^2) cryo-TEM images of unstabilized lyophobic sol of Compound 1. (A) Age = 1 hr (B) Age = 23 hr.

Fig 4. Low dose (10 electrons / \AA^2) cryo-TEM images of lyophobic sol of Compound 1 stabilized with PVP. (A) Age = 3 hr (B) Age = 48 hr.

ANALYSIS OF SMALL PARTICLES VIA HRTEM LATTICE IMAGES: CONTRAST MECHANISMS AND EFFECTS OF PARTICLE SHAPE

John C. Barry

Centre for Microscopy and Microanalysis, University of Queensland, Brisbane Queensland 4072,
AUSTRALIA.

It is well known that because of their large surface area, small particles possess unusual physical properties. What is not so well known is that small particles often exhibit unusual diffraction behaviour. The diffraction behaviour of small particles is a function of their size, shape and chemical composition. This diffraction behaviour is essentially the same for small precipitates within a parent matrix as it is for small particles dispersed on the surface of a thin film. The unusual diffraction behaviour of small particles falls into two categories.

1) The apparent lattice fringe spacing may differ significantly from the actual lattice parameter for particles of irregular shape.

2) One of the surprises of dynamical diffraction is that structures with heavy atoms do not necessarily give strong scattering into Bragg beams. For small particles this means that light elements are often visible on the surfaces of heavy-atom particles.

In this paper an analysis of small particles is made with reference to the microscopic diamonds found in oxidized acid residues from carbonaceous chondrite meteorites.

Residues prepared by Halbout, Robert and Javoy¹ from the Orgueil meteorite were studied by high resolution electron microscopy (400 kV, Cs = 1.0 mm, structure resolution limit = 1.7 Å). Typical images of the small diamonds are shown in Fig. 1. These diamonds resemble those reported in the literature² in that they have diameters ranging from 10 to 60 Å. The particle fringe spacings were measured directly from the negatives using a travelling stage microscope.

Fig. 2 shows the distribution of d-spacings measured from the small diamond particles. The average measured d-spacing is 2.062 Å (111 diamond = 2.059 Å). The average measured d-spacing is very close to the value for bulk diamond however there is quite a spread (about 3%) of values. Part of the spread (1.5%) in measured d-spacing is due to measurement error. The other 1.5% of the spread must be due to particle shape effects. The shape effects may be explained by reference to Fig. 3. The diamond particles were not equiaxed and have an average aspect ratio of 1.5. Fig. 3 shows a schematic diagram of diffraction streaks from a small particle which is not exactly aligned with a zone axis and where the surface normal of the flattest face on the crystal is not parallel to the electron beam. Because of the way that the diffraction streaks intersect the Ewald sphere in Fig. 3 the measured d-spacing differs from the actual d-spacing in the crystal. For crystal dimensions of 20 Å, the difference could easily be 3% or so for the 111 spacing in diamond.

The fact that particles with heavy atoms do not necessarily give strong scattering into Bragg beams is demonstrated in Fig. 4. Fig. 4 shows the pendellosing behaviour of the central beam in diamond, aluminium and silver. The simulations are for beam amplitude for the [110] zone axis, at 400kV. The pendellosing behaviour in diamond is very strong with the central beam reduced to less than one quarter of its initial value at 130Å thickness. The scattering into Bragg beams is less in aluminium, and much less in silver. In small particles, we could expect to see much stronger lattice fringe contrast in diamond than in either aluminium or silver³.

References

1. J. Halbout, F. Robert, and M. Javoy, *Geochim. Cosmochim. Acta* (1986) 50, 1599-1609.
2. R.S. Lewis, T. Ming, J.F. Wacker, E. Anders and E. Steel, *Nature* (1987) 326, 160-162.
3. The author would like to acknowledge support from the Australian Research Council, and also the support of, and the use of the facilities at the Centre for Microscopy and Microanalysis at the University of Queensland.

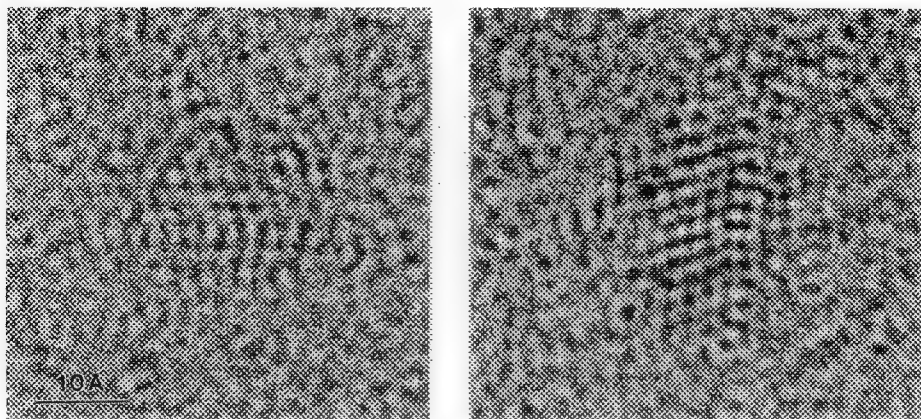


Fig. 1. Typical images of the small diamonds from the Orgueil meteorite.

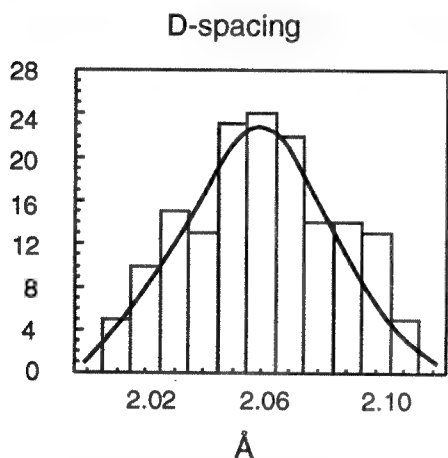


Fig. 2. The distribution of d-spacings measured from the small diamond particles.

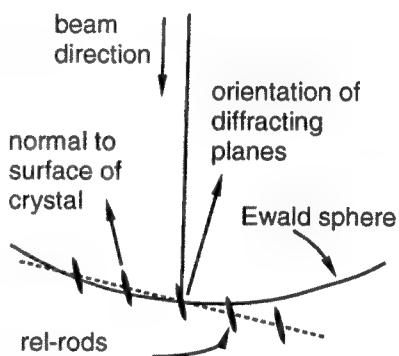


Fig. 3. A schematic diagram of diffraction streaks from a small particle.

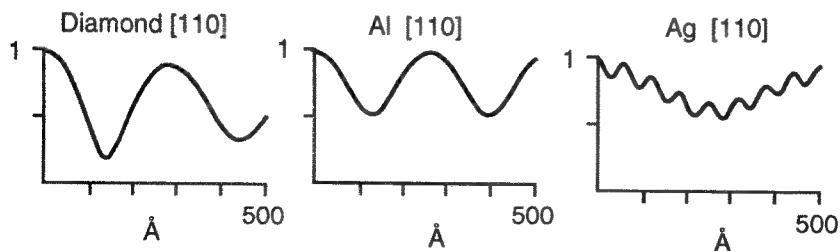


Fig. 4. Pendellosung behaviour of the central beam for the [110] zone axis.

TRANSMISSION ELECTRON MICROSCOPY STUDIES OF BORON NITRIDE THIN FILMS PRODUCED BY PULSED LASER DEPOSITION

D.L. Medlin, T.A. Friedmann, P. B. Mirkarimi, K.F. McCarty, and M.J. Mills

Sandia National Laboratories, Livermore, California 94551 USA

We are synthesizing boron nitride films by pulsed laser ablation in order to study the deposition conditions necessary to produce the cubic phase (cBN) which has a number of useful applications as a hard coating, semiconductor, and optical material. The yield of cubic material is controlled in part by the simultaneous irradiation of the growing film with a low energy beam of N_2 and Ar ions. In order to understand how this transformation process occurs, we are using TEM to investigate how the microstructure and phase distribution varies with film deposition conditions.

In many ways analogous to carbon, boron nitride forms both sp^3 - and sp^2 -bonded phases. The cubic phase (cBN), which is sp^3 bonded, has the zinc blende structure, and in addition, BN can also form an sp^3 bonded hexagonal phase with the wurtzite structure (wBN). An sp^2 -bonded hexagonal structure (hBN) is the stable room temperature phase, but like its analog, graphite, the sp^2 -bonded material can also exist in a highly disordered state, often referred to as turbostratic (tBN). In the turbostratic material, the basal planes form out of registry and are severely bent. Such distortion complicates electron diffraction analysis by broadening the hBN (100) and (101) peaks to form a broad "(10)" peak at about 2.13 \AA^{-1} . This can cause identification of the cBN (111) peak (2.088 \AA) to be ambiguous, although the tBN (10) peak is of lower intensity and somewhat more diffuse. The analysis is further complicated if the cBN crystallites are of nanometer dimensions since the weak cBN (200) peak may not be distinguishable above the background of the broadened cBN (111) peak².

Because of such complications, we have used several complementary techniques to assess the distribution of the hexagonal and cubic phases. Figure 1 shows electron diffraction intensities from films grown with and without ion irradiation. The ion irradiated sample matches well with the expected peak positions for cBN, although the presence of a broad peak at about 3 nm^{-1} indicates that some of the hexagonal/turbostratic material is present as well. This interpretation is further confirmed by EELS measurements of these films (Figure 2). Here, the π^* peak, which is characteristic of the sp^2 bonding in the hexagonal phase, is absent from the spectrum taken from a crystallite within the irradiated region. The absence of the π^* peak indicates that the ion-irradiated material is primarily sp^3 -bonded. High resolution TEM observations of these films further demonstrate that within the unirradiated film (Figure 3), the material is indeed disordered and turbostratic, whereas within the irradiated region, the material consists of cBN crystallites that are heavily faulted and possess a large number of twins³.

References

1. J. Thomas, Jr., N. E. Weston, and T. E. O'Connor, J. Amer. Chem. Soc. (1963) **84**, 4619.
2. D.R. McKenzie, W.G. Sainty, and D. Green Materials Science Forum (1990) **54-55**, 193.
3. This research is supported by the U.S. Department of Energy, Office of Basic Energy Sciences, Division of Material Sciences, under contract DE-AC04-76DP00789. EELS measurements were conducted at the Center for High Resolution Electron Microscopy, Arizona State University, which is supported by the National Science Foundation under grant number DMR-9115680. The authors gratefully acknowledge the assistance of Prof. P. Rez in obtaining the EELS results.

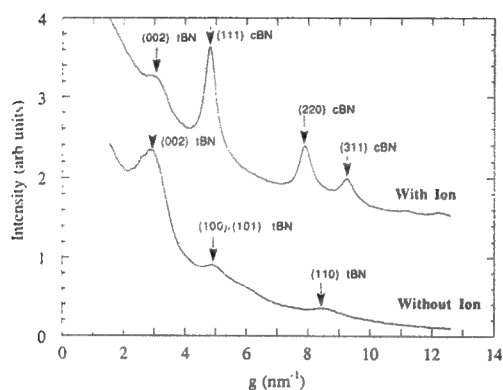


FIG. 1.-- Electron diffraction intensities from boron nitride films deposited with and without ion irradiation. Results indicate a two phase mixture of the turbostratic and cubic structures in the ion irradiated film.

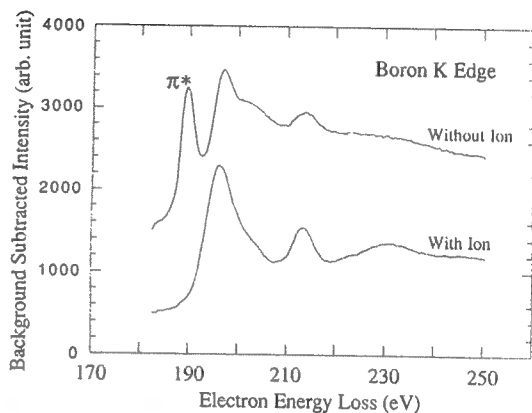


FIG. 2.-- Electron energy loss spectra from films deposited with and without ion irradiation. Absence of π^* peak in ion irradiated film indicates that material is primarily sp^3 -bonded.

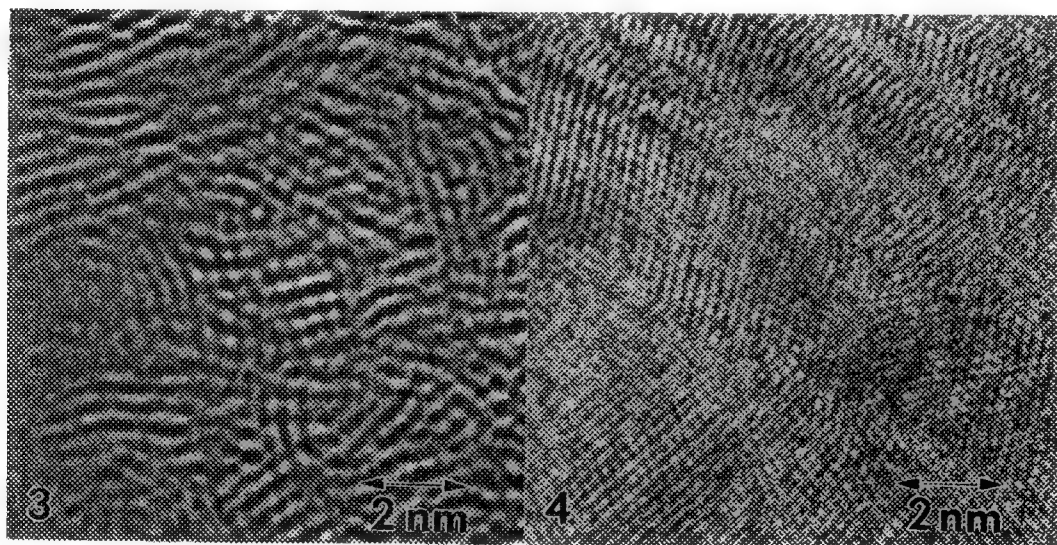


FIG. 3.--HRTEM image of turbostratic material in BN film deposited without ion irradiation.

FIG. 4.--HRTEM image of twinned cBN crystallites in film deposited with ion irradiation.

HREM STUDY OF STRONG METAL-SUPPORT INTERACTION IN Pt/TiO₂

Ming-Hui Yao

Department of Physics and Center for Solid State Science, Arizona State University, Tempe, AZ 85287, USA

The chemisorption ability and catalytic properties of metal particles supported on reducible oxides are often altered by high temperature reduction (HTR) in a process known as strong metal-support interaction (SMSI) [1]. Different models [2-4] have been proposed to explain the SMSI mechanism. In recent years, experimental evidences [5-8] have favored the "decoration model", which suggests that SMSI is due to the encapsulation of the metal particles by oxide overlayer species that have migrated from the support. HREM profile imaging was the most useful tool to directly relate these surface decorations to the SMSI effects. The profile imaging can provide atomic-scale information about supported particles and their surfaces without image being obscured by overlapping contrast from the support [10].

In the present work, the SMSI effect in Pt/TiO₂ and Pt/CeO₂ model catalysts have been studied using HREM profile imaging and multislice simulations. HREM observations were made with a JEM-4000EX microscope, operated at 400 kV. Fig. 1(a) shows a typical profile image of TiO₂ after HTR in H₂ at 923K. On well-faceted {111} surfaces, crystalline monolayers (marked A) are clearly visible along <110> projection, whereas surfaces in other directions on some larger particles (>2nm) appear relatively rough and covered by a less-ordered oxide overlayer (marked B). In contrast to the stable monolayer observed on {111} surfaces, the thicker overlayers changed under electron irradiation. Fig. 2 shows this process of structural change. The oxide layer on the particle marked A was gradually etched away by the electron beam, whereas the overlayer on the particle marked B showed growth under the beam. It seems unlikely that the layer is Pt oxide because of the facts that the sample was thoroughly reduced in H₂ and no similar layer was found on Pt/CeO₂ in a similar HTR state. It is possible that the oxide overlayer represents a suboxide of Ti, which migrated from the support, blocked certain atomic sites on the Pt surface and thereby caused the substantial drop of butane hydrogenolysis activity [11]. The relatively clean surfaces for Pt/TiO₂ visible in Fig. 1(b) could explain catalytic reversibility [11] after low temperature reduction and oxidation.

Unlike the thicker oxide overlayers on Pt surfaces, the monolayers on {111} surfaces exhibited high contrast and clear atomic positions. The average periodicity in the monolayer was close to that of Pt in the {111} plane, but the spacing between the monolayer and the top {111} plane of Pt is about 20% larger than that of Pt {111}. Most black dots corresponding to atomic column positions in the monolayer are somewhat elongated along {100} plane. Multislice image simulations were attempted to identify the monolayer and a few simulated images are shown in Fig. 3. It appears that the elongation of the black dots in the surface layers could be due to oxygen termination.

It is concluded that the HREM profile technique and multislice simulations are useful tools for studying the surface structure of supported fine particles on atomic scale. Crystalline monolayers on {111} Pt/TiO₂ surfaces in HTR state were observed by profile imaging. It was believed that they could contribute to the SMSI state in Pt/TiO₂ catalysts.

References

- [1] S. J. Tauster, S. C. Fung, and R. L. Garten, *J. Am. Chem. Soc.* 100 (1978)170.
- [2] S. J. Tauster and S.C. Fung, *J. Catal.* 55 (1978)29.
- [3] J.M. Herrmann, and P. Pichat, *J. Catal.* 78 (1982)425.
- [4] J. A. Horsley, *J. Amer. Chem. Soc.* 55 (1979)29.
- [5] J. Santos, J. Phillips, and J. A. Dumesic, *J. Catal.* 81, (1983)147.
- [6] R. T. Baker, E. B. Prestidge and L. L. Murrell, *J. Catal.* 79 (1983)348.
- [7] A. D. Logan, E. J. Braunschweig, A. K. Datye and D. J. Smith, *Langmuir*, 4(1988)827.
- [8] E. J. Braunschweig, A. D. Logan, A. K. Datye and D. J. Smith, *J. Catal.* 118 (1989)227.
- [9] L. Wang, G. W. Qiao, H. Q. Ye, K. H. Kuo, and Y. X. Chen, *Proc. 9th International Congress on Catalysis*, p.1253. The Chemical Institute of Canada, Ottawa, 1988.
- [10] M. H. Yao and D. J. Smith, these proceedings.
- [11] K. J. Blenkinsop and A. K. Datye, *J. Catal.*, 128 (1991)186.
- [12] The author is grateful to Dr. D. J. Smith for helpful advice and Dr. A. K. Datye for providing catalyst samples. The microscopy was conducted at the Center for High Resolution Electron Microscopy supported by NSF Grant DMR-9115680.

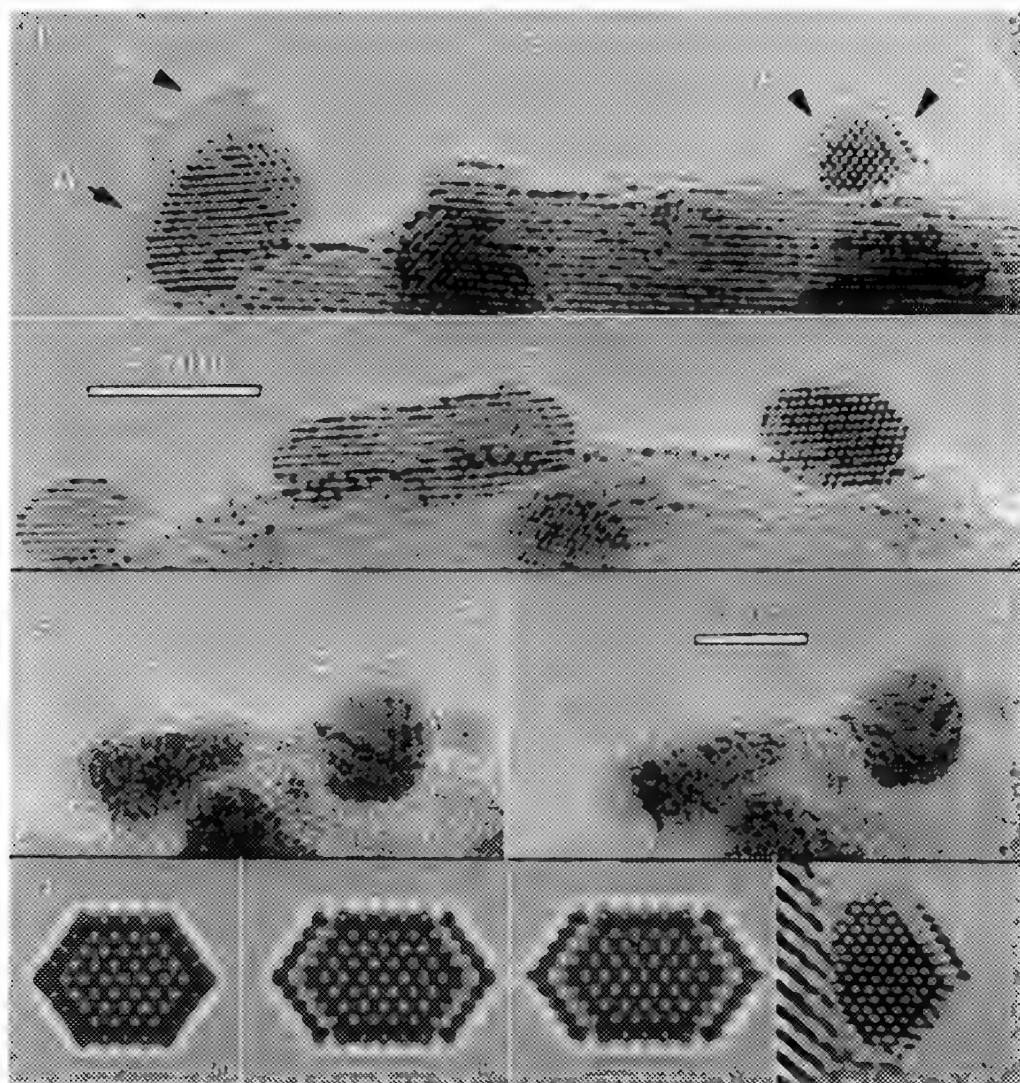


Fig.1. (a) Profile view of overlayers on Pt/TiO₂ (H₂ @923K). (b) Clean surfaces of Pt/TiO₂ (H₂ @773 K, O₂ @673 K).

Fig.2 Structure changes of surface oxide overlayers on Pt/TiO₂ under electron beam.

Fig.3. (a)-(c) Simulated images at 400 kV and defocus of 51 nm. (a) Pt particle with clean surfaces. (b) (111) surfaces of Pt particle covered by Ti monolayers (c) TiO surface layer on Pt particle. (d) Electron micrograph of Pt particle in SMSI state recorded at 400 kV. The (111) surface is covered by a monolayer.

HREM IMAGE SIMULATIONS FOR SUPPORTED METAL PARTICLE CATALYSTS

Ming-Hui Yao and David J. Smith

Department of Physics and Center for Solid State Science, Arizona State University, Tempe, AZ 85287

The chemical properties of catalysts often depend on the size, shape and structure of the supported metal particles. To characterize these morphological features and relate them to catalysis is one of the main objectives for HREM study of catalysts. However, in plan view imaging, details of the shape and structure of ultra-fine supported particles (<2nm) are often obscured by the overlapping contrast from the support, and supported sub-nanometer particles are sometimes even invisible. Image simulations may help in the interpretation at HREM images of supported particles in particular to extract useful information about the size, shape and structure of the particles. It should also be a useful tool for evaluating the imaging conditions in terms of visibility of supported particles. P. L. Gai et al have studied contrast from metal particles supported on amorphous material using multislice simulations[1]. In order to better understand the influence of a crystalline support on the visibility and apparent morphological features of supported fine particles, we have calculated images of Pt and Re particles supported on TiO₂(rutile) in both plan view and profile view.

The simulations were performed on a VAX/VMS computer using the EMS package[2], which is an implementation of the multislice algorithm. Most supported particles used in our calculation were configured as perfect cuboctahedra with sizes ranging from 0.6 nm(13 atom one-shell model) to 2.3 nm(309 atom 4-shell) in diameter. Unit cells used in computing (Super cell) were constructed sufficiently large that interference between particles in different super cells was negligible. In the profile image simulations, half of the super cell was filled with atoms and the other half was vacuum, and the supported particle was placed on the crystal-vacuum interface parallel to the beam direction. In plan view, the particle was on the support surface perpendicular to beam direction. HREM images were simulated for support thicknesses from 2 to 15 nm at various defocus values. 256x256 and 512x256 sampling points were used for dynamical wave function calculations in plan view and profile view respectively.

Some of the simulated images are shown in Fig.1-Fig.5. It was found that Scherzer defocus, also known as the optimum defocus, was not a favorable imaging condition in terms of visibility of supported ultra-fine particles. Particles smaller than 2 nanometer showed poorest visibility in plan view at the defocus(about 50 nm for 400keV, Cs = 1.0 mm). For example, an isolated ReO₄ cluster on TiO₂ of 2 nm in thickness (Fig.4) is invisible at this defocus in <001> projection, but it is visible at 140 nm defocus. Generally, it was found that the visibility of supported particles improved as the defocus value increased. Especially, at half-spacing defoci and reverse-contrast defoci the supported subnanometer particle(ReO₄ and 13 atom Pt particle) showed up better than at other defocus values, although the detailed information about the atomic arrangements and particle shape was still not available. For larger particles, it is possible to resolve the atomic configuration and particle shape at some defoci greater than the optimum. In fig.2(d) and (e), atom columns and even the particle shape for a 55-atom cuboctahedron seem resolvable at support thickness of 2 nm. The apparent size of subnanometer particles is smaller than the actual size around optimum defocus, but may appear larger at defoci that are significantly greater. Particles usually appear detectable for support thickness up to five times of its diameter. For example 309-atom Pt particles(2.3 nm in diameter) are even visible on supports of 12 nm in thickness. In comparison with previous results, it seems that particles supported on crystals have better visibility than those on amorphous supports. This is probably because: (1) Particles are more easily detectable above periodic background than for random noise; and (2) Simulations were done for greater defocus values instead of just around the optimum defocus. The Fresnel fringe and relatively low contrast from supports at greater defocus enhanced visibility significantly.

Fig.5 confirms that the profile imaging method can provide atomic-scale information about supported particles without the images being affected by contrast from the support. At optimum defocus, atom columns in 13-atom cluster are clearly visible. More importantly, the surfaces of supported particles can be studied on the atomic scale by profile imaging. It may even be possible to establish whether a surface is terminated by oxygen atoms using assistance from image simulations[3].

Reference

- [1]P.L. Gai, M. J. Goringe and J. C. Barry, J. of Microsc. 142(1986)9.
- [2]P.A. Stadelmann, Ultramicroscopy 21(1987)131.
- [3]M.H. Yao, These proceedings.
- [4]This work has been partially supported by a grant from Mobil R&D, Paulsborro, NJ.

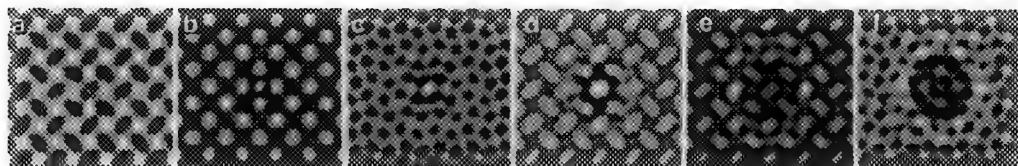


Fig. 1. 13 atom cuboctahedral Pt particle on TiO_2 support. Support thickness = 3 nm
The defocus (from left to right): 50, 60, 70, 80, 120, 140 nm. Scherzer defocus: 50 nm

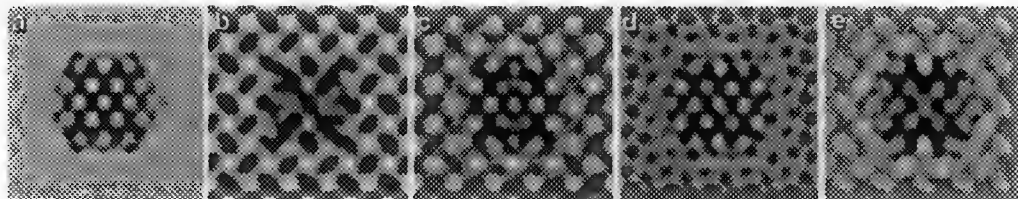


Fig. 2. 55 atom cuboctahedral Pt particle along $\langle 110 \rangle$ projection. (a) $\text{Df} = 60$ nm, without support.
(b)-(e): Defocus = 50, 60, 70, 80 nm. TiO_2 support thickness = 2 nm.

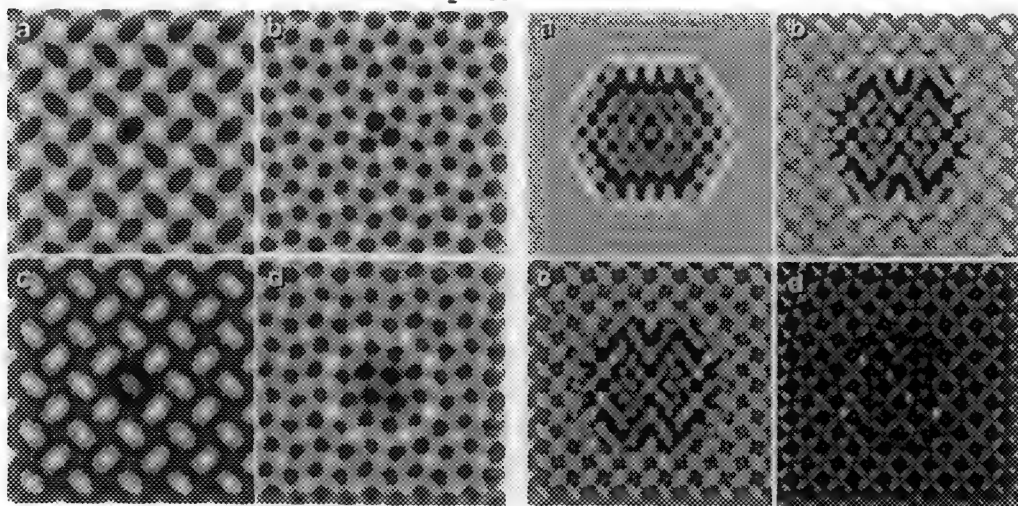


Fig. 3. ReO_4 cluster on TiO_2 . Thickness = 3 nm
Defocus = 50, 80, 120, 140 nm

Fig. 4. 309 atom Pt particle. $\text{Df} = 80$ nm
Support thickness = 0, 3, 5, 10 nm

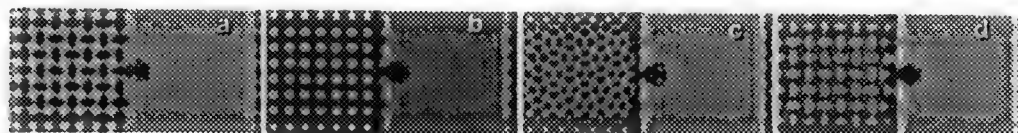


Fig. 5. Profile images of 13 atom particle on TiO_2 (110) surface. Support thickness along the beam direction is 3 nm. Defocus: 50, 60, 70, 80 nm

AUTOMATED PARTICLE ANALYSIS IN ELECTRON MICROSCOPY

Tim B. Vander Wood

MVA, Inc., 5500 Oakbrook Parkway #200, Norcross, GA 30093

The ability to quickly and economically characterize particle samples is increasingly important. A knowledge of particle size distributions can be critical in a wide variety of processes, from powder metallurgy to ethical drug delivery. Powdered materials may be contaminated at levels of only one particle in one thousand and still be unsuitable for use. Particulate samples may represent a variety of materials from many sources, requiring complex analyses for complete characterization. The traditional analytical approach to these problems, dictated by the need for economy, has been the application of batch techniques (e.g. light scattering) to the problem of particle sizing and trace component and bulk techniques (e.g. atomic absorption, x-ray fluorescence) to the problems of particle analysis. Scanning electron microscopy (SEM), combined with energy-dispersive x-ray spectrometry (EDS), is capable of directly measuring the required individual particle sizes, morphologies and compositions but has not been widely applied due to the high cost of analysis of several hundred to thousands of particles which may be required to adequately represent an entire population.

However, an SEM/EDS system operating under computer control can automatically determine the size and composition of as many as thousands of individual particles in a matter of hours. Advances in EDS and computer hardware, the application of standard image processing algorithms for particle recognition and morphology measurement, and the availability of sophisticated spreadsheet programs for data handling and presentation make direct determination of individual particle characteristics competitive with batch and bulk techniques. Systems for performing automated analyses by SEM are now commercially available from a variety of manufacturers and emerging applications of this technology are supplanting and complementing batch and bulk techniques in the analysis of complex samples.

Sizing of powders in manufacturing is commonly done by light scattering, despite recognized difficulties in data interpretation. Calibration of this equipment against ground truth data supplied by microscopical particle size measurements can improve its accuracy.¹ Figure 1 compares the results of uncalibrated light scattering particle size measurements of particles with those determined by direct measurement using image analysis and an automated SEM. The uncalibrated light scattering instrument (LS) determined a broader and flatter size distribution than could be confirmed by direct measurement.

A more sophisticated use of automated SEM employs EDS to acquire elemental composition data for every particle detected by image analysis. Interesting particles at trace levels in a sample that cannot be distinguished solely by morphological properties can be found on the basis of elemental composition. Needle-in-a-haystack applications include the detection and quantification of free silica in industrial minerals and gun shot residue detection.^{2,3} In other applications, characterization and sizing of all particle types present is required; e.g., contaminant particles in ultra clean water systems or mineralogical characterization of smelter dusts.^{4,5}

One application with aspects of both needle-in-a-haystack and full sample characterization requirements is the analysis of particulate air pollution. An airborne particulate sample collected in a Prague, Czechoslovakia traffic tunnel contains a wide variety of materials from natural and anthropogenic sources.⁶ Automated SEM/EDS analysis of several hundred particles allows the determination of the types of particles present, their size distributions and

other morphological characteristics and can generate estimates of bulk population composition for comparison to results from more traditional methods.

Figure 2 shows the distribution based on number of particles for twelve particle types found in the tunnel air. Most particles appear to be soil derived aluminosilicates and carbonates, but some types appear to be anthropogenic. Particularly interesting are particles containing high levels of lead and bromine. These particles are derived from gasoline combustion, and represent a health hazard due to their high lead content. Some of this hazard would be ameliorated if the Pb-Br particles were in a size fraction that was not easily respirable. Figure 3 shows this to not be the case: these Pb-Br particles are concentrated in an easily respirable fraction ($<2\mu\text{m}$ diameter). Figure 4 presents a comparison between the bulk composition derived from the individual particle data and from XRF measurements. There is reasonable agreement between XRF and the SEM/EDS data for elements other than Pb and Br. The SEM/EDS data underrepresents these elements due to the use of higher energy x-ray lines (M and L, respectively) for their detection. Corrections for all elements based on normalized k-ratios are under investigation.

References

1. J. Hefter and L. Steriti, *Part. Sci. and Tech.*, 10(1992)91.
2. T. Vander Wood and W. Boltin, in D. Hausen, et al., Ed., *Process Mineralogy XI* (1991)37.
3. M. Germani, *Jour. For. Sci.* 36(1991)331.
4. T. Vander Wood and L. Detter, in K. Mittal, Ed., *Proc. 2nd Symp. on Part. in Gas. and Liq.* (1991).
5. T. Vander Wood, *Proc. Ann. EMSA Meeting* 50(1992)1492.
6. Sample provided by R.D. Willis, ManTech Environmental Technology, Inc.

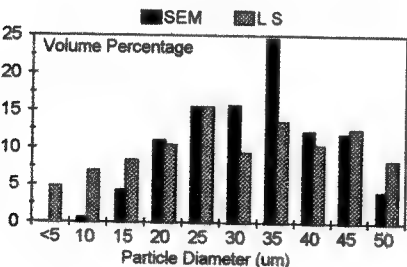


Figure 1: Comparison of particle sizing, SEM vs. light scattering.

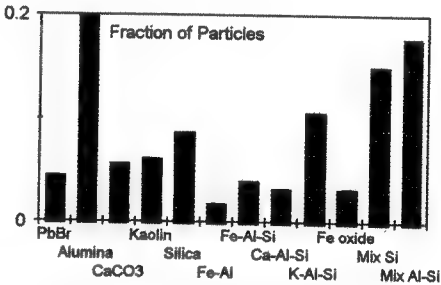


Figure 2: Particle type distribution in Prague tunnel.

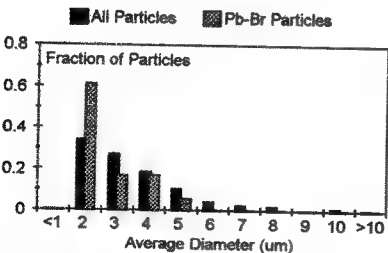


Figure 3: Size distribution of Prague tunnel particles.

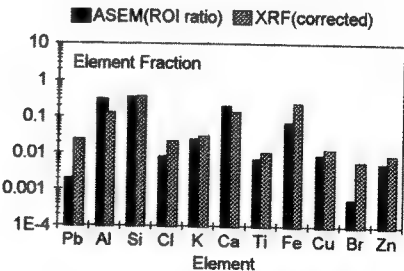


Figure 4: Element concentration in Prague tunnel particles.

ORIGINS OF FINE PARTICLES IN A POWER PLANT-PLUME AS DETERMINED USING INDIVIDUAL-PARTICLE ANALYSIS

Karen A. Katrinak and John P. Hurley

Energy and Environmental Research Center, University of North Dakota, Grand Forks, North Dakota 58202-9018 U.S.A.

Individual particles from the fine fraction of samples of entrained ash from a coal-burning power plant were analyzed using an automated scanning electron microscope with an energy-dispersive x-ray spectrometer. The particles were of concern as a probable cause of high levels of opacity in the plant emissions. Both the mass loading and the number size distribution of fine particles peak in the size range of 0.4 to 0.8 μm diameter.

Most of the fine particles are Na-, S-, P-, or Cl-rich. The coal is likely to be the major source for these particles. Minerals and organically-associated metals in the coal can remain in the solid phase during combustion, forming ash particles of varied sizes, including those in the submicron range. Elements are also vaporized during combustion, and Na- and S-bearing particles may form when gas-phase Na_2SO_4 condenses homogeneously in the convective pass of the boiler. Phosphate and chloride particles may also condense homogeneously. These submicron particles are too small to be removed by the wet scrubber, and thus ultimately become part of the plant emissions. Fine particles may also form when solids precipitate from the scrubber water. Many of the particles contain varied proportions of Al, Si, and Mg. The scrubber water contains high levels of Al, Si, and Mg, as well as Na and S, and thus may be another source for the fine particles.

Transmission electron microscope imaging showed that both submicron and supermicron ash particles are composed of many tiny spherules combined into aggregates (Figs. 1, 2). Each spherule has a diameter of between approximately 0.05 and 0.10 μm . In some instances, the spherules appear to be sintered together, suggesting aggregation may have occurred at elevated temperatures or that vapor-phase condensation may have occurred after aggregation, smoothing the spherule surfaces through deposition of coatings.

Calculations based on Mie theory^{1,2} show that particle size is the major factor influencing scattering (Fig. 3), the primary means of light extinction in the plume studied here. Both Na_2SO_4 and scrubber-precipitate particles thus evidently cause the plume opacity, although the Na_2SO_4 particles are the major contributors because of their greater concentration. The effect of the fine particles on plume opacity is maximized because their size distribution peaks near a diameter equal to the wavelength of visible light, the particle size with the greatest amount of scattering per unit mass.

References

1. G. Mie, Ann. Phys. 25 (1908) 377.
2. C.F. Bohren and D.R. Huffman, Absorption and Scattering of Light by Small Particles, New York: John Wiley & Sons (1983) 477.

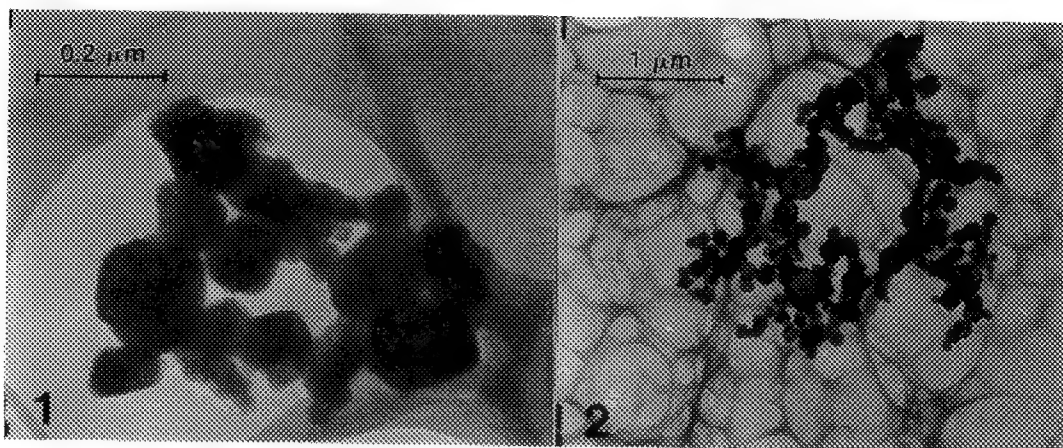


FIG.1--Transmission electron microscope image of a submicron ash aggregate.

FIG.2--Transmission electron microscope image of a supermicron ash aggregate.

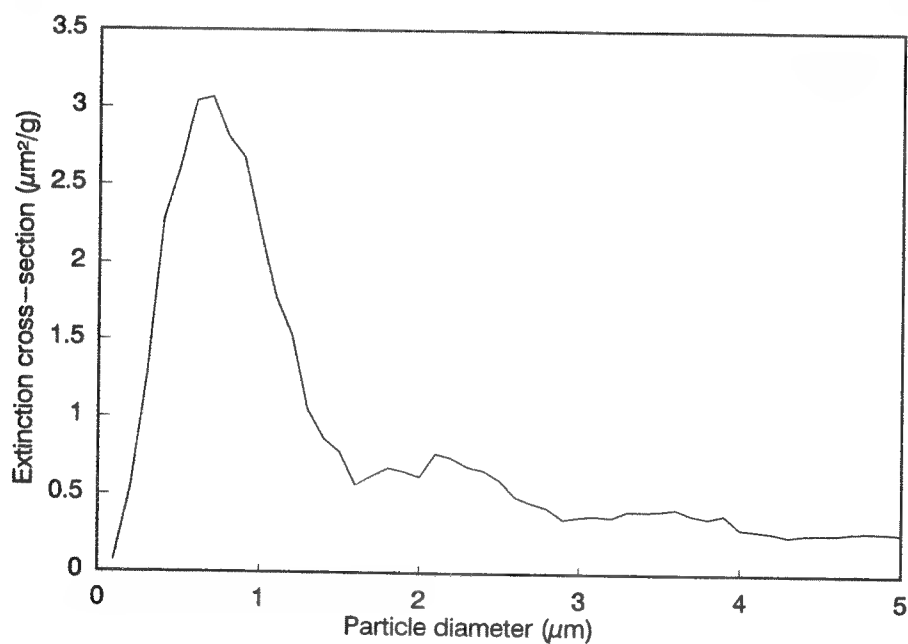


FIG.3--Calculated extinction cross-sections per unit mass for Na₂SO₄ particles of varied diameter.

LONG-TERM VARIATIONS IN INDIVIDUAL PARTICLE TYPES IN THE AEROSOL OF PHOENIX, ARIZONA, AS DETERMINED USING AUTOMATED ELECTRON MICROPROBE ANALYSIS AND MULTIVARIATE STATISTICAL TECHNIQUES

Karen A. Katrinak,^{1*} James R. Anderson,² and Peter R. Buseck^{1,2}

Departments of Geology¹ and Chemistry,² Arizona State University, Tempe, Arizona 85287 U.S.A.
(*Current address: Energy and Environmental Research Center, University of North Dakota, Grand Forks, North Dakota 58202-9018 U.S.A.)

Aerosol samples were collected in Phoenix, Arizona on eleven dates between July 1989 and April 1990. Elemental compositions were determined for approximately 1000 particles per sample using an electron microprobe with an energy-dispersive x-ray spectrometer. Fine-fraction samples (particle cut size of 1 to 2 μm) were analyzed for each date; coarse-fraction samples were also analyzed for four of the dates.

The data were reduced using multivariate statistical methods.^{1,2} Cluster analysis was first used to define 35 particle types. 81% of all fine-fraction particles and 84% of the coarse-fraction particles were assigned to these types, which include mineral, metal-rich, sulfur-rich, and salt categories. "Zero-count" particles, consisting entirely of elements lighter than Na, constitute an additional category and dominate the fine fraction, reflecting the importance of anthropogenic air pollutants such as those emitted by motor vehicles. Si- and Ca-rich mineral particles dominate the coarse fraction and are also numerous in the fine fraction. Metal-, S-, and salt-bearing particles are minor contributors, found mainly in the fine fraction.

Eighteen particle types each comprised >1% of the particles in at least one sample; they were used for principal components analysis. Four principal components (PCs) with eigenvalues ≥ 1.0 prior to Varimax rotation were identified, accounting for 88% of the variance in the data matrix. PC1 consists of ten particle types, mostly mineral-rich. PC2 comprises three S-bearing particle types, two of which are also Na-bearing. PC3 has eight particle types, including five metal-rich and three mineral-rich. PC4 includes two particle types, one a Br-bearing aluminosilicate type, the other S-rich.

Absolute principal component scores³ for PC1 are highest for samples collected on the two dates associated with episodes of urban haze (Figs. 1 and 2), suggesting local crustal sources for the mineral-rich particles it represents. PC2 is absent from the coarse-fraction samples on the two haze dates, suggesting a distant source such as a power plant or smelter. Absolute principal component scores for PC3 are highest for the coarse-fraction samples on the two haze dates, suggesting local sources, possibly industrial, for these compositionally varied particles. The chemical composition of particles in PC4 suggests they represent, at least in part, a secondary aerosol source.

Lower Pb concentrations in the 1989-90 samples compared with samples collected in the early 1980's⁴ probably reflect decreased usage of leaded gasoline. A difference in the number of S-bearing particles was also noted; S-bearing particles comprised 30% of the fine fraction of the earlier samples but only 17% of the fine fraction in the 1989-90 samples.⁵

References

1. D.A. Saucy et al., *Atmos. Environ.* 21 (1987) 1649.
2. T.W. Shattuck et al., *Anal. Chem.* 63 (1991) 2646.
3. G.D. Thurston and J.D. Spengler, *Atmos. Environ.* 19 (1985) 9.
4. J.R. Anderson et al., *Environ. Sci. Technol.* 22 (1988) 811.
5. This research supported in part by NSF grants #ATM-9007796 and ATM-8707070.

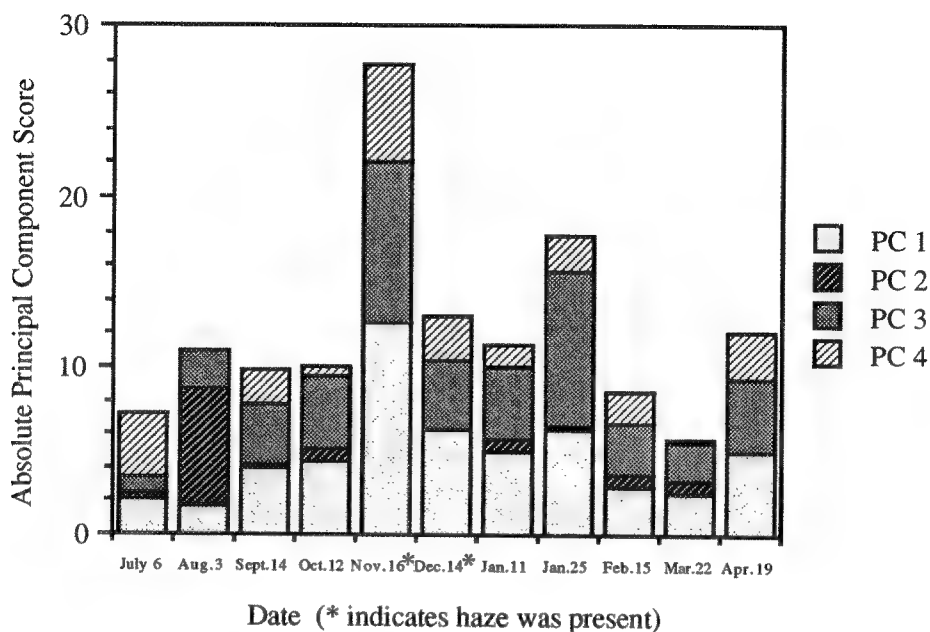


FIG. 1--Absolute principal component scores for fine fraction of Phoenix aerosol samples, showing four principal components.

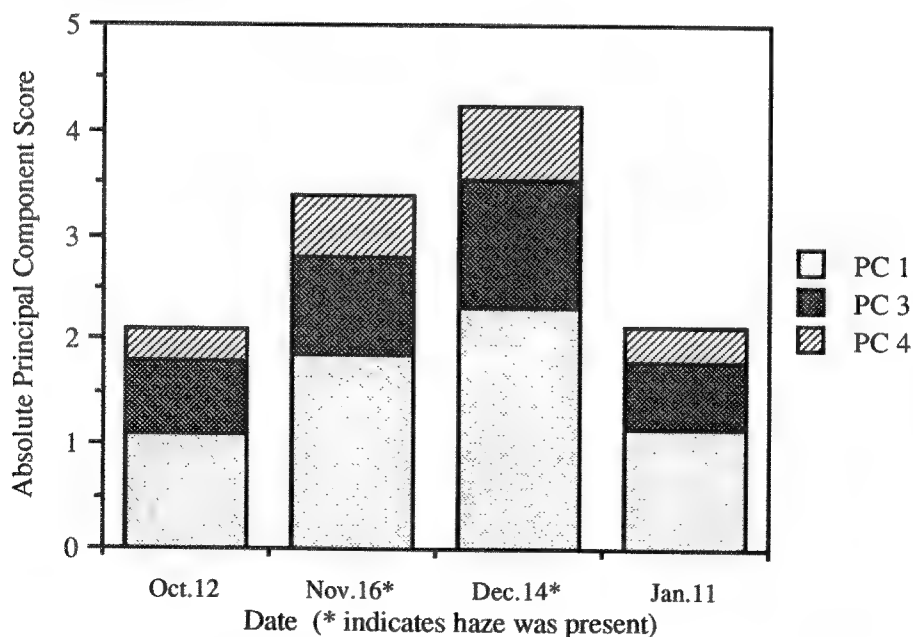


FIG. 2--Absolute principal component scores for coarse fraction of Phoenix aerosol samples. PC2 is absent from the coarse fraction.

CHEMICAL TWINNING IN THE $\text{Ti}_4\text{C}_2\text{S}_2$ -TiS SYSTEM

Mingjian Hua, C. I. Garcia and A. J. DeArdo

Basic Metals Processing Research Institute, Materials Research Center, Department of Materials Science and Engineering, University of Pittsburgh, Pittsburgh, PA 15261

Titanium carbosulfide $\text{Ti}_4\text{C}_2\text{S}_2$ (H phase, $P6_3/mmc$, $a=0.321$ nm and $c=1.120$) and titanium sulfide TiS ($R\bar{3}m$, $a=0.3417$ nm and $c=2.65$) are frequently found to coexist within a sandwich-like composite particle in ultra-low carbon interstitial-free (IF) steels.¹ This morphology seems to suggest that a direct transformation from TiS to $\text{Ti}_4\text{C}_2\text{S}_2$ may be a major mechanism for the stabilization of C at higher temperatures in these steels. The deduced orientation relationship between $\text{Ti}_4\text{C}_2\text{S}_2$ and TiS is in agreement with a reported crystal structure model.² However, the transformation mechanism between these two phases appears to be strongly related to their defect structures.

At the as-cast condition, most of the S- and C-rich particles in the studied IF steels were identified as pure $\text{M}_4\text{C}_2\text{S}_2$ ($M=\text{Ti, Nb}$). After a re-heating treatment at 1300°C , $\text{M}_4\text{C}_2\text{S}_2$ disappeared but TiS and a new phase were observed. This new phase can be indexed as a trigonal sulfide polytype with $a=0.33$ nm and $c=5.3$ nm (Figure 1). After a second re-heating treatment at 1220°C , $\text{Ti}_4\text{C}_2\text{S}_2$ appeared at the center layer of the multi-phase particles (Figure 2). It should be noted that (i) some planar defects were observed inside the new phase and $\text{Ti}_4\text{C}_2\text{S}_2$ carbosulfide (Figure 1a and 2a). Similar faults were also reported in $(\text{Ti,Nb})_4\text{C}_2\text{S}_2$ particles in a superalloy,³ (ii) frequently, the TiS layers outside the $\text{Ti}_4\text{C}_2\text{S}_2$ layer are found to have a twin relationship (Figure 2b) and (iii) sometimes the $\text{Ti}_4\text{C}_2\text{S}_2$ layer between such TiS layers is just a single $(0001)_H$ thick (1.12 nm, Figure 3). These observations seem to imply that (i) the faulted planes may not be simple stacking faults, but rather may have resulted from the incomplete transformation reaction from TiS or sulfide polytype towards $\text{Ti}_4\text{C}_2\text{S}_2$, and (ii) the TiS- $\text{Ti}_4\text{C}_2\text{S}_2$ transformation could occur by a special intergrowth mechanism known as chemical twinning.⁴ It follows that the non-stoichiometric composition of the precipitates may be related to two factors. The major factor is the multi-phase nature of the particle, while the minor one is the transformation characteristics, or defect, in the TiS- $\text{Ti}_4\text{C}_2\text{S}_2$ system.

It is well-known that (i) the formation of stacking faults and polytypes in the sulphide is relatively easy,^{5,6} and (ii) some transformations among the sulfides occur by chemical twinning.⁴ The present work suggests that similar phenomena exist in the TiS- $\text{Ti}_4\text{C}_2\text{S}_2$ system, and also that there may exist an internal relationship among various planar defects. For example, a simple stacking fault along $(0001)_H$ can absorb S atoms or expel C atoms thus can become an extended stacking fault (i.e., Suzuki atmosphere) while repeated stacking faults may result in TiS or sulfide polytypes. Similarly, a twin boundary along $(0003)_{\text{TS}}$ can absorb Ti and C atoms and can result in chemical twinning, while abundant chemical twinning can result in $\text{Ti}_4\text{C}_2\text{S}_2$. Moreover, the chemical twinning in the TiS- $\text{Ti}_4\text{C}_2\text{S}_2$ system may be equivalent to a special sequence of extended stacking faults. In other words, various terminologies may be just different ways of describing the same phase transformation phenomenon. A recent study on the defect structure of $\text{Nb}_{1+x}\text{S}_2$ also revealed such a possibility.^{6,7}

References

1. Mingjian Hua, C. I. Garcia and A. J. DeArdo, Scripta Met., 28, No. 8, 1993, in press.
2. E. P. Whelan and M. S. Grzedzielski, Metals Technology, 1, 186 (1974).
3. R. Vincent, Acta Metall., 33, 1205 (1985).
4. M. Bakker and B. G. Hyde, Phil. Mag. A, 38, 615 (1978).
5. J. J. Legendre et al., Progress in Crystal Growth and Characterization, Vol. 7, Ed. P. Krishna, p309, Pergamon Press, Oxford; New York, 1983.
6. C. Zhou and L. W. Hobbs, Proc. 50th Ann. Meeting of EMSA, Ed. G. W. Bailey, J. Bentley and J. A. Small, p38, EMSA, San Francisco Press, Inc., CA, 1992.
7. This work is supported by the Research Center of the LTV Steel Corp., Independence, OH, and Niobium Products Company Inc., Pittsburgh, PA.

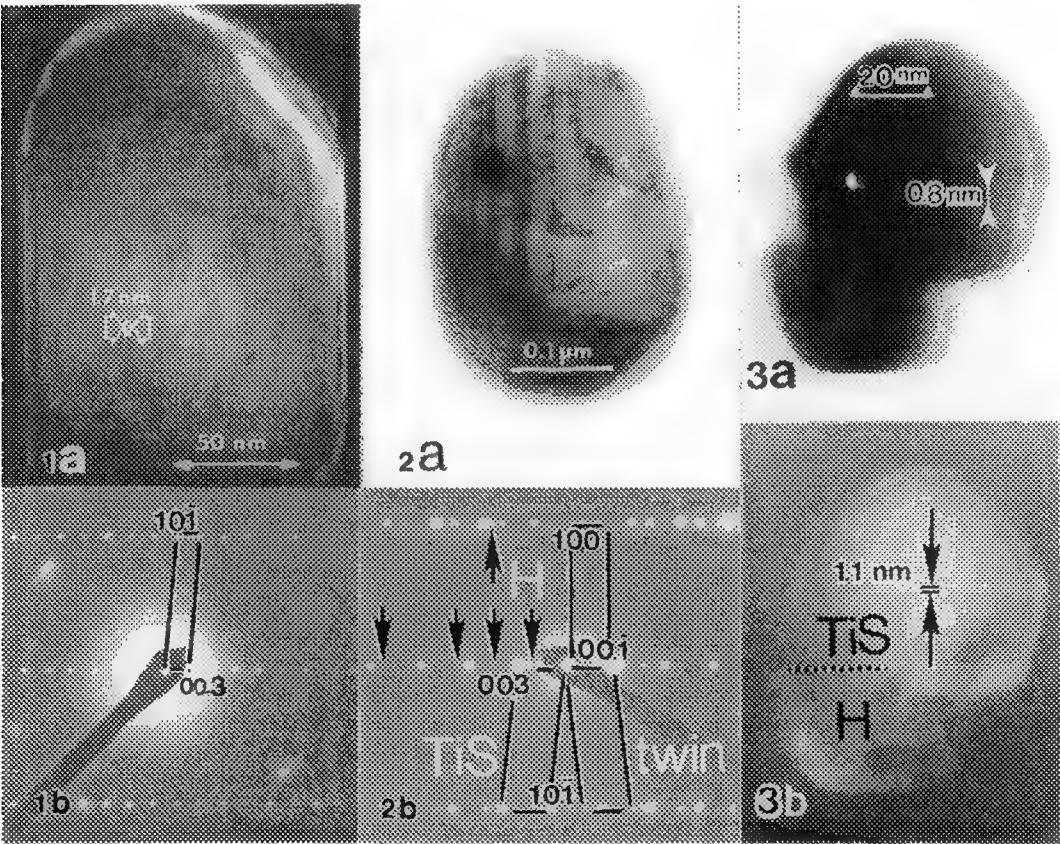


FIG. 1.--a) Dark field (DF) lattice image and b) corresponding diffraction pattern (DP) of a new phase, indexed as $[12\bar{1}0]$ of a trigonal lattice, note the a^* is equivalent to that of TiS.
FIG. 2.--a) Typical micrograph of a multi-phase particle and b) DP of $[\bar{1}2\bar{1}0]_{\text{TiS}} \parallel [\bar{1}2\bar{1}0]_{\text{twin}} \parallel [\bar{1}2\bar{1}0]_{\text{H}}$.
FIG. 3.--a) Bright field and b) DF lattice image showing a single (0001) TiC_2S_2 layer.

IMPURITY GETTERING IN RAPIDLY SOLIDIFIED ADVANCED STEELS

G. Ghosh and G. B. Olson

Department of Materials Science and Engineering, Robert R. McCormick School of Engineering and Applied Science, Northwestern University, Evanston, IL 60208-3108, USA

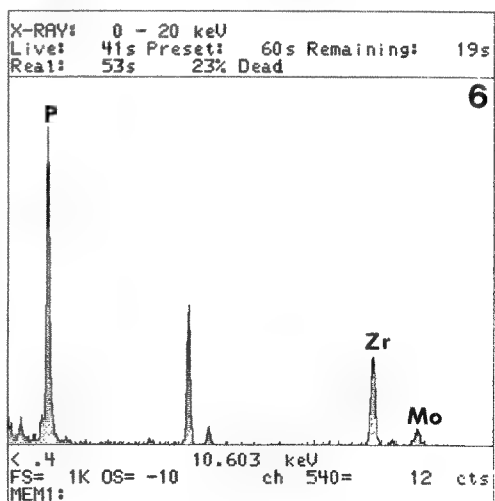
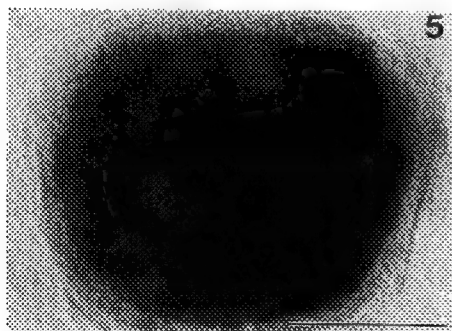
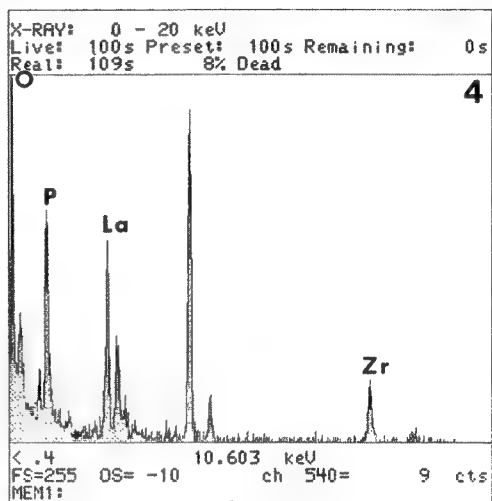
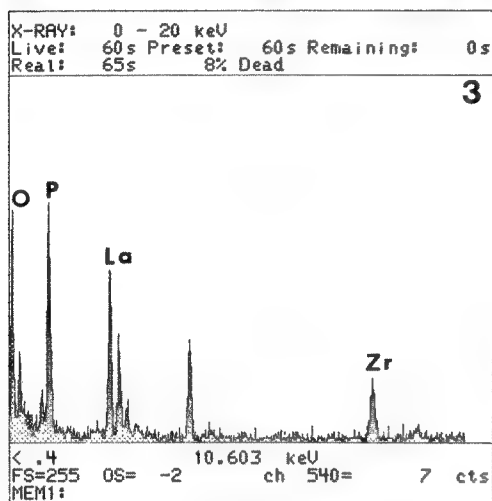
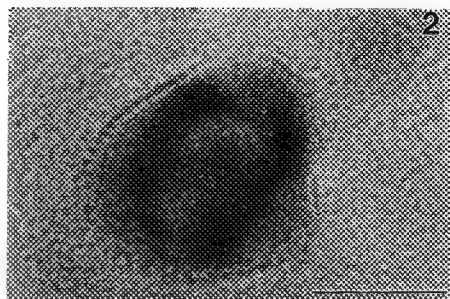
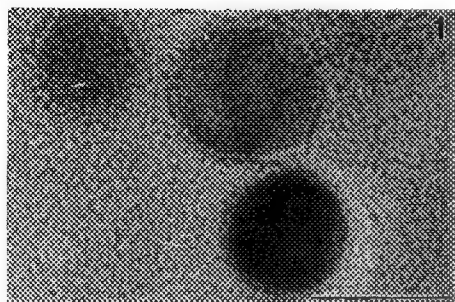
It is well known that gettering of the elements responsible for intergranular stress-corrosion cracking (SCC), such as P and S, leads to significant improvement in resistance to SCC in ultrahigh-strength (UHS) steels. Using rapid solidification processing (RSP) and with the addition various impurity getteres, such as La, Ti and Zr, it is possible to obtain very fine dispersion of various phases. Formation of very stable P- and S-bearing compounds not only improves SCC¹ but also provide grain coarsening resistance during high temperature consolidation/austenization treatments². In a recent study of La gettered Ni-Mo steels, highly stable fine dispersions of LaPO_4 and $\text{La}_2\text{O}_3\text{S}$ were claimed to have been observed¹. But, the major drawback was that the structure of these phases and quantitative estimate of any stoichiometry were not carried out. Furthermore, above experiment was done using thin foils which are certainly not suitable for making any kind of quantitative estimate involving light elements. In an effort to understand processing-structure-property relationship, this study deals with identifying various phases formed in rapidly solidified UHS steels using extraction replicas.

Several rapidly solidified steels containing about 2wt% Ni, 1.5wt% Mo and 0.4wt% C were studied. These alloys were also treated with various levels of La, Ti and Zr as impurity getters. Extraction replicas were prepared from compacted and solution treated specimens. A cold field emission Hitachi HF2000 atomic resolution analytical electron microscope (ARAEM) was used for phase identification. The ARAEM is equipped with ultra-thin window X-ray detector (LINK). Both X-ray microanalysis and convergent beam electron diffraction were used for characterizing the phases.

Figures 1 and 2 show very fine scale La-Zr-P-O compounds which are typically 15 to 40 nm in diameter. X-ray microanalysis revealed a wide variety of La, P and O contents in these particles. Two such X-ray spectra are shown in Figures 3 and 4. While the intensity of Zr peak is very similar, different relative intensities of La and oxygen peaks can easily be noticed in these two Figures 3 and 4. Since X-ray spectra were not collected in two-beam condition or near any zone axis, the possibility of channelling effect can be ruled out. Rather, Figures 3 and 4 represent two different phases. In order to determine the La/O ratios we used La_2O_3 as standard. After determining the K-factors by standard procedures, the La/O ratios in Figures 3 and 4 were estimated to be 0.29 and 0.40, respectively. Various La-phosphates and La-oxophosphates have been reported³. Based on the available data, the spectra in Figure 3 is most likely to correspond to LaPO_4 and that in Figure 4 corresponds to $\text{La}_7\text{P}_3\text{O}_{18}$. Other P-bearing compounds were found to exist in such alloys. Figure 5 shows a Zr-phosphide particle, the X-ray spectra corresponding to this particle is shown in Fig. 6. Even though the Zr-P binary phase diagram does not exist, several Zr-P compounds have been reported⁴. Similarly, a wide variety of S-bearing phases involving La, Ti and Mo were also found in the RSP alloys. Characterization of these finely dispersed phases by convergent beam electron diffraction and X-ray microanalysis will be presented in detail. Kinetics of formation of various phases during rapid solidification will also be addressed⁵.

REFERENCES

1. J. F. Watton, Sc. D. Thesis, MIT (1987).
2. M. Suga, J. L. Goss, G. B. Olson and J. B. Vander Sande, Proc. 2nd Int. Conf. Rapid Solidification Processing: Principles and Technologies, Claitor's, Baton Rouge (1980), p. 364.
3. H. D. Park and E. R. Kreidler, J. Am. Cer. Soc. (1984), 23, 67.
4. Pearson's Handbook of Crystallographic Data of Intermetallic Phases, ASM International, Materials Park, OH (1991)
5. This work was supported by the Office of Naval Research.



FIGS. 1 & 2.--Bright-field TEM micrographs showing nanoscale La-Zr-P-O phases. Bar = 20nm.
FIGS. 3 & 4.--X-ray spectra from the La-Zr-P-O phases.
FIG. 5.--Bright field TEM micrograph showing a Zr-phosphide particle. Bar = 25 nm.
FIG. 6.--X-ray spectra from the particle in Figure 5.

HOLLOW-CONE ANALYSIS OF INTERCALATED PARTICLES IN LAYERED $\text{H}(\text{Ca}_2\text{Na}_{n-3}\text{Nb}_n\text{O}_{3n+1})$ MATERIALS

M. M. J. Treacy*, M. E. Bisher* & A. J. Jacobson**

*NEC Research Institute, Inc., 4 Independence Way, Princeton, NJ 08540

**Dept. of Chemistry, University of Houston, Houston, TX 77204

The series of compounds $\text{H}(\text{Ca}_2\text{Na}_{n-3}\text{Nb}_n\text{O}_{3n+1})$ form tetragonal perovskite-related layer structures that are strongly bound in two dimensions, but more weakly bound in the third.¹ These materials can be delaminated by intercalating basic surfactant molecules into the layers, which spontaneously exfoliate the structure to form stable dispersions in a polar solvent.² On drying a diluted droplet of this dispersion on an amorphous carbon film supported on a TEM specimen grid, all sheets are observed to lie flat on the carbon, with the thin tetragonal *c*-axis parallel to the optic axis. Typical sheet dimensions are $1\ \mu\text{m} \times 1\ \mu\text{m} \times 1.4\ \text{nm}$. Layered materials prepared in this way make fascinating specimens for transmission electron microscopy because the thickness, composition and orientation are known. Depending on the dispersion density, sheets will occasionally overlap with parallel *c* axes, but with random relationship between the *a* axes.

Layers of exfoliated $\text{H}(\text{Ca}_2\text{Nb}_3\text{O}_{10})$ material were examined in a Hitachi H9000NAR microscope equipped with a high angle electronic hollow cone unit.³ Images were collected on a Gatan slow scan model 690 CCD at camera magnifications of 50K. To enhance the scattering from these thin materials, a 100kV operating voltage was used. To assist focusing, and to help label areas of interest, 10 nm gold colloid particles were co-deposited on the grid, after excess surfactant had been washed off with distilled water. The hollow cone angular width was constant at $(\alpha_2 - \alpha_1) \approx 3\ \text{mrad}$, and the objective aperture angular radius was $\sim 10\ \text{mrad}$. A series of hollow cone images were collected as a function of hollow cone inner collection angle α_1 .

Figure 1 shows eight images taken from this series. The darkest regions are the carbon film. Regions showing single $\text{H}(\text{Ca}_2\text{Nb}_3\text{O}_{10})$ sheets, as well as two and three overlapping sheets are visible. The single sheets show uniform contrast at all hollow cone angles. However, at low hollow cone angles ($\leq 60\ \text{mrad}$) the overlapping sheets exhibit a random "blister-like" contrast. These blisters, which typically have radius $\sim 10\ \text{nm}$, can co-exist with Moiré fringes, and change contrast as the hollow cone angle changes. Frequently, the blisters show a small white dot at their centers. Tilted dark field analysis reveals that the blister regions exhibit Ashby-Brown type contrast.⁴ The circular symmetry of the blisters arises from the hollow cone averaging of the Ashby-Brown contrast over the diffraction zone. We believe that these contrasts are due to small contaminant particles that were trapped (intercalated) between the perovskite sheets during sample preparation. Similar blisters are observed around gold colloid particles which had been deliberately intercalated during sample preparation. A schematic cross-sectional view of the specimen geometry is shown in Figure 2. In hollow-cone terms, the blister contrast can be thought of as arising from coherent electron scattering within, and between, the upper and lower perovskite layers.

The data in Figure 1 indicate that coherent scattering can be important in hollow cone images from thin crystals when $\alpha_1 \leq 60\ \text{mrad}$ (at 100 kV). The Z-contrast improves at higher angles; the 10 nm gold particles are not detectable when $\alpha_1 \leq 22\ \text{mrad}$, yet show strong contrast when $\alpha_1 \geq 70\ \text{mrad}$.

References

1. A. J. Jacobson, J. W. Johnson, & J. T. Lewandowski, *Inorg. Chem.* (1985), 3727–3729.
2. M. M. J. Treacy *et al.*, *Chem. Matls.* (1990) 2, 279–286.
3. W. Krakow & L. A. Howland, *Ultramicroscopy* (1976) 2, 53–67.
4. M. F. Ashby & L. M. Brown, *Philos. Mag.* (1963) 8, 1649.

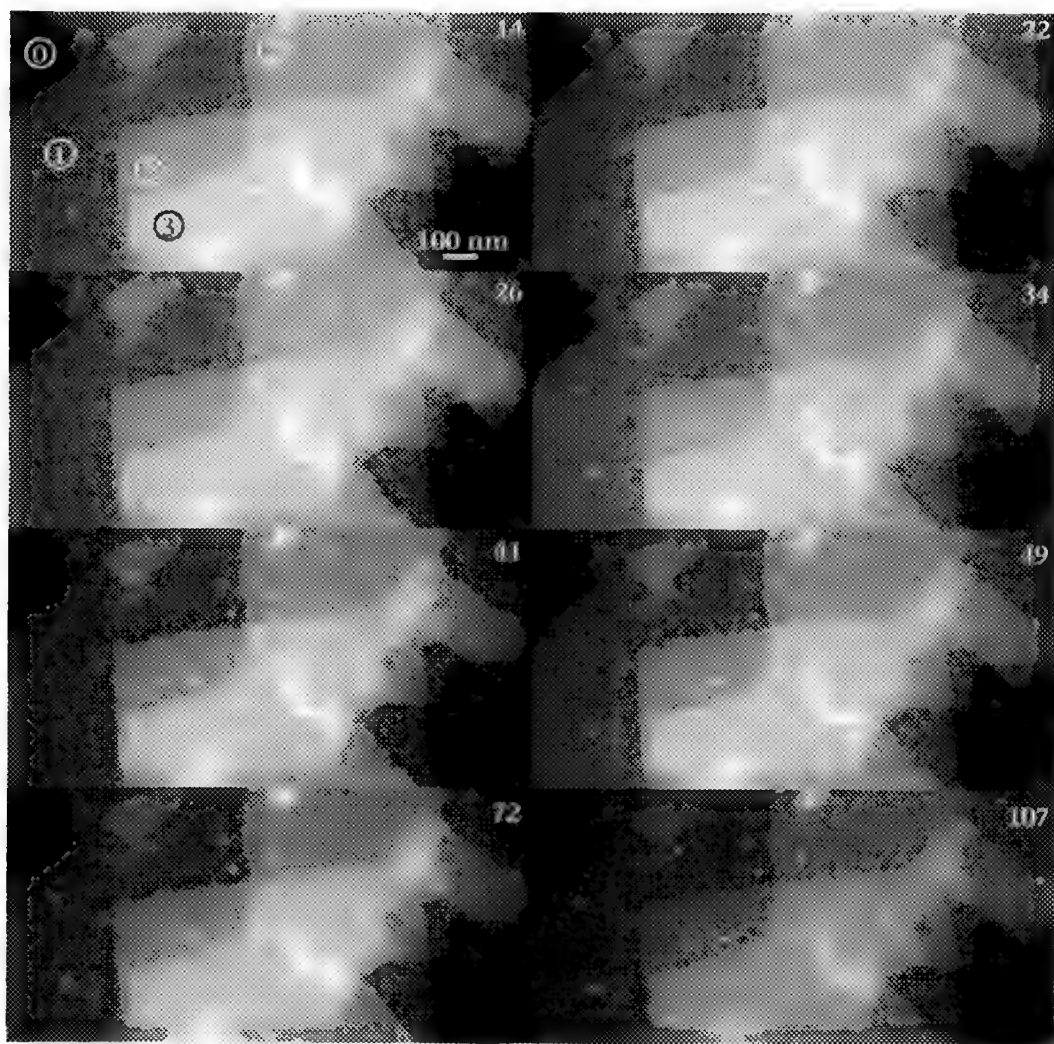
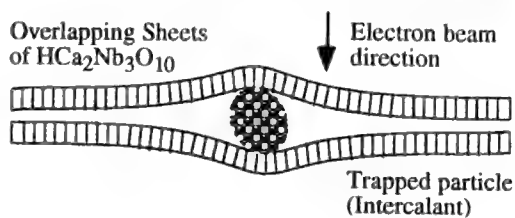


FIG. 1 Hollow cone dark field images of $\text{H}(\text{Ca}_2\text{Nb}_3\text{O}_{10})$ layers. The numbers in the upper right refer to the hollow cone inner angular radius, α_1 , in mrad. The hollow cone upper angle, α_2 is given by, $\alpha_2 = \alpha_1 + 3$ mrad. The objective aperture angular radius was ~ 10 mrad. The numbers in circles indicate the number of overlapping layers at those regions.

FIG 2. Diagram illustrating the distortion of layers due to intercalated particle. This mechanism is thought to be responsible for the blistered contrasts observed in FIG 1.



STRUCTURAL PHENOMENA IN THE GROWTH OF CARBON NANOTUBES

Jun Jiao

Department of Physics, University of Arizona, Tucson, AZ 85721

HREM studies of the carbonaceous material deposited on the cathode of a Huffman-Krätschmer arc reactor have shown a rich variety of multiple-walled nano-clusters of different shapes and forms. The preparation of the samples, as well as the variety of cluster shapes, including triangular, rhombohedral and pentagonal projections, are described elsewhere¹.

The close registry imposed on the nanotubes, focuses attention on the cluster growth mechanism. The strict parallelism in the graphitic separation of the tube walls is maintained through changes of form and size, often leading to 180° turns, and accommodating neighboring clusters and defects. Iijima et. al.^{2,3} have proposed a growth scheme in terms of pentagonal and heptagonal defects and their combinations in a hexagonal graphitic matrix, the first bending the surface inward, and the second outward. We report here HREM observations that support Iijima's suggestions, and add some new features that refine the interpretation of the growth mechanism. The structural elements of our observations are briefly summarized in the following four micrographs, taken in a Hitachi H-8100 TEM operating at an accelerating voltage of 200 kV and with a point-to-point resolution of 0.20 nm.

Figure 1 shows an example of the "turn-around growth" in a nanotube that causes a change in the external diameter from 20 nm to 12 nm. Probably induced by a defect in the center of the "turn-around stack" (indicated by arrows "t"), the outer seven layers reverse the growth direction, taking twice their thickness out of the continuation of the growth. The outer rim of the turn-around growth circumscribes a plane that is slanted with respect to the tube axis, as clearly shown in the fringe pattern across the tube. The number of turn-around layers is the same on either side, although their registry with respect to the center differs. The inner layers continue to grow straight on the left-hand side of the image, whereas all of them try to participate in the turn-around on the right side. But they are forced back into straight growth again. Note that an apparent defect in the tube wall (indicated by arrow "d") has caused the direction of growth to change. The d-spacing at the defect area is 0.39 nm, slightly larger than the graphitic spacing of 0.34 nm⁴.

Figure 2 shows a symmetric cap that according to Iijima's model precludes helicity in the tube walls². The rim of the turn-around region is still slanted (indicated by arrow "r"), however, possibly indicating the effect of helicity in this part of the growth. The thinner parts of the tubes shown in Figs. 1 and 2 show a phenomenon commonly observed in the tubes in Fig. 3. Bridges cross the hollow core, usually consisting of only two layers (indicated by arrow "b"). If the curvatures oppose each other, closed contours can result in an additional two-layer bridge following the closed contour. The duplicity of the walls of the internal "close-offs" reflects possibly steric elements of a basic topography, like the arrangement of hexagons and pentagons in separate planes³.

The last Fig. 4 shows a series of bridges that form tubes inside tubes, separated from each other at times by an empty space (arrows) so that they cannot influence each other but by the peripheral stacks. As with the other images the observations reported here favor certain growth features over others less likely to occur. Continuation and expansion of the HREM studies we present here will help to close the gaps still existing in our understanding of the growth mechanism⁵.

References:

1. S. Seraphin, D. Zhou, J. Jiao, J. C. Withers and R. Loutfy, Carbon, 1993 (in press)
2. S. Iijima, P. M. Ajayan, and T. Ichihashi Phys. Rev. Lett. 69, 3102 (1992)
3. P. M. Ajayan, T. Ichihashi and S. Iijima, Chem. Phys. Lett. 202, 384 (1993)
4. J. M. Cowley, M. Q. Liu, (to be published)
5. The author gratefully acknowledges helpful discussions with S. Seraphin, D. R. Huffman, L. Lamb, and J. C. Withers.

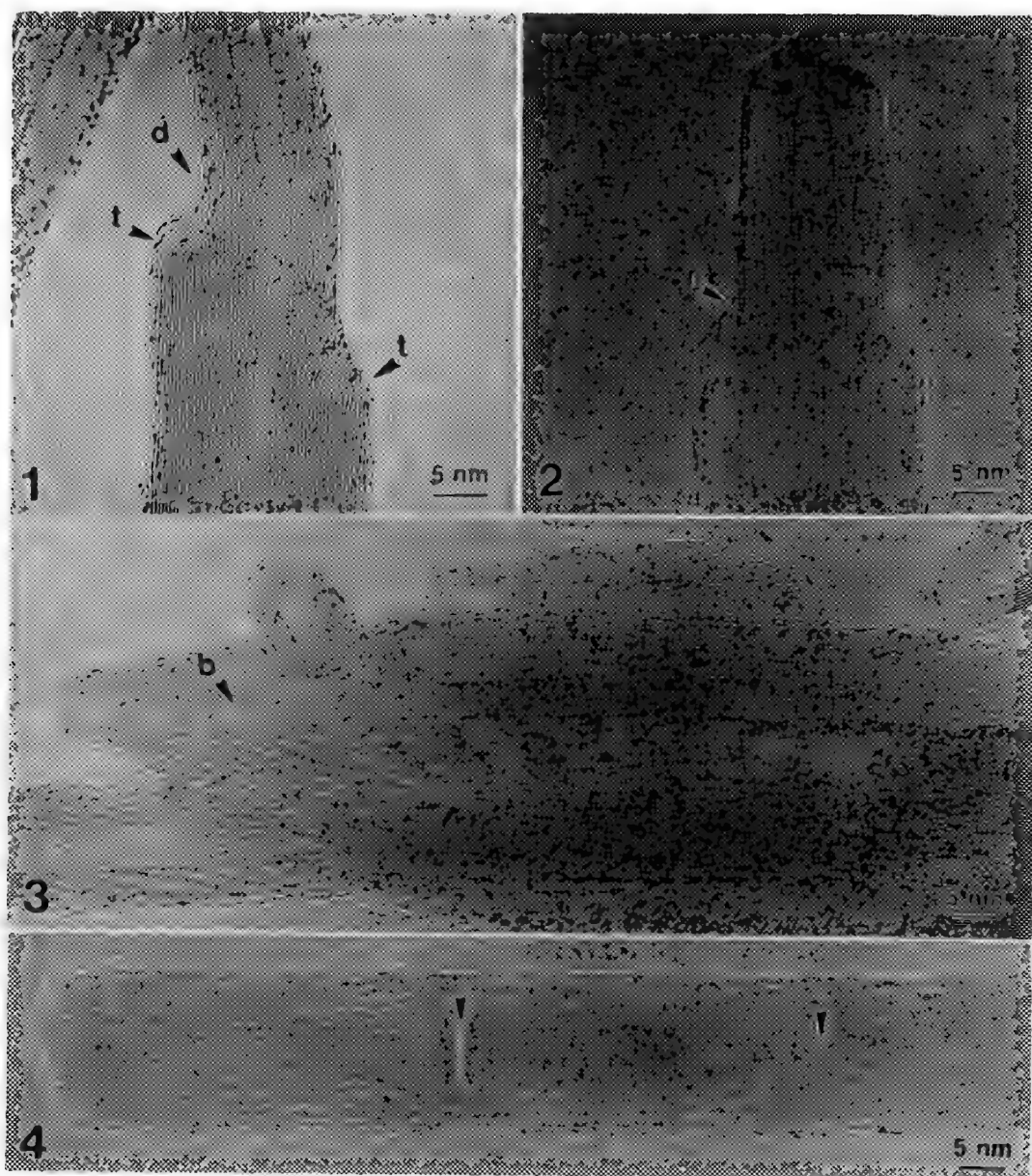


FIG. 1. -- A HREM image of a carbon nanotube illustrating the "turn-around growth" (arrow "t") that causes a change in the diameter of the tube. Arrow "d" indicates growth defects of tube walls with a d-spacing of 0.39 nm instead of a typical d-spacing of 0.34 nm.

FIG. 2. -- An image of a tube with symmetric caps. The rim of the turn-around region (arrow "r") is slanted indicating the effect of helicity.

FIG. 3. -- An image of tubes showing the internal close-offs. Most of the bridges across the hollow cores consist of double layers. Arrow "b" indicates an example of the bridges.

FIG. 4. -- An image of tubes inside a tube. Arrows indicate the separations of the internal tubes.

GROWTH BEHAVIOR AND STRUCTURES OF CARBON NANOTUBES

Mingqi Liu and John M. Cowley

Department of Physics and Astronomy, Arizona State University, Tempe, AZ 85287-1504

Recent discovery of the novel hollow graphitic tubules of nanometer dimensions^{1,2}, so called carbon nanotubes, has greatly stimulated the studies in the field of carbon fiber growth. Their potential applications in electronic and materials industries have been suggested³. In the present study, carbon nanotubes were fabricated by an arc-discharge method⁴. The microstructures of nanotubes thus obtained were examined with a JEM-2000FX high-resolution transmission electron microscopy (HRTEM) and with an electron nanodiffraction technique in a VG HB-5 scanning transmission electron microscopy (STEM).

HRTEM images show that nanotubes, consisting of 3 to 30 carbon sheets, have a length up to 1 μm and a diameter of 6 to 26 nm. Some nanotubes have a symmetric uniform sheet spacing of 0.34 nm. Others show non-symmetric uneven fringes (Fig. 1), indicating that they may have a polyhedral cross section. Most nanotubes are closed by cone-like or polyhedral shaped caps (Figs. 2 and 3). The closure angle varies from 17 to 40° and the internal sheets have a tendency to be closed in pairs. Fig. 4 shows the image of a growing tubes. Carbonaceous residues and low-contrast fringes are seen at tube top and side surfaces, indicating that tube extension is achieved by an open end growth and tube thickening is accomplished by simultaneous nucleation of new sheet on existing surface². Some growth defects are identified, such as disordered sheet stacking, uncompleted sheets, and U-turn growth (Fig. 4).

An electron beam of 0.5-1.0 nm in diameter, which is much smaller than either the tube wall thickness or the center hollow region, was scanned across the tube and along the tube axis. Based upon the nanodiffraction patterns obtained from multi-sheet nanotubes (Fig. 5), four structures are identified. The first one is a nonhelical structure. The pattern obtained at the center hollow region is a single set of $\{hk0\}$ spots. All sheets have a $[100]$ orientation with respect to the tube axis so that there is no helix row. The second one is a helical structure but without rotational disorder between neighboring sheets. Doubled reflections are obtained from tube top and tube bottom, respectively. The third one, which takes the majority of the tubes examined, is a helical structure with rotational disorders between neighboring sheets. The nanodiffraction pattern obtained in the center hollow region is a continuous $\{hk0\}$ ring. The fourth one shows relatively sharp diffraction patterns, corresponding to ordered hexagonal or rhombohedral graphite stacking and coming from planar regions of tube having polyhedral cross section.

References

1. S. Iijima, *Nature*, (1991)354, 56.
2. S. Iijima, P.M. Ajayan and T. Ichihashi, *Phys. Rev. Letters* (in press).
3. P.M. Ajayan and S. Iijima, *Nature*, (1993)361, 333.
4. T.W. Ebbesen and P.M. Ajayan, *Nature*, (1992)358, 220.
5. This work was supported by National Science Foundations (NSF) grant DMR 90-14975 and made use of the facilities in the Center for High Resolution Electron Microscopy at ASU.

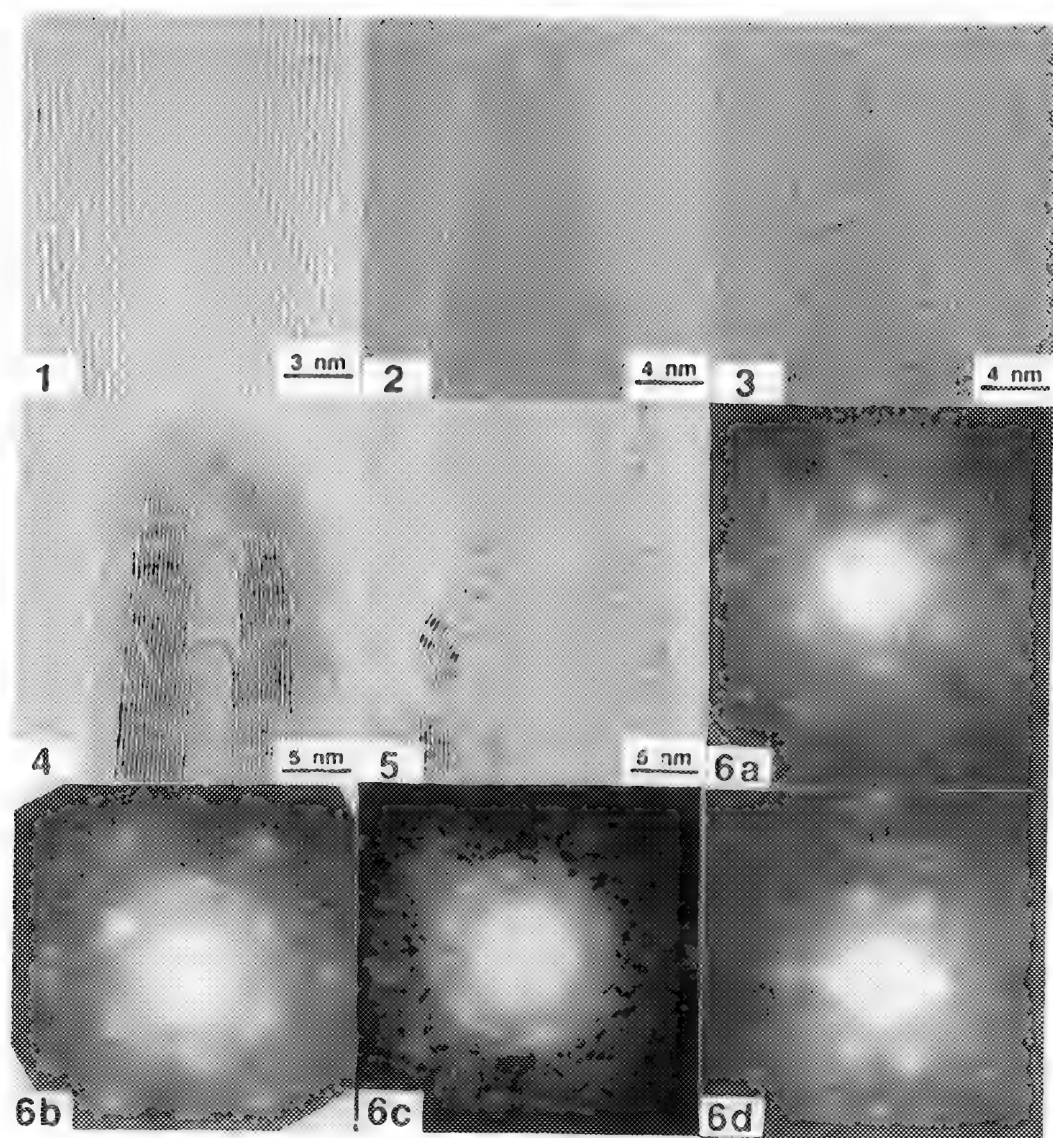


Fig. 1.--(002) lattice fringes of non-symmetric nanotube. The d-spacing is 0.39 nm on right.
 Fig. 2.--Image of cone-like cap that is seen only in symmetrical cylindrical nanotubes.
 Fig. 3.--Polyhedral shaped cap that is seen in both cylindrical and polyhedral nanotubes.
 Fig. 4.--Image of growing nanotube. Low-contrast fringes are seen on top and side surfaces.
 Fig. 5.--U-turn growth of intermediate sheets. Tilted sheet top contours are seen.
 Fig. 6.--Nanodiffraction patterns of nonhelical tube (a), single helix angle tube (b), multiple helix angle tube (c), and polyhedral cross section tube with ordered sheet stacking (d).

THE THREE-DIMENSIONAL SHAPE OF CARBON NANOTUBES BY HIGH RESOLUTION ELECTRON MICROSCOPY

* Z. G. Li, ** L. Liang, * P.J.Fagan, * M.van Kavelaar

* Du Pont Company, Experimental Station, P. O. Box 80356, Wilmington, DE 19880-0356 and **
A.T. Corp., Mesa, AZ 85202

Following the discovery of a large scale synthesis of fullerenes[1], the existence of the related carbon nanotubes was suggested by high resolution electron microscopy (HREM) [2]. Larger scale syntheses of these nanotube-rich materials has now been reported and has sparked interest worldwide. Because the HREM technique essentially observes the projection of a three dimensional object onto a two-dimensional plane, the three dimensional shape of the object is usually not apparent in typical HREM images. However, as we report here, by rotating along the axis of single carbon nanotube, and recording the images in succession by HREM, the non-cylindrical nature of these tubes is revealed, especially near the sealed ends of the nanotubes. In addition, from electron diffraction and X-ray diffraction, we find the spacing between the planes to be $3.398(8) \text{ \AA}$ on average. This is in contrast to earlier reports which suggested an interlayer distance of 3.35 \AA , similar to the graphite interplanar spacing.

Fig. 1 is a HREM image of the cap of carbon nanotubes. In order to ascertain the three-dimensional shapes of these coaxial nanotubes, an individual tube was examined by tilting the carbon needle around its axis in the electron microscope. The direct images and SAED patterns of the tube were systematically recorded and compared. If the tubes had cylindrical shape, the diameter of the nanotube should not change as it is rotated about the long axis. However, Fig. 2 shows two images corresponding to tilt angles of -20° and $+30^\circ$. The diameter of the carbon needle at the section indicated by an arrow on the left side of Fig. 2 does not change after 50° of rotation in the microscope. Furthermore, the layer-like structure in the projected images, and the equal numbers of lattice fringes on both sides of the nanotube remained the same at the different tilt angles. This is good evidence that this section of the tube has the originally proposed[2] coaxial nested-tube structure. The innermost diameter of the nanotube is measured to be about 4.4 nm and the outermost one, 14.6 nm at this point. But the dimensions of the carbon needle at the section indicated by the arrow on the right of Fig. 2 were significantly different when viewed at the various angles. The dimension of the outermost tube increased from 14.6 nm to 15.8 nm upon rotation, which indicates a non-cylindrical shape for this section of nanotube. The nanotube in Fig. 2 consisted of 15 layers of carbon sheets which were separated by a distance of about 3.40 \AA . This separation distance is *larger* than that of the graphite (002) plane.

SAED patterns of single carbon needles were also recorded at different tilting angles. The spacings of strongly diffracted spots reflecting the interlayer distances remained unchanged with a value of 3.40 \AA even after 50° of tilting, which is again evidence for a coaxial structure. Weakly diffracted spots were frequently found with an angular range of $70-80^\circ$ with respect to the strongly diffracted spots. X-ray powder diffraction results of the carbon nanotube containing materials confirmed HREM results. Fig. 3 shows that the first peak contains two spacings: a strong one centered at 3.40 \AA and a weaker one at 3.35 \AA . The latter could correspond to graphite (002) planar spacing as the samples examined were not pure tubes and likely contain some graphitic material. Combined with our SAED patterns of a single needle, it is proposed that the spacing of 3.40 \AA reflects interlayer distances within each nanotube.

In conclusion, we have found that the diameter and/or cylindrical shapes of the carbon nanotubes can change along the axis. This may ultimately have an effect on physical properties. We have also accurately measured an interlayer distance of 3.40 \AA which is 0.05 \AA larger than the graphite interplanar spacing [3].

REFERENCES

1. W.Kratschmer, L.D.Lamb, K.Fostiropoulos, D.R.Huffman, Nature 347 (1990) 354.
2. S. Iijima, Nature, 354 (1991) 56.
3. We wish to thank Dr. Su Wang for very constructive discussions on nanotube and graphite structure.

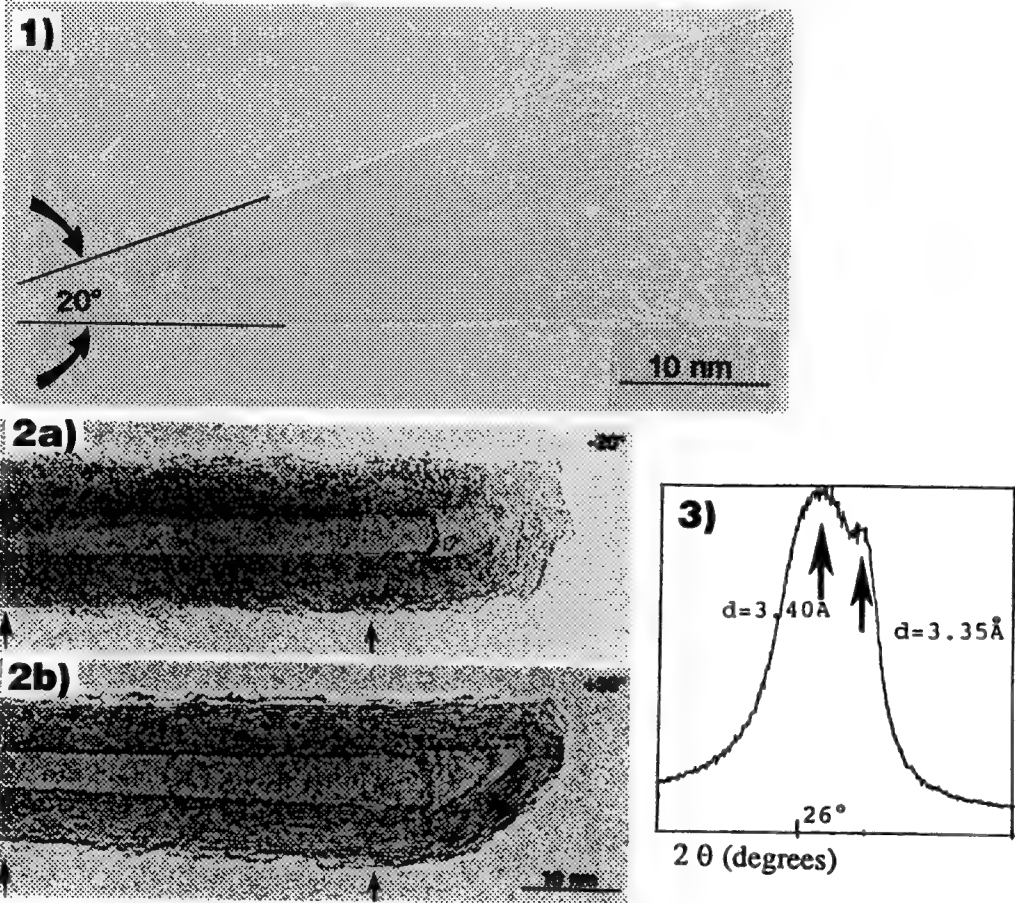


Figure 1. HREM image of the cap of carbon nanotubes.

Figure 2. A single carbon nanotube rotated about the long axis at tilt angles of (a) -20° and (b) +30° with respect to the electron beam.

Figure 3. A portion of X-ray powder diffraction pattern for the carbon nanotube sample.

SEM STUDY OF STRUCTURE AND FORMATION OF THE CARBON CLUSTER IN THE ARC-DISCHARGE DEPOSITS

DAN ZHOU, SUPAPAN SERAPHIN, and JUN JIAO*

Department of Materials Science and Engineering, University of Arizona, Tucson, AZ 85721

*Department of Physics, University of Arizona, Tucson, AZ 85721

The richly structured surfaces of the graphite electrodes in carbon arc discharges have been the subject of numerous studies in the past, due to the strong technological importance of the carbon arc lamp. However, since they were not known until recently [1], no attention was paid to the existence of carbon nanocluster which the discharge produces [2]. Our previous results show that the variations of the production processing conditions will affect the properties of the individual carbon nanotube [3]. We present here a scanning electron microscopy (SEM) study of the topography of the deposits at the graphite cathode, and attempt to correlate the growth behavior of nanotubes to the structural elements of the cathode surface.

The starting material in this study is the carbonaceous deposit (i.e. slag) formed on the initial flat cathode as the anode is consumed during the arc discharge. The slag was carefully cleaved to make a SEM sample and the topography of the slag was characterized in both top view and cross-section. Fig.1 shows an overview SEM image of the slag with parts of the shell removed. Note that both the core and the shell regions have layer structure of different nature and thickness. The layers are aligned in the direction perpendicular to the current flow. The core region shows onion-type layers. Two distinct types of layer structures are observed: the first type is a columnar structure shown in Fig. 2a. It is the dominant structure of the core part. The interface of the onion layers is pitted, possibly reflecting the movement of the arc over the surface. The layer thickness is several hundreds microns and increases from the center of the core to the shell. Fig.2b shows that the columnar structures contain a high density of tubes mixed with a few polyhedral particles. Note that the nanotubes have random orientation and are not aligned along the current flow direction. The second type of the layer structure is shown in Fig. 3a, in which the thin layers stack together like lamellae. Most of the shell region is also constructed of the lamellae structure which consists of carbon spherical particles (Fig.3b) and carbon flakes (Fig.3c). No nanotubes are observed in the shell region. The columnar growth changes to lamellae stacking at the intersection of the core and the shell. The results suggest that the temperature and cooling rate are critical for nanotubes formation. Fig. 4a shows the fibrils, collected from the end of the run where the potential difference between electrodes was low. The fibrils contain a high density of the nanotubes as shown in Fig. 4b. Furthermore, a disc from the core region was cleaved and examined. The results indicate that the occurrence and density of the tubes on both surfaces of the disc are not radially uniform, and that the yield of tubes depends on the columnar growth.

The observations reported here indicate that the properties of the arc, its local current density and fluctuations, strongly influence the topography of the cathode deposit, and in turn the occurrence as well as the growth of the nanoclusters. Since the potential distribution at the reaction zone is highly non-linear, the columnar structure, which is greatly affected by the electrical condition of the arc discharge during the deposition process, is critical for the structure and formation of the nanotubes. A better definition and constancy of the arc will be required to correlate the observed structures to the different processing conditions. The methods to characterize the physical mechanism of plasma will be required, in addition to SEM observations, to make the production of the carbon nanoclusters systematically controlled by the arc discharge processing conditions. Work in this direction is in progress [4].

References

- [1] W. Krätschmer, L.D. Lamb, K. Fostiropoulos, and D.R. Huffman, *Nature* **347**, 354(1990).
- [2] S. Iijima, *Nature* **354**, 56(1991).
- [3] S.Seraphin, D.Zhou, J.Jiao, J.C. Withers, and R.Loutfy, *Carbon* (1993), in press.
- [4] We are grateful to the MER. Corp. for providing the samples, and to K.A. Jackson, P. Calvert, and J.C. Withers for valuable discussions.

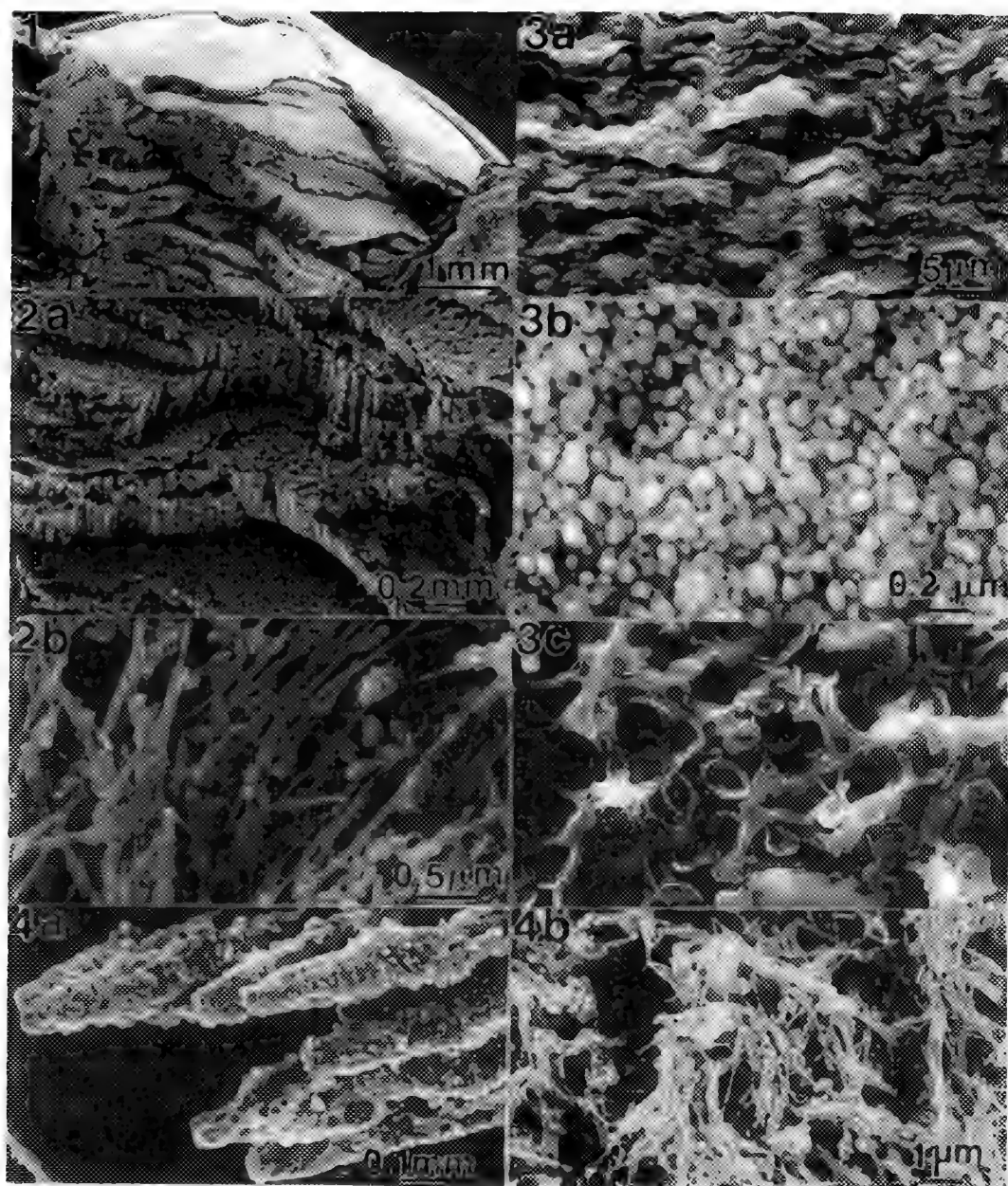


Fig. 1-- A SEM image of the carbonaceous deposit showing the core and the shell regions.
 Fig. 2-- SEM images: (a) the columnar structure in the core region, (b) the nanotubes mixed with a few polyhedral particles in the columnar region.
 Fig. 3-- Cross-section images of the shell region: (a) thin layers stacked together like lamellae. The lamellae consist of (b) carbon particles, and (c) flakes.
 Fig. 4-- Images of the fibrils collected from the end of the slag: (a) an overview image, (b) the compact tubes in fibrils.

INSERTION OF YTTRIUM CARBIDE INTO CARBON NANOCCLUSERS BY VAPOR TRANSPORT DURING GROWTH

Supapan Seraphin and Dan Zhou

Department of Materials Science and Engineering, University of Arizona, Tucson, AZ 85721

Jun Jiao

Department of Physics, University of Arizona, Tucson, AZ 85721

Carbon nanoclusters have basic features in common, although they vary greatly in shapes.^{1,2} Concentric graphitic layers separated by 0.34 nm surround a hollow core a few nanometers in diameter. Encapsulating materials into this hollow core changes the physical properties drastically.^{3,4} The insertion offers the possibility to study materials of small dimensions in a closed-off environment. Technological promise is given for the production of nanowires,⁵ and other applications in which the nanoscale is of importance. Recent work takes a variety of approaches, inserting lead into nanotubes by capillary suction through open ends,⁶ or encapsulating microcrystals of LaC_2 into the polyhedral cages.⁷ We report a method for filling carbon clusters of various shapes *in situ* through vapor transport from a composite anode of a graphite rod filled with yttrium oxide paste at a center hole.⁸

Both materials pass through the arc discharge, and grow as composite carbon nanoclusters at the pure graphite cathode. The growing slag contains nanoclusters in which a graphitic cage surrounds an yttrium carbide core. Fig. 1 shows a TEM micrograph of a 10-nm diameter nanotube filled with material up to a dividing wall that separates two internal cavities of different diameter. Note that the thinner hollow core of the tube is not filled. The filling material extends over 200 nm along the length of the tube and does not wet the internal surface of the cavity completely. The tube tips remain closed and show no sign of any damage. This is in contrast to the filling by capillary action which damages the tube tips.⁶ Fig. 2 shows a tetrahedral particle sitting on a bent nanotube. The particle is half-filled with a crystalline material having lattice spacings of 0.315 nm which match the interplanar spacing of (101) planes of yttrium carbide. Arrows indicate the ripples of the graphitic fringes whose spacings are less than the typical value of 0.34 nm. The outer surface of the tube has no sign of rupture or crack illustrating the high elasticity of the nanotube structure. Based on our observations of various kinks and curves of several other nanotubes, it is suggested that the ripple is not a part of the growth process but rather a result of the compressive stress. The presence of the inserted material affects the yield strength and topography of the growing graphitic cage significantly. The fraction of filled clusters is about 50%, sufficient to encourage the study of the physics of particles of reduced size on the one hand, and efforts to realize the promise of technological applications on the other.

Electron energy-loss spectroscopy (EELS) was performed by placing the electron beam of nanometer size on the filling material inside a narrow channel of the tube. The obtained spectrum shows the M-edge of yttrium and the K-edge of carbon (Fig. 3). No oxygen signal is detected. This analysis confirms the presence of yttrium carbide and not yttrium oxide inside the tube.⁹

References

1. Iijima, S., Ichihashi, T. & Ando, Y. *Nature* **356**, 776-778 (1992).
2. Seraphin, S., Zhou, D., Jiao, J., Withers, J.C. & Loutfy, R. *Carbon*, in press.
3. Mintmire, J.W., Dunlap, B.I. & White, C.T. *Phys. Rev. Lett.* **68**, 631-634 (1992).
4. Hamada, N., Sawada, S. & Oshiyama, A. *Phys. Rev. Lett.* **68**, 1579-1581 (1992).
5. Smalley, R.E. *Materials Science & Engineering B*, in press.
6. Ajayan, P.M. & Iijima, S. *Nature* **361**, 333-334 (1993).
7. Ruoff, R.S., et al. *Science* **259**, 346-348 (1993).
8. Seraphin, S., Jiao, J., Zhou, D., Withers, J.C. & Loutfy, R. Submitted to *Nature*.
9. We acknowledge the MER Corp. for providing nanotube samples, J.M. Cowley and P. Calvert for valuable discussions.

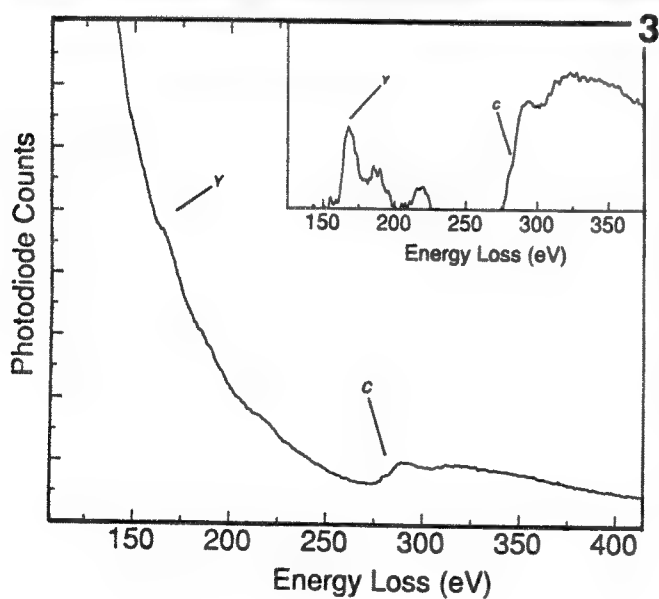


FIG. 1.--HREM image of a nanotube with two different sizes of inner cores. The larger core is filled with material extended over 200 nm.

FIG. 2.--HREM image of a half-filled tetragonal particle sitting on a bent tube. Arrows indicate ripples caused by compressive stress.

FIG. 3.--EELS spectra of nanotube filled with material. The spectrum shows the M-edge of yttrium and the K-edge of carbon. The spectrum after removing the background is shown in the inset.

HIGH-RESOLUTION MICROSCOPY OF CARBON NANOTUBES

Stuart McKernan, Paul G. Kotula, Dale W. Owens, C. Barry Carter and J. H. Weaver

Department of Chemical Engineering and Materials Science, Amundson Hall, University of Minnesota, Minneapolis, Minnesota 55455.

The presence of fullerenes and carbon nanotubes in the residue of plasma discharge electrodes has recently been documented.¹⁻⁵ The occurrence of 5-fold and 7-fold coordinated carbon rings in otherwise 6-fold coordinated graphene sheets apparently provides sufficient variation of the familiar graphite morphology to form spheres and cylinders. The spherical structure of the fullerenes has been studied in relatively more depth than the cylindrical structure of the carbon nanotubes.^{5,6}

Carbon nanotubes may be considered as individual graphene sheets rolled up into cylinders. These cylinders are stacked concentrically with a spacing between the layers analogous to the stacking of sheets in graphite of $c=3.4 \text{ \AA}$. This spacing imposes geometrical constraints on the circumference of the cylinders. Variations of the cylinder diameter from the value required to give the exact spacing may be expected, due to the discrete nature of the sheets. For large cylinders this variation may not be very noticeable, and may be accommodated as small strains within the tube. For nanotubes, which have a relatively small radius, these variations would lead to large strains, which are not observed experimentally. For tubes rolled about an axis parallel to the $\langle 10\bar{1}0 \rangle$ or $\langle 11\bar{2}0 \rangle$ directions, the diameters of the tubes must increase in multiples of $a/2$ or $a\sqrt{3}$ respectively. Smaller increments may be obtained if the tubes are rolled in a helical fashion, but in this case the atomic arrangements of successive tubes will not be aligned. The tubes are generally terminated by a curved or faceted end-cap. This frequently terminates only a few of the layers at a time, requiring several such end caps to terminate a complete tube. High-resolution lattice images of these nanotubes have been obtained from a JEOL 4000EX operating at 400kV. The images were recorded using minimum dose techniques, as the tubes damaged rather quickly in the beam.

Images of the nanotubes show strong (0002) fringes parallel to the tube axis with a gap in the center corresponding to the tube core. The fringes in thicker tubes tend to have higher contrast nearer the outside of the tube than they do near the core. Figure 1 shows the region close to the end of a nanotube. Three different end caps may be seen terminating different portions of the nanotube. The fringes at the terminations show discrete changes in orientations, rather than smoothly bending around. Finer fringes are also observed with a spacing of approximately 2.04 \AA running approximately perpendicular to the tube axis. In other nanotubes, similar fringes are observed running parallel to the nanotube axis or some large angle to it. A small, single walled circular structure is arrowed on the surface of the nanotube. This image is consistent in size with the projection of a small carbon fullerene sphere as has been reported previously.^{6,7}

Image simulations have been performed of graphite close to the $\{1\bar{1}0\}$ or $\{11\bar{2}0\}$ zone axes (figure 2). The results of these simulations show that the characteristic $\sim 3.4 \text{ \AA}$ (0002) fringes seen in the nanotubes may still be observed from graphite planes that are tilted over by as much as 15° . The fine fringes have also been simulated by constructing a model of the nanotube with the upper and lower halves specified separately to allow for helical and non-helical tubes (figure 3). Again the results show that fine fringes may be observed even for tilted helical tubes.

An analysis of the bend angles in the end caps of many different nanotubes indicates that several different angles are represented, which would not be expected if the tube closure were caused solely by the presence of 5- or 7-fold rings. The facets formed in the end caps therefore represent tilt grain-boundaries. Possible structures for these boundaries will be discussed. The morphology of the nanotubes will be critically examined in the light of these results, with particular emphasis on whether they can be considered as tubes or as polygonal prisms.⁸

1. S. Iijima, *Nature* **354**, 56 (1991)
2. T. W. Ebbesen and P. M. Ajayan, *Nature* **358**, 220 (1992)
3. D. Ugarte, *Nature* **359**, 707 (1992)
4. X. F. Zhang et al. submitted for publication (1993)
5. V. P. Dravid et al., *Science* **259**, 1601 (1993)
6. Yaccaman et al., *Journal of Materials Research*, **8**, 200 (1993)
7. P. M. Ajayan and S. Iijima, *Nature* **358**, 23 (1992)
8. This research is supported by the DoE under grant No DE-FG02-89ER45381 and the NSF under grants No. DMR-8901218 and No. DMR 91-08419 and in part by the user program of the HTML Facility at Oak Ridge National Labs and by the DoE under contract DE-AC05-84OR21400 with Martin Marietta Energy Systems, Inc. The material was provided by L-S. Wang and R. E. Smalley of Rice Quantum Institute and Department of Chemistry & Physics, Rice University, Houston Texas.

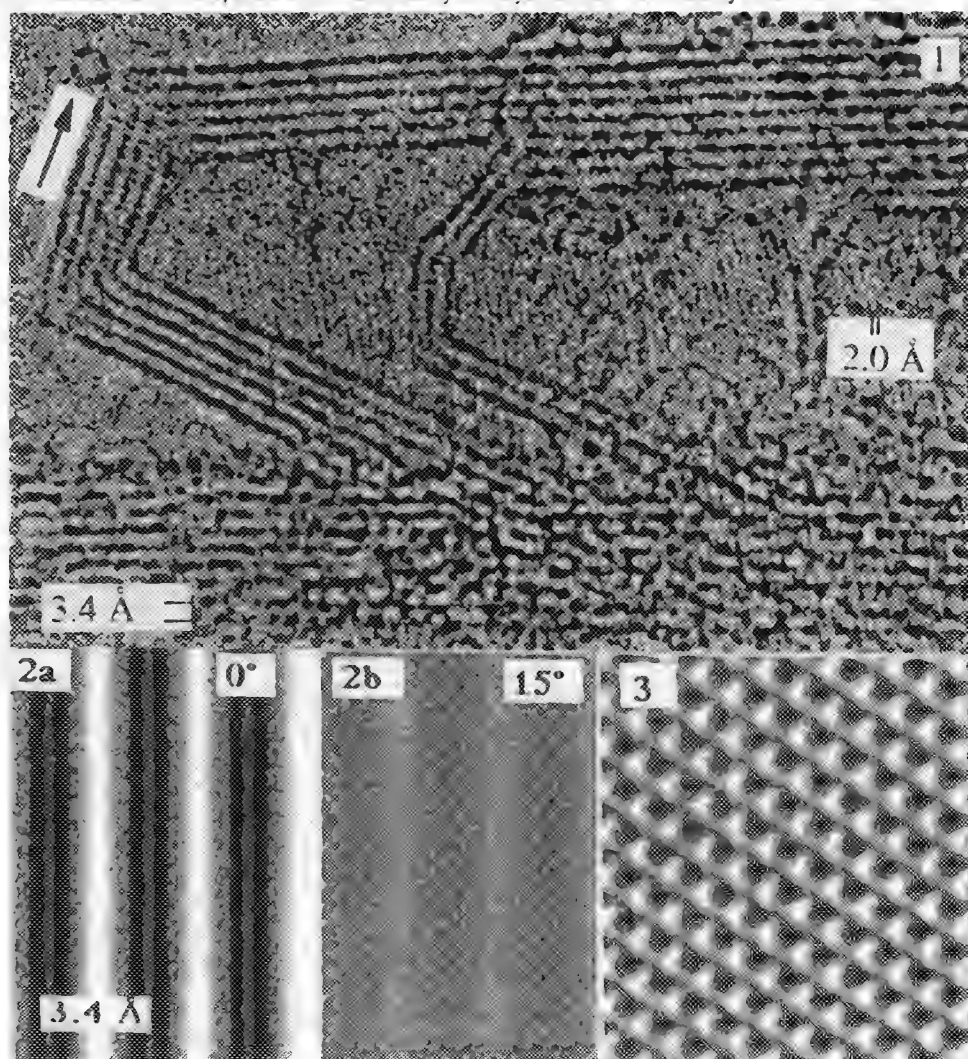


FIG. 1.— High-Resolution lattice image from tip of carbon nanotubule.

FIG. 2.— Image simulation of graphite (0001) planes tilted by a) 0° and b) 15° towards [0001].

FIG. 3.— Image simulation of graphite planes stacked to resemble core region from carbon nanotubule.

SCANNING ELECTRON MICROSCOPY 1928-1965

D. McMullan

Cavendish Laboratory, Cambridge University, Madingley Road, Cambridge, ENGLAND

The beginning of the general use of the scanning electron microscope (SEM) can be accurately dated to 1965 when the Cambridge Instrument Company in the U.K. marketed their Stereoscan 1 SEM (to be followed about 6 months later by JEOL in Japan). But development had been in progress intermittently over the previous 30 years in Germany, the U.S.A., France, and the U.K. where in 1948 work was begun in Charles Oatley's department at the Cambridge University Engineering Department which led directly to the Stereoscan. The purpose of this paper is to trace the development of the SEM and to show that some of the ideas put forward by the early workers were well ahead of their time and only became technologically practicable much later.

The first proposal for the application of scanning to microscopy was made in 1928 by Synge,¹ an Irish scientific dilettante, who conceived the near-field scanning optical microscope but did not attempt to build one. Patents were granted in 1929 to Stinzinger,² a German physical chemist, for surface analysis apparatus using a scanned x-ray or electron probe, but a working instrument was not developed.

SEM was a direct offshoot of television technology although its invention in 1934 was the work of Knoll, the co-inventor with Ruska of the TEM at the Berlin Technische Hochschule in 1931. The following year he joined the Telefunken company to develop TV camera tubes which were then in their infancy. Enlarged images of the surface structure of the targets of such tubes could be produced by reducing the amplitude of the scans and Knoll realised that this was a useful technique which could also be used on other types of sample. He went on to build a low-magnification (10X) electron beam scanner which had the following advanced features:³

- Sample in UHV and the contrast produced by variations in secondary electron emission ratio.
- TV-rate images on CRT monitor.

In 1936, von Ardenne, who was a private consultant in Berlin and who also had had experience on the development of TV camera tubes, was contracted by Siemens A.G. to investigate the possibility of using a scanned electron probe to avoid the effects of objective lens chromatic aberration with thick samples in TEM. Following the building of the first STEM he published papers which contained:^{4,5}

- A detailed analysis of electron probe formation, lens aberrations and beam current limitations.
- Diagrams showing the placing of detectors for bright-field, dark-field and surface imaging.
- A study of the effects of beam and amplifier noise on imaging.

Because of the lack of a suitable low-noise electron detector he used photographic film and there was no immediately visible image. Von Ardenne's STEM proved to have no advantages over TEM and when he tried to use it as a SEM on bulk samples he was unsuccessful because of the detector problem; even so he made the following advances:⁶

- A proposal for the use of an electron multiplier as a secondary electron detector.
- Elucidation of the effect of electron scattering on resolution and the formation of contrast.⁷

In 1941 at RCA, New Jersey, a team headed by Zworykin, the inventor of the iconoscope TV camera, published their work on SEM which included the following important innovations:⁸

- An attempt to use a field-emitter gun..
- Low-voltage operation (800V) with deceleration of a 10-keV scanning beam close to the specimen in an electrostatic immersion lens.
- Secondary electrons accelerated back to the detector.
- A detector using a phosphor screen + photomultiplier.

This SEM had drawbacks, the most serious being that the images were not directly visible on a

monitor and took 8 minutes to record on a fax machine. It also had to compete with replica methods which were then starting to give excellent images of surfaces in TEMs. RCA therefore decided to discontinue the project and concentrate on the development of the EMB TEM.

During the next few years there was virtually no interest in SEM and the general consensus among electron microscopists was that as a concept it was seriously flawed and that further development would be "a complete waste of time". However in 1948, Charles Oatley at the Cambridge University Engineering Department decided that a further attempt at developing a SEM might be a suitable project for a Ph.D. student. The present writer was selected, having had experience in TV electron optics and circuits, and he built an electrostatically focussed SEM with a high-energy beam (up to 40keV) and an electron multiplier detecting mainly the backscattered electrons.⁹ The sample was placed at an angle to the beam, and topographic images were displayed on a monitor at 0.9 frame/s and recorded over 300s. The resolution was about 50nm, limited by astigmatism and insufficient magnetic shielding. Z contrast was attempted and cathodoluminescent imaging demonstrated.¹⁰

K.C.A. Smith, this year's MSA Distinguished Scientist (Physics), took over the Cambridge SEM in 1953, introduced stigmation and other improvements, and obtained 25-nm resolution.^{10,11} He increased the detection efficiency, demonstrated the importance of the low-energy secondaries, and, with Oatley, used a plastic scintillator for detecting the high-energy back-scattered electrons.¹¹ He examined a wide variety of samples including thermal decomposition of silver azide, a germanium point contact rectifier, fungus spores in water vapour in an environmental cell, and paper fibres.^{11,16} He went on to build the first magnetically focussed SEM,¹² completed in 1958, for the Pulp and Paper Research Institute of Canada; this instrument was the precursor of the Stereoscan.

It must be mentioned that, from 1954, scanning x-ray analysers were being developed in the U.K., France, Japan, and elsewhere but the electron imaging in these instruments was relatively crude.

In the period up to 1965 three further SEMs were built in Oatley's department by Wells, Stewart, and Pease and Nixon, and there were many advances in technique.¹⁶ These included: Z contrast and stereomicroscopy (Wells); secondary electron detector (Everhart and Thornley); low-voltage SEM (Thornley); voltage contrast (Oatley and Everhart); 10-nm resolution (Pease and Nixon); ion etching in SEM (Stewart); high temperature samples (Ahmed and Beck); microfabrication (Broers).

Oatley experienced great difficulties^{13,15} in finding a firm to manufacture and market the SEM and his efforts came to fruition only in 1965 when the Cambridge Instrument Company delivered the first Stereoscan¹⁴ (a prototype) to the du Pont Corporation in the U.S.A.

References

1. E.H. Syngé, *Phil. Mag.* (1928)6, 356-362.
2. H. Stintzing, German patents nos. 485155 and 485156 (1929).
3. M. Knoll, *Z. tech. Phys.* (1935)16, 467-475.
4. M. von Ardenne, *Z. Phys.* (1938)109, 553-572.
5. M. von Ardenne, *Z. tech. Phys.* (1938)19, 407-416.
6. M. von Ardenne, "Elektronen-Übermikroskopie", Springer, Berlin (1940).
7. See "Historical Review of BSE in SEM" by O.C. Wells in this volume.
8. V.K. Zworykin, J. Hillier and R.L. Snyder, *A.S.T.M. Bull.* (1942)117, 15-23.
9. D. McMullan, *Proc. Inst. Elect. Eng. II*(1953)100, 245-259.
10. K.C.A. Smith and C.W. Oatley, *Brit. J. Appl. Phys.* (1955)6, 391-399.
11. K.C.A. Smith, "The SEM and its fields of application", Ph.D. Dissertation, Cambridge University.
12. K.C.A. Smith, *Pulp. Paper Mag. Can. Tech. Sect.* (1959)60, T366-T371.
13. P. Jervis, *Research Policy* (1970)1, 174-207.
14. A.D.G. Stewart and M.A. Snelling, *Proc. 3rd EUREM*, Prague 1965, pp. 55-56.
15. C.W. Oatley, *J. Appl. Phys.*(1982)53, R1-R13.
16. Bibliographies: "Beginnings of Electron Microscopy" by C.W. Oatley, D. McMullan and K.C.A. Smith in *Adv.E.E.P. Suppl.* 16, pp. 443-482 (1985); D. McMullan, *J. Microsc.* (1989)155, 373-392.

ELECTRON SOURCES: PAST, PRESENT, AND FUTURE

⁺David C Joy

EM Facility, University of Tennessee, Knoxville, TN 37996-0810, and

⁺Oak Ridge National Laboratory, Oak Ridge, TN 37831

The electron source is the most important component of the Scanning electron microscope (SEM) since it is this which will determine the overall performance of the machine. The gun performance can be described in terms of quantities such as its brightness, its source size, its energy spread, and its stability and, depending on the chosen application, any of these factors may be the most significant one. The task of the electron gun in an SEM is, in fact, particularly difficult because of the very wide range of operational parameters that may be required e.g a variation in probe size of from a few angstroms to a few microns, and a probe current which may go from less than a pico-amp to more than a microamp. This wide range of operating parameters makes the choice of the optimum source for scanning microscopy a difficult decision.

Historically, the first step up from the sealed glass tube 'cathode ray generator' was the simple, diode, tungsten thermionic emitter. With the addition, in the 1930's, of the Wehnelt control-grid cylinder to form a triode gun the thermionic emitter was able to reach its theoretical brightness limit and a source size of a few tens of microns.¹ With the relatively poor lenses, vacuums, and detectors that were then available this level of performance was adequate and permitted significant advances to be made in the application and understanding of the instrument itself. However, with the development in 1959 of the Everhart-Thornley secondary electron detector it became clear that the potential of the SEM for high spatial resolution imaging would only be achieved with better electron sources. Two types of improvement were investigated. Firstly, the 'pointed' filament, developed by Fernandez-Moran and other workers and designed to minimize the effect of space-charge on the cathode and to produce a smaller source size.² Although pointed filaments do have a brightness which is 2 to 3x higher than that of a conventional tungsten emitter the fragility of the device, its susceptibility to mechanical and thermal damage, and its consequent shortened life-span, make it unsuitable for most purposes. Secondly the LaB₆ cathode, originally proposed by Lafferty, was turned into a practical reality by the work of Broers and others.³ The LaB₆ emitter gives an increase in brightness of from 3 to 5 times over a tungsten thermionic emitter, a reduction in source size of typically from 50µm down to about 5 µm, and only half the energy spread coupled with, in the case of the modern indirectly-heated LaB₆ cathode, a long lifetime (>1000 hours) and stable emission.

The event which took the performance of the SEM to the next level was the development of practical field emission (FE) sources. Field emitters were not new, for example Zworykin and collaborators had used one in their prototype SEM in the 1940's, but two major problems had to be overcome before they were anything more than laboratory curiosities. The first was the provision of practical, reliable, and clean, ultra-high vacuum systems in which to run the emitter. This goal was met by the late 1960s, though improvements in the technology of demountable metal gaskets, bakeable vacuum systems, and in ion and getter pumps, which made the attainment of ultra-high vacuums a relatively routine matter. The second was the development of an electron gun design which would allow the full potential of the field emitter to be realized. Here the work of Crewe and his group provided a design which minimized the effect of gun aberrations on the brightness of the emitter while providing convenient and flexible electron-optical properties.⁴ Their design, which forms the basis of most of the current generation of high resolution SEMs, was so effective that just the gun alone could form a probe a few angstroms in diameter containing sufficient current for high resolution imaging and microanalysis. Further they were able to demonstrate that a comparable level of performance could be obtained even at accelerating voltages of only one or two kV, so opening a new field of SEM investigation. Most recently still, the work of Vu Thien Binh and others has led to the concept of nano-FE tips which achieve a brightness two orders of magnitude higher than that of a regular FE source by starting from a source of atomic dimensions.⁵

Despite the advances discussed briefly above there is still not one single choice of electron source which is optimum for all applications and instruments. The best electron source for conventional electron beam microanalysis needs quite different properties to those found in a source optimized for ultra-high resolution imaging, or to those for a source designed for application in electron beam lithography, and so the scanning microscopist will continue to have to deal with a variety of electron guns.

References

1. M E Haine and P A Einstein, (1952), *Brit. J.Appl.Phys.*, **3**, 40
2. H Fernandez-Moran, (1966), *Proc.6th Int.Cong.on EM*, Kyoto, 27
3. A N Broers, (1969), *J.Phys.E.*, **2**, 273
4. A V Crewe et al, (1968), *Rev. Sci.Instr.* **39**, 576
5. Vu Thien Binh and N Garcia, (1991), *J.Phys.L.*, **1**, 605

THE ORIGINS OF HIGH-RESOLUTION SECONDARY-ELECTRON MICROSCOPY

M.R. Scheinfein^{*,#}, J.S. Drucker[#], J.K. Weiss[#]

^{*}Department of Physics and Astronomy, Arizona State University, Tempe, AZ 85287-1504

[#]Center for Solid State Science, Arizona State University, Tempe, AZ 85287-1704

The production or generation of SE by focused, fast electron beams is a multistage process which includes excitation of target electrons by the energetic incident beam, subsequent decay yielding hot SE, transport to the surface, and transmission over the surface potential barrier¹. The ultimate spatial resolution of a SE image formed by scanning a well focussed probe across a surface is limited by the excitation events' spatial delocalization through the transverse momentum transferred to the specimen.

The accepted model for SE production¹ is not well characterized since it is extremely difficult to separate experimentally the generation, transport and transmission processes during a given SE creation event. Here, we examine the SE generation pathway by correlating SE of a given energy produced by an initial inelastic excitation using time coincidence detection²⁻⁵. This technique can be used, for example, to isolate the role of plasmon decay⁶ in the SE generation process. The experiments were performed in a Vacuum Generators HB501-S UHV scanning transmission electron microscope (STEM), operating at base pressures of 5×10^{-11} torr. The microscope is equipped with an electron energy loss spectroscopy (EELS). Surface microanalysis is performed within the magnetic field of the objective lens using the parallelizer principle. Collected electrons are deflected by an astigmatic Wein filter, and energy analyzed by a 100 mm radius, 180° spherical electrostatic energy analyzer operated at a fixed retard ratio of 5. In the coincidence experiments, time correlation spectra (TCS) are formed by starting the timing electronics with EELS pulses, and using the delayed SE pulses to gate the stop. The EEL spectrometer pass energy is ramped while the SE spectrometer remains fixed at a particular energy with a 1 eV energy window. A time correlation spectrum is acquired at each EEL energy, and the true and false coincidence signals, which are integrals under the TCS peak and background, are extracted and stored.

EELS, coincidence and generation probability spectra for p-type ($n_h = 10^{15} \text{ cm}^{-3}$) Si<111> are shown in Figs. 1a and 1b. The SE generation probability spectrum is defined as the ratio between the coincidence and EELS spectra, and is a measure of SE generation efficiency for a particular inelastic excitation. The plasmon excitation visible at 17.7 eV is the dominant peak in the EELS spectrum (Fig. 1a). The role of plasmon decay in SE production remains controversial. These excitations have large cross sections and the accompanying planar surface plasmons are localized within a SE escape depth of the surface. We observe that most of the generation probability for SE creation lies at excitation energies above the volume plasmon excitation energy (Fig. 1), suggesting that SE production resulting from the decay of plasmons is not the primary production mechanism in p-type Si <111>. The data of Fig. 1 provide evidence that large densities of states (along L) at -7.24 and -10.17 eV⁷ ($E_F = 0$ in this highly doped p-type Si) are the source of many generated SE.

Coincidence electron spectra were accumulated between 2.5 eV SE and primary inelastically scattered electrons at discrete energies, 17eV (the plasmon energy in Si), 34 eV and 51 eV. In each case, three effective angular apertures were defined with the post specimen lens optics such that electron energy loss excitations with perpendicular momentum transfer wave vectors up to 1.00 \AA^{-1} , 0.18 \AA^{-1} and 0.15 \AA^{-1} were accepted into the spectrometer. The ratios of the number of SE produced by primary electrons which have scattered through a certain angle can be obtained by fitting this data (not shown). With the 1.00 \AA^{-1} (the cut-off wave vector for plasmon excitations in Si is 1.1 \AA^{-1}) transverse momentum data used for the normalization, 44% of all SE produced in thin Si(111) crystals result from primary electrons which have scattered through at least 0.18 \AA^{-1} , and 87% are the result of scattering by at least 0.15 \AA^{-1} . The spatial resolution of an image can be estimated from the degree of delocalization from the inelastic scattering

distribution and the Heisenberg uncertainty principle⁵. For the angularly resolved coincidence data, and the EEL spectra which produced these SE, we estimate the spatial delocalization to be 0.35 nm for images formed with all SE generated from all high angle inelastic events. This work was performed at the NSF supported Center for High Resolution Electron Microscopy at ASU, Grant No. DMR-91-15680.

References

1. D.M. Suszcynsky, J.E. Borovsky, Phys. Rev. **A45**(9), 6424 (1992); M. Rosler, W. Brauer, phys. stat. sol. (b) **104**, 161 (1981); M. Rosler, W. Brauer, phys. stat. sol. (b) **104**, 575 (1981); M. Rosler, W. Brauer, phys. stat. sol. (b) **148**, 213 (1988); J. Schou, Scanning Micr. **2**, 607 (1988); R. Bindi, H. Lateri, P. Rostaing, Scanning Micr. **1**, 1475 (1987); V.E. Henrich, Phys. Rev. **B7**, 3512 (1973); R. Willis et. al, Phys. Rev. **B9**, 1926 (1974).
2. D. Voreades, Surf. Science, **60**, 325 (1976).
3. H. Mullejans, A.L. Bleloch, A. Howie, C. McMullan, Inst. Phys. Conf., Ser. No. **119**(3), 117 (1991); H. Mullejans, Ph. D. Thesis, University of Cambridge, 1992.
4. P. Kruit, H. Shuman, A.P. Somlyo, Ultramicrosc. **13**, 205 (1984);F.J. Pijper, P. Kruit, Phys. Rev. **B44**(17), 9192 (1991).
5. M.R. Scheinfein, J.S. Drucker, J.K. Weiss, Phys. Rev. **B47**(7), 4068 (1993); J.S. Drucker, M.R. Scheinfein, Phys. Rev. **B** (in press, 1993).
6. T.E. Everhart, M.S. Chung, J. Appl. Phys. **43**(9), 3707 (1972); M.S. Chung, T.E. Everhart, Phys. Rev. **B15**(10), 4699 (1977);J.P. Ganachaud, M. Callier, Surf. Sci. **83**, 498 (1979); J.P. Ganachaud, M. Callier, Surf. Sci. **83**, 519 (1979).
7. J.R. Chelikowsky, M.L. Cohen, Phys. Rev. **B14**(2), 556 (1976).

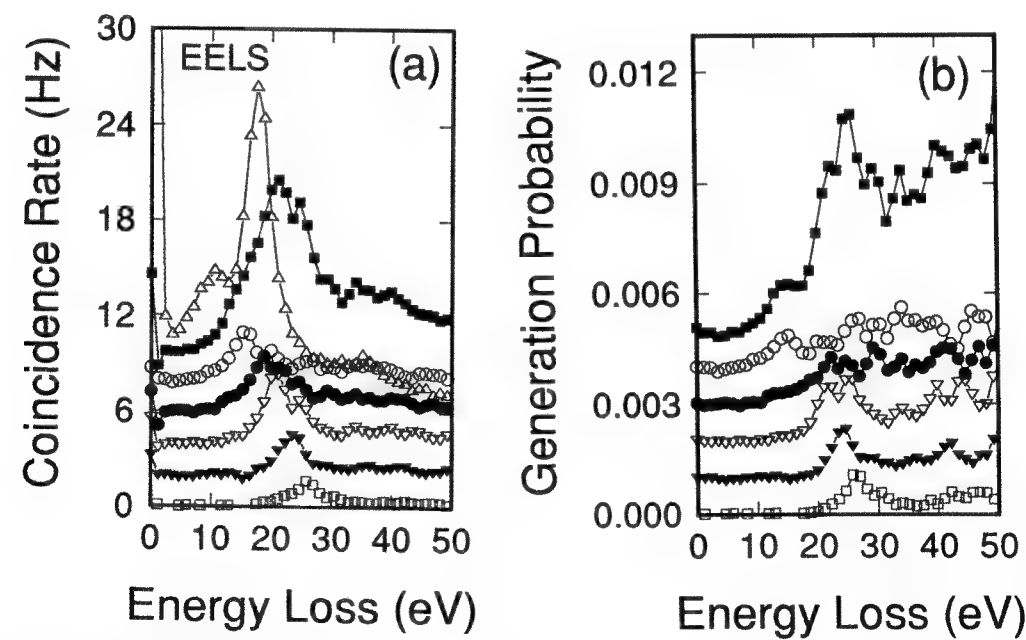


Fig 1: (a) EELS (open triangles) and coincidence spectra (total (top), 2.5 eV, 5.0 eV, 7.5 eV, 10.0 eV, and 12.5 eV(bottom) SE) for Si <111>. (b) Generation probability spectra extracted from (a).

THE BRIGHT FUTURE OF DIGITAL IMAGING IN SCANNING ELECTRON MICROSCOPY

M. T. Postek and A. E. Vladar*

National Institute of Standards and Technology, Gaithersburg, MD 20899**

One of the major advancements applied to scanning electron microscopy (SEM) during the past 10 years has been the development and application of digital imaging technology. Advancements in technology, notably the availability of less expensive, high-density memory chips and the development of high speed analog-to-digital converters, mass storage and high performance central processing units have fostered this revolution. Today, most modern SEM instruments have digital electronics as a standard feature. These instruments, generally have 8 bit or 256 gray levels with, **at least**, 512 x 512 pixel density operating at TV rate. In addition, current slow-scan commercial frame-grabber cards, directly applicable to the SEM, can have upwards of 12-14 bit lateral resolution permitting image acquisition at 4096 x 4096 resolution or greater. The two major categories of SEM systems to which digital technology have been applied are:

1. Analog "slow scan" SEM systems. In the analog SEM system the scan generator is normally operated in an analog manner and the image is displayed in an analog or "slow scan" mode. TV rate is available, but is not the preferred mode of operation. These systems have been the mainstay of the SEM market and many thousands of instruments are currently out in the field. Analog systems are not directly or economically upgradable by the SEM manufacturer to digital imaging, but it is possible to install accessory digital image processing and analysis systems such as those provided by third-party companies. These systems include digital imaging incorporated into x-ray microanalysis systems or other computer-based stand alone systems. External access of the system is through a port referred to as a digital beam interface (DBI). The DBI changes the voltage levels, signal polarities, biases and impedances in order to properly connect the standard inputs and outputs of the analog and digital converters of the external computer to the SEM. This port is either standard on the instrument or it can be added later.

2. Digital SEM Systems. In the digital SEM system, the scan generator is operated either in an analog or digital manner. The image is stored, processed and displayed transparently through an image memory routinely at TV rate. Internal or external hard-disk mass storage of the digital images is also possible for archiving. The stored digital image may be photographed directly from the frame memory or hard disk. High resolution photography is accomplished through direct analog or digital scanning. High-speed frame-grabbing is also possible with an accessory computer through a standard video output (RS-170 or PAL).

*Guest Researcher from the Research Institute for Technical Physics of the Hungarian Academy of Sciences.

**Contribution of the National Institute of Standards and Technology. Not subject to copyright.

External communication to other third party systems is accomplished through a DBI or other standard communication channels such as the Small Computer Standard Interface (SCSI).

Pre-digital electronics SEMs were plagued by the problem of a poor signal-to-noise ratio, especially at low accelerating voltages and TV scan rates. Recent developments in field emission filament technology improved that situation, but parallel development of the modern digital imaging technology brought both of these technologies together into an extremely powerful tool with exceptional flexibility. Some of the advantages afforded by digital imaging include:

TV Rate Scanning. Essentially the "slow scan" presentation of the SEM is gone and is replaced with a real-time TV image. Integration of poorer signal-to-noise images is transparently accomplished by frame buffering and frame averaging of the video signal. TV rate scanning has been shown to be useful in reduction of charging on many samples.

Digital Image Storage. Image archiving of the digital images either to floppy disk or hard disk provides a permanent record that is easy to retrieve. Image quality is identical to the originally stored image. Standardized file storage such as the TIFF file format enables importation of the images into desk-top computers and word processing programs.

Paperless Image Transmission. The image data can be transmitted via data lines to remote locations. It is conceptually possible to view the SEM image from a remote location and actually operate the SEM from that location.

Real-time Pseudocolorization. High speed frame grabbers built into fast computers enable the pseudocolorization of the SEM image at TV rate. This allows the highlighting by color coding of certain information valuable to the viewer.

Real-Time Image Analysis/Processing. Digital enhancement of the image can be done transparently, as the image is acquired, and the image can be processed at the SEM console.

Optimization of Operating Conditions. Digital SEMs can automatically optimize the operating conditions, such as the brightness, contrast, focus and astigmatism correction. The operator can save optimum operating conditions then re-load them as needed.

Until a few years ago, digital imaging was severely limited by the power of the computer systems available and, therefore much of the digital imaging was done through interfacing to the powerful mini-computer coupled to an x-ray microanalysis systems. Today, many desktop computers have computing capabilities surpassing these early mini-computers. Computer systems are now small and inexpensive enough to be directly incorporated into the SEM electronics console as a standard component by the manufacturer. Thus, the architecture of the modern SEM has changed, in that, the instrument has become more a computer with an SEM column being only a peripheral component. This concept is a major advantage because the digital architecture of modern SEMs now permits the application of a whole host of peripheral technologies associated with, and being developed for, the personal computer industry to be readily applied to the SEM. These technologies enable the data to be more readily taken, stored and processed. Indeed, the future is bright for this technology.

EXPLANATION OF THE HIGH RESOLUTION BACKSCATTERED ELECTRON IMAGE IN THE SCANNING ELECTRON MICROSCOPE BY THE TWIN-POPULATION THEORY - A HISTORICAL REVIEW

Oliver C. Wells

IBM Thomas J. Watson Research Center,
 PO Box 218, Yorktown Heights, NY 10598

Several different "twin-population" theories have been proposed to explain the high resolution backscattered electron (BSE) image in the scanning electron microscope (SEM). In all of these, the BSE are divided into local BSE that give an image having a resolution that is significantly better than the electron penetration depth R and diffused BSE that give a less sharp image. Other theories attach more importance to the diffused BSE.

The BSE image was originally proposed by von Ardenne in 1940 with the specimen at right angles to the incident electron beam⁽¹⁾ (Fig. 1). This has been summarised by McMullan.⁽²⁾ Von Ardenne predicted high resolution secondary electron (SE) imaging by local SE (now⁽³⁾ called SE-I) and pointed out the advantages of low voltage operation, but failed to realise that there was a high resolution BSE signal also. McMullan⁽⁴⁾ distinguished between the BSE image as defined above (Fig. 2(b)) where the principal contrast mechanism is compositional and the reflected electron image in which the sample is tilted by typically 45° and forward-scattered BSE are collected (Fig. 2(a)). The contrast is then mainly topological. Forward scattered BSE are localised to some degree. These can be energy-filtered to give the low-loss electron image.⁽⁴⁻⁷⁾

Smith⁽⁸⁾ (in addition to pioneering the SE image) built a large-angle BSE detector with an aluminised scintillator and photomultiplier. This writer⁽⁹⁾ and Robinson⁽¹⁰⁾ built quasi-symmetrical scintillator BSE detectors with a hole for the beam to pass through. BSE have also been detected using solid-state diodes⁽¹¹⁾ or a multichannel-plate (MCP).^(12,13)

The spatial distribution of BSE was calculated by Murata⁽¹⁴⁾ using the Monte Carlo method. A central peak (the "Murata peak"⁽¹⁵⁾) caused by singly and plurally scattered BSE provides a localised signal for high resolution BSE imaging (Fig. 3). Energy distribution curves by Kulenkampf and Spyra⁽¹⁶⁾ show a higher fraction of faster BSE for high-Z elements. This suggests a bimodal spatial distribution of BSE with diffused and localised components.⁽¹⁷⁾

Ogura et al⁽¹⁸⁾ obtained high resolution BSE images from a GaAs/AlAs superlattice with a repetition distance of 22 nm or less that was many times smaller than the penetration depth ($R \approx 1 \text{ mg/cm}^2 \approx 1.9 \text{ } \mu\text{m}$ in GaAs at 25 keV) (Fig. 4). The sample was mounted between the polepieces of the lens to minimise aberrations. One possible scattering model to explain this success involves beam spreading that blurs the image and a wide-angle scattering event towards the detector⁽¹⁹⁾ (Fig. 5). For the future it will be interesting to see whether the BSE image under these conditions can resolve individual atomic columns as is the case when a thinned single crystal sample is examined by the Z-contrast method.^(20,21) The physics is very similar but there is a signal-to-noise ratio penalty of $\sim 10,000$.

It is possible that the slower BSE might contribute high resolution information in Fig. 5 as follows.⁽¹⁹⁾ Consider a deflection ϕ of probability $p(\phi)d\phi$ in a high-Z inclusion at depth z by a wide-angle scattering event where $0 < \phi < \pi/2$ and where $z \ll R$. The escape probability of this electron is given (very nearly) by the BSE coefficient $\eta(\phi)$ for an incident angle ϕ . This is greater than $\eta(0)$ for normal incidence. Thus there will be a contribution to the signal from slow BSE arising from forward scattering at depth z proportional to $\int p(\phi) (\eta(\phi) - \eta(0)) d\phi$ for $0 < \phi < \pi/2$. Experiments are planned to measure this contribution.

FIG. 1

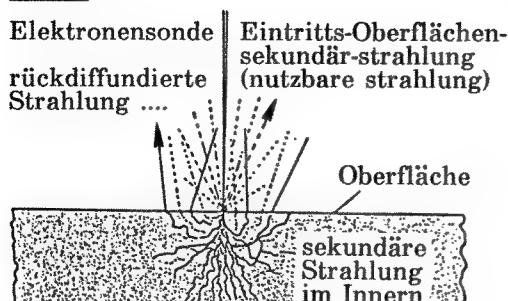


FIG. 2(a)

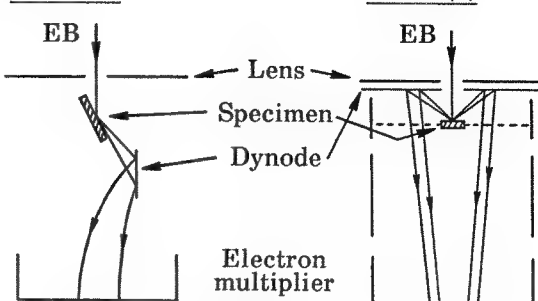


FIG. 2(b)

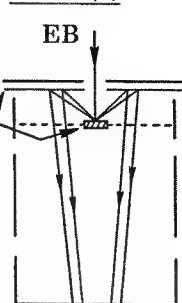


FIG. 3

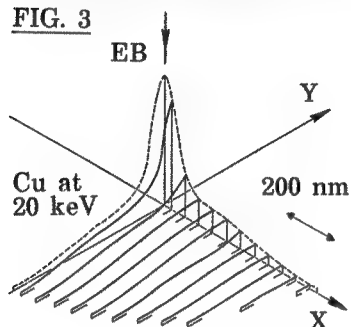


FIG. 4

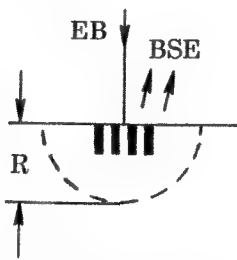


FIG. 5

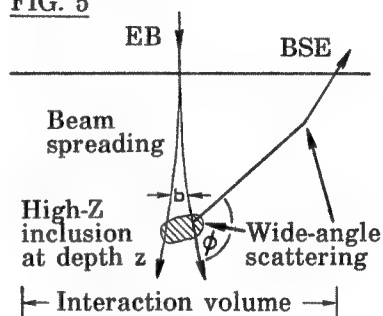


FIG. 1. Diffusion model for BSE image (relettered from von Ardenne⁽¹⁾).

FIG. 2. (a) Reflection imaging and (b) BSE imaging after McMullan⁽⁴⁾.

FIG. 3. Spatial distribution of BSE from Cu at 20 keV calculated by Murata⁽¹⁴⁾.

FIG. 4. High resolution BSE imaging of superlattice based on Ogura et al.⁽¹⁸⁾

FIG. 5. Electron scattering model⁽¹⁹⁾ to explain Fig. 4.

- (1) M. von Ardenne, *Elektronen-Übermikroskopie*, Springer, Berlin (1940); Edwards, Ann Arbor (1943). Summary: ref. 2.
- (2) D. McMullan, *Proc. Royal Microsc. Soc.* **23** (1988) 283.
- (3) K-R Peters, *SEM/1982* (1982) 1359.
- (4) D. McMullan, *Proc. IEE (England)* **100 Pt. II** (1953) 245.
- (5) O.C. Wells, *Appl. Phys. Lett.* **19** (1971) 232.
- (6) O.C. Wells, F.K. LeGoues and R.T. Hodgson, *Appl. Phys. Lett.* **56** (1990) 2351.
- (7) R.T. Hodgson, F.K. LeGoues and O.C. Wells, U.S. Patent 4,962,306 (Oct. 9, 1990).
- (8) K.C.A. Smith, Ph.D. Diss., Cambridge Univ., England, (1956).
- (9) O.C. Wells, Ph.D. Diss., Cambridge Univ., England, (1957).
- (10) V.N.E. Robinson, *J. Phys. E: Sci. Instrum.* **2** (1974) 650.
- (11) S. Kimoto and H. Hashimoto, *The Electron Microprobe* (T.D. McKinley et al, eds.), (Wiley, New York, 1966) 480.
- (12) P.E. Russell and J.F. Mancuso, *J. Microsc.* **140 Pt.3** (1985) 323.
- (13) M.T. Postek, *Rev. Sci. Instrum.* **61** (1990) 3750.
- (14) K. Murata, *J. Appl. Phys.* **45** (1974) 4110.
- Fig. 3 is relettered from: K. Murata, *SEM/1973* (Part II) 267.
- (15) K-R Peters, private discussions. For experimental data, see: Ong Sing Poen and J.B. Le Poole, *Appl. sci. Res. (Netherlands)* **7B** (1958) 233.
- (16) H. Kulenkampff and W. Spyra *Z. Phys.* **137** (1954) 416.
- (17) O.C. Wells, *Proc. 24th. Ann. Conf. MAS; (Asheville, NC)*, (1989) 227.
- (18) K. Ogura et al., *Proc. 48th. Ann. Conf. EMSA 2* (1990) 404.
- (19) O.C. Wells and M. Nacucchi, *Proc. Int. School on Electron Microscopy in Materials Science* (Mesagne, Italy, Oct. 1991), World Scientific Singapore (in press).
- (20) S.J. Pennycook and D. McMullan, *Ultramicroscopy* **11** (1983) 315.
- (21) S.J. Pennycook and D.E. Jesson, *Ultramicroscopy* **37** (1991) 14.

CRYSTALLOGRAPHIC PHASE IDENTIFICATION IN THE SCANNING ELECTRON MICROSCOPE: BACKSCATTERED ELECTRON KIKUCHI PATTERNS

J. R. Michael and R. P. Goehner

Materials and Process Sciences Center, Sandia National Laboratories, Albuquerque, NM 87185

The use of the recently developed charge coupled device (CCD)-based detector for the acquisition of high quality backscattered electron Kikuchi patterns (BEKP) has allowed on-line crystallographic phase identification studies to be conducted in the scanning electron microscope.¹ High quality patterns suitable for analysis have been obtained in a wide variety of materials with little special specimen preparation. Phase identification through a combination of BEKP and energy dispersive x-ray spectrometry (EDS) is demonstrated by the identification of crystals present on ruthenium oxide thin films on Si. The crystals were identified as RuO₂, a tetragonal phase.

The CCD-based detector has been described previously and will only be briefly described here.¹ The detector consists of a scientific grade slow scan CCD coupled to a YAG scintillator by a fiber optic reducer. During operation the CCD is cooled to -40°C by a thermoelectric cooler. This detector allows high quality patterns to be recorded with beam currents as low as 10⁻¹⁰A and exposure times of 1 to 10 seconds. The images obtained with the detector were significantly improved by a procedure called flat-fielding. The raw patterns collected with the detector consist of the detailed crystallographic information superimposed on a slowly changing background intensity and a fine 'chicken wire' pattern. The chicken wire pattern is due to defects at the sub-bundle boundaries in the fiber optic reducer. A flat field image is obtained by scanning the electron beam over a large area of the specimen that includes many crystal orientations which washes out any crystallographic detail. The raw image is then normalized by the flat field image. The flat fielding procedure corrects for any variations in pixel response and for any defects in the fiber optic bundle and the YAG scintillator.³ The CCD-based detector produces digital images which are immediately available for analysis.

BEKP's were obtained from crystals which were on substrates tilted 70° from the horizontal position. The specimen height was carefully reproduced by focusing with the mechanical height control to ensure that the location of the pattern on the detector does not change. Patterns were obtained at 40 kV by holding the beam stationary, in a manner similar to the collection of x-ray spectra, on the faces of crystals like the one shown in Figure 1. It was not possible to mount the individual crystals so that facets on the crystals were at a 70° angle, but this did not hinder the collection of BEKP's from the crystals. EDS analysis of the crystals on the ruthenium oxide films contained Ru and possibly oxygen.

Figure 2 a shows a BEKP obtained from a crystal on the ruthenium oxide thin films. Initial analysis of the pattern is accomplished by measurement of the angles between the crystallographic zone axes visible in the patterns. The center of the pattern and the camera length must be accurately known. The measured interzonal angles can then be compared with those calculated for candidate compounds. This technique is quite useful for non-cubic materials, but is not diagnostic for cubic crystals since the interzonal angles are fixed and independent of the lattice parameter. The d-spacing for a given crystallographic plane is proportional to the spacing between Kikuchi line pairs in the BEKP. There is some uncertainty associated with the d-spacing measurements, but the measurements are accurate enough to use for further candidate compound screening.

Once the number of candidate compounds is narrowed down, patterns of the candidate compounds are simulated. The simulation utilizes centering restrictions and intensity corrections in order to more accurately simulate the observed patterns. The intensity corrections are used to exclude Kikuchi lines from the simulation that are either not allowed by the space group or do not yield significant relative intensities. It has been our observation that the relative intensities of the Kikuchi lines, both positive and negative, are in good agreement with calculated intensities. Figure 2b is a simulations of the pattern

shown in Figure 2 a for RuO_2 with some of the major zone axes labeled. The excellent agreement between the experimental and simulated pattern indicates that the crystals on the ruthenium oxide thin film are RuO_2 , a tetragonal compound.

Through the combination of BEKP and EDS, crystals that grew on ruthenium oxide thin films were identified as RuO_2 . Identification would be very difficult utilizing conventional techniques such as x-ray diffraction and electron diffraction in the transmission electron microscope due to the size and small area fraction of the crystals on the substrate. Phase identification utilizing BEKP has been used to identify crystallographic phases in many metals, semiconductors and ceramics. The ability of the CCD-based detector to collect high quality patterns without the use of photographic emulsions enables on-line analysis of the BEKP's. The combination of diffraction information from BEKP with EDS information holds the promise of a powerful new tool for materials science that will eventually allow rapid phase identification in the SEM.

References

1. R. P. Goehner, et al. Proc. Ann. EMSA Meeting 50 (1992) 1310.
2. J. R. Michael and R. P. Goehner, MSA Bulletin (1993) 23 in press.
3. S. Kujawa and D. Krah, Ultramicros. (1992) 46, 395.
4. This work was supported by the U. S. Department of Energy under contract DE-AC04-76DP00789.

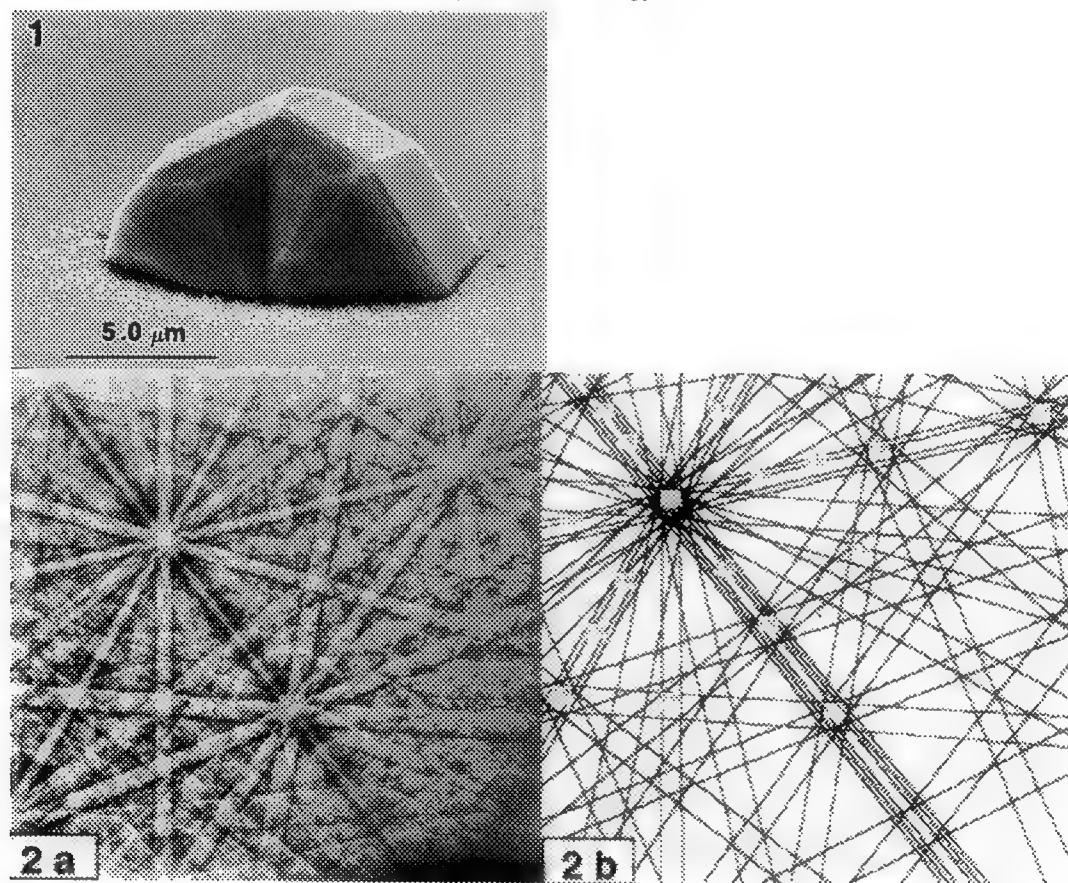


FIG. 1 SEM image of a crystal grown on a ruthenium oxide thin film on Si.

FIG. 2.a. BEKP taken at 40 kV from the crystal shown in FIG 1, and b) simulated BEKP of RuO_2 at 40 kV.

FACET CRYSTALLOGRAPHY BY ELECTRON DIFFRACTION IN THE SEM

J.A. Sutliff

GE Corporate Research and Development, 1 River Road, Schenectady, NY 12309

The study of fracture in engineering materials often involves an analysis of the crystallography of the fracture surface. In particular, the question is often asked, "What, if any, low index plane corresponds to the plane of a particular fracture surface facet?" To determine the crystallographic plane of a surface facet, it is necessary to determine the orientation of the grain and the orientation of the facet plane relative to the grain. For example, if a euhedral crystal of known orientation is fractured, an optical reflection goniometer can be used to measure the angles between a facet and known crystal faces in order to deduce the direction of the facet normal. Laue x-ray diffraction patterns taken from well aligned facets can also be analyzed to determine the orientation of the crystal normal to the facet. In many engineering materials, the facets are small, usually as a result of a small grain size in the material, and it becomes impractical to use these techniques. The electron back-scattering pattern (EBSP) technique^{1,2} in the SEM is a rapidly growing technique which can be applied to the problem of facet crystallography in small grain size material. The EBSP technique can be applied in a Laue-like fashion, with the added SEM benefits of high resolution imaging and beam positioning.

To apply the EBSP technique to facet analysis can be simple. If the local topology of the sample surface allows, the facet is observed in a normal SEM mode while the sample is tilted and rotated in a eucentric stage until the facet normal is perpendicular to the optic axis. The microscope stage is then "zeroed" and the sample tilted a specific amount so that the surface of the facet is well oriented to produce a diffraction pattern (e.g. twenty degrees). The EBSP is analyzed to determine the orientation of the crystal and the facet plane is simply found from the solution using the known tilt. It is assumed, as is necessary for most EBSP studies, that the detection system has been calibrated using an orientation standard such as a cleaved single crystal. Two types of problems can arise for samples having complex fracture surfaces. First, the fracture surface may either block the SEM probe from striking the facet under conditions necessary for formation of a usable diffraction pattern or block the back-scattered electrons from striking the EBSP detector. Second, the fracture surface may block the view of the facet at those tilts required to "zero" the stage. To alleviate the first kind of problem it may be necessary to cut the sample into smaller pieces to gain access to the region of interest. If "zeroing" the stage as described above is impossible, it may be possible to determine a different, specific, non-perpendicular, reference tilt for the facet by photographing the facet at a number of tilts and measuring the position of features on the facet.

To demonstrate the use of the procedure outlined above, a crystallographic analysis was made of facets on a well formed crystal of diamond. Figure 1 is a SEM micrograph of the diamond with the facets analyzed indicated. Figure 2 is an EBSP pattern from the GaAs crystal used as a standard. Figures 3, 4, and 5 show EBSPs from facets marked in Figure 1. All patterns were taken with the respective facet normal tilted 70 degrees to the beam direction and rotated to make a primary facet edge parallel to the microscope x-axis. Figure 6 is a {100} pole figure which shows the orientation of the {100} crystal poles when each facet was oriented. The expected [001], [111] and [110] orientations of the normal to the facets, which should fall on the center of the figure can be easily deduced. The principle error in the measurements results from the lack of precision and accuracy in the microscope stage.

References

1. J.A. Venables and C.J. Harland, *Phil. Mag.* **27** (1973) 1193.
2. D.J. Dingley, *Scanning Electron Microscopy/1984*, ed. Johari, Chicago: SEM Inc. (1984) 569.

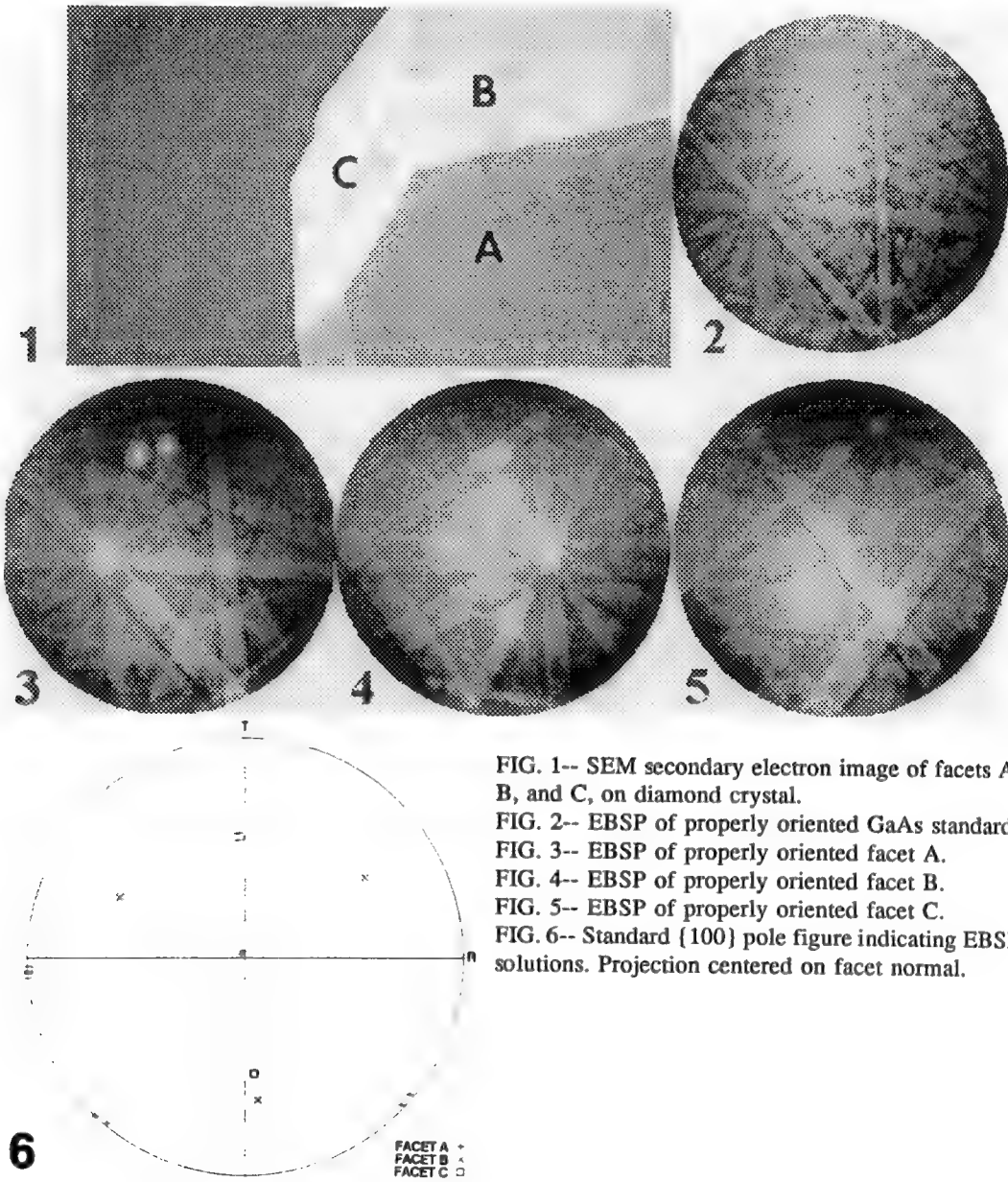


FIG. 1-- SEM secondary electron image of facets A, B, and C, on diamond crystal.
FIG. 2-- EBSP of properly oriented GaAs standard.
FIG. 3-- EBSP of properly oriented facet A.
FIG. 4-- EBSP of properly oriented facet B.
FIG. 5-- EBSP of properly oriented facet C.
FIG. 6-- Standard {100} pole figure indicating EBSP solutions. Projection centered on facet normal.

Scanning Electron Microscope Magnification Calibration Interlaboratory Study

Michael T. Postek, Andras E. Vladar,¹ Samuel N. Jones and William J. Keery

National Institute of Standards and Technology,^{2,3} Gaithersburg, MD 20899

The National Institute of Standards and Technology (NIST) is in the process of developing a new scanning electron microscope (SEM) magnification calibration reference standard useful at both high and low accelerating voltages. This standard will be useful for all applications to which the SEM is currently being used, but it has been specifically tailored to meet many of the particular needs of the semiconductor industry.^{4,5} A small number of test samples with the pattern were prepared on silicon substrates using electron beam lithography at the National Nanofabrication Facility at Cornell University. The structures were patterned in titanium/palladium with maximum nominal pitch of approximately 3000 μm scaling down to structures with minimum nominal pitch of 0.4 μm . Several of these samples were sent out to a number of university, research, semiconductor and other industrial laboratories in an inter-laboratory study. The purpose of the study was to test the SEM instrumentation and to review the suitability of the sample design. The laboratories were asked to take a series of micrographs at specific magnifications and accelerating voltages designed to test several of the aspects of instrument performance related to general SEM operation and metrology. This study represents data from a pool of 35 participating laboratories representing a total of 49 instruments.

A number of studies were done on the data submitted.⁶ These studies included: analysis of the micrometer marker relative to the image, measurement of the image magnification, measurement of the X and Y squareness, and analysis of the accelerating voltage compensation. The analysis of the micrometer marker length to the measured image of the prototype sample was made from the submitted micrographs. Overall, most of the SEMs involved in this study demonstrated some error in the adjustment of the micrometer bar. This is a very difficult adjustment to make since it is generally made directly from the micrograph, often from a relatively short fiducial line. Box plots of the percent error demonstrated by all the instruments of this study relative to the magnification range (for all accelerating voltages reported) are shown in Fig 1a. The mean of the error of these measurements was 2.23% with a standard deviation of $\pm 13.01\%$.

The actual magnification of the micrographs was also determined and compared to NIST measurements of the same sample in another portion of the study. The graphical representation of the magnification error is shown in Figure 1b. This figure represents box plots of the magnification error data obtained from all the instruments. In this figure, the mean of the error of these measurements was 1.77% with a standard deviation of $\pm 12.03\%$.

It can be concluded from this study that the NIST calibration sample could be issued without further modification, but several excellent suggestions made by the participants of the study

will be incorporated in the final issued version. However, even with the issuance of an accurate standard capable of meeting the needs of modern SEM use, the coarseness of the calibration system of the instrument will become the limiting factor to the accuracy of the magnification calibration procedure.

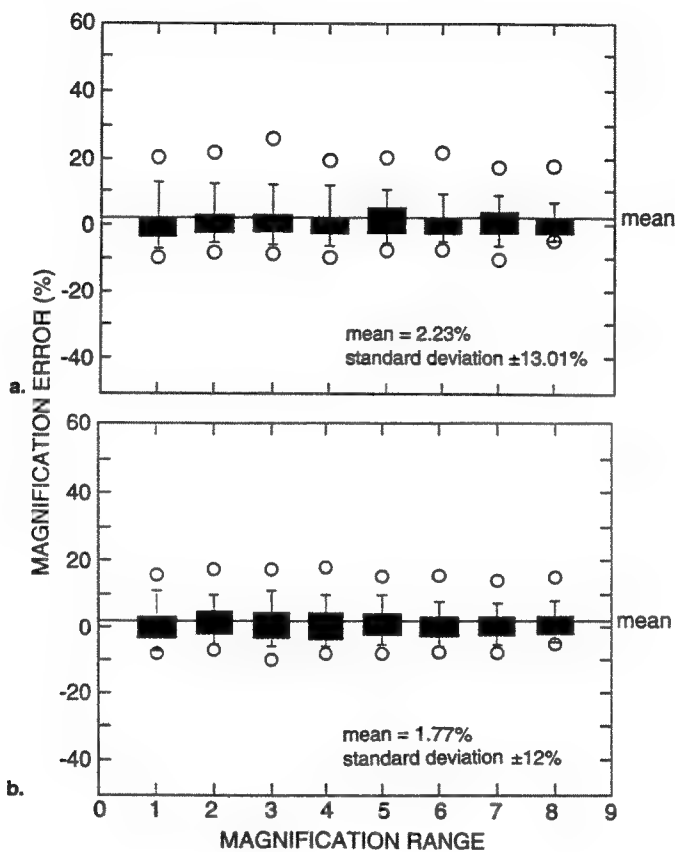


FIG 1.-- SEM magnification calibration error. (a) Measurement of the error of the image magnification to the micrometer marker. (b) Measurement of the error of the magnification to the NIST measurements of the same sample.

References

1. Guest Researcher from the Research Institute for Technical Physics of the Hungarian Academy of Sciences
2. Contribution of the National Institute of Standards and Technology. Not subject to copyright.
3. M.T. Postek and R.C. Tiberio, Proc. Ann. EMSA Meeting, 46(1988)198-199.
4. M.T. Postek, Scanning Microscopy 3(4),(1989) 1087-1099.
5. M.T. Postek et al., NIST J. Research, in press.

THE SEM IN PRESENT DAY SEMICONDUCTOR FABS

Marylyn Hoy Bennett

Semiconductor Process and Design Center, Texas Instruments Inc.,
P.O. Box 655012 MS 944, Dallas, TX 75265

Computers, cars, HDTV, and microwave ovens: what great modern conveniences! Why do these marvels of technology work the way they do? The Scanning Electron Microscope has a lot to do with it. For the last decade, the shrinking geometries of integrated circuits have necessitated the use of the Scanning Electron Microscope (SEM) for inspection and metrology.¹ The current device feature sizes in production are as small as $0.5\mu\text{m}$, and current feature sizes under development are $0.25\mu\text{m}$ or smaller. The semiconductor industry depends on the SEM to tell us if our processes, whether production or developmental, are correct. Neither leading edge fabs nor developmental fabs could function very well without the SEM.

The uses of the SEM are many and varied, both inside and outside the fab. Inside the fab, there are many inspection steps to be performed. Although the optical microscope is still a viable option for, and is still routinely used for, in-line wafer inspection, the SEM is indispensable for inspection (Fig. 1) of small geometries such as $0.35\mu\text{m}$ lines and spaces and $0.5\mu\text{m}$ contact holes. The resolution of the SEM is also required to perform measurements of features about $1.0\mu\text{m}$ and below (Fig. 2). Current automation features on either of these types of SEM's allow for multiuser function and high utilization in the fab.

Outside the fab, the SEM is used for process characterization, failure analysis, and elemental analysis.² The nature of this type of work lends itself to experienced, dedicated SEM users for optimal resolution and use of the tool. Main uses of the SEM are process characterization/verification by cross section (Fig. 3), failure analysis by strip-back process, and elemental analysis (EDS/WDS) for contamination (Fig. 4). Other techniques utilized are back-scattered electron imaging (BEI), electron channeling pattern (ECP), electron beam induced current (EBIC), and voltage contrast.

The SEM can only become more indispensable to the IC fab in the future, with new and improved techniques allowing for more non-destructive wafer inspections. Integration of SEM metrology with cluster lithography tools will most likely occur. Increased use of backscattered electron imaging for metrology and in-line inspection to reduce charging effects, and low voltage electron probe microanalysis (EPMA) for in-line inspection and elemental analysis will be utilized.

References

1. T.T.H. Fu et al, Proceedings SPIE. (1992)1673, 526.
2. M.H. Bennett-Lilley et al, Proceedings of EMSA. (1991), 896.

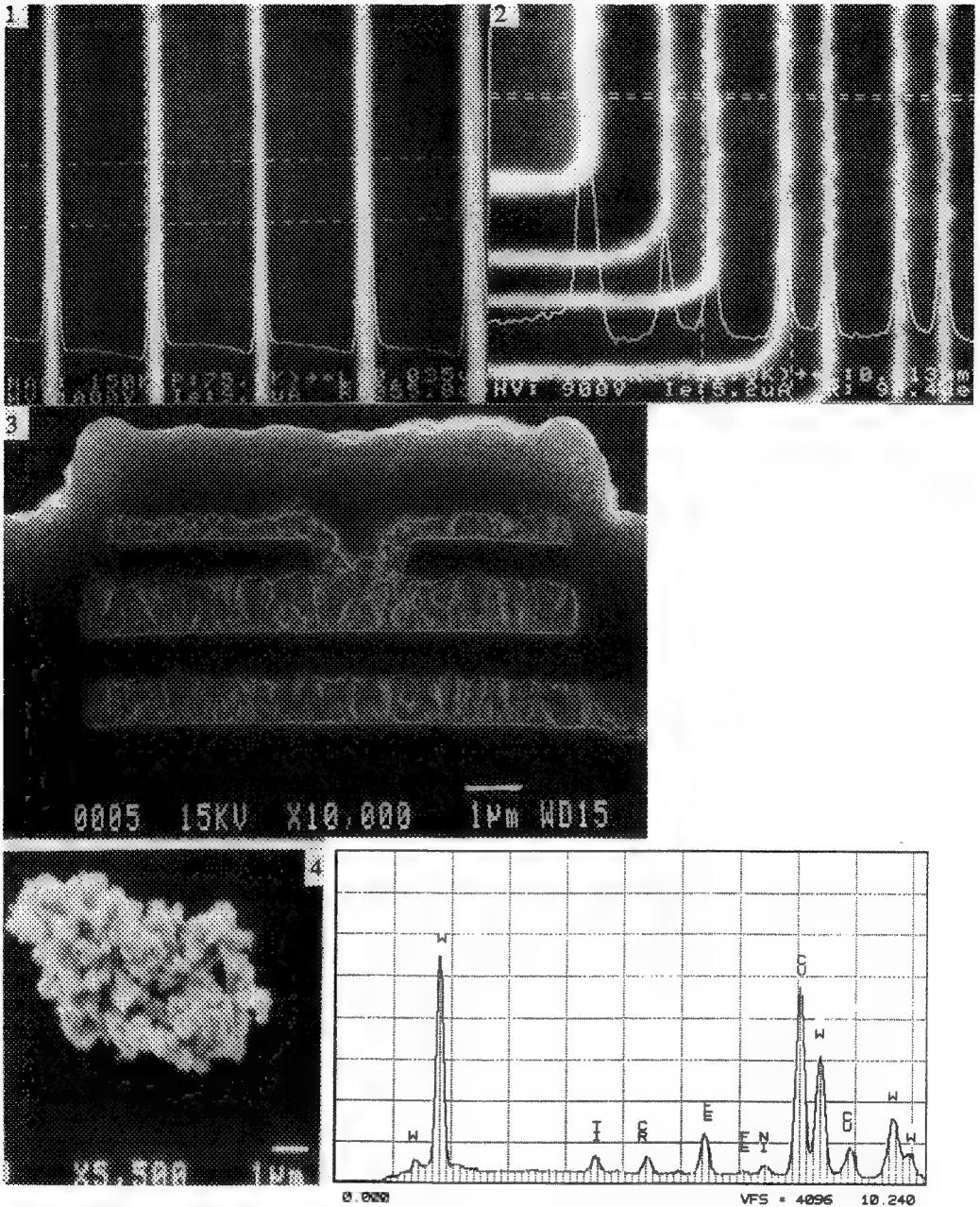


FIG. 1. High resolution micrograph of very small ($0.035\mu\text{m}$) resist lines and $0.2\mu\text{m}$ spaces on silicon substrate to check design rules.
 FIG. 2. Linewidth measurement of $0.613\mu\text{m}$ polysilicon line on silicon wafer.
 FIG. 3. Cross-sectional micrograph to characterize/verify processes.
 FIG. 4. Micrograph showing particle contamination from a metallization reactor, with accompanying EDS spectra.

APPROACHING AN *ABSOLUTE* WITH S E M METROLOGY

George H. McAfee

Analytical Support, Harris Semiconductor, 1700 Fostoria Rd., Findlay, Ohio 45840

The Scanning Electron Microscope remains one of the most universal tools in the semiconductor industry. While it gained prominence in the areas of inspection and analysis, it is also a very capable metrology tool. There is a wide selection of S.E.M.'s available that are dedicated to line width measuring; however, this article discusses film thickness measuring during cross-sectional S.E.M. analysis.

As with any metrology system, a process should begin with a certified and traceable measurement standard. N.I.S.T. SRM 484f was the standard employed for this experiment. A gauge and capability study was first performed on a Nanometrics CWIKSCAN II FE S.E.M.. Long range repeatability was calculated at 1.57%. Figures 1 and 2 show the micrograph and video signal data respectively from the N.I.S.T. standard. Note the cursor position and measurement value on figure 2. The 1.072 μ m value agrees very well with the certified value of 1.067 μ m.

- It is important to note that the aspect ratio on most CRT screens is not 1:1. Therefore, if any electronic manipulation of the image is required for cursor alignment, the system calibration must be performed at the same orientation where the measurements will be taken.

The film selected for this experiment was a standard aluminum (1% silicon) metallization film. Aluminum, by nature, is very malleable and therefore very difficult to cross-section. The sectioned edge is often distorted, making quantification nearly impossible. For this reason an encapsulating layer of silicon di-oxide was thermally deposited on top of the metallization layer. The sectioned edge was then exposed to a heated phosphoric acid solution that effectively recessed the aluminum such that a cavity was formed between the silicon substrate and the encapsulating oxide. This cavity was then measured for a near absolute metal thickness. This cavity is displayed in figure 3 with the video data shown in figure 4. The measured value of 8590Å is within 1.0% of the nominal 8500Å value.

Standard aluminum delineation is given by the following equation:



Note that only aluminum will be removed during this reaction. Both the substrate and the encapsulation will remain in tact. This allows the cavity to represent a near absolute metal thickness. The cavity must be positioned perpendicular to the electron beam for precise measurements. This is critical due to the trigonometric relationship among the beam, sectioned edge, and the measurement cursor.

Film thickness quantification with the S.E.M. provides an actual physical measurement at a relatively high magnification. This is an obvious advantage over non-destructive measurement techniques because of the few factors involved in the process. Ambient conditions can have a dramatic impact on the measurement accuracy of non-contact metrology tools. Therefore, the physical measurement provided by cross-sectional S.E.M. analysis is a superior approximation of the absolute film thickness.

References

1. G. McAfee and S. Dean, Improvements in S.E.M. Productivity...
American Physical Society, May, 1992.

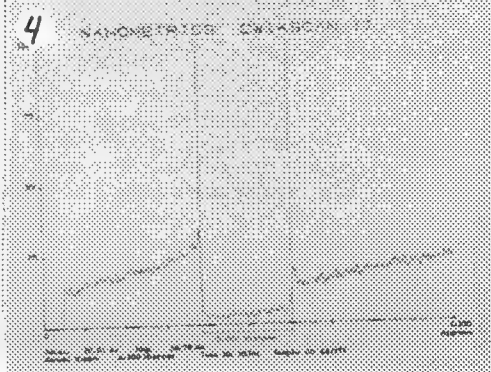
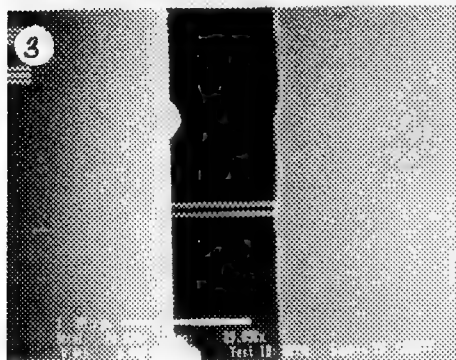
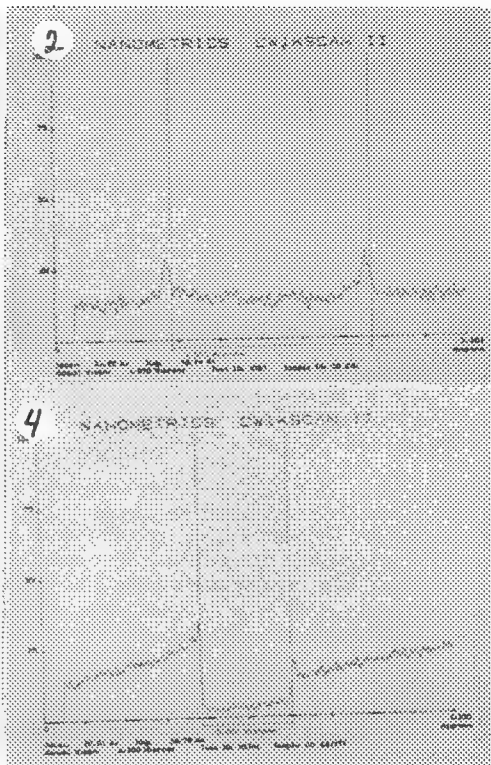
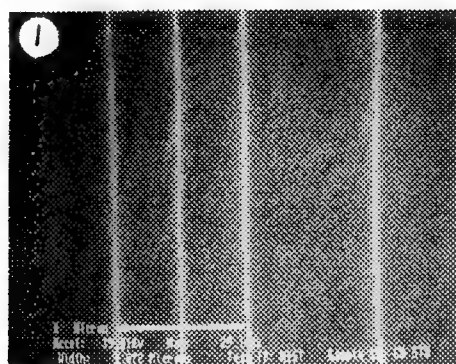


Figure 1: S.E.M. micrograph showing N.I.S.T. certified linewidths. The larger width is $1.067\mu\text{m}$. A leading edge pitch measurement was used for the experiment.

Figure 2: Video signal plot from the $1.067\mu\text{m}$ line set, showing actual cursor position during measurement.

Figure 3: S.E.M. micrograph showing etched cavity, with cursor position during measurement.

Figure 4: Video signal plot from the sectioned edge. The minimum signal is from the cavity area. Note the cursor width and position.

OBSERVATION OF SUPPORTED CATALYST PARTICLES BY HIGH-RESOLUTION SEM

Ming-Hui Yao, David J. Smith and Abhaya K. Datye*

Department of Physics and Center for Solid State Science, Arizona State University, Tempe, AZ 85287, USA

* Department of Chemical & Nuclear Engineering, University of New Mexico, Albuquerque, NM 87131, USA

Supported metal particle catalysts have found wide application in the chemical industry and for environmental control. Many microscopy techniques have been employed to study these catalysts. Although scanning electron microscopy (SEM) is not commonly used, its ability to provide surface topological information as well as the ease of sample preparation and observation are positive attractions for catalysis research. Due to limited SEM resolution in the past, as well as severe charging of the insulating catalyst supports, very few studies of catalysts using SEM appear to have been reported. Recent development of in-lens specimen immersion systems and cold field emission sources of high brightness have made it possible to image specimen surfaces with secondary electrons at subnanometer resolution[1]. Using a high resolution Hitachi S-5000 in-lens field emission SEM, we have studied Pt particles supported on TiO_2 and CeO_2 . The purpose of this study was to evaluate relative merits and demerits of high resolution SEM for catalysis research, in particular with respect to TEM and STEM techniques.

The SEM observations were performed at an accelerating voltage of 30kV, with a guaranteed resolution of 0.6 nm. Images were recorded at magnifications ranging from 100kX to 1000kX. Fig.1 shows a typical low magnification SE micrograph of the Pt/ TiO_2 catalyst. The supported Pt particles range from 0.8 nm to 14 nm in diameter while the TiO_2 supports range from 20 nm to 100 nm. The image contrast and profile clearly reveal topological information about the spherical TiO_2 supports in three dimensions. Fig.2 is a high resolution SEM micrograph initially recorded at 1000kX. Fig.3 and Fig.4 are pictures of the same sample taken, respectively, by TEM, and STEM with a high-angle annular dark field (HAADF) technique. Steps and ledges on the TiO_2 surfaces are clearly visible in Fig.2. These surface features are not seen at all in plan view using TEM and HAADF. It appears that larger Pt particles are more likely to be located in the vicinity of kinks on the TiO_2 support surfaces. In comparison with TEM and HAADF in STEM, high resolution SEM thus has a much stronger capability for providing surface topological information. This better knowledge of the surface topology of the catalyst support should provide better understanding of the factors responsible for particle nucleation and growth and any interaction between the particles and their supports.

High resolution SEM can also be used to study the size distribution of supported particles. In contrast to HAADF, the areal density of particles observed in the HRSEM image was about half of that in HAADF image (Fig.3), simply because only particles on the top surface of the support were recorded with the SE detector. In this respect, imaging by HRSEM could again be considered as an advantage over HAADF and TEM since, with the latter techniques, it is impossible to determine the side on which the supported particles are located. In SEM, the locations of the supported fine particles are uniquely determined. Moreover, particles can be imaged on catalyst supports of any thickness so that sample preparation and observation become much easier. It is no longer necessary to locate particles protruding over the edges of grid bars or carbon film as in TEM and STEM.

The major drawback of HRSEM for catalyst characterization is its lack of characteristic features such as lattice fringes which facilitate identification of metal crystallites in TEM. It also appears that the detectability of supported particles is likely to be relatively low when the support surface is rough or when the particles of oxide support particle are small (<20nm) or comparable to that of supported particle. Fig.5 and Fig.6 show a comparison of HR images of Pt/ CeO_2 taken from TEM and HRSEM. Small Pt particles can hardly be seen in Fig.6, whereas Pt particles of 1 nm are very clearly visible in Fig.5.

Reference

- [1] T. Nagatani, S. Saito, S. Sato and M. Yamada, Scanning Microsc. 1 (1987)901.
- [2] The electron microscopy was conducted at the Center for High Resolution Electron Microscopy, supported by NSF Grant DMR-9115680. The authors would like to thank Mr. Mikhail Reilly for assistance, and thank Mark Appleget and Hitachi Scientific Instrument for access to the Hitachi S-5000 FESEM.

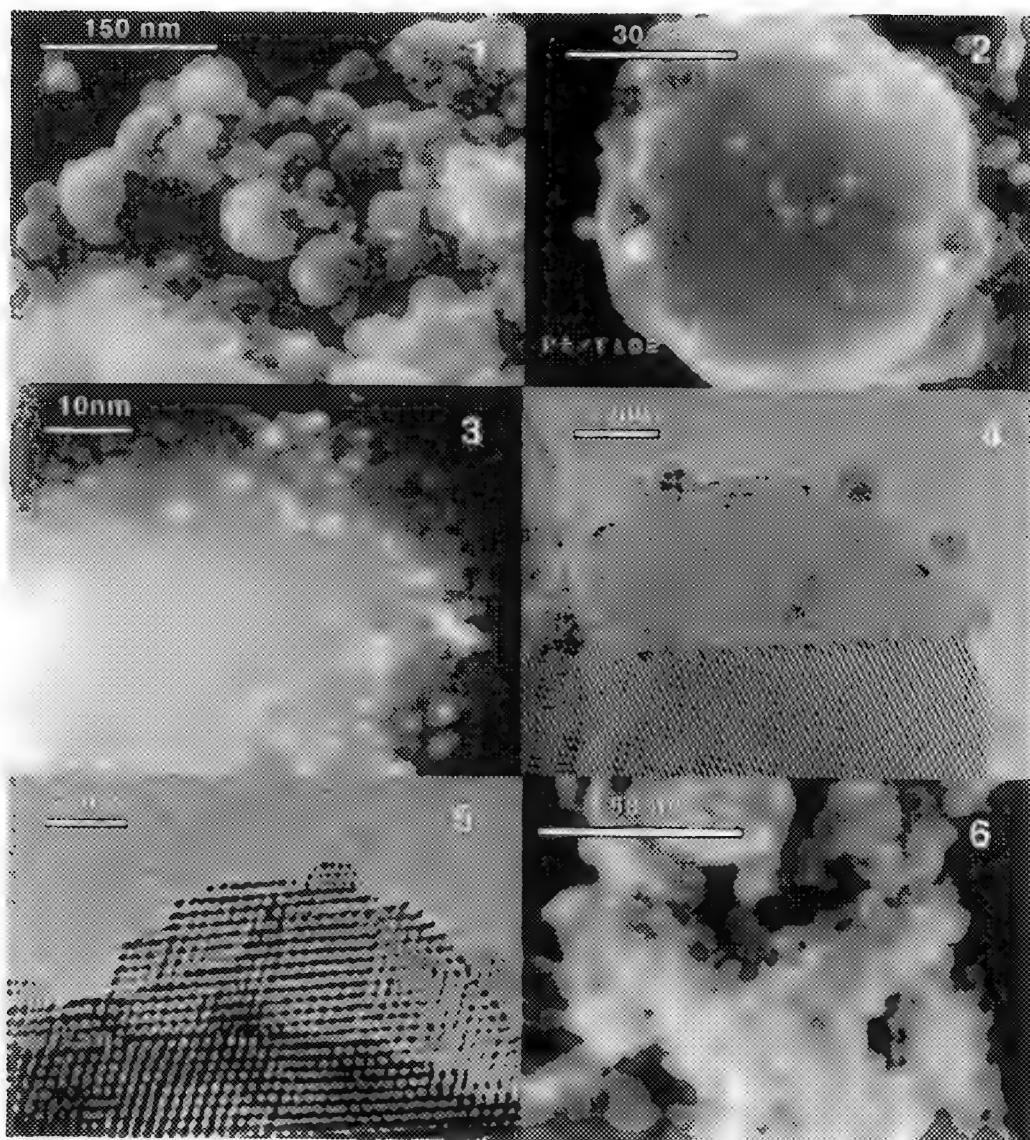


Fig.1. HRSEM image of Pt/TiO₂ recorded at 30kV and initial magnification of 180kX.
 Fig.2. HRSEM image of Pt/TiO₂ recorded at 30kV and initial magnification of 1000 kX.
 Fig.3. HAADF image of Pt/TiO₂ recorded on VG HB501 at 100kV and 1000kX.
 Fig.4. HRTEM micrograph of Pt/TiO₂ recorded by JEM-4000EX at 400kV and 1000kX.
 Fig.5. HRTEM image of Pt/CeO₂. Pt particles of 1 nm in size are clearly visible.
 Fig.6. HRSEM image of Pt/CeO₂ recorded at 700kX.

OBSERVATION OF A SUPPORTED METAL CATALYST IN AN ULTRA-HIGH-RESOLUTION FIELD-EMISSION SEM

J. Liu* and G. E. Spinnler**

* Center for Solid State Science, Arizona State University, Tempe, AZ 85287

** Shell Development Company, Westhollow Research Center, P. O. Box 1380, Houston, TX 77287

Zeolites loaded with noble-metal particles are interesting catalytic systems. The relative positions of small metal particles on and within the support structure may have significant consequences for catalytic activity. Small metal particles dispersed on model and commercial catalyst supports have been observed by using secondary and Auger electrons in a UHV STEM.¹ In this paper we further report preliminary results of observing a metal/zeolite catalyst in a commercial high-resolution field-emission SEM and investigate the contrast variations of SEM images with the change of incident beam energies.

Metal-loaded zeolite samples were ground to fine powders and were dispersed onto a thin holey carbon film coated on a copper grid. The samples were directly observed without being coated with conducting materials. Such coating would obscure fine-scale surface details and make imaging of small metal particles impossible. The experiments were performed in a field-emission Hitachi S-5000 SEM, operating from 0.5 to 30 kV. This microscope has a spatial resolution of 0.6 nm at 30 kV and 3.5 nm at 1 kV. Fig. 1a shows a typical SE micrograph of the metal/zeolite sample obtained at 30 kV. Fig. 1b shows a typical high-angle annular dark-field (HAADF) image of the same catalyst system obtained in a HB501 STEM. The HAADF image clearly reveals all the metal particles by atomic number contrast. The topography of the metal/zeolite sample, however, is clearly shown in the SE image. The binder materials on the surfaces of the zeolite particles are also revealed in the SE image. Furthermore, some of the metal particles ranging from 2 to 10 nm in diameter are clearly visible in the SE image with bright contrast, indicating that these particles are actually located on the surfaces of the zeolite support. The SE image intensity of a small metal particle increases with the size of that particle.² From many SE and HAADF images similar to the ones shown in Fig. 1, one can deduce information about the size distribution and dispersion of the small metal particles which are important parameters for catalyst characterization.

The resolution of SE images, the charging of insulating samples and the surface sensitivity of SE signals all depend on the primary beam voltages used.³ At low beam voltages the probe size is broadened due to chromatic aberration. Therefore the image resolution is definitely deteriorated at low voltages as compared with that at high voltages. The surface sensitivity of SE signals varies with the incident beam voltage. Figs. 2a, 2b and 2c show, respectively, low magnification SE images of metal/zeolite powders supported on a holey carbon film obtained at 1.5, 3 and 30 kV. Figs. 3a, 3b and 3c show the corresponding high magnification images of the framed area shown in Fig. 2a. At low magnifications the large-scale surface morphology of the zeolite powders is best represented in Fig. 2a. Fig. 2c, however, shows much finer surface details while Fig. 2b does not show much surface topography at all. At high magnifications the small metal particles and fine details of the binder materials as well as nano-scale surface morphology of the zeolite support are clearly visible at high voltages (Fig. 3c). At 1.5 kV (Fig. 3a) the surface morphology of the zeolite agglomerate is still revealed but finer details are not resolved. The larger metal particles are still visible in Fig. 3a with a weak bright contrast. By comparing these images one can conclude that the form of SE images of the same sample area changes with incident beam energy. The surface sensitivity of the collected SE signal is determined by the relative spatial distribution of type I and type II secondary electrons which depend on the incident beam energy. It should also be mentioned that the sample shows charging effect at low beam voltages. This charging up of the sample distorts the beam profile of low energy incident electrons which affects the image resolution and the image contrast. The contrast variations, the surface sensitivity and the charging effect at different beam voltages will be discussed.⁴

References

1. J. Liu and G. E. Spinnler, Proc. 49th Annu. Meeting of EMSA (1991) 502;
J. Liu et al., Surface Sci. 262 (1992) L111; Catal. Lett. 15 (1992) 133.
2. J. Liu et al., Proc. 50th Annu. Meeting of EMSA (1992) 1288.
3. D. C. Joy and J. B. Pawley, Ultramicroscopy 47 (1992) 80.
4. The authors are grateful to Mark Appleget and Hitachi Scientific Instruments for generously providing access to the Hitachi S-5000 FEG-SEM and to Dr. R. Roberts for assistance. This work was supported by Shell Development Company and made use of the ASU CHREM supported by NSF DMR-9115680.

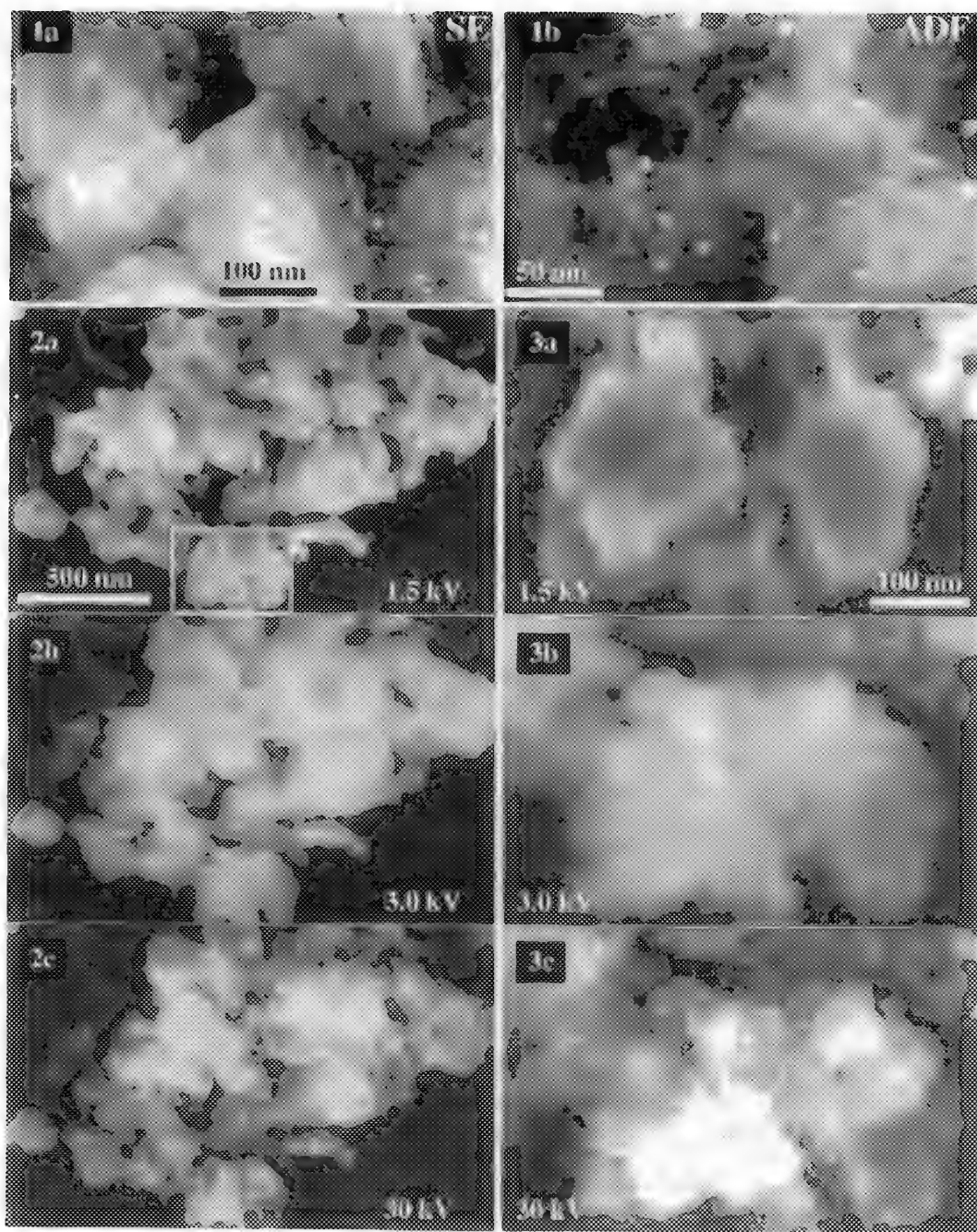


Fig.1--(a) SE image of metal/zeolite sample obtained at 30 kV and (b) HAADF image of same sample.
 Fig.2--Low magnification SE images of metal/zeolite sample at (a) 1.5 kV, (b) 3 kV and (c) 30 kV
 Fig.3--High magnification SE images of metal/zeolite sample at (a) 1.5 kV, (b) 3 kV and (c) 30 kV.

UNIVERSAL ESEM

G.D. Danilatos

ESEM Research Laboratory, 98 Brighton Boulevard, North Bondi (Sydney), NSW 2026, Australia

The environmental scanning electron microscope (ESEM) has evolved as the natural extension of the scanning electron microscope (SEM), both historically and technologically.¹ ESEM allows the introduction of a gaseous environment in the specimen chamber, whereas SEM operates in vacuum. One of the detection systems in ESEM, namely, the gaseous detection device (GDD) is based on the presence of gas as a detection medium.^{2,3} This might be interpreted as a necessary condition for the ESEM to remain operational and, hence, one might have to change instruments for operation at low or high vacuum. Initially, we may maintain the presence of a conventional secondary electron (E-T) detector in a "stand-by" position to switch on when the vacuum becomes satisfactory for its operation. However, the "rough" or "low vacuum" range of pressure may still be considered as inaccessible by both the GDD and the E-T detector, because the former has presumably very small gain and the latter still breaks down. However, it can be shown that a single instrument of ESEM can be made to work under all environmental conditions of operation, including the vacuum of an SEM. To this single instrument we refer as a *universal ESEM*.

A universal system of detectors can now be incorporated in ESEM so that the complete pressure range from high pressure to high vacuum can be used.⁴ A schematic of such a system is shown in Fig. 1. The GDD is integrated with solid scintillating materials together with an optimized gas dynamics system. An array of electrodes (grids and apertures) serve in the detection, separation and control of various signals. They are combined with highly efficient scintillating materials and/or light pipes. This system (drawn not to scale) should be incorporated at the lower part of an electron optics column. Thus, all main modes of detection can be represented. Secondary (SE) and backscattered (BSE) electron signals, cathodoluminescence (CL) and x-ray microanalysis can be practised at any pressure. In addition, a mass spectrometer can be interfaced for analysis of the gas flowing through PLA1. By directing the electron beam at the feature of interest, ESEM produces an ablation mass spectrometer with very high resolution and sensitivity, in an equivalent but much better system than that used with a laser beam. The system in Fig. 1 constitutes a powerful way to image and analyze virtually any specimen.

The parameter of gas pressure is considered as the independent variable which determines the limits (or range) of operation of all other variables (or parameters). Some of those other variables are the accelerating voltage, beam current, specimen positioning (distance and tilt), temperature and detection efficiency. They, in turn, determine a host of other variables such as beam spot, contrast and resolution, specimen stability, etc. Formally, we can state that

$$\text{Universal ESEM} \xrightarrow{p \rightarrow 0} \text{SEM}$$

The art of establishing the interrelationships and ultimate physical limits of operating parameters, as we vary the pressure of gas in the specimen chamber of the microscope, constitutes the science of

ESEM. Our understanding of the limits and relationships between various parameters, and the development of various apparatuses continually evolve.

The present state of the art in ESEM, with reference to its universal potential, will be reviewed. This includes the possibility of using all types of electron gun, low and high keV, with virtually any specimen. Those applications that exclusively require vacuum, rough vacuum, low pressure or high pressure can be carried out within a single instrument. An updated bibliography on ESEM can be found in a recent publication.⁵

References

- 1. G.D. Danilatos, Advances in Electronics and Electron Physics 71, Academic Press, 109-250 (1988).
- 2. G.D. Danilatos, Advances in Electronics and Electron Physics 78, Academic Press, 1-102 (1990).
- 3. G.D. Danilatos, Scanning Microscopy (Ed. Johari O.), Vol 4, No. 4, 799-823 (1990).
- 4. G.D. Danilatos, Scanning Microscopy (Ed. Johari O.), in press (1993) .
- 5. G.D. Danilatos, J. Miscrosc. Res. Technique, in press (1993).

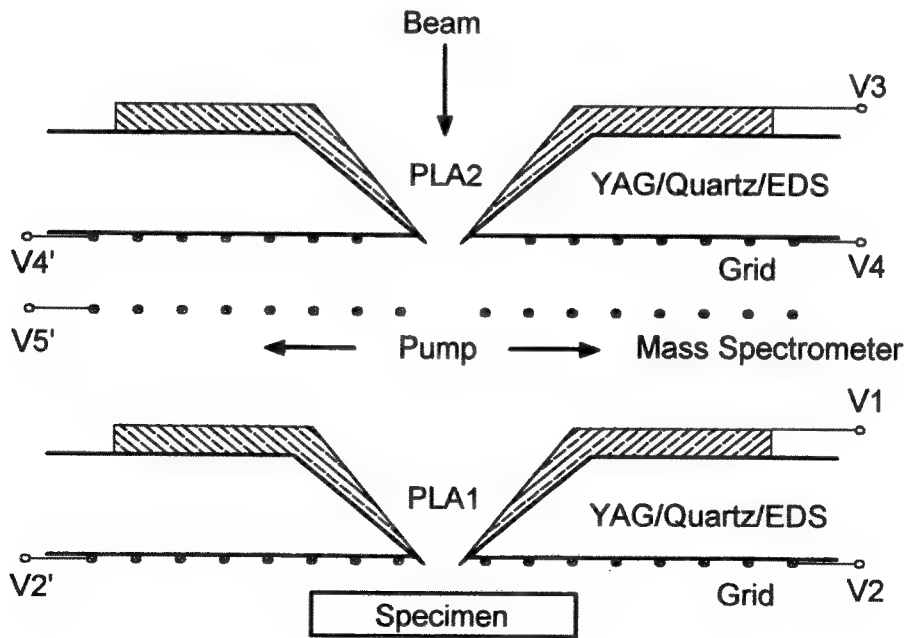


FIG. 1. Schematic of system of detectors for a universal ESEM. Variable voltages (V1, V2, V2', V3, V4, V4', V5) are applied to corresponding electrodes which, together with YAG and/or Quartz material, detect, separate and control SE, BSE and CL signals. An EDS detector can be placed either "below" of above pressure limiting aperture PLA1, depending on the design of electron optics column.

IN SITU HIGH-TEMPERATURE CORROSION WITH THE ENVIRONMENTAL SCANNING ELECTRON MICROSCOPE

L. A. Touryan and L. W. Hobbs

Department of Materials Science and Engineering
Massachusetts Institute of Technology
Cambridge, MA 02139

Electron microscopy has greatly aided in understanding the microstructure and morphological development of corrosion scales formed by high temperature oxidation and sulfidation of metals. However, this knowledge has been limited by the fact that the microstructure and morphological features could only be studied after corrosion had occurred. The recent development of the environmental scanning electron microscope (ESEM) permits actual in-situ observation of the evolution of high temperature corrosion scales at the scale-gas interface, allowing for a better understanding of the detailed mechanisms of scale growth. The objective of this study is to investigate the evolution of oxidation and sulfidation scales on various metals and alloys.

R.A. Rapp and associates¹ adapted a conventional SEM for oxidation studies by developing a stage that could be heated in excess of 1000 C. Because of the vacuum restrictions of the SEM, a gas pipe directed at the surface of the samples was utilized in order to increase the local oxygen partial pressure, and this resulted in low (0.2 Torr) but sufficient pressures for oxidation. Their investigations included studies of the continuous evolution of scales on pure Fe, Cu, Ni and Cr².

The Electroscan ESEM used in this investigation has a high temperature stage capable of reaching 1000 C, and can be used to examine specimens in gaseous environments with pressures up to 15 torr. Initial studies, which have been designed to test the capabilities and limitations of the instrument, have shown that scales can be grown in-situ on Cu, Ni and Fe powders. Figure 1a shows a NiO scale grown in an air environment in a furnace, and Figure 1b shows a similar scale grown under observation in the ESEM (also in air). Figures 1c and 1d present results for whiskers grown on Fe, both in a furnace and in-situ, respectively.

Further studies of the corrosion of flat polished Cu, Ni and Fe pure metals and alloys in various gaseous environments are in progress, and preliminary results are shown in Figures 1e and 1f. In addition, the development of convolutions in chromia scales will be studied. High temperature corrosion studies in the ESEM are essentially undocumented, and there is much to be learned from observing the actual morphological development of scales in this exciting new instrument³.

1. S.K.Verma, G.M.Raynaud, R.A.Rapp, Ox. of Metals 15(1981) 471.
2. R.A.Rapp, Met. Trans. B. 15B(1984) 195.
3. This research was supported by the National Science Foundation.

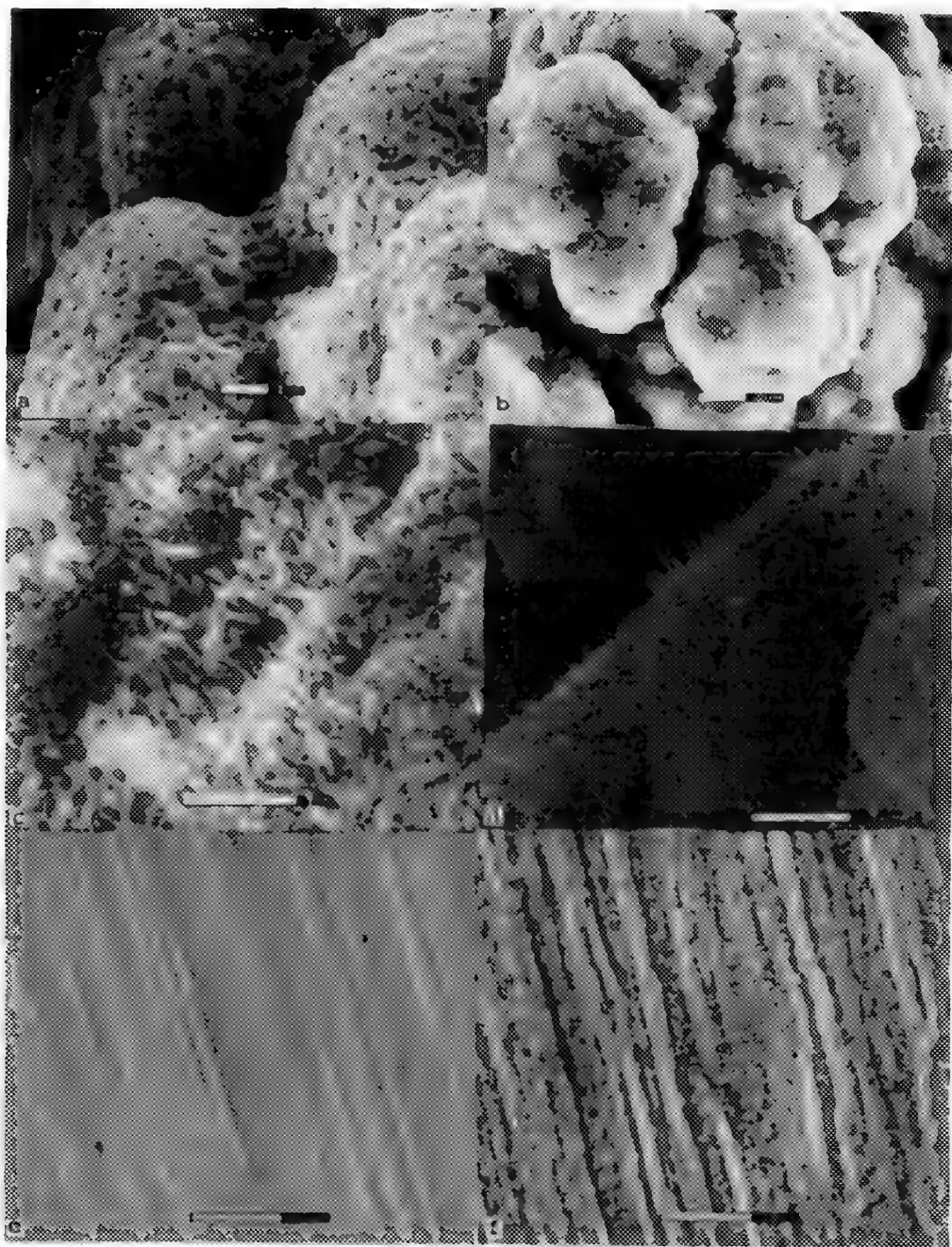


Figure 1. a. NiO scale grown on Ni powder in furnace; b. NiO scale grown in ESEM; c. FeO scale grown on Fe powder in furnace; d. FeO scale grown in ESEM; e. Ni foil before oxidation in ESEM; f. Oxide grown on Ni foil in ESEM. All oxides grown in air environment.

IMAGING PERISTOME MOVEMENT IN THE ENVIRONMENTAL SEM

J.C. Long, D.M.J. Mueller

Electron Microscopy Center, Dept. of Biology, Texas A&M University, College Station, Texas
77843-2257

The ElectroScan Environmental Scanning Electron Microscope is a powerful new tool in the study of spore dispersal mechanisms in bryophytes. The ESEM is similar in many ways to a conventional SEM, but with a few important differences. While the ESEM column remains at high vacuum (10^{-7} torr), the specimen chamber typically operates in a water vapor environment at low vacuum (1 to 20 torr). The secondary electron signal is generated by gaseous signal amplification and is collected by the Environmental Secondary Detector.

This new technology has significant implications regarding sample preparation and specimen requirements. First, there is no need to dry the sample, thus observations in the natural state are possible. Second, the water vapor dissipates charge build up, therefore a conductive coating is not necessary.

The ESEM lends itself directly to the understanding of spore dispersal in mosses, which involves the sensitivity of the peristome to changes in ambient moisture (hygroscopicity). Using conventional SEM techniques, it is not possible to view peristome movement directly, however, using the ESEM, the movements can be observed and recorded via video tape in real time.

In many mosses the peristome is an integral part of the spore release mechanism which regulates the release of spores from the capsule. Peristomes consist of the thickened portions of concentric rings of cell walls of contiguous layers of cells. These cell wall remains are responsive to changes in ambient moisture and exhibit movement with these hygroscopic changes in such a way as to effect the release of spores (facilitating the release in some mosses, hindering the too rapid release of spores in others).

Using a microinjector, water can be applied directly to the peristome, in order to stimulate these movements. In turn, these movements are recorded, in real time, on videotape with sufficient magnification and resolution to view, for the first time, the intricacies of movement as it reflects the variable composition and construction of the cell wall layers making up these structures.

References

1. D.M.J. Mueller and A.J. Neumann, *Advances in Bryology* (1988) 3:135-158
2. A.J. Neumann and D.M.J. Mueller, *Memoirs of the New York Botanical Garden* (1987) 45:71-86
3. This work was support by the Electron Microscopy Center and staff, Texas A&M University, College Station, Texas

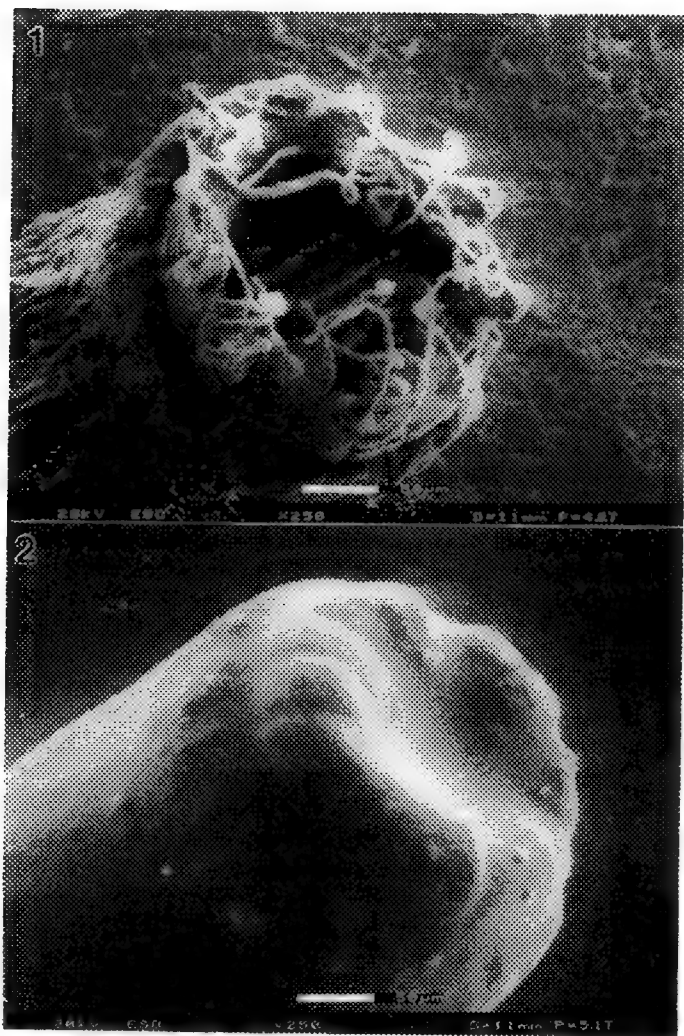


Figure 1. - Peristome under dry conditions.

Figure 2. - Peristome after wetting with drop of water.

EFFECTS OF A THIOL ANTIOXIDANT ON LEUCOCYTE ADHERENCE TO AORTIC ENDOTHELIUM DURING ATHEROGENESIS: QUANTITATIVE SEM ASSESSMENT

Keith A. Robinson^{1,2}, Russell M. Medford¹, R. Wayne Alexander¹

¹Division of Cardiology, Department of Medicine, Emory University School of Medicine; ²Integrated SEM & Microanalytical Facility, Yerkes Research Center of Emory University, Atlanta, Georgia, 30322

Dysfunction of arterial endothelial cells (EC) leading to adherence of circulating leucocytes (WBC) is a pivotal step in atherogenesis, preceding fatty streak formation. The attachment process is mediated at least in part by inducible endothelial-leucocyte adhesion molecules (ELAMs) on the EC surface which interact with WBC counterreceptors¹. Expression of VCAM-1, a monocyte selective adhesion molecule, by IL-1 and TNF stimulated vascular EC *in vitro* was shown to be inhibited by a thiol antioxidant (pyrrolidine dithiocarbamate, PDTC)². In this study we analyzed the effect of PDTC administered to cholesterol-fed rabbits, on WBC attachment to lesion-prone sites of the aorta using SEM morphometry.

New Zealand White (NZW) rabbits (2-3 kg) were fed 1% cholesterol for 3 d. The day before feeding, venous cannulas were introduced, and PDTC (20 mg/kg) or vehicle (0.1 M PBS) was given twice daily throughout. The animals were euthanatized at 4 d and the aortas pressure perfusion fixed with buffered 2.5% glutaraldehyde after rinse with Ringer's solution containing heparin (10 u/ml). The aortic arch and segments containing the 1st and 4th pairs of intercostal arteries were excised, postfixed with 1% OsO₄, and dehydrated in ethanol series. The samples were critical point dried from liquid CO₂ using thermoregulation and flow monitoring, opened longitudinally and attached to supports, and sputter coated with 20 nm Au/Pd alloy.

Specimens were staged below the lens in a DS-130 SEM (Topcon) equipped with a LaB₆ emitter operated at 10-15 kV. The dual-screen function at 10X differential magnification was used in conjunction with a grid over the low-magnification CRT, to count cells within 64 adjacent (8x8) fields 100 μ m² in size, in a modification of a previously described technique³. Areas sampled included a 1 mm² area of the ventral surface on the posterior half of the arch apex, as well as 4 mm² areas centered at each intercostal branch ostial region. Results were expressed as mean \pm SD of total WBC counted in all sampled areas from each animal, and compared using an unpaired 2-tailed t-test.

At 1000X magnification in rapid scan mode, WBC were easily distinguished, allowing efficient counting of the sampled areas (Figs. 1,2). Attached cells were round or in various stages of spreading (Fig. 2), and frequently displayed pseudopodial extensions penetrating the endothelium (Fig. 3). There were significantly fewer WBC adherent to the lesion-prone sites of PDTC-treated animals (n=9) compared to controls (n=6) given sham injections (145 \pm 68 vs. 379 \pm 267 total WBC, p=0.02, Fig. 4). However, blood cholesterol levels were similar (334 \pm 67 vs. 324 \pm 155 mg/dl, p=0.9).

The quantitative method used allows measurement of *in vivo* luminal EC-WBC adhesion phenomena. EC-WBC adhesion in this model of atherogenesis may be mediated in part by an oxidant-sensitive mechanism involving EC expression of VCAM-1 or other ELAMs, since it was inhibited by administration of the thiol antioxidant PDTC.

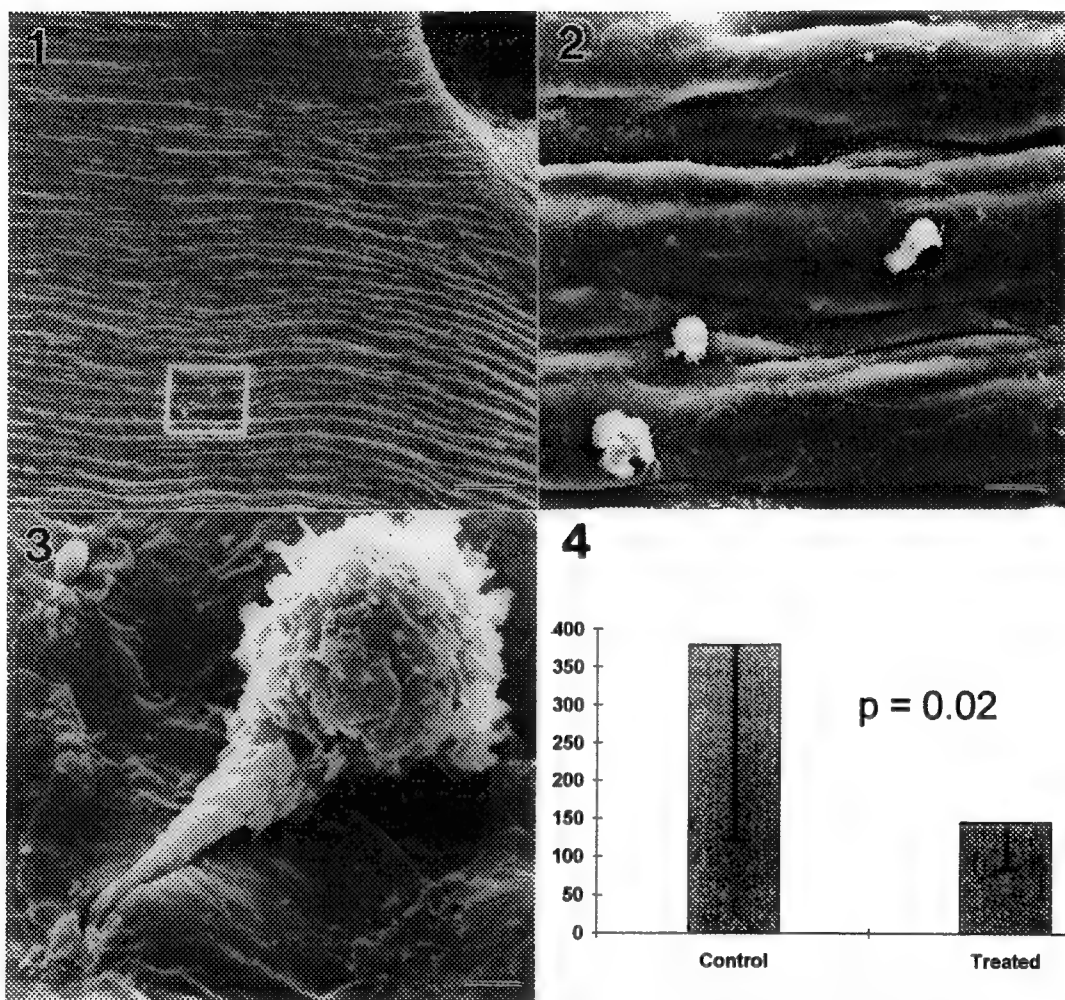


Fig. 1. Low-magnification SEM of the distal lateral circumcostal region, 1st left intercostal artery, from a PDTC-treated rabbit. Area in box is shown in following figure. Bar=100 μ m.
 Fig. 2. Area in Fig. 1. Three variably spread WBC are observed. Bar=10 μ m.
 Fig. 3. Adherent WBC with pseudopod extended to an EC junctional area. Bar=2 μ m.
 Fig. 4. Effect of PDTC on total WBC adherence to lesion-prone sites in aortas of cholesterol-fed rabbits, measured using quantitative SEM.

References

1. M.I. Cybulsky and M.A. Gimbrone, Science (1991) 251, 788.
2. N. Marui et al. Proc. VII Int. Symp. Biol. Vasc. Cell. (1992), 106.
3. M. Richardson et al. J Ultrastruct Res (1985) 91, 159.
4. The authors thank Robert Apkarian for technical advice. This work was supported in part by NIH grants RR-00165 from the National Center for Research Resources to the Yerkes Research Center, and RO1 HL48667(RWA&RMM). RMM is an established investigator of the American Heart Association.

OBSERVATION OF *CORYNEBACTERIUM* SPECIES USING SCANNING ELECTRON MICROSCOPY

Toya S. McWilliams*, Ernest C. Hammond**, and Marlene B. Luzarraga*

*Division of Comparative Medicine, Johns Hopkins University School of Medicine, 720 Rutland Avenue, Baltimore, MD 21205

**Department of Physics, Morgan State University, Hillen Road and Cold Spring Lane, Baltimore, MD 21239

Bacteria of the genus *Corynebacterium* are considered part of the bacterial flora of skin and mucosa. Even *C. diphtheriae*, a long recognized pathogen, may be isolated from the throat of healthy individuals. Recent evidence indicates that other *Corynebacteria* are associated with opportunistic conjunctival infections in aging laboratory mice.²

Our goal of using scanning electron microscopy was to expand previous studies and to observe the association of the bacteria with the conjunctival surface of aged mice. To accomplish this, we needed a point of reference for identification of the corynebacteria which were frequently present in the company of other bacteria. We studied cultures of known corynebacteria of ocular origin during the exponential growth phase. These cultures contained pleomorphic cells that were round, ovoid and rod shaped, clustered together and surrounded by a biofilm. Several of the cylindrical rods appeared as V-shaped pairs, classic features of the genus *Corynebacterium*. The V-shape arrangement is accomplished by a snapping postfission movement. These pairs further separate when postfission is completed yielding two progeny cells that are round to ovoid resembling those seen in the our colonies.¹

These ultrastructural features will serve as identifying characteristics of the bacteria when studying the interaction of the corynebacteria with the colonized host tissue.

References

1. P.E. Kolenbrander and R.J. Hohman, Journal of Bacteriology, (1977)130,1345
2. T.S. McWilliams, Laboratory Animal Science, publication in press
3. This study was supported by PHS grants RR07002 and RR00130 from the National Institutes of Health.

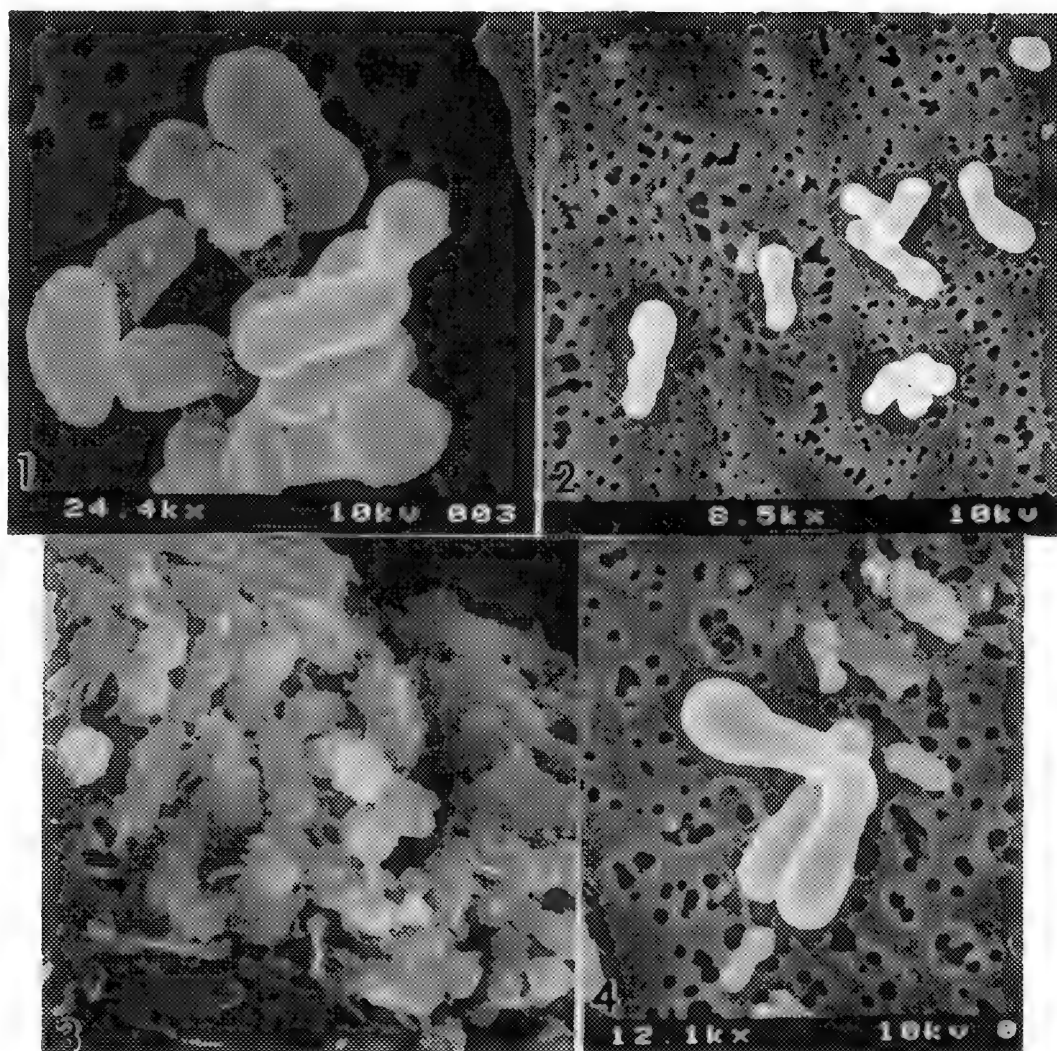


Figure 1. Rod-shaped cells of the *Corynebacterium* spp. beginning to elongate.

Figure 2. Various stages of growth of the *Corynebacterium* spp with elongation occurring and asymmetric cellular division.

Figure 3. Colony of the *Corynebacteria* surrounded by a biofilm. 5,000X

Figure 4. V-shaped cell pairs prior to separation.

THE APPLICATION OF TRANSMISSION ELECTRON MICROSCOPY TO SEMICONDUCTOR DEVICE PROBLEMS

Brian Cunningham and J. Daniel Mis

IBM East Fishkill, Route 52, Hopewell Junction, NY 12533

In the last 5-10 years there has been a large increase in the application of TEM to semiconductor device problems. This increase is due to several factors. Higher density chips and decreasing device dimensions have led to structural components which are frequently in the nanometer range. The ease with which present day microscopes can measure nanometer dimensions along with the advances in specimen preparation techniques now make the TEM invaluable as a tool for routine constructional analysis. As device dimensions shrink, the structure and composition of thin interfacial layers becomes increasingly important to device performance. In fact, in some cases, such as the emitter polysilicon to single crystal interface in bipolar transistors, the interface can dominate device parametrics such as current gain and emitter resistance. The ability to examine these interfaces in actual devices is therefore extremely important, and TEM is again proving to be uniquely suited to this task. Another important factor to consider when reducing device dimensions is that the properties of large area semiconductor structures can differ from those of sub-micron structures. This *dimensional effect* occurs frequently in silicide formation, where the formation of silicides in small contacts and on narrow lines can differ from silicide formation on large area structures. Whereas Rutherford Backscattering Spectroscopy, Auger spectroscopy and ion mass spectroscopy can be used to study thin film reactions in *blanket* films, these techniques lack the necessary spatial resolution to examine the structure of thin films in the small contacts encountered in many of today's semiconductor devices.

The value and uniqueness of TEM in the constructional analysis of semiconductor devices can be best shown in the examination of the thin dielectric films used for gate oxides in FET technologies and for trench liners in storage capacitors.^{1,2} Figure 1 shows a thin gate oxide. The thickness of the oxide can be easily, and accurately, determined from the silicon lattice fringe spacing. The geometry of the oxide at the gate edges can also be examined.

Figure 2 shows the emitter contact region of a typical polysilicon emitter bipolar transistor. It has been shown that reducing the emitter size below 1 micron has a significant effect on the electrical characteristics of the devices. Energy dispersive spectroscopy has shown that this *small emitter effect* is due to a lower arsenic concentration in the emitter polysilicon of small devices compared to large devices processed on the same chip.³ Since the effect is only observed in sub-micron devices, it is extremely difficult to detect by the normal spectroscopic techniques used to determine dopant concentrations.

Silicides are often used on the gate contacts of FETs to lower the series resistance. Unfortunately, silicide formation can also degrade the electrical properties of the gate oxide. Figure 3 shows a reaction between a TiSi_2 layer and a thin gate oxide which resulted in degraded breakdown voltage. A similar analysis of CoSi_2 layers showed no reaction with the oxide and no degradation of the breakdown voltage.

The above examples are meant to show the variety of applications to which the TEM is suited and are by no means meant to be exhaustive. No discussion on the application of TEM to semiconductor devices would be complete however without mention of one more field of study. For many years now the TEM has been used to examine defects, primarily dislocations, generated during device processing.⁴ Dislocations have been in the past, and will continue to be in the future, one of the major yield detractors in semiconductor device manufacturing. Device engineers appear to have the never-ending ability to devise new processes for generating dislocations. An example of such

a process is that of overlapping an ion implant with a stress field from a trench isolation. Neither process on its own generated dislocations but the combination produced the structure shown in Figure 4.⁵

The applications of TEM to semiconductor device problems will continue to grow not only as device geometries shrink, but also as advances are made in the design and development of microscopes such as the field emission TEM. The small probe analytical capabilities of the FETEM should prove to be invaluable to studies of semiconductor structures and devices.

References

1. H. Oppolzer et al., *Inst. Phys. Conf. Ser.* 87 (1987) p.433.
2. M. Song et al., *J. Electron. Microsc* 41 (1992) p.337.
3. B. Cunningham et al., *J. Appl. Phys.* 70 (1991) p.5318.
4. B.O. Kolbesen and H. Strunk, *Inst. Phys. Conf. Ser.* 57 (1981) p.21.
5. P.M. Fahey et al., *IBM J. Res. Develop.* 36 (1992) p.158.

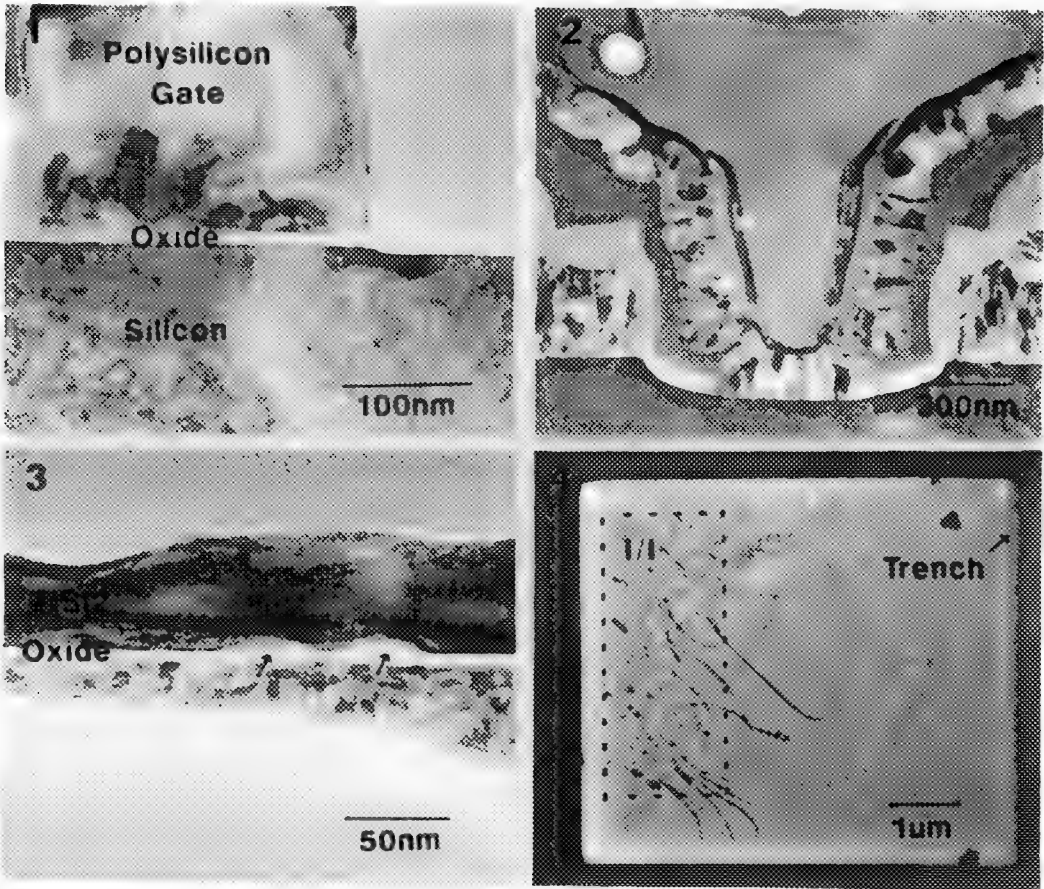


Figure 1. Cross-sectional micrograph of thin gate oxide.
Figure 2. Typical polysilicon emitter bipolar transistor.
Figure 3. Reaction of TiSi₂ film with gate oxide.
Figure 4. Dislocations generated by the interaction of trench stresses and ion implantation.

ELECTRON MICROSCOPY OF DEFECTS IN SILICON-ON-INSULATOR STRUCTURES FORMED BY SELECTIVE EPITAXIAL GROWTH

Z. S. H. Weng-Sieh*, J. C. Lou**^, W. G. Oldham**, and R. Gronsky*

* Department of Materials Science & Mineral Engineering, University of California Berkeley, and the National Center for Electron Microscopy, Lawrence Berkeley Laboratory, Berkeley, CA.

** Department of Electrical Engineering & Computer Science, University of California Berkeley, Berkeley, CA. ^ present address: National Jiao-Tung University, Dept. EEIE, Hschien, Taiwan.

In the interest of obtaining increased integrated circuit device density, a relatively new technology known as selective epitaxial growth (SEG) of silicon is being explored, especially for improved isolation of devices including possible three dimensional (vertical) integration. This technology involves the deposition and selective nucleation and growth of silicon from the vapor phase, seeded by the silicon substrate. The process is "selective" because nucleation and growth occurs on the silicon substrate but is prohibited on the oxide. The epitaxial silicon proceeds to grow upward and laterally over the oxide.

Silicon deposition was performed in a horizontal hot-walled low pressure chemical vapor deposition (LPCVD) reactor. A dry thermal oxide was grown on the substrates, patterned, and etched to create seed windows. A 900 °C prebake was performed at a pressure of 6 torr in a hydrogen ambient for a period of 15 minutes, with in some cases, a small concentration (approximately 0.025%) of dichlorosilane (DCS) gas, and deposition was performed at 850 °C through the decomposition of DCS gas:
 $\text{SiH}_2\text{Cl}_2 \rightarrow \text{Si(s)} + 2\text{HCl(g)}$.

Electron microscopy was performed to evaluate the integrity of these silicon-on-insulator structures. For oxides with sidewalls orientated along the <110> directions, twinned regions, propagating from the sidewall to the surface of the epitaxial film were observed, and an interesting region of one such twin band is shown in figure 1. For oxides with <100> sidewalls, no twins were formed.

The quality of the homoepitaxial interface is dependent upon the removal of the native oxide and other contaminants prior to epitaxial growth.¹ Without proper removal, inclusions, such as the one displayed in figure 2, are found along the homoepitaxial interface, causing the formation of dislocations within the epitaxial film. With partial removal of the native oxide and contaminants, dislocations loops, not inclusions, are formed along the interface. In our LPCVD system, the removal of the native oxide occurs by the addition of dichlorosilane gas which decreases the partial pressure of oxygen and water vapor in the furnace, thereby promoting the decomposition of the oxide through the formation of volatile SiO(g):
 $\text{Si(s)} + \text{SiO}_2\text{(s)} \rightarrow 2\text{SiO(g)}$.

Even with a 'perfect' homoepitaxial interface, near the oxide shape, at the region of the bottom oxide corner, various defects such as {311} defects, vacancy-type stacking fault tetrahedra, and dislocations, are observed, as shown in figures 3 and 4. These defects at the region of the bottom oxide corner are believed to be caused by a combination of a high concentration of silicon interstitials² as well as strain, induced by the differential contraction of the thermal oxide and the surrounding silicon substrate upon cooling from the growth temperature to room temperature.³

1. Z. S. Weng et. al., Mat. Res. Soc. Symp. Proc. Vol. 238 (1992) 707.

2. A. Bourret, Inst. Phys. Conf. Ser. 87 (1987) 39.

3. S. M. Hu, J. Appl. Phys., 67 (1990) 1092.

4. This work was supported by Cypress Semiconductor and National Semiconductor as part of the California MICRO Program and by the Director, Office of Basic Energy Sciences, Materials Science Division of the U.S. Department of Energy under contract number DEAC0376SF00098. The assistance of the staff and access to the facilities of the National Center for Electron Microscopy is gratefully acknowledged.

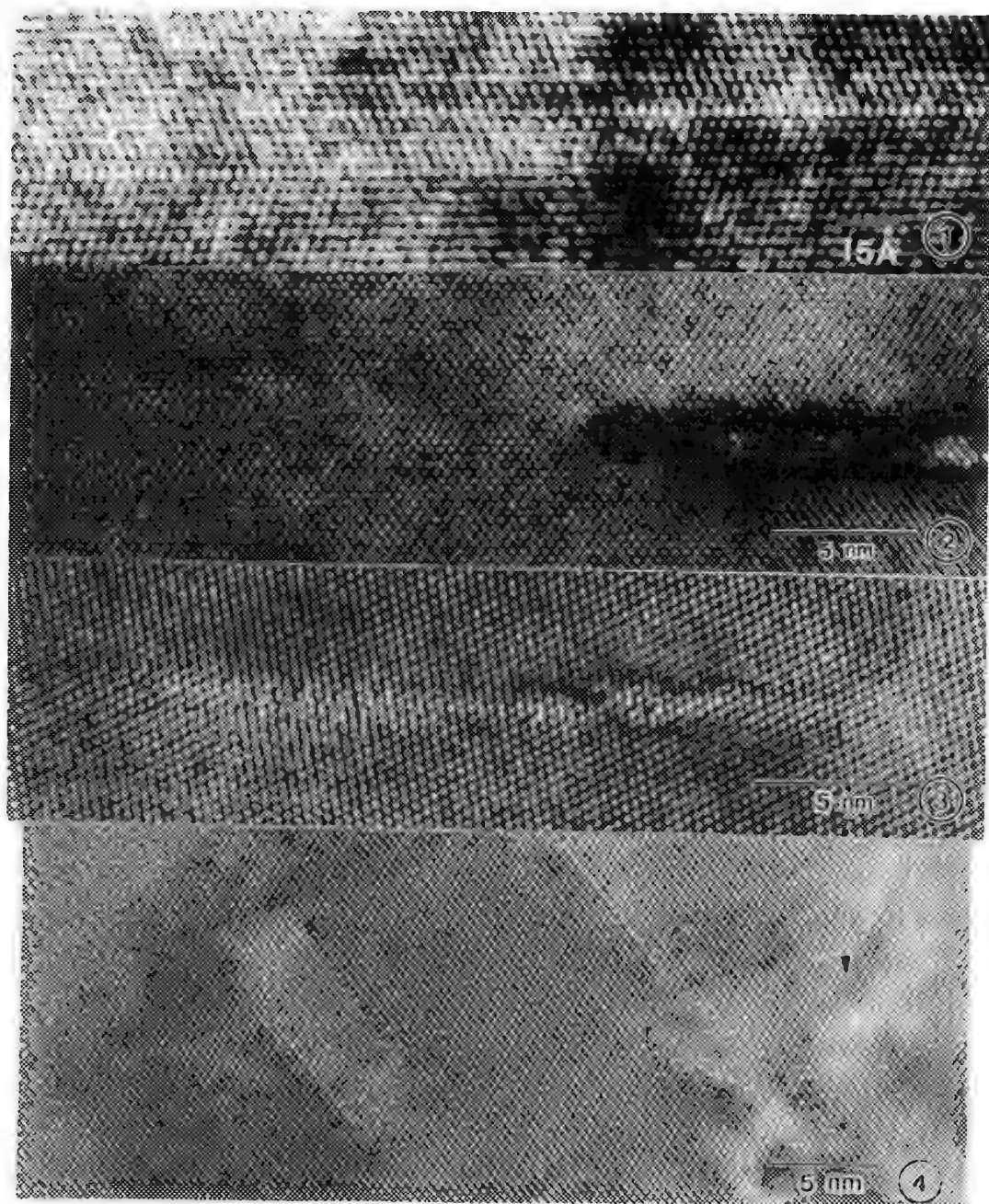


Figure 1- Multiply stepped twin boundary found in the epitaxial film near an oxide with $\langle 110 \rangle$ sidewalls.
 Figure 2- Ellipsoidal inclusion along the homoepitaxial interface.
 Figure 3- $\{311\}$ defect found at the bottom oxide corner region.
 Figure 4- Other defects found at the bottom oxide corner region: SiOx precipitate, intrinsic (vacancy-type) stacking fault tetrahedron, and extrinsic stacking fault.

CHARACTERIZATION OF Al/GaAs SCHOTTKY BARRIERS WITH THIN Si INTERFACIAL LAYERS

M.W. Bench,* T.J. Miller,** M.I. Nathan,** and C.B. Carter*

*Department of Chemical Engineering and Materials Science and **Department of Electrical Engineering, University of Minnesota, Minneapolis, MN 55455

It has been shown in previous reports that barrier height variations can be achieved in GaAs Schottky diodes grown using molecular beam epitaxy by utilizing a thin epitaxial Si layer (a few monolayers) between the GaAs and the Al contact.^{1,2} The effective barrier height was found to be dependent on the thickness and growth conditions of the Si layer. However, there has remained a question as to the exact nature of the interfacial Si layer. In the present investigation, samples with different Si layer thicknesses (no Si, 6 Å Si, and 20 Å Si, as determined *in situ* during growth using reflection high energy electron diffraction (RHEED)) were characterized using transmission electron microscopy (TEM) to determine the nature of the Si layers. In the present study, it was also found that the presence of the interfacial Si layers affected the growth orientation and morphology of the Al layers.

The layer structures investigated were grown using molecular beam epitaxy in a system described elsewhere.² The structures were fabricated on GaAs substrates by growing an initial GaAs layer at 590°C, followed by growing the Si layers at 400°C, and finally the Al layers were grown after cooling to less than 100°C (see ref. 2 for a detailed description of the growth conditions). Samples for TEM examination were made using standard cross-section preparation techniques. The microscopy was performed in a Philips CM30 operating at 300 kV.

The determination of the nature of a thin interfacial layer between two dissimilar layers can prove difficult. Possible methods of measuring the thickness of the Si interfacial layer are now considered. Imaging in dark-field using a GaAs superlattice reflection, a technique that would be commonly used to image a Si layer buried in the GaAs, is not possible in this case since the Si is at the GaAs surface. However, due to the different extinction distances characteristic of each material, using a reflection present in both the Si and GaAs can also produce different intensities in each layer. As an example, Figure 1 shows a $g=400$ dark-field image where the Si layer is brighter than the other layers. The Al layer in this case is polycrystalline with at least two growth orientations ($(200)_{\text{Al}} // (400)_{\text{GaAs}}$, $[200]_{\text{Al}} // [022]_{\text{GaAs}}$ and $(220)_{\text{Al}} // (400)_{\text{GaAs}}$, $[220]_{\text{Al}} // [022]_{\text{GaAs}}$) as compared to a continuous single-crystal film ($(220)_{\text{Al}} // (400)_{\text{GaAs}}$, $[220]_{\text{Al}} // [022]_{\text{GaAs}}$) that was found in the absence of a Si layer. When the Si interfacial layer thickness was increased to 20 Å, the Al layer was also polycrystalline, but had no obvious preferential orientation relationship with the substrate. Again considering the contrast in Figure 1, the width of the bright contrast region is 10-15 Å. This dimension is considerably greater than the 6 Å expected based on the RHEED measurements performed during growth. A possible reason for this difference is that the projected width of the Si layer is wider than the actual layer width when the sample is tilted into the $g=400$ Bragg condition. With the microscope operating at 300 kV, the sample tilt required to orient the sample will increase the projected width of the layer by 3.5 Å for a 1000 Å thick foil, and the foil was at least this thick for the image in Figure 1. If this is the cause of the difference, it should be possible to eliminate this effect if an image can be formed with the sample oriented so that the interface is parallel to the electron beam direction. An image of this nature is shown in Figure 2. In this figure the image is formed using the direct beam with the sample tilted into the planar symmetric condition (i.e. parallel to the interface plane) along the $[400]$ Kikuchi band a few degrees away from the $[110]$ zone axis. As can be seen, there is a thin bright line at the GaAs/Si/Al interface that is 6-7 Å wide. This measured thickness agrees very well with that determined by RHEED. In order to confirm that this contrast at the interface is due to the Si layer and is not an imaging artifact, similar images were formed using a sample with an expected 20 Å Si layer and one with no Si at the interface. Figure 3 shows an image formed in the 20 Å Si sample under the same conditions used for Figure 2. The bright band in this case measures 20 Å. In the sample with no Si there was not a bright band at the interface. Thus, images formed in the planar symmetric orientation demonstrate that thin continuous Si layers are present at the expected thicknesses. Details of the orientation relationships of the Al layers will be presented.³

1. J.C. Costa et al., Appl. Phys. Lett. 58 (1991) 382.
2. J.C. Costa, T.J. Miller, F. Williamson, and M.I. Nathan, J. Appl. Phys. 70 (1991) 2173.
3. Research supported by the University of Minnesota Center for Interfacial Engineering (mwb and cbc) and NSF grant DMR-9116436 (tjm and min)

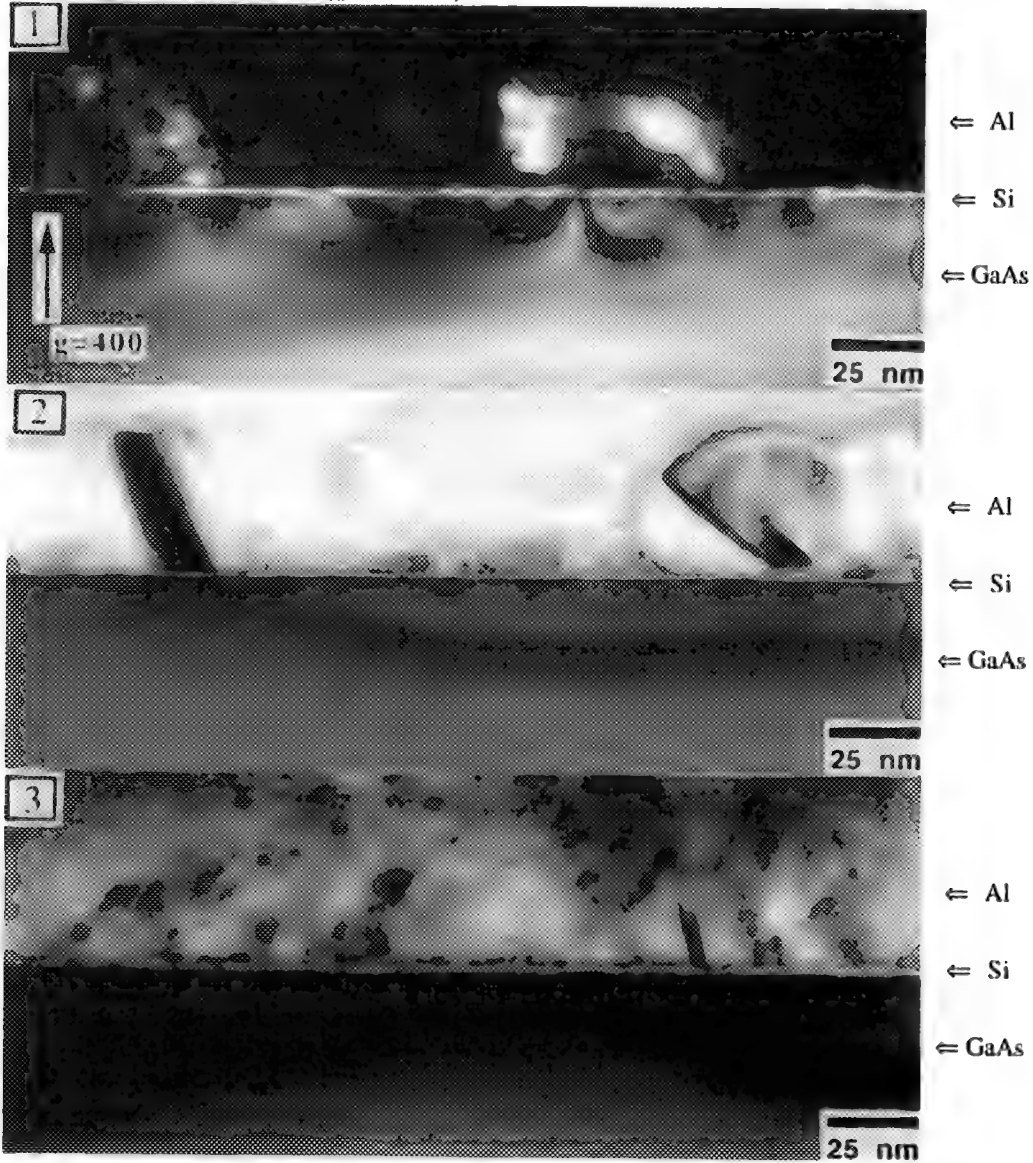


Figure 1. Dark-field image formed with $g=400$ (in GaAs) of an Al/Si/GaAs layered sample with an expected Si layer thickness of 6 Å. The measured thickness of the bright band is 10-15 Å.
 Figure 2. Bright-field image of the sample in Figure 1 formed with the beam parallel to the interface. The bright band measures 6-7 Å.
 Figure 3. Bright-field image formed under the same conditions as Figure 2 of an Al/Si/Ga sample with an expected Si thickness of 20 Å. The bright band measures 20 Å.

Z-CONTRAST IMAGING OF AN ORDERED INTERFACE STRUCTURE IN THE Si/CoSi₂/Si SYSTEM

M. F. Chisholm, D. E. Jesson, S. J. Pennycook, and S. Mantl*

Solid State Division, Oak Ridge National Laboratory, Oak Ridge, TN 37831-6030

*Institut für Schicht- und Ionentechnik, Forschungszentrum Jülich, Germany

We show the atomic structure of buried CoSi₂/Si(001) boundaries involves a 2×1 ordering of the interfacial Co atoms. The ability to directly image and interpret this unforeseen structure is possible through the Z-contrast technique, and presents a new level of insight into the important and controversial relationship between the atomic structure and electronic properties, such as the energy barrier for electron transport across metal-semiconductor interfaces.¹

The buried CoSi₂ layer was produced by implanting Co⁺ ions (200 keV, 2×10^{17} ions/cm²) in a Si(001) substrate heated to 350°C. The substrate was capped with 200 nm of SiO₂ and then given a two-step anneal in high purity argon (750°C for 30 s + 1150°C for 10 s). This treatment results in a continuous buried CoSi₂ layer ~70 nm thick, ~90 nm below the substrate surface. The layer and the substrate are oriented such that the cubic CaF₂ unit cell of CoSi₂ is aligned parallel to the cubic unit cell of Si. Both the top and bottom interfaces were found to consist of {001} terraces separated by an occasional {111} faceted step.

The atomic structure of the CoSi₂/Si(001) interface was characterized in cross section by high-resolution Z-contrast imaging using a VG Microscopes HB501 UX scanning transmission electron microscope. In this imaging mode, each atomic column can be imaged independently with high compositional sensitivity.² Figure 1a, a Z-contrast image of the CoSi₂/Si(001) interface, reveals the 2×1 ordered structure of the boundary. In this <110> projection, the ordering is clearly seen to involve the interfacial Co atoms doubling the periodicity along the [110] direction. This is a structure which has not been previously considered. The right side of Fig. 1b is a 1×2 domain of the same structure seen in Fig. 1a and in the left hand portion of Fig. 1b. The domains are related by a 90° rotation about the [001] direction and are separated by a dislocation with $\mathbf{b} = a/4\langle 111 \rangle$. This interface structure is sensitive to 100 keV electron irradiation. The gradual destruction of the 2×1 order may explain the many structures reported for this interface.³ Figure 2 is the atomic structure derived from the Z-contrast images. In this first order model, we have assumed the tetrahedral coordination and bond lengths of Si are maintained, even though the images reveal an expansion of the {001} spacing at the interface. The interfacial Co atoms necessarily have reduced coordination in this model, but the 2×1 ordering reduces the number of 6-fold coordinated Co when compared with a flat 1×1 interface. The model suggests the {001} interface breaks down to atomic sized {111} facets. Another possible model is produced by rotating CoSi₂ relative to the Si lattice 90° about the {001} direction. In this model, the Co maintains 8-fold coordination everywhere, but the Si in the interfacial region is either overbonded or has dangling bonds.

Simulation of the Z-contrast image (Fig. 1c) based on the model structure reproduces the essential features of the experimental images but is inconsistent with the Si dimer models. Phase contrast simulations based on the new model structure (Fig. 3) do produce images consistent with the published observations of interface reconstruction in both the NiSi₂/Si(001)⁴ and CoSi₂/Si(001)^{5,6} systems.⁷

References

1. For a useful summary, see J. Vrijmoeth et al., *Phys. Rev. B* **42** (1990) 9598.
2. S. J. Pennycook and D. E. Jesson, *Acta. Metall. Mater.* **40** (1992) S149.
3. For review, see S. Mantl, *Materials Science Reports* **8** (1992) 71.
4. J. L. Batstone et al., *Proc. EMSA* **47** (1989) 460.
5. C. W. T. Bulle-Lieuma et al., *Proceedings of the 12th International Congress for Electron Microscopy* (San Francisco Press, San Francisco, 1990) 344.

6. D. Loretto et al., *Phys. Rev. Lett.* **63** (1989) 298.
 7. This research was sponsored by the Division of Materials Sciences, U.S. Department of Energy, under contract DE-AC05-84OR21400 with Martin Marietta Energy Systems, Inc.

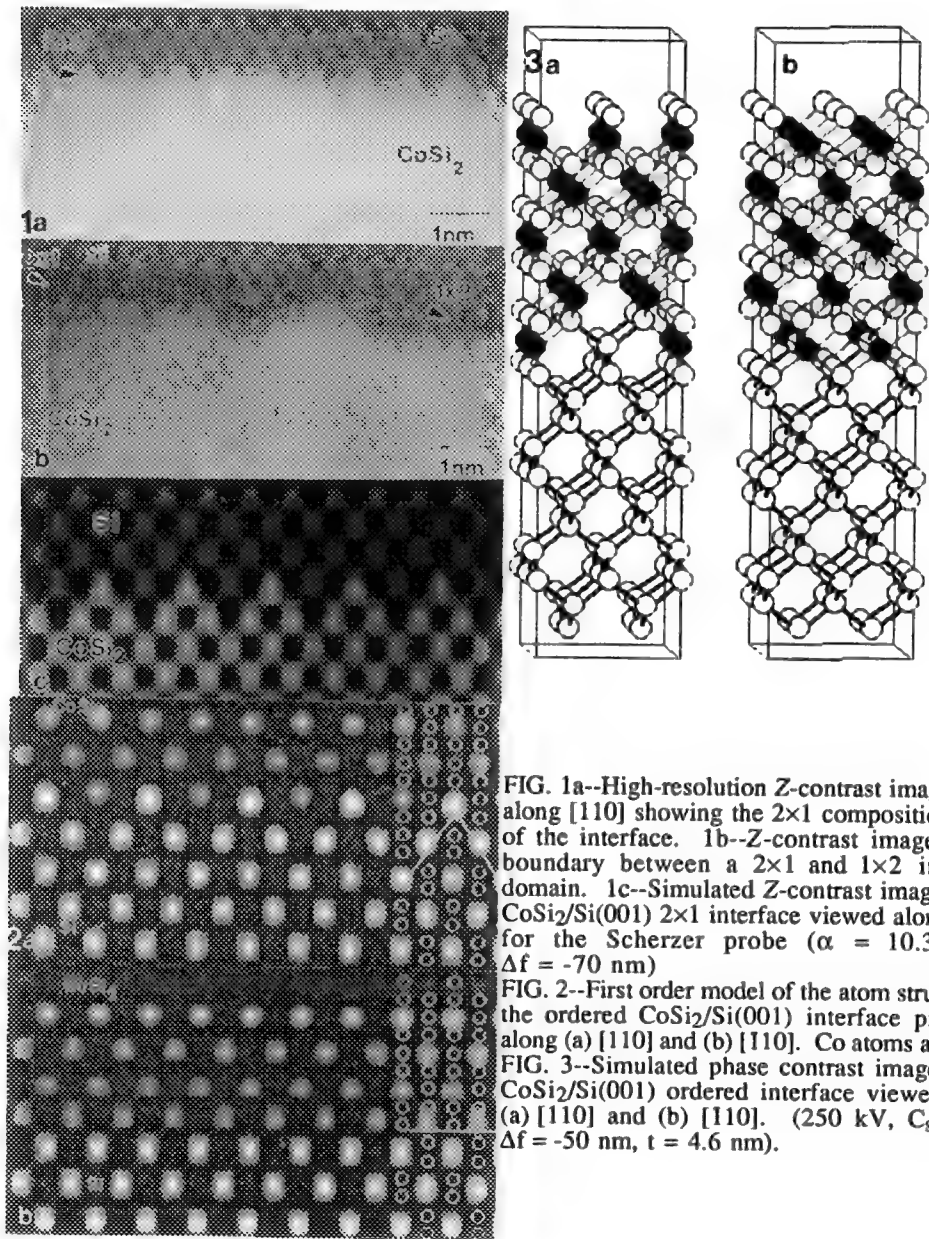


FIG. 1a--High-resolution Z-contrast image taken along [110] showing the 2x1 composition order of the interface. 1b--Z-contrast image of the boundary between a 2x1 and 1x2 interface domain. 1c--Simulated Z-contrast image of the CoSi₂/Si(001) 2x1 interface viewed along [110] for the Scherzer probe ($\alpha = 10.3$ mrad, $\Delta f = -70$ nm)
 FIG. 2--First order model of the atom structure of the ordered CoSi₂/Si(001) interface projected along (a) [110] and (b) [110]. Co atoms are solid.
 FIG. 3--Simulated phase contrast image of the CoSi₂/Si(001) ordered interface viewed along (a) [110] and (b) [110]. (250 kV, $C_s = 1.2$, $\Delta f = -50$ nm, $t = 4.6$ nm).

A TEM STUDY OF LOW-TEMPERATURE Ge GROWTH ON Ge(001)2x1⁽¹⁾

H.Z. Xiao, G. Xue, I.M. Robertson, H.K. Birnbaum, and J.E. Greene

Materials Research Laboratory and Department of Materials Science and Engineering, University of Illinois, Urbana, IL 61801

One approach to a solution of the doping problem in the molecular beam epitaxy (MBE) growth of the group IV semiconductors, e.g., segregation, low incorporation, and control of the dopants, is to lower the growth temperatures. It has been found that the room temperature Si deposition becomes amorphous after growth of a limiting epitaxial thickness which increases rapidly with the growth temperature.⁽²⁾ However, the mechanism for this structural transition is not well understood. In the present paper, we report the preliminary results of a study on the mechanism of the low temperature MBE growth of Ge on Ge(001)2x1 over the temperature range of 20-100 °C at deposition rates $R=0.05$ and 0.1 nm s^{-1} in an MBE system which has a base pressure of 5×10^{-11} Torr which increases to about 2×10^{-9} Torr during deposition. The structural transitions were investigated using a combination of *in-situ* reflection high-energy electron diffraction (RHEED) and post-deposition high resolution cross-sectional transmission electron microscopy (XTEM).

Figures 1-3 show typical high resolution XTEM images taken along the [110] direction of the Ge epilayers grown with $R=0.05 \text{ nm/s}$ at 30, 60, and 100 °C, respectively. The position of the substrate-epilayer interface, estimated using R and total time of deposition, was indistinguishable and the position of the interface in the film grown at 30 °C is defined by a solid line, as shown in Fig. 1. The growth direction (GD) is marked on the micrographs 1-3. No interfacial defects or impurity particles were observed in either high or low resolution images. All samples exhibited three regions as a function of the epilayer thickness. The initial layer is epitaxial and defect-free with a thickness which increases with increasing the growth temperature. This is followed by an intermediate layer which, while still epitaxial, contains planar defects (microtwins and stacking faults) whose density increases with the growth temperature, see Figs. 1-3. The third is an amorphous layer labelled by A in the micrographs 1-3. As shown in Figs. 1-3, the growth front of the second layer becomes rough due to the formation of three-dimensional (3D) pyramidal-shaped islands bounded primarily by {111} planes and the average size of the islands increases with the growth temperature. This is in agreement with RHEED observations.

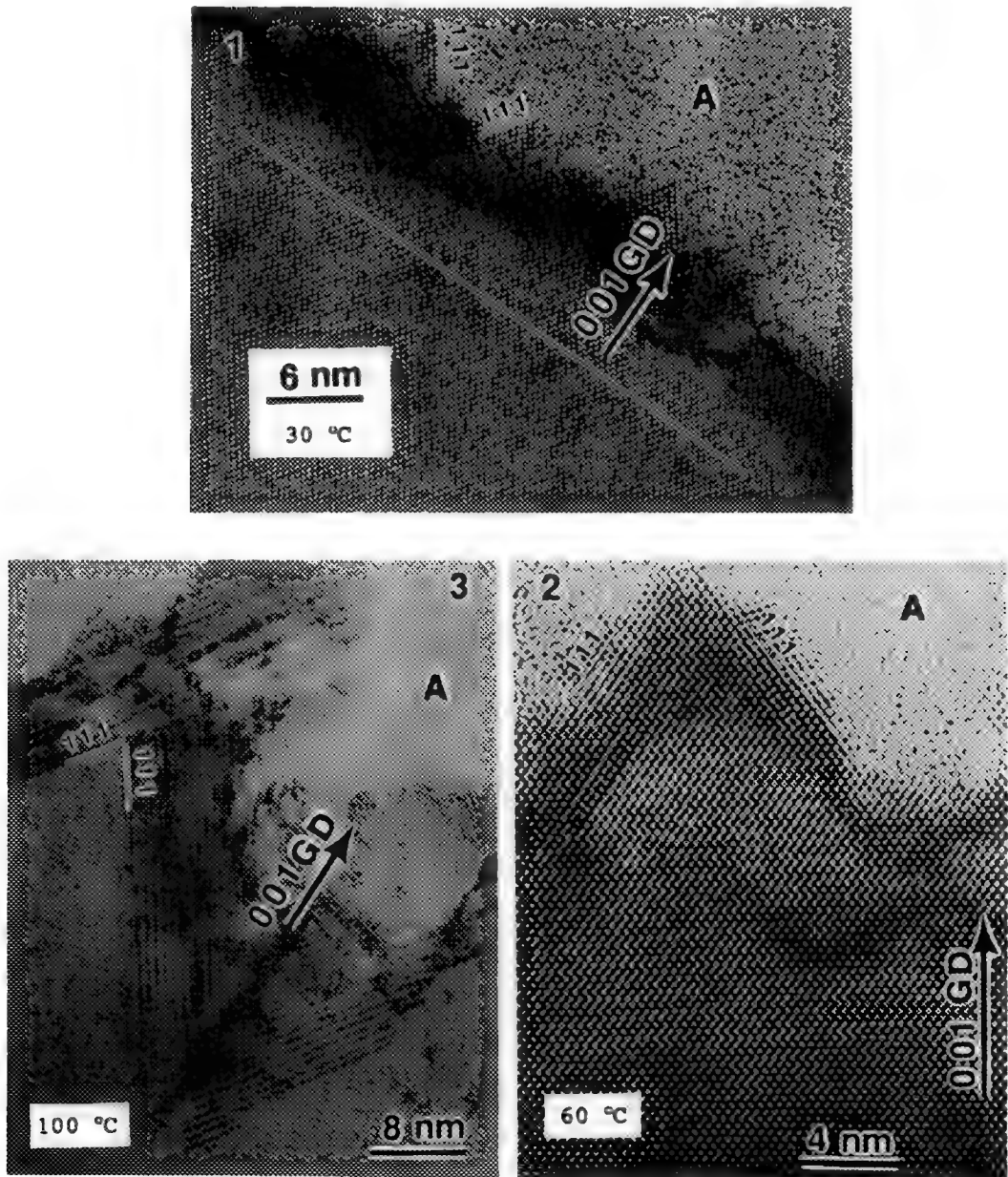
Compared to {100} surfaces, {111} planes have higher atom densities, exhibit more complex reconstructions, and require higher deposition temperatures than on {100} planes to grow epitaxial layers.⁽³⁾ This causes that the structural transition occurs from an epitaxial to an amorphous state once the {111} planes are formed. Increasing growth temperature enhances surface diffusivity resulting in larger average terrace size, thereby delaying the onset of the amorphous growth, increasing the total epilayer thickness, and leading to higher stacking fault densities.

References

1. This work is supported by the Joint Services Electronics Program, SRC, and the US Department of Energy under grant DE-FG02-91ER45439.
2. D.J. Eaglesham, H.-J. Gossmann and M. Cerullo, Phys. Rev. Lett., (1990)65, 1220.

3. H.-J. Gossmann and L.C. Feldman, Phys. Rev. B, (1985)B32, 6.

Figures 1-3. High resolution XTEM micrographs obtained along the [110] direction of MBE Ge layers grown on Ge(001)2x1 with R=0.05 nm/s at 30, 60, and 100 °C, respectively.



GROWTH OF Si ON Ge(001)2x1 BY GAS-SOURCE MOLECULAR BEAM EPITAXY*

H.Z. Xiao, R. Tsu, I.M. Robertson, H.K. Birnbaum, and J.E. Greene

Materials Research Laboratory and Department of Materials Science and Engineering, University of Illinois, Urbana, IL 61801

The growth of SiGe strained-layer superlattices (SLS) has been received considerable attention due to the electronic and optoelectronic properties of these layers. In addition, these structures offer tantalizing possibilities for "band gap engineering" through the use of strain and chemically ordered alloys. The remaining barriers to grow the SiGe SLS structures with high quality result from the generation of large densities of defects, such as dislocations, twins, stacking faults, etc., at the heterointerfaces arising from the misfit strain relaxation. Other problems associated with the growth of the SiGe SLS structures are segregation and low incorporation of the dopants and inter-diffusion of Si and Ge. In the present study, the inter-mixing of Si and Ge and the generation of the defects in Si epilayers grown on Ge(001)2x1 at 550 °C by gas-source molecular beam epitaxy (MBE) from Si₂H₆ were studied using transmission electron microscopy (TEM), *in-situ* reflection high-energy electron diffraction (RHEED), scanning tunneling microscopy (STM) and electron energy-loss spectroscopy (EELS).

At 550 °C, two-dimensional islands growth were observed for the Si coverage up to 1.5 ML. The islands were essentially pure Ge (Ge has a lower surface energy and segregates to the surface). At higher coverage, the Ge surface coverage decreased, the surface was observed to roughen, the roughness increased with thickness, and two-dimensional multi-layer island growth was observed up to about 8 ML above which three-dimensional island growth was obtained. Overlayers with a thickness of ≤ 7.5 ML were defect free as judged by high resolution cross-sectional TEM. This structure is shown in Fig. 1 which is a high resolution micrograph of a Si epilayer with a thickness of 8 ML. The rough surface can be seen and the amorphous region is epoxy. The surface roughness is produced by the Ge segregation which is enhanced by the misfit strain field. For thick layers (≥ 75 ML), no Ge was detected at the surface. In the epilayers with thickness in a range of 10-40 nm, misfit dislocations, stacking faults, and large three-dimensional islands bounded primarily by the (001) and {113} planes were observed. Fig. 2 is a bright field image of a plan-view sample with a thickness of 30 nm close to the [001] zone axis. The moire fringes result from the difference of the lattice spacings of Si and Ge. The distortion of this pattern is produced by the strain fields of the three-dimensional islands. Misfit dislocations are easily seen in Fig. 3 which is a weak beam dark field micrograph obtained under a condition of $g(3g)$, where g is the (220) diffraction vector. The dislocations are pure edge ones with Burgers vectors of $1/2[101]$ and $1/2[011]$ and dislocation line directions of $[010]$ and $[100]$, respectively. In addition to the dislocation network, the strain fields of the islands have irregular shape (white contrast). In cross-sectional samples, it was found that the misfit dislocations were generated in the layers, but close to the substrate-epilayer interface, and the stacking faults in the epilayers. An example of the stacking faults is shown in Fig. 4 and the faults are marked by arrows.

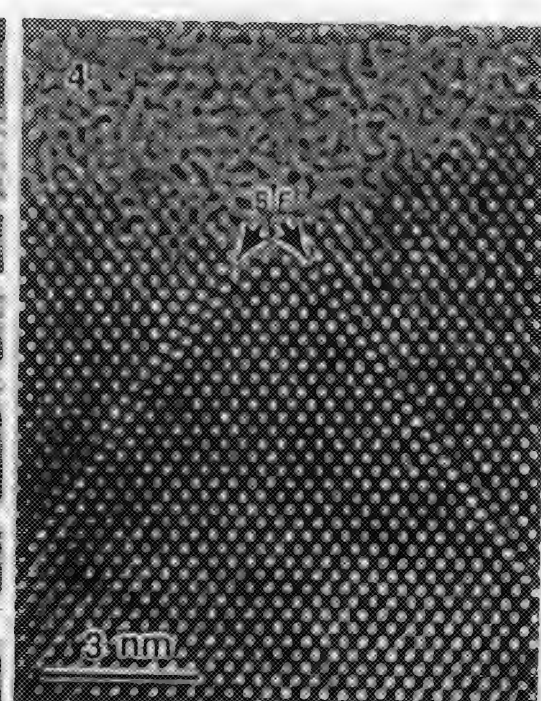
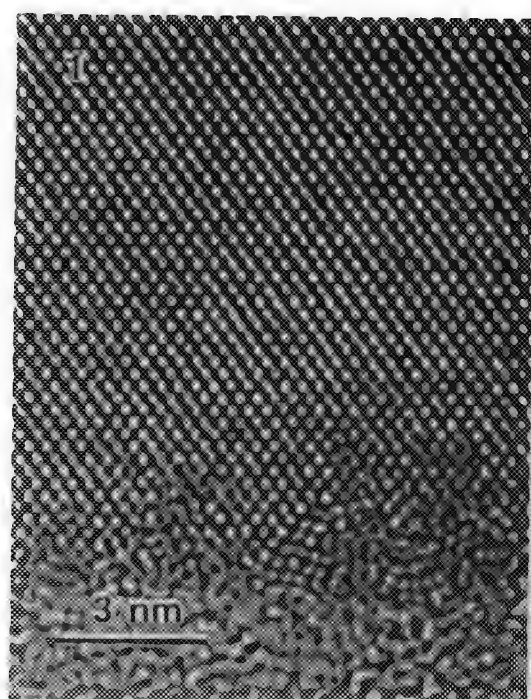
*: This work is supported by the US Department of Energy under grant DE-FG02-91ER45439.

FIG. 1. A high resolution cross-sectional micrograph of a Si epilayer with a thickness of 8 ML.

FIG. 2. A bright field moire pattern of a plan-view sample of a thick epilayer (30 nm).

FIG. 3. A weak-beam dark field image of the misfit dislocation network in a thick film (30 nm).

FIG. 4. A high resolution cross-sectional micrograph of the stacking faults in the thick film (30 nm).



FORMATION OF β -FeSi₂ BY THERMAL ANNEALING OF Fe-IMPLANTED (001) Si

X.W. Lin*, Z. Liliental-Weber*, J. Washburn*, J. Desimoni^{†,a)}, and H. Bernas[†]

*Materials Science Division, Lawrence Berkeley Laboratory, CA 94720

[†]C.S.N.S.M., Bât. 108, 91405 Orsay Campus, France

Epitaxy of semiconducting β -FeSi₂ on Si is of interest for optoelectronic device technology, because of its direct bandgap of ≈ 0.9 eV.¹ Several techniques, including solid phase epitaxy (SPE)² and ion beam synthesis,³ have been successfully used to grow β -FeSi₂ on either Si (001) or (111) wafers. In this paper, we report the epitaxial formation of β -FeSi₂ upon thermal annealing of an Fe-Si amorphous layer formed by ion implantation.

Si (001) wafers were first implanted at room temperature with 50-keV Fe⁺ ions to a dose of $0.5 - 1 \times 10^{16}$ cm⁻², corresponding to a peak Fe concentration of $c_p \approx 2 - 4$ at.%, and subsequently annealed at 320, 520, and 900°C, in order to induce SPE of the implanted amorphous layer. Cross-sectional high-resolution electron microscopy (HREM) was used for structural characterization.

We find that the implanted surface layer (≈ 100 nm thick) remains amorphous for samples annealed at 320°C for as long as 3.2 h,⁴ whereas annealing above 520°C results in SPE of Si, along with precipitation of β -FeSi₂. In the latter case, three types of orientation relationships between β -FeSi₂ and the Si matrix are observed:

- I: β -FeSi₂ [0 $\bar{1}$ 0]//Si [110], (Fig. 1)
- II: β -FeSi₂ [010]//Si[110], (Fig. 2a)
- III: β -FeSi₂ [1 $\bar{1}$ 1]//Si[110], (Fig. 2b)

with a commonly shared interface β -FeSi₂ (20 $\bar{2}$)//Si ($\bar{1}$ 11), along which the corresponding precipitates are faceted. As illustrated in Fig. 3, these relationships correspond to three closely related azimuthal orientations in the β -FeSi₂ (20 $\bar{2}$)//Si ($\bar{1}$ 11) plane, i.e., type II is a twin of type I, while type III is equivalent to type II.

Figure 2 shows that the β -FeSi₂/Si interface is basically curved, except the above-mentioned facet. The curved interface exhibits a better coherency for type II precipitate (Fig. 2a) than for type III (Fig. 2b). In addition, Si twins associated with precipitates are often observed (Figs. 1 and 2b). We also find that type II and III precipitates are always predominant in the crystallized samples, as compared with type I, probably due to their relatively low interfacial energy.⁵

References

- a) on leave from Dpto. de Fisica, UNLP, under a CONICET fellowship, Argentina
1. J. Derrien *et al.*, Appl. Surf. Sci. **56/58**, 382 (1992); S. Mantl, Mater. Sci. Reports **8**, 1 (1992).
2. N. Cherief *et al.*, Appl. Phys. Lett. **55**, 1671 (1989); J. Mahan *et al.*, Appl. Phys. Lett. **56**, 2126 (1990).
3. D.J. Oostra *et al.*, Appl. Phys. Lett. **59**, 1737 (1991); K. Radermacher *et al.*, Appl. Phys. Lett. **59**, 2145 (1991).
4. However, if the samples are subjected to ion-beam irradiation at the same temperature, cubic FeSi₂ and α -FeSi₂ will be formed, depending on the Fe dose. [see: Desimoni *et al.*, Appl. Phys.

Lett. 62, 306 (1993); Lin *et al.*, Mat. Res. Soc. Symp. Proc. 279, xx (1992)]
 5. This work was supported by the Director, Office of Energy Research, Mater. Sci. Div., U. S. Department of Energy under Contract No. DE-AC0376 SF00098.

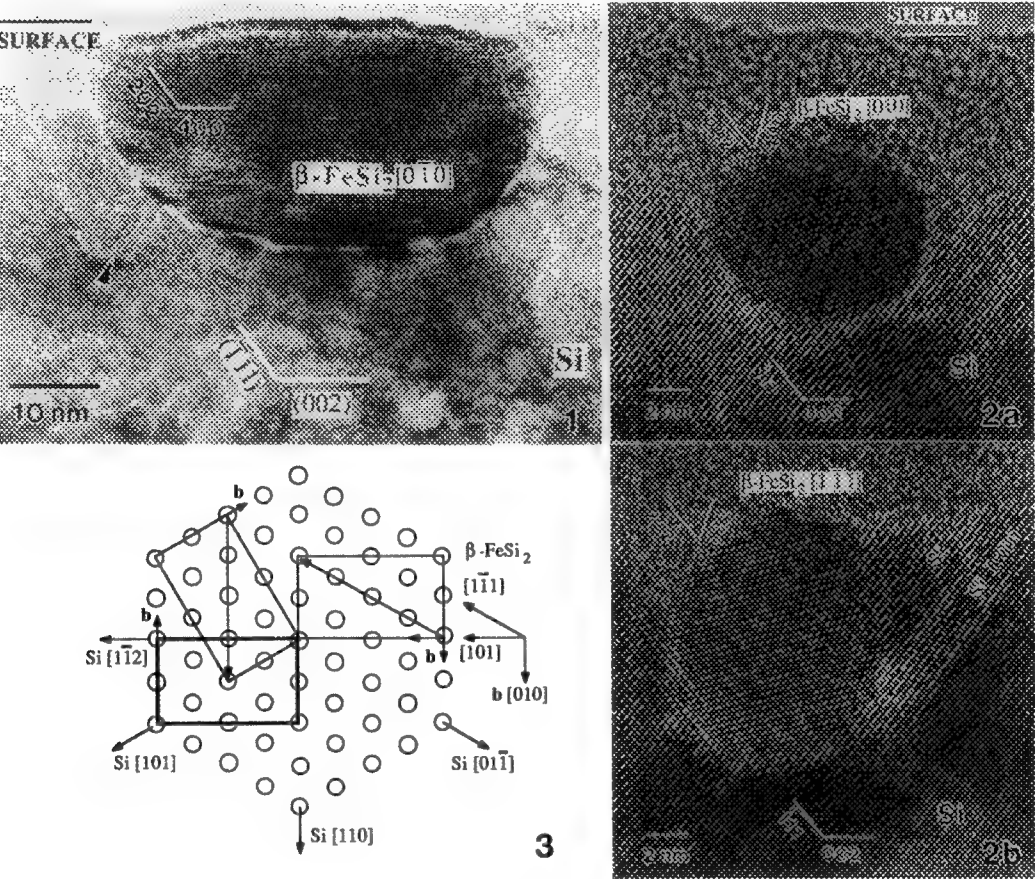


Figure 1: HREM micrograph of a β -FeSi₂ precipitate formed in a sample ($c_p \approx 4$ at.% Fe) annealed at 900°C for 3 min. The image is viewed along β -FeSi₂ [0 $\bar{1}$ 0]//Si [110].
 Figure 2: HREM images of β -FeSi₂ precipitates formed in a sample ($c_p \approx 2$ at.% Fe) annealed at 520°C for 2.5 h. Viewed along (a) β -FeSi₂ [010]//Si[110] and (b) β -FeSi₂ [1 $\bar{1}$ 1]//Si[110].
 Figure 3: Schematic diagram showing the orientations of β -FeSi₂ in the matching plane β -FeSi₂ (20 $\bar{2}$)/Si ($\bar{1}11$). Each rectangle on top of Si ($\bar{1}11$) represents a unit mesh of β -FeSi₂ (20 $\bar{2}$). Type I: thick rectangle with $-\mathbf{b}$ //Si[110]; Type II: rectangle with \mathbf{b} //Si[110]; Type III: rectangle whose diagonal [1 $\bar{1}$ 1] is parallel to Si[110]. $\mathbf{b} \equiv \beta$ -FeSi₂ [010].

CBED STUDY OF LOW-TEMPERATURE InP GROWN BY GAS SOURCE MBE

R. Rajesh*, M.J. Kim*, J.S. Bow*, R.W. Carpenter*, G.N. Maracas**

*Center for Solid State Science, Arizona State University, Tempe, AZ 85287

**Department of Electrical Engineering, Center for Solid State Electronics Research, Arizona State University, Tempe, AZ 85287

In our previous work on MBE grown low temperature (LT) InP,¹ attempts had been made to understand the relationships between the structural and electrical properties of this material system. Electrical measurements had established an enhancement of the resistivity of the phosphorus-rich LT InP layers with annealing under a P₂ flux, which was directly correlated with the presence of second-phase particles. Further investigations, however, have revealed the presence of two fundamentally different types of precipitates. The first type are the surface particles, essentially an artefact of argon ion milling² and containing mostly pure indium. The second type and the one more important to the study are the dense precipitates in the bulk of the annealed layers. These are phosphorus-rich and are believed to contribute to the improvement in the resistivity of the material.³

The observation of metallic indium islands solely in the annealed LT layers warranted further study in order to better understand the exact reasons for their formation. Figure 1a shows a TEM image of the LT InP layer containing both types of precipitates. Figure 1b shows a HREM image of a surface indium island with Moiré fringes visible in the core. Since all the LT layers were grown with excess phosphorus over the stoichiometric amount, the explanation was that the annealing was depleting the surface of phosphorus owing to inadequate phosphorus over-pressure. Consequently, the annealed layers approached stoichiometry closely, particularly near the top surface, and subsequent milling with argon ions further depleted the phosphorus preferentially, leading to the formation of indium islands. This theory is supported by convergent beam electron diffraction (CBED) studies which reveal a lattice parameter variation from the top of the LT layer to the interface, corresponding to a phosphorus gradient. The experimental procedure involved traversing a focussed probe (~2 nm in diameter) across the 1.5 µm LT InP layer, from the top to the interface and taking bright field CBED patterns off the <112> zone axis at various points along the scan. The microscope used was a Philips 400 FEG operating at 98.6 keV. The precise operating voltage of the microscope was determined by comparing a zone axis pattern (ZAP) obtained from a (111) Silicon crystal with theoretical patterns that were simulated for varying voltages around 100 keV. A series of theoretical <112> ZAPs for the InP crystal were then simulated by varying the lattice parameter slightly till they could be brought into agreement with the patterns experimentally obtained.⁴ The HOLZ-line technique is used to determine lattice parameter variations of a few parts in 10000. Each of figures 2 and 3 show the experimental and simulated CBED patterns from the top and bottom of the LT layer respectively. The findings revealed an absolute lattice parameter increase of ~0.09 nm (+/- 0.01 nm) from the top to the interface, equivalent to a 0.15% increase ($\delta a/a$). The corresponding change in stoichiometry was established by using Vegard's equation for the case of (InP + P), assuming a linear variation of the lattice parameter with the addition of excess phosphorus. An excess phosphorus content of about 3% (P/In molar ratio ~1.03) was thus detected, with the interface being the richer region due to the reduced depletion of the group V element from the interfacial regions during annealing.

References

1. R. Rajesh et al., Proc. Ann. MSA Meeting 50 (1992) 1380.
2. N.G. Chew et al., Ultramicroscopy 23, pp. 175-198, (1987).
3. A.C. Warren et al., Appl. Phys. Lett. 57 (13), pp. 1331-1333, (1990).
4. P.M. Jones et al., Proc. R. Soc. Lond., A354 (1977) 197.
5. This research was supported by a grant from the Army Research Office, No. DAAL 03-89-K-0038, and performed at the ASU/NSF HREM Facility supported by NSF-DMR-9115680 (Dr. L. Inglehart).

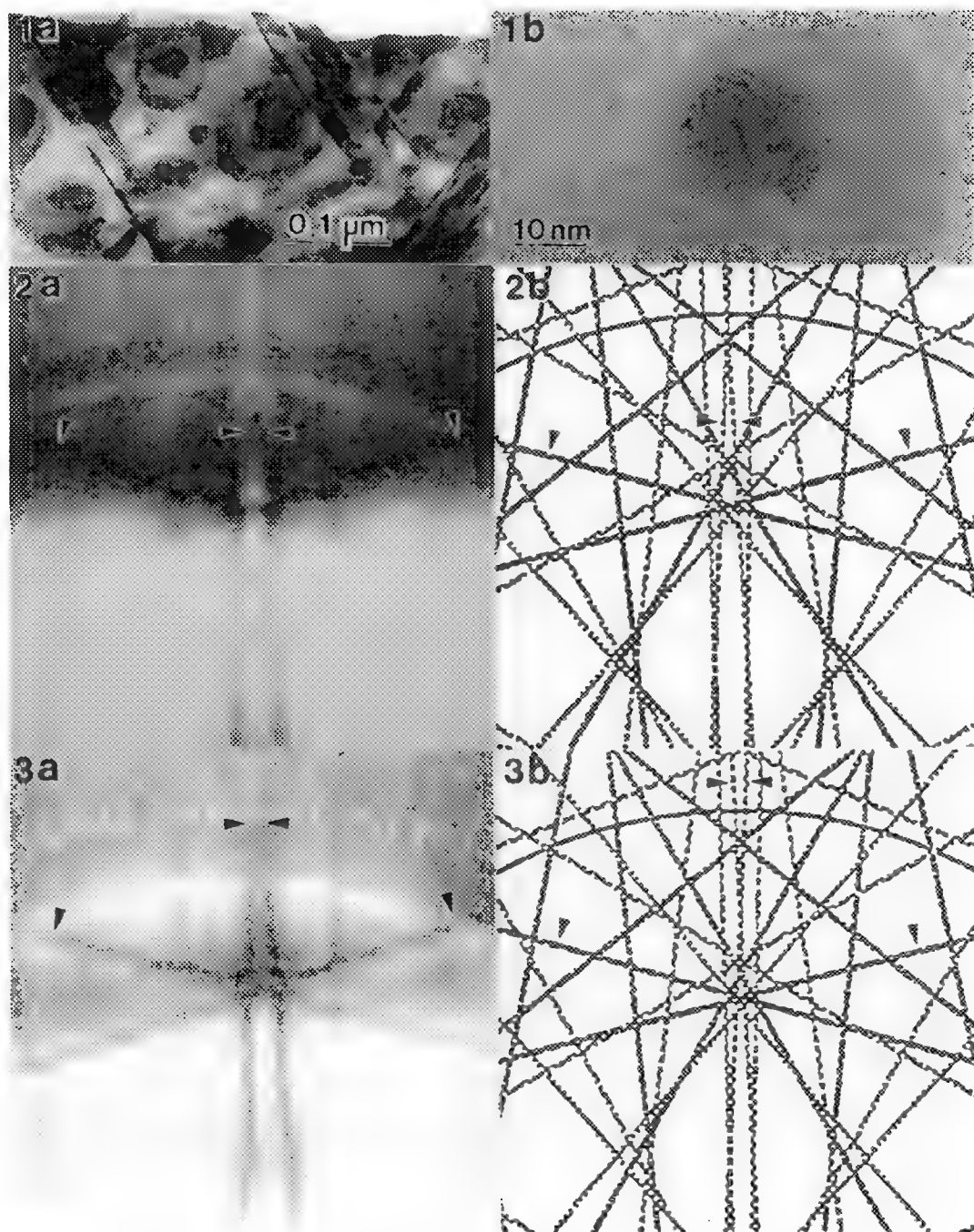


FIG. 1a--TEM image of annealed LT InP showing two types of precipitates and defect structure.
 FIG. 1b--HREM image of surface precipitate showing Moire fringes through indium-rich core.
 FIG. 2--Experimental and simulated CBED patterns from top of LT layer.
 FIG. 3--Experimental and simulated CBED patterns from bottom of LT layer.

A STUDY OF ORDERED DOMAINS IN $\text{Ga}_{0.5}\text{In}_{0.5}\text{P}$ GROWN BY MOVPE

Jane G. Zhu, D. J. Friedman, M. M. Al-Jassim and J. M. Olson

National Renewable Energy Laboratory, Golden, Colorado 80401

Atomic ordering in III-V alloys is known to influence the physical properties of these materials.¹ Therefore, the understanding and the control of the formation of ordered alloys are very important. Ordering in $\text{Ga}_{0.5}\text{In}_{0.5}\text{P}$, which is lattice matched to GaAs, occurs on two out of four $\{111\}$ planes, i.e., $(\bar{1}\bar{1}1)$ and $(1\bar{1}\bar{1})$.² The substrate orientation can affect the selection between the two ordered variants.³ Studies on atomic ordering in III-V alloys have been carried out during the past several years.⁴

Transmission electron microscopy (TEM) and selected-area diffraction have been used in this study to investigate the ordered domains in $\text{Ga}_{0.5}\text{In}_{0.5}\text{P}$ layers. The samples were grown on misoriented (100) GaAs substrates, mostly 2° towards $[001]$ unless otherwise specified, by metalorganic vapor phase epitaxy at 670°C with a growth rate $\sim 5\ \mu\text{m/hr}$. The layer thicknesses range from 1.5 to $12\ \mu\text{m}$. Plan-view specimens were prepared by chemical etching from the substrate sides and examined using a Philips CM30 microscope operated at 300 kV.

From the $12\text{-}\mu\text{m}$ -thick $\text{Ga}_{0.5}\text{In}_{0.5}\text{P}$ layer, a rough surface containing hillocks elongated along the $[011]$ direction has been observed (see Normarski image in Fig. 1a).⁵ To study the ordered domains, plan-view TEM specimens were tilted inside the microscope $\sim 20^\circ$ along the $[011]$ direction to the vicinity of $[411]$ orientation. Reflections arising from both $\{111\}$ -type variants are present in this (411) diffraction pattern as shown in Fig. 1b. The ordered domains can be imaged by using the excited $1/2(113)$ -type superlattice spots. The dark-field images recorded using the superlattice spots are shown in Figs. 1c and 1d respectively. The two variants are well separated and the "superdomains," which are formed with individual domains of the same ordering variant, correspond to the different sides of the hillocks. The sizes of the individual domains are as big as $\sim 0.1\ \mu\text{m} \times 1\ \mu\text{m}$. The domain sizes are much smaller in a $\text{Ga}_{0.5}\text{In}_{0.5}\text{P}$ layer that is $1.5\ \mu\text{m}$ thick and exhibited a smooth surface viewed under the optical microscope. Dark-field images recorded using $1/2(113)$ and $1/2(\bar{1}\bar{1}3)$ spots from the same area are shown in Figs. 2a and 2b, respectively. The ordered domains have similar features to those in the $12\text{-}\mu\text{m}$ -thick layer, but on a much finer scale. The domain sizes are $\sim 20\ \text{nm} \times 0.6\ \mu\text{m}$. From the samples in this study, it is shown that the sizes of both the superdomains of the same variant and the individual domains become bigger as the thickness of the $\text{Ga}_{0.5}\text{In}_{0.5}\text{P}$ layer increases. The surface features are correlated with the superdomains of the ordering variants. The contrast seen between the ordered domains may be resulted from the change from the ordered to disordered alloy or the change of the ordering parameter in some areas. Ordered domains with almost isotropic shapes have also been observed. In a $\text{Ga}_{0.5}\text{In}_{0.5}\text{P}$ layer that was grown on a (100) GaAs substrate misoriented 4° to $[011]$, only one ordering variant is present. Figure 3 shows a dark-field image from this sample with the ordered areas in bright contrast. Further investigation is necessary to determine the controlling factors on the domain shapes. In a sample containing defects, most of the ordering domains cross the stacking faults (Fig. 4) unchanged, although some stop at the stacking faults. A diffraction pattern in Fig. 5 is recorded at $[411]$ orientation from an area with a twin defect. All the extra spots (compared to Fig. 1b) arise from an inclined (111) twinning.

References

1. A. Gomyo et al., Appl. Phys. Lett. 50(1987)673.
2. A. Gomyo et al., Phys. Rev. Lett. 60(1988)2645.
3. P. Bellon et al., J. Appl. Phys. 66(1989)2388.
4. G. S. Chen and G. B. Stringfellow, Appl. Phys. Lett. 59(1991)324.

5. D. J. Friedman et al., Mat. Res. Soc. Symp. Proc. (1992) in press.
 6. This work has been supported by the U.S. Department of Energy under contract number DE-ACO2-83CH10093.

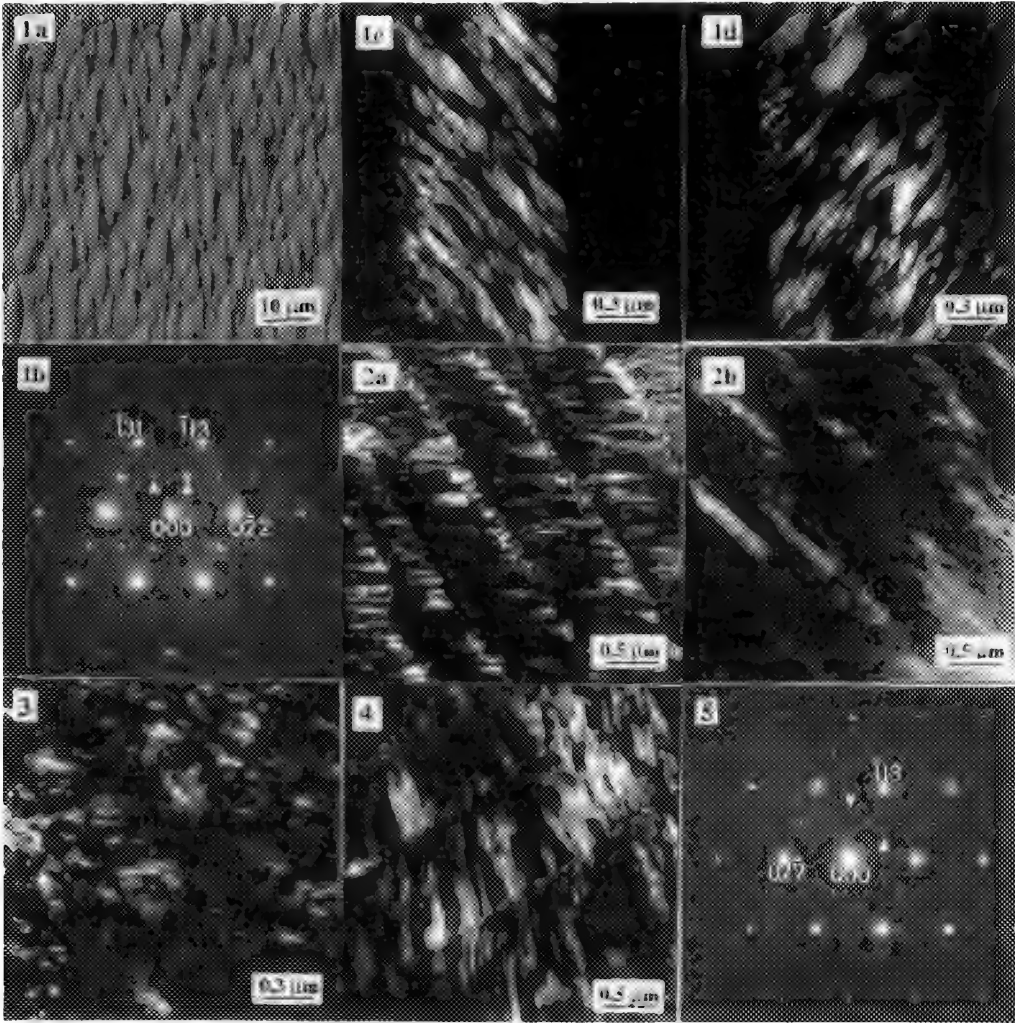


Fig. 1. (a) Normarski image; (b) Diffraction pattern at [411] orientation with the white triangles indicating the spots due to ordering; (c) and (d) Dark-field images recorded using the ordering spots from a Ga_{0.5}In_{0.5}P layer with thickness ~ 12 μm.
 Fig. 2. (a) and (b) Dark-field images (using ordering reflections) of the same area in a 1.5-μm-thick Ga_{0.5}In_{0.5}P layer.
 Fig. 3. Dark field image recorded using the ordering reflection of a 10-μm-thick Ga_{0.5}In_{0.5}P layer grown on (100) GaAs substrate misoriented 4° towards [011].
 Fig. 4. Dark-field image (using an ordering reflection) of an area with stacking faults.
 Fig. 5. (411) diffraction pattern with extra spots (indicated by white triangles) arising from an inclined (111) twin boundary.

CRYSTALLINE NANOSTRUCTURES IN POROUS SILICON AND THEIR RELATION TO OPTICAL AND ELECTRONIC PROPERTIES

Anthony G Cullis

DRA Malvern, St Andrews Road, Malvern, Worcs WR14 3PS, UK

Although Si normally emits only extremely weak infrared photoluminescence (PL) due to its relatively small and indirect band gap, light-emitting devices based upon Si would find many applications in both VLSI and display technologies. Therefore, there has been much interest in the recent demonstration¹ of very efficient visible light emission from highly porous, electrochemically etched Si. Although it was originally proposed that the efficient PL was due to recombination of quantum-confined carriers^{1,2} in pore walls, evidence for this was only indirect and transmission electron microscopy (TEM) studies³ have been required to provide a detailed understanding of the light emission mechanism.

Porous Si samples are generally prepared by anodization in HF solution and porosities as high as ~80% are required for efficient PL emission. Typical PL spectra from highly porous Si are shown in Fig. 1 where it is evident that emission is usually in the red and near infra-red regions of the spectrum. When electron transparent specimens are examined by TEM, crystalline Si nanostructures are found. Figure 2a presents the (001) projection of a high porosity layer anodized to give only very weak light emission: the remaining Si skeleton comprises rod-like bridging members with diameters down to ~5nm. The material is completely crystalline, as is clear from the corresponding diffraction pattern given in Fig. 3a (400- and 220-type spots are labelled W and X, respectively). For comparison, Figs. 2b and 2c-f show samples which gave, respectively, moderate and strong PL emission. In both cases, although the structures are more irregular, narrow undulating Si columns are clearly visible with diameters in a size range down to <3nm. Calculations indicate³ that Si wires of these dimensions would be expected to emit visible radiation. Once again, the porous material is completely crystalline, as is clear from the related diffraction patterns in Figs. 3b-d: the strong arcing of main spots in some areas and the appearance of aligned reflections which would not ordinarily occur (eg 311 (Y) and 111 (Z) in Fig. 3d) indicates the formation of isolated, misoriented nanocrystallites due to fragmentation of the Si skeleton.

Potential alternative luminescence mechanisms have been proposed based upon the presence of either hydrogenated amorphous Si⁴ or the light emitting compound siloxene⁵. However, both of these phases exhibit significant thermal instability and the recent observation⁶ of efficient PL from porous Si oxidised at high temperature essentially eliminates these candidates. The variation in PL spectrum with rapid (30sec) thermal oxidation temperature is shown in Fig. 4 and it is clear that oxidation at 950-1000°C leads to high efficiency emission. It has further been shown⁷ that this material, although mainly oxide, contains large numbers of residual Si nanocrystallites which yield aligned electron diffraction spots and appear bright in dark-field TEM images (see Fig. 5: image taken using a 220-type reflection). High resolution lattice images (see Fig. 6) confirm that the nanocrystallites, which often exhibit {111} facets, are present down to the 3-5nm size range. While the role of surface states must be clarified, these nanocrystallites are likely to be the entities responsible for the strong luminescence emission from oxidized porous Si, in accordance with the carrier quantum-confinement model¹.

References

1. L.T. Canham, Appl. Phys. Lett. (1990)27, 1046.
2. A. Bsiesy, J.C. Vial, F. Gaspard, R. Herino, M. Ligeon, F. Muller, et al, Surf. Sci. (1991)254, 195.
3. A.G. Cullis and L.T. Canham, Nature (1991)353, 335.
4. R. Fathauer, T. George, A. Ksendzov, T. Lin, W. Pike and R. Vasquez, Appl. Phys. Lett. (1992)60, 995.
5. M.S. Brandt, H.D. Fuchs, M. Stutzmann, J. Weber and M. Cardona, Sol. State Commun. (1992)81, 307.
6. V. Petrova-Koch, T. Muschik, A. Kux, B. Meyer, F. Koch and V. Lehman, Appl. Phys. Lett. (1992)61 943.
7. A.G. Cullis, L.T. Canham, G.M. Williams, P.W. Smith and O.D. Dosser, J. Appl. Phys. *in the press*.

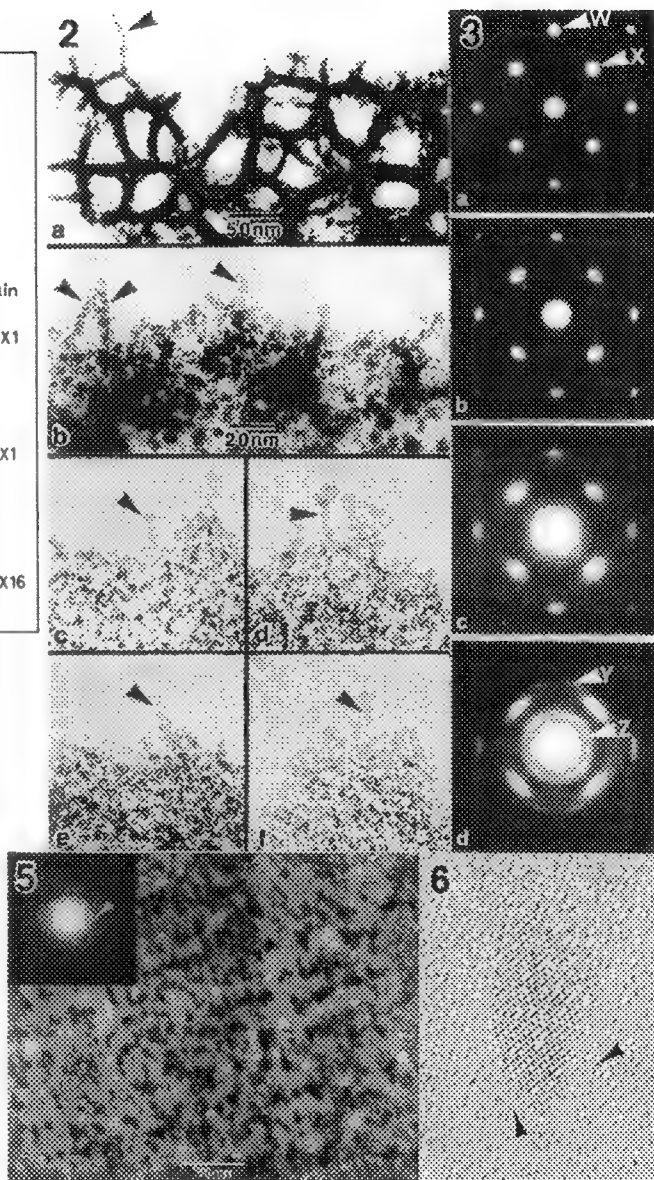
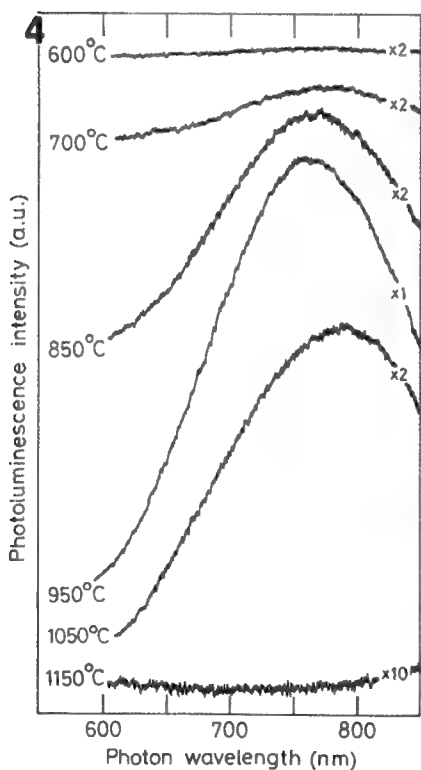
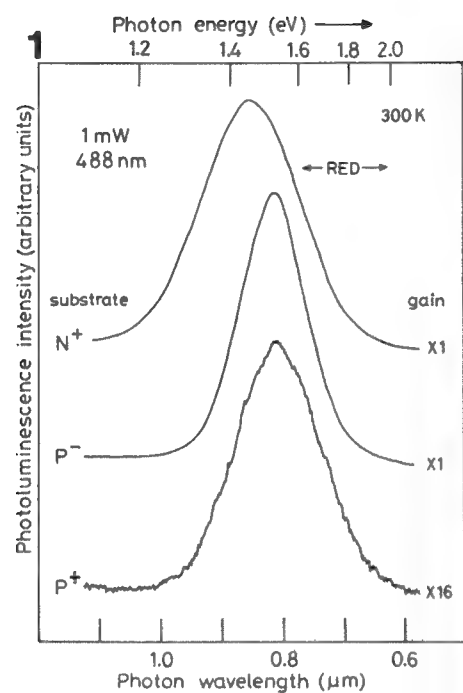


FIG. 1.—PL spectra from as-anodized porous Si.
 FIG. 2.—Bright field TEM images of porous Si.
 FIG. 3.—TEM diffraction patterns from porous Si.
 FIG. 4.—PL spectra from porous Si oxidized at various temperatures.
 FIG. 5.—Dark field TEM image and EDP from oxidized porous Si.
 FIG. 6.—High resolution [110] lattice image of oxidized porous Si.

CONDUCTION EDGE STRAIN SPLITTING IN GE-SI QUANTUM WELLS USING EELS

P.E. Batson and J.F. Morar

IBM Thomas J. Watson Research Center, Yorktown Heights, New York 10598

Ge/Si quantum well structures show a high hole mobility as the heavy hole bands are shifted to lower energy under bi-axial strain produced by lattice mismatch between the well and the Si substrate. This strain can also split and shift the conduction band edge in the well to below that of Si, producing a Type I quantum well capable of photo-luminescence. In previous work, we have shown that the conduction bandstructure can be obtained using EELS in the relaxed Ge/Si alloy system.¹ Also, we have noticed that the heterojunction band offset can be obtained from EELS because the Si 2p core level is a constant energy reference level throughout the alloy composition.² In this report, we show that a detailed fitting of the shape of the Si $L_{2,3}$ edge can obtain the bi-axial strain splitting of the conduction band edge as a function of position inside a quantum well. This information can then be correlated with annular dark field images of the cross sectioned well.

The specimens examined were both MBE and UHV-CVD grown single wells grown on Si with a Si capping layer. We describe here the MBE results. Undoped epitaxial SiGe layers were grown on undoped Si buffer layers by stoichiometric co-evaporation of Si and Ge from electron beam evaporators onto Si(100) substrates held at between 550-600°C. Growth took place in a Vacuum Generators V80 Molecular Beam Epitaxy chamber.³ Coherently strained alloys below 30% composition displayed relatively intense band edge luminescence thereby verifying a high level of crystalline ordering and purity.

The IBM high resolution spectrometer fitted to the VG Microscopes HB-501 STEM has been described elsewhere.⁴ The microscope was operated at 100 KeV using a 0.8nm diameter probe. The work reported here used a diode array detection system, requiring a relatively large probe to maximize signal. Currently, similar results are being obtained with a CCD detector using the 0.2-0.3 nm probe at 120 keV. The energy resolution was about 0.25 eV, limited by statistical considerations in unfolding the 0.35eV wide asymmetrical field emission energy distribution from the data.⁵ The $2p^{3/2}$ absorption edge shape was extracted from the 2p scattering using methods described elsewhere.⁶

In Figure 1, we show the Si $2p^{3/2}$ scattering in the 98-104eV range to point out the major features of the spectra. We have fitted the data using a model s,d-projected DOS which includes contributions from the band edge (Δ_1), L_1 , L_3 and a saddle point in the Λ_1 band. The DOS is inserted into a scattering theory which includes core excitonic distortion, plasmon collective effects, lifetime damping and instrumental resolution.⁷ We show results from Si and a relaxed 40% Ge alloy. In the alloy case, Δ_1 and L_3 shift upwards, L_1 shifts downwards, and the Λ_1 saddle point appears. In Figure 2, we show the extreme near edge regions plotted with respect to the Si valence band edge position, compared with a result from the center of a 3nm 40% well. L_1 in the strained alloy is identical to the relaxed case. The Δ_1 band edge moves down to within 25 meV of the Si position. This edge is fitted with a 4-,2-fold split DOS shape. Figure 3a shows the annular dark field image (at 0.8nm resolution) of the well. Line scans across the image show an asymmetric distribution of Ge. Figure 3b shows the band edge positions and splitting across the well. L_1 is seen to approach the 40% alloy position gradually, attaining it only in the center of the well. Δ_1 splits as expected, giving a value of 0.28 eV. Also, the splitting occurs gradually, showing the asymmetric behavior apparent in the dark field image. We wish to thank F.K. LeGoues for many discussions and access to cross sectioned samples.

References:

1. P.E. Batson and J.F. Morar, Appl. Phys. Lett., 59 3285 (1991).
2. J.F. Morar, P.E. Batson and J. Tersoff, Phys. Rev. B47 4107 (1993).

3. J.F. Morar and P.E. Batson, *J. Vac. Sci. Technol.* **B10** 2022, (1992).
4. P.E. Batson, *Rev. Sci. Inst.*, 57 43 (1986), and *Rev. Sci. Inst.*, 59 1132 (1988).
5. P.E. Batson, D.W. Johnson, and J.C.H. Spence, *Ultramicroscopy*, 41 137 (1992).
6. P.E. Batson, *Ultramicroscopy*, in press.
7. P.E. Batson and J. Bruley, *Phys. Rev. Lett.*, 67, 350 (1991), and P.E. Batson, *Phys. Rev. B*, in press.

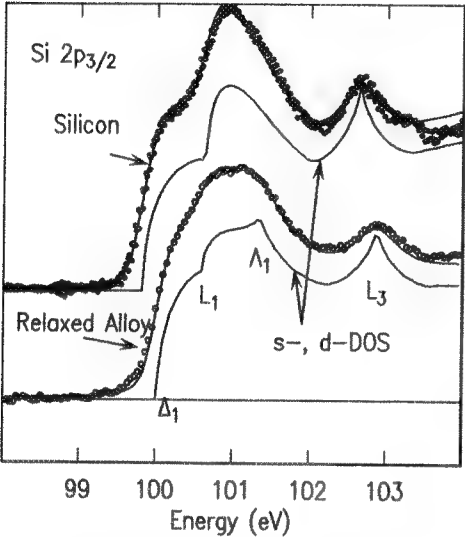


Figure 1. Wide energy summary of relaxed Si and 40% Ge alloy 2p_{3/2} spectra. The energy shifts of Δ₁, L₁ and L₃ are significant.

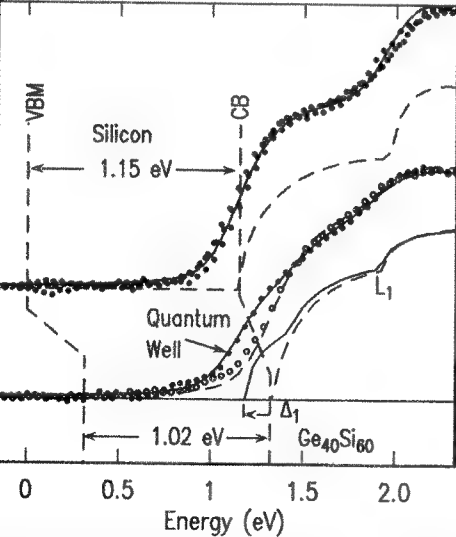


Figure 2. Narrow energy comparison of Si, relaxed 40% alloy and strained well results. Δ₁ must be split into two components to allow a good fit to the data.

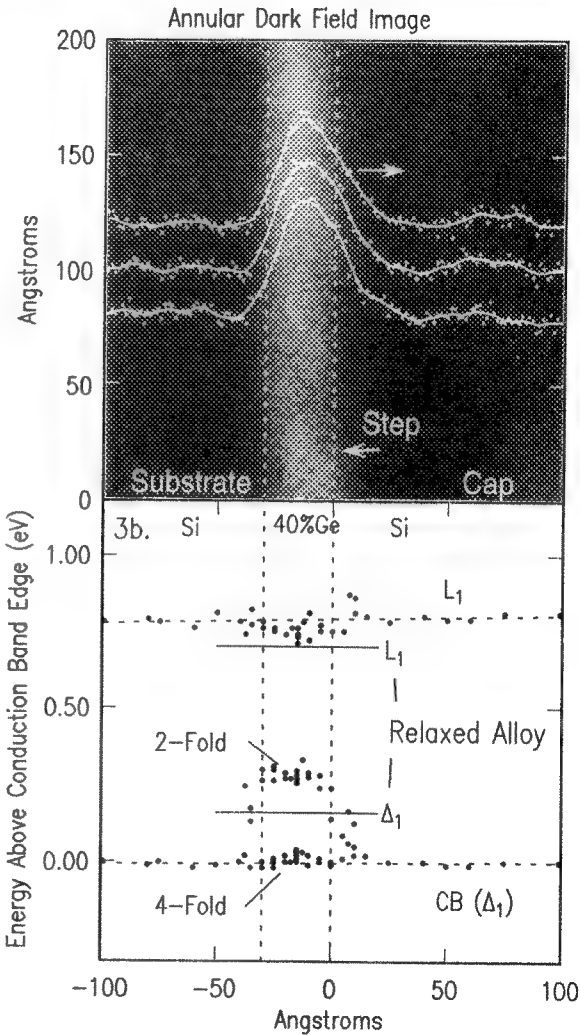


Figure 3a. Dark field image of 3nm 40% Ge quantum well. Line scans show an asymmetric distribution of Ge. (3b.) Positions of Δ₁, L₁ and the bi-axial strain splitting as a function of position through the well.

TEM STUDY OF CHEMICALLY CONVERTED SiC THIN FILM ON NANOMETER CURVED Si SURFACE

A. N. Stepanova*, J. Liu, K. N. Christensen, U. T. Son**, K. J. Bachmann, E. I. Givargizov*, J. J. Hren

Department of Materials Science and Engineering, North Carolina State University, Raleigh, NC 27695

*Institute of Crystallography, Russian Academy of Sciences, Moscow, Russia

**Agency for Defense Development, Korea

Silicon whiskers with nanometer curvature have a variety of applications such as probes in STM and AFM, or field emission cathodes for vacuum microelectronic devices. For these and other applications it is essential to stabilize the sharply curved silicon surface during usage. Carburization of the silicon surface seems to be a very suitable solution to this problem, since SiC crystals have excellent physical properties and are chemically quite inert. There have been a number of reports of the carburization of flat surface silicon wafers by chemical reaction using both CVD and MBE methods.¹⁻³ However, to carburize while maintaining a very sharp silicon tip is extremely difficult. It is also desirable to carburize only a very thin layer, so as to avoid excessive mechanical strain arising from the large difference (~20%) in lattice parameters.

Our carburizations were carried out in a turbo-pumped ultra-high vacuum system. The silicon specimens were oxidation sharpened and cleaned in a buffered HF solution. They were next transferred to the vacuum system and mounted onto a tantalum heating strip. Finally, the tips were recleaned at ~900°C under a vacuum of 10^{-9} Torr to remove the remaining native oxide. Flowing ethylene (C₂H₄) gas was introduced into the system at 5×10^{-3} Torr during the carburization reaction at 900-950°C.

Some of the TEM specimens were studied in a TOPCON 002B using a specially fabricated holder. Others were examined by high resolution SEM and some were studied by FEM/FIM. Only the results of the TEM studies are reported here.

Significant oxidation of the HF cleaned silicon whiskers occurred under ambient conditions. This is contrary to the results reported for flat wafers but can be attributed to the especially high reactivity of the nm sized tips. These native oxides could be completely removed by annealing *in vacuo* at 850-900°C at 10^{-9} Torr. The removal of all oxide was confirmed by field emission and/or field ion microscopy. Clean emitters are next carburized at 900-950°C in C₂H₄ at $P \geq 5 \times 10^{-3}$ Torr for 2-5 min. Time, temperatures, and pressures are critical as can be concluded from Figures 1-4. The optimum measured conditions were for $T \approx 900^\circ\text{C}$ and $P \approx 5 \times 10^{-3}$ Torr. However, absolute value of the temperature on the tip itself is difficult to be measured.

References:

1. C. J. Mogab and H. J. Leamy, *J. Appl. Phys.*, 45(3), 1075(1974).
2. I. Golecki, F. Reidinger, and J. Marti, *Appl. Phys. Lett.*, 60(14), 1703(1992).
3. S. Motoyama and S. Kaneda, *Appl. Phys. Lett.*, 54(3), 242(1989).

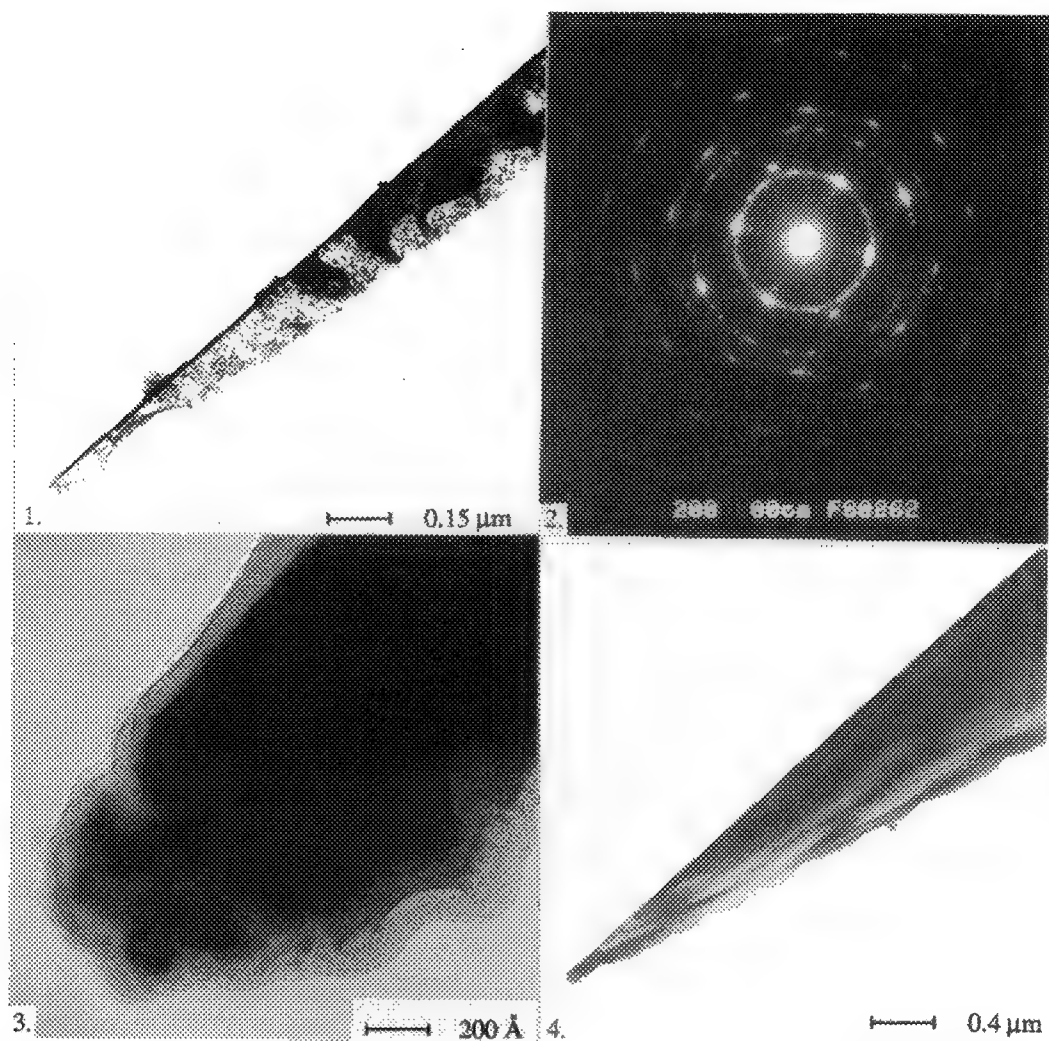


Fig. 1. Si Tip carburized at 950°C for 5 min results in complete SiC phase in tip.
 Fig. 2. The polycrystalline 3C-SiC diffraction pattern of Figure 1.
 Fig. 3. The Si tip with a thin layer of SiC film after a treatment of 2 min. at 900°C.
 Fig. 4. TEM micrograph of the whole Si specimen shown in Fig. 3.

STEM CHARACTERIZATION OF A 6Å DIAMETER Mo₃Se₃ FIBER

M. Hornbostel*,†, F.J. DiSalvo,** S. Hillyard***, and J. Silcox***

*Physics Department, Cornell University, Ithaca, NY 14853

†Current address Chemistry Department, University of Oregon, Eugene, OR 97403

**Department of Chemistry, Cornell University, Ithaca, NY 14853

***Department of Applied Physics, Cornell University, Ithaca, NY 14853

LiMo₃Se₃ is a highly anisotropic conductor¹ containing 6Å diameter one dimensional chains of Mo₃Se₃ triangles.² This compound can be dissolved in polar solvents to produce solutions containing micron length Mo₃Se₃ fibers³. Choice of solvent and solution concentrations allows some control of fiber diameters, from a few hundred angstroms down to the molecular limit of a single 6Å diameter chain.⁴ These fibers have been deposited from solution on holey carbon substrates by vacuum evaporation of the solvent to produce free-standing, one dimensional wires.

High resolution microscopy at 100kV was carried out in a VG HB501A STEM and confirms the presence of many different sized bundles extending all the way down to the single strands. Figure 1a shows an ADF image of a medium sized strand which commonly occurred in a sample prepared with the solvent propylene carbonate. The flexibility of the fiber and its seeming attraction to the edges of carbon holes is apparent as it snakes its way along the surface. Figure 1b shows a BF image of the 7Å spacing between the separate Mo chains of the same fiber where it is suspended over the hole (Although the single fibers are 6Å across, in the bundles Li acts as a spacer). The 2.24Å spacing along the chains was also seen in the bundles of this size. Beam damage prevented imaging of the 2.24Å spacing along a single isolated chain. Although the single free standing fibers seemed to hold up well under lower magnification, at the higher magnifications they were seen to vibrate and finally shake apart. In order to attempt to prevent this, imaging at 60kV was done. Figure 1c shows a group of the single 6Å fibers common to a sample prepared in a dimethyl sulfoxide solution. The inset diffraction pattern shows the 2.24Å spacing along the chains. Although some improvement in the lifetime of the strands was noted at 60kV, we were still unable to image the spacing along the single fibers. Figure 1d shows the damage done by high magnification imaging to the smaller strands at the lower right hand side of the image. The coating around some of the fibers is believed to be decomposed solvent, which seemed to be of some help in protecting the strands from beam damage.

The electronic structure of the fibers was studied by serial EELS. A bulk plasmon was identified at 23eV and studied as a function of fiber diameter and scattering angle. The plasmon energy was found to be independent of fiber diameter for fibers with diameters between 30Å and 600Å. The plasmon dispersion is also found to be independent of diameter. Surprisingly, the dispersion is also found to be independent of scattering angle relative to the long axis of the fiber. The only evidence of one-dimensionality is seen in a lack of Landau damping of the plasmon at large scattering angles, as predicted by Willams and Bloch.^{5,6}

1. Tarascon et al., Solid State Comm. 52 (1984) 227
2. Tarascon et al., Materials Research Bull. 19 (1984) 915
3. Tarascon et al., J. Solid State Chem. 58 (1985) 290
4. M. D. Hornbostel, PhD Thesis 1993 Cornell Univ.
5. Willams and Bloch, Phys Rev B 10 (1974) 1097
6. This work was supported by DoE (Grant #DE-FG02-87ER45322 & DE-FG02-87ER45298). Sean Hillyard holds a DoED fellowship. The UHV-STEM was acquired through NSF (Grant #DMR-8314233) and is operated by the Cornell Materials Science Center (NSF Grant #DMR-9121654).

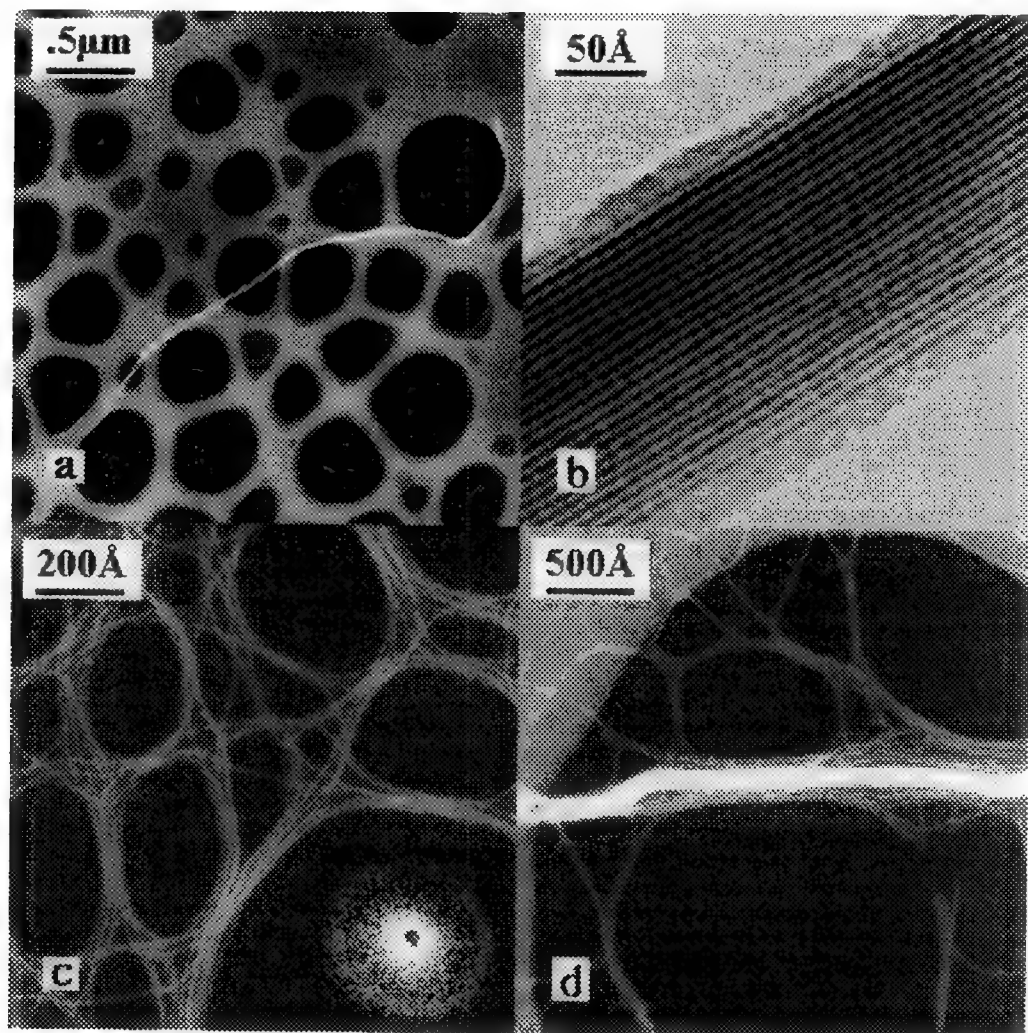


Figure 1

a) ADF STEM image of Mo_3Se_3 fiber on a holey carbon substrate taken at 100kV.

b) BF Image of same fiber at a higher magnification.

c) ADF image showing single 6\AA chains. Inset is a diffraction pattern showing the 2.24\AA spacing along the chains. Electron energy was 60keV

d) ADF image. Note the beam damage in the lower right corner due to high magnification imaging of the single fibers in that area. Electron energy was 60keV.

LATERAL DOPANT PROFILING OF SUBMICRON VLSI DEVICE STRUCTURES USING SCANNED-PROBE MICROSCOPY

J. A. Slinkman *

IBM Technology Products Division, 1000 River Rd, Essex Jct., VT 05452

Present day very large scale integrated circuit (VLSI) technology requires accurate knowledge of the spatial extent in three dimensions (3D) of active impurity dopants which have been purposely incorporated into the device structures. The active region of a typical device, where most electrical conduction is confined, is engineered to contain dopants such as As, B, or P in a concentration range of 10^{15} to 10^{20} cm^{-3} . It is necessary to control the variation of the dopant "profiles" to a resolution of 100 nm for device reliability. The devices themselves occupy a footprint of, typically, 10 μm^2 .

Except in 1D, it has been impossible to achieve a high degree of precision in the metrology of dopant profiles in actual device structures. Existing methods which have been developed for 2D dopant profiling, such as junction-staining or TEM, generally yield only qualitative information and are destructive measurements. Secondary ion mass spectrometry (SIMS) yields quantitative data but the technique is time and labor intensive, but it, too, is destructive.

Two techniques are described here which have been developed^{1,2} to measure 2D dopant profiles with a resolution of 100 nm in an essentially nondestructive fashion: 1) Scanning Capacitance-Voltage Microscopy (SCVM), and 2) Kelvin Probe Force Microscopy (KPFM). Because KPFM is a close cousin of SCVM, the latter is emphasized. Figure 1 shows a schematic of the metallic or metal-coated Si tip, (which is typically 50 nm radius) being scanned over a non-uniformly doped Si region. The tip is maintained 1 to 3 nm away from the sample. The contours represent equiconcentrations of dopant. The inset shows this system can be represented as an equivalent series capacitor stack. A block diagram of the SCVM apparatus is shown in Figure 2. The heart of the system is a capacitance sensor which can detect local capacitive changes between the tip and the sample on the order of 3×10^{-22} F/_Hz. In order to perform measurements on a submicron scale, the tip is controlled by a feedback loop, at frequency ω_1 as indicated, which maintains the capacitive signal constant as the tip is rastered across the sample surface by piezo-tube scanners. The tip, being non-contacting is dithered vertically at kHz frequencies providing a means of measuring the important quantity, dC/dz . A signal generator provides an ac or dc bias between the tip and the sample. A second lock-in (ω_2) fixes the response at ω_2 . This makes it possible to obtain a "C-V curve" at any fixed position, or to obtain dC/dV images at constant dc bias as the tip is scanned. Both dC/dz (topographic) and dC/dV images can be acquired and displayed. KPFM differs from SCVM in that the first feedback loop uses a laser heterodyne interferometric loop for topographic control. The second loop still requires a tip-to-sample bias, but the lock-in is configured to force the local electric field

*Work done in collaboration with Dartmouth College and University of Utah.

between tip and sample to zero. This is a measure of the local "contact potential difference" (CPD)². The dopant modifies the local capacitance-voltage signal in a well-known way¹. Thus, the signal as a function of tip scan position can be deconvolved to obtain the quantitative profile. Figure 3 shows a 2D dC/dV image in the vicinity of a p-n junction. The position of the dopant atoms in the lightly-doped p-region (10^{15} cm^{-3}) to the left are discernable. The region to the right is n-doped at 10^{19} cm^{-3} . Finally Figure 4 shows KPFM images of both topography and contact potential difference in the vicinity of an electrostatically-shortcd contact on a 16Mb DRAM chip. Note the essentially different features between the images.

1) C.C. Williams et. al., Appl. Phys. Lett. 55, 203(1989).
 2) M. Nonnenmacher et. al, Appl. Phys. Lett, 61, 518(1992)

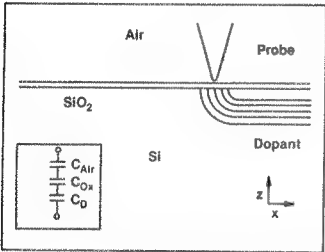


Figure 1. Schematic of the tip-sample configuration near a p-type dopant pocket in a n-type background. Inset shows the equivalent circuit.

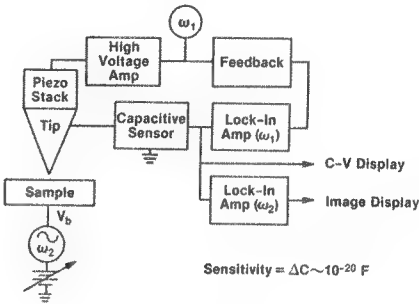


Figure 2. Block diagram of the SCVM apparatus showing the two feedback loops for topographic and capacitive detection.

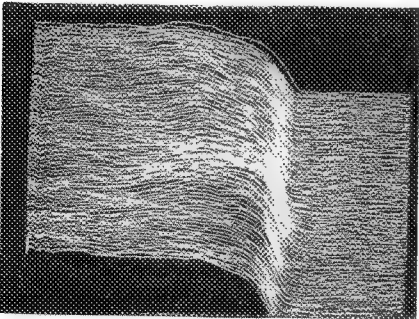


Figure 3. A 2D scan of dC/dV in the vicinity of a p-n junction. Left is low-doped p-type region.

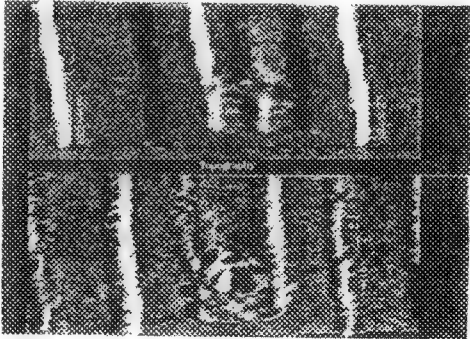


Figure 4. KPFM images of a "blown" contact: top is topography; bottom is CPD.

ELECTROCHEMICAL ATOMIC LAYER EPITAXY OF SEMICONDUCTOR CdTe THIN FILMS

Baoming M. Huang

Department of Chemistry, University of Georgia, Athens, GA 30602-2556

Semiconductor thin films have important applications in areas such as photovoltaics and luminescent displays¹. Electrodeposition of these films is a potential low cost, room temperature production technique. Electrochemical atomic layer epitaxy (ECALE) involves alternatively depositing individual element monolayer amount per ECALE cycle, taking advantage of the under-potential deposition (UPD) phenomena^{2,3}.

A series of CdTe thin films have been deposited using ECALE methodology in an electrochemical flow cell system. The 0.5 mM Te^{4+} , Te blank, 5mM Cd^{2+} , and Cd blank solutions are made with purasonic grade TeO_2 and CdSO_4 , research grade electrolyte, and 18 M ohm water. The gold foil substrates are cleaned electrochemically before each experiment. An ECALE cycle starts with depositing monolayer amount Te, rinsing with Te blank, then depositing monolayer amount of Cd, and ending with rinsing with Cd blank solution. The whole flow cell system is controlled by a computer with house-written codes, and the deposition process can be fully programmed.

Deposits have been made with 5,20,35,50,75 and 100 ECALE cycles. These deposits have been characterized by scanning electron microscopy (SEM), electron prob microanalysis (EPMA), atomic force microscopy (AFM) and inductively coupled plasma-atomic emission spectrometry (ICP-AES). As shown in Figures 1-4, the SEM pictures revealed the morphologies of these films, changing from smooth deposits at the initial ECALE cycles to grains formed at higher ECALE cycles. The EPMA data in Figure 7 shows that all but the 100-cycle deposits are stoichiometric, and the amounts of Cd and Te increase with the number of ECALE cycles. ICP-AES analysis on the 50-cycle deposit gives the absolute amount of Cd in the deposit, which corresponds to about 30 full monolayers. To measure the thickness of the deposits, another sample is deposited onto gold thin film vacuum evaporated on mica. A photo-resist pattern is formed on the gold before the deposition. The photo-resist is washed out with acetone after the deposition of CdTe. Figure 5 is the SEM picture of part of the pattern. Figure 6 is the AFM picture of the number "4". Measurement of the thickness with the section function in AFM gives the thickness of the deposit about 20 nm. These preliminary results demonstrate that ECALE can be used to deposit stoichiometric CdTe thin films, and that the films are deposited about half monolayer per ECALE cycle.

References

1. K. Rajeshwar, Adv. Mater. (1992) 4, 23.
2. B. W. Gregory and J. L. Stickney, J. Electroanal. Chem. (1991) 300, 543.
3. B. W. Gregory, D. W. Suggs and J. L. Stickney, J. Electrochem. Soc. (1991) 138, 1279.
4. This work is supported by National Science Foundation (Grant # DMR-9017431) and the Office of Naval Research (Grant # N00014-91-J-1919).

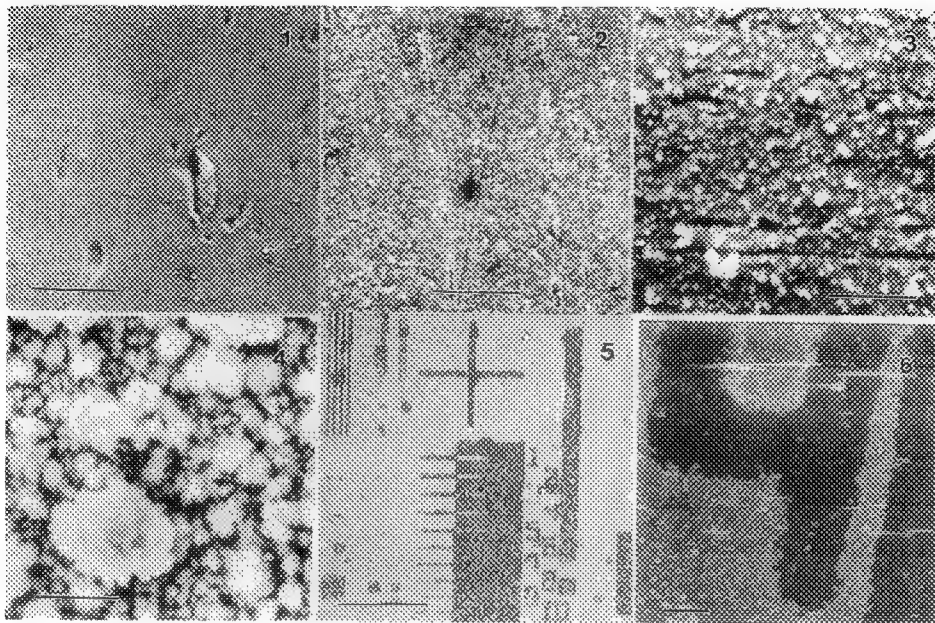


Fig.7 Electron Probe Microanalysis

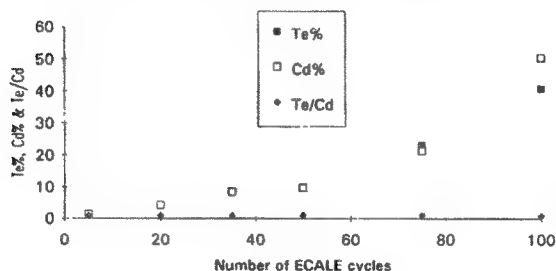


Fig. 1-4 SEM of 20-, 50-, 75- and 100-cycle deposits, respectively. The morphologies of these films change from smooth deposits at initial ECALE cycles to grains formed at higher ECALE cycles. Bars = 5 μ m.

Fig. 5 SEM of the 20-ECALE-cycle CdTe pattern formed on gold on mica.

Fig. 6. AFM (without filtering) of the number "4" of the 20-ECLAE-cycle CdTe pattern. Measurement with the section program in AFM gives the thickness of the deposit about 20 nm. Bar = 50 μ m.

Fig. 7 Electron probe microanalysis data of the series of deposits, showing that all the deposits but the 100-cycle one are stoichiometric, and the amounts of Te and Cd increase with the number of ECALE cycles. Bar = 2 μ m.

INTERFACIAL PROPERTIES OF GaSb/InAs SUPERLATTICES

M. E. Twigg, B. R. Bennett*, J. R. Waterman, J. L. Davis, B. V. Shanabrook, and R. J. Wagner

Electronics Science and Technology Division, U. S. Naval Research Laboratory, Washington, D. C. 20375-5347, *NRL-NRC Research Associate

Recently, the GaSb/InAs superlattice system has received renewed attention. The interest stems from a model demonstrating that short period $\text{Ga}_{1-x}\text{In}_x\text{Sb/InAs}$ superlattices will have both a band gap less than 100 meV and high optical absorption coefficients, principal requirements for infrared detector applications.¹ Because this superlattice system contains two species of cations and anions, it is possible to prepare either InSb-like or GaAs-like interfaces. As such, the system presents a unique opportunity to examine interfacial properties.

We used molecular beam epitaxy (MBE) to prepare an extensive set of GaSb/InAs superlattices grown on an GaSb buffer, which, in turn had been grown on a (100) GaAs substrate. Through appropriate shutter sequences, the interfaces were directed to assume either an InSb-like or GaAs-like character. These superlattices were then studied with a variety of ex-situ probes such as x-ray diffraction and Raman spectroscopy.² These probes confirmed that, indeed, predominantly InSb-like and GaAs-like interfaces had been achieved.

In Figure 1 we show a high-resolution transmission electron microscope (HRTEM) image of a [100]-oriented cross-sectional sample recorded on an Hitachi H-9000UHR operating at 300kV with a spherical aberration coefficient of 0.9 mm and a defocus of 65 nm. The material in the cross-section was taken from an MBE-grown 40 period superlattice in which each period consists of 12 MLs (monolayers) of GaSb, followed by 8 MLs of InAs. A shutter sequence designed to produce only InSb bonding at the interface was used. Pendellosung modulations suggest a sample thickness of 19 nm. According to the HRTEM image simulation³ shown in Figure 2a, the interface for a perfect InSb bonded GaSb/InAs superlattice should reveal bright dots only on the (low Z) Ga and As columns; the (high Z) In and Sb atomic columns of the InSb interface should remain relegated to the dark background. Because MBE growth may not be capable of controlling deposition on an atomic level, we naturally expect that the actual interface would not resemble exactly the simulation in Figure 2a.⁴ Indeed, in addition to the features expected for InSb-like interfaces, we can see some evidence of zipper-like features that are similar to the GaAs-like interfaces shown in the simulation in Figure 2b.

The results of Raman spectroscopy and x-ray diffractometry indicate that the fraction of GaAs bonding at the nominally InSb-like interface cannot be greater than 10%. Similarly, our preliminary HRTEM observations, which reveal a relatively low incidence of zipper-like features in interfacial images, suggest that the incidence of GaAs bonding in nominally InSb-like interfaces is less than 10%. The existence of GaAs bonding in this material may be due to either incomplete coverage or a tendency for islanding. It is interesting to consider that the HRTEM observations of GaAs interfacial regions may be the most reliable evidence of a true departure from atomic control of growth in GaSb/InAs superlattices. Although the presence of $\langle 110 \rangle$ -oriented interfacial steps can also give rise to a departure from the simple image simulation shown in Figure 2a, the effect of such steps does not give rise to a zipper-like interface. Instead, a more diffuse interface, shown in Figure 2c, is the result.

References

1. C. Mailhot and D. L. Smith, J. Vac. Sci. Technol. (1989)A7, 445.
2. J. R. Waterman et al., Semicond. Sci. Technol. (1993)8, S106.
3. P. Stadelmann, Ultramicrosc. (1987)21, 131.
4. A. Ourmazd et al., Ultramicrosc. (1990)34, 237.

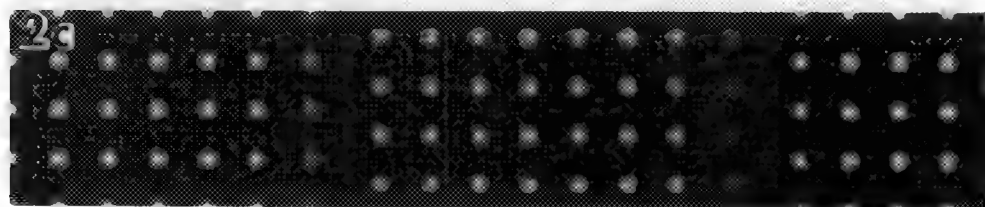
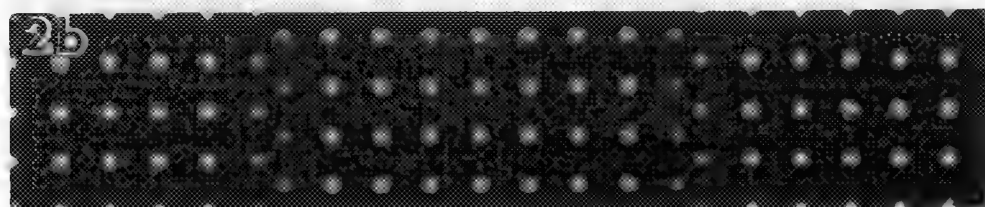
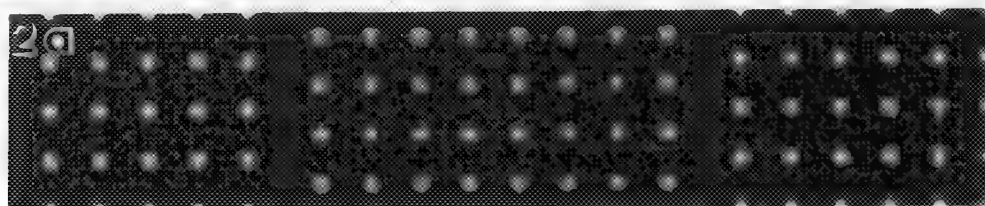
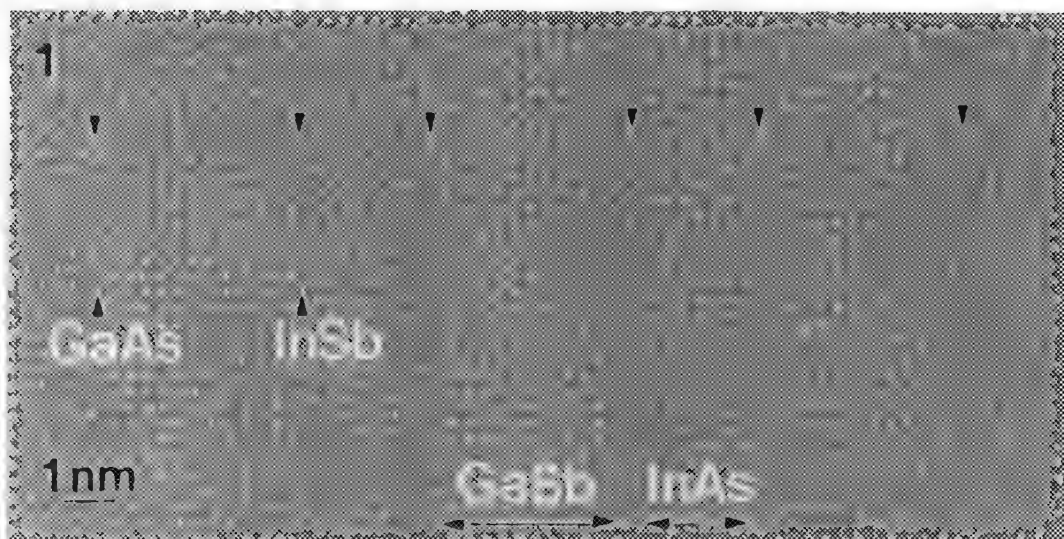


FIG. 1.--HRTEM image of InSb-like 12 GaSb/8 InAs superlattice recorded at 65 nm defocus. Double arrows designate interfacial regions of clearly GaAs-like or InSb-like character. Single arrows designate remaining interfaces.

FIG. 2.--HRTEM simulations of 12 GaSb/8 InAs superlattice for sample thickness of 19 nm and defocus of 65 nm. Each simulation places InAs layer in the center with GaSb layers are at each end. Bright dots in GaSb and InAs correspond to Ga and As columns, respectively. (a) InSb-like interface. (b) GaAs-like interface. (c) InSb-like interface with interfacial step.

REFLECTION ELECTRON MICROSCOPY OF TRIANGULAR QUANTUM WELLS

M. Gajdardziska-Josifovska

Center for Solid State Science, Arizona State University, Tempe, AZ 85287

Asymmetric triangular quantum wells (ATQW) have recently been developed to improve the absorption and emission characteristics of opto-electronic devices.¹ A triangular compositional gradient is produced during epitaxial growth of $\text{Al}_x\text{Ga}_{1-x}\text{As}$ on GaAs by either continuous variation of x or by alternate deposition of thin layers of the two compounds where the ratio of the layer thickness produces an average alloy composition. The knowledge of the compositional profile of the actual ATQW, as derived from HREM, has proven essential for the description of the photo-emission properties of the device.² Recently, the technique of reflection electron microscopy has also been applied to multiple rectangular quantum wells of $\text{GaAs}/\text{Al}_x\text{Ga}_{1-x}\text{As}$ with the encouraging result that layers with 1% Al can be distinguished from the GaAs layers.³ In this work we investigate the applicability of REM to characterization of ATQW.

Triangular quantum wells were grown by MBE, employing the digital alloy method.² Fig. 1 shows a schematic representation of the nominal thickness and composition of the studied ATQW. Specimens with dimensions of $\sim 0.5 \times 1 \times 0.2 \text{ mm}$ were mounted as sketched in Fig. 2, with the surface for imaging being cleaved immediately before loading in the microscope. REM studies were performed in Philips 400T and 400T-FEG microscopes, the latter being equipped with a Gatan 679 slow-scan CCD camera. Both room temperature and liquid nitrogen cooled specimen holders were tested.

Fig. 3a shows a reflection electron micrograph recorded with the reflection arrowed in the inset RHEED pattern. Large atomically flat areas can be seen on the cleaved (110) surface of the GaAs substrate, and the quantum wells are clearly visible on the right side of the micrograph even at low magnification. A faint line can also be seen at the position where a GaAs buffer layer (330nm thick) was grown onto the GaAs substrate prior to deposition of the quantum well structure. Digitization of the electron micrograph with an optical CCD camera allows extraction of intensity profiles: The digitized image section in Fig. 3b was averaged parallel to the interfaces to give the profile in Fig. 3c. The qualitative agreement between this experimental profile and the nominal Al composition of the wells, shown in Fig. 1, is remarkable. The intensity of the reflection used for imaging was lower from $\text{Al}_{0.3}\text{Ga}_{0.7}\text{As}$ compared to GaAs at the three diffracting conditions studied (Fig. 3 and 4). Even in cases when the cleavage was imperfect (e.g. Fig. 4) it was always possible to find regions on the specimen from which the ATQW could be imaged. The bi-layers in this digital triangular well, nominally 2.5nm thick, could not be discerned in the images, in agreement with previous observations.³ The resolution of REM under the conditions used is typically $\sim 1 \text{ nm}$, and it is not clear at the moment why it appears to be poorer for the GaAs/AlGaAs system. Surface contamination and radiation damage were cited as possible causes, but in our preliminary studies with different specimen holders and electron doses we could not observe any difference.

The images in Fig. 4 were acquired directly in digital form by utilizing a CCD camera attached to the microscope. In this manner the analysis was further speeded which, when combined with the fast specimen preparation time of $\sim 1/2$ hour, would enable quick feedback for optimization of the growth procedures for asymmetric triangular quantum wells.⁴

References

- 1 D. S. Gerber et al., *Appl. Phys. Lett.* (1993)62,525.
- 2 D. L. Mathine et al., *J. Appl. Phys.* (1993) submitted.
- 3 L.-M. Peng et al., *Phil. Mag Lett.* (1992)66,9.
- 4 This research was conducted at the Center for HREM at ASU supported by NSF grant DMR-9115680. The author is grateful to Prof. J. C. H. Spence for financial support, and to Dr. D. Gerber for providing the MBE samples.

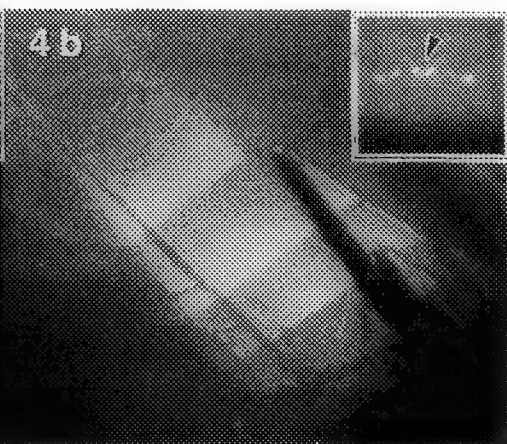
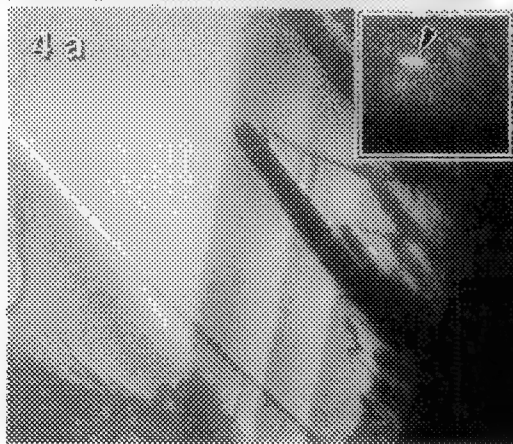
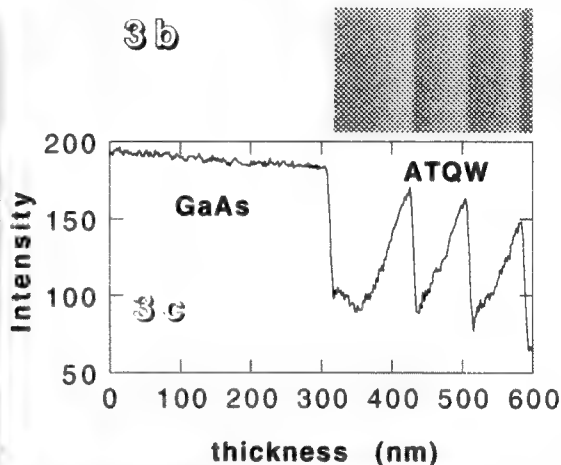
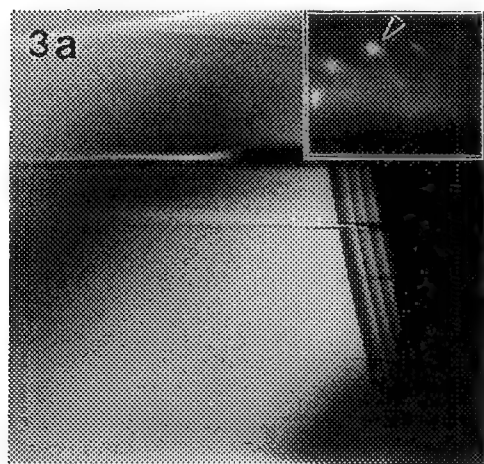
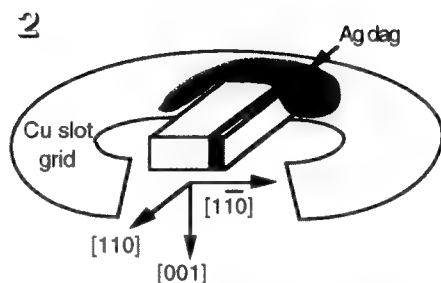
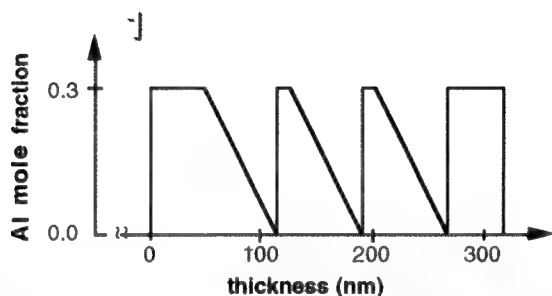


FIG. 1.--Schematic of nominal thickness and composition of as grown ATQW used for REM studies.

FIG. 2.--Sketch of specimen orientation and mounting for REM.

FIG. 3.--Low magnification reflection image (a) and reflection high energy electron diffraction pattern (inset) of studied ATQW recorded on photographic plates. Digitized part of image (b) was used for averaged intensity profile (c).

FIG. 4.--Digital REM images and RHEED patterns (inset) acquired with CCD camera using 880 reflection from sample with rough surface cleavage: (a) azimuthal tilt; (b) symmetrical orientation.

IN SITU HREM OF INTERFACE REACTIONS

Robert Sinclair and Toyohiko J. Konno

Department of Materials Science and Engineering, Stanford University, Stanford CA94305, USA

We have applied in situ high-resolution electron microscopy (HREM) to the study of interface reactions, particularly in metal-semiconductor systems. There is contrasting behavior whether or not the manufactured interface undergoes a chemical reaction. The in situ technique allows determination of the reaction mechanisms on an atomic scale.

Reactive interfaces are characterized by systems in which new chemical compounds are formed (e.g., silicides for metal-silicon interfaces, metal gallides and arsenides for GaAs, etc.). We found that the equilibrium phase formation is often preceded by a solid-state amorphization reaction. In situ observations allow very precise measurement of the reaction rate in a sufficient temperature range to confirm that this process is diffusion controlled.^{1,2} Crystallization of the amorphous material can be followed as well as the development of any crystallographic orientation relationships. A ledge growth mechanism can easily be distinguished from a random process.

It might be expected that non-reactive interfaces are stable upon heating. However, significant changes can take place which give rise to easily measured exotherms in differential scanning calorimetry experiments. For instance in Al-Si multilayer samples, 12kJ per mole is released upon heating to about 200°C. Neither equilibrium nor metastable compounds are produced : rather the amorphous semiconductor films (Si) crystallize at an abnormally low temperature. In situ investigation shows that the Si nucleates within the Al layers and that Si crystal growth continues by the rapid diffusion of Si through the Al matrix. In multilayers, this gives the appearance of the Si "growing along" the Al lines (e.g., Fig.1). The Al atoms must diffuse in the opposite direction to that of the Si, and this is manifested by the Al grain growth and "splitting" as the reaction proceeds.³ Equivalent behavior is found in similar systems such as Ag-Si and Ag-Ge. High-resolution recordings confirm the above atomic interdiffusion directly.

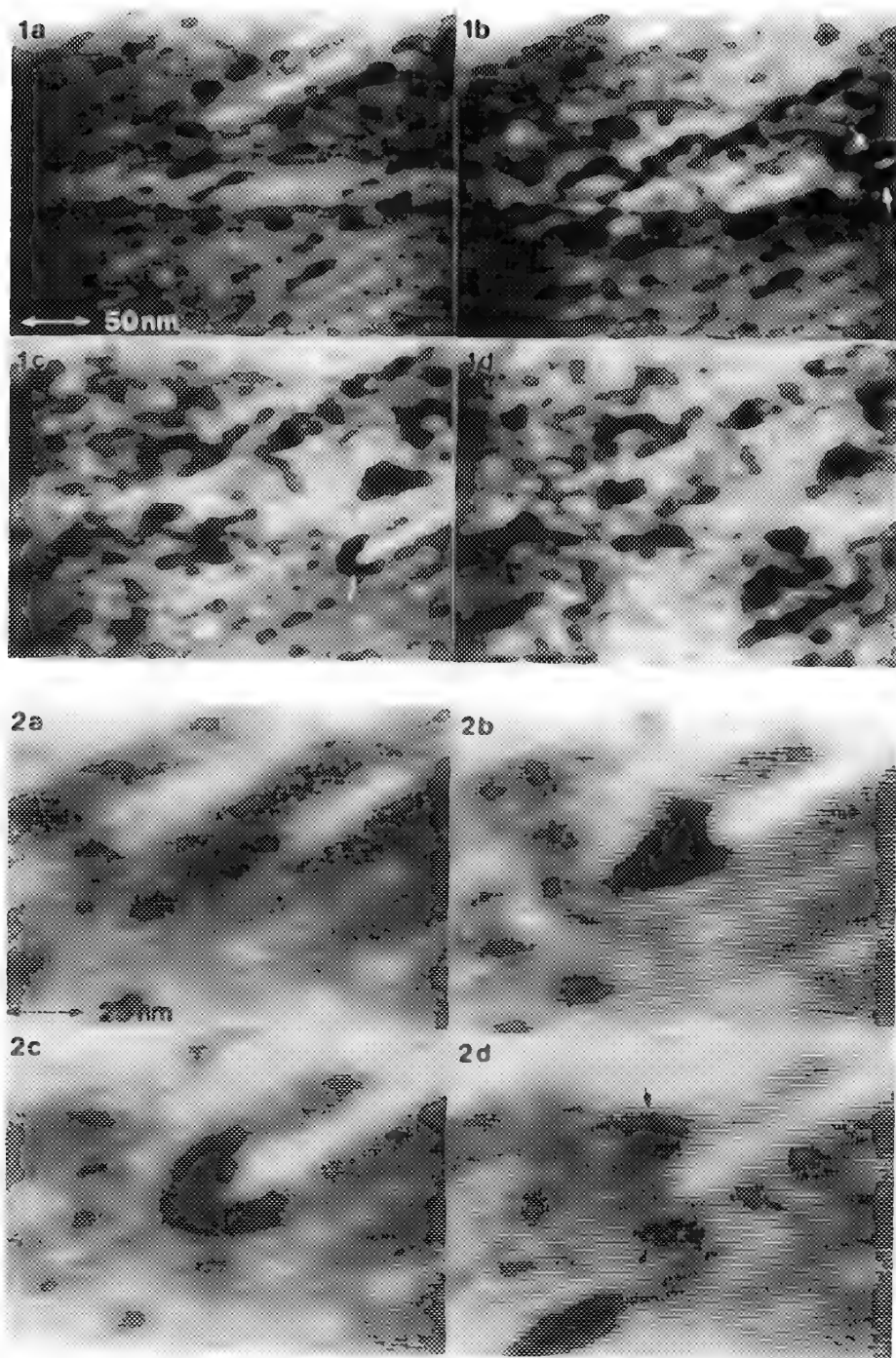
Many interface reactions are open to study by in situ HREM. In our experience of semiconductor systems, the result duplicate those seen in bulk samples in the great majority of cases (e.g., ref. [4]), but at the moment we still recommend in situ and ex situ parallel studies. The information provided, however, remains unique.⁵

References

1. K.L. Holloway and R. Sinclair, *J. Less-Common Metals*, 140 (1988) 139
2. D.-H. Ko and R. Sinclair, *J. Appl. Phys.*, 72 (1992) 2036
3. T.J. Konno and R. Sinclair, *Phil. Mag. B66* (1992) 749
4. R. Sinclair et al., *Acta Crystallog. A44* (1988) 965
5. This research is supported by the National Science Foundation (Grant No. DMR 8902232)

Fig. 1 A sequence of video images (about 1min. apart) of the reaction in Al-Si multilayers at 200°C. The reaction proceeds from the upper right corner of the images with Si crystals growing along the Al layers.

Fig. 2 Higher magnification views of the Al grain arrowed in fig. 1 (c), showing the enlargement and splitting of the Al grains as the Si crystals grow.



HREM AND AEM STUDY OF Pt/SiC INTERFACE ANNEALED AT HIGH TEMPERATURE

J.S. Bow*, L.M. Porter**, M.J. Kim*, R.W. Carpenter*, and R.F. Davis**

* Center for Solid State Science, Arizona State University, Tempe, AZ 85287-1704

**Department of Materials Science and Engineering, North Carolina State University, Raleigh, NC 27695-7907

High temperature applications of SiC semiconductor devices will be essentially limited by the metal/SiC interface interconnect properties. Pt/SiC was reported to have more stable and better electrical properties¹ than other metal/6H-SiC after annealing above 700°C under UHV condition. Some work on the Pt/SiC interface has been conducted by AES and other low spatial resolution surface techniques^{2,3}, but there is no detailed direct image data reported. Here, we characterize the microstructure of the Pt/SiC interface after high temperature annealing in UHV at near atomic resolution and reported the first nanospectroscopic energy loss data for the system.

As-deposited Pt film is polycrystalline with grain size of 10 ± 3 nm (Fig.1). The thin amorphous layer visible at the interface in Fig.1, gradually disappearing in the thick regions, was attributed to oxygen-induced ion-milling damage⁴. Similar results were observed frequently in other metal/ceramic system. We consider the amorphous layer to be due to residual oxygen on the ceramic surface during synthesis, since trace oxygen was only detected at the as-deposited Pt/6H-SiC interface. A pronounced reaction zone, showing bright contrast in XTEM (Fig.2), formed after 750°C/20 min. annealing. HREM images (Fig.3a) indicated that this bright contrast product (marked A) was an amorphous phase. EELS mapping showed the A-phase contained carbon (Fig.3d), and EELS point spectra indicated that it contained both carbon and platinum. Besides forming as a continuous layer, the A-phase also occurred as tiny particles from 0.5 to 2 nm diameter distributed throughout the Pt film, as shown in the HREM image. This phase is the origin of the ring pattern in the micro-diffraction pattern of Pt (Fig.3b) and the carbon K-edge in EELS spectra acquired from the Pt film.

A crystalline phase of strip-shape, showing dark contrast, occurred between the A-phase and the SiC substrate. Two sets of d-spacings, 0.2015 and 0.2785 nm, which were orthogonal to each other were measured from both optical digital diffraction patterns as well as micro-diffraction patterns from this phase, and were considered to be $d[112]$ (0.2025 nm) and $d[110]$ (0.2781 nm) corresponding to tetragonal Pt₂Si. The Pt-silicide was epitaxially related to SiC with $[\bar{1}\bar{1}2]_{\text{Pt}_2\text{Si}} // (0001)_{\text{SiC}}$ and $[110]_{\text{Pt}_2\text{Si}} // (1100)_{\text{SiC}}$ (Fig.3c), and was not completely isolated from Pt by the A-phase layer. Some tunnels could be seen in some locations.

Contrary to previous reports^{2,3}, we would like to believe that the A-phase formed first, followed by nucleation and growth of the silicide according to two features of the microstructure. First, most of the silicide strips only contacted SiC at their ends, and a thin layer of A-phase usually separated them. Second, the morphology of silicide tended to be parallel to that of the A-phase. For example a large silicide precipitate formed at the location where an A-phase island formed, as shown in Fig.3a. These characteristics also indicated that the A-phase provided a fast diffusion path for Si and Pt.

References

1. L. M. Porter et al., Mat. Res. Soc. Symp. Proc. (1992), to be published.
2. N. A. Papanicolaou et al., J. Appl. Phys. 65(9) (1989) 3526.
3. V. M. Bermudez et al., J. Mat. Res. 5(12) (1990) 2882,
4. J. S. Bow, F. Shaapur, et al., these proceedings.

5. This research was partly supported by NSF-DMR-8901841 and partly supported by the Office of Naval Research via contract N00014-88-K-0341. The microscopy was performed at NSF/ASU HREM facility under grant NSF-DMR-9115680.

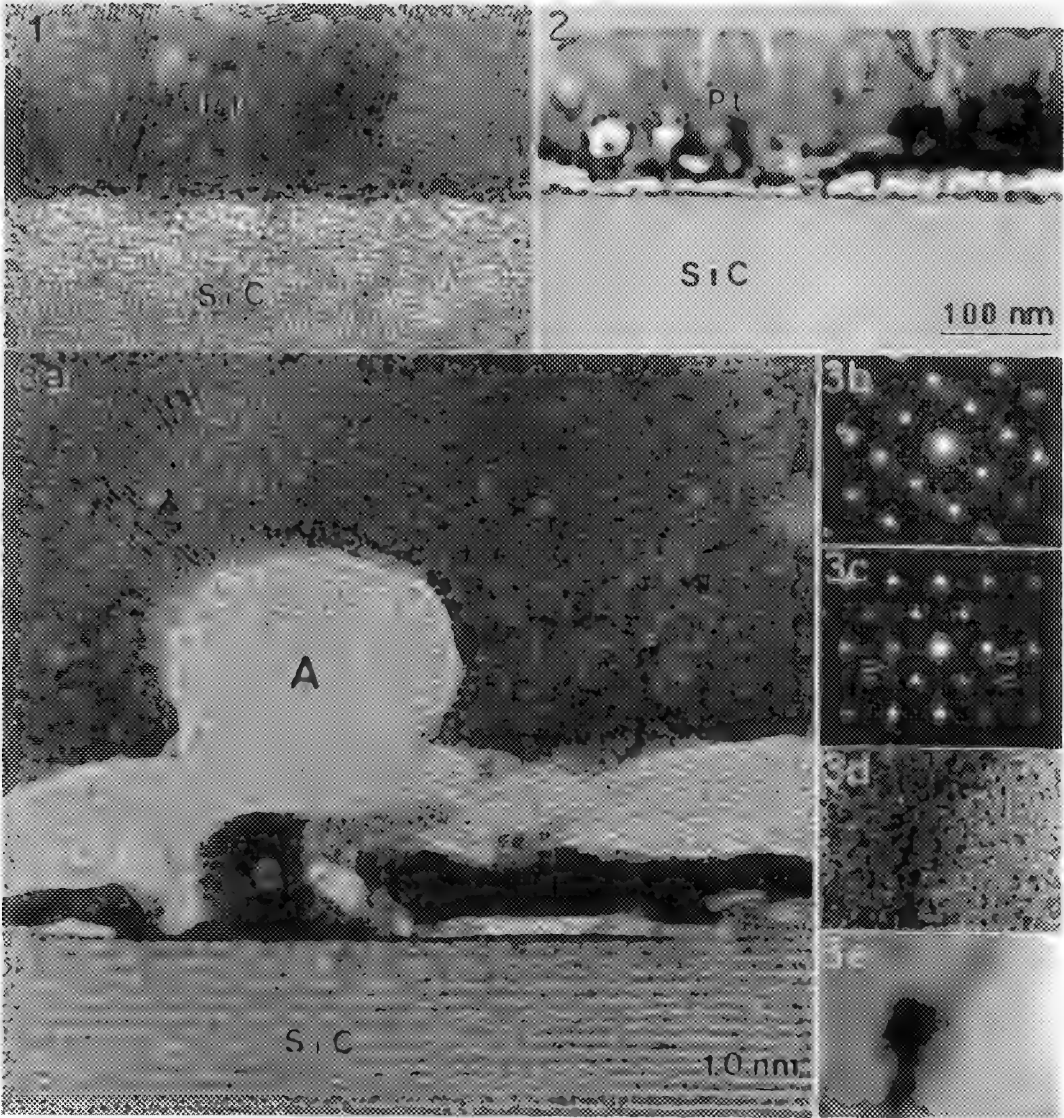


Fig.1 HREM image of as-deposited Pt/6H-SiC.
 Fig.2 TEM micrograph of 750°C / 20 min. annealed Pt/SiC.
 Fig.3 (a) HREM image of 750°C / 20 min. annealed Pt/6H-SiC, (b) microdiffraction pattern of Pt, (c) microdiffraction pattern of "C" in (a), arrowed spots are of 6H-SiC, (d,e) EELS mapping of carbon and silicon respectively (reduced magnification, 55° anti-clockwise rotated)

HREM OF EPITAXIALLY GROWN Fe/TiO₂ AND Cu/TiO₂ INTERFACES

P. Lu and F. Cosandey

Department of Materials Science and Engineering, Rutgers University, Piscataway, NJ 08855

High-resolution electron microscopy (HREM) has been used to provide information on atomic structures of metal/oxide interfaces, which are of both scientific and technological interest.¹ In this report, we present results of a study on Fe/TiO₂ and Cu/TiO₂ interfaces by HREM. The Fe/TiO₂ and Cu/TiO₂ interfaces were formed by vapor deposition of Fe and Cu on TiO₂ (110) surface, respectively, in a UHV chamber with a base pressure of $\sim 1 \times 10^{-10}$ torr.² Cross sectional HREM specimens were prepared using standard techniques involving mechanical polishing, dimpling and ion-milling. The samples were examined in an Topcon-002B high-resolution electron microscope. HREM simulations were performed using the EMS program.³

Figs. 1a and 1b show a HREM micrograph and a select area diffraction pattern of Fe/TiO₂ interface, respectively, taken along the TiO₂ [001] direction. From Fig.1a and Fig.1b, the following orientation relationship is obtained: [001]Fe//[001]TiO₂ and (100)Fe//(110)TiO₂. With this orientation, there is about 12.6% lattice misfit along the TiO₂ [1 $\bar{1}$ 0] direction. The interface is atomically flat and free of any interfacial phases. Despite the large lattice misfit present between the Fe and TiO₂, the interface is partially coherent and contains a high density of dislocations. The dislocations, visible in Fig.1, have a projected Burgers vectors of $1/2\langle 110 \rangle$. The strain field associated with the interfacial dislocations are present mainly in the Fe lattice.

Figure 2a is a HREM micrograph showing Cu epitaxially grown on (110) TiO₂ substrate. A select area diffraction pattern from the interface is shown in Fig.2b. The HREM micrograph and electron diffraction pattern indicate that the Cu layer has an epitaxial orientation relationship given by [1 $\bar{1}$ 0]Cu//[001]TiO₂ and (111)Cu//(110)TiO₂. With this orientation, there are two equivalent domains in the film which are related by a 180° rotation about the substrate normal. Within each domain, the film also contains some stacking faults and microtwins on {111} planes, which are easily visible, as indicated in Fig.2a. The lattice misfit along the TiO₂ [1 $\bar{1}$ 0] direction is about 2%. The partial dislocations associated with the faulted plane termination might be responsible for misfit accommodation. The Cu/TiO₂ interface is atomically flat, sharp and free of any interfacial phases. Two interface structures are observed by HREM, which at the interface, give rise to either a dark line or a bright line in the image taken near scherzer defocus. These difference in image contrast are due to different TiO₂ surface structures corresponding to either O- or Ti- and O-termination. HREM simulations have been used to determine the atomic models for these two interfaces. As an example, Fig.3a shows an experimental image with in Fig.3b the interface model and in Fig.3c the corresponding simulated image. The interface in Fig.3 is found to be terminated by Ti- and O-atoms. A detailed study of interface structures is under way.⁴

References

1. "Metal-Ceramic Interfaces", Ed. M.Ruhle, A.G.Evans, M.F.Ashby and J.P.Hirth, Acta-Scripta Metallurgica Proc. Ser. Vol. 4, 1990.
2. B.L.Maschhoff, J.M.Pan and T.E. Madey, Surf. Sci. 259, 190 (1991).
3. P. Stadelmann, Ultramicroscopy 21, 131 (1987).
4. Thanks to Drs. U. Diebold, J.M. Pan and T.E.Madey for vacuum deposition of Fe and Cu film on TiO₂ substrate. This work is supported by the National Science Foundation under no. NSF-MRG-89-07553.

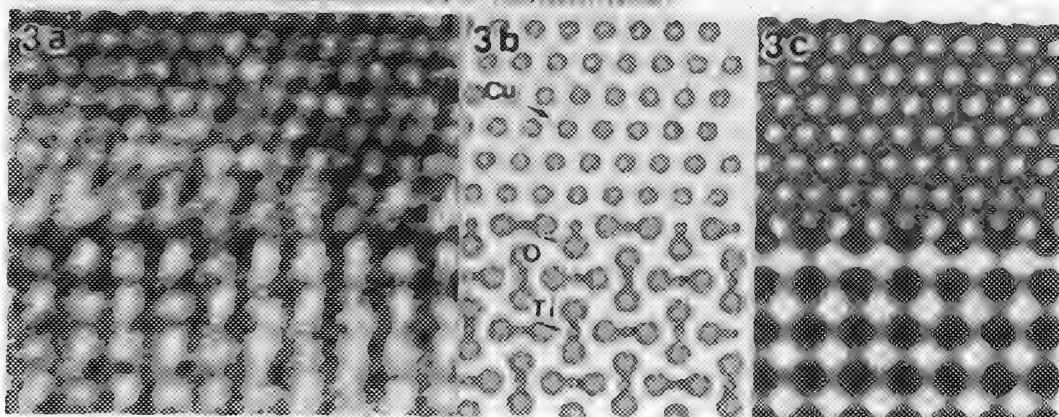
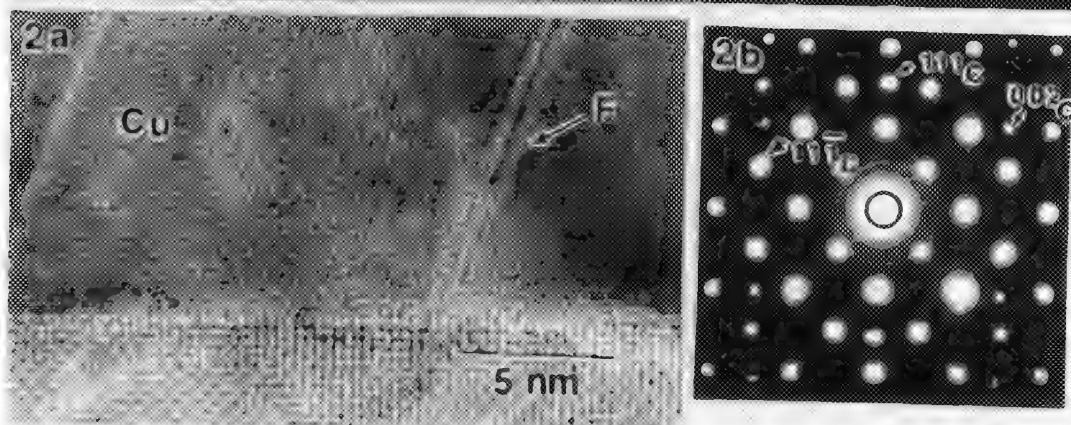
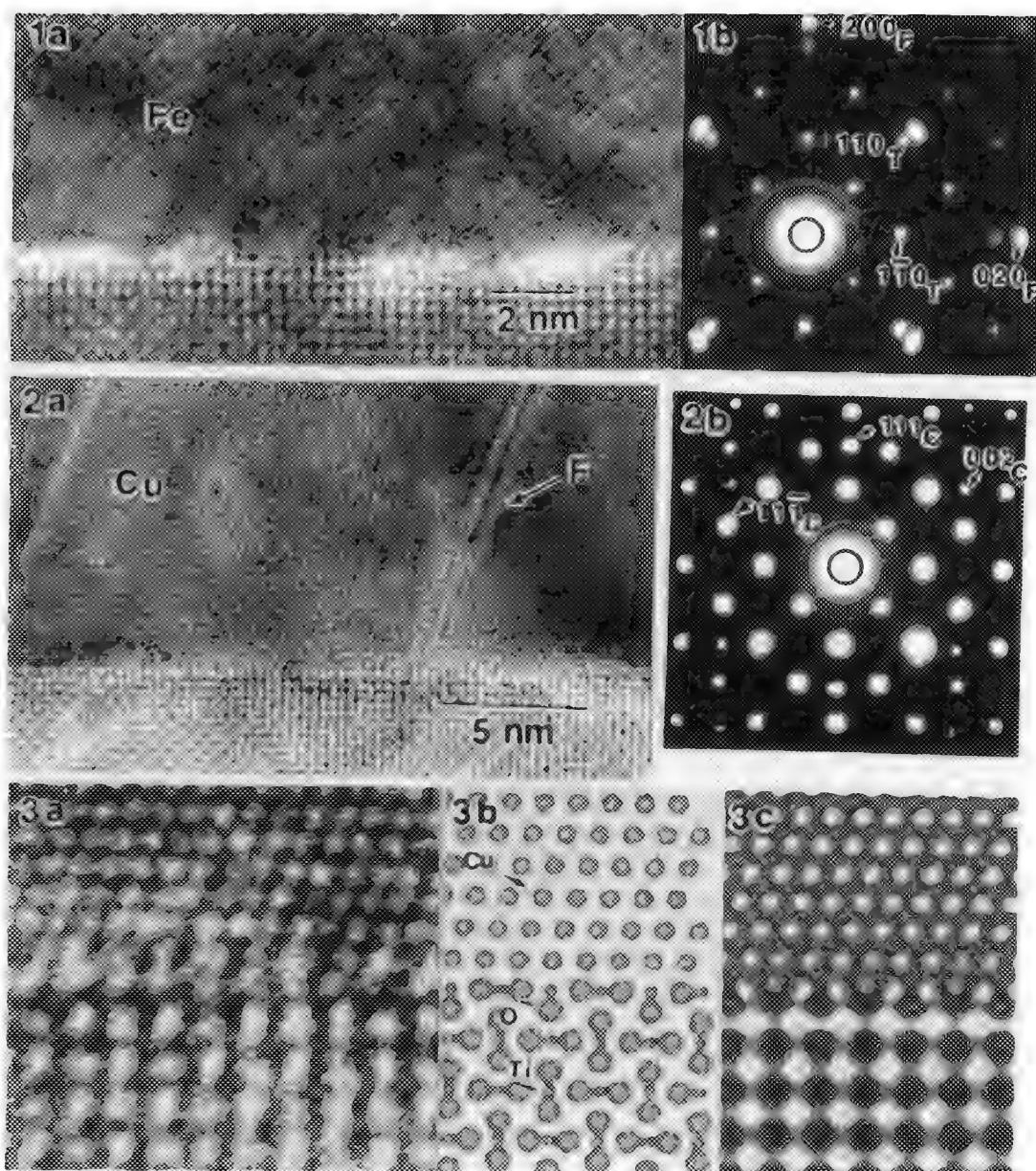


Fig.1 (a) HREM micrograph and (b) selected area diffraction pattern of Fe/TiO₂ interface taken in the TiO₂ [001] direction.

Fig.2 (a) HREM micrograph and (b) selected area diffraction pattern of Cu/TiO₂ interface taken in the TiO₂ [001] direction.

Fig.3 (a) HREM micrograph, (b) model and (c) simulated image of Cu/TiO₂ interface. The image simulation was carried out at a defocus value of about -30nm and a crystal thickness of 3.6nm.

ATOMIC STRUCTURES OF FACETED LOW-ENERGY Pd/Al₂O₃ INTERFACES

F. Cosandey*, P. Lu*, N. Brun^o and S. Hagege[#]

* Materials Science, Rutgers University, Piscataway NJ 08854, USA

^o Institut des Sciences des Matériaux, Université Paris-Sud, 91405 Orsay, FRANCE

[#] CNRS-CECM, 94407 Vitry-sur-Seine, FRANCE

Recently, it has been demonstrated that alpha alumina fibers having the stable trigonal structure can be grown in Pd by internal oxidation.¹ The alumina fibers are oriented with respect to Pd and exhibit strong faceting. In this paper, we present HREM results on the atomic structures of the faceted interfaces.

Oxidation experiments were done in air at 1000 °C for 48 hrs on a Pd-10.8 at. % Al alloy. Selected samples were subsequently annealed at 1000 °C for 0.5 hrs in an Al vapor. All HREM observations were done using a Topcon-002B high resolution microscope. For image analysis, the interfaces were modeled using EPITAX² and multislice image simulations were performed using EMS³ programs.

The alumina fibers grown by internal oxidation, grow along the <110>Pd oxidation front direction. The orientation relationship between Al₂O₃ fibers and Pd is not unique, however, most fibers are faceted with primary low energy interfaces between Pd and Al₂O₃ corresponding to (110)//(0001), (111)//(0001) and (111)//(11-20). Other secondary facets are also observed corresponding to (001)//(11-20) and (113)//(11-22).

A fourier filtered HREM image of a (110)//(0001) Pd/Al₂O₃ interface taken along the common <110>//<1-100> direction is shown in Fig. 1a. This image, taken at a defocus value of ~45 nm, was obtained for a sample annealed in oxygen. The (110) Pd interface is tilted with respect to (0001) Al₂O₃ by an angle of 3.5°. This misorientation angle give rise to a tilted interface which minimize interfacial misfit. In addition, all images reveal an open structure with a large rigid body expansion normal to the interface. This large volume expansion give rise, at larger defocus values, to a strong fresnel contrast⁴, whose effect on atomic image contrast, can be minimized by the filtering process. A rigid sphere supercell model of this tilted interface is shown in Fig. 1b with, in superposition, the simulated image obtained for a defocus value of ~43 nm and a sample thickness of 6.9 nm. The (0001) Al₂O₃ surface is polar and terminates, at the interface, by an oxygen layer. In the simulation, an additional white contrast is also observed which is caused by the open structure of this interface.

A fourier filtered HREM image of a (111)//(11-20) Pd/Al₂O₃ interface taken along the common <110>//<1-101> direction is shown in Fig. 2a. This interface was obtained for a sample annealed in an Al vapor. The unrelaxed rigid sphere model of this interface is shown in Fig. 2b. Under the imaging conditions of defocus value of ~40 nm and sample thickness of 6.2 nm, the white contrast in alumina corresponds to the open channels. The (11-20) Al₂O₃ surface is polar and terminates, at the interface, by an oxygen layer. In addition, the rigid body expansion normal to the interface is large and this displacement is accommodated to within the first three (11-20) Al₂O₃ atomic planes. Further refinements of the structures are in progress.⁵

References

1. F. Cosandey and P. Lu, Acta Met & Mater (1993) In Press
2. F. Guillet and S. Hagege, J. Appl. Cryst. (1991)24, 950.
3. P. Stadelmann, Ultramicroscopy (1987)21, 131.
4. F. Cosandey and P. Lu, Proc. 50th EMSA Meeting (1992),
5. Thanks to Pierre Stadelmann for his contribution to the image processing. This work was supported in part by the CNRS and by the National Science Foundation under grant # NSF-MRG-89-07553.

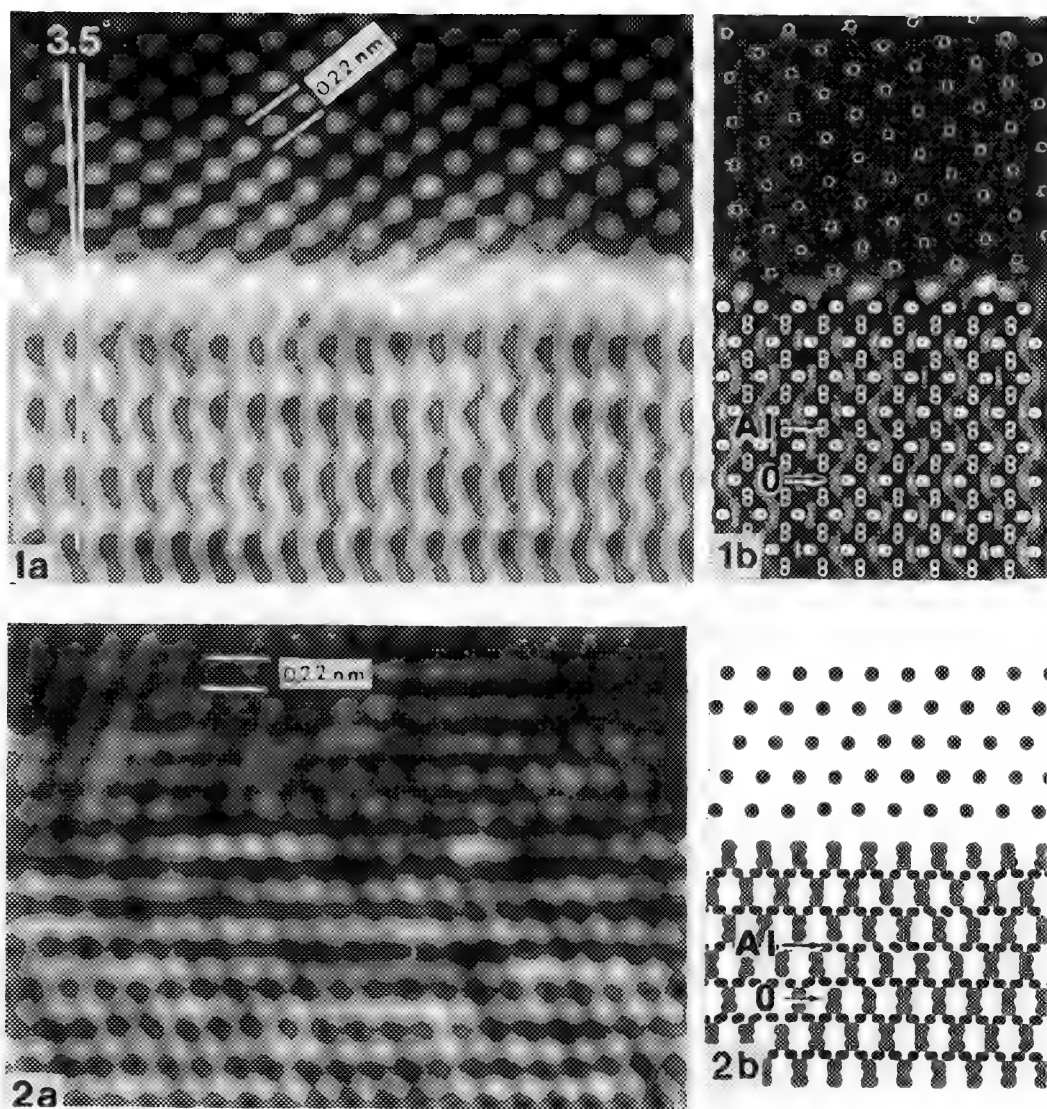


Fig. 1a. HREM image of a (110)/(0001) Pd/Al₂O₃ interface taken along the common $\langle 110 \rangle // \langle 1-100 \rangle$ direction and for a defocus value of ~ 43 nm with in Fig. 1b the supercell model of the interface superposed to a simulated image. Sample thickness ~ 6.6 nm and defocus value ~ 44 nm. Fig. 2a. HREM image of a (111)/(11-20) Pd/Al₂O₃ interface taken along the common $\langle 110 \rangle // \langle 1-101 \rangle$ direction and for a defocus value of ~ 40 nm with in Fig. 2b a rigid sphere model of the interface.

THIN-SPECIMEN PREPARATION FOR HETEROPHASE INTERFACES

C. E. Lyman, R. Anderson*, and T. Malis**

Dept. of Materials Science and Engineering, Lehigh University, Whitaker Lab, 5 E. Packer Ave., Bethlehem, PA 18015; *IBM ZIP E-40, Hopewell Junction, NY 12533; **Metals Technology Laboratories, CANMET, Ottawa, Ontario, Canada K1A-0G1

Imaging and analysis of heterophase interfaces in cross-sectional view requires demanding thin specimen preparation techniques. The term heterophase refers to the juxtaposition of a heavy and a light element or a metal and an insulator on either side of the interface. No single thinning method can be recommended for all such interfaces in all materials. In fact, the desired information might, of necessity, only be obtained by the use of several methods. This paper provides an overview of three different thinning methods for heterophase interfaces: conventional ion-beam thinning (IBT), tripod polishing (TP), and ultramicrotomy (UM).

The ideal thin specimen of a heterophase interface is rarely achieved. Regardless of the final thinning method, the information obtainable often depends on the mechanical alignment of the interface prior to final thinning. Typical alignment parameters are: 1) angle between interface and specimen surface, 2) crystallographic orientation about the normal to the interface, and 3) lateral location of thinned area along interface. Optimization of these parameters is obtained through appropriate specimen handling prior to the final thinning. In addition, several practical aspects must be considered that include total thinning time, amount of transparent area, final thickness at interface, temperature rise, mechanical damage, compositional integrity, subsurface artifacts, spurious coatings, and surface topography. The three methods under consideration each possess varying degrees of these qualities and thus are often complementary (Table 1).

For many years ion-beam thinning (IBT) of sandwiched cross-sectional specimens has been used to thin interfaces for TEM.¹ However, long thinning times in the IBT produced specimens with irregular topography, and in recent years mechanical polishing and dimple grinding have been used to reduce the time required under the ion beam. Precision alignment of the interface as described above has been generally left to the ingenuity of the investigator.

Recent hand polishing methods (TP) for cross-sectioning silicon integrated circuits are generally successful,² but thinning of specimens containing phases greatly dissimilar to silicon continues to provide challenges. Fortunately, the geometry and crystallography of VLSI structures are well-defined so that control of alignment parameters (1)-(3) above becomes a matter of using suitable jigs prior to and during final hand polishing. In the examples shown in Figure 1, the specimens were polished to a plane through the feature of interest, inverted and polished to 100 nm or less from the opposite side. No ion milling was necessary. The main use of ion milling in these cases is for cleaning the specimen and flattening the asperities in composite specimens via very low-angle milling (2°) for times of about 10 minutes. Although the TP method was developed for the preparation of Si-based VLSI structures, it has seen wide applicability in the preparation of metal, ceramic, mineral, and composite specimens.

Ultramicrotomy (UM) often can yield useful thin specimens where other methods fail.³ The process usually begins with embedding the material of interest in a hard epoxy. The alignment parameters (1)-(3) above are important in the embedding process; however, useful jigs for alignment of the interface again rely on the ingenuity of the individual investigator. Consider the example of an Al-SiC metal matrix composite (MMCs) for which no single thinning method works perfectly. Figure 2a shows that hundreds of thin sections may be cut from a trimmed block of embedded MMC using a diamond knife microtome, but only a fraction of these retain the second phase. A thin section containing a piece of SiC which remained attached to the matrix aluminum is

shown in Figure 2b. While sections containing such useful interface structure are rare, there are generally tens or hundreds of sections that may contain regions of interface. In less demanding MMC's such as Al-Al₂O₃, the proportion of usable interface rises significantly.

References

1. J. C. Bravman and R. Sinclair, *J. Elect. Microsc. Tech.* **1** (1984) 53.
2. J. Benedict, R. Anderson, and S.J. Klepeis, in *Specimen Preparation for Transmission Electron Microscopy of Materials - III*, MRS Sympos. Vol. 254, R. Anderson, B. Tracy, and J. Bravman (eds.), Materials Research Society, Pittsburgh, PA, (1992), p. 121.
3. T. Malis and D. Steele, *ibid.*, p. 257.

Table 1. Comparison of Practical Aspects of Three Interface Thinning Techniques

Characteristic	Ion-Beam Thin	Tripod Polish	Ultramicrotomy
Alignment of interface	Various methods	Easy with jigs	System dependent
Total preparation time	1-2 days	1/2 day	1-2 days
Transparent area	Moderate	Large	Moderate
Control of thickness	Moderate	Good	Good
Temperature rise	Often significant	Very small	None
Mechanical damage	Moderate	Small	Can be severe
Compositional integrity	Moderate	Good	Very good
Internal artifacts	Moderate	Moderate	Moderate
Surface topography	Often significant	Planar	Planar

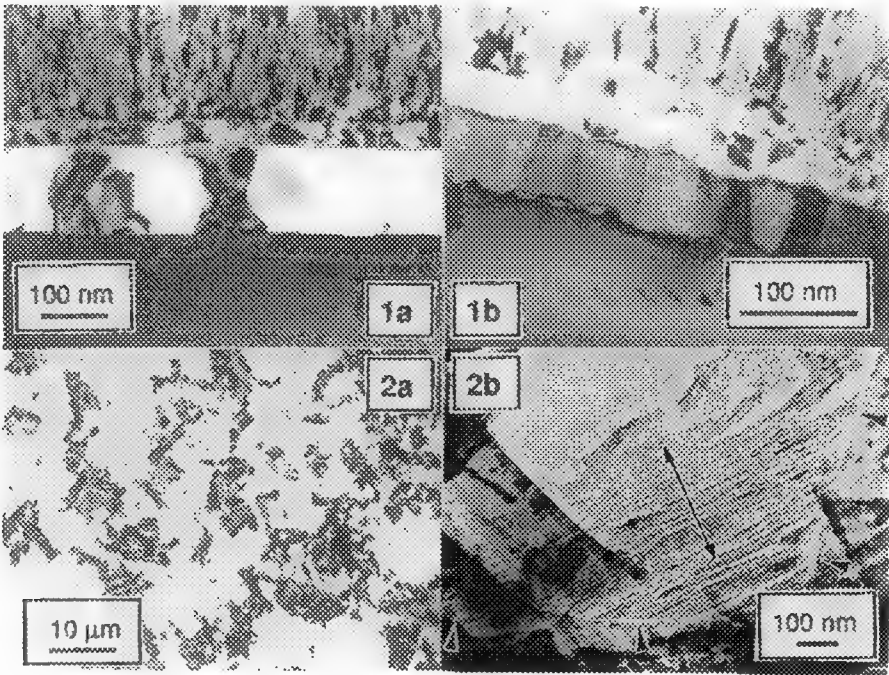


Figure 1. Examples of tripod polishing to electron transparency (<100nm thick) without ion milling. (a) stack of poly-Si, Ti, and Cr on Si substrate, (b) layers of Cr, Ti, and PtSi on Si.
Figure 2. Ultramicrotomy of Al-SiC metal matrix composite. (a) many random sections of similar thickness, (b) section showing usable interface (arrows) of SiC particle and Al matrix.

ULTRAMICROTOMY FOR STUDY OF INTERFACES AND COATINGS

G. Williams and T. Malis

Metals Technology Laboratories, CANMET, 568 Booth St., Ottawa, Canada K1A 0G1

While grain and phase boundaries in conventional alloys are examined quite readily by classic TEM specimen preparation methods such as electropolishing and ion thinning, the plethora of metal, ceramic and/or polymer combinations in many advanced materials have proven to be a much stiffer challenge. Whether in the form of composites, coatings, multilayers or thin films, such material systems have given rise to newer methods such as low angle ion thinning, mechanical (tripod) polishing to electron transparency and diamond knife sectioning. The damage incurred during the latter method may be offset by the advantages of a controlled thickness which is fairly insensitive to the type of material.

Fig. 1 demonstrates that the high degree of deformation generated in ductile materials by no means prohibits conventional grain boundary imaging due to the substantial degree of dislocation self-recovery which generally occurs in thin sections. Alloy phase boundaries also are amenable to examination after sectioning, although the particle/matrix interface may debond somewhat as the hardness difference increases. When the second phase becomes, in fact, a very hard composite reinforcement as found in metal matrix composites (MMC's) the challenge begins in earnest. As noted in an overview elsewhere in this proceedings¹, the ceramic reinforcement generally shatters upon sectioning and falls out of the section. Nonetheless, even for the most demanding cases, such as SiC-reinforced Al, some regions can be found where significant portions of the phase interface are retained². Fig. 2 shows an Al₂O₃-reinforced commercial Zn-Al alloy where, not only were many particles largely retained, but the complex, multiphase alloy matrix was rendered much more suitable for visual examination, elemental mapping, line profiles and the like by the uniformity of the thin section.

"Natural" coatings (eg corrosion products and oxides) have long been studied by way of ultramicrotomy³, where matrix damage does not interfere visually and the coating may have less damage by virtue of its more brittle and/or amorphous nature. Fig. 3 shows a thin corrosion layer on pure Mg where the severe shear lamellae of the Mg does not carry over to the corrosion layer. 'Artificial' coatings, such as on galvanized steel⁴, or the composite coating on a polymer substrate shown in Fig. 4, do suffer from a tendency to debond from the substrate. With reasonable care, enough useful portions of the coating can be retained to accomplish both the visual and microchemical goals of a research task.

Some specific measures which can enhance the chances of producing useful interface regions are:

Grain or twin boundaries:

- for ductile metals, experiment with different thicknesses to obtain a low defect density. For HREM, moderate heating of very thin sections may reduce the density even more.

Phase boundaries:

- anodic attack of matrix and or particle with respect to the water bath can occur in many material systems. Rapid section collection may prove sufficient. If not, dry sectioning is an alternative.

Composite interfaces:

- resist the urge to shape very hard MMC's into a suitable block by 'brute force' methods such as grinding. The material may work harden and/or microcrack to the point where the section disintegrates as fast as it is cut. A diamond saw is crucial for rough trimming and a worn diamond knife is usually essential for forming the facet. The sectioning knife should be cleared of 'debris' from shattered reinforcing particles periodically. Sectioning of a soft metal (eg Al) may serve this purpose well.

- retention of reinforcing phase appears to be higher with 55° conventional diamond knives and the so-called histo knives which are more economical (if somewhat more likely to produce knife marks)⁴.

Coatings and films:

- perform final trimming with care and inspect the coating/substrate interface optically. If trimming has caused debonding visible on this scale, usually the entire interface 'unzips' during sectioning. Retrim.

- our preference is to section with the coating roughly perpendicular to the knife edge, thereby preserving structure and geometry at the expense of portions invariably being torn away. (The parallel orientation

can produce substantial compression and debonding of the entire interface). A slight inclination from the perpendicular (coating to impact the knife edge first) may lessen the force normal to the interface.

- debonded fragments may be saved by use of coated grids, but beware of support film decomposition⁵.
- if there is a suspicion of outer layers spalling away, Au-coating prior to sectioning is useful (Fig.3).

References

- 1.C.E. Lyman et al, these proceedings.
- 2.T.F. Malis & D. Steele, Spec. Prep. for TEM of Materials, Mat. Res. Soc. Symp., 199 (1990)
- 3.J.D. L'Ecuyer et al, Proc. 12th Int. Congress Electron Microscopy, 4 (1990) 1036.
4. T. Malis, Proc. 50th EMSA Meeting (San Francisco Press, 1992) 390. Also, with G. McMahon, these proceedings.
- 5.T. Malis & D. Steele, Spec. Prep. for TEM of Materials III, Mat. Res. Soc. Symp., 254 (1992) 257.

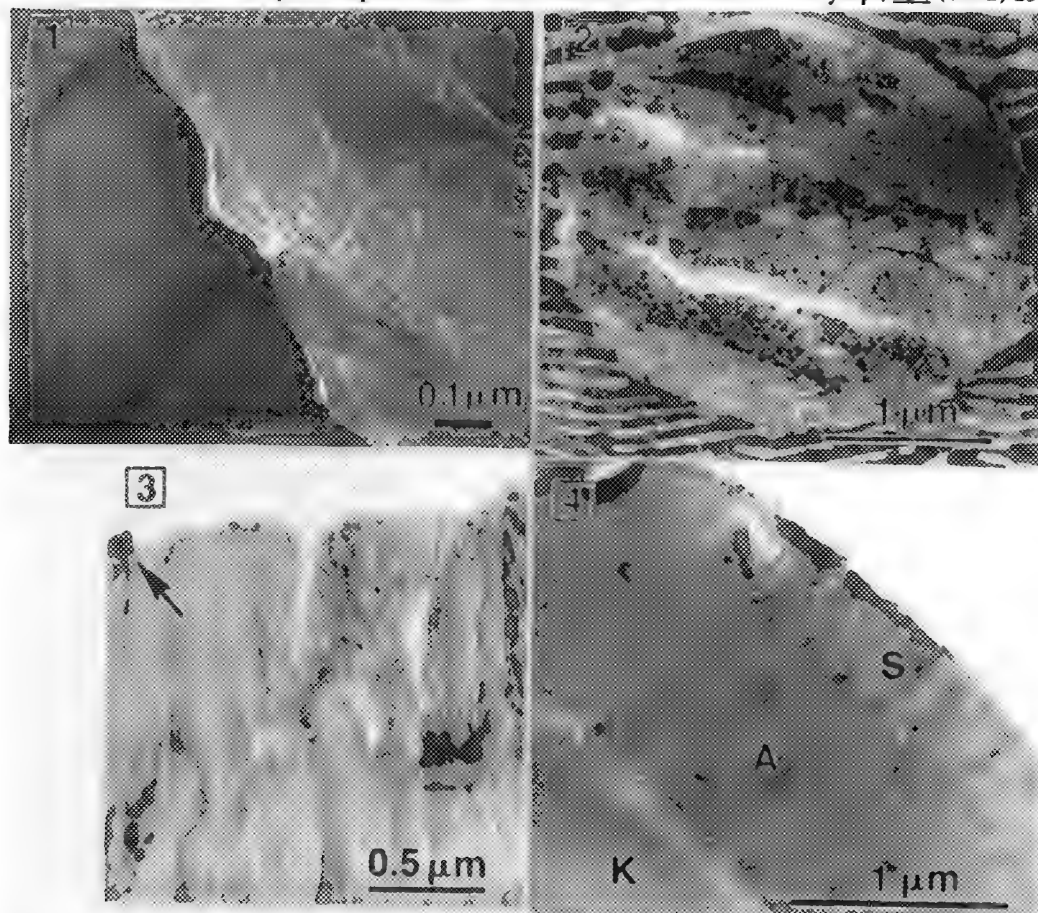


Fig.1 Weak beam image of tilt boundary and adjacent grain in pure Al. Section thickness ~90nm.
 Fig.2 Good Al_2O_3 particle retention in an MMC with a Zn-28Al (eutectic) matrix. Thickness ~ 80nm.
 Fig.3 Corrosion layer and corrosion pit on Mg. Remnant of Au-coating to mark surface is arrowed.
 Fig.4 Composite coating of silica (S) and alumina (A) on kapton (K). Section thickness ~70nm.

THE USE OF TRANSMISSION AND ANALYTICAL ELECTRON MICROSCOPY IN STUDYING REACTIONS AND PHASE TRANSFORMATIONS IN THIN FILMS

K. Barmak

Department of Materials Science and Engineering, Lehigh University, Whitaker Laboratory, 5 East Packer Avenue, Bethlehem, PA 18015

Generally, processing of thin films involves several annealing steps in addition to the deposition step. During the annealing steps, diffusion, transformations and reactions take place. In this paper, examples of the use of TEM and AEM for *ex situ* and *in situ* studies of reactions and phase transformations in thin films will be presented.

The *ex situ* studies were carried out on Nb/Al multilayer thin films annealed to different stages of reaction. Figure 1 shows a multilayer with $d_{\text{Nb}} = 383$ and $d_{\text{Al}} = 117$ nm annealed at 750°C for 4 hours. As can be seen in the micrograph, there are four phases, Nb/Nb_{3-x}Al/Nb_{2-x}Al/NbAl₃, present in the film at this stage of the reaction. The composition of each of the four regions marked 1-4 was obtained by EDX analysis. The absolute concentration in each region could not be determined due to the lack of thickness and geometry parameters that were required to make the necessary absorption and fluorescence corrections. Instead, the NbAl₃ and Nb were used as internal composition references, i.e., the Nb was taken as essentially pure Nb (<0.5 at.% Al) and the composition of the NbAl₃ was fixed at 75 at.% Al. The relative compositions of the other two phases, Nb_{3-x}Al and Nb_{2-x}Al, were then corrected using these internal standards and are plotted in figure 1(b). This procedure allowed us to confirm the presence of four phases rather than three (Nb, Nb_{3-x}Al, and NbAl₃) that had been observed by x-ray diffraction analysis alone. Since the presence of the sigma Nb_{2-x}Al phase affects the composition of the superconducting Nb_{3-x}Al phase, a knowledge of its presence is important. This knowledge was obtained through the use of TEM and AEM.

In addition, TEM was critical in revealing the unusual morphology of the reaction front between the NbAl₃ phase and the sigma Nb_{2-x}Al phase. Figure 2 is a micrograph from a multilayer with $d_{\text{Nb}} = 342$ and $d_{\text{Al}} = 158$ nm annealed to 930°C at 50°C/min. It can be seen that the consumption of NbAl₃ occurs by penetration of the sigma phase into the grain boundaries of the NbAl₃ phase resulting in radial shrinkage of the individual grains of NbAl₃. In kinetic models of thin film reactions it is often assumed that the reaction front is planar(e.g.²). The sample in figure 2 provides contrary evidence to this assumption and requires a non-planar model to describe the reaction kinetics.

In this study of Nb/Al reactions⁽¹⁾, TEM and AEM were critical in providing information on the number and relative composition of the phases present as well as the morphology of the reaction front. This was in addition to information on thickness and grain size of each phase. The TEM and AEM observations were used in conjunction with calorimetry, x-ray diffraction and superconducting measurements to provide a detailed picture of the phase formation sequence in these films.

Another way in which TEM can provide essential information in the study of phase transformations in thin films is through *in situ* hot stage studies of these transformations. The crystallization of codeposited amorphous Co_{0.33}Si_{0.67} films was studied by differential scanning calorimetry and *in situ* resistivity studies and it was shown that the Avrami exponent for the transformation was close to three⁽³⁾. This exponent can result either from a constant nucleation rate and two-dimensional growth or from three-dimensional growth from a fixed number of nuclei. Calorimetry and *in situ* resistivity studies cannot distinguish between these two processes, because these techniques do not provide separate information about nucleation and growth. However, *in situ* annealing of a 100 nm thick codeposited Co_{0.33}Si_{0.67} at 161°C in the microscope clearly showed that the number of crystalline grains reached a saturation value early in the crystallization process and remained almost unchanged during prolonged annealing (figures 3(a) and 3(b)). Consequently, the Avrami exponent of three could be unambiguously interpreted as three-dimensional growth from a fixed number of nuclei⁽³⁾.

In summary, the examples presented here show how TEM and AEM provide information on the presence of phases, their relative composition, the morphology of reaction fronts, nucleation and growth modes and microstructural features such as grain size and layer thickness. Thus, TEM and AEM

contribute greatly to the study of phase transformations and reactions in thin films and are expected to play an even greater role as film dimensions decrease.

REFERENCES

1. K. Barmak, K.R. Coffey, D. A. Rudman, S. Foner, J. Appl. Phys. **67**(1990)7313.
2. U. Gösele, K.N. Tu, J. Appl. Phys. **53**(1982)3252.
3. Q.Z. Hong, K. Barmak, L.A. Clevenger, J. Appl. Phys. **72** (1992)3243.

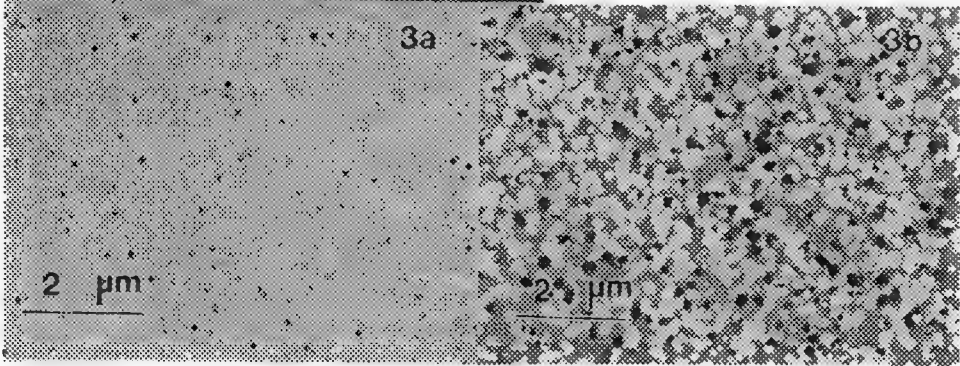
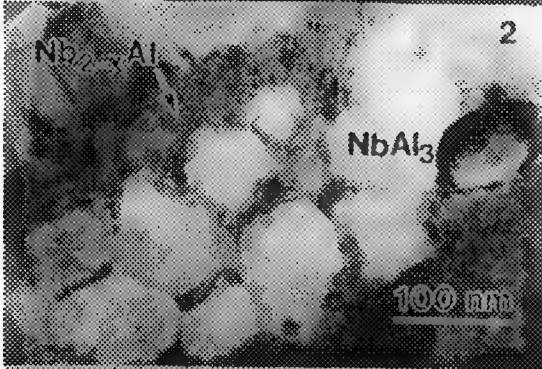
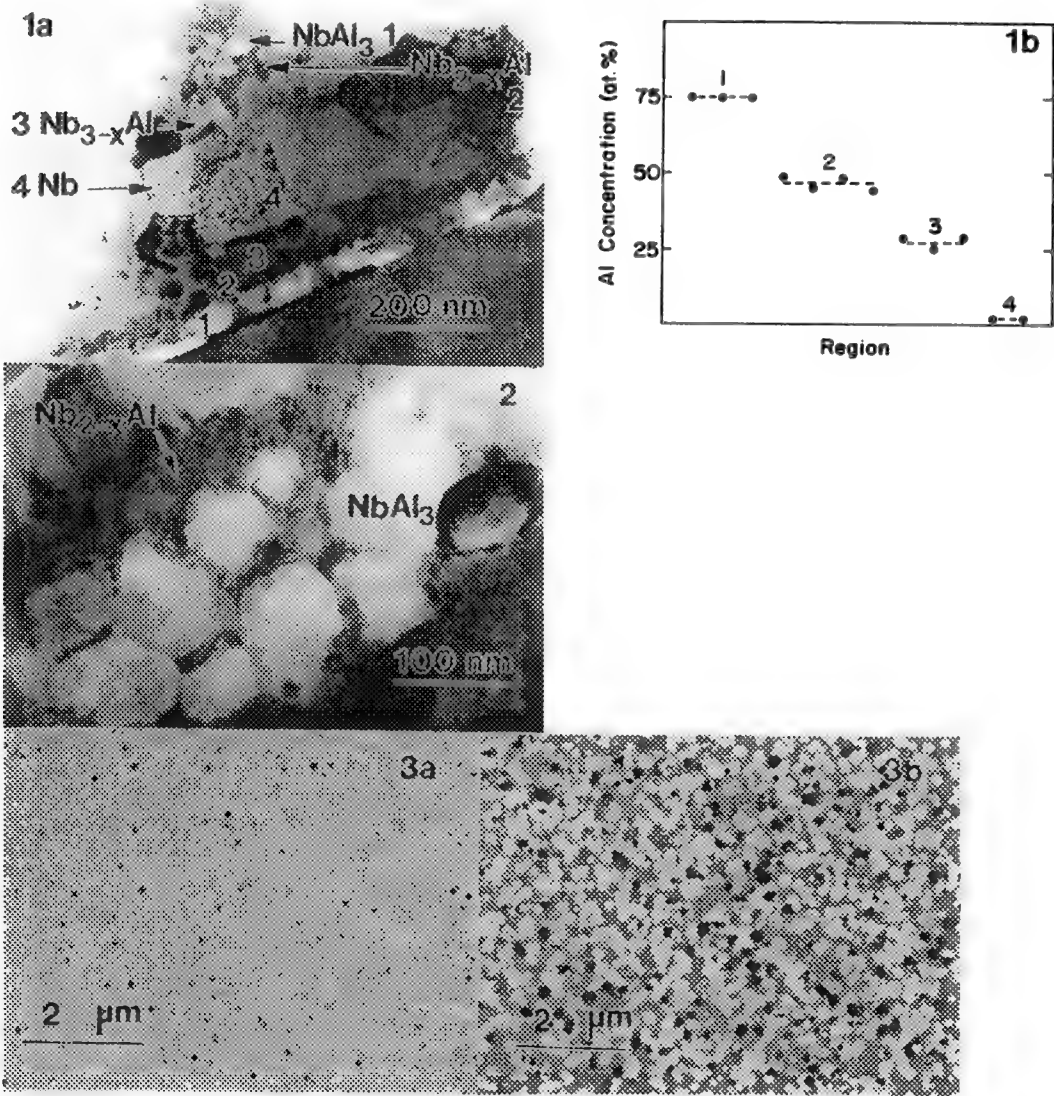


Figure 1 - (a) Cross-sectional micrograph of a Nb/Al multilayer with $d_{Nb} = 383$ and $d_{Al} = 117$ nm annealed for 4 hours at $750^{\circ}C$. (b) EDX analysis of regions 1-4 of (a).

Figure 2 - Cross-sectional micrograph of a Nb/Al multilayer with $d_{Nb} = 342$ and $d_{Al} = 158$ nm annealed to $930^{\circ}C$ at $50^{\circ}C/min$.

Figure 3 - *In situ* bright-field images of 100 nm thick $Co_{0.33}Si_{0.67}$ film annealed at $161^{\circ}C$ for (a) 5.5 and (b) 15.5 min.

NUCLEATION AND INITIAL GROWTH OF Pd₂Si CRYSTALS ON Si(111)

Xianghong Tong, Oliver Pohland and J. Murray Gibson

Department of Physics/Material Research Laboratory, University of Illinois at Champaign-Urbana, 104 S. Goodwin Av., Urbana, Illinois 61801

The nucleation and initial stage of Pd₂Si crystals on Si(111) surface is studied in situ using an Ultra-High Vacuum (UHV) Transmission Electron Microscope (TEM). A modified JEOL 200CX TEM is used for the study. The Si(111) sample is prepared by chemical thinning and is cleaned inside the UHV chamber with base pressure of 1×10^{-9} τ . A Pd film of 20 Å thick is deposited on to the Si(111) sample in situ using a built-in mini evaporator. This room temperature deposited Pd film is thermally annealed subsequently to form Pd₂Si crystals. Surface sensitive dark field imaging is used for the study to reveal the effect of surface and interface steps.

The initial growth of the Pd₂Si has three stages: nucleation, growth of the nuclei and coalescence of the nuclei. Our experiments shows that the nucleation of the Pd₂Si crystal occurs randomly and almost instantaneously on the terraces upon thermal annealing or electron irradiation. Surface defects are not found to act as nucleation centers. Experiments has also been done on samples with dislocation and stacking faults. The stacking faults are found not to affect the nucleation of Pd₂Si in any way. Surface steps and SiC pinning sites, however, affect the nucleation of the Pd₂Si crystals. The nucleation sites are observed to occur mostly on the flat terraces and a zone of no nucleation is observed along the steps. The strain field caused by the surface steps is believed to play an important role in determining the preferred nucleation sites.

Once the Pd₂Si nuclei are formed, they start to grow epitaxially on the substrate. The final size of the second stage is limited by the strain caused by the mismatch between Pd₂Si and the Si(111) substrate. The strain energy starts to build up with the size of the grain until it is energetically unfavorable to continue to increase the size. The measured Pd₂Si grain size at this stage are about 70-90Å. This is just the right size predicted from the bulk values of the misfit before misfit dislocations will have to be introduced to release the strain. An activation barrier for the introduction of a misfit dislocation can only be overcome by further annealing.

In situ real time experiments shows that the Pd₂Si grains grows by coalescing on further thermal annealing. This is the third stage of Pd₂Si growth. This is different from previous models which proposed that the Pd₂Si crystal grows by interfacial step propagation¹, or layer by layer². However, the growth mode may be thickness and /or deposition condition dependent.

References:

1. D. Cherns, Phil. Mag., (1981)A 55, 107.
2. P. A. Bennett et al, Physical Review Letters, (1992)69, 2539
3. This project was supported by DOE grant DEFGO2-91ER45439/11

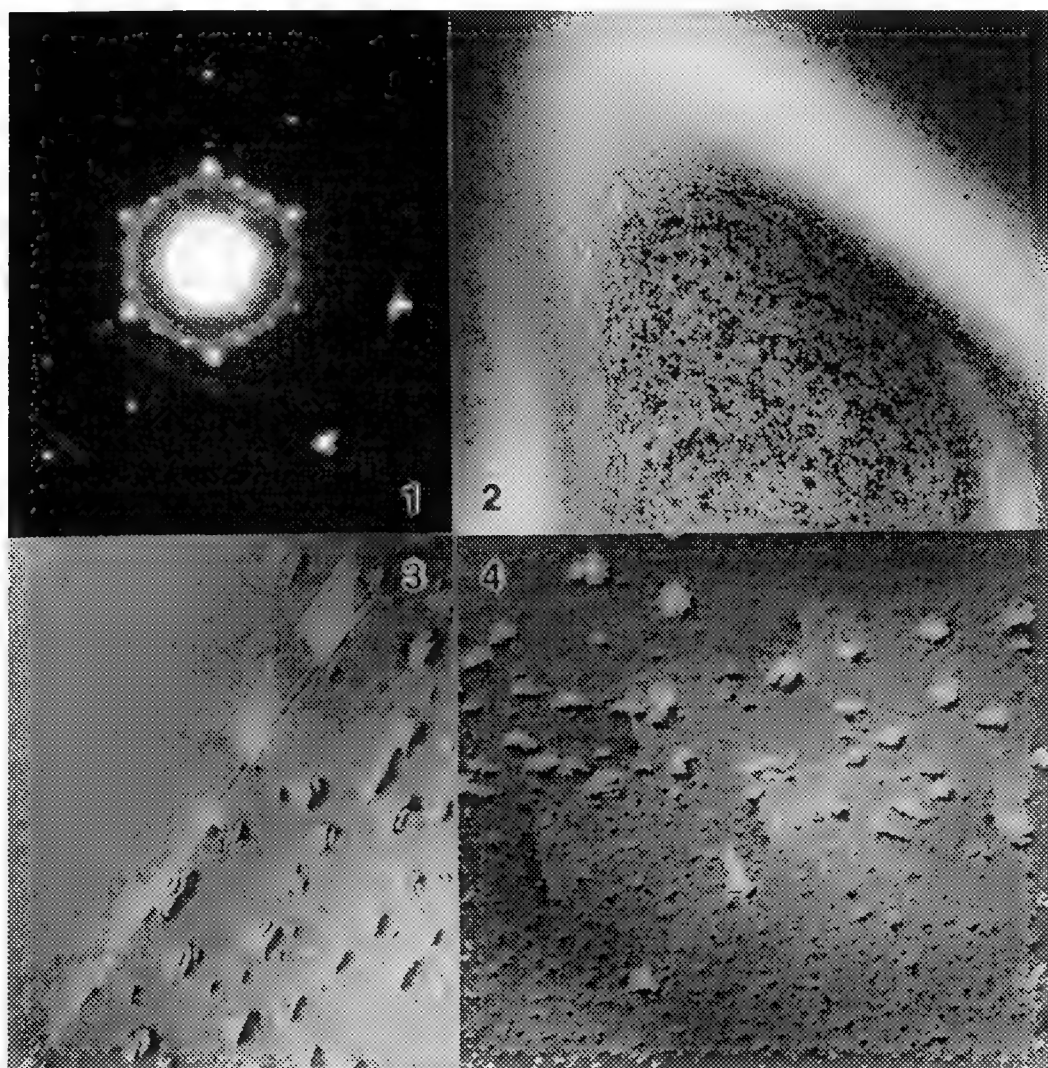


Fig. 1.--Diffraction pattern of Pd₂Si nuclei of size 70Å-90Å at the interface of 20Å of Pd film and Si(111) substrate.

Fig. 2.--Dark field image of Pd₂Si nuclei. Notice that the lines formed along the steps.

Fig. 3.--Pd₂Si grains near a stacking fault. Shows that the stacking fault does not affect the formation of the Pd₂Si crystals.

Fig. 4.--Pd₂Si grains near dislocations.

ORIENTATION RELATIONSHIP BETWEEN Γ PHASE AND α -FE IN COMMERCIAL GALVANNEAL STEEL COATING

C. S. Lin

Department of Materials Science and Engineering
Northwestern University, Evanston, IL 60208

The steel coatings' forming technology and their resulting mechanical performance are of primary concern to the automobile and appliance industries, for they determine directly the long-term structural integrity of the final products. In automobile industry, steel coating plays a crucial role for extended warranty of their product. The recent trend in coatings is an increase in galvanized coatings.

The iron-zinc compound coatings produced by galvannealing bring about a dramatic improvement, in terms of coating performance, compared to pure zinc coatings. The improvement includes corrosion resistance, weldability and paintability in addition to energy and material efficiency. However, there is still one serious obstacle which prevents the industry-wide use of galvannealing as the dominant steel coating technology: Its powdering and flaking tendency during press forming processes. There are a number of empirical hypotheses which propose that the presence of various Fe-Zn intermetallic phases influences the powdering/flaking tendency of galvanized coatings [1,2,3,4]. Nevertheless, not enough microstructural information is available except those obtained by SEM and X-ray diffraction. The microstructural information in optimizing coating performance from TEM is essential. The scarcity of TEM microstructural information on galvanized coating is mainly due to difficulties encountered in sample preparation. To this end we have developed a reproducible cross-sectional sample preparation method based on a modification of the "sandwich" method, and using this, successfully obtained detailed interfacial, microstructural and phase information on galvanized steel coatings. A few examples are cited in this report.

Fig.1(a) and (b) show the $[111]$ zone selected area diffraction pattern(SADP) of α -Fe and Γ phases respectively. Noting the similarity between the configuration of most intense reflections $\{330\}$ ($d=2.137\text{\AA}$) in Γ phase and that of the $\{110\}$ ($d=2.027\text{\AA}$) reflections in α -Fe; it is suggested that the larger d-spacing of $\{330\}$ (compared to the d-spacing of $\{110\}$ of α -Fe) observed in Γ phase is resulted from the replacement of Fe by larger Zn atoms. The atomic arrangement of Γ phase is based on the α -Fe structure by this reason. The existence of low lattice misfit orientation relationship between Γ and α -Fe phases supports this assumption. Fig.2(a) shows the SADP taken from the interface between Γ phase and α -Fe. The orientation relationship between Γ/α -Fe was determined as $[100]_{\Gamma}/[130]_{\alpha\text{-Fe}}$ and $(013)_{\Gamma}/(001)_{\alpha\text{-Fe}}$. The lattice misfit calculated based on this relationship is about 1%, suggesting coherent bonding between Γ phase and α -Fe. Fig.2(b) shows a SADP from another region at Γ phase and α -Fe interface as shown in Fig.3. The orientation relationship between Γ/α -Fe was determined as $[\bar{1}11]_{\Gamma}/[\bar{1}12]_{\alpha\text{-Fe}}$ and $(330)_{\Gamma}/(110)_{\alpha\text{-Fe}}$. The lattice misfit calculated based on this relationship is 9.6%, suggesting semi-coherent interface between Γ phase and α -Fe at this region. The interface between Γ and δ phases appears to be incoherent. The shear-lap test indicates that the bonding strength between Γ phase and α -Fe is stronger than that between δ phase and Γ phase as expected from the coherence of these two interfaces. The observation indicates the path to improve powdering resistance of galvanized coatings, that is, the improved δ - Γ interface.

In this microstructural study of galvanized steel coating [5] not only have we accurately determined the presence of various Fe-Zn intermetallic phases, we also identify the orientation relationships between Γ phase and α -Fe phase. The development of a reproducible and widely applicable TEM cross-sectional sample preparation technique can now be available to study the microstructure of various galvanized coatings. Utilizing this technique, one can obtain a complete picture of how phase evolution of galvanized steel coating taking place in the various stages of galvannealing process. The

THE APPLICATION OF HIGH-RESOLUTION SEM AND EPMA TO THE STUDY OF COATINGS AND INTERFACES OF MATERIALS

Joseph I. Goldstein

Department of Materials Science and Engineering, Lehigh University, Bethlehem, PA 18015

Microchemical and micro-structural analysis are often required when characterizing coatings and interfaces in materials. For coatings the interface between substrate and coating and between coating and the surface are of particular interest. The scanning electron microscope (SEM) and electron probe microanalyzer (EPMA) are often employed in characterizing interfaces in materials particularly because solid samples can be studied and sample preparation is usually restricted to developing a suitable flat polished surface for analysis. Both these instruments are essentially the same although the EPMA is equipped with wavelength dispersive detectors (WDS) and is dedicated to quantitative microchemical analysis.

The spatial resolution for high resolution SEM where microstructural analysis of the surface is desired is now in many ways comparable to the transmission electron microscope (TEM). Magnifications of over 100,000 X are available in SEMs equipped with a field emission gun using the secondary electron mode. Figure 1 shows the interface region of a retained austenite region in the Tazewell iron meteorite shown in both TEM and SEM mode¹ and Figure 2 shows the morphology of crystals, 0.3 μm wide by 1.5 μm long containing ledges 30-50 nm wide in an electrodeposited Zn coating on a steel in both TEM and SEM mode². Although the SEM cannot provide information about the structure and composition of the various phases observed at high magnification, one can observe larger numbers of specimens since surface preparation is much easier.

The spatial resolution for micro-chemical analysis with the SEM-EPMA, at or near interfaces in coatings and multiphase samples, is about 1 μm both laterally across the polished surface of the sample and in depth. The spatial resolution is controlled by elastic scattering of the beam electrons by the solid sample. Although low accelerating voltage can be used to minimize the scattering, and low energy characteristic x-rays can be measured, sub-micron x-ray spatial resolution is rarely achieved with the SEM-EPMA. Spatial resolutions for microchemical analysis at the submicron can be achieved with x-ray analysis in the analytical electron microscope (AEM). This enhanced spatial resolution can only be obtained, however, by preparing electron microscope thin sections of coatings and specific interface areas. This preparation technique is very time consuming and in some specific systems extremely difficult to perform.

Figure 3 shows detailed x-ray microanalysis data across the interface of a chromium coating on a steel substrate³ and Figure 4 shows a similar type of diffusion profile across the two phase interface in a diffusion couple between two Cu-Al alloys⁴. Both of these examples show the use of x-ray microanalysis to determine both interface compositions and diffusion profiles in complex samples. Figure 5 shows the application of x-ray scanning to determine the distribution of Cr and Fe across the interface of a chromium coating on a steel substrate³ and the distribution of the light elements boron, B, and O at the bond interface between Ti and a borate glass⁵. With suitable data storage, pixel by pixel in the scan, quantitative chemistry can also be extracted micron by micron within the analysis area.

References

1. K. B. Reuter et al, *Geochem Cosmochim Acta*. (1988)52, 617.
2. C. A. Drewien, Ph D Thesis, Lehigh University, 1992.
3. B. J. Smith and A. R. Marder, *Surface Modification Technologies*, Warrendale, PA, TMS (1991)471
4. A. D. Romig and J. I. Goldstein, *Met. Trans.* (1983)14A,1224.
5. S. Saha and J. I. Goldstein, to be published, *Materials Res Soc.* (1993).

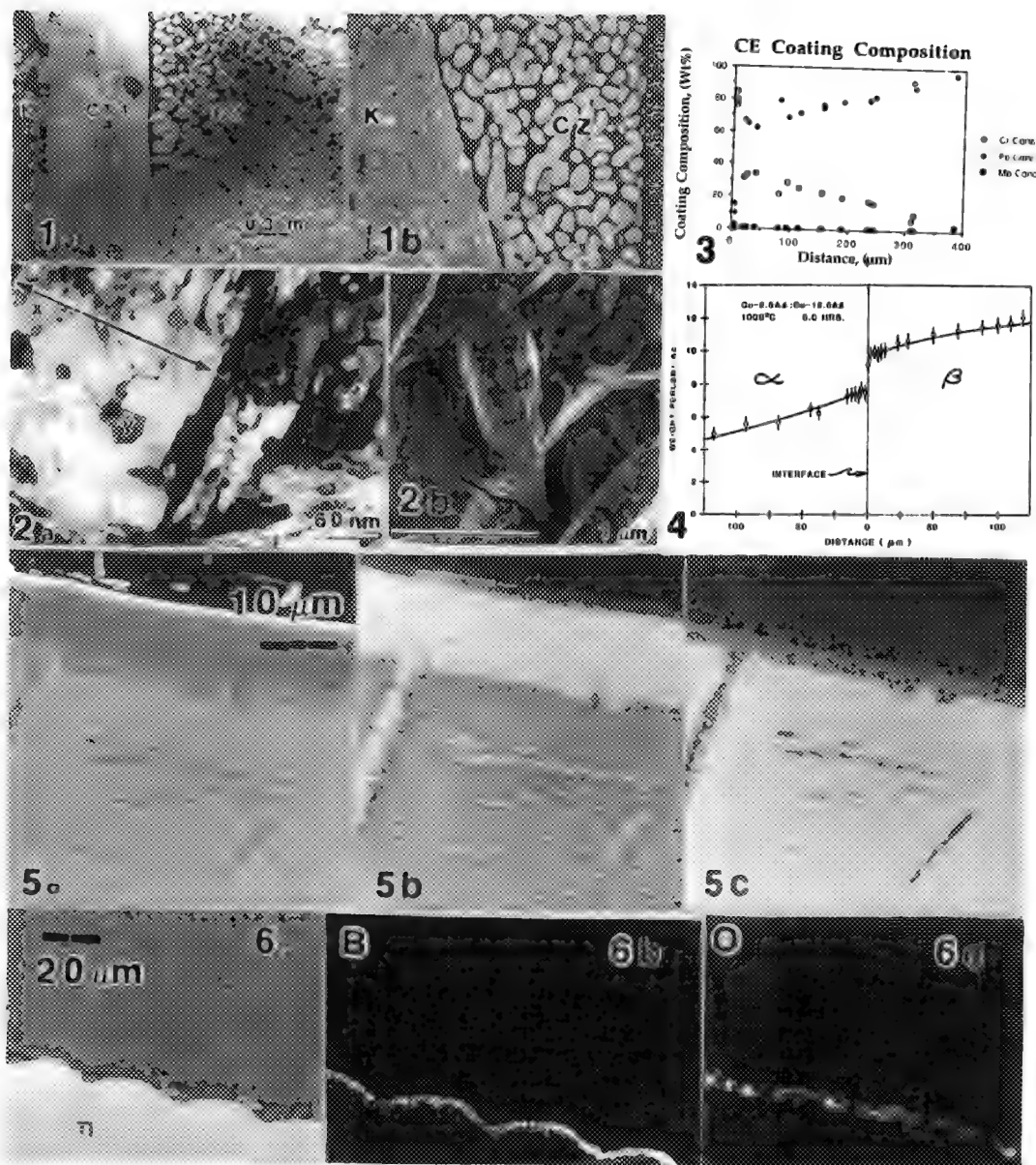


FIG. 1. --Metallography of Ni-rich taenite in the Edmonton iron meteorite. a) thin-foil TEM micrograph¹ b) field emission SEM micrograph of polished section
 FIG. 2. -- Micrographs of a 6wt% Fe-Zn coating on Fe. a) TEM b) field emission SEM
 FIG. 3. -- X-ray microanalysis trace across Cr coating on an Fe-Mo steel
 FIG. 4. -- X-ray microanalysis trace across interface of a Cu-2.5 wt% Al: Cu-12.5 wt% Al diffusion couple heat treated at 1000°C.
 FIG. 5. -- X-ray scanning photographs of Cr coating on an Fe-Mo steel: a) SE, b) Cr, c) Fe
 FIG. 6. -- X-ray scanning photographs of the interface in a Ti-B₂O₃ glass diffusion couple heat treated at 800°C for 48 hrs: a) Back Scattered Electrons, b) B, c) O.

MICROSTRUCTURAL CHARACTERIZATION OF A CORROSION-RESISTANT HYDROTALCITE COATING ON ALUMINUM

C. A. Drewien, C. R. Hills, and R. G. Buchheit

Materials and Process Sciences Center, Sandia National Laboratories, Albuquerque, NM 87185

Aluminum-lithium-hydroxycarbonate hydrate ($\text{Li}_2\text{Al}_4\text{CO}_3(\text{OH})_{12}\cdot 3\text{H}_2\text{O}$) or hydrotalcite coatings are novel corrosion resistant coatings being considered for replacement of environmentally sensitive chromate conversion coatings. Hydrotalcite coatings provide corrosion protection to aluminum alloys used in atmospheric environments.¹ In order to model the electrochemical corrosion behavior and to assess the impact of changing processing variables on the overall corrosion performance, a detailed baseline characterization of the microstructure was required.

Hydrotalcite coatings were formed by immersion of an 1100 aluminum alloy into a room temperature, alkaline bath of lithium carbonate and lithium hydroxide for 15 minutes. Microstructural characterization of the coating was performed using both scanning (SEM) and transmission (TEM) electron microscopy. In Figure 1a, the secondary electron image of the surface, obtained on a JEOL 6400 SEM operated at 15 kV, reveals a porous network of hydrotalcite crystals oriented perpendicular to the plane of viewing. In order to determine whether the pores were continuous to the substrate and to provide further characterization, cross-sectional TEM was performed. The TEM samples were prepared by cutting 10 mm x 3 mm wide slices from the hydrotalcite coated aluminum substrate. The coated surfaces were glued face-to-face under pressure with Epon 828 epoxy to form a block. After curing, slices were cut, ground through 1 μm diamond to a thickness of $\sim 200 \mu\text{m}$, and sectioned into 3 mm diameter disks. The disks were dimpled and then ion-milled to perforation. Thin foil samples were examined using a JEOL 2000 FX, operated at 200 kV and equipped with an EDS detector. The cross-sectional TEM micrograph in Figure 1b shows that the coating consists of two layers. The outer layer of the coating appears porous and is similar in appearance to the SEM images. In this region, which is up to 5 μm in width, only aluminum could be detected with EDS. The selected area diffraction pattern (SADP) in Figure 2a shows a ring pattern, indicating that the layer is composed of small crystalline regions. Indexing of the pattern was consistent with the hexagonal hydrotalcite structure. The inner layer adjacent to the aluminum substrate appears to be less porous and is 0.5 to 1 μm in width. Energy dispersive spectroscopy suggests that this region is aluminum-poor relative to the outer layer. In order to verify this layer is composed predominantly of light elements, further composition analysis using electron energy loss spectroscopy needs to be performed. The SADP in Figure 2b for the inner layer shows a nearly amorphous structure. Near the interface of the inner and outer layer, precipitates containing iron are observed. These are thought to be FeAl_3 precipitates that were originally part of the aluminum substrate.

Microstructural analysis has revealed that coating porosity is not continuous to the substrate, because of the presence of a uniform, more dense inner layer. Thus, an open pathway for the electrolyte to reach the substrate in a corrosion experiment is not provided, and any model of the coating should account for the porosity of the outer layer and the continuity of the inner layer. Electrochemical impedance experiments on the coating indicated that two resistive-capacitive loops exist for this coating. Two possible models of the coating and equivalent electrical circuits² are shown in Figures 3a and b. Microstructural characterization confirms that the model in Figure 3b is appropriate for this coating.³

1. R. G. Buchheit, G. Stoner, and M. Bode, submitted to Corrosion (1993).
2. K. Juttner et al., Corrosion Science, (1983) 2, 279.
3. This work was supported by U.S. Department of Energy under contract number DE-AC04-76DP00789.

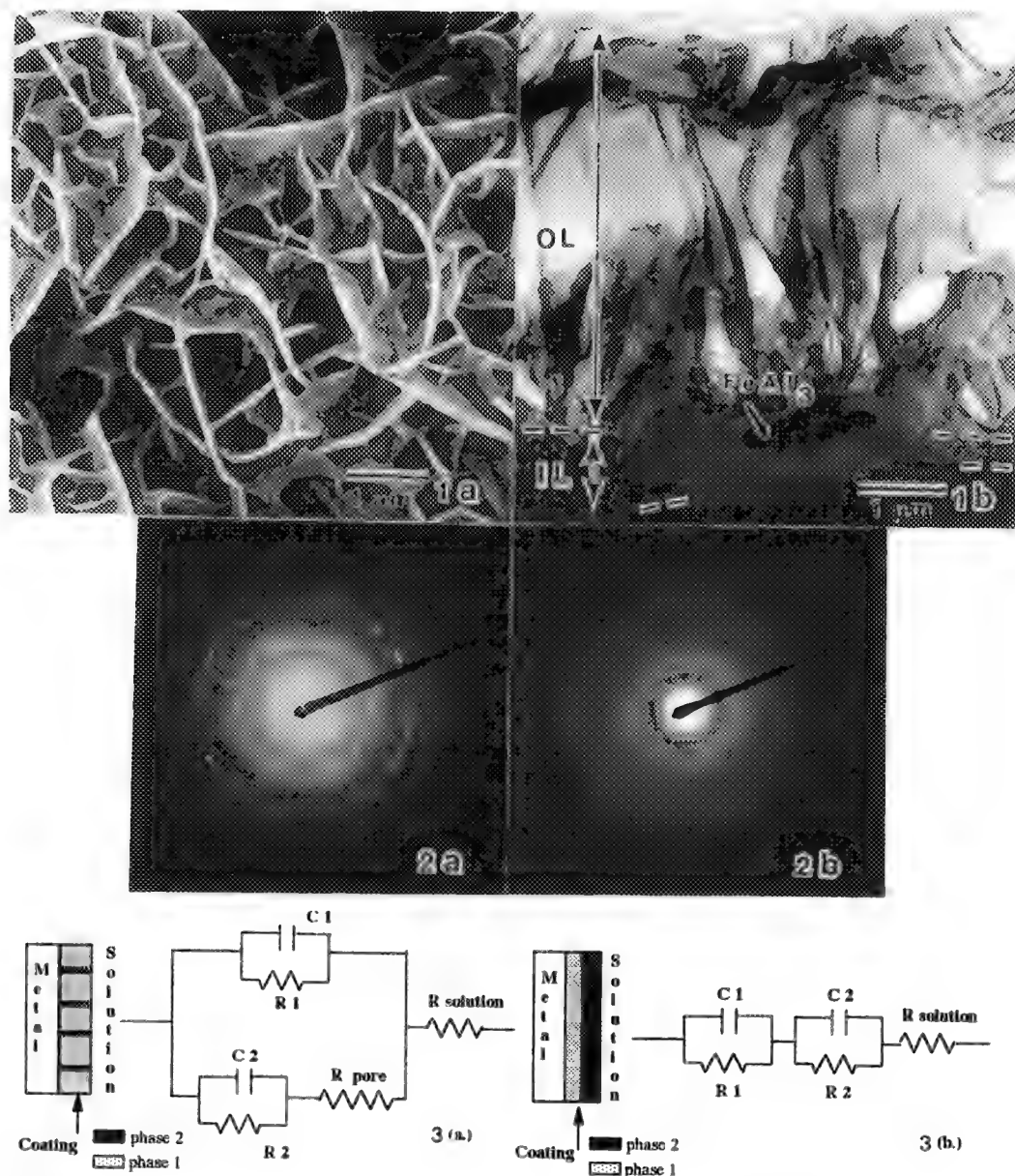


FIGURE 1.--a.) Secondary electron SEM image of coating surface and b.) cross-sectional TEM image of coating and substrate. Dashed line shows boundaries of inner layer (IL) and outer layer (OL).
 FIGURE 2.--Selected area diffraction patterns of a.) inner and b.) outer layers in coating.
 FIGURE 3.--Coating models and equivalent electrical circuit models for a.) a two phase coating whose phases are perpendicular to the plane of the substrate as in the case of porosity or pitting and b.) a two phase coating whose phases are parallel to the plane of the substrate.

ELECTRON MICROSCOPY OF PULSED-LASER-DEPOSITED THIN FILMS FOR TRIBOLOGICAL APPLICATIONS

Scott D. Walck, Jeffrey S. Zabinski, and Michael S. Donley

Materials Directorate, Wright Laboratory, WL/MLBT, Wright Patterson AFB, OH 45433-7750

Pulsed laser deposition (PLD) is a novel thin film deposition technique which has recently been applied to tribological materials with great success.¹⁻³ PLD has several inherent advantages over conventional deposition techniques, including excellent film adhesion, replication of target chemistry, and low film deposition temperature. Because load-bearing materials are typically hardened, heat treated alloys, these properties of PLD are ideally suited for tribological applications. In addition to being a relatively simple deposition technique, considerable processing flexibility is inherent with PLD. Dense, nonporous, stoichiometric films of solid lubricants, such as MoS₂, have been grown having long wear lives with low coefficients of friction.¹ Hard coating materials, such as TiC, have been grown at room temperature that were polycrystalline and had excellent wear properties.⁴

A significant feature of pulsed laser deposited (PLD) thin films is the incorporation of spherical particles within the films. Figure 1 shows these particles embedded in a film of PLD MoS₂ deposited at room temperature. The number and size distribution of these particles depend on both the target material and laser deposition parameters. For PLD MoS₂ films, the presence of these particles is benign, however, their accumulation during film growth produces increasing surface topography with thickness that eventually leads to porosity. Figure 2 shows PLD films of MoS₂ and the particles in cross section. The origin of the surface topography is due to the hillocks which form over the particles due to the line-of-sight deposition process. The porosity which evolves in relatively thick films is seen in Figure 3. Figure 4 shows the same film in cross section. The transition from being fully dense to porous occurs at a thickness of approximately 450 nm. By decreasing the volume fraction of particles, thicker, fully dense films will result, but the tradeoff is reduced deposition rates.

Because the particles project their presence to the surface, the TEM can be used to determine the projected area of the particles in differential thicknesses of deposited films and correlate it to the evolution of porosity. A simple model which simulates the PLD growth process using a constant projected area fraction per unit of film thickness, A_{Δ} , indicates that the critical thickness for the onset of porosity occurs at a projected area fraction for the particles in the film, P_A , of about 35%. P_A as a function of thickness for constant A_{Δ} is given by the expression, $P_A(t) = 1 - \exp(-A_{\Delta} \cdot t)$.

Future aerospace applications will require sophisticated tribological materials for the broad range of temperatures and environmental conditions that they will encounter and will probably be in the form of engineered, thin film, composite coatings. PLD can be used for these coatings, but the deposition parameters which affect the microstructure and tribological properties must be understood.

REFERENCES

1. M. S. Donley et al., Surf. and Coat. Techn., 36, (1988) 329.
2. M. S. Donley et al., Lecture Notes on Physics, 389, New York, Springer-Verlag, (1991): 271.

3. M. S. Donley et al., in *Photons and Low Energy Particles in Surface Processing*, 236, Pittsburgh, MRS (1992) 461.
4. W. J. Sessler et al., submitted to *Surf. and Coat. Techn.*, 1992.

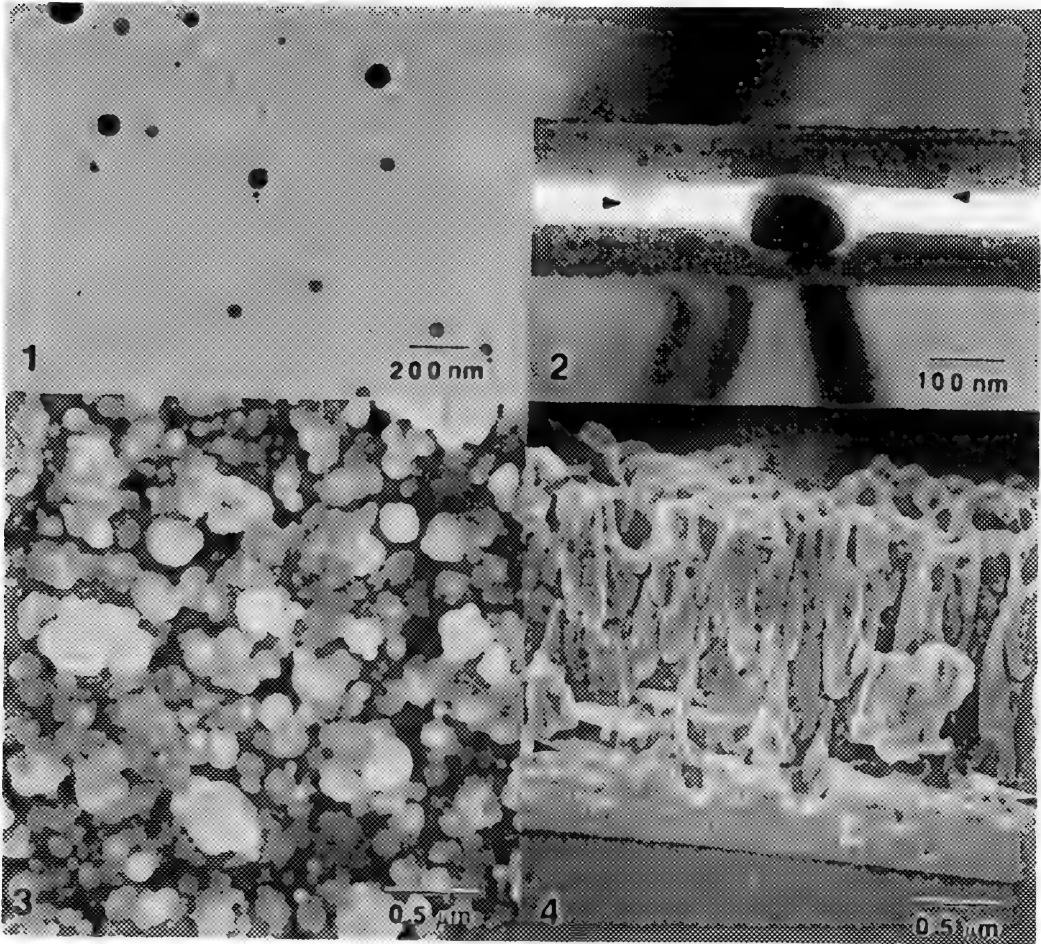


Fig. 1.--TEM of RT-PLD MoS₂ deposited on silicon. The spherical particles are crystalline and the film is amorphous.
 Fig. 2.--XTEM of RT-PLD MoS₂ deposited on silicon. The arrows indicate the surface protrusions from the embedded particles.
 Fig. 3.--SEM of 1900 nm of RT-PLD MoS₂ deposited on silicon.
 Fig. 4.--XSEM of 1900 nm of RT-PLD MoS₂ deposited on silicon. The arrows indicate 450 nm.

INTERGRANULAR SEGREGATION IN PRESSURE-VESSEL STEELS

M.G. Burke and E.A. Kenik*

Westinghouse Science & Technology Center, Pittsburgh, PA 15235-5098

*Metals and Ceramics Division, Oak Ridge National Laboratory, Oak Ridge, TN 37831-6376

The degradation of low alloy pressure vessel steels in the presence of neutron irradiation is of fundamental importance in the nuclear industry. Numerous studies have been performed to evaluate the irradiation-induced changes in mechanical properties, and to a lesser extent, the changes in microstructure, of these pressure vessel materials. Irradiation results in an increase in the ductile to brittle transition temperature and a decrease in the upper shelf energy of the steels. The exact contribution of intergranular segregation to the concomitant degradation in mechanical properties is, however, unclear. To understand the microstructural changes caused by neutron irradiation and to clarify this contribution, it is important to fully characterize the material prior to irradiation. In this initial investigation, the techniques of analytical electron microscopy (AEM), high spatial resolution field emission gun scanning transmission electron microscopy (FEG-STEM) and energy dispersive x-ray spectroscopy (EDS) microanalysis have been employed to evaluate the microstructure of a low alloy steel as a first step in addressing this issue.

General microstructural characterization of the steel was performed using a Philips CM12 analytical electron microscope equipped with a Link Analytical LZ5 EDS system. The FEG-STEM microanalytical study was conducted at ORNL using the Philips EM400T/FEG interfaced with an EDAX EDS detector and a PV9100 analyzer. All FEG-STEM EDS analyses were performed using a Gatan liquid nitrogen analytical double tilt holder at -130°C . The specimen current was ~ 1 nA, and the probe size was approximately 2 nm in diameter.

The general ferritic-bainitic microstructure of the steel is shown in the micrographs of Fig. 1. M_3C carbides were frequently observed along lath and subgrain boundaries. The elements comprising M for the M_3C carbides as measured by STEM-EDS microanalysis were 14.5 at.% Mn - 0.7 at.% Si - 0.6 at.% Mo - 0.2 at.% Ni - bal Fe. A non-uniform distribution of fine needle-shaped Mo_2C carbides was also observed. Both inter- and intragranular Mo_2C were present in the steel, Fig. 2. FEG-STEM microanalysis of several boundaries in this steel revealed that significant Mo segregation had occurred. This was occasionally accompanied by local enrichments ($\sim 200\%$) in P levels at the boundaries. No increases in Mn, Si, or Ni levels were detected at any of the boundaries analyzed. The effect of intergranular precipitation on the extent of Mo segregation was demonstrated in the analysis of two grain boundaries containing alloy carbides. The Mo content along a boundary containing an M_3C carbide was observed to increase by $\sim 350\%$ as the carbide interface was approached. Conversely, significant Mo depletions were observed along boundaries in the vicinity of intergranular Mo_2C carbides, with the grain boundary Mo levels varying from 200% enrichments decreasing to approximately 0.12 at.% (measured matrix Mo content) within 5 nm of the Mo_2C carbide. This variation in the experimentally measured Mo contents along the grain boundaries and in the vicinity of the M_3C and Mo_2C carbides can be explained in terms of solute rejection accompanying precipitation. In summary, the segregation of Mo and P to grain boundaries in these low alloy steels has been confirmed using FEG-STEM microanalysis. With this baseline information, it may be possible to evaluate the contribution of neutron irradiation in promoting additional segregation in these materials in the future.

Reference

1. The authors thank J.J. Haugh of the Westinghouse Science & Technology Center for his technical assistance. This research was sponsored in part by the Division of Materials Sciences, U.S. Department of Energy, under contract DE-AC05-84OR21400 with Martin Marietta Energy Systems, Inc. and through the SHaRE program under contract DE-AC05-76OR00033 with Oak Ridge Institute for Science and Education.

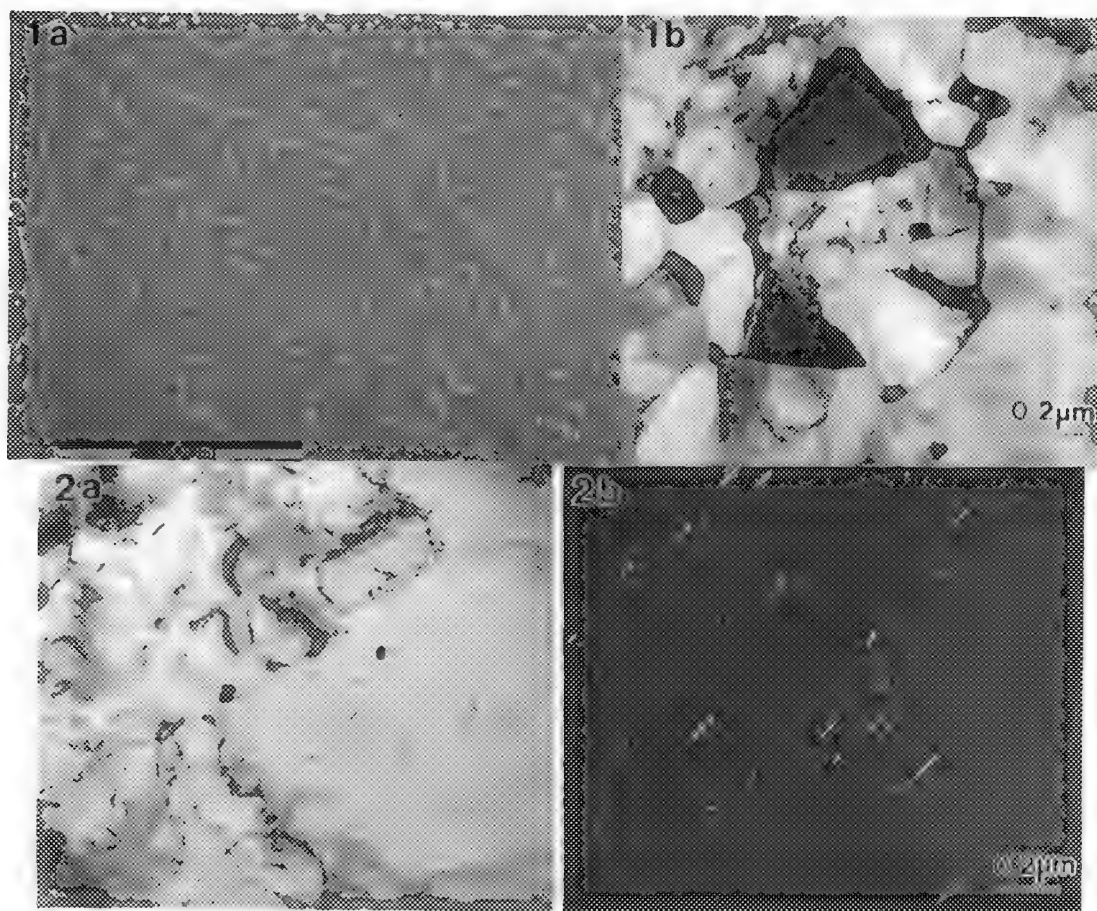


FIG. 1.--(a) SEM of pressure vessel steel showing M_3C carbides along grain and lath boundaries; (b) TEM showing subgrains, M_3C carbides, and general defect structure.
FIG. 2.--(a) Bright and (b) dark field micrographs of the intragranular Mo_2C carbides observed in the low alloy steel.

ION MICROSCOPE AND MICROPROBE STUDIES OF SURFACES AND INTERFACES

Dale E. Newbury

National Institute of Standards and Technology, Gaithersburg, MD 20899

Secondary ion mass spectrometry (SIMS) in its spatially-resolved forms, the ion microscope and ion microprobe, offers elemental, isotopic, and molecular detection, wide dynamic intensity range spanning major to trace concentrations in the part per million (ppm) range or lower, high lateral spatial resolution in the micrometer to sub-micrometer range, shallow sampling depths to the nanometer range, and the possibility of "microanalytical tomography", the reconstruction of three-dimensional distributions.^{1,2} With this broad range of capabilities, SIMS has special advantages for the characterization of surfaces and interfaces that complement the measurement capabilities of other microanalysis/surface analysis techniques such as electron probe x-ray microanalysis (EPMA), analytical electron microscopy (AEM), Raman and infrared microscopy, scanning Auger electron microanalysis (SAM/AES), and spatially-resolved x-ray photoelectron spectroscopy (XPS). Examples of applications will highlight the special contributions of SIMS to surface/interface characterization studies.

1. Surface studies

Figure 1 shows an example of characterization with extreme surface sensitivity. Changes in surface chemistry induced on a passivated silicon surface by scanning tunneling microscopy in air are revealed by time-of-flight secondary ion mass spectrometry (TOF-SIMS).³ The TOF-SIMS is a type of ion microprobe with a 100 nm focused ion beam derived from a high brightness liquid gallium source. Because of the low primary ion currents in the 100 nm probe, sputtering rates are very low so that TOF-SIMS is exceptionally surface sensitive. Because of the effectively parallel collection of secondary ions achieved in the TOF mode, the entire mass range of interest can be sampled, allowing detection and measurement of unexpected species. TOF-SIMS also has a rapid imaging mode based on collection of ion-induced secondary electrons that can be used to image specimen topography. The combination of imaging/mass spectrometry makes TOF-SIMS complementary to analytical electron microscopy.

2. Depth profiling

One of the most powerful SIMS operating modes is depth profiling, usually accomplished by controlled sputtering from the outer surface. The maximum depth reached in this mode is generally less than 10 μm due to ion extraction considerations. To reach greater depths, the specimen can be prepared as a cross section, and the lateral resolution of the imaging mode can then be employed to measure a profile through the section. Figure 2 shows an application of this technique to the measurement of lithium depletion below a surface oxide layer in heat-treated Al-Li-Cu-Mg alloy.⁴ Because of the high inherent signal rate of SIMS, lateral images even of trace constituents can be recorded in a few seconds. Such images can reveal lateral inhomogeneities in physical/chemical processes such as diffusion.

3. Microanalytical tomography

The penultimate SIMS characterization method is "microanalytical tomography" with the ion microscope or ion microprobe, which is achieved by recording lateral images as a function of sputter depth and then using computer algorithms to reconstruct synthesized cross sections from the data. An example of this type of analysis is shown in Figure 3, which depicts the distribution of carbon in a $\text{YBa}_2\text{Cu}_3\text{O}_7$ high T_c superconductor. The carbon is preferentially concentrated at the outer surface and along the grain boundaries, possibly as a result of incomplete calcining, or else because of subsequent attack by atmospheric carbon dioxide. Since these images were recorded with a magnetic spectrometer, only one species could be detected at a time. Although peak switching data collection is utilized with such spectrometers, valuable information is lost because of the non-simultaneity of the data collection. This situation can be overcome with the "ultimate" arrangement, microanalytical tomography by TOF-SIMS, where all species are recorded at all locations. The data flow required overwhelms existing systems for collection and manipulation, although future developments may obviate this problem.

References

1. Newbury, D. E., Joy, D. C., Echlin, P., Fiori, C. E., and Goldstein, J. I., Advanced Scanning Electron Microscopy and X-ray Microanalysis, Plenum Press, New York (1986) 243.
2. Newbury, D. E., Nanotechnology, **1** (1990) 103.
3. Dagata, J. Schneir, J., Harary, H. H., Bennett, J. and Tseng, W., *J. Vac. Sci. Tech. B* **9**, (1991) 1384.
4. Soni, K.K., Williams, D.B., Newbury, D.E., Chi, P., Downing, R.G., and Lamaze, G., *Corrosion*, **49** (1993) 31.
5. Gillen, G., Chi, P., and Simons, D. S., Secondary Ion Mass Spectrometry. SIMS VII, eds. A. Benninghoven, et al., Wiley, New York (1990) 697.

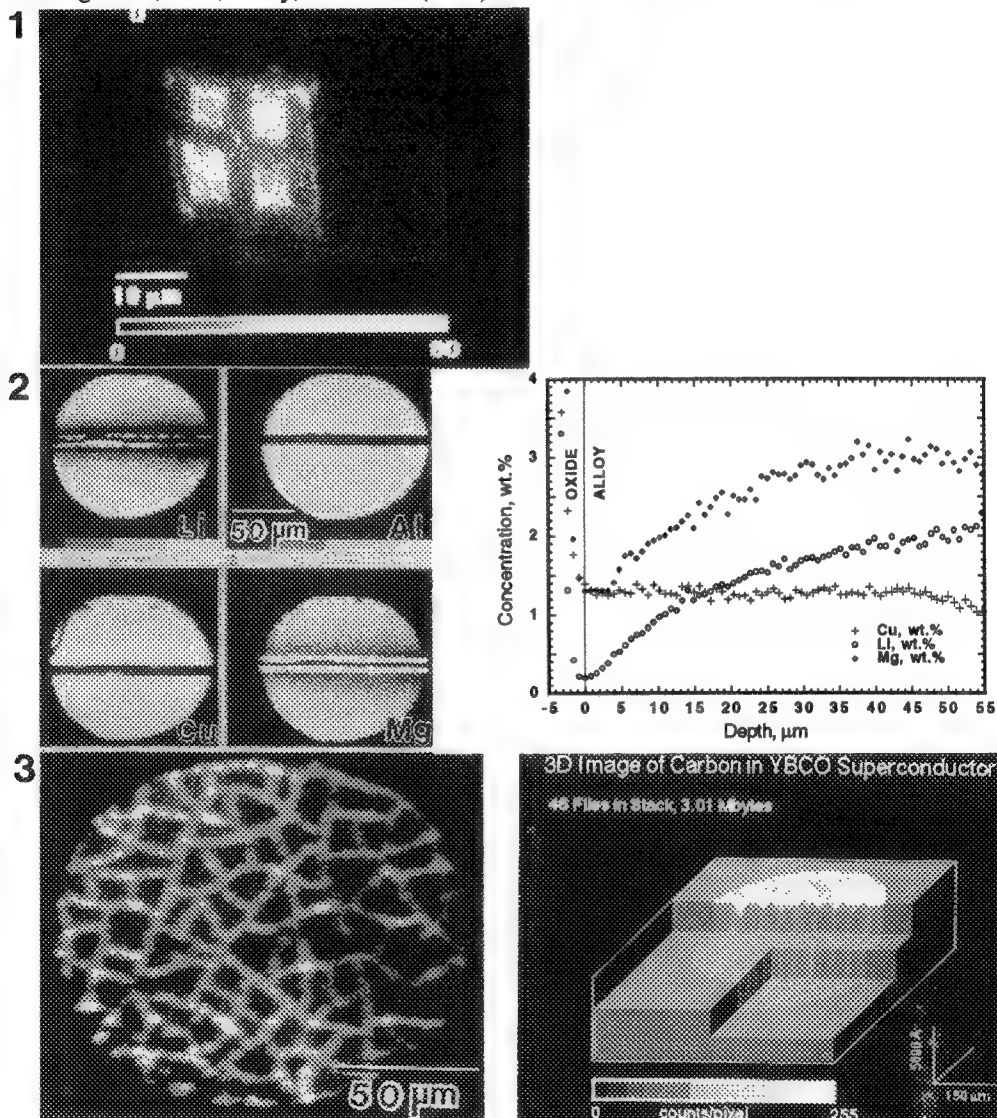


Figure 1 $^{16}\text{O}^-$ TOF-SIMS image of Si surface modified by scanning tunneling microscope scan.³

Figure 2 (a) Cross-sectional Li, Al, Cu, Mg ion images; (b) depth profiles following oxidation.⁴

Figure 3 (a) C surface image (b) C depth distribution in $\text{YBa}_2\text{Cu}_3\text{O}_7$ vert. = 15 nm; horiz. = 150 μm .⁵

EELS STUDY OF NiSi₂/Si(111) INTERFACE IN STEM

Kaikee Wong*, P. E. Batson** and John Silcox*

* Department of Applied Physics, Cornell University, Ithaca, NY 14853

** IBM Thomas J. Watson Research Center, Yorktown Heights, NY 10598

Experimental studies of the NiSi₂/Si(111) interface are difficult since the interface is only 3 Å wide and separating the interfacial signals from bulk signals is hard. When equipped with an EELS detector, a STEM becomes a powerful tool in studying the electronic properties of an interface. By locating the electron probe at the interface, at bulk Si and at bulk silicide, the electronic properties of the NiSi₂/Si(111) interface can be identified.

An A-type NiSi₂ template was grown using Tung's scheme.¹ To increase the film thickness to 200 Å, 60 Å of Ni was deposited on the template and annealed at 550°C for 10 min. A cross-section TEM sample was prepared by dimpling and ion-milling. Within 70 Å of the interface, the specimen stoichiometry was found to be that of NiSi₂ with TEM lattice imaging and x-ray EDS. Beyond that the concentration of Ni increased and approached that of NiSi. EELS measurements were carried out at the IBM VG HB501 STEM operating at 120 keV equipped with a CCD EELS detection system and a Wien filter.² The probe size was estimated to be 4 Å. The spectra were recorded with an energy resolution of 0.4 eV and a step size of 0.05 eV. The convergence and collection half-angles were about 13 and 1 mrad respectively. The spectra were recorded within an area 60 Å across centering on the interface to minimize variation in thickness, which was estimated from the plasmon intensity to be 600 Å.

Fig.1 shows the plasmon loss spectra obtained from bulk Si, the interface and bulk silicide. The plasmon energies of Si, interface and silicide are 16.9, 18.1 and 19.8 eV respectively. The shift of the plasmon energy at the interface is well defined and the interfacial plasmon energy is close to the geometric mean of the other two plasmon energies (18.3 eV), suggesting the free electron model is accurate in describing the valence electron excitations even at the interface in the high energy limit.³ The width of the plasmon loss increases from 4.6 eV for Si, 6.5 eV for the interface to 7.9 eV for NiSi₂. The relatively small width for the silicide again suggests that the valence electrons are mainly free-electron like in the high energy limit. Fig.2 shows the Si L_{2,3} edges obtained from bulk Si and at the interface. The pre-edge backgrounds of the two spectra have been fitted to a E^{-r} power law and subtracted. There is a shift of 0.15 eV to a lower binding energy at the interface and may be due to charge transfer from the Si to the Ni atoms. The interfacial spectrum has a slightly higher intensity at E_F. The increase may be due to interfacial states responsible for Fermi energy pinning that lie within the band gap.^{4,5} The Si L₃ spectra of Si and the silicide (fig.3) can be obtained by deconvoluting the background-subtracted core loss spectra with two delta functions separated by the spin-orbit splitting of the Si 2p electrons (0.61 eV) and with a statistical ratio of 2 to 1. A sharp threshold is seen for the silicide L₃ spectrum and suggests a continuous DOS across E_F, which is consistent with many calculations.⁴ The mid-point of the threshold gives an E_F of 99.6±0.1 eV, which compares favorably with 99.5±0.4 eV from a photoemission study.⁶

The Ni L_{2,3} core edges were recorded serially from the same specimen at the Cornell VG HB501A STEM operating at 100 keV and are shown in fig.4 with background subtracted. Both the convergence and collection half-angles were about 10 mrad. One spectrum was recorded at the interface and the other at the bulk silicide with a 5 Å probe. The two points were within 40 Å to reduce the thickness variation and the thickness was estimated to be about 300 Å from the low loss spectra. The bulk spectrum was recorded with an energy step of 0.25 eV and with a dwell time of 2 s per step. To avoid specimen drift, a series of spectra with a dwell time of 0.25 s per energy step was recorded at the interface. If the specimen had drifted the probe was moved back to the interface and the spectrum was discarded. At the end 27 interfacial spectra were summed. To improve the signal, every five energy steps were binned together and so the interfacial spectrum shown in fig.4 has a step size of 1.25 eV. The interfacial spectrum has stronger L₃ and L₂ white lines compared to the bulk. A Ni atom at the bulk is surrounded by 8 Si atoms while at the interface the coordination number is reduced to 7 with the same

nearest neighbor distance.⁷ The breaking of bonds lead to an increase in the nonbonding d-DOS, which gives rise to the white lines. Therefore the white lines should be stronger, as observed in experiment.⁸

References

1. R. Tung et al., Phys. Rev. Lett. (1983) 50, 429.
2. P. E. Batson, Rev. Sci. Inst. (1988) 59, 1132.
3. H. Raether, in Excitation of Plasmons and Interband Transitions by Electrons, New York: Springer Verlag (1980): 144.
4. O. Bisi et al., Phys. Rev. B (1990) 42, 5735.
5. P. E. Batson, Phys. Rev. B (1991) 44, 5556.
6. A. Franciosi et al., Phy. Rev. B (1982) 26, 546.
7. D. Cherns et al., Phil. Mag. A (1982) 46, 849.
8. This work was supported by the MRL Program of the NSF under Award No. DMR-9121654.

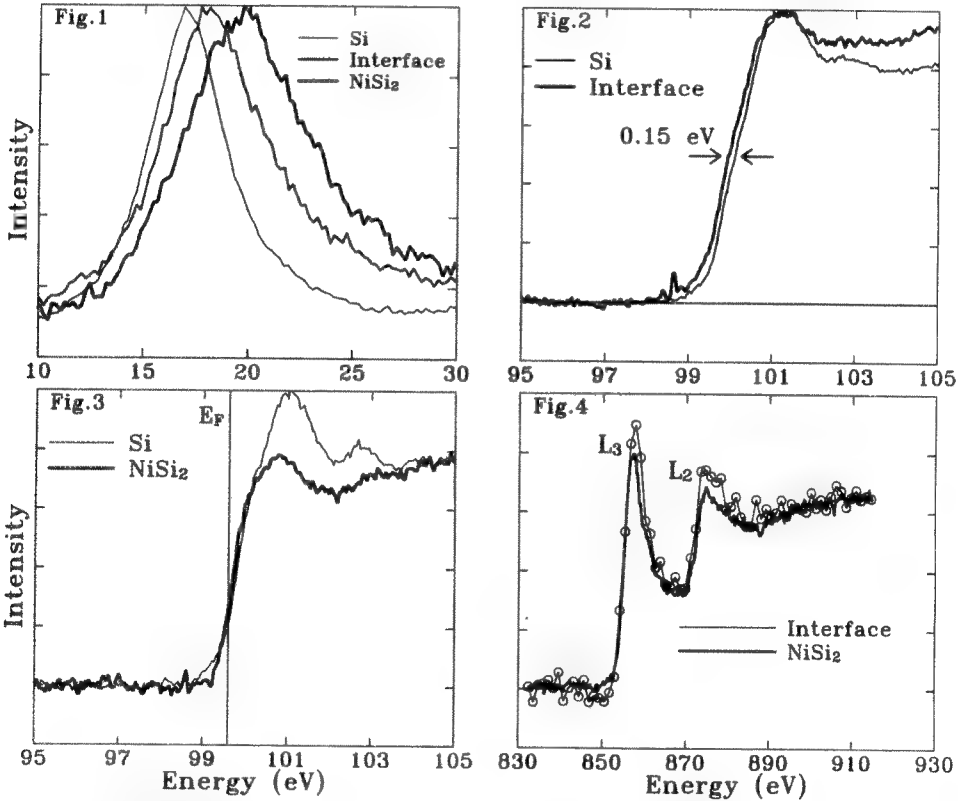


Fig.1: Low loss spectra of Si, NiSi₂/Si(111) A-type interface and NiSi₂. Spectra intensities normalized at plasmon energy.
 Fig.2: Si L_{2,3} core loss spectra of Si and interface with backgrounds subtracted. Spectra intensities normalized at maxima to demonstrate readily the energy shift.
 Fig.3: Si L₃ edge of Si and silicide normalized at 105 eV with E_F indicated. See text for details.
 Fig.4: Ni L_{2,3} core loss spectra of interface and silicide with backgrounds subtracted. Spectra scaled to same intensity after the L₂ edge.

COPPER ENRICHMENT ON AL 2024 SURFACE AFTER DE-OXIDIZING TREATMENT

C. A. Drewien, R. G. Buchheit, K. R. Zavadil and T. E. Neil

Materials and Process Sciences Center, Sandia National Laboratories, Albuquerque, NM 87185
USA

Coatings of lithium-aluminum-carbonate-hydroxide are being developed for corrosion protection of aluminum alloys against atmospheric and saline environments. Coating is performed by immersion of the aluminum part into a lithium carbonate-lithium hydroxide solution of pH=11.5.¹ Before coating, the aluminum alloy is degreased in trichloroethylene, cleaned in a sodium carbonate-sodium silicate bath, and de-oxidized in nitric acid containing ammonium bifluoride. Coating of most aluminum alloys is easily accomplished, and the coatings pass the ASTM B117 salt spray test. However, aluminum alloys that contain copper, specifically 2024-T3 and 7075-T6, yield coatings that fail the salt spray test, i.e. pitting and general corrosion is observed. Photographs of coatings after 168 hr salt spray exposure are shown in Figure 1 for Al 1100 and 2024-T3 alloys. A study has been undertaken to determine the influence of copper upon the corrosion properties of the coating.

The surface of 2024-T3 was analyzed after each processing step in order to determine if copper enrichment at the specimen surface was occurring. A PHI Scanning Auger system model 595 was operated at 5 keV to examine the surface and the bulk of each sample. In order to remove adventitious carbon, a 20 Å layer was sputtered from the surface prior to surveying the surface composition using KLL peak transitions for Al, Mg, O, C, F, Na, and Si and LMM peak transitions for Cu and Fe. A beam size of ~100 Å was used to survey the sample at three or more points spaced at least 250 µm apart. Then, the sample was sputtered at 100 Å/min (as calibrated against an SiO₂ sputter rate standard) for 3 minutes while Al, O, and Cu profiles were measured. Finally, surveys were taken from the bulk of the sample, and composition ratios were determined by measuring the peak-to-peak heights of the differentiated peak intensities.

As shown by the composition profiles in Figure 2a, the surface of the sample subjected to only degreasing contained levels of copper that did not vary with sputtering into the bulk of the material. The surface of the sample that had been de-oxidized had a thin oxide layer by comparison with the degreased sample and had considerable enrichment of copper at the surface; the profile in Figure 2b shows the copper concentration decreasing as the sample is sputtered. The relative intensities of copper and magnesium versus the aluminum are summarized in Table 1. These data indicate a factor of 2 increase in surface Cu concentration after immersion in the acid deoxidizing bath. Analysis of the x-ray induced Cu LMM Auger line shape, acquired on a VG ESCALAB 5, showed that the surface copper was in a zero valence state. To demonstrate that the copper from the alloy could plate onto the alloy surface during the acid de-oxidizing treatment, a degreased and cleaned Al 1100 coupon was de-oxidized in a bath containing copper nitrate. Copper was detected on the sample surface.

It appears that the presence of copper in the Al 2024 alloy leads to plating of metallic copper on the alloy surface during the acid de-oxidizing treatment. It is expected that this observed enrichment of copper on the alloy surface after the deoxidizing step directly results in degradation of the protective properties of the coating.^{2,3}

References

1. R. G. Buchheit, G. Stoner, and M. Bode, submitted to Corrosion (1993).
2. The authors thank G. Nelson and R. W. Buttry for their technical support.
3. This work was supported by the U. S. Department of Energy under contract number DE-AC04-76DP00789.

Table 1.--Copper vs. Aluminum and Magnesium vs. Aluminum on Surface and in Bulk of Al 2024-T3

Sample	Degreased		Alkaline Non-Etch		Acid De-oxidized	
	Surface	Bulk	Surface	Bulk	Surface	Bulk
Cu	0.092±0.01	0.10±0.013	0.11±0.026	0.078±0.016	0.193±0.017	0.098±0.017
Mg	0.046±0.008	0.031±0.004	0.095±0.023	0.075±0.017	0.086±0.020	0.064±0.005

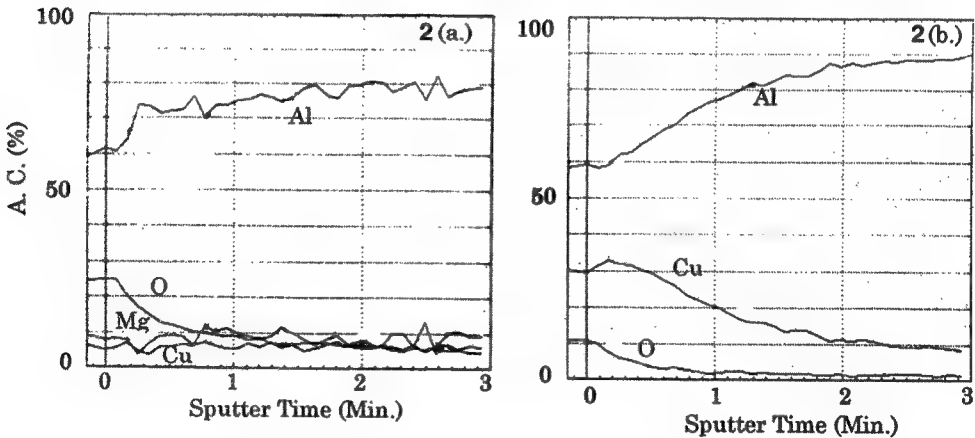
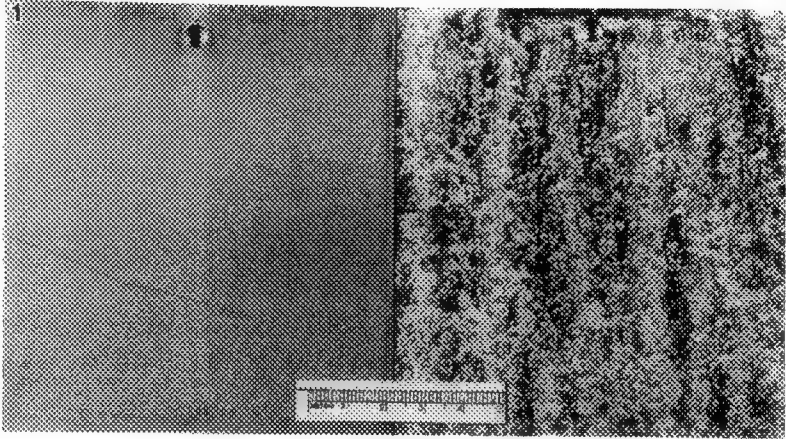


Figure 1.--Photographs of lithium-aluminum-carbonate-hydroxide coating on Al 1100 and 2023-T3 after 168 hr salt spray exposure.

Figure 2.--AES profiles, plotted as atomic concentration versus sputter time, for Al 2024-T3 subjected to a.) degreasing by trichloroethylene and b.) alkaline non-etch followed by acid de-oxidizing.

APPLICATIONS OF ATOM-PROBE FIELD-ION MICROSCOPY TO THE STUDY OF INTERFACES

M.G. Burke and M.K. Miller*

Westinghouse Science and Technology Center, Pittsburgh, PA 15235-5098

*Metals and Ceramics Division, Oak Ridge National Laboratory, Oak Ridge, TN 37831-6376

The near-atomic resolution and elemental sensitivity of the atom probe field-ion microscope (APFIM) permit the detailed microstructural and microchemical analysis of phases and interfaces in a variety of materials. To overcome the limitation of this technique in terms of volume of material sampled, it is frequently necessary to perform complementary microstructural studies by other techniques such as analytical electron microscopy (AEM) or auger electron spectroscopy (AES). With such complementary data, the microstructural significance of the APFIM data can be exploited. In addition to specifically evaluating segregation at interfaces, the high spatial resolution of the APFIM technique can be used to determine microcompositional fluctuations in the vicinity of interfaces. In this overview, some selected examples illustrating the application of the APFIM technique to the evaluation of segregation to interfaces are presented.

Considerable research has been performed on low alloy steels, particularly those such as A533B which are used in the pressure vessels of nuclear reactors. Field-ion micrographs of grain boundaries in ex-reactor steels have clearly demonstrated that segregation of solute elements such as Mo, P, C, N, Ni and Mn can occur. Indeed, a 1 to 2 atom layer thick film of Mo-rich carbonitrides have been observed in irradiated steels, Figure 1.^{1,2} This type of grain boundary decoration (but to a significantly lesser extent) has also been observed in unirradiated pressure vessel steels, Figure 2. Localized compositional variations in the vicinity of such interfaces have been measured by APFIM analysis. An example of such a microchemical variation is shown in Figure 3, which is an APFIM composition profile through a coarse (~50 nm) CuMn precipitate in a pressure vessel steel. As the precipitate-ferrite interface is approached, there is a local enrichment of Mn and Ni. Note that the fine scale of these compositional changes makes such measurements extremely difficult, if not impossible, with the use of conventional AEM techniques.

Other applications of APFIM to the characterization of interfaces include the analysis of ordered intermetallic precipitates in Ni-based and Fe-based alloys.^{3,4} In addition to microchemical variations measured by atom probe microanalysis, field-ion micrographs of the ordered phase with the disordered matrix can provide direct evidence of coherency. The field-ion micrograph of Figure 4 shows several brightly-imaging L1₂-ordered Ni₃(Al,Ti,Nb) γ' precipitates in Alloy 718. The continuity of the rings (atom planes) through the precipitates and the matrix is direct evidence of the coherency of the precipitate with the matrix.

The application of APFIM to the characterization of interfaces in appropriate materials has provided unique and complementary microstructural and microchemical data important in furthering our understanding of the role of microstructure in controlling materials behavior.

References

1. M.K. Miller and M.G. Burke, J. Nuclear Mat., 195(1992)68.

2. M.K. Miller and M.G. Burke, in *Effects of Rad. on Mat.* ASTM-STP 1175(1993) in press.
3. M.G. Burke and M.K. Miller, in E. Loria, Ed., *Superalloys 718, 625 and Various Derivatives*, Warrendale:TMS (1991)337.
4. M.K. Miller and M.G. Burke, *Micros. Microanal. Microstruct.* 3(1992)387.
5. This research was sponsored in part by the Division of Materials Sciences, U.S. Department of Energy, under contract DE-AC05-84OR21400 with Martin Marietta Energy Systems, Inc. and through the SHaRE program under contract DE-AC05-76ORO0033 with Oak Ridge Institute for Science and Education.

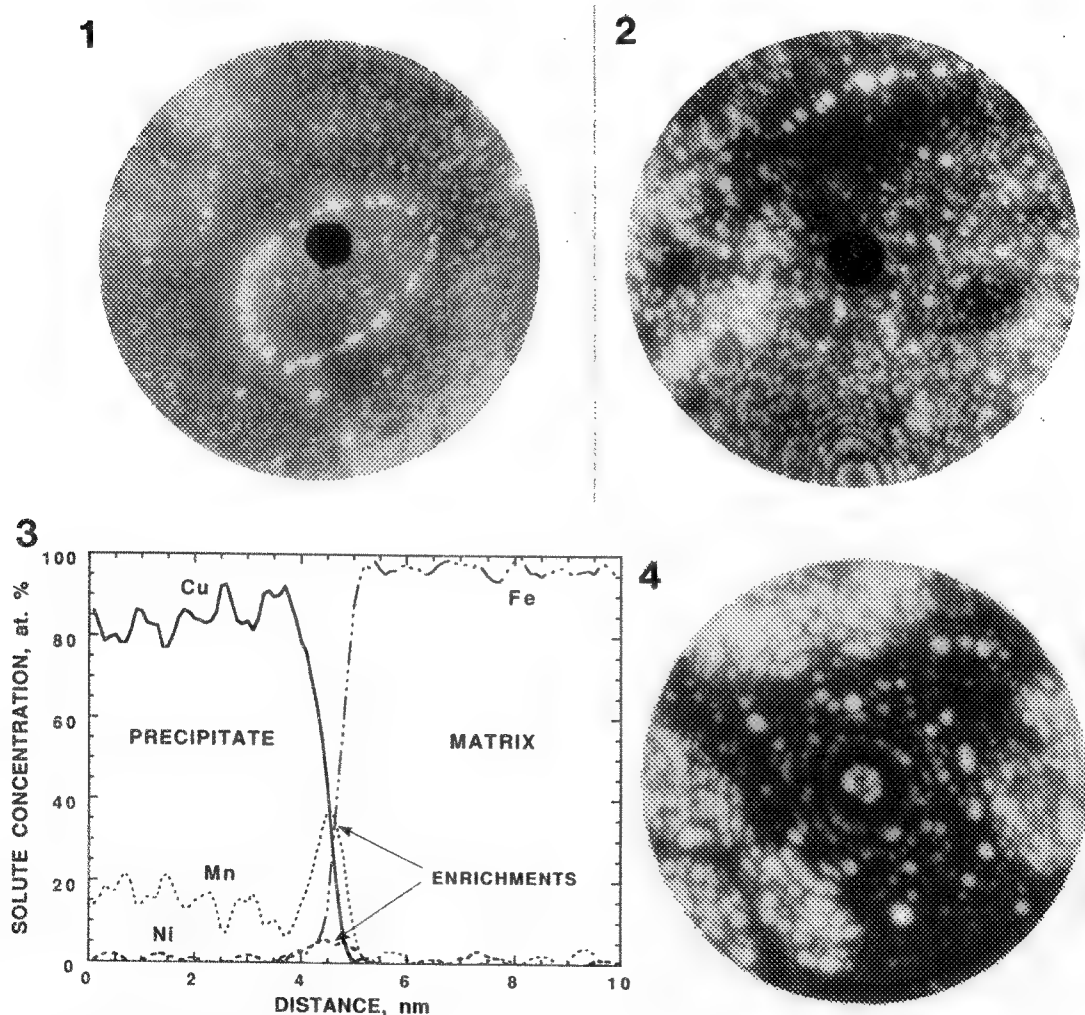


FIG. 1.--FIM of Mo-rich carbonitride decorated grain boundary in irradiated A533B pressure vessel steel. FIG. 2.--FIM of grain boundary in unirradiated pressure vessel steel. FIG. 3.--AP composition profile through a CuMn precipitate in an irradiated A533B weld. FIG. 4.--FIM of brightly imaging γ' precipitates and γ matrix in Alloy 718.

CHARACTERIZATION OF SHEARED LIQUID CRYSTALLINE POLYMERS BY LIGHT MICROSCOPY

Christopher Viney* and Wendy S. Putnam†

*Molecular Bioengineering Program, Center for Bioengineering WD-12, and †Department of Materials Science and Engineering FB-10, University of Washington, Seattle, WA 98195, USA

It is widely observed that nematic and cholesteric liquid crystalline materials develop a one-dimensional periodic microstructure during and/or after a uniaxial draw or simple shear (Fig.1). This property is common to lyotropic and thermotropic examples of both small-molecule and polymeric liquid crystals. The periodic microstructure gives rise to a banded texture between crossed polars (Fig 2).

A material under load will extend more readily if the microstructure contains crimps that can be straightened, compared to the extension that is achieved if covalent backbone bonds are highly aligned along the direction of load. The microstructure in Fig.1 therefore is regarded as a stiffness-reducing defect. Two classes of stiff polymer that are produced from lyotropic solutions do not exhibit banded textures: the highest modulus variant of poly(*p*-phenyleneterephthalamide) (Kevlar), and various natural silk fibers. However, a banded texture *is* present in the less stiff variants of Kevlar, and also in silk fibers that have been drawn by hand from natural secretions, which demonstrates that the defect is not intrinsic to liquid crystalline molecular order, but is related to processing.¹

The banded texture has been characterized by several techniques of microscopy and diffraction: polarized and phase contrast light microscopy, transmission and scanning electron microscopy, as well as x-ray and electron diffraction. The band spacing often approaches the limits of light-optical resolution, which, coupled with the one-dimensional character of the microstructures, can lead to some otherwise unusual image artifacts.² Also, even if there is no question about the banded texture being resolved properly, light microscopy may not always be an accurate indicator of how the angle of molecular misorientation (relative to the shear direction) varies as a function of position measured along the shear direction. This problem occurs because the extinction directions observed between crossed polars may not correspond in any straightforward way to the local direction of molecular orientation: the apparent in-plane molecular orientation direction may be affected by out-of-plane components. Electron microdiffraction, or electron microscopy of etched or decorated samples, is required to reveal the in-plane component of molecular orientation unambiguously.³

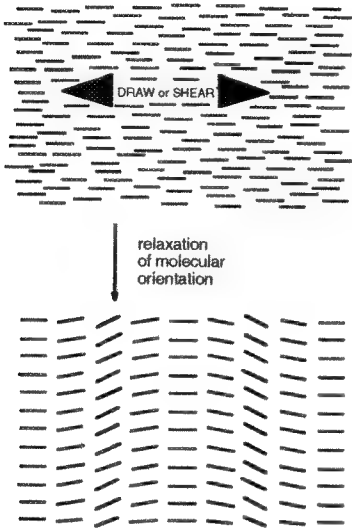
Several groups have attempted to quantify the processing conditions under which banded textures form. The "hydrogen atom" for experimentation is hydroxypropyl cellulose (HPC), a semiflexible polymer available from several different suppliers in a variety of molecular weights. *In situ* evolution of banded textures has been studied extensively in different shear flow geometries that are accessible to light microscopy. Figure 3 schematically shows the parallel plate apparatus used in our experiments, in which banded textures were observed to form after cessation of shear.⁴ The experimental arrangement ensures that the velocity gradient is constant through any vertical column of material in the field of view (unlike the situation between rotating parallel disks), and the thickness is also constant (unlike the situation in cup-and-cone geometries). However, we are limited to applying shear in a given direction for only a (short) finite length of time.

The rate at which the banded microstructure evolves (equivalent to microstructural mobility, and depending on a compromise between driving and resisting forces), can be quantified by locating the minimum in plots of average band spacing vs elapsed time since shear ceased (Fig.4). We have determined that the following variables are significant for HPC: solvent type, solution concentration, and shear rate. Band relaxation is governed by a trade-off between chain entanglements (which retard microstructural evolution more effectively at higher concentration in a thermodynamically poor solvent, but at lower concentration in a good solvent), and the elastic constants for director field deformation (which retard microstructural evolution at higher concentration in all types of solvent, but more so in good solvents). Attempting to use these observations to understand the different behavior of naturally spun and hand drawn fibers of silk fibroin (also a lyotropic semiflexible polymer), we note that solvent type and shear rate are comparable in both systems, as is the initial concentration. So the absence of a banded texture in the naturally spun material must be due to the particular *rate of concentration change* that is characteristic of this process.⁵

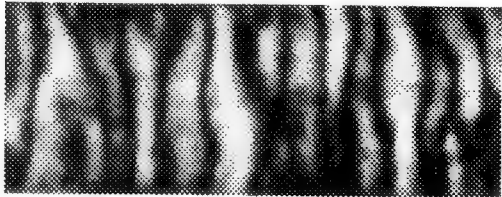
References

1. K. Kerkam *et al.*, in M. Alper *et al.*, Eds., Materials Synthesis Based on Biological Processes, Pittsburgh: Materials Research Society (1991) 239.

2. C. Viney and A.H. Windle, Philosophical Magazine A 55 (1987) 463.
3. S.E. Bedford and A.H. Windle, Polymer 31 (1990) 616.
4. W.S. Putnam and C. Viney, Molecular Crystals and Liquid Crystals 199 (1991) 189.
5. Support from the College of Engineering at the University of Washington, the Washington Technology Center, and the US Army RD& E Center (Natick) is acknowledged gratefully .



← FIG.1. Variation of local molecular orientation in sheared liquid crystalline sample (top), and after partial relaxation (bottom).



↑
FIG. 2. Banded texture of fiber drawn by hand from *Bombyx mori* (silkworm) silk secretion. Polarizer N-S and analyzer E-W; fiber oriented E-W. Bar = 10 μ m.

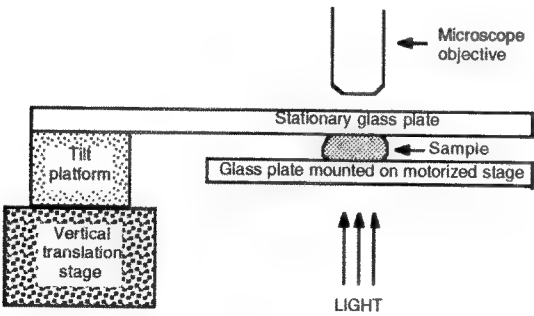


FIG. 3. Schematic representation of microscope stage for shearing samples between parallel glass plates. Glass plate attached to motorized stage is under joystick control, and can be displaced unidirectionally in either N-S or E-W direction.

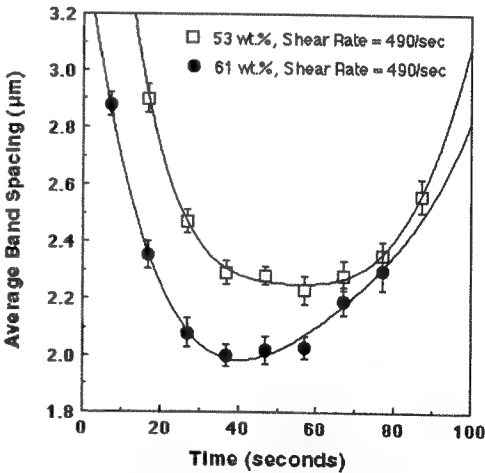


FIG. 4. Band spacing after cessation of shear; HPC weight average molecular weight = 80,000; solvent is water.

RECENT DEVELOPMENTS IN LOW-VOLTAGE SEM OF POLYMERS

S.J. Krause* and W.W. Adams**

*Chemical, Bio, and Materials Engineering, Arizona State University, Tempe AZ 85287

**Air Force Materials Laboratory, Polymer Branch, Wright-Patterson OH 45433

Over the past decade low voltage scanning electron microscopy (LVSEM) of polymers has evolved from an interesting curiosity to a powerful analytical technique. This development has been driven by improved instrumentation and in particular, reliable field emission gun (FEG) SEMs. The usefulness of LVSEM has also grown because of an improved theoretical and experimental understanding of sample-beam interactions and by advances in sample preparation and operating techniques. This paper will review progress in polymer LVSEM and present recent results and developments in the field.

In the early 1980s a new generation of SEMs produced beam currents that were sufficient to allow imaging at low voltages from 5keV to 0.5 keV. Thus, for the first time, it became possible to routinely image uncoated polymers at voltages below their negative charging threshold, the "second crossover", E2 (Fig. 1). LVSEM also improved contrast and reduced beam damage in sputter metal coated polymers.¹ Unfortunately, resolution was limited to a few tenths of a micron due to the low brightness and chromatic aberration of thermal electron emission sources. In the mid 1980s FEG SEMs achieved high resolution (<10nm) images of uncoated polymers at low voltages (~1keV).² A new understanding of detailed morphology of polymer surfaces, comparable to transmission electron microscopy replication techniques, began progressing. Improvements in instrumentation continue today: resolution at 1 keV is below 5nm (Fig. 2); fast scan frame grabbers reduce sample charging and beam damage; LV backscattered electron (BSE) channel plate detectors have achieved resolution in topographic and atomic number contrast similar to secondary emission (SE) electron images. Currently, energy dispersive X-ray light element analysis is being explored but, low X-ray yield, low critical voltage, and low FEG current may limit this technique.

A fascinating area of study in LVSEM of polymers is the nature of the "second crossover" E2. Uncoated polymers charge positively in LVSEM between E1 and E2 when the ratio of current emitted from the surface to beam current is greater than one. Imaging is possible with positive charging mostly compensated by recapture of low energy SEs. Areas imaged above E2 will be brighter from negative charging and areas below E2 will be darker from positive charging. Various factors affect E2 including composition,³ microtexture (Fig. 3), tilting, and scan rate. Tilting increases E2 and may, for some samples, such as rods or fibers, cause anomalous contrast opposite to that found in conductors. Compositional imaging has been used in microtomed surfaces in polymer blends where contrast is enhanced when operating in the vicinity of E2.⁴ The sensitivity of E2 to surface condition also makes it probe for measuring changes in surface condition with time. E2 changes with temperature could provide insight on molecular motion which is important in areas such as adhesion and biologically active surfaces. E2 effects from treatments like solvent cleaning, UV exposure, or electrical discharge could be used to monitor time dependent changes such as chemical degradation, oxidation, aging, and hydrophobicity.⁵ Charging effects are different for thin insulating samples on a conducting substrate. As voltage increases, beam film penetration increases the charge conducted away by the substrate until positive charging begins at a new crossover, E3, which is not fixed, and will increase with increasing film thickness.⁶ Figure 4 shows polyethylene single crystals on Si with multiple 10nm layers of spiral overgrowth. The first layer is darker than the substrate due to positive charging above E3 while the thicker center has contrast reversal from negative charging.

Improvements in sample preparation and observation techniques can enhance resolution and/or contrast and provide additional information about samples. Any increase in E2 to higher voltages will permit better machine resolution; eg. 4nm at 1keV, 3nm at 2keV, and 2nm at 3keV. Methods to increase E2 include; tilting, faster scan rate, flash metal coating (ie. a few seconds of metal sputtering)⁷, and microtexturing through solvent etching or plasma etching (Fig. 5).

In summary, it can be seen that utilitarian high resolution (<10nm) SEM imaging of uncoated polymers is possible with low voltage FEG SEMs. It is likely that further improvements will occur in resolution, compositional information, and easier use. Advances in the understanding of E2 will improve image resolution, contrast, and charging and the use of E2 as a dynamic time dependent probe. It is also likely that entirely new applications and new in-situ techniques will be developed. Additionally, there is much work to be done in quantification in sample-beam interactions and image calculation and in correlating LVSEM results to other contemporary surface analysis techniques such as atomic force microscopy.

References

1. J. Pawley and D.C. Joy, EMSA Proc. 50 (1992) 1278.
2. S.J. Krause, W.W. Adams, S. Kumar, T. Reilly, and T. Suzuki, EMSA Proc. 45 (1987) 466.
3. J.H. Butler et. al., Microscopy, 22 (1992) 103.
4. V.K. Berry, Scanning 10 (1988) 19.
5. S.J. Krause, J. Mohr, G.H. Bernstein, D.K. Ferry, and C.C. Joy, MAS Proc. 24 (1989) 459.
6. W.W. Adams and D.L. Vezie, EMSA Proc. 49 (1991) 1040.
7. J. Chang, S.J. Krause, and W.W. Adams, EMSA Proc. 49 (1991) 1038.

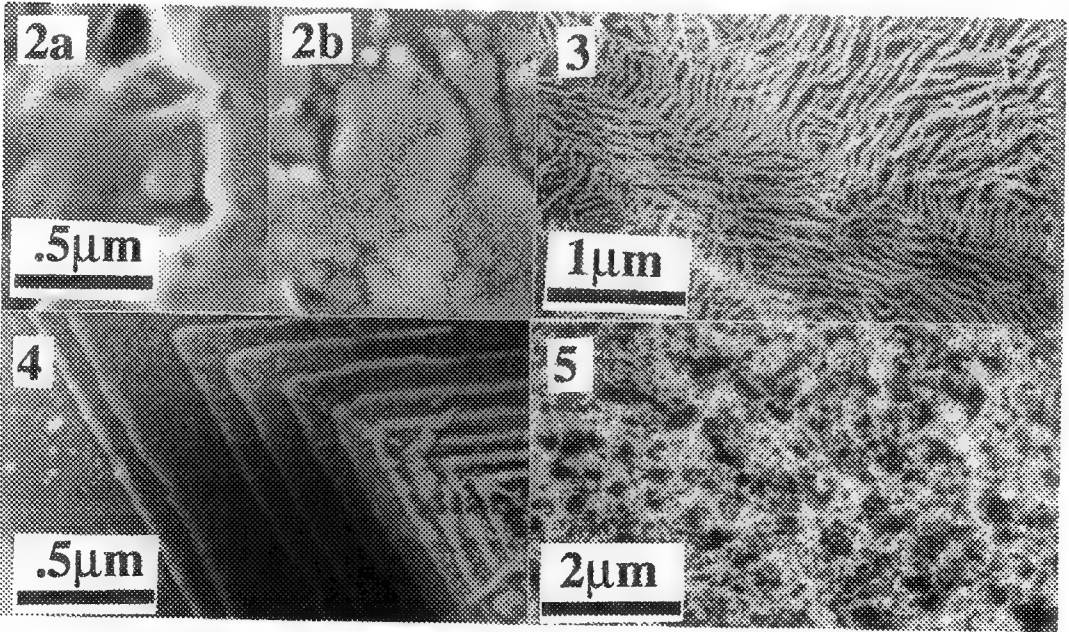
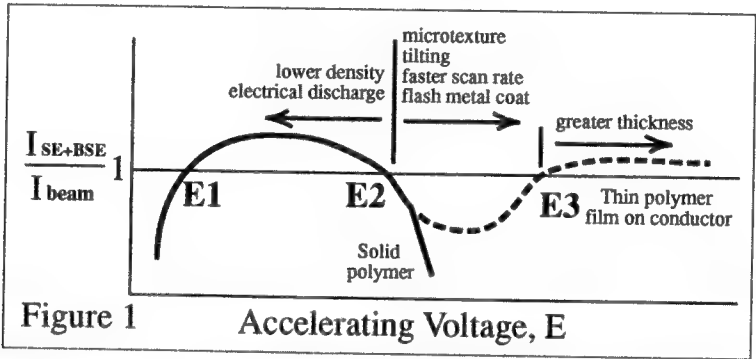


FIG. 1.-- Schematic of electron emission ratio for various effects on E2 and for polymer film thickness on E3.
FIG. 2.-- Resolution of Au sputtered on nylon showing resolution of a) 5nm at 1 keV and b) 2nm at 5keV.
FIG. 3.-- Microtexture of lamallae on biaxially drawn polyethylene film increases E2 and reduces charging effects.
FIG. 4.-- Overgrowth layers on a PE single crystal showing + charging on lower layers and - charging on upper layers.
FIG. 5.-- Plasma etched surface develops fibrillar network structure which increases E2 and reduces charging effects.

LOW-VOLTAGE HIGH-RESOLUTION SEM: A VALUABLE RESOURCE FOR THE POLYMER MORPHOLOGIST

D. L. Vezie,* W. W. Adams,** and E. L. Thomas*

*Department of Materials Science and Engineering, M.I.T., Cambridge, MA 02139

**Materials Directorate, Wright Laboratory, Wright-Patterson Air Force Base, OH 45433

The elucidation of polymer morphology has historically been accomplished using optical microscopy (OM), conventional transmission electron microscopy (TEM), X-ray scattering and more recently for crystalline polymers, high resolution TEM (HRTEM). Significant work using scanning electron microscopy (SEM) to study synthetic polymers began in the late 1960's, but for twenty years after these first studies, the smallest features imaged by SEM in polymer samples have typically been 1-10 μm . The evolution of the low voltage high resolution SEM (LVHRSEM) now provides polymer scientists with the opportunity to image structures topographically on the order of 50-100 \AA , a level of microstructure important in basic polymer physics research. The potential for improved understanding of polymer morphology is significant, especially when HRSEM data is combined with information from other complementary techniques such as TEM, X-ray scattering, and the scanning probe microscopies (SPM, AFM, STM).

The advantages of LVHRSEM over conventional thermionic source SEM as a polymer characterization technique include^{1,2}: i) low keV operation reduces or eliminates charging in uncoated insulating polymers, ii) the high brightness, low energy spread, small spot size field emission gun allows for operation at low keV without significant loss of resolution (practically, resolution on the order of 50 \AA at 1.0 keV in a polymer sample is attainable), iii) imaging of surface topography is improved at low keV as the beam/sample interaction volume is smaller and closer to the surface, resulting in more secondary electrons being generated within the secondary electron escape depth, and iv) the immersion lens system improves the signal to noise ratio by decreasing the noise component in the secondary electron signal. However, there are some disadvantages that include: i) the immersion lens system limits depth of field, tilt range and sample size, and ii) the electron beam is susceptible to stray fields at low keV operation. Also, polymers are inherently difficult to image with electron microscopy techniques because their low atomic number and low density results in poor electron scattering which gives low contrast. Most polymers are also very susceptible to radiation damage in the form of chain scission and/or crosslinking.

There are several possible contrast mechanisms that can be present when imaging a polymer surface at low keV. Each mechanism can act singularly or in conjunction with another contrast mechanism. The contrast mechanisms we address are the result of the detection of secondary electrons, although the production of secondary electrons can be affected by factors such as surface topography, the backscattered electron coefficient (sample composition), crossover effects, beam/sample geometry, sample conductivity,

and for thin polymers such as single crystals the substrate plays a large role in the observed contrast. Image interpretation is not always a straightforward process and great care must be taken to understand the effects of microscope configuration as well as the contribution of each contrast mechanism to the final image.

The usefulness of LVHRSEM is demonstrated for diverse polymer systems, both amorphous and crystalline, with structurally interesting features on a 50-1000Å length scale. Our studies include polyethylene single crystals, deformation of polyethylene blown films, defect textures in liquid crystalline nematic polymers³ and cholesteric macromolecules⁴, surface morphology of styrene-butadiene block copolymers⁵, kinking in high performance polymer fibers⁶, ion-implantation of rigid-rod polymer fibers⁶, silk fibers, starch fibers, and the morphology of carbon fibers⁷.

LVHRSEM is certain to become an increasingly valuable complementary technique to TEM, X-ray diffraction and the scanning probe microscopies in the study of polymer morphology and polymer structure-property relationships. Recent high resolution technology allows for operation at low voltage with resolution of 50 Å and the low voltage operation reduces or eliminates charging problems common to uncoated polymers. The potential rewards of LVHRSEM are great but a thorough understanding of this technique is necessary to properly interpret polymer image data because understanding the contrast present in low voltage images is not always straightforward. As the technology continues to mature, as contrast mechanisms are more quantitatively understood, and as the price decreases for these instruments (!?), LVHRSEM should prove an ever more valuable resource for the polymer morphologist.

References

1. D. C. Joy, Hitachi Instrument News, 16 EM Ed., 3, July 1989.
2. J. B. Pawley, Scanning Electron Microscopy, Part I, 153, (1972).
3. S.D. Hudson, D.L. Vezie, and E.L. Thomas, Makromol. Chem., Rapid Commun., 11, 657,(1990).
4. T. Bunning, Ph.D. Thesis, University of Connecticut, 1992.
5. D.W. Schwark, et al., J. Mat. Sci. Lett., 11, 352, (1992).
6. D.L. Vezie, Ph.D. Thesis, Massachusetts Institute of Technology, 1993.
7. D. L. Vezie and W. W. Adams, J. Mat. Sci. Let., 9, 883, (1990).

"DYNAMIC" CHARGING OF POLYMERS IN THE LVSEM

J. H. Butler*, D. C. Joy† and G. F. Bradley†

*Exxon Chemical Company, P.O. Box 5200, Baytown, TX 77522

†EM Facility, University of Tennessee, Knoxville, TN 37996

Recently we have been using a field emission LVSEM with an immersion-type objective lens extensively for the examination of polymers at low (<2 keV) incident beam energies.¹ During the course of these studies it became apparent that, even though operating in the vicinity of E2 (the accelerating voltage at which no electrostatic charge builds up on the sample surface), sample charging effects of a most curious nature do, in fact, abound.

In general the LVSEM has been successful in producing a wealth of exciting information. However, when nonconducting polymers are the subject of observation at E2, an unexpected and unusual charge build-up behavior is almost always encountered on the sample surface under irradiation (c.f. Figure 1). Thus for strongly insulating materials, it is not as easy to work in the realm of E2 as earlier predicted. For example, in some polymeric materials, it appears that charging is a function of magnification: at very high magnifications the sample will charge "positively", at lower magnifications (with all other parameters the same) the same sample will charge negatively, and at even lower magnifications the same sample will revert back to a positive charging situation. Another practical observation is that the charging is very much worse when the beam is exactly focused on the sample, while at slight under or over focus the charging is much less; this is striking in samples which do not lie completely flat relative to the objective focal plane as charging then sweeps back and forth across the sample as the focus is changed. Another strange phenomenon is the appearance of both positive and negative charging within a single field of view. Yet a fourth phenomenon is the incredible ability for polymers to store charge at various depths below the surface for periods ranging up to several months! Charging levels even vary as a function of the sample temperature. Because of the non-static behavior of these charging effects, we have collectively labeled them as "dynamic" charging.

This work shows that simple considerations of charge balance at a surface are not sufficient to explain all of the phenomena that are observed. In particular it is evident that both beam current and current density affect the magnitude and the sign of the charging that occurs. The likely explanation for this is that conductivity induced in the specimen by the beam (i.e. electron beam induced conductivity, EBIC) must also be included as a component in the charge balance equation. This, in turn, requires that the spatial distribution of both the energy deposited by the beam, and the distribution of the trapped charge, be known. Monte Carlo simulation is being applied to try and quantitatively model this situation. There is also evidence to suggest that the immersion lens geometry provides a secondary influence on "dynamic" charging effects.

On the basis of our new understanding we have developed a modestly successful procedure for producing charge free high resolution images. Continuing work is focused on further development of the semiempirical theory of secondary electron emission for wide band gap insulators, on the implementation of a micro-channel plate backscattered detector, and on the installation of a digital beam control and data acquisition system.

Reference

1. J. H. Butler et al., *Microscopy: The Key Research Tool* (1992)22, 103.

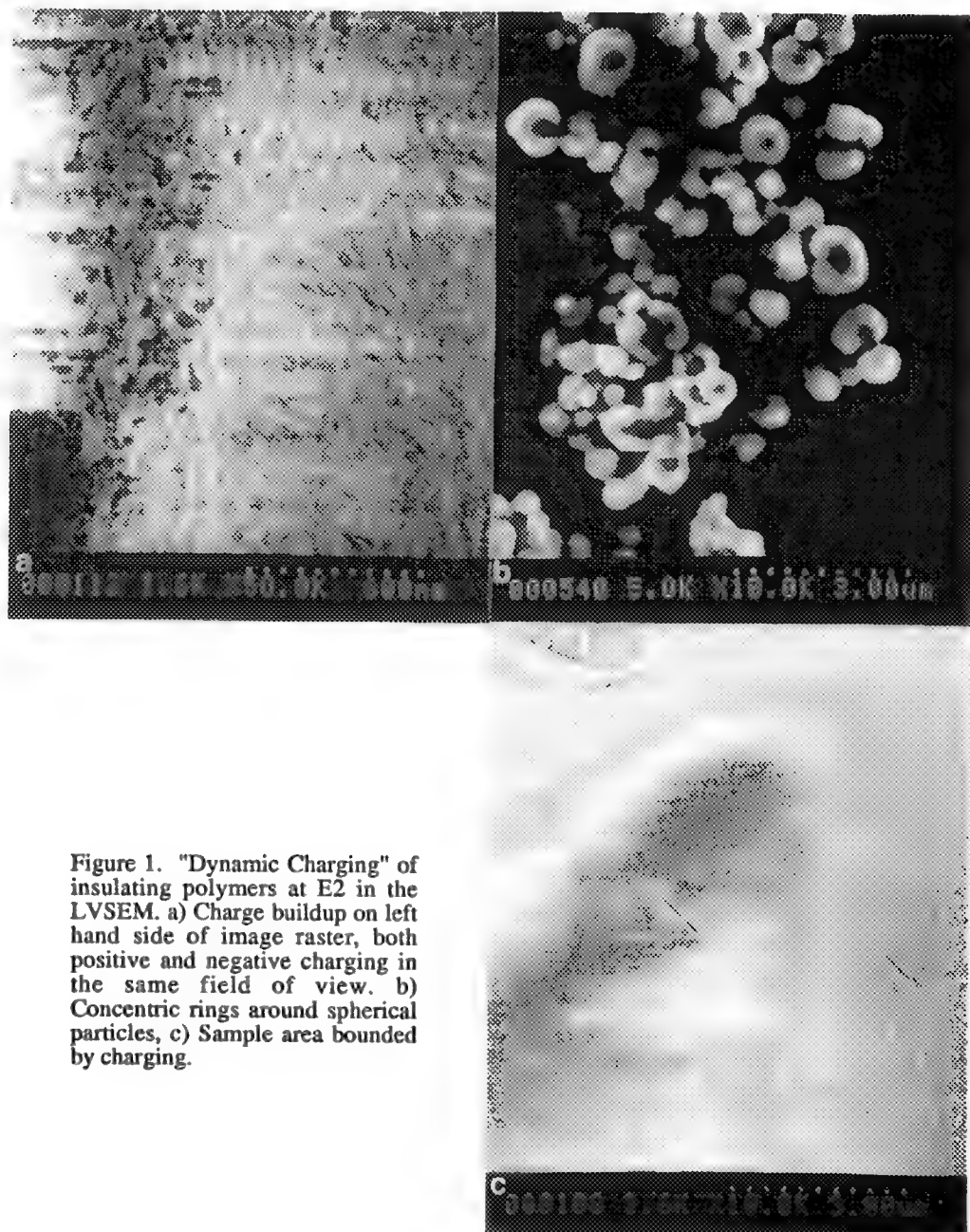


Figure 1. "Dynamic Charging" of insulating polymers at E2 in the LVSEM. a) Charge buildup on left hand side of image raster, both positive and negative charging in the same field of view. b) Concentric rings around spherical particles, c) Sample area bounded by charging.

IMAGING NANOSTRUCTURES ON ABLATED KAPTON POLYIMIDE

Daniel L. Callahan, H. M. Phillips*, and R. Sauerbrey*

Department of Mechanical Engineering and Materials Science, *Department of Electrical and Computer Engineering, Rice University, Houston, TX 77005

Excimer laser irradiation has been used to interferometrically ablate submicron line patterns on to Kapton polyimide [1]. Such patterned material may exhibit highly anisotropic conduction as was predicted from previous studies showing enhanced conductivity from uniformly ablated material [2]. We are currently exploiting this phenomenon to create integrated devices using conventional polymers as both dielectrics and conductors. Extensive scanning electron microscopy (SEM) and limited transmission electron microscopy (TEM) have been conducted in order to characterize the morphology of such patterned nanostructures as a function of processing conditions.

The ablation technique employed produces an interference pattern on the polymer surface of period equal to half that of a diffraction grating period, independent of the laser wavelength [3]. In these experiments, a 328 nm grating has been used to produce line patterns of 164 nm line-spacings as shown in Figures 1 and 2. A 200 Å Au coating has been used to both prevent charging and, perhaps more importantly, enhance contrast. "Beading" or "bubbling" at the ablated valley / unablated ridge interface gives rise to a double row morphology. It is clear from glancing angle SEM, however, that these beads form on the edges of the unablated ridges. Samples for glancing angle SEM may be prepared uniquely from thin polymers and possibly metal foils by wrapping the material about a small cylinder. Such a mounting allows the examination of the sample at a continuous range of glancing angles and is particularly useful for highlighting depressed regions. As illustrated in Figure 3, this technique reveals the excellent depth resolution which is on the order of the lateral resolution.

Plan-view TEM samples of thin commercial Kapton films (~12 µm) can also be made readily using conventional methods. High quality electron transparent samples have been consistently obtained by single-sided argon ion-milling with a 0.4mA current at 5.5 kV first at 25° incidence for 1 hour followed by 1 hour at 15° incidence. A TEM thin film made from a polyimide coated with ~200 Å of Au observation is shown in Figure 4. The strong contrast highlighting the ablated regions reflects the preferential sputtering of gold onto the unablated raised regions. This effect is believed due to the depth and narrowness of the ablated valleys as illustrated in a glancing SEM profile. The inhomogeneous deposition has probably enhanced the morphological contrast considerably in the SEM and may itself be of use in device design.

References:

1. H. M. Phillips, R. L. Callahan, R. Sauerbrey, G. Szabo, and Z. Bor, Appl. Phys. Lett **58**, 2761-2763, 1991.
2. M. Schumann, R. Sauerbrey, and M. C. Smayling, Appl. Phys. Lett **58**, 428-430, 1991.
3. H. M. Phillips, R. L. Callahan, R. Sauerbrey, G. Szabo, and Z. Bor, Appl. Phys. A, **54**, 158-165, 1992.

FIG. 1 line period = 164 nm

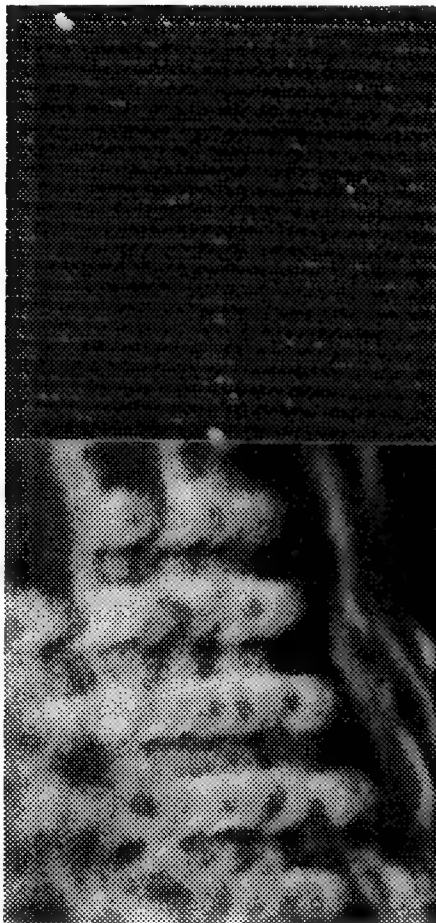


FIG. 2 line period = 164 nm

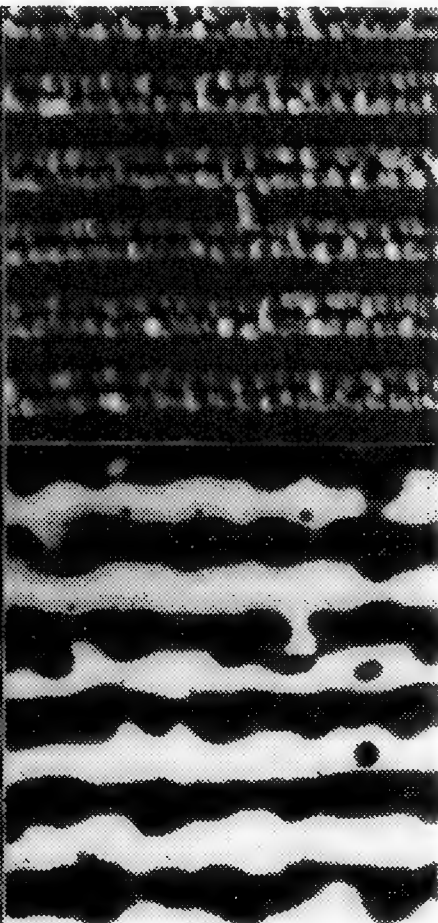


FIG. 3 line period = 164 nm

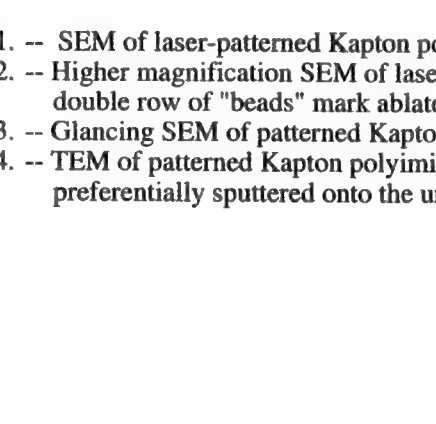


FIG. 4 line period = 164 nm

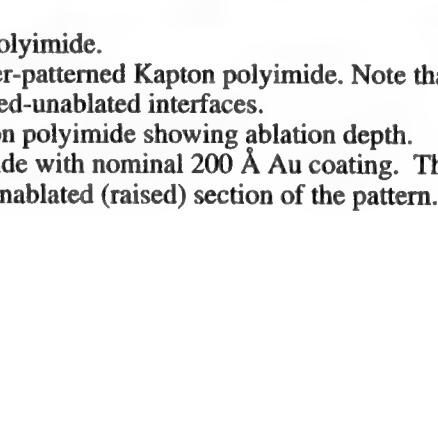


FIG. 1. -- SEM of laser-patterned Kapton polyimide.

FIG. 2. -- Higher magnification SEM of laser-patterned Kapton polyimide. Note that the double row of "beads" mark ablated-unablated interfaces.

FIG. 3. -- Glancing SEM of patterned Kapton polyimide showing ablation depth.

FIG. 4. -- TEM of patterned Kapton polyimide with nominal 200 Å Au coating. The Au has preferentially sputtered onto the unablated (raised) section of the pattern.

SCANNING-PROBE MICROSCOPY OF POLYMERS

Darrell H. Reneker, Rajkumari Patil, Seog J. Kim, and Vladimir Tsukruk

The Maurice Morton Institute of Polymer Science, The University of Akron, Akron, Ohio 44325-3909

Scanning probe microscopy techniques, particularly atomic force microscopy (AFM) and scanning tunneling microscopy (STM) are finding a rapidly growing number of applications to both synthetic and biological polymers¹. Segments of individual polymer molecules can often be observed with atom scale resolution. Observation of polymeric objects as large as 100 microns with nanometer resolution is possible with contemporary AFM, although features caused by the convolution of the shape of the sample and the shape of the tip must be recognized and properly interpreted. The vertical resolution of the atomic force microscope readily provides precise data about the heights of molecules, crystals, and other objects.

Lamellar crystals of polyethylene are well characterized objects with many features which can be observed with scanning probe microscopes. Figure 1 shows the fold surface near a fold domain boundary of a lamellar crystal of polyethylene, as observed with an AFM. The folded chain crystal is about 15 nm thick. The ability to observe sub-nanometer changes in thickness as a function of position led to the discovery that there are broad patches that are up to a nanometer thicker than the surrounding material. Figure 2 shows a small area on the surface of a high performance polyimide fiber. Here, the spacings between the high points of the image correspond to the repeat units along the chain and to the spacing between the chains.

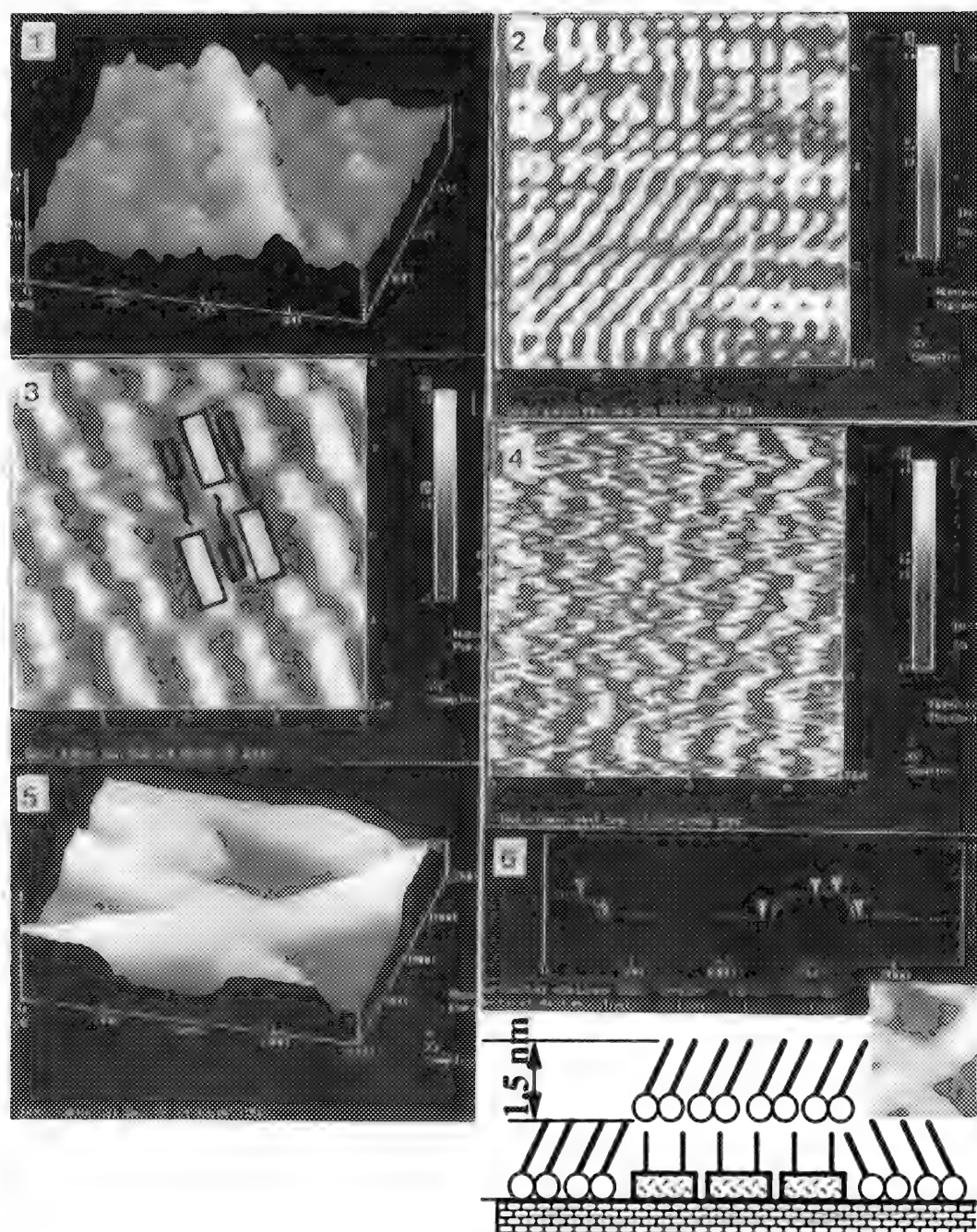
Molecular images of self-assembled monolayer films of discotic liquid crystals² on silicon surfaces are shown in Figure 3. These discotic liquid crystals are composed of molecules in which a charge transfer donor molecule is linked at its edge, with a short flexible chain, to an acceptor molecule. If the link is short, each molecule must participate in two stacks, as indicated in the unit cell superimposed on the image.

Rod-like molecules of poly- γ -glutamate³, in thin films prepared by Langmuir-Blodgett techniques, offer a route to the fabrication of wave guides for light waves. AFM observations of bilayers of this polyglutamate in Figure 4 show that the molecules are aligned, but relatively easy to deform by forces transverse to the chain direction, which can be applied by the scanning tip.

Single crystals of a cyanine dye absorbed on a lipid monolayer and collected on glass or silicon surfaces⁴ are shown in Figure 5. Flat bottomed holes 1.5 nm deep were observed between the crystals, as shown in cross section in Figure 6. The flat dye molecules have ionic groups attached to their edges, so that these molecules are expected to stand on edge on the substrate. The edge to edge dimension of the dye corresponds to the depth of the hole if the tilt of the lipid is the same on the dye crystal and the substrate. The diagram in Figure 6 shows thicknesses deduced from grazing angle x-ray diffraction. The x-ray and AFM data taken together show that the dye crystal is only one molecule thick.

This research was supported by the EPIC/NSF Center for Molecular and Microstructure of Composites, a National Science Foundation State/Industry/University cooperative research center.

1. D.H. Reneker, et al., "Observation of Oligomers, Polymers, and their Crystals by Scanning Tunneling and Atomic Force Microscopy", in *Polymer Characterization*, Ed. by M. Dosiere, Kluwer Academic Press, London, 1993.
2. M. Möller, et al., *Liquid Crystals*, **12**, 17, 1992.
3. A. Mathy, et al., *Thin Solid Films*, **215**, 98, 1992.
4. S. Kirstein and H. Mohwald, *Chemical Physics Letters*, **189**, 408, 1992.



CRYO-TEM OF AMPHIPHILIC POLYMER AND AMPHIPHILE/POLYMER SOLUTIONS

Yeshayahu Talmon

Department of Chemical Engineering, Technion-Israel Institute of Technology, Haifa 32000, Israel

To achieve complete microstructural characterization of self-aggregating systems, one needs direct images in addition to quantitative information from non-imaging, e.g., scattering or rheological measurements, techniques. Cryo-TEM enables us to image fluid microstructures at better than one nanometer resolution, with minimal specimen preparation artifacts. Direct images are used to determine the "building blocks" of the fluid microstructure; these are used to build reliable physical models with which quantitative information from techniques such as small-angle x-ray or neutron scattering can be analyzed.

To prepare vitrified specimens of microstructured fluids, we have developed the Controlled Environment Vitrification System (CEVS), that enables us to prepare samples under controlled temperature and humidity conditions, thus minimizing microstructural rearrangement due to volatile evaporation or temperature changes.¹ The CEVS may be used to trigger on-the-grid processes to induce formation of new phases, or to study intermediate, transient structures during change of phase ("time-resolved cryo-TEM").² Recently we have developed a new CEVS, where temperature and humidity are controlled by continuous flow of a mixture of humidified and dry air streams. This computer-controlled system is especially useful for temperature jump experiments at fixed air humidity, and for controlled on-the grid drying experiments.³

Our work has covered a wide range of complex fluids from biological systems to synthetic surfactants. This presentation will focus on the application of our experimental approach in the study of amphiphilic polymers and amphiphile/polymer systems. For example, we were able to observe the interaction (binding) between sodium dodecyl sulfate (SDS) and a strongly hydrophobic polyelectrolyte, poly(disodium maleate-co-hexadecylvinylether), a polysoap. Due to the strong hydrophobic interactions between the hexadecyl side chains and water, PS16 adopts in aqueous solution a very compact, thread-like micellar conformation.⁴ Cryo-TEM provides direct visual evidence of the disruption of the long thread-like micelles of PS16 into their constituting elements, i.e., individual polymer chains, upon addition of SDS. This disruption is clearly the result of the incorporation of SDS into the PS16 microdomains, and also into the junctions between polymer chains. In PS16 solutions each polymer chain end becomes incorporated into an SDS micelle and the ends lose their capacity to self-associate into aggregates resembling thread-like micelles. This is illustrated in Fig.1. This study is being extended now to polysoap/nonionic surfactant interactions.

Results of our study of the interactions between poly(ethyleneoxide) (PEO) and SDS, and between modified cellulose derivatives, such as ethyl hydroxyethyl cellulose (EHEC),⁵ and cationic or nonionic surfactants will also be presented.⁶

References

1. J.R. Bellare et al., J. Electron Microsc. Tech. (1988)10, 87.
2. Y. Talmon et al. Electron Microsc. Tech. (1990)14, 6.
3. Y. Fink and Y. Talmon, Microsc. Res. Tech. (to be submitted).
4. D. Cochin et al., Macromolecules (1992)25, 4220.
5. B. Lindman and K. Thalberg, in *Polymer-Surfactant Interactions*, Goddard, E.D. and Ananthapadmanathan, K. P., Eds., CRC Press, Chapter 6, in press.
6. This research has been supported by grants from United States-Israel Binational Science Foundation (BSF), Jerusalem and from the Procter & Gamble Company, Cincinnati. The work has been done in collaboration with Prof. R. Zana, Dr. Y. Cohen, Ms. M. Goldraich, and Mr. Y. Fink.

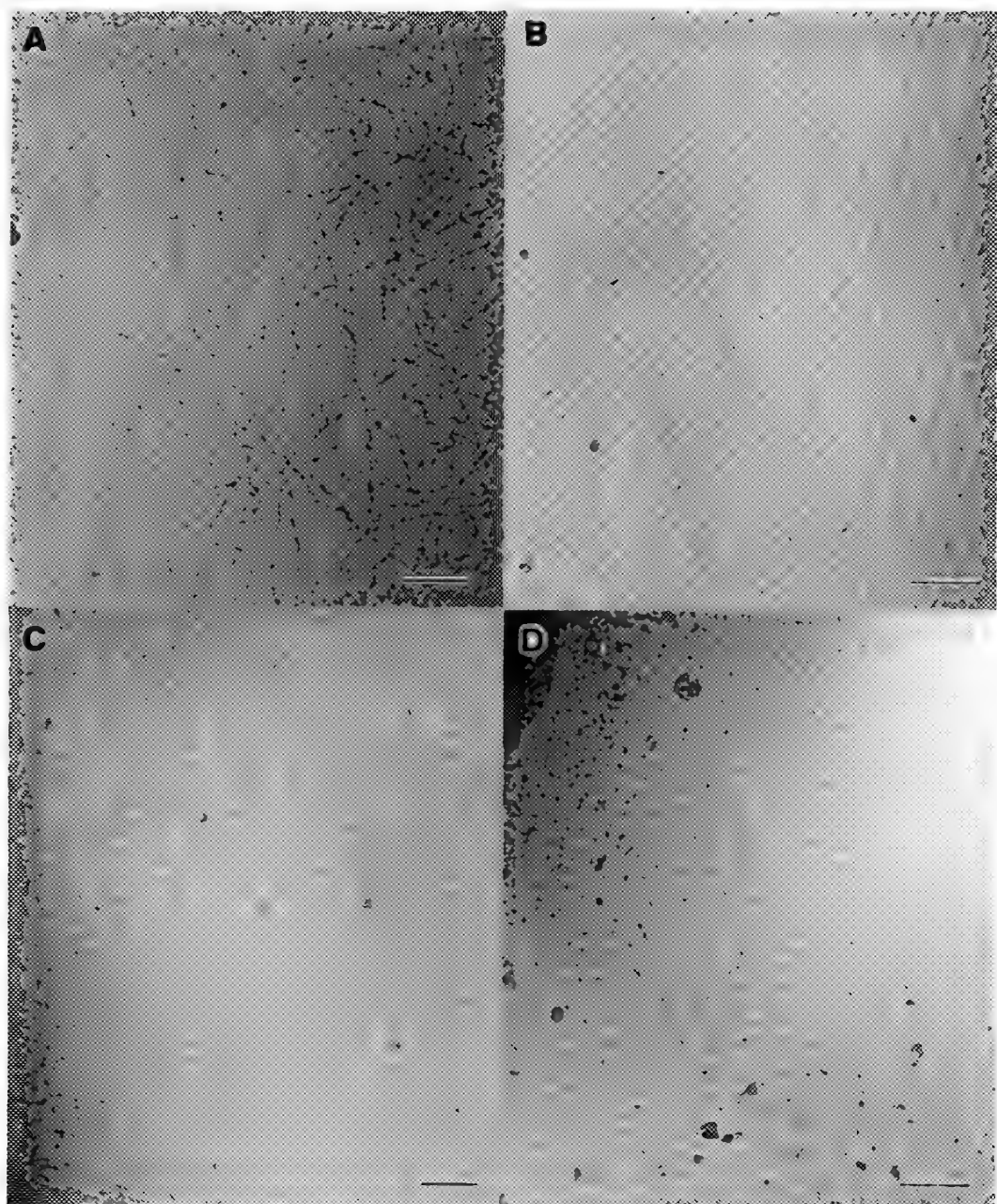


Fig. 1. Cryo-transmission electron micrographs of 9 mM PS16 solutions with increasing amounts of SDS; $R = [\text{SDS}]/[\text{PS16}]$: (A) and (B) $R = 0.57$; note long, entangled thread-like micelles, which are disordered in A, but somewhat oriented in B as a result of sample preparation; at $R = 0.79$ (C), thread-like micelles are still predominant, but some shorter micelles can be seen, too; when $R = 1.0$ (D), only short thread-like micelles coexisting with spheroidal micelles are observed. Bars equal 100 nm.

POLYMER-INDUCED WORMLIKE-TO-SPHERICAL MICELLE TRANSITION IN SURFACTANT SOLUTIONS

ZUCHEN LIN

Department of Chemical Engineering and Materials Science
University of Minnesota, Minneapolis, MN 55455-0132, U.S.A.

In various applications important to chemical, pharmaceutical, petroleum, and mineral processing industries, surfactant molecules are present in solution not alone but along with synthetic or biological macromolecules. The presence of polymer molecules gives rise to changes in the solution and its interfacial properties as compared to the corresponding polymer-free systems.¹⁻³

The interaction between surfactant and polymer results in association of the two, which affect many properties of the system, especially the rheological ones. Recently, a polymer induced transition from non-Newtonian to Newtonian behavior was observed in the CTAB/NaSal system.⁴ This effect was attributed to a polymer-induced break-up of the worm-like micelles into spherical ones. This interpretation can be tested directly by microscopic observation.

In this study, interactions between poly(vinylmethylether) (PVME) or poly(propyleneoxide) (PPO) (Aldrich, WI) and the nonionic surfactant pentaethylene glycol mono-dodecyl ether ($C_{12}E_5$) (Nikkol, Japan) or the cationic surfactant cetyltrimethylammonium bromide (CTAB) (Aldrich) with presence of sodium salicylate (NaSal) (Mallinkordt, MO) were examined by cryo-TEM and rheometry.

Figure 1 shows a cryo-TEM image of a 25 mM CTAB/15 mM NaSal aqueous solution. Long entangled wormlike micelles, about 60 Å in diameter, are evident in the micrograph. Their lengths cannot be determined accurately because of overlapping, but some micelles are estimated to be more than 1 μm long. By adding PVME or PPO to this CTAB/NaSal solution, the wormlike micelles undergo wormlike-to-spherical micelle transition. Figure 2 shows micelles in a CTAB/NaSal solution containing 1 g/L PVME; there are still some wormlike micelles. They coexist with many spherical micelles. The mean length of the wormlike micelles has diminished to several hundred Å. With addition of more PVME to the solution, all the wormlike micelles transform to spherical micelles, as shown in Figure 3. Addition of PPO had a similar effect. The transition is presumably due to the transfer of hydrophobic polymer segments from the aqueous phase to the micellar surroundings. This would increase the volume of the hydrophobic core of the micelle, to favor formation of polymer-bound spherical micelle.³ As the result of this transition, the solution lost its viscoelastic behavior and became Newtonian.^{4,5}

Addition of polymer into $C_{12}E_5$ aqueous solutions, however, had little effect on the wormlike micelles in the solution.³ Figure 4 shows cryo-TEM images of 2 wt% $C_{12}E_5$ in water. Highly flexible wormlike micelles formed in the solution. Steady shear measurement showed the solution viscosity to be about 4 times higher than water viscosity, and unchanging over shear rate in the range 0.1 s^{-1} to 1000 s^{-1} : evidently even though wormlike micelles form, the solution

remains Newtonian. Figures 5 and 6 show cryo-TEM images of 2 g/L and 5 g/L PPO, respectively, added to 2 wt% $C_{12}E_5$ aqueous solutions. Micelles in both images are still wormlike micelles but may be somewhat shorter, which is consistent with the observation that the viscosities of the solutions were lowered.

Thus cryo-TEM images strongly supported the hypothesis that micellar structure change is responsible for the changes in rheological properties of the solutions.

1. E. D. Goddard, *Colloids & Surfaces* 19(1986)255.
2. S. Saito, in M. J. Schick, Ed., *Nonionic Surfactants*, New York: Marcel Dekker (1987)881.
3. R. Nagarajan, *J. Phys. Chem.* 90(1989)1980.
4. J. C. Brackman et al., *J. Am. Chem. Soc.* 112(1990)872.
5. J. C. Brackman et al., *Langmuir* 7(1991)2097.
6. This research was supported by NSF Center for Interfacial Engineering at University of Minnesota.
7. Author thanks Profs. H. T. Davis, L. E. Scriven, and Y. Talmon for stimulating discussions.

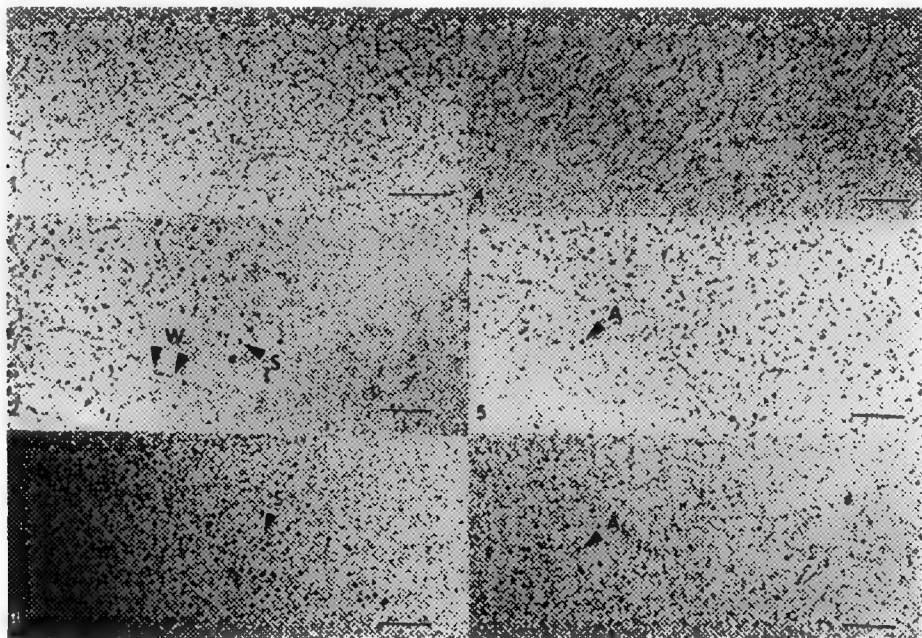


FIG. 1. — 25 mM CTAB and 15 mM NaSal. Entangled wormlike micelles. Bar = 50 nm.

FIG. 2. — 25 mM CTAB, 15 mM NaSal, and 1 g/L PVME. Short wormlike micelles coexist with spherical micelles. Bar = 50 nm.

FIG. 3. — 25 mM CTAB, 15 mM NaSal, and 5 g/L PVME. Only spherical micelles appear. Bar = 50 nm.

FIG. 4. — 2 % $C_{12}E_5$. Highly flexible wormlike micelles. Bar = 50 nm.

FIG. 5. — 2 % $C_{12}E_5$, and 1 g/l PPO. Polymer does not change shape of micelles. Bar = 50 nm.

FIG. 6. — 2 % $C_{12}E_5$, and 5 g/l PPO. Polymer does not change shape of micelles but shortened them. Bar = 50 nm.

CRYO-TEM STUDY OF NOVEL MORPHOLOGY IN MIXED SURFACTANT-LIPID SYSTEMS

S. Chiruvolu

Department of Chemical and Nuclear Engineering, University of California, Santa Barbara, CA 93106

Microstructured fluids arise in a number of biological, chemical, and physical systems as interfaces, films, emulsions, membranes, gels, and liquid crystals. We have recently discovered a wealth of new types of microstructure formed by mixed surfactant systems in water, including the first system of spontaneous, equilibrium vesicles formed by simple cationic and anionic surfactant mixtures.¹ Many of these systems present unusual rheological or phase behavior, and accompanying technological opportunities. However, these systems do not lend themselves to simple characterization by conventional light, X-ray, or neutron scattering, NMR, etc. This is due to the indirect nature of these probes; structural information is inferred from these measurements, and a model is often necessary to infer structural information. For mixed surfactant systems, the microstructure is often so unexpected as to make it impossible to construct a model; or worse, a model built on simple structural concepts leads to erroneous interpretation.² Cryo-electron microscopy is a necessary alternative to these techniques as the structural information provided is much more direct and model independent.

Specimens for cryo-electron microscopy are prepared by making thin films (50 - 250 nm) of the sample liquid on a holey-film grid in an environmental controlled chamber.³ The specimen is vitrified by plunging into a bath of liquid propane cooled by liquid nitrogen. The grid is transferred under liquid nitrogen to a Gatan 626 cryo-stage and imaged directly at -168° C in a JEOL 2000FX TEM. Images are recorded on Kodak SO163 plates and developed using D-19 developer at full strength and then photographically enlarged.

Cryo-electron microscopy has proved to be extremely useful in elucidating the structure of mixed phospholipid and surfactant assemblies. Rather subtle changes in the surfactant additive to the phospholipid produce dramatic changes in the microstructure of the composite that were impossible to determine from simple scattering experiments. Fig. 1 shows disc-like micelles formed by mixing dipalmitoylphosphatidylcholine (DPPC) with diheptanoylphosphatidylcholine (DHPC) at a molar ratio of 4:1 and 25 mM total concentration in water. At 25° C, 30 - 100 nm disc-micelles coexist with micron-sized rigid bilayer fragments which show clear evidence of the rippled structure of the P_g phase (Pure DPPC forms flat L_g bilayers and pure DHPC forms cylindrical micelles under these conditions). This observation suggests that there is likely a lateral phase separation of the DHPC, which prefers a highly curved, micelle-like structure, to the edges of the DPPC-rich bilayer fragments and discs. Previous light scattering and NMR measurements suggested that the microstructure in the mixed DPPC-DHPC system consisted of closed, unilamellar vesicles,² which is clearly incorrect.

In a similar system, dimyristoylphosphatidylcholine (DMPC) and geraniol (a branched chain alcohol which is precursor to Vitamin A) mixed in a 4:1 mass ratio at 3 wt% total concentration in water produces a two phase mixture.⁴ The top phase is translucent and extremely viscoelastic, while the bottom phase is Newtonian and transparent. Fig. 2 shows that the top phase consists of giant wormy vesicles spanning several microns. The vesicles are typically multilamellar and appear quite fluid. The bottom phase (not shown) consists of polydisperse collection of unilamellar vesicles of sizes ranging from 10 nanometers to several microns. Under flow, we observe large normal stress effects (e.f. the Weissenberg effect) in the top phase caused by the distortion of the entangled giant multilamellar vesicles. Entanglements of objects of this size have never before been observed. What is quite surprising is the great difference in microstructures observed between these two samples of generally similar chemical composition. Both samples show the power of cryo-TEM in determining new structures, thereby allowing simple correlations to be drawn between fluid properties and microstructure.⁵

1. E. W. Kaler, A. K. Murthy, B. Rodriguez, and J. Zasadzinski, *Science*, **245**, 1371 (1989).
2. N. E. Gabriel and M. F. Roberts, *Biochemistry*, **23**, 4011 (1984).
3. J. Bellare, et al., *J. Electron Microscope Tech.*, **10**, 87 (1988).
4. The DMPC/geraniol sample was provided by C. R. Safinya.
5. We acknowledge financial support from the donors of the PRF, NSF grant #CTS90-15537, the MRL program of the NSF, award #DMR-9123048, and the NIH under Grant #GM47334.

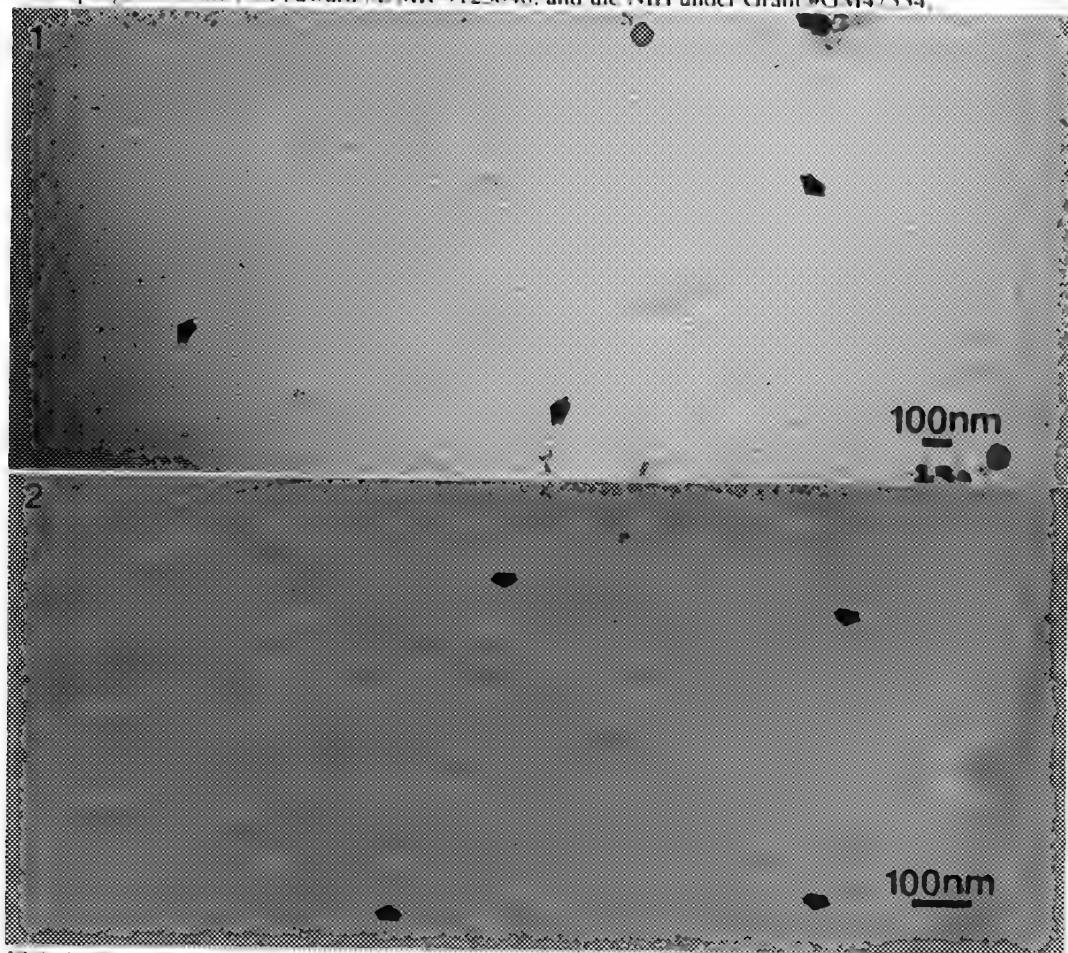


FIG. 1. Cryo-electron micrograph showing disk-micelles from a DPPC/DHPC (4:1 by mole) mixture 25mM total lipid concn. and vitrified at 25°C. Disk-micelles are seen at different projections which cause them to appear different in contrast level, with a line projection being the darkest and the circle appearing the faintest in the micrograph.

FIG. 2. Top phase of DMPC/Geraniol (4/1) mixture showing long (several microns) undulating wormy vesicles. The bilayers appear extremely flexible and unbound from a multilayered L_α state known for pure DMPC at 25°C. The entangled vesicles give rise to the highly viscoelastic behavior observed in solution.

MORPHOLOGICAL STUDY OF STRUCTURED LATEX PARTICLES BY TRANSMISSION ELECTRON MICROSCOPY

Iris Segall*, Olga L. Shaffer, Victoria L. Dimonie, and Mohamed S. El-Aasser

Emulsion Polymers Institute, Lehigh University, Bethlehem, Pennsylvania, 18015

Transmission electron microscopy plays an important role in the study of the influence polymerization conditions have on the morphology of structured latex particles and thus in the understanding of the morphological effect of such particles on the structure-property relationships of polymeric end products.

Structured latex particles are prepared by seeded emulsion polymerization, where the first stage is a polymerization of "the core" poly(*n*-butyl acrylate) (PBA), followed by a second stage polymerization of "the shell" poly(benzyl methacrylate/styrene) (P(BM/St)) at various ratios. The changes in polymerization conditions include such variables as the polymerization mode (batch vs. semicontinuous), core/shell ratio, shell thickness, and shell composition. Morphology studies of the structured latex particles are performed by transmission electron microscopy on preferentially stained samples. In a small vial, a few drops of latex sample are combined with a few drops of uranyl acetate (UAc) 2% solution. The uranyl acetate serves as a negative staining to better delineate the particles edges. A drop of the mixture is deposited on a stainless steel grid covered with formvar film and allowed to dry. Subsequently, the grid with the latex sample is subjected to ruthenium tetroxide (RuO₄) vapors for preferential staining which facilitates differentiating the rubbery PBA from the glassy phases.¹ PS and PBM stain dark by RuO₄ due to the presence of a ring in their chemical structure while PBA remains light in color.

Figure 1 shows a core/shell latex prepared by batch polymerization where the PBA seed particles appear to be only partially covered by the PBM second stage polymer. Figure 2 shows that PBA/PBM latex prepared by semicontinuous addition of the BM second stage monomer yields a better, though not complete, coverage of the seed latex particles. Figures 3, 4, and 5 allow for the comparison of the morphology differences due to variations in the shell polymer composition; PBM (in 3), P(BM/St) (in 4), and PS (in 5). Latex particles with the 100% PS shell polymer appear to have one thicker patch, and a larger uncovered surface; latex particles with shells comprised of 95/5 P(BM/St) appear to have patches of different thicknesses all around the core particles, while 100% PBM tend to cover the PBA with a continuous shell. Figures 6 and 7 indicate the morphological differences caused by the presence of IOMP (a chain transfer agent mixed with the BM monomer prior to the second stage polymerization).²

As seen by the sequence of transmission electron micrographs, microscopy is a powerful technique in following on the effect process parameters have on the morphology of structured latex particles and eventually in understanding the mechanical properties of products made with these structured latex particles.³

References

1. J.S. Trent, J.I. Scheinbeim, and P.R. Couchman, *Macromolecules* 16(1983)589.
2. I. Segall, Structured latex particles for the toughening of polycarbonate, Ph.D. Dissertation, Lehigh University, (1992).
3. This project was partially supported by Enichem America Inc.

*Currently at Department of Materials Science & Engineering, University of Cincinnati, Cincinnati, Ohio, 45221.

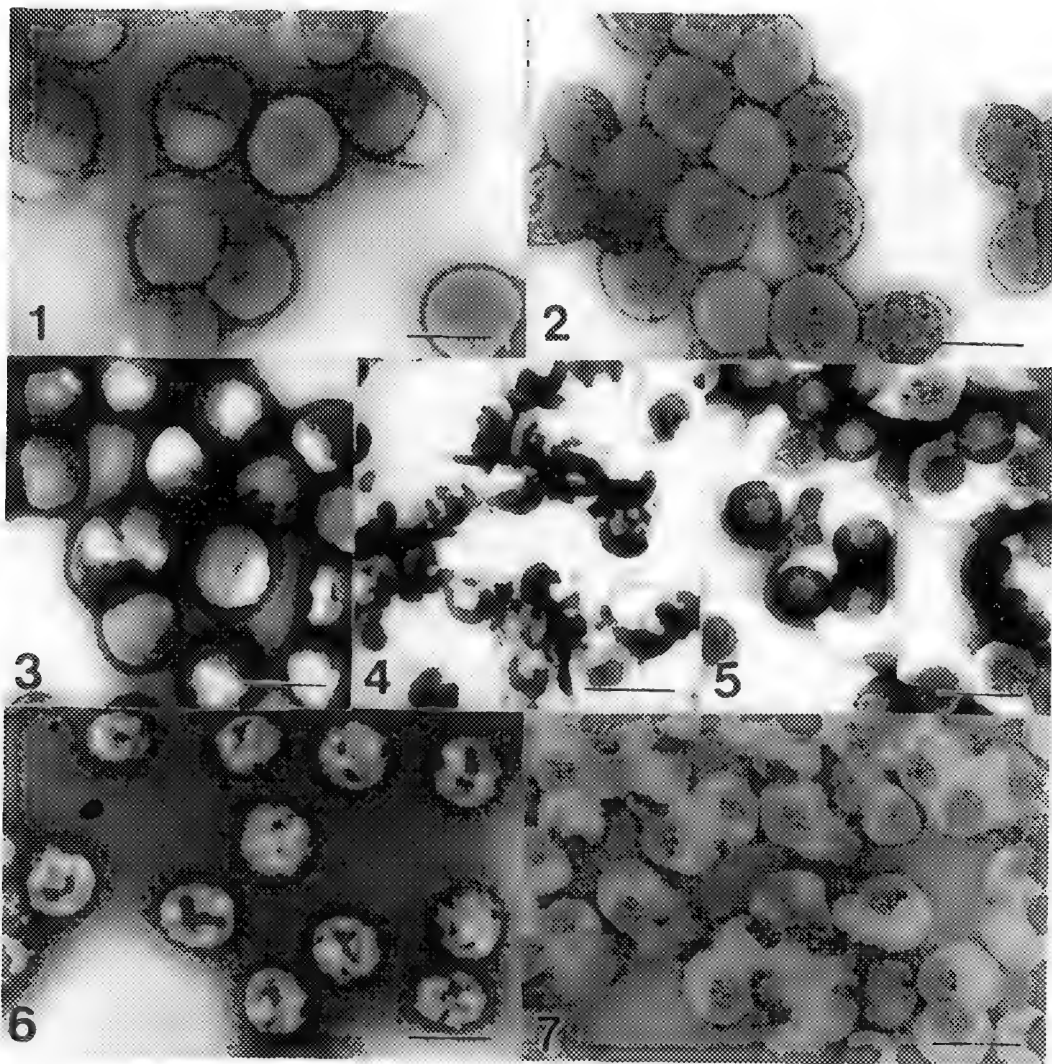


FIG. 1. TEM of 1/3 PBA/PBM latex particles. Second stage prepared via batch polymerization. Bar = 0.3 μm .

FIG. 2. TEM of 1/3 PBA/PBM latex particles. Second stage prepared via semicontinuous polymerization. Bar = 0.3 μm .

FIG. 3. TEM of 1/1 PBA/PBM core/shell latex particles. Bar = 0.3 μm .

FIG. 4. TEM of 1/1 PBA/P(BM/St) core/shell latex particles. Bar = 0.3 μm .

FIG. 5. TEM of 1/1 PBA/PS core/shell latex particles. Bar = 0.3 μm .

FIG. 6. TEM of 1/0.4 core/shell latex particles. Core is PBA. Shell is PBM synthesized in the absence of chain transfer agent. Bar = 0.3 μm .

FIG. 7. TEM of 1/0.4 core/shell latex particles. Core is PBA. Shell is PBM synthesized in the presence of chain transfer agent. Bar = 0.3 μm .

TRIPLY-PERIODIC NANOSTRUCTURES IN SURFACTANT, BLOCK COPOLYMER, AND BIOMEMBRANE SYSTEMS, and SIMULATION OF TEMs

David M. Anderson and Tomas Landh

Department of Biomaterials, SUNY @ Buffalo, NY 14214

First discovered in surfactant-water liquid crystalline systems, so-called 'bicontinuous cubic phases' have the property that hydrophilic and lipophilic microdomains form interpenetrating networks conforming to cubic lattices on the scale of nanometers¹. Later these same structures were found in star diblock copolymers², where the simultaneous continuity of elastomeric and glassy domains gives rise to unique physical properties. Today it is well-established that the symmetry and topology of such a morphology are accurately described by one of several triply-periodic minimal surfaces, and that the interface between hydrophilic and hydrophobic, or immiscible polymer, domains is described by a triply-periodic surface of constant, non-zero mean curvature³. One example of such a dividing surface is shown in figure 5.

The study of these structures has become of increasing importance in the past five years for two reasons:

1) Bicontinuous cubic phase liquid crystals are now being polymerized to create microporous materials with monodispersed pores and readily functionalizable porewalls⁴; figure 3 shows a TEM from a polymerized surfactant / methylmethacrylate / water cubic phase⁴; and

2) Compelling evidence has been found that these same morphologies describe biomembrane systems in a wide range of cells⁵.

A crucial part of our studies of these systems has been the simulation of TEM projections, as well as SAXS intensities and NMR self-diffusion data⁶, by the use of the constant-mean-curvature models. Computer modeling using these precisely-defined models is in some cases augmented by the use of an image restoration method that performs a maximum entropy restoration on the power spectrum of the image, and thus tests periodic features for statistical support⁷.

Striking fits to TEM data for several tilt angles provide strong evidence of validity of a model -- which in the case of TEM data of the endoplasmic reticulum casts serious doubt on the traditional model of biomembranes, and leads us to look at ordered, bicontinuous morphologies as providing spatial discretization within the cell. Figures 1 and 2, for example, show actual and simulated TEM data for the ER in a river lamprey retinal epithelial cell (reprinted from ref. 8 with permission).

1. V. Luzzati and D. Chapman, *Biological Membranes*, NY: Academic (1968).
2. E. L. Thomas et al., *Macromolecules* 19 (1986) 2197.
3. D. M. Anderson et al., *Adv. Chem. Phys.* 77 (1990) 337.
4. D. M. Anderson and P. Strom, *Polymer Association Structures*, ACS Symposium Series 384, Ed. M. El-Nokaly, 1989, p. 204.
5. T. Landh, in *The Language of Shape*, Elsevier/Pergamon (in press).
6. P. Strom and D. M. Anderson, *Langmuir* 8 (1992) 691.
7. D. M. Anderson, D. C. Martin, E. L. Thomas, *Acta Cryst.* A45 (1989) 686.
8. P. Ohman, *Acta Zool.* 55 (1974) 245.

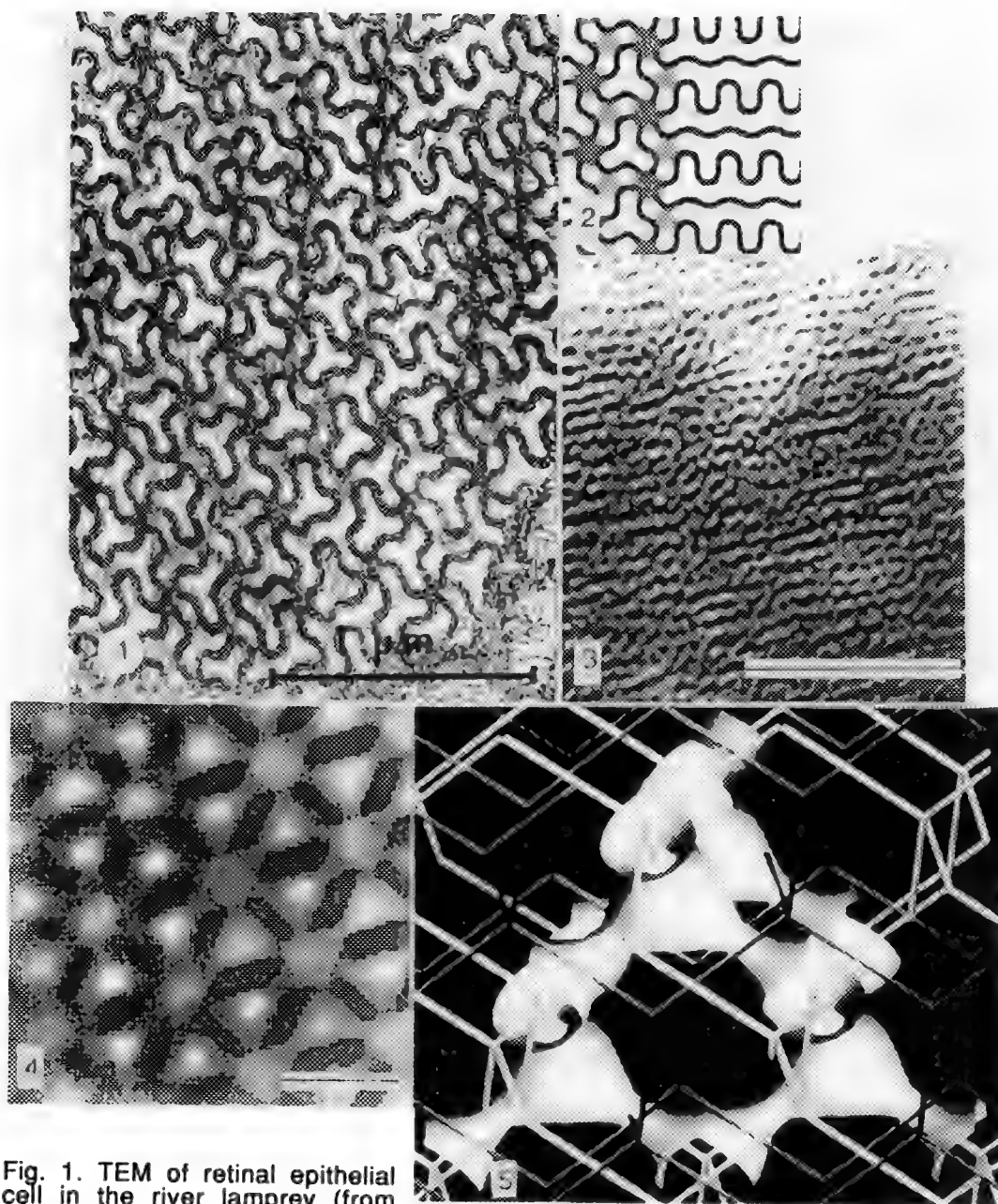


Fig. 1. TEM of retinal epithelial cell in the river lamprey (from ref. 8). Bar=1 μ m.

Fig. 2. A computer simulation of Fig. 1.

Fig. 3. TEM of polymerized cubic phase. Bar=50 nm.

Fig. 4. Left half: restored TEM data of polyisoprene-polystyrene star diblock copolymer; right half: computer simulation. Bar=20 nm.

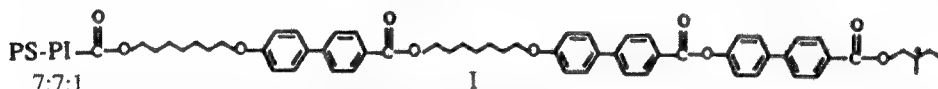
Fig. 5. The model used for the simulation in Fig. 4.

THE MORPHOLOGY AND STRUCTURE OF A ROD-COIL POLYMER AND ITS MOLECULAR OBJECT DERIVATIVES

L. S. Li and S. I. Stupp

Department of Materials Science and Engineering, University of Illinois at Urbana-Champaign
 Urbana, IL 61801

Several non-crystalline ordered structures are known in polymer science; these include liquid crystalline structures and long range ordered microdomain structures of amorphous block copolymers with well defined block lengths. It would be very interesting to combine these two types of structures together to form a block copolymer in which a rigid board-like or rod-like mesogen block is connected to a coil-like chain. These copolymers, containing a mesogenic block and a short block of polyisoprene (PI), polystyrene (PS) or a diblock sequence have been synthesized in our laboratory^{1,2}. The chemical structure of one of the copolymers is shown below:



If a molecular object, such as molecular sheet or rod could be formed through microphase separation and cross-linking among the PI blocks, a nanocomposite with liquid crystalline, rubbery and glassy regions could be formed. In order to reveal the morphology and structure of the rod-coil copolymer and its molecular object we studied the copolymer using electron microscopy and electron diffraction techniques.

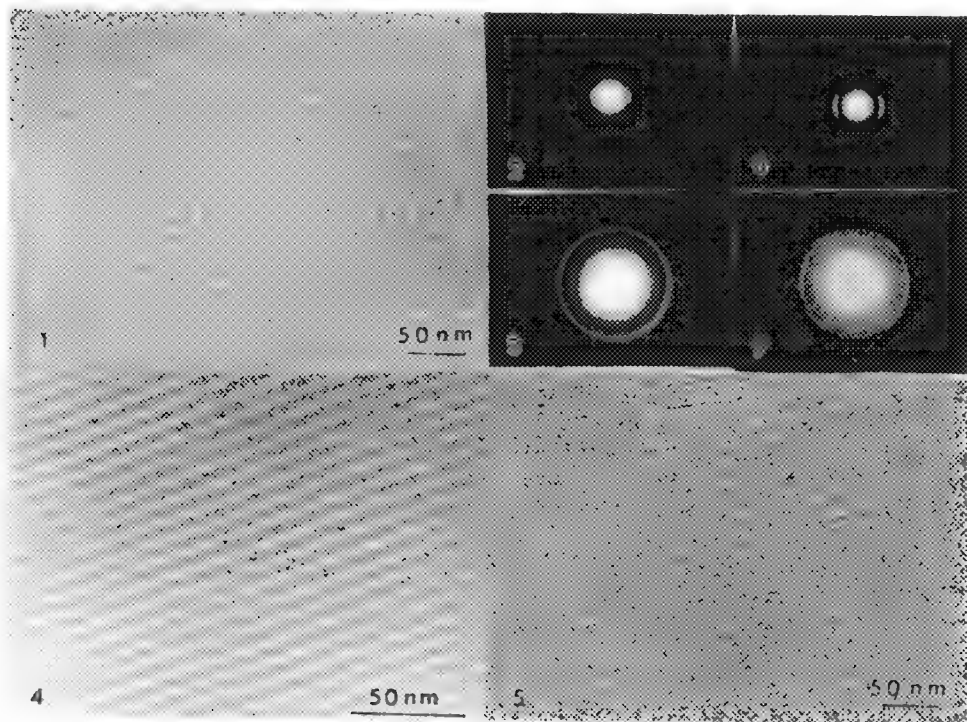
Thin films of the copolymer (I) were prepared using a solution casting technique and examined in a Philips CM-12 electron microscope at 120 KV. Fig.1 is an electron micrograph of the thin film. This figure shows a lamellar structure with alternating dark and light layers indicating microphase separation. The dark layer is the mesogenic core phase and the light layer contains the PI and PS diblock phase. Fig.2 is a small angle electron diffraction pattern of the film, indicating that the periodic spacing of the lamellae is 83 Å. The chain axes of the copolymer are in the plane of the film and perpendicular to the layers. The PI and PS chains are more or less stretched. Fig.3 is a wide angle electron diffraction pattern. The sharp reflections in the pattern can be indexed as 212 (4.50 Å) and 417 (3.04 Å) (weak, not shown in the print) corresponding to orthorhombic unit cell parameters of $a = 15.25$ Å, $b = 5.60$ Å and $c = 83$ Å. The results indicate that the mesogenic core phase is probably a smectic E phase. Fig.4 is an electron micrograph of the thin film stained with OsO₄. This figure shows a lamellar structure with dark (1), narrow light (2), dark (3) and wide light (4) sublayers alternating along the direction perpendicular to the layers. One of the dark sublayer is the mesogenic core phase, another dark sublayer contains PI blocks stained with OsO₄, the narrow light line is the interphase between mesogenic cores and stained PI blocks and is probably associated with the aliphatic spacer of the mesogen and the wide light sublayer is the PS phase. Therefore there appears to also be microphase separation between the PI and PS blocks in the film. Fig.5 is an electron micrograph of the thin film heated at 130°C for two days under vacuum, in order to form molecular objects by cross-linking PI blocks, and then slowly cooled to room temperature. This figure shows even clearer lamellae with mesogenic core and PI-PS sublayers alternating along the normal to the layers. Fig.6 is a small angle electron diffraction pattern of the heated film, indicating long range order in the lamellar structure. Fig.7 is a wide angle electron diffraction pattern of the heated film. In this pattern, in addition to 212 and 417 reflections, four new reflections (012, 014, 016 and 018) appear at smaller angles indicating that the order in the mesogenic core sublayer is improved and both \vec{c} and \vec{b} are aligned in the plane of the film. Because of cross-linking two-dimensional polymers shaped as sheets are formed. Each sheet consists of a mesogenic core sublayer, a cross-linked PI sublayer and a PS sublayer.

Therefore liquid crystalline, rubbery and glassy properties should be combined in a single molecule at room temperature.

Based on the electron microscopy and electron diffraction results the following conclusions can be reached: (1) Thin films of the rod-coil copolymer exhibit a lamellar morphology with a mesogenic core sublayer, an interphase between mesogenic cores and PI blocks, a PI sublayer and a PS sublayer alternating along the normal to the layers. (2) The mesogenic cores are packed in an orthorhombic lattice with their long axes aligned in the plane of the film and perpendicular to the layers. The PI and PS blocks are more or less stretched and confined in separated sublayers. (3) The heated film of the copolymer is composed of molecular sheets. Each sheet consists of a mesogenic core sublayer, a cross-linked PI sublayer and a PS sublayer. The mesogenic cores are packed in an orthorhombic lattice with *b* and *c* aligned in the plane of the film.

References

1. L. H. Radzilowski et al, *Macromolecules* (1993) 26, 879
2. S. I. Stupp et al, *ACS Polymer Preprints*, (1993) 34 (1)



- Fig.1--- Electron micrograph of the thin film of the rod-coil copolymer.
Fig.2--- Small angle electron diffraction pattern of the film.
Fig.3--- Wide angle electron diffraction pattern of the film.
Fig.4--- Electron micrograph of the film stained with OsO₄.
Fig.5--- Electron micrograph of the heated film.
Fig.6--- Small angle electron diffraction pattern of the heated film.
Fig.7--- Wide angle electron diffraction pattern of the heated film.

ELECTRON TOMOGRAPHY OF MICROSTRUCTURAL ELEMENTS IN STRONGLY SEGREGATED BLOCK COPOLYMERS

Richard J. Spontak,* Steven D. Smith† and David A. Agard‡

*Department of Materials Science & Engineering, North Carolina State University, Raleigh, NC 27695

†Corporate Research Division, The Procter & Gamble Company, Cincinnati, OH 45239

‡Howard Hughes Medical Institute and Department of Biochemistry & Biophysics, University of California, San Francisco, CA 94143

Block copolymers are composed of long contiguous sequences (blocks) of chemically dissimilar monomer species. By themselves or in microphase-separated blends, these materials readily undergo self-organization into either disordered micelles or ordered morphologies, much in the same way as do small-molecule amphiphiles.¹ In the strong-segregation regime, wherein only repulsive monomer interactions and periodic morphologies prevail, a copolymer can assemble into spherical or cylindrical dispersions of one block in a continuous matrix of the other or alternating lamellae. Recent efforts^{2,3} have also shown that an ordered bicontinuous double-diamond morphology (OBDD) exists between the cylindrical and lamellar morphologies. Ongoing studies continue to reveal the existence of other non-classical morphologies, such as the lamellar catenoid,⁴ in both pure copolymers and in blends.⁵ Attempts to elucidate the 3-D structure of these materials have relied upon computer simulation of idealized periodic surfaces and comparison between "slices" of simulated structures with projections from transmission electron microscopy (TEM).^{4,6} Here, we employ electron tomography to discern the 3-D structure of block copolymer morphologies *in-situ*, regardless of microstructural periodicity.

The three systems used in this study, described in detail below, all consisted of block copolymers composed of styrene (S) and isoprene (I) monomers. In each case, 5% (wt/v) toluene solutions were cast into Teflon molds. Following slow solvent evaporation (ca. 3 weeks), the resultant films were heated to remove residual solvent and subjected to high vacuum (ca. 10^{-5} torr) and Ar prior to annealing at 165° C for 1 week. Thin specimens measuring about 70 nm thick were produced by sectioning at -100° C on a Reichert-Jung FC-4E cryoultramicrotome with a 35° Diatome cryodiamond knife. The isoprene-rich microphases were selectively stained with OsO₄ vapor from a 2% aqueous solution for 90 min. One surface of each specimen was first coated with polylysine to promote hydrophilicity and then decorated with 20 nm colloidal gold. Digital TEM images were recorded from -60° to +60° in 2.5° increments with a Gatan 679 CCD detector on a Philips 430 electron microscope. Each projection was subsequently corrected for mass thickness and aligned with respect to the gold beads. Three-dimensional volume elements were generated with the filtered back-projection protocol.⁷

Figure 1 is a pair of images clearly displaying the OBDD morphology, at two different orientations, in a 60/40 (wt%/wt%) blend of two strongly-segregated diblock copolymers, both of which possess a molecular weight (M) of 80 kDa. The first copolymer is 50/50 S/I and exhibits a lamellar morphology, while the second is 85/15 S/I and exhibits dispersed isoprene spheres in a styrene matrix. Upon reconstruction, the resultant volume element of the OBDD morphology can be analyzed by "slice" along any axis in cartesian space. The montage presented in Fig. 2. consists of x-y slices (where the x and y axes are \perp to the electron beam) along the z axis. Each image in this montage contains structural information which is unobscured by specimen thickness. A 3-D rendering of the volume element, partially eroded from the fore-ground, is shown in Fig. 3. Note that the channel network inferred from an idealized *Pn3m* periodic surface is visible here. Figure 4 is a montage of x-y slices from a 50/50 blend of a diblock and an octablock copolymer, each possessing M=120 kDa and 50/50 S/I. Due to the difference in molecular architecture, the copolymers undergo macrophase separation. The interface separating the macrophases is of interest, since S and I are present in each phase in equal proportion. Close examination of the images in Fig. 4 reveals that the spatial arrangement by which analogous lamellae in each phase are connected varies with position along the interface front.

References

1. D.M. Anderson et al., *Adv. Chem. Phys.* (1990)77, 337.
2. E.L. Thomas et al., *Macromolecules* (1986)19, 2197.
3. H. Hasegawa et al., *Macromolecules* (1987)20, 1651.
4. E.L. Thomas et al., *Nature* (1988)334, 598.
5. R.J. Spontak et al., *Macromolecules* (1993)26, 956.
6. D.M. Anderson et al., *J. Coll. Interface Sci.* (1992)148, 398.
7. R.H.T. Bates and M.J. McDonnell, *Image Restoration and Reconstruction*, Oxford: Clarendon (1986):166-170.
8. RJS gratefully acknowledges financial support from NCSU. We also thank A. Ashraf, J. Fung, and M.B. Braunfeld for their valued assistance in this study.

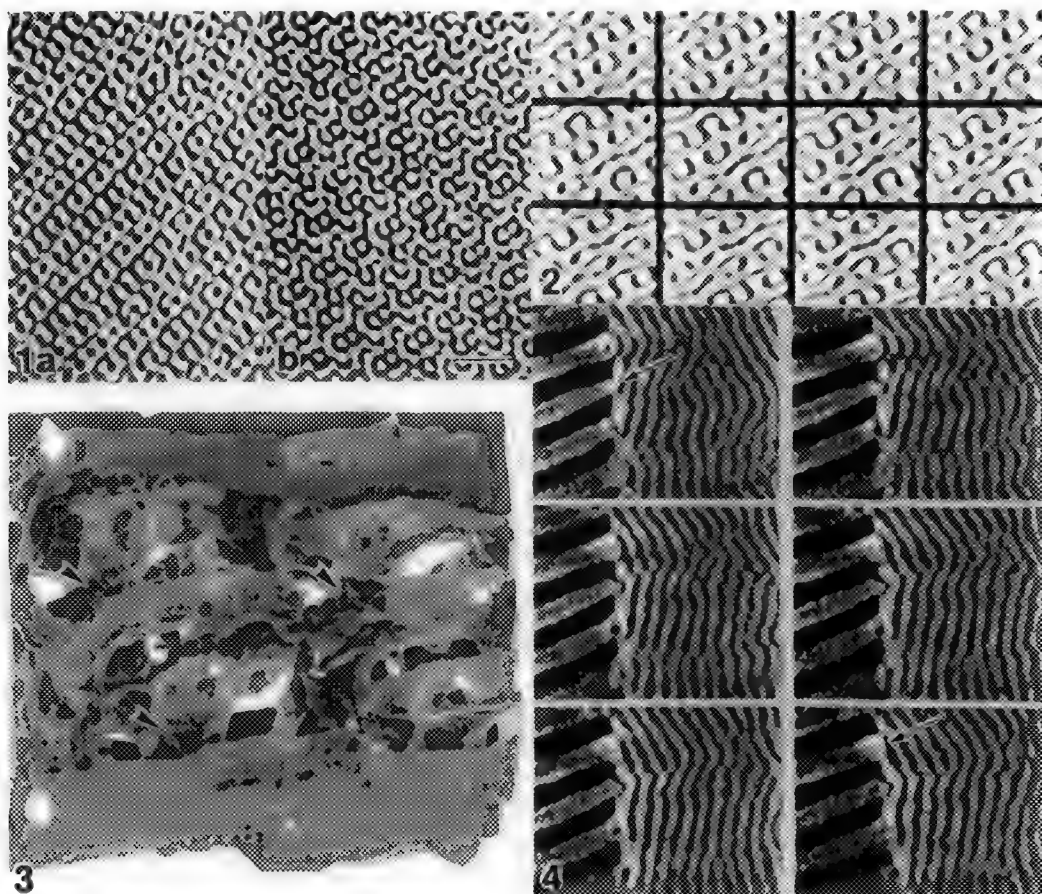


FIG. 1.--Pair of TEM images obtained at different orientations revealing OBDD morphology in 60/40 blend of two ordered diblock copolymers. All images shown here are contrast-reversed. Bar = 200 nm.
 FIG. 2.--Montage of x-y slices along z axis (z is || to electron beam) from reconstructed OBDD morphology. Images collected at 2.1 nm/pixel. Sequence is from left to right and then top to bottom.
 FIG. 3.--Reconstructed three-dimensional OBDD morphology, generated with Renderman® on SGI workstation. It is partially eroded from foreground to show internal channel network (arrowheads).
 FIG. 4.--Montage of x-y slices of macroscopic interface arising in diblock/octablock blend. TEM images acquired at 1.7 nm/pixel. Note change in interfacial lamellar connectivity with z (arrows).

DYNAMIC LOW-DOSE ELECTRON DIFFRACTION AND IMAGING OF PHASE TRANSITIONS IN POLYMERS

David C. Martin and Jun Liao

2022 H. H. Dow Building, Materials Science and Engineering and the Macromolecular Science and Engineering Center,
The University of Michigan, Ann Arbor, MI 48109-2136

By careful control of the electron beam it is possible to simultaneously induce and observe the phase transformation from monomer to polymer in certain solid-state polymerizable diacetylenes [1]. The continuous change in the crystal structure from DCHD diacetylene monomer ($a=1.76$ nm, $b=1.36$ nm, $c=0.455$ nm, $\gamma=94$ degrees, $P2_1/c$) [2] to polymer ($a=1.74$ nm, $b=1.29$ nm, $c=0.49$ nm, $\gamma=108$ degrees, $P2_1/c$) [3] occurs at a characteristic dose (10^{-4} C/cm²) which is five orders of magnitude smaller than the critical end point dose (20 C/cm²) [4]. Previously we discussed the progress of this phase transition primarily as observed down the [001] zone (the chain axis direction) [1]. Here we report on the associated changes of the dark field (DF) images and selected area electron diffraction (SAED) patterns of the crystals as observed from the side (i.e., in the [hk0] zones).

High resolution electron micrographs (HREM), DF images, and SAED patterns were obtained on a JEOL 4000 EX HREM operating at 400 kV. The data was collected on an image intensified YAG screen and recorded on video tape. The exposure was controlled with a minimum dose system (MDS) and beam blanking device. Images and diffraction patterns were digitized from the video tape with a Scion frame grabber board on a Mac IIsi and analyzed with the Image 1.44 processing software.

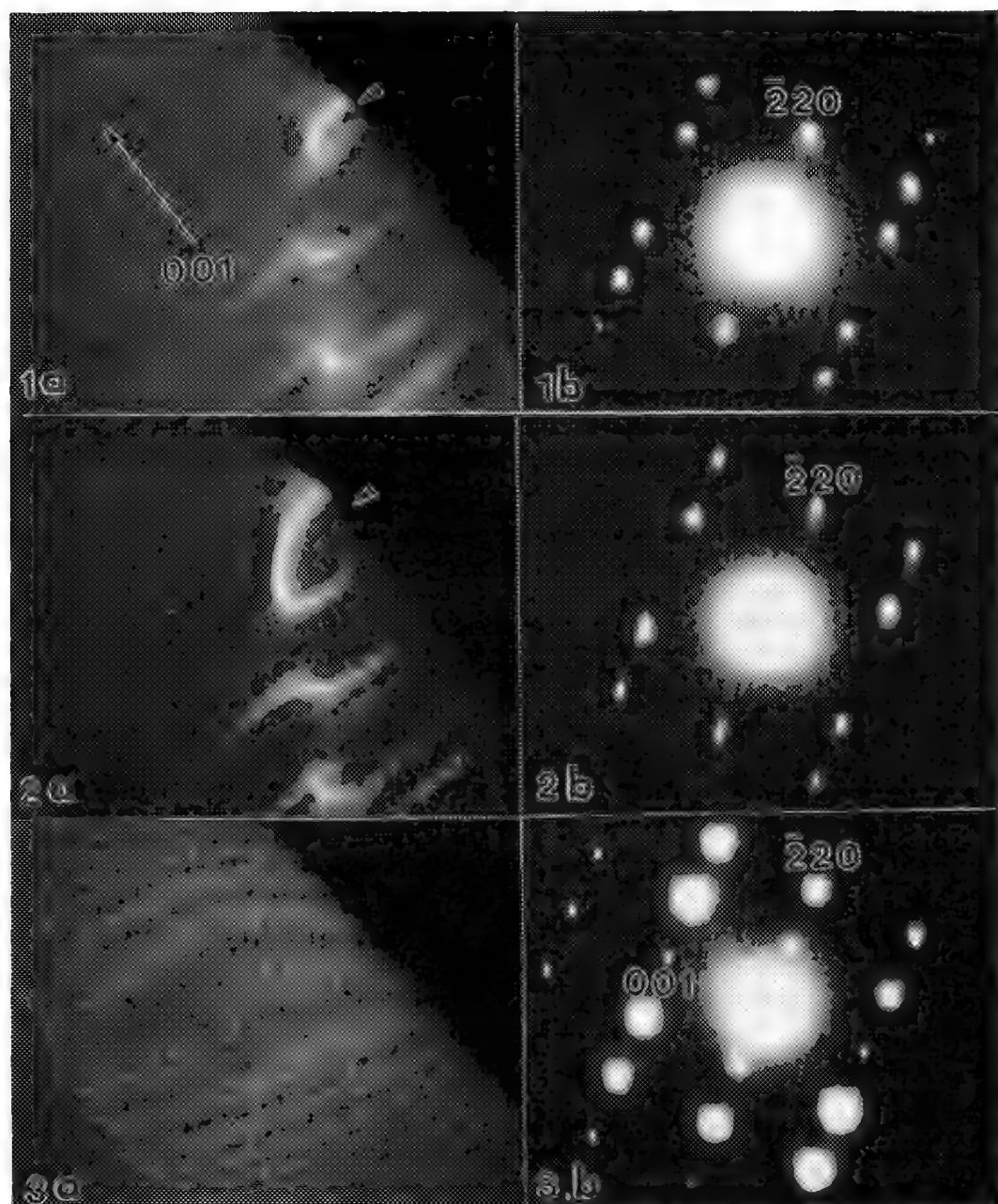
Figures 1, 2, and 3 show DF and SAED patterns of the monomer ($J=1 \times 10^{-5}$ C/cm²), partly converted ($J=5 \times 10^{-5}$ C/cm²), and polymer ($J=10 \times 10^{-5}$ C/cm²) crystals. The SAED patterns change in a continuous manner, indicating the reaction proceeds through a series of crystalline intermediate states. Characteristic streaking develops in the [200] and [110] directions (Figure 2b), giving information about planar defects which develop during the reaction. These defects are associated with local fluctuations in the extent of conversion of monomer to polymer. The streaking disappears after the reaction is complete. Quantitative analysis of the diffraction spot broadening is consistent with conversion fluctuations of up to 20% during the intermediate stages of the transition.

The DF images indicate the dramatic changes in the mechanical properties of the crystals as they are polymerized. The monomer crystals (Figure 1a) have profuse bend contours which arise due to local fluctuations in orientation. As the material polymerizes, the bend contours move due to changes in the crystallographic angle, extent of structural disorder, and reorientation of the crystalline domains (Figure 2a). After polymerization the crystals are nearly free of bend contours (Figure 3a). This is consistent with a increased stiffness of the polymer crystals due to the connectivity of the chain. However, the diffraction patterns remain highly crystalline until fading occurs at the critical dose.

We have also seen changes in the degree of order along the chain axis during polymerization. After polymerization there are additional sharp reflections on upper order layer lines indicating improved organization in this direction. The nature and extent of this change appears to be dependent on the structural disorder originally present in the precursor monomer crystals.

References

1. J. Liao and D. Martin, Science, (1993), in press.
2. V. Enkelmann, et al., Chem. Phys. Lett., 52, 314, (1977).
3. P. A. Apgar and K. C. Yee, Acta Cryst., B34, 957, (1978).
4. R. T. Read and R. J. Young, J. Mat. Sci., 19, 327, (1984).
5. The authors would like to thank the Electron Microbeam Analysis Laboratory at the University of Michigan for access to facilities and the National Science Foundation (DMR-9024876, NYI Program) for financial support.



A series of dark-field (DF) and selected area diffraction patterns from the $[110]$ zone axis of DCHD diacetylene during the solid-state phase transformation from monomer to polymer.

Fig. 1. (a) DF and (b) SAED pattern of DCHD monomer ($J = 1.0 \times 10^{-5} \text{ C/cm}^2$)

Fig. 2. (a) DF and (b) SAED pattern of DCHD during the intermediate stages of the transformation ($J \sim 5 \times 10^{-5} \text{ C/cm}^2$)

Fig. 3. (a) DF and (b) SAED pattern of DCHD polymer ($J > 10 \times 10^{-5} \text{ C/cm}^2$)

REAL-TIME CRYO-DEFORMATION OF POLYPROPYLENE AND IMPACT-MODIFIED POLYPROPYLENE IN THE TRANSMISSION ELECTRON MICROSCOPE

Robert C. Cieslinski^{*}, H. Craig Silvis^{**}, and Daniel J. Murray^{**}

^{*} The Dow Chemical Company, Analytical Sciences; 1897 Bldg., Midland, MI 48667

^{**} The Dow Chemical Company, Central Research; 1707 Bldg., Midland, MI 48674

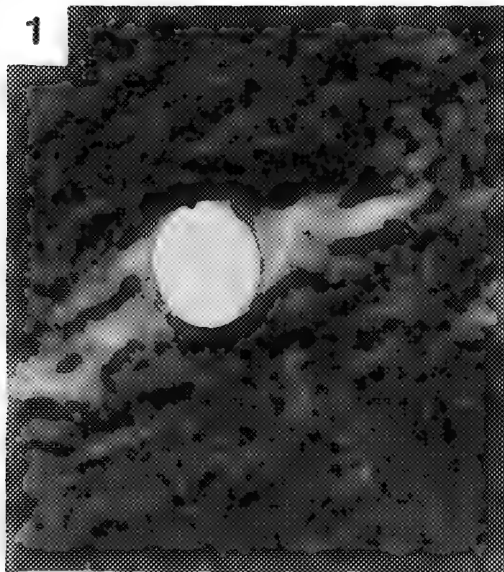
An understanding of the mechanical behavior polymers in the ductile-brittle transition region will result in materials with improved properties. A technique has been developed that allows the real-time observation of dynamic plane stress failure mechanisms in the transmission electron microscope (1). With the addition of a cryo-tensile stage, this technique has been extended to -173 °C, allowing the observation of deformation during the ductile-brittle transition.

The technique makes use of an annealed copper cartridge in which a thin section of bulk polymer specimen is bonded and plastically deformed in tension in the TEM using a screw-driven tensile stage. In contrast to previous deformation studies on solvent-cast films (2-4), this technique can examine the frozen-in morphology of a molded part.

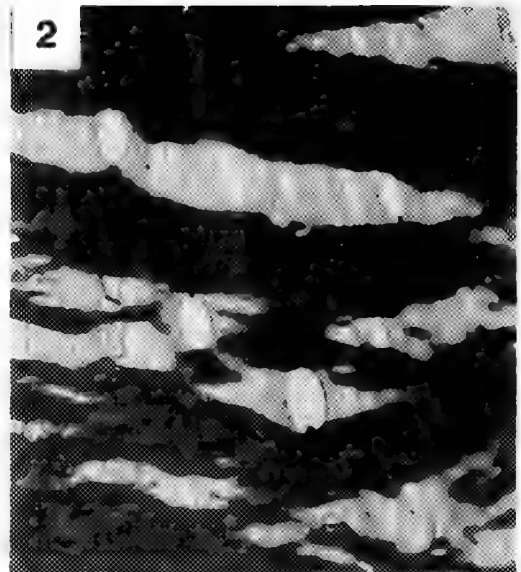
The deformation behavior of polypropylene and polypropylene impact modified with EPDM (ethylene-propylene diene modified) and PE (polyethylene) rubbers were investigated as function of temperature and the molecular weight of the impact modifier. Figure 1 shows voids initiating from the polypropylene (PP) nucleating agent as the specimen is pulled in tension. Shearing is the predominate deformation mechanism in the surrounding PP at room temperature. As the temperature is lower though the ductile-brittle transition (approx. -10 to -20 °C) the propensity for crazing to occur is observed by the narrowing and sharpening of the shear tip until fibrillation and crazing occurs (Figure 2). Impact modification was found to nucleate and stabilize a much larger damage zone. The impact modifiers expand during deformation and also provide rubber fibrils which bound to the PP, stabilizing the cracks during deformation (Figures 3 and 4). The behavior of the rubber fibrils with temperature which is a function of the molecular weight is explored in this paper and is discussed in terms of tie molecule and molecular entanglement concentration (5).

References

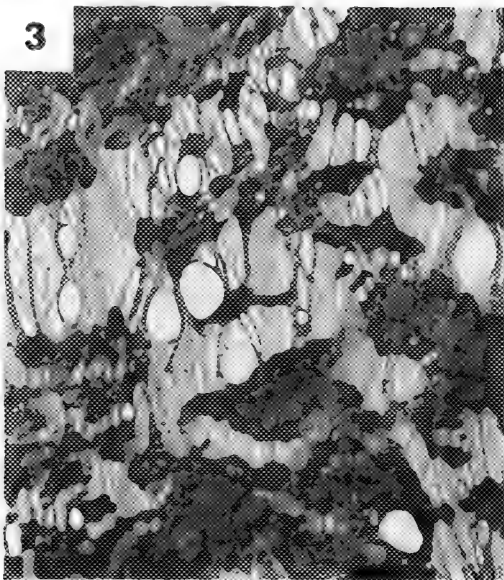
1. R. C. Cieslinski, J. Mater. Sci. Letters. **11** (1992) 813.
2. B. D. Lauterwasser and E. J. Kramer, Phil. Mag. **39** (1979) 469.
3. A. M. Donald and E. J. Kramer, J. Mater. Sci. **17** (1982) 2351.
4. R. P. Kambour, J. Polym. Sci. **D7** (1973) 1.
5. Y. Huang and N. Brown, J. Polym. Sci., Phys. Edn. **29** (1991) 129.



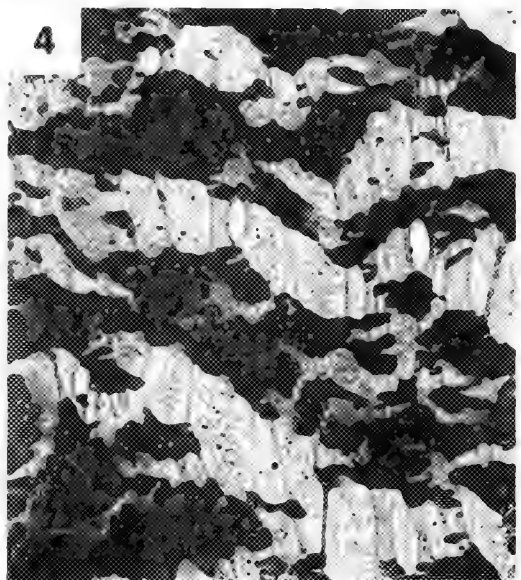
1.0 μm



1.0 μm



5.0 μm



5.0 μm

- FIG 1. Void formation and matrix shearing in polypropylene deformed at room temperature.
 FIG 2. Crazes produced during deformation in polypropylene at -15°C .
 FIG 3. EPDM rubber fibrils and PP matrix shearing produced during room temperature deformation
 FIG 4. EPDM rubber fibrils and PP matrix crazing produced during -15°C deformation.

A QUANTITATIVE IMAGE ANALYSIS METHOD FOR THE DETERMINATION OF COCONTINUITY IN POLYMER BLENDS

William A. Heeschen

The Dow Chemical Company, 1897-D Building, Midland, MI 48667

Two new morphological measurements based on digital image analysis, CoContinuity and CoContinuity Balance, have been developed and implemented for quantitative measurement of morphology in polymer blends. The morphology of polymer blends varies with phase ratio, composition and processing. A typical morphological evolution for increasing phase ratio of polymer A to polymer B starts with discrete domains of A in a matrix of B ($A/B < 1$), moves through a cocontinuous distribution of A and B ($A/B \approx 1$) and finishes with discrete domains of B in a matrix of A ($A/B > 1$). For low phase ratios, A is often seen as solid convex particles embedded in the continuous B phase. As the ratio increases, A domains begin to evolve into irregular shapes, though still recognizable as separate domains. Further increase in the phase ratio leads to A domains which extend into and surround the B phase while the B phase simultaneously extends into and surrounds the A phase. This condition is typically given the descriptor "cocontinuous" because both phases appear to be continuous throughout the observed field. Yet-higher phase ratios yield an inversion where the A phase is now the continuous matrix and the B phase is present as separated domains surrounded by the A phase. The CoContinuity value is an attempt to describe this type of morphology with a single number. The CoContinuity Balance is useful in quantitatively determining the relative contributions of the two phases to the measured CoContinuity. The current discussion will be limited to a two-phase system.

The basis of these CoContinuity measurements is the extent to which the phases of a polymer blend mutually surround each other. The fundamental DIA measurements are the areas and convex areas of all features in both phases. Sums and ratios of these measurements are combined in a prescribed fashion to ultimately produce the CoContinuity and CoContinuity Balance. Both functions are dimensionless and scale-invariant, thus allowing objective comparisons of dissimilar systems. The CoContinuity is zero for perfectly convex particles in a matrix and increases with increasingly cocontinuous morphology. An expected value for a "typical" cocontinuous morphology would be about two, although there is no theoretical upper bound. The CoContinuity Balance is a simple ratio which ranges from 0 to ∞ where 0 and ∞ indicate perfectly convex particles in a matrix and a value of 1 indicates that each phase is equally continuous throughout the field of view. With the morphology reduced to a number, quantitative correlation can be made between morphology and physical properties.

An example of morphological evolution is shown in the binary images of Figures 1(a) through 1(f) taken from the work of Skochdopole.¹ The magnification in Figures 1(a)-1(c) is approximately 3 times greater than in Figures 1(d)-1(f). The dark phase is a 70/30 styrene/acrylonitrile copolymer (SAN) and the light phase is polycarbonate (PC). The phase ratios are 10%, 20%, 30%, 40%, 50% and 75% SAN in PC, respectively. The morphology in Figures 1(a) through 1(c) shows discrete domains of SAN in a matrix of PC with domain shape becoming less regular with increasing SAN. Figures 1(d) and 1(e) exhibit cocontinuity, although Figure 1(e) is just beginning to show formation of discrete domains of PC in SAN. In Figure 1(f), the morphology has "inverted", with PC domains in a matrix of SAN. The images were analyzed for CoContinuity and CoContinuity Balance and the results are plotted in Figure 2 as a function of %SAN with solid and dash lines, respectively. The measured CoContinuity was low for 10% SAN, increased with increasing SAN content and reached a maximum value at 40% SAN then decreased at successively higher SAN content. The CoContinuity Balance (CCB) was less than one for low SAN, indicating that PC is the dominant continuous phase. As SAN content increased, the CCB increased reaching a value close to one for

40% SAN, indicating similar continuity for both phases. As SAN went above 40%, the CCB continued to increase, indicating SAN as the continuous phase.

Physical properties of the various blends were measured and were largely found to vary directly with PC/SAN ratio. The most noticeable exception was ultimate impact energy which dropped dramatically at the point where the CoContinuity reached a maximum value and the CoContinuity Balance passed through the value "1", indicating that the continuous PC morphology inverted to continuous SAN. This result is plotted in Figure 2 with the dot line. This behavior is consistent with a continuous tough PC matrix being replaced with a continuous brittle SAN matrix.

1. R.E. Skochdopole et al., *Polymer Engineering And Science* (1987) 27, 2, 627 - 631.

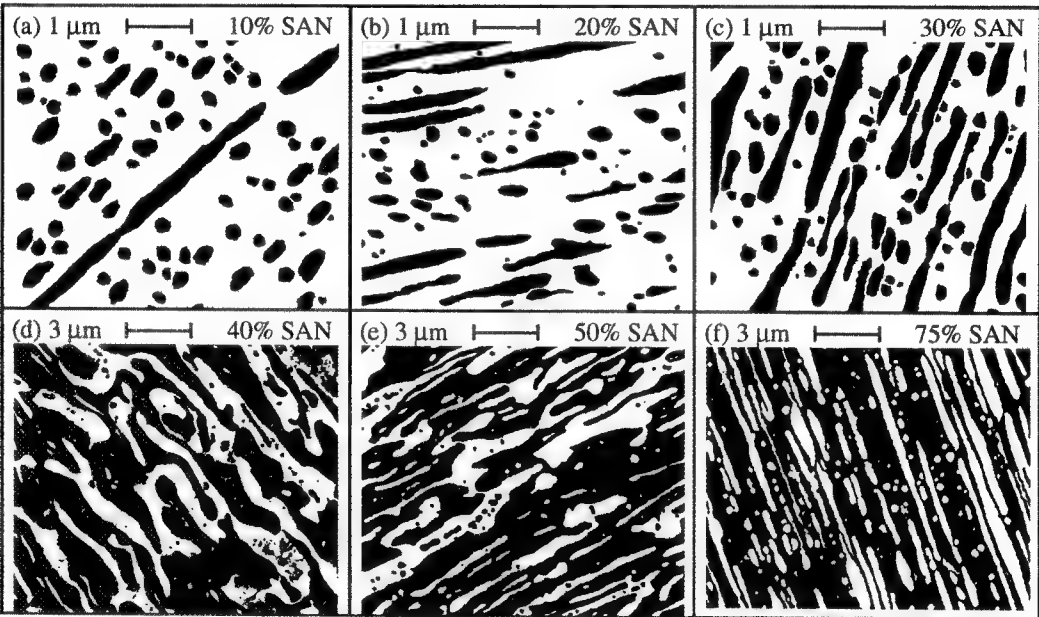


Figure 1. Binary Images Of Polycarbonate / Polystyrene-co-(30%)acrylonitrile (PC/SAN) Blends. Light phase is PC. Dark phase is SAN.

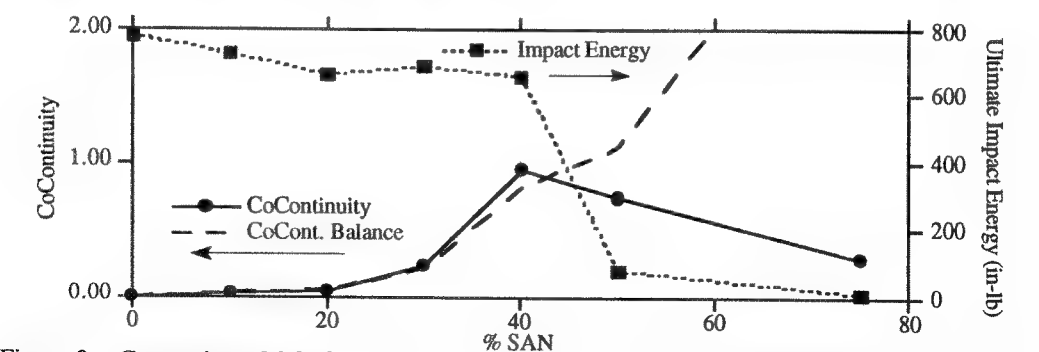


Figure 2. Comparison Of CoContinuity and CoContinuity Balance With Ultimate Impact Energy For Varying SAN ratio in PC/SAN blends.

TEM AND IMAGE ANALYSIS TO QUANTITATIVELY DESCRIBE THE PHASE BEHAVIOR IN COPOLYMER / HOMOPOLYMER / HOMOPOLYMER BLENDS: EFFECT OF THE COPOLYMER SEQUENCE DISTRIBUTION

Karen I. Winey* and Mary E. Galvin**

* Department of Materials Science and Engineering, University of Pennsylvania, Philadelphia, PA 19104-6272

** AT&T Bell Laboratories, Murray Hill, NJ 07974

Polymers are typically immiscible with one another, that is phase separated, in the absence of specific favorable intermolecular interactions, because the combinatorial entropy of mixing is small. Copolymers, polymer molecules containing more than one type of monomer unit, are frequently used to induce miscibility in homopolymer mixtures. Extensive work has previously established the importance of the copolymer composition, though the sequence of monomers within the copolymer has received less attention.^{1, 2} Copolymers with random and with alternating sequences of monomers have been synthesized and mixed with homopolymers to evaluate the importance of the sequence distribution on blend miscibility.² Blend miscibility determinations using differential scanning calorimetry and visual inspection can be erroneous when the glass transition temperatures of the phases are similar or the domains are small compared to the wavelength of light. Thus, we have used transmission electron microscopy to study the phase behavior of these polymer blends.

Blend samples (~30 mg) of poly(styrene-co-methyl methacrylate) (PS-PMMA), homopolystyrene (PS), homopoly(methyl methacrylate) (PMMA) were prepared by casting from tetrahydrofuran and annealing at 150°C for 7 days. Small flecks of the brittle polymer film were stained using the vapors above an aqueous RuO₄ solution. The stained samples were placed into partially cured epoxy and subsequently heated to 60°C overnight to fully cure the embedding medium. This heat treatment does not alter the morphology of the polymer blends, because the glass transition temperatures of the polymers are above 100°C. At room temperature, a Reichert-Jung Ultracut S with a glass knife was used to remove excess epoxy and prepare a block face. Sections (~60 nm) for TEM were microtomed at room temperature using a Diatome 35° angle knife. Sections were retrieved from the water surface using a "perfect loop" and viewed in a Phillips 400T without further staining.

Figures 1 and 2 show examples of binary and ternary blends, respectively, in which the sequence distribution of the copolymer, random or alternating, alters the phase behavior. Analysis of the TEM images determines the volume fractions of the phases using the following method. TEM negatives were digitized using a Macintosh IIfx, Adobe PhotoShop, and a scanner with a transmission attachment. This method is faster and provides better resolution than making a photographic print to subsequently digitize using a standard reflective scanner. The area fractions of the images are measured using IMAGE, a public domain software package originating from NIH. We assume that the area fraction of the projected TEM image equals the true area fraction of the sample; this assumption is reasonable when the domains are much larger than the thickness of the microtomed section, as is typically the case here.

The area fractions of the phases are equated with the volume fractions of the phases, because the sample morphology is assumed to be isotropic.

The measured volume fractions of the phases, the known overall compositions of the blends, and mass balance equations are used to determine the coexistent curves or phase boundaries. This information is presented in ternary phase diagrams as found in Figure 3 for the PS-PMMA / PMMA / PS blends having random or alternating sequence distributions. As evidenced by comparing Figures 3a and 3b, the sequence distribution in PS-PMMA copolymers significantly influences the phase behavior. TEM and subsequent image analysis provide a reliable method of producing quantitative phase diagrams.

References

1. C. Zhikuan and F. E. Karasz, *Macromolecules* (1992) 25, 4716 and 6113.
2. M. E. Galvin, *Macromolecules* (1991) 24, 6354.
3. This research was supported by a grant from the University of Pennsylvania's Research Foundation. The authors acknowledge the experimental contributions of M. L. Berba and L. Cerini.

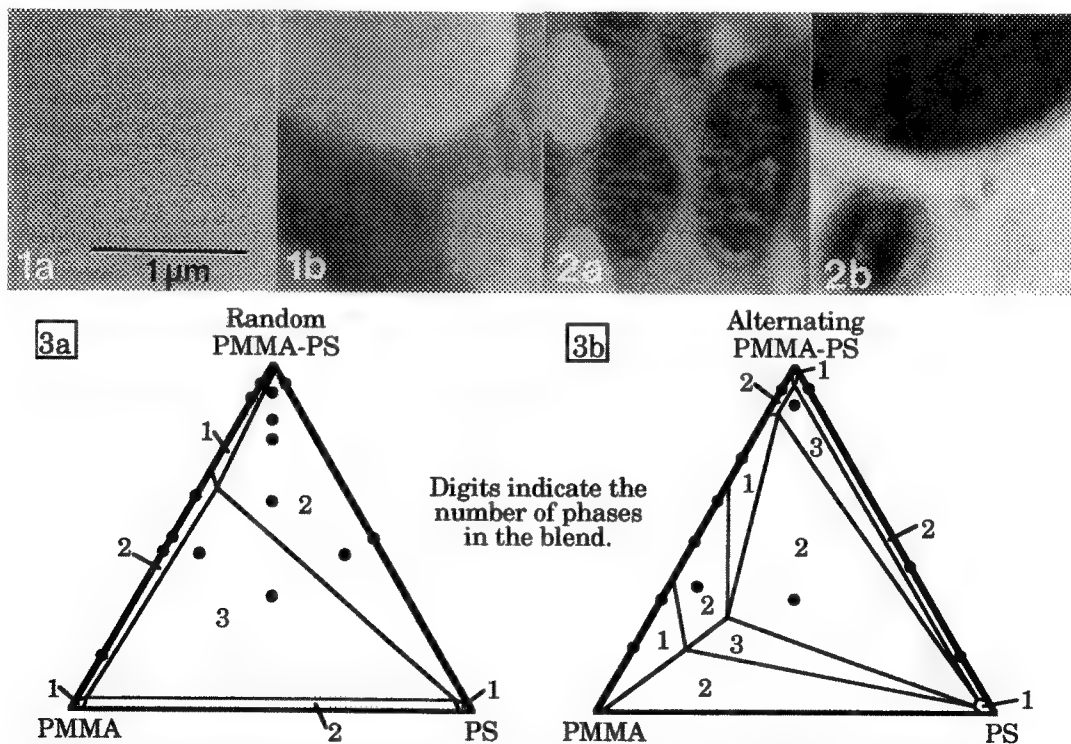


FIG. 1 - TEM of blends containing ~95% PS-PMMA and ~5% PMMA. a.) Random copolymer, one phase. b.) Alternating copolymer, two phases.

FIG. 2 - TEM of blends containing ~33% PS-PMMA, ~34% PMMA, and ~33% PS.

a.) Random copolymer, three phases. b.) Alternating copolymer, two phases.

FIG. 3 - Ternary phase diagrams for PS-PMMA, PMMA, and PS blends. a.) Random copolymer. b.) Alternating copolymer.

MICROWAVE-STIMULATED HEAVY METAL STAINING OF POLYMER BLENDS FOR TRANSMISSION ELECTRON MICROSCOPY

Barbara A. Wood

Corporate Center for Analytical Sciences, Du Pont Experimental Station, P.O. Box 80323,
Wilmington, DE 19880

Microwave methods for fixation and staining of biological samples for microscopy have been under development for a decade.¹ While microwave ovens are routinely used in the synthetic polymer field for sample digestion and ashing, potential microwave staining techniques for TEM of polymers have yet to be thoroughly investigated. Preliminary experiments have demonstrated that copper grids do not cause arcing problems in the microwave, and that most types of polymer sections can be safely and conveniently stained in an industrial microwave oven. The staining agent used was ruthenium tetroxide vapor generated from ruthenium trichloride.² Improvements in the speed and selectivity of staining are attributed in part, but not entirely, to the increased reaction rates at higher temperatures compared to standard room temperature vapor staining techniques. Stringent waste disposal regulations make microwave staining an attractive method from the industrial hygiene point of view, with a minimum of toxic waste generation compared to staining with $\text{RuO}_4/\text{CCl}_4$ solutions.

A CEM MDS81 laboratory microwave oven equipped with a stainless steel interior and an exhaust fan was installed in a chemical fume hood. The RuCl_3 /bleach reaction mixture was prepared in a conical flask, and a Buchner funnel with cryoultramicrotomed sections on 200 mesh grids placed over the holes was inserted into the neck of the flask. The staining apparatus was transferred to the microwave oven with the exhaust fan running. The oven was operated at a power setting of 17% (to avoid boiling) for periods up to 30 minutes. Polymers loaded with carbon black would be susceptible to intense heating and were avoided. Depending on the application, satisfactory staining was accomplished in as little as 10 minutes, versus 2 hours using room temperature vapor staining.

Materials successfully stained include conventional and ultrahigh molecular weight polyethylene, segmented block copolymers, ethylene-propylene copolymers, and polystyrene. Interfacial staining at the boundary of polyethylene domains dispersed in HIPS was enhanced relative to room temperature staining. Selective deposition of RuO_2 at blend interfaces has previously been described and may signify staining of segregated additives, impurities rejected during crystallization, or oriented chains of one or both polymers.³ The polyethylene-rich regions also contain small unstained domains of crosslinked polyethylene as well as two other ethylene copolymers (Figure 1). A comparison of TEM images of occluded PS particles in the HIPS prepared using microwave versus conventional RuO_4 shows greater contrast at the HIPS/rubber interface, which may contain some grafted polymer, in the case of microwave staining.

Neither polyethylene nor polystyrene alone was susceptible to microwave heating. The symmetry of the RuO_4 molecule also suggests a lack of a dipole moment and therefore low susceptibility to heating. Although it may be possible for microwaves of the appropriate frequency to excite cooperative motions of polymer chains which would stimulate diffusion of small molecules, this is not believed to occur under the fixed frequency conditions used in the experiment. Changes in staining behavior are attributed to heating of the aqueous reaction mixture, enhanced reaction rate, and improved interactions between water and hydrocarbon polymers. The temperature dependence of surface interactions between polyethylene and water is known from contact angle data.⁴ Using this information, one would expect a more favorable interaction between "wet" ruthenium tetroxide vapor and the polymer as the vapor temperature increases, despite the fact that polyethylene itself is not susceptible to microwave heating under the conditions used. Microwave staining with OsO_4 is also possible using an OsCl_3 /bleach reaction instead of crystalline OsO_4 and could substantially reduce exposure time requirements compared to conventional techniques.

REFERENCES

1. M. Boon and L. Kok, Microwave Cookbook of Pathology, Leiden:Coulomb Press Leyden (1989).
2. D. Montezinos et al., J. Polym. Sci. Polym. Lett. Ed. 23(1985)421.
3. B. Wood, Advances in Polymer Blends and Alloys Technology - Volume 3, Lancaster:Technomic Publishing Co. (1992)24.
4. S. Wu, Polymer Interface and Adhesion, New York: Marcel Dekker, Inc. (1982)145.

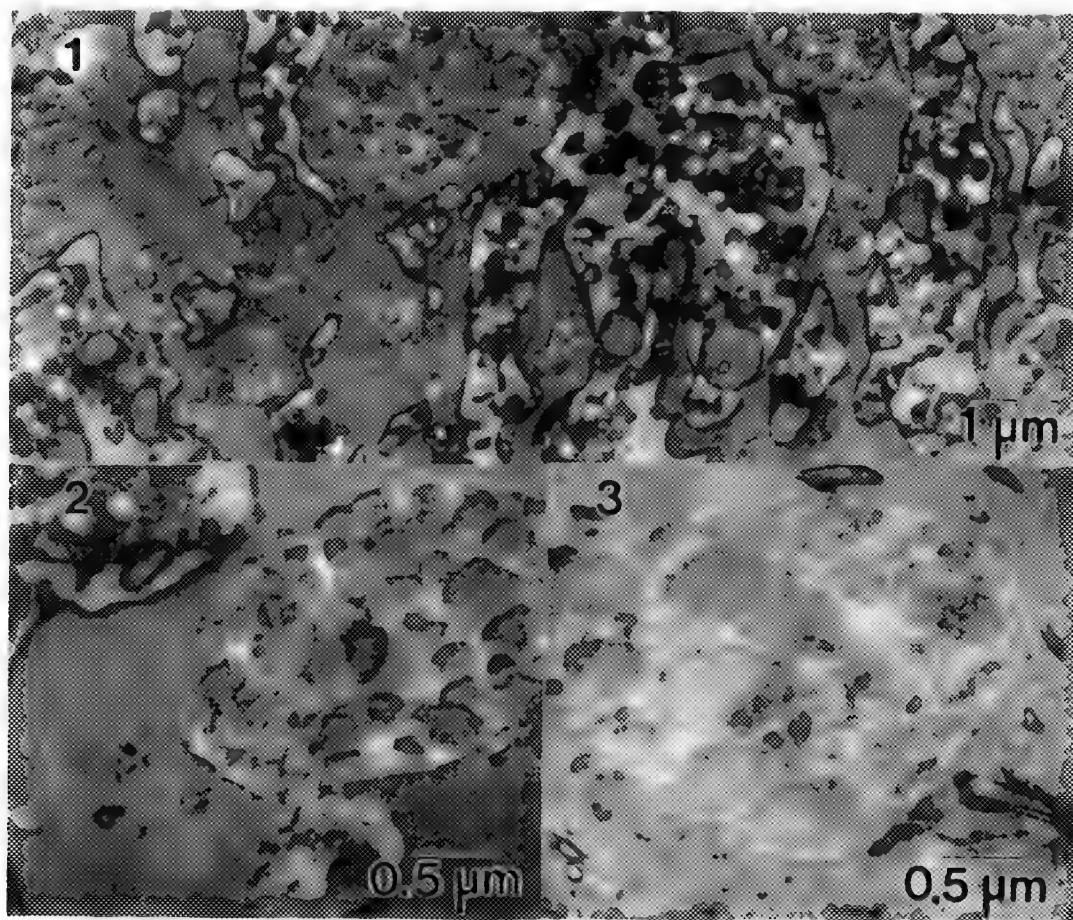


FIG. 1. -- 120 KV TEM of section of HIPS/PE/ethylene copolymer blend subjected to RuO_4 staining in microwave oven. Note selective staining at HIPS/PE interface.

FIG. 2. -- Higher magnification of HIPS region of material in FIG. 1.

FIG. 3. -- HIPS prepared by conventional RuO_4 staining; rubber phase appears white.

SOLVENT-ASSISTED OSMIUM STAINING OF BUTYL ACRYLATE AND ETHYLENE-PROPYLENE-DIENE IN A STYRENE ACRYLONITRILE MATRIX

Gudrun A. Hutchins

GE Corporate Research and Development, PO Box 8, Schenectady, NY 12301

In order to optimize the toughening effect of elastomers in engineering polymers, it is necessary to characterize the size, morphology and dispersion of the specific elastomer within the polymer matrix. For unsaturated elastomers such as butadiene or isoprene, staining with osmium tetroxide is a well established procedure.¹ The residual carbon-carbon double bond in these materials is the reactive site and forms a 1,2-dilato complex with the OsO₄. Incorporation of osmium tetroxide into the elastomer not only produces sufficient contrast for TEM, but also crosslinks the elastomer sufficiently so that ultramicrotomy can be accomplished at room temperature with minimal distortion.

Blends containing saturated elastomers such as butyl acrylate (BA) and ethylene propylene diene monomer (EPDM) cannot be stained directly with OsO₄ because effective reaction sites such as C=C or -NH₂ are not available in sufficient number. If additional reaction sites can be introduced selectively into the elastomer by a chemical reaction or the absorption of a solvent, a modified, two-step osmium staining procedure is possible. This would eliminate the very time-intensive cryo-microtomy of blends containing saturated elastomers.

Results are reported here for the two-step staining of BA and EPDM in styrene acrylonitrile (SAN). Faced microtomy specimens were soaked in 1,7 octadiene at room temperature for times ranging from 2 hrs to 16 hrs depending on the rubber loading; preferential absorption of octadiene in the rubber phase introduced stainable C=C sites. The specimens were then dried in a hood and stained in 1% aqueous OsO₄ at 60°C. Subsequent microtomy was completed at room temperature with a diamond knife. Styrene monomer could not be utilized for selective solvent absorption as recommended by Sue et. al.² because the blends were slightly soluble in it.

Figures 1 and 2 show results for BA from two sources. Both large and small particles are stained evenly (Fig. 1), and poorly dispersed particles that are clustered together are still recognizable as separate particles (Fig. 2). The BA particles show a staining texture that appears to be related to the absorption of the solvent and is larger or smaller for different sources of BA. The same specimens were stained by the two-step staining procedure developed by Hamazaki et.al.³ in which the specimen is first reacted with hydrazine hydrate to produce acrylic acid hydrazides (-NH₂ reaction sites) and then reacted with OsO₄. This procedure was not as satisfactory because the shape of the rubber particles was distorted during the hydrazine reaction and it was difficult to distinguish a large particle from a poorly dispersed clump of small particles. The morphology of cryo-sectioned specimens vapor stained with ruthenium tetroxide⁴ was in good agreement with the morphology of the octadiene/OsO₄ stained specimens.

Results for two sources of EPDM with very different morphologies are given in Figures 3 and 4. Inclusions of SAN within the EPDM are readily visible in both samples. Large particles within the second specimen (Fig. 4) show fibular segments which are probably crystalline and therefore not absorbing the solvent.⁵ The crystalline material was not visible in RuO₄ stained cryo-sections. Some artifacts were seen within the matrix of the octadiene/OsO₄ stained EPDM blends since large solvent-swollen EPDM particles caused occasional crazes within the adjacent SAN.

References

1. K. Kato, *J. Elect. Microsc.*, **14**, 219 (1965).
2. H. J. Sue, E. I. Garcia-Meitin, B. L. Burton, and C. C. Garrison, *J. of Pol. Sci. B*, **92**, 1623 (1991).
3. T. Hamazaki, Y. Kanchiku, R. Handa, and M. Izumi, *J. Appl. Pol. Sci.*, **21**, 1569 (1977).
4. J. S. Trent, J. I. Scheinbeim, and P. R. Couchman, *Macromolecules*, **16**, 589 (1983).
5. M. Kakugo and H. Sadatoshi, *J. of Pol. Sci. C*, **24**, 171 (1986).

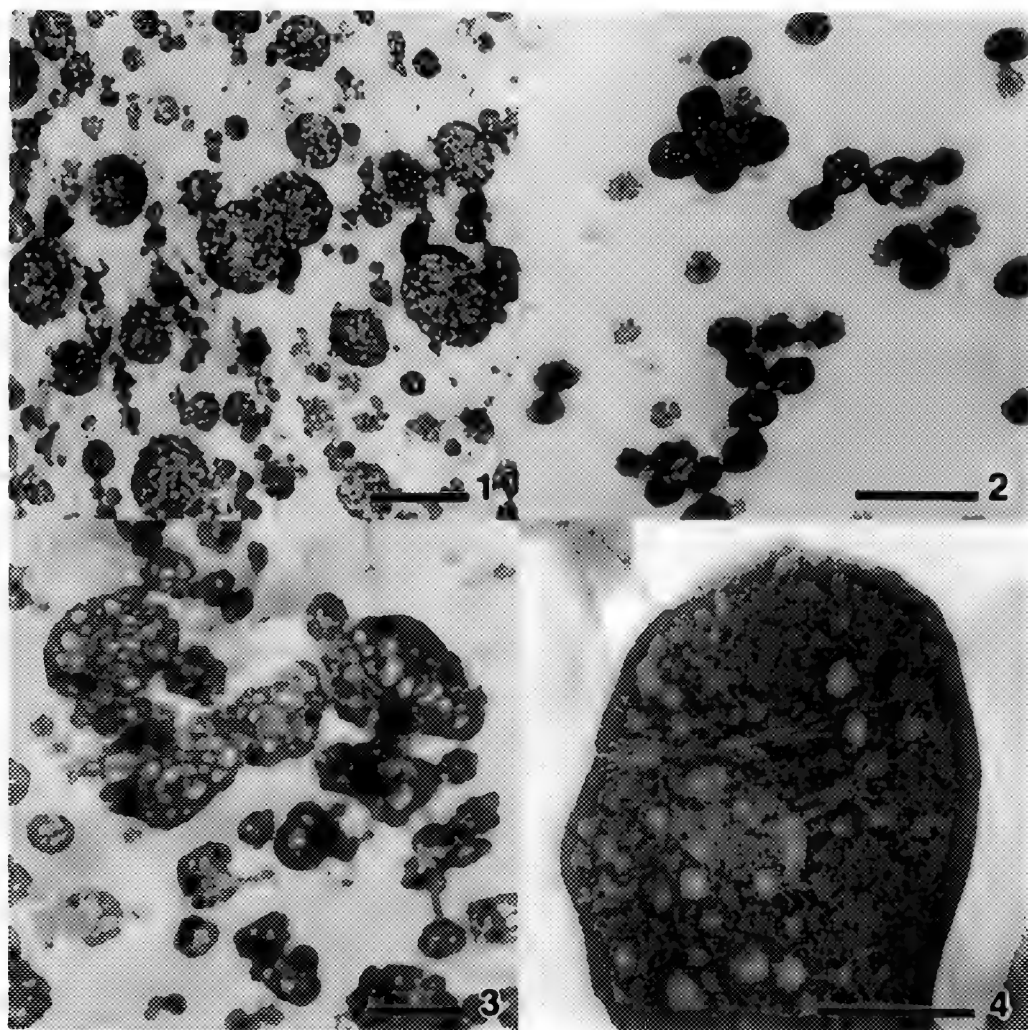


Fig. 1 and 2: BA in SAN matrix, octadiene/OsO₄ stained.
 Fig. 3 and 4: EPDM in SAN matrix, octadiene/OsO₄ stained.
 All markers = 0.5μm

X-RAY MICROSCOPY IN POLYMER SCIENCE: PROSPECTS OF A NEW IMAGING TECHNIQUE

H. Ade¹, B. Hsiao², G. Mitchell³, S. Cameron⁴, S. Costello⁴

¹Dept. of Physics, North Carolina State University, Raleigh, NC 27695-8202, ²Experimental Station, PuPont, Wilmington, DE 19880-0302, ³Dow Chemical, ASL, Midland, MI 48667, ⁴Exxon Research and Engineering, Annandale, NJ 08801

The ultimate bulk and surface properties of heterophase polymers are strongly tied to their morphology. Light and electron microscopies are often successfully used to characterize such morphologies, but these techniques are inherently limited in their applicability and versatility. We present a new, relatively non-invasive imaging technique which employs highly focused, tunable x-rays that can be used to investigate the surface and bulk characteristics of heterophase polymeric materials with chemical¹ and orientational sensitivity. In X-ray Absorption Near Edge Structure (XANES) imaging, a highly monochromatic soft x-ray beam is focused onto the sample, and the transmitted flux through a thin specimen is collected to produce images with presently 55 nm Rayleigh resolution on the X1A beamline at the National Synchrotron Light Source.^{1,2} With judicious choice of photon energy, the technique is sensitive to the chemical (valence) state and local orientation of each component present and is, for instance, capable of distinguishing among chemical functionalities such as C-C, C=C, C≡C, C=O, COOH, and C=N. To demonstrate this chemical sensitivity we imaged several unstained heterophase polymers with very high contrast. In Fig. 1, a poly(styrene-*r*-acrylonile)-polypropylene blend was imaged at a photon energy of 285.5 eV, where styrene is highly absorbing, while the polypropylene matrix is practically transparent.¹ Fig. 2 shows the chemical contrast of a polycarbonate-poly(ethylene terephthalate) (PC-PET) blend at a photon energy of 285.7 eV. Again, high contrast is achieved without staining. Furthermore, XANES is polarization dependent³ and the resulting x-ray dichroism can be used to image orientation in (partially) order samples. Figs. 3a and 3b are micrographs of a 100 nm thick section of a poly(p-phenylene terephthalamide) (PDD-T) fiber imaged with the electric field vector in the left-right direction (3a) and up-down direction (3b), respectively. Strong contrast changes are readily observable.

So far, we mostly employed the carbon K-edge to acquire images and spectra, but nitrogen, oxygen, chlorine and fluorine edges, as well as other core shells with energies in the 250-750 eV range, should be accessible with the X1A microscope. For optimum signal-to-noise the samples should be 0.1-0.5 μm in thickness for transmission experiments. In principle, it is also possible to make the technique surface sensitive, probing selectively about 1 nm, 10 nm, and 100 nm of the sample surface, by monitoring the near edge cross sections via the Auger-, secondary electron-, and fluorescence yield, respectively.³ We believe that the unique contrast mechanisms presented will make XANES microscopy a valuable characterization tool in polymer science.

References

1. H. Ade *et al.*, Science 258 (1992) 972, X. Zhang *et al.*, these proceedings.
2. C. Jacobsen *et al.*, these proceedings.
3. J. Stohr, NEXAFS Spectroscopy, Springer Series in Surface Science Vol. 25 (Springer, Berlin, 1992).
4. Part of this work was performed while HA was at SUNY, Stony Brook, and was supported by NSF grant DIR 9005893. We thank J. Kirz, C. Jacobsen, S. Williams, X. Zhang, S. Wirrick, E. Anderson, D. Attwood, and M. Rivers for their support and help with the X-ray microscope.

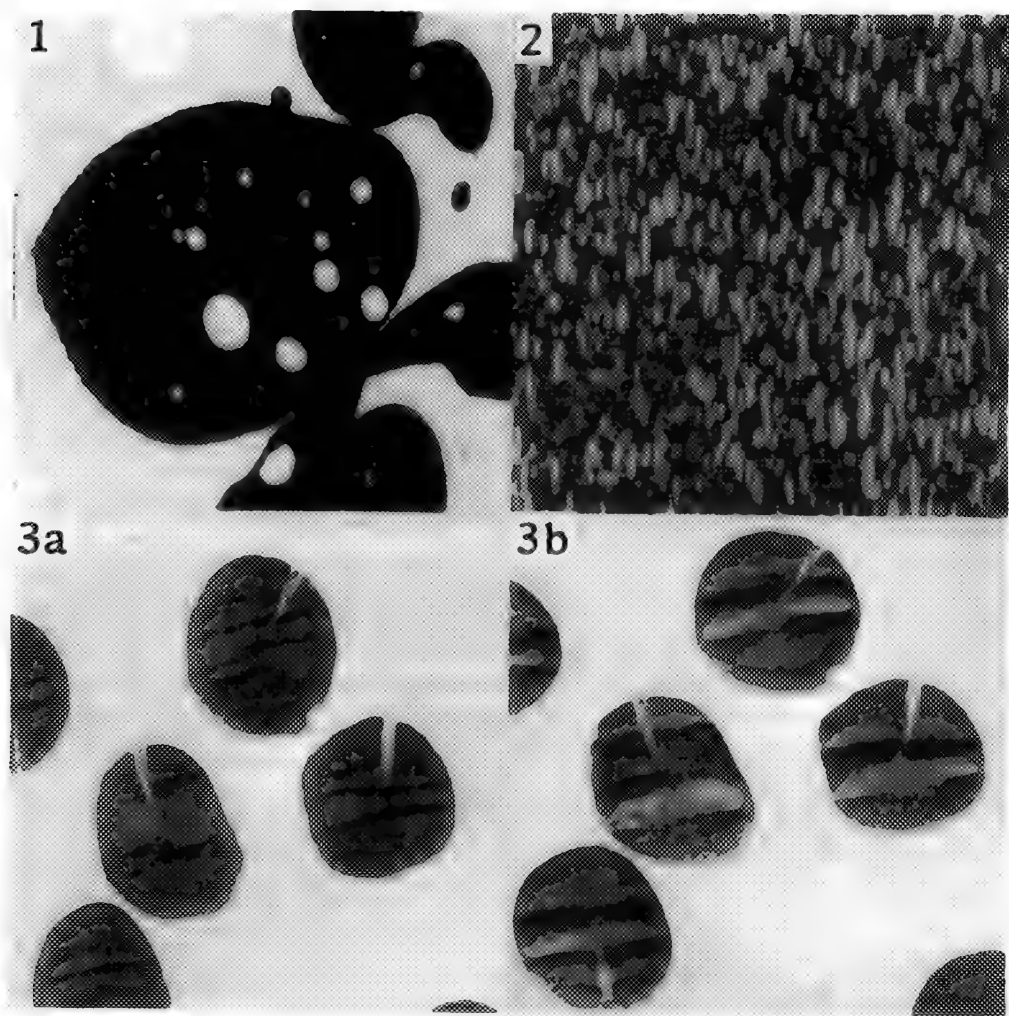


Fig. 1. -- Micrograph of 0.5 μm thick section of poly(styrene-*r*-acrylonitrile)-polypropylene blend acquired at a photon energy of 285.5 eV. Styrene is strongly absorbing at this energy and the phase containing it appears dark, while polypropylene is virtually transparent. Black and white levels of the micrograph are from zero to incident intensity, i.e. contrast is not enhanced (Field of view: 30x30 μm)

Fig. 2. -- Micrograph of PC/PET blend, demonstrating contrast between homopolymer phases without staining (Field of view: 30x30 μm)

Fig. 3. -- Micrographs of 0.1 μm thick PDD-T fiber section (45° relative to fiber axis) imaged with electric field vector in left-right direction (a) and in up-down (b) direction at 285.5 eV photon energy. This energy selects aromatic group of fiber polymer and contrast changes between two images arise due to x-ray dichroism reflecting orientational order in sample. In these particular images weak butterfly-like patterns are due to radial symmetry of fiber, while stronger features are due to anisotropies introduced during sectioning. (Note different X-Y magnification. Field of view: 40x40 μm).

ELECTRON ENERGY-LOSS SPECTROMETRY OF LASER-IRRADIATED KAPTON POLYIMIDE

J. Bentley*, H.M. Phillips†, D.L. Callahan§, and R. Sauerbrey†

*Metals and Ceramics Division, Oak Ridge National Laboratory, P.O. Box 2008, Oak Ridge, TN 37831-6376

†Department of Electrical and Computer Engineering, and §Department of Mechanical Engineering and Materials Science, Rice University, P.O. Box 1892, Houston, TX 77251-1892

It has recently been demonstrated that the electrical resistivity of a high temperature polymer, polyimide, can be changed permanently from $10^{17} \Omega\text{cm}$ to $10^{-1} \Omega\text{cm}$ by KrF (248 nm) excimer laser irradiation.¹ Further, using a holographic technique, an array of 500-nm-wide electrically conducting wires has been produced on polyimide by direct laser ablation.² There is obvious interest in exploiting this phenomenon to create integrated microelectronic devices with conventional polymers as both dielectrics and conductors.³ The imaging of such patterned nanostructures by scanning and transmission electron microscopy (SEM and TEM) is reported elsewhere.⁴ Knowledge of compositional changes that accompany the structural changes is necessary for understanding formation mechanisms, but analytical electron microscopy (AEM) of polymers is usually severely limited by electron beam damage effects, especially when high spatial resolution microanalysis is attempted with focussed probes. However, parallel-detection electron energy-loss spectrometry (PEELS) has been successfully used to investigate laser-induced compositional changes in polyimide (Kapton™, E.I. DuPont) with no apparent signs of beam damage.

Specimens with a uniform starting thickness of 12 μm were prepared for AEM by argon ion milling ($\sim 5 \text{ kV}$ and 0.4 mA) from the non-irradiated side, beginning at 25° and finishing at 15° incidence. Electron microscopy was performed at 100 kV in a Philips EM400T equipped with a field emission gun (FEG) and Gatan 666 PEELS. Usually, specimens were cooled to -130°C in a Gatan 636 double tilt cooling holder to minimize contamination, but some specimens were analyzed at room temperature. No beam damage was observed at either temperature. Spectra were acquired with Gatan EL/P software in both conventional and second difference (with offsets $\Delta = \pm 4 \text{ eV}$) modes.⁵ Typical conditions for PEELS were: incident beam divergence $\sim 3 \text{ mrad}$, collection semi-angle (defined by the PEELS entrance aperture) $\sim 14 \text{ mrad}$, 1 to 3 nA probe currents, $\sim 0.5 \text{ eV/channel}$ dispersion, $< 1.5 \text{ eV}$ energy resolution, and acquisition times of up to 180 s.

Comparison of spectra from an ion-milled but unirradiated Kapton specimen (e.g. Fig. 1a) with spectra from a microtomed Kapton thin section (e.g. Fig. 1b) revealed that no major compositional changes were induced by the ion milling. Analysis of conventional spectra (e.g. Fig. 2a) gave N:C and O:C ratios within 15% of those expected from the composition of Kapton ($\text{C}_{22}\text{N}_2\text{O}_5\text{H}_{10}$). Irradiation with 250 pulses of 30 ns duration at an energy density of 28 mJ/cm^2 from a KrF laser (just above the 20 mJ/cm^2 ablation threshold) resulted in the formation of $\sim 20 \text{ nm}$ clusters at the polymer surface (see Fig. 3). The N:C and O:C ratios are reduced by ~ 2 in spectra recorded from regions between the clusters (Fig. 1c) and reduced by ~ 4 in spectra recorded from a cluster overlapping such matrix material (Fig. 1d). Spectra obtained from individual clusters at the specimen edge (i.e. no overlapped matrix material) in a specimen irradiated with 2000 pulses at 40 mJ/cm^2 (Fig. 1e) showed nitrogen levels of $< 4\%$ and oxygen levels of $< 15\%$ of those in the control materials, corresponding to $< 0.3 \text{ at. \%}$ nitrogen and $< 2.5 \text{ at. \%}$ oxygen. For the irradiated specimens, the low visibility of O and N edges in conventional spectra precluded even qualitative measurements. To quantify the second difference spectra, the signal amplitude from the first minimum to first maximum was used as a simple measure of edge intensity and the unirradiated and microtomed specimens were used as standards. This procedure assumes that the laser irradiation does not change the shape of the edge near its onset, but has the advantage that the near edge structure is expected to be almost immune to multiple scattering, which is important for spectra from thicker than ideal specimens (for the microtomed sections $t/\lambda = 1.3$). The more sophisticated approach of multiple-least-squares fitting of reference spectra⁵ was considered to be unnecessary for the accuracy required in the present work. Conventional spectra from individual clusters (e.g. Fig. 2b) show a more pronounced π^* peak (arrowed) that is consistent with graphitization.

The microanalysis data indicate that laser irradiation results in the formation of carbon-enriched (possibly partially graphitic) $\sim 20 \text{ nm}$ clusters, consistent with pyrolysis studies that show oxygen and nitrogen loss.⁶ Other work suggests that the clusters grow together with an increasing number of laser pulses, which with

the temperature dependence of the electrical resistivity and sharp threshold for the appearance of electrical conductivity, suggests a percolative insulator-conductor phase transition in the laser-irradiated polymer.⁷

1. M. Schumann, R. Sauerbrey and M.C. Smayling, *Appl. Phys. Lett.* **58** (1991) 428.
2. H.M. Philips, R.L. Callahan, R. Sauerbrey, G. Szabó, and Z. Bor, *Appl. Phys. Lett.* **58** (1991) 2761.
3. H.M. Philips et al., *Proc. SPIE Conf. on Laser Radiation Photophysics*, Los Angeles, Jan 16-23, 1993.
4. D.L. Callahan, H.M. Philips, and R. Sauerbrey, these proceedings.
5. R. Leapman, in *Transmission Electron Energy Loss Spectrometry in Materials Science*, M.M. Disko, C.C. Ahn, and B. Fultz, eds., Warrendale, PA: The Minerals, Metals and Materials Society (1992) 47.
6. M. Inagaki et al., *Carbon* **27** (1989) 253.
7. This research was supported by the National Science Foundation, the Office of Naval Research, the Robert A. Welch Foundation, and by the Division of Materials Sciences, U.S. Department of Energy, under contract DE-AC05-84OR21400 with Martin Marietta Energy Systems, Inc., and through the SHaRE Program under contract DE-AC05-76OR00033 with Oak Ridge Associated Universities. The authors thank Dr. E.H. Lee at ORNL for providing the microtomed Kapton specimen.

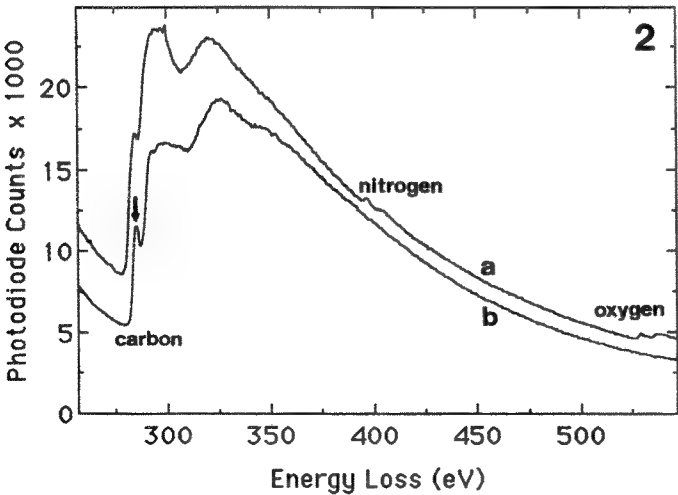
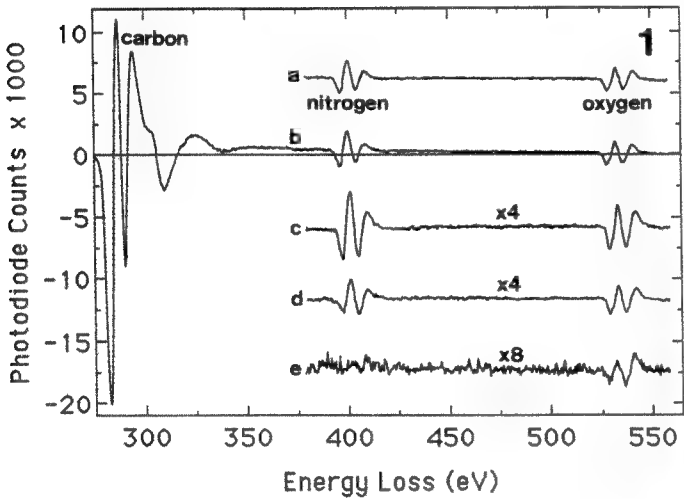


FIG. 1.--Second difference PEELS data from Kapton. (a) ion-milled, unirradiated, (b) microtomed, (c) laser irradiated, 250 pulses, 28 mJ/cm², between clusters, (d) laser irradiated, 250 pulses, 28 mJ/cm², on cluster, (e) laser irradiated, 2000 pulses, 40 mJ/cm², on cluster. All spectra normalized to carbon signal and expansion factors indicated.

FIG. 2.--Conventional PEELS data from Kapton. (a) microtomed, (b) laser irradiated, 2000 pulses, 40 mJ/cm², on cluster.

FIG. 3.--TEM image of ~20 nm clusters in laser irradiated Kapton, 250 pulses, 28 mJ/cm².

MICROSCOPY OF CERAMICS: THROUGH THE LOOKING GLASS AND OUT THE OTHER SIDE

Linn W. Hobbs

Massachusetts Institute of Technology, Room 13-4062, Cambridge, MA 02139

INTRODUCTION

Because this exposition will be followed by nine distinguished symposium contributions detailing better than could any single individual the modern approaches to microscopical analysis of surfaces and interior microstructures of ceramic solids, I have thought it the wiser course to adopt an historical approach¹ and identify those significant points of departure where substantial leaps were made in our understanding of ceramic materials through the application of microscopical techniques. Developments in two techniques are outlined here.

LIGHT MICROSCOPY

The light microscope was developed in the Netherlands by Hans Jensen and his son Zacharias between 1590 and 1610. This was a *compound* microscope, consisting of two lenses, but it was the *single lens* microscope, extensively exploited by Anthony van Leeuwenhoek and Robert Hooke in the 17th century, that provided the first significant microscopical advances, notably in biology. In 1733 an English barrister, Chester More Hall, discovered that a compound *lens* comprising glass elements of different dispersion could correct the chromatic aberration which limited the resolution of the compound microscope, although the principle was not applied to microscopy until 1791; and not until 1830 that another barrister, Joseph Lister, set forth the principles underlying correction of spherical aberration. Light polarization was discovered in 1808 by E. L. Malus, but it was William Nicol who in 1829 first described the method of producing polarized light using calcite prisms ("nicols"). In 1848, the young English geologist Henry Clifton Sorby introduced the making of thin sections from hard substances, like rocks, and recognized immediately the possibilities for examination of geological specimens by transmitted-light microscopy. The characteristic colors exhibited by birefringent minerals examined in the petrographic microscope, with polarizers situated above and below the sample, were catalogued by Albert Michel-Lévy in 1906, by which time petrographic microscopy in mineralogy was on a firm footing.

Mineralogical examination methods were first applied to clays for the ceramics industry in 1913,² although photomicrographs did not start appearing in the *Transaction of the American Ceramic Society* until 1917. Petrographic microscopy of ceramics and glasses was respectively pioneered by Albert Peck³ and Herbert Insley⁴ in the 1920's, and was applied to the setting of hydraulic cement in the 1920's and 1930's. By 1937 an extensive cumulative bibliography of ceramic microscopy had appeared.⁵ Current practice of conventional light microscopy of ceramics is still well described in Insley and Fréchette's 1955 book,⁶ after which time electron microscopies increasingly replaced light microscopy for microstructural analysis. More recent developments are detailed in this symposium by McCrone.

ELECTRON MICROSCOPY

Transmission electron microscopy was developed in the early 1930's by Ernst Ruska and Bodo von Borries in Germany and in the late 1930's and 1940's by E. F. Burton's group in Toronto, by C. E. Hall at Kodak and by James Hillier and Arthur Vance at RCA in the United States. Among the first studies of ceramics was an investigation of high-temperature sintering by W. G. Burgers,⁷ of Burgers circuit fame, in 1937. Other notable applicants were W. H. Eitel, who made early contributions to clays,⁸ minerals⁹ and cements,¹⁰ and his countryman Manfred Baron von Ardenne, who invented the scanning transmission electron microscope in 1937 and applied it to characterization of clays,⁸ microstructures of cements,¹⁰ and sintering of ceramics and fusion of glasses¹¹. Baron von Ardenne's microscope was unfortunately destroyed in an allied air raid in 1944. By 1946, James Hillier was able to compile an extensive bibliography of electron microscopy applications in ceramics.¹²

Ceramic technology, of course, lent itself to early electron microscopy because of the particulate nature of the raw materials. Investigation of monolithic ceramics required thinning to electron transparency, which could be done only with strong acids at high temperatures. Notable studies by Groves and colleagues of MgO in 1960,¹³ by Amelinckx and Kirkpatrick¹⁴ of MgO and BaTiO₃ in 1962 and by Tighe¹⁵ of Al₂O₃ in 1964 utilized this approach. Ion-beam thinning was invented by Raymond Castaing in 1955¹⁶ but initially applied to metals. Its application to thinning monolithic ceramics to electron transparency by Drum in 1964¹⁷ and more extensively by Barber in 1970¹⁸ led the way to widespread TEM of ceramics. The state of progress a little more ten years ago was documented in an issue of the *Journal of the American Ceramic Society*¹⁹. More recent progress is detailed in the contributions to this symposium by Shaw, Bentley and Kriven.

1. Linn W. Hobbs and Jean-Paul Revel, "The Invisible World," *The Microverse*, ed. B. Preiss and W. R. Alschuler, Bantam Books, New York, 1989, pp. 22-47.
2. W. J. McCaughey, "Mineralogical examination of clays," *Trans. Amer. Ceram. Soc.* **15** (1913) 322-27.
3. Albert B. Peck, "Applications of the polarizing microscope in ceramics," *J. Amer. Ceram. Soc.* **2** (1919) 695-707.
4. Herbert Insley, "Petrographic microscope as an instrument for glass technologist," *J. Amer. Ceram. Soc.* **11** (1928) 812-28.
5. T. N. McVay, "Bibliography of ceramic microscopy," *Bull. Amer. Ceram. Soc.* **16** (1937) 33-62.
6. Herbert Insley and Van Derck Fréchette, *Microscopy of Ceramics and Cements*, Academic Press, New York, 1955.
7. W. G. Burgers, "Direct observation of structural changes at high temperatures by use of an electron microscope," *Z. Metallkunde* **29** (1937) 250-51.
8. W. H. Eitel, H. O. Müller and O. E. Radzewski, "Ultramicroscopic Examination of Clay Minerals," *Ber. deut. keram. Ges.* **20** (1939) 165-80. M. von Ardenne, K. Endell and V. Hofmann, "Investigation of first fraction of bentonite and clay soil with the universal electron microscope," *Ber. deut. keram. Ges.* **21** (1940) 209-27.
9. W. H. Eitel, "Importance of electron microscopy for mineralogical investigations," *Fortschr. Mineral. Krist. Petrog.* **23** (1939) 115-20.
10. O. E. Radzewski, H. O. Müller and W. Eitel, "Hydration of tricalcium aluminate," *Naturwissenschaften* **27** (1939) 837-38. M. von Ardenne and K. Endell, "Fusing of clinker materials C₃A and C₄AF as well as the fraction less than three microns of some Portland cement clinker in a heated electron microscope," *Zement* **31** (1942) 313-16.
11. M. von Ardenne, K. Endell and H. Lehmann, "Sintering of ceramic raw materials in a heated electron microscope," *Ber. deut. keram. Ges.* **24** (1943) 73-88. K. Endell and M. von Ardenne, "Visualization of sintering and fusion of glass mixtures, soda, and soda slags in the heated electron microscope," *Glastech. Ber.* **21** (1943) 121-28.
12. James Hillier, "Electron microscopy," *Amer. Ceram. Soc. Bull.* **25** (1946) 438-48.
13. G. W. Groves, J. Washburn, A. Kelly and G. K. Williamson, *Phil. Mag.* **5** (1960) 991.
14. S. Amelinckx and H. B. Kirkpatrick, *Rev. Sci. Instrum.* **33** (1962) 488.
15. N. J. Tighe, *Rev. Sci. Instrum.* **35** (1964) 520.
16. R. Castaing, *Rev. Met.* **52** (1955) 669.
17. C. M. Drum, *Proc. Eur. Reg. Conf. on Electron Microscopy*, ed. M. Titlbach, Czechoslovak Academy of Sciences, Prague, 1964, p. 329.
18. D. J. Barber, "Thin foils of non-metals made for electron microscopy by sputter etching," *J. Mater. Sci.* **5** (1970) 1-8.
19. "Application of transmission electron microscopy to engineering practice in ceramics," ed. A. H. Heuer and N. J. Tighe, *J. Amer. Ceram. Soc.* **62** (1979) 225-98.

LIGHT MICROSCOPY OF CERAMICS

Walter C. McCrone

McCrone Research Institute, Chicago, Illinois 60616-3292

An excellent chapter on this subject by V.D. Fréchet appeared in a book edited by L.L. Hench and R.W. Gould in 1971 (1). That chapter with the references cited there provides a very complete coverage of the subject. I will add a more complete coverage of an important polarized light microscope (PLM) technique developed more recently (2). Dispersion staining is based on refractive index and its variation with wavelength (dispersion of index). A particle of, say almandite, a garnet, has refractive indices of $n_F = 1.789$ nm, $n_D = 1.780$ nm and $n_C = 1.775$ nm. A Cargille refractive index liquid having $n_D = 1.780$ nm will have $n_F = 1.810$ and $n_C = 1.768$ nm. Almandite grains will disappear in that liquid when observed with a beam of 589 nm light (D-line), but it will have a lower refractive index than that liquid with 486 nm light (F-line), and a higher index than that liquid with 656 nm light (C-line). Consequently, when illuminated with white light, one observes colored borders for that almandite grain. On focusing above best focus, a red halo (Becke line) will be observed moving inside the grain while, simultaneously, a blue halo will move out into the liquid. At best focus each grain will show deep purple borders as the red and blue Becke lines coalesce.

These color effects are easily observed with a special 10X objective on the PLM. One can purchase a 10X dispersion staining objective for under \$500 to fit any PLM or one can modify an ordinary 10X objective by placing a 4 ± 1 mm droplet of india ink in the center of an 18 mm round coverslip which is then placed on the top of the objective as it is screwed into place in the PLM. This, plus a stopped-down aperture diaphragm, in the substage condenser yields a black field of view against which most transparent particles show vivid colors when mounted in an appropriate liquid. The colors represent the complementary color of any wavelength at which the particle and the liquid have identical refractive indices. In practice, it soon becomes easy to estimate the wavelength of match (λ_0) for any color observed. Accurate refractive indices can then be calculated from these wavelengths.

Grains of anisotropic substances show different colors depending on their orientation relative to the vibration direction of the light. They will show specific colors when mounted in specific liquids so that a microanalytical scheme can be based on this effect.

A group of olivine grains mounted in a common permanent mounted medium (Aroclor® 5442, $n_D = 1.662$) shows yellow borders if oriented to show the γ index direction, magenta for the β index and blue for the α index. Intermediate orientations showing "prime" values of index show intermediate colors. Yellow, orange or magenta colors always indicate higher indices than the liquid; deep purple, a match in index at 589 nm (D-line), and blue to pale blue-green indicate lower indices. A major mismatch in index is indicated by white borders. A considerable mismatch, however, will still often show pale yellow (higher index than the liquid) or pale blue-green (lower index).

Particles with indices close together (low birefringence) show good colors in all possible orientations in the proper liquids. High birefringent particles show good colors in a few orientations in a given liquid; otherwise, they show pale yellow, pale blue or white borders on the black field.

In practice, one often uses dispersion staining to look for trace substances in mixtures, e.g., amosite asbestos in dust, insulation, or other industrial products. Mounted in 1.680 Cargille high dispersion liquid amosite fibers show blue (for a light vibration direction perpendicular to the length) and golden yellow (parallel to the length). The presence of tremolite in talc, quartz in general dust samples, cocaine or TNT in dust from an automobile trunk is a rapid and certain identification procedure.

Dispersion staining is also a rapid method for the identification of manmade fibers, minerals, street drugs, explosives, etc., or to differentiate different glass samples, e.g., headlight, window, bottle or optical glass.

The principal refractive indices of any crystals can be quickly determined. Isotropic particles will show a single color in a given liquid in all orientations relative to the light vibration direction. The refractive index at 589 nm corresponds to a deep purple color. This is usually determined most precisely by plotting a graph of matching wavelengths for the particles in several liquids in the range yielding wavelengths in the visible range (400-700 nm). The best line through these data points from a plot of matching wavelength versus refractive index of the liquids yields an intercept at 589 nm for the index n_D of those particles. The index of the particle at 486 nm (n_F) and at 656 nm (n_C) can also be calculated from the same graph. The intersection at 486 nm is the wavelength at which the particle and the liquid have the same refractive index. A table of dispersion data for that liquid whose n_D is known from the graph yields n_F of both liquid and particle; n_C is determined correspondingly.

Anisotropic particles give at least two curves of matching wavelength versus n_D of the liquid; one for the highest index (lowest matching wavelength) and one for the lowest index (highest matching wavelength). Biaxial crystals yield three curves, one each for the α , β , and γ directions. These will correspond to γ and α for biaxial substances or ϵ and ω for uniaxial substances. If all particles in the preparation show the same color during stage rotation the corresponding index is ω of a uniaxial substance. The use of dispersion staining for the identification of many common minerals is covered in a paper on soil mineral analysis (4). Quartz, microcline, gypsum, orthoclase, aragonite, nepheline, chrysotile, labradorite, anhydrite, beryl, and talc all show good colors in 1.550 High Dispersion liquid; tourmaline, barite, fluorapatite, prehnite, calcite, forsterite, spodumene, strontianite, augite, dolomite, aragonite, and hornblende in 1.662 (Aroclor®); and kyanite, spinel, rhodonite, periclase, epidote, grossularite, corundum and almandite in 1.74 (methylene iodide). Without belaboring the subject it is clear that a great deal of useful identification data is quickly determined by dispersion staining.

An interesting way to apply dispersion staining to ceramic materials is to examine a roughly polished thin-section. Each grain will show colors characteristic of its orientation and composition at each interface between the liquid and the crystal. The roughened surface of each grain will show dispersion staining colors corresponding to its composition. Most of the dispersion staining data for the identification of extraneous substances is contained in the *Particle Atlas* (3) now available on CD-ROM disk.

References:

1. V.D. Fréchet (1971) Chapter titled "Petrographic Analysis" in Characterization of Ceramics edited by L.L. Hench and R.W. Gould, Marcel Dekker, New York, 257-271.
2. McCrone, W.C. et al. Dispersion Staining Chapter 10 of Polarized Light Microscopy, McCrone Research Institute, 4th Printing, (1984) 169-196.
3. McCrone W.C. et al. Particle Atlas, Electronic Edition, MicroDataware, CD-ROM (1993).
4. McCrone, W.C., Forensic Soil Analysis, Microscope (1992) 40:1, 109-121.

CERAMICS IN THE ENVIRONMENTAL SCANNING ELECTRON MICROSCOPE

Stuart McKernan

Department of Chemical Engineering and Materials Science, Amundson Hall, University of Minnesota,
Minneapolis, Minnesota 55455

Several recent advances have had a major potential impact on the microscopy of ceramic materials. The ability of modern scanning electron microscopes to image uncoated materials, at low voltage for example, whilst still maintaining high resolution should make possible a wide variety of experiments that were hitherto impossible to contemplate. This ability to look at the unmodified surface of a ceramic enables iterative or dynamic experiments to be done with a lot more confidence in the results than has been possible before. A second advance has been the introduction of microscopes capable of operating at higher pressures than was previously possible. This makes possible the ability to image specimens in a variety of different environments. The environmental scanning electron microscope (ESEM) exploits both of these novel areas.¹ The aim of this review is to highlight areas where the unique capabilities of the ESEM may be applied to advance our understanding of ceramics.

Because of the charge-compensating nature of the detector system in the ESEM, ceramic specimens may be imaged without coating them first. This has several advantages, some more obvious than others. For dynamic experiments the fact that there is no metal layer on the surface, for example, should make meaningful observations more realistic. Reactions may thus be followed *in situ*, and in real time. A second feature of the ESEM is that the activity of the surrounding atmosphere may be varied by imaging in different gases and by varying the gas pressure. An good example showing the usefulness of this technique is shown in figure 1. Here a sample of the bismuth, calcium, cuprate superconductor has been heated in oxygen in the microscope. Most of the sample was allowed to melt, only the small black dots, which were later identified as calcium oxide, remained solid. The morphology of the resulting structure could be followed as the specimen was allowed to cool. The morphology of samples heated in oxygen or argon showed significant differences.

The conditions that exist at the specimen surface may not yet match those found in industrial settings, but the higher pressure available, and the presence of water vapor, mean that specimens such as sol-gel films or the curing of cements² may be examined in an appropriate manner.

Because the secondary electron detection system in the ESEM relies so heavily on the gas present in the specimen chamber, any outgassing or evolution of volatile material from the sample during a heating experiment will affect the gas pressure in the chamber. Although the microscope will quickly compensate for this, the instantaneous increase in brightness is apparent on the micrographs. The appearance of these bright streaks may be correlated with features in DTA analyses.

Another image contrast feature which may be useful has been observed in the oxidation of metal layers. The efficiency of production of secondary electrons from the metal is much greater than from the oxide. Therefore, in an oxidation proceeds the image brightness will be reduced.

Other techniques for analysing ceramic materials in the ESEM will be discussed, with examples of applications in different areas of research.³

References

1. G. D. Danilatos *Journal of Microscopy*; **160**, 9 (1990)
2. D. A. Lange, K. Sujata and H. M. Jennings; *Scanning* **90**, 75 (1990)
3. Support was provided by the Center for Interfacial Engineering, an NSF Engineering Research Center.

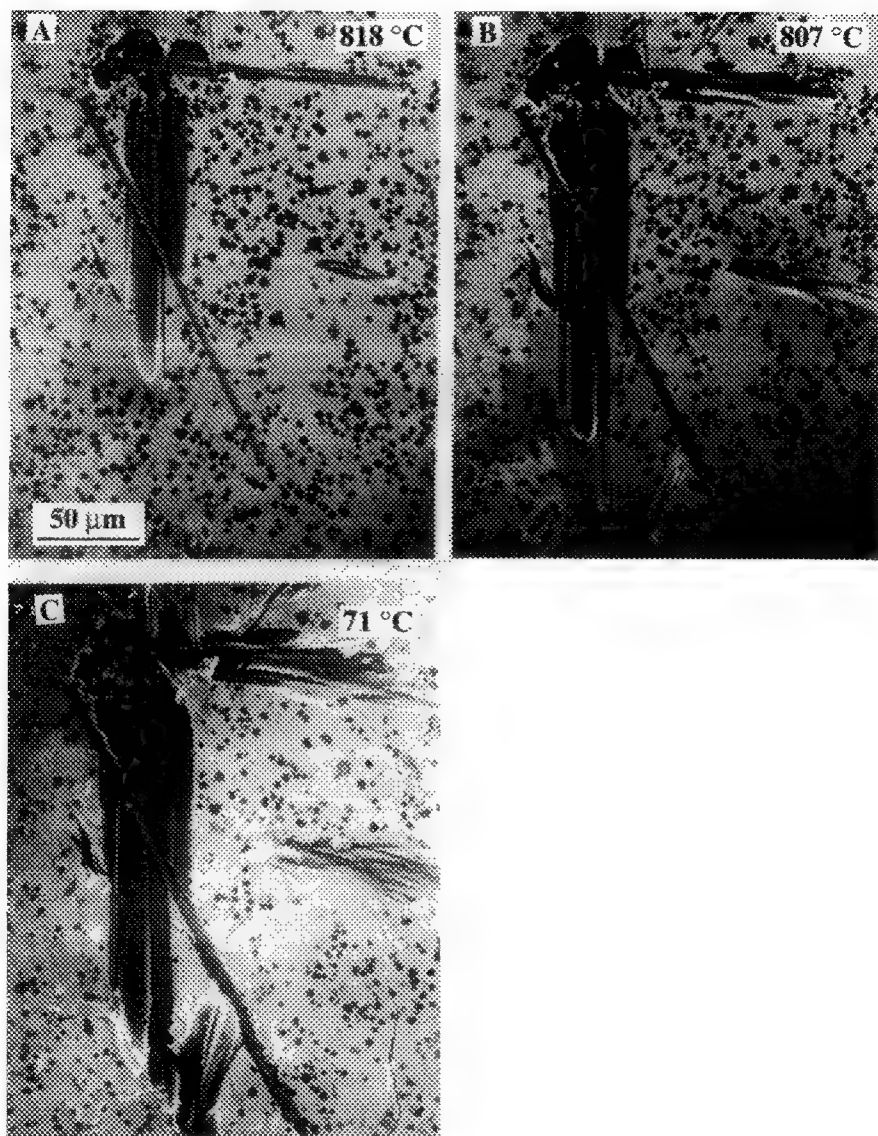


FIG 1 —Solidification of calcia-rich $\text{Bi}_2\text{Sr}_2\text{CaCu}_2\text{O}_8$ melts in oxygen environments. Long needle-like crystallites are the superconducting phase, small, dark dots are calcia, and the ground is apparently still molten in a) at 818°C and b) at 807°C. In c) the specimen has been cooled to close to room temperature.

DISLOCATION DECOMPOSITION AND DISSOCIATION IN MOLYBDENUM DISILICIDE

S. A. Maloy, J. J. Petrovic and T. E. Mitchell

Center for Materials Science, Los Alamos National Laboratory, Los Alamos, NM 87545

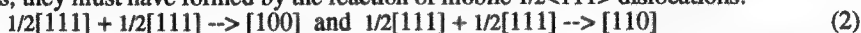
Molybdenum disilicide (MoSi_2) is being investigated as a potential high temperature structural material. It has the tetragonal C11_b crystal structure, space group $I4/mmm$, with $a=3.204\text{\AA}$ and $c=7.848\text{\AA}$. The shortest Burgers vector is $\langle 100 \rangle$ and such dislocations are commonly observed^{1,2}. The $\{110\}$ planes have pseudo-hexagonal symmetry and so the next larger Burgers vectors, $1/2\langle 111 \rangle$ and $\langle 110 \rangle$, both have $b = 4.531\text{\AA}$, followed by $1/2\langle 331 \rangle$ and $\langle 001 \rangle$ both with $b = 7.848\text{\AA}$. The easiest slip systems are $\{011\}\langle 100 \rangle$ and $\{110\}1/2\langle 111 \rangle$ ². These have zero Schmid factors for crystals deformed along $[001]$, forcing other systems such as $\{103\}1/2\langle 331 \rangle$ into operation^{3,4}. Here we will describe and discuss TEM observations of dislocations produced in Czochralski-grown MoSi_2 single crystals by deformation along the $[001]$ compression axis at temperatures from 1000 to 1500°C.

Specimens tested at 1000°C yielded in a series of load drops starting at a stress of 680MPa and continuing to 1400MPa (the limit of the machine) when the plastic strain was 0.3%. The slip system was found to be $\{103\}1/2\langle 331 \rangle$. A typical dislocation structure for a foil cut parallel to the (103) slip plane is shown in Figure 1. Burgers vectors were determined by **g.b** analysis. The microstructure consists of $1/2[331]$ screw dislocations plus mixed $1/2[111]$ and $[110]$ dislocations, mostly lying parallel to $[010]$, which result from the energetically favorable decomposition reaction:



The dislocation loops in Figure 1 have $[100]$ Burgers vectors. These are seen more clearly in the foil cut perpendicular to the slip plane in Figure 2. The $[100]$ loops occur in strings along the $[010]$ direction and are clearly formed from dipoles. Initially, $1/2[331]$ dipoles are formed by edge-trapping along $[010]$; the $1/2[111]$ dislocations formed from reaction (1) can then annihilate by cross-slip on (101) , leaving a $[110]$ dipole. The $[010]$ screw portion of $[110]$ can also annihilate by cross-slip, leaving a $[100]$ edge dipole, which can then break-up into a series of loops by pipe diffusion and self-climb.

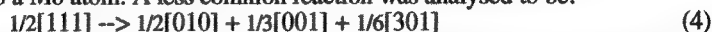
Specimens tested at 1200°C did not yield plastically within the load limits of the machine. Apparently reaction (1) prevents large-scale movement of $1/2\langle 331 \rangle$ dislocations at these temperatures. Specimens tested at higher temperatures yielded at lower stresses and the dislocation microstructures showed strong influence from climb processes. For example, Figure 3 shows a typical microstructure from a specimen deformed 1% at 1500°C. The dislocations are almost all in small-angle $\{100\}$ and $\{110\}$ tilt boundaries consisting of $\langle 100 \rangle$ and $\langle 110 \rangle$ edge dislocations respectively. Since these have zero Schmid factors, they must have formed by the reaction of mobile $1/2\langle 111 \rangle$ dislocations:



followed by climb into low energy configurations. In none of the above cases was dislocation dissociation detected even by weak-beam dark-field microscopy. However, for a specimen oriented 10° off $[001]$, deformed at 1400°C, the microstructure consisted mostly of dissociated $1/2[111]$ dislocations with concomitant fault contrast, as shown in Figure 4. The most common dissociation was found by **g.b** analysis to be:



This reaction is energetically favorable; the associated fault is an anti-phase boundary (APB), i.e., the displacement connects a Si to a Mo atom. A less common reaction was analysed to be:



This dissociation is also energetically favorable and there are two complex stacking faults between the three partials. Both dissociations (3) and (4) appear to occur by climb after the $1/2\langle 111 \rangle$ dislocations have become immobilized. These various decompositions and dissociations are of key importance in controlling the unusual anisotropy in the plastic behavior of MoSi_2 single crystals; investigations are continuing in order to understand the mobility of the various $\langle 100 \rangle$, $1/2\langle 111 \rangle$ and $1/2\langle 331 \rangle$ dislocations.

1. O. Unal, J. J. Petrovic, D. H. Carter, T. E. Mitchell, J. Amer. Ceram. Soc. 73(1990)1752.
2. S. A. Maloy, A. H. Heuer, J. J. Lewandowski, T. E. Mitchell, Acta Met. Mater. 40(1992)3159.
3. Y. Umakoshi, T. Sagami, T. Hirano, T. Yamane, Acta Met. Mater. 38(1990)909.
4. S. A. Maloy, T. E. Mitchell, J. J. Lewandowski, A. H. Heuer, Phil. Mag. Lett. (1993).
5. This research was supported by the US DOE-OBES.

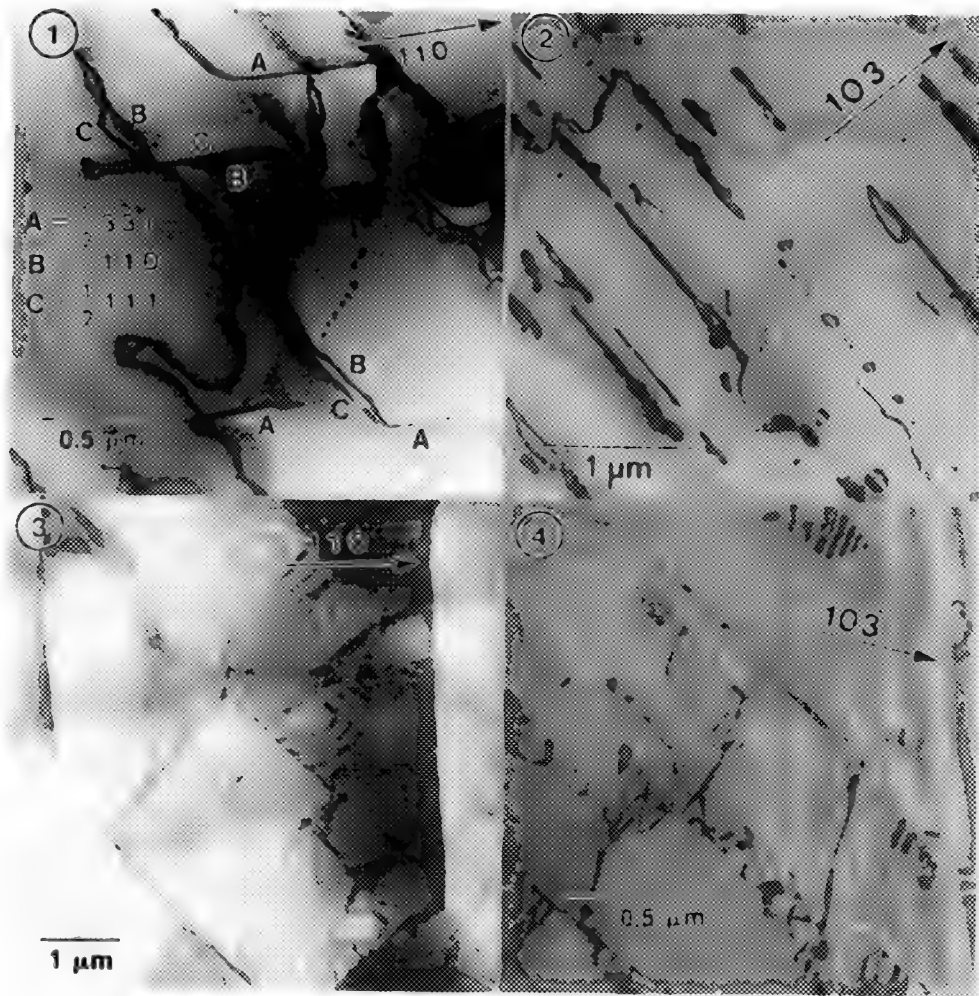


Fig. 1 MoSi₂ deformed at 1000°C, showing $\frac{1}{2}\langle 331 \rangle$, $\frac{1}{2}\langle 111 \rangle$ and $\langle 110 \rangle$ dislocations.
 Fig. 2 Same as Fig. 1, but viewed perpendicular to the slip plane, showing strigs of $\langle 100 \rangle$ loops.
 Fig. 3 MoSi₂ deformed at 1500°C, showing $\{100\}$ and $\{110\}$ small angle tilt boundaries.
 Fig. 4 MoSi₂ deformed at 1400°C (10° off $\{001\}$), showing dissociated $\frac{1}{2}\langle 111 \rangle$ dislocations.

ORIGIN OF THE ALTERNATE BRIGHT/DARK CONTRAST IN HREM IMAGES OF HEXAGONAL CRYSTALS, PARTICULARLY 6H-SiC

J.S. Bow, R.W. Carpenter, and M.J. Kim

Center for Solid State Science, Arizona State University, Tempe, AZ 85287-1704

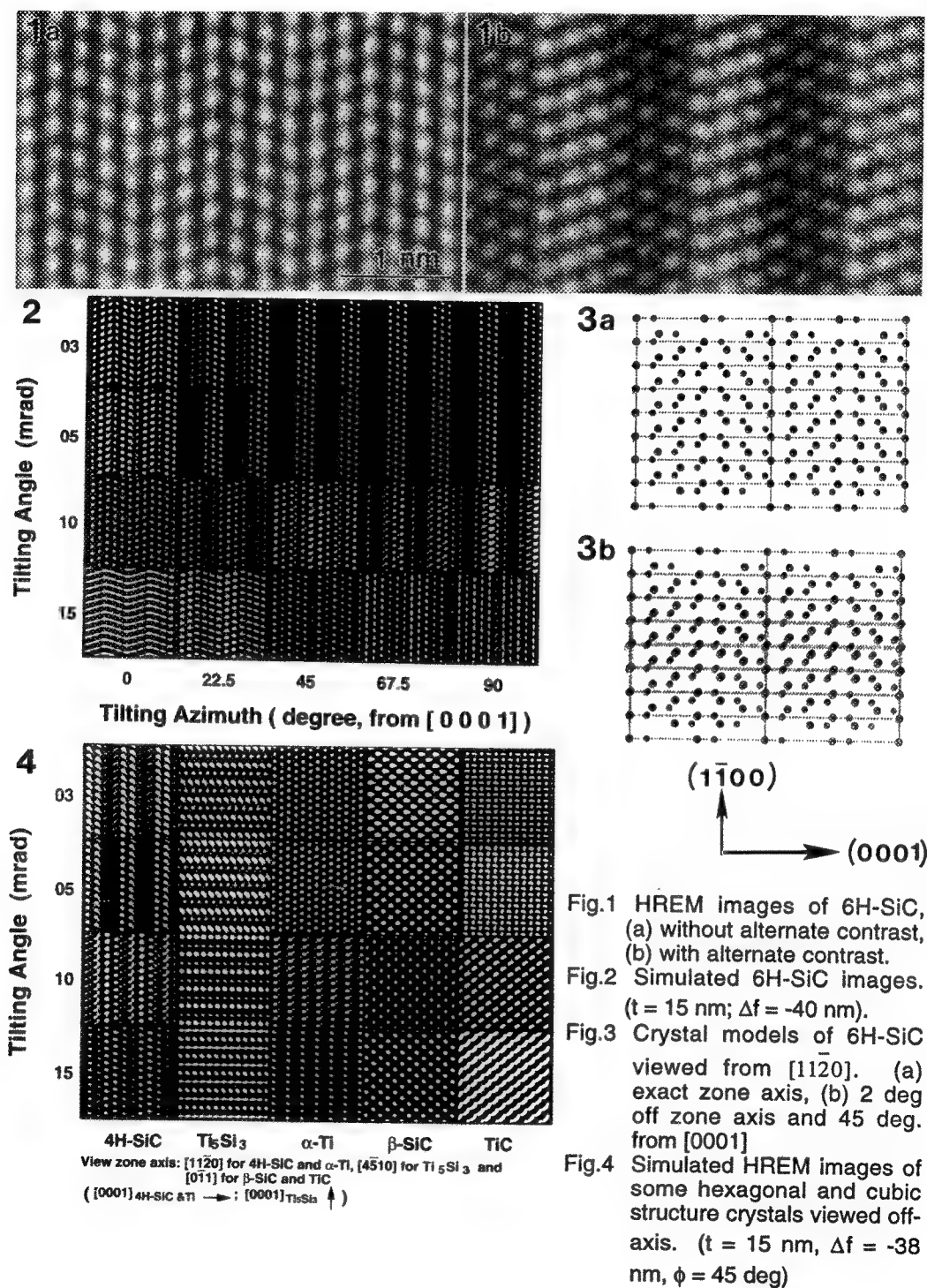
A prominent characteristic of high-resolution images of 6H-SiC viewed from $[11\bar{2}0]$ is a zigzag shape with a period of 6 layers as shown in Fig.1. Sometimes the contrast is same through the 6 layers of (0006) planes (Fig.1a), but in most cases it appears as in Fig.1b -- alternate bright/dark contrast among every three (0006) planes. Alternate bright/dark contrast is most common for the thicker specimens. The SAD patterns of these two types of image are almost same, and there is no indication that the difference results from compositional ordering. O'Keefe et al.¹ concluded this type of alternate contrast was due to crystal tilt in thick parts of the specimen. However, no detailed explanation was given. Images of similar character from Ti_3Al , which is also a hexagonal crystal, were reported by Howe et al.² Howe attributed the bright/dark contrast among alternate (0002) Ti_3Al planes to phase shifts produced by incident beam tilt.

Crystal model construction and high resolution image simulation were performed using CERIUS 3.1 programs to investigate the effect of crystal tilt on HREM images of crystals with hexagonal structure. Fig.2 shows some simulated images of a 15 nm thick 6H-SiC crystal with different tilting angles and different tilting azimuths. Azimuth is degree ccw from $[0001]$ and θ is mrad tilt in the azimuthal direction from the incident beam direction to $[11\bar{2}0]$. Except those of tilting toward $[0001]$ direction ($\phi = 0$), all other images display the characteristics of alternate bright/dark contrast. The highest contrast occurs when the tilting angle θ is 5 mrad, which equals the Bragg angle of the (0006) and the (1100) planes for 6H-SiC. The different contrast indicates that different scattering conditions occurred between these two sets of (0006) planes. The reason for the different scattering conditions is not easily deduced from simulated images.

Using the CERIUS programs, the crystal models can be viewed with arbitrary tilting and azimuth angles. Fig. 3a shows a 6H-SiC crystal model, of $4 \times 4 \times 2$ unit cell dimensions, viewed along the exact $[11\bar{2}0]$ zone axis. From this model, we found that the relative position of carbon atoms with respect to the closest Si atom switch for every three (0006) planes. We may divide these six (0006) planes into 2 sets by carbon atom position. Tilting a certain angle away from $[11\bar{2}0]$ zone along a direction of $\phi = 45^\circ$ from $[0001]$, the projected distances between carbon and silicon atoms of one set of (0006) planes become smaller, while that of other set does not change much. Thus two kinds of phase object are expected. This model also explains why this effect is more prominent for thick specimens. Similar work was performed on some other hexagonal crystals, compounds and elements, and also for several cubic crystals, to better understand the effect of crystal tilt on high resolution images of crystals with hexagonal structure. One set of results are shown in Fig.4. The images of other hexagonal compounds show characteristics similar to those of 6H-SiC when viewed off-axis. Detailed explanation of these contrast effects will be given.

References:

1. M. A. O'Keefe et al., in Proc.50th EMSA Ann. Meeting ed. by G.W.Bailey, J.Bentley, and J.A.Small (1992) p.116
2. J. M. Howe et al., Microscopy Res. and Tech., 23 (1992) 230
3. This research was supported by USDOE grant DE-FG02-87ER-45305. The microscopy was performed at ASU HREM Facility supported by Arizona State University and NSF-DMR-9115680. The specimens were supplied by Mrs. Potter and Dr. Davis from North Carolina State University.



STACKING FAULTS IN DEFORMED α -SILICON NITRIDE SINGLE CRYSTALS

H. Suematsu, J. J. Petrovic* and T. E. Mitchell

Center for Materials Science(*Materials Science and Technology Division), Los Alamos National Laboratory, Los Alamos, New Mexico 87545, U. S. A.

Silicon nitride(Si_3N_4) is well known for its high toughness and strength. This is the reason why it is selected for ceramic turbo charger rotors in automobile engines. However, the high strength of most sintered Si_3N_4 products drops above 1200°C because sintering aids like Y_2O_3 and MgO are required which form glassy phases with low melting points on the grain boundaries. This secondary phase degrades the high temperature characteristics of Si_3N_4 . In order to overcome this deficiency, much work has been reported which aims at crystallizing or removing the glassy phase. If this aim could be successful, resulting in an increase in high temperature strength, other processes would determine the high temperature performance of Si_3N_4 , such as diffusional creep and dislocation slip. Line and planar defects in Si_3N_4 play an important role in such the processes particularly in slip, however, available knowledge about them is limited¹. In the present work, stacking faults in deformed Si_3N_4 single crystals are investigated using high resolution electron microscopy(HREM).

Single crystals of Si_3N_4 were made using a chemically vapor deposition technique by Union Carbide Coating Service. The crystals have a hexagonal pyramid shape with a base diameter of ~5mm and a height of ~10mm. Samples for high temperature compression tests were cut into parallelepipeds 1x1x3mm with a diamond cutting blade. The compression tests were performed in vacuum at a temperature of 1820°C. Details of this test are described elsewhere². After the compression tests, a 0.1mm thick disc was cut for a HREM sample. The specimen was ground with diamond paste and finally thinned with 5kV Ar ions into a suitable thin foil. TEM observation was performed in a Philips CM30ST microscope operated at 300kV.

In the deformed Si_3N_4 , dislocations² and stacking faults were observed as well as dislocation loops which are also found in undeformed sample³. Typical stacking faults are shown in Fig.1. Many of the faults are bent sharply through angles of 90°. Trace analysis shows that they lie on the (0001) and $\{1\bar{1}00\}$ planes. A HREM image of one of the stacking faults is shown in Fig.2. A horizontal fault line can be seen clearly and the distorted region around the fault is restricted to within 0.2nm. This means that this fault is parallel to the $[11\bar{2}0]$ zone axis and lies on the (0001) plane. The (0001) interplanar spacing is 0.56nm in α - Si_3N_4 ; however, the planes are seen to be closer together at the stacking fault. Thus, the fault has a displacement vector \mathbf{R} with a component perpendicular to the fault plane. On the other hand, no shear is observed when sighting along the $(1\bar{1}01)$ lattice planes. The direction of \mathbf{R} must therefore lie in the $(1\bar{1}01)$ plane, parallel to $[\bar{1}102]$.

Another stacking fault is shown in Fig.3. It is clear this fault is also parallel to the imaging zone axis. Compared with the fault in Fig.2, this fault is not straight. Some sections of the fault are approximately on the $(10\bar{1}0)$ plane. Shaw et al. reported that 60° rotation boundaries are frequently found in α - Si_3N_4 single crystal¹. However, the fault in Fig.3 is different from the fault previously reported. Since $(10\bar{1}0)$ interplanar spacing is expanded across the fault, this fault has a component of \mathbf{R} perpendicular to the fault plane. Atomic structures of the both faults are still under investigation⁴.

References

1. T. M. Shaw, J. W. Steeds and D. R. Clarke, Mat. Res. Soc. Symp. Proc. 31, 325-330 (1984).
2. H. Suematsu, J. J. Petrovic and T. E. Mitchell, Mat. Res. Soc. Symp. Proc. (1993), in press.
3. H. Suematsu, J. J. Petrovic and T. E. Mitchell, Proc. EMSA, 342-343 (1992).
4. This work was supported by the US DOE-OBS.

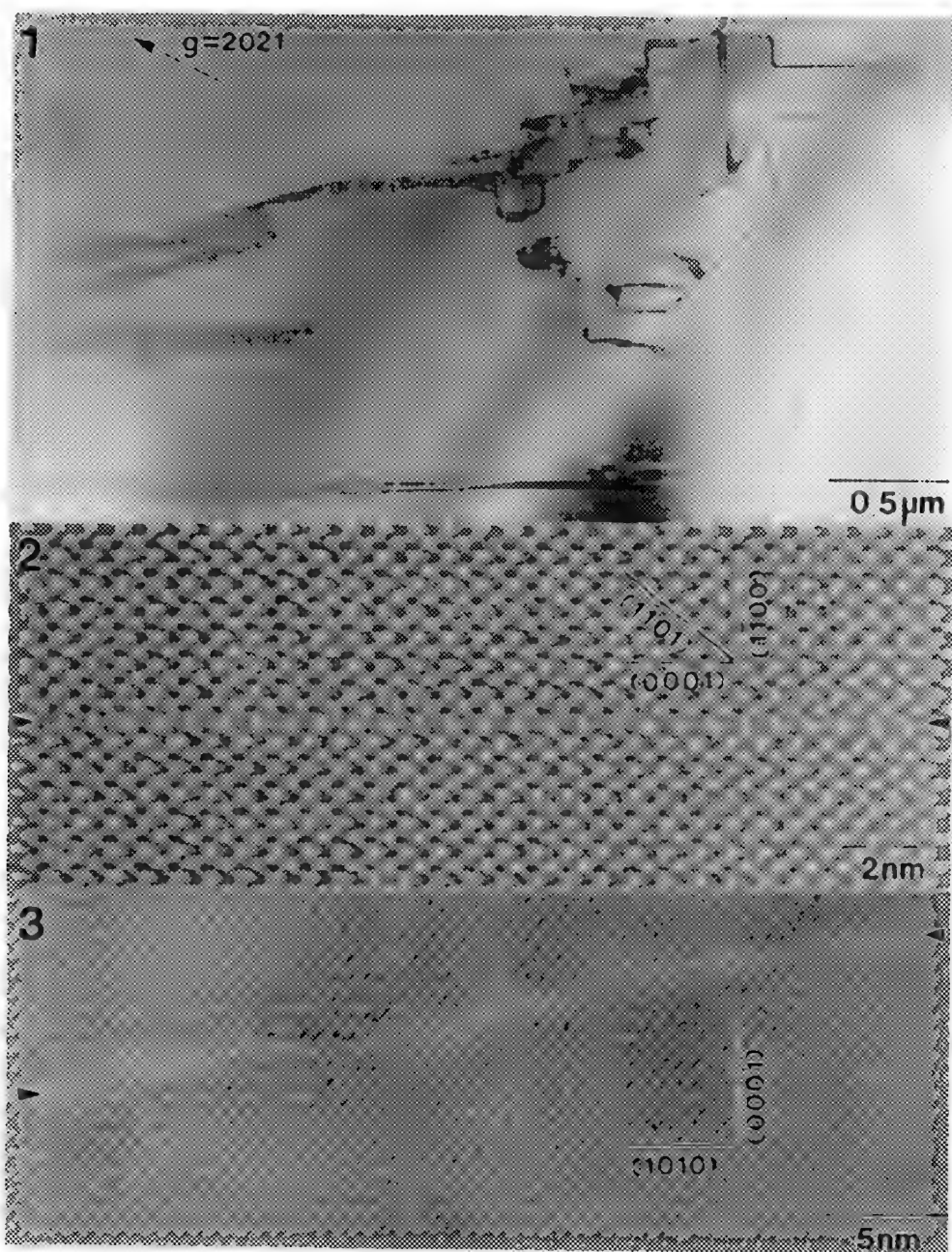


Fig.1 Bright field electron micrograph of stacking faults in deformed Si_3N_4 .
 Fig.2 High resolution electron micrograph of a stacking fault on the (0001) plane. \mathbf{R} is $[\bar{1}102]$.
 Fig.3 High resolution electron micrograph of a stacking fault on the $(10\bar{1}0)$ plane.

LOW-TEMPERATURE Mo-CATALYZED GROWTH OF CRYSTALLINE Si_3N_4 BY CVD

K.L. More, R.A. Lowden, and T.M. Besmann

High Temperature Materials Laboratory, Oak Ridge National Laboratory, Oak Ridge, TN 37831-6064

Silicon nitride possesses an attractive combination of thermo-mechanical properties which makes it a strong candidate material for many structural ceramic applications. Unfortunately, many of the conventional processing techniques used to produce Si_3N_4 , such as hot-pressing, sintering, and hot-isostatic pressing, utilize significant amounts of densification aids (Y_2O_3 , Al_2O_3 , MgO , etc.) which ultimately lowers the utilization temperature to well below that of pure Si_3N_4 and also decreases the oxidation resistance. Chemical vapor deposition (CVD) is an alternative processing method for producing pure Si_3N_4 .^{1,2} However, deposits made at temperatures less than $\sim 1200^\circ\text{C}$ are usually amorphous and at slightly higher temperatures, the deposition of crystalline material requires extremely low deposition rates ($\sim 5 \mu\text{m/h}$). Niihara and Hirai¹ deposited crystalline $\alpha\text{-Si}_3\text{N}_4$ at 1400°C at a deposition rate of $\sim 730 \mu\text{m/h}$. Hirai and Hayashi³ successfully lowered the CVD temperature for the growth of crystalline Si_3N_4 by adding TiCl_4 vapor to the SiCl_4 , NH_3 , and H_2 reactants. This resulted in the growth of $\alpha\text{-Si}_3\text{N}_4$ with small amounts of TiN at temperatures as low as 1250°C . Under similar deposition conditions, $\beta\text{-Si}_3\text{N}_4$ with small amounts of TiN was produced at 1350°C .

It has recently been discovered that the addition of MoCl_5 to the reactant gases SiCl_4 , NH_3 , and H_2 resulted in the codeposition of MoSi_2 and $\beta\text{-Si}_3\text{N}_4$ at a temperature of 1150°C at deposition rates approaching $200 \mu\text{m/h}$. Deposition experiments were performed using a cold-wall CVD reactor and graphite substrates. Not only is 1150°C the lowest reported temperature for the growth of crystalline Si_3N_4 , but the high deposition rates obtained make Mo-catalyzed growth extremely practical. The $\text{Si}_3\text{N}_4\text{-MoSi}_2$ coating system is particularly attractive because both phases are refractory, and together in a composite coating can possibly have a greater fracture toughness than either alone (K_{1C} values are being determined). The addition of MoSi_2 also improves the oxidation resistance.

The general microstructure of a $\text{MoSi}_2\text{-Si}_3\text{N}_4$ coating is shown in the TEM image of Figure 1. The coating was removed from the graphite substrate, mechanically thinned to $\sim 75 \mu\text{m}$, dimpled, and ion milled to perforation. Small particles of MoSi_2 , identified by both X-ray and electron diffraction techniques and arrowed in Figure 1, were homogeneously dispersed throughout the matrix and ranged in size from $\sim 5\text{-}100 \text{ nm}$. The $\beta\text{-Si}_3\text{N}_4$ matrix, also positively identified by both X-ray and electron diffraction, was highly textured towards the $\langle 0001 \rangle$ basal orientation and had a relatively large average domain size ($> \sim 10 \mu\text{m}$). However, each of these large domains contained a high density of sub-grain/low-angle grain boundaries, as arrowed in Figure 2. The MoSi_2 particles were found along these low-angle boundaries as well as at the high angle boundaries separating the larger domains. Figure 3 shows a group of these much smaller grains ($\sim 50 \text{ nm}$ in size) separated by low-angle boundaries, with each small sub-grain oriented close to $\langle 0001 \rangle$. The larger MoSi_2 particles found along the low-angle boundaries had no apparent orientation relationship with respect to the surrounding $\beta\text{-Si}_3\text{N}_4$ grains. Work is ongoing to further characterize the grain boundaries and will include cross-section in addition to plan view samples, and to determine the limits for the low temperature, Mo-catalyzed, CVD growth of crystalline Si_3N_4 .⁴

1. K. Niihara and T. Hirai, *J. Mat. Sci.* 11 (1976) 593.
2. A.C. Airey, S. Clark, and P. Popper, *Proc. Brit. Ceram. Soc.* 22 (1973) 305.
3. T. Hirai and S. Hayashi, *J. Amer. Cer. Soc.* 64 (1981) C-88.
4. Research sponsored by (1) the U.S. DOE Interagency Agreement 1692-1692-A1, sponsored by the Materials Laboratory, Wright Research Laboratories (WRL/MLBC) under contract AFWAL MIPR FY1457-89-N5001 and (2) the U.S. DOE, Assistant Secretary for Conservation and Renewable Energy, Office of Transportation Technologies, as part of the High Temperature Materials Laboratory Users Program, under contract DE-AC05-84OR21400 managed by Martin Marietta Energy Sys., Inc.

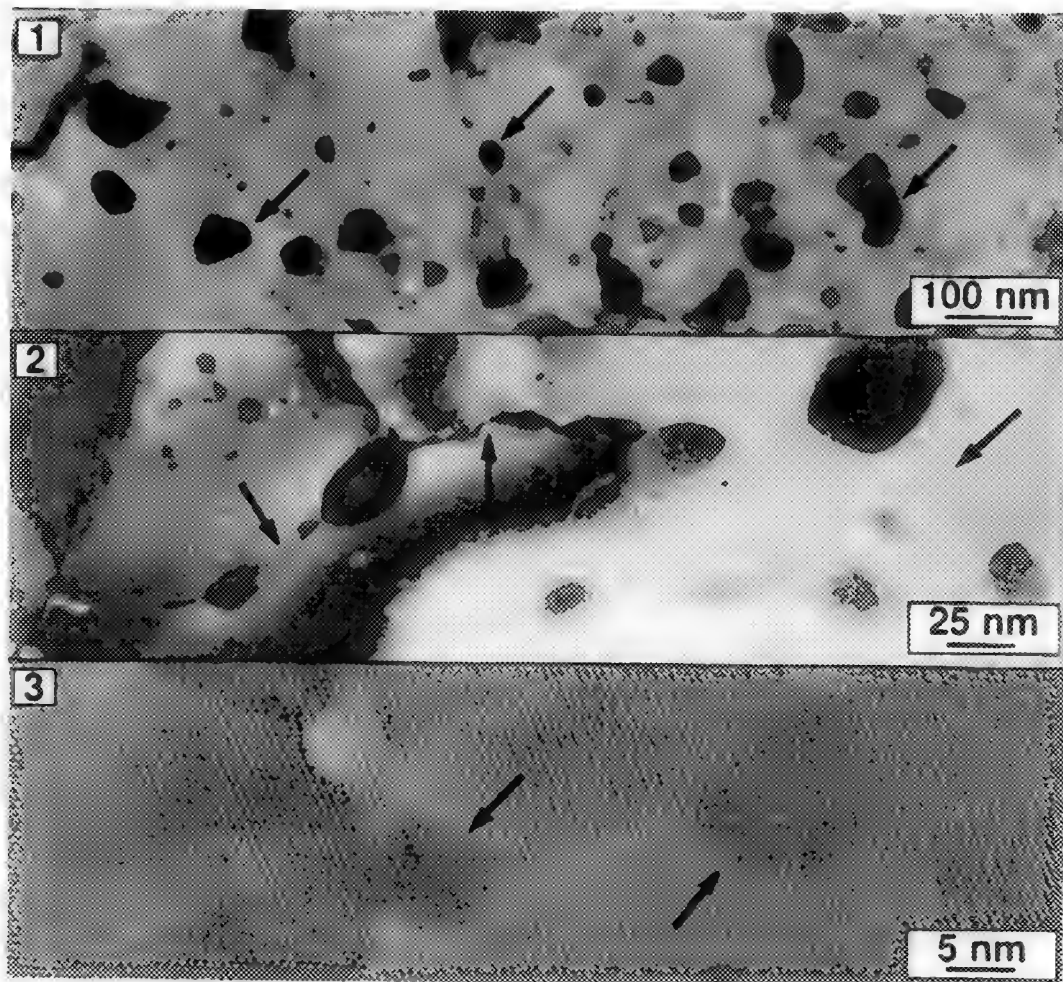


FIG. 1. -- Low magnification TEM image showing general microstructure of $\text{MoSi}_2\text{-Si}_3\text{N}_4$ coating. Several MoSi_2 particles are arrowed.

FIG. 2. -- Low-angle grain boundaries found within larger $\beta\text{-Si}_3\text{N}_4$ domains (arrowed). Most of the MoSi_2 particles were found along the low-angle boundaries.

FIG. 3. -- Group of $\beta\text{-Si}_3\text{N}_4$ sub-grains within larger domains, all oriented close to $\langle 0001 \rangle$. Two MoSi_2 particles are arrowed.

GRAIN BOUNDARIES IN SILICON NITRIDE

K Das Chowdhury⁺, R. W. Carpenter and W. Braue*

Center for Solid State Science, Arizona State University, Tempe, AZ 85287-1704, *German Aerospace Research Establishment, D5000, Cologne 90, Germany

+ Present Address: Dept. of Materials Science and Engineering, MIT, Cambridge, MA 02139

Research on whisker/matrix interfaces and matrix grain boundaries in Si_3N_4 and Al_2O_3 composites reinforced with SiC whiskers by HREM imaging have shown that disordered layers exist in these regions [1-3]. The disordered interfacial regions are often considered amorphous layers, particularly when they are thicker than ~1nm. They appear to be discontinuous in the whisker/matrix interfaces and continuous in matrix grain boundaries [3]. Thin amorphous layers in composites and conventionally synthesized ceramics, particularly those based on Si_3N_4 , are expected to contain oxygen from sintering aids and powder particle surface impurities. In this paper we report the results of an investigation of silicon nitride matrix grain boundaries in $\text{Si}_3\text{N}_4/\text{SiC(w)}$ composites (CMC) and polycrystalline CVD silicon nitride, using very high spatial resolution position resolved EELS and HREM imaging. Interfaces between SiC and silicon nitride in CMC materials have been discussed elsewhere (1).

The CMC's were prepared by pressing and presintering Toyo-Soda α -silicon nitride (TS10) powder with 5.5 wt% Yttria and 1.1 wt% Alumina as sintering aids and 20 vol% β -SiC Huber whiskers at 1500°C in 0.1MPa Argon. Complete densification was achieved by hot-isostatic-pressing the compact at 1780°C in 190 MPa Argon. The CVD silicon nitride was synthesized from a low pressure gas mixture of SiCl_4 and NH_3 on substrates in the 1300°C to 1400°C range (4). Planar TEM specimens were made by conventional mechanical thinning, dimpling and Ar-ion-milling. The structure of grain boundaries was examined in an Akashi 002B microscope with a point resolution of 0.18nm at 200KeV. The chemistry at and around the interfaces was determined by position-resolved EELS technique with a Philips 400ST TEM fitted with a field emission gun, coupled to a Gatan666 parallel EELS detector. The field emission gun was operated at 100KeV, with an approximately 3nm diameter probe with a current density of the order of 10^8 A/m^2 at the specimen level. A liquid nitrogen cooled specimen holder was used to eliminate specimen borne contamination. All the experiments were carried out in the diffraction mode with the entrance aperture for the parallel EELS detector centered around the transmitted beam. The acceptance half angle for the parallel EELS detector was 10mrad.

Figure 1 shows an HREM image of a grain boundary in silicon nitride prepared by CVD. Grain A was in $\langle -24-23 \rangle$ zone axis orientation and grain B was in $g = \langle 1 \ 0 \ 1 \ 0 \rangle$ two beam orientation. No amorphous layer was visible at the grain boundary within the resolution limit of the microscope used, but a disordered region with structural width approximately equal to the SiN_4 tetrahedron size for this material was visible, as expected. Good planar matching between the $\langle 1 \ 0 \ 1 \ 0 \rangle$ lattice fringes in grains A and B was observed in figure 1. Position resolved EELS analysis across the boundary did not show any light element impurity segregation, particularly oxygen at the boundary. Figure 2a shows an HREM image of another silicon nitride grain boundary in the HIPped SiC whisker reinforced CMC. A 0.5 nm wide disordered region was visible at this grain boundary. Position resolved EELS analysis for oxygen distribution across this boundary showed a sharp rise in oxygen concentration at the boundary (figure 2b). This observation confirmed that the disordered region is oxygen rich. The wide difference observed between the structural width (in fig 2a) and the chemical width (in fig 2b) has been explained in detail elsewhere (1).

It is commonly believed that the origin of the oxygen containing amorphous layer at the grain boundaries in CMC or conventionally synthesized polycrystalline ceramics is the addition of sintering aids for densification. From the observation of clean boundaries in CVD silicon nitride it can be strongly inferred that the existence of an oxygen rich amorphous grain boundary layer or disordered zone is dependent upon the presence of sintering aids and/or impurity content of the bulk material. However, the

structural width of the "amorphous layer" or disordered zone can be very small ($< 0.5\text{nm}$) in either case and is not an indicator of the presence or absence of oxygen segregation. Spectroscopy is required for definitive impurity analysis (5).

REFERENCES

1. K. Das Chowdhury, R. W. Carpenter, and W. Braue, Ultramicroscopy (1992) 40, 229.
2.W. Braue, R. W. Carpenter and D. J. Smith, J. Mat. Sci., 25, 2949 (1990).
3..K. Das Chowdhury, R. W. Carpenter, and W. Braue, J. in preparation.
4. R. E. Engdahl, Synterials Inc. private communications.
5. This research was supported by the US Dept. of Energy, Basic Energy Sciences (DE-FG02- 87ER 45305) and performed in the NSF/ASU HREM Center.

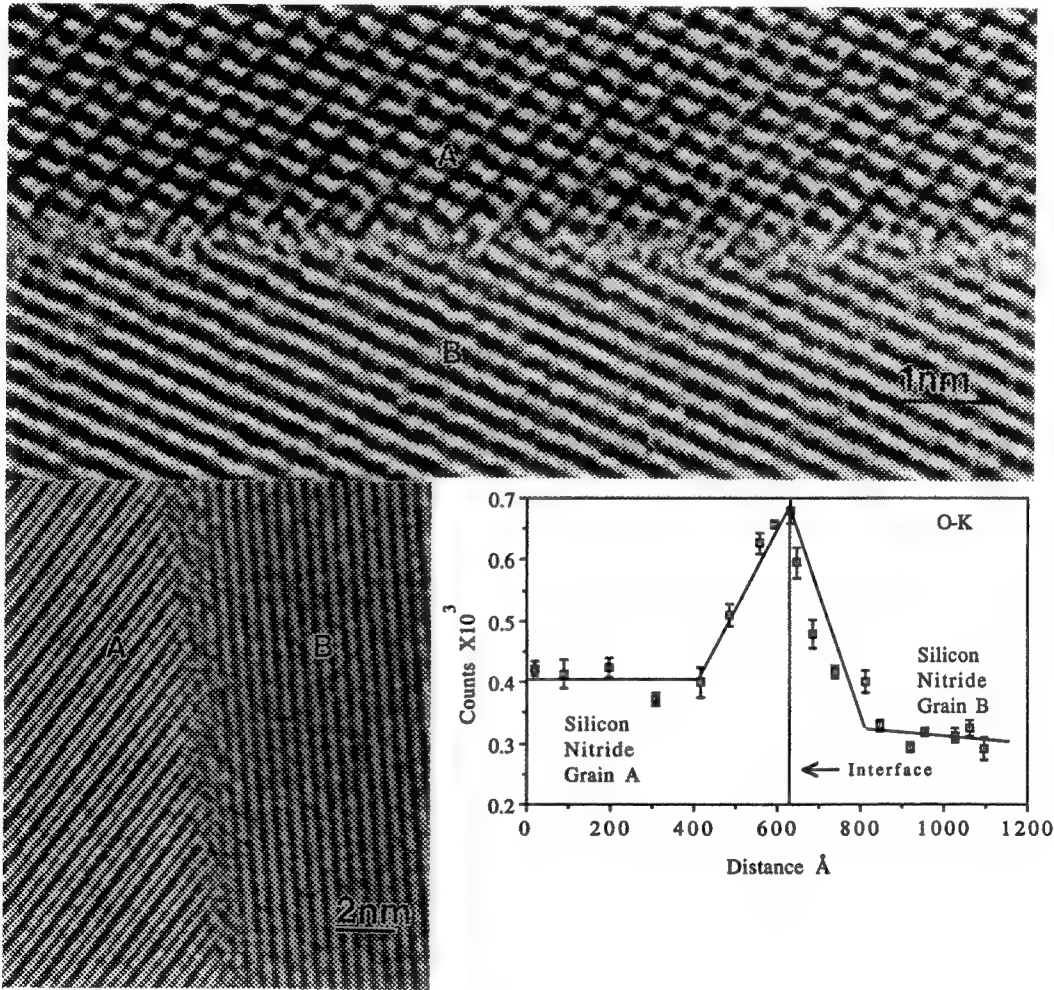


Figure.1 HREM image of a Silicon Nitride grain boundary prepared by Chemical Vapor Deposition, indicating presence of very thin disordered region. No oxygen was detected at the boundary.
Figure 2 (a) HREM image of a Silicon Nitride boundary in HIPped SiC(w) reinforced CMC material indicating a 0.5 nm interfacial layer. (b) Variation of oxygen distribution across the grain boundary shown in (a).

EVALUATION OF MATRIX AND INTERFACE PROPERTIES IN SiC/SiC COMPOSITES

A.D. Surrent, K.L. More, and R.A. Lowden

High Temperature Materials Laboratory, Oak Ridge National Laboratory, Oak Ridge, TN 37831-6064

It has become increasingly important to characterize composite matrix materials in terms of processing-microstructure-property relationships. The characteristics of composite matrices can differ significantly from monolithic materials processed using more conventional techniques such as hot-pressing or sintering. Knowledge of the mechanical and thermophysical properties of the matrix as a function of processing parameters is necessary for the modeling and design of composite materials. In this study, the microstructure and mechanical properties of the matrix in the Nicalon/SiC composite system have been characterized as a function of processing temperature.

The composites were fabricated by stacking multiple layers of plain-weave Nicalon fabric rotated in a 30°-60°-90° sequence within the cavity of a graphite holder. The preforms were then coated with carbon at 1375 K and 3 kPa. The coated preforms were densified using a forced chemical vapor infiltration (FCVI) technique developed at ORNL.¹ The SiC matrix was produced by the decomposition of methyltrichlorosilane carried in hydrogen at temperatures of 1000, 1100, 1200, 1300, and 1400°C in order to reveal the effect of temperature on the properties of the composite and matrix. A combination of techniques was used to characterize the composites, including AFM, SEM, and TEM.

Vickers hardness numbers (VHN), as a function of processing temperatures for the SiC matrix, are compiled in Table 1. The matrix hardness values for the composites processed at 1000, 1100, and 1200°C were approximately equal whereas the values for the composites processed at 1300°C and 1400°C were lower. These same trends were observed for composite flexure strength and matrix cracking as a function of processing temperature, also summarized in Table 1. These results can be directly related to observed microstructural changes. A comparison between TEM images of the fiber/matrix interface region clearly shows the differences in the microstructural evolution of the SiC matrix during processing at different temperatures. Fig. 1 shows that at temperatures less than 1200°C, the SiC nucleates randomly as small grains. Within less than 50 nm from the fiber surface, columnar growth begins. The TEM micrograph in Fig. 2 shows that at 1400°C, the grain size is not only larger, but the grain orientation is completely random. The preferred orientation, or lack of, is reflected in the diffraction patterns associated with each TEM image. In fact, this effect was observed at 1300°C to a lesser extent; the "nucleation zone" close to the fiber is wider (>200 nm). Other characterization techniques were also used to evaluate the matrix microstructure. The SEM image in Fig. 3 shows the characteristic radial growth of the SiC grains off the fiber surface. Fig. 4 is an image obtained by AFM. This method was used to obtain three-dimensional images to correlate with the SEM images.

This paper has presented characterization of the matrix of SiC/SiC composites. Future work will concentrate on other composites containing Si-C-O, alumino-silicate, or carbon fibers. Fiber push-out tests on these composites will be performed in order to obtain the interfacial shear stress, which will be correlated with the fiber surface roughness found by AFM. These techniques, along with previously collected data, will be instrumental in characterizing the composites as a whole.²

1. D.P. Stinton, A.J. Caputo, and R.A. Lowden, Amer. Cer. Soc. Bull., (1986) 65(2), 347-50.

2. Research sponsored by (1) Office of Industrial Tech., Improved Energy Productivity Div. and Adv. Industrial Concepts Div. and (2) Office of Transportation Technologies, as part of the HTML User Program, both sponsored by the U.S. DOE, Assistant Secretary for Conservation and Renewable Energy, under contract DE-AC05-84OR21400, managed by Martin Marietta Energy Systems, Inc.

TABLE 1.

Processing Temp. (°C)	VHN (GPa)	Composite Strength (MPa)	Matrix Cracking (MPa)
1000°C	41.5 ± 3.1	324 ± 31	116 ± 15
1100°C	41.7 ± 3.2	359 ± 28	141 ± 15
1200°C	44.3 ± 4.8	379 ± 19	184 ± 22
1300°C	36.1 ± 1.6	295 ± 5	116 ± 12
1400°C	32.8 ± 4.5	290 ± 31	118 ± 5

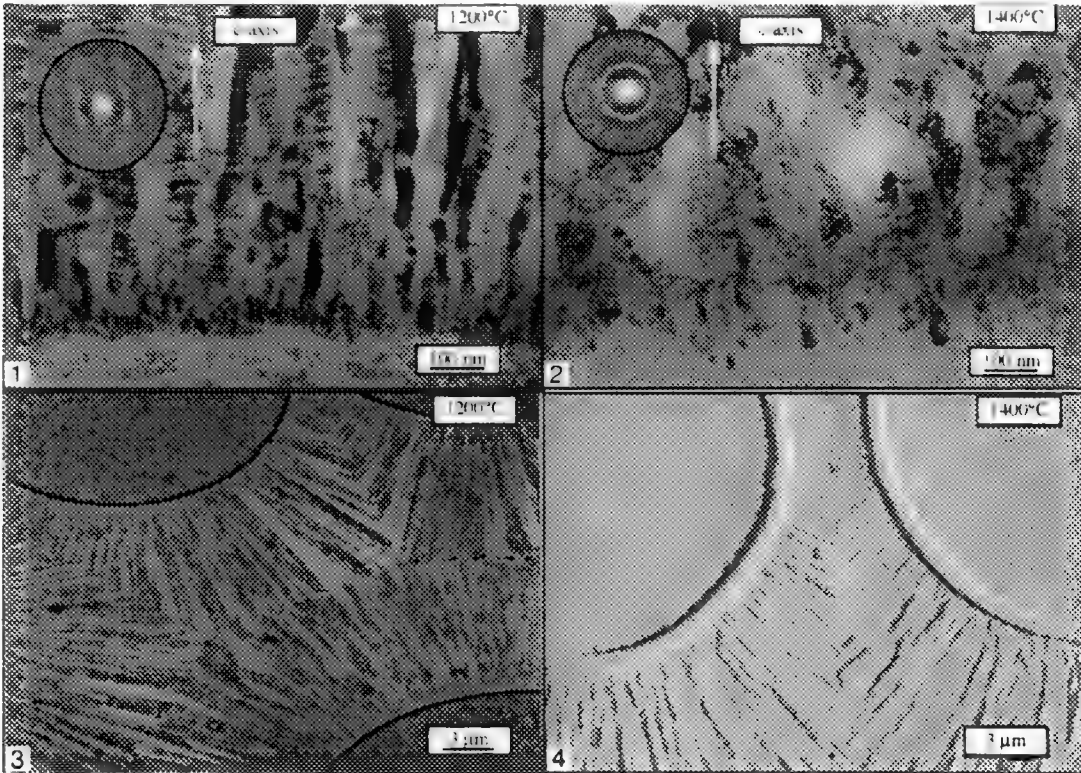


FIG. 1.--TEM image of Nicalon/SiC composite processed at 1200°C. Note columnar growth of SiC grains.

FIG. 2.--TEM image of Nicalon/SiC composite processed at 1400°C. No preferred growth orientation.

FIG. 3.--SEM image demonstrating radial growth of SiC grains in composite processed at 1200°C.

FIG. 4.--AFM image showing three-dimensional view of fiber/matrix region.

STRUCTURES OF CHEMICALLY STABILIZED CERAMICS

Pratibha L. Gai #, M. A. Saltzberg, L.G. Hanna and S.C. Winchester

Central Research and Development Department, Du Pont Science and Engineering Laboratories,
Microstructural Lab., Experimental Station, Wilmington DE 19880-0356

Silica based ceramics are some of the most fundamental in crystal chemistry. The cristobalite form of silica has two modifications, α (low temperature, tetragonal form) and β (high temperature, cubic form). This paper describes our structural studies of unusual chemically stabilized cristobalite (CSC) material, a room temperature silica-based ceramic containing small amounts of dopants, prepared by a wet chemical route. It displays many of the structural characteristics of the high temperature β - cristobalite (~270°C), but does not undergo phase inversion to α -cristobalite upon cooling. The Structure of α -cristobalite is well established (1), but that of β is not yet fully understood (2).

Compositions with varying Ca/Al ratio and substitutions in cristobalite were prepared in the series, $\text{CaO}:\text{Al}_2\text{O}_3:\text{SiO}_2 : 3-x: x : 40$, with $x=0-3$. For CSC, a clear sol was prepared from Du Pont colloidal silica, Ludox AS-40®, aluminium nitrate nonahydrate, and calcium nitrate hexahydrate in proportions to form a final composition 1:2:40 composition. The precursor was calcined at 1100°C for 24 hours to yield CSC. Well ordered α -cristobalite was prepared by crystallizing Aerosol®, a very pure form of amorphous silica at 1400°C. Other compositions with varying Ca/Al were also prepared with different calcination temperatures, and examined. Chemically stabilized compositions using transition metals, and alkali metals were synthesized as above.

Since the true-structures of these materials is unclear, we have chosen to call the samples synthesized by our new route which do not undergo phase transformation - thus they are 'stabilized' :- chemically stabilized cristobalite, or CSC.

High resolution electron microscopy (HREM) and electron diffraction were performed using a CM30 supertwin HREM operating at 300 keV and fitted with a windowless EDX detector for simultaneous microcomposition analysis (3,4).

X-ray diffraction patterns of the room temperature CSC indicated a well-crystallized structure, in contrast to the relatively broad reflections observed in synthetic cristobalites and in natural cristobalitic opals reported in the literature.

Electron diffraction examinations reveal remarkable differences between the CSC and the undoped α - cristobalite. As shown in Fig. 1 (a), the local structure of undoped α -cristobalite in (010) projection reveals a high concentration of stacking faults and twins along $\langle 101 \rangle$ directions. The electron diffraction (b) shows faint streaks along $\langle 101 \rangle$ when the concentration of faults is high. Microstructure of the room temperature CSC with the composition $\text{CaO}:\text{2Al}_2\text{O}_3:\text{40SiO}_2$ with no stacking faults (confirmed by tilting) and the corresponding EDX spectrum indicating the incorporation of Ca and Al into the structure, are shown in Fig. 2(a) and (b), respectively. Electron diffraction patterns generally show complex and substantial diffuse scattering (Fig.2c). The HREM structure image of the CSC is shown in Fig. 3 in (101) projection, indicating a cubic symmetry. The electron and X-ray diffraction data show that the structure is related to the high-cristobalite.

In-situ electron microscopy results suggest that the disorder is structural and is static, and these, and the related NMR data will be reported in Journal of Solid State Chemistry. (# Address for corresp.).

References

1. M.O'Keefe and B.G. Hyde, Acta.Cryst., (1976)B32, 2923.
2. T.R. Welberry, G.L. Hua and R.L. Withers, J.Appl.Cryst., (1989)22,87.
3. E.D. Boyes et al, Physica C (Elsevier), (1989)159, 802.
4. P.L. Gai and J.M. Thomas, Supercond.Rev., Gordon & Breach, (1992)1, 1.

Fig.1. (a) Pure α -cristobalite (tetragonal) with stacking faults along $\langle 101 \rangle$
(b) Electron Diffraction in (010)

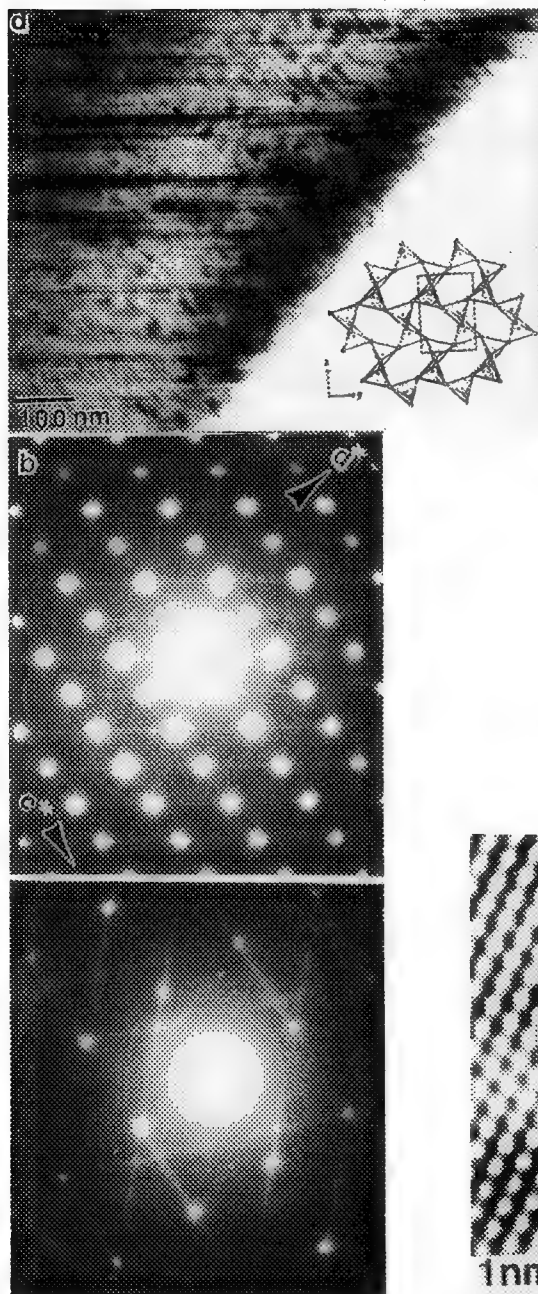


Fig.2 (a) Chemically Stabilized Ceramic with no stacking faults
(b) EDX with Al and Ca dopants

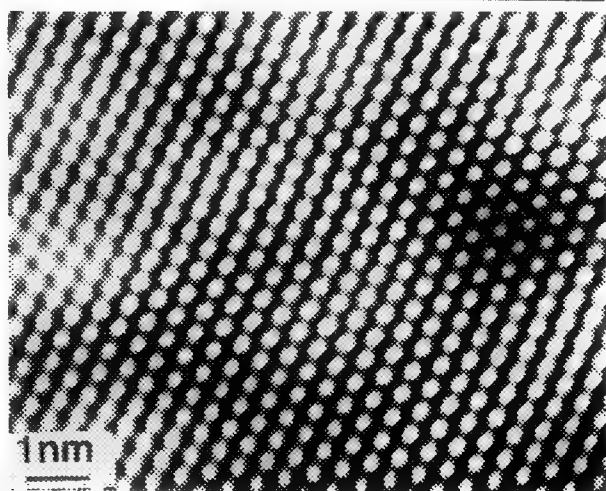
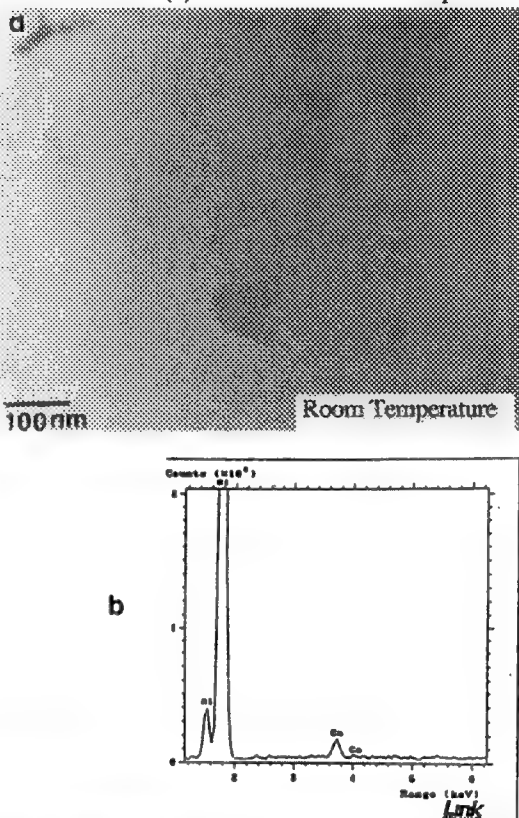


Fig.2(c) Strong diffuse streaking from 'ordered' CSC

Fig.3 HREM structure image of CSC

ELECTRON DIFFRACTION STUDY OF THIN COBALT OXIDE FILMS GROWN BY PULSED LASER DEPOSITION ON ZIRCONIA SUBSTRATES

Stuart McKernan, Sundar Ramamurthy and C. Barry Carter

Department of Chemical Engineering & Materials Science, Amundson Hall, 421 Washington Avenue SE, University of Minnesota, Minneapolis, MN 55455

The technique of pulsed laser deposition (PLD) has been applied to many different materials systems.¹ Thin films of metal, ceramic, semiconductor and polymer material have successfully been deposited on different substrates. The nature of the deposited film varies according to the target used and the exact conditions under which the deposition occurred. Among other properties, the films may be amorphous or fully crystalline, they may be homogeneous or contain particulates from the target, and the films may be smooth or textured. Because of the nature of the deposition process the films need not be in the thermodynamically lowest energy state. Following earlier work, we have grown several ceramic films on single crystal oxide targets, to characterize the interfacial reactions involved.^{2,3}

In this study crystalline cobalt oxide ceramic films have been grown on (001) zirconia substrates by PLD. The deposition was performed in an oxygen partial pressure of ~ 6 mtorr, with the substrate heated to 750°C. Under these conditions a very clean interface between the CoO layer and the zirconia was formed. A very strong crystallographic texture was evident in cross-section samples with the {111} planes of the CoO lying parallel (001) deposition surface of the zirconia substrate. When viewed in plan-view, i.e. with the electron beam parallel to the growth direction, the diffraction pattern shown in figure 1 was observed. This 12-fold ring of bright diffraction spots can be shown to originate from two sets of grains which are rotated at approximately 90° to each other. The multiple dark-field image in figure 3 shows that the intensity in alternate reflections originates in different grains of the film. The apparent 12-fold symmetry is therefore a convolution of the 4-fold symmetry of the substrate and the 3-fold symmetry of the <111> textured film. The two major orientation relations observed between the CoO and the zirconia substrate were therefore: <111> CoO // [001] zirconia and either {220} CoO // (100) zirconia, or {220} CoO // (010) zirconia. A small number of grains were observed with a slightly different orientation relation. Although the <111> CoO was still parallel to the [001] zirconia, the CoO grains were rotated about the <111> axis by a small amount ~8° so that the 220 planes in the CoO did not match up with the 200 planes in the zirconia.

The fainter, inner set of spots arise from double diffraction between the two CoO grains rotated by approximately 90°. A small departure of about 1° from exactly 90° is responsible for these spots not lying on a circle, but rather forming a hexagonal shape around the transmitted beam. The double diffraction routes for the strongest reflections are shown schematically in figure 2. The amount of the misorientation can be determined most accurately by examination of the double diffraction spots.

The boundaries between the grains are inclined to the growth direction, and give rise to stacking-fault-like fringes in strong-beam images. Convergent beam diffraction patterns obtained from grains on either side of a set of fringes show the Kikuchi bands rotated by 90°. Convergent beam diffraction patterns obtained from a set of fringes (figure 4) showed, in addition to the 12 expected 220 discs, lens shaped regions of intensity. This intensity occurred not at the position of any reflections due to double diffraction shown in figure 1, but in the region where such discs would overlap. Only six of the twelve possible overlap regions showed any intensity however.

References

1. See for example, papers in Mater. Res. Soc. Symp. Proc. **191** (1990)
2. Y. K. Simpson et al, J. Am. Cer. Soc. **70**, C149-151 (1987)
3. P. G. Kotula and C. B. Carter, Mat. Res. Soc. Symp. Proc. **285** (1992)

4. This research is supported by the DoE under grant No DE-FG02-92ER45465 and NSF under grant No. DMR-8901218, and in part by the DoE under contract DE-AC05-84OR21400 with Martin Marietta Energy Systems, Inc. & through the SHaRE Program under contract DE-AC05-76OR00033 with ORAU.

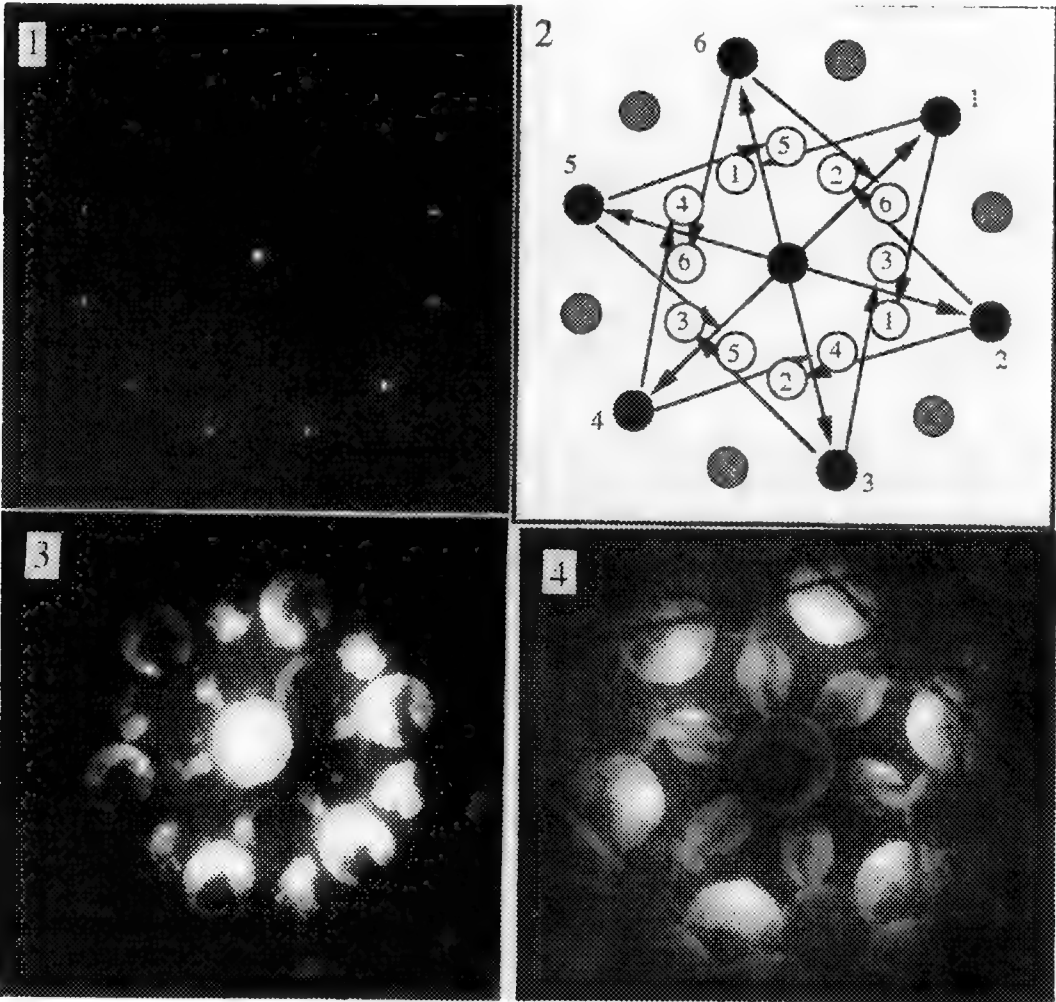


FIG. 1.—Selected area electron diffraction pattern from CoO thin film, oriented with the electron beam parallel to the growth direction.
 FIG. 2.—Schematic diagram of fig 1. Black and gray filled circles are 220 spots from different grains, open circles are double diffraction spots. Numbers denote double diffraction routes assuming black spots are on top.
 FIG. 3.—Multiple dark-field image of the film, showing alternate 220 spot intensity arising from different areas of specimen.
 FIG. 4.—Convergent beam diffraction pattern from overlapping grains of different orientation.

IN SITU CRYSTALLIZATION OF SILICATE GLASS FILMS DEPOSITED ON α -Al₂O₃

Michael P. Mallamaci, James Bentley,* and C. Barry Carter

Department of Chemical Engineering and Materials Science, University of Minnesota,
421 Washington Avenue SE, Minneapolis, MN 55455-0132

*Metals and Ceramics Division, Oak Ridge National Laboratory, P. O. Box 2008,
Oak Ridge, TN 37831-6376

Polycrystalline alumina compacts often contain amorphous films at grain boundaries and triple junctions as a result of the liquid-phase sintering process. An anorthite-based composition (CaAl₂Si₂O₈) is typical of the glassy phases observed in these materials. With appropriate heat treatments the glass phase can be crystallized, which can influence the properties of the bulk material.¹ Deposition of a thin film of glass on single-crystal α -Al₂O₃ is being used to study the influence of specific crystallographic orientations on the alumina-glass interface properties. Vapor-phase growth of glass on different orientations of α -Al₂O₃ has been accomplished previously and, through subsequent thermal treatments, the alumina was shown to facet preferentially when in contact with a glassy phase.² In the present study, calcium-aluminosilicate glass films were grown on single-crystal α -Al₂O₃ at relatively low substrate temperatures (<950°C) by pulsed-laser deposition. These films were then heated in the electron microscope to determine the effect of α -Al₂O₃ crystallography on crystallization of calcium-aluminosilicate glasses.

Single-crystal (0001) α -Al₂O₃ substrates in pre-thinned form were used for the initial film depositions. The samples were then observed in plan-view to characterize the as-deposited film microstructure; no post-deposition thinning was required. Pre-thinned substrates were prepared with a procedure described elsewhere.^{3,4} Film deposition was achieved using a KrF excimer laser operating at 10 Hz with a 200mJ pulse energy. The laser was focused on a rotating target inside a vacuum chamber, where an oxygen partial pressure of 5 mTorr was maintained during deposition. The substrates were mounted on a resistively-heated block, and a series of substrate temperatures ranging from ambient to 950°C was chosen to determine any effect of substrate temperature on the film composition or structure. An anorthite-based glass target was used, and the deposited film was amorphous at each substrate temperature. Film compositions were determined by energy-dispersive x-ray spectrometry (EDS) in a Philips CM12 analytical electron microscope (AEM) with a procedure to remove the substrate contribution that is described elsewhere.⁴ The composition of the glass target was also determined in the AEM. The composition of the film was nearest to that of the glass target for depositions at ambient temperature; depositions at higher substrate temperatures resulted in a systematic decrease in the silicon content. However, no significant differences in the film microstructures were detected. The typical structure, shown in Figure 1, consisted of a uniform amorphous film, except for the presence of spheroidal particulates that have a range of compositions but are generally enriched in calcium relative to the surrounding film.

Following EDS of each glass film, crystallization experiments were performed in the electron microscope with the specimen mounted in a Gatan 628 single-tilt heating holder. The crystallization process was video recorded with a Gatan 673 camera. Four glass films were crystallized in this manner, corresponding to substrate temperatures during deposition of 23, 200, 500, and 950°C. Early experiments indicated no distinct changes below 1000°C; subsequently, specimens were heated rapidly to 1000°C. During this initial heating, the edges of some particulates became more diffuse, while the edges of others remained well-defined. This behavior may be associated with the compositional variations of the particulates. After each specimen was held at 1000°C for 10-20 minutes, the temperature was increased in 50° increments and observed at each interval for at least 5 min. The glass films deposited at 23, 200, and 500°C crystallized between 1150 and 1200°C. Nucleation and growth began in featureless regions of the film, presumably at the glass/substrate interface, and not at the spheroidal particulates. After crystallization, the film deposited at 23°C was polycrystalline, as shown

in Figure 2, and had a smaller grain size than the crystallized films which had been deposited at 200 and 500°C. The microstructures of the latter two films were similar and consisted of much larger crystallites having special orientation relationships with the substrate, as shown in Figure 3. These larger crystallites often contained low-angle grain boundaries. For the films grown at 23, 200, and 500°C, the crystallization product was single-phase, with a composition corresponding to anorthite based on the calcium-to-silicon ratio obtained by EDS. The glass film deposited at 950°C crystallized at 1125°C and consisted of at least two major phases (Figure 4), both different from the phase in lower-temperature films. This glass film had a significantly lower silicon content than the lower-temperature films ($\text{Ca/Si} \gg 0.5$, as opposed to $\text{Ca/Si} \leq 0.5$ for all others), which presumably affected the crystallization product. Work on identifying all of the crystallized phases from electron diffraction patterns is in progress.⁵

1. C. A. Powell-Doğan and A. H. Heuer, *J. Am. Cer. Soc.* **73**, 3684 (1990).
2. Y. K. Simpson and C. B. Carter, *J. Am. Cer. Soc.* **73**, 2391 (1990).
3. D. W. Susnitzky and C. B. Carter, *J. Am. Cer. Soc.* **75**, 2463 (1992).
4. M. P. Mallamaci et al., "Microanalysis of Silicate Glass Films Grown on $\alpha\text{-Al}_2\text{O}_3$ by Pulsed-Laser Deposition," these proceedings.
5. Research supported by the U. S. Department of Energy under Grant No. DE-FG02-92ER45465 and partially supported by the Division of Materials Sciences, U. S. Department of Energy, under contract DE-AC05-84OR21400 with Martin Marietta Energy Systems, Inc., and through the SHaRE Program under contract DE-AC05-76OR00033 with Oak Ridge Associated Universities. MPM is also with the Department of Materials Science and Engineering, Cornell University, Ithaca, NY.

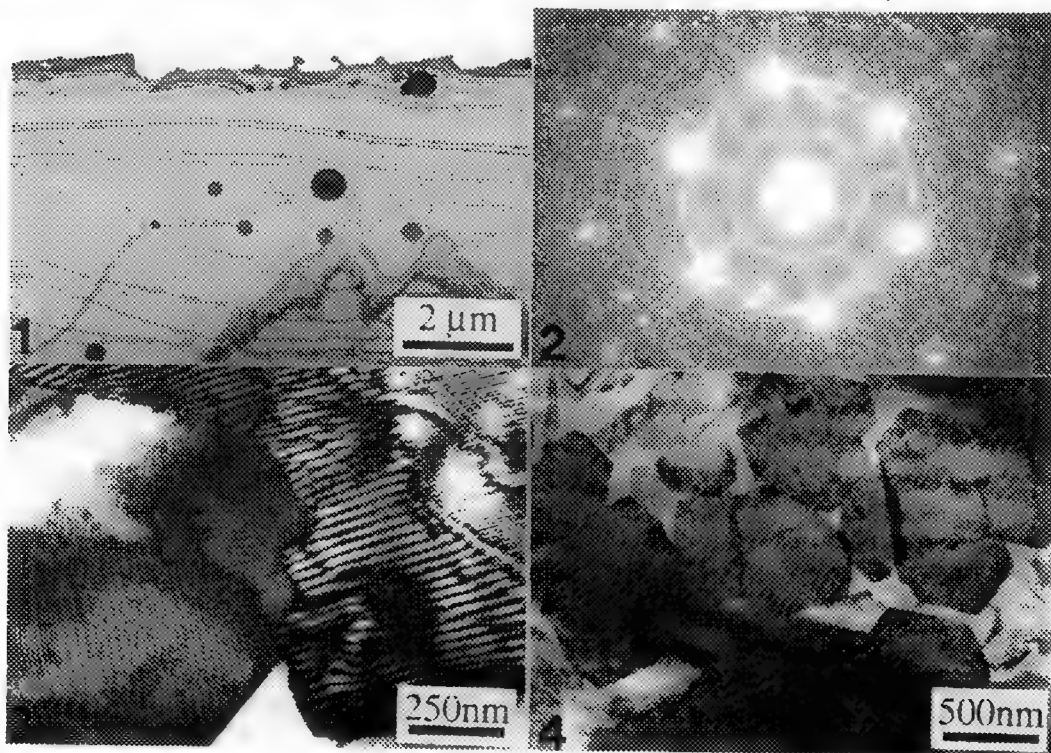


FIG. 1 Bright-field image of a typical as-deposited glass film on (0001) $\alpha\text{-Al}_2\text{O}_3$.

FIG. 2 Selected-area diffraction pattern from the polycrystalline film crystallized at 1200°C from the glass film deposited at 23°C.

FIG. 3 Bright-field image of crystallites grown from the glass film deposited at 200°C.

FIG. 4 Bright-field image of crystallites grown from the glass film deposited at 950°C.

DOMAIN STRUCTURES IN DONOR-DOPED BARIUM TITANATE CERAMICS

S. K. Sundaram, Yolande Berta, and Robert F. Speyer,

School of Materials Science and Engineering, Georgia Institute of Technology, Atlanta, GA 30332

The effects of cooling rate and soaking time on the positive temperature coefficient of resistivity (PTCR) of donor-doped barium titanate ceramics have been well studied.^{1,2} Daniels and Wernicke³ presented a model which predicted that an increasing grain boundary thickness led to a continuous transition from a PTC thermistor to an intergranular capacitor. Common in grain boundary potential layer models⁴ of PTC behavior, is the assumption that the polarization vector is parallel to the domain boundary (180° domains). Haanstra and Ihrig⁵ observed only 90° domains (perpendicular polarization vectors in neighboring domains) in these materials. They did not observe any intergranular second phase in their microstructures, which had grain boundary thicknesses of 2 - 10 nm. They discarded the potential barrier model proposed by Hoffmann⁶ in which a 500 nm thick second phase layer (possibly Ti-rich) was assumed to be present at the grain boundary. In the present investigation, the domain structures and grain boundary thicknesses in BaTiO₃ PTC thermistor, and the intergranular capacitor specimens were studied.

0.3 atom% Sb₂O₃-doped BaTiO₃ (containing 0.01 mole of excess TiO₂) was prepared by a conventional solid state reaction at 1100°C for 4 hours, cold pressed at 350 MPa, and sintered at 1350°C for 0, 20, and 40 hrs. A heating and cooling rate of 5°C/min was maintained for all specimens. DC resistance was measured using a resistance bridge (GR 1666). In-Ga alloy was used as an electrode. TEM samples were cut into 3 mm discs, thinned mechanically to 120 μm, dimpled to 40 μm, and then Ar ion milled to electron transparency using a liquid nitrogen cold stage.

Figure 1 shows the effect of temperature on DC resistivity with increasing soaking time at the sintering temperature. The specimen soaked for 0 hr displays a 4 orders of magnitude PTC jump, which decreases to 3 orders in the specimen soaked for 20 hrs. After 40 hrs of soaking, the PTC jump is insignificant. The room temperature resistivity increased with increasing soaking time implying a PTC thermistor to intergranular capacitor transition. Selected area diffraction (SAD) as well as dark field microscopy (Figure 2) showed that the grain boundary phase was crystalline. Electron microprobe analysis (EMPA-WDS) confirmed the presence of a Ti-rich second phase (suggested by Hoffmann) in coarser grain boundary regions. The thicknesses of these crystalline grain boundaries ranged from 100 to 600 nm in the PTC thermistor (soaked for 20 hours), and 577 to 840 nm, in the intergranular capacitor (soaked for 40 hours). Examples are shown in Figure 3.

Figures 4 (a) and (b) show domain structures in the PTC thermistor, and the intergranular capacitor, respectively. The pendelloesung fringes in the domain walls⁵, arising from changes in the crystal periodicity, indicate that these were 90° domains. 180° domains were not observed in these specimens.

In agreement with reference 5, 90° domains were observed in this work. However, in contrast to Haanstra and Ihrig, the observations herein are in agreement with references 3 and 6, wherein PTC thermistor behavior was observed with ~500nm thick grain boundaries. It is therefore suggested that an improved model based on these latter references be developed.

References:

1. W. Heywang, *Solid-State Electron.*, (1961) **3**, 51.
2. S. K. Sundaram, *J. Phys. D: Appl. Phys.* (1990) **23**, 103.

3. J. Daniels, and R. Wernicke, *Philips Res. Repts*, (1976)**31**, 544.
4. H. Ihrig in *Advances in Ceramics*, Volume 7, (1981), The American Ceramic Society, 117.
5. H. B. Haanstra, and H. Ihrig, *J. Amer. Cer. Soc.*, (1980)**63**(5-6), 288.
6. B. Hoffmann, *J. Appl. Phys.*, (1979)**50**(2), 1156.

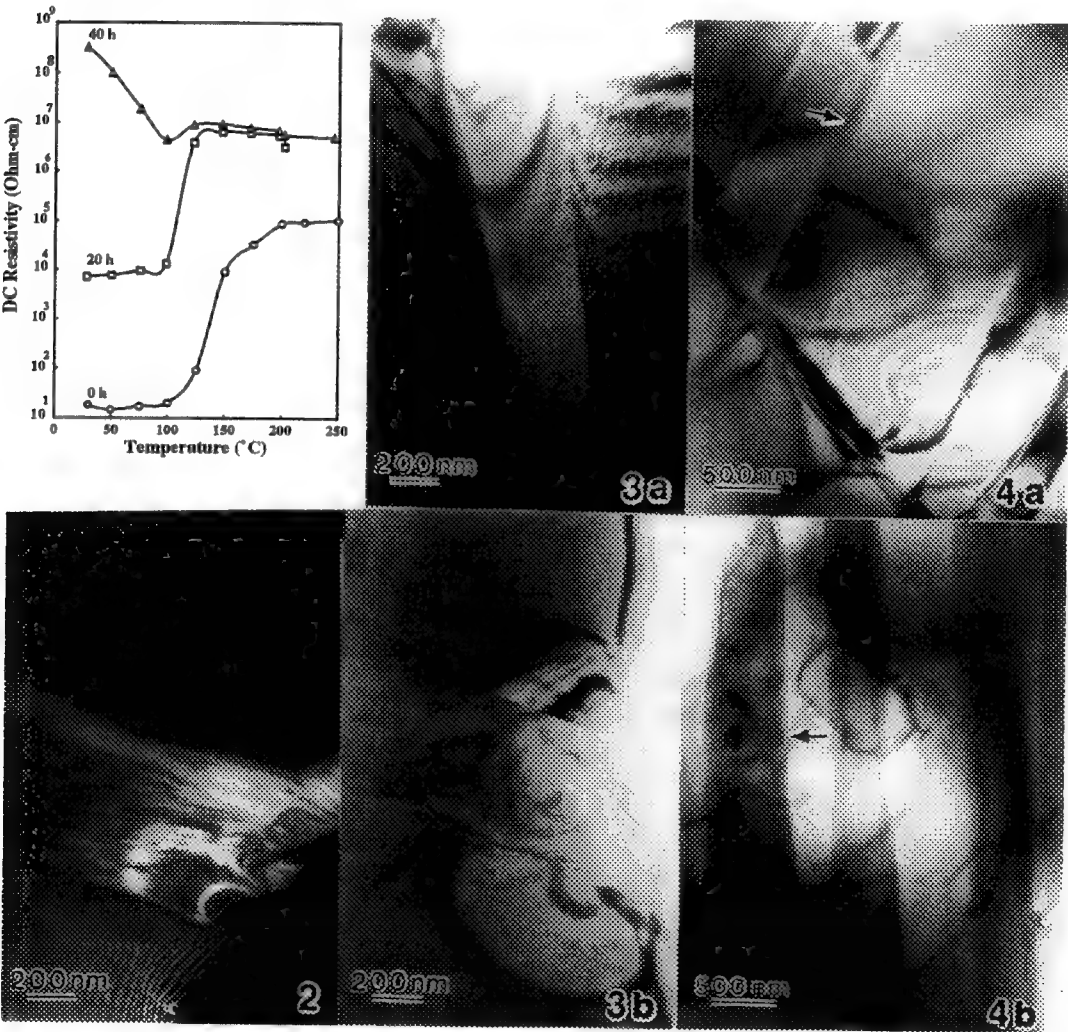


Figure 1: DC resistivity as a function of temperature showing PTC thermistor to intergranular capacitor transition with increasing soaking time. Above the Curie temperature (~120°C), all specimens demonstrated standard negative temperature coefficient characteristics.

Figure 2: Dark field TEM micrograph of crystalline grain boundary of a PTC thermistor.

Figure 3: Typical grain boundaries in (a) a PTC thermistor (thickness ~ 350 nm), and (b) an intergranular capacitor (thickness ~ 600 nm) .

Figure 4: 90° domains, as implied by marked pendelloesung fringes in (a) a PTC thermistor, and (b) an intergranular capacitor.

TEM CHARACTERIZATION OF SYNTHETIC HILLEBRANDITE: STRUCTURE, MICROSTRUCTURE, AND DEHYDRATION

Y. J. Kim and W. M. Kriven

Department of Materials Science and Engineering, University of Illinois at Urbana-Champaign, Urbana, IL 61801

Hillebrandite ($\text{Ca}_2\text{SiO}_4 \cdot \text{H}_2\text{O}$) occurs in nature as a white, fibrous mineral. Synthetic hillebrandite was prepared hydrothermally from calcia and silica.¹ On heating, hillebrandite dehydrated to $\beta\text{-Ca}_2\text{SiO}_4$ which is stable at room temperature. The crystal structure, microstructures and the dehydration mechanism of the synthetic hillebrandite prepared by Ishida *et al.*¹ were investigated by conventional TEM, HREM, and *in situ* hot-stage TEM.

Most hillebrandite fibers showed their fiber axis to be parallel to the b axis and tended to lie on $\{001\}$ cleavage planes. SADP's frequently displayed continuous streaking, and corresponding dark field images revealed stacking disorders perpendicular to the fiber axis (Fig. 1). The observed $[001]$ SADP (Fig. 2) was very different from the expected $[001]$ SADP based on published XRD data² (space group, $P2_1/a$). For all $hk0$ reflections, (i) if $k = \text{odd}$, no individual spots are shown but weak continuous streaking exists, (ii) if $k = 2$, reflections of $h = \text{even}$ are extinct, and (iii) if $k = 4$, reflections of $h = \text{odd}$ are extinct. The morphology, stacking disorders and extinction conditions of $\{hk0\}$ reflections of hillebrandite resembled those of the mineral wollastonite (CaSiO_3)³. As in the case of wollastonite, periodic (100) faults with a displacement vector $1/2 b$, which separate blocks consisting of one or several units of basic hillebrandite are proposed to be the major origin of the streaking and systematic absences. A HREM image (Fig. 3) suggested that the basic hillebrandite unit may be triclinic ($d \approx 8.3 \text{ \AA}$) rather than monoclinic. *In situ* TEM heating at 700°C for an hour resulted in dehydration of some hillebrandite fibers. No significant changes in fiber morphology occurred by dehydration, except for lateral shrinkage and occasional bending of fibers (Fig. 4A). SADP's of the dehydrated fiber (Fig. 4B) indicated a possible structural relationship between hillebrandite (hil) and $\beta\text{-Ca}_2\text{SiO}_4$ (β) to be a_{hil}/c_β such that b_{hil}/b_β .

References

1. H. Ishida *et al.*, J. Am. Ceram. Soc. (1992) 75, 2427.
2. L. Heller, Mineral. Mag. (1953) 30, 150.
3. H.-R. Wenk *et al.*, *Electron Microscopy in Mineralogy* (1976) 324.
4. This research was supported by the Center for Science and Technology of Advanced Cement-Based Materials at the University of Illinois at Urbana-Champaign.

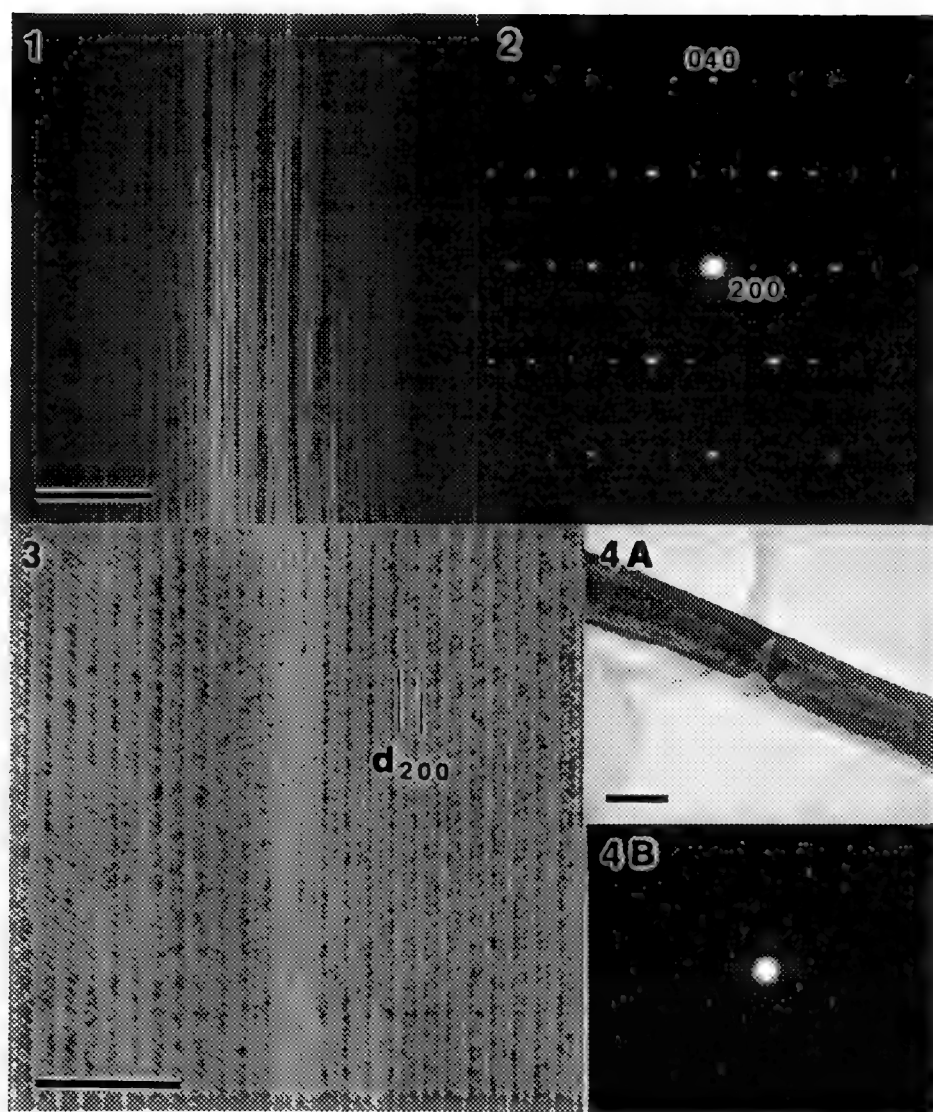


FIG. 1. DF image of a hillebrandite fiber. Note the variation of the stack widths and their contrast changes across the stacking. Bar = $0.1\ \mu\text{m}$.

FIG. 2. The observed [001] SADP of a hillebrandite fiber.

FIG. 3. High-resolution image in the [001] orientation. Note the distinct (200) planes ($d \approx 8.3\ \text{\AA}$) lying parallel to the fiber axis. Bar = $5\ \text{nm}$.

FIG. 4. A dehydrated ($\beta\text{-Ca}_2\text{SiO}_4$) fiber (A) and its [100] SADP (B). Bar = $0.1\ \mu\text{m}$.

ELECTRON MICROSCOPY OF CERAMIC SUPERCONDUCTORS

M. Grant Norton* and C. Barry Carter**

* Mechanical and Materials Engineering, Washington State University, Pullman WA 99164

** Chemical Engineering and Materials Science, University of Minnesota, Minneapolis MN 55455

The microstructure of ceramic superconductors plays a crucial role in the transport properties of these materials. For example, it has been shown that high-angle grain boundaries can act as weak links¹ and atomic scale defects can act as pinning centers.² The nature and spatial distribution of such defects is related to the way in which the material is processed. Transmission electron microscopy (TEM) is an essential technique for understanding the relationship between microstructure, processing, and properties and for defect characterization. The advantage of TEM is that it is possible to combine various imaging modes with electron diffraction and other analytical techniques such as x-ray energy dispersive spectroscopy in order to obtain both structural and chemical information.

Early measurements of critical current densities (J_c) across individual tilt grain boundaries in $\text{YBa}_2\text{Cu}_3\text{O}_{7-\delta}$ (YBCO) thin films demonstrated that J_c decreased with increasing misorientation angle.¹ More recently, however, it has been observed that this phenomenon may not be the case for all high-angle grain boundaries.^{3,4} Examination of high-angle tilt grain boundaries in YBCO thin films using high-resolution electron microscopy showed that for boundaries that had very similar misorientation angles, the microstructure of the boundaries could be quite different.⁵ Some of the boundaries are structured and free from extraneous phases, whilst others show considerable disorder at the boundary region. Structural differences have also been observed in the same grain boundary depending on the local boundary orientation. In order to correlate grain boundary structure and properties, it is necessary to know not just the boundary tilt angle but also the atomic structure of the boundary including the boundary plane, the presence of interfacial strain, and the local chemical composition. Thus in any study of the behavior of grain boundaries in YBCO, the structure of each individual boundary must be related to its physical properties, rather than assuming that all boundaries of the same misorientation have the same structure.

The highest J_c 's have been obtained in epitaxial thin films of YBCO. Understanding and controlling the introduction of defects into these films requires studies of film nucleation and the early stages of the growth process.^{6,7} TEM analysis is an essential component of these studies and when it is used in combination with other characterization techniques provides a powerful method for understanding film growth and microstructure development. A recent example of this approach has been in a study of the growth of barium bismuthate films on MgO using molecular beam epitaxy. Examination of the initial stages of growth revealed that a disordered BaO layer must form before the Bi begins to stick further growth results in the formation of BaBi_2O_y .⁸ This phase has been used to nucleate high quality epitaxial $\text{Ba}_{1-x}\text{K}_x\text{BiO}_3$ films and has also been used as a barrier layer in the fabrication of superconductor-insulator-superconductor heterostructures. Examination of heterostructures and superlattices is an area where electron microscopy is invaluable. A recent example is the use of Z-contrast scanning transmission electron microscopy in the study of YBCO/PrBCO superlattices.⁹

In the Ti-Ca-Ba-Cu-O and Bi-Ca-Sr-Cu-O systems several closely related polytypes, each having a different superconducting transition temperature, exist and this makes fabrication of single phase material very difficult. Mixed phase (Ti-2223 and Ti-2122) films grown on SrTiO_3 by electron beam evaporation have recently been examined using TEM.¹⁰ The films, which were c-axis oriented, consisted of a layered microstructure with large coherent domains of the Ti-2122 phase and somewhat smaller domains of Ti-2223 in different grains. This syntactic growth behavior on a microstructural basis is similar to that found in large crystals where occasionally even a larger and/or

different combination of phases are observed. These complexities make the establishment of relationships between microstructure and processing difficult for this class of superconductor and highlight the important role that TEM can play in these studies.

In this presentation the role of electron microscopy in the study of ceramic superconductors will be reviewed and future challenges examined. Some of these challenges in the area of grain boundaries and phase boundaries are listed in Table I. Particular attention will be drawn to relationships between the processing of these materials, in various forms, and their microstructure.

References

1. D. Dimos, *et al.*, Phys. Rev. Letters 61, 1653 (1988).
2. J.L. Vargas and D.C. Larbalestier, Appl. Phys. Letters 60, 1741 (1992).
3. S.E. Babcock, *et al.*, Nature, 347, 167 (1990).
4. S.-W. Chan, *et al.*, in: High T_c Superconducting Thin Films: Processing, Characterization and Applications, AIP Conference Proceedings 200, 172 (1990).
5. S. McKernan, M.G. Norton, and C.B. Carter, J. Mater. Res. 7, 1052 (1991).
6. M.G. Norton and C.B. Carter, J. Cryst. Growth 110, 641 (1991).
7. M.G. Norton and C.B. Carter, J. Mater. Res. (1993 submitted for publication).
8. M.G. Norton, *et al.*, Physica C 205, 347 (1993).
9. S.J. Pennycook, *et al.*, Phys. Rev. Letters 67, 765 (1991).
10. B. Morosin, *et al.*, J. Mater. Res. (1993 in press).

Table I. Challenges for transmission electron microscopy in the study of high- T_c superconductors.

Feature	Challenges for TEM
<u>Grain Boundaries</u> Examples: low angle high angle grain boundary films boundary morphology	Determination of the atomic structure and chemical composition of the grain boundary. Relationship between J_c and microstructure for individual boundaries. Relating grain boundary structure to processing conditions.
<u>Phase Boundaries</u> Examples: heterojunctions metal/ceramic interfaces nucleation of films multilayers "polymorphs"	Establishing the relationship between microstructure and processing for thin films and multilayers. Determination of the mechanism of film growth and the introduction of defects. Examination of interdiffusion and reactions.

FLUX-PINNING-RELATED DEFECT STRUCTURES IN MELT-PROCESSED $\text{YBa}_2\text{Cu}_3\text{O}_{7-x}$

Z. L. Wang, R. Kontra*, A. Goyal, D. M. Kroeger and L.F. Allard

Metals and Ceramics Division, Oak Ridge National Laboratory, P.O. Box 2008, Oak Ridge, TN 37831;
* presently at IBM, D324, Bldg. 967-2, Essex Jct., VT 05402

Previous studies of $\text{Y}_2\text{BaCuO}_5/\text{YBa}_2\text{Cu}_3\text{O}_{7-\delta}$ ($\text{Y}_{211}/\text{Y}_{123}$) interfaces in melt-processed and quench-melt-growth processed $\text{YBa}_2\text{Cu}_3\text{O}_{7-\delta}$ using high resolution transmission electron microscopy (HRTEM) and energy dispersive X-ray spectroscopy (EDS) have revealed a high local density of stacking faults in Y_{123} , near the $\text{Y}_{211}/\text{Y}_{123}$ interfaces.¹ Calculations made using simple energy considerations suggested that these stacking faults may act as effective flux-pinner and may explain the observations of increased J_c with increasing volume fraction of Y_{211} . The present paper is intended to determine the atomic structures of the observed defects. HRTEM imaging was performed using a Philips CM30 (300 kV) TEM with a point-to-point image resolution of 2.3 Å. Nano-probe EDS analysis was performed using a Philips EM400 TEM/STEM (100 kV) equipped with a field emission gun (FEG), which generated an electron probe of less than 20 Å in diameter.

Stacking faults produced by excess single Cu-O layers: Figure 1 shows a HRTEM image of a Y_{123} film viewed along [100] (or [010]). The Y and Ba atoms are resolved and show dark contrast in the image. For Y_{123} , since the locations of the oxygen atoms in the unit cell are not identical when the structure is projected along [100] or [010] there are two possible stacking faults that can be produced by introducing an excess Cu-O layer in the a-b plane. The first has glide (G) plane symmetry corresponding to a displacement of $1/6[031]$ when viewed along [100], and the other has mirror (M) symmetry produced by a displacement of $1/6[301]$ when viewed along [010]. The simulated images of these two types of stacking faults are inserted in the figure. The Ba-Ba separation across the stacking faults is about 6.2 Å, in good agreement with the expected value from the Y_{123} structural model. The EDS and EELS analyses also support the proposed chemistry of the stacking faults.

Stacking faults produced by excess double Y-O and Cu-O layers: Figure 2 shows a HRTEM image of a Y_{123} containing some stacking faults without any displacement along the a- (or b-) axis. The image contrast near these stacking faults is different from that of the stacking faults produced by an excess single Cu-O layer having mirror-symmetry. The simulated images based on a perfect Y_{224} structure show reasonable agreement with the observed image, suggesting that the stacking faults are produced by the introduction of double Y-O and Cu-O layers. The presence of Y rather than Ba was confirmed by EDS nano-probe compositional analysis on and off the stacking faults. The Ba-Ba atomic column separation across the two sides of the stacking fault is measured as being about 8 Å, significantly larger than that for a stacking fault produced by excess single Cu-O layer and is in good agreement with the expected value based on the Y_{224} structure. This type of stacking fault is usually observed near the Y_{211} particles, in agreement with the EDS results showing Y enrichment and Ba depletion near the $\text{Y}_{211}/\text{Y}_{123}$ interfaces.

Figure 3 shows a HRTEM observation of stacking faults and the associated dislocations. Stacking faults 1 and 2 display a shift along $1/6[032]$ and are produced by the insertion of double Cu-O and Y (or Ba)-O layers. However, the observed b/2 shift did not match the structure of double Y-O and Cu-O stacking faults illustrated in figure 2. Stacking faults 3 and 4 show a displacement of $1/6[302]$, but it is not clear if Y or Ba is involved in the faulted layer.

In conclusion, stacking faults which lie parallel to the (001) basal plane are observed near the $\text{Y}_{211}/\text{Y}_{123}$ interfaces in Y_{123} . These stacking faults are produced by either excess single Cu-O layers or double Cu-O and Y-O layers. Y enrichment and Ba depletion were observed near the $\text{Y}_{211}/\text{Y}_{123}$ interface, and this effect is consistent with dissolution of trapped Y_{211} . Such diffusion effects and stress due to lattice mismatch at $\text{Y}_{211}/\text{Y}_{123}$ interfaces may be the mechanisms for generating stacking faults around the Y_{211} particles in the Y_{123} matrix. Finally, a new type of defect with displacement vector $1/6[032]$ or $1/6[302]$ was also observed.²

1. Wang, Z.L., Goyal, A. and Kroeger, D.M., Phys. Rev. B, 1993, in press; Wang, Z.L., Goyal, A., Kroeger, D.M. and Armstrong, T., in Layered Superconductors: Fabrication, Properties and Applications, D.T. Shaw, C.C. Tsuei, T.R. Schneider and Y. Shiohara eds., Proc. of MRS, 1992, 275, 181.
2. Research was supported by the U. S. Department of Energy, Office of Advanced Utility Concepts - Superconducting Technology Program, under contract DE-AC05-84OR21400 with Martin Marietta Energy Systems, Inc.

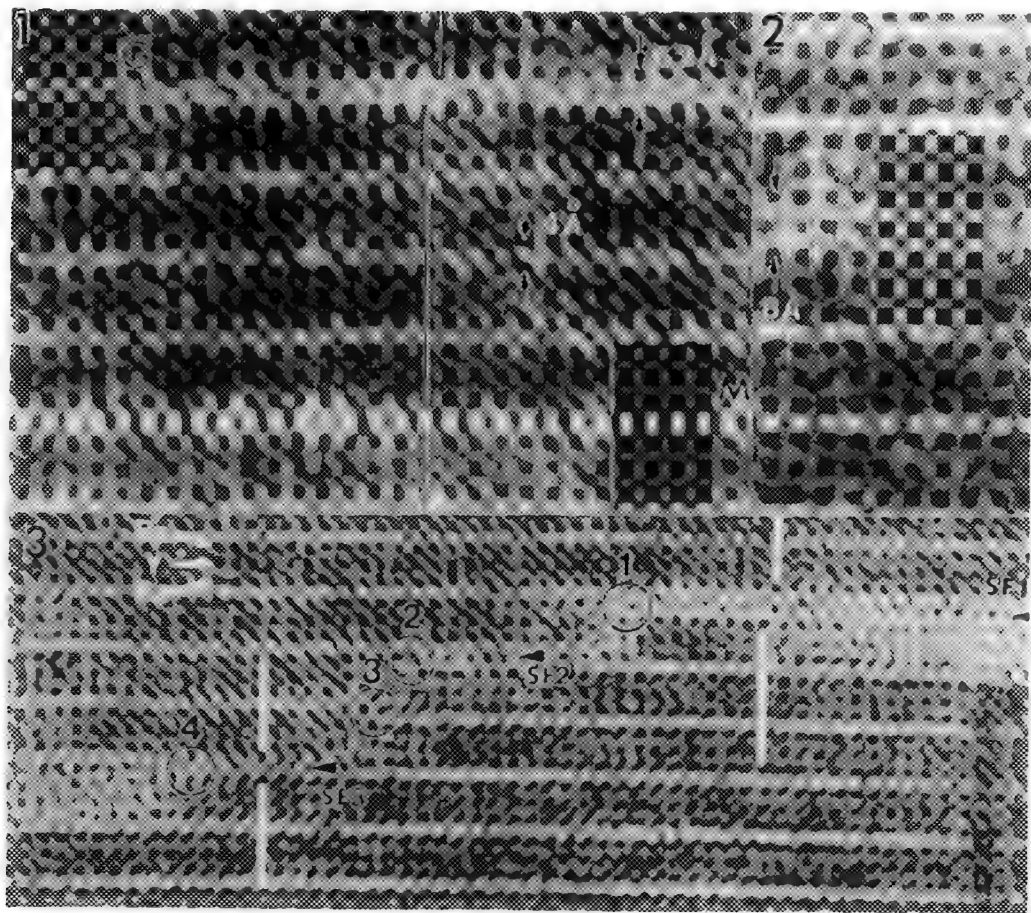


FIG. 1.--HRTEM image of stacking faults with glide plane (G)- and mirror (M)-symmetry produced by excess single Cu-O layers. Inserts are the simulated images for two models. Simulations were performed for following parameters: objective lens spherical aberration coefficient $C_s = 2.0$ mm, accelerating voltage 300 kV, crystal thickness 27 Å, defocus -560 Å, objective aperture radius 0.7 Å^{-1} , divergence of semi-angle 1.5 mrad, and spread of defocus 100 Å.

FIG. 2.--HRTEM image of stacking faults produced by excess double Y-O and Cu-O layers. Ba-Ba distance across stacking fault is considerably larger than that of stacking fault produced by excess single Cu-O layer in Y123, but agrees with expected value according to standard Y224 structure. Conditions for image simulations were same as those for figure 1.

FIG. 3.--HRTEM image of stacking faults and associated dislocations with displacements of $1/6[032]$ (labeled 1 and 2) and $1/6[302]$ (labeled 3 and 4).

THE INTERFACIAL STRUCTURE OF ORTHOGONALLY ORIENTED TWINS IN $\text{YBa}_2\text{Cu}_3\text{O}_7$

Yimei Zhu, M. Suenaga, and J. Taftø¹

Materials Science Division, Brookhaven National Laboratory, Upton, NY 11973

Interfaces such as the twin boundary and grain boundary in $\text{YBa}_2\text{Cu}_3\text{O}_{7-\delta}$ are thought to be important in reconciling the large discrepancy between the low critical-current density observed in bulk polycrystalline. Recently, we studied another type of frequently encountered interface, i.e., the interface between the orthogonally orientated (110) and (-110) twins. In the vicinity of the interface, the crystal has a characteristic geometry because of additional constraints due to the impediment and the local orientational difference. The impinging twins usually have a wedge shape (Fig.1a), and when the wedge slope is large, the tip of the twin splits (Fig.1b). A HREM image of a tapered twin is shown in Fig.2. Four twin variants give rise to five boundaries. Boundaries between IV-III, III-IV, IV-II, and II-IV are twin boundaries, while II-III, which has no apparent structure, is the interface of the orthogonal twins. If there is no constraint, the orientation of II and III should be equivalent (Fig.3a and 3b); however, we observed that the lattice in II does not align with that in III.

We analyzed the local crystal orientation by means of an optical analogue of moiré pattern on HREM images, and by electron diffraction observing the change of the splitting of the (hh0) Bragg spots while moving the electron beam from II to III. We found that the crystal lattice of the impinging set of twins rotates around the c-axis when they confront the orthogonally oriented twins. Every second one of the impinging twins is pointed, but does not taper off to zero width, yielding a small-angle grain boundary ($\sim 2^\circ$); the other twin forms a coherent boundary with a twin belonging to the orthogonal set (Fig.3c and 3d). Thus, the interface of the orthogonally orientated twins comprises an alternation of twin boundaries and grain boundaries. The tapering off of one set of the impinging twins can be attributed to the higher energy of the grain boundary. We also found that there is a limiting wedge-angle ($\sim 15^\circ$) for the tapered twins; if this angle is exceeded, the tip of the twin splits. Splitting might begin at the interface when the resolved shear stress reaches a critical value, simultaneously generating an additional twin variant I' having twinning orientation with twin II and twin III' (Fig.4). When the new twin variant grows away from the interface, it reduces the wedge angle of the tapered twin at the expense of increasing the length of the twin boundary. The equilibrium of the constraint at the twin tip, and the interfacial energy of twin boundary, as well as the grain boundary determines the splitting and the final shape of the twin tip, and hence, the structure of the interface where the (110) and (-110) twins meet. The shape of the tapered twin was calculated based on the observed twinning dislocations and twinning steps in $\text{YBa}_2\text{Cu}_3\text{O}_{7-\delta}$,² and shows good agreement with our observations.³

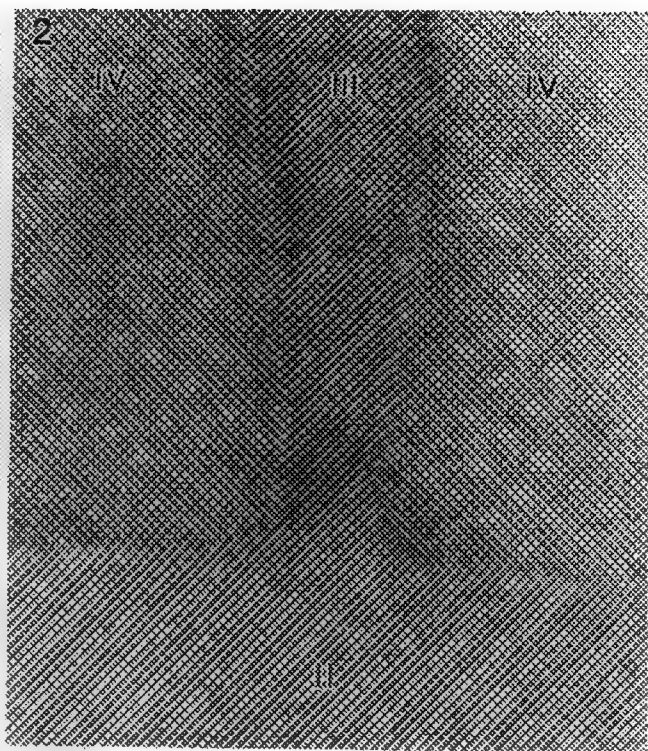
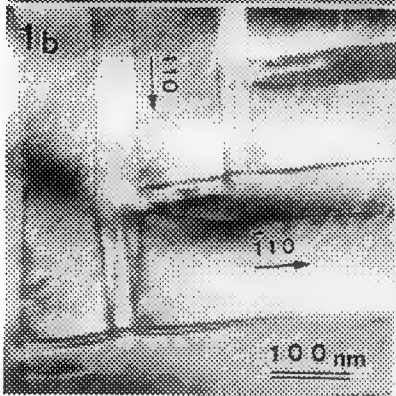
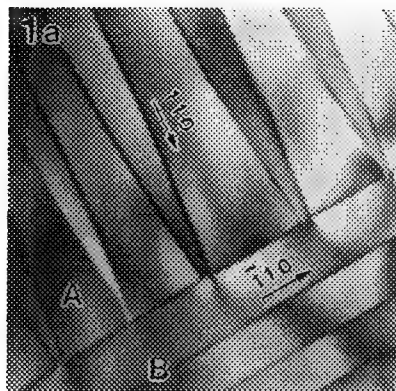
Reference

1. Visiting scientist, Department of Physics, University of Oslo, Blindern, Norway
2. Y.Zhu, M.Suenaga, *Phil.Mag.A*, **66** (1992) 457, Y.Zhu, M.Suenaga, and J.Taftø, *Phil.Mag.A* (1993) in press
3. This research was supported by U.S. Department of Energy, Division of Materials Sciences, Office of Basic Energy Sciences under Contract No. DE-AC02-76CH00016.

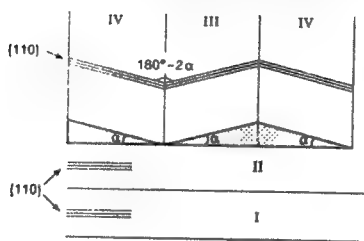
Fig.1 Typical bright-field images of two orthogonal sets of twins near the (001) projection. Note, the split twin tips (1b) has a similar wedge angle θ as those of unsplit ones (1a).

Fig.2 High-resolution image of a twin tip and the interface of the orthogonal twins.

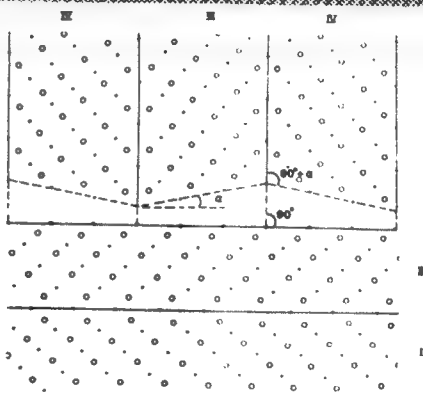
Fig.3a-3b Ideal crystallographic orientations of twin variants uninfluenced by constraint; neither IV-II nor III-II can have a twinning relationship. 3c-3d: Increasing the angular mismatch between III and II from α to 2α results in twinning of IV and II and a small-angle grain boundary between III-II. The triple lines represent (-110) planes and (110) planes. Fig.4 Sketch of the observed interface; TB-twin boundary, GB-grain boundary.



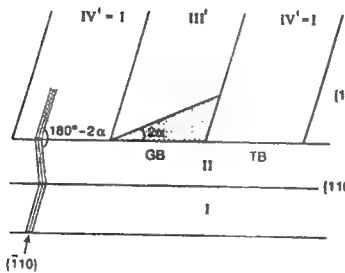
3a



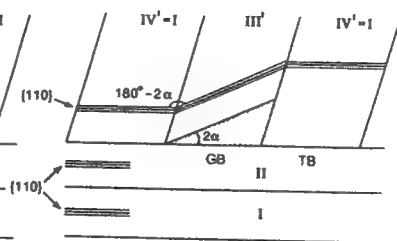
3b



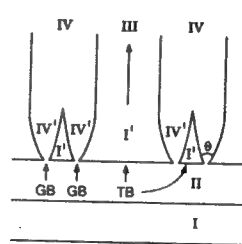
3c



3d



4



LOW- T_c PHASE FORMATION AT THE GRAIN BOUNDARIES AND ELECTROMAGNETIC GRANULARITY IN $(\text{Bi,Pb})_2\text{Sr}_2\text{Ca}_2\text{Cu}_3\text{O}_x$ SILVER-SHEATHED TAPES

Yi Feng, A. Umezawa, H. S. Edelman and D. C. Larbalestier

Applied Superconductivity Center, University of Wisconsin-Madison, Madison, WI 53706

High resolution transmission electron microscopy (HRTEM) was performed on progressively heat treated Ag-clad $(\text{Bi,Pb})_2\text{Sr}_2\text{Ca}_2\text{Cu}_3\text{O}_x$ (2223) tapes and was correlated with their transport critical current densities, DC magnetization and AC susceptibility. HRTEM reveals the presence of a small number of half layers of the low T_c $\text{Bi}_2\text{Sr}_2\text{CaCu}_2\text{O}_x$ (2212) phase clustered at the numerous (001) twist grain boundaries. This residual 2212 phase produces electromagnetic granularity in a temperature range around 77K and thus directly controls the critical current.

The Bi(Pb)-Sr-Ca-Cu-O (BSCCO) Ag-clad tapes with the stoichiometric 2:2:2:3 starting composition were prepared by a standard powder-in-tube method. Sample A was heat treated at 817°C for 5 hours only. Sample B was first heat treated at 817°C for 24 hours, and then heat treated for 100 hours at the same temperature after two intermediate pressings. Sample C was heat treated at 830°C for 72 hours, and then heat treated for additional 196 hours after one intermediate pressing. All heat treatments were done in a 7.5% O_2/Ar atmosphere. Electromagnetic measurements were performed on each sample (Details can be found in ref. 1). Thin longitudinal cross sections were ion milled at 4.5 KV on a liquid nitrogen cooled stage and then examined in a Hitachi HF-2000 and a Phillips EM20 ultra-twin.

Fig. 1 shows the temperature dependence of the real (χ') component of the AC susceptibility for the A, B and C samples. There is a small diamagnetic transition at about 109 K (in all three traces) and then a lower transition temperature (T') in the range from 80 to 105 K (in traces A and B only, corresponding to samples A and B). Similar features were observed in DC magnetic moment measurements using a SQUID magnetometer. Fig. 2 shows the T' values of these three samples against their transport current densities (J_c at 77K, 0T). It is evident that the J_c increases steeply as T' comes close to the 109 K superconducting transition of the 2223 phase. HRTEM images (Fig. 3) were taken from these samples with the incident beam normal to the [001] axis. The double Bi-O planes are particularly evident and permit layers having the 2212 lattice spacing $c/2 = 1.55$ nm to be easily distinguished from layers having the 2223 spacing $c/2 = 1.85$ nm. A strong tendency of the 2212 layers to cluster at the (001) twist boundaries was found in sample A, as shown in Fig. 3a (about ten 2212 half layers at the twist boundary). The frequency of 2212 that clusters at the twist boundaries was very much reduced for the longer time reacted sample B (Fig. 3b). In sample C, which was heat treated for the longest time, we have not found any 2212 phase at the (001) twist boundaries (Fig. 3c).

From the strong correlation between the electromagnetic properties and the microstructure shown above, we conclude that the changes in T_c and J_c are directly controlled by the presence of a small amount of the lower T_c 2212 phase which remains preferentially at the (001) twist boundaries of the 2223 phase. These residual 2212 layers require a long reaction time for their elimination and directly control the critical current while they are present.

References

1. A. Umezawa, Y. Feng, H. S. Edelman, Y. E. High, D. C. Larbalestier, Y. S. Sung, E. E. Hellstrom and S. Fleshler, *Physica C* 198 (1992) 261.
2. This work was supported by DARPA (N00014-J-4115) and EPRI (RP8009-05). We thank E.E. Hellstrom for helpful discussions.

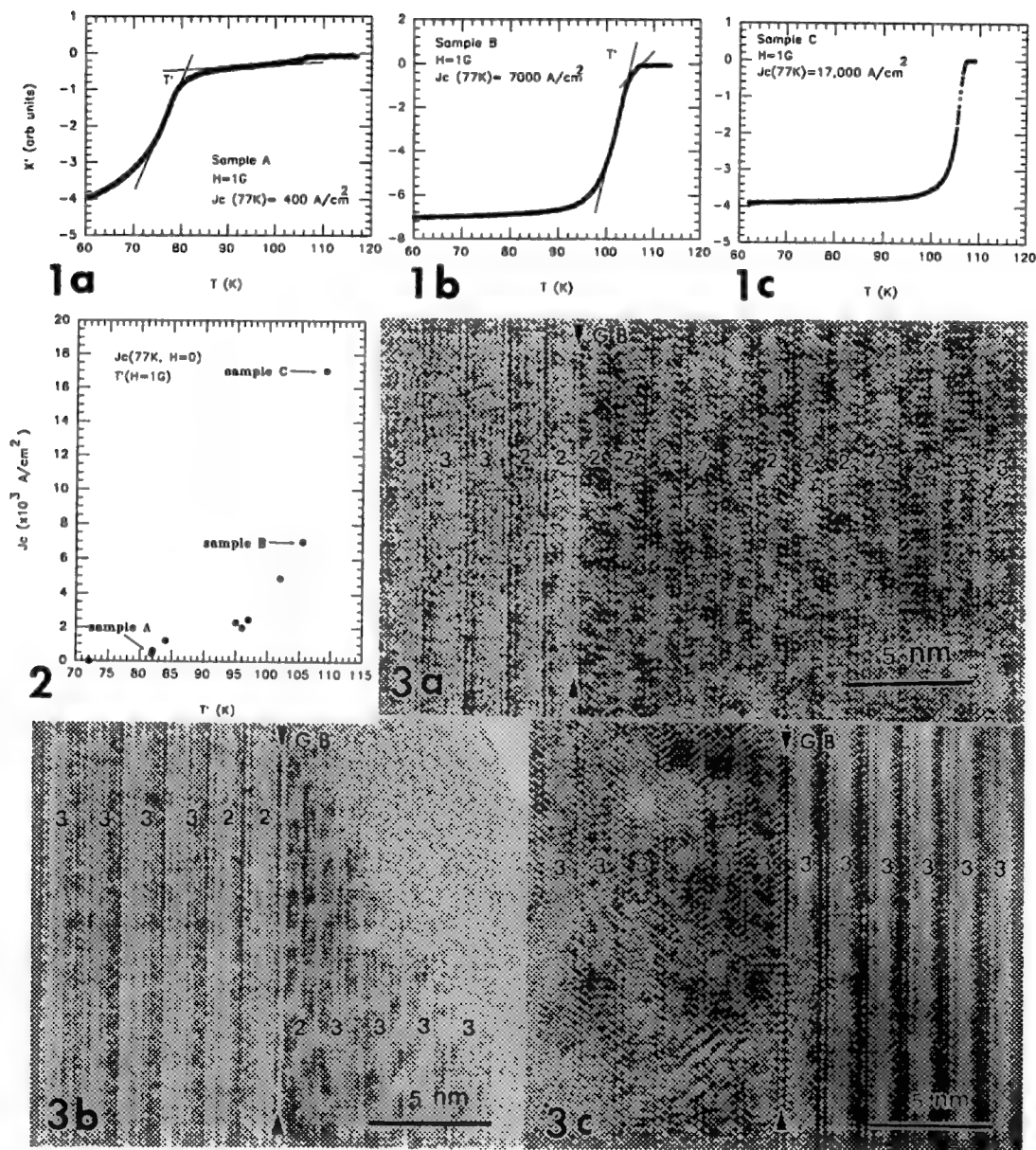


FIG. 1. The temperature dependence of the real (χ') component of the AC susceptibility for the A, B and C samples. ($H = 1 \text{ G}$ perpendicular to the plane of the tape.)

FIG. 2. Comparison of J_c with T^* for the A, B and C samples.

FIG. 3. Representative HRTEM images of a region near a (001) twist boundary for sample A (Fig. 3a), B (3b) and C (3c). "2"-2212 phase; "3"- 2223 phase. Incident beam normal to the [001] axis.

STRUCTURAL ANALYSIS OF A $\Sigma 5$ GRAIN BOUNDARY IN $\text{YBa}_2\text{Cu}_3\text{O}_{7-\delta}$

J.-Y. Wang,¹ Y. Zhu,² A.H. King,¹ and M. Suenaga²

1. Dept. of Mater. Sci. & Eng., State Univ. of New York at Stony Brook, Stony Brook, NY 11794

2. Materials Science Division, Brookhaven National Laboratory, Upton, NY 11973

One outstanding problem in $\text{YBa}_2\text{Cu}_3\text{O}_{7-\delta}$ superconductors is the weak link behavior of grain boundaries, especially boundaries with a large-angle misorientation. Increasing evidence shows that lattice mismatch at the boundaries contributes to variations in oxygen and cation concentrations at the boundaries, while the strain field surrounding a dislocation core at the boundary suppresses the superconducting order parameter.¹ Thus, understanding the structure of the grain boundary and the grain boundary dislocations (which describe the topology of the boundary) is essential in elucidating the superconducting characteristics of boundaries. Here, we discuss our study of the structure of a $\Sigma 5$ grain boundary by transmission electron microscopy. The characterization of the structure of the boundary was based on the coincidence site lattice (CSL) model.

Fig.1 shows two-beam images of the grain boundary near the $[001]$ projection. An array of grain boundary dislocations, with spacings of about 30nm, is clearly visible in Fig.1(a), but invisible in Fig.1(b). Analysis using the $\mathbf{g}\cdot\mathbf{b}=0$ extinction criterion shows that the Burgers vector of the dislocations is $[001]$. Misorientation measurement using a computer-generated Kikuchi pattern (Fig.2(a)) across the boundary suggests that its geometry can be described by rotating the left grain (grain i) 37.28° respect to the right grain (grain ii) about the $[0.192\ 0.152\ 0.970]$ axis. The misorientation is, thus, very close to that of an ideal $\Sigma 5$ boundary (36.87° of rotation angle and $[001]$ of rotation axis). The corresponding diffraction patterns of grain i, ii, and the boundary region (i+ii) are shown in Fig.2(b), (c), and (d), respectively. Note, Fig.2(c) cannot be deduced from the overlap of Fig.2(b) and (d). The extra spots are due to double diffraction when Bragg reflections of grain i, acting as new incident beams, were scattered by the reflections of grain ii. Figure 3 depicts the analysis.

A detailed analysis of the observed dislocation array was achieved using the concept of the O2 lattice. For a large-angle grain boundary, the primary grain boundary dislocations are very closely spaced, so, the observable dislocations are often the secondary grain boundary dislocations, which accommodate the deviation from the exact coincidence orientation. In the present case, the deviation can be described by a 3.03° (O2 angle) rotation about $[0.545\ 0.833\ 0.032]$ (O2-axis) from the ideal $\Sigma 5$ boundary. By making such a rotation, an O2-lattice can be generated (Fig.4). The O-sites represent the regions of perfect match, while the regions between them represent the worst lattice match. The intersection of the grain boundary with the worst-match regions yields the array of dislocations. From such an approach, the dislocation Burgers vector \mathbf{b} , dislocation line direction \mathbf{l} , and dislocation spacing d can be determined ($\mathbf{b}=[001]$ (a DSC vector²), $\mathbf{l}=[110]$, and $d=300\text{\AA}$); the results show good agreement with experimental observations. The grain boundary was found to facet in the a - b plane with steps along the c -axis. The present observations give additional support in showing the applicability of the CSL model in grain boundary characterization in complex materials such as $\text{YBa}_2\text{Cu}_3\text{O}_{7-\delta}$.³

Reference

1. Y.Zhu, Z.L.Wang and M.Suenaga, *Philos.Mag.A* **69** (1993) 11.
2. A.Singh, N.Chandrasekhar and A.H.King, *Acta Crystallogr.B* **46** (1990) 117.
3. This research was supported by U.S. Department of Energy, Division of Materials Sciences, Office of Basic Energy Sciences under Contract No. DE-AC02-76CH00016.

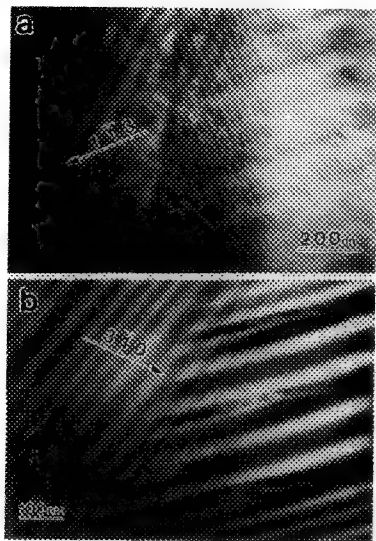


Fig.1 Two-beam images of a large-angle grain boundary in $\text{YBa}_2\text{Cu}_3\text{O}_{7-\delta}$. Note, the dislocation array is visible in (a) (dark-field, $g_1=113$), while invisible in (b) (bright-field, $g_1=310$).

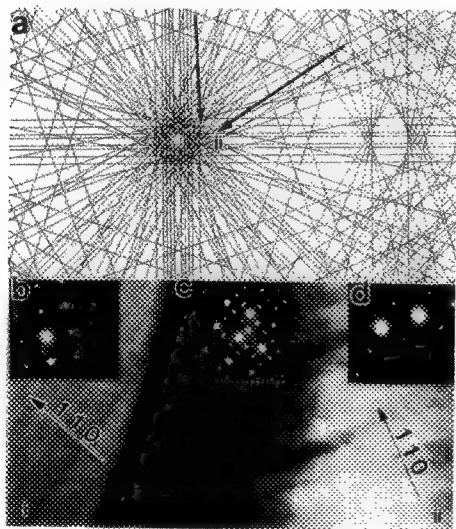


Fig. 2 (a) Calculated Kikuchi pattern near the $[001]$ pole showing the beam direction of grain i and ii. The arrows represent reference directions of a beam-stopper for each grain. (b)-(d) Select area diffraction pattern from grain i (b), the grain boundary region (c), and grain ii (d), respectively.

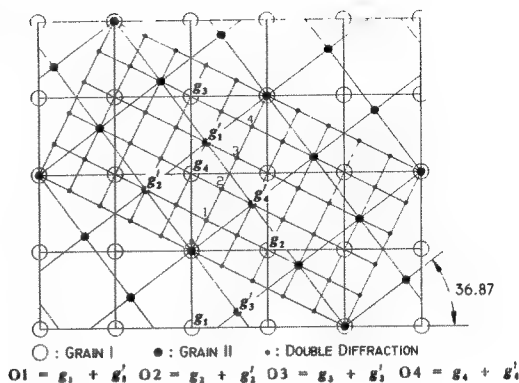


Fig. 3 Analysis of the diffraction pattern shown in Fig. 2(c). The extra spots (small solid dots), which do not belong to grain i and ii, arise from double diffraction.

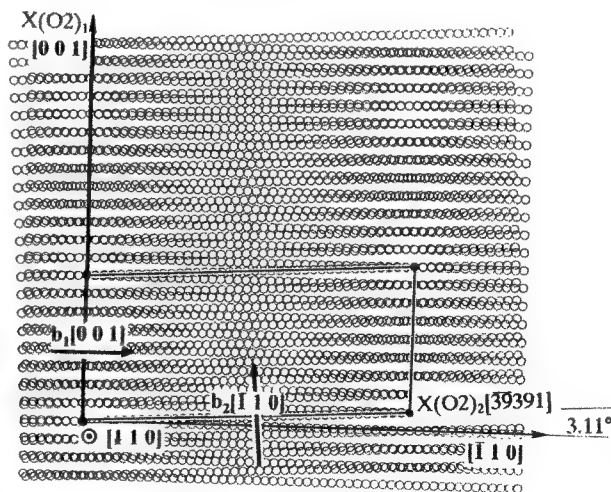


Fig.4 The O_2 -lattice configuration used to characterize the secondary grain boundary dislocations of the near $\Sigma 5$ boundary. The rectangular-like cell represents the projection of the worst-match region; the corresponding Burgers vector of the dislocations is also indicated.

ELECTRON SPECTROSCOPY OF CERAMICS

Vinayak P. Dravid, Yun-Yu Wang and Hong Zhang, Dept. of Materials Science & Engineering and STcS, Northwestern University, Evanston, IL 60208

High resolution, analytical and conventional TEM techniques/analyses have had considerable impact on ceramic science and engineering. Recently, the focus is shifted to the use of less traditional such as transmission EELS and novel techniques such as electron holography, STM, AFM etc.. In this contribution we illustrate the power and potential for transmission EELS in high spatial/energy resolution analysis of charge carriers in ceramic superconductors. Traditionally, optical and x-ray spectroscopies have been successfully utilized to probe the electronic structure of solids. The oxide superconductors, however, are marred by inhomogeneity of structure, chemistry and consequently the electronic structure. Thus, though very powerful, dedicated EELS¹ has its limitations. Furthermore, these compounds possess highly anisotropic crystal and electronic structure. As an alternative, we have demonstrated²⁻⁴ that our 200 keV Hitachi HF-2000 cFEG TEM offers adequate energy, momentum transfer (q) and spatial resolution (< 0.5 eV at zero loss, $\sim 0.10\text{\AA}^{-1}$ and $< 1\text{-}2$ nm, respectively) to realistically address these issues.

$\text{Ba}_{1-x}\text{K}_x\text{BiO}_3$ (BKBO, $0 \leq x \leq 0.5$) exhibit an insulator-metal transition at about $x = 0.35$. EELS indicates shifting of the low energy excitation (2.4 - 1.7 eV) towards lower energy with K-doping. The abrupt change in the oscillator strength of the low energy excitation signals the insulator-metal transition⁴ (Figure 1). q -resolved EELS spectra clearly show that for $x < 0.3$, the low energy excitation is rigid in the momentum space, indicative of its high effective mass (Figure 2a). On the other hand, for $x > 0.35$, the excitation disperses with q in a well-defined manner (Figure 2b), which is a characteristic of a free charge carrier plasmon. An optically forbidden transition is also observed and confirmed for $x = 0$ (Figure 2a). The O-K and Cu L_3 core loss edges are analyzed in terms of formation of holes and charge transfer in p -doped superconductors. $\text{YBa}_2\text{Cu}_4\text{O}_8$ (Y124) displays a O-K pre-edge indicative holes on oxygen sites¹, which are estimated to be about 85 % of those present in $\text{YBa}_2\text{Cu}_3\text{O}_7$ (Y123)³. Momentum transfer (q) resolved low loss EELS indicates clear confinement of charge carriers within the ab -planes, while there is very little coupling along c -direction (Figure 3). High spatial resolution and adequate sensitivity to hole concentration offered by EELS are also utilized to probe the connection between charge carriers at grain boundaries (GBs) and the transport critical current (J_c). The prevailing model of GB junction assumes Dayem bridge configuration where normal regions are separated by weak-links along the GBs⁵. We have shown that there is considerable inhomogeneity of hole concentration along GBs in YBCO. The ratio of O-K pre-edge to main edge intensity (Figure 4a) is plotted against distance along an asymmetrical tilt-GB. The variation in this parameter (Figure 4b) indicates variation in hole concentration, thus the oxygen stoichiometry. A modified Dayem bridge model which is consistent with experimental observation is proposed.⁶ It will be argued that transmission EELS with a cFEG TEM very much complements optical and soft x-ray spectroscopies with the added advantage of high spatial resolution and ability to perform local structural and chemical characterization of ceramics.⁷

References:

- 1) J. Fink et al., Studies of High Tc Superconductors, Vol. 6, (Nova Science Publishers, NY, 1990).
- 2) V.P. Dravid and H. Zhang, Physica (C), **200**, 349 (1992).
- 3) Y. Wang et al., Physica C, in press (1993).
- 4) Y. Wang et al., Phys. Rev. B, in press (1993).
- 5) Sarnelli et al., Appl. Phys. Lett., **62**(7), 777 (1993).
- 6) V.P. Dravid et al., Appl. Phys. Lett. submitted.
- 7) The research is supported by the NSF-DMR through the Science and Technology Center for Superconductivity (STcS, NSF Cooperative Agreement No. NSF-DMR-91-20000).

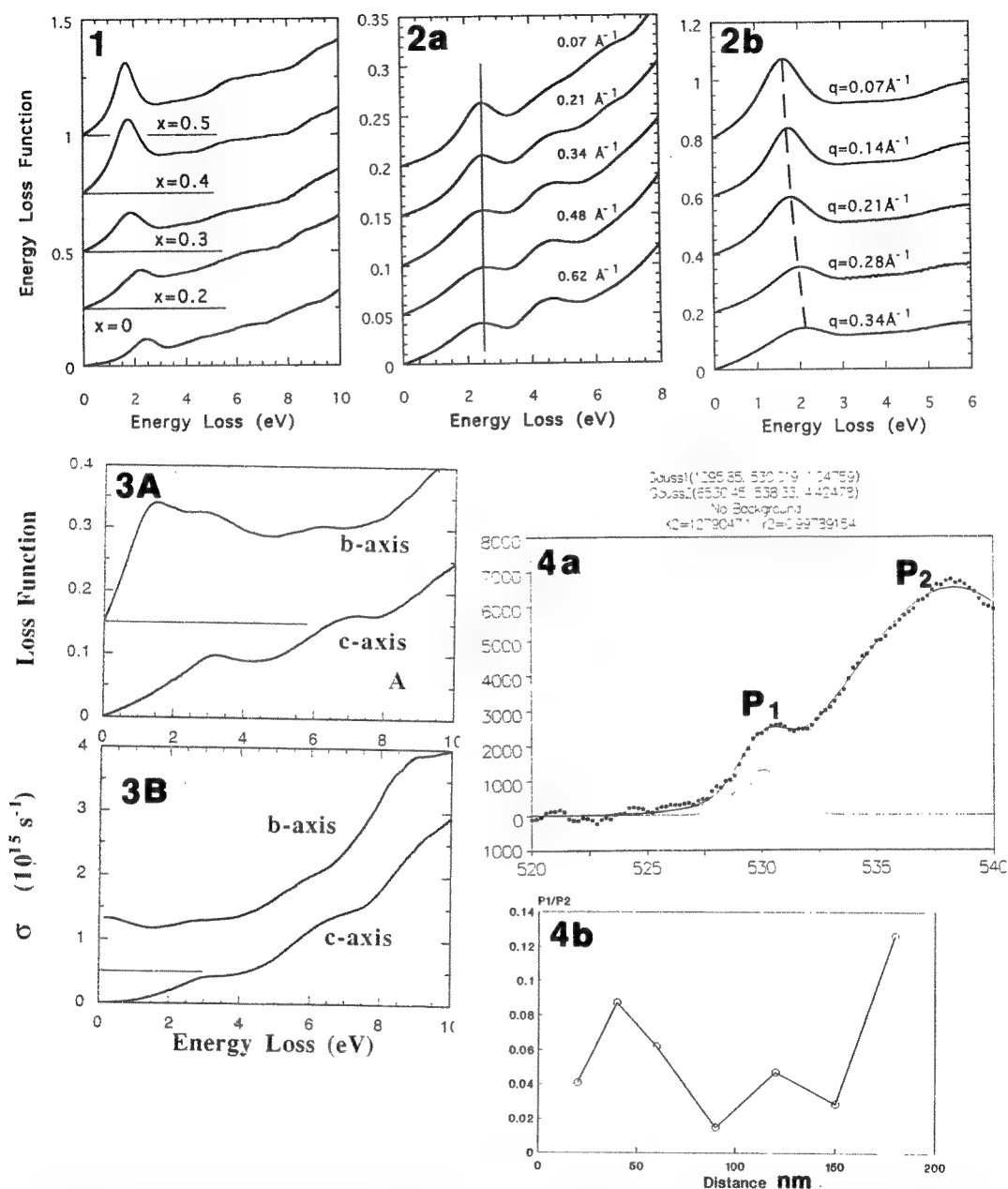


Figure 1: Low loss EELS spectra of BKBO with x . **Figure 2:** (a) q -resolved EELS for $x=0$ and for (b) $x=0.5$, **Figure 3:** Loss function (A) and AC conductivity (B) of Y124 along ab -planes and c -axis (b). Free charge carrier plasmon (and conductivity) is present only within the ab -planes. **Figure 4:** (a) Curve fitting of O-K edge for quantification of hole concentration along GB. (b) Plot of relative oscillator strength of the pre-edge (P1) to the O-K main edge (P2) as a function of distance along GB.

APPLICATION OF SCANNING ELECTRON MICROSCOPY TO THE STUDY OF MULTI-PHASE CERAMIC COMPOSITES

Helen M. Chan, Martin P. Harmer and Gary A. Miller

Materials Research Center and Dept. of Materials Science & Engineering, Lehigh University,
Bethlehem, PA 18015

Recent on-going research at Lehigh has focussed on the tailoring of multi-phase ceramic composite structures for enhanced mechanical behavior. Results have shown that by suitable control of the morphology and nature of the phases present, improvements may be obtained in properties such as microstructural stability, flaw tolerance, and strength¹. What follows is a brief discussion of examples illustrating applications of scanning electron microscopy (SEM) to this type of study for several specific systems.

Work by French et al.² revealed that relative to single phase materials, duplex structures (which consist of ~ 50:50 vol.% mixtures of mutually insoluble phases) show significantly enhanced resistance to grain coarsening. It was postulated that the slower grain growth rate in the duplex material resulted from the necessity for long-range diffusion. To test this hypothesis, the grain growth behavior of two duplex $\text{Al}_2\text{O}_3\text{:ZrO}_2$ materials was compared, the difference being that a grain boundary glassy phase was deliberately incorporated into one of the structures. As can be seen from Figure 1, the intergranular glass behaved as a rapid pathway for diffusion, hence resulting in greater grain growth compared to the glass-free composite.

Figure 2 shows a SEM micrograph of an alumina composite containing 25 vol.% of calcium hexaluminate ($\text{CaAl}_{12}\text{O}_{19}$). As clearly illustrated by Figure 2B, the hexaluminate phase forms dispersed plate-like grains. Preliminary measurements using the indentation-strength-in-bending technique reveal that the composite shows superior strength behavior over a wide range of flaw sizes. Examination of indentation cracks in the material indicates that this results from the hexaluminate grains behaving as crack bridging sites.

The work of Niihara et al.³, which showed that alumina composites containing fine dispersions of SiC particles can exhibit significantly improved fracture strengths (> 1500 MPa), has excited much interest in these materials⁴. Figure 3 shows the morphology of the same indentation crack in an $\text{Al}_2\text{O}_3\text{:5 vol.% SiC}$ composite, both before and after annealing. Careful comparison of Figs. 3A and 3B reveals evidence of crack closure, and possibly crack healing. Interestingly, this is not observed for cracks in single phase alumina. Research is currently underway to rationalize this difference in behavior, and relate it to bulk mechanical properties.

References

1. M.P. Harmer, H.M. Chan and G.A. Miller, *J. Am. Ceram. Soc.* (1992)75, 1715
2. J.D. French et al., *J. Am. Ceram. Soc.* (1990)73, 2508
3. K. Niihara and A. Nakahira, in "Advanced Structural Inorganic Composites", Ed. P. Vincenzi, Elsevier, 1990, pp. 637-64
4. J. Zhao et al., *J. Am. Ceram. Soc.* (1993)76, 503

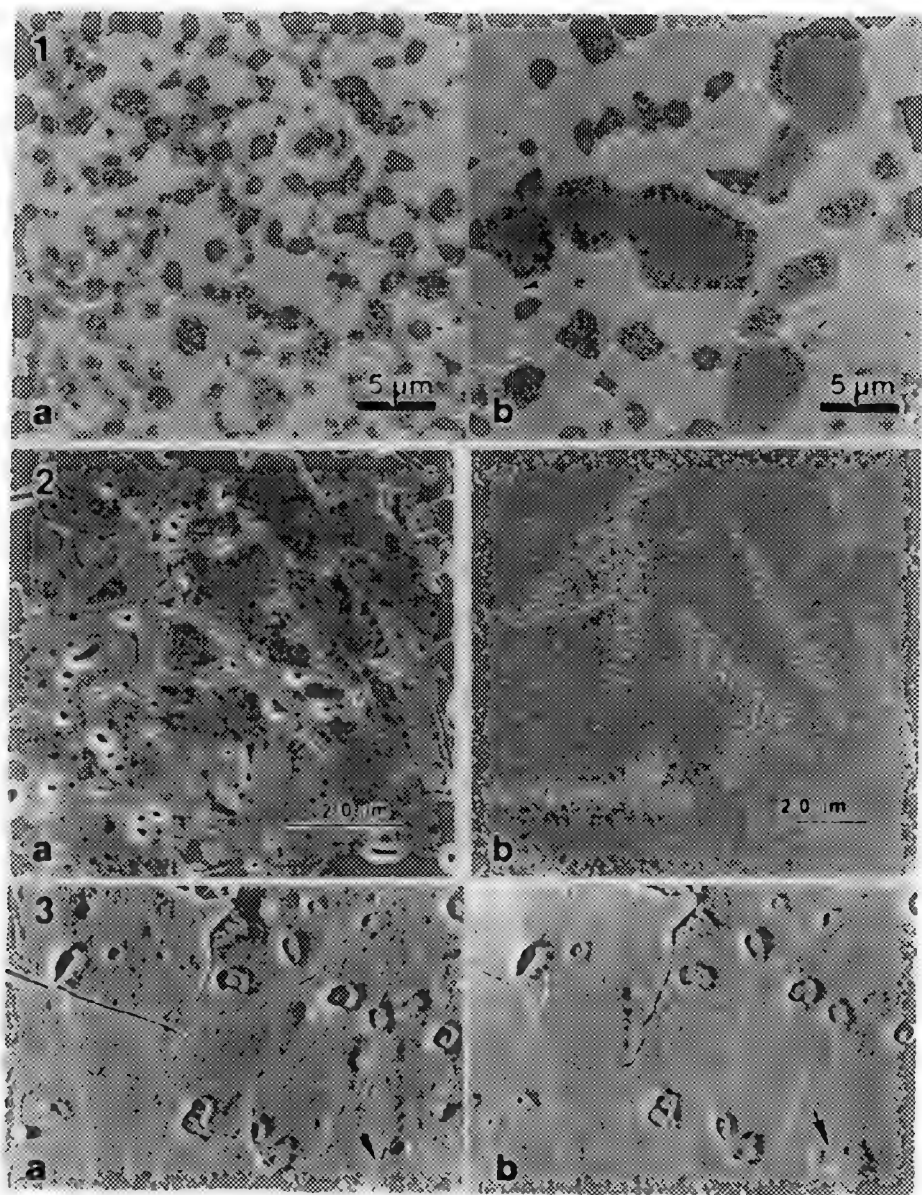


FIG. 1.--SEM micrograph showing microstructure after annealing 65 h at 1600 °C . A) Al_2O_3 :50 vol.% c-ZrO₂, B) Al_2O_3 :50 vol.% c-ZrO₂ + 1 vol. % anorthite glass (and 0.1 wt.% MgO). Courtesy S. Dill and J.D. French.

FIG. 2.--A) SEM micrograph of Al_2O_3 :25 vol.% CaAl_2O_6 (+ 1 vol.% anorthite glass), B) Calcium K- α x-ray map of same region. Courtesy L. An.

FIG. 3.--SEM micrograph of the tip region of an indentation crack in an Al_2O_3 :5 vol.% SiC composite. (Uncoated, operating voltage 3.1 keV). A) As indented, B) After annealing for 2 h at 1300 °C in an Argon atmosphere. Courtesy M. Thompson.

MICROSTRUCTURE OF DENSE MgO PENETRATED BY A SILICATE LIQUID

Sundar Ramamurthy, Michael P. Mallamaci, C. Barry Carter, Peter R. Duncombe* and Thomas M. Shaw*

Department of Chemical Engineering and Materials Science, University of Minnesota,
421 Washington Avenue SE, Minneapolis, MN 55455-0132

*IBM Research Division, T. J. Watson Research Center, Yorktown Heights, NY 10598

Grain boundaries control most of the critical properties of ceramic materials and devices. The presence of an intergranular amorphous phase in many polycrystalline ceramic compacts has been reported.^{1,2} Grain boundaries may also involve regions of ordered structure and amorphous (glassy) phase.^{3,4} Dense polycrystalline compacts are processed by liquid-phase sintering routes. The addition of sintering aids such as CaO, MgO and SiO₂ influence the densification process substantially. During sintering the grain boundaries are wet by liquid phases, and amorphous films are often found at the grain boundaries and triple junctions in the sintered product. The presence of such films not only influences the sintering behavior but it also affects the final properties in the sintered product. These films have therefore been the subject of intense investigation. Silicate-based compositions are the typical glass phases observed in these materials.

In the present study, polycrystalline, dense MgO cubes have been penetrated by liquid monticellite (CaMgSiO₄) at 1700°C. High-purity monticellite was prepared by melting exact proportions of CaO, MgO and SiO₂ at 1700°C in a Pt crucible. The resulting compound was crushed and investigated by x-ray diffraction to confirm the presence of crystalline monticellite. MgO cubes were weighed and calculations made to ascertain the exact amounts of monticellite required to obtain cubes penetrated by different volume percent monticellite. Accurately weighed flakes of monticellite were placed on the top surface of the MgO cube and the samples were heated at 1700°C in air for 44 hours, in order to allow sufficient time for the liquid to interact with all the grain boundaries in the material. Complete penetration by the liquid phase was confirmed by the absence of any silicate phase on the top surface. A series of penetrated samples was prepared by incrementing the amount of liquid phase from two to twenty volume percent.

The microstructure of these samples has been studied using visible-light microscopy, scanning electron microscopy (SEM) and conventional transmission electron microscopy (TEM). The morphology of the grains in the polished sections of the penetrated samples have been studied in the SEM. Most of the grains are found to be completely penetrated but there is also evidence of unpenetrated boundaries (Figure 1). TEM studies of these samples reveal that the penetrated microstructure is complicated, showing MgO grains immersed in a matrix of highly-defective monticellite. A majority of the grain-boundary phase is confirmed to be crystalline although some regions of amorphous phase have also been found.

In order to provide an understanding of the microstructure, as-received highly dense MgO samples were studied using the TEM. Highly-defective grains, faceted pores and dispersed particles of zirconia are the typical characteristics of the microstructure. The zirconia particles are found at the grain boundaries, triple points and within the grains. Electron diffraction studies reveal interesting topotactic relationships of these zirconia particles in the MgO matrix (Figure 5) which indicates that they were introduced at high-temperature during the initial processing of the MgO.⁵

1. D. R. Clarke and G. Thomas, *J. Am. Cer. Soc.* **60**(11-12), 491 1977
2. O. L. Krivanek et al, *J. Appl. Phys.* **50**, 4223 1979
3. C. B. Carter and Z. Elgat, *Adv. Ceram.* **6**, 73 1983
4. P. L. Flaitz and J. A. Pask, *J. Am. Cer. Soc.* **70**(7), 449 1987

5. Research supported by the U. S. Department of Energy under Grant No. DE-FG02-92ER45465. The authors wish to thank Prof. Stan Erlandsen for access to the Hitachi S-900 FESEM and Chris Frethem for technical assistance.

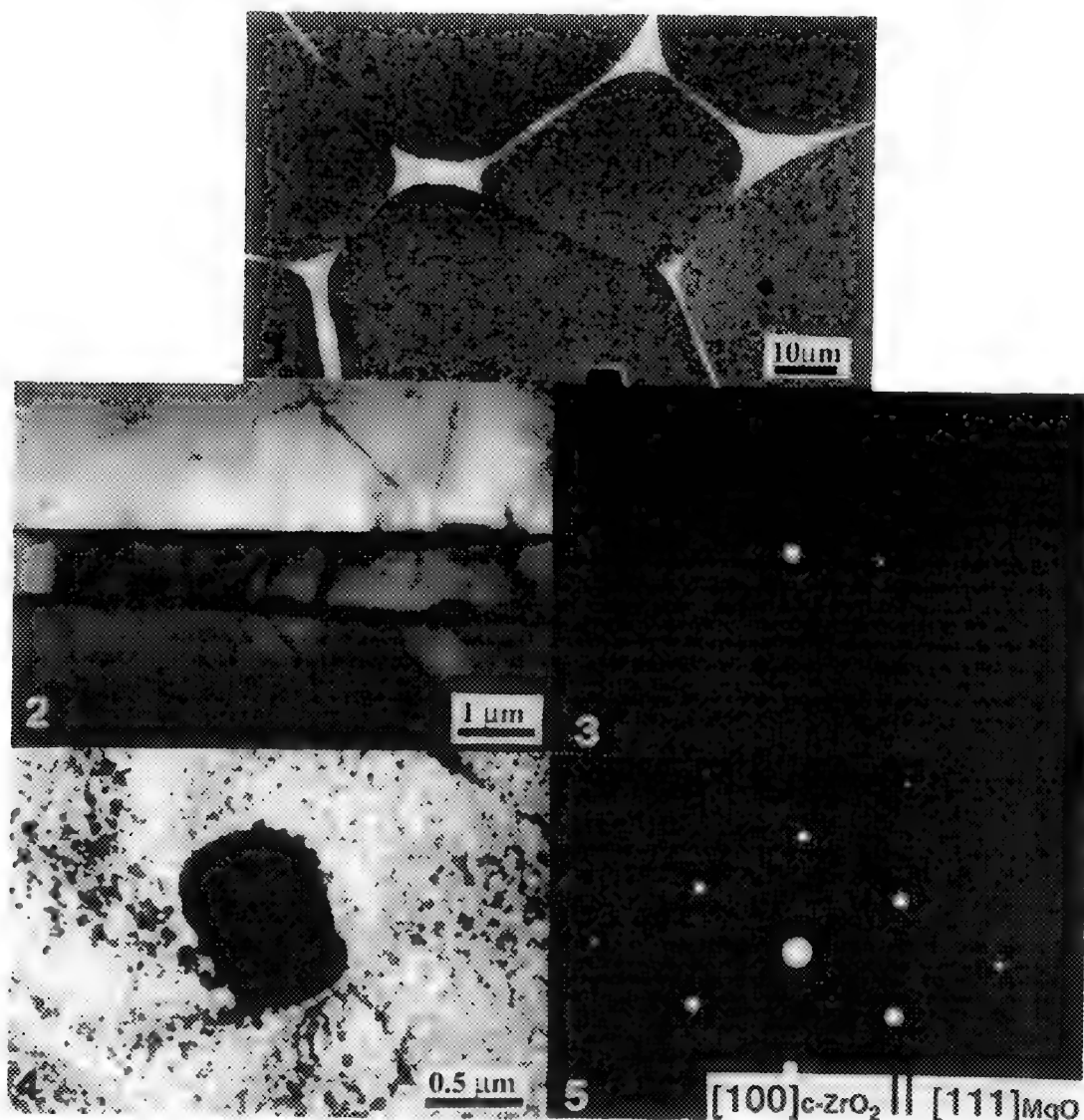


FIG. 1 Typical back-scattered electron image of polycrystalline MgO penetrated by liquid (2 vol. %).
 FIG. 2 Typical bright-field TEM image showing dislocations in the intergranular phase. Also seen are zirconia particles at the grain boundary.
 FIG. 3 Selected-area diffraction pattern from a grain boundary showing monticellite "on axis" and additional spots from the adjacent MgO grain.
 FIG. 4 Bright-field TEM image of intragranular zirconia particle.
 FIG. 5 Selected-area diffraction pattern from the zirconia particle topotactically aligned with the MgO.

THE EFFECT OF TIME AND TEMPERATURE ON THE SEGREGATION OF FOREIGN IONS TO GRAIN BOUNDARIES IN GROWING α -Al₂O₃ SCALES

B. A. Pint, A. J. Garratt-Reed and L. W. Hobbs

H. H. Uhlig Corrosion Laboratory, Massachusetts Institute of Technology, Cambridge, MA 02139

The addition of small quantities of certain oxygen-active or "reactive" elements (REs) such as Y, Zr, Hf and Ce produces a tremendous improvement in the oxidation behavior of both chromia and alumina-forming alloys. However, few of the hypotheses that have been put forth to explain this phenomenon have been confirmed by careful characterization of the oxidation process.

The segregation theory emphasizes the role of RE segregation to oxide grain boundaries and has been successful in correlating the presence of Y and Zr segregants to changes in the oxidation mechanism (thus reducing the oxidation rate) of chromia^{1,2} and alumina scales.³⁻⁵ Improvements in oxide adhesion have been attributed to the segregation of REs to the metal-alumina interface on doped β -NiAl and FeCrAl alloys.^{3,5} All of these studies employed FEG-STEM equipped with XEDS in order to detect the interfacial segregation.

The RE is also found in the scale as RE-rich particles which have been observed after high temperature oxidation using XEDS on SEM and FEG-STEM and detected using glancing-angle (0.5° incident angle) x ray diffraction.^{3,6} It has been proposed that the RE segregation detected after oxidation is a result of the RE diffusing outward in the oxygen potential gradient in the oxide scale (from the metal-Al₂O₃ oxygen dissociation pressure to the gas phase oxygen pressure).^{3,5} Once the RE diffuses out to the gas interface, RE-rich particles are formed or are ripened.

In order to study the segregation-diffusion phenomenon further, the current study has focused on the segregation phenomenon in α -Al₂O₃-formers at various times and temperatures. Y-implanted (2×10^{16} cm⁻²) and Zr-doped(0.23wt%) β -NiAl and commercial oxide dispersion strengthened FeCrAl alloys, Inco's MA956(Y₂O₃) and Kanthal's APM(ZrO₂) were studied in order to compare the behavior of Y and Zr in different substrates. Samples were made in the scale near the gas interface parallel to the metal-oxide interface.⁷ The segregation was quantified by using the Cliff-Lorimer method to determine the apparent weight percentages of Zr and Al on the boundary. Based on a recent study by Furdanowicz, et al., the effect of sample thickness was ignored.⁸

The segregation data for Y, Ti and Zr are shown in Tables I and II respectively. There is a consistent increase in the amount of segregation between 1000° and 1200°C, however, in most cases the quantity decreases at higher temperatures. This is most likely due to the increased formation of RE-rich particles at higher temperatures.¹⁰ It is proposed that at higher temperatures the RE is more easily incorporated into RE-rich particles, thus reducing the quantity of grain boundary segregation. RE-rich particles are presumably a lower energy state for the RE than as segregants.

The effect of time has not been conclusively identified and requires further study. At 1400° and 1500°C, the amount of segregant drops with time, again presumably because the RE ions on the boundaries are being incorporated with time into RE-rich particles. After 50hr at 1500°C, only Y-rich particles are observed with no detectable boundary segregation in the scale formed on Y-implanted β -NiAl, Table I. There has not yet been a careful study made of the effect of time at lower temperatures.

It is difficult to compare the segregation between different substrates because of the different types of RE additions: ion implantation, oxide dispersions and alloy additions. There are also different quantities and distributions in the substrates. For instance, β -NiAl (0.23wt%Zr) and APM (0.1wt%Zr) not only have

different Zr contents but there could be a difference in the amount of outward transport due to the Zr in the substrate being present as a metal solute or as a stable oxide (ZrO_2) respectively. However, the overall trends appear to confirm the model that the REs are diffusing outward in the scale to the gas interface and forming RE-rich particles.¹¹

References

1. K. Przybylski and G. J. Yurek, Materials Science Forum 43 (1989) 1.
2. C. M. Cotell, et al., Oxid. Met. 34 (1990) 173 .
3. B. A. Pint, Ph.D. Thesis, Massachusetts Institute of Technology, Cambridge, MA, (1992).
4. B. A. Pint, et al., Oxid. Met. (1993) in press.
5. B. A. Pint and L. W. Hobbs, Electrochem. Soc. Extended Abstracts 93-1 (1993) in press.
6. B. A. Pint, et al., in Proc. 3rd Int. Symp. on the High Temp. Corrosion and Protection of Materials, J. Physique (1992) in press.
7. L. W. Hobbs and T. E. Mitchell, in 'High Temperature Corrosion', R. Rapp ed., NACE, Houston, TX, (1983) 76.
8. Furdanowicz, et al., Inst. Phys. Conf., 119:10 (1991) 437.
9. K. Przybylski, et al., J. Electrochem Soc., 134 (1987) 3207.
10. B. A. Pint, et al., Proc. 2nd Int. Conf. on the Microscopy of Oxidation, Institute of Materials, Cambridge, U.K., (1993) in press.
11. The authors would like to thank Dr. J. Stringer and the Electric Power Research Institute for financial support; Dr. J. Doychak at NASA Lewis, Dr. W. Lipscomb at Inco and Mr. B. Jonsson at Kanthal for providing materials.

Table I. Average apparent XEDS weight percentage ratios on $\alpha\text{-Al}_2\text{O}_3$ grain boundaries near the gas interface in scales grown on Inco MA956 ($\text{FeCrAl} + \text{Y}_2\text{O}_3$) and Y-implanted $\beta\text{-NiAl}$ after various oxidation kinetics.

Alloy/ Conditions	MA956 Y/Al ratio	MA956 Ti/Al ratio	Y-implanted $\beta\text{-NiAl}$ Y/Al ratio
1000°C, 100hr ⁸	0.014	0.037	n/a
1200°C, 25hr	0.049	0.071	n/a
1200°C, 50hr	n/a	n/a	0.089
1400°C, 25hr	0.017	0.003	n/a
1500°C, 0.2hr	n/a	n/a	0.029
1500°C, 50hr	n/a	n/a	0.000

Table II. Average apparent XEDS weight percentage ratio (Zr/Al) on $\alpha\text{-Al}_2\text{O}_3$ grain boundaries near the gas interface in scales grown on Kanthal APM ($\text{FeCrAl} + \text{ZrO}_2$) and $\beta\text{-NiAl} + 0.23\text{wt}\%\text{Zr}$ after various oxidation kinetics.

Alloy/ Conditions	APM	$\beta\text{-NiAl} + \text{Zr}$
1000°C, 50hr	n/a	0.030
1000°C, 100hr	0.018	n/a
1200°C, 50hr	n/a	0.048
1200°C, 100hr	0.130	n/a
1400°C, 1hr	0.065	0.110
1400°C, 25hr	0.038	n/a

PHASE TRANSFORMATIONS IN CERAMICS

W. M. Kriven

Department of Materials Science and Engineering, University of Illinois at Urbana-Champaign,
Urbana, Illinois, 61801

The study of phase transformations in ceramic has received limited coverage in ceramic text books¹, other than for example, ferroelectric transformations, (e.g., in barium titanate), zirconia and amorphous to crystalline transformations in glass. While Newnham² has comprehensively reviewed the crystal chemistry of "ferroic" (ferroelectric, ferroelastic or ferromagnetic) ceramics, the success of "transformation toughening" as a mechanism for reducing the brittleness of ceramics has stimulated the search for other potential transformation tougheners alternative to zirconia.³

While phase transformations have been widely studied in metals over the past 50 years, caution needs to be exercised in transplanting conventional wisdom from metals to ceramics. The differences in bonding in ceramics (mixed covalent and ionic), can lead to profound differences in crystal structures and transformation mechanisms. An alternative approach which has been particularly helpful in our work is that of Hyde et al.,^{4,5} which emphasizes cation arrangements, into the interstices of which, the anions are inserted, rather than the inverse perspective of putting cations into a packed anion array. The aim of this abstract is to list known examples of non-perovskite - type transformations which generally have significant volume and/or unit cell shape changes (Table 1).

Judicious use of such transformations in ceramic composites may have beneficial effects on the mechanical properties of composites. Alternatively, a better understanding of the precise crystallography of the transformation mechanisms may lead to their application as new types of large-force actuator materials. When coupled with conventional perovskite transformations currently used in "smart" or adaptive ceramics they could produce a more powerful mechanical response. In the case of martensitic transformations which proceed with the speed of sound, the response times are comparable with current sensor and actuator materials.

In addition to those compounds listed in Table 1, other reports of displacive phase transformations in ceramics include: a tetragonal to monoclinic-like transformation in zircon (ZrSiO_4) on heating at 827 °C;⁶ a $\beta \rightarrow \gamma$ transformation in Li_3PO_4 at $\approx 340^\circ\text{C}$ ⁷; a monoclinic to rhombohedral transformation in the NaSiCON type, $\text{LiSn}_2(\text{PO}_4)_4$ ⁸; as well as transformations in aluminium titanate (Al_2TiO_5), barium orthotitanate (Ba_2TiO_4) and cerium pyrosilicate (CeSiO_4).

References

1. W. D. Kingery, et al., Introduction to Ceramics, 2nd Ed, John Wiley and Sons Publ. (1975).
2. R. E. Newnham, Crystal Chemistry of Non-Metallic Materials, Springer-Verlag (1975).
3. W. M. Kriven, J. Am. Ceram. Soc. **71** [12] (1988) 1021-1030.
4. M. O'Keeffe and B. G. Hyde, Structure and Bonding 61, Springer Verlag, (1985) 77.
5. B. G. Hyde and S. Andersson, Inorganic Crystal Structures, John Wiley and Sons, 1989.
6. Z. Mursic, T. Vogt and F. Frey, Acta Cryst B48 (1992) .
7. C. Ibarra-Ramirez et al., J. Mater. Sci. **20** (1985) 812.
8. J. Angenault et al., J. Mater. Sci. Lett. **11** (1992) 1705.
10. This was supported by the US Air Force Office of Scientific Research, Grant AFOSR-URI-90-0174.

Table 1. Examples of First Order Displacive Transformations in Ceramics

<u>Compound</u>	<u>Crystal Symmetries</u>	<u>Transformatⁿ Temperature (T_o on cooling)</u>	<u>Volume Change (ΔV)</u>	<u>Unit Cell Shape Change(°)</u>
ZrO ₂	tetragonal→ monoclinic	950	(+)4.9% (R.T.)	9
Ln ₂ O ₃ (type)	monoclinic→ cubic	600–2200	(+)10%	10
Ca ₂ SiO ₄ (K ₂ SO ₄ -type)	monoclinic→ orthorhombic	490	(+)12%	4.6
Sr ₂ SiO ₄ (K ₂ SO ₄ -type)	orthorhombic → monoclinic	90	0.2%	2
NiS	rhombohedral → hexagonal	379	(+)4%	—
2Tb ₂ O ₃ •Al ₂ O ₃ (type)	orthorhombic → monoclinic	1070	(+)0.67%	18.83
PbTiO ₃	cubic→ tetragonal	445	(+)1%	0
KNbO ₃	tetragonal → orthorhombic	225	~0%	0
LuBO ₃	hexagonal → rhombohedral	1310	(+)8%	—
MgSiO ₃ (CaSiO ₃ -type) (FeSiO ₃ -type)	orthorhombic → monoclinic	865	(-)5.5%	18.3
YNbO ₄ (LnNbO ₄ -type)	tetragonal → monoclinic	900	(-) 1.8%	4.53
LnBO ₃ (type)	hexagonal → hexagonal	550–800	(-)8.2%	—

NEW TITANIUM OXIDE PRECIPITATES IN Ti-DOPED SAPPHIRE

S. Q. Xiao, D. A. Phillips*, A. H. Heuer

Department of Materials Science and Engineering, Case Western Reserve University,
Cleveland, OHIO 44106

* Los Alamos National Laboratory, Los Alamos, New Mexico 87545

When Ti-doped α -Al₂O₃ single crystals are annealed at 1400°C, needle-like rutile TiO₂ precipitates form on the basal plane of α -Al₂O₃ and cause the asterism in star sapphire[1]. Tetragonal rutile has $a = 0.459$ nm and $c = 0.296$ nm, and has the following orientation relationship with the α -Al₂O₃ matrix: $(100)_r // (0001)_s$ and $\langle 011 \rangle_r // \langle 1\bar{1}00 \rangle_s$, where the subscripts r and s refer to the rutile and sapphire, respectively. Moon and Phillips [2] studied the precipitation in natural blue sapphire containing both Fe and Ti. They found that rutile precipitates formed after annealing at 1350°C but an orthorhombic α -TiO₂ precipitate formed after annealing at 1150°C. In this study, Ti-doped α -Al₂O₃ single crystals were annealed at 1300°C. TEM specimens were prepared with their plane normals parallel to $\langle 11\bar{2}0 \rangle_s$, $\langle 1\bar{1}00 \rangle_s$ and $\langle 0001 \rangle_s$, respectively, and ion beam thinned to electron transparency.

Three different types of precipitates are present in the α -Al₂O₃ matrix. The first is the needle-like rutile precipitate lying on $(0001)_s$, with the needle axes parallel to $\langle 1\bar{1}00 \rangle_s$. The second forms as oblate spheroids, their plate normal being parallel to $\langle 0001 \rangle_s$ (Fig.1). Electron diffraction study revealed that this precipitate was α -TiO₂ with $a = 0.455$ nm, $b = 0.550$ nm and $c = 0.476$ nm; this is a high pressure phase of TiO₂. The precipitates are twinned along $(02\bar{1})_\alpha$, where the subscript α refers to the α -TiO₂ and the following orientation relationship was determined: $\langle 100 \rangle_\alpha // \langle 0001 \rangle_s$, $(002)_\alpha // (11\bar{2}0)_s$ and $(021)_\alpha // (1\bar{2}10)_s$. Both the crystal structure and the morphology of the precipitate are very similar to the results of Moon and Phillips in natural blue sapphire[2].

The third type of precipitates are also oblate spheroids with an orthorhombic structure, but their plate normal is parallel to $\langle 1\bar{1}00 \rangle_s$ (Fig.2). Their lattice constants are: $a = 0.433$ nm, $b = 0.476$ nm and $c = 0.296$ nm. The following orientation relationship between the precipitate and the α -Al₂O₃ matrix was determined: $\langle 001 \rangle_o // \langle 1\bar{1}00 \rangle_s$, $(100)_o // (0003)_s$, and $(020)_o // (11\bar{2}0)_s$, where the subscript o refers to the orthorhombic lattice. The composition of this precipitate is being determined.

Both of the oblate spheroid precipitates have coherent interface with the sapphire matrix.

References

- [1]: D. A. Phillips, A. H. Heuer and T. E. Mitchell, Phil. Mag. A (1980) 42(3) 385
- [2]: A. R. Moon and M. R. Phillips, Phys. Chem. Minerals (1991) 18, 251

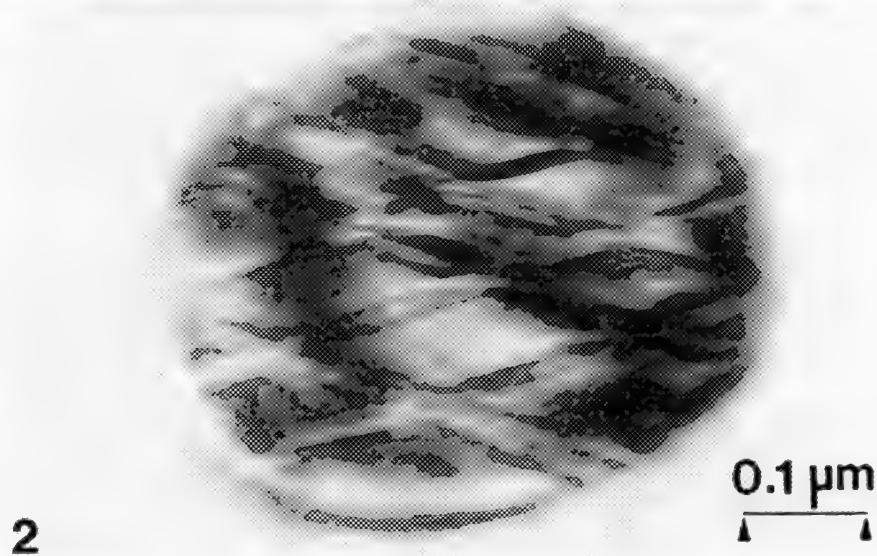
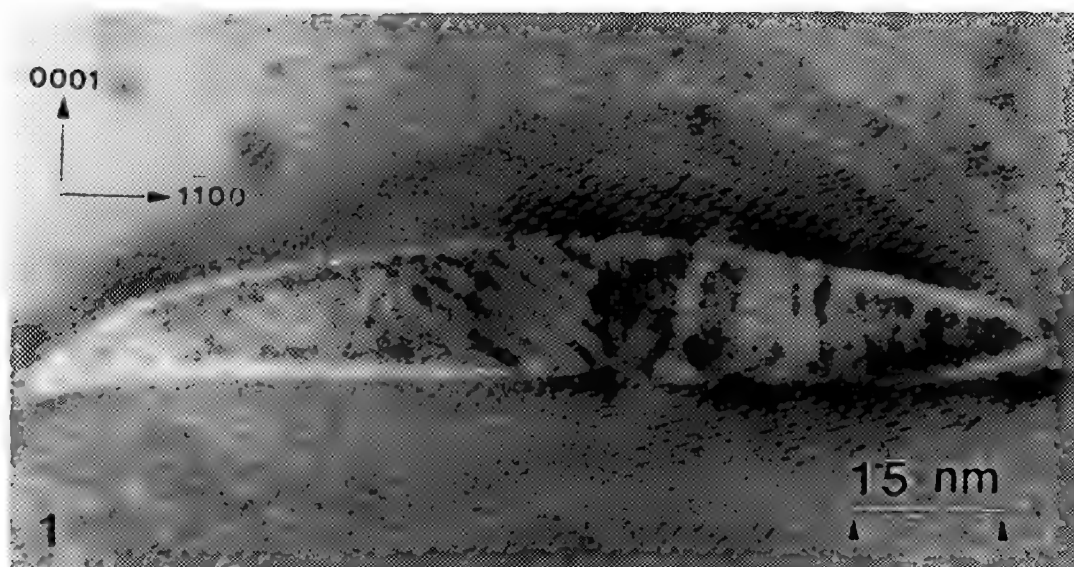


Fig.1: HREM of a α - TiO_2 precipitates viewing along $\langle 11\bar{2}0 \rangle_g$. Only one of the two twinned portions of the precipitate is on the zone axis and can be imaged high resolution.
 Fig.2: Bright field TEM micrograph of a new orthorhombic precipitate viewed near $\langle 1\bar{1}00 \rangle_g$.

MICROSTRUCTURE AND PHASE TRANSFORMATION IN KNbO_3

Oludele O. Popoola and Waltraud M. Kriven

Department of Materials Science and Engineering, University of Illinois at Urbana-Champaign, 105 South Goodwin Avenue, Urbana IL 61801

KNbO_3 is a perovskite ferroelectric ceramic material with important electro optical and non linear optical properties [1 - 2]. It can be used in an optical parametric oscillator, secondary harmonic generator and photo refractive holographic storage devices. Its macroscopic properties depend on a number of inter-related features such as crystal structure, domain structure, defects and impurity content. KNbO_3 has four known solid phases with decreasing symmetry with temperature:

Cubic $\xrightarrow{418^\circ\text{C}}$ Tetragonal $\xrightarrow{225^\circ\text{C}}$ Orthorhombic $\xrightarrow{-10^\circ\text{C}}$ Monoclinic. The paraelectric to ferroelectric transition occurs during the cubic to tetragonal transformation. The dielectric properties of KNbO_3 have been extensively studied and related to the various phase transformations. The aim of this investigation is to study the orthorhombic to tetragonal phase transformations using TEM.

Thin slices were cut from a flux grown crystal and mechanically polished to a thickness of 100 μm with a 1 μm surface finish using diamond paste and isopropyl alcohol as the lubricant. Discs (3 mm in diameter) were then ultrasonically drilled, dimpled on one side to a thickness of about 50 μm , and mounted on Cu grids for support. Final perforation to electron transparency was achieved by argon ion beam milling under an accelerating voltage of 6 kV and a gun current not exceeding 1 mA. Under these conditions, no domain boundary motion, domain or defect (dislocations) nucleation was expected. Hot stage TEM experiments were performed on a Philips EM 420 using a single tilt specimen holder. The heating rate was about $10^\circ\text{C} / \text{minute}$. A dwell time of 20 minutes was allowed after each 50°C increment to allow for structural relaxation.

Figure 1a is a bright field (TEM) image of the domain configurations commonly observed in KNbO_3 . The associated diffraction pattern (Figure 1b), taken across many boundaries, shows no spot splitting in [001] direction and contrast behavior similar to Friedel's law failure was frequently observed. These are characteristics of 180° domains. 90° domains, characterized by spot splitting in the [001] diffraction patterns are also frequently observed. On heating a [011] foil, the orthorhombic to tetragonal transformation started at 188°C and was completed at 192°C . The reverse transformation (i.e. tetragonal to orthorhombic) occurred between 174°C and 167°C . In Figure 2, the microstructural modifications that took place during the transformation of an area containing 180° domains is seen. The transformation manifested itself by the disappearance of the domains at 192°C (Figure 2a). On subsequent cooling, many domain variants reappeared (Figure 2b). This behavior, observed during repeated experiments, indicated that the transformation had no microstructural reversibility. The diffraction patterns associated with Figures 2a and 2b are seen in Figure 3. The [011] orthorhombic direction changed to the [001] tetragonal without any tilting or rotation of the specimen. Although no orthorhombic / tetragonal phase boundary could be imaged due to the rapidity of the transformation, these two patterns were sufficient to establish the reversible orientation relation between the two phases. This relation was $[011]_o // [001]_t$ and $(100)_o // (100)_t$. Since the $(100)_t$ and the $(010)_t$ were interchangeable, two symmetry equivalent options at 90° to each other could be expected in the tetragonal phase, as observed in the microstructure (Figure 4).

References

1. S. A. Ingle and A. P. David, *Ferroelectrics* (1989) 97, 201.
2. T. Malis and H. Gleiter, *J. Appl. Phys.* (1976) 47, 12, 5195.
3. This research was supported by AFOSR-URI-90-0174.

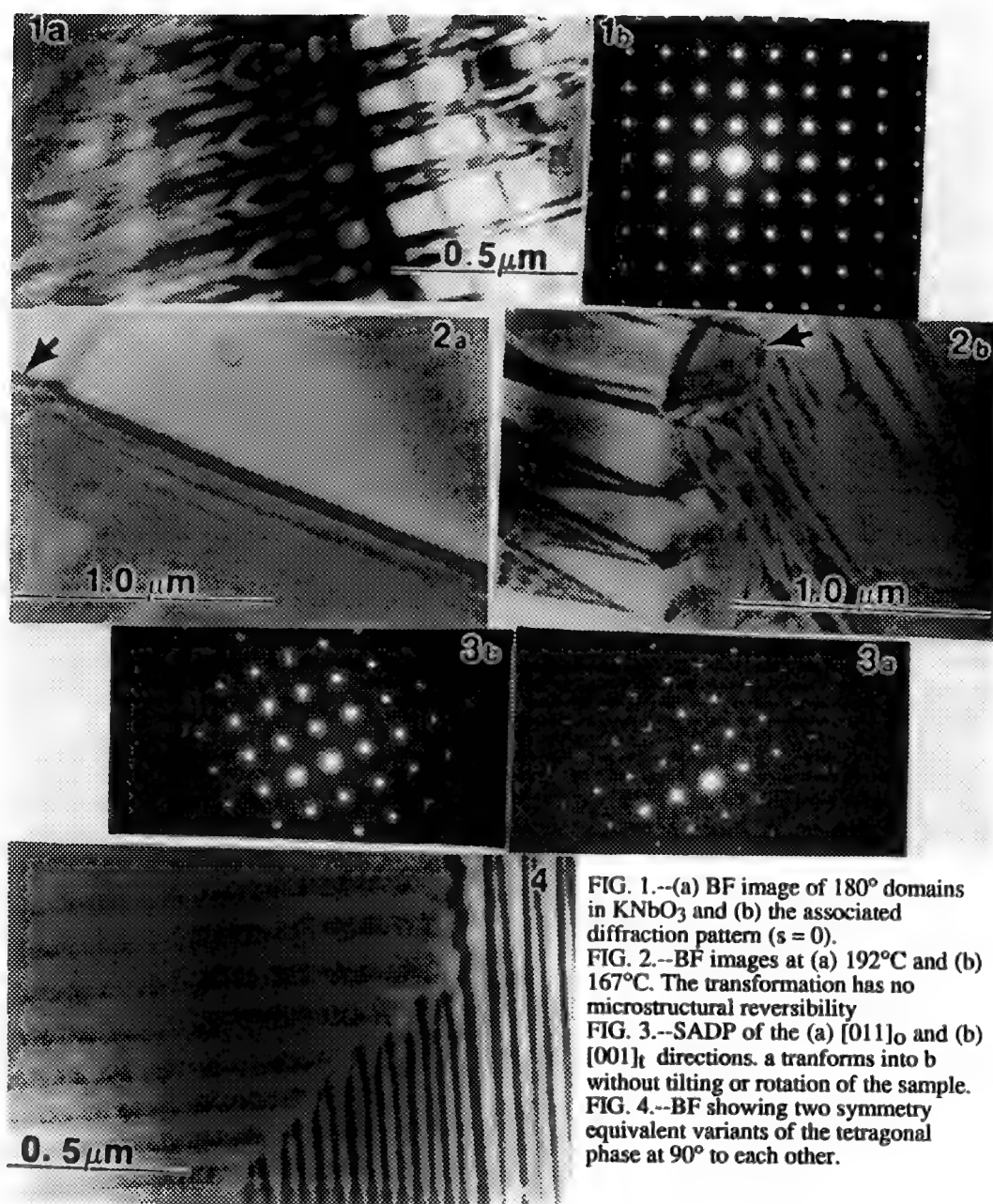


FIG. 1.--(a) BF image of 180° domains in KNbO_3 and (b) the associated diffraction pattern ($s = 0$).
 FIG. 2.--BF images at (a) 192°C and (b) 167°C . The transformation has no microstructural reversibility
 FIG. 3.--SADP of the (a) $[011]_O$ and (b) $[001]_T$ directions. a transforms into b without tilting or rotation of the sample.
 FIG. 4.--BF showing two symmetry equivalent variants of the tetragonal phase at 90° to each other.

ION MIXING OF THIN ZrO_2 FILMS ON $\alpha\text{-Al}_2\text{O}_3$ BY Cr^+ OR Kr^+ IONS

N. D. Evans*, D. L. Joslin and C. J. McHargue

* Oak Ridge Institute for Science and Education, P.O. Box 117, Oak Ridge, TN 37831-0117
Department of Materials Science and Engineering, The University of Tennessee, Knoxville, TN 37996-2200

Analytical electron microscopy (AEM) has been used to study ion beam mixing in an oxide-oxide system: ZrO_2 thin films on $\alpha\text{-Al}_2\text{O}_3$. This mixing process is useful in applications such as adhesion enhancement.

Films of ZrO_2 (~80 nm thick) were deposited on $\alpha\text{-Al}_2\text{O}_3$ by radio frequency (rf) sputter deposition and annealed for 2 h at 500°C in 96%Ar+4% H_2 to remove excess oxygen. Samples were bombarded at room temperature with either 340 keV Cr^+ or 475 keV Kr^+ ions to a fluence of 4×10^{12} ions/ m^2 . An area of each specimen was masked during implantation to permit analysis of unimplanted interfaces. Specimens for AEM were mounted in cross-section, ground and dimpled to a thickness of ~20 μm , and Ar^+ ion milled to electron transparency. Specimens were sputter-coated with ~5 nm of carbon to reduce charging effects. The AEM was performed in a Philips EM400T/FEG operated in the scanning transmission mode with a probe diameter of <2 nm (FWTM prior to beam spreading). All AEM was performed with specimens in a double-tilt, liquid-nitrogen-cooled holder to minimize contamination under the focussed probe. Concentration profiles of Al and Zr cations, which indicate the degree of mixing, as well as Cr and Kr profiles, were obtained by energy-dispersive x-ray spectrometry (EDXS). With the $\text{Al}_2\text{O}_3/\text{ZrO}_2$ interface tilted edge-on relative to the beam, EDXS was performed with either a stationary probe or from analog line scans acquired in a direction normal to the interface. Spectra were hole count corrected, or where necessary, corrected for a surface film associated with the argon ion milling.¹ Ion ranges and recoil distances, used to explain implanted morphologies, were calculated by the use of Monte Carlo simulations of binary collisions between a moving ion and stationary target atoms (TRIM-88).²

The $\text{Al}_2\text{O}_3/\text{ZrO}_2$ interface and the cation profiles prior to bombardment are shown in Figure 1. Zero on the abscissa of all line scans corresponds to the measured $\text{Al}_2\text{O}_3/\text{ZrO}_2$ interface composition obtained from a stationary probe. Data from the ZrO_2 film are plotted to the right of zero. In Fig. 1b, the secondary excitation of Al $K\alpha$ is manifested by the significant amount of Al detected even far from the $\text{Al}_2\text{O}_3/\text{ZrO}_2$ interface.³ EDXS spectra acquired in a spot mode at a constant position in the ZrO_2 far from the alumina yielded a tilt-dependent concentration of 9 to 18 at.% Al for specimen tilts of 12° to 48°. This result supports the explanation that secondary excitation of Al is occurring.

Following Cr^+ ion bombardment, ballistic mixing is evident at the $\text{Al}_2\text{O}_3/\text{ZrO}_2$ interface and in the EDXS line scans shown in Figure 2. In Fig. 2a, the indicated region A is ZrO_2 . Regions B and C are in the alumina. Diffraction patterns revealed that region B is an amorphous layer; it slowly crystallizes under the focussed probe. The extent of the amorphous layer (~30 nm) corresponds to the range of Cr through the ZrO_2 into the Al_2O_3 ; the influence of the Cr on the amorphous layer is uncertain at this time. The recoil distance of Zr in alumina extends into Region C. Alumina implanted with Zr^+ ions at room temperature is known to amorphize.⁴ Region C is damaged alumina; the extent corresponds to the end-of-range of recoiled oxygen atoms displaced from the ZrO_2 by Cr^+ ions. Region D is unaltered alumina. The line scans from this specimen also indicate Zr is present in the amorphized alumina after implantation; a significant increase in the amount of Zr in the interface has occurred. The profiles in Fig. 2b were corrected for a uniform surface film; the apparent increase in Al content near the hole in the specimen suggests that the film is not uniform.

In Figure 3, ballistic mixing is observed at the $\text{Al}_2\text{O}_3/\text{ZrO}_2$ interface and corresponding line scans from a specimen bombarded with Kr^+ ions. The morphology is analogous to that of Fig. 2a in that it contains ZrO_2 (region A), a ~7-10 nm wide amorphous layer (region B) in the alumina immediately below the ZrO_2 , damaged alumina (region C), and undisturbed alumina (region D). The width of the amorphous layer in this specimen is less than that for the Cr^+ ion implanted specimen (Fig. 2b) and is due to there being comparatively less Zr at the $\text{Al}_2\text{O}_3/\text{ZrO}_2$ interface and in the alumina (Fig. 2b).⁵

1. J. Bentley and E. A. Kenik, Proc. Ann. EMSA Meet. **50** (1992) 1230-1.
2. J.F. Ziegler et al., *The Stopping and Range of Ions in Solids*, Vol 1, New York: Pergamon Press (1985).
3. E. A. Kenik and J. Bentley, *Microbeam Analysis 1990*, San Francisco Press (1990) 289-92.
4. C. J. McHargue et al., Mater. Res. Soc. Symp. Proc. **157** (1990) 505-12.
5. Research sponsored by the Ceramic Technology Project, Office of Transportation Technologies, and the Division of Materials Sciences, U.S. Department of Energy under contract DE-AC05-84OR21400 with Martin Marietta Energy Systems, Inc., and through the SHaRE Program at Oak Ridge National Laboratory under contract DE-AC05-76OR00033 with Oak Ridge Associated Universities. Discussions with Drs. J. Bentley and E. A. Kenik are appreciated.

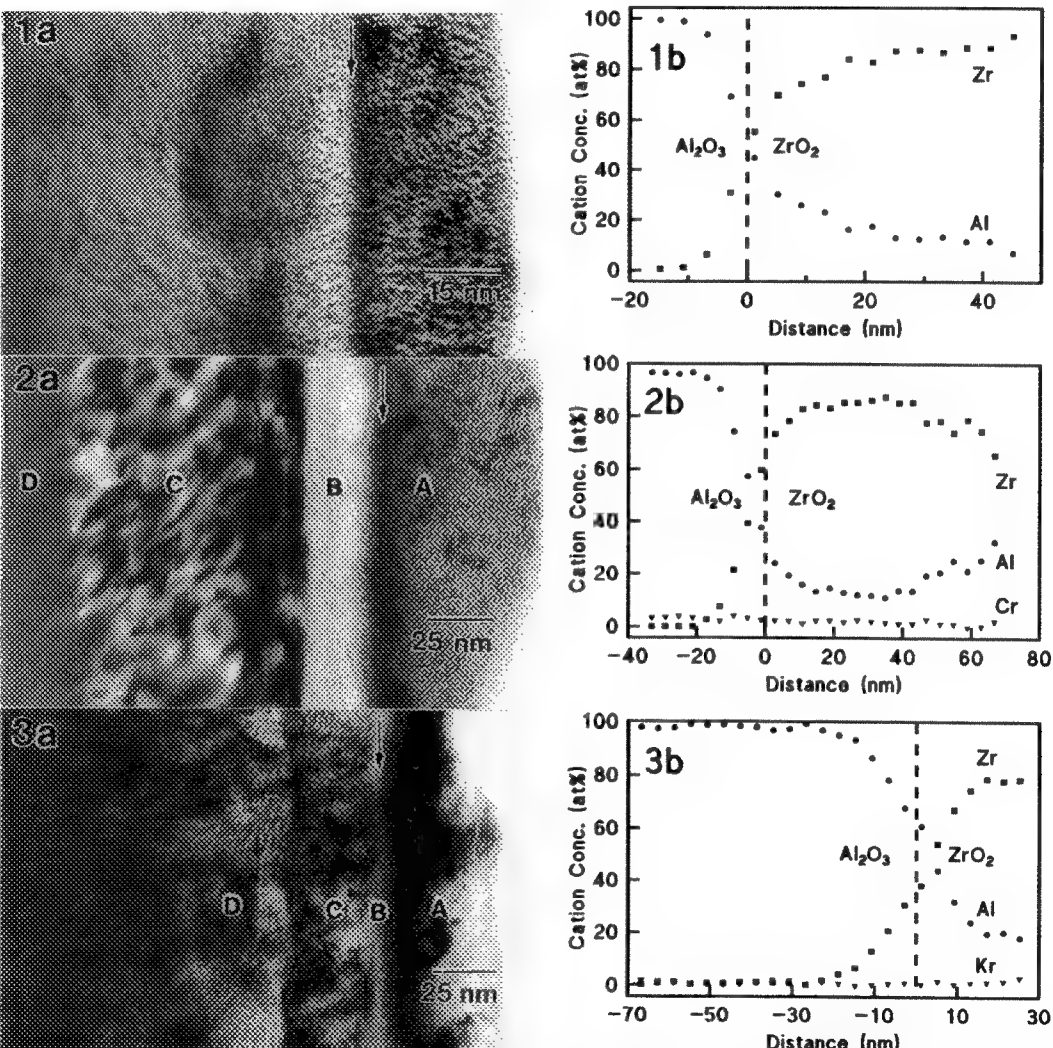


FIG. 1.--a) Unimplanted $\text{Al}_2\text{O}_3/\text{ZrO}_2$ interface; b) elemental profiles through interface
 FIG. 2.--a) $\text{Al}_2\text{O}_3/\text{ZrO}_2$ interface, Cr^+ implanted at room temperature; b) elemental profiles through interface
 FIG. 3.--a) $\text{Al}_2\text{O}_3/\text{ZrO}_2$ interface, Kr^+ implanted at room temperature; b) elemental profiles through interface

GRAIN BOUNDARIES IN CERAMICS FOR SOLID OXIDE FUEL CELLS

F. Tsai and J. M. Cowley

Department of Physics and Astronomy, Arizona State University, Tempe, AZ 85287-1504

S. S. Jiang and J. B. Wagner, Jr.

Center for Solid State Science, Arizona State University, Tempe, AZ 85287-1704

Calcium stabilized zirconia (CSZ) and ceria (CeO_2) doped with rare-earth oxides have been used as electrolytes in solid oxide fuel cells (SOFC). Such ceramics are usually good ionic conductors for oxygen ions at elevated temperatures. A few studies have attempted to correlate the microstructures with ionic conductivity [1-4]. It was suggested that the grain boundaries play a role in depressing the ionic conductivity [1]. In their study, it was found that continuous "thick" boundary layers of secondary phases existed on the grain boundaries and blocked ion transport [1,3].

In the present studies, high resolution transmission electron microscopy has been used to investigate the microstructures of grain boundaries in zirconia doped with calcium ($\text{ZrO}_2 + 13\% \text{CaO}$) and ceria ceramics doped with calcium ($\text{CeO}_2 + 10\% \text{CaO}$). The ceramics were made in our Solid State Ionics Laboratory. Transport number measurements on zirconia samples showed that the transport number $t_{\text{O}^{2-}} = 1$ from $\text{P}_{\text{O}_2} = 10^{-17}$ atm to $\text{P}_{\text{O}_2} = 1$ atm. Measurements showed that the transport number of the oxygen ions in ceria was small only when the P_{O_2} was very low between 600°C and 1000°C . The CSZ was used in a galvanic cell $\text{P}_{\text{O}_2} | (\text{CaO})\text{ZrO}_2 | \text{P}_{\text{O}_2} = 1$ (atm). The open circuit EMF values measured between 600°C and 1000°C agreed well with the calculated values [5]. The TEM ceramic samples were cut into $2.5 \times 2.5 \times 0.5$ (mm) discs, then dimpled and ion milled with argon ions.

Fig. 1(a) shows a bright field image of grain boundaries in CSZ. It can be noticed that pores of different sizes are located in the grains and grain boundaries. X-ray dispersive spectroscopy (EDX) has been used to identify the secondary phases and no continuous secondary phase boundary layers have been found on grain boundaries. Fig. 1(b) shows a high resolution lattice image of a grain boundary in the zirconia. One grain is tilted to $[100]$ orientation. There is little evidence that secondary phases are present on the grain boundary but small voids of about a few hundred angstroms may exist at the grain boundary. Fig. 2(a) shows a bright field image of grain boundaries in ceria sample. EDX has been used to examine the chemical compositions over a fairly large area. Little secondary phase in grains nor thick boundary layer on grain boundaries has been found. Fig. 2(b) is a high resolution lattice image of a grain boundary in ceria, which shows the discontinuity of crystal lattices at grain boundaries.

In previous studies by other authors on the microstructures of grain boundaries in CSZ [1,2] and ceria with CaO [3,4], it was suggested that the presence of continuous secondary phase boundary layer on grain boundaries might interrupt the ionic transport. However, for the ceramics used as electrolytes for SOFC, no continuous boundary layers should be present on grain boundaries. Then, in the absence of boundary layers the main blocking of ion transport may be the discontinuity of the crystal structures at grain boundaries because oxygen ion transport through the crystal lattices is the main transport process and the discontinuity of the crystal lattices at grain boundaries may interrupt the ion transport. Pores of different sizes usually exist in ceramic materials. No TEM evidence has been made convincing the effects of pores on ionic transport. It is suggested that the pores at grain boundaries will increase the discontinuity and reduce the ion transport through the grain boundaries.

1. A. J. A. Winnubst, M. J. Verkerk and A. J. Burggraaf, in "Additives and Interfaces in Electronic Ceramics", Eds. by M. F. Yan and A. H. Heuer, (1982) 177, Ohio, the American Ceramic Society, Inc.
2. S. P. S. Badwal and J. Drennan, Sol. St. Ionics, 53(1992)769.
3. R. Gerhardt, A. S. Nowick, M. E. Mochel and I. Dumler, J. Am. Ceram. Soc., 69(1986)647.
4. K. Eguchi, T. Kunisaki and H. Arai, J. Am. Ceram. Soc., 69(1986)c282.
5. K. Kuikkola and C. Wagner, J. Electrochem. Soc., 104(1957)379.

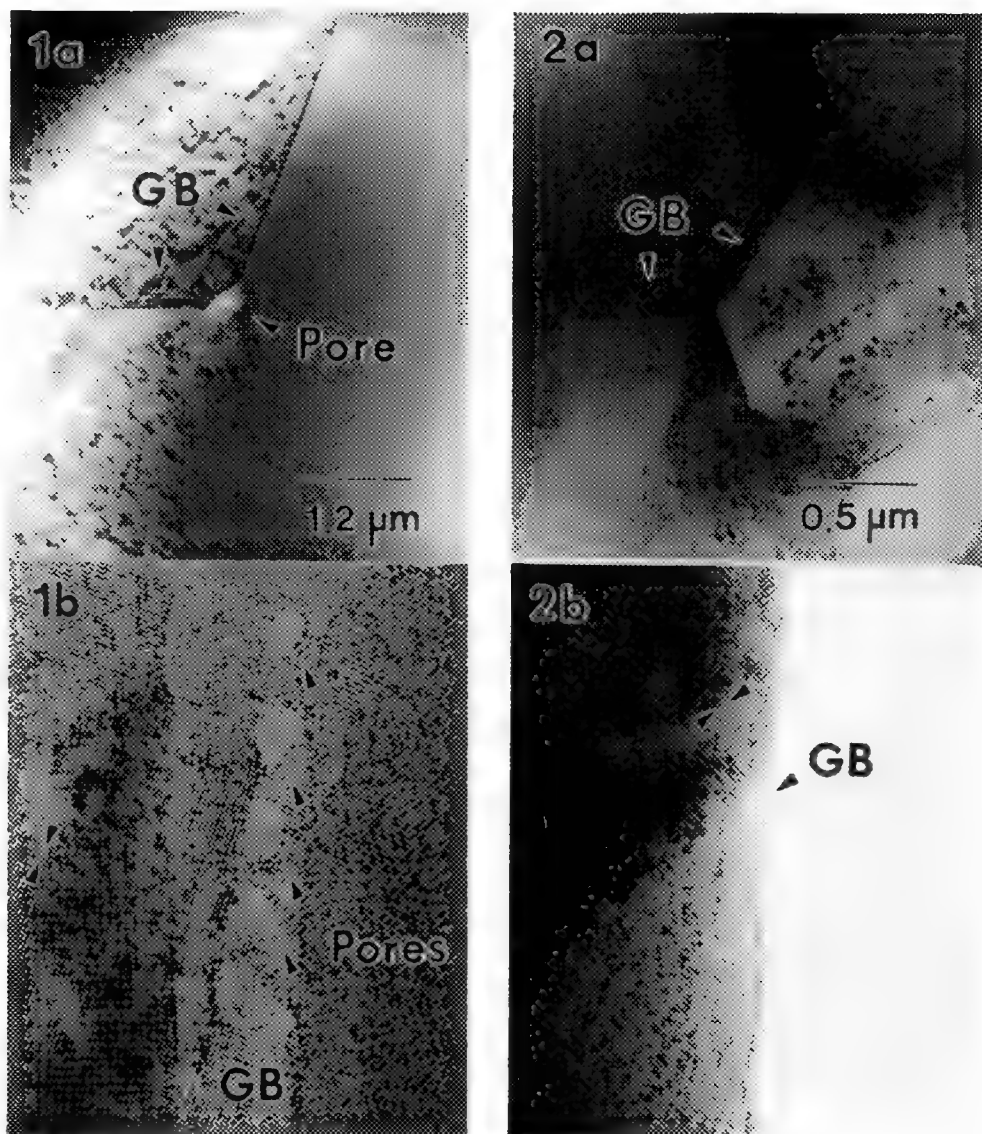


Fig. 1(a). A bright field image of grain boundaries in zirconia showing no boundary layers at grain boundaries; (b). A high resolution image showing the lattice image of a grain boundary of random orientation. One grain is tilted to [001] orientation. The lattice spacings are about 2.7 Å.

Fig. 2(a). A bright field image of grain boundaries in ceria showing no boundary layers at grain boundaries; (b). A high resolution image showing the lattice image of a grain boundary of random orientation. One grain is tilted to [001] orientation. The lattice spacings are about 2.7 Å.

Acknowledgements: The research is supported by NSF grant DMR 91-10386 and made use of the ASU Facility for High Resolution Electron Microscopy supported by NSF grant DMR 89-13384.

HIGH-RESOLUTION MICROSCOPY OF CERAMIC SURFACES

J. Bentley

Metals and Ceramics Division, Oak Ridge National Laboratory, P.O. Box 2008, Oak Ridge, TN 37831-6376

The characterization of ceramic surfaces plays an important role in understanding a wide variety of properties such as fracture, wear, crack initiation, oxidation, sintering, and thin film growth on substrates. Three major microscopies are employed to obtain nanometer-scale resolution of ceramic surfaces: scanning electron microscopy (SEM), (scanning) transmission electron microscopy (STEM or TEM) especially in the glancing-incidence reflection modes, and scanning tip microscopies - most notably atomic force microscopy (AFM). Each technique has its own set of characteristics, advantages, and disadvantages and is usually complementary to the others.¹

Conventional SEM is quick and easy to implement. As a mature technique, the contrast mechanisms, although sometimes complex, are largely well understood;² computer programs for image simulation are available. The technique is applicable to a wide range of materials and specimen sizes; usually, little specimen preparation is involved. Charging of electrically insulating ceramics has traditionally been overcome by coating but, at high resolution, the faithful representation of the structure then becomes of some concern. With the increasingly widespread availability of SEMs equipped with field emission guns (FEG), high resolution imaging at low accelerating voltages has become an attractive alternative to coating. Recently, a deliberate and significant increase in pressure at the specimen in an environmental SEM (ESEM) has been found to be effective in eliminating charging effects. The availability of low magnification ($>10\times$) SEM images is of great help in placing the high resolution images in context. Rough surfaces (e.g. growth or fracture surfaces of fine-grained polycrystalline materials) are obvious candidates for SEM. The adaptability to in-situ experiments and the ability to record dynamic processes (e.g. slow crack growth in toughened ceramics and composites) makes SEM particularly appropriate for such studies. ESEMs further expand the range of studies to in-situ gas reactions and observation of hydrated specimens. X-ray microanalysis with energy- or wavelength-dispersive spectrometers (EDS and WDS) adds an often important capability to studies of ceramic surfaces, especially at low accelerating voltages when for appropriate specimens the surface sensitivity and spatial resolution are enhanced.³ Instrumentation being developed to obtain high spatial resolution crystallographic information, based on static probes and cameras to record the backscattered Kikuchi patterns, will further complement SEM imaging.

Several completely different techniques have been developed for studying surfaces in the TEM.⁴ Profile imaging by high resolution electron microscopy (HREM) provides single atomic column resolution at the thin edge of a foil but beam-stimulated atomic migration and reduction are commonly observed. For thinned plan-view specimens, HREM can reveal surface reconstruction and TEM imaging with weak "forbidden" reflections can reveal atomic-height surface steps. Selected area diffraction patterns are an important adjunct in such work. Plan-view TEM has also been effectively used in the elegantly direct studies of thin film nucleation and growth on prethinned ceramic substrates.⁵

Reflection electron microscopy (REM) performed in a TEM (or the scanning equivalent, SREM, in a STEM) has been the technique of choice for imaging individual atomic-height surface steps on unthinned "bulk" specimens,⁶ although equivalent SEM observations have been reported.⁷ REM requires no modifications of the TEM or specimen holders and specimen preparation is usually much more straightforward than for transmission work. The (dark-field) diffracting conditions are adjusted by reference to the reflection high-energy electron diffraction (RHEED) pattern. Although the lateral resolution is usually limited to ~ 1 nm, and several times this in the direction parallel to the incident beam, the technique is especially sensitive to atomic-height surface steps because of the large associated phase change. Such phase contrast is enhanced with the use of a FEG.⁸ Electron holographic REM has also been reported,⁹ and a SREM method for achieving atomic resolution with atomic number discrimination (Z-contrast) has been proposed.¹⁰ As a result of image foreshortening and the need for Bragg diffraction, REM is limited to studies of nearly atomically flat surfaces of single crystal or large-grained materials.

Ceramic surfaces produced by polishing and annealing or by fracture (cleavage) have been studied with REM.¹¹ Although most REM images are not bright by most TEM standards, the intensity is high enough to permit video recording, opening up the possibility for dynamic processes to be followed in-situ. Video recordings have been made of surface step migration and terrace nucleation and growth on cleaved α -alumina (012) surfaces at up to 1670 K.¹² Step velocities of $\sim 0.1 \mu\text{m/s}$ were easily recorded even though images at such high temperatures are degraded by the increased diffuse scattering. The studies are relevant for understanding the development of substrate surfaces (e.g. silicon on sapphire) and have the potential for allowing measurements of activation energy of surface diffusion or desorption processes. Similar in-situ annealing studies on MgO did not show step migration but rather a phase transformation.¹³ Above 1400 K, a rough surface developed and extra reflections appeared in the RHEED patterns. Additional conventional TEM observations were used in the identification of a surface film of MgO₂ present as different crystallographic variants a few tens of nm in diameter. The work also revealed the potential for incorrect structural interpretation of additional rods in RHEED patterns. The formation of MgO₂ stable in bulk form only at high temperatures and high oxygen partial pressure, is of significance for the widespread use of MgO as a substrate for thin film growth. Experiments on stable oxides such as Al₂O₃ and MgO give meaningful information even in the poor quality vacuum environment of an unmodified TEM, but this is not so for all classes of materials. Non-oxide ceramics may require true ultra-high vacuum specimen environments. Recent work on in-situ annealing of SiC has also demonstrated the importance of residual impurities.¹⁴

A useful surface analysis technique that is complementary to REM and RHEED is reflection electron energy-loss spectrometry (REELS).⁸ Since the spectra originate mostly from electrons that have penetrated just a few atomic layers, REELS provides surface-sensitive information on composition and bonding. Signal-to-background ratios are much lower than in transmission (TEELS) but are still usable, especially with parallel detection. Quantification is complicated by mostly unavoidable dynamical diffraction and channeling discrimination effects, but a technique based on the measurement of effective ionization cross sections by TEELS has been developed.¹⁵ Adsorbed surface species and terminating atomic layers have been identified for a number of oxide ceramics and related materials.^{8,13,15}

The technique with potentially the highest resolution, both parallel and normal to the surface, is AFM. In principle, it is applicable to the widest range of specimens in a range of environments including, most significantly, ambient conditions. Image formation involves convolution of the surface with the profile of the stylus tip. For more-or-less flat surfaces with atomic height steps or for surfaces with roughness on a scale much larger than the tip dimensions, image interpretation can be relatively straightforward. For a surface with roughness on the same scale as the tip dimensions, images contain misleading information and are difficult to interpret. The problem is one of knowing when this situation applies. Other current practical limitations are the unavailability of a low magnification image to locate the area to be imaged at high resolution and long acquisition times for images that preclude following rapid changes during in-situ dynamic experiments. Some of the limitations are intrinsic to the technique; others may be overcome in the future and merely await the implementation of novel solutions in this new and rapidly developing field.¹⁶

1. e.g. papers by H. Chan and D. Bonnell, these proceedings.
2. J.I. Goldstein et al., *Scanning Electron Microscopy and X-ray Microanalysis*, New York: Plenum (1981).
3. E.D. Boyes et al., *Proc Ann. EMSA Meet.* **50** (1992) 1630.
4. K. Yagi, in P. Buseck, J. Cowley, and L. Eyring, eds., *High Resolution Transmission Electron Microscopy*, New York: Oxford University Press (1988) 568.
5. e.g. M.G. Norton, S.R. Summerfelt, and C.B. Carter, *Appl. Phys. Lett.* **56** (1990) 2246.
6. e.g. Collection of papers in *Microscopy Research and Technique* **20**(4) (1992) 317-462.
7. R.H. Milne, *Ultramicroscopy* **27** (1989) 433; Y. Uchida et al., pp. 406-412 in ref. 6.
8. Z.L. Wang and J. Bentley, pp. 390-405 in ref. 6.
9. N. Osakabe et al., *Jpn. J. Appl. Phys.* **27** (1988) L1772; N. Osakabe, pp. 457-462 in ref. 6.
10. Z.L. Wang and J. Bentley, *Ultramicroscopy* **37** (1991) 39.
11. e.g. P.A. Crozier et al, pp. 426-438 and G.C. Ndubuisi et al., pp. 439-449 in ref. 6.
12. Z.L. Wang and J. Bentley, *Proc. Ann. EMSA Meeting* **49** (1991) 660; *Ultramicroscopy*, in press.
13. Z.L. Wang et al, *Surf. Sci.* **273** (1992) 88.
14. J. Bentley, S. Tanaka, and R.F. Davis, unpublished research 1992.
15. Z.L. Wang and J. Bentley, *Microsc. Microanal. Microstruct.* **2** (1991) 301; *Ultramicroscopy*, in press.
16. This research was supported by the Division of Materials Sciences, U.S. Department of Energy, under contract DE-AC05-84OR21400 with Martin Marietta Energy Systems, Inc.

THE MORPHOLOGY OF ACID-CLEANED HEAT-TREATED MgO (100) SURFACES

Simon King and C. Barry Carter

Department of Chemical Engineering and Materials Science, Amundson Hall, 421 Washington Av SE,
University of Minnesota, Minneapolis, MN 55455

The widespread use of the (100) MgO surface as a substrate for the deposition particularly of high-Tc super-conductors,^{1,2} and a wide variety of other materials such as titania,³ has provoked considerable interest in the morphology of the surfaces employed. In the above studies, (100) oriented MgO specimens have generally been prepared according to the method of Norton et al. in which foils are cleaned in acid, with the active ingredient being aqua-regia, after perforation by ion-milling and before a heat treatment in air, typically for 10-15 mins at 1350°C.^{4,5} The surface morphology of specimens prepared in this manner is explored in this paper.

Many of the features common to the aqua-regia cleaned and heat-treated thin-films are shown in the (100) zone-axis bright-field (BF) image of fig 1(a). The general morphology of these foils includes a high density of holes within the thinnest regions, whilst pores are in evidence in thicker areas. Both holes and pores, which often are associated with pre-existing dislocations, result from the acid treatment necessary to remove ion-mill sputter damaged and contaminated surface regions. The faceting of the holes (e.g., at A) is explored in another paper in these proceedings.⁶ The background contrast in these foils undergoes abrupt changes indicative of surface-steps. In foils prepared using aqua regia, the step traces are generally highly curved and, hence, are not aligned along any particular direction, although short sections are occasionally observed to be faceted.^{6,7} Terraces between these steps range from a few tens to hundreds of nanometers across.

Particularly noticeable features of these micrographs are the narrow contrast bands, examples of which are arrowed. At B in figure 1(a), a wide (~35nm), single dark band is indicated. Notice, however, in the dark-field (DF) image of fig 1(b), that this band is now visible as a succession of six dark-bright fringes. This contrast may be explained as arising from step-faces which are shallowly inclined to the foil plane.⁷

Further corroborative evidence is provided in figure 2, in which a narrow contrast band visible in a zone-axis BF micrograph (fig 2(a)) is not seen in a corresponding, short extinction length, DF micrograph (fig 2(b)). It appears extremely unlikely that this band should represent an individual terrace, yet should not be visible in the "higher resolution", near-weak-beam micrograph; instead, figure 2 shows the statistically unusual case where the foil thicknesses either side of the step bracket an extremum in $|g \cdot r|$ for the BF case, but not for the DF case.

As mentioned above, steps in these foils are commonly found not to be aligned with any particular direction. The high density of holes and pores in these foils provides a vivid demonstration of the etching nature of aqua regia, leading to highly localized variations in average foil-normal orientations and relatively rapid changes in foil thickness. Steps, therefore, may be constrained artificially by the substrate morphology, such that significant faceting along low-energy directions is inhibited by the necessity that the step traces follow contours of constant thickness.

To investigate this possibility, specimens have recently been prepared by static polishing in orthophosphoric acid at ~100-120°C (the polishing plateau encompasses a wide temperature range; at least 90-150°C). Polishing with phosphoric acid, which in the past has successfully been employed when etching considerations have been paramount, such as for a TEM study of grain boundaries in MgO bicrystals,⁸ should lead to 'flatter' foils.

A preliminary observation of a phosphoric acid thinned specimen is shown in figure 3. Most step traces are now faceted along $\langle 011 \rangle$. Notice that, in common with the specimens prepared using aqua regia, these straight step traces also apparently have faces inclined to the (100) foil-plane normal, as is shown by the

narrow contrast bands (an example is arrowed) visible particularly in the short extinction length DF image of figure 3(b). A curious feature is that whilst holes in the aqua regia prepared samples have their dominant facet along $\langle 001 \rangle$, holes in the phosphoric acid prepared samples are faceted along $\langle 011 \rangle$. Further details of these, and other, morphological features in these foils will be discussed.⁹

References

- ¹ M.G. Norton and C.B. Carter; *Scanning Microsc.*, **6**, 385-398 (1992)
- ² M.G. Norton and C.B. Carter; *Physica C*, **172**, 47-56 (1990)
- ³ S.L. King and C.B. Carter; "*TiO₂ on MgO by PLD: The Effect of the Substrate Treatment*", this conference.
- ⁴ M.G. Norton and C.B. Carter; *J. Cryst. Growth* **110**, 641-651 (1991)
- ⁵ M.G. Norton et al; *Appl. Phys. Lett.*, **56**, 2246-2248 (1990)
- ⁶ S.L. King et al; "*TEM Observations of Surface-step and Hole-edge Faceting in Acid-etched and Annealed MgO Thin-foils*"; this conference.
- ⁷ S.L. King and C.B. Carter; *Proc. Symp. B*, M.R.S. Fall Meeting, Boston (1992) - in press
- ⁸ C.P. Sun and R.W. Balluffi; *Scripta Met.*, **13**, 757-761 (1979)
- ⁹ The authors acknowledge the support of the D.O.E. under grant number DE-FG02-92ER45465

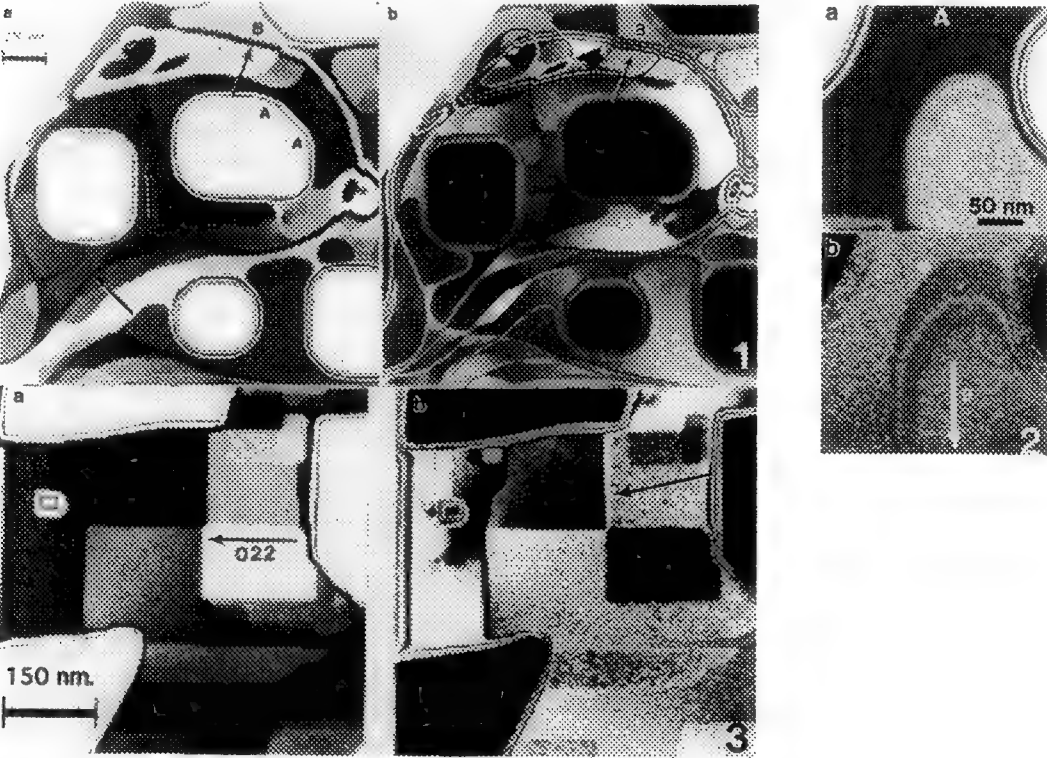


Fig.1: (a) and (b) (100) zone-axis BF, and near weak-beam DF micrographs of aqua-regia etched specimen annealed for 15.5 mins at 1350°C. See text for details.
 Fig.3: (a) and (b) (100) zone-axis BF, and near weak-beam DF micrographs of phosphoric acid etched specimen annealed for 10 mins at 1350°C. See text for details.

THE NATURE OF OXIDE SURFACES: TOPOGRAPHIC AND ELECTRONIC STRUCTURE

Dawn A. Bonnell and Yong Liang
The University of Pennsylvania, Philadelphia, PA 19104

Recent progress in the application of scanning tunneling microscopy (STM) and tunneling spectroscopy (STS) to oxide surfaces has allowed issues of image formation mechanism and spatial resolution limitations to be addressed. As the STM analyses of oxide surfaces continues, it is becoming clear that the geometric and electronic structures of these surfaces are intrinsically complex. Since STM requires conductivity, the oxides in question are transition metal oxides that accommodate aliovalent dopants or nonstoichiometry to produce mobile carriers. To date, considerable effort has been directed toward probing the structures and reactivities of ZnO polar and nonpolar surfaces¹, TiO₂ (110)² and (001)³ surfaces and the SrTiO₃ (001)^{4,5} surface, with a view towards integrating these results with the vast amount of previous surface analysis (LEED and photoemission)⁶ to build a more complete understanding of these surfaces. However, the spatial localization of the STM/STS provides a level of detail that leads to conclusions somewhat different from those made earlier. Furthermore, trends in oxide surface morphology and local structure are becoming clear. This paper illustrates these trends with an examination of the dependence of the morphology of the SrTiO₃ (001) surface on thermochemical history.

A SrTiO₃(001) single crystal surface was annealed under three different conditions: (1) UHV annealing in a vacuum of 5×10^{-10} Torr at 600 °C for 15 min. (2) UHV annealing under the same conditions for 35 min. (3) Reoxidation in a partial pressure of oxygen of 8×10^{-6} Torr at 800 °C for 45 min. Auger electron spectroscopy showed that annealing in UHV yielded a clean surface and LEED patterns exhibit weak 1×1 structure with streaking, indicating a two dimensional nature of the surface. STM images show that the three different conditions yielded three different surface morphologies on the nanometer scale, which can be characterized as: (1) low structural ordering for short time reduction; (2) high structural ordering (row-like structure) for a longer time reduction; (3) random structure after reoxidation.

The short time reduction produced a rough, cluster-type surface with features predominantly aligned along the [100] direction as shown in Fig.1. The size of the clusters typically ranges from 15 Å to 50 Å. One interesting consequence of the ordering is that the surface exhibits 2-fold symmetry instead of the 4-fold symmetry expected for a bulk-truncated perovskite (001) surface. On extending the annealing time for 35 min., distinct row-like features are observed in some areas of the surface as shown in Fig.2. The orientation of the rows is also along [100] direction with typical spacings of 12 Å, and 20 Å existing as lamellae. Four angstrom features, both along the rows and between the rows, are evident in some regions of the image. The vertical height of the corrugations is approximately 2 Å. The widths of the lamellae appears larger for the rows with 20 Å spacing than those with 12 Å spacing. The surface morphology underwent a significant change after annealing under oxygen ambient. The morphology of the reoxidized surface changed from previously highly ordered structures to a random structure with cluster-like features that are much larger than those on the reduced surfaces.

The STM images are consistent with formation of local phases of $\text{Sr}_{n+1}\text{Ti}_n\text{O}_{3n+1}$ where the order, i.e. n , depends upon the local degree of oxygen deficiency. Fig.3 illustrates the structures that result when $n=1$ (Sr_2TiO_4), and $n=2$ ($\text{Sr}_3\text{Ti}_2\text{O}_7$). The sizes of the unit cells are 12 Å along [001] direction (c direction) for Sr_2TiO_4 and 20 Å along [001] direction for $\text{Sr}_3\text{Ti}_2\text{O}_7$, respectively. The displacement described in Fig.3 results in a protrusion with a height of 2 Å and spacing of 12 Å for Sr_2TiO_4 and 20 Å for $\text{Sr}_3\text{Ti}_2\text{O}_7$, respectively, consistent with the STM images. We tentatively attribute the 4 Å feature to the perovskite subunit of the unit cell structure.

The formation of suboxides with periodic structures was also observed on TiO_2 surfaces and the cluster-like features have been observed on ZnO as well as TiO_2 . The potential generalization of this behavior in transition metal oxides will be discussed in detail in forthcoming publications.

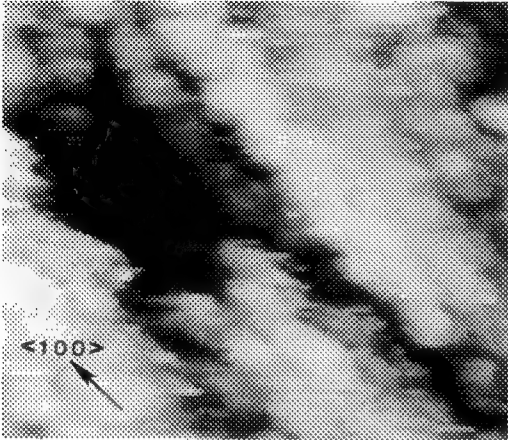


Fig. 1. Constant current STM image of 115 Å x 115 Å area; reduced 15 min.

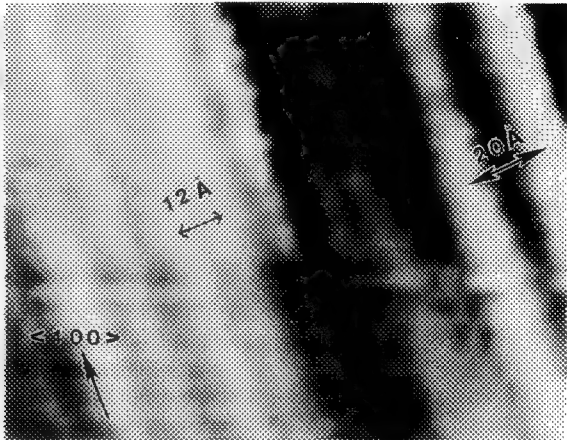


Fig. 2. Constant current STM image of 110 Å x 110 Å area; reduced 30 min.

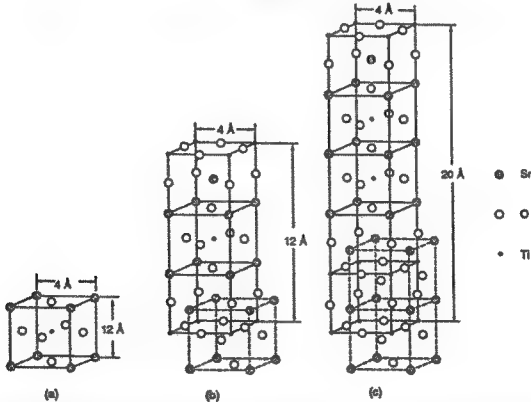


Fig. 3. Relationship between ideal perovskite (a) and the Sr_2TiO_4 (b) and Sr_3TiO_7 (c).

- 1 G. S. Rohrer, D. A. Bonnell *Surf. Sci.* **247** (1991) L195-L200.
- 2 G. S. Rohrer, V. Henrich, D. A. Bonnell *Science* **260** (1991) 1230-1241.
- 3 G. S. Rohrer, V. Henrich, D. A. Bonnell *Surf. Sci.* **274** (1992) 35-43.
- 4 P. Murray, F. Leibsle, H. Fisher, C. Flipse, C. Muryn, G. Thornton *Phys Rev. B.* (1992).
- 5 Y. Liang, D. A. Bonnell *Surf. Sci.* (1992)
- 6 Y. Liang, D. A. Bonnell *Proc. of Mat. Res. Soc.* (1993).
- 7 T. Matsumoto, H. Tanaka, T. Kawai, S. Kawai *Surf. Sci.* **278** (1992) L153.
- 8 See for example V. Henrich *Rep. Prog. Phys.* **48** (1985) 1481.

ZERO-LOSS ENERGY FILTERED REM AND RHEED OBSERVATIONS ON RUTILE (110) SURFACE

L. Wang, J. Liu* and J. M. Cowley

Department of Physics, Arizona State University, Tempe, AZ 85287

*Center for Solid State Science, Arizona State University, Tempe, AZ 85287

In reflection electron microscopy (REM), the surface reflection electrons undergo both elastic and inelastic scattering within a crystal. The dominant inelastic processes are phonon scattering, valence electron excitation, bulk and surface plasmon excitation and combinations of these processes. Multiple inelastic scattering processes are also probable as the mean traveling distance of surface reflection electrons is about 10 to 100 nm. In reflection high energy electron diffraction pattern (RHEED), 50% to 90% of the electrons contributing to surface reflection spots used for imaging have suffered energy loss of more than 10 eV, thus the main limitation on REM image resolution is due to the chromatic aberration effects given by the energy spread from inelastic scattering.¹ An energy filter fitted inside a TEM microscope can remove most of the inelastic scattering contribution and so improve the contrast and resolution.² Oxygen-annealed rutile (001), (100) and (110) surfaces were previously studied by REM and RHEED techniques without energy filtering.^{3,4} In this paper, we report further investigation of oxygen-annealed rutile (110) surface by using energy filtered REM and RHEED.

The sample preparation is the same as in the previous work.^{3,4} The experiment was carried out at 120 kV with a Zeiss 912 TEM, which is fitted with an omega magnetic imaging energy filter and a Gatan 679 CCD camera with suitable software to record "parallel EELS" results.⁵ All REM images and RHEED patterns were recorded digitally into picture of 1024x1024 pixels. The sample was kept at -140°C with a cold-stage sample holder.

Figure 1 presents a zero-loss REM image obtained by using an omega filter with an energy window about 9 eV. Most inelastically scattered electrons are removed from the image and the contribution of phonon diffuse scattering is reduced with the use of a cold-stage sample holder. The contrast is improved in the elastic REM image. The imaging condition is shown by the inset RHEED pattern. Extra half-order spots (arrowed in inset) are clearly revealed. These half-order spots may be due to a surface reconstruction. Figure 2a shows an unfiltered convergent beam RHEED pattern obtained with the incident beam along the $[1\bar{1}1]$ zone axis. Figure 2b is a zero-loss convergent beam RHEED pattern with the same settings of the energy filter as for figure 1. The contrast is dramatically increased in figure 2b and the details of the elliptical arcs, typical of those for a convergent beam pattern, are seen much more clearly. It is to be noted that the Kikuchi lines and parabolas in figure 2b, due to thermal diffuse scattering followed by elastic scattering are sharper and clearer than in figure 2a since the small-angle inelastic scattering was excluded. However, the electrons undergoing phonon diffuse scattering can not be removed by the filter,⁶ thus they still contribute to the image contrast in figure 1 and figure 2b.⁷

References

1. J. M. Cowley, Proc. Ann. EMSA Meeting 49(1991)482.
2. J. C. H. Spence and J. Mayer, Proc. Ann. EMSA Meeting 49(1991)616.
3. J. Liu et al., Proc. Ann. EMSA Meeting 49(1991)646.
4. L. Wang et al., Proc. Ann. EMSA Meeting 50(1992)1462.
5. S. Lanio, Optik 73(1986)99. See also S. Kujawa et al. 86(1990)39.
6. L. M. Peng and J. M. Cowley, Ultramicroscopy 29(1989)168.
7. This work was supported by NSF grant DMR-9110386 and Shell Development Company and made use of the ASU Center for HREM supported by NSF grant DMR-9115680. The authors thank Dr. M. McKelvy, D. Wright and T. Karcher for help with sample annealing.

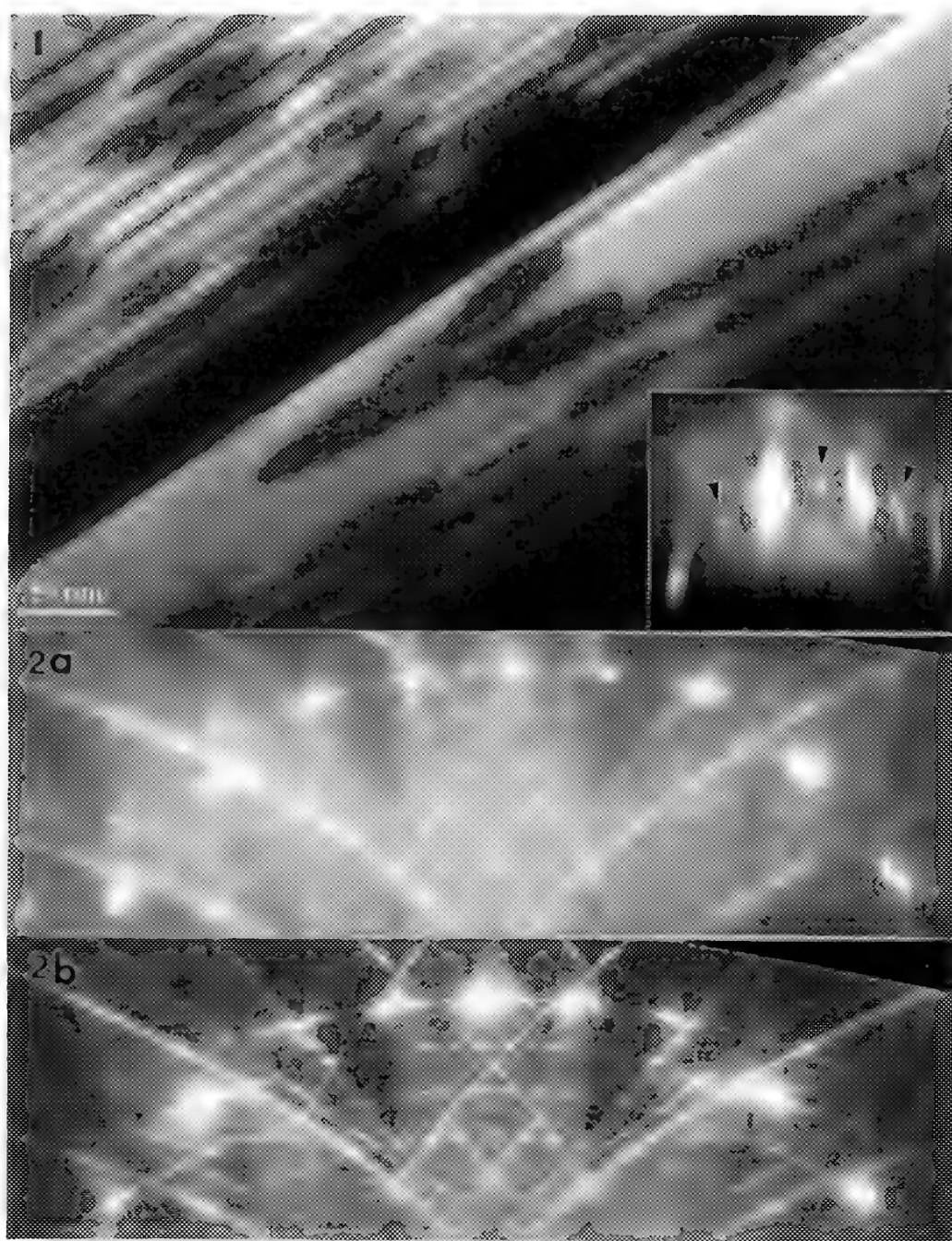


Fig. 1.--Zero-loss REM image of oxygen annealed rutile (110) surface.

Fig. 2a.--Unfiltered CB-RHEED pattern of rutile (110) surface with incident beam along $[1\bar{1}1]$ zone axis.

Fig. 2b.--Zero-loss CB-RHEED pattern of rutile (110) surface with incident beam along $[1\bar{1}1]$ zone axis.

SPHERICAL ABERRATION-FREE OBSERVATION OF RECONSTRUCTED Au(011)2×1 SURFACE BY HRTEM USING DEFOCUS-MODULATION IMAGE PROCESSING

Yoshizo Takai, Yoshifumi Taniguchi, Takashi Ikuta* and Ryuichi Shimizu

Department of Applied Physics, Faculty of Engineering, Osaka University,
2-1 Yamada-oka, Suita, Osaka, 565 Japan

*Department of Applied Electronics, Osaka Electro-Communication University,
18-8 Hatsu-machi, Neyagawa, Osaka, 572 Japan

The surface profile imaging technique by HRTEM has a good potential for observing surface reconstructions¹. It also has possibilities for measuring with high accuracy the displacement of atoms in the direction perpendicular to the surface². However, surface profile images have been strongly influenced by imaging parameters such as defocus and spherical aberration. Therefore atom images generally appear to be appreciably displaced from their actual positions in crystal. In order to correct the spherical aberration in the image, the authors have recently developed a novel approach based on defocus-modulation image processing³ and experimentally confirmed that spherical aberration can be corrected very well by this method⁴, as shown in a symmetric Thon diagram reproduced from amorphous carbon images,

In the present paper, a reconstructed (011) gold surface has been observed by HRTEM (HF-2000) with a field emission gun at an accelerating voltage of 200kV. Phase shift caused by spherical aberration has been corrected by an attached defocus-modulation image processing system, which records through focus images by changing the objective lens current while controlling image shift coils to compensate image drift. Fig.1 shows HRTEM images of a (011) gold crystal which were taken at just focus for (a), near Scherzer focus (71 nm) for (b) and 159 nm under-focus for (c). Although the shape can be seen most clearly at the Scherzer condition, all the images are insufficient to determine actual atom positions in the crystal, because of the appearance of extra interference fringes outside the crystal region in (a), weak lattice contrast in (b) and blurring of the edge shape in (c). Fig.2 shows a processed phase contrast image, which was reconstructed by image integration of 256 original through-focus images with a positive-negative weighting function. The image corresponds to a phase contrast image at just focus by an ideal lens without spherical aberration. The lattice image near the surface is clearly seen with strong bright contrast and the atomic steps can be seen clearly without blurring. In the image, one can find, locally, areas which show the 2×1 missing-row reconstruction. Some of the intensity maxima of the top surface indicated by arrows seem to be shifted a little inside of the normal atom positions in crystal. Using through-focus images calculated on the basis of an electron dynamical diffraction theory⁵ and an image formation theory⁶, a computer simulation of the same image processing was performed and is inserted below in Fig.2. By comparison of the two processed images, the observed distortion of the lattice image near the surface has been confirmed not to be due to the effect of spherical aberration or an artifact of the processing but to the displacement of atoms in the crystal, because no displacement of atom images can be seen in the result calculated by the model without distortion.

References

1. L.D. Marks, Surface Science (1984)139,281.
2. N.Ikarashi et al., Ultramicroscopy (1988)26,195.
3. T.Ikuta, J Electron Microscopy (1989)38,415.
4. Y.Taniguchi et al., Ultramicroscopy (1992)41,323.
5. A.Howie, M.J.Whelan, Proc R Soc (1961)A263,217.
6. K.Ishizuka, Ultramicroscopy (1980)5,55.

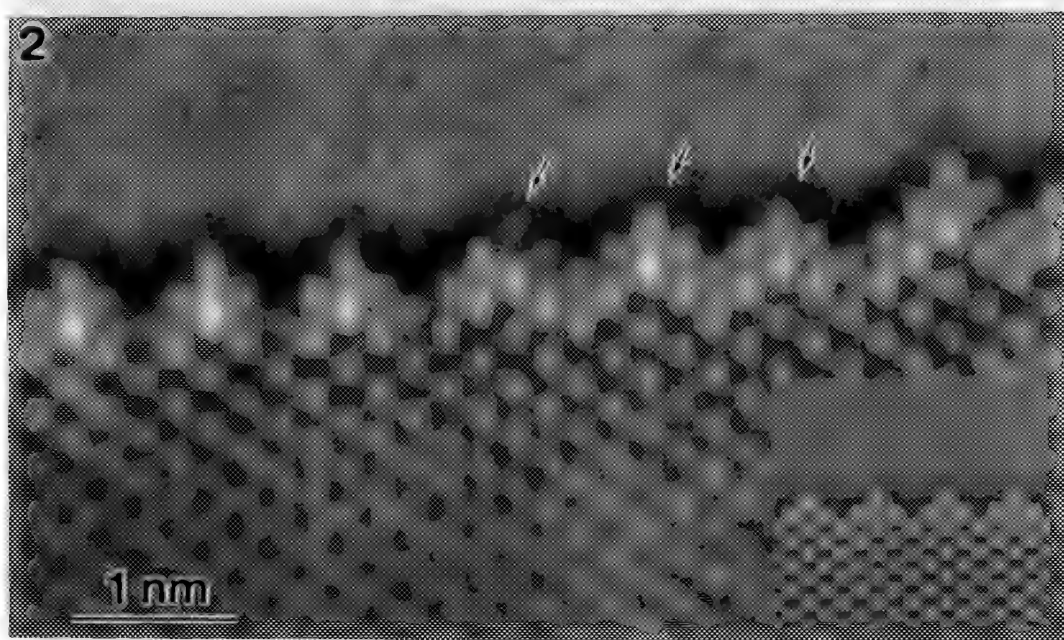
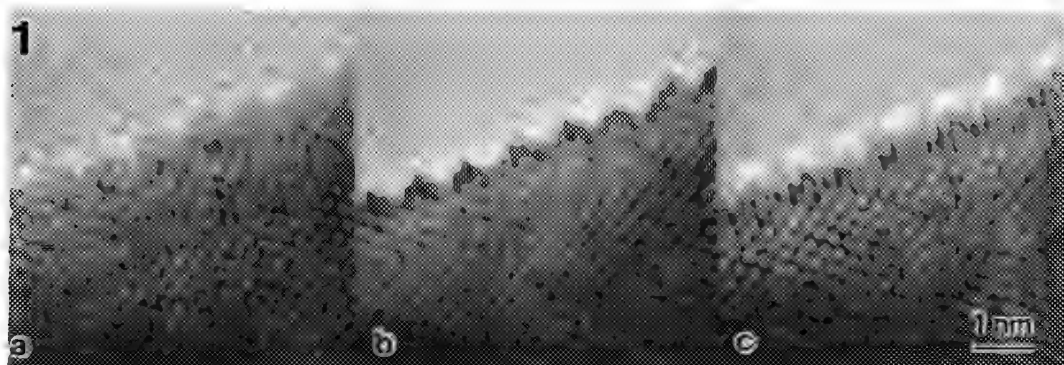


Fig.1. Through-focus images by profile imaging. (a) just focus, (b) 71 nm under-focus (Scherzer defocus), (c) 159 nm under-focus.
 Fig.2. Phase contrast image of reconstructed Au(011)2x1 surface by defocus-modulation image processing.

THREE-FOLD ASTIGMATISM: AN IMPORTANT TEM ABERRATION

O.L. Krivanek and M.L. Leber

Gatan Research and Development, 6678 Owens Drive, Pleasanton, CA 94588

Three-fold astigmatism resembles regular astigmatism, but it has 3-fold rather than 2-fold symmetry. Its contribution to the aberration function $\chi(q)$ can be written as:

$$\chi_3(q) = [A_3 \lambda^2 q^3 \cos 3(\phi - \phi_3)] / 3 \quad [1]$$

where A_3 is the coefficient of 3-fold astigmatism, λ is the electron wavelength, q is the spatial frequency, ϕ the azimuthal angle ($\phi = \tan^{-1}(q_y/q_x)$), and ϕ_3 the direction of the astigmatism.

Three-fold astigmatism is responsible for the "star of Mercedes" aberration figure that one obtains from intermediate lenses once their two-fold astigmatism has been corrected. Its effects have been observed when the beam is tilted in a hollow cone over a wide range of angles¹, and there is evidence for it in high resolution images of a small probe obtained in a field emission gun TEM/STEM instrument². It was also expected to be a major aberration in sextupole-based C_s correctors, and ways were being developed for dealing with it on C_s -corrected STEMs³. However, many high resolution electron microscopists appear to be unaware of it, even as they are pushing to improve the resolution of the microscopes to a level at which this aberration is likely to make its presence strongly felt.

The lack of general awareness of the importance of three-fold astigmatism is probably due to two factors that have helped to make it "invisible". First, since it is antisymmetric, its contributions from $+q$ and $-q$ spatial frequencies to a diffractogram cancel, and thus it has no noticeable effect on a single diffractogram. Second, because the antisymmetric lobes it adds to images of individual atoms may cancel out when the atoms are placed in a centrosymmetric array, its effects may be masked in weak phase images of centrosymmetric crystals. However, non-centrosymmetric images (such as images of defects) and images of single atoms taken both in TEM and STEM modes will be fully affected by it. The expected strength of the three-fold astigmatism of the objective lens is of the same order of magnitude as the lens's inherent normal astigmatism (two-fold astigmatism that would be present if the electromagnetic stigmators were switched off) - typically around 1 μm .

The three-fold astigmatism of the objective lens is best detected by tilting the incident beam in a hollow cone pattern, and measuring either the resultant image shift, or the variation of tilt-induced apparent astigmatism. In the absence of any astigmatism or beam misalignment, when the beam is tilted around the cone, the image shift will trace a perfect circle of radius $r = C_s \theta^3 + \Delta Z \theta$, where C_s is the coefficient of spherical aberration, θ is the induced beam tilt, and ΔZ is the defocus. The tilt-induced apparent 2-fold astigmatism vector will trace out a perfect circle of radius $C_s \theta^2$. When 3-fold astigmatism is present, the shift circle will become distorted as shown in Fig. 1, with the peak distortion amounting to $A_3 \theta^2$. The astigmatism circle will be distorted in a similar manner, with the distortion amounting to $2 A_3 \theta$. These results were obtained by taking the first and second derivative of $\chi_3(q)$ with respect to q , and will be reported in full elsewhere⁴. Note that because the distortion of the circle of apparent astigmatism contains θ to the first power, the effect is present with θ of only a few mrad. The shift distortion depends on θ^2 , and the presence of the 3-fold astigmatism will only be detectable for relatively large θ of the order of 30-100 mrad with the shift method.

Using the tilt-induced two-fold astigmatism method on a particular HREM (Philips CM12ST) gave the experimentally measured astigmatism variation as a function of the azimuthal angle shown in Fig. 2. The figure also shows the best theoretical fit, calculated for three-fold astigmatism of 0.57 μm magnitude pointing in the direction of 63°. The microscope was equipped with a slow scan CCD camera (Gatan 694) and software which implemented the required beam tilts, acquired a number of images, computed their digital diffractograms, and worked out the two-fold astigmatism variation by automatic diffractogram

analysis (Gatan's DigitalMicrograph). The hollow cone semi-angle was 5 mrad.

0.57 μm of 3-fold astigmatism is probably on the low side of the range of values that will be encountered in most HREMs. The amount of maximum aberration function distortion that $A_3 = 1 \mu\text{m}$ will produce in a 200 keV microscope for different spatial frequencies is listed in Table 1. Remembering that a change of 0.5 in $\chi(q)$ reverses the contrast of the spatial frequency q from white to black (or vice versa), one can see that $A_3 = 1 \mu\text{m}$ is barely tolerable at 2 Å resolution, and that if one is trying to reach 1 Å resolution, 3-fold astigmatism larger than 0.1 μm will prevent its attainment.

In summary, careful analysis of the imaging properties of the objective lens of any high resolution electron microscope is likely to find 3-fold astigmatism of a strength that may just permit 2 Å resolution, but which will need correcting if 1 Å resolution is to be achieved. A pair of crossed sextupoles placed next to the objective lens stigmators inside the microscope column will be sufficient for the correction. The adjustment of the sextupoles will be best done by a computer-automated analysis using a slow scan CCD camera and suitable software, and it may well become the first microscope tuning task that humans will not be able to carry out without the assistance of a computer.

References

1. M.M.J. Treacy, unpublished results.
2. J.K. Weiss, R.W. Carpenter and A.A. Higgs, Ultramicroscopy **36** (1991) 319.
3. P.E. Mooney, private communication.
4. O.L. Krivanek et al., to be published.

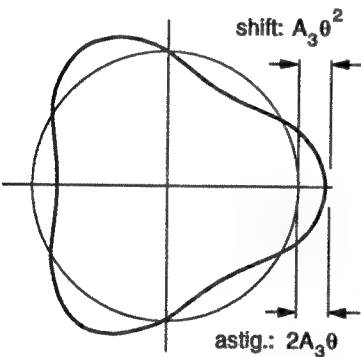


Fig. 1 Patterns traced out by image shift and apparent 2-fold astigmatism as the beam is tilted in a hollow cone pattern. Circle: no 3-fold astigmatism. 3-fold figure: 3-fold astigmatism present.

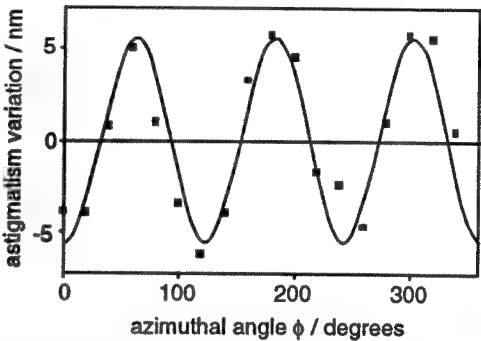


Fig. 2 Points: variation of the magnitude of apparent 2-fold astigmatism measured as the beam was tilted in a hollow cone pattern. Philips CM12ST, 120 keV. Curve: theoretical fit for $A_3 = 0.57 \mu\text{m}$.

resolution (Å)	spatial frequency q (nm^{-1})	$\chi_3(q)$
5	2	0.02
3	3.3	0.06
2	5	0.26
1.5	6.7	0.62
1.0	10	2.08

Table 1. The effect of 3-fold astigmatism of 1 μm amplitude on the aberration function of a 200 keV electron microscope.

USING CONVERGENCE AND SPREAD-OF-FOCUS PARAMETERS TO MODEL SPATIAL AND TEMPORAL COHERENCE IN HRTEM IMAGE SIMULATIONS

Jan-Olle Malm* and Michael A. O'Keefe

National Center for Electron Microscopy, University of California, LBL B72, Berkeley, CA 94720

*Permanent address: National Center for HREM, Lund University, S-221 00 Lund, Sweden

In all HRTEM images, the incident electron beam suffers from the effects of limited spatial and temporal coherence. These effects produce a smearing of the image, and provide the ultimate limits as to how high a spatial frequency can be transferred to the image (i.e. resolution¹). The effect of partial temporal coherence is manifested as a spread of focus², and that of partial spatial coherence as incident beam convergence.³ The effects of partial coherence can be included in HRTEM image simulations by summing images in real space³, or by applying an appropriate transmission cross-coefficient (TCC) when computing the image intensity spectrum in reciprocal space.⁴ Figure 1 shows a method of including the effects of incident beam convergence by real-space summation. The degree of convergence is estimated by measuring the spot size in the experimental diffraction pattern (a). Each spot in the diffraction pattern is sub-sampled (b), and a series of images is computed at incident beam angles appropriately sampling the convergence cone. The images are added to produce the final result (c), which matches experiment.³ In reciprocal space, an approximately equivalent result can be obtained by modelling each diffraction spot with a top-hat function of appropriate size; then the TCC result matches real-space summation results (and also experiment).⁵

For linear images (from specimens thin enough to behave as weak phase objects), the TCC can be simplified and described in terms of "damping envelope" functions that multiply the usual phase-contrast transfer function⁶. The envelope for a top-hat convergence model is then $2J_1(x)/x$, where $x = \{2\pi\alpha(\epsilon + \lambda^2 C_s k^2)k\}$. A further approximation is to use a gaussian model for the diffraction spot intensity, giving an envelope of the form $\exp(x)$, where $x = \{-\pi^2\sigma^2(\epsilon + \lambda^2 C_s k^2)^2 k^2\}$ with σ the standard deviation of the gaussian. In the case of the top-hat model, the radius of the top-hat is obviously correct when set to the convergence semi-angle α ; for the gaussian model the standard deviation σ of the gaussian is proportional to α . We need to determine the proportionality constant, especially since many simulation programs use a gaussian model to form the TCC used in simulating images. Comparisons of plots of top-hat and gaussian damping functions show that they match when σ is set to 0.77α (fig. 2). Several other expressions for gaussian convergence damping envelopes exist, but none of these appears to have been tested against the top-hat result. Spence⁷ and Reimer⁸ use a gaussian with α set to the half-width at half maximum (HWHM), Krivanek⁹ uses the spot diameter (2α) as the FWHM, and Stadelmann¹⁰ chooses half the HWHM. The standard deviations used by these authors to compute the damping envelope will thus range over a factor greater than two for the same value of α . Less variation occurs in the gaussian spread-of-focus envelope, which has the form $\exp\{-\frac{1}{2}\pi^2\lambda^2\sigma^2 k^4\}$, where σ is the standard deviation of a one-dimensional gaussian. O'Keefe¹ and Spence⁷ set σ equal to the spread of focus, Δ ; Reimer⁸, Krivanek⁹, and Stadelmann¹⁰ set Δ equal to the FWHM of the gaussian. Figure 3 shows the different damping envelopes obtained for the same nominal values of α and Δ by the various expressions (the numbers on the curves indicate the references). This result illustrates how differences in TCCs, and thus simulated images, can arise.¹¹

1. M.A. O'Keefe, *Ultramicroscopy* **47** (1992) 282-297.
2. P. Fejes, *Acta Cryst.* **A33** (1977) 109-113.
3. M.A. O'Keefe and J.V. Sanders, *Acta Cryst.* **A31** (1975) 307-310.
4. M.A. O'Keefe, *37th Ann. Proc. EMSA*, San Antonio, Texas (1979) 556-557.
5. G.R. Anstis and M.A. O'Keefe, *34th Ann. Proc. EMSA*, Miami Beach, Florida (1976) 480-481.
6. J. Frank, *Optik* **38** (1973) 519-536.
7. J.C.H. Spence, *Experimental HREM*, Oxford University Press, 1988.
8. L. Reimer, *Transmission Electron Microscopy*, Springer-Verlag, 1989.
9. O.L. Krivanek, *HRTEM and Associated Techniques*, Oxford University Press, Chapt 12, 1992.
10. P.A. Stadelmann, *Ultramicroscopy* **21** (1987) 131.
11. Work supported by the Director, Office of Energy Research, Office of Basic Energy Sciences, Material Sciences Division of the U.S. Department of Energy, under contract No. DE-AC03-76SF00098.

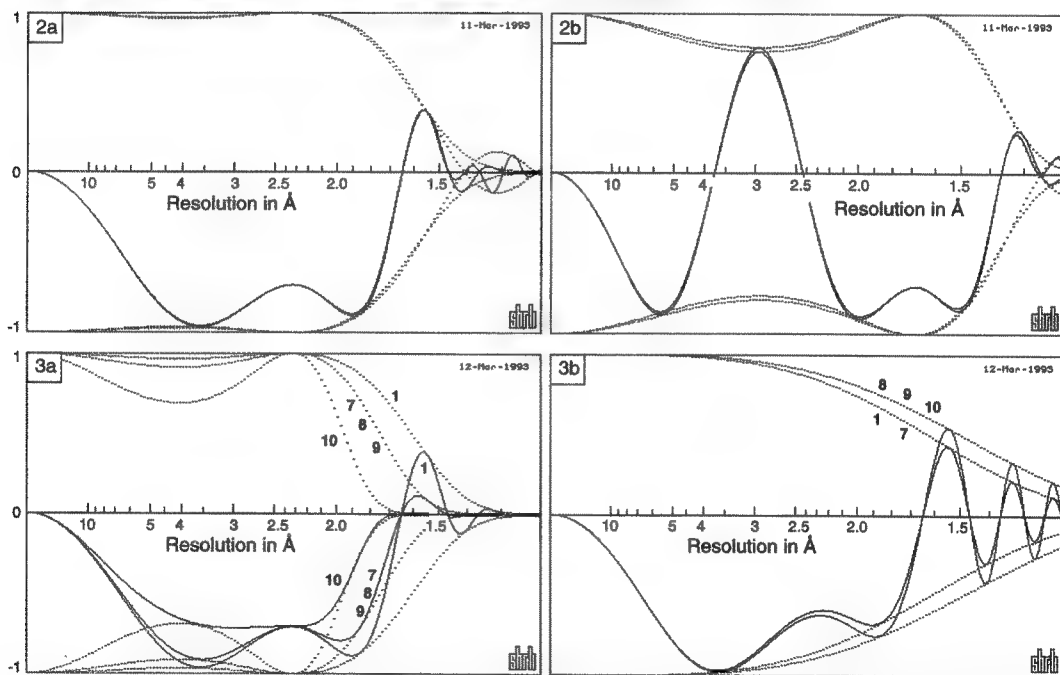
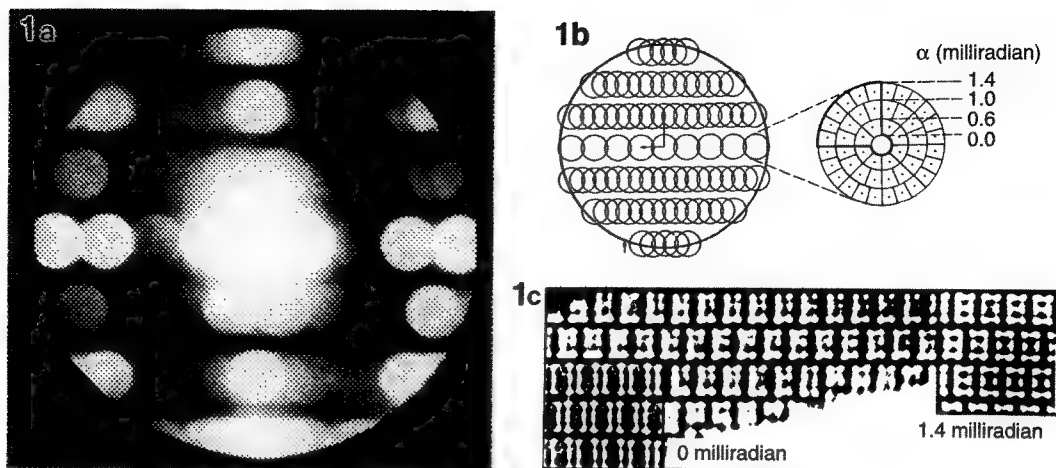


Figure 1. (a) Experimental diffraction pattern of $\text{Nb}_{12}\text{O}_{29}$ with illumination set for imaging, showing the degree of incident beam convergence and the objective aperture size. (b) Model of (a) showing the 49 sampling angles used for each spot. (c) A simulation without summation (left) does not match the experimental image, whereas one with summation over the full 49 angles does (right).

Figure 2. Phase-contrast transfer functions (solid lines) and convergence damping functions (dotted) for the gaussian and top-hat models. The curves match (except that the gaussian envelope falls smoothly to the axis, whereas the top-hat envelope crosses it) for $\sigma=0.77\alpha$. Plots for 400keV, $C_s=1.0\text{mm}$, $\alpha=1.0$ milliradian, and defocus values of (a) $\sqrt{1.5}$ scherzers, and (b) $\sqrt{5.5}$ scherzers.

Figure 3. Phase-contrast transfer functions and damping functions for (a) gaussian model of convergence at $\alpha=1.0$ milliradian, (b) gaussian model of spread of focus at $\Delta=60\text{\AA}$. Numbers on the curves refer to expressions used in the references. Plots for 400keV, $C_s=1.0\text{mm}$, and defocus value of $\sqrt{1.5}$ scherzers.

THICKNESS-DEPENDENT ANNULAR DARK-FIELD STEM

Sean Hillyard,* and John Silcox*

*Applied and Engineering Physics, Cornell University, Ithaca, NY 14853

The demonstration of Z-contrast atom structure images¹ and high spatial resolution² using annular dark field STEM³ has drawn considerable interest. This approach is well suited for quantitative image and diffraction pattern acquisition.⁴ Experimental data has been used to validate calculations of convergent beam electron diffraction (CBED) patterns in silicon⁵ and ADF STEM images of (100) InP.⁶ These procedures can be extended to explore the dependence of images on factors such as thickness.

Energy filtered CBED patterns over an angular range of over 150 mrad and covering a range of over four orders of magnitude in intensity from silicon were recorded with a VG HB501A STEM for thicknesses of 217Å, 326Å and 543Å. Simulation using a "frozen phonon" approximation successfully modeled⁵ this data provided an accurate phonon amplitude was used. A similar quantitative study for images has been carried out for (100) oriented InP. This sample contains indium columns at the corner of a 2.9Å square and phosphorus atoms at the square center. Both the experimental images and the simulated images are consistent with the incoherent imaging model.⁶ This makes it possible to factor out effects due to the contrast transfer function and determine an instrument independent specimen scattering function as a function of thickness.

Simulations of (100) InP images at different thicknesses up to 587Å were carried out and treated to compensate for probe shape effects. That component of the image associated with scattering from the indium columns was found to saturate at approximately 100Å thickness whereas that associated with the phosphorus signal grew steadily (but more slowly) up to the thickness limit. This behavior corresponds to the predicted channeling effects that arise when the probe is located either on the indium or phosphorus atom columns. The channeled probe first grows and then shrinks, disappearing completely after 100Å when located on the indium columns⁷.

To provide experimental evidence for this, we note that the intensities of the two lattice fringes at 2.9Å and 2.1Å spacing behave differently with thickness (see figure 1). By determining the ratio of the two intensities at different thicknesses, it should be possible to eliminate intensity variations. In figure 2, we show experimental data compared with the predictions of figure 1. Thickness is determined by plasmon intensity measurements. Good agreement is obtained if the effective source size is permitted to vary within reasonable limits.⁸

1. S.J. Pennycook, *Ultramicroscopy* 30 (1989) 58.
2. P. Xu, E. J. Kirkland, J. Silcox and R. J. Keyse, *Ultramicroscopy* 32 (1990) 93.
3. A. V. Crewe et al., *Physical Aspects of Electron Microscopy and Microbeam Analysis*, eds. B. M. Siegel and D.K. Beaman, New York: Wiley (1975) 47.
4. E. J. Kirkland, *Ultramicroscopy* 32 (1990) 349.
5. R. F. Loane et al., *Acta Cryst. A* 47 (1991) 267; P. Xu et al., *Ultramicroscopy* 38 (1991) 127.
6. R. F. Loane et al., *Ultramicroscopy* 40 (1992) 121.
7. S. Hillyard et al., *Ultramicroscopy* (1992) to appear.
8. This work was supported by DoE (Grant #DE-FG02-87ER45322). Sean Hillyard holds a DoED fellowship. The UHV-STEM was acquired through NSF (Grant #DMR-8314255) and is operated by the Cornell Materials Science Center (NSF Grant #DMR-9121654).

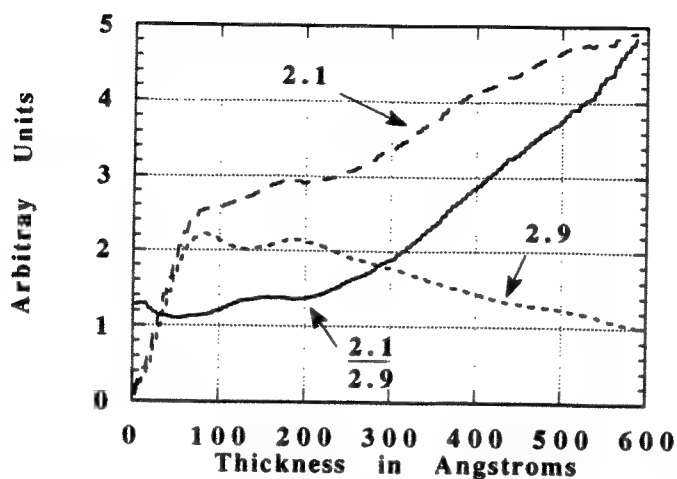


Figure 1. Result of simulations of Fourier fringe intensities at 2.9 Å and 2.1 Å spacings as a function of thickness. The divergence at thicknesses above c 100 Å reflects the saturation of the indium column signal and growth of the phosphorus column signal. The solid line shows the change in the ratio of the intensity of the 2.1 Å fringe relative to the 2.9 Å fringe.

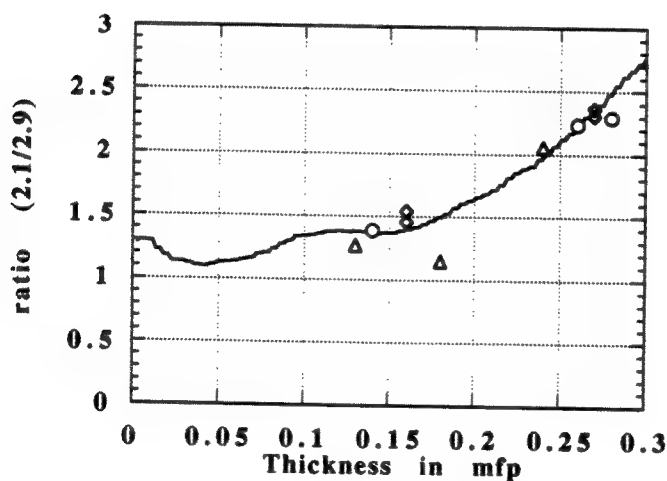


Figure 2. Experimental measurements (symbols) of the intensity ratio 2.1/2.9 compared with the simulation (see figure 1) as a function of thickness in terms of plasmon mean free path (~1300 Å). Different symbols reflect different runs.

INCOHERENCE IN ATOMIC-RESOLUTION Z-CONTRAST IMAGING

D. E. Jesson and S. J. Pennycook

Solid State Division, Oak Ridge National Laboratory, Oak Ridge, Tennessee 37831-6030

Incoherent imaging of atomic clusters, monolayer rafts, or low index crystal projections at atomic resolution in a scanning transmission electron microscope (STEM) offers a number of distinct advantages over coherent imaging methods. These include an improved "interpretable" resolution and no experimental contrast reversals with specimen thickness or objective lens defocus. However, considerable controversy and confusion has arisen concerning the conditions under which the image of a given object can be interpreted using incoherent imaging theory. Here, we attempt to clarify the situation.

Firstly, we consider the case of very thin specimens, such as heavy atoms, clusters of atoms, or extremely thin crystals. Experimentally, these specimens demand a relatively low annular detector inner radius to achieve an acceptable signal-to-noise ratio in the image. It is usual, therefore, to match the detector inner radius to the radius of the directly transmitted disc. In this conventional geometry, the annular dark-field signal will be dominated by coherent scattering, and the use of incoherent imaging theory may give rise to appreciable error close to the resolution of the STEM instrument.¹ However, it is possible to circumvent this problem² by increasing the inner detector angle θ_i as demonstrated in Fig. 1. This figure plots the ratio of the detected/incoherent signal as a function of θ_i for two silicon atoms separated by 1.0 and 1.5 Å. At small θ_i , there is significant departure from incoherent imaging, although this is reduced to less than 10% by increasing θ_i to 30 mrad. Physically, this improvement is linked to sampling an increased number of interference fringes around the detector periphery.

A more general criterion for the minimum detector angle θ_i^{inc} for incoherent imaging is

$$\theta_i^{\text{inc}} = \frac{1.22\lambda}{\Delta R} \quad (1)$$

which corresponds to the second minima in Fig. 1 where the detected and incoherent signals differ by about 5%. Here λ is the electron wavelength and ΔR is the atomic separation. In practice, many of the early STEM images of atomic clusters were obtained under conditions consistent with Eq. (1) so that the use of incoherent imaging theory was valid for the transverse direction. It is important to emphasize, however, that an ADF detector will not destroy interference between atoms in a column. In particular, the intensity of an atomic column should increase as the number of atoms in the column squared. Since a single atom will appear a factor of 4 fainter than two atoms with the same projected coordinate, it would be quite possible to misinterpret such weak features in an image. This might explain the apparent linear imaging observed by Isaacson et al.³ since by ignoring the intensity level of a single atom, n^2 increases almost linearly between $n = 2$ and 4. For longer columns, the phase object approximation breaks down, and the high-angle coherent signal is rapidly replaced by thermal diffuse scattering (TDS).

Recently, we have derived a TDS absorption model⁴ based on the Warren shell approach to thermal vibrations.⁵ This is equivalent to replacing the absorptive form factors in the usual Einstein model⁶ with form factors involving the sum over correlated atoms within a shell. At high angles, the model shows that transverse incoherence is again a good approximation so that atomic columns can be considered to scatter independently. In practice, this independence can prove to be a significant asset in the study of unknown interfacial structures.^{7,8} However, residual correlations preserve to some extent along the column so that the high-angle signal originates from the collective scattering of "atom packets" (Fig. 2). Since for moderate angles the size of these packets is typically much smaller than a column length, each packet can be considered to scatter incoherently, although the phase relationships within a packet can amplify the high-angle signal. The effective correlation factor^{4,5} between the zeroth and n -th atom within a column is calculated in Fig. 3 (solid line). Perfect coherence would correspond to a correlation factor of unity along the column whereas total incoherence (the Einstein model) is equivalent to a delta function

at the zeroth atom. The phase preservation in our absorption model has important implications not only for high-angle scattering, but also for the attenuation of tightly bound fast electron states in general. This should be amenable to study in a 300 kV STEM, which will provide a column-by-column absorption map of *s*-states.⁹

References

1. J. M. Cowley, *Ultramicroscopy* **2** (1976) 3.
2. D. E. Jesson and S. J. Pennycook, *Proc. Roy. Soc.* (in press).
3. M. Isaacson, M. Ohtsuki, and M. Utlaut in *Introduction to Analytical Electron Microscopy* (ed. J. J. Hren, J. Goldstein, and D. C. Joy) Plenum Press, New York-London (1979) 343.
4. D. E. Jesson and S. J. Pennycook (in preparation).
5. B. E. Warren, *X-Ray Diffraction*, Dover Publications, Inc., New York (1969).
6. See, for example, C. R. Hall and P. B. Hirsch, *Proc. Roy. Soc. A* **286** (1965) 158.
7. S. J. Pennycook and D. E. Jesson, *Acta Metall. Mater.* **40** (1992) S149.
8. D. E. Jesson, S. J. Pennycook, and J.-M. Baribeau, *Phys. Rev. Lett.* **66** (1991) 750.
9. This research was sponsored by the Division of Materials Sciences, U.S. Department of Energy, under contract DE-AC05-84OR21400 with Martin Marietta Energy Systems, Inc.

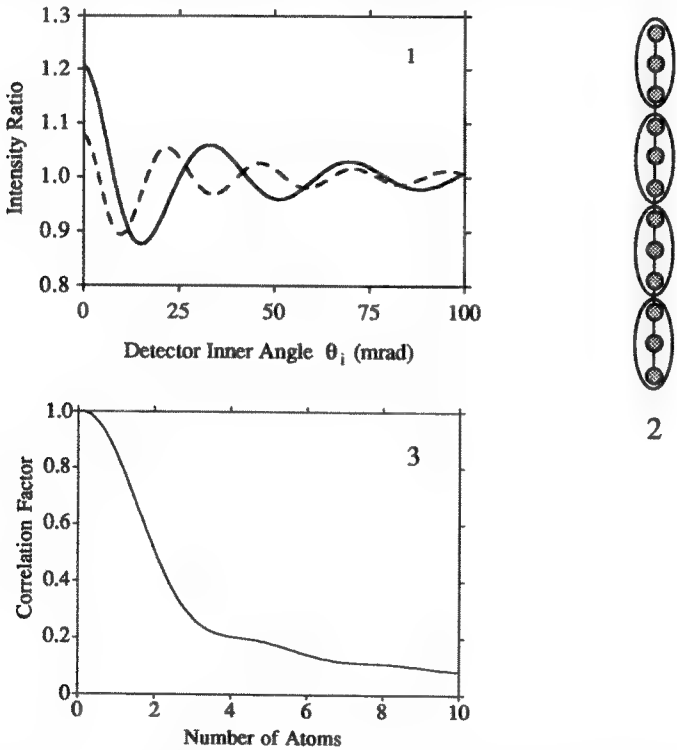


FIG. 1.--Ratio of the ADF signal to the coherent signal from two Si atoms separated by 1.0 Å (solid line) and 1.5 Å (dashed line) as a function of inner detector angle θ_i .
 FIG. 2.--Schematic representation of an atomic column which is considered to scatter as correlated "packets".
 FIG. 3.--Correlation factor between the zeroth and *n*-th atom of an atomic column (see text).

THE EFFECTS OF SMALL CRYSTAL TILTS ON DYNAMICAL SCATTERING: WHY SIMULATED IMAGES ARE THINNER THAN EXPERIMENTAL ONES

Michael A. O'Keefe and Velimir Radmilovic[♦]

National Center for Electron Microscopy, University of California, LBL B72, Berkeley, CA 94720

[♦]Permanent address: University of Belgrade, Dept. of Physical Metallurgy, Belgrade, Yugoslavia

It is now well-established that high-resolution transmission electron microscope image simulation can accurately reproduce experimental HRTEM images when imaging parameters are accurately known. These parameters include specimen properties such as unit cell structure, crystal orientation, and specimen thickness, as well as microscope parameters such as beam energy and coherence (both spatial and temporal), objective aperture size, and objective lens defocus and spherical aberration. Of these parameters, the most difficult to measure, and thus to include accurately, is the specimen thickness (and also the temporal coherence; on the other hand, although spatial coherence is easily measured, its effects are not always accurately included in all simulations¹). In many investigations that utilize matches between experimental and simulated HRTEM images, specimen thickness is treated as a disposable parameter; i.e. the experimental specimen thickness is not measured, but assigned to be the thickness that was used in the simulation program to produce the simulated image that best matched the experimental one. Such a procedure can be dangerous, because image character is not unique; i.e. the same image can be found at a different thickness if other conditions are allowed to vary within measurement errors. For example, image maps show that there is a trade-off between objective lens defocus and specimen thickness.²

Changes in image character with increasing specimen thickness occur due to changes in the amplitudes of the diffracted beams leaving the specimen exit surface; changes in the phase of a diffracted beam alter its contribution to the image by altering its transference into terms in the image intensity spectrum; similarly, changes in its magnitude alter the proportions of its linear and second-order contributions to the image intensity spectrum. The rate of change of image character with increasing specimen thickness is thus governed by the degree of dynamical scattering within the specimen. In turn, this "dynamicity" of the specimen is a function of its projected potential, as "seen" by the electron beam. Of course the magnitude of the specimen projected potential is strongly dependent upon crystal tilt. In tilted crystals, columns of atoms no longer stack exactly along the electron beam direction and the projection of the tilted columns produces much lower amplitudes in projected potential, a condition that reduces dynamical scattering. Thus small tilts can produce large changes in "dynamicity", and in the rate of change of image character with specimen thickness. Simulated images attain a specific image character faster than experimental ones because simulations are done exactly on-axis and experimental specimens are rarely so. Tilting the crystal off the zone axis will reduce the "dynamicity" of the simulation and slow down the rate of image change, making the crystal "act thinner". Note that increasing ionicity in the simulation has the opposite effect.³

For tilted crystals, Moodie has shown that, although the symmetry of images from thicker crystals will be in error, images from thinner areas will retain the correct symmetry in first order.³ This behavior has been confirmed by simulations of tilted crystals.⁴ Additionally, since they decrease the rate of image change with thickness, small tilts can extend the range of thicknesses over which a "good" (or thin-crystal) image can be obtained (and may unknowingly be selected for this reason).⁵ Perhaps this is why crystallographic image processing often confirms the presence of small tilts in HRTEM images.⁶ Thinner crystals can also tolerate more tilt and enjoy more tilt-induced quenching of dynamical scattering; small (15-50Å) metal particles produce two-dimensional images when oriented up to several degrees from a zone-axis.⁷

Simulated images of aluminum in [001] orientation display less dynamical characteristics when the specimen crystal is tilted; the proportion of second-order contributions⁸ is lower, and the image appears to come from a thinner crystal. Figure 1 illustrates this effect for 80Å thickness and tilts up to 16 milliradian. Interestingly, even though the potential is quite smeared out at the higher tilts, the images appear much less so. Simulations show no significant effect for the 1 milliradian tilt (the peak potential drops from 106 volts to 99 volts); this means that normal beam convergences (usually near 1 milliradian) need not be included in the diffraction calculation, at least up to 80Å thickness for atoms as light as aluminum.⁹

1. J.-O. Malm and Michael A. O'Keefe, *51st Ann. Proc. EMSA*, Cincinnati, Ohio (1993).
2. M.A. O'Keefe, U. Dahmen & C.J.D. Hetherington, *Mat. Res. Soc. Symp. Proc.* **159** (1989) 453.
3. G.R. Anstis, D.F. Lynch, A.F. Moodie and M.A. O'Keefe, *Acta Cryst.* **A29** (1973) 138-147.
4. D.J. Smith, W.O. Saxton, M.A. O'Keefe, G.J. Wood & W.M. Stobbs, *Ultramicro.* **11** (1983) 263.
5. M.A. O'Keefe and V. Radmilovic, *50th Ann. Proc. EMSA*, Boston, Massachusetts (1992) 116-117.
6. D.N. Wang, S. Hovmöller, L. Kihlberg and M. Sundberg, *Ultramicroscopy* **25** (1988) 303-316.
7. J.-O. Malm and Michael A. O'Keefe, *SCANDEM-93*, Lund, Sweden (1993).
8. M.A. O'Keefe, *37th Ann. Proc. EMSA*, San Antonio, Texas (1979) 556-557.
9. Work supported by the Director, Office of Energy Research, Office of Basic Energy Sciences, Material Sciences Division of the U.S. Department of Energy, under contract No. DE-AC03-76SF00098.

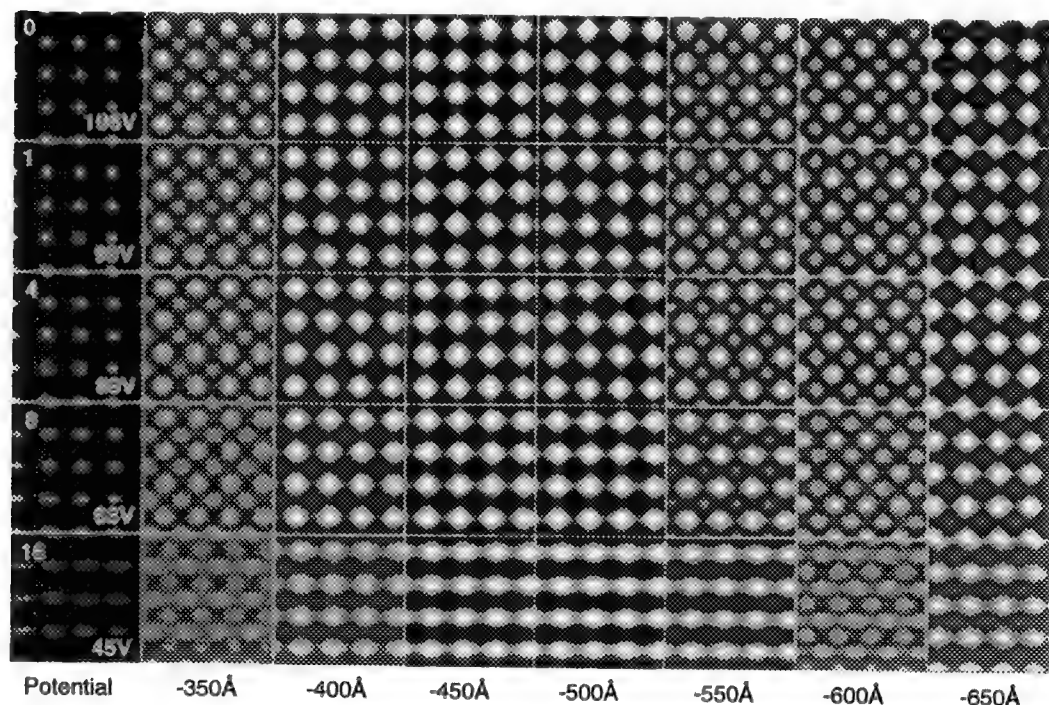


Figure 1. Projected potentials (left column), and simulated images for aluminum in [001] orientation. Each potential (left) is marked with tilt (upper left in milliradian) and potential peak (lower right in volts). Increasing tilt smears out the projected crystal potential (left column) and lowers the peak from the untilted maximum of 106 volts to 45 volts. Simulations are for 400keV, $C_s = 1\text{mm}$, convergence semi-angle of 1.0mrad (i.e. gaussian halfwidth of 0.77 milliradian¹), spread of focus of 60Å halfwidth, and defocus values (marked) from -350Å to -650Å in steps of -50Å. The optimum defocus image ("black-atom" image) is near the center of the defocus range. Non-linear second-order contributions produce white dots in the centers of the blacks when the specimen is untilted (top); this effect decreases with increasing tilt.

THE EFFECT OF BEAM AND CRYSTAL TILT ON QUANTITATIVE HREM MEASUREMENTS OF GRAIN BOUNDARY VOLUME EXPANSION

M. I. Buckett and Karl L. Merkle

Materials Science Division, Argonne National Laboratory, Argonne, IL 60439

The effects of both beam and crystal tilt on quantitative high resolution electron microscopy (HREM) measurements of grain boundary volume expansion have been investigated. As volume expansion - or rigid body translation normal to a given boundary - has been found to directly vary with the grain boundary energy, it is important that accurate measurements of this quantity can be made. The type of measurement we consider is a technique first outlined by Stobbs and co-workers¹ and modified by Merkle.² The technique utilizes a linear least squares fit to the centers of gravity of either peak or valley positions in the HREM image. The interplanar distances on both sides of the boundary outside the strain fields of the core are first determined, and the measured width of the boundary region is extrapolated. The volume expansion is then determined as the difference between this measured width and the effective unrelaxed width of an ideal boundary. This method is reported to be accurate to displacements of 0.001 ± 0.004 nm for the Cu $\Sigma 5$ boundary¹ and to better than 0.01 ± 0.009 nm for grain boundaries in Au.² Beam and crystal tilt are well known to affect the appearance of HREM images,^{3,4} however the effect on quantitative measurements with regard to boundary displacements is not well characterized.

Figure 1 illustrates the technique on a relaxed Au $\Sigma 11$ (113)/(113) boundary (volume expansion = $0.029 \cdot a_0$) simulated under ideal imaging conditions (a); with a beam tilt of 3.4 mrad perpendicular to the boundary (b); and with a beam tilt of 2.6 mrad parallel to the boundary (c). The simulations shown are for a 5 nm crystal thickness and -70 nm defocus. Instrumental parameters for the JEM4000EX were used: $C_s = 1.0$ mm; focal spread of 8.0 nm, semi-convergence angle of 0.5 mrad; and objective aperture radius of 6.0 nm^{-1} . The dimensions of the supercell used to create the boundary were $X = 9.6377$ nm, and $Y = 0.9587$ nm (1024 x 128 array size).

Shown in Figure 2 are the measured volume expansions for the Au $\Sigma 11$ boundary normalized to the lattice parameter (a_0) under various imaging conditions. Crystal thicknesses of 5.0 nm and 8.3 nm were both considered. All images analyzed were at -70 nm defocus, which gave rise to 'white dot' conditions. The volume expansion measured in the ideal simulation was essentially the same as the true value, thus illustrating the utility of this technique under ideal imaging conditions. Introduction of beam tilt perpendicular to the boundary shows little effect up to 2.6 mrad for a crystal thickness of 5.0 nm and 2.0 mrad for a crystal thickness of 8.3 nm. This suggests that even with increasing crystal thickness, moderate amounts of beam tilt normal to this boundary can be tolerated without significant error. Parallel to the boundary, however, a negative deviation from ideal by nearly 4% is already seen with a beam tilt of only 1.7 mrad. Crystal tilts of up to 4 mrad parallel and perpendicular to the boundary show only a small effect (< 0.4% change) on the volume expansion measurement. While only one particular type of boundary has been considered here, it serves to illustrate that proper beam tilt alignment is critical for accurate measurement of the volume expansion. Small deviations of the beam tilt alignments which may be barely noticeable in the image can give rise to significant errors in the measurement.

REFERENCES

1. W. M. Stobbs et al., *Ultramicroscopy* 14 (1984) 130.
2. K. L. Merkle, *Ultramicroscopy* 40 (1992) 281.
3. David J. Smith et al., *Ultramicroscopy* 11 (1983) 263.
4. J. M. Howe and S. J. Rozeveld, *Microscopy Research and Technique* 23 (1992) 230.

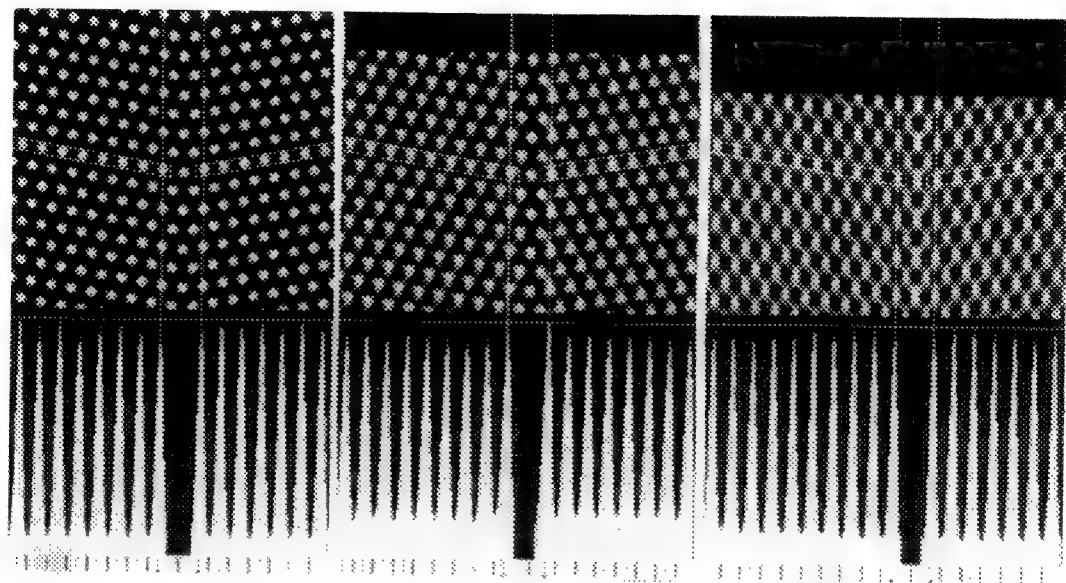


FIG. 1 Simulations of a Au $\Sigma 11$ boundary showing the planes used to make the volume expansion measurement. Thickness = 5 nm, defocus = -70 nm. (a) no beam or crystal tilt; (b) beam tilt of 3.4 mrad normal to boundary; (c) beam tilt of 2.6 mrad parallel to boundary.

Measured Volume Expansion as a Function of Beam and Crystal Tilt

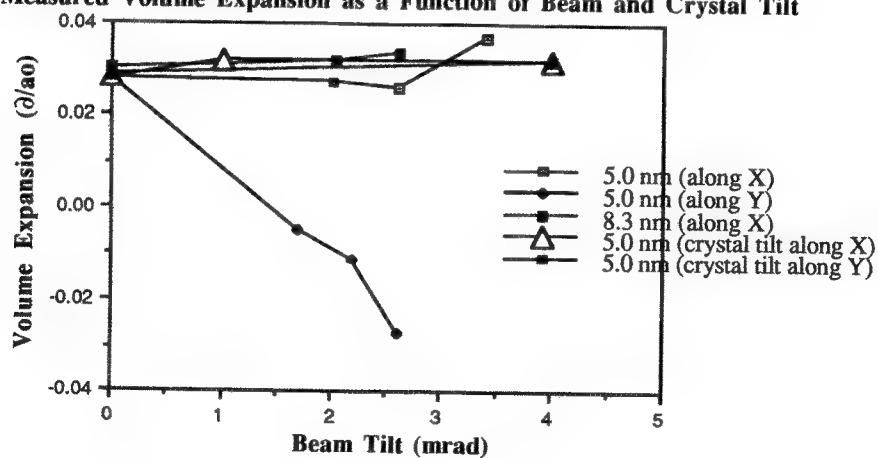


FIG. 2 Measured volume expansion as a function of beam and crystal tilt in the Au $\Sigma 11$ boundary. X = dimension normal to boundary. Y = dimension parallel to boundary. Crystal thickness is given in the legend.

STRUCTURE OF THE $\Sigma=5$ (310) INTERFACE IN NiAl

Richard W. Fonda and David E. Luzzi

Laboratory for Research on the Structure of Matter and Department of Materials Science and Engineering, University of Pennsylvania, Philadelphia, PA 19104-6272

The atomic structure of the $\Sigma=5$ [001] (310) grain boundary in NiAl was examined by high resolution electron microscopy and multislice image simulation. As in most other intermetallic compounds, the grain boundaries in NiAl are intrinsically brittle at low temperatures.¹ Although there have been few studies on this alloy, the energies of NiAl grain boundaries have been calculated using embedded atom potentials for both stoichiometric² and non-stoichiometric³ structures. These studies are consistent with the results of Bradley and Taylor⁴, which indicate that nickel-rich compositions result from nickel antisite defects on the aluminum sublattice, while aluminum-rich compositions produce constitutional vacancies on the nickel sublattice, and with recent field ion microscopy results on nickel-rich alloys.⁵⁻⁶

The $\Sigma=5$ grain boundary was prepared by diffusion bonding at 1000 °C. A JEOL 4000EX was used for HREM imaging and the NUMIS multislice simulation program was used to simulated images. Analysis of these images considered the effects of grain boundary expansion, rigid body displacements along the boundary, grain boundary stoichiometry, and point defects at the boundary. The observed rigid body displacement severely constrained the physically possible structures for this grain boundary.

Imaging this grain boundary in the [001] orientation (Fig. 1) aligns the columns of pure Ni and pure Al with the electron beam direction. The thickness and defocus were determined to be approximately 58 Å and -700 Å, respectively, which produces a strong superlattice of white atom contrast, with the nickel sites brighter than the aluminum sites. This superlattice contrast extends up to the grain boundary, indicating a continuous chemical ordering up to the boundary. This grain boundary displays an asymmetry produced by a $\frac{1}{2} d_{1\bar{3}0}$ (0.46 Å) rigid body translation of the top grain toward the right, but does not exhibit a measurable grain boundary expansion. The lateral displacement of the two grains removes the mirror symmetry of the boundary and causes the grain boundary lattice sites of the upper and lower grains to become distinct. The structure of the grain boundary will therefore be different for grain boundary atoms located at lattice sites of the upper grain, at lattice sites of the lower grain, or at some intermediate position. Associating the grain boundary atoms with the upper grain (and including a grain boundary expansion of $0.18 d_{310}$ (0.16 Å), which is within the experimental measurements) retains the matrix interatomic spacings around these atoms. Other placements of the grain boundary atoms significantly reduces their interatomic separation. This grain boundary structure displays a very even distribution of atoms across the grain boundary. However, the separation between atom sites adjacent to the grain boundary plane is fixed by the observed rigid body displacement. These atom sites are almost 30% closer to each other than sites within the matrix. In addition, the brightness of some atom sites at and near the grain boundary in simulated images of this structure differs from the experimentally observed image.

The steric crowding between sites adjacent to the grain boundary can only be decreased by introducing vacancies into these sites. This would lead to a predicted structure in which the pairs of sterically crowded sites contain only one atom between them. These sites may thus be more



Fig. 1 High resolution image of the $\Sigma=5$ [001](310) grain boundary in NiAl imaged along the [001] zone axis.

appropriately viewed as two low energy positions for a single atom. This description of the grain boundary, based solely on the restrictions of the observed rigid body displacements, is consistent with the image simulations in all respects except in the aluminum sites adjacent to the grain boundary plane. Image simulations indicate that the atoms which partially occupy these sites are nickel rather than aluminum, producing a structure in which all atomic sites adjacent to the grain boundary plane are identically occupied by 50% nickel atoms and 50% vacancies (Fig. 2). This grain boundary structure both removes the steric overcrowding at the grain boundary and produces a simulated image which matches the observed grain boundary image in all respects, even at different thicknesses.⁷

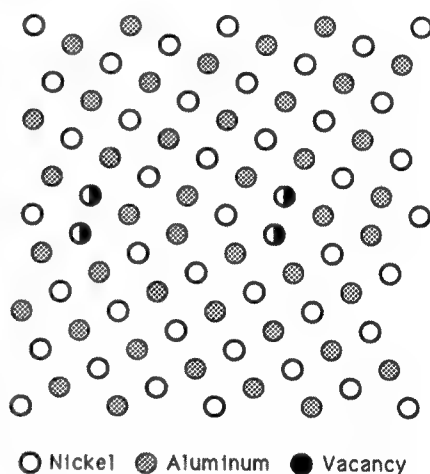


Fig. 2 Schematic of the grain boundary structure which best matches the experimental results.

References

- 1.E. P. George and C. T. Measurable, *J. Mater. Res.* **5** (1990) 754.
- 2.G. Petton and D. Farkas, *Scripta Met.* **25** (1991) 55.
- 3.S. P. Chen *et al.*, *Mat. Res. Soc. Symp. Proc.* **133** (1989) 149.
- 4.A. J. Bradley and A. Taylor, *Proc. Roy. Soc.* **A159** (1937) 56.
- 5.P. P. Camus *et al.*, *J. de Physique* **49** (1988) C6-329.
- 6.M. K. Miller *et al.*, *Scripta Metall.* **26** (1992) 679.
- 7.Support of this project was provided by the National Science Foundation under grants 91-11775 and 91-20668 and by the central facilities of the Penn-MRL.

ATOMIC STRUCTURE OF UNDOPED $\Sigma=5$ SYMMETRICAL-TILT GRAIN BOUNDARY IN STRONTIUM TITANATE

V. Ravikumar

Department of Materials Science and Engineering, Northwestern University, Evanston, IL 60208.

Strontium titanate is an important electroceramic material which, under appropriate processing and dopant additions exhibits both varistor and Grain Boundary Layer Capacitor (GBLC) behavior.^{1,2,3} The presence of electrically active grain boundaries is essential for obtaining these properties. The first step towards correlating the grain boundary structure to properties is to determine the detailed atomic structure of the boundary, which includes its geometric structure, chemistry and electronic structure. We present here our TEM investigation of the atomic structure of an undoped ("pristine") symmetrical tilt grain boundary in SrTiO₃. This provides the basic reference structure, changes to which can be studied as a function of doping and/or processing parameters, and correlated to electrical and dielectric properties.

Self-supported TEM samples were made from bicrystals of SrTiO₃ through the conventional sample preparation route. Fig. 1 shows a high resolution electron micrograph (Hitachi H9000) of a representative grain boundary region in the sample. Flat and straight regions having a compact core with a periodically repeating structural unit are separated by monatomic steps (indicated by arrows). No glassy or second phases are present at the boundary. The SAED pattern (inset, Fig. 1) conforms to that of a $\Sigma=5$ tilt boundary with a common [001] tilt axis, and from Fig. 1, it can be seen that this is a symmetrical tilt boundary with (130)-type grain boundary plane. The composition profile across the grain boundary was determined at high spatial resolution (< 5 nm) by EDS (Hitachi HF-2000 FE-TEM with a Link UTW-EDS detector and a Gatan 666 PEELS unit) using a fine probe (≈ 2 nm) and Fig. 2 shows the peak intensity ratio ($\text{Ti}_{K\alpha}:\text{Sr}_{L}$) as a function of distance across the interface. There does not seem to be any appreciable cation non-stoichiometry or an indication of any foreign impurity segregation at this boundary, within the limits of this experimental technique. While this does not rule out the possibility of very low levels of segregation and/or non-stoichiometry, the atomic structure of the boundary can be expected to be representative of a pristine undoped boundary. Fig. 3 shows a comparison of the EELS low loss spectra acquired with the fine probe placed on the grain boundary and in the bulk region. Any changes in the local optical or dielectric function at the interface is localized to spatial extents within a nanometer on either side of the interface since no appreciable changes in the position or relative intensities of the corresponding peaks can be observed.

Analysis of the high resolution micrographs revealed an in-plane RBT of $(1/2)d_{130}$. No appreciable plane-normal RBT (lattice expansion) could be observed, but there was considerable individual atomic relaxation at the core of the interface. Based on these observations, an empirical model has been proposed and is shown in Fig. 4(a), which includes the observed RBT and also estimated individual atomic displacements near the core of the boundary (based on comparisons between simulated and experimental images, to get better fits of the core structure). One comparison between the simulated image (multislice simulations using NUMIS⁴) and the experimental image is given in Fig. 4(b), where the simulated image (defocus = -45nm, $t = 98$ Å) is shown as an inset in the experimental image. Theoretical calculations using static lattice energy minimization schemes are currently being performed to determine the relaxed atomic structure of this boundary, and preliminary results of these calculations will also be discussed.⁵

References

1. N. Yamaoka and T. Matsui in *Grain Boundary Phenomena in Electroceramics*, edited by L. M. Levinson and D. C. Hill (Advances in Ceramics Vol 1, ACerS Publishers, Columbus, OH, 1986) p.232.
2. M. Fujimoto and W. D. Kingery, J. Am. Ceram. Soc **68** [4] (1985) 169.
3. N. Yamaoka et. al., Am. Ceram. Soc. Bull **62** [6] (1983) 698.
4. NUMIS®, High Resolution Image Simulation Program, Northwestern University
5. This research is supported through a seed grant by the MRL program of the National Science Foundation at the Materials Research Center of Northwestern Univ. under award no. DMR9120521, and the U. S. Department of Energy - Basic Energy Sciences, Grant No. DE-FG02-92ER45475.

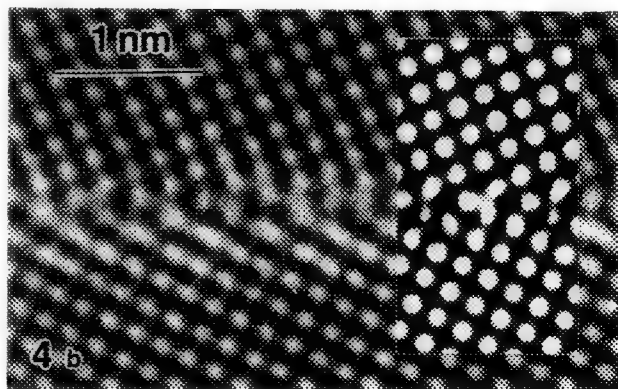
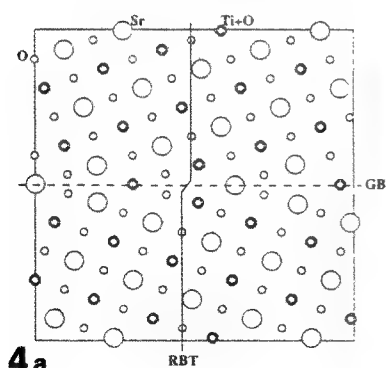
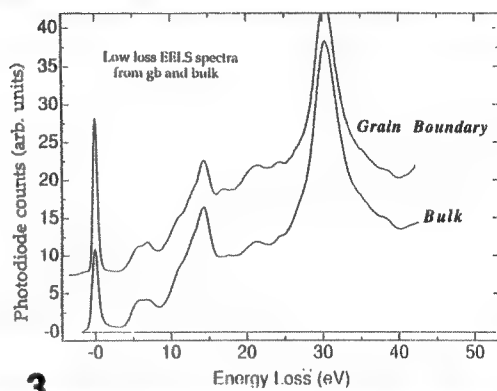
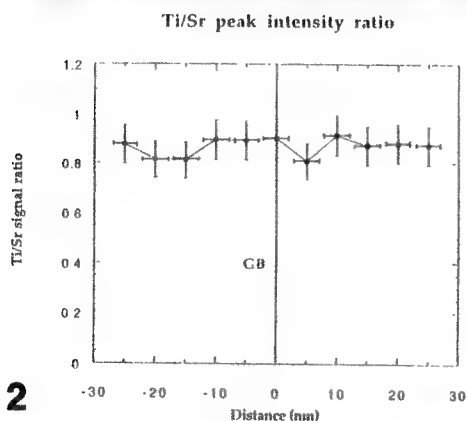
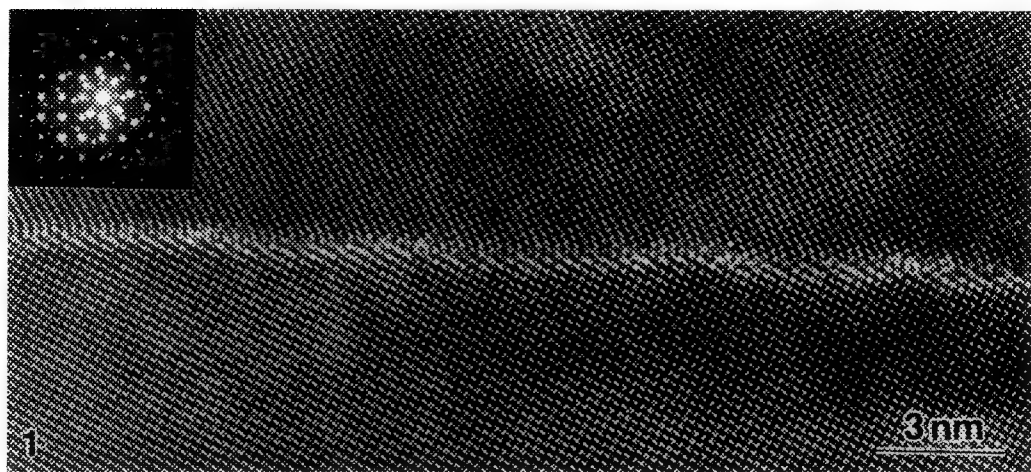


FIG. 1. -- HRTEM of a representative region in the $\Sigma=5$ (130) grain boundary, and the SAED pattern.
 FIG. 2. -- Ratio of the $\text{Ti}_{K\alpha}$ to $\text{Sr}_{L\alpha}$ x-ray peak intensity as a function of distance across the boundary.
 FIG. 3. -- EELS low loss spectra from the grain boundary and the bulk.
 FIG. 4(a).-- Proposed semi-empirical model of the $\Sigma=5$ boundary.
 FIG. 4(b).-- Comparison between the experimental image and the simulated image (inset).

ATOMIC MORPHOLOGY OF THE γ/γ' INTERFACE

Richard W. Fonda, Xuegen Jin, and David E. Luzzi

Laboratory for Research on the Structure of Matter and Department of Materials Science and Engineering, University of Pennsylvania, Philadelphia, PA 19104-6272

Nickel-based superalloys are well known for their high temperature strength. These alloys consist of two phases, γ and γ' , which in combination produce an alloy of higher strength than either phase alone. A significant factor in this strength increase is the interface between the two phases. The γ phase is a fcc solid solution of nickel, while the γ' phase has a $L1_2$ structure based on Ni_3Al . The difference in lattice parameter between these two phases is very small, producing large regions of coherent interface between the two phases. This interface between γ and γ' was examined by high resolution electron microscopy

The nickel-based superalloy (René N4) was generously supplied by Dr. R. Field of GE Aircraft Engines. TEM samples were cut from this oriented single crystal, mechanically thinned, then electropolished in a solution of 10% perchloric acid in ethanol. A Philips 400T TEM was used for conventional imaging and a JEOL 4000EX was used for high resolution imaging.

This alloy consists of cuboidal precipitates of the γ' phase surrounded by a small volume fraction of the γ phase (Fig. 1). These cuboids of γ' range in size from less than 0.5 μm to about 1.0 μm . A selected area diffraction pattern of this two phase material (Fig. 2) shows the 100 superlattice reflections, which are forbidden reflections for the fcc phase and arise from the difference in atomic scattering of Ni and Al in the $L1_2$ phase, as well as allowed fcc reflections. This diffraction pattern shows these two phases to be related by a cube-on-cube orientation relationship and demonstrates that the cuboid morphology is caused by a preference for the $\{100\}_{\gamma} \parallel \{100\}_{\gamma'}$ interface between the two phases.

Contrary to what may be expected from the macroscopic dominance of the $\{100\}_{\gamma} \parallel \{100\}_{\gamma'}$ interfacial habit, high resolution imaging of the γ/γ' interface (Fig. 3) reveals it to be non-faceted. All γ/γ' interfaces which were examined exhibited this rough morphology at the atomic scale. Imaging the two phases in this common [001] orientation clearly shows the fundamental structure of the γ phase (top) and the superlattice structure of the γ' phase (bottom). This clarity is primarily due to the [100] orientation of the sample, which aligns the electron beam directly along columns of pure nickel and pure aluminum and maximizes the contrast produced by chemical ordering. The interface between these two phases does not adhere to a specific interfacial plane or have discrete ledges in the imaging direction. The roughness of this interface is observed both along the interface, which results in a wavy appearance of the interface, and in the beam direction, which produces a gradual diminution of the superlattice contrast across the interface. The analysis of Penisson *et al.*¹ on this interface in the [011] sample orientation also predicted a rough interface, but the reduced chemical resolution in the [011] orientation precluded an accurate delineation of the interfacial morphology. The superior resolution of the chemical ordering in the [100] orientation permits an accurate examination of the morphology of this interface.²

References

1. J. M. Penisson *et al.*, *Phil. Mag. Lett.*, **64**(5) (1991) 269.
2. Support of this project was provided by the National Science Foundation under DMR 91-11775 and 91-20668. The authors acknowledge the use of the central facilities of the Penn-MRL.

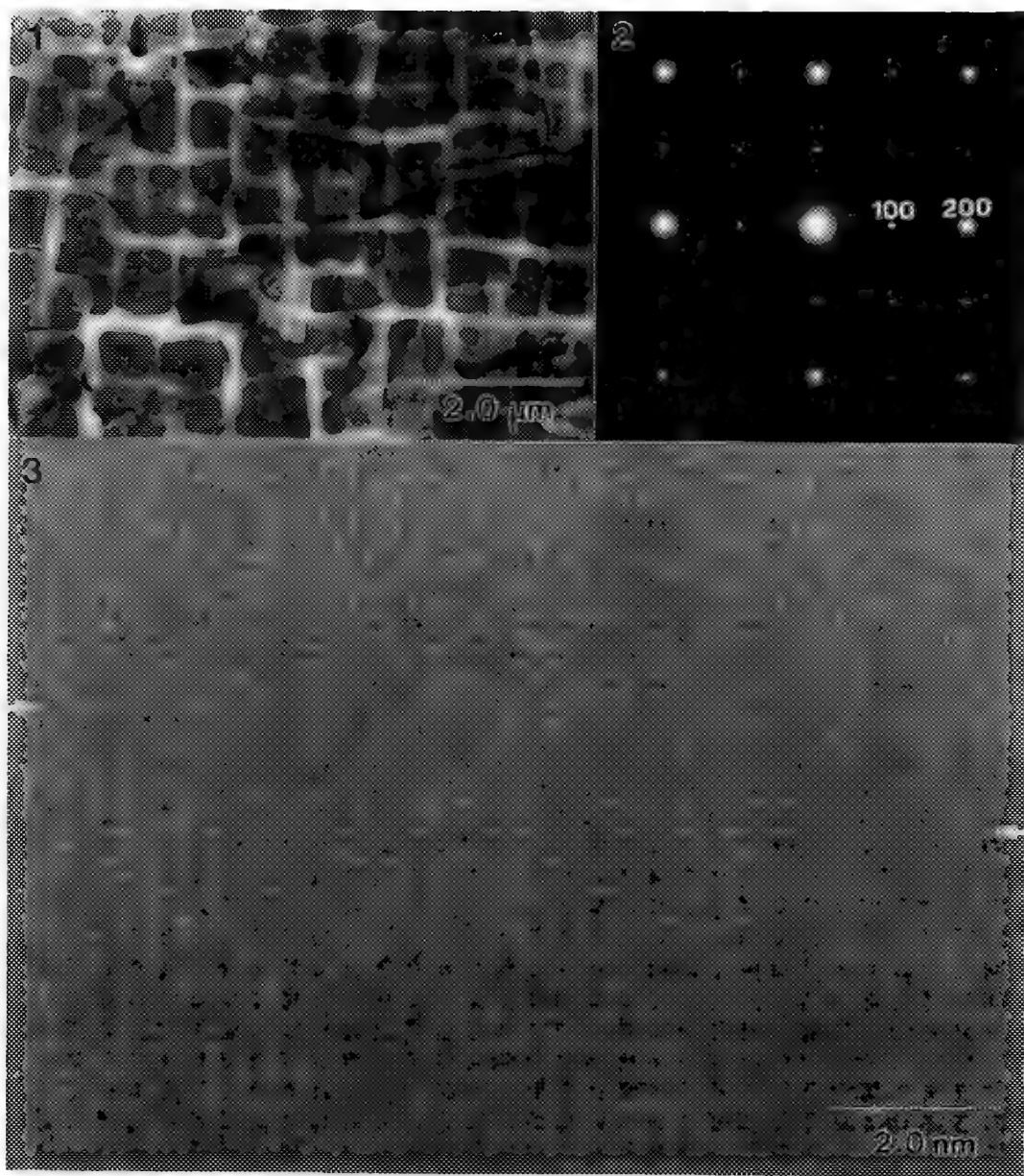


Fig. 1 Typical morphology of the nickel-based superalloy, consisting of cuboidal γ' in a γ matrix.
 Fig. 2 Diffraction pattern showing the cube-on-cube orientation relationship between the two phases.
 Fig. 3 High resolution TEM image of a typical interface between γ (top) and γ' (bottom), showing the atomically rough morphology of the interface.

STRUCTURE AND CHEMICAL COMPOSITION OF NANOPHASE PARTICLES IN Mg-BASED ALLOYS

V. Radmilovic and G. Thomas

Department of Materials Science and Mineral Engineering, University of California,
Berkeley, CA 94720, USA, and National Center for Electron Microscopy,
Lawrence Berkeley Laboratory, Berkeley, CA 94720

Conventional and high resolution transmission electron microscopy, as well as microchemical analyses, are playing an important role in identifying precipitates in Mg based alloys for aerospace applications, especially for nanometer sizes. During aging of Mg-Al-Nd-Zn based alloys, Al-Nd-Zn based particles precipitate which affect the mechanical properties. These alloys, which serve as the metal matrix for MMC materials containing SiC particulates as reinforcement, are processed by rapid solidification/powder metallurgy techniques, and they are designed for relatively high temperature (250-300° C) applications.

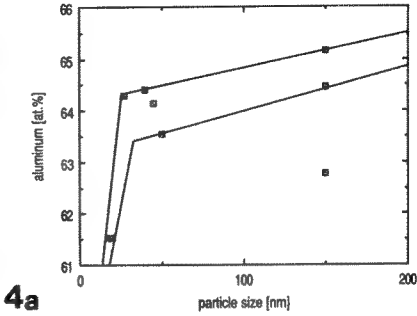
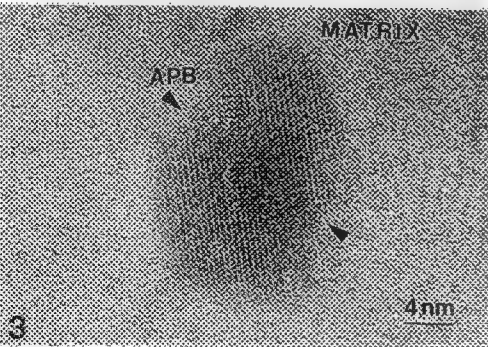
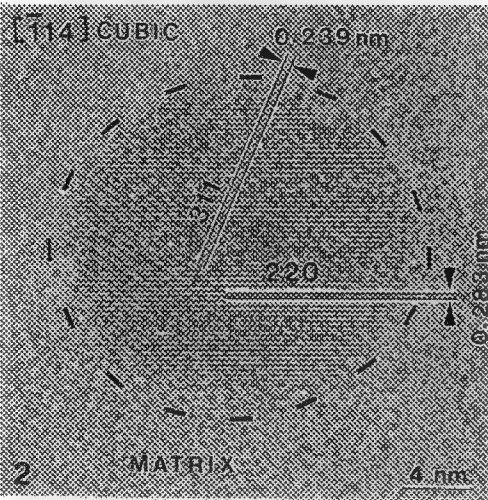
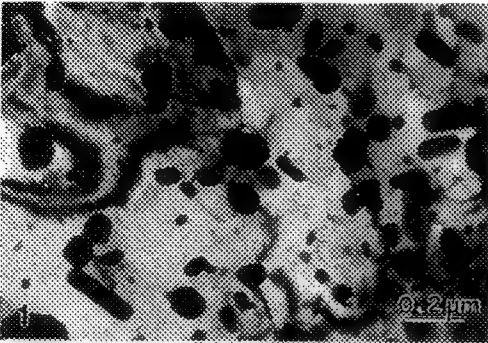
Figure 1 shows the typical structure of second-phase particles in the Mg-based matrix. The spread in the particle size range is quite large, e.g., roughly between 70 and 100 nm. Close examination of these particles shows (Fig. 2) that there is no coherency with the Mg-based matrix, and no specific crystallographic relationship has been established. In some cases the growing direction of large particles was found to be within 5° of the C-axis of the Mg matrix. Also, the presence of moiré fringes clearly visible in several cases indicates the existence of possible crystallographic orientation relationships to the matrix. Analyses of some small particles indicate their crystal structure is close to the cubic Al₂Nd type, with a lattice parameter of 0.8 nm. However, it is not possible to define uniquely what the structure is, especially because the angles between atomic planes do not correspond exactly to the calculated values of the cubic phase, and because the chemical composition of extracted particles shows the presence of Zn atoms. On the other hand, the experimental values for the spacing between 220 and 311 planes are 0.283 (0.275) and 0.239 (0.244) nm, respectively, and they are in very good agreement with the values in the PDP files No. 29-54 for the Al₂Nd compound: $d_{220} = 0.2828$ nm and $d_{311} = 0.2412$ nm. It is interesting to note that the Al₂Nd cubic structure is observed only in small particles with diameter up to 5 nm. Occasionally, an antiphase boundary within an ordered particle is observed (Figure 3). The presence of a disordered region could arise when particles impinge whose lattices are in antiphase. The formation of a common APB would require a higher energy than if a region of disordered phase is left between both particles. An optical diffraction pattern of the particle in Figure 3 does not show spot splitting due to the existence of antiphase-oriented domains, as is the case for single translation interfaces,^{1,2} and therefore the intensities from higher-order reflections from the antiphase domains are very weak.

Microchemical analyses of very fine spherical, plate-like, and elliptical particles show that their average composition is Al₇NdZn. However, depending on the size of the precipitate, a compositional variation occurs and initial Al/Zn and Al/Nd atomic ratios, typical for the particles in size up to 30 nm, are not the same for precipitates of different size and shape. With increasing particles size up to approximately 40 nm, the amount of Al and Nd increases and Zn decreases sharply (see Figure 4). Above an average particle size of 40 nm the concentration of the present elements changes in the same manner but more slowly.³

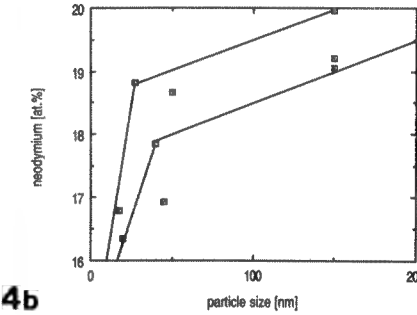
References

1. H. Warlimont, in G. Thomas, Ed., *Electron Microscopy and Structure of Materials*, Berkeley: University of California Press (1972) 505.
2. D. Van Dyck, G. Van Tendeloo, and S. Amelinckx, *Ultramicroscopy* 357 (1984) 15.

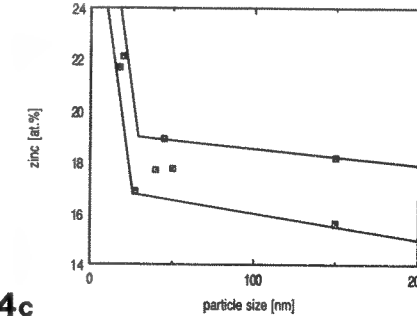
3. This work was supported by the Director, Office of Energy Research, Office of Basic Energy Sciences, Materials Sciences Division of the U.S. Department of Energy under Contract No. DE-AC03-76SF00098. V. R. also acknowledges a grant from AlliedSignal Inc.



4a



4b



4c

Fig. 1.--TEM micrograph of Al-Nd-Zn base particles in Mg based matrix.
 Fig. 2.--HREM micrograph of Al₂Nd cubic-type particle in 114 zone axis.
 Fig. 3.--HREM micrograph of Al₂Nd cubic-type particle with 111 planes edge-on; note presence of antiphase boundary.
 Fig. 4.--The compositional variation of Al, Nd, and Zn as a function of particle size.

CHARACTERIZATION OF THE DISLOCATION CORE STRUCTURE OF PARTIAL DISLOCATIONS IN $SiC\langle 011 \rangle$ USING HRTEM: A THEORETICAL STUDY

T. Geipel and P. Pirouz

Dept. of Mat. Sci. and Eng., Case Western Reserve University, Cleveland OH 44106

The mobility of a dislocation in compound semiconductors of zincblende or wurtzite structure depends on its core structure i.e. its chemical composition. Present analytical techniques are not able to resolve the nature of the atomic species at the dislocation core and although HRTEM is capable of resolving the atomic arrangement in the core, its chemical characterization is difficult. In single crystalline regions the chemical composition can be determined using chemical mapping [1] but this method cannot be applied to dislocations, viewed end-on, because these are non-periodic features. In a HRTEM image of a compound material, different scattering factors of the constituent elements may lead to spots of different brightness, but these contrast differences are very small. The only distinct characteristic of a HRTEM image is the spacings between bright or dark spots which can be measured easily. In this paper a practical concept for chemical distinction between Si and C in the cores of partial dislocations in $SiC\langle 011 \rangle$ is presented.

For the 90° and the 30° glide partial dislocations (Fig. 1) there are two possible core structures corresponding to $Si(g)$ and $C(g)$. The HRTEM image contrast of $SiC\langle 011 \rangle$ is determined by a strong 111 'lattice' contrast and a weaker 200 'chemical' contrast assuming maximum contrast conditions. In case that the 'chemical' 200 and $\bar{2}00$ beams and/or the 'lattice' $11\bar{1}$ and $\bar{1}1\bar{1}$ beams have different amplitudes, the 200 pattern shifts with a changing defocus with respect to the 111 pattern [2]. Fig. 2 shows that for a specimen thickness of $H = 15.4nm$, the 200 beams make a large contribution to the resulting HRTEM contrast. For a defocus of $\Delta f = -70nm$, both 111 and 200 beams have maximum contrast. It turns out that in this case the bright spots correspond to the C positions in the lattice. Figs. 3 and 4 show the simulated HRTEM images corresponding to $Si(g)$ and $C(g)$ cores of Fig. 1. The distances between the bright spots in the $C(g)$ and $Si(g)$ cores of the 90° partial can be measured to be $d_C = 0.23nm$ and $d_{Si} = 0.37nm$, respectively, which can be distinguished easily. The two core types of 30° glide partials cannot be determined directly because the image contrast differences are too small. For a 60° dislocation dissociated into a 30° and a 90° partial, a knowledge of the 90° core type indirectly determines the chemical composition of the 30° partial also.

The accuracy of the proposed method decreases with decreasing amplitudes of the 200 beams but can be also applied to other thicknesses. It can also be applied to other compound materials depending on the differences of the scattering factors of the constituent elements. It should be mentioned that the experiment requires a very good alignment of the microscope, the specimen thickness has to be known to an accuracy of about 20% and the defocus has to be known to about $\Delta(\Delta f) = \pm 15nm$.

References

1. A. Ourmazd et al., Ultramicroscopy (1990) 34, 237.
2. T. Geipel and M. Hohenstein, Ultramicroscopy (1992) 45, 167.

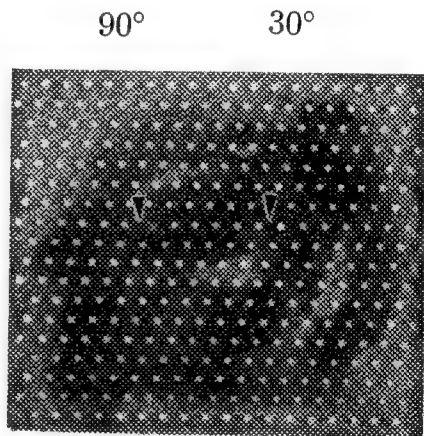
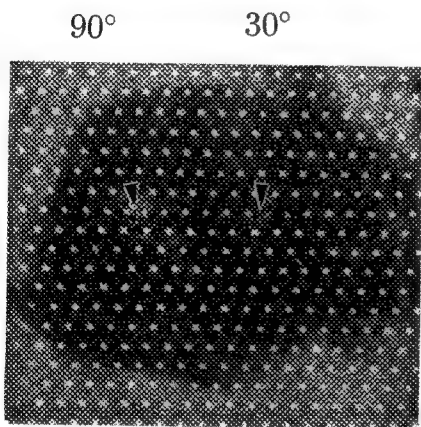
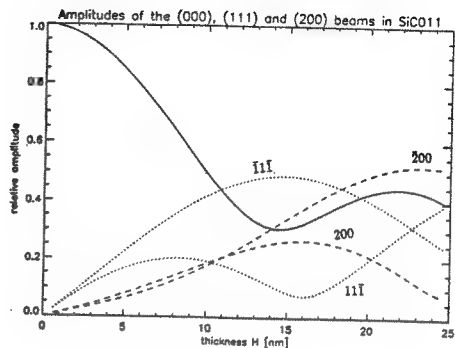
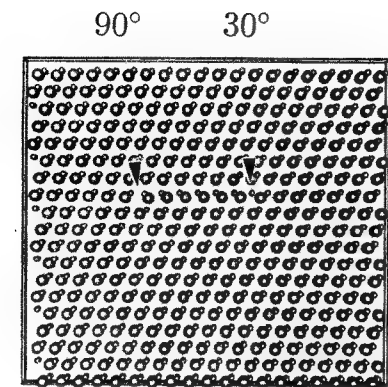


Figure 1: $SiC\langle 011 \rangle$ with a 90° partial dislocation on the left hand side and a 30° partial dislocation on the right hand side bounding an intrinsic stacking fault in between. For the $C(g)$ case i.e. the dislocation core is built up from C atoms, in this case the small circles in the figure correspond to C columns and the large circles correspond to Si columns. For the $Si(g)$ case the configuration is reversed.

Figure 2: Amplitudes of Bragg beams in $SiC\langle 011 \rangle$ from dynamical simulations. The solid line corresponds to the 0 beam, the dotted lines to 111 and the dashed lines to 200.

Figure 3: Simulated HRTEM image using the imaging parameters of a JEOL 4000EX for the supercell of Fig. 1 with a $C(g)$ core. $H = 15.4nm$, $\Delta f = -70nm$.

Figure 4: Simulated HRTEM image for the $Si(g)$ core with the same conditions as in Fig. 3.

BAYESIAN REMOVAL OF NOISE FOR INCREASED SENSITIVITY IN VECTOR PATTERN RECOGNITION LATTICE IMAGING OF INTERFACES

L. Fei and P. Fraundorf

Department of Physics and Astronomy, University of Missouri-St. Louis, St. Louis, MO 63121

Interface structure is of major interest in microscopy. With high resolution transmission electron microscopes (TEMs) and scanning probe microscopes, it is possible to reveal structure of interfaces in unit cells, in some cases with atomic resolution. A. Ourmazd et al.¹ proposed quantifying such observations by using vector pattern recognition to map chemical composition changes across the interface in TEM images with unit cell resolution. The sensitivity of the mapping process, however, is limited by the repeatability of unit cell images of perfect crystal, and hence by the amount of delocalized noise, e.g. due to ion milling or beam radiation damage. Bayesian removal of noise, based on statistical inference, can be used to reduce the amount of non-periodic noise in images after acquisition. The basic principle of Bayesian phase-model background subtraction, according to our previous study,² is that the optimum (rms error minimizing strategy) Fourier phases of the noise can be obtained provided the amplitudes of the noise is given, while the noise amplitude can often be estimated from the image itself.

The implementation of noise removal can be summarized as follows: Fourier transform the original image to obtain Fourier phase and amplitude; the noise amplitude then can be obtained by extrapolating background from purely noise regions into signal peak regions with same local averaging to remove statistical fluctuation. In order to not over estimate the background, our algorithm uses the original amplitude in the place where the model noise amplitude exceeds the measured Fourier amplitude. We then subtract the background from the original image in Fourier space (it can also be done in real space) and back Fourier transform to obtain the noise removed image. Fig.1 (a) is a TEM GaAs/AlAs interface image and (b) is after Bayesian phase model noise/background removal of (a).

In order to see the improvement quantitatively, we applied a vector pattern recognition mapping procedure similar to that A. Ourmazd et al.¹ proposed. The templates of two different phases are obtained by averaging the unit cells in pure phases on both sides of the interface. Treat each pixel in the template as one component of a multi-dimensional vector, and the mapping is just a cross correlation calculation of each unit cell in the image with the templates. In multi-dimensional space, such a correlation yields the cosine angle Θ between unit cell vector and template vector. Fig 2 (a) and (b) are $\Theta_A \sim \Theta_B$ plots of the mapping performed on images Fig 1 (a) and (b) respectively. The plots clearly show that after noise removal, the angular vector pattern variability of healthy unit cells are reduced by 20-30% (e.g. from 30 degrees down to 20 degrees). Thus the accuracy of individual cell composition estimates is significantly decreased. Moreover, the angular variability of unit cells in the interface region has no measurable change. This indicates that Bayesian background subtraction has caused little or no Fourier

bleeding,³ our original reason for using Bayesian noise removal instead of conventional Fourier window filtering. Thus artifactual "blurring" of the interface during noise removal is kept to a minimum.⁴

1. A. Ourmazd et al., *Ultramicroscopy*, **34**, (1990)237.
2. P. Fraundorf, *Physical Review Letters*, **64** (1990)1031.
3. P. Fraundorf and K. Pollack, *Ultramicroscopy*, **37**, (1991)72.
4. Thanks to A. Ourmazd and M. Bode of AT&T Bell Labs for providing the images used for this work, and to the University of Missouri-St. Louis, Graduate Summer Research Fellowship.

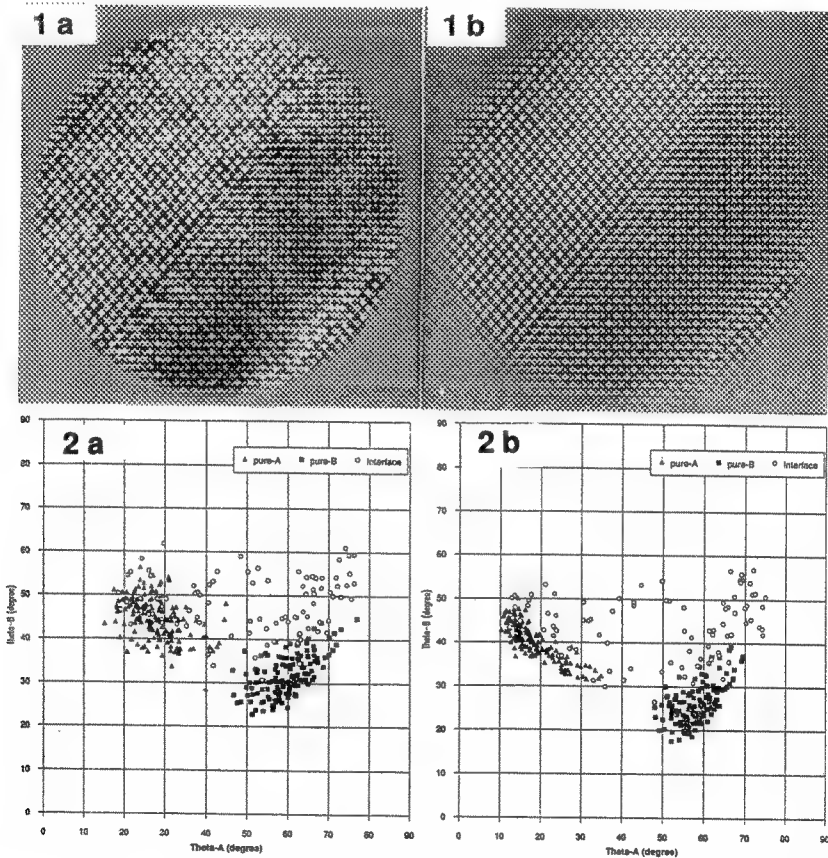


Fig. 1--(a) Original TEM image of GaAs/AlAs showing the interface in the field of view. (b) After Bayesian background subtraction of image in (a). The interface region remains intact.

Fig. 2--(a) and (b), with respect to fig. 1 (a) and (b), are plots of mapping angles between unit cell vectors across the images and template vectors obtained with averaging over unit cells in pure phases only. These angles measure the disagreement between each unit cell in the image, and reference cells corresponding to "pure" structures A and B on opposite sides of the interface. Triangles are "pure" A structures, squares are "pure" B structures and open circles are cells in interface region.

TOWARDS 1-ÅNGSTROM-RESOLUTION STEM

H.S.von Harrach, D.E. Jesson* and S.J. Pennycook*

VG Microscopes, Fisons Instruments, East Grinstead RH19 1UB, UK
*Solid State Division, Oak Ridge National Laboratory, P.O.Box 2008, Oak Ridge, TN 37831, USA

Phase contrast TEM has been the leading technique for high resolution imaging of materials for many years, whilst STEM has been the principal method for high-resolution microanalysis. However, it was demonstrated many years ago that low angle dark-field STEM imaging is a priori capable of almost 50% higher point resolution than coherent bright-field imaging (i.e. phase contrast TEM or STEM)^{1,2}. This advantage was not exploited until Pennycook developed the high-angle annular dark-field (ADF) technique which can provide an incoherent image showing both high image resolution and atomic number contrast³.

This paper describes the design and first results of a 300kV field-emission STEM (VG Microscopes HB603U) which has improved ADF STEM image resolution towards the 1 angstrom target.

The instrument uses a cold field-emission gun, generating a 300 kV beam of up to 1 μ A from an 11-stage accelerator. The beam is focussed on to the specimen by two condensers and a condenser-objective lens with a spherical aberration coefficient of 1.0 mm. A single projector lens is used to vary the collection angle for ADF detection from 25 to 200 mr. The detectors are arranged as shown in Fig.1, such that in addition to the bright-field image, either an ADF image can be collected by a photomultiplier or a diffraction pattern viewed by an intensified CCD camera.

A silicon <110> single crystal specimen was used to test the ADF STEM resolution, theoretically 130 pm at Scherzer defocus. The images were obtained with an angular range of 40 mr to 200 mr. Fig.2 shows an ADF image with the dumbbells at 136 pm spacing clearly resolved.

Calculations of the image contrast were carried out by considering the columns of atoms as independent scatterers convoluted with the probe profile⁴. Fig.3 is a simulated through-focus series based on a probe size of 130 pm. As predicted by the simulation no contrast reversals are observed as a function of focus or specimen thickness.

The probe current used for obtaining the above images was 0.12 nA and the effective brightness is about 2×10^9 Acm⁻²sr⁻¹. The brightness is thus about 10 times higher than for Schottky and thermal field-emission gun systems.

These results show that ADF STEM imaging can produce directly interpretable images at 130 pm resolution without the need for image processing, unlike phase-contrast imaging. It is estimated that the 1 angstrom target could be reached either by reducing the spherical aberration coefficient below 0.5 mm or raising the beam voltage to 400 kV. Alternatively, it may be reached indirectly through image reconstruction which is particularly simple in the case of incoherent imaging.

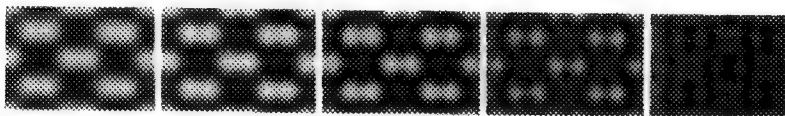
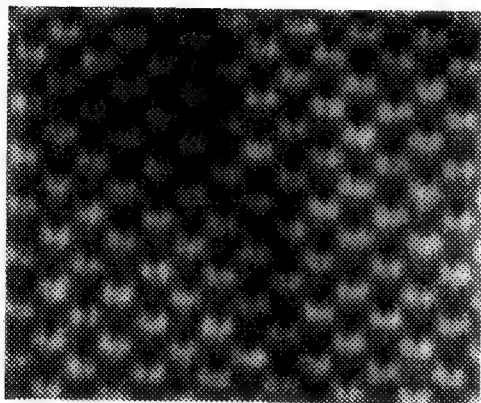
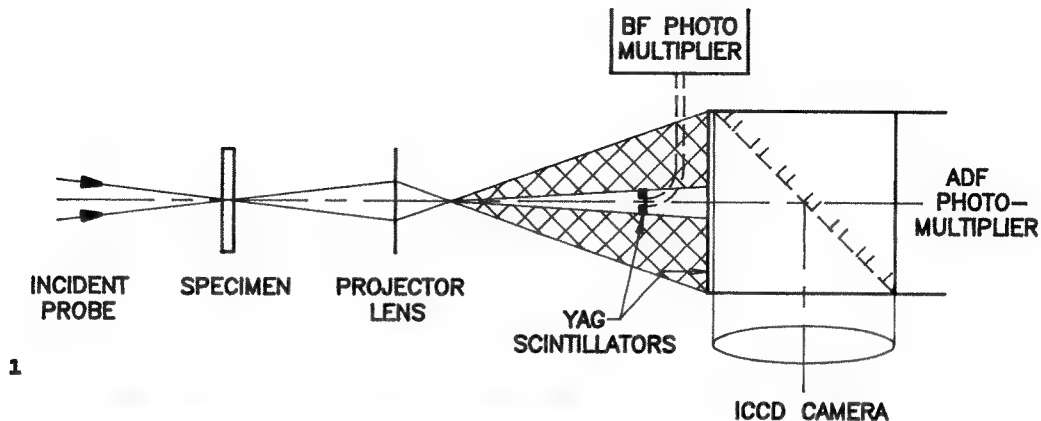


FIG.1--Schematic diagram of detector arrangement in HB603U.
 FIG.2--High-angle ADF image of silicon (110), bar= 1 nm
 FIG.3--Simulated images for a range of defocus values (-30, -40, -50, -60, -70 nm), calculated at 300 kV, $C_s=1.0$ mm, convergence angle = 9.4 mr.

REFERENCES

1. A.V.Crewe, J.P.Langmore and M.S.Isaacson (1975) in 'Physical Aspects of Electron Microscopy and Microbeam Analysis' B.M.Siegel and D.R.Beaman (eds.), New York, Wiley, p.47.
2. J.Cowley in 'Principles of Analytical Electron Microscopy' (1986) D.C.Joy,A.D.Romig,J.I.Goldstein(eds.)p.105.
3. S.J.Pennycook and D.E.Jesson Ultramicroscopy (1991)37,14.
4. S.J.Pennycook and D.E.Jesson Acta Metall.Mater.(1992)40, suppl. S149

IN SITU STUDIES OF HETEROGENEOUS REACTIONS USING SURFACE ELECTRON MICROSCOPIES.
LEEM, MEM, and PEEM

W. Engel, B. Rausenberger, W. Swiech*, C. S. Rastomjee, A. M. Bradshaw and
E. Zeitler

Fritz-Haber-Institut der Max-Planck-Gesellschaft, Faradayweg 4-6, 14195 Berlin 33,
Germany; *On leave from Inst. of Experimental Physics, Univ. of Wroclaw, Poland

The preferred imaging techniques for the observation of physical and chemical processes at solid surfaces with high temporal and spatial resolution are low-energy electron microscopy (LEEM), mirror electron microscopy (MEM) and photoemission electron microscopy (PEEM). In these techniques the energy transfer to the surface during the imaging process itself is small so that surface processes such as adsorption, diffusion, chemical reactions etc. remain largely undisturbed.

LEEM, MEM and PEEM, which all can be performed in an ultra-high-vacuum surface microscope of the Bauer/Telieps type¹, have been applied to the study of CO/O reaction-diffusion fronts on a Pt(100) surface saturated with CO. These fronts develop after admission of oxygen to the surface (10^{-6} mbar) at surface defects which provide adsorption sites for oxygen and thus initiate the autocatalytic oxidation process. The formed CO₂ is instantaneously desorbed, freeing adsorption sites which are then occupied by oxygen from the gas phase. The front propagates over the whole surface, leaving behind an oxygen-covered region.

The front propagation is strongly influenced by the surface microtopography, which can be characterized as a system of parallel step bunches separated by $\sim 1 \mu\text{m}$ wide terraces as seen in fig. 1. The front velocity parallel to the step bunches is $1.5 \mu\text{m/s}$ and 3 times higher than that orthogonal to them.

The CO/O reaction-diffusion fronts have an unexpected, rather complicated, structure which is not yet clarified in all details. PEEM, which is capable of imaging slight differences of local work functions with high contrast, reveals altogether six zones with different work functions (see fig. 2a). The zone boundaries are sharp. Although the contact potentials at these boundaries are only of the order of 0.1 V, rather strong electrical microfields exist that give rise to strong contrasts in MEM (see fig. 2b). The reaction-diffusion front is also seen in LEEM (fig. 2c), but the particular contrast mechanism of LEEM is not capable of revealing all the zones with sufficient contrast. The possibility of selected-area low-energy electron diffraction (LEED) measurements within the microscope turned out to be extremely useful. Most of the zones could be identified as well known ordered adsorption phases (see fig. 3).

References

1. W. Telieps and E. Bauer, Ultramicroscopy 17 (1985) 57.

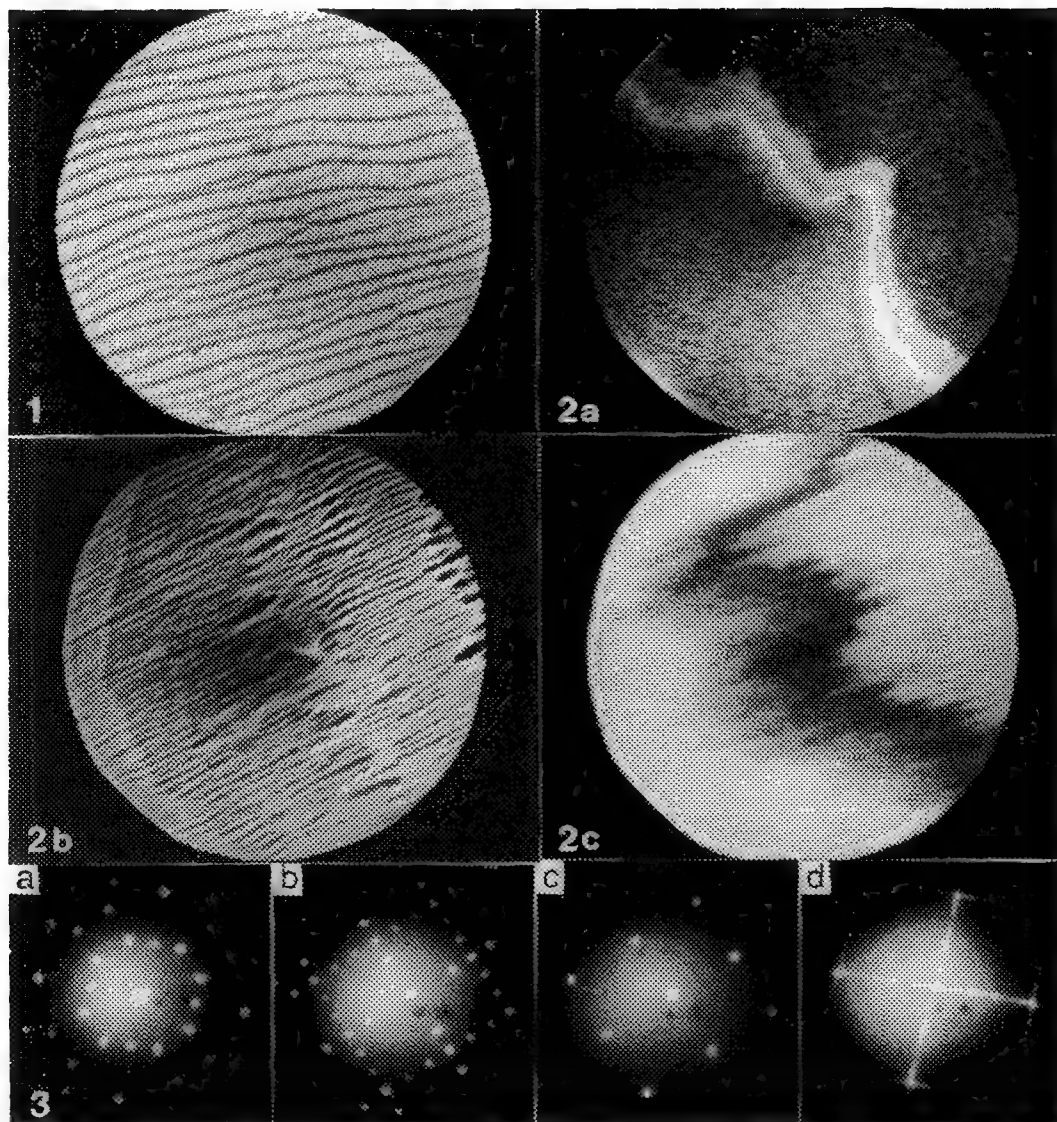


FIG. 1.--LEEM image of a Pt(100) surface revealing the surface topography. Image diameter 17 μm .

FIG. 2.--Images of reaction diffusion fronts obtained by (a) PEEM, image diameter 250 μm ; (b) MEM, image diameter 35 μm ; (c) LEEM, image diameter 35 μm . The fronts propagate from the upper right to the lower left.

FIG. 3.--LEED patterns of four of the adsorption phases which comprise a CO/O reaction diffusion front: (a) CO $c(4\times 2)$, (b) CO $(\sqrt{2}\times\sqrt{2})R45^\circ$, (c) CO $(\sqrt{2}\times\sqrt{2})R45^\circ$, (d) oxygen (5×1) .

MULTISLICE CALCULATIONS OF RHEED PATTERNS FROM VICINAL Si (001)

Scott Lordi

University of Illinois, Materials Research Laboratory, 104 South Goodwin, Urbana IL, 61801

Vicinal Si (001) surfaces are interesting because they are good substrates for the growth of III-V semiconductors.¹ Spots in RHEED patterns from vicinal surfaces are split due to scattering from ordered step arrays and this splitting can be used to determine the misorientation angle, using kinematic arguments.² Kinematic theory is generally regarded to be inadequate for the calculation of RHEED intensities; however, only a few dynamical RHEED simulations have been attempted for vicinal surfaces.³ The multislice formulation of Cowley and Moodie⁴ with a recently developed edge patching method⁵ was used to calculate RHEED patterns from vicinal Si (001) surfaces. The calculated patterns are qualitatively similar to published experimental results^{6,7} and the positions of the split spots quantitatively agree with kinematic calculations.

RHEED patterns were calculated for unreconstructed (bulk terminated) Si (001) surfaces misoriented towards [110], with an energy of 15 keV, at an incident angle of 36.63 mrad ([004] bragg condition), and a beam azimuth of [110] (perpendicular to the step edges) and the incident beam pointed down the step staircase. All angles are measured relative to the (001) plane. Double domain surfaces with monolayer steps and single domain surfaces with bilayer steps were both simulated. Fig 1a is a graph of the intensity along the specular rod versus exit angle for a double domain surface misoriented by $\beta=9.89$ mrad. Instead of the single peak at the specular beam position (36.63 mrad) which a flat surface would give, the curve has several maxima which correspond to the split spots in a RHEED pattern. The exact peak shapes (approximately $\sin(x)/x$) are artifacts of the calculation. Fig 2 is a graph of the angular positions of the intensity maxima along the specular rod versus misorientation angle. Solid lines are spot positions predicted by kinematic theory.

Fig 1b shows the intensity along the specular rod versus exit angle for a single domain surface misoriented by $\beta=9.89$ mrad. Calculations were performed for two incident angles (36.63 mrad and 59.52 mrad) and several misorientation angles ($\beta=9.89, 14.89, 19.92, 24.73, 29.2$ mrad). For the same misorientation angle calculated patterns for double and single domain surfaces exhibited differences qualitatively similar to the differences between fig 1a and 1b. These differences indicate that RHEED may be useful in determining the relative numbers of monolayer and bilayer steps on a vicinal surface.

Bulk terminated surfaces with regularly spaced steps are not very realistic models for actual vicinal surfaces. Future calculations will include the (1x2) and (2x1) surface reconstructions, irregularly spaced steps, and unequal step heights in order to determine what effect these complications have on RHEED intensities. Calculations for rough surfaces are also planned. This work demonstrates the feasibility of using the multislice method to calculate RHEED patterns from stepped surfaces.

1 JE Griffith and GP Kochanski, Crit. Rev. Solid State Mater. Sci. 16(1990) 255.

2 PR Pukite et al, Appl. Phys. Lett. 44(1984) 456.

3 T Kawamura, Prog. Theor. Phys. Suppl. 106(1991) 295.

4 JM Cowley and AF Moodie, Acta. Cryst. 10(1957) 609.

5 Y Ma and LD Marks, Acta. Cryst. A47(1991) 707.

6 PR Pukite and PI Cohen, Appl. Phys. Lett. 50(1987) 1740.

7 H Toyoshima et al, Surf. Sci. 264(1992) 10.

8 This work was supported by Department of Energy Grant DEFG02-91ER45439.

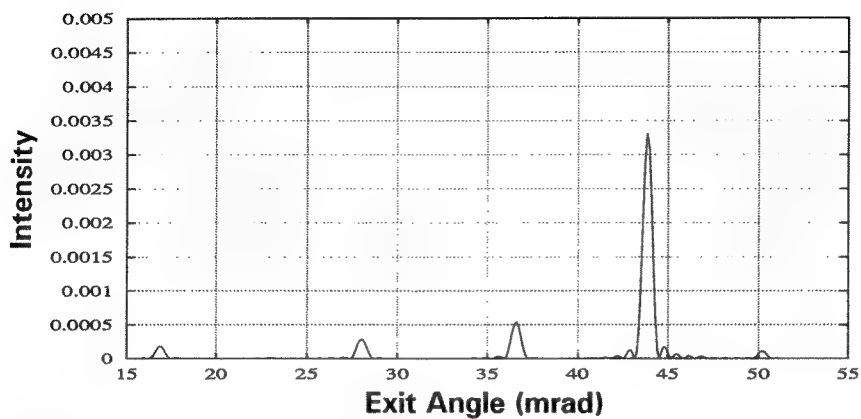


Fig 1a: Double domain surface.

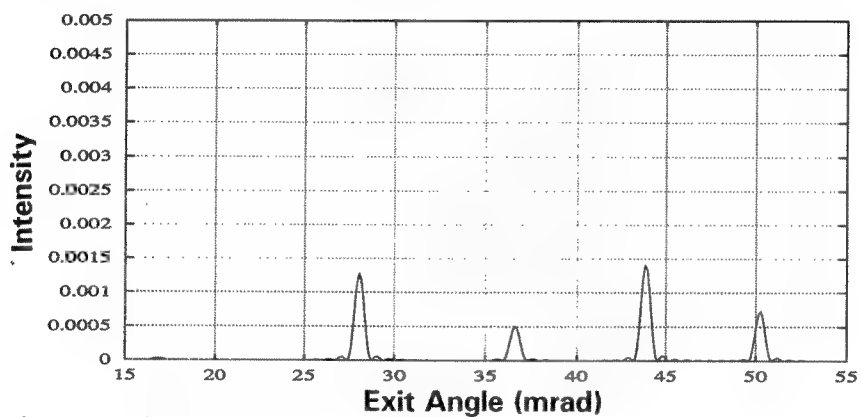


Fig 1b: Single domain surface.

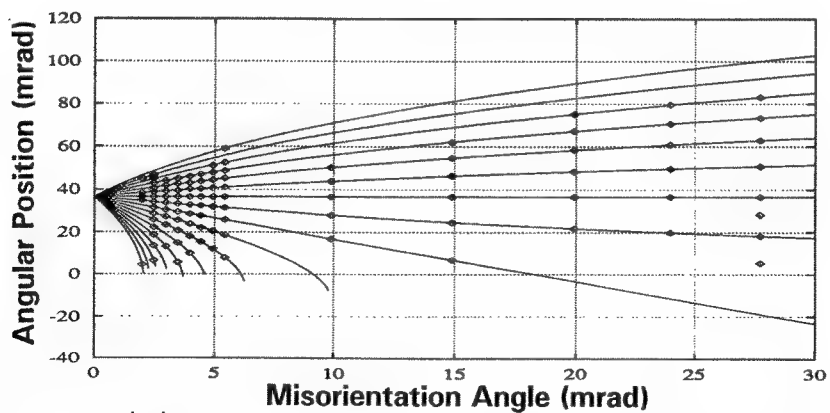


Fig 2: Positions of intensity maxima along specular rod.

UHV-TED STUDY OF CLEAN Si(100) SURFACE STRUCTURES

Ganesh Jayaram

Department of Materials Science and Engineering, Northwestern University, Evanston, IL 60208

Detailed information about the structure of silicon surfaces is very important prior to deposition of metal contacts. Though transmission electron diffraction is sensitive to the atomic structures of both the surface and the bulk, under appropriate conditions, information on the structure of the surface can be obtained from a careful analysis of the diffraction spot intensities¹.

Since Si(100) surface is highly reactive² (sticking coefficient for water = 1), preparation and observation of clean surfaces necessitates ultra-high vacuum (UHV) conditions. A thin sample of Si(100) (B doped to 1 ohm-cm) was prepared for observation inside a Hitachi UHV-H9000 300keV electron microscope (stable operation pressure $\sim 9 \times 10^{-11}$ Torr). It was mechanically polished, dimpled and ion-milled before being transferred into a UHV surface science chamber attached to the microscope³. *In situ* sample preparation carried out inside this chamber involved a combination of sputtering using 2-4 keV argon ions (to clean the surface) and electron-gun annealing cycles (to order the surface).

Though various complicated reconstruction patterns have been reported for the clean Si(100) surface⁴, this experimental investigation revealed only the simple 2×1 type. Since the surface atoms forming this reconstruction form dimers (symmetric and/or asymmetric along the (110) directions), the goal of this experiment was to solve the structure from a rigorous analysis of the diffraction patterns. Fig.1 shows a selected area diffraction pattern from an area with the 2×1 and 1×2 reconstructions. The reasonably strong diffraction spots due to these two domains are located at positions $(m/2, n)$ and $(m, n/2)$ in surface unit cell notations, where m and n are integers. The common characteristic of all diffraction patterns is the strong intensity of the (1,2) and (3/2,0) type spots (relative to the reconstruction spots). The intensity of the (1,1) type spots is very weak and in all cases shows streaking, a characteristic of the defects in the bulk. While the intensity of the surface reconstruction spots decayed as a function of time (2-3 hours), the intensity of the (1,2) type spots stayed unaffected during the same period of observation as can be seen in Fig.2 (decay seems to be caused by the residual water vapor in the system).

Diffraction patterns of the reconstructions thus obtained have been scanned using a microdensitometer. The relative intensity value for each spot was obtained by cleaning off the background using a high pass filter and then integrating the intensity around each surface cell spot. Under pseudo-kinematical conditions (Fig.1), the intensity of surface reconstruction spots would be sensitive to only the surface and possibly a few layers below it. These experimental values have been matched to the calculated intensities obtained using multislice simulations (for only a few layers into the bulk) for the two different dimer structures incorporating multilayer relaxations. Preliminary data analyses yield R-factors in both cases of ~ 0.1 -0.2 with a slight preference for the asymmetric structure (Fig.3). Analyses of diffraction data at different tilt conditions are being carried out at the present moment to fit the model to more rigorous multislice calculations (incorporating actual specimen thickness and tilt). This would better represent not only the registry of the reconstruction but also the strain field associated with it⁵.

REFERENCES

1. L. D. Marks, P. Xu and D. N. Dunn, Submitted to Surface Science.
2. P. A. Thiel and T. E. Madey, Surface Science Reports 7(1987)211.
3. L. D. Marks et al., Ultramicroscopy 37(1990)90.
4. N. Roberts and R. J. Needs, Surface Science 236(1990)112.
5. This work has been supported by the National Science Foundation on grant # DMR-92-14505.

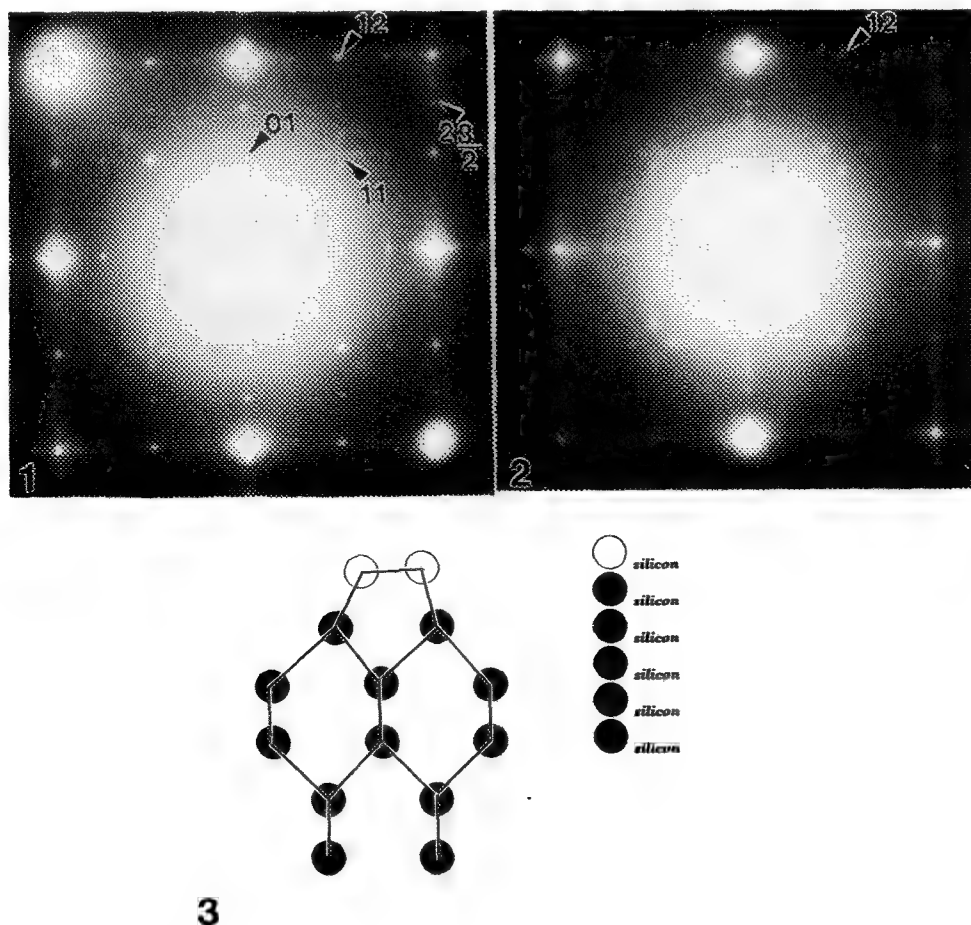


Fig.1 SAD pattern from a region with the 2x1 and 1x2 domains.

Fig.2 Typical SAD pattern after about 2-3 hours of observation inside the microscope showing no reconstruction. Note the strong intensity of the (1,2) spots.

Fig.3 A schematic of the 2x1 asymmetric dimer structure viewed along a (100) direction obtained from a multislice matching of the intensities of the diffraction spots in Fig.1. Hollow circles denote atoms in the topmost layer and the filled circles denote atom positions in the next five layers into the bulk.

CONTRASTS OF PLANAR DEFECTS IN REFLECTION ELECTRON MICROSCOPY

Feng Tsai and J. M. Cowley

Center for Solid State Science and Department of Physics and Astronomy, Arizona State University, Tempe, AZ 85287-1504

Reflection electron microscopy (REM) has been used to study surface defects such as surface steps[1], dislocations emerging on crystal surfaces[2], and surface reconstructions[3, 4]. However, only a few REM studies have been reported about the planar defects emerging on surfaces[5]. The interaction of planar defects with surfaces may be of considerable practical importance but so far there seems to be only one relatively simple theoretical treatment of the REM contrast[5] and very little experimental evidence to support its predications. Recently, intersections of both 90° and 180° ferroelectric domain boundaries with BaTiO_3 crystal surfaces have been investigated by Tsai and Cowley[6] with REM.

The REM observations of several planar defects, such as stacking faults and domain boundaries have been continued by the present authors. All REM observations are performed on a JEM-2000FX transmission electron microscope. The sample preparations may be seen somewhere else[6]. In REM, the incident electron beam strikes the surface of a crystal with a small glancing angle. One of the reflection-diffraction beam is used to form a foreshortened image of the surface. Therefore, a planar defect will appear quite different in the REM image depending on its position and orientation to the electron beam. Fig.1 is the illustration of the REM imaging of a planar defect in different orientations.

The intersections of stacking faults with surfaces are usually associated with surface steps. Shuman[5] considered the contrast due to the stacking fault in the crystal without considering the phase contrast due to the associated surface step. In practice the phase contrast due to the surface step tends to dominate the contrast and the oscillatory contrast predicated by Shuman has not been observed. Fig.2 shows an image of a stacking fault enclosed by two dislocations in GaAs. It is suggested that the stacking fault is enclosed by a dislocation loop. Because the step may be one or two slip vectors and the fault image is focus, the phase contrast is weak and sharp black line appears as a result of diffraction contrast. The mechanism of creation of the stacking fault is related to the growth of crystal.

The intersections of a twin boundary with a crystal surface will not produce a surface step but a diffraction contrast will be produced due to the difference of diffraction conditions at boundaries. 90° domain boundary in BaTiO_3 are good examples because they are twin boundaries on $\{110\}$ planes. An example of 90° domain boundaries in REM is given in Fig.3. The contrast of the 90° domain boundaries has been suggested as diffraction contrast and additional dark or bright line contrast appears to be from lattice distortions in the vicinity of 90° domain boundaries[6].

The 180° domain boundaries in BaTiO_3 are antiphase domain boundaries. Some 180° domain boundaries in REM are indicated in Fig.3. It has been found the contrast of 180° domain boundaries are very sensitive to the deviations in orientation from the zone axis. The origin of the contrast of 180° domain boundaries is still unknown. It may be related to the lattice distortions of intersections of 180° domain boundaries with the crystal surface. Further study is being carried on.

REFERENCES

1. T. Hsu and J. M. Cowley, *Ultramicro.*, 11(1983)551.
2. L. M. Peng and J. M. Cowley, *Ultramicros.*, 26(1988)161.
3. Y. Tanishiro, K. Tanyanaigi and K. Yagi, *J. Microscopy*, 142(1986)211.
4. G. Lehmppfuhl, Y. Uchida and N. Wang, *Ultramicros.*, in press.
5. H. Shuman, *Ultramicros.*, 2(1977)361.
6. F. Tsai and J. M. Cowley, *Ultramicros.*, 41(1992)53

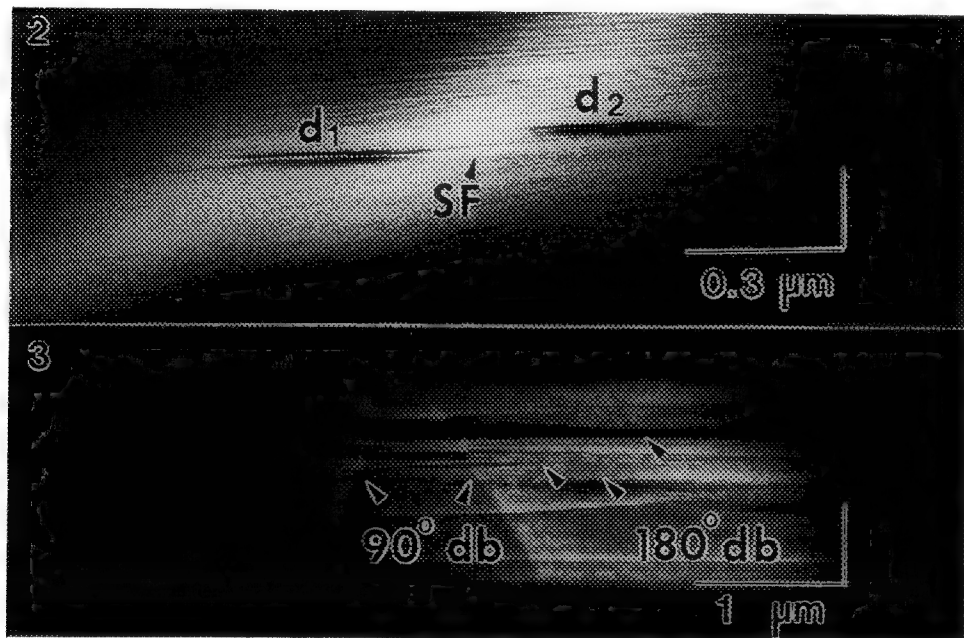
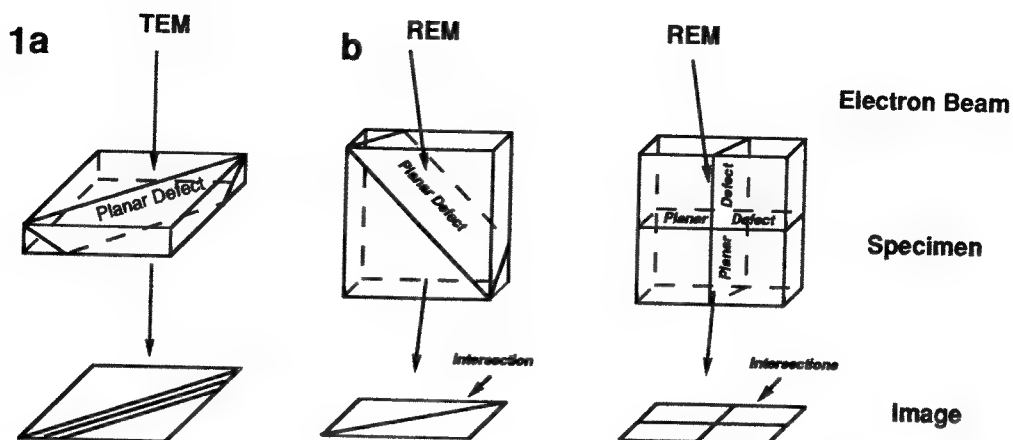


Fig.1. The schematic representation of TEM and REM imaging of a planar defect, (a)TEM; (b)+(c): REM.

Fig.2. A REM image of a stacking fault enclosed by two dislocations of the opposite signs emerging on the (110) surface of GaAs single crystal.

Fig.3. A REM image of the intersections of 90° and 180° domain boundaries (arrowed) emerging on (100) surface of $BaTiO_3$ single crystals. The intersections are nearly parallel to the direction of the incident electron beam, which is nearly parallel to [010] zone axis.

Acknowledgement: The authors wish to thank Dr. J. M. Zho for many useful discussions on REM. The work is supported by NSF grant DMR 91-10386 and made use of the ASU Facility for High Resolution Electron Microscopy supported by NSF grant DMR 89-13384.

REFLECTION ELECTRON MICROSCOPY OF AS-GROWN DIAMOND SURFACES

Z.L. Wang*, J. Bentley, R.E. Clausing, L. Heatherly and L.L. Horton

Metals and Ceramics Division, Oak Ridge National Laboratory, Oak Ridge, TN 37831-6376;

* and Department of Materials Science and Engineering, The University of Tennessee, Knoxville, TN 37996-2200

It has been found that the abrasion of diamond-on-diamond depends on the crystal orientation.^{1,2} For a {100} face, the friction coefficient for sliding along $\langle 011 \rangle$ is much higher than that along $\langle 001 \rangle$. For a {111} face, the abrasion along $\langle 11\bar{2} \rangle$ is different from that in the reverse direction $\langle \bar{1}12 \rangle$. To interpret these effects, a microcleavage mechanism was proposed^{1,2} in which the {100} and {111} surfaces were assumed to be composed of square-based pyramids and trigonal protrusions, respectively. Reflection electron microscopy (REM) has been applied to image the microstructures of these diamond surfaces.³

{111} surfaces of synthetic diamond: The synthetic diamonds used in this study were obtained from the De Beers Company. They are in the as-grown condition with grain sizes of 0.5-1 mm without chemical treatment or mechanical polishing. By selecting a strong reflected beam in the reflection high-energy electron diffraction (RHEED) pattern, the dark-field REM image of the surface is formed (Fig. 1). The dark "patches" on the surface are probably surface contaminants, which cannot be removed by ultrasonic washing in acetone. Besides these contaminants, unequally spaced contrast fringes, separated by approximately 3-6 nm and running parallel or almost parallel to the incident beam direction (from the top to the bottom of the micrograph), are observed. It appears that these fringes arise from surface topography rather than interference effects.

It was proposed that the diamond {111} surfaces were composed of small trigonal protrusions of about 5 nm in size,^{1,2} which are oriented, the corners pointing to the edges of the triangular outline of the octahedral faces (Fig. 2). When observed along $[0\bar{1}1]$, these features could appear in rows due to the foreshortening effect of REM, forming the observed topography fringes (Fig. 1).

{100} surfaces of as-grown CVD diamond: Single crystal diamond thin films grown with a hot filament assisted chemical vapor deposition (CVD) system on single crystal natural diamond {100} substrates were also studied by REM. The as-grown film is a [100] single crystal. The surface microstructure appears complex in REM images (Fig. 3). The features can be summarized as: (1) regions of dark contrast (possibly contaminants); (2) lines of contrast running parallel to the beam direction [010] with separations of 6-11 nm; and (3) "hill" and "valley" topography, each hill showing piled-up steps. The observed fringes appear to be due to surface topographic contrast and may correspond to the existence of square-based pyramids (Fig. 4) on the {100} surface as expected.^{1,2} In addition, nanometer-scale structures have also been observed on polished natural diamond {100} surfaces, and the friction tracks produced during abrasion experiments have been directly imaged, even for a single pass of measurement, with REM.³

In conclusion, REM has revealed that the diamond {111} and {100} surfaces in as-grown conditions may be composed of regularly arranged nanometer-scale protrusions, in agreement with the expected result of abrasion experiments.^{1,2} Atomically flat surfaces of as-grown diamonds are rarely seen. Further studies using atomic force microscopy are in progress.⁴

References:

1. A.G. Thornton and J. Wilks, J. Phys. D: Appl. Phys., **9** (1976) 27.
2. E.M. Wilks and J. Wilks, J. Phys. D: Appl. Phys., **5** (1972) 1902.
3. Z.L. Wang, Z. Feng and J.E. Field, Philos. Mag., **A 63** (1991) 1275.
4. This research was sponsored by the Division of Materials Sciences, U.S. Department of Energy, under contract DE-AC05-84OR21400 with Martin Marietta Energy Systems, Inc.

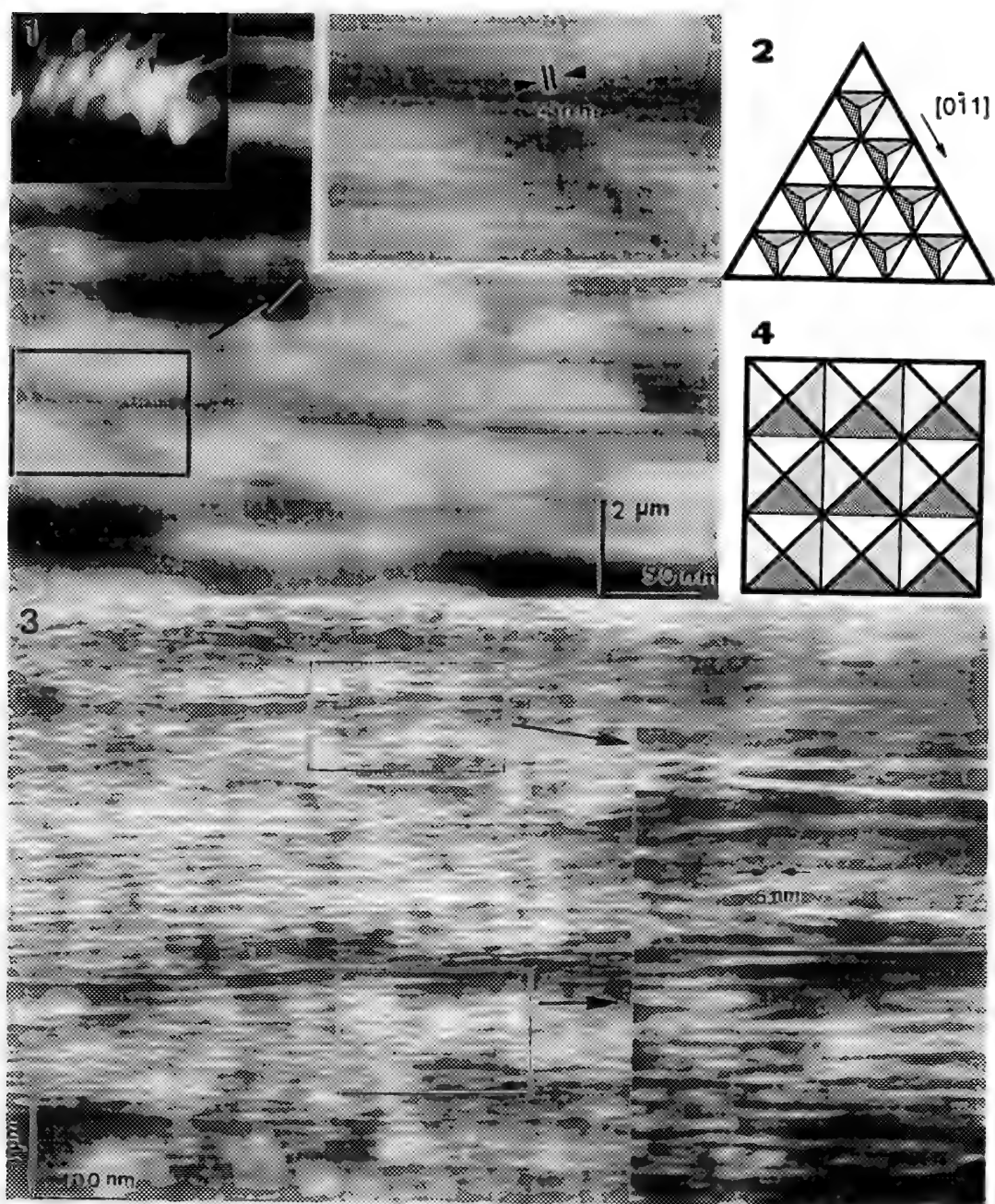


FIG. 1.--REM image of synthetic diamond (111) surface. Difference in scale is due to foreshortening effect along beam direction $[0\bar{1}1]$ in REM geometry.

FIG. 2.--Schematic showing expected nm size trigonal protrusions on diamond (111) surface.

FIG. 3.--REM image of as-grown CVD $[100]$ single crystal diamond film, showing nanometer-scale surface growth topographic features.

FIG. 4.--Schematic showing expected nanometer square-based pyramids on diamond (100) surface.

STRUCTURE DETERMINATION OF MBE-GROWN GaAs(001)-2X4 SURFACES BY QUANTITATIVE RHEED ANALYSES

Y. Ma, S. Lordi and J. A. Eades

Materials Research Laboratory, University of Illinois at Urbana-Champaign

The GaAs(001) surface is the most widely used gallium arsenide face in the MBE growth of multilayer electronic device structures. Various reconstructions on this face have been reported. They range from the As-rich (2x4) to the Ga-rich (4x2).¹ The As-rich (2x4) surface is the most important one of these, since MBE growth usually starts and ends with this surface. A multislice formalism of Cowley & Moodie² with a recently developed edge patching method^{3,4} has been applied to quantitative analyses of the RHEED patterns from MBE grown GaAs(001)-2x4 surfaces.⁵ The analyses are based on the ordering of visually estimated spot intensities of the observed RHEED patterns from the GaAs(001)-2x4 surfaces, which is similar to the approach used in early X-ray structure determinations. The surface structure has been proved to be a dimerized vacant 2x4 reconstruction with one dimer of every four missing, which is consistent with previous STM observations.⁶ The results show that the relaxation of reconstructed atoms in the top surface layer (δ) is the parameter most sensitive to the intensities of observed RHEED patterns. It has been refined to be 10 ± 5 %. The dimer length (l_d) was determined semi-quantitatively as $2.0 < l_d < 2.5 \text{ \AA}$, with the help of the observed RHEED pattern acquired in the [110] azimuth.⁷ The effects of dimer twist on the intensities of RHEED patterns were also briefly assessed, which indicated that twist of dimers on the GaAs(001)-2x4 surface is unlikely. There was no match between kinematically calculated and observed spot intensities. This demonstrates again that RHEED is basically a dynamical process and the kinematic approximation cannot be used for quantitative analysis.

Fig. 1 shows diagrams of three dimer vacancy models of GaAs(001)-2x4 surfaces: two-dimer-missing reconstruction (a, b) and one-dimer-missing reconstruction (c). Both STM imaging and the RHEED results here confirm that (c) is the structure of the stabilized GaAs(001)-2x4 surfaces. Fig.2 illustrates three experimental RHEED patterns from the GaAs(001)-2x4 surfaces along the [110] azimuth, at different angles of incidence. The calculated RHEED intensities for different surface relaxation values are listed in Table 1, together with the visually estimated intensities of experimental patterns in Fig.2 for comparison. The minimum R-values are obtained at about $\delta=10\%$ for all three angles of incidence. It becomes more evident that the three calculated patterns for $\delta=10\%$ match the observed patterns best, if one compares the intensity ordering of near-neighbor spots. This work was supported by the Department of Energy, Grant No. DEFG02-91ER45439. The authors would like to thank Dr. P. K. Larsen for the experimental RHEED patterns he provided and useful discussions.

1. P. Drather et al., Surface Sci., 77(1978)L162.
2. J. M. Cowley and A. F. Moodie, Acta Cryst., 10(1957)609.
3. Y. Ma, Acta Cryst., A47(1991)37.
4. Y. Ma and L. D. Marks, Acta Cryst., A47(1991)707.

5. P. K. Larsen and G. Meyer-Ehmsen, *Surface Sci.*, **240**(1990)168.
6. M. D. Pashley et al., *Phys. Rev. Lett.*, **60**(1988)2176.
7. P. K. Larsen and D. J. Chadi, *Phys. Rev.*, **B37**(1988)8282.

Figure 1. Diagrams of three models of GaAs(001)-2x4 surfaces.

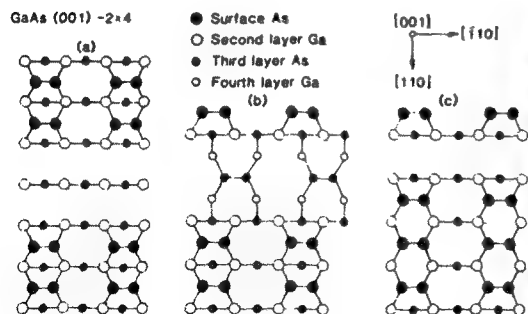


Figure 2. Experimental RHEED patterns from GaAs(001)-2x4 surfaces (P. K. Larsen).

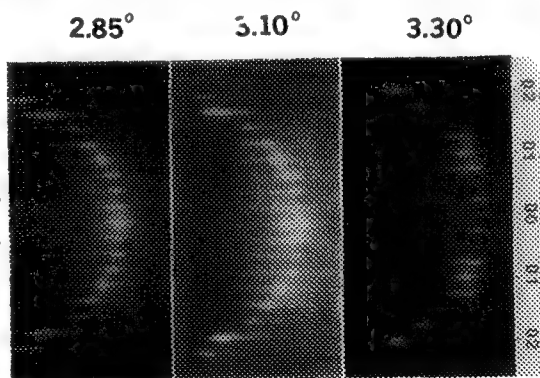


Table 1

		Vision In.			Calculated In. (Relaxation)				
	(0,k)	Let.	Numer.	-20%	-10%	0%	10%	20%	30%
2.85deg	0	ss	1.000	1.0000	1.0000	1.0000	1.0000	.3887	.0961
	1/4	w	.250	.0417	.0468	.0577	.0906	.0612	.0155
	1/2	w	.200	.0082	.0099	.0049	.0002	.0076	.0316
	3/4	m	.400	.1716	.1528	.2212	.4319	.3899	.2231
	1	s	.750	.0095	.0841	.2847	.7654	.8456	.5740
	5/4	w	.250	.4289	.4275	.3686	.2612	.0357	.0502
	3/2	ww	.050	.1663	.0923	.0692	.1290	.1803	.2375
	7/4	m	.500	.3045	.2964	.4079	.8449	1.0000	1.0000
	2	ww	.010	.0061	.0050	.0037	.0041	.0055	.0079
	R-value			0.36	0.31	0.16	0.09	0.36	0.60
3.10deg	0	s	.800	1.0000	1.0000	.7237	.4295	.2500	.1681
	1/4	m	.300	.0064	.0033	.0414	.1136	.2137	.2602
	1/2	w	.100	.0363	.0164	.0165	.0419	.0906	.1213
	3/4	m	.250	.0534	.0747	.0827	.0839	.0913	.0783
	1	s	.750	.0458	.1586	.3936	.6736	1.0000	1.0000
	5/4	m	.500	.1535	.1385	.0859	.0507	.0480	.0418
	3/2	w	.100	.1454	.2335	.2872	.3062	.3129	.2041
	7/4	ss	1.000	.6241	.8834	1.0000	1.0000	.9838	.6611
	2	ww	.050	.1268	.1464	.1041	.0463	.0221	.0585
	R-value			0.36	0.26	0.17	0.17	0.25	0.32
3.30deg	0	ww	.030	.1411	.0228	.0119	.0627	.1001	.1267
	1/4	w	.050	.0332	.0529	.0595	.0472	.0352	.0275
	1/2	ww	.010	.0349	.0481	.0508	.0357	.0229	.0151
	3/4	m	.300	.0884	.1281	.1353	.1049	.0768	.0556
	1	m	.500	.2291	.4265	.4593	.3185	.1964	.1165
	5/4	w	.050	.0250	.0336	.0257	.0116	.0063	.0070
	3/2	ww	.010	.4266	.3987	.2487	.1065	.0458	.0229
	7/4	w	.200	.5417	.5464	.3836	.1860	.0819	.0301
	2	ss	1.000	1.0000	1.0000	1.0000	1.0000	1.0000	1.0000
	R-value			0.30	0.22	0.09	0.06	0.12	0.18

RECENT ADVANCES AND OPPORTUNITIES IN MAGNETIC RECORDING MATERIALS

Mark H. Kryder

Engineering Research Center in Data Storage Systems,
Carnegie Mellon University, Pittsburgh, PA 15213-3890

Recording densities in magnetic recording products manufactured today are of the order of 200 Mbit/in². However, it is projected that densities as high as 10 Gbit/in² will be achieved in the future. To achieve this, substantial improvements in the thin film magnetic materials used for magnetic heads and media are required.

To support higher recording density in thin film media, it is necessary to increase the coercivity, while simultaneously achieving small grain size and small intergranular coupling. To achieve high coercivity, materials with large magnetocrystalline anisotropy are used, while to achieve small, well-isolated grains, special materials are used and deposited under conditions which promote either heavily voided grain boundaries or the segregation of non-magnetic species to the grain boundaries. It is also thought to be important to control the orientation of the crystallites so that a preferred axis of magnetization lies parallel to the direction of recording. Although current thin film magnetic disk media are based on hcp-Co alloys, for future applications SmCo/Cr{110} films¹ and Ba-ferrite thin films are also of interest. Both of these materials offer considerably stronger magnetocrystalline anisotropy and therefore higher coercivity than the hcp-Co alloys. In this talk the relationships between processing conditions, microstructure, and magnetic properties of new thin film recording media will be discussed.

To write on high coercivity media, improved recording heads with higher saturation flux density are needed. To this end researchers have been investigating new magnetic alloys with higher magnetization than Sendust (FeAlSi) or Permalloy (NiFe) which are commonly used today. Some of the most promising materials are FeN/SiO₂ or FeN/Al₂O₃ multilayers, deposited by sputtering. These materials have saturation flux densities twice that of Permalloy or Sendust. Simultaneously achieving all the soft magnetic properties necessary for a good magnetic recording head material requires careful selection of a third element addition to the reactively sputtered FeN to control grain size and proper multilayering to simultaneously achieve high permeability and zero magnetostriction.

To obtain large signals during readback it is desirable that improved magnetoresistive materials be developed. To that

end, giant magnetoresistive multilayer materials and spin valve materials are being actively pursued in a large number of laboratories around the world. These materials exhibit large differences in resistance, depending upon whether the magnetization of neighboring magnetic layers are parallel (low resistance state) or antiparallel (high resistance state). Exchange coupling between antiferromagnetic and ferromagnetic layers is used in the spin valve materials to bias the magnetization into the desired directions.

In this talk the physics of the magnetic recording process which necessitates these properties, the relationships between the processing, microstructure and desired magnetic properties, as well as the use of high resolution microscopy techniques used to investigate the microstructural properties will be discussed.

MICROSTRUCTURE AND MAGNETIC STRUCTURE OF Co-BASED THIN-FILM RECORDING MEDIUM

M. Futamoto, Y. Honda, N. Inaba, Y. Matsuda, and M. Suzuki

Central Research Laboratory, Hitachi Ltd., Kokubunji, Tokyo 185, JAPAN

Knowledge of the relationship between microstructure and microscopic magnetization configuration is strongly required to improve Co-based thin film media. The purpose of this paper is to report some of these properties measured for a thin film longitudinal recording medium and to discuss their inter-relationship.

Figure 1 shows an SEM micrograph of fractured cross-section of CoCrPt/CoCrPtSi dual-layered medium which was used to demonstrate the feasibility of 2 Gb/in² magnetic recording^{1,2}. The Cr underlayer is used to control the orientation, size, and distribution of magnetic crystals. Magnetic crystal grains, whose size ranges between 20-30nm, form chain-like clusters consisting of several crystals as shown in the plan-view TEM micrograph(Fig.2). Neighboring clusters are separated physically with an average distance of 3nm. Magnetic separation among magnetic crystals and/or clusters is important to reduce the medium noise which is related to magnetic coupling between crystals. The crystalline easy axes of the grains are randomly oriented in the film plane. High-resolution cross-sectional TEM(Fig.3) shows that magnetic crystals are grown epitaxially on Cr crystals with a relationship of (100) or (101) hcp Co-alloy // (110)bcc Cr. The easy magnetization axis of the Co-alloy grain lies about 30 degrees off the interface plane. Figs 4 and 5 show MFM images of magnetization pattern recorded with a thin film recording head at the same head-to-medium spacing^{3,4}. The width of magnetization transition is estimated to be about 0.1 μm . The signal spread of magnetization beyond the recording track edge estimated from the MFM data decreased from 0.2 to 0.1 μm corresponding to the linear recording density increase from 20 to 100 kFCI. The magnetization configuration depends on the magnetic field distribution of the recording head as well as the medium microstructure^{3,4}. Comparison between the SEM, an AFM, and the MFM images obtained from the same medium suggests that the size of the image irregularities in MFM reflects the presence of magnetic cluster which consists of several crystal grains and that the cluster tends to behave as one unit when magnetized. This is due to a stronger magnetic coupling along the chain-like magnetic crystals. Fig.6 depicts the magnetization structure of tracks recorded with an extremely narrow track-width-head showing the feasibility of ultra-high density magnetic recording well over 1 Gb/in² using longitudinal magnetic recording. The effect of microstructure on the magnetization configuration is clearly more enhanced when the recording unit cell approaches the size of magnetic crystal. A series of magnetization structures observed by MFM suggests a strong need to investigate the crystalline-order micromagnetics utilizing a well considered combination of high resolution structural and magnetic microscopies in order to improve the thin film recording medium for ultra-high density magnetic recording applications.

References

1. M. Futamoto et al, *IEEE Trans. Magn.* Vol.27(1991)4678.
2. Y. Matsuda et al, *J. Magn. Soc. Japan* Vol. 15 (1991) 1001.
3. Y. Honda et al, *Proc. 1993 Intermag Conference*, (submitted to *IEEE Trans. Magn.*).
4. Y. Honda et al, *Japan J. Appl. Phys.* Vol.31(1992)L1061.

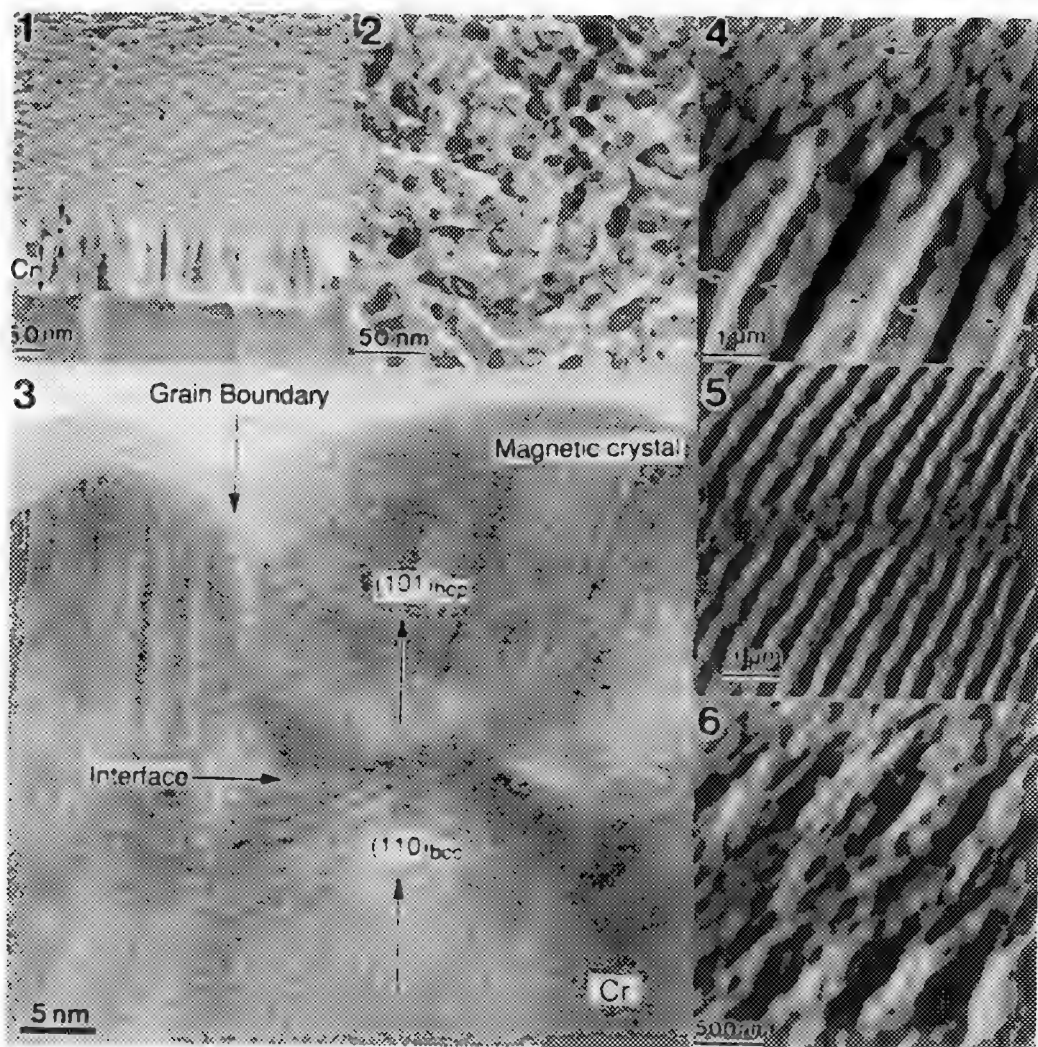


FIG.1 -SEM of longitudinal recording medium consisting of C(10nm)/CoCrPt(15nm)/CoCrPtSi(15nm)/Cr(150nm)/Glass. * shows magnetic layer.
 FIG.2 -Distribution of magnetic crystals in thin film medium observed by plan-view TEM.
 FIG.3 -High resolution TEM of cross-sectional medium structure.
 FIG.4 -MFM of magnetization structure recorded at a linear density of 20 kFCI. The arrows show magnetization directions.
 FIG.5 -MFM of magnetization structure recorded at a linear density of 100 kFCI. Two tracks are recorded with a separation guard-band width of 1 μm .
 FIG.6 -Magnetization structure of tracks recorded with 0.8 μm track-width head.

APPLICATIONS OF TRANSMISSION ELECTRON MICROSCOPY TO MICROSTRUCTURE, EPITAXY, AND PREFERRED ORIENTATION IN MAGNETIC THIN FILMS

Michael Andrew Parker

IBM Fellow Program, IBM ADSTAR, San Jose, California 95193

J. Kent Howard, some years ago, published an extensive review of the phenomenon of what he referred to as "grain-to-grain" or "polycrystalline" epitaxy in thin films.¹ Of the six or so different applications of this phenomenon, from superconductors to magnetics, none has greater technological significance than applications to magnetic thin films. This derives from the magnetic anisotropy of these thin films which has such a profound influence on their magnetic properties. In particular, magnetocrystalline anisotropy is often used to engineer thin films with the desired orientation of the easy axis of magnetization for magnetic recording media applications.^{2,3} Magnetocrystalline anisotropy is intimately connected to the crystallographic preferred orientation of the grains composing the magnetic layer which can be controlled through the skillful use of epitaxy with a suitable sublayer. The techniques of AEM, especially elongated probe microdiffraction (EPMD)⁴, have proven themselves invaluable for characterizing the microstructure of such thin films. In the following, we present a number of examples of the application of not only AEM, but also XTEM, CTEM, and HRTEM, to the elucidation of crystallographic structure/property relationships in magnetic thin films.

Fig. 1 illustrates the application of XTEM⁵ and CTEM to elucidate the microstructure of CoPtCr/Cr bilayers used for magnetic recording media. Conventional bright field (BF) and dark field (DF) images are used to great effect in characterizing the grain size, and intergranular separation in the magnetic layer as a function of the Cr sublayer thickness. The epitaxy between the Cr sublayer and the magnetic CoPtCr layer is clearly demonstrated by the continuity of columnar grains from the Cr right through the CoPtCr in the DF image. From quantification of the microstructural features in these images, the structure/property relationships illustrated in Fig. 2 were derived.⁶ Fig. 3 shows an example of the application of AEM, specifically the EPMD technique, to examine the epitaxy between the sublayer and CoPtCr as a function of alloy additions of V to the Cr sublayer. By elongating the electron probe using the condenser stigmators, it was possible to profile the preferred orientation in the various individual layers lying at different depths within the structure when examined in cross-section.⁴ For the 80/20 (atomic %) CrV alloy, increased epitaxy between the {200} sublayer grains and {1120} CoPtCr grains is indicated by the absence of any other reflections in the direction perpendicular to the plane of the film. Increased numbers of {200} sublayer grains are favored for compositions of the sublayer with concentrations of V between 80% and 50% which give rise to increasing numbers of {1120} CoPtCr grains with the easy axis of magnetization in the film plane. This offers some explanation for the enhancement of coercivity for films with sublayers of this composition shown in Fig. 4.⁷ Fig. 5 shows HRTEM images of epitaxial Ba-hexaferrite on sapphire substrates with various orientations. The continuity of {0001} basal planes of close-packed oxygen ions across the interface clearly shows that the easy axis of magnetization [0001] (which is also the easy axis for CoPtCr alloys) changes orientation depending upon the orientation of the substrate.⁸ Ba-hexaferrite has applications both for magnetic recording and microwave filters.

References

1. J. K. Howard, J. Vac. Sci. Technol. A (1986)4, 2975.
2. J. K. Howard, R. Ahlert, and G. Lim, J. Appl. Phys. (1987)61, 3834.
3. K. E. Johnson et al., J. Appl. Phys. (1990)67, 4686.
4. M. A. Parker et al., Elec. Micro. Soc. Amer. Proc. (1991)49, 762.
5. M. A. Parker et al., Mat. Res. Soc. Symp. Proc. (1990)199, 331.
6. M. A. Parker et al., IEEE Trans. Magn. (1991)MAG-27, 4730.
7. M. A. Parker et al., J. Appl. Phys. (1992 Mag. Mag. Mats. Conf.) submitted.
8. T. L. Hylton, M. A. Parker, and J. K. Howard, Appl. Phys. Lett. (1992)61, 867.

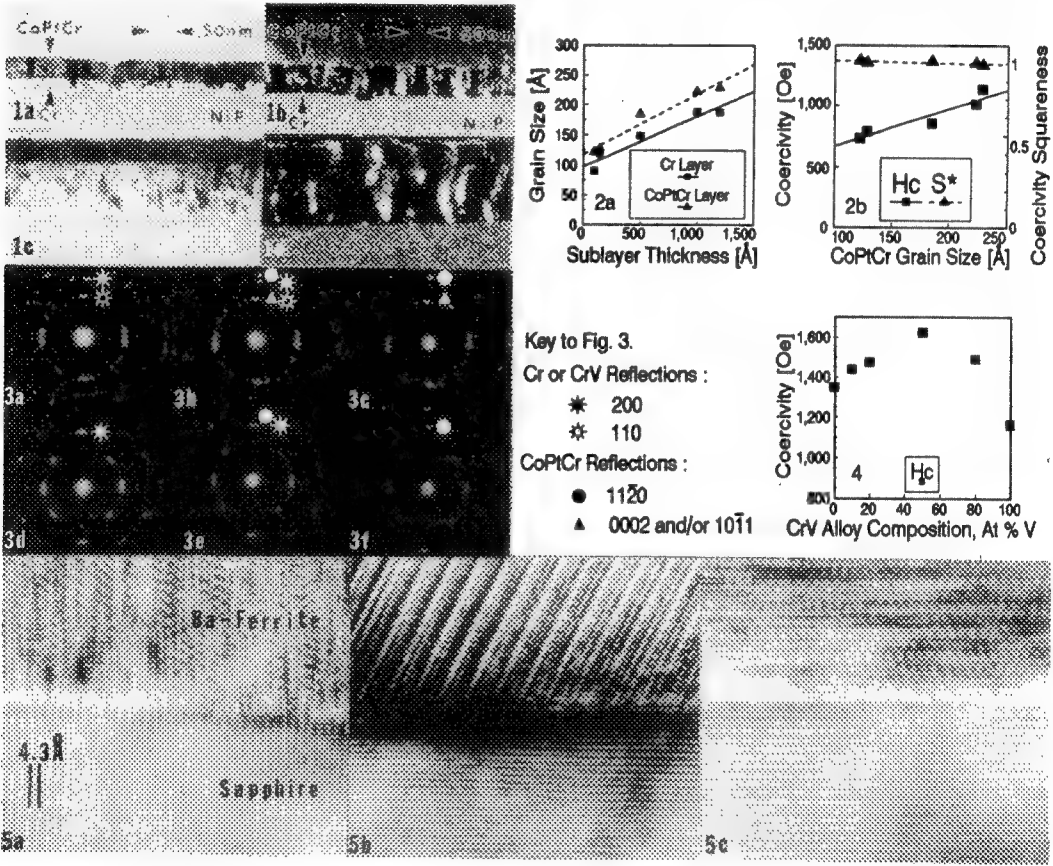


FIG. 1.--XTEM images of CoPtCr/Cr with 15nm Cr in a) BF, and b) DF, and with 120nm Cr in c) BF, and d) DF. Bar = 50 nm.
FIG. 2.--Structure/Property relationships inferred from CTEM for a) grain size, GS, in CoPtCr and Cr vs. Cr thickness; and b) coercivity, H_c , and coercivity squareness, S^* , vs. CoPtCr grain size, GS_{Co} .
FIG. 3.--EPMD patterns comparing a) the pure Cr layer with d) the 80/20 CrV layer, comparing the CoPtCr/sublayer interface on b) pure Cr with that on e) 80/20 CrV, and the CoPtCr layer on c) pure Cr with that on f) 80/20 CrV.
FIG. 4.--Coercivity of CoPtCr vs. composition of CrV sublayers.
FIG. 5.--HRTEM image of epitaxial Ba-hexaferrite on a) (1120), b) (1102), and c) (0001) sapphire substrates.

CORRELATION OF MICROSTRUCTURAL AND MAGNETIC PROPERTIES OF LONGITUDINAL RECORDING MEDIA USING TEM

T. P. Nolan*, R. Sinclair*, T. Yamashita** and R. Ranjan**

*Department of Materials Science and Engineering, Stanford University, Stanford, CA 94305

**Komag Inc., 591 Yosemite Drive, Milpitas, CA 95035

Cobalt alloy on chromium thin film media are used in industry because of their large values of coercivity (H_c), remanent magnetization (M_r), squareness (S^*), and relatively low noise. The magnetic properties depend strongly on processing conditions and, as will be shown, the resulting microstructure.

A complete structure-processing-properties analysis requires effective measurement of both magnetic and microstructural properties. Direct micromagnetic-microstructural comparison is not yet readily available, but bulk hysteresis loop parameters are reproducible and highly correlated with both desired recording characteristics and microstructures, and so provide a valuable, albeit indirect comparison. Signal to noise (S/N) measurements are also used as a more direct measure of usefulness in a high density disk drive. The nanoscale microstructural features which dramatically affect these bulk magnetic properties are difficult to observe. However, careful combination of TEM techniques, including bright-field, dark-field, high-resolution, selected area diffraction and elongated-probe microdiffraction can determine the subtle microstructural differences.⁶ It will be shown that the processing of the NiP plated aluminum substrates, the chromium underlayer, and the Co alloy magnetic layer independently and in collusion, determine the effectiveness of the resulting magnetic medium.

The NiP plated layer (FIG. 1) is stiff and easily polished to give different surface morphologies. At low temperature NiP is amorphous and non-magnetic, giving an isotropic growth surface, and the resulting magnetic properties are independent of polishing. At higher temperatures the growth surface is unchanged, but anisotropic polishing can result in magnetic anisotropy.¹⁻³ TEM shows that the Co alloy crystallography can follow the local substrate surface normal, which changes the out-of-plane component of the Co alloy's magnetic easy axis and changes magnetic properties.

The Cr underlayer (FIG. 1) grows in a crystalline, columnar structure on the amorphous NiP. TEM shows that low temperature chromium nucleates with a weakly preferred $\langle 200 \rangle$ surface normal orientation, but $\langle 110 \rangle$ orientation is weakly preferred during growth.⁴ The result is a film with nearly random crystallographic orientation and a morphologically rough surface. At higher temperature, the preferred $\langle 200 \rangle$ nucleation becomes increasingly strong, and is maintained during growth. The strong Cr $\langle 200 \rangle$ orientation is required for the in-plane Co alloy easy axis and the substrate induced anisotropy.

The Co alloy layer (FIG. 1) forms a crystalline, columnar structure on the Cr underlayer. At low temperature the topography has little effect upon the crystallography of the Co alloy, but has a much greater effect upon the physical morphology. At higher temperature the morphology of the Co alloy layer is largely unaffected by the substrate, but the growth orientation can be precisely controlled with the aid of a coherent Co alloy-Cr interface. The quality and extent of coherence depends dramatically on the Co alloy-Cr lattice match, and thus on the temperature, alloy composition, and even the physical topology.⁵ TEM shows that Pt addition to a CoCr alloy increases the lattice parameter mismatch with Cr, and the stacking fault density. Ta addition physically separates grains, improving noise performance.

These relationships and many more must be optimized in order to produce the best possible recording media, and it is clear that TEM will become an increasingly important tool for understanding these relationships as the critical size of most important features reach the nanometer scale.

References

1. E. Teng and N. Ballard, IEEE Trans. Magn., **22**, 579 (1986).
2. S. Uchinami, et al., IEEE Trans. Magn., **23**, 3408 (1987).
3. Nolan et al., J. Appl. Phys., in press, May 15 (1993).
4. Nolan et al., IEEE Trans. Magn., **29**, 292 (1993).
5. Nolan et al., J. Appl. Phys., in press, May 15 (1993).
6. Nolan et al., Ultramicroscopy, **47**, 437 (1992).

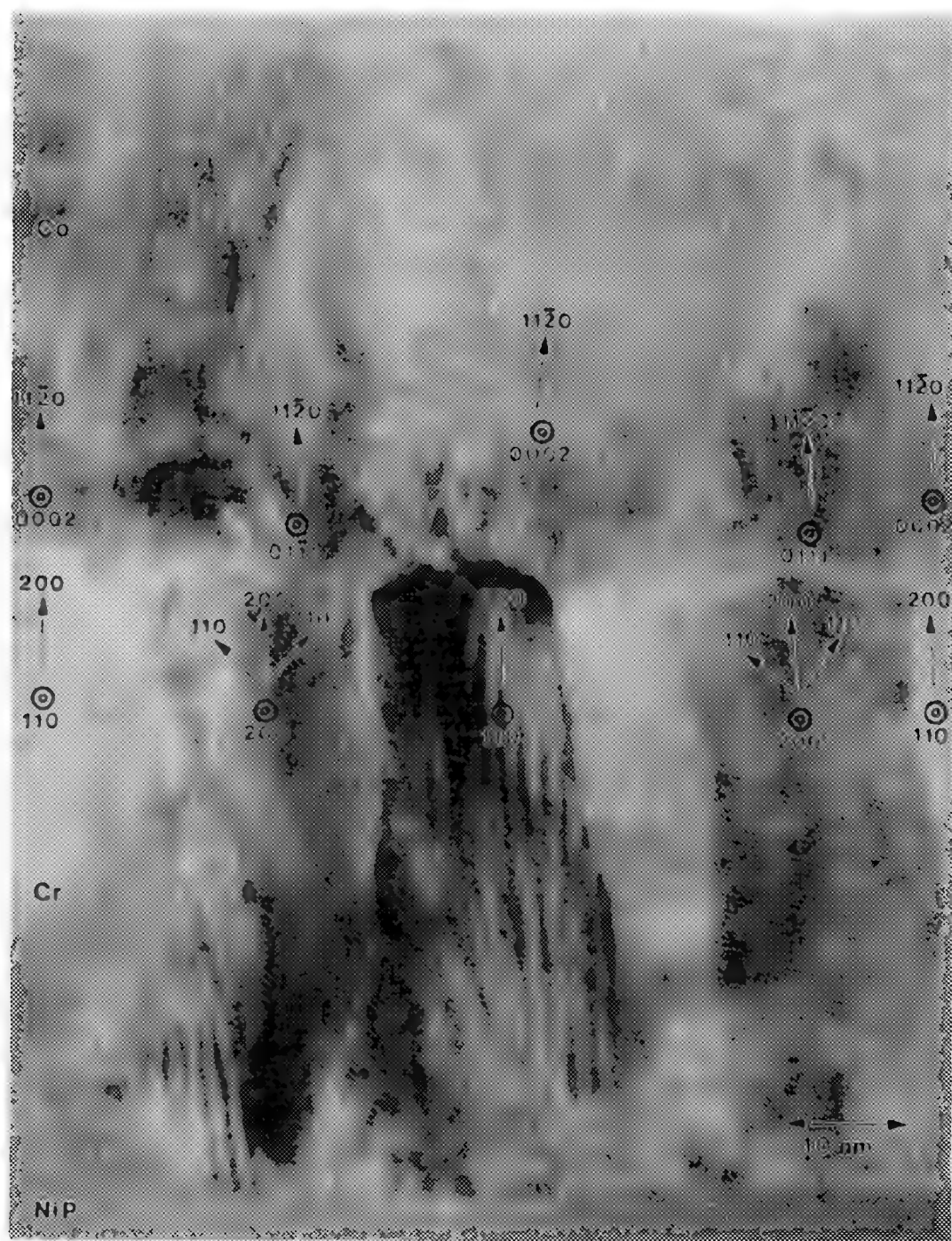


FIG. 1—Low magnification, high-resolution cross-section TEM image of a CoCrTa/Cr/NiP medium deposited under high mobility conditions, showing the morphology and crystallography of the layers.

Materials Science Aspects in Designing Giant Magnetoresistance in Heterogeneous $\text{Cu}_{1-x}\text{Co}_x$ Thin Films

Andreas Hütten and Gareth Thomas

Department of Materials Science and Mineral Engineering, University of California, and National Center for Electron Microscopy, Lawrence Berkeley Laboratory, Berkeley CA 94720, U.S.A.

The recent discovery^{1,2} of giant magnetoresistance (GMR) in heterogeneous $\text{Cu}_{1-x}\text{Co}_x$ thin films has brought new insights in the phenomenon of GMR, which was previously believed to be restricted to multilayered structures only. Subsequent theoretical analyses³ of GMR in this new materials class have shown that GMR is mainly controlled by the mean radius and the volume fraction of single domain ferromagnetic particles. In addition to these parameters, the mean free path for electron in the non-magnetic matrix as well as coherency between particles and matrix are influencing the amplitude of GMR. Clearly, the key to increase the amplitude of GMR is to determine the decomposition kinetics and from which to optimize the single domain ferromagnetic Co particle size distribution in heterogeneous $\text{Cu}_{1-x}\text{Co}_x$ thin films.

$\text{Cu}_{81}\text{Co}_{19}$ films, 50 nm in thickness, have been deposited by dc magnetron sputtering¹ from separate Cu and Co targets onto 30 nm thick silicon nitride electron transparent grids. These samples have been subsequently *in-situ* annealed in the JEOL 200 CX AEM electron microscope operating at 200 keV at the National Center for Electron Microscopy. $\text{Cu}_{65}\text{Co}_{35}$ melt-spun ribbons are made by standard melt-spinning techniques. Field ion microscope (FIM) tips are prepared from these ribbons by first mechanically grinding to a quadratic cross-section and then electropolishing in perchloric acid and ethyl alcohol in the proportion 1:10. Analytical field ion microscopy (APFIM) studies are performed at the University of Göttingen, Germany.

The Gibbs free energy of the fcc phase in Cu-Co has been calculated from available thermodynamic data utilizing the CALPHAD method⁴. Taking the second derivative of Gibbs free energy with respect to the atomic fraction of Co, the chemical as well as the coherent spinodal have been calculated and the differences between both are very small (Figure 1). Because the specimens have nominal composition in the spinodal region, their decomposition should be of the spinodal type. A detailed kinetics study shows that the fastest growing wavelength of concentration fluctuations is about 2 nm during annealing at 450°C - 950°C. At these temperatures the equilibrium composition of Co precipitates is reached in less than two seconds at 450°C and only 10⁻⁴ seconds at 950°C. Hence it is extremely difficult to achieve homogeneous melt-spun ribbons. As a result, melt-spun ribbons are already decomposed during preparation. Figure 2 shows a FIM micrograph of a melt-spun $\text{Cu}_{65}\text{Co}_{35}$ ribbon. The bright areas correspond to Co precipitates with an average diameter of 3.2 nm whereas the matrix appears dark. The Co particle composition has been determined with APFIM to be at equilibrium. Figure 3 shows the microstructure of a $\text{Cu}_{81}\text{Co}_{19}$ thin film after annealing for one hour at 530°C. Despite the predicted fast decomposition there is no contrast that indicates the appearance of precipitates. The Ashby-Brown contrast, which is expected for coherent precipitates, is not observed because the large volume fraction of Co particles results in overlap and cancellation of strain fields. The corresponding ring pattern matches with the fcc phase of Cu as well as the fcc phase of Co since both lattice parameters differ only by 1.7%. In addition, the separation of pure Cu at the surface of

these films is observed and can be explained as a consequence of the lower surface tension of Cu in comparison to Co.⁶

References

1. A.E. Berkowitz, J.R. Mitchell, M.J. Carey, A.P.Young, S. Zhang, F.E. Spada, F.T. Parker, A. Hütten and G. Thomas, *Phys. Rev. Lett.* **68** (1992) 3745.
2. J.Q. Xiao, J.S. Jiang and C.L. Chien, *Phys. Rev. Lett.* **68** (1992) 3749.
3. S. Zhang, *Appl. Phys. Lett.* **61** (1992) 1855.
4. R. Bormann, private communication.
5. M.F. Ashby and L.M. Brown, *Phil. Mag.* **8** (1963) 1063.
6. This work was supported by the Director, Office of Basic Energy Science, Materials Science Division under Contract Number DE-AC03-76SF00098. A. Hütten acknowledges a fellowship from the Heraeus Foundation, Germany.

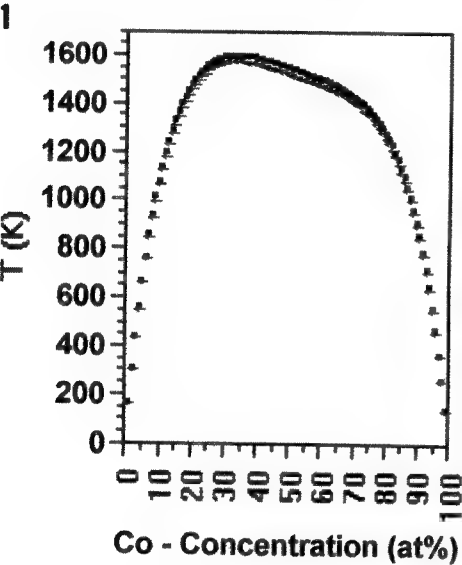
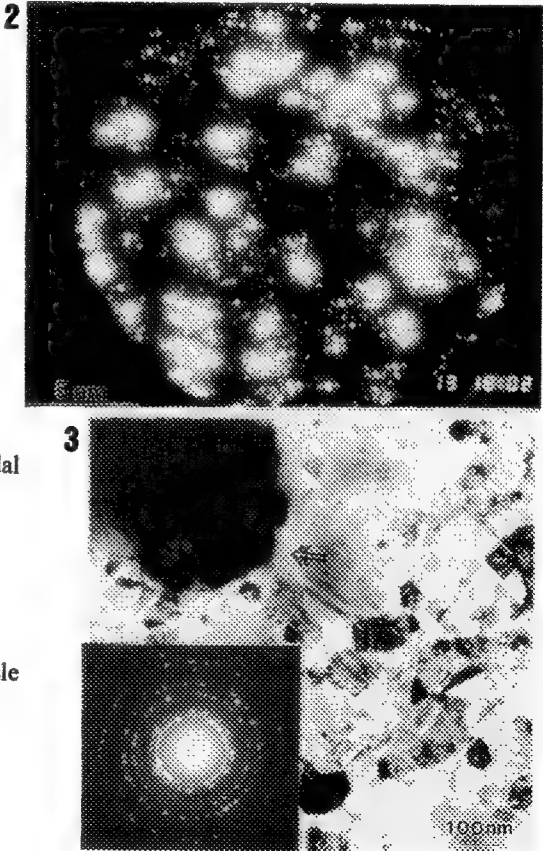


Fig. 1. Calculated chemical and coherent spinodal in the Cu-Co system.

Fig. 3. TEM micrograph of Cu₈₁Co₁₉ thin film annealing for one hour at 530°C. The arrow is indicating a large pure Cu particle at the surface of the film.

Fig. 2. FIM micrograph of melt-spun Cu₆₅Co₃₅.



MICROSTRUCTURAL ANALYSIS OF COBALT ALLOY SINGLE AND MULTILAYER LONGITUDINAL RECORDING MEDIA

M.Kuwabara and M.R.Visokay

Applied Electronics Center, Kobe Steel USA Inc., Palo Alto, CA 94304

Co-based alloys have been successfully used as sputtered thin film media for hard disk drives. Media with higher recording density and lower media noise are required for the future hard disk drives. The magnetic properties can be controlled by processing and alloy composition. However, the origin of the magnetic properties, such as film coercivity and transition noise, are not fully understood yet. In this paper the analysis of the magnetic properties versus microstructure of Co-based alloy single and multilayer media is reported.

Co-alloy media were prepared by DC magnetron sputtering of Cr, Co-alloy (CoCrNi and CoCrPt) and overcoat materials (C and Zr) on Ultra Densified Amorphous Carbon (UDAC) substrates.¹ The sputtering pressure and deposition temperature were 3-5 mTorr and between 30°C and 300°C, respectively.

The coercivity of CoCrNi and CoCrPt media increases with the deposition temperature in the range between room temperature and a few hundred degree Celsius.² Figure 1 shows cross-section TEM(XTEM) images of CoCrPt media. Fig.1-(a) and (b) are images of media deposited at 30°C and at 250°C, respectively. The Cr underlayer and Co media layer have a columnar structure and Co layer has a replica structure of Cr layer. One significant difference is their grain size. The media processed at low temperature has smaller grains than that processed at higher temperature. Therefore it is concluded that one of the factors affecting the film coercivity is the grain size. Figure 2 is a plan-view image of CoCrPt deposited at 200°C. The films are highly dense and there is no physical separation nor amorphous-like material between grains. This media has high coercivity (2500 Oe) and low media noise (1.9µV at 50KFCI). Therefore it is possible to obtain media with high coercivity and low noise without physical grain separation. Even though x-ray diffraction analysis does not indicate the presence of the fcc phase of Co, HREM images reveal the existence of well-defined fcc grains in the film. Although at this moment there are no clear quantitative data, more fcc grains are observed in the films deposited at elevated temperature. The fcc phase may also be influencing the film coercivity. It has been also speculated that Cr segregation at the grain boundaries of Co alloy films is another important phenomenon controlling the film coercivity. It is known that suitable annealing of the media increases the coercivity significantly. Microprobe EDS results indicate that the Cr concentration at the grain boundaries increases after annealing.³

One way to reduce media noise is by using multilayer magnetic films separated by non-magnetic materials. It is also reported that the film coercivity of the multilayer is different from that of single layer media. Figure 3 shows XTEM images of CoCrNi multilayer films separated by Cr (10nm in thickness). The 10nm Cr layer separates the magnetic films completely. A dark field (Fig.3-a) and a HREM image (Fig.3-b) clearly indicate that the underlayer, separation layer and magnetic layers have a strong crystallographic relationship in a column. In the case of a Zr separation layer, however, the two magnetic layers tend to lose their crystallographic orientation relationship and the film has a lower coercivity value. Therefore it is concluded that a strong crystal relationship between layers in a column is important to achieve high film coercivity in these multilayers.⁴

References

1. K.Muramatsu et al., R&D Kobe Steel Eng. Rep. 39 (1989) 35.

2. M.Kuwabara et al., to be published in J. Appl. Phys.
3. Y.Onishi et al., Intermag 1993.
4. The work was carried out in collaboration with H.Saffari, Y.Onishi, M.Sato and H.Hayashi.

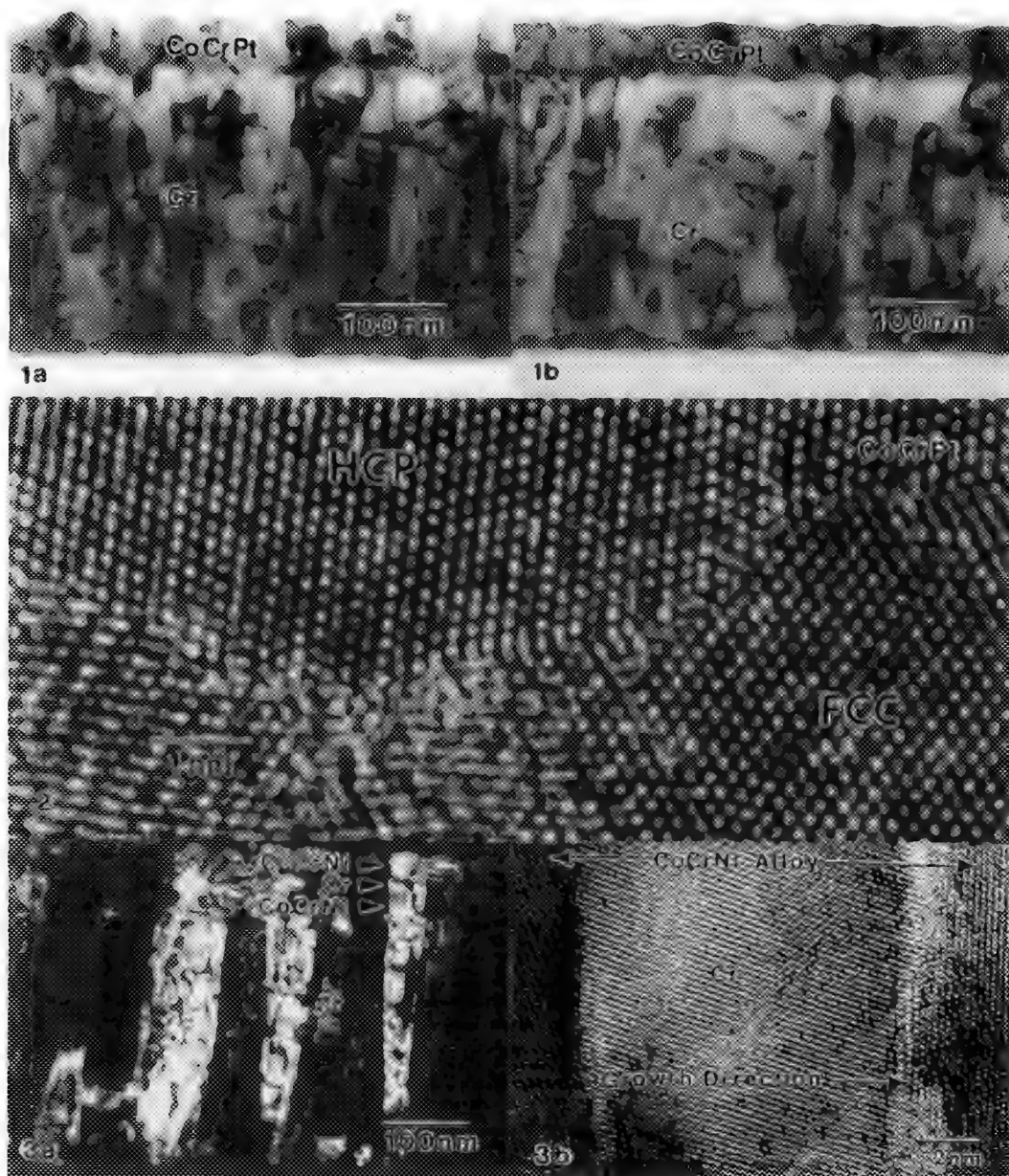


Fig. 1 Cross-section TEM images of CoCrPt media deposited at a) 30°C, b) 250°C.
 Fig. 2 Plan-view HREM image of CoCrPt media deposited at 200°C.
 Fig. 3 Cross-section images of CoCrNi multilayer media, a) dark field, b) HREM.

MAGNETIC-DOMAIN IMAGING TECHNIQUES

Ian R. McFadyen

IBM Research Division, Almaden Research Center, 650 Harry Road, San Jose CA 95120-6099

The concept of domains in ferromagnets was introduced by Weiss in 1906. However, they were not observed until 1931 when Bitter showed that domain boundaries could be observed by decorating them with fine magnetic particles. Since then the field of magnetic domain imaging has expanded enormously.

The original Bitter technique involved the decoration of a magnetic sample with a colloidal suspension of fine magnetic particles (usually magnetite) and observation by dark field optical microscopy. This is still a commonly used method and has been extended to finer particles, which include clusters directly deposited on the magnetic sample from a chemical vapor and observation of the clusters in the SEM or TEM at magnifications in excess of $20,000\times$ ¹.

Another very popular means of observing magnetic domains employs the magneto-optic Kerr effect. Both polar and longitudinal Kerr techniques have been utilized. In the polar Kerr technique a magnetic sample is illuminated by a beam of plane polarized light normal to the sample surface. Upon reflection from the sample the plane of polarization is rotated clockwise or anticlockwise depending upon the direction of the component of magnetization perpendicular to the sample surface. An analyzer can then be used to obtain contrast between oppositely magnetized domains. In the longitudinal Kerr effect a polarized light beam illuminates a sample at an angle to the normal. Upon reflection the light is elliptically polarized. In this case the sense of ellipticity is determined by the component of magnetization parallel to the sample surface and in the plane of illumination. Kerr microscopy is generally limited to the spatial resolution of standard optical microscopy but has the advantages of being able to image through thick, optically transparent overcoats and it is also suitable for dynamic domain studies².

Electrons interact with magnetic materials in a number of ways, the most well known of which is the Lorentz force. This was first utilized by Fuller and Hale to image magnetic domain walls in a transmission electron microscope³. As a beam of electrons passes through a magnetic sample it is deflected by those components of the local magnetic induction which are perpendicular to the beam. By focusing on a plane below the specimen the domain walls are revealed as dark or bright lines corresponding to a deficiency or an excess of electrons. This is known as the Fresnel technique. The domains themselves can be observed by blocking all of the electrons which are deflected in a given direction. This is easily done by displacing an aperture in the diffraction plane of the microscope. In neither of these techniques, however, does the domain contrast relate linearly to the magnetic induction. Another Lorentz technique, differential phase contrast (DPC), addresses this problem. A focussed probe of electrons impinges on the sample and is deflected by an angle $\beta_L \propto \int \mathbf{B} \times \mathbf{k} dz$ where \mathbf{B} is the magnetic induction due to the sample and \mathbf{k} is the unit vector along the electron trajectory. Provided β_L is small compared to the probe $\frac{1}{2}$ angle, which is usually the case, the magnitude and direction of the deflection angle can be measured using a quadrant detector⁴.

Magnetic imaging due to the Lorentz force can also be carried out on bulk samples in the SEM. In the 'type I' imaging mode the stray fields above the sample deflect the secondary electrons emitted by the sample and this deflection is detected by an asymmetric detector. In the 'type II' imaging mode the effect of internal magnetic fields on the trajectories of scattered primary electrons results in a variation of the backscattered yield which is dependent on both the internal fields and the sample geometry. This technique has been used to probe the magnetic structure of thin film heads as a function of depth⁵.

More recent electron techniques for imaging magnetic structures at surfaces include secondary electron microscopy with polarization analysis (SEMPA) where the polarization of the secondary electrons emitted from a sample in an SEM is determined. This technique can probe all three components of surface magnetization but due to the very poor efficiency ($\approx 10^{-4}$) of polarization detectors the images take 10-15 minutes to acquire⁶.

Another recent technique, spin polarized low energy electron microscopy (SPLEEM) promises similar information to SEMPA but much higher imaging rates. Here a beam of polarized low energy ($\approx 10\text{eV}$) electrons strikes a sample and is reflected from it. The probability of reflection is dependent on the orientation of the sample magnetization with respect to the polarization direction of the in-coming electron beam. Subtracting two images obtained with oppositely polarized primary beams results in strong domain contrast that can be obtained in a few video frames. Since the imaging electrons are very low energy great care must be taken to shield the instrument from external electric and magnetic fields⁷.

A related technique to SPLEEM is magnetic x-ray circular dichroism (MCD) where a circularly polarized x-ray beam hits the sample and ejects low energy photoelectrons which can then be imaged using the imaging optics of a low energy electron microscope. The probability of ejecting a photoelectron is dependent on the orientation of the magnetic moment with respect to the spin vector of the circularly polarized x-ray beam. Therefore, the intensity in the image carries information on the magnetic structure of the sample⁸. Both SPLEEM and MCD imaging are very recent developments which require sophisticated equipment and both show promise for many magnetic studies.

No review of imaging techniques would be complete without considering the probe microscopies. Magnetic force microscopy is based on the AFM and forms an image by sensing the force between a magnetic sample and a magnetic tip scanned across the sample surface⁹. MFM is now well established and has recently become available as an addition to a number of commercial AFMs.

Variations on magnetic imaging with a scanning probe microscope include using a flexible tunnelling tip which responds to the magnetic field above the sample by moving towards or away from the sample thus modulating the tunnelling current¹⁰. One of the scanning probe methods which promises the highest spatial resolution relies on tunnelling between a magnetically polarized tip and a magnetic sample. In this case the magnitude of the tunnelling current is dependent on the relative orientation of the moment in the tip with respect to that in the sample¹¹.

Magnetic imaging is now a well established field and spans all of the major imaging modes. As well as being of scientific interest it has aided in the solution of many technological problems and will undoubtedly continue to do so.

References

1. K. Goto, M. Ito, T. Sakurrai, *Jpn. J. Appl. Phys.* 19 (1980) 1339-1346
2. B. Petek, P.L. Trouilloud, B. E. Argyle, *IEEE Trans. Magn.*, MAG-26 (1990) 1328-1330
3. Fuller and Hale, *J. Appl. Phys.* 31 (1960) 238
4. J. N. Chapman et al. *IEEE Trans. Magn.*, MAG-26 (1990) 1506-1511
5. R. P. Ferrier and S. McVitie, in "Microbeam Analysis" 1991 395-396
6. M. R. Scheinfein et al. *Rev. Sci. Instrum.* 61 (1990) 2501-2526
7. M. S. Altman et al., *Mat. Res. Soc. Symp. Proc.* 232 (1991) 125-132
8. J. Stohr et al., *SCIENCE* 259 (1993) 658-661
9. D. Rugar et al., *J. Appl. Phys.* 68 (1990) 1169-1177
10. R. Gomez et al., *IEEE Trans. Magn.*, MAG-28 (1992) 3141-3143
11. R. Weisendanger et al., *Phys. Rev. Lett.* 65 (1990) 247-250

Flux-Line Observation by Electron Holography

Akira Tonomura

Advanced Research Laboratory, Hitachi, Ltd.

&

Tonomura Electron Wavefront Project, ERATO, JRDC
Hatoyama, Saitama 350-03, Japan

In electron microscopy, the intensity of an electron beam transmitted through an object can be observed. While in electron holography, the phase of the electron beam can also be observed and displayed as an interference micrograph [1]. Using a technique unique to holography, the precision of phase measurements can be increased to 1/100 of the electron wavelength. An interference micrograph of a magnetic object can be interpreted in a straightforward way: Contour fringes directly indicate projected magnetic flux lines and a constant magnetic flux of h/e ($= 4 \times 10^{-15}$ Wb) flows between two adjacent fringes (See Fig. 1).

Examples of magnetic recordings are shown in Fig. 2. Flux lines inside and outside of the magnetic tapes, recorded in different ways, can directly and quantitatively be observed as interference micrographs. Figure 2 (a) shows an example of in-plane magnetic recording [2]. Two magnetization streams, pointed in opposite directions, merge and produce vortices in the transition region similar to those produced by streams of water. The width of the transition region shows the limit of high density recording. In this type of recording, the magnetization directions are parallel to the direction in which the magnetic head is driven and, therefore, lie in the tape plane.

On the other hand, in perpendicular recording, the magnetization directions are perpendicular to the tape plane. In this case, the width of the transition region becomes much smaller because it is similar to the width of a 180° domain wall. This feature can be seen in Fig. 2 (b), where magnetization is recorded perpendicularly to the driven direction of the magnetic head and also in the tape plane. In order to observe flux lines in perpendicular recording, the tape has to be sliced and studied from a direction perpendicular to the section, or parallel to the original tape plane. Only flux lines outside the tape can be observed in Fig. 2 (c), which confirms a bit length of only 700 Å [3].

- [1] A. Tonomura: *Physics Today* 22 (April 1990) 22.
- [2] N. Osakabe et al.: *Appl. Phys. Lett.* 42 (1983) 746.
- [3] S. Hasegawa et al.: *J. Appl. Phys.* 65 (1989) 2000.

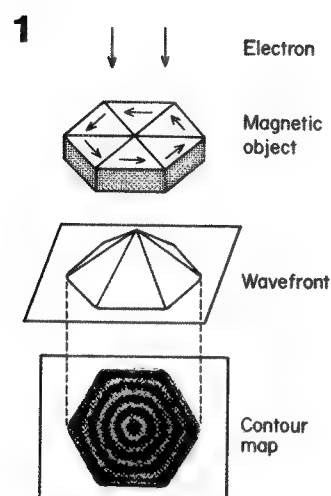


Fig. 1. Contour fringes in an electron interference micrograph indicating in-plane magnetic lines of force.

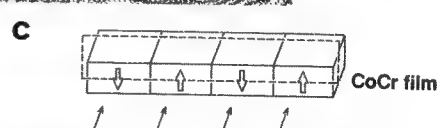
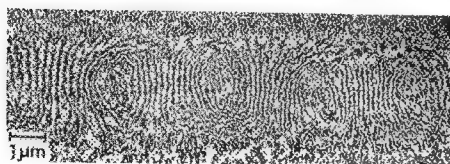
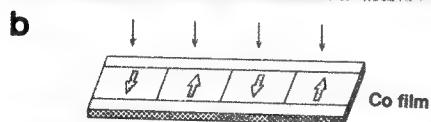
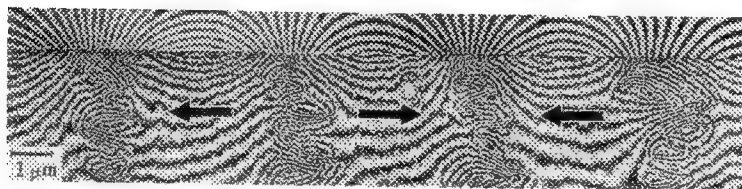
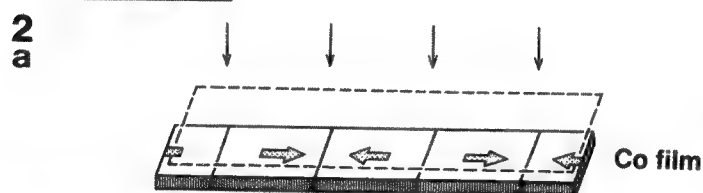


Fig. 2. Magnetization patterns recorded in different ways.

STEM OF ORDER AND DYNAMICS IN NOVEL MAGNETIC MATERIALS

Marian Mankos, J.M.Cowley, R.V.Chamberlin, M.Scheinfein and J.D.Ayers*

Department of Physics and Astronomy, Arizona State University, Tempe, AZ85287-1504

*Naval Research Laboratory, Washington, DC20375-5000

The new detection system of the HB5 STEM enables the operation of the microscope in a variety of modes [1]. If the specimen is placed inside the objective lens, high resolution bright and dark field images revealing the microstructure can be obtained. Since the specimen is located in a high magnetic field, magnetic ordering phenomena are disturbed and no magnetic structure contrast is observed. In the out-of-field position, magnetic structure may be revealed in the Fresnel and Differential Phase Contrast modes of Lorentz Microscopy [2]. Fresnel images are obtained with a static beam, i.e. the scanning coils are not excited. In the Fresnel mode the objective lens focus is changed slightly and domain walls appear in the shadow image as dark and bright lines, switching contrast when the objective lens is changed between overfocussing and underfocussing. Electrons, passing through the sample, are deflected by the Lorentz force and appear to converge towards or diverge from the domain walls. Shadow images are observed in this mode through a low light level SIT camera with usual TV speed (1 frame ~ 30 ms) or a CCD camera with variable acquisition time from 1 ms to several seconds. In the Differential Phase Contrast mode the beam is scanned over the sample [3]. The central beam is deflected at different angles and in different directions as it passes through sections of the specimen with different magnetization. A properly aligned annular detector generates a signal carrying the information about the bulk magnetization and images showing magnetic domain contrast may be observed on the STEM slow scan TV screen (1 frame ~ 100 ms). The instrument presents a unique combination of high spatial resolution (~2Å in bright and dark field modes, ~5nm in magnetic contrast modes) and relatively high temporal resolution (30ms continuous acquisition or 1ms windows with defined delay). In addition, the HB501 microscope equipped with an energy dispersive x-ray spectrometer (Link Analytical) and electron energy loss spectrometer (Gatan) is used for compositional analysis.

Nanocrystalline magnetic alloys (Fe-Si-Nb-B-Cu and Fe-Zr-B-Cu) having superior soft magnetic properties have been described only recently [4]. Domain structure in a $\text{Fe}_{73.5}\text{Si}_{13.5}\text{B}_9\text{Nb}_3\text{Cu}_1$ alloy annealed for 1 hour at 820K is obtained in the Bright Field (Fig.1a), DPC (Fig.1b) and Fresnel (Fig.1c, d) modes. Underfocussed and overfocussed Fresnel images of a small particle of about 130nm in diameter, located at the surface of this alloy are shown in Fig.2a,b, a HAADF image of the same particle is in Fig.2c. The microstructure and magnetic structure of a granular Co film, 300Å thick and grown at 300K, can be compared in Fig.3a (in-lens BF) and Fig.3b (Fresnel mode). Medium-ranged ("mesoscopic") correlations have been predicted to exist in magnetic materials [5]. An attempt is made to visualize these correlations in magnetic thin films. Dynamic phenomena, revealing relaxation effects of granular Co thin films in an external magnetic field are observed (Fig.4a-e).

References.

1. M. Mankos et al., Proc. Ann. EMSA Meeting 50(1992)102
2. J.N. Chapman, J. Phys. D: Appl. Phys. 17(1984)623
3. S.Kraut and J.M.Cowley, Microsc. Res. Tech. In press.
4. Y.Yoshizawa and K.Yamauchi, J. Appl. Phys. 64, No.10(1988)6044
5. R. V. Chamberlin and M. Scheinfein, Ultramicroscopy 47(1992)408
6. This study is supported under NSF grant DMR-9014975 and made use of the ASU Center for HREM supported by NSF grant DMR-8913384.

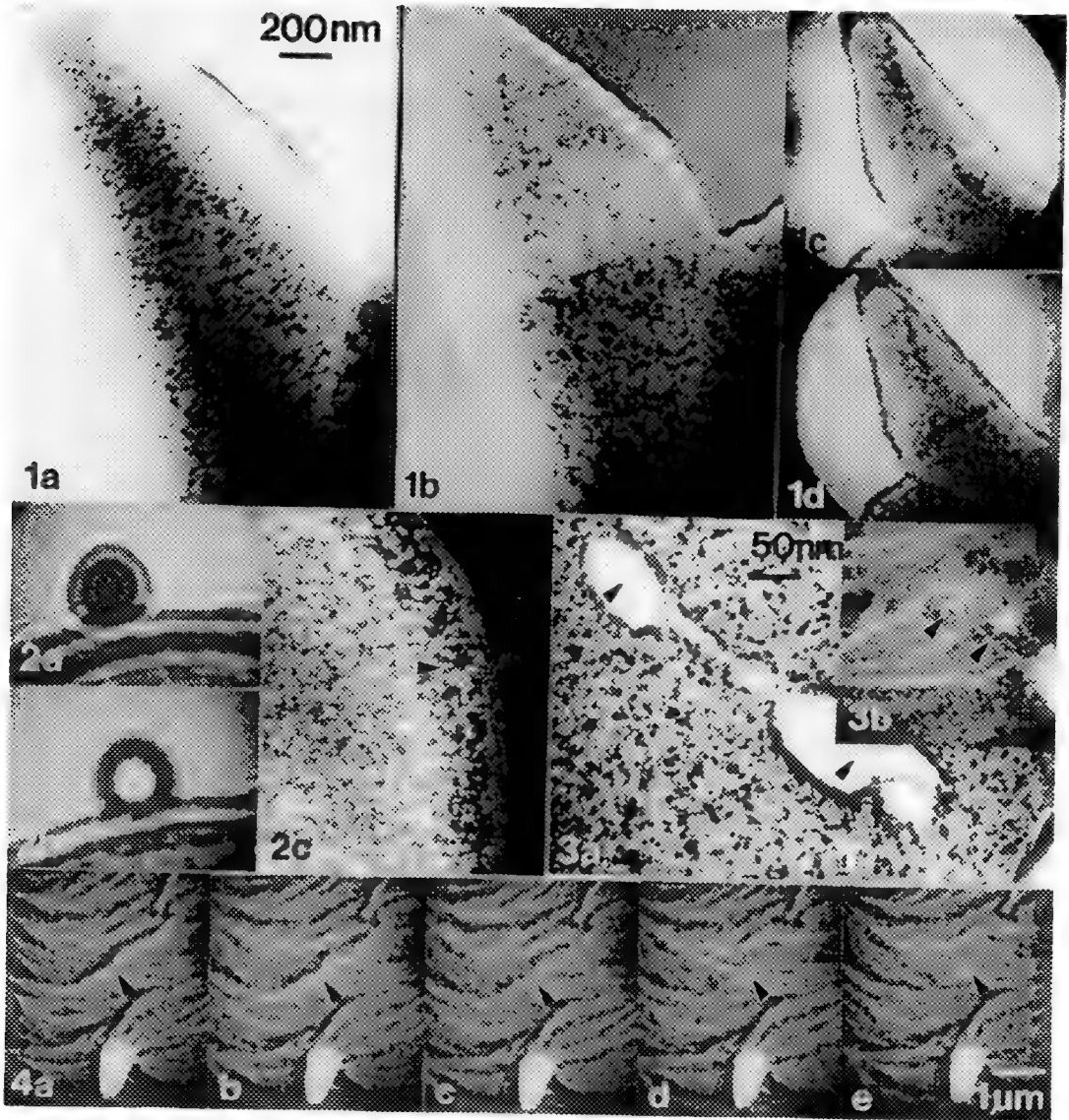


Figure 1. $\text{Fe}_{73.5}\text{Si}_{13.5}\text{B}_9\text{Nb}_3\text{Cu}_1$ alloy imaged in BF (a), DPC (b) and Fresnel modes (c, d).
 Figure 2. Small particle located on the surface of $\text{Fe}_{73.5}\text{Si}_{13.5}\text{B}_9\text{Nb}_3\text{Cu}_1$ alloy in Fresnel (a,b) and HAADF (c) modes.
 Figure 3. Granular Co thin film in BF (a, in-lens) and Fresnel (b, out-of-lens) modes.
 Figure 4. Relaxation phenomena in a granular Co film. Successive frames with 30ms acquisition time, the first frame is recorded 250ms after a strong magnetic field was switched off.

APPLICATION OF ELECTRON HOLOGRAPHY TO MATERIAL SCIENCE

Studies on magnetic domain states of small particles

T. Hirayama, Q. Ru, T. Tanji and A. Tonomura

Tonomura Electron Wavefront Project, ERATO, JRDC
P.O. Box 5, Hatoyama, Saitama, 350-03
JAPAN

The observation of small magnetic materials is one of the most important applications of electron holography to material science, because interferometry by means of electron holography can directly visualize magnetic flux lines in a very small area.¹ To observe magnetic structures by transmission electron microscopy it is important to control the magnetic field applied to the specimen in order to prevent it from changing its magnetic state. The easiest method is turning off the objective lens current and focusing with the first intermediate lens. The other method is using a low magnetic-field lens,² where the specimen is set above the lens gap.

Figure 1 shows an interference micrograph of an isolated particle of barium ferrite on a thin carbon film observed from approximately [111]. A hologram of this particle was recorded by the transmission electron microscope, Hitachi HF-2000, equipped with an electron biprism. The phase distribution of the object electron wave was reconstructed digitally by the Fourier transform method³ and converted to the interference micrograph Fig 1. This particle has a well-defined crystal habit and magnetic flux lines emerging from the N-pole and converging into the S-pole which can be seen very clearly. In general, magnetic materials have domain structures to minimize their total magnetic energy. The energy of a magnetic domain-wall in a small particle is proportional to the area (the square of size) of the domain wall. On the other hand the magnetostatic energy is proportional to the volume (the cube of size) of the particle. Therefore, as the particle size decreases, the relative contribution of the domain-wall energy to the total magnetic energy of the particle increases. Finally, a single domain state in a particle becomes most stable below a certain critical size.⁴ This phenomenon is a typical example of "size effect". The existence of single-domain particles was first proved by Goto⁵ et al. with the "Colloid-SEM Method". In Fig.1 a single-domain particle, proven by its flux line pattern, has been observed directly and clearly for the first time. Furthermore, the direction of the flux lines is determined by the phase distribution map of the particle. As described above, electron holography is extremely useful for observing microstructures of magnetic materials. Figure 2 shows an interference micrograph of two small cobalt particles sticking to each other, where the phase shift of the object wave is amplified eight times. The shape of the flux lines indicates that each particle is in the single-domain state. Electron holography using the low magnetic field lens allows us to observe flux lines of these small particles. This technique is eminently suitable for studying magnetic materials less than 0.1 μm .

The authors would like to thank Prof. Kimiyoshi Goto of Yamagata University and Mr. Tomoaki Sakurai of Tohoku University for preparing the barium ferrite samples and for valuable suggestions.

References:

1. A. Tonomura, *Advances in Physics*, **41** (1992) 59.
2. K. Shirota et al., *J. Electron Microsc.* **25** (1976) 303.
3. Q. Ru et al., *J. Opt. Soc. Am. A* **8** (1991) 1739
4. J. Frenkel et al., *Nature* **126** (1930) 274
5. K. Goto et al., *Jpn. J. Appl. Phys.* **19** (1980) 1339

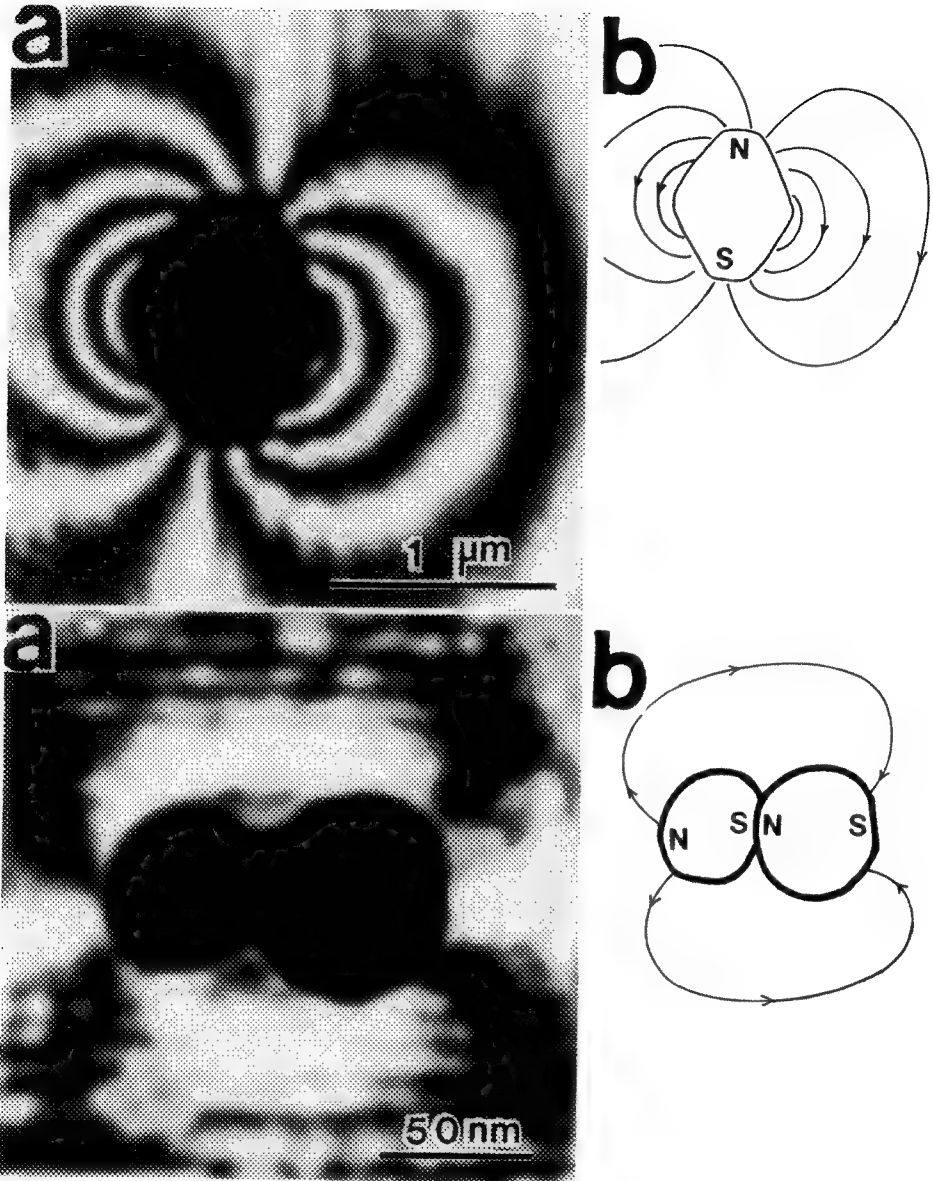


Fig. 1 -- Typical example of single-domain particle of barium ferrite showing (a) interference micrograph, where magnetic flux lines can be seen to emerge from N-pole and converge into S-pole and (b) schematic of domain state and magnetic flux lines.

Fig. 2 -- Two cobalt particles sticking to each other showing (a) interference micrograph, where shape of magnetic flux lines indicates that each particle is in single-domain state and (b) schematic of the domain state and flux lines.

MICROSCOPY OF MAGNETIC MATERIALS USING AN OPTIMISED FEG CTEM/STEM INSTRUMENT

J N Chapman, R P Ferrier and B Bormans*

Department of Physics and Astronomy, University of Glasgow, Glasgow G12 8QQ, UK

* Philips Electron Optics, Building AAE, 5600 MD Eindhoven, The Netherlands

Modern magnetic materials, as well as being of major scientific interest, are being developed intensively for a wide range of technological applications. To achieve superior properties great attention is devoted to the ways in which materials are produced in that many of the desirable attributes are induced by a particular growth process rather than being intrinsic to the material itself. Thus development of enhanced macroscopic properties requires that the magnetic microstructure be determined and its dependence on the physical microstructure understood. Furthermore, the information needed is not restricted to the materials in their as-grown state but on how they are affected by application of magnetic fields and changes in temperature.

To satisfy all these requirements a highly modified electron microscope has been developed. The main criteria it had to fulfill were: (i) sufficient room around the specimen to house a small "micromagnetic laboratory" to allow a range of in-situ experiments to be undertaken; (ii) CTEM and STEM imaging modes to be accessible with state-of-the-art resolution with the specimen situated in magnetic field-free space; and (iii) a high sensitivity analytical capability to allow structural and/or compositional information to be obtained from regions where magnetic features of interest are observed. The instrument itself is based on a Philips CM20 FEG which has undergone substantial modifications around the specimen region. Specifically the specimen is located at the centre of an objective lens with an increased gap (20mm) which remains unexcited during normal domain imaging. Instead, image formation makes use of two high performance mini-lenses sited symmetrically above and below the specimen. If CTEM imaging modes, such as Fresnel and Foucault microscopy¹, are to be employed in an investigation the lower "Lorentz" lens is used as a non-immersion objective with a line resolution of $\approx 1\text{nm}$. Conversely, if a scanning mode such as modified differential phase contrast (MDPC) imaging² is preferred, the upper "Lorentz" lens acts as the probe forming lens allowing a resolution better than 5nm to be attained. We should note that it is desirable to have access to both CTEM and STEM imaging modes. The former are more readily implemented and give direct access to information on domain geometry and the approximate direction of magnetisation in each domain, whilst the latter are particularly well suited for probing domain wall structures and deriving the detailed spatial distribution of induction in a small region of the specimen. The objective lens itself plays two roles. Simply switching it on and off at selected excitations allows the specimen to be subjected to a user-selected magnetisation cycle and the changes in magnetic microstructure introduced by the field can be studied. Alternatively with the lens excited the instrument reverts to a high performance electron microscope with a specification only slightly diminished from that of the standard instrument, the small performance loss being due to the presence of the enhanced gap. Specifically the CTEM line and point resolution in the modified instrument are 0.14nm and 0.36nm respectively whilst the STEM edge resolution is $\approx 1\text{nm}$. One purpose of the large gap is to allow a magnetising stage to be mounted orthogonal to the specimen rod so that the specimen can be subjected to horizontal as well as vertical magnetic fields. As the standard goniometer has been retained, the specimen can be mounted in a heating or cooling rod thereby allowing experiments to be undertaken in which the material of interest is subjected to simultaneous changes in field and temperature.

In the preceding paragraph a brief description of the overall instrument has been given. For the remainder of the paper we give an example of how a coherent beam imaging system can be used to realise novel developments in imaging techniques. The mode involved is Foucault imaging in which a portion of the magnetically-split central spot of the diffraction pattern is obscured by a suitably positioned aperture and the specimen used to illustrate the new information obtainable is a set of small permalloy elements defined by electron beam lithography. The central portion of the diffraction pattern and the position of the aperture are shown schematically in figure 1 whilst the corresponding images are displayed in figure 2. Interference patterns reminiscent of those produced by processing electron holograms are present in all the elements.³ They arise as a consequence of removing parts of the "streaking" which surrounds each sub-spot; these in turn are a direct result of the presence of the edges delineating the structures. Simple calculations show that the flux enclosed between adjacent fringes is h/e , again as is the case in holographic imaging. However, one advantage of the modified Foucault technique is that the fringes can be seen directly on the microscope viewing screen or on a monitor if a TV camera is employed. Thus, not only can the experimenter rapidly determine the direction of induction in a particular domain but he can see where there are any deviations in regularity (as at a cross-tie wall in the central element in figure 2) and he can obtain a direct measure of the product of saturation magnetisation and film thickness. Quantitative data of this nature is not easily obtained using any of the more commonly used techniques referred to above. A cautionary note must be sounded in that careful positioning of the aperture is crucial to avoid artefacts appearing and that information on all directions of magnetisation are not accessible using a single aperture position. Nonetheless, the results displayed serve to illustrate that new and exciting possibilities exist through the use of an advanced electron optical instrument designed to allow detailed investigations of magnetic materials.

1. J N Chapman, J. Phys. D: Appl. Phys., 17 (1984) 623.
2. J N Chapman, I R McFadyen and S McVitie, IEEE Trans. Mag. 26 (1990) 1506.
3. A Tonomura, Rev. Mod. Phys., 59 (1987) 639.

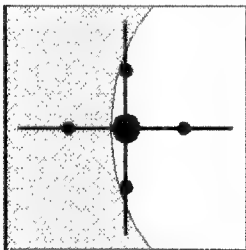
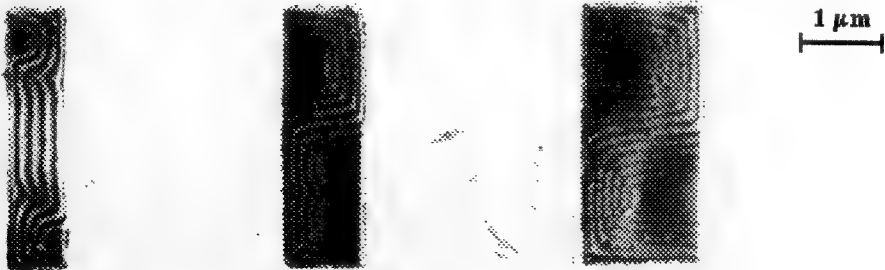


Figure 1: Schematic of the central portion of the diffraction pattern with a suitably positioned aperture to yield magnetic interferograms.

Figure 2: Foucault interferograms showing the magnetisation distributions in small permalloy elements.



IMAGING MAGNETIC MICROSTRUCTURE WITH SEMPA

M. H. Kelley, J. Unguris, R. J. Celotta, and D. T. Pierce

National Institute of Standards and Technology, Gaithersburg, MD 20899

By measuring the spin polarization of secondary electrons generated in a scanning electron microscope, scanning electron microscopy with polarization analysis (SEMPA) can directly image the magnitude and direction of a material's magnetization^{1,2}. Because the escape depth of the secondaries is only on the order of 1 nm, SEMPA is especially well-suited for investigating the magnetization of ultra-thin films and surfaces. We have exploited this feature of SEMPA to study the magnetic microstructure and magnetic coupling in ferromagnetic multilayers where the layers may only be a few atomic layers thick. For example, we have measured the magnetic coupling in Fe/Cr/Fe(100) and Fe/Ag/Fe(100) trilayers and have found that the coupling oscillates between ferromagnetic and antiferromagnetic as a function of the Cr or Ag spacer thickness^{3,4}.

The SEMPA apparatus has been described in detail elsewhere⁵. The sample consisted of a magnetic sandwich structure with a wedge-shaped interlayer as shown in Fig. 1. The substrate was the atomically flat (100) surface of a single crystal Fe whisker. Fe whiskers that were divided into two opposite magnetic domains were selected in order to test for any instrumental offsets. The spacer layer wedge was grown by precisely moving a shutter in front of the sample during evaporation. The spacer layer was then covered by an Fe film. All of the sample preparation was done in situ so that the magnetization, the composition, and the atomic-scale roughness could be monitored during sample preparation by using SEMPA, scanning Auger spectroscopy and reflection high-energy electron diffraction (RHEED), respectively.

The magnetic coupling between the Fe films was determined by simply measuring the magnetization of the top Fe film with SEMPA and seeing how it was aligned with the substrate magnetization. As can be seen from the Cr and Ag spacer layer results shown in Fig. 2 and Fig. 3, respectively, the coupling oscillates between ferromagnetic and antiferromagnetic as a function of the interlayer thickness. The spacer thickness was measured directly from the sample by measuring spatially resolved RHEED oscillations. Analysis of these measurements revealed that both the Cr and Ag oscillatory coupling was composed of a long and a short period component. For Cr the periods are 2.11 (0.304) and 12 (1.7) layers (nm), and the short period dominates. For Ag the periods are 2.37 (0.483) and 5.73 (1.17) layers (nm), and the long period dominates. The observed periods support a model of the oscillatory coupling where periodicities are determined by the size and shape of the Fermi surface of the material.

References

1. J. Unguris et al., in Chemistry and Physics of Solid Surfaces VIII, Springer-Verlag, (1990) 239.
2. K. Hayakawa et al., Hitachi Inst. News **14**, (1988) 11.
3. J. Unguris et al., Phys. Rev. Lett. **67**, (1991) 140.
4. J. Unguris et al., J. Mag. and Mag. Mat., (to be published).
5. M. R. Scheinfein et al., Rev. Sci. Instr. **61**, (1990) 2501.
6. This work was supported in part by the Office of Naval Research.

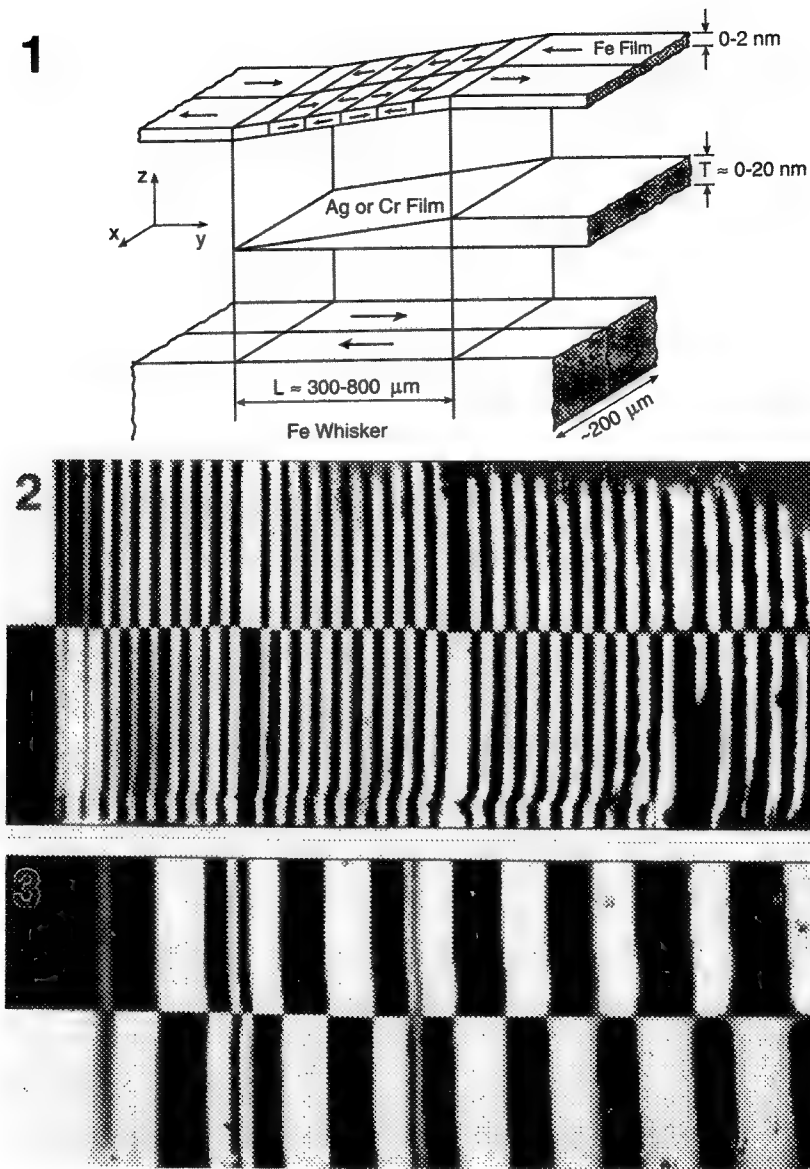


FIG. 1. - A schematic exploded view of the sample structure showing the Fe(100) single crystal whisker substrate, the evaporated wedge, and the Fe overlayer. The arrows in the Fe show the magnetization direction in each domain. The z-scale is expanded approximately 5000 times.

FIG. 2. - A SEMPA image of an Fe/Cr/Fe(100) sandwich. Going from left to right the Cr thickness increases from 0 to 80 atomic layers. Dark and light contrast correspond to magnetization pointing towards the left and right, respectively.

FIG. 3. - A SEMPA image of an Fe/Ag/Fe(100) sandwich. The Ag thickness varies from 0 to 50 atomic layers

TUNNELING STABILIZED MAGNETIC-FORCE MICROSCOPY¹

John Moreland

Electromagnetic Technology Division, National Institute of Standards and Technology, Boulder, Colorado 80303

Magnetic force microscopy (MFM) can be done by making a simple change in conventional scanning tunneling microscopy (STM) where the usual rigid STM tip is replaced with a flexible magnetic tip. STM images acquired this way show both the topography and the magnetic forces acting on the flexible tip. The z-motion of the STM piezo tube scanner flexes the tip to balance the magnetic force so that the end of the tip remains a fixed tunneling distance from the sample surface. We present a review of some "tunneling-stabilized" MFM (TSMFM) images showing magnetic bit tracks on a hard disk,² Bloch wall domains in garnet films,³ and flux patterns in high- T_c superconductor films.⁴ The image resolution of TSMFM is routinely $0.1\text{ }\mu\text{m}$ using Au coated magnetic tips cut from Ni or Fe films. Recent results show that a TSMFM resolution of less than 40 nm is possible with micromachined cantilevers coated with a very thin Au-Fe bilayer.⁵

In TSMFM, the physical tunneling gap is maintained constant in the usual STM sense while the tip flexes in reaction to magnetic forces. In contrast, conventional MFM is a variation of atomic force microscopy (AFM) where the end of the AFM flexible cantilever tip is magnetic. The motion of a conventional MFM tip can be detected using optics or a tunneling detector on the back side of the tip. The benefits of conventional MFM are that it is possible to separate topography from magnetic force action on the probe and that the samples need not be conductive. However, if the TSMFM tunneling probe has a low enough spring constant the contribution of topography to the magnetic field map of the surface will be small enough as to be negligible. In addition, TSMFM has the potential for improving upon conventional MFM resolution limits due to the closer proximity of the magnetic tip.

The TSMFM images in this abstract are made with tips consisting of free-standing, triangular, Ni films, about $0.5\text{ }\mu\text{m}$ thick and 1 mm in size, fastened to a support wire with silver paint. The spring constants of the tips are about 0.01 N/m. Apparently the native oxide layer on the films has a high enough resistance to cause the tips to rub on the sample surface. Therefore, 60-nm-thick Au films are evaporated onto the assembled tip and the sample surface to insure good tunneling conditions. Images consist of 400 line scans with 400 samples per line scan. The images were taken at a scan rate of 1.0 line/s. The tunneling current and voltage were 0.5 nA and 700 mV. The data were taken in height mode to show the z motion of the piezoelectric scanner in response to magnetic forces on the tip.

Figures 1-3 show typical TSMFM images along with a diagram illustrating the motion of the tip above the sample. Interpretation of TSMFM images relies on theoretical modeling of the tip-sample interaction. In brief, the TSMFM signal is determined by hard and soft domain structures in the tip. In general, domains in the sample will dominate the image if the tip is magnetically hard, while domain walls will dominate the image if the tip is magnetically soft. Pertinent references have been included in the figure captions.

References

1. Contribution of the National Institute of Standards and Technology, not subject to copyright.
2. J.Moreland and P.Rice, Appl. Phys. Lett. 57, (1990)310; J. Appl. Phys. 70, (1991)520.
3. R.R.Katti, et al., IEEE Trans. Mag. 28, (1992)2913; J.Oti and P.Rice, J. Appl. Phys. 73, in print.
4. P.Rice and J.Moreland, IEEE Trans. Mag. 27, (1991)5181; A Wadas, et al., Z. Phys. B 88, (1992)317.
5. A.Wadas, H.J.Hug, and H.-J.Güntherodt, Appl. Phys. Lett. 61, (1992)357.

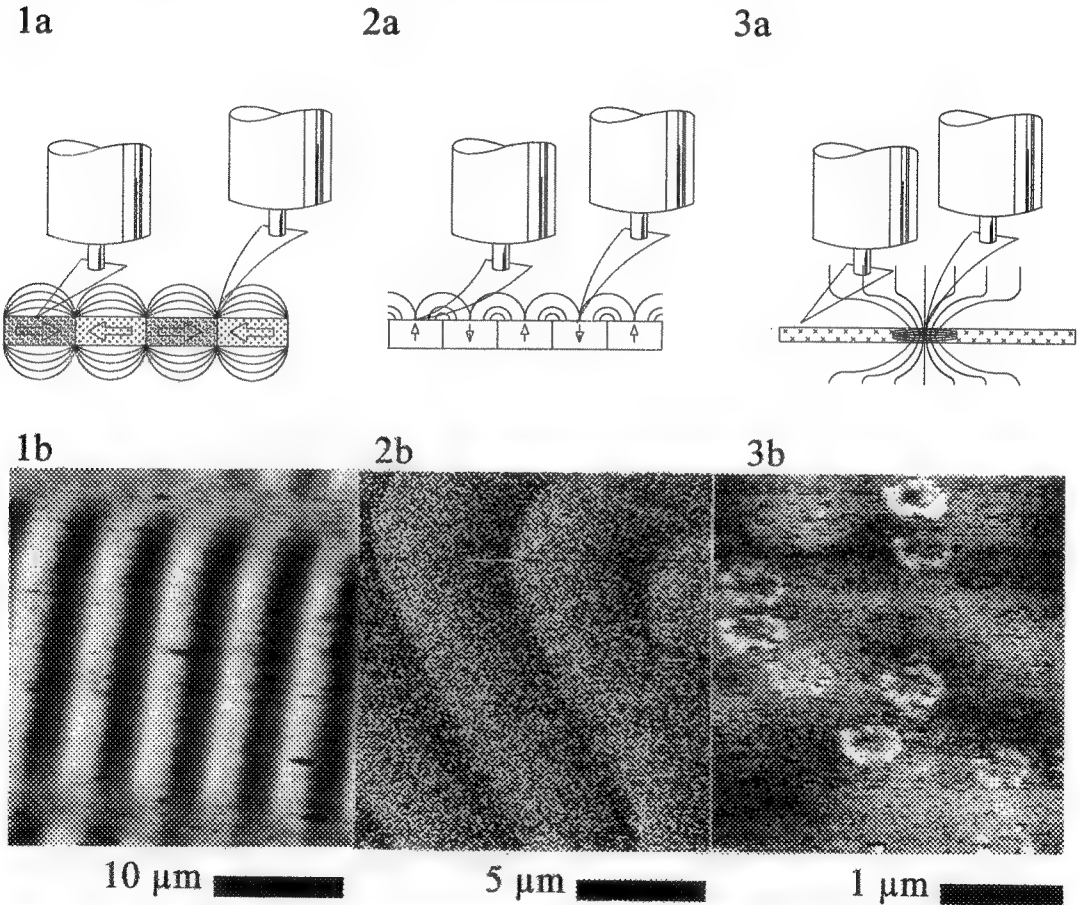


FIG. 1.--Longitudinal magnetization in a hard disk.² a) piezo tube scanner and tip motion above the sample. b) bit tracks written by recording head.

FIG. 2.-- Vertical magnetization in a garnet film.³ a) piezo tube scanner and tip motion above the sample. b) undulatory domain structure separated by vertical Bloch walls.

FIG. 3.-- Magnetic vortex cores in superconductors.⁴ a) piezo tube scanner and tip motion above the sample. b) $\text{YBa}_2\text{Cu}_3\text{O}_{7.6}$ thin film in a 50 mT field normal to the c-axes, $T = 76\text{K}$.

Transmission Electron Microscopy Study of Co/Pd and Co/Au Multilayers

A.E.M. De Veirman, F.J.G. Hakkens, W.M.J. Coene and F.J.A. den Broeder

Philips Research, P.O.Box 80.000, 5600 JA Eindhoven, the Netherlands

There is currently great interest in magnetic multilayer (ML) thin films (see e.g. ¹), because they display some interesting magnetic properties. Co/Pd and Co/Au ML systems exhibit perpendicular magnetic anisotropy below certain Co layer thicknesses, which makes them candidates for applications in the field of magneto-optical recording. It has been found that the magnetic anisotropy of a particular system strongly depends on the preparation method (vapour deposition, sputtering, ion beam sputtering) as well as on the substrate, underlayer and deposition temperature. In order to get a better understanding of the correlation between microstructure and properties a thorough cross-sectional transmission electron microscopy (XTEM) study of vapour deposited Co/Pd and Co/Au (111) MLs was undertaken (for more detailed results see ref. ²⁻⁵).

The Co/Pd films (with fixed Pd thickness of 2.2 nm) were deposited on mica substrates at substrate temperatures T_s of 20°C and 200°C, after prior deposition of a 100 nm Pd underlayer at 450°C. The Co/Au MLs (with fixed Au thickness of 2.4 nm) were deposited on glass substrates at $T_s=20^\circ\text{C}$, after deposition of a 100 nm Au base layer at 20°C, which has been recrystallized at 150°C for 20 minutes. TEM studies were performed on a Philips CM30 SuperTWIN transmission electron microscope, operating at 300 kV.

The deposition of the ML films under conditions of limited atomic surface mobility results in columnar ML structures with a convex curvature of the layers ⁵. In fig.1 it is demonstrated for the Co/Pd MLs that increasing T_s from 20°C to 200°C gives rise to an increase in column width from 20 to 50 nm. The deviation of the (111) growth plane, visible as a continuous layer curvature over the entire column width for $T_s=20^\circ\text{C}$ is only localized at the column boundaries for $T_s=200^\circ\text{C}$. The influence of the layer curvature on the magnetic anisotropy is explained in ref. ². Although the subsequent layers may have a pronounced curvature, the (111) lattice planes in general remain horizontal (i.e. parallel to the substrate surface). Only for the Co/Au MLs, containing thin Co layers, an additional curvature of the crystal lattice was observed, which is thought to be related to the large (14%) misfit for Co/Au. Figs. 2 and 3 show high resolution TEM (HRTEM) images of a Co/Pd and a Co/Au ML respectively.

Due to the limited thickness of the Co layer as well as to the layer curvature and the interface roughness in the viewing direction, it is impossible to get a clear HRTEM image of the thin Co layer ². For Co/Au MLs with a thicker Co layer it was shown that there are interface steps of 1 to 2 atomic steps in height. As a consequence the thin Co layer of fig. 3 is not continuous and at several locations successive Au layers make contact.

In view of the magnetic properties it is also important to establish whether the growth is coherent or semicoherent. Both Co/Au (14% misfit) and Co/Pd (9% misfit) MLs grow semicoherently from one Co monolayer onward. Misfit dislocations can be distinguished at the interfaces. For MLs with thicker Co layers the Burgers vector was established to be $a/2\langle 110 \rangle$, which is the same as derived for a Co/Au bilayer ⁴. Whereas the average misfit relaxation over the whole layer can be obtained from electron diffraction patterns, moiré fringes (fig. 4) occurring at the interfaces due to layer curvature and/or interface roughness in the viewing direction, allow to determine the relaxation at the interfaces. Both analyses give a 80-85% misfit relaxation and thus 20-15% residual strain for both Co/Au and Co/Pd MLs ².

References

1. in Ultramicroscopy 47 (1992) 313, 323, 375, 437
2. F.J.G. Hakkens et al., J. Mater. Res. 8 (1993)
3. F.J.G. Hakkens, W.M.J. Coene and F.J.A. den Broeder, Mater. Res. Soc. Symp. Proc. Vol. 231 (1991) 397
4. A.E.M. De Veirman et al., Mater. Res. Soc. Symp. Proc. Vol. 263 (1992) 119
5. A.E.M. De Veirman, F.J.G. Hakkens and A.G. Dirks, accepted for publication in Ultramicroscopy

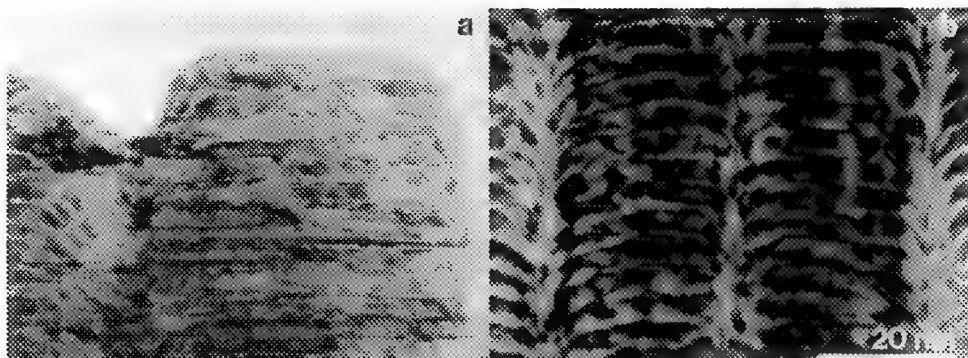


Fig.1 XTEM images of Co/Pd MLs
(a) 0.4 nm/2.2 nm, $T_s=200^\circ\text{C}$
(b) 0.8 nm/2.2 nm, $T_s=20^\circ\text{C}$.

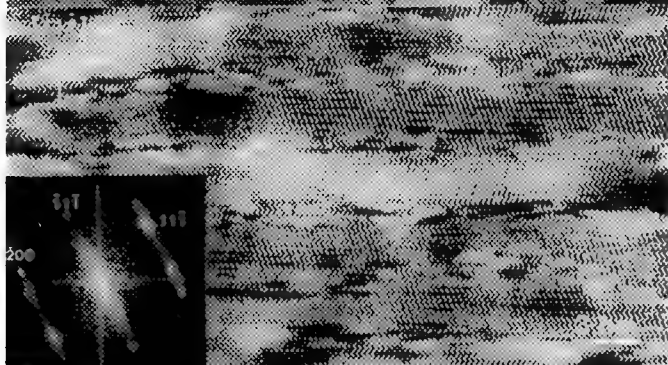


Fig.2 HRTEM images of 0.6 nm Co/2.2 nm Pd ML, $T_s=200^\circ\text{C}$. The inset shows the numerical diffractogram.

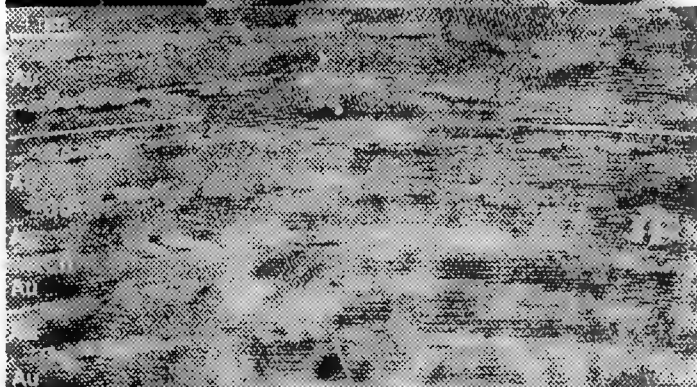


Fig.3 HRTEM image of 0.4 nm Co/2.4 nm Au ML, $T_s=20^\circ\text{C}$. Misfit dislocations are indicated by white arrows.

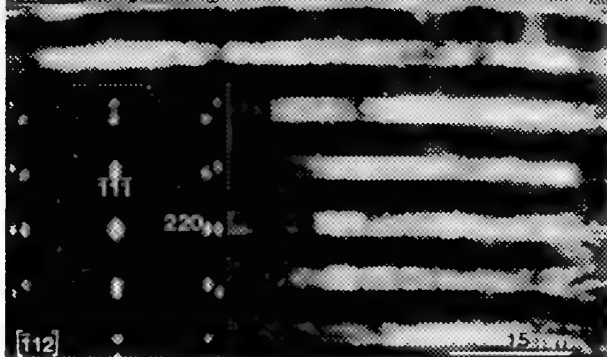


Fig.4 XTEM image of 2.4 nm Co/2.4 nm Au ML, $T_s=20^\circ\text{C}$, $\langle 112 \rangle$ zone-axis orientation (see corresponding diffraction pattern).

GRAIN SEPARATION ENHANCED MAGNETIC COERCIVITY IN Pt/Co MULTILAYERS.

G.A. Bertero and R. Sinclair

Department of Materials Science and Engineering, Stanford, CA 94305-2205

Pt/Co multilayers displaying perpendicular (out-of-plane) magnetic anisotropy and 100% perpendicular remanent magnetization are strong candidates as magnetic media for the next generation of magneto-optic recording devices.¹ The magnetic coercivity, H_c , and uniaxial anisotropy energy, K_u , are two important materials parameters, among others, in the quest to achieving higher recording densities with acceptable signal to noise ratios (SNR). The relationship between K_u and H_c in these films is not a simple one since features such as grain boundaries, for example, can have a strong influence on H_c but affect K_u only in a secondary manner. In this regard grain boundary separation provides a way to minimize the grain-to-grain magnetic coupling which is known to result in larger coercivities and improved SNR as has been discussed extensively in the literature for conventional longitudinal recording media.²

We present here results from the deposition of two Pt/Co/Tb multilayers (A and B) which show significant differences in their coercive fields. The processing of the two multilayers differ only in the substrate temperature at which the 100Å thick Pt underlayer was deposited. The two films were sputter deposited onto thermally oxidized silicon wafers with a SiO_2 thickness of 2000Å. The Pt underlayer for sample A was deposited at approximately 500 °C and for sample B at 600 °C. In both cases the subsequent deposition of the multilayer was carried out with the substrate at room temperature in a 3 mTorr Ar atmosphere. The magnetic coercivities displayed in out-of-plane vibrating sample magnetometry measurements were 0.5 kOe and 2.2 kOe for samples A and B respectively.

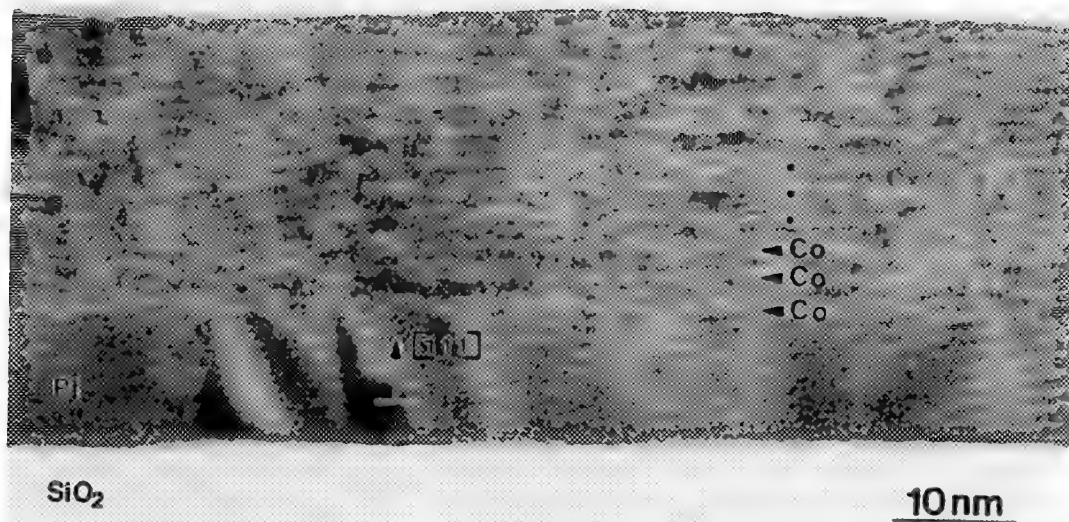
Figures 1 and 2 show cross-section high resolution TEM micrographs from samples A and B. It is clear from the figures that the grain boundary structures are very different. In particular sample B (Fig. 2) shows well separated grains with a Pt underlayer displaying extensive grain boundary grooving. Both samples display a strong $[111]_{\text{Pt}}$ texture, desired to promote perpendicular magnetic anisotropy. The grain strongly diffracting in the film of Fig. 2 is in a $[011]$ -type zone axis with the (111) reflection parallel to the out of plane normal. A large number of stacking faults on (111) planes can be seen under this diffracting condition. These defects are mostly visible in those grains aligned along the $[011]$ zone axis and were frequently seen in both samples. The horizontal fringes elsewhere arise from a predominantly three-beam condition formed with (111) -type reflections. In these areas, not so strongly diffracting, the composition modulation can be clearly seen. No significant difference in the layering was found between the samples.

In summary, the two microstructures look very similar except for the grain boundary grooving of the Pt underlayer and the subsequent grain separation seen in the multilayer of sample B. It is speculated therefore that this feature is responsible for the differences in magnetic properties. This phenomenon may be of significant technological importance for the magnetic recording industry and will thus be studied in further detail.³

REFERENCES:

- [1] W.B. Zeper, H. van Kesteren, and P. Carcia, *Adv. Mater.*, **3** (1991), No. 7/8, 379
- [2] R. Ranjan et al, *IEEE Trans. Magn.*, MAG-26, 1990, 322
- [3] The financial support of Kobe Steel USA is greatly appreciated.

1



2



Figure 1: High Resolution TEM micrograph of a Pt/Co/Tb multilayer (sample A) with the 100Å thick Pt underlayer deposited at 500 °C.

Figure 2: High Resolution TEM micrograph of a Pt/Co/Tb multilayer (sample B) with the 100Å thick Pt underlayer deposited at 600 °C.

Co-THICKNESS DEPENDENCE OF THE MICROSTRUCTURE OF Pt/Co MULTILAYERS

Z.G. Li, P.F. Carcia

Du Pont Research & Development, Experimental Station, P.O.Box 80356, Wilmington, DE 19880-0356

For Co layer thicknesses less than about 12 Å, Pt/Co multilayers have perpendicular magnetic anisotropy [1]. However, the best magnetic properties are obtained when Co is only ~4 Å thick, or nearly two atomic layers, and the Pt layer at least twice as thick. We have revealed the microstructure dependence of the Pt/Co multilayers on the Co thicknesses by using high resolution electron microscopy.

We found that for thin Co (~4 Å), Pt/Co multilayers had (111)-fcc texture and a coherent lattice with interplanar spacing of ~2.2 Å. The lattice coherence depended only on the Co thickness and was independent of the film preparation method. However, multilayers synthesized by vapor-deposition or Xe-sputtering, which impart less energy [2,3] to the growing film, consisted of a larger single crystal volume of Pt/Co superlattice, and also had better (111) texture than Ar- or Ne-sputtered multilayers. Fig. 1) and Fig. 2) illustrate these points with atomic resolution images of Ne-sputtered and vapor-deposited multilayers. We also found that the major defect type in the thin Co thickness multilayers was twinning. In Xe-sputtered and vapor-deposited multilayers with thin Co, the twinning planes were usually parallel to the substrate.

As the Co thickness increased, coherence was lost, and thicker Co layers were hcp with (002) texture, and the film surface roughness increased for less energetic deposition conditions, as shown in Fig. 3). Individual layers commonly adopted their own unique structure and lattice constants. Only infrequently were there locally coherent regions that included both Pt and Co layers. Thick Co layers usually had characteristic hcp close-packing, AB/AB structure shown Fig. 3), with a smaller (002) lattice spacing ~2.0 Å. Pt layers had fcc close-packing structure with their (111) lattice spacing ~2.26 Å. Twin defects were also common in multilayers with thick Co layers. Atomic planes in consecutive Pt layers, separated by a Co or a Co-rich layer, often had a twin-like relationship.

Because twins are more numerous in Ar and Ne sputtered Pt/Co multilayers, and they have lower coercivity, it seems unlikely that twin defects pin domain wall motion and contribute to coercivity. Column boundaries, which are sharper in Xe-sputtered and vapor-deposited multilayers, which have relatively large coercivity, more likely pin domain walls and thus contribute to coercivity.

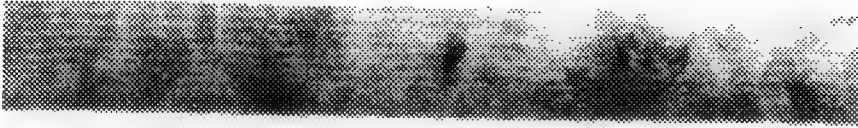
In summary, the microstructure of Pt/Co multilayers depended on Co thickness. As the Co layer thickness increased from ~4 Å to ~20 Å, the surface roughness of the multilayer increased, lattice coherence of Pt and Co layers was lost, and the number of defects increased. Also, the structure of Co layers became hcp. We noticed that coincident with a coherent structure (thin Co), Pt/Co multilayers have a large perpendicular magnetic anisotropy [4].

References

1. F. J. A. M. Greidanus, W. B. Zeper, B. A. J. Jacobs, J. H. M. Spruit, and P. F. Carcia, Japanese J. Appl. Phys. (1989) 28, 37, Supplement 28-3.
2. Z.G. Li, P.F. Carcia, J. Appl. Phys. (1992) 71, 842.
3. Z.G. Li, P.F. Carcia, Ultramicroscopy, (1992), 47, 313.
4. We thank to wish to thank Dr. Y.Cheng for collaboration and the Arizona State University high resolution microscopy facility for their cooperation in this study.

1)

Pt/Co multilayers



Si

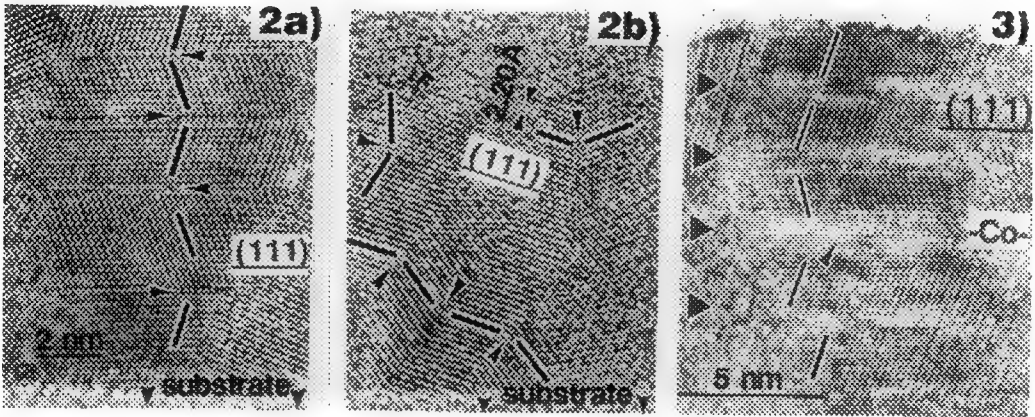


Fig.1. Cross sectional image of a Ne-sputtered multilayers, 10x(4 Å Co+10 Å Pt).

HREM cross sectional images of Fig. 2a) a vapor-deposited multilayers, 13x(6 Å Co+9 Å Pt), and Fig. 2b) a Ne-sputtered multilayers, 10x(4 Å Co+10 Å Pt). They both have coherent structure in the grains, but vapor-deposited multilayers exhibit better (111) texture than Ne-sputtered multilayers.

Fig. 3). HREM image of 15x(10Å Co+16Å Pt), multilayers, Xe-sputtered at 5 mTorr. The position of Co layers is indicated by arrows. The AB/AB Co hcp stacking is also indicated.

MICROSTRUCTURE AND MAGNETO-OPTIC PROPERTIES OF UNANNEALED AND ANNEALED Fe/Pt AND Co/Pt MULTILAYERS

Mark R. Visokay

Department of Materials Science and Engineering, Stanford University, Stanford CA 94305

Two requirements for magneto-optical storage media are remanent perpendicular magnetization and large magneto-optic Kerr rotations. Several film structures and material systems have been proposed for this purpose, including amorphous rare earth-transition metal alloys, Co/Pt multilayer films and Co/Pt alloys. Another structure that has potential for magneto-optic applications are thin films of ordered alloys based on the $L1_0$ structure, with two possible materials systems being Fe/Pt and Co/Pt.¹ Ordered CoPt and FePt both adopt the $L1_0$ crystal structure, are ferromagnetic, and are magnetically easy along the unique axis. Thin films oriented such that the c axis is out of the film plane are expected to have large perpendicular anisotropy, and both FePt and CoPt are known to have large Kerr rotations, so both of the requirements mentioned above can be met with these materials.²

In order to produce the ordered structures oriented with the c axis out of the plane epitaxial multilayers of the two constituents were produced by magnetron sputtering onto epitaxial Pt [001] seed layers deposited onto MgO [001], resulting in multilayers stacked along Pt [001]. These films were then annealed in vacuum ($<5 \times 10^{-7}$ Torr) to produce the ordered, oriented structures.

The initial film structure of a $(46 \text{ \AA} \text{ Fe}/59 \text{ \AA} \text{ Pt})_{30}$ multilayer is shown in Figure 1. Figure 1A is a cross section bright field image showing the overall microstructure consisting of a well layered structure with conformal roughness. The orientation relationship for the unannealed films is Fe (001) \parallel Pt (001) and Fe [110] \parallel Pt [100] (the Bain relationship), which is confirmed in Figure 1B, a high resolution image of the multilayer with the Pt and Fe in the [110] and [100] zone axis orientations, respectively. Upon annealing of the multilayers the tetragonal FePt phase is formed such that FePt (001) \parallel MgO (001) and FePt (100) \parallel MgO (100). The presence and orientation relationship of this phase can be seen in Figure 2A, a cross section selected area diffraction pattern (SADP) of the film and substrate in the [010] orientation. The changes in structure shown by electron and x-ray diffraction are accompanied by changes in the magnetic and magneto-optic properties. Figure 2B shows the magnetization as a function of applied field for a $(23 \text{ \AA} \text{ Fe}/29.5 \text{ \AA} \text{ Pt})_8$ multilayer, as deposited and after annealing at 475 °C for 14 h. Before annealing there is a magnetic hard axis out of plane which switches to an easy axis upon annealing, with a perpendicular anisotropy of 8×10^6 erg/cc. Magneto-optic measurements show a post anneal remanent Kerr rotation of 0.5°. These characteristics compare very favorably with those of the other aforementioned magneto-optical systems.

Similar results have been obtained for Co/Pt films. Figure 3 shows high resolution images of the as deposited structure of a $(14 \text{ \AA} \text{ Co}/19 \text{ \AA} \text{ Pt})_{32}$ multilayer taken in the MgO [110] orientation. The low magnification image (3A) shows the composition modulation present in the film, whereas the higher magnification image (3B) shows that the structure is in fact a compositionally modulated fcc structure. Annealing of this structure forms the CoPt phase oriented with the c axis out of the film plane. Again the structural changes are accompanied by improvements in the magnetic and magneto-optic properties.³

References

1. B.M. Lairson et al., Applied Physics Letters, 62, 6 (1993) 639.
2. T. Katayama et al., Journ. Magn. and Magn. Mat., 104-107 (1992) 1002.
3. This work supported by Kobe Steel Inc. Many thanks to Bruce Lairson, Professor Robert Sinclair and Professor Bruce Clemens for encouragement and helpful discussions

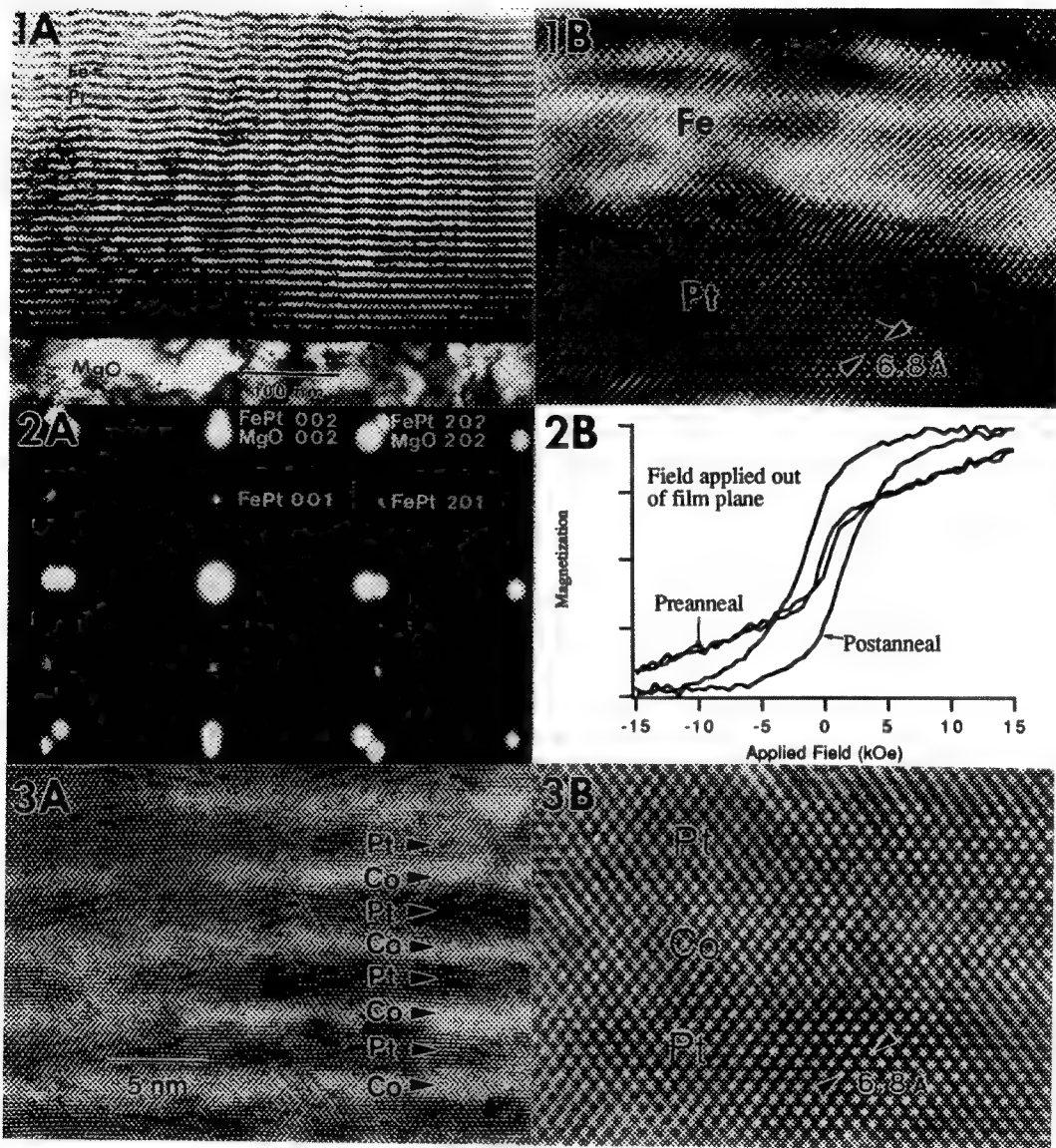


Fig. 1: Bright field (A) and HREM (B) images of a (46 Å Fe/59 Å Pt)₃₀ [001] stacked multilayer. Zone axes imaged: Fe [100], Pt [110]. The growth direction is vertical.
 Fig. 2: SADP (A) and magnetization data (B) for a (23 Å Fe, 29.5 Å Pt)₈ annealed multilayer. The SADP shows the presence of oriented FePt that was absent in the unannealed film, the formation of which causes a change from a hard to an easy magnetic axis out of the film plane, shown in B.
 Fig. 3: Low (A) and high (B) magnification HREM images of a (14 Å Co/19 Å Pt)₃₂ [001] stacked multilayer. The zone axis imaged is [110]. The growth direction is vertical.

MAGNETIC DOMAIN WALL MOVEMENT IN IRON SILICON

J.E. Wittig

Department of Materials Science and Engineering, Vanderbilt University, Nashville, Tennessee

Lorentz microscopy in the transmission electron microscope directly images magnetic domains. By changing the magnetic field of the electromagnetic lenses relative to the specimen plane, the movement of the magnetic domain walls and their interaction with microstructural features can be observed *in situ*. This type of experiment has successfully analyzed the microstructure-domain wall interactions in spinel ferrites and iron-rare-earth-boron magnetic materials^{1,2}. The domain wall motion reveals the qualitative pinning potential of grain boundaries, precipitates, inclusions, stacking faults, and cracks. In addition, these *in situ* experiments display the dynamics of magnetic domain nucleation. The current study investigates the magnetic domain wall movement in iron silicon alloys. Since magnetic properties such as intrinsic coercivity and permeability are structure sensitive, the influence of microstructure on domain wall movement dictates the soft magnetic behavior.

Thin foils of iron-6.5 wt% silicon were prepared by electropolishing ribbons produced by melt spinning techniques. The magnetic domain walls were imaged in the defocused (Fresnel) mode with a Philips CM20T operated at 200 kV. The Free Lens Control capability can manipulate the magnetic field at the specimen position by increasing the objective lens current from zero to a few hundred mA or by changing the TWIN lens current which has a slight leak field into the objective-lens space³. Either changing the magnetic field strength in the specimen space or tilting the specimen in the presence of a low level field produced magnetic domain movement. These small magnetic fields did not affect the quality of the magnetic domain wall images. Maximizing the current in both the intermediate and second projector lenses while reducing the first projector lens current increased the magnification over the standard low magnification (LM) imaging mode. The diffraction lens defocused the image to provide the Fresnel contrast.

Figures 1-3 represent a typical sequence of Lorentz images from a dynamic experiment. Figure 4 is a bright field image of this area which reveals the presence of a high angle grain boundary, a low angle grain boundary, individual dislocations, and silicon oxides within the grains. A magnetic domain wall intersects the high angle grain boundary in figure 1. The domain wall was pinned in this position since the sample had to be tilted more than 10° before the domain wall suddenly jumped to the new position in figure 2. The wall did not move smoothly, but released stored energy when it changed positions. The domain wall stopped when it became pinned by the silicon oxides within the grain. Cross tie walls are also evident in figure 2. Tilting the sample back to the initial position resulted in the domain wall configuration shown in figure 3. The tilting experiment returned the domain wall to the original orientation but also created a new set of reverse domain walls attached to the original wall. Qualitatively, oxide particles were more effective at pinning domain walls than grain boundaries. These oxides produced the strongest pinning effect when they were less than 100 nm in size. Single dislocations or low angle grain boundaries did not reveal any observable influence on the domain wall motion⁴.

References

- 1- I.N. Lin et al., IEEE Trans. Mag., 20 (1984) 134
- 2- R. Ramesh and G. Thomas, J. Appl. Phys. 67 (1990) 6968
- 3- M.T. Otten, private communication
- 4- Helpful discussions with Prof. W.F. Flannagan are gratefully acknowledged.

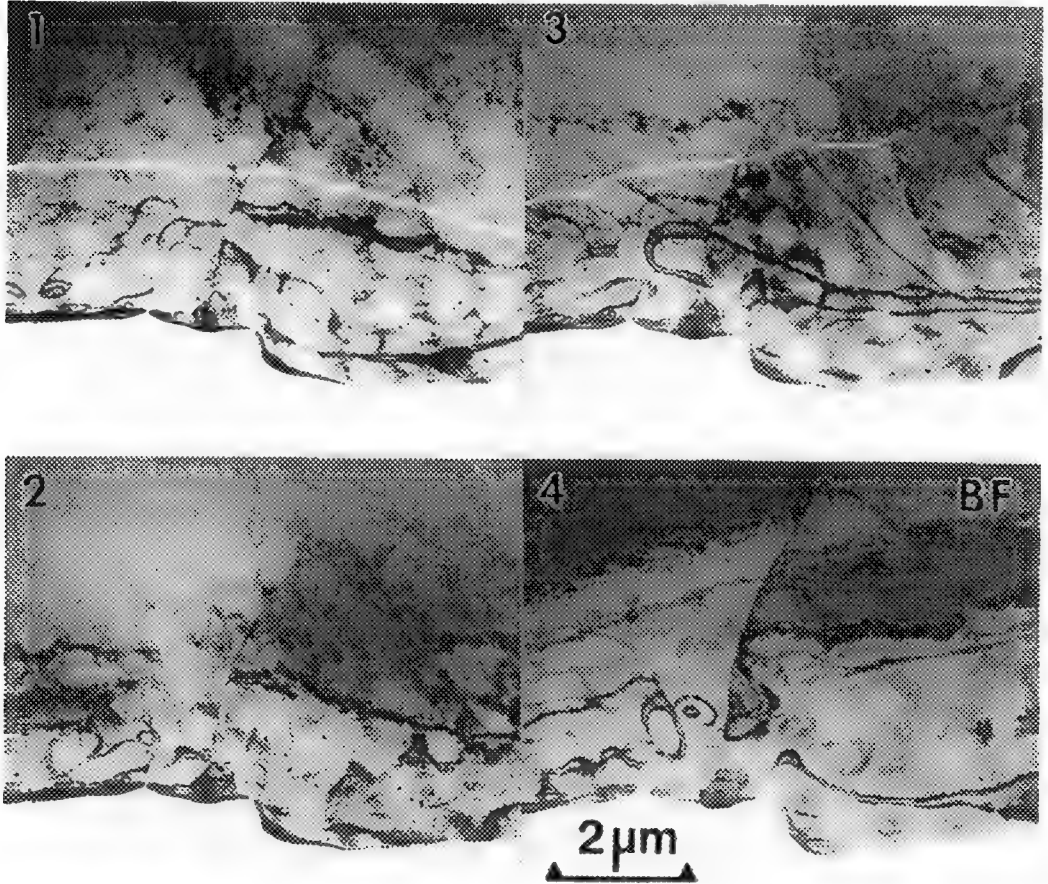


FIG. 1 - Fresnel contrast Lorentz image of a magnetic domain wall intersecting a high angle grain boundary.

FIG. 2 - Lorentz image showing the new position of the magnetic domain wall from FIG. 1 after tilting the sample 12° in the presence of the leakage field from the TWIN lens.

FIG. 3 - Lorentz image after tilting the sample back to its initial position.

FIG. 4 - Bright field image of the area for Lorentz microscopy.

DOMAINS AND DOMAIN NUCLEATION IN MAGNETRON-SPUTTERED CoCr THIN FILMS

B. G. Demczyk

North Campus Electron Microbeam Analysis Laboratory, The University of Michigan, Ann Arbor, MI 48109-2143

CoCr thin films have been of interest for a number of years due to their strong perpendicular anisotropy, favoring magnetization normal to the film plane. The microstructure and magnetic properties of CoCr films prepared by both rf and magnetron sputtering have been examined in detail. By comparison, however, relatively few systematic studies of the magnetic domain structure and its relation to the observed film microstructure have been reported. In addition, questions still remain as to the operative magnetization reversal mechanism in different film thickness regimes. In this work, the magnetic domain structure in magnetron sputtered Co-22 at.%Cr thin films of known microstructure were examined by Lorentz transmission electron microscopy. Additionally, domain nucleation studies were undertaken *via* in-situ heating experiments.

It was found that the 50 nm thick films, which are comprised of columnar grains, display a "dot" type domain configuration (Figure 1d), characteristic of a perpendicular magnetization. The domain size was found to be on the order of a few structural columns in diameter. Thinner (~10 nm) films with no perceptible column structure exhibit well-defined in-plane 180° domain walls (Figure 1b). Films of intermediate thickness show a "feather-like" structure (Figure 1c), indicating that both in-plane and out-of-plane magnetization components are present. In addition, the thinnest films (≤ 5 nm), which are practically amorphous, appear to have a perpendicular anisotropy component as well (Figure 1a), as has been predicted theoretically¹. Domain nucleation studies seem to indicate that films with in-plane magnetization reverse by domain wall motion and those with perpendicular anisotropy by rotation. This is consistent with ferromagnetic resonance and vibrating sample magnetometry measurements of the magnetic properties of these materials.

References

1. Gay, J. G. and Richter, R., Phys. Rev. Lett. **56**, 2678 (1986).
2. Samples were prepared under a grant from the Division of Materials Research, National Science Foundation, Grant No. DMR-8613396.

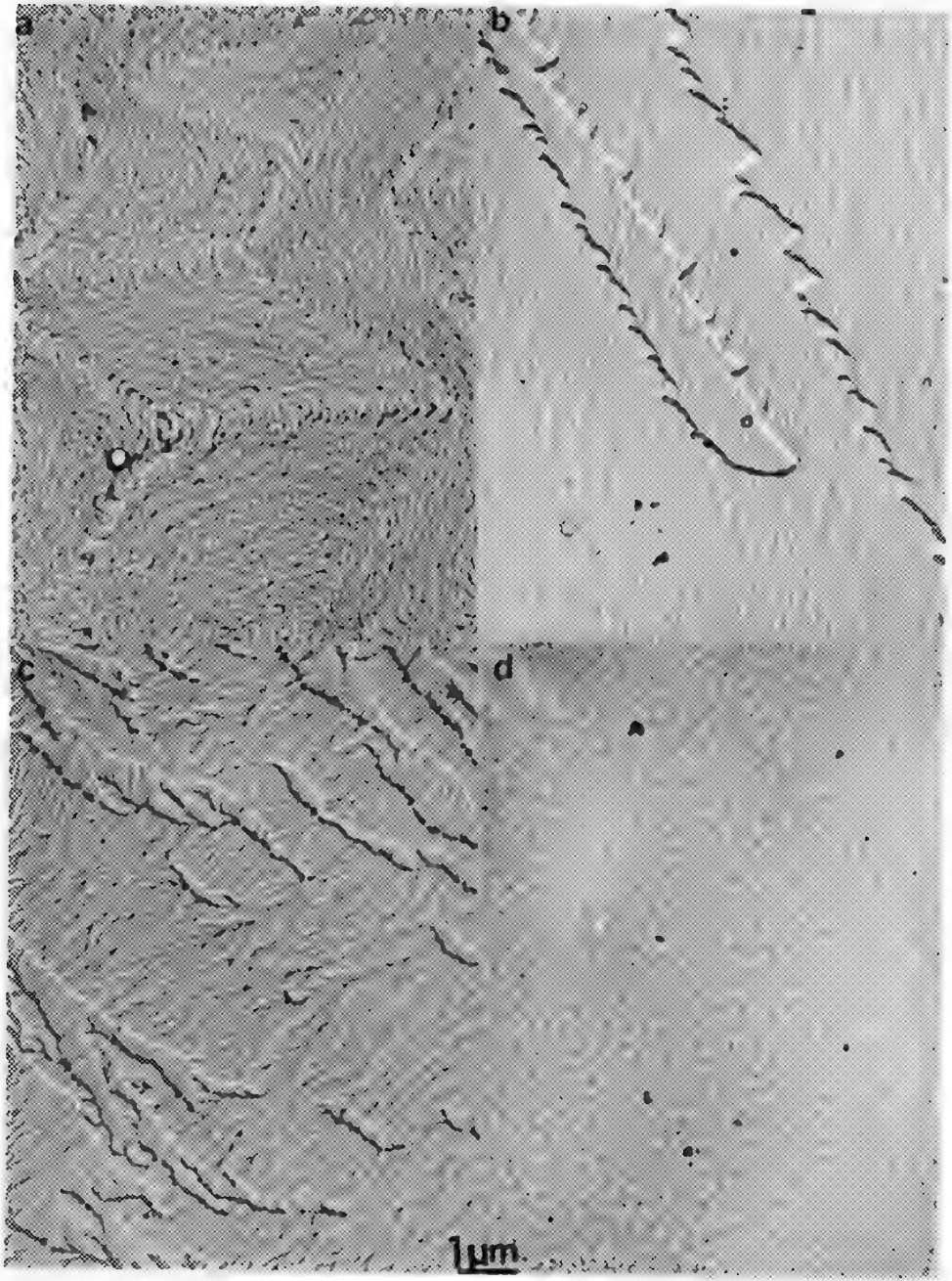


Fig. 1 Magnetic domain structures in: a) 5 nm, b) 10 nm, c) 20 nm and d) 50 nm thick CoCr thin film.

Transmission Electron Microscopical Examination Of The Magnetic Domain Boundaries in a Duplex Austenitic- Ferritic Stainless Steel

G. Fourlaris and T. Gladman

School of Materials , The University of Leeds , Leeds LS2 9JT, England

Duplex austenitic- ferritic stainless steels (DSS) offer significant advantages when compared to standard austenitic stainless steels, in several areas of industrial applications, due to their higher mechanical strength , superior resistance to corrosion and a lower price because of their lower nickel content [1,2] . Despite the extensive research carried out so far in the area of DSS the characterisation of their magnetic properties , under stress or under a static field , has attracted significantly less attention. This is contrary to the fact that in certain naval constructions the suitability of a given type of steel is judged not only by its tensile , impact , and corrosion properties but also by its magnetic behaviour.

A 2205 type austenitic- ferritic DSS has been cold rolled to different cold rolling reductions , with an aim of achieving a 0.2 % proof strength of at least 700 MPa with an elongation value of greater than 20 %. Samples of this steel were subjected to SEM and TEM examination following the cold rolling experiments. A Philips 430 ST High Voltage Electron Microscope was used. In addition magnetic property assessment was also carried out , in a static field , using as a reference for comparison the properties exhibited by a medium carbon-low alloy steel.

In Figure 1 a composite SEM micrograph is presented showing the general details of the ferritic-austenitic microstructure in the three orthogonal directions . It can be seen that the microstructure consists of austenite and ferrite in equal amounts. This has also be verified by TEM examination where it can be seen that austenitic regions exhibit a high dislocation density and are heavily twinned (Fig.2) . Also , some secondary austenitic islands are present within the ferritic areas (Fig.3). The magnetic hysteresis loop , under a static field , is presented in Figure 4 where the hysteresis loop of an En 24 type medium carbon low alloy reference steel of equivalent strength is also presented, in order to show the significant differences in terms of both the low value of maximum magnetic induction and the low value of coercivity achieved in the 2205 type DSS. It can be concluded that the presence of high amounts of ferrite (ferromagnetic phase) in the DSS microstructure does not prevent the material from exhibiting surprisingly weak magnetic behaviour. An explanation for this behaviour can be found when the material is examined in the Low Magnification mode of the Philips TEM , where the objective lens magnetic field is non operational . It can be seen in Figure 5 that the magnetic domain boundaries are clearly imaged within the ferritic regions of the DSS sample , appearing as bands of alternate light and dark contrast.

Concluding this presentation it can be said that the 2205 austenitic- ferritic DSS exhibits not only excellent mechanical , impact and corrosion properties but also a weak magnetic response. Such behaviour is due to the lamellar interwoven austenitic-ferritic microstructure and it is only surpassed by fully austenitic stainless steels.

References.

1. J.O. Nilsson : Mater.Sci.Technol., 1992, **8** , 685 .
 2. S.Bernhardsson: Proc.Conf. 'Duplex Stainless Steels 91 ' , **185**; , 1991, Les Ulis, France , Les Editions de Physique.
- This work is supported by Procurement Executive , Defence Research Agency , U.K.

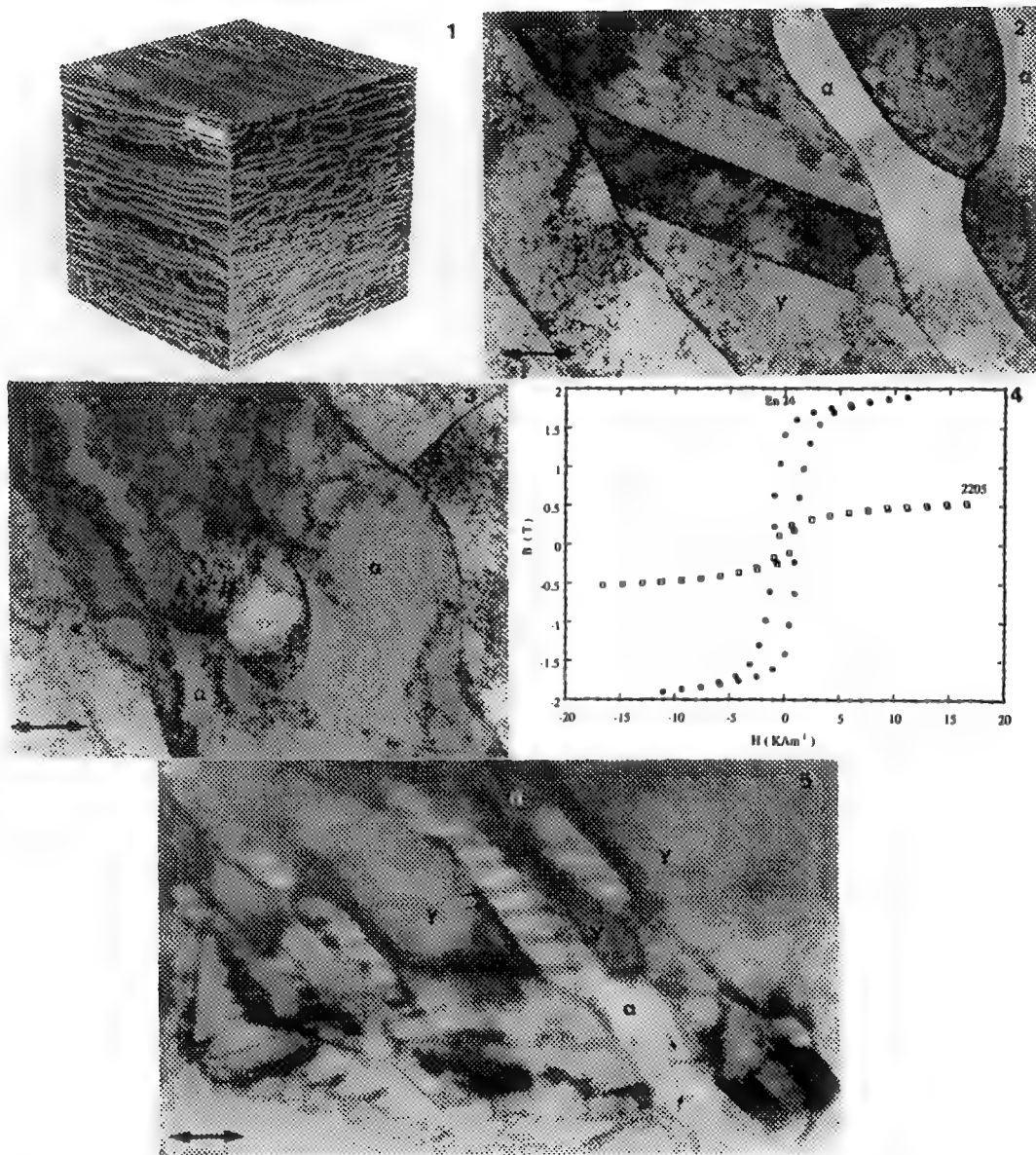


Figure 1 : Composite SEM micrograph of the ferritic-austenitic microstructure.

Figure 2 : TEM Bright field micrograph showing the high dislocation density and the heavily twinned appearance of the austenitic regions . Bar 800 nm.

Figure 3 : TEM Bright field micrograph showing the presence of secondary austenitic islands in the ferritic regions. Bar 800 nm.

Figure 4 : Hysteresis loops produced , under a static field , in an austenitic -ferritic DSS and a medium carbon low-alloy steel of similar strength.

Figure 5 : Low magnification Bright field TEM micrograph showing the magnetic domain wall boundaries within the ferritic regions . Bar 1.15 μ m.

REAL-TIME OBSERVATION OF VORTEX LATTICES IN A SUPERCONDUCTOR

K. Harada, T. Matsuda, J.E. Bonevich, M. Igarashi*, S. Kondo, H. Kasai, T. Yoshida, G. Pozzi,**
U. Kawabe* and A. Tonomura

Advanced Research Laboratory, Hitachi, Ltd., Hatoyama, Saitama 350-03, JAPAN

*Central Research Laboratory, Hitachi, Ltd., Kokubunji, Tokyo 185, JAPAN

**Department of Materials Science, University of Lecce, via Arnesano, 73100 Lecce, ITALY

Previous observations of magnetic flux-lines (vortex lattices) in superconductors, such as the field distribution of a flux-line,^{1,2} and flux-line dynamics activated by heat³ and current,⁴ have employed the high spatial resolution and magnetic sensitivity of electron holography.⁵ And recently, the 2-D static distribution of vortices was also observed by this technique.⁶ However, real-time observations of the vortex lattice, in spite of scientific and technological interest, have not been possible due to experimental difficulties. Here, we report the real-time observation of vortex lattices in a thin superconductor, by means of Lorentz microscopy using a 300 kV field emission electron microscope.⁷ This technique allows us to observe the dynamic motion of individual vortices and record the events on a VTR system.

The experimental arrangement is shown in Fig. 1. A Nb thin film for transmission observation was prepared by chemical etching. The grain size of the film was increased by annealing, and single crystals were observed with a thickness of 50~90 nm. The specimen was set on a low temperature stage tilted at 45° to both the incident electron beam and the applied magnetic field. Vortices were visible in a defocused image (Lorentz micrograph) with spot-like contrast, one side light and the other side dark. The dividing line between spots is the projection of the flux-line field.

Figure 2 shows the equilibrium Lorentz micrograph of a vortex lattice at B=150 G and T=4.5 K. Each spot with light and dark contrast is a vortex, the black lines are bend contours. The specimen has a fairly uniform thickness in the region shown, but the vortex lattice is irregular in some places (arrowed). When the specimen was heated, the vortices hopped to form a more regular triangular lattice. But the vortices at the arrowed points did not move about, as they were strongly pinned. There was no observable diffraction contrast from these areas, presumably the pinning sites consisted of impurities (e.g. substitutional atoms) in the Nb.

After turning off the applied field, 90% of the vortices disappeared. Those that remained, being trapped at pinning sites, moved by hopping in the direction of decreasing vortex density. Examples of the vortex movements as reproduced from videotape (30 frames/s) are shown in Fig. 3. Figure 3 (a) was 48 s after turning off magnetic field, and this distribution of vortices was stable for 1.3 s. The distribution shown in Fig. 3 (b) was stable for 1.8 s. The interval of time between Fig. 3 (a) and (b) was 0.4 s. Furthermore, the vortices oscillated briefly (0.3 s) after hopping before becoming stable. Figure 3 (c) was recorded after 6.2 s and was stable for 1.3 s. From these results we can infer that although the vortex distribution is relatively stable (a few seconds), the hopping process is a quick phenomenon usually requiring less than 0.1 s.

Based on this real-time and transmission observation, it is now possible to study the movement of vortex lattices and pinning sites in superconductors.

References

1. T. Matsuda et al., Phys. Rev. Lett. (1989) 62, 2519.
2. S. Hasegawa et al., Phys. Rev. B (1991) 43, 7631.
3. T. Matsuda et al., Phys. Rev. Lett. (1991) 66, 457.
4. T. Yoshida et al., Proc. 50th Ann. EMSA Meeting 1(1992)68.
5. A. Tonomura, Rev. Mod. Phys. (1987) 59, 639.

6. J.E. Bonevich et al., *these proceedings*.
 7. K. Harada et al., *Nature* (1992) 360, 51.

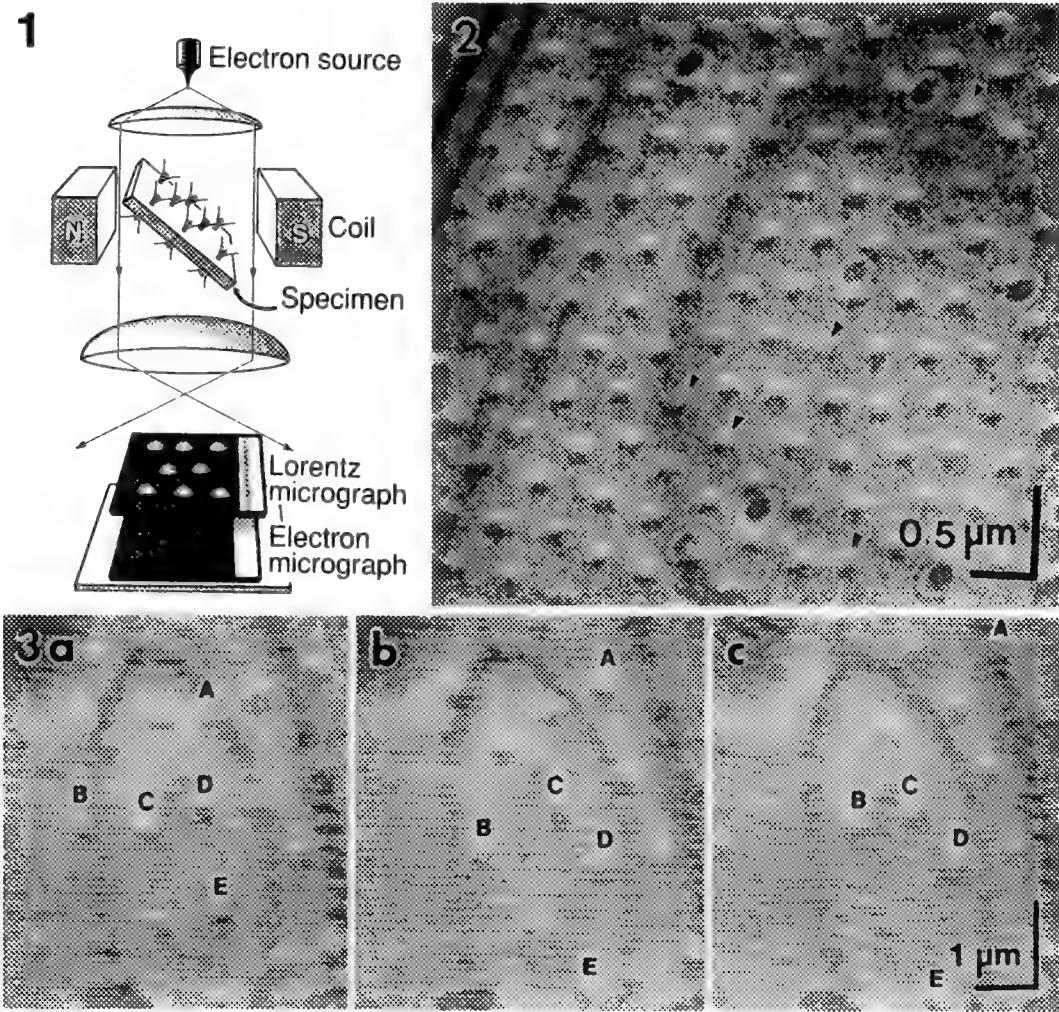


FIG. 1 Schematic diagram of vortex lattice observation.
 FIG. 2 Lorentz micrograph of vortex lattice in Nb thin film at 150 G and 4.5 K. Vortices are observed as small spots of light and dark contrast. Arrows indicate strongly pinned vortices.
 FIG. 3 Dynamics of the vortices seen at times t after magnetic field has been switched off from 100 G; (a) $t=t$ s, (b) $t=t+1.7$ s, (c) $t=t+8.3$ s ($t=48$ s). The letters indicate identical vortices.

LORENTZ ELECTRON MICROSCOPY OF COBALT BORIDES IN A PLATINUM COBALT MATRIX

N. Qiu and J.E. Wittig*

Department of Mechanical Engineering, Yale University, New Haven, Connecticut

*Department of Materials Science and Engineering, Vanderbilt University, Nashville, Tennessee

The presence of cobalt borides significantly increases the intrinsic coercivity (H_{ic}) of a Pt-Co alloy^{1,2}. Whereas the maximum H_{ic} for a binary Pt-Co alloy is less than 5 kOe, a ternary $Pt_{42}Co_{45}B_{13}$ (at%) alloy exhibits intrinsic coercivity as large as 15.2 kOe. The optimum microstructure for the maximum H_{ic} consists of a dispersion of cobalt boride precipitates having the orthorhombic Co_3B structure in an $L1_0$ Pt-Co matrix. Lorentz electron microscopy of the magnetic structure of these cobalt borides has been used to elucidate their strong influence on the magnetic properties of this alloy. Magnetic domain wall thickness measurements assist with modeling of the magnetic hardening mechanism.

Processing the $Pt_{42}Co_{45}B_{13}$ (at%) material utilized an initial rapid solidification step followed by annealing at 800°C. Samples for Lorentz electron microscopy were prepared by dimple grinding and ion milling to electron transparency. The Lorentz imaging employed the standard Fresnel contrast method by operating a Philips CM20T at 200 kV in the low magnification (LM) mode. In the LM mode, the objective lens is weakly excited and the diffraction lens is used to defocus the image. Since the magnification of the LM mode is limited, a Gatan 622 image intensified video camera provided additional magnification of the Lorentz images. The magnetic domain wall width was measured by using the technique developed by Wade which compares convergent and divergent domain wall half-width images⁴. Typical defocus settings were +/- 150 microns.

Analysis of the optimum hard magnetic microstructure revealed that the average cobalt boride size was less than 500 nm in diameter. Lorentz imaging of particles smaller than 500 nm showed no evidence of magnetic domain walls, thus this particle size must be within the single magnetic domain regime. Overaging the rapidly solidified structure past the peak coercivity increased the average cobalt boride size. Figure 1 shows some of these overaged cobalt borides which now exhibit multiple magnetic domains. The measured cobalt boride magnetic domain wall thickness was 10 nm (+/- 4 nm). This large experimental error arises from the difficulty of measuring the width of the defocused wall image for a large defocus and a small domain wall width. Nevertheless, a theoretical domain wall thickness of 12 nm (estimated from available magnetic data) provides confidence in the measured domain wall dimension. Using the experimental value of the domain wall thickness, the calculated magnetic anisotropy constant (K) is 16×10^6 ergs/cm³ and the domain wall energy is 20 ergs/cm². These data predict the theoretical single magnetic domain size to be 390 nm which is in close agreement with the experimental observations. The magnetic hardening mechanism of the ternary alloy is proposed to be related to difficult reverse magnetic domain nucleation in these single domain size cobalt borides⁵.

References

1. N. Qiu et al., J. of Appl. Phys., 70 (1991) 6137
2. N. Qiu and J.E. Wittig, IEEE Trans. Mag., 28 (1992) 2865
3. N. Qiu and J.E. Wittig, J. of Appl. Phys., in press
4. R.H. Wade, Proc. Phys. Soc., 79 (1962) 1237
5. This work was supported by the NASA Office of Commercial Programs and the Engelhard Corporation.

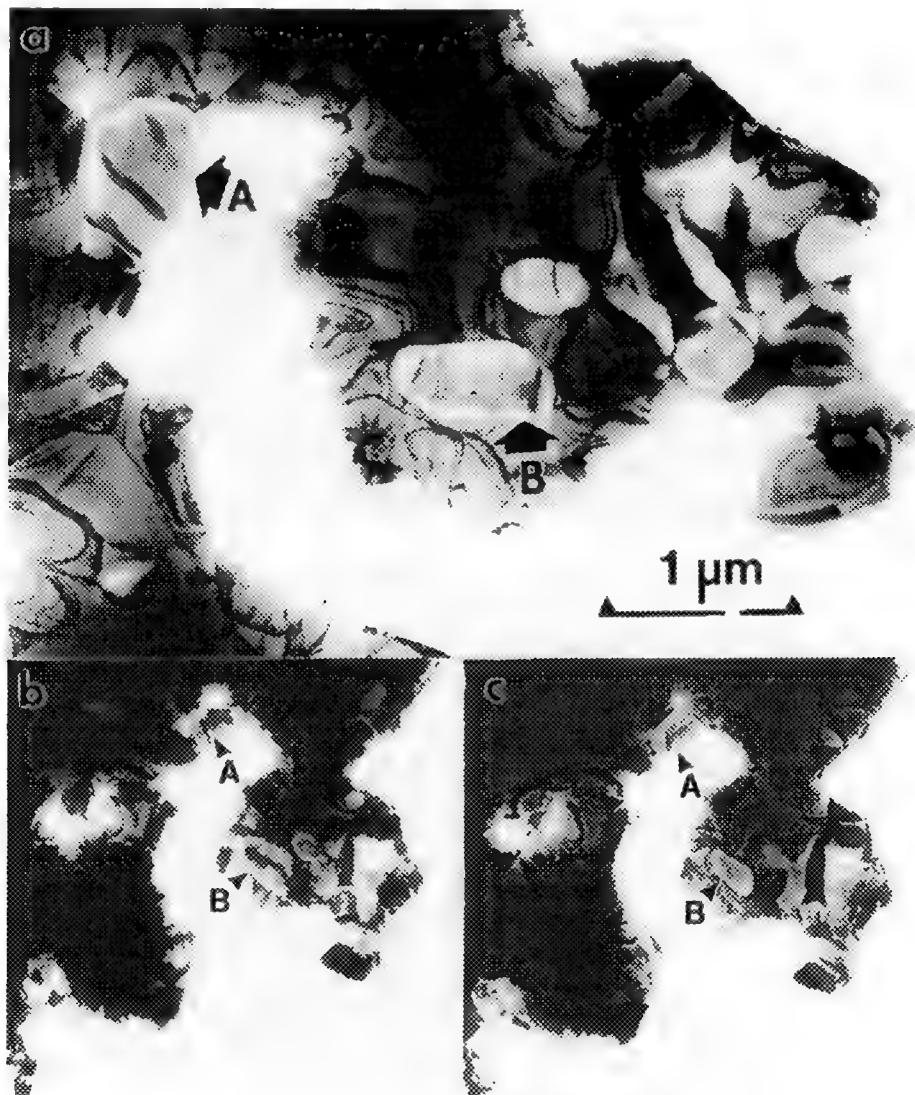


FIG. 1- a) BF image of cobalt boride precipitates in the L1₀ Pt-Co matrix. b&c) Fresnel underfocused and overfocused Lorentz images of multiple magnetic domain cobalt borides marked A and B.

EXPLORATORY WORK ON COHERENT DIFFRACTION AND ELECTRON HOLOGRAPHY USING A HITACHI HF 2000

J W Steeds, R Vincent, P Spellward and X F Deng

Physics Department, University of Bristol, Bristol, BS8 1TL, UK

Now that coherent electron diffraction can be performed routinely on appropriately chosen specimens in a standard commercial instrument^{1,2} there are a number of applications of the technique which are in progress.

One of these is in crystal structure determination. For sufficiently thin crystals, the fringes in the overlap between adjoining reflections n and $n+1$ give the relative phases $(\phi_{n+1} - \phi_n + \delta)$ of their complex structure factors, apart from an unknown phase factor, δ , which depends on the probe position. In a systematic row of reflections, the next overlap between reflections $n+1$ and $n+2$ gives $(\phi_{n+2} - \phi_{n+1} + \delta)$ and so the difference between these two phasings becomes $(2\phi_{n+1} - \phi_n - \phi_{n+2})$, eliminating the unknown factor δ . Now that coherent diffraction has been achieved in the zero order Laue zone of a zone axis pattern it is possible to phase the whole two dimensional mesh relative to the central beam (Figure 1). In addition, the existence of coherent diffraction effective in higher order Laue zone diffraction² permits the extension of direct measurements of relative phases to the third dimension. Until recently, the coherent electron diffraction patterns were recorded photographically and included both elastic and inelastic contributions. However, the addition of an energy selecting imaging filter and slow scan CCD system (Gatan imaging PEELS) to our Hitachi HF2000 means that purely elastic data may be directly recorded in a digital form. We are therefore in a position to extract effectively the amplitude and phase information from our results for the first time.

By using a very small selecting area aperture ($\sim 1\mu\text{m}$ diameter) it has also been possible to stay within the lateral coherence of the source and obtain coherent large angle convergent beam electron diffraction patterns from two adjoining reflections. These patterns contain large numbers of fringes³ (~ 120 have been recorded) and allow relatively straightforward identification of particular features of the specimen such as dislocations, stacking faults or grain boundaries. Moreover, the angular view is sufficiently large for the effects of spherical aberration to alter the fringe spacing near the periphery of the pattern relative to its centre. Such patterns may be regarded as a form of Fraunhofer hologram (although without an unaffected reference beam) and have been processed to provide information about the specimen and the lens aberrations.

Since slightly out-of-focus coherent electron diffraction patterns reveal lattice fringes in the region of overlap between adjoining discs (as in Figure 1) high resolution spatial information is also available in this mode of operation. It is therefore interesting to compare the two different techniques for studying defects or interfaces in specimens, and also to compare the reciprocal space methods with off-axis real-space holograms generated using a Möllenstedt biprism. Out-of-focus coherent electron diffraction patterns contain large numbers of reflections but a relatively small field of view. Thus it is hard to locate a specific region in the specimen. However, the multiplicity of reflections has distinct advantages in attempting to distinguish strain effects from microscopic electric or magnetic fields associated with the extended defect. Suppose the defect has a displacement \underline{R} associated with it. Then the magnitude of $\underline{g} \cdot \underline{R}$ will dictate the strain contrast observed and different regions of the pattern will show systemically greater or smaller effects. However, the effect of local electric or magnetic fields will generally have quite different properties which may be used for distinguishing the separate effects. The large number of ZOLZ and HOLZ reflections which can occur in such patterns might be used to make very accurate deductions about displacements associated with the defect. Coherent large angle diffraction

patterns will have the advantage in studying more complex defects or defect arrays because of the larger field of view. Moreover the large number of fringes generated makes possible the effective application of holographic techniques to study effects associated with the defects. Neither of the techniques so far discussed have the direct spatial resolution which can be achieved by real-space off-axis holograms where sub-Angstrom resolution is projected⁴ and slightly poorer resolutions have already been achieved⁵. By comparison, the highest resolution which we have achieved so far in our coherent electron diffraction experiments is 7.5Å.

References

1. W. J. Vine, R. Vincent, P. Spellward and J. W. Steeds, *Ultramicroscopy*, 41(1992)423.
2. J. W. Steeds, R. Vincent, W. J. Vine, P. Spellward and D. Cherns, *Hitachi News*, 24(1992)3.
3. R. Vincent, W. J. Vine, P. A. Midgley, P. Spellward and J. W. Steeds, submitted to *Ultramicroscopy*.
4. H. Lichte, *Ultramicroscopy*, 47(1992)223.
5. T. Kawasaki and A. Tonomura, *Phys. Rev. Lett.*, 69(1992)293.

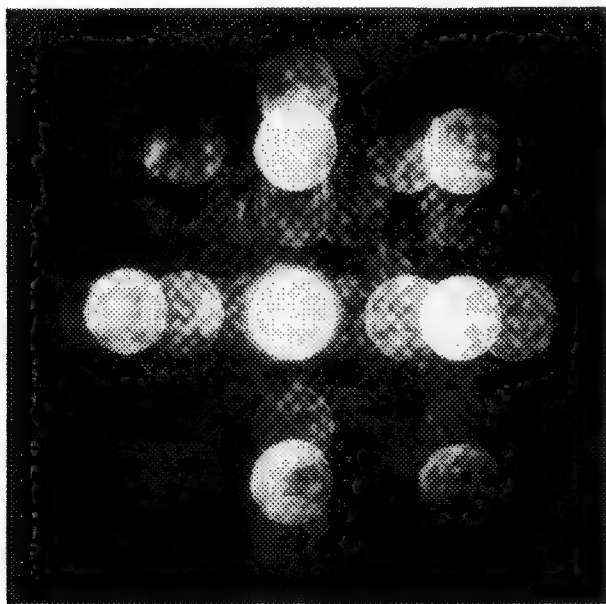


FIG. 1.--Coherent electron diffraction pattern of BaCuO₂ taken at 200kV at the [001] zone axis of the tetragonal lattice.

CONVERGENT BEAM ELECTRON DIFFRACTION INTERFEROMETRY USING AN ELECTRON BIPRISM (CBED+EBI)

R.A. Herring, G. Pozzi*, T. Tanji, and A. Tonomura

Tonomura Electron Wavefront Project, ERATO, JRDC, P.O. Box 5, Hatoyama, Saitama 350-03 Japan

* Department of Material Science, University of Lecce, Via Arnesano, 73100 Lecce, Italia

Recently, a new method of interferometry has been realized [1] which is capable of providing important information of crystals, crystal defects and electron-optical information of the microscope such as its spherical aberration surface. The method produces interferograms by using an electron biprism to interfere diffracted beams produced from a small convergent beam probe of ~10 nm. The electron biprism uses an applied voltage of ~15 to 100 V to deflect and compensate for the diffracted beam(s) of $2\theta_B$ (typically ~5 mrad) (Fig. 1). The biprism (~0.3 μm dia) is inserted in between and perpendicular to the diffracted beam(s). Two biprism positions were successfully used. An "upper" biprism is placed in the selected area aperture position which is between the objective lens and 1st intermediate lens. A "lower" biprism is further down the optic axis and is placed between the 1st and 2nd intermediate lenses. In Fig. 1, the virtual image of a biprism is shown with respect to the specimen plane. The virtual image of the biprism is reduced in size by the (de)magnification of the post-specimen lens which enable it to be placed in between the diffracted beams without intersecting them. The difference in magnification of the biprisms enabled the lower biprism's focus probe positions, S1 and S2 in Fig. 1, to lie closer to the specimen plane resulting in a finer fringe spacing for the same interfering beams. The image of the specimen within the CBED disk lies in the back-focal-plane between the fraunhofer and near-image plane, i.e., fourier space, which depends on the magnifying condition of the microscope's lenses and strongly depends on the convergence angle (C1 current), objective (de)focus, and I1 lens current. Examples of some interferograms produced from a GaAs crystal are shown in Fig. 2 and Fig. 3. At a zone axis many interferograms can be produced simultaneously. As well, since the interference originates from the same place in the crystal a coherent beam is not necessary for CBED+EBI and thus it is possible to use an extended source such as a LaB₆. Fig. 2 also shows the sensitivity of the CBED+EBI method to spherical aberration effects where the fringe spacing of the main beam overlaid by the 222 beam is 1) not equal to half that of the main beam overlaid by the 111 beam and 2) not equal to the 111 beam overlaid by the $\bar{1}\bar{1}\bar{1}$ beam, as might be expected. In fact, for the interference of two beams relatively far from the optic axis the deviation from the fringe spacing and linearity of the fringes can become very great (Fig. 3). Simulations are being performed to explain the above results (Fig. 4), although some microscope parameters still need measuring, using the following theoretical model.

The amplitude and phase difference contained within the interferogram is related to the (de)focus condition of the specimen, as well as, the structure factor of the diffracted beam(s). For exact overlaying of the diffracted beam the amplitude and phase difference related to the (de)focus condition of the microscope is given by [2],

$$I(u) = |C(u)f_1(u)|^2 + |C(u)f_2(u)|^2 + 2|C(u)^2 f_1(u)f_2(u)| \cos[4\pi r_b K_b - \gamma(u + g_1) + \gamma(u + g_2) + \Delta\phi] \quad (1)$$

where u is a reciprocal lattice vector, $C(u)$ is the condenser aperture function, f_1 and f_2 are the amplitudes of the two interfering beams, r_b is the coordinate of the biprism axis, K_b is the biprism spatial frequency (α/λ), $\gamma(u)$ is the contrast transfer function, g is the reciprocal lattice vector of the diffracted beams ($2\theta_B/\lambda$) and $\Delta\phi$ is the phase difference between the two beams. For the kinematical condition, f and ϕ are given by their respective structure factors,

$$F(h,k,l) = \sum_n f_n \sum_{u,v,w} e^{-i\phi_{ann}} \quad (2)$$

where n is the atom type, $f = \sum f_n$, $\phi(h,k,l) = [2\pi(hu + kv + lw)]$, and (h,k,l) are the beam's Miller indices and u, v , and w are the coordinates of the atoms. For the bright field condition the main beam and a diffracted beam interfere and the phase information of the diffracted beam is contained within its interferogram. Whereas in dark field, where any two diffracted beams can interfere, their relative phase difference is contained within the interferogram. The deviation of the fringe spacing shown in Fig. 2 and Fig. 3 is given by the change in spherical aberration, as the beams deviate from the optic axis, which is contained within the contrast transfer function of Equation 1. Further results of experiments and modeling will be presented at the meeting. Applying CBED+EBI to holographic studies of crystals and their internal structures is presented elsewhere [3].

1) R.A. Herring, G. Pozzi, T. Tanji, and A. Tonomura, Ultramicroscopy, Accepted for publication.

2) G. Pozzi, Optik 65 1 (1983) 77.

3) R.A. Herring and T. Tanji, these MSA proceedings.

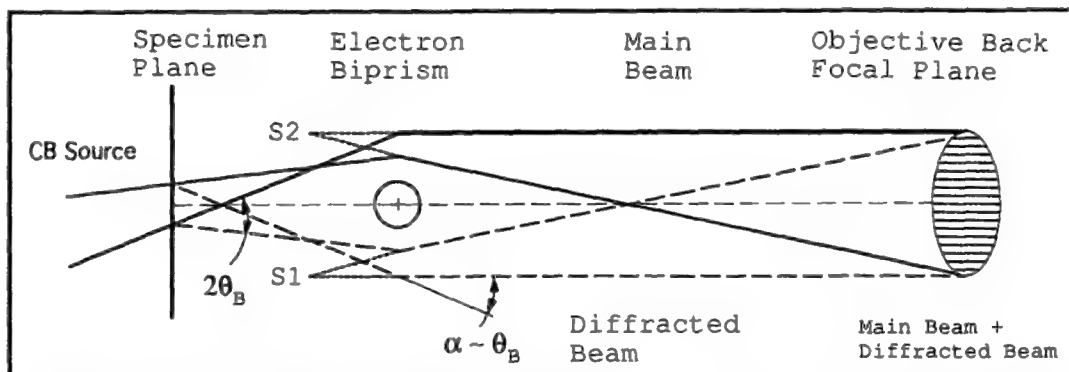


Fig 1 Simplified electron ray diagram, i.e., without the lens system present, showing the CBED+EBI method where the main beam is overlaid by the diffracted beam by use of the electron biprism. See text.

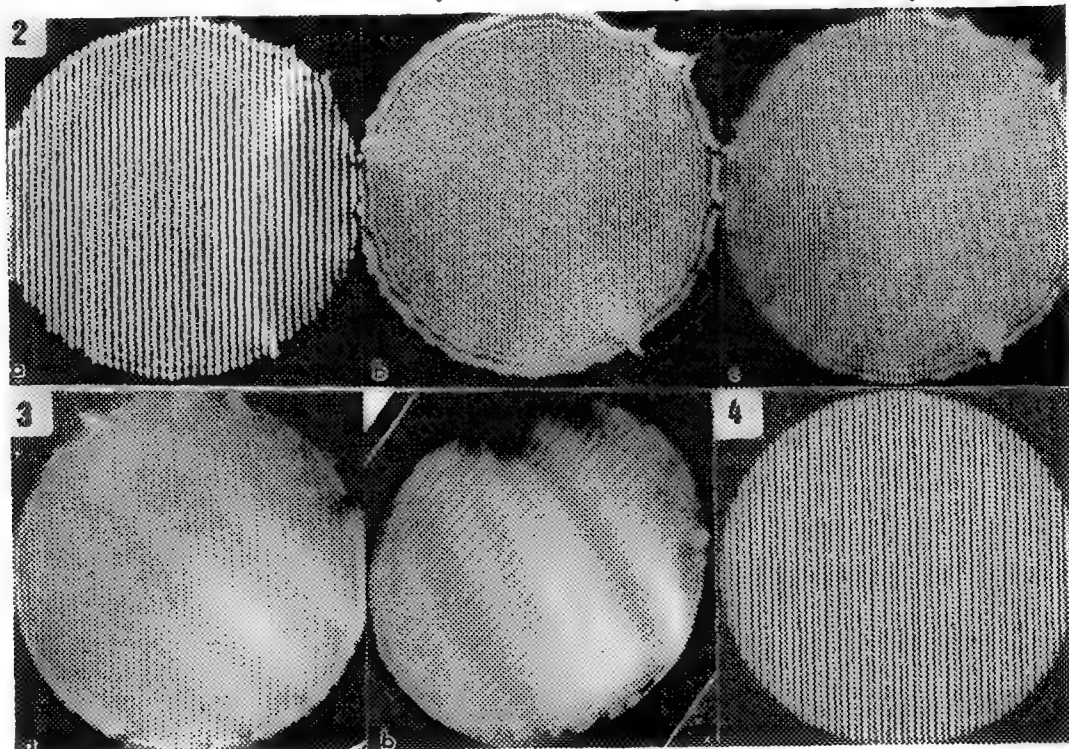


Fig. 2 Interferograms produced from a GaAs crystal showing a) the main beam overlaid by the 111g beam, b) the main beam overlaid by the 222g beam and c) the 111g beam overlaid by the 111g beam. Note that b) and c) were produce simultaneously and that the fringe spacing in b) is not 1/2 of a) and, b) does not equal c).

Fig. 3 Interferograms produced from a GaAs crystal showing a) the main beam overlaid by the 001g beam and b) the 001g beam overlaid by the o11g beam. Note the curvature of the fringes in b).

Fig. 4 Initial simulation results of an interferogram produced by the model presented in the text.

COHERENT ELECTRON NANODIFFRACTION FROM CLEAN SILVER NANO PARTICLES IN A UHV STEM

J. Liu*, M. Pan* and G. E. Spinnler**

* Center for Solid State Science, Arizona State University, Tempe, AZ 85287

** Shell Development Company, Westhollow Research Center, P. O. Box 1380, Houston, TX 77287

Small metal particles have peculiar chemical and physical properties as compared to bulk materials. They are especially important in catalysis since metal particles are common constituents of supported catalysts. The structural characterization of small particles is of primary importance for the understanding of structure-catalytic activity relationships. The shape and size of metal particles larger than approximately 5 nm in diameter can be determined by several imaging techniques.¹ It is difficult, however, to deduce the shape of smaller metal particles. Coherent electron nanodiffraction (CEND) patterns from nano particles contain information about the particle size, shape, structure and defects etc.^{2,3} As part of an on-going program of STEM characterization of supported catalysts we report some preliminary results of CEND study of Ag nano particles, deposited in situ in a UHV STEM instrument, and compare the experimental results with full dynamical simulations in order to extract information about the shape of Ag nano particles.

The experiments were performed in a UHV HB-501S STEM, known by the acronym MIDAS (a Microscope for Imaging, Diffraction and Analysis of Surfaces). The probe size used was approximately 1.5 nm in diameter. Small Ag particles were formed by evaporating Ag, in situ, onto pre-heated thin (< 5 nm in thickness) carbon film. Detailed descriptions of the deposition process and the characterization of these clean Ag particles have been reported elsewhere.⁴ The nanodiffraction patterns were recorded on videotape and played back frame by frame for photographic reproduction and digital analysis.

Fig. 1a shows a CEND pattern from a small Ag particle < 2 nm in diameter. This diffraction pattern shows 10 spots on an inner ring and 10 spots on an outer ring with almost ten-fold symmetry. Fig. 1b shows a simulated CEND pattern of an icosahedral particle (~1.5 nm) with the incident beam along the five-fold axis. The major features of these patterns are similar. It has been found that the intensity distribution of a CEND pattern is very sensitive to the relative beam position and the specific shape and size of the metal particle. Fig. 1c shows another CEND pattern from the same Ag particle but obtained after approximately 2 minutes electron beam irradiation. The ten-fold pseudosymmetry is no longer visible and the particle appears to have reoriented. Fig. 1d is a simulated CEND pattern of the icosahedron with the incident beam along the three-fold axis. The general appearance of Fig. 1c is similar to Fig. 1d although detailed spot arrangements are different due to a variety of factors including the exact beam position and orientation relative to the particle. By comparing these experimental CEND patterns with simulated ones we concluded that this particular Ag particle has an icosahedral shape.

Larger Ag nano particles are stable under electron beam irradiation, thus many nanodiffraction patterns can be obtained from different positions on a small Ag particle and a variety of unique features of CEND patterns from nano-particles can be explored. With a coherent convergent incident beam interference effect will occur which depends on the shape of the particle and the form of the potential field within the area illuminated by the probe.⁵ Therefore the diffraction spots may appear split, sharpened or even distorted depending on the beam position and the particle orientation. For example, Figs. 2a and 2b show CEND patterns from a Ag particle approximately 3 nm in diameter. Figs. 2c and 2d show simulated diffraction patterns of a FCC cuboctahedral particle with the incident beam close to the particle edges along the [011] zone axis. Based on the CEND patterns shown in Fig. 2 and many other experimental and simulated CEND patterns we deduced that the Ag particle giving CEND patterns shown in Fig. 2 has a cuboctahedral shape. Ag particles were also observed with CEND patterns showing evidence for twinning. Other small Ag particles, however, gave patterns that could not be easily explained. Fig. 3 is a CEND pattern from a very small Ag particle, the six outer strong spots represent {220} spots of a FCC structure with the incident beam along the [111] zone axis. The appearance of the six inner spots with fine structures, however, is difficult to understand since they are not {110} type forbidden reflections. Further experiments are in progress to study the particle shape-size relationships. Other unique features of CEND patterns from clean nano metal particles will be discussed.⁶

References

1. M. Jose-Yacaman and M. Avalos-Borja, Catal. Rev.-Sci. Eng. 34 (1992) 55.
2. W. B. Monosmith and J. M. Cowley, Ultramicroscopy 12 (1984) 177.

3. M. Pan et al., *Ultramicroscopy* 30 (1989) 385.
4. J. Liu et al., *Surface Sci.* 262 (1992) L111; *Catal. Lett.* 15 (1992) 133.
5. J. M. Cowley and J. C. H. Spence, *Ultramicroscopy* 6 (1981) 359.
6. This research was supported by Shell Development Company and ASU Industrial Associate Program and made use of the ASU Center for HREM supported by NSF grant DMR-9115680.

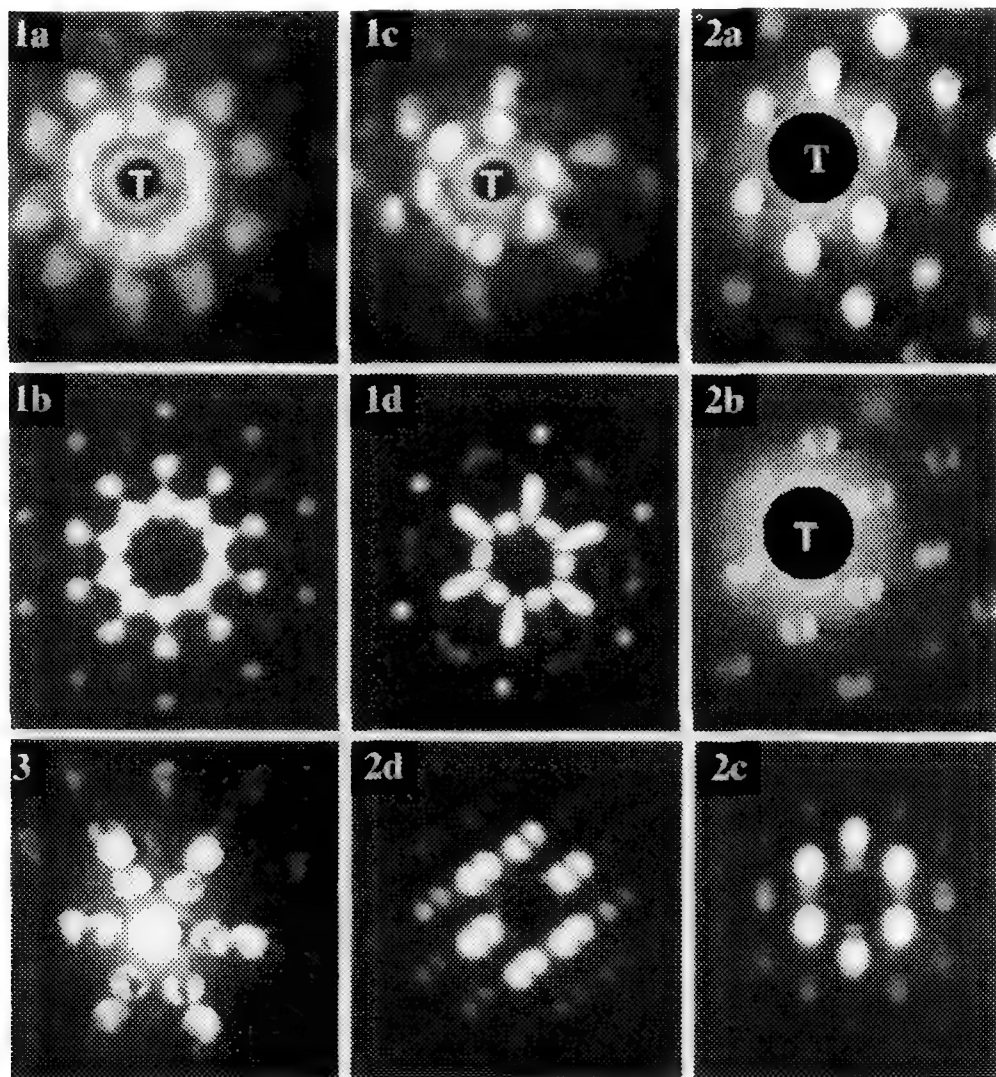


Fig.1--Experimental nanodiffraction patterns (a, c) from small Ag particle and simulated patterns (b, d) of icosahedral metal particle with incident beam along (b) five-fold axis and (d) three-fold axis.

Fig.2--Experimental nanodiffraction patterns (a, b) from 3 nm Ag particle and simulated patterns (c, d) of cuboctahedral metal particle with incident beam along [011] zone axis.

Fig.3--Unusual electron nanodiffraction pattern from clean Ag nano particle.

PERIMENTAL LOW-VOLTAGE-POINT PROJECTION MICROSCOPY

J.C.H. Spence, W. Qian, J. Liu and W. Lo

Department of Physics, Arizona State University, Tempe, Arizona, U.S.A. 85287

The remarkable achievement of atomic resolution by low voltage point projection microscopy¹ has revived interest in this instrument^{2,3}, and, since resolution is approximately equal to virtual source size, demonstrates field-emission from tip regions of atomic dimensions. Ray-tracing calculations⁴ show the aberration coefficients and size of the virtual source to be subnanometer. The brightness of such a nanotip has been measured⁵ to be $7.7 \times 10^{10} \text{ A cm}^{-2} \text{ sr}^{-1}$ (at 100 kV), somewhat greater than conventional cold field emitters or synchrotrons. The images require the theory of transmission LEED for interpretation^{6,7} and are always out of focus by the tip to sample distance⁸ z_1 . Their relationship to HREM images and coherent CBED is discussed elsewhere⁸. The instruments hold promise for imaging small organic molecules (across holey carbon grids), LB and other thin organic films where radiation damage is dominated by inner-shell processes⁹. Our instrument, (figure 1), ultimately intended for reflection holography, has $z_2=12 \text{ cm}$ from sample to detector. Fine Kapton and gold wires, Boron nitride (BN), and titanium (Ti) are used. A Burleigh ARIS UHV inchworm (I.W.) was chosen for its clamping action, maintained by stored charge during imaging when leads are disconnected, with PZT deflection tube (T1), and single crystal [111] tungsten tip (T) either welded to a tungsten heating loop or fitted directly to T1. The crystal axis is aligned with the center of the detector. Unlike STM, reduction of AC magnetic fields and vibration transmitted on tip heating wires are important. The microscope sits on a viton stack, enclosed in a mu-metal cylinder. An inertial stick-slip stage¹⁰ which accepts a 3mm TEM grid (MG) was designed. The kinematic mounting uses three balls (two riding on sapphire rods (SR), one on a plate) to provide one-dimensional coarse motion. Two-dimensional deflection of the tube T1 then allows a three micron by 3 mm strip to be examined. The stage is driven by a 100 volt saw-tooth waveform applied to piezo tube motor T2 exercised in stretching mode against weight W. Differences in static and dynamic friction cause linear motion of the center of mass if the force passes thro the center of friction. The (bakeable) microscope chamber is mounted on a (non-bakeable) pneumatic table. A single stage channel plate and screen are used as detector. Since the sensitivity of these falls rapidly for beam energies below about 100 volts, useful energy filtering is obtained. Figure 2 shows trimer and monomer field-ion images of a [111] tip obtained after heating and neon sputtering on the same instrument, used for brightness measurement. Figure 3 shows images of a baked holey carbon film on a Mo TEM grid, obtained at 100 volts, 1 nA beam current. Here $M=169,000$, so $z_1 = z_2 / M = 710 \text{ nm}$. This large defocus z_1 produces the many Fresnel fringes seen. Width of small hole is 17.7 nm. Tip heating and neon sputtering have been tried for tip formation¹, but best results¹² came using KOH etch, HF^{11} and field evaporation without heating. This simplifies tip support and reduces sensitivity to vibration.

References.

1. H. W. Fink, H. Schmid, H. J. Kreuzer and A. Wierzbicki, Phys. Rev. Letts. (1991) 67, 1543.
2. G. A. Morton and E. G. Ramberg, Phys. Rev. (1939) 56, 705.
3. A. J. Melmed and J. Smit, J. Phys. (1979) E12, 355.
4. W. Qian, M. Scheinfein and J. C. H. Spence, Appl. Phys. Letts. (1993) 62, 315
5. W. Qian, M. Scheinfein and J. C. H. Spence, J. Appl Phys. (1993) in press.
6. H. Kreuzer, K. Nakamura, A. Wierzbicki, H.-J. Fink and H. Schmid, Ultramic. (1992) 45 381.
7. W. Qian, J. Spence and J. M. Zuo, Acta Cryst. A (1992) in press.
8. J. Spence and W. Qian, Phys. Rev. B45 (1992) 10271 also J. Spence, Optik (1992) 92, 57
9. A. Howie, F. J. Ruca and U. Valdre, Phil Mag. (1985) 52, 751.
10. D.W. Pohl, Rev. Sci. Instr. (1986) 58, p. 54
11. L. A. Hockett and S. E. Creager, Rev. Sci. Instr. (1993) 64, 263.
12. We thank A. Melmed for advice on tip formation and M. Scheinfein. Support: NSF:DMR91-12550.

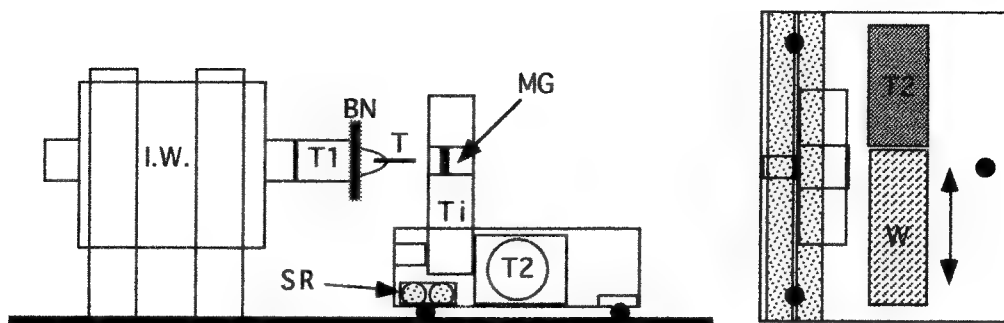


FIG. 1. Point projection microscope. Stage moves normal to page. Top view of stage at right.

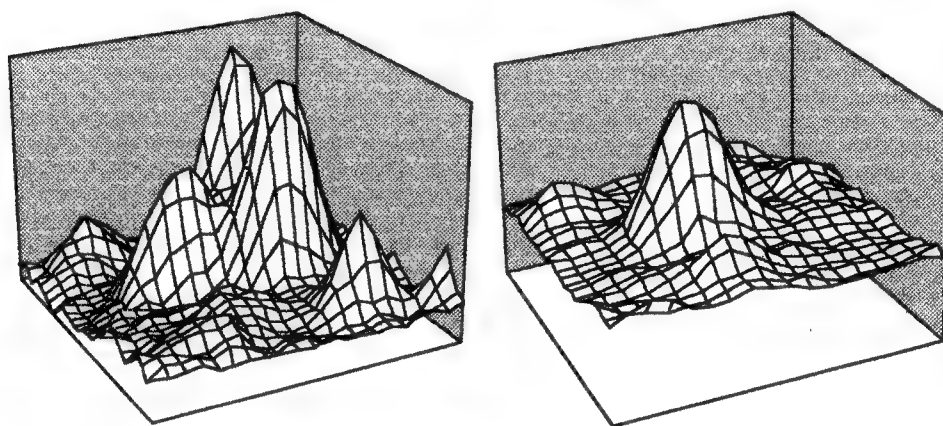


FIG. 2 Field-ion image of atomic trimer (left) and monomer (right) on W [111] after sputtering.

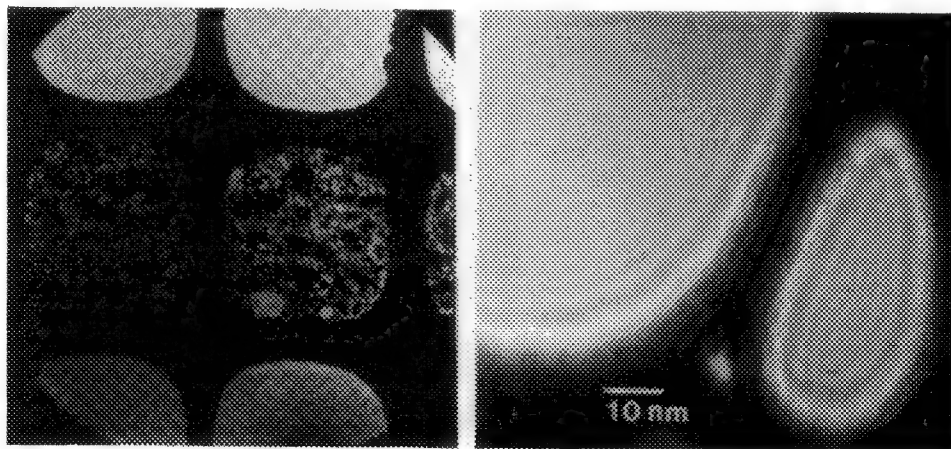


FIG. 3 Left: Low mag. carbon grid imaged at 200 volts, 2 nA. Right: High mag. Fresnel fringes.

SIGNAL TRANSFER EFFICIENCY OF SLOW-SCAN CCD CAMERAS

W.J. de Ruijter, P.E. Mooney and O.L. Krivanek

Gatan Research and Development, 6678 Owens Drive, Pleasanton, CA 94588, USA

Slow-scan CCD cameras are helping transmission electron microscopy and electron holography become increasingly quantitative. Accurate characterization of the performance of the cameras can extend this trend by making it possible to extract weak signals from noisy images with optimal precision. The property to be characterized is the performance of the camera in transferring a particular spatial frequency contained in the input electron image to the output image captured by a computer, as a function of the input intensity. Using the concepts and notation of standard signal processing theory¹, we characterize this performance by introducing *signal transfer efficiency* (STE) defined as:

$$STE(\mathbf{k}) = \frac{SNR_{out}(\mathbf{k})}{SNR_{in}(\mathbf{k})}, \quad (1)$$

where $SNR_{in}(\mathbf{k})$ and $SNR_{out}(\mathbf{k})$ are signal-to-noise ratios at the input and the output of the image detector as a function of spatial frequency \mathbf{k} . Signal-to-noise ratio is defined as $SNR(\mathbf{k}) = S_{II}(\mathbf{k})/S_{nn}(\mathbf{k})$, where $S_{II}(\mathbf{k})$ and $S_{nn}(\mathbf{k})$ denote the power spectra of the signal and the noise. STE could be regarded as an extension of the use of detection quantum efficiency as a figure of merit for electron image detectors.²

Operation of the slow-scan CCD camera is illustrated in Fig.1: primary electrons are converted into photons which in turn are detected by a charge coupled device (CCD). We will derive the signal transfer efficiency of slow-scan CCD cameras using the schematic representation given in Fig.2, in which I_i is the image at the input, n_1 is the shot-noise contained in I_i , n_2 and n_3 describe the noise introduced by the camera, Γ is the camera's modulation transfer function and I_o is the captured image.

The power spectrum of the input image I_i is given by $S_{I_i I_i}(\mathbf{k}) = P(\mathbf{k})N_e^2$, where N_e denotes the mean number of electrons per pixel and $P(\mathbf{k})$ represents the normalized power spectrum of I_i . The noise in every pixel is governed by Poisson statistics and since contrast in electron images is in general low (5-10%) it follows that the noise at the input n_1 is stationary and white with variance $\text{var}(n_1) = N_e$. The power spectrum of the noise at the input is given by $S_{n_1 n_1}(\mathbf{k}) = N_e / MN$, where M and N are the number of pixels in the x and the y directions of the image region under study. The input signal-to-noise ratio is then given by:

$$SNR_{in}(\mathbf{k}) = MN P(\mathbf{k})N_e. \quad (2)$$

The noise n_2 is due to variations in path length of incident electrons through the scintillator material (which includes back scattered electrons) and to granularity of the scintillator. We assume n_2 white with variance $\text{var}(n_2) = FN_e$.³ The noise n_3 is due to the combined effects of spread in CCD well-electron generation and electronic readout noise. It is reasonable to assume $\text{var}(n_3) = N_e G^{-1} + R$, where G is the average number of CCD well-electrons generated per primary electron incident on the scintillator, and R is the variance of the electronic readout noise expressed in primary electrons equivalent. The noise due to the spread in CCD well-electron generation should be white, and furthermore, we determined from Fourier analysis of dark images, recorded with no electrons incident onto the scintillator, that the electronic readout noise is also white. It follows from Fig.2 that the power spectrum of the signal at the output can be written as $S_{I_o I_o}(\mathbf{g}) = P(\mathbf{g})\Gamma^2(\mathbf{g})N_e^2$. The power spectrum of the noise at the output is determined by the combined effects of the mutually independent white noise contributions n_1 , n_2 and n_3 and is $S_{n_o n_o}(\mathbf{k}) = [(1+F)N_e\Gamma^2(\mathbf{k}) + N_e G^{-1} + R]/MN$. The signal-to-noise ratio at the output is therefore:

$$SNR_{out}(\mathbf{k}) = \frac{MN P(\mathbf{k})\Gamma^2(\mathbf{k})N_e^2}{(1+F)N_e\Gamma^2(\mathbf{k}) + N_e G^{-1} + R}. \quad (3)$$

Division of (3) by (2) gives the signal transfer efficiency:

$$STE(k) = \left[1 + F + \frac{1}{\Gamma^2(k)} \left(\frac{1}{G} + \frac{R}{N_e} \right) \right]^{-1}. \quad (4)$$

Fig.3 presents surface plots of the *STE* for Gatan 679 and 694 cameras equipped YAG and P43 scintillators as function of spatial frequency k and electron dose N_e . Approximate parameter values are $F=0.25$, $G=60$, $R=0.2$ for YAG and $F=0.5$, $G=300$, $R=0.04$ for P43. Experimental measurements show that $\Gamma(k) = \exp[-4|k|]$, with $0 \leq k \leq 0.5$, is a reasonable approximation for the modulation transfer function of both YAG and P43 scintillators.⁴ The *STE* drops with decreasing electron dose due to detector noise caused by the electronic readout process (R/N_e term). At high spatial frequencies *STE* is reduced because of signal attenuation by the modulation transfer function which allows readout noise and photon shot-noise ($1/G$ term) to become a factor. The maximum attainable *STE* for high electron dose is mainly determined by electron path length variations in the scintillator (F term), and is smaller for a P43 scintillator due to its granularity. The maximum attainable *STE* for P43 scintillators is, in contrast to YAG scintillators, frequency independent because of the (5 times) higher electron-photon transfer efficiency. For YAG scintillators, the maximum achievable *STE* decreases for high frequencies due to photon shot-noise. An important consequence of this analysis is that the modulation transfer function can typically be restored to unity for all frequencies. If the electron dose exceeds 10-100 e/px, this can be accomplished without significant effects on the signal-to-noise ratio for high frequencies.⁵

References

1. M.B. Priestley, Spectral Analysis and Time Series (Academic Press, 1981).
2. K.-H. Herrmann and D. Krah, J. Micros. 127 (1982) 17.
3. U. Fano, Phys. Rev., 72 (1947) 26.
4. W.J. de Ruijter and J.K. Weiss, Rev. Sci. Instrum. 63 (1992) 4314.
5. P.E. Mooney, W.J. de Ruijter and O.L. Krivanek, these proceedings.

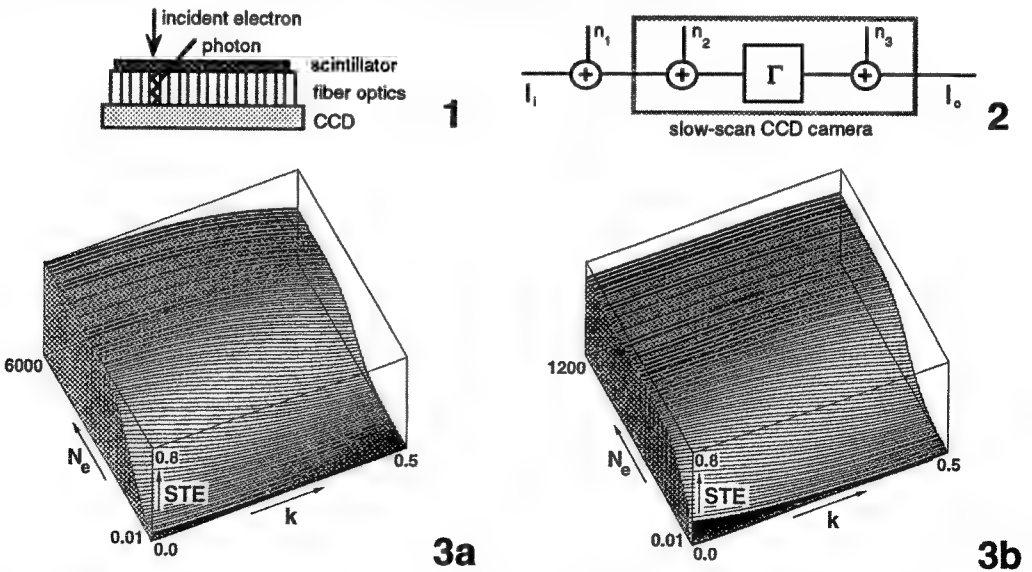


FIG. 1.--The image conversion chain in slow-scan CCD cameras suitable for electron detection.
 FIG. 2.--Diagram showing transfer functions and noise sources for slow-scan CCD cameras.
 FIG. 3.--Surface plots of *STE* as function of spatial frequency and the logarithm of the electron dose for Gatan slow-scan CCD cameras with (a) YAG and (b) P43 scintillators. Electron energy 120 kV.

ON-LINE RECONSTRUCTION OF ELECTRON HOLOGRAMS

W.D. Rau

Inst. f. Ang. Physik der Universität Tübingen, Auf der Morgenstelle 12, D-7400 Tübingen, GER.

Electron-off-axis holography has proven to be a most promising tool for the collection of the complete information about amplitude and phase modulation of the complex electron image wave $b(\vec{r}) = A(\vec{r})e^{i\phi(\vec{r})}$ in one single micrograph. Then amplitude and phase can be reconstructed numerically, offering almost any wave-optical possibility for the evaluation of the electron object wave at the exit surface, including the elimination of the influence of coherent aberrations of the objective lens in the image wave.¹ Bottle-neck of the whole two step – registration and reconstruction – procedure has long been the need for highly accurate conversion of the holograms to numerical data as well as the available computational power, since the necessary Fast Fourier Transforms are time consuming numerical operations. Modern CCD slow-scan detectors and the permanently increasing computing power speed up this process and, combined with state of the art FEG microscopy, supply the reconstructed amplitude and phase of the image wave to the microscopist on-line.^{2,3}

The impact of the microscope aberrations on the object wave $o(\vec{r}) = a(\vec{r})e^{i\phi(\vec{r})}$ is described in the back focal plane of the objective lens as a multiplication of the object spectrum $O(\vec{q})$ with a complex phase plate $\exp(-i\chi(\vec{q}))$, where the wave aberration $\chi(\vec{q})$ includes spherical aberration, astigmatism and defocus. A correction is therefore performed by numerical division of the reconstructed complex spectrum of the image wave by an appropriate phase plate in Fourier space. Fig.1 shows a correction at the example of a hologram of amorphous carbon foil that was taken at a Philips EM420 at 100 keV by means of a CCD detector, which – based on a Photometrics camera with a Thompson THX 31156 chip – was developed and tested in Tübingen.² The whole reconstruction procedure with a VME-bus system of TIETZ GmbH (Munich, Ger.) consisting of a 68030 CPU and an array processor (40 MFlop) for the Fast Fourier Transforms takes about 20 seconds. First, the distortion visible in the reconstructed phase has to be corrected by complex division with the reconstruction of an empty reference hologram (fig.1b). Second, the astigmatism has to be eliminated (fig.1c). Finally spherical aberration and defocus are corrected with the phase plate shown in fig.1d. After correction almost all information on the object wave is found in the phase as expected for a weak phase object at an ideal imaging process.

The precision of correction is strongly influenced by the properties of the chosen image detector. The number of resolved pixels, determining the field of view in real- and Fourier space, give an upper limit for the maximal correctable spatial frequencies.⁴ Furthermore, the asymmetric influence of the Modulation Transfer Function on the reconstructed wave can lead to an undesirable crosstalk between amplitude and phase. Additionally, a high linearity over the full dynamic range is indispensable. In the end, a high sensitivity combined with low noise figures are important for the efficiency of the correction algorithms. Our new detector system used at a CM30 FEG microscope consists of a dual speed (2MHz/150kHz) CCD camera (TEK 1024) of Photometrics Ltd with $1024 \times 1024 \times 24 \mu\text{m}$ pixels fibre-optically coupled to a thin (1.5 mg/cm^2) P20 scintillator.

The contrast transfer at the pixel to pixel Nyquist frequency is 10 %. With this resolution and pixel number a correction up to 0.17 nm is in reach. Further use of the CM30 FEG information limit of less than 0.1 nm can be obtained only with a CCD chip consisting of 2048² pixels.⁵

References

- 1. Q. Fu et al., Phys. Rev. Lett. (1991) Vol.67 No.2 p.2319
- 2. I. Daberkow et al., Ultramicroscopy (1991) Vol.38 p.215
- 3. W.D. Rau et al., J. Comp. Ass. Micr. (1991) Vol.3 No.2 p.51
- 4. H. Lichte, Parameters for high resolution holography, Ultramicroscopy, in press
- 5. This work was supported by the Körber Stiftung, Hamburg, the Volkswagenstiftung and the European Community (BRITE/EURAM).

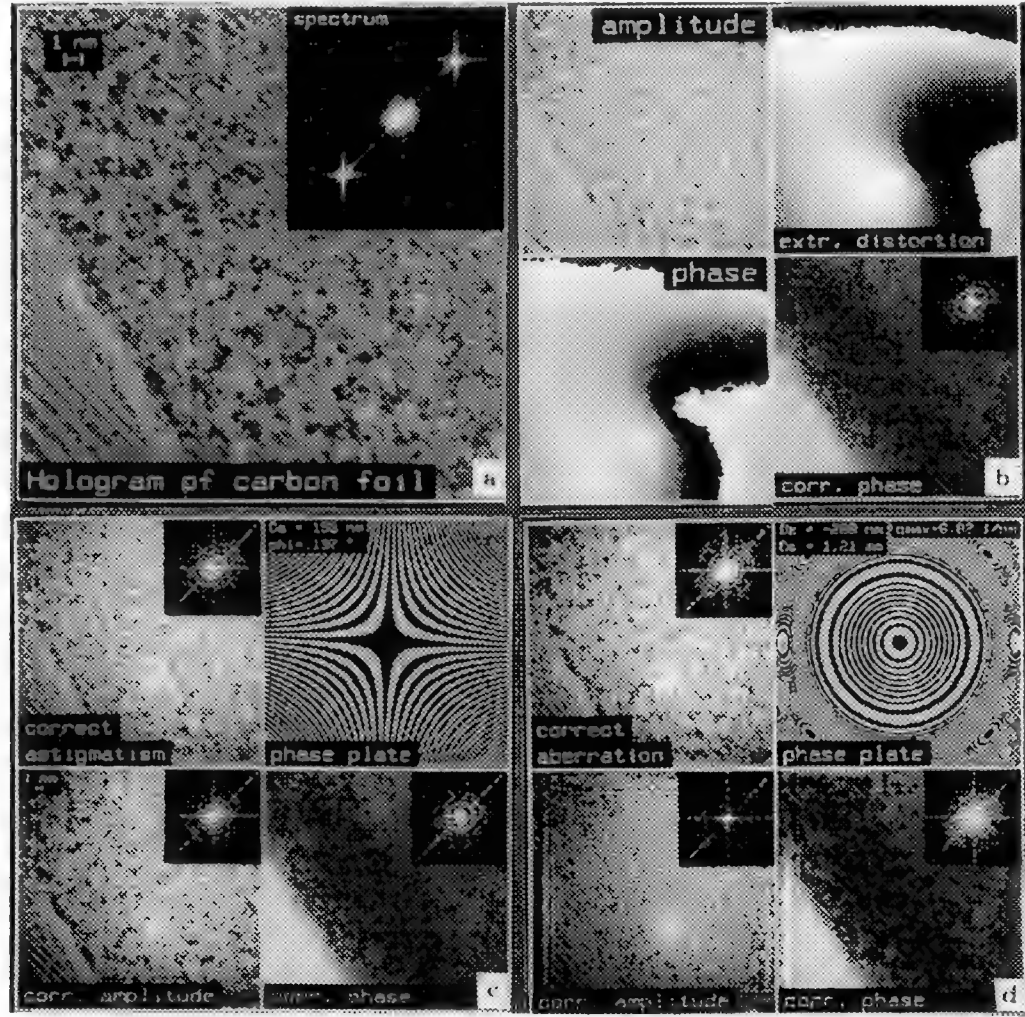


Fig.1 Correction of distortion (b), astigmatism (c), spherical aberration and defocus (d) at the example of a thin amorphous carbon foil (a).

DIGITAL PROCESSING OF HIGH-RESOLUTION ELECTRON HOLOGRAMS

E. Völkl and L. F. Allard

High Temperature Materials Laboratory, Oak Ridge National Laboratory, Oak Ridge, TN 37831

Electron Holography has been shown to be an useful tool in high resolution imaging for obtaining more information from the electron image than is possible in conventional microscopy.¹ In our laboratory we presently record our images on photographic material, and then digitize them by using a 4096 pixel line scan by EKTRON. Digitizing photographic material and correcting for its nonlinearities is a time consuming process which will soon be alleviated by the installation of the GATAN retractable slow-scan CCD-camera. Both camera and microscope will be operated from a Macintosh computer using the software "Digital Micrograph®" and "Advanced Acquisition®", the first of which is used already for image processing of our negatives.

From an electron hologram, e.g. an hologram of a PMN ferroelectric material (FIG. 1a), the diffraction pattern of the object (FIG. 1b) can be obtained and evaluated from areas as small as one unit cell.² It is thus possible to align any small area of the specimen, e.g. an area directly at an interface, at the microscope, without changing the illumination or going to diffraction mode, by evaluating the ratio of the intensities I_1 and I_2 of opposite diffracted beams. The change of the ratio I_1/I_2 depends primarily on the parameters tilt and thickness of the specimen from the point of view of kinematic diffraction theory. Investigating the dependence of the ratio of I_1/I_2 as a function of the crystal tilt, it should be possible to retrieve the thickness of the investigated area, i.e. its morphology, thus increasing the reliability of matching simulated images with the experimental images.

Working with small image areas, i.e. with small pixel numbers, yields a seemingly decreased resolution in Fourier space, as diffracted beams fall between pixels or are very close together. Further-more, using round apertures in Fourier space with small pixel numbers, causes artefacts. This may be overcome by the following definition of an alternative Fourier transform aFT and its inverse aFT⁻¹ of a (1 dim.) pixel line P_m , with $m = 1, 2, \dots, M$; $k = 1, 2, \dots, K$; and $K := t \cdot M$, (extendable to 2 dim.):

$$P_k := \text{aFT}\{P_m\} := 1/\sqrt{K} \sum_{m=1}^M P_m \exp(-2\pi i \cdot (k-1) \cdot (m-1)/K) \quad \text{and}$$

$$P_m := \text{aFT}^{-1}\{P_k\} := 1/\sqrt{K} \sum_{k=1}^K P_k \exp(2\pi i \cdot (k-1) \cdot (m-1)/K) \quad \text{as its inverse.}$$

FIG 2. shows a comparison of a discrete ($M = 32$) and continuous cos-function confined to an interval, while FIG 3. shows the spectra, i.e. the absolute value of their Fourier transforms - conventional and alternative.³ For $t = 8$, the alternative Fourier transform yields a larger, in terms of pixels, discrete spectrum which is much closer to the spectrum of the continuous Fourier transform.⁴

References

1. H. Lichte, Ultramicroscopy, **20**, 293 (1986)
2. E. Völkl, H. Lichte, Optik Supplement 4 (Vol. 88) 1991
3. Mathematica 2.1, Wolfram Research, Inc. Champaign, Illinois, 1992
4. Research sponsored by the Directed R&D Program of Oak Ridge National Laboratory, managed for the DOE by Martin Marietta Energy Systems, Inc. under contract DE-AC05-84OR21400.

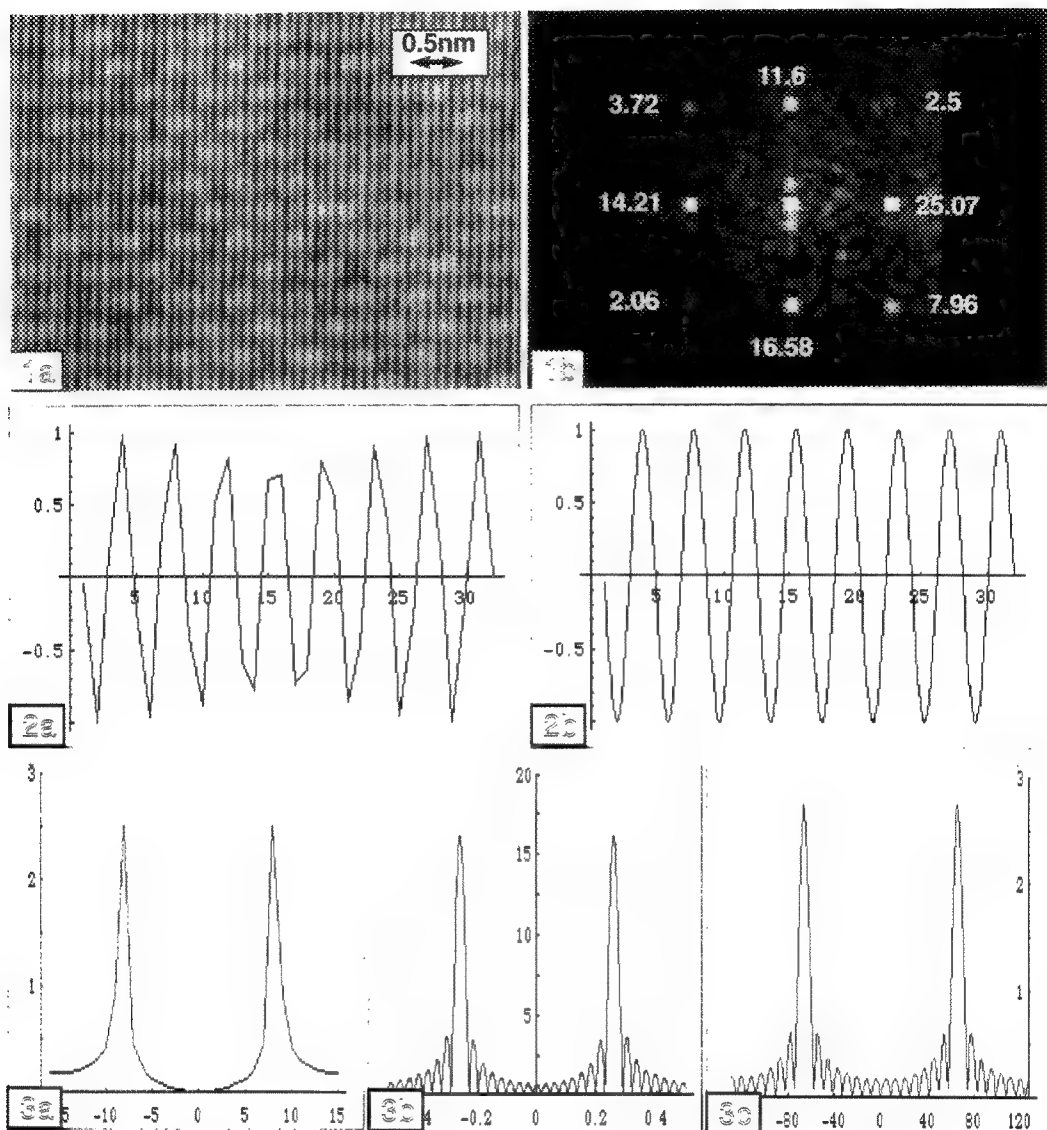


FIG. 1a -- Small part of a hologram of PMN ferroelectric material in $\langle 100 \rangle$ direction. FIG. 1b -- The diffraction pattern as obtained from FIG. 1a shows clearly the misalignment of this area. The tilt direction is towards to the lower right corner. Diffracted beam intensities are inset.

FIG. 2a -- Cos- function sampled at $M = 32$ and a sampling rate of 3.88. It is not straightforward to realize that this is a plane cos pattern. FIG. 2b -- In comparison, the continuous cos- function.

FIG. 3a -- Spectrum of the discrete set as in FIG. 2a. FIG. 3b -- Spectrum of the continuous function as in FIG. 2b. FIG. 3c -- The alternative spectrum of the discrete set as in FIG. 2a is close to FIG.3b.

DIRECT STRUCTURE INFORMATION USING THE FOCUS-VARIATION METHOD

D. Van Dyck, M. Op de Beeck

University of Antwerp (RUCA), Groenenborgerlaan 171, B-2020 Antwerpen, Belgium

1. Introduction

In [1], a new method was proposed to reconstruct the exit wavefunction of an object from a combination of images at closely spaced focus values. Recently, in the framework of a Brite-Euram project, the method has been implemented on a Philips CM20 ST electron microscope equipment with Field emission source and CCD camera. The first experimental results for the high TC superconductor $\text{YBa}_2\text{Cu}_4\text{O}_8$ are presented in [2,3]. In this case, the object is very thin so that the phase of the wavefunction directly reveals the projected potential of the atom columns. The oxygen columns could be observed with a resolution of 0.13 nm. However, when the object is thicker, the one-to-one correspondence between the wavefunction and the projected structure is not so straightforward due to the dynamical diffraction. This is shown in Figure 1 for $\text{Ba}_2\text{NaNb}_5\text{O}_{15}$ where the heavy columns are revealed in the amplitude and the bright columns in the phase. Hence, there is an urgent need for a theory which enables to reverse in a sense the dynamical scattering, i.e. to retrieve the object potential from the exit wavefunction. A solution to this problem can only be expected in case the object is a crystal viewed along a zone axis. A number of ideas have been proposed in [4] all based on reversing the dynamical equations in an iterative way. However, due to the large number of beams involved, these method only converge for moderate crystal thicknesses and are very sensitive to noise. A workable inverse method should be much more robust and stable. Recently we proposed a simple real space channelling theory which has these advantages [5]. The basic idea is the following. The wavefunction in the crystal is governed by the high energy equation

$$-i 4\pi \frac{\hbar^2 k}{2m} \frac{\partial \psi(\mathbf{R}, z)}{\partial z} = \mathcal{H} \psi(\mathbf{R}, z) \quad (1)$$

where

$$\mathcal{H} \phi_n(\mathbf{R}) = E_n \phi_n(\mathbf{R}) = \left[\frac{\hbar^2}{2m} \Delta - e U(\mathbf{R}) \right] \phi_n(\mathbf{R}) \quad (2)$$

The solution of (1) can be expanded in eigenfunctions of the Hamiltonian

$$\psi(\mathbf{R}, z) = \sum_n C_n \phi_n(\mathbf{R}) \exp \left[-i\pi \frac{E_n}{E_0} kz \right] \quad (3)$$

with

$$E_0 = \frac{\hbar^2 k^2}{2m} \quad (4)$$

the incident electron energy. k is the electron wavevector. For $E_n < 0$ the states are bound to the columns. Taking account of the boundary conditions at the entrance plane we can rewrite (3) as

$$\psi(\mathbf{R}, z) = 1 + i\pi \frac{eU(\mathbf{R})}{E_0} kz + \sum_n C_n \phi_n(\mathbf{R}) \left[\exp \left[-i\pi \frac{E_n}{E_0} kz \right] - 1 + i\pi \frac{E_n}{E_0} kz \right] \quad (5)$$

The first two terms yield the well-known weak phase approximation. In the third term only these states will appear in the summation for which

$$|E_n| \geq \frac{E_0}{kz} \quad (6)$$

For an isolated column and an incident energy which is not too high, only one state obeys (6). If for all other states the energies are assumed sufficiently small, (5) can be approximated as

$$\psi(\mathbf{R}, z) = 1 + \left[\exp \left[-i\pi \frac{E}{E_0} kz \right] - 1 \right] \phi(\mathbf{R}) \quad (7)$$

This result holds for each isolated column. In a sense, the whole wavefunction is uniquely determined by the eigenstate $\phi(\mathbf{R})$ and its energy E which are both functions of the "density" of the column and the crystal thickness z .

Suppose all atom potentials would be exactly proportional to the atomic number Z one could expect that the eigenstate $\phi(\mathbf{r})$ and its energy E could scale with $\frac{Z}{d}$ with Z the atomic number of the atom and d the repeat distance of the column. In this way, the wavefunction could be completely parametrised in terms of $\frac{Z}{d}$ and z . Even if eq. (7) would only be qualitatively correct, this would allow to determine the position of each column very accurately and the "weight" of the column and the crystal thickness approximately. Figure 2 shows the bound state scaled with $Z^{1/2}$ for all atoms of the periodic table (calculated using Smith & Burge parameters). Figure 3 shows that E roughly scales with $\frac{Z}{d}$. From this it is clear that the proposed scaling is correct to some extent and that in principle the direct structure retrieval should be possible.

1. D. Van Dyck, M. Op de Beeck, *Proc. XIIth Int. Congress on Electron Microscopy*, Seattle, San Francisco Press (1990), p. 26-27.
2. M. Op de Beeck, W. Coene, D. Van Dyck, in preparation.
3. W. Coene, G. Janssen, M. Op de Beeck D. Van Dyck, *Phys. Rev. Lett.* (1992), Vol. 29, nr. 26, p. 3743.
4. D. Van Dyck, in *Advances in Electronics and Electron Physics*, ed. P. Hawkes, Academic Press (1985), p. 295-355.
5. D. Van Dyck, M. Op de Beeck, W. Coene, *Optik* (1993).

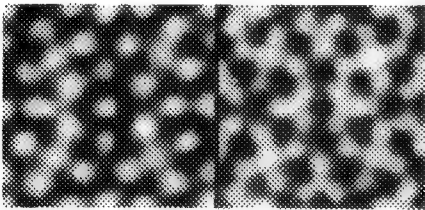


Fig.1.-- Experimentally retrieved amplitude (left) and phase (right) for $\text{Ba}_2\text{NaNb}_5\text{O}_{15}$.

Fig.2.-- Scaled eigenfunctions for different Z .

Fig.3.-- Energy of the bound state vs. Z/d .

Fig. 1.

Fig.2

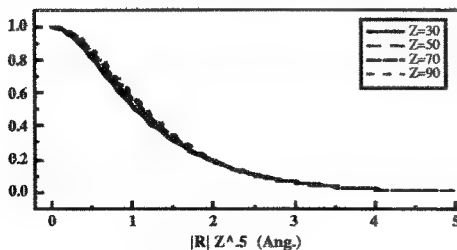
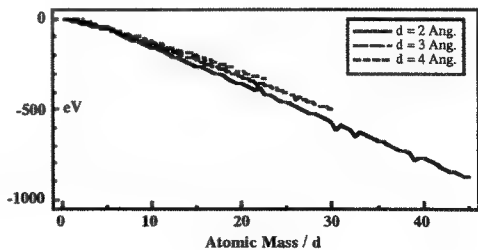


Fig. 3



FOCUS-VARIATION IMAGE RECONSTRUCTION IN FIELD-EMISSION TEM

W.M.J. Coene⁽¹⁾, A.J.E.M. Janssen⁽¹⁾, M. Op de Beeck⁽²⁾, D. Van Dyck⁽²⁾,
E.J. Van Zwet⁽³⁾, H.W. Zandbergen⁽³⁾

(1) Philips Research Laboratories, PO Box 80000, 5600 JA Eindhoven, The Netherlands

(2) University of Antwerp (R.U.C.A.), Belgium

(3) National Center for HREM, Delft University of Technology, The Netherlands

The use of a field emission gun (FEG) in high resolution TEM (HRTEM) improves the information limit much below the point resolution. This is due to the FEG's high brightness and low energy spread which yield a very good coherence. In the area between point and information resolution of the FEG-TEM, image interpretation is complicated by the lens aberrations and focus effects, which cause scrambling of the information from the specimen. This problem is solved by 'holographic' techniques, which retrieve aberration-corrected amplitude and phase information of the electron wave ϕ at the exit plane of the specimen. We follow the route of 'in-column' or 'non-linear' holography by digital processing of a focal series of HRTEM images [1].

Different reconstruction algorithms can be used for that purpose depending on the assumptions that are made in the HRTEM imaging model. We have devised two workable algorithms. A first method, called the "paraboloid method" (PAM), aims at filtering out recursively the nonlinear contributions in the images, so that high-speed linear reconstruction can be applied [2]. Secondly, we have developed a new variant of the Kirkland reconstruction scheme [3] within a "maximum-likelihood" (MAL) framework. In MAL, the electron wave ϕ at the object's exit plane (object wave) is matched to the measured intensities in the HRTEM images by minimizing a least-squares functional, using the steepest descent approach. This leads to a twofold iteration cycle in which (1) images are simulated for the current estimate of the object wave ϕ , and (2) the image difference with respect to the experimental image is fed back into a new update of the object wave. Our MAL algorithm is further tailored to the coherence properties of the FEG as follows: the very high brightness of the FEG implies very good spatial coherence so that the spatial coherence envelope in the transmission-cross-coefficient (TCC) can be satisfactorily factorized. For temporal coherence, the focal averaging over the chromatic focal spread is built in explicitly [1], e.g. the estimated image intensity results then from the integration of several partial image intensities at slightly different focus settings. We can then benefit from fast Fourier transforms, hereby avoiding time-consuming weighted correlations in frequency space with the TCC, for the propagation between specimen and image plane. The first guess for ϕ in the MAL iteration procedure is either the PAM solution or a constant 'dc' level, compatible with the mean image intensity. Two actions are further undertaken for the positional alignment of the images in the focal series. Prior to the reconstruction, a pre-alignment is carried out, based on simple cross-correlation of successive images in the series, and this without compensation for contrast changes or reversals due to the variation of focus in the series. For each iteration step during the reconstruction, a positional match of experimental and estimated images is performed with sub-pixel accuracy. We further improved the computational performance of MAL considerably by introduction of some intrinsic parallelism: MAL reconstruction for 20 images of 512² pixels and with 20 iterations requires +/- 15 CPU minutes on an IBM/RS6000 computer.

Recent results of image reconstruction on Philips FEG-TEMs are shown in figs. 1 and 2. Fig. 1 shows the reconstructed phase for $\text{YBa}_2\text{Cu}_4\text{O}_8$ [100] orientation at 200 kV, in which all atoms can be directly identified. Even the oxygen atoms in the O-Y-O stacks (O-Y distance = 0.14 nm) are observed as faint white dots close to the larger white dots representing the yttriums. Fig. 2 shows the reconstructed amplitude for Si [110] at 300 kV. The individual atoms in the Si dumbbells, only 0.136 nm separated from each other, are clearly resolved.

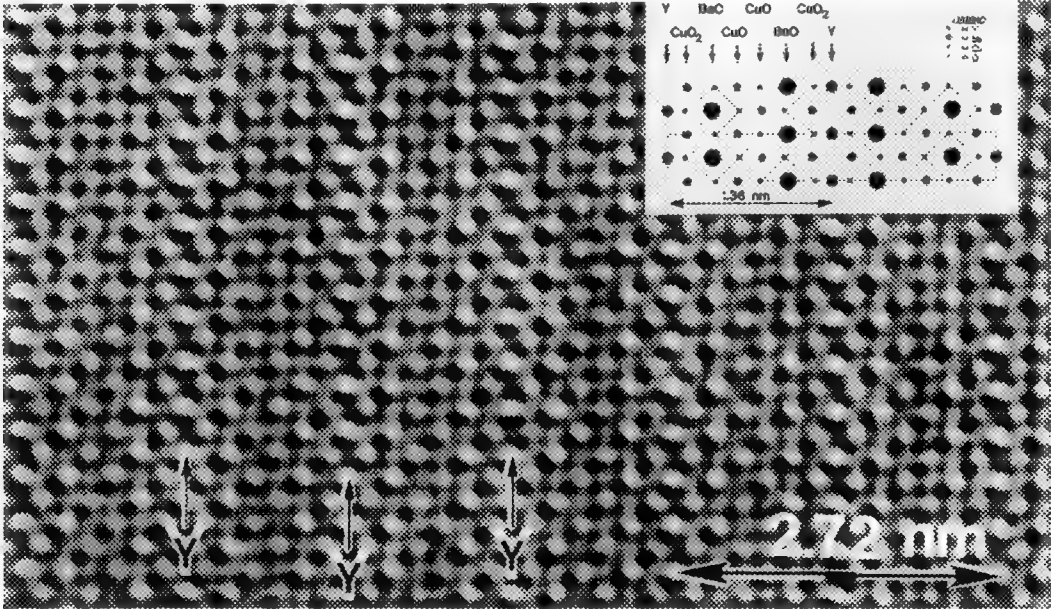


Fig. 1. Reconstructed phase from [100] - oriented $\text{YBa}_2\text{Cu}_4\text{O}_8$ (CM20-FEG; 200 kV).

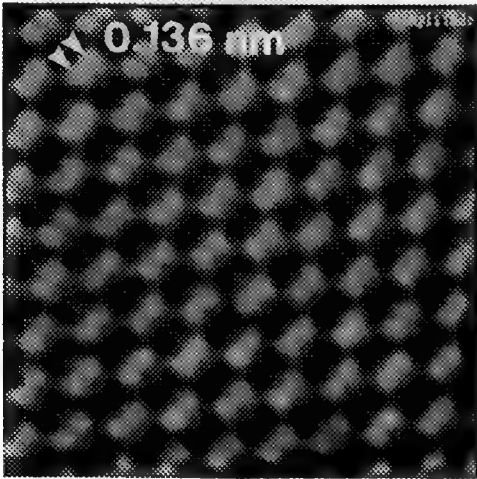


Fig. 2. Reconstructed amplitude from [110] - oriented Si (CM30-FEG; 300 kV).

References

[1] W.M.J. Coene, A.J.E.M. Janssen, M. Op de Beeck, D. Van Dyck, Phys. Rev. Lett. (1992) **69**, p. 3743-3746.
 [2] M. Op de Beeck, D. Van Dyck, W.M.J. Coene, Ultramicroscopy (1993), submitted.
 [3] E.J. Kirkland, Ultramicroscopy (1984) **15**, p. 151-172.

HIGH-RESOLUTION IMAGING WITH THE SCHOTTKY EMITTER FEG TEM

Max T. Otten

Philips Electron Optics, Applications Laboratory, Building AAE, 5600 MD Eindhoven, The Netherlands

The Philips CM-series Field Emission TEMs, equipped with the Schottky field emitter and operating at 200 kV (CM20 FEG and the newer CM200 FEG) and 300 kV (CM30 FEG) have a dramatically improved performance in HRTEM imaging relative to their LaB₆ equivalents (Table 1). The spatial and temporal coherence of these microscopes far exceeds that of similar microscopes equipped with LaB₆ filaments. As a result, the information in the HRTEM images proceeds well beyond the point resolution (the information limit for the 200 kV microscopes typically lies around 0.6x their point resolution) (Fig. 1).

The information limit is determined by brightness (controlling the illumination semi-angle α and thus the spatial coherence) and the energy spread (controlling the temporal coherence). These two factors are inversely related — if one goes up, the other goes down. The energy spread under HRTEM conditions is ~ 0.8 eV, a value that is not inherent to the Schottky emitter but is due to the total system including the emitter and high-tension tank and accelerator. The spatial coherence is more difficult to determine but from a measured brightness of the order of $4\text{--}8 \times 10^8$ A cm⁻²srad⁻¹ and results on the CM20 FEG-TWIN (point resolution 0.27 nm, information limit around 0.17 nm) values between 0.05 and 0.2 mrad for the illumination semi-angle α appear reasonable.

Accurately measuring the performance of these instruments poses a serious problem due to the absence of suitable test specimens. Ideally the specimen should be amorphous, scatter well beyond 0.2 nm, be easily and reproducibly made and should not degrade with time. In practice, we have been unable to find such a specimen. The amorphous carbon previously used¹ has proved to be too thick and scatter too weakly at small spacings. Amorphous germanium performs better on both counts but typically is still limited to 0.17–0.15 nm in information transfer (Fig. 1). It is also quite unstable and tends to degrade over time, resulting in a worsening of the information transfer. Ultra-thin, amorphous tungsten appears to show information transfer down to very small spacings (Fig. 2), but is not easy to produce and is rather fragile. Crystalline specimens cannot be used because the intensity of the diffracted beams depends too much on orientation and thickness.

Several aspects of HRTEM imaging were seen that were or could not be observed with LaB₆ microscopes. Apart from the difficulty of correcting astigmatism, focussing and coma-free alignment², these concern specimen stability and orientation. The orientation proves to be more critical on FEG TEMs than on LaB₆ microscopes, due to the sensitivity of the high-order beams, whose reflections lie well off the Ewald sphere.

In search of the limits on HRTEM imaging we have found that the quality and stability of the specimen play a major role. The detectability of small metal particles (catalysts), for example, does not depend on the background of the substrate but on the stability of the particles in the beam. Particle size and the rate of structural rearrangement show a clear relation. Whereas larger particles (above 3 to 5 nm) are reasonably stable and do not change much over several minutes, very small particles (1 nm or smaller) reconstruct at such a rapid rate that they are often invisible in the HRTEM image as recorded on negative (Fig. 3) or SSC camera. Only on a TV-rate camera is it possible to see these particles and to follow the structural rearrangements.

References

1. M.T. Otten, *Mat. Res. Symp. Proc.* (1989) 139, 251.
2. M.T. Otten and W.M.J. Coene, *Ultramicroscopy* (1993) 48, 77.

TABLE 1. Point resolution and estimated information limits of the CM series FEG TEMs.

Voltage Objective lens	200 kV			300 kV	
	UltraTWIN	SuperTWIN	TWIN	SuperTWIN	TWIN
Point resolution	0.19 nm	0.24 nm	0.27 nm	0.20 nm	0.23 nm
Information limit LaB ₆	0.17 nm	0.21 nm	0.25 nm	0.18 nm	0.21 nm
Information limit FEG	0.12 nm	0.15 nm	0.17 nm	0.11 nm	0.14 nm

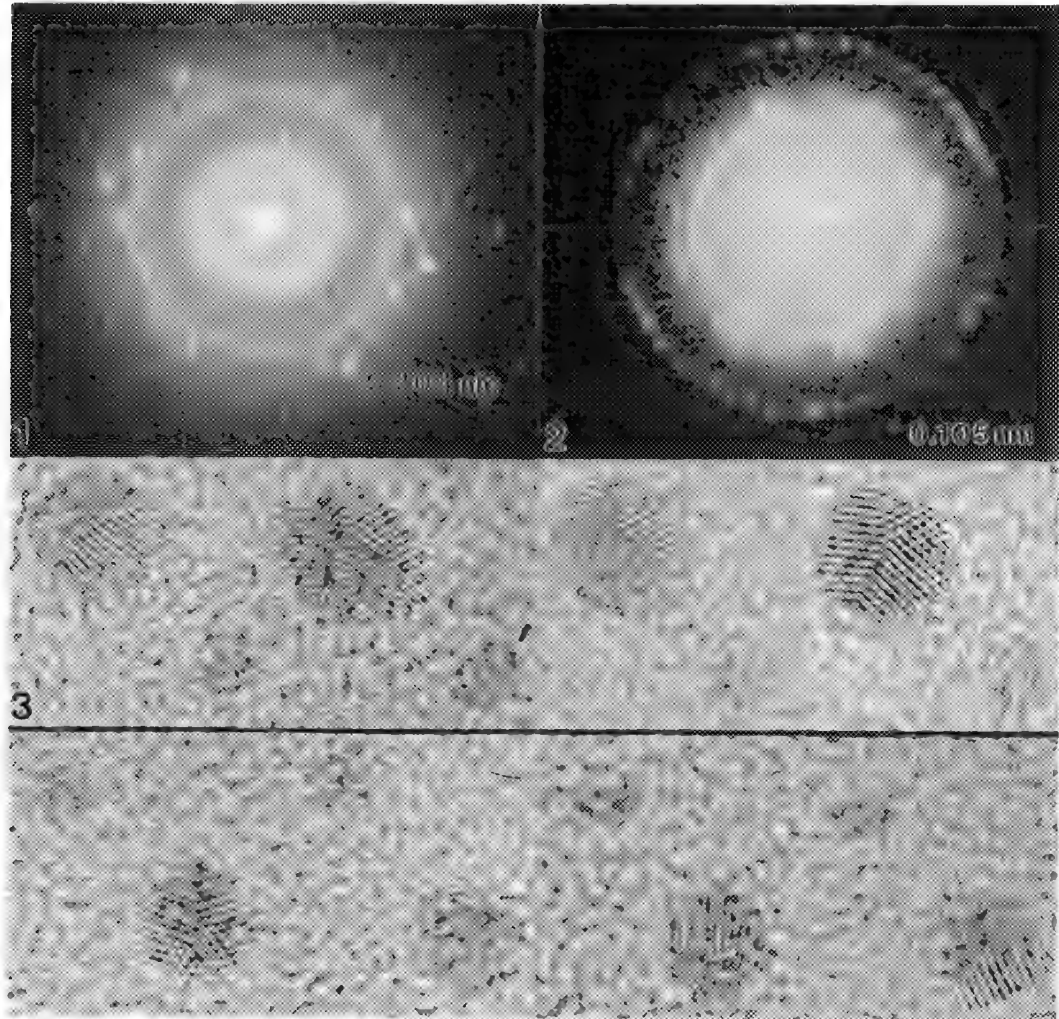


FIG. 1. Diffraction pattern of amorphous germanium with gold islands (CM20 FEG-SuperTWIN) allows determination of the point resolution, but not of the information limit because specimen thickness is too high. FIG. 2. Diffraction pattern of amorphous tungsten with small crystallites (CM30 FEG-SuperTWIN) shows rings down to 0.105 nm. Courtesy of Prof. H. Lichte, University of Tübingen, Germany. FIG. 3. HRTEM images of gold-palladium colloid (CM30 FEG-SuperTWIN), showing two time series (10 s intervals). Structural rearrangements in larger particles can be followed, but those of very small particles (arrowed) are too fast unless recorded with a TV-rate camera.

ELECTRON HOLOGRAPHY WITH A CM30-FEG-Special-Tübingen MICROSCOPE

Hannes Lichte

Institut für Angewandte Physik, Universität Tübingen, Auf der Morgenstelle 12,
W-7400 Tübingen, Germany

Electron holography offers the advantage over conventional microscopy that full use of the object information can be made especially if numerical reconstruction is applied: By coherent optical coupling of a computer to the electron microscope, the electron object wave is completely available for a very flexible wave optical analysis. For example, besides the correction of the coherent aberrations [1] (e.g. spherical aberration, defocus and astigmatism) and the unique accessibility of both amplitude and phase of the object wave in real space and in Fourier space, techniques like nanodiffraction or Selective Imaging can be used to improve our knowledge about the object structure at atomic dimensions [2].

However, there are limits imposed on this scheme by the restrictions given by today's technology for the two steps of data acquisition and processing, i.e. taking the hologram and reconstructing the wave.

First, the information collected in a hologram is limited by incoherent effects. Recording of the sub-Angstrom hologram fringes at a sufficient visibility needs a high degree of coherence consequently a high brightness electron gun; of course, extreme care has to be taken about ac-stray field, vibrations and noise. A principal limit is set by the incoherent aberrations of the objective lens because the information limit cannot be overcome by holographic reconstruction.

Second, the holographic reconstruction procedure is limited by the characteristics of the hologram pick-up and processing system: The pixel number must be sufficient to sample the wave aberration for correction of aberrations; MTF and DQE reduce the S/N in the reconstructed wave and can lead to artefacts.

Corresponding estimations show that the 100keV electron microscope used so far for the development of the holographic technique will not allow to reach a point resolution of, say, beyond 0.16nm [3]. To reach 0.1nm, a holographic imaging system must meet the following requirements:

- 300kV electrons for a moderate wave aberration up to 0.1nm
- Brightness better than $5 \cdot 10^8$ A/cm²/sr
- Information limit better than 0.1nm
- Magnification of 2 Mio and 4 Mio for adaption of the point spread function of the microscope and of the detector, for film and CCD-camera, respectively.
- Pixel number of the image processing system 2k*2k.

According to these specifications, the CM30-FEG-Special-Tübingen electron microscope was designed and built by the Philips company and installed in Tübingen. The performance tests show that the specifications are met. An information limit of 0.105nm was recently measured by means of on-line-diffractometry with a 1k*1k Photometrics CCD-camera and a Tietz image

processing system (fig.1); the result is in good agreement with the data given in [4]. The test specimen consisted of a carbon grid with a very thin tungsten layer to enhance the diffraction efficiency.

First tests show that there are no severe obstacles in taking high resolution holograms with 0.05nm fringe spacing (fig.2). Holograms with 0.03nm fringes, which are needed for 0.1nm holography, have already been observed on the monitor.

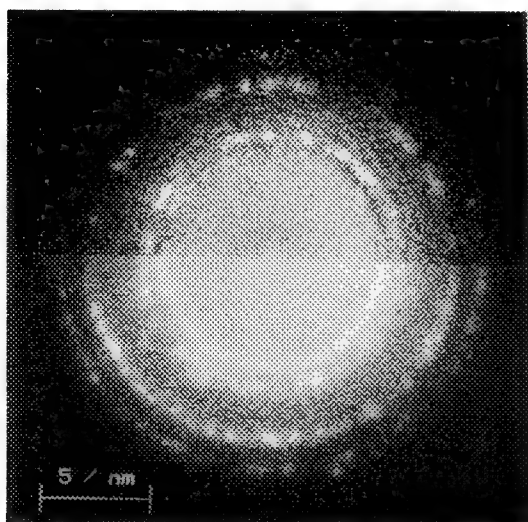


Fig.1 Diffractograms of carbon foil with 0.3nm tungsten. Top: Scherzerfocus 60nm. Bottom: 420nm underfocus. Oscillations due to PCTF can be found beyond the (221) reflectons corresponding to 0.105nm.

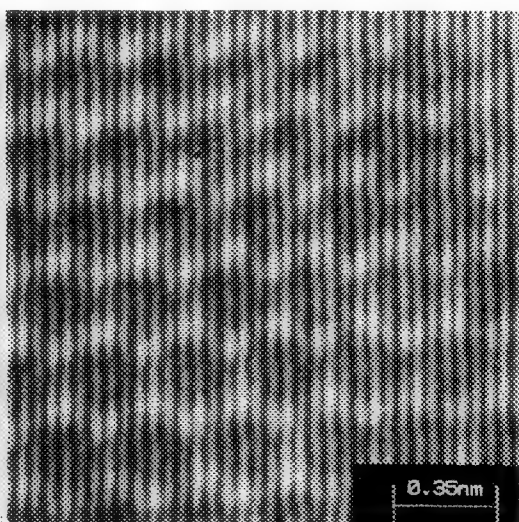


Fig.2 Hologram of WSe₂ in (001)orientation with a fringe spacing of 0.05nm. Exposure time 7sec.

- [1] Q. Fu, H. Lichte and E. Völkl, Phys. Rev. Letters 67(1991), 2319
- [2] H. Lichte, E. Völkl and K. Scheerschmidt, Ultramicroscopy 47(1992),231
- [3] H. Lichte, Parameters for High Resolution Electron Holography, Ultramicroscopy, in press
- [4] M.A. O'Keefe, Ultramicroscopy 47(1992), 282
- [5] For our development of holography the support from Körber-Stiftung, Hamburg, Volkswagen-Stiftung, Deutsche Forschungsgemeinschaft and the European Community (BRITE/EURAM) was indispensable. The discussion with the BRITE/EURAM-partners is highly appreciated.

OPTICAL CHARACTERISTICS OF THE HITACHI HF-2000 COLD FIELD-EMISSION TEM

L. F. Allard, E. Völkl and T. A. Nolan

High Temperature Materials Laboratory, Oak Ridge National Laboratory, Oak Ridge, TN

The illumination system of the cold field emission (CFE) Hitachi HF-2000 TEM operates with a single condenser lens in normal imaging mode, and with a second condenser lens excited to give the ultra-fine 1 nm probe for microanalysis. The electron gun provides a guaranteed high brightness of better than 7×10^8 A/cm²/sr, more than twice the guaranteed brightness of Schottky emission guns. There have been several articles in the recent literature (e.g. refs. 1,2) which claim that the geometry of this illumination system yields a total current which is so low that when the beam is spread at low magnifications (say 10 kX), the operator must "keep his eyes glued to the binoculars"² in order to see the image. It is also claimed that this illuminating system produces an isoplanatic patch (the area over which image character does not vary significantly) at high magnification which is so small that the instrument is ineffective for recording high resolution images. We have investigated these and other such claims, and report here some actual experimental results.

For standard imaging, a 300 μ m aperture in the first condenser lens is typically used, giving a convergence semi-angle of 6.2 mrad. At a typical emission current of 30 μ A, and with the beam spread to cover the full viewing screen, an imaging current of 45 pA/cm² is obtained at 10 kX magnification. We compared this imaging current to that which is used for typical operation of our JEOL 2000FX TEM, and found that with a 200 μ m second condenser aperture, a LaB₆ emitter at 15 μ A emission current produces 48 pA/cm², close to that obtained on the HF-2000. However, the HF-2000 can easily be used with the C1 aperture removed and with the beam spread over a very large area, to get imaging currents of better than 100 pA/cm², far greater than needed for convenient operation. Thus, contrary to published claims, illumination at low magnifications is quite adequate.

For high resolution imaging, the instrument must be carefully adjusted for coma-free alignment so that the isoplanatic patch³ is centered precisely in the field of view. This adjustment is required for high resolution imaging on any instrument. Coma-free images of an amorphous Ge film were recorded at 300 kX and at 25 mA emission (which gives an energy spread from the gun of 0.5 eV) for various times from 1-10 s on Mitsubishi MEM film. Fig. 1 shows diffractograms from center and edges of an image not corrected for coma, showing the strong departure from isoplanicity from one edge to the other of the negative. After coma correction, similar diffractograms show little departure from isoplanicity across the negative (Fig.2). Only for exposures less than 2 s was there any significant departure from isoplanicity at the edges of the negative area. This is a consequence of the high gun brightness provided by the CFE gun, which permits the beam to be spread over an area much larger than the image area, thus increasing the effective size of the isoplanatic patch. Isoplanatic images at various defoci were acquired to determine the optical transfer characteristics of the objective lens ($C_s = 1.2$ mm). Fig. 3 shows a rotationally averaged diffractogram, with its intensity profile matched to a lens transfer function (CTF) calculation for a defocus spread of 3.5 nm and illumination semi-angle of 0.1 mrad. This exhibits contrast transfer consistent with an information limit, at the $1/e^2$ (14%) contrast level, of 0.15 nm. Such diffractograms can be matched very accurately to transfer function plots, allowing easy evaluation of the defocus. Fig. 4 shows a plot of O.L. clicks below minimum contrast versus defocus, determined from comparison to the CTF plot, illustrating the excellent results which can be obtained

from such an experiment. This data generated an average defocus per fine O.L. click of 0.45 nm, about half of the factory preset value.⁴

References

1. M. T. Otten and W. M. J. Coene, *Electron Microscopy*, Vol. 1, EUREM 92, Granada, Spain (1992).
2. M. J. C. DeJong and M. T. Otten, *J. Computer-Assisted Microscopy* (1992)4(2), 191.
3. K. J. Hanszen, R. Lauer and G. Ade, *Ultramicroscopy* (1985)16, 257.
4. Res. spons. by the Laboratory Directed R&D Program of Oak Ridge National Laboratory, managed for the Department of Energy by Martin Marietta Energy Systems, Inc. under contract DE-AC05-84OR21400.

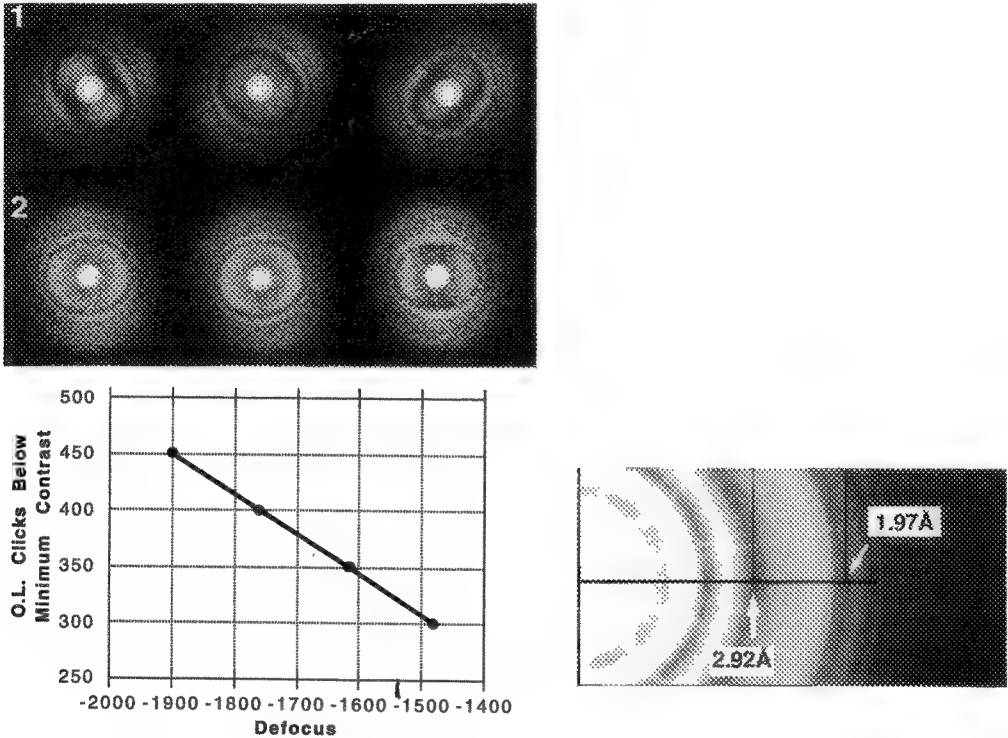


FIG. 1.--Optical diffractograms from left, center and right edges of a 300 kX image of a 5nm amorphous Ge film, showing the effects of coma.
FIG. 2.--Optical diffractograms from a similar image after coma correction, showing little variation in the image from one edge of the negative to the other. Some residual astigmatism exists.
FIG. 3.--Contrast transfer function calculation (top) compared to the intensity profile (center) of the rotationally averaged diffractogram of the 5 nm Ge film. Contrast transfer to near 0.15 nm is shown.
FIG. 4.--Plot of O.L. clicks below minimum contrast versus defocus determined from matching CTF calculations to optical diffractograms at several defoci. The straight line generated suggests that minimum contrast can be chosen with a precision of ± 0.15 nm, and also that the data are self-consistent.

PERFORMANCE AND APPLICATIONS OF THE HOLOGRAPHY ELECTRON MICROSCOPE

Akira Tonomura

Advanced Research Laboratory, Hitachi, Ltd., and Tonomura Electron Wavefront Project, ERATO, JRDC, Hatoyama, Saitama 350-03, Japan

Electron holography is a two-step imaging method. However, the ultimate performance of holographic imaging is mainly determined by the brightness of the electron beam used in the hologram-formation process. In our 350kV holography electron microscope¹ (see Fig. 1), the decrease in the inherently high brightness of field-emitted electrons is minimized by superposing a magnetic lens in the gun, for a resulting value of 2×10^9 A/cm² sr. This high brightness has led to the following distinguished features. (1) The minimum spacing (d) of carrier fringes is $d = 0.09$ Å, thus allowing a reconstructed image with a resolution, at least in principle, as high as $3d=0.3$ Å. (2) The precision in phase measurement can be as high as $2\pi/100$, since the position of fringes can be known precisely from a high-contrast hologram formed under highly collimated illumination. (3) Dynamic observation becomes possible because the current density is high. Several different techniques are now being developed for real-time observation².

An example of dynamic observation³ is shown in Fig. 2, which shows a snapshot of flux lines penetrating a superconductor with an exposure time of 1/30 second. One fringe corresponds to a magnetic flux of $\Phi_0/2$, or a phase shift of π , since the photograph is amplified two times. The original photograph (b) is noisy due to the small number (~ 20) of carrier fringes. However, image quality can be improved as shown in Fig. 2 (c) through image processing, making use of the fact that magnetic field distribution in a free space is of a harmonic form². The high-energy characteristics of this electron beam have recently been exploited to observe the flux-line lattice in the transmission mode⁴. In this experiment, Lorentz microscopy was used for real-time observation. However, with any type of microscopy, a coherent and penetrating electron beam plays a crucial role in detecting such a small phase object as a flux line.

References

1. T. Kawasaki et al., Jpn. J. Appl. Phys. (1990)29, L508.
2. Q. Ru et al., J. Opt. Soc. Am. (1991)8, 1739.
3. T. Matsuda et al., Phys. Rev. Lett. (1989)62, 2519.
4. K. Harada et al., Nature (5 November 1992)360, 51.

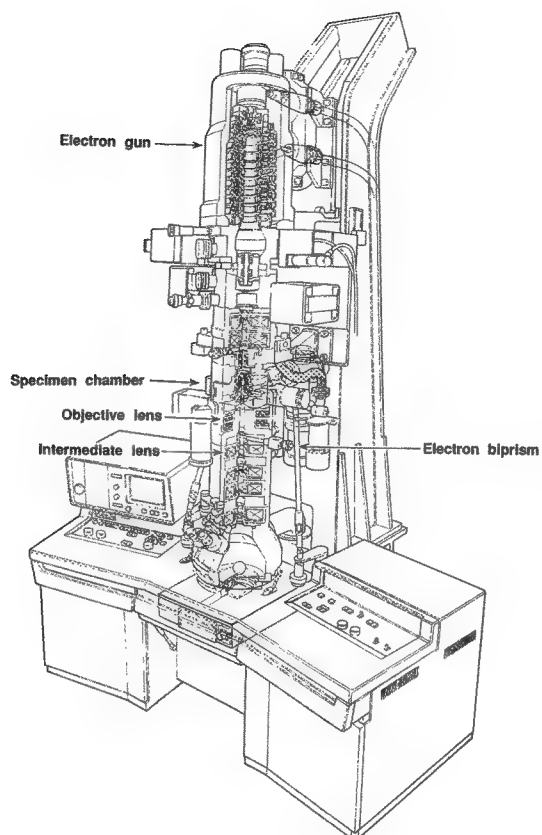


Fig. 1. 350 kV holography electron microscope.

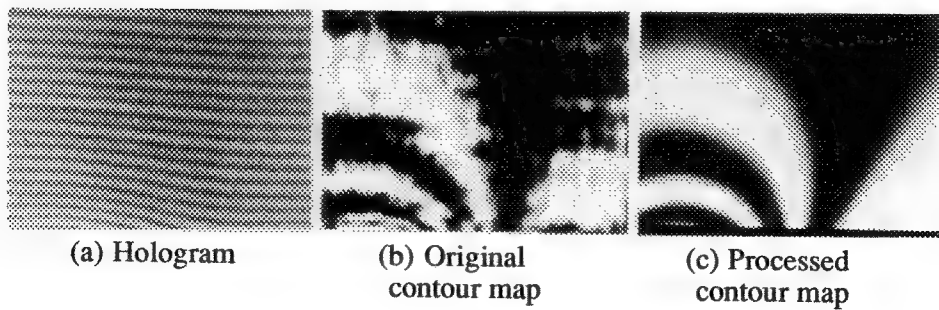


Fig. 2. A snapshot of flux lines penetrating a superconductor.

DEVELOPMENT OF A 300 KV FIELD EMISSION TEM

Y. Ishida*, Y. Bando**, Y. Kitami**, T. Tomita*, and M. Kersker*

*JEOL, Ltd., Musashino 3-1-2, Akishima, Tokyo; **National Institute for Research in Inorganic Materials, Namiki, Sakura-mura, Niihari-gun, Ibaraki 305, Japan

The 300 kV analytical electron microscope, as compared with the 100 to 200 kV instruments, have excellent features such as the high resolution of TEM images, high P/B ratio of EDS and PEELS, and high spacial resolution in analysis.¹⁾

We hereby report the principal specifications of an ultrahigh sensitivity and ultrahigh resolution field emission type electron microscope, which, capable of giving full play to the above-mentioned features of the 300 kV analytical instrument, allows elemental analysis at the single atomic layer level (nm regions).

Its electron gun, simply operated by CPU control, allows emission current to be obtained at the touch of a single button. As the emitter, a W (100)-TF emitter, which can be used simply, stably, and for a long period of time, is employed. After build-up,²⁾ this emitter can obtain about 10 times the angular current density of the W (310) emitter. Around the emitter are provided three electrodes to make emission current variation and electrostatic lens function independent of each other. The ultrahigh vacuum in the electron gun chamber, which is essential for emission stability, is attained by evacuating the accelerating tube with a 150 μ /s SIP and the electron gun chamber with a 15 μ /s SIP, after baking out the electron gun chamber and accelerating tube by means of TMP evacuation and heating by the oven system. Also, for the stabilization of high voltage, which is as important as the vacuum for the stable operation of the field emission type electron gun, the instrument is provided with 10 accelerating electrodes, which is fully sufficient for application of 300 kV.

For the objective lens, a polepiece has been adopted which has a spherical aberration of 1.1 mm and a chromatic aberration of 1.8 mm and is capable of $\pm 30^\circ$ double tilt. This is in order to fully utilize the characteristics of a high-brightness electron source, for obtaining a practical probe diameter for analysis and obtaining high-contrast high-resolution images due to high coherence. And a point resolution of 0.195 nm has been obtained at 300 kV by means of a condenser objective lens. The calculated phase transfer function in this optical system is shown in Figure 1 and Figure 2 shows calculated values of the probe diameter versus probe current. Optical diffraction pattern by TEM image of amorphous Si film was shown in Figure 3 and Figure 4 shows measured line profiles of the minimum probe at the two rectangular direction. The probe was recorded on the imaging plate, which has wide range linearity for the dose of the electrons.³⁾

In order to carry out micro-volume analysis of nanometer-order regions by changing over to the probe mode after obtaining high-resolution high-magnification images in the TEM mode, the EDS is given a take-off angle of 26 degrees for better P/B ratio and a solid angle of 0.2 str. for higher sensitivity.

references

- 1) Y.Bando et al., Ultramicroscopy, 18 (1985) 117.
- 2) L.H.Venellasen and B.M.Siegel, J. Appl. Phys., 43 (1972) 1600.
- 3) N.Mori, J. Electron microscopy, 39 (1990) 433.

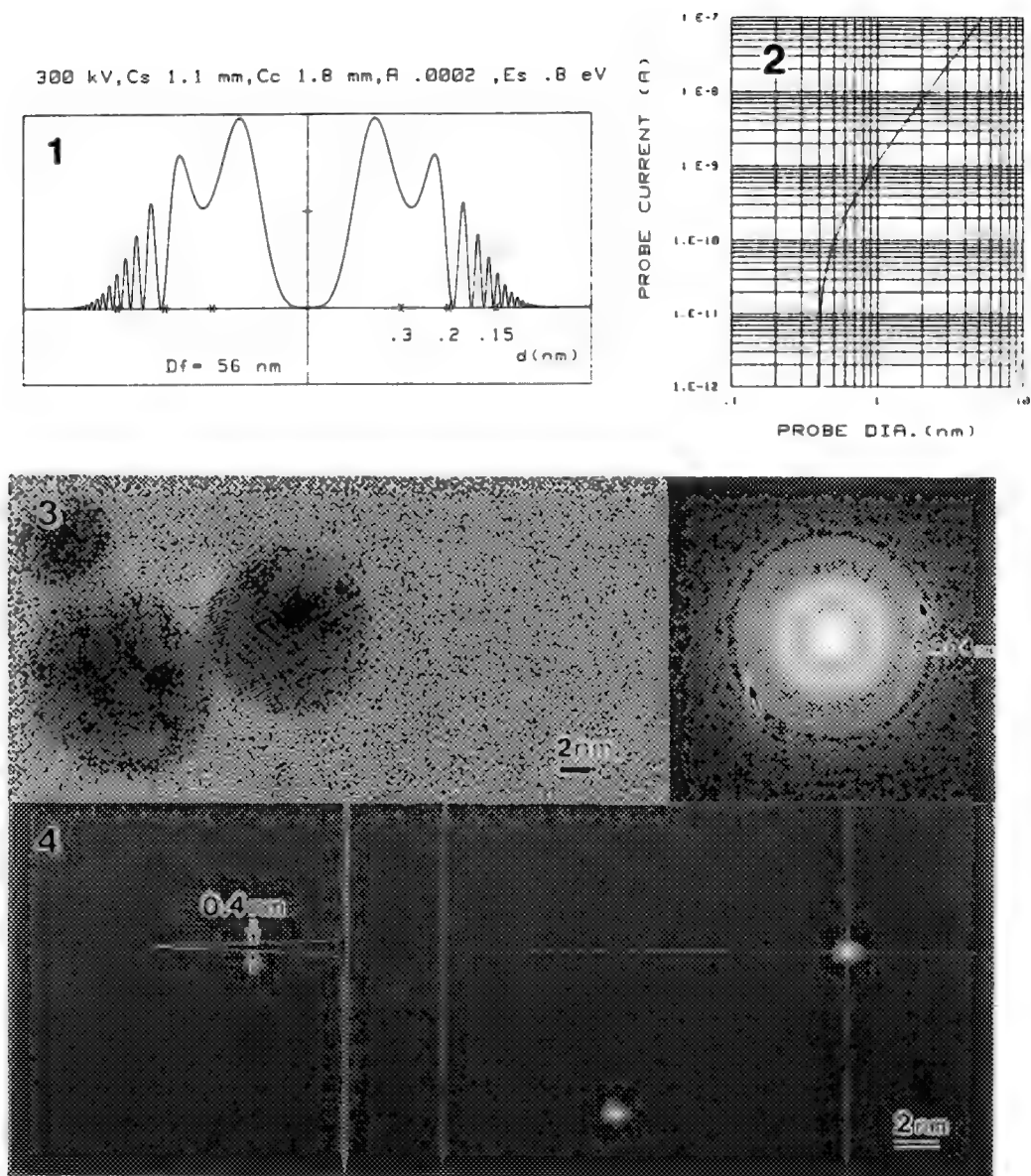


FIG. 1. Calculated phase transfer function for Cs=1.1mm, Cc=1.4mm and $2\alpha = 0.2\text{mrad}$. at 300kV.

FIG. 2. Calculated values of the probe diameter versus probe current for Cs=1.1mm at 300kV.

FIG. 3. TEM image and optical diffraction pattern near the sherzer focus.

FIG. 4. Measured probe size at 300kV using the imazing plate.

HIGH-RESOLUTION COHERENT IMAGING IN STEM

J.M. Cowley, M.A. Gribelyuk*

Department of Physics and Astronomy, Arizona State University, Tempe, AZ 85287-1504 USA
*Now at: MPI fur Metallforschung, Seestrasse 92, W-7000 Stuttgart 1, Germany

The ultimate aim of high resolution electron microscopy is the accurate determination of the positions and types of the atoms in a specimen. The coherent imaging theory for STEM is reviewed with the emphasis on its potential for achieving this aim by holographic methods. The STEM modes of holography are in many respects equivalent to the corresponding TEM modes[1], but have the advantage that, because with a FEG electron source the focussed probes have sub-nanometer diameter, a strong signal is obtained from the illuminated region and the problem of shot-noise is much less important.

The original proposal for holography by Gabor[2] envisaged the use of a reconstruction process on the recorded hologram to correct for the lens aberrations and hence improve the image resolution. The more general and more challenging problem is to reconstruct the aberration-free wave function at the exit face of the specimen (with its real and imaginary, or amplitude and phase, components) and then to invert the dynamical diffraction process and derive the projected potential distribution of the object[3,4].

Several forms of electron holography are discussed in view of their particular promise for achieving the atomic resolution. If a set of nanodiffraction patterns is recorded from the overlapping regions of an object while the focussed probe is scanning the sample, atomic positions can be obtained from the analysis of autocorrelation (AC) functions[5]. The method has been demonstrated experimentally for the case of a known structure of a thin Si(110) crystal; atomic positions have been determined with the accuracy of 0.1-0.15Å. In the future, necessary conditions should be formulated under which the analysis of AC functions leads to unique and true solutions; for an analysis of an unknown structure, methods of experimental imaging parameters determination should be developed which do not rely on simulation. Both the in-line and off-axis[1] versions of Veneklasen's method[6] use a mask placed in the STEM detector plane to multiply the hologram intensity. This has the advantage that no off-line reconstruction is required. The development and placement of masks which can remove the effects of aberrations and conjugate images remains the main practical problem. Recently suggested detector functions[1] appear promising when applied to thin objects[7]. Further work is in progress utilizing a recently-acquired detector system.

In the sideband off-axis STEM holography[8] a biprism placed in the illumination system of the microscope produces two focussed probes in the specimen plane. One probe passes through the vacuum while the other is scattered by the object. The interference pattern (hologram) is recorded in the diffraction plane behind the specimen. It has been shown by computer analysis that it is possible to achieve the resolution $d_1=1.6\text{\AA}$ (VG HB5) and $d_2=1.2\text{\AA}$ (300kV STEM) with the reconstruction scheme suggested[8]. The reconstruction is performed off-line at each position of the two probes where a hologram (up to 512x256pix for the required resolution $d=1.2\text{\AA}$) is taken. The choice of experimental parameters (defocus, separation of two probes, scanning step) has been optimized to achieve highest accuracy and the minimum number of reconstructions. The reconstruction of a region 100x100Å requires only $t<2\text{h}$ with a VAX 11/750 computer. The experimental realization of the method is promising and requires a dedicated acquisition system based on the CCD camera which provides fast accumulation of data.

Most methods of electron holography are found very sensitive to the accuracy with which experimental imaging parameters are known. Recently a method of their determination has been

suggested[9] which is based on the assumption that the aberration-free reconstructed wave function should obey the phase grating approximation (PGA) at least in the region between atomic positions. All the relevant experimental parameters are refined in one iteration cycle. The low absolute error for defocus $\Delta f < 11 \text{ \AA}$ and spherical aberration coefficient $\Delta C < 0.015 \text{ mm}$ is maintained for any crystal thickness t as long as $\alpha = \sigma V(r)t < 5$. This is far beyond the validity domain of PGA ($\alpha=1$) and covers most of the possible situations which are met in high resolution imaging. The method has been found general enough to be implemented in most forms of electron holography. In particular, for TEM off-axis sideband holography, it is realized that experimental imaging parameters can be found with an accuracy such that the imaginary part of the residual transfer function, $\sin(\chi_{\text{res}}(u))$, where $\chi_{\text{res}}(u) = \pi\lambda\Delta f u^2 + 0.5\pi\Delta C\lambda^3 u^4$ does not exceed the limit ± 0.2 for most of reciprocal lattice vectors. The amplitude and the phase of the reconstructed wave reveal a good agreement with model data (Fig. 1).

It is concluded that further progress in holographic methods in STEM is very promising and should follow simultaneously two parallel lines; development of alternative imaging modes and relevant quantitative methods on one hand and experimental implementation of these on the other which requires acquisition of dedicated instrumentation. It appears that the latter process controls further progress at this state.

This work has been supported by the NSF grant DMR-8810238. The authors are very grateful to Paul R. Perkes, Center for HREM, ASU, for assistance with computing.

References

1. J.M. Cowley, *Ultramicroscopy* 41 (1992) 335.
2. D. Gabor, *Proc. Roy. Soc. (London) Ser.A* 197 (1949) 454.
3. D. Van Dyck, in *Advances in Electronics and Electron Physics*, ed. by P.W. Hawkes, Academic Press, New York (1985) 295.
4. M.A. Gribelyuk, *Acta Cryst.* A47 (1991) 715.
5. J. Konnert, P. D'Antonio, J.M. Cowley et al., *Ultramicroscopy* 30 (1989) 371.
6. L.H. Veneklasen, *Optik* 44 (1975) 447.
7. S.Y. Wang, M. Mankos, J.M. Cowley, *Proc. of 50th EMSA* (1992), Boston, 982.
8. J.M. Cowley, *Ultramicroscopy* 34 (1990) 293.
9. M.A. Gribelyuk, J.M. Cowley, *Ultramicroscopy* 45 (1992) 115.

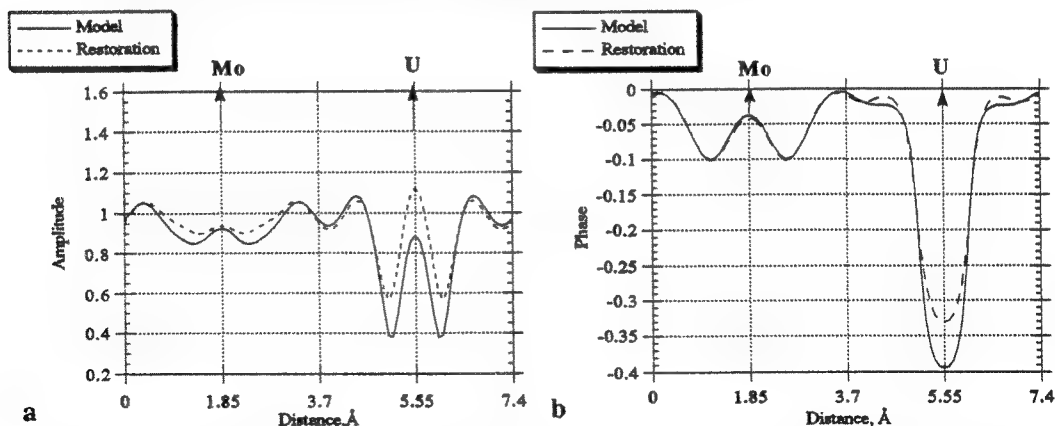


Fig. 1 Reconstructed and model amplitude and phase of the wave function for 300keV TEM off-axis holography for 40Å thickness of a U-Mo oxide.

OBSERVATION OF CRYSTAL STRUCTURES BY IMAGE RESTORATION IN ELECTRON HOLOGRAPHY

Takayoshi Tanji and Kazuo Ishizuka

Tonomura Electron Wavefront Project, ERATO, JRDC
P.O.Box 5, Hatoyama, Saitama 350-03, Japan

Off-axis electron holography has been applied to crystal structure images using digital image processing.

Three important factors pertaining to the correction of aberrations in electron holography are:

- (1) interference fringes narrower than one third of the required resolution,
- (2) a Signal to Noise (S-N) ratio in the hologram which is high enough for high resolution reconstruction, and
- (3) the estimation of the amount of aberrations.

We have obtained interference fringes with a spacing of below 0.03 nm [1], which is sufficient for a resolution of 0.1 nm in the reconstructed image. The S-N ratio depends on the instrument used to record the hologram and whether the specimen causes strong scattering or weak scattering.

Some ways of estimating the amount of aberration have been proposed [2-5]. Here we adopted an algorithm which involves minimizing the contrast of the reconstructed image by optimizing the processing parameters (Cs and df), because it is applicable not only to weak phase objects but also to general phase objects and, in principle, only one hologram is needed to determine the parameters.

The standard deviation of the amplitude distribution was monitored with varying Cs and df. In the case of an amorphous carbon film, the standard deviation of the processed amplitude has one minimum, as shown in Fig. 1(a), where Cs is fixed at 1.7 mm. On the other hand, the standard deviation for a crystal specimen ($W_8Nb_{18}O_{69}$) sometimes has a few minima as shown in Fig. 1(b), where Cs=0.55 mm. Even in this case, the best values of Cs and df for a certain reconstruction aperture are found at or close to the lowest minimum. Figure 2(a) shows an electron hologram of $W_8Nb_{18}O_{69}$, as recorded by a Hitachi HF-2000 FE-TEM equipped with a standard objective lens and electron biprisms. In Fig. 2(b), the Fourier transform of this hologram shows that the carrier frequency (19 nm^{-1}) is high enough for the reconstruction aperture ($r=4.2 \text{ nm}^{-1}$) indicated on the side band. The reconstructed phase distribution in Fig. 2(c) represents a 4x4 block structure, which is the structure image, after restoration with parameters of Cs=1.7 mm and df=-300 nm (under-focus). Although the minimum standard deviation is found at df=-290 nm for this hologram, the best parameter for correction is found at a point shifted by 10 nm. It must be pointed out that these parameters are not always the actual values, but the suitable ones for restoration. The phase of an electron wave is delayed in the specimen and if it is perfectly corrected, its distribution shows similar B/W contrast to that of structure images obtained by electron microscopy. Figure 3 shows a hologram (a) obtained with a higher resolution objective lens and the phase distribution restored with Cs=0.55 mm and df=-126 nm (b). The size of the reconstruction aperture was 4.5 nm^{-1} (d=0.22 nm). The Scherzer limit of this lens is 0.21 nm, but the low S-N ratio of the hologram prevented improvement of the resolution. This low S-N ratio is due to the thickness of the specimen.

The resolution of electron holography has reached the same level as that of electron microscopy. In the near future, sources with more coherency and detection systems with higher efficiency will enhance the information limit of holography to the same level as that of the microscope. The algorithm which we adopted here to estimate the parameters restricts the specimens to pure phase objects, which is the

reason why the best correction parameters were not always at the minimum standard deviation. Improvement of this algorithm is a remaining problem to achieve a resolution as high as the information limit.

References

- [1] T.Tanji, K.Urata, K.Ishizuka, Q.Ru and A.Tonomura, Ultramicroscopy in print
- [2] F.J.Franke, K.-H.Herrmann and H.Lichte, Scanning Electron Microsc. Suppl. 2 (1988) 59.
- [3] T.Tanji, J.Ito and K.Yada, Ultramicroscopy 35 (1991) 245.
- [4] A.F.de Jong, W.M.J.Coene and A.J.Koster, Proc. 50th Annl.Mtg.qr EMSA (1992) 136.
- [5] M.A.Gribelyuk and J.M.Cowley, Electron Microscopy, 1. EUREM 92 (1992) 649.

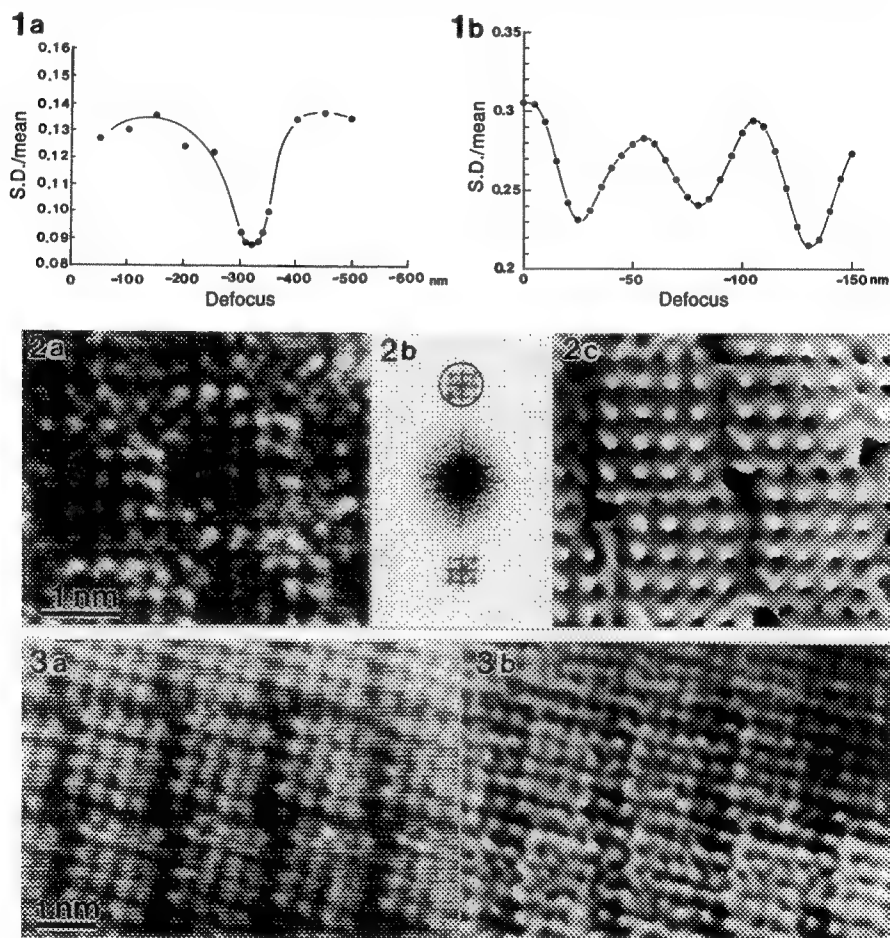


FIG.1---Standard deviation of restored amplitude for a thin carbon film at Cs=1.7 mm (a), and for the crystal, W₈Nb₁₈O₆₉, at Cs=0.55 mm (b) with varying df.
 FIG.2---Electron hologram of W₈Nb₁₈O₆₉ (a), its Fourier transform (b) and the phase distribution restored with Cs=1.7 mm and df=-300 nm (under-focus) (c).
 FIG.3---Electron hologram of W₈Nb₁₈O₆₉ recorded with a high resolution lens (a) and the restored phase distribution with Cs=0.55 nm and df=-126 nm.

CBED+EBI HOLOGRAPHY (CBED+EBH) OF MATERIALS STRUCTURES

R.A. Herring and T. Tanji

Tonomura Electron Wavefront Project, ERATO, JRDC, P.O. Box 5, Hatoyama, Saitama 350-03 Japan

A new method of holography is presented using the CBED+EBI technique [1, 2] of interferometry. The CBED+EBI method produces interferograms by using an electron biprism to interfere diffracted beams produced from a convergent beam probe. Holography is made possible by the fact that the beams continue to interfere as they are displaced from each other slightly, Fig. 1. This fact enables an object beam to be taken from one part of a crystal (e.g. a crystal defect) and a reference beam to be taken from another part of the crystal (e.g. the perfect crystal). The interference results in a phase shift around the dissimilar region. As well, for small defects which do not disturb or phase shift one beam (say the main beam) significantly but do so with the diffracted beam, directly overlaying the two beams results in a significant phase shift at the small defect. These methods are very easy to apply although the interpretation of phase shifted regions still requires knowledge of the crystal, its diffraction characteristics and interference effects. Examples of phase shifted regions are shown in Fig. 2 for the superlattice materials of GaAs/In_{0.2}Ga_{0.8}As and Si/Si_{0.65}Ge_{0.35}, in Fig. 3 for small amorphous Si regions created by high-energy As implantation, and Figure 4 for a threading dislocation in a GaAs epi layer. In Fig. 2 for the GaAs superlattice the fringes are nearly parallel to the superlattice layers and a Fresnel fringe (dark band inside light region) is apparent, whereas, in the SiGe superlattice the fringes are not parallel to the superlattice and a Fresnel fringe is not apparent.

The phase shift at the GaAs/In_{0.2}Ga_{0.8}As interface is $\sim 3\pi/8$ and at the Si/Si_{0.65}Ge_{0.35} interface is $\sim 3\pi/4$. The model given in [2] shows the relationship of phase shift with composition, although strain at the interface must also be considered. In Fig. 3 for the small amorphous zones in Si the interpretation of the fringe shift is much easier. There is a π phase shift at regions which are 100% amorphous due to the intensity of the 004g beam being zero and a fraction thereof for any mixed amorphous/crystal regions. This allows CBED+EBH to detect and quantify partially amorphous regions which are very difficult to do by standard high resolution techniques. It is interesting to note that the amorphous regions in Fig. 3 are interconnected which lends insight into the interpretation of their formation process. In Fig. 4 for the dislocation in GaAs the interpretation of the phase shift requires detailed knowledge of the imaging condition which includes its Burgers vector, habit plane, diffraction vector, deviation parameter and possibly depth within the crystal. A π phase shift is possible at the dislocation core as seen in Fig. 4.

Since the diffraction image is defocused, obtaining the true image requires using a digital method [3] to first correct for the defocusing and to reduce the carrier fringes and then to separate the amplitude and phase distributions from the reconstructed in-focus image. Localization of the image features is enhanced by imaging the back focal plane in fourier space to the near-imaging condition by appropriately adjusting the electro-optical system. As well, a null-hologram (without an object) under the same imaging condition is recorded and reconstructed for eliminating the system's aberration errors. The resolution limit for imaging reconstruction appears to be quite high (3x the fringe spacing [4]) and will be discussed in detail at the meeting. Because the interference fringes disappear with displacement of the beams, the CBED+EBH method is enhanced by the use of a coherent source where the maximum displacement of the beams for visible fringes is equal to the beam's lateral coherence.

For CBED+EBH, conventional holographic interpretation of phase shifts, i.e. mean inner potential, magnetic and electric fields, is possible for defects or dissimilar crystal regions which are not influenced by the diffraction condition of the interfering beams. Thus it may be possible to use CBED+EBH for detecting compositional gradients and static electric fields at dislocation cores, grain boundaries, and compositional interfaces, as well as, magnetic field distributions at domain boundaries and magnetic flux vortices.

Studying crystals structures by the CBED+EBH method offers many advantages over the conventional holography method which typically splits and interferes a single beam into an object beam and a reference beam using a biprism. These advantages include being able to produce holograms in relatively thick specimen having abundant, high-contrast, straight fringes. Many of these advantages will be discussed at the meeting.

- 1) R.A. Herring, G. Pozzi, T. Tanji, and A. Tonomura, Ultramicroscopy, In press.
- 2) R.A. Herring, G. Pozzi, T. Tanji, and A. Tonomura, These MSA proceedings.
- 3) M. Takeda and Q. Ru, Appl. Opt. **24** (1985) 3068.
- 4) K.J. Hanszen, J. Phys. D: Appl. Phys. **19** (1986) 373.

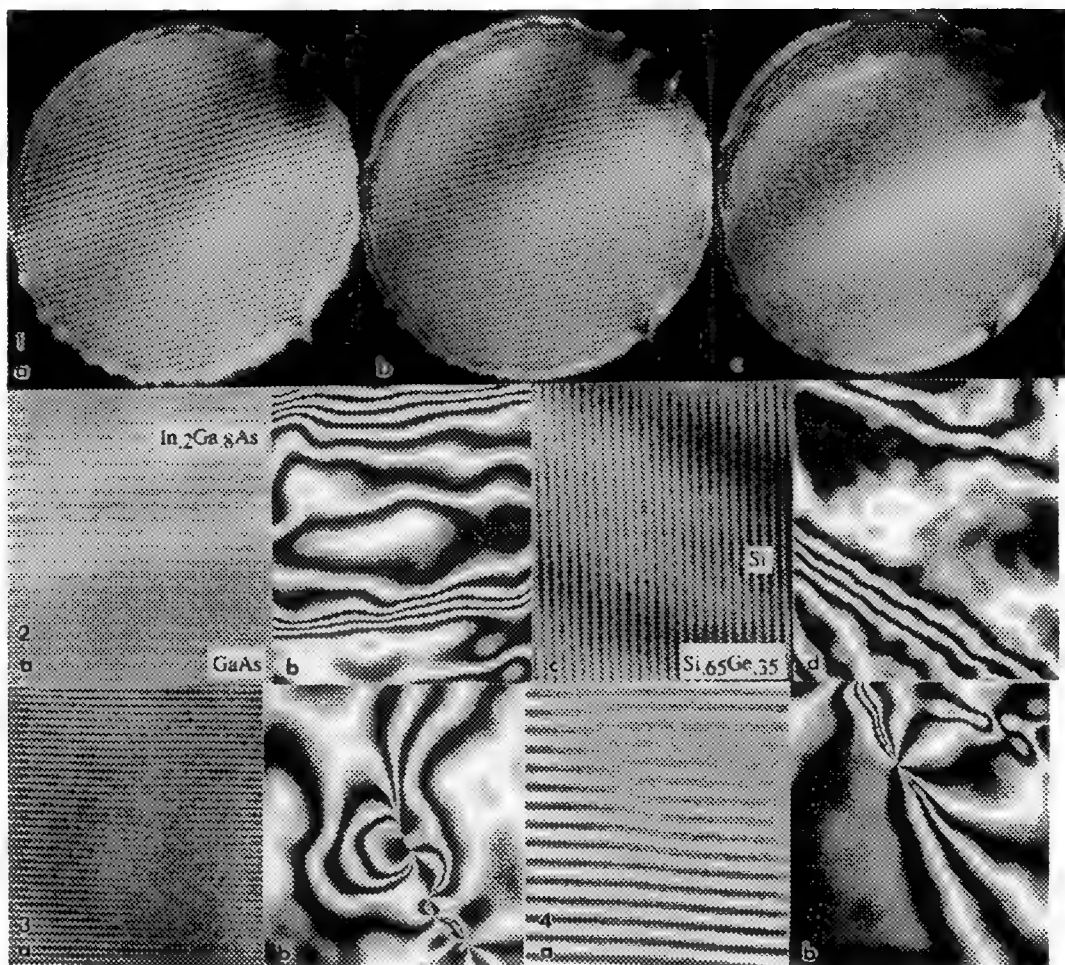


Fig. 1 CBED+EBI of GaAs produced by the main beam overlaid by the 111g beam showing exact overlap in a), a shift in overlap in b), and a further shift in c). The interference of the beams decreases with an increase in shift from the exact overlap position. For significance see the main text.

Fig. 2 CBED+EBH showing holograms and phase images of GaAs/In₂Ga₈As in a) and b), which used the main beam with the 002g, and of Si/Si₆₅Ge₃₅ in c) and d), which used the main beam and the 111g, respectively, where the phase is amplified by 8x in b) and 16x in d). Note the dark band (fresnel fringe) in the In₂Ga₈As layer.

Fig. 3 CBED+EBH showing in a) a hologram which used the main beam with the 004g, and b) a phase image of small amorphous regions in high-energy As implanted Si, where the phase is amplified by 8x in b).

Fig. 4 CBED+EBH showing in a) a hologram which used the main beam and the 220g, and b) a phase image of a threading dislocation in a GaAs epi layer, where the phase is amplified by 8x in b).

Although the exact magnification scale for these images is not known at this time, the fringe spacing in the holograms is approximately 2x the interplanar spacing of the diffracting vector used to interfere with the main beam.

ELECTRON HOLOGRAPHY OF INTERFACES IN ELECTROCERAMICS

Vinayak P. Dravid, V. Ravikumar and Richard Plass

Dept. of Materials Science & Eng., Northwestern University, Evanston, IL 60208

With the advent of coherent electron sources with cold field emission guns (cFEGs), it has become possible to utilize the coherent interference phenomenon and perform "practical" electron holography. Historically, holography was envisioned to extent the resolution limit by compensating coherent aberrations. Indeed such work has been done with reasonable success in a few laboratories around the world. However, it is the ability of electron holography to map electrical¹ and magnetic fields² which has caught considerable attention of materials science community.

There has been considerable theoretical work on formation of space charge on surfaces and internal interfaces. In particular, formation and nature of space charge have important implications for the performance of numerous electroceramics which derive their useful properties from electrically active grain boundaries. Bonnell and coworkers,³ in their elegant STM experiments provided the direct evidence for GB space charge and its sign, while Chiang et al.⁴ used the indirect but powerful technique of x-ray microchemical profiling across GBs to infer the nature of space charge. Recently attempts have been made to probe the nature of polarization and space charge associated with electroceramic interfaces with electron holography. Zhang et al.⁵ reported biprism fringe bending across 90° domain boundaries in ferroelectric BaTiO₃. They went on to model the domain boundaries and obtained values for domain boundary width and polarization. Spence⁶ challenged these results and argued that thickness effects, dynamical effects due to polarity changes and strain are probably responsible for such observations.

Using off-axis electron holography, we have seen very intriguing and surprising fringe shifts. One such hologram is shown in Figure 1 for an internal interface in PbTiO₃. While grain boundaries (GBs) in ionic materials could be charged, for example due to local point defects (e.g. oxygen vacancies), clear and cogent explanation for such fringe shifts have not yet been possible. Such dramatic offsetting of biprism fringes led us to further investigate electron holography of charged grain boundaries. There is considerable evidence for the presence of charged GBs and oppositely charged space-charge regions on either side of GBs in ionic systems (see schematic representation in Figure 2A). Since the charged GB and space charge directly modify the potential of the region, electron holography should, in principle, be able to detect the presence and extent of GB space charge. It can be anticipated that the presence of charged grain boundary and space-charge translates into changes in the local mean inner potential (MIP) which should impart phase shift(s) (see Figure 2B). Indeed, we have observed fringe shifting across GBs in ZnO doped with Bi₂O₃.⁷ Whenever fringe shifts were observed, Bi-segregation to the GBs could be detected by XES. However, there have also been instances of no fringe bending even when boundary was segregated with Bi. Since Bi-segregation leads to oxygen vacancies at the GB region, one can envision the presence of negatively charged GB and positive space charge in Bi-doped ZnO. Complete theoretical treatment for such cases is now being pursued, including effect of thickness, perturbation of reference wave and crystallographic orientation effects. To eliminate the crystallographic and channeling contribution to differential phase change, we are utilizing oriented tilt-bicrystals of SrTiO₃ for such experiments. These experimental results and theoretical analysis of holography of charged grain boundaries will be presented.⁸

References:

1. G. Matteucci et al., *Physica B*, 151, p.223 (1988).
2. A. Tonamura, *Rev. Mod. Phys.*, 59, p. 639 (1987).
3. D.A. Bonnell and I. Solomon, *Ultramicroscopy*, 42-44, p. 788 (1992).
4. Y.-M.

Chiang and T. Takagi, J. Am. Ceram. Soc., 73[11], p. 3286 (1990). 5. X. Zhang et al., Appl. Phys. Lett., 60, p. 784 (1992). 6. J.C.H. Spence et al., App. Phys. Lett., submitted, and private communication. 7. V.P. Dravid et al., unpublished research. 8) This research is partially supported by the NSF-STCS-91-20000, U.S. Dept. of Energy-DE-FG02-92ER45475 and NSF-DMR 9203722.

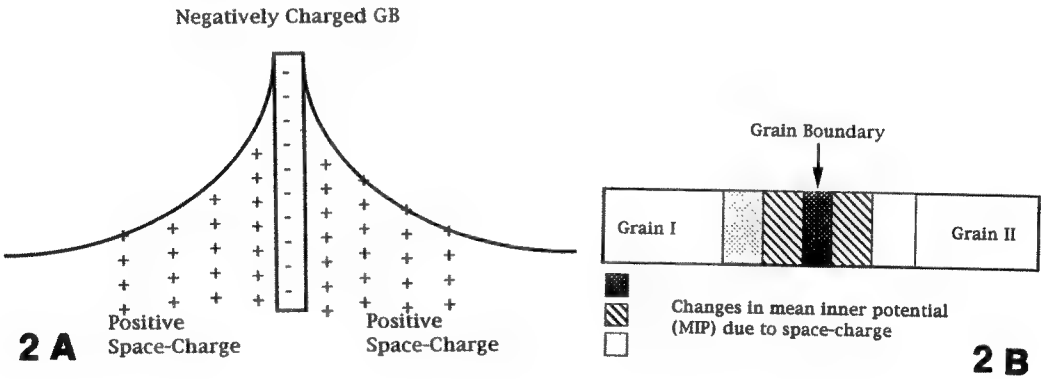
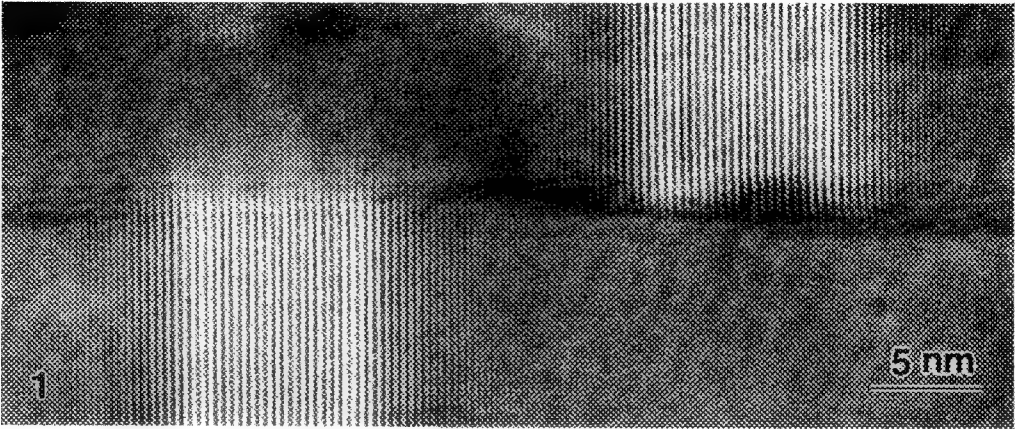


Figure 1:Unusual biprism fringe bending (offset) across a charged interface in PbTiO3. **Figure 2A:** Schematic illustration of charged grain boundary and space-charge region in electroceramics. **Figure 2B:** Schematic illustration of change in mean inner potential (MIP) across charged grain boundary as in Figure 2.

QUANTITATIVE ELECTRON HOLOGRAPHY APPLIED TO CRYSTAL WEDGES AND INTERFACES

M. Gajdardziska-Josifovska

Center for Solid State Science, Arizona State University, Tempe, AZ 85287

Electron holography is unique among transmission electron microscopy techniques in that it allows retrieval of phase of the electron wave, information which is lost with other imaging techniques. With access to the phase, interactions of the incident electron wave with the electrostatic and magnetic potentials of the specimen can be studied directly with high spatial resolution.¹ Besides resolution enhancement, the original goal for electron holography, applications to wide range of materials problems are currently under investigation.² This work will address applications to measurements of mean inner potential of crystals and to epitaxial crystal interfaces.

In non-magnetic materials, in the absence of external electrical fields and/or charge layers, the electrostatic potential which alters the phase of the exit surface wave results from the atomic potentials. For amorphous and polycrystalline samples of known thickness, the phase change depends on the volume average of the atomic potentials, i.e. the mean inner potential V_0 .³ Recently, we have found that phase images from amorphous and/or polycrystalline interfaces, as found in multilayered materials, can be interpreted in terms of V_0 differences.⁴ In order to extend these studies to interfaces between single crystals we have developed an accurate method for measurement of mean inner potential of crystals: By using cleaved crystal wedges of known angle, combined with digital recording and numerical reconstruction of holograms, the phase change of the transmitted electrons with thickness $(d\phi/dt)_{\text{exp}}$ was determined experimentally for crystal orientations away from low index zone axes and Kikuchi bands (Table 1).⁵ In the kinematical approximation this phase change is directly proportional to V_0 ($V_0^{\text{kin}} = 1.082 \times 10^{-7} d\phi/dt$ Vm/rad for 100keV electrons used for data in Table 1). Dynamical calculations of the phase change of the transmitted beam due to multiple scattering $(d\phi/dt)_{\text{dyn}}$ show that, for the studied materials and crystal orientations, the kinematical approximation gives values which are lower than the true value of V_0 by $\leq 5\%$.

In the case of epitaxial interfaces, the only option for reducing dynamical effects is to tilt to systematic row orientations where the transmitted beam is in the center of a Kikuchi band parallel to the interface. Fig. 1 shows an example of a CoSi₂/Si interface where the zone axis (a,b) and the systematic row (c,d) orientations yield markedly different phase profiles from the same specimen region. In Fig. 1d the phase advances more in CoSi₂ compared to Si, which is qualitatively consistent with CoSi₂ having larger mean inner potential. However, in the zone axis case (Fig. 1b), the diffraction contributions cause a reversal of the phase contrast. Fig. 2 shows a case of GaAs/AlGaAs quantum wells where the phase contrast is entirely due to diffraction effects (a), and disappears when the specimen is tilted parallel to the interfaces but away from the zone axis (b). In conclusion, the application of holography to crystal interfaces will require measurements and calculations of both mean inner potential variations and diffraction contributions.⁶

References

- 1 A. Tonomura, *Rev. Mod. Phys.* (1987)59, 639.
- 2 H. Lichte et al., *Ultramicroscopy* (1992)47, 231.
- 3 R. Buhl, *Z. Phys.* (1959)155, 395; C. Jönsson et al, *Phys. Kondens. Mater.* (1965)3, 193.
- 4 J. K. Weiss et al, *Ultramicroscopy*, submitted; also: Proc. 49th Annl. Mtg. EMSA (1991)674; Proc. 50th Annl. Mtg. EMSA (1992)244.
- 5 M. Gajdardziska-Josifovska et al, *Ultramicroscopy*, submitted; also Proc. 50th Annl. Mtg. EMSA (1992)134.
- 6 This research was conducted at the Center for HREM at ASU supported by NSF grant DMR-9115680. The author is grateful to Prof. J. C. H. Spence for financial support and to Dr. R. Tung and Dr. D. Gerber for providing MBE samples.

Table 1. Mean inner potentials V_o for four materials obtained by adding calculated phase change with thickness due to diffraction $(d\phi/dt)_{dyn}$ to phase slope $(d\phi/dt)_{exp}$ measured from electron holograms. Kinematical approximation applied to same experimental data results in lower $(V_o)_{kin}$ values.⁵

crystal	$(\frac{d\phi}{dt})_{experimental} \left[\frac{rad}{nm}\right]$	$(V_o)_{kin} [V]$	$(\frac{d\phi}{dt})_{dynamical} \left[\frac{rad}{nm}\right]$	$V_o [V]$
Si	0.08422 ± 0.00014	$9.11\pm0.5\%$	0.001350 ± 0.000003	$9.26\pm0.5\%$
MgO	0.11816 ± 0.00035	$12.78\pm0.6\%$	0.002137 ± 0.000007	$13.01\pm0.6\%$
GaAs	0.13064 ± 0.00118	$14.13\pm1.2\%$	0.003728 ± 0.000055	$14.53\pm1.2\%$
PbS	0.15118 ± 0.00060	$16.35\pm0.7\%$	0.007130 ± 0.000033	$17.19\pm0.7\%$

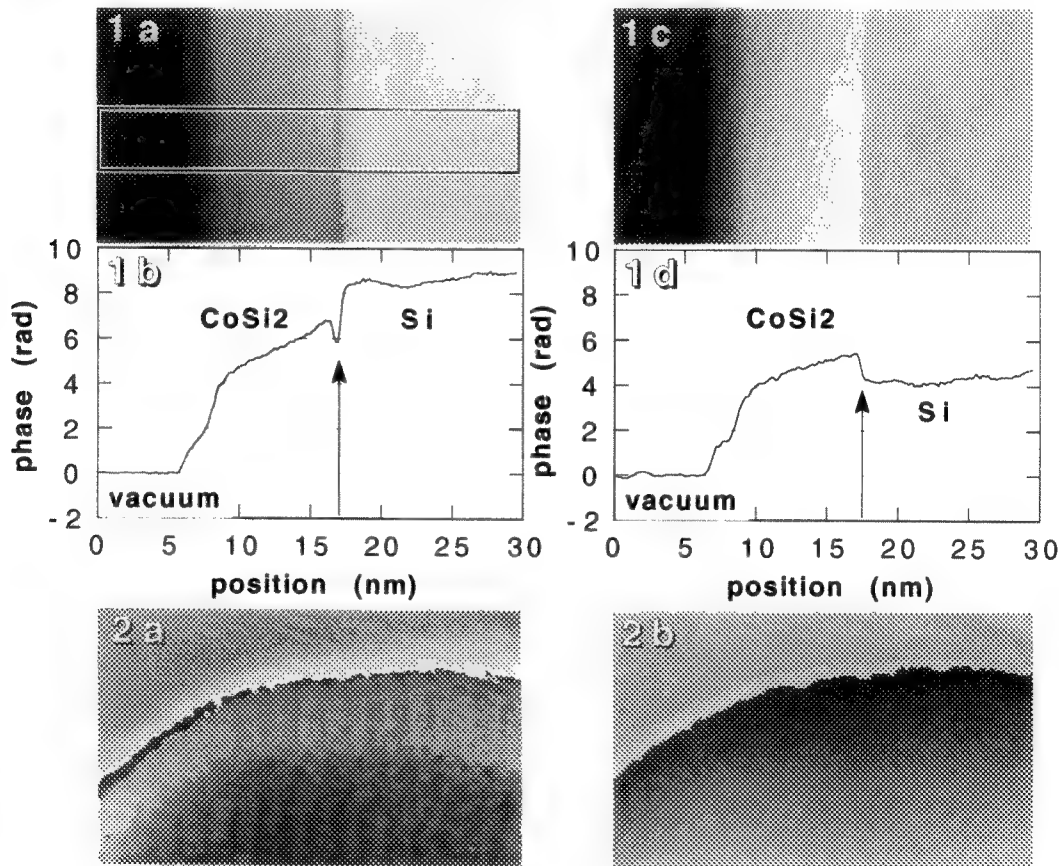


FIG.1.--Phase images and phase profiles from epitaxial CoSi₂/Si interface oriented edge-on to electron beam: (a and b) at [110] zone axis, (c and d) at 200 systematic row. Box in (a) denotes region used for phase averaging over 30pixel (4.4nm) parallel to interface to obtain phase profiles.

FIG. 2.--Phase images from GaAs/Al_{0.3}Ga_{0.7}As quantum wells show contrast between layers at [100] zone axis (a), and no contrast at 200 systematic row (b). Width of images is 37nm.

APPLICATION OF ELECTRON HOLOGRAPHY TO FERROELECTRIC STUDY

X. Zhang, D. C. Joy*, L. F. Allard*, and T. A. Nolan*

Electron Microscope Facility, The University of Tennessee, Knoxville, TN 37996,
and *Metals and Ceramics Division, Oak Ridge National Laboratory, Oak Ridge, TN 37831

With the development of FE TEM, electron holography becomes a reality to materials scientists, which opens a new window for materials study.¹ Weak phase objects, such as a thin transparent specimen or an electric or a magnetic field, which have little or no effect on the intensity of the transmitted wave, can readily be observed via holography because of the phase shift that they produce. Application of the electron holographic method has been extended to the study of ferroelectric domain wall structures.² This work presents the most recent results in this area.

Polarization gradients within domain walls are extremely important for the understanding of the extrinsic elastio-dielectric properties of ferroelectrics. Electron holographic studies of the local domain wall profiles provide essential input parameters for phenomenological theories of domain structure and of the macroscopic properties derived from the theories. Figure 1(a) is an electron hologram of the ferroelectric (BaTiO_3) 90° domain wall area. The interference fringe bending due to the phase shift is a direct measure of the electrostatic field across the domain wall, which permits not only the determination of the domain wall thickness but also the quantitative analysis of the polarization changes associated to the wall.² The study shows that the phase shift at any point across the wall is directly related to P_z , the component polarization parallel to the electron beam direction. The shape and the magnitude of the fringe bending profile therefore quantitatively displays $P_z(x)$, the spatial variation of spontaneous polarization across the wall. Figure 1(b) plots the normalized variation of P_z versus the normalized position across the domain wall where $X/W = 0$ is the center position of the wall. The solid line represents the variation of P_z predicted based on the Zhirnov thermodynamic model.³ The dash line in Figure 1(b) is the match of the experimental result with the Landau p^6 -model for first order phase transition.⁴ The parameters associated with the model are thus experimentally determined. These parameters can be subsequently used in the complete characterization of the domain wall structures.

The understanding of the phase transition is of direct importance of the domain formation and the domain wall movement. We have conducted some preliminary electron holographic studies of the phase transition of BaTiO_3 crystal. The specimen is heated while the phase shift across the domain wall is continuously monitored by a TV camera. When the specimen temperature is taken close to the Curie point, the domain wall thickness increases (see Figure 2). At near the Curie-Weiss temperature the fringe bending disappears with the loss of spontaneous polarization. The fringe bending does not reappear until the temperature is again dropped below T_C . Using the experimentally determined p^6 -model one is able to predict the changes of domain wall thickness versus the increment of temperature (Figure 2). A good agreement is reached between the prediction and the measured values.

The distinct anomalous interference fringe pattern shown in Figure 3 (a) is believed to be due to the charged point defect within the BaTiO_3 domain wall.² In Figure 3, the charge center is located at the tip of a newly formed 90° domain wall when the specimen temperature is dropped below T_C . Because of the possible pinning effect of the point defect, the domain size is about one third of the initial parent domain before the heating. Figure 3 (b) is the isopotential contour map of the area of (a). The character-

istic of the charge singularity at the domain tip is revealed. The electrostatic potential distribution around the charge centers is displayed in detail.

References

1. A. Tonomura, Rev. Modern Phys., 59(1987)639
2. X. Zhang, T. Hashimoto, and D.C. Joy, Appl. Phys. Lett., 60(1992)784
3. V.A. Zhirnov, Sov. Phys. JETP, 35(1959)822
4. Y. Ishibashi, Ferroelectrics, 98(1989)193
5. The authors are grateful to Drs. C. Randall and W. Cai of Penn State University for providing the BaTiO₃ specimens and valuable discussions. Research sponsored in part by the Laboratory Directed Research and Development Program of Oak Ridge National Laboratory, managed for the U.S. Department of Energy by Martin Marietta Energy Systems, Inc. under contract DE-AC05-84OR21400.

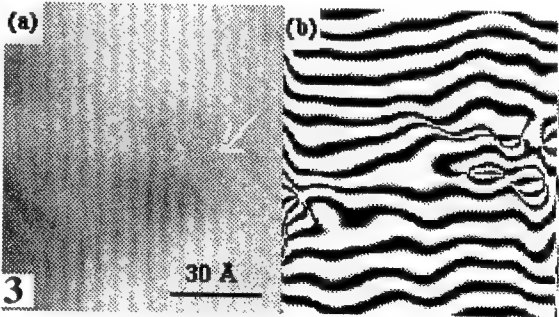
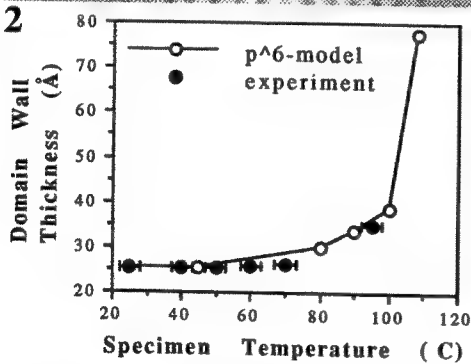
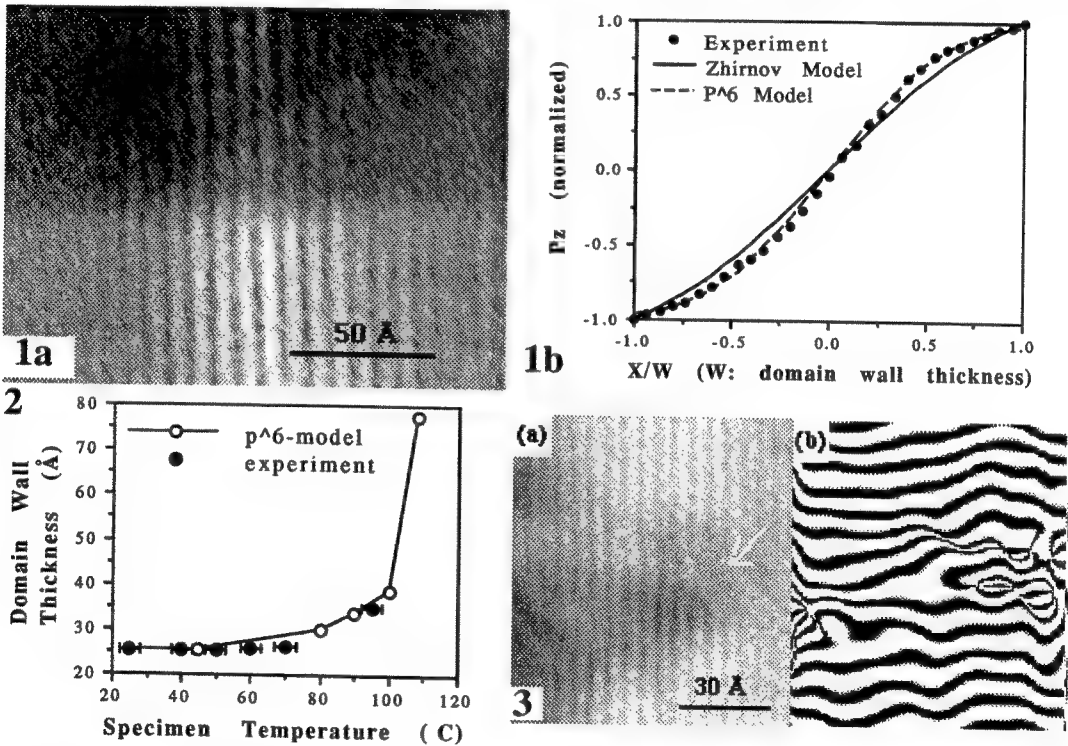


Fig.1(a) Electron hologram of 90° domain wall of BaTiO₃, (b) experimentally measured P_z(x) across wall. Theoretical prediction from Zhirnov model and p⁶-model are superimposed on data. Fig.2 Domain wall thickness change vs specimen temperature (experiment and prediction). Error bars on experimental data show uncertainty of temperature measurement. Fig.3(a) Electron hologram of tip of newly formed 90° domain wall of BaTiO₃ showing anomalous fringe pattern, (b)isopotential contour map.

ELECTRON HOLOGRAPHY OF ELECTROSTATIC FIELDS

D. C. Joy*, X. Zhang, A. Mohan, and B. Cunningham†

EM Facility, University of Tennessee, Knoxville, TN 37996-0810,

*and Oak Ridge National Laboratory, Oak Ridge, TN 37831

†IBM, East Fishkill, Rte 52, Hopewell Junction, NY 12533

Electron Holography allows both the amplitude and phase of a transmitted wavefront to be stored and subsequently recovered by a reconstruction of the hologram. Since both magnetic and electric fields change the phase of an electron wave that passes through them electron holography can therefore be used to directly, and quantitatively, image such fields. Significant experimental applications have already been made of this technique to the study of magnetic fields and materials, and electric fields have been studied in ferroelectric materials.^{1,2} Such a technique has particular value when applied to the study of semiconductor devices since these rely for their operation on the electric fields produced internally at P-N junctions or Shottky barriers. Holographic imaging of these fields will make it possible to accurately find the active regions of junctions as well as making it possible to measure the electrostatic fields that are present. Consider a cross-sectioned P-N junction of thickness t placed normal to the beam (figure 1). The phase shift $\phi(x,y)$ of the transmitted beam relative to a reference beam which passes only through vacuum is given in the phase object approximation by³

$$\phi(x,y) = \left(\frac{\pi}{\lambda E} \right) \int V(x,y,z) dz \quad (1)$$

where x,y are coordinates in the plane of the specimen, and z is along the optic axis. λ is the de Broglie wavelength and E is the accelerating voltage. This integral is computed along the electron path parallel to the optic axis both inside and outside the specimen. The phase shift $\phi(x,y)$ thus stores the potential distribution as projected onto the XY plane. The phase shift from a junction geometry such as that in figure (1) consists of two components. The first comes from the inner potential $V_{in,pot}$ of the sample, which is constant across the sample, and (if the beam is passing through the depletion region) from the barrier potential V_{junc} of the junction, which may vary along the length of the depletion region (equation 2). The second term comes from the external leakage field which extends around the specimen. If the specimen thickness t is much less than the width of the depletion region, a condition which is usually met, then it is this leakage term which dominates.³

$$\phi_{int}(x,y) = \left(\frac{\pi}{\lambda E} \right) \cdot (V_{in,pot} + V_{junc})_{x,y} \cdot t \quad (2)$$

As an illustration figure 2 shows the off-axis hologram, generated at 200keV on an Hitachi HF-2000 field emission gun TEM, and the corresponding computer reconstructed phase image, recorded from a region at the point where a PN junction crosses the edge of a silicon sample. The image has been processed so that contours of equal phase shift are produced, each contour line representing an increment of $\pi/4$ radians. The two-dimensional leakage field, spreading out from the intersection of the edge with the junction region, is clearly visible. Both outside and inside the sample the measured phase shift may then be interpreted from equation (1) to obtain the actual potential distribution. Since the lateral spatial resolution of the reconstructed image can be of the order of a few nanometers, and since phase shifts as small as $\pi/100$ may be measured, this technique offers the ability to probe field distribu-

tion in and around semiconductor devices with unmatched resolution and sensitivity.⁴

References

- (1) Tonomura A, et al., (1982), Phys.Rev. B 25, 6799
- (2) Zhang X, et al, these proceedings.
- (3) Frabboni S, et al., (1985), Phys.Rev.Lett., 55, 2196
- (4) This work was sponsored in part by the Laboratory Directed Research and Development Program of Oak Ridge National Laboratory, managed by Martin Marietta Energy Systems Inc., for the United States Department of Energy under contract DE-AC05-84OR21400

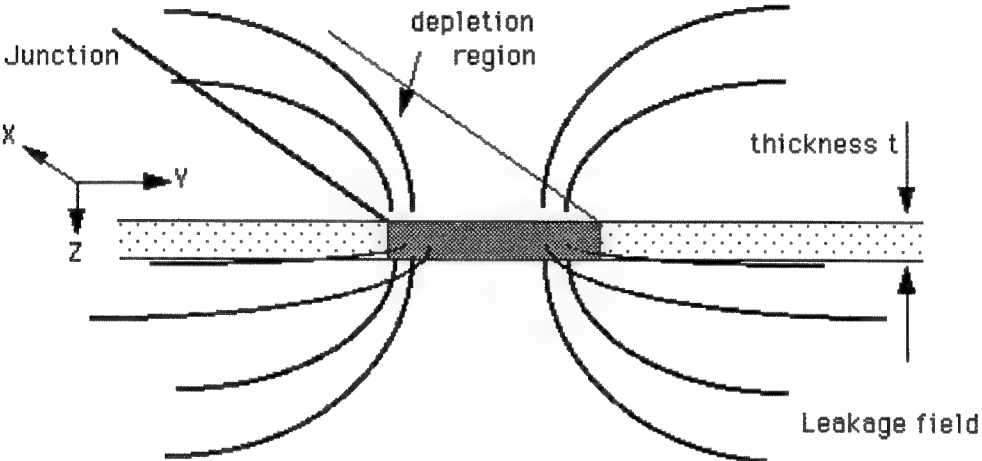


Fig.1 Schematic arrangement of a P-N junction specimen for electron holography, and the position of the depletion layer and leakage fields which give rise to measurable phase shifts in the interferogram.

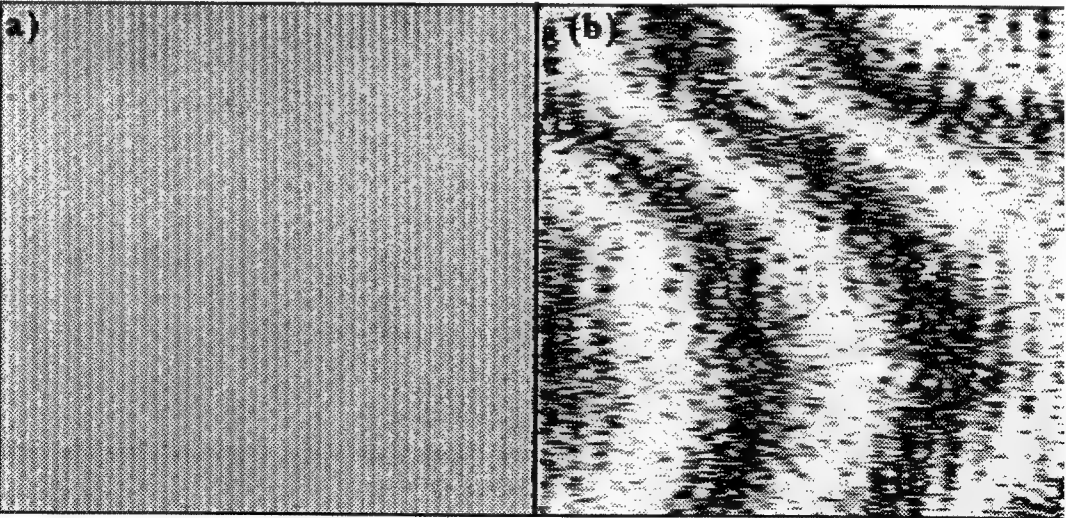


Fig.2 (a) Hologram recorded from P-N junction region in silicon at 200keV on Hitachi HF-2000 FEG TEM. (b) phase image reconstructed from (a) showing iso-potential contours of the leakage field.

ELECTRON HOLOGRAPHY OF VORTEX LATTICES IN SUPERCONDUCTORS

J.E. Bonevich, K. Harada, T. Matsuda, H. Kasai, T. Yoshida, G. Pozzi* and A. Tonomura

Advanced Research Laboratory, Hitachi Ltd., Hatoyama, Saitama 350-03, Japan

*Department of Materials Science, University of Lecce, via Arnesano, 73100 Lecce, Italia

The recent success in observing magnetic vortices in superconductors by means of transmission electron microscopy techniques has opened a new window to investigate the behavior of vortex lattices.¹ We report the first direct observation of 2-D vortex lattices in niobium thin films taking advantage of the high resolution and sensitivity of electron holography.

The experiments were conducted in a 300 keV field emission electron microscope equipped with a cold stage that allows magnetic fields to be applied while the specimen can be maintained from 30 K down to 4.5 K.² The Nb specimen is tilted by 45° to the electron beam and the magnetic field is applied in the horizontal direction. The microscope also has a rotatable electron biprism used to form holograms. The thin (70±20 nm) foil specimens were prepared by chemically polishing 2 mm × 2 mm × 30 μm sections of Nb that had been annealed to ~2000°C in a vacuum of 10⁻⁶ Pa. The electron optical conditions were such that the overall magnification was ~1800× and the hologram carrier fringe spacing referred back to the specimen was ~30nm.

The experimental procedure was to first cool the Nb specimen down to 4.5 K in a field of 100 G. Regions with trapped vortices were then identified by Lorentz microscopy.¹ Once suitable regions were found, holograms were formed. Images were subsequently reconstructed from the holograms, either optically or numerically, as phase amplified interference micrographs. These micrographs indicate the magnetic lines of the force in the specimen projected along the electron beam direction.

A typical interference micrograph, Fig. 1, shows that while the projected magnetic lines of force flow in the direction of the applied magnetic field as a whole, they become locally dense at the circled regions. These regions were found to spatially coincide with the contrast observed in the Lorentz micrograph (Fig. 2). The interference micrograph is 16× phase amplified such that the phase difference between two contours is $\pi/8$. Thus the magnetic flux flowing through each vortex appears to be equivalent to a phase difference of about $\pi/2$. This is the expected phase difference for a single vortex ($\Phi_0 = h/2e$) in a thin superconducting specimen tilted by 45° to the electron beam.³ Furthermore, the vortex core measures about 100 nm in diameter (Fig. 3), indicating that the vortex inner core structure is observed in the interference micrographs.

To fully interpret the experimental results, the vortex lattices were simulated by implementing a flux tube lattice model that considers the effects due to finite core sizes.⁴ The calculated phase differences agreed well with the experimental data and thus confirms that the interference micrographs are sensitive to the phase differences produced by singly quantized vortices.

In summary, we have directly observed projected magnetic lines of force of 2-D vortex lattices in a superconductor by electron holography. The experimental results can be compared with the Lorentz micrographs and have been interpreted by a theoretical model accounting for the finite vortex size.

References

1. K. Harada, et al., *Nature* (1992) 360, 51.
2. J.E. Bonevich, et al., *Phys. Rev. Lett.* (1993), submitted.
3. A. Migliori, G. Pozzi and A. Tonomura, *Ultramicroscopy* (1993) 49, 87.
4. G. Pozzi, J.E. Bonevich and A. Tonomura, *these proceedings*.

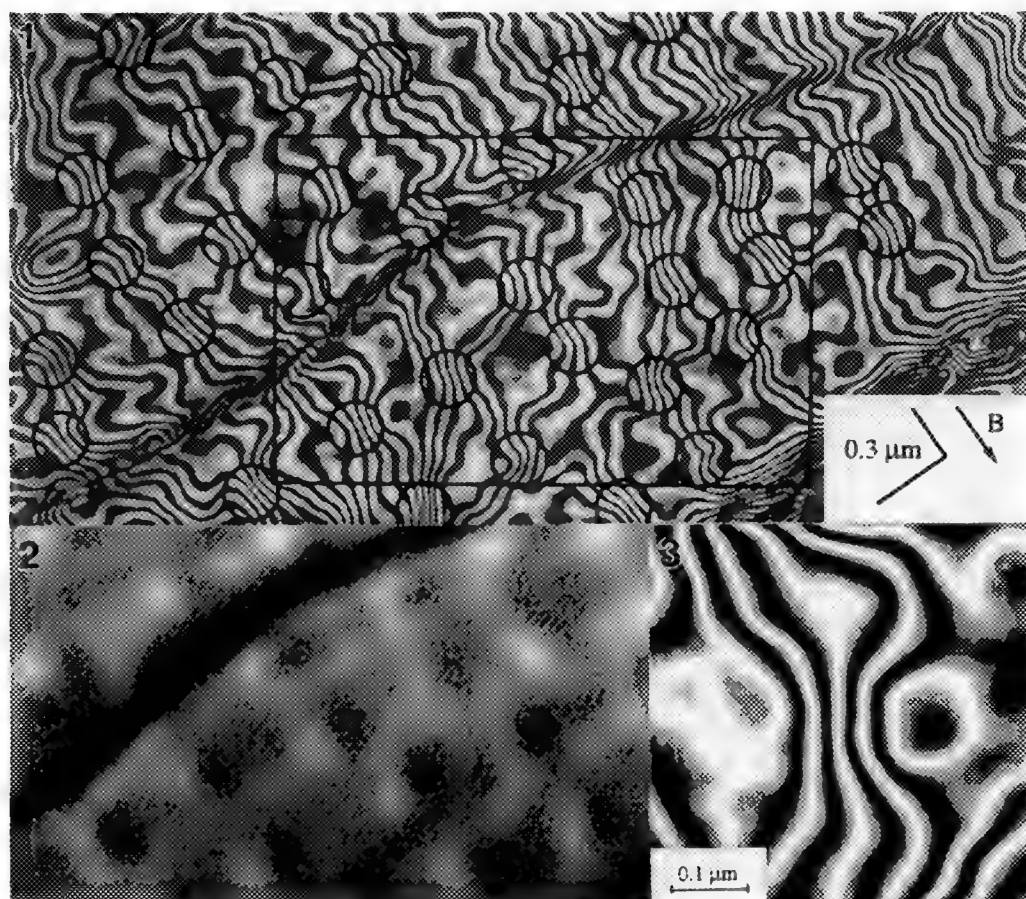


FIG. 1. 16 \times phase amplified contour map of Nb specimen at 4.5 K and 100 G. Contours indicate projected magnetic lines of force and become locally dense at circled regions, i.e. vortex positions. FIG. 2. Corresponding Lorentz micrograph of the boxed region. The phase difference produced by vortices is manifested in a 20 mm defocused plane as adjacent spots of light and dark contrast. FIG. 3. Interference micrograph of single vortex (16 \times phase amplified) where the phase difference (measured from left to right) is 0.55π . The vortex core measures ~ 100 nm in diameter.

TEM OF ELECTRON-BEAM INDUCED CRYSTALLIZATION OF AN AMORPHOUS $\text{AuFe}_{0.3}/\text{Si}$ SPIN-GLASS MULTILAYER

D.A. Howell, L. Hoines, M.A. Crimp, J. Bass, and J.W. Heckman

Center for Fundamental Materials Research, Michigan State University, East Lansing, MI, 48824

The use of thin film multilayers for the study of physical phenomena (e.g. spin-glass dc magnetic susceptibility, giant magnetoresistance, and x-ray reflectivity) has grown recently as the technology for their preparation has improved. The multilayers in this study were produced for an investigation of finite-size effects in a $\text{AuFe}_{0.3}$ spin-glass.¹

We prepared the samples by dc sputtering of a $\text{AuFe}_{0.3}$ alloy and a Si target in an UHV system. The specimen in this investigation had 67 bilayers of 3 nm spin-glass layers alternating with 7 nm amorphous silicon (a-Si) layers on a (001) single-crystal silicon substrate for a total film thickness of 670 nm. Ultrathin cross-sections were prepared by cleaning the thin-film surface in Freon TF and gluing this surface to a clean ground-glass slide with epoxy. We removed the thin-film from its silicon substrate by peeling the substrate from the film which remained on the glass slide. This film was freed from the glass slide by digesting the epoxy with sodium ethoxide in ethanol and then imbedded into Spurr's resin for sectioning to ≈ 70 nm with a 55° diamond knife. Sections were collected on 1000 mesh copper grids and carbon coated. TEM was performed on a Hitachi H-800 TEM operated at 200 keV with a beam current of 10 μA and a 5 μm spot size and a JEOL 100 CX II operated at 120 keV with a 2 μm spot size.

Figure 1a shows the specimen as it appeared prior to the beam induced transformation. The dark layers are believed to be the spin-glass alloy and the lighter layers the amorphous silicon. Direct measurement of diffraction contrast images from finite thickness multilayers containing amorphous silicon layers can give rise to misleading apparent relative layer thicknesses. A High-Angle Annular Dark-Field (HAADF) technique or the method of Donovan must be used for true layer thickness measurements.^{2,3} Figure 1b strongly suggests that the silicon and the spin-glass layers are both amorphous. Figure 2a shows the effect of condensing the beam to cross-over. Once this occurs, darker contrasting material coalesces into 70-300 nm regions, some with boundaries following the initial layering. Figure 2b shows that some of the material has crystallized, giving rise to polycrystalline electron diffraction patterns. Figure 3a is a dark-field image (spot indicated in Figure 3b) of the area in Figure 2a and reveals portions of the material that have crystallized. A feature of the altered specimen is that the apparent thicknesses of the light and dark contrast layers are now reversed. Interestingly, the apparent thicknesses of the light and dark layers are now closer to the intended fabrication parameters. One explanation for the observed images and behavior is possible interfacial mixing of the two materials (spin-glass and silicon) during deposition to form a metastable amorphous silicide (dark layer in Figure 1) that subsequently exsolves during beam modification. Future investigations involving a VG-H501 STEM to analyze unaltered individual layer compositions and altered regions are currently being undertaken.

References:

1. G.G. Kenning et al., *Physical Review*, B42 (1990) 2393.
2. J. Liu et al., *Ultramicroscopy*, 40 (1992) 352.
3. P. Donovan et al., *J. Appl. Phys.*, 69 (1991) 1371.

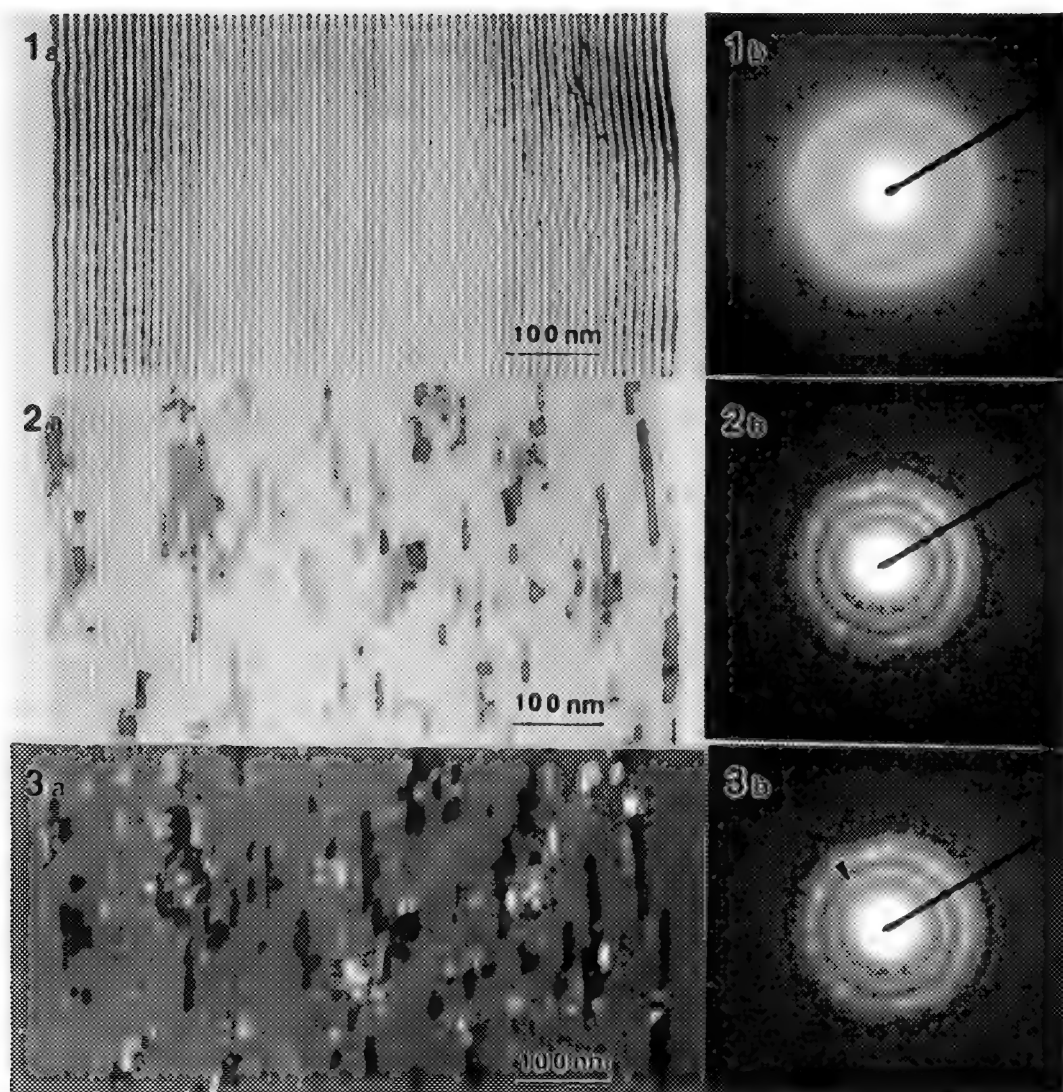


Fig. 1 a) Bright-field TEM image of $\text{AuFe}_{0.9}/\text{Si}$ multilayer before alteration. b) Electron diffraction pattern of unaltered multilayer.

Fig. 2 a) Bright-field TEM image of same multilayer after beam induced transformation. b) Electron diffraction pattern after transformation.

Fig. 3 a) Dark-Field of area in Figure 2. b) Electron diffraction pattern of transformed material with arrow indicating area used to create dark-field image.

ELECTRON-DIFFRACTION STUDIES OF AMORPHOUS CARBON THIN FILMS

David A. Muller*,†

*Electron Microscope Unit, University of Sydney, Sydney 2001, AUSTRALIA

†Current Address: Physics Department, Cornell University, Ithaca NY 14853, USA

The sp^2 rich amorphous carbons have a wide variety of microstructures ranging from flat sheetlike structures such as glassy carbon¹ to highly curved materials² having similar local ordering to the fullerenes. These differences are most apparent in the region of the graphite (0002) reflection of the energy filtered diffracted intensity obtained from these materials (Fig. 1). All these materials consist mainly of threefold coordinated atoms. This accounts for their similar appearance above 0.8 \AA^{-1} . The fullerene curves (b,c) show a string of peaks at distance scales corresponding to the packing of the large spherical and oblate molecules. The beam damaged C_{60} (c) shows an evolution to the sp^2 amorphous carbons as the spherical structure is destroyed although the (220) reflection in fcc C_{60} at 0.2 \AA^{-1} does not disappear completely. This 0.2 \AA^{-1} peak is present in the 1960 data of Kakinoki et. al.³ who grew films in a carbon arc under conditions similar to those needed to form fullerene rich soots. Under normal conditions, a-C produced in a carbon arc (d) lacks the 0.2 \AA^{-1} peak although its radial distribution function matches that from (c) up to 6 \AA so the short range ordering is similar.

A system for collecting energy filtered electron diffraction patterns was developed using a GATAN 666 Parallel EELS (PEELS) mounted beneath a Philips EM430 TEM. In an earlier paper⁴ techniques were described for correcting memory effects and channel to channel gain variations inherent in the diode array. The usable dynamic range of the photodiode array was about a factor of 1000 from the largest to smallest measurable signal. At large scattering angles, the scattering intensity is proportional to the fourth power of the scattering angle so a doubling of the maximum collected scattering angle would require a sixteen fold improvement in dynamic range. The computer controlled acquisition methods allowed dramatic improvements in resolution, dynamic range and acquisition times to be made compared to earlier PEELS⁴ and serial EELS (SEELS)⁵ setups. By automatically selecting an acquisition time appropriate to the signal strength and correcting for nonlinearities arising from charge leakage in the photodiode array of the PEELS at large collection times, a tenfold improvement in the dynamic range was obtained for routine collections. This means that the thermal vibrations which lower the intensity of the diffraction pattern at the large scattering angles cannot be ignored (Fig. 2). Fig.3 shows that the SNR in the reduced intensity function of tetrahedral amorphous carbon obtained using the PEELS system is considerably better than that obtained with the SEELS detector. After further processing the reduced density function of Fig. 4 is obtained. The termination ripple is more pronounced in the SEELS curve.

A simulated annealing technique for generating three-dimensional structural models from the pair correlation function, $g(r)$, was developed. It is a mean field theory in which each pair of atoms is assumed to act independently of the other pairs which have been averaged into a background potential. The partition function of the canonical ensemble can then be written as $Z_N = \prod Z_{ij}$, where it can be shown that Z_{ij} is proportional to $g(r_{ij})$. A physically plausible structure can be obtained by minimizing the approximate Helmholtz free energy $A = A_0 + kT \sum_{ij} \ln[g(r_{ij})]$. The question of uniqueness loses some of its meaning for amorphous materials. As the simulated structure is much smaller than the experimentally measured one, a "correct" solution might be regarded as one which matched some region of the real material. Structural refinement of the C_{60} molecule using the experimentally measured $g(r)$ gives the structure and bond length splittings to 0.02 \AA of the accepted structure. It offers some interesting insights into the classification of amorphous materials by their many-body interactions and should prove to be a more robust fitting routine than a least-squares refinement.⁶

References

1. D.C. Green et. al. in *Properties and Characterisation of Amorphous Carbon Films*, eds, J.J. Pouch and S.A. Alterovitz, Trans Tech, Nedermansdorf **103** (1990).
2. S.J. Townshend et. al. *Phys. Rev. Lett.* **69**(6), p.921 (1992).
3. J. Kakinoki et. al., *Acta Cryst.* **13** 171 and 448 (1960).
4. D.J.H. Cockayne et. al. *Microscopy, Microanalysis, Microstructures* **2** (1991) p359.
5. Cockayne D.J.H. and McKenzie D.R., *Acta. Cryst.* **A44** (1988) p870.
6. The author would like to thank his research advisors David McKenzie and David Cockayne for their guidance. David Muller was supported by an Australian Postgraduate Research Award. Helpful discussions with John Silcox are also acknowledged.

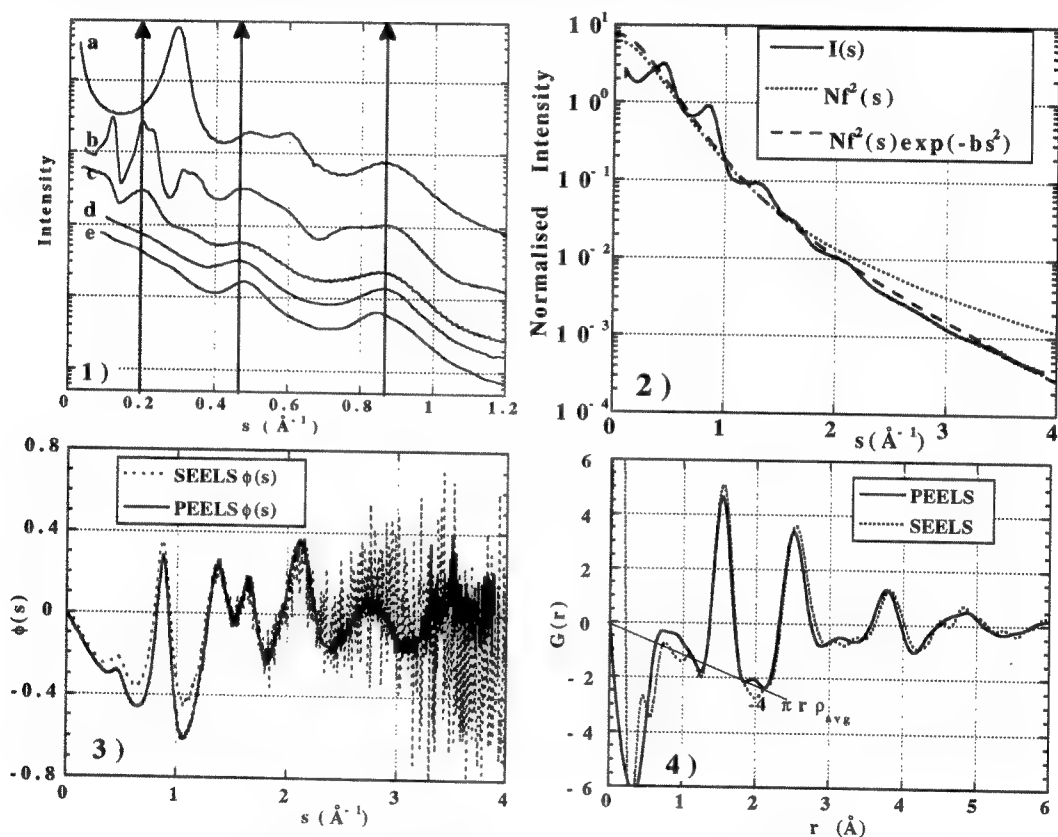


Fig. 1. $I(s)$ for various carbon thin films: a) glassy carbon; b) C_{60} ; c) Beam Damaged C_{60} (immersed in 300kV electron beam for two hours); d) sp^2 a-C (Carbon Arc); e) sp^2 a-C (electron beam). The vertical arrows show the first three diffraction peaks reported by Kakinoki et. al.

Fig. 2. Correction for the Debye-Waller factor is equivalent to replacing the form factor $f(s)$ by $f(s)\exp(-bs^2)$. The two fits are compared to the diffracted intensity $I(s)$ for sp^3 amorphous carbon. Here $b=0.04$ and the scattering vector $s=(2\sin\theta)/\lambda$.

Fig. 3. Comparison of the reduced intensity function for tetrahedral amorphous carbon collected using the SEELS and PEELS methods. The SEELS signal is lost in the noise beyond 2.5 \AA^{-1} .

Fig. 4. Comparison of $G(r)$ obtained by SEELS and PEELS filtering. (from data of Fig. 3.) The peak below 0.5 \AA is the residual of the mismatch between $I(s)$ and the background $f(s)\exp(-bs^2)$.

HREM OF ELECTRON-IRRADIATED SILICAS¹

L.C. Qin

Massachusetts Institute of Technology, Department of Materials Science and Engineering, Cambridge, MA 02139

Silica (SiO₂) crystals exist in various polymorphs which have different densities and different crystal structures, such as quartz, tridymite, and cristobalite, though all of these have in common the network structure which is formed by corner-sharing of SiO₄ tetrahedra. All these structures are sensitive to electron irradiation. Amorphization occurs when they are irradiated by energetic electrons.

In the present study three polymorphs of silica crystals, α -quartz, α -tridymite and α -cristobalite crystals² were used as starting materials. Electron irradiation experiments were carried out *in situ* in the electron microscope. The structural changes of the specimens were monitored using high-resolution electron microscopy (HREM).

The amorphization of α -quartz crystals was found to progress through two morphologies: (a) nucleation and growth of amorphous nuclei with a sharp boundary with the crystalline matrix (figure 1); and (b) crystallinity lost gradually and more uniformly. Figure 2 shows a series of HREM images showing the amorphization of a tridymite crystal. An amorphous region forms first and grows as electron irradiation continues; this is similar to the amorphization process found in electron irradiated α -quartz³. However, it was found that under the same conditions, tridymite transforms more rapidly than quartz. The crystalline-to-amorphous transition process of cristobalite is depicted in figure 3. Cristobalite was found to be the most sensitive to electron irradiation of the three polymorphs and to amorphize most homogeneously.

Fourier analysis of the HREM images has been used to examine the regularities that persist in the intermediate stage of the transformation. Digital Fourier transformation of partially periodic images shows that, as irradiation continues, there is a gradual increase of the diffuse background in the diffractogram that is characteristic of an amorphous structure. Auto-correlation analysis has also been applied to detect any remnant regularities in the images.

Computer simulations of HREM images have been made to assist in quantitative interpretation of the experimental images. Specimen models consist of amorphous clusters embedded in crystalline matrices (*cf.* fig.1) and crystals with amorphous layers (*cf.* figs.2 & 3).

As in quartz, the transformation in tridymite and cristobalite appears to be a radiolytic process. A knock-out mechanism is possible, but dominates only at higher energies⁴. Since the density of the amorphous state is closer to that of cristobalite or tridymite than the density of quartz, the energy required to re-arrange the linkage of the SiO₄ tetrahedra to reach the metamict states, as has been analyzed in terms of topological network connectivities⁵ in these structures, for tridymite or cristobalite is thus expected to be less than that for quartz. This is likely to be one of the reasons for the more rapid transformations in tridymite or cristobalite. It should also be noted that for the specimens of tridymite and cristobalite, since they are prepared from natural mineralogical material, there exists a higher concentration of impurities, which can be the preferred nucleation sites, than for the synthetic quartz specimens. Radial distribution function (RDFs) for the metamict states have also been reconstructed from energy-filtered electron diffraction⁶ and are being used to help characterize the atomic arrangements in the metamict states.

References

1. Research supported by the DOE grant DE-FG02-89ER45396 under the supervision of Professor L.W. Hobbs.
2. Cristobalite (catalog # 128694) and tridymite (catalog # 119881) samples were obtained from Dr. C. Francis of the Harvard Mineralogical Museum.
3. L.W. Hobbs and M.R. Pascucci, *J. Physique* (1980) **41**, C6-237.
4. H. Inui, H. Mori, T. Sakata and H. Fujita, *J. Non-Cryst. Solids* (1992) **116**, 1.
5. C.S. Mariani and L.W. Hobbs, *J. Non-Cryst. Solids* (1990) **119**, 269; **124**, 242.
6. L.C. Qin, A.J. Garratt-Reed and L.W. Hobbs, *Proc. 50th EMSA* (1992) p.350.

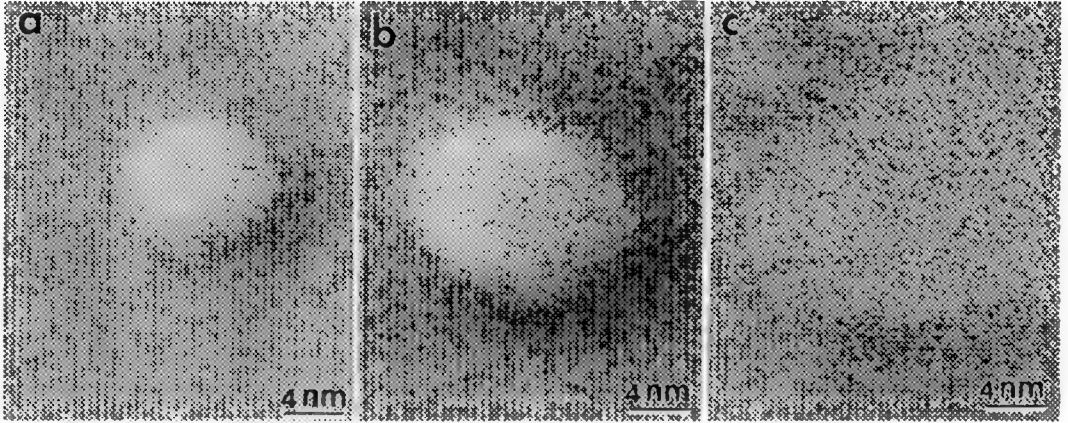


Figure 1. The growth of an amorphous nucleus in α -quartz under electron irradiation: (a) small nucleus forms; (b) its volume expands; and (c) amorphization completes as it intersects with an adjacent uniform amorphization front.

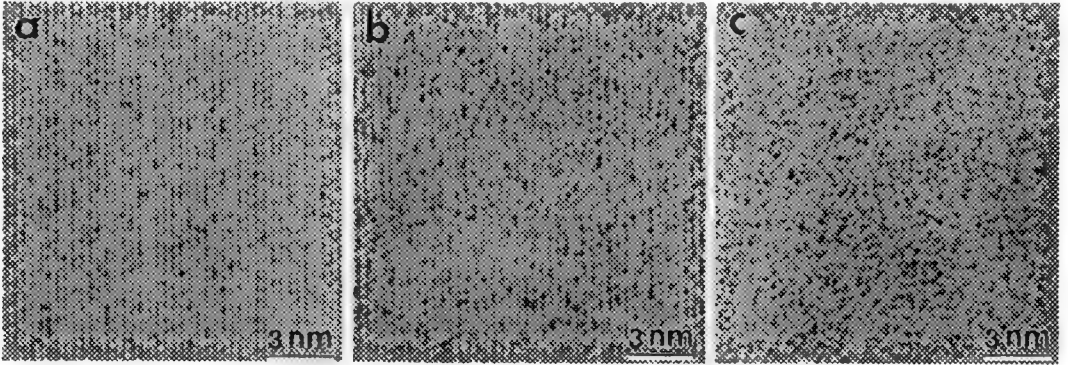


Figure 2. Time-sequence of HREM images showing the amorphization of tridymite under electron irradiation: (a) perfect crystalline lattice image; (b) amorphous region begins to form and grow; and (c) uniform metamict state.

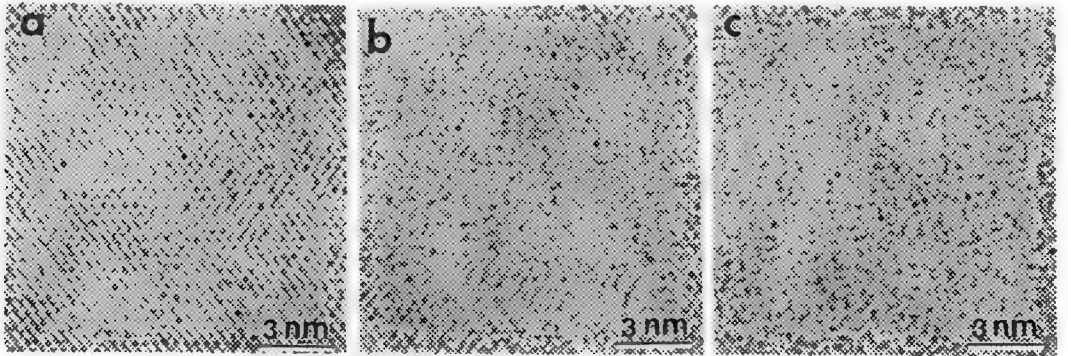


Figure 3. HREM images of the amorphization process of cristobalite under electron irradiation: (a) before amorphization occurs; (b) partially amorphized; and (c) amorphization completed.

HRTEM STUDY OF HEAVY ION IRRADIATION DAMAGE IN $\text{Ca}_2\text{La}_8(\text{SiO}_4)_6\text{O}_2$

L.M. Wang¹ and W.J. Weber²

¹Department of Earth and Planetary Sciences, University of New Mexico, Albuquerque, NM 87131

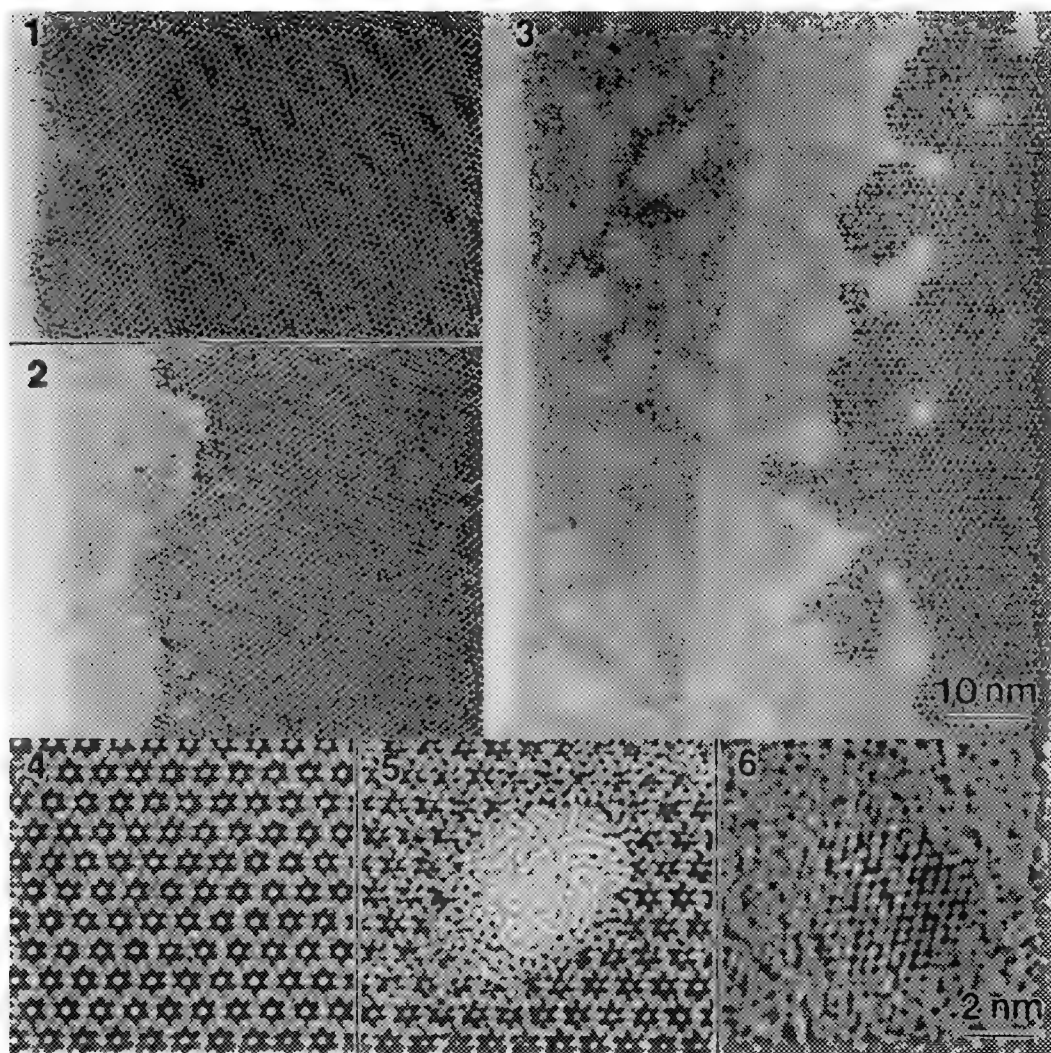
²Department of Materials Science, Pacific Northwest Laboratory, Richland, WA 99352

Radiation effects in complex ceramic materials, including the crystalline phases with the apatite structure are of interest to the materials science, geoscience and biomedical communities. It has been shown by in situ TEM experiments that these materials can easily be rendered amorphous under heavy ion irradiations.^{1,2} Detailed study at atomic level using HRTEM on this crystalline to aperiodic transition is necessary for the fundamental understanding of the process. The results reported below are from a systematic HRTEM study on 1.5 MeV Kr ion irradiated synthetic $\text{Ca}_2\text{La}_8(\text{SiO}_4)_6\text{O}_2$.

The TEM samples were prepared from (0001) thin foils by Ar ion-milling which was finished at 3.5 kV and 13°. As shown in fig. 1, the width of the amorphous rim at the sample edge after ion milling is less than 2 nanometers. The pre-thinned TEM samples were irradiated at room temperature with 1.5 MeV Kr ions in the HVEM-Tandem Facility at Argonne National Laboratory.³ The HRTEM was performed using several state-of-the-art 200 keV microscopes after the ion irradiation. Fig. 2 is a micrograph taken from the sample irradiated to a dose of 0.5 ion/nm². At this dose, the width of amorphous rim has increased by ~10 nm indicating a thin layer of amorphous material has formed. Adjacent to the amorphous rim, brighter spots of the size of 1 to 2 nm can be observed, however, the lattice fringes were not disrupted within these spots. No irradiation damage was seen in the thicker regions. According to TRIM⁴ calculations, the passage of 1.5 MeV Kr ions leaves displacement cascades of 1 to 5 nm in dimensions in a 10 nm thick $\text{Ca}_2\text{La}_8(\text{SiO}_4)_6\text{O}_2$ foil, smaller size in a thinner foil. Also, previous studies has suggested that amorphization in this material may occur directly in the displacement cascades². The brighter spots adjacent to the amorphous rim in fig. 2 are believed to be the results of displacement cascades which are sandwiched in a crystalline matrix. Image simulation of structures containing various amount of amorphous volumes has displayed similar contrast and has shown that when the fraction of the amorphous material is less than 30% of the total sample thickness, the lattice fringes may not be disrupted^{5,6}. When the Kr dose is increased to 1 ion/nm², the thickness of the amorphous material in the sample increased. The amorphous rim in the very thin region has extended to about 30 nm from the specimen edge (fig. 3). However, at the thicker region, "perfect" structural image can still be obtained because the amorphous fraction in thickness is still small in the region (fig. 4). At intermediate thickness, isolated spots where lattice fringes are disrupted can be observed due to the overlapping of the displacement cascades through the thickness.(fig. 5). Also, nanocrystallites nucleated within displacement cascades are observed at the very thin region where the material has mostly become amorphous (fig. 6). One important conclusion of this study is that the HRTEM image of radiation damage varies greatly with the sample thickness even after an uniform dose of irradiation, one must use the images from the same thickness for comparison studies on the dose dependence of damage structure.

References

1. L.M. Wang and R.C. Ewing, Material Research Society Bulletin XVII (5) (1992) 38.
2. W.J. Weber and L.M. Wang, Mat. Res. Sym. Proc. 279 (1993), in press.
3. C.W. Allen et al., Nucl. Instr. and Meth. B40/41 (1989) 553.
4. J.F. Ziegler, J.P. Biersack and U. Littmark, The stopping and Range of Ions in Solids (Pergamon Press, New York, 1985).
5. M.L. Miller and R.C. Ewing, Ultramicroscopy 48 (1993) 203.
6. L.M. Wang, M.L. Miller and R.C. Ewing, Ultramicroscopy (1993), in press.
7. HRTEM was completed at the demonstration centers of Philips, JEOL, Topcon and Hitachi in the Netherlands and Japan. The assistance and contribution of M.T. Otten and J.G. Bakker (on a Philips CM20UT), M. Suzuki and M. Kawasaki (on a JEM 2010), K. Moriyama (on a Topcon 002B) and T. Tamori (on a Hitachi H-8100) are gratefully appreciated. This work is supported by the US DoE/BES under Contract DE-AC06-76RLO 1830.



- FIG. 1.— HRTEM micrograph of an as-ion-milled $\text{Ca}_2\text{La}_8(\text{SiO}_4)_6\text{O}_2$ sample. Note, the width of the "amorphous rim" at the edge (on the left) is < 2 nm.
- FIG. 2.— HRTEM micrograph of a $\text{Ca}_2\text{La}_8(\text{SiO}_4)_6\text{O}_2$ sample after 1.5 MeV Kr ion irradiation to a dose of 0.5 ion/nm^2 at room temperature.
- FIG. 3.— HRTEM micrograph of a $\text{Ca}_2\text{La}_8(\text{SiO}_4)_6\text{O}_2$ sample after 1.5 MeV Kr ion irradiation to a dose of 1 ion/nm^2 at room temperature.
- FIG. 4.— HRTEM micrograph from the thicker region of the $\text{Ca}_2\text{La}_8(\text{SiO}_4)_6\text{O}_2$ sample shown in Fig. 3 (right side). Note, the irradiation damages are not observed.
- FIG. 5.— HRTEM micrograph from a region of intermediate thickness of the same sample shown in Figs. 3 and 4. Overlapping of displacement cascades through the sample thickness caused the disruption of the lattice fringes in the center of the micrograph.
- FIG. 6.— HRTEM micrograph from a very thin region of the same sample shown in Figs. 3, 4 and 5 (left side of Fig. 3). A newly nucleated crystallite with the size of a displacement cascade is observed in an "amorphous" matrix.

RADIATION DAMAGE IN ION-IRRADIATED PYROLYTIC GRAPHITE

E.A. Kenik, D.F. Pedraza, and S.P. Withrow†

Metals and Ceramics Division, †Solid State Division, Oak Ridge National Laboratory, Oak Ridge, TN 37831-6376

Several grades of graphite are used in nuclear applications; as moderators in fission reactors, primary fuel containment in high temperature gas-cooled reactors, and plasma facing materials in fusion reactors. Whereas high temperature ($>800^{\circ}\text{C}$) radiation damage response is reasonably well understood, the low temperature response is less well understood, including amorphization under irradiation. This study examined this response for ion-irradiated, highly-oriented pyrolytic graphite (HOPG). Electron transparent flakes of HOPG were prepared by repeated cleavage. Folding grids were used to hold the flakes during ion irradiation and electron microscopy. Specimens were irradiated with either 35 or 165 keV carbon or 300 keV xenon ions to fluences up to 1×10^{16} and 3×10^{15} ions/cm², respectively, at nominal temperatures from room temperature to 600°C . The low energy carbon and xenon ions were selected to give similar ion ranges (~ 84 nm). The range of the 165 keV carbon ions was 330 nm. Microscopy was performed either on a Philips CM12 or a Philips EM400T/FEG equipped with a Gatan 666 parallel-detection electron energy loss spectrometry (PEELS) system.

Fig. 1 shows the microstructure of HOPG as irradiated with 1.7×10^{15} carbon ions/cm² (165 keV) at room temperature. With slight tilting of the specimen, it was possible to expose an area of the specimen which had been shadowed by a grid bar on the ion incident side. This permitted side-by-side examination of irradiated and unirradiated regions of HOPG with similar thickness, orientation, and original microstructure. Fig. 2(a) gives the selected-area diffraction pattern (SADP) from the irradiated area shown in Fig. 1, which exhibits broadened single crystal reflections. In a higher dose specimen, diffuse rings become visible [Fig. 2(b)], indicating the amorphization of the HOPG. The single crystal reflections decrease in intensity and eventually disappear as the diffuse rings become dominant. Attendant with this change was the gradual decrease in contrast of bend and thickness contours. At room temperature the dose required for complete amorphization is $\sim 3 \times 10^{15}$ ions/cm² for xenon and $> 5 \times 10^{15}$ ions/cm² for 165 keV carbon. The higher amorphization dose for carbon irradiation results from the lower recoil energy deposited per carbon ion relative to that per xenon ion. At higher irradiation temperatures, the dose required for amorphization increases; such that at 600°C a specimen irradiated with xenon remains predominantly crystalline up to 3×10^{15} ions/cm², with only slight evidence of amorphization.

Diffraction patterns of the partially amorphized HOPG exhibited unusual behavior upon specimen tilting; the broadened single reflections continuously changed positions perpendicular to the tilt axis. Starting from the symmetric basal zone, the net of single crystal reflections elongated in a continuous fashion consistent with the presence of strong 0001 reirods. As a result of the inhomogeneous deposition of damage energy by ions as a function of depth, the amorphization of the HOPG varies along the ion range (i.e.; depth in the specimen). Fig. 3 shows SADPs from two areas of different thickness in a specimen irradiated to 1×10^{16} ions/cm² with 35 keV carbon ions. In the thin area, both broadened spots and diffuse rings are present. As thickness increases, the relative spot intensity decreases until the spots are not visible, indicating that regions further along the ion range have little or no crystallinity. Measurement of plasmon energies by PEELS in these same regions indicated an irradiation-induced decrease in the density of valence electrons (i.e.; decreased atomic density by $\sim 12\%$, which is near the density difference between graphite and amorphous carbons). There are attendant changes in the carbon K-edges (Fig. 4). Both the π^* and σ^* peaks are broadened and decreased in intensity for the

irradiated HOPG. The decrease in the π^* peak relative to the entire carbon K-edge is indicative of a reduction in sp^2 bonding during the irradiation-induced amorphization.¹

Reference

1. Research sponsored by the Office of Fusion Energy and the Division of Materials Sciences, U.S. Department of Energy under contract DE-AC05-84OR21400 with Martin Marietta Energy Systems, Inc.

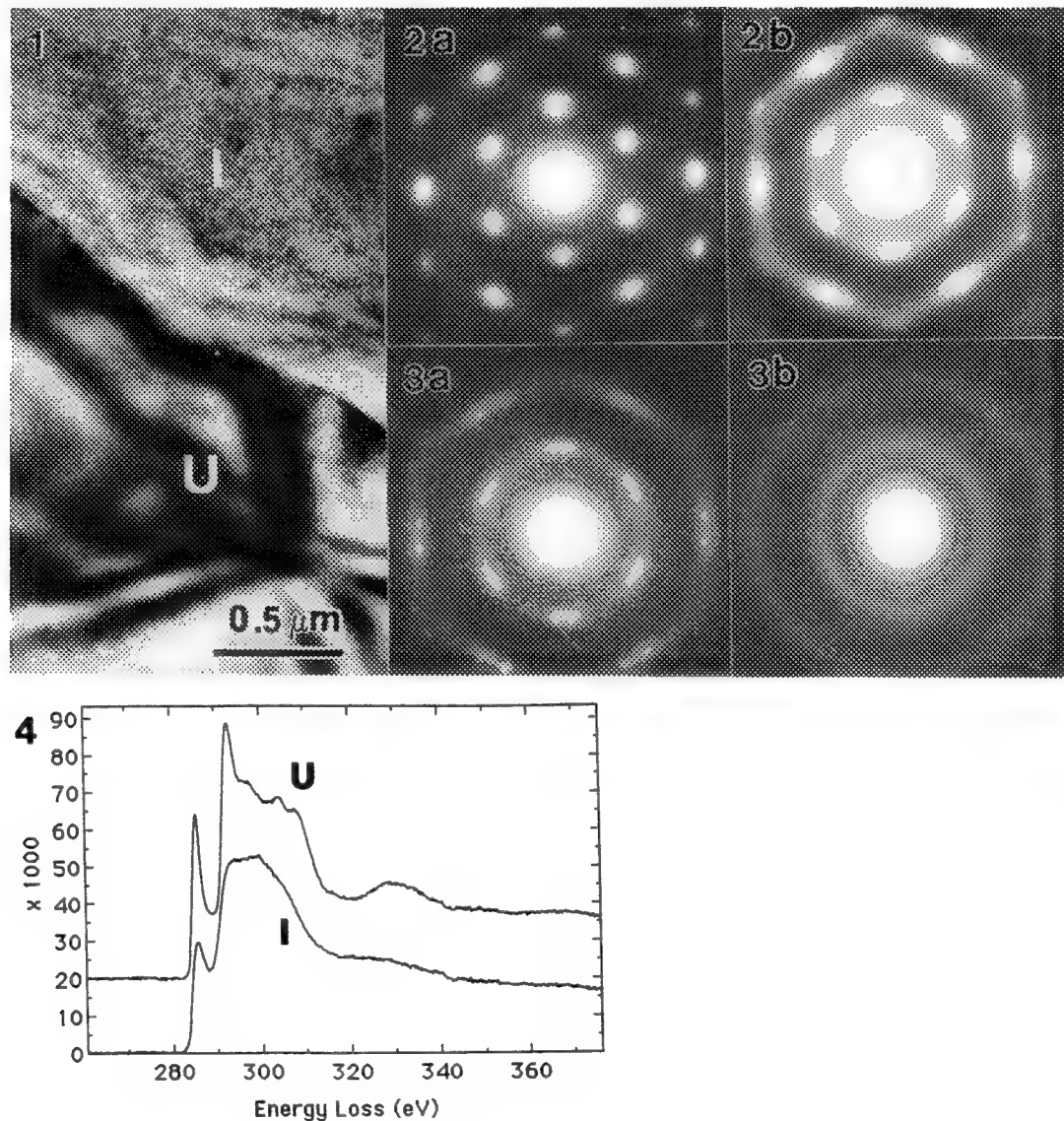


FIG. 1.—Adjacent irradiated (I) and unirradiated (U) HOPG; 1.7×10^{15} carbon ions/cm² at 165 keV. FIG. 2.—SADPs of a) irradiated area in Fig. 1 and b) area irradiated to 5×10^{15} carbon ions/cm² at 165 keV. FIG. 3.—SADPs of a) thin ($t/\lambda \sim 0.3$) region and b) thick ($t/\lambda \sim 0.8$) region of HOPG irradiated to 1×10^{16} carbon ions/cm² at 35 keV. FIG. 4.—Background-stripped, single scattering C K-edges from unirradiated (U) HOPG and HOPG irradiated (I) to 1×10^{16} carbon ions/cm² at 35 keV; $t/\lambda \sim 0.8$ for both spectra.

ORIGIN OF THE DEFECT STRUCTURES IN OXYGEN-IMPLANTED SILICON-ON-INSULATOR MATERIAL

D. Venables, S.J. Krause, J.D. Lee, J.C. Park and P. Roitman*

Department of Chemical, Bio and Materials Engineering, Arizona State University, Tempe, AZ 85287

* National Institute of Standards and Technology, Gaithersburg, MD 20899

Silicon-on-insulator material fabricated by high-dose oxygen implantation (known as SIMOX) has been used for high speed and radiation hard devices and is under consideration for use in low power applications.[1] However, a continuing problem has been crystalline defects in the top silicon layer.[2] SIMOX is fabricated by two distinct methods: a single oxygen implant to a dose of $1.8 \times 10^{18} \text{ cm}^{-2}$ followed by a high-temperature anneal ($\geq 1300^\circ\text{C}$, 4-6 hr) or by multiple lower dose implants ($\sim 6 \times 10^{17} \text{ cm}^{-2}$) with high-temperature anneals after each implant. To date, there has been no systematic comparison of the defect structures produced by these two fabrication methods. Therefore, we have compared the defect structure and densities in multiple vs. single implant wafers. In this paper we describe the origin and characteristics of the defect structures in SIMOX and show how their densities are controlled by the processing method and conditions.

Silicon (100) wafers were implanted in a high current implanter at $\sim 620^\circ\text{C}$ to doses of 1.8×10^{18} or $0.6/0.6/0.6 \times 10^{18} \text{ cm}^{-2}$ and annealed at 1325°C , 4 hr in 0.5% or 5% O_2 in Ar. Cross-section (XTEM) and plan-view (PTM) samples were studied with bright field and weak beam dark field techniques in a transmission electron microscope operating at 200 keV.

The results indicate that the defects in SIMOX can be conveniently placed in three categories: through-thickness defects (TTDs) which thread from the wafer surface to the buried oxide; partial-thickness defects (PTDs) which extend up from the buried oxide only partially into the top silicon layer; and interface-vicinity defects which occur at the upper buried oxide interface. All three defect types occur in both single and multiple implant material, however, at varying densities. The dominant defects in single implant material are TTDs that occur in pairs at a density of $\sim 10^6 \text{ cm}^{-2}$. Figure 1 illustrates the formation of these TTD pairs. They originate from large, extrinsic, prismatic $1/2\langle 110 \rangle$ dislocation half-loops that form during the implantation process by stress-assisted dislocation climb.[3] The half-loops expand further into the top silicon layer during subsequent annealing, although segments of some of the dislocations become pinned by SiO_2 precipitates. Eventually the half-loops intersect the buried oxide, thus creating a pair of TTDs with identical total Burgers vectors. At temperatures between 1000 and 1100°C , these dislocations dissociate into Shockley partials bounding a narrow stacking fault so that the final defect structure consists of a pair of dissociated dislocations. This dissociation reaction can occur on two $\{111\}$ glide planes and therefore each defect in the pair often consists of two segments dissociated onto different glide planes.

The formation of partial thickness defects is illustrated in Figure 2. These defects consist of narrow stacking faults pinned to residual precipitates at one end, and to the buried oxide at the other end. The large residual precipitates arise during annealing as a result of a preferential precipitation process on as-implanted defects known as multiply-faulted defects. The preferentially nucleated precipitates grow larger than any others in the top silicon layer and can survive into the late stages of annealing at high temperature.[4] When the precipitates dissolve, most of these defects are unstable and anneal out. However, if two narrow stacking faults intersect one another at the end of the precipitate dissolution process, a stable defect configuration may result. The third defect type in SIMOX occurs when the narrow stacking faults pinned to a residual precipitate are less than a critical length ($\sim 530\text{\AA}$). Our calculations [5] show that it is then energetically favorable for them to transform to a partially or fully formed stacking fault pyramid (SFP) at the buried oxide interface (see Figure 3). These SFPs consist of a pyramid of stacking faults on four $\{111\}$ planes with stair rod dislocations along the intersection of the faults. SFPs are more common in multiple ($\sim 10^6 \text{ cm}^{-2}$) than in single implant material ($< 10^5 \text{ cm}^{-2}$). This difference in SFP density occurs because the residual precipitates are closer to the buried oxide after the third and final implant in multiple implant material, and thus the narrow stacking faults are shorter than the critical length for the transformation to SFPs.

In summary, the three major defect types in SIMOX are through-thickness defect (TTDs) pairs, partial-thickness defects (PTDs) and, at the buried oxide interface, stacking fault pyramids (SFPs). All three defect types occur in both multiple and single implant material, however, at varying densities. Single implant material is dominated by $\sim 10^6 \text{ cm}^{-2}$ TTDs and contains PTDs and SFPs at densities $< 10^5 \text{ cm}^{-2}$. In contrast, multiple implant material is dominated by $\sim 10^6 \text{ cm}^{-2}$ SFPs and contains PTDs at densities of 10^5 to 10^6 cm^{-2} and TTDs at densities $\leq 10^4 \text{ cm}^{-2}$. This improved understanding of defect origins in SIMOX should continue to contribute to the development of low-defect-density processing methods.

REFERENCES

1. G.W. Cullen and M.T. Duffy, ECS Proc. **90-6**, 10 (1990).
2. D.G. Plattetter and T.F. Cheek, IEEE Trans. Nuc. Sci. **35**, 1350 (1988).
3. D. Venables and K.S. Jones, Nuc. Inst. Meth B, in press.
4. J.C. Park, J.D. Lee, D. Venables, S.J. Krause and P. Roitman, MRS Proc. **279** (1993), in press.
5. J.D. Lee, J.C. Park, D. Venables, S.J. Krause and P. Roitman, submitted to Appl. Phys. Lett.
6. Support by NSF grant #DMR8901370, DNA grant #DNA-IACRO-88-800, NIST, and staff support and use of the National Center for High Resolution Electron Microscopy, ASU, under NSF grant #DMR-9115680 is acknowledged.

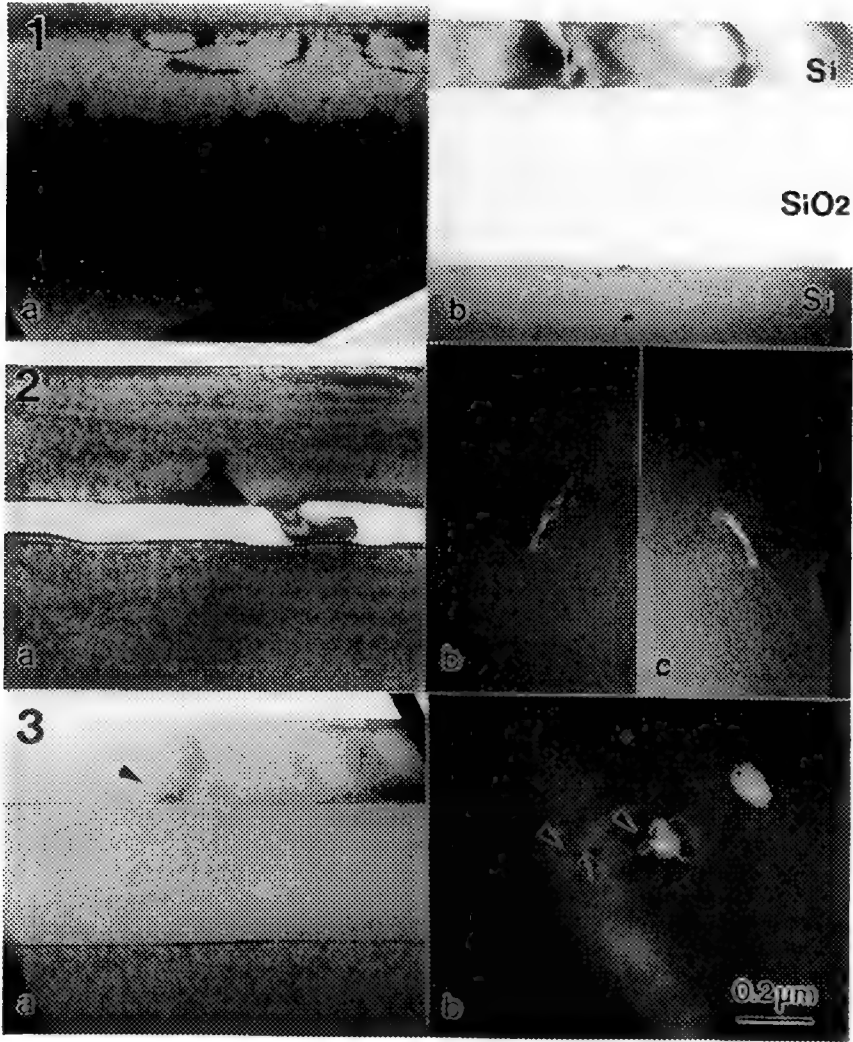


Fig 1. XTEMs of single implant material: a) as-implanted half-loops; b) through-thickness defect pair after annealing.
Fig 2. Partial-thickness defects in multiple implant material after first implant/anneal: a) XTEM; b) and c) PTEM.
Fig 3. Partially and fully formed stacking fault pyramids in multiple implant wafer after final anneal: a) XTEM; b) PTEM.

DETERIORATION OF POLYSILICON/ GATE-OXIDE STRUCTURES UPON H₂ ANNEALING

N. David Theodore and Merit Hung*

Motorola Inc., Materials Technology Center, MD-M360, 2200 W. Broadway Rd., Mesa, AZ 85202

*Motorola Inc., Advanced Custom Technologies, MD-M350, 2200 W. Broadway Rd., Mesa, AZ 85202

Silicon device-technology makes extensive use of polysilicon layers for capacitors¹, contact-materials², thin-film diodes, transistors and resistors¹. In metal-oxide-semiconductor field-effect transistors (MOSFETs) polysilicon is used as the gate electrode on top of a thin gate-oxide layer. The microstructure and stability of the polysilicon and gate-oxide layers can strongly influence electrical behavior of the transistors. Any microstructural deterioration that occurs as a result of processing can result in reduced charge-to-breakdown and lowered breakdown voltages. It is known that interfacial oxides inadvertently present at interfaces of silicon/polysilicon structures break-up as the structures are annealed.^{3,4} Whereas agglomeration of oxide is beneficial in some structures, in MOSFETs such deterioration would be disastrous. The stability of polysilicon/ gate-oxide structures for various processing conditions likely to be used during device-fabrication needs to be characterized. The present study investigates the thermal stability of polysilicon gate-electrode/ gate-oxide structures annealed in a hydrogen ambient at temperatures varying from 800°C to 1050°C.

The starting material consisted of n-type <001> 10-20 Ω-cm phosphorus doped Czochralski silicon substrates. After a standard RCA clean, dry-thermal oxidation was performed at 950°C to form a 10nm gate-oxide. Polysilicon layers (~50nm thick) were then deposited upon the gate-oxide using chemical-vapor deposition at 620°C. Annealing was performed in a H₂ ambient at 800°C, 950°C, 1000°C and 1050°C for ten minutes. After the anneal, 40nm of silicon nitride was deposited on top of the polysilicon layers to protect the structures during subsequent specimen preparation. Cross-section transmission electron-microscopy (XTEM) specimens were made by cleaving strips of annealed wafers, glueing these strips face-to-face, grinding and dimpling in a <110> direction. Argon ion-milling was performed at 5 keV to obtain electron-transparent material at the region of interest. A JEOL 200CX transmission electron microscope (TEM) was used for analysis. The TEM was operated at 200 kV.

Figure 1 presents an XTEM micrograph obtained from a polysilicon/ oxide/ substrate-Si sample annealed at 800°C for 10 minutes in hydrogen. The structure is intact; polysilicon and gate-oxide are both quite uniform. Figure 2 presents an XTEM image of a wafer annealed at 950°C for 10 minutes in H₂. Once again, the gate oxide and polysilicon layers appear intact. Figures 3-4 present the microstructures of polysilicon/ gate-oxide/ silicon annealed at 1000°C and 1050°C respectively, for 10 minutes in H₂. In both cases, the oxide layer is no longer continuous. Gaps have appeared in the gate oxide. These gaps have allowed polysilicon to come into contact with underlying Si-substrate. Recrystallization of the polysilicon has occurred with the substrate-Si acting as a seed for epitaxial recrystallization. The gate oxide itself is extremely non-uniform. If this extent of deterioration were to occur in a MOSFET, the device would cease to function electrically. It is relevant to note that in regions where the oxide has disappeared, the polysilicon top layer has dropped, losing co-planarity with polysilicon still present upon oxide. The experimental results indicate that for anneal temperatures above 950°C polysilicon and gate-oxide have been consumed by some process. The only explanation that correlates with data from the literature is the reaction (in a low-oxygen ambient) between silicon-dioxide and silicon to produce volatile silicon-monoxide⁵: $\text{Si} + \text{SiO}_2 \rightarrow 2\text{SiO}$. This reaction has been observed to cause pitting of silicon wafers at high temperatures and in low-oxygen ambients. Pitting occurs due to localized consumption of Si. The formation of SiO can occur at temperatures greater than about 900°C. In the present study, experimental results suggest that SiO can escape as a gas via grain boundaries in polysilicon. It is relevant to note that nitride layers present on top of polysilicon (Figs. 1-4) were deposited onto the structures after the H₂ anneal. There was no nitride present during the anneal to cap the polysilicon layers and to prevent diffusion of SiO up grain boundaries (followed by escape of SiO into the ambient). The formation of SiO occurs at triple points between polysilicon grains and oxide. As polysilicon and SiO₂ are consumed, a small void forms at the triple point. The void then grows along the polysilicon/ silicon interface due to SiO formation at the Si/SiO₂ edge in the void. Internal surface diffusion of silicon atoms (on the internal-surface of the void) can also provide silicon for the reaction to continue. When the void is large enough, polysilicon slumps down onto the SiO₂. This sequence of events occurs until gate-oxide is consumed and polysilicon breaks through to contact the substrate-Si. Being now aware of this phenomenon, it is necessary to maintain anneal-cycles for device fabrication at temperatures <950°C (for ten-minute H₂ anneals), or to use a different anneal ambient.

References

1. S. Inoue et al, IEDM Tech. Dig. 31 (1989).
2. T. Kamins, Polycrystalline Silicon for IC applications (Kluwer Academic Publishers, Boston, 1988).

3. J.C. Bravman et al, J. Appl. Phys., 57, 2779 (1985).
 4. Q. Wolstenholme et al, J. Appl. Phys., 61, 225 (1986).
 5. A. Ishizaka and Y. Shiraki, J. Electrochem. Soc. 133, 667 (1986).

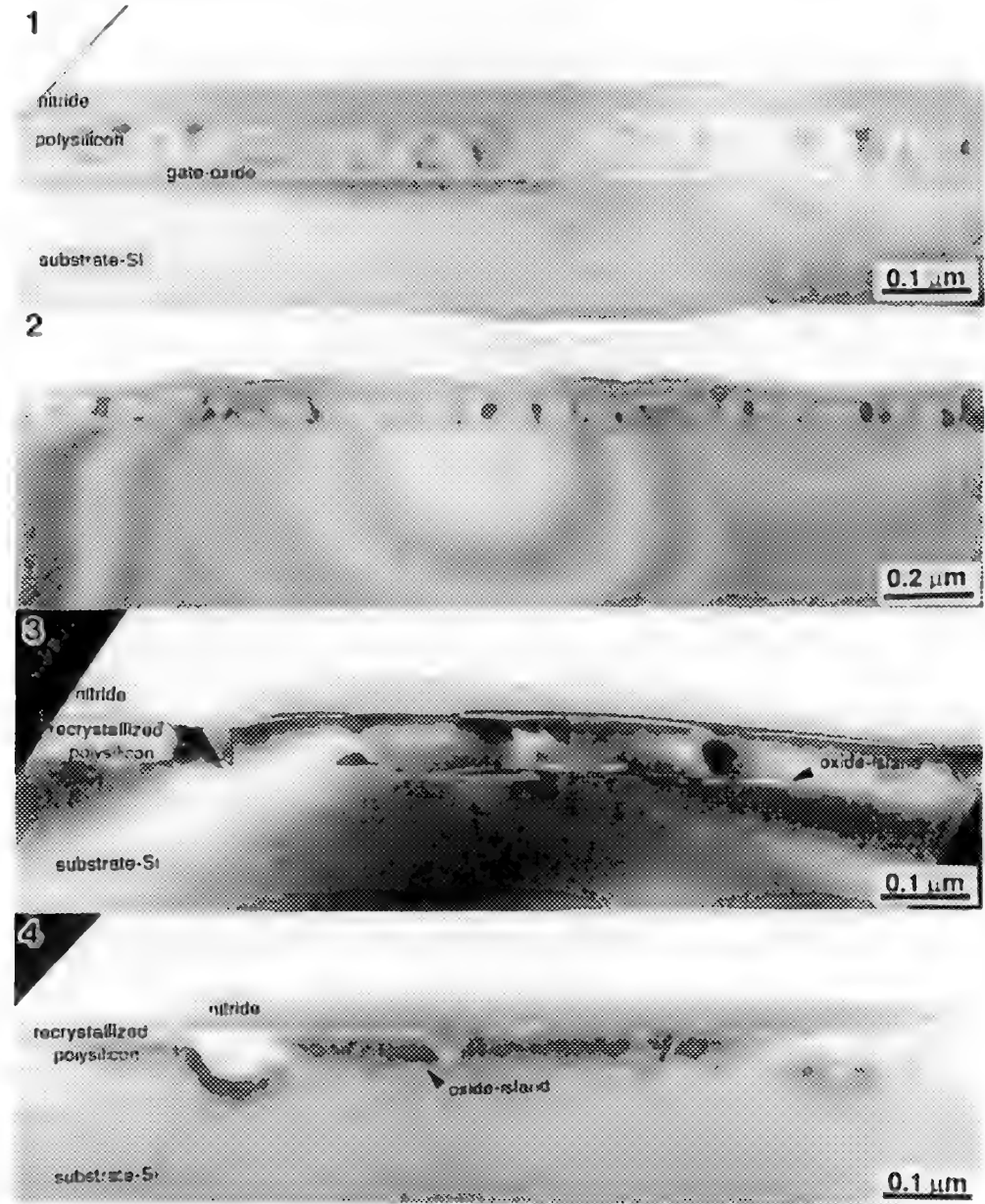


Fig. 1 XTEM micrograph showing polysilicon/ oxide/ Si annealed at 800°C (10 minutes, H₂ anneal).
 Fig. 2 XTEM micrograph showing polysilicon/ oxide/ Si annealed at 950°C (10 minutes, H₂ anneal).
 Fig. 3 XTEM micrograph showing polysilicon/ oxide/ Si annealed at 1000°C (10 minutes, H₂ anneal).
 Fig. 4 XTEM micrograph showing polysilicon/ oxide/ Si annealed at 1050°C (10 minutes, H₂ anneal).

IMPLANT-INDUCED STRAIN-RELAXATION IN SiGe/Si LAYERS

N. David Theodore and Gordon Tam*

Motorola Inc., Materials Technology Center, MD-M360, 2200 W. Broadway Rd., Mesa, AZ 85202

*Motorola Inc., Advanced Custom Technologies, MD-M350, 2200 W. Broadway Rd., Mesa, AZ 85202

SiGe is being extensively investigated for use in heterojunction bipolar-transistors (HBT) and high-speed integrated circuits.^{1,2} SiGe is typically used as an epitaxial base material in HBTs. To obtain extremely high-performance bipolar-transistors it is necessary to reduce the extrinsic base-resistance. This can be done by increasing the base-doping or by widening the base link-region by ion implantation. A problem that arises however with the use of implantation is that blanket implants have been found to enhance strain-relaxation of SiGe/Si.³ Strain relaxation will cause the bandgap-difference between Si and SiGe to decrease; this difference is maximum for a strained SiGe layer. The electrical benefits of using SiGe/Si arise largely from the presence of a significant bandgap-difference across the SiGe/Si interface. Strain relaxation reduces this benefit. Furthermore, once misfit or threading dislocations result (during strain-relaxation), the defects can give rise to recombination-generation in depletion regions of the device; high electrical leakage currents result. It is relevant therefore to understand the interaction between ion-implantation and strain-relaxation in SiGe/Si structures. The present study investigates the lateral interaction between implant damage and unimplanted strained epi-Si/SiGe/Si-substrate structures.

Epitaxial Si/SiGe/Si layers were grown by chemical vapor deposition (CVD), and were doped in-situ with $1 \times 10^{19} \text{ cm}^{-3}$ boron. The structures consisted of (i) 50nm epi-Si/ 40nm $\text{Si}_{0.9}\text{Ge}_{0.1}$ / Si-substrate, and (ii) 50nm epi-Si/ 50nm $\text{Si}_{1-x}\text{Ge}_x$ (x: 0-0.1 linearly graded)/ Si-substrate. A 190nm oxide-nitride stack was deposited on the layer, then patterned in strips to act as an implant mask. The wafers were then implanted with 20 keV- $3.7 \times 10^{15} \text{ cm}^{-2}$ boron. After capping with plasma-enhanced CVD oxide, the wafers were rapid-thermal annealed (RTA) at 1000°C for 30 seconds. Plan-view transmission electron microscopy (TEM) specimens were then made from patterned regions of the wafer. TEM analysis was performed using a JEOL 200CX TEM operating at 200 kV.

Figure 1 presents a schematic of the SiGe/Si layers together with implant configurations. Implanted regions are present in strips parallel to $[110]$ directions. Adjacent strips have not been exposed to the implant. Figure 2 presents a plan-view TEM (PTM) micrograph showing an unimplanted epi-Si/ $\text{Si}_{0.9}\text{Ge}_{0.1}$ / Si structure annealed at 1000°C for 30 seconds. Dark horizontal bands are regions where a thin oxide remains from an oxide-nitride stack intended for later use as an implant mask. Misfit dislocations are absent from the structure. It is relevant to note that SiGe layer thicknesses used in the present study (~50nm) are greater than calculated equilibrium critical-thicknesses for misfit-dislocation formation (~30nm). Figure 3 is a PTM micrograph showing an implanted epi-Si/ $\text{Si}_{0.9}\text{Ge}_{0.1}$ / Si structure RTA annealed at 1000°C for 30 seconds. Dark horizontal bands (top and bottom of micrograph) correspond to regions protected by the implant mask. The bright region across the center of the micrographs has been exposed to the 20 keV- $3.7 \times 10^{15} \text{ cm}^{-2}$ boron implant. Extensive damage is visible within the implanted region. The damage arises from implant-induced point-defects coalescing to form dislocation loops. When the loop density is very high, loop segments interact with one another to form dislocation tangles within the implanted region. At edges between implanted and unimplanted regions, extended dislocation half-loops are evident. Two types of loops are present: type "A" defects have long dislocation segments parallel to $[110]$ directions; type "B" defects have long dislocation-segments parallel to $[1\bar{1}0]$ directions. These defects are indicated in Fig. 3. Graded SiGe structures show similar defect-geometries. Figure 4 is a schematic that shows configurations for type "B" half-loops. These defects lie upon (111) glide planes for "B"-defects at the top edge of the implanted region in Fig. 3, and upon $(\bar{1}\bar{1}1)$ glide planes for "B"-defects at the bottom edge of the implanted region. Type "A" defects lie upon $(\bar{1}\bar{1}1)$ and (111) glide planes. It is evident from micrographs (e.g., Fig. 3) that type "A" and type "B" defects originate from the implanted region and propagate out into unimplanted regions on $\{111\}$ glide planes. The defects expand downwards until they reach a SiGe/Si interface, at which stage they expand horizontally leaving a segment of misfit dislocation at the SiGe/Si interface. Since the glide loops originate at the implanted region, this means that implant loops have to act as, or form dislocation sources. It has been seen in the past that an implant loop can transform to create a Frank-Read dislocation source by having a Shockley partial sweep across the loop. The driving force for formation of dislocation glide-loops is the presence of strain at the SiGe/Si interfaces. The strain provides the impetus to overcome an energy barrier for the formation of dislocation-sources from implant loops. Once a glide half-loop reaches a SiGe/Si interface, the energy required to form additional lengths of misfit dislocation at the interface (by extension of glide-loop segments) is counter-balanced by the SiGe strain energy relieved by the extending misfit-dislocation. The fact that extended misfit-dislocation segments are seen at the ends of glide-loops in Fig. 3 indicates that the strain-energy relieved per unit length of misfit dislocation is greater than the dislocation line-energy (per unit length of misfit-dislocation). There is hence a positive driving force for indefinite extension of the glide loops to produce misfit dislocations

extending across the whole wafer. Figure 3 shows that type "B" defects propagate only ~150nm into the unimplanted region; these defects do not extend all the way across the wafer despite the presence of a positive driving force for such propagation to occur. This behavior indicates that the kinetics of misfit-dislocation propagation limits the extent of defect-propagation. The extent of such propagation should be determined by the velocity-time product for the misfit/threading dislocation. Under normal circumstances, the velocity-time product for the high temperature anneal used in this study should be sufficient for misfit-dislocation segments to propagate across the wafer. The fact that such propagation does not occur indicates that some phenomenon is occurring to hinder dislocation motion. It is known that dislocation immobility can result from the formation of Cottrell (impurity atom) atmospheres around glide dislocations. In the present case, boron from the implanted region can diffuse down glide-dislocations, form atmospheres around the defects and hinder their motion. Such hindrance will then result in limited propagation of misfit dislocations into unimplanted SiGe/Si regions. Knowledge of this behavior is important for determining implant/structure geometries for SiGe-based transistors.

References

1. G.L. Patton et al, IEEE EDL 11(4), 171 (1990).
2. J.D. Cressler et al, IEEE EDL 12(4), 166 (1991).
3. R. Hull et al, Appl. Phys. Lett. 56, 2445 (1990).

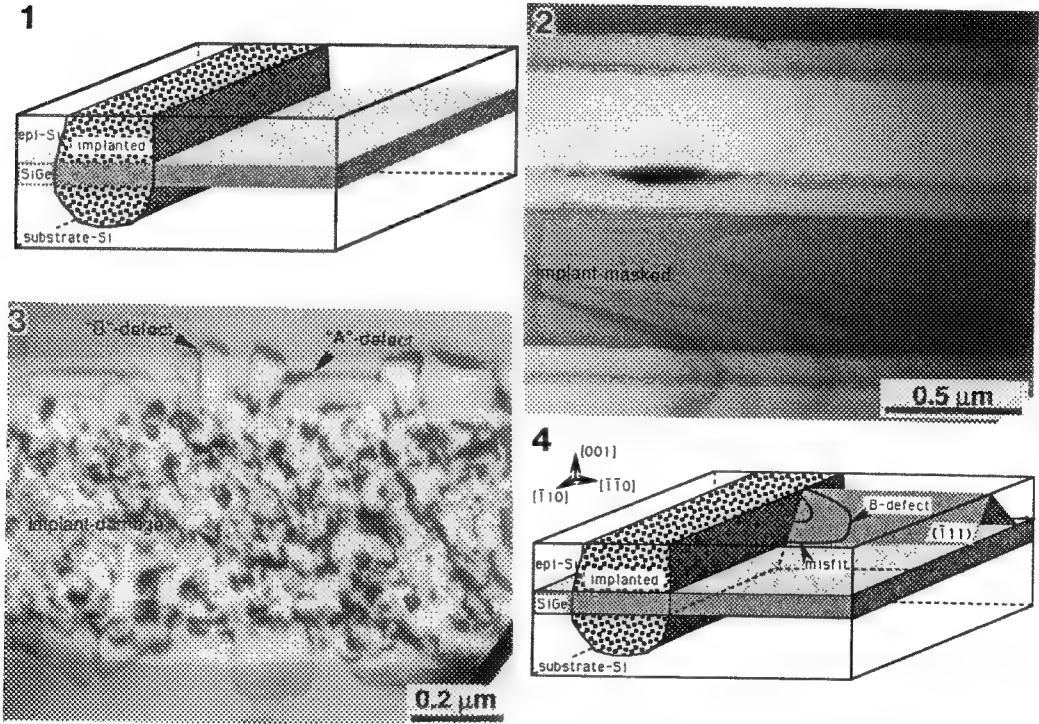


Fig. 1 Schematic showing epi-Si/SiGe/Si layers and implant configurations.
 Fig. 2 PTEM micrograph showing unimplanted epi-Si/Si_{0.9}Ge_{0.1}/Si structure (RTA 1000°C-30")
 Fig. 3 PTEM micrograph showing epi-Si/Si_{0.9}Ge_{0.1}/Si structure implanted in strips (RTA 1000°C-30").
 Fig. 4 Schematic showing configuration of type "B" defects.

DRY-ETCH-INDUCED DAMAGE IN GaAs INVESTIGATED VIA TEM

M.W. Cole and G.F. McLane

Army Research Laboratory, Ft. Monmouth, NJ 07703

Plasma-assisted etching is an important III-V semiconductor fabrication technique for patterning device structures on the nanometer scale with high accuracy. The quality of the processed surface is of primary importance for most electronic applications. It is well documented that reactive ion etching (RIE), with its high self-biases, usually incurs material damage via ion bombardment which ultimately limits device performance.¹ Magnetron ion etching (MIE) is an attractive alternative to RIE. Specifically, MIE has a lower sheath voltage than RIE and the discharge contains low to moderate energy ions, both of which allow wafer processing with less ion-induced damage.² This study investigated the nature and extent of near surface disorder resultant from MIE with freon-12 (CCl_2F_2) via cross-sectional transmission electron microscopy (TEM). The effect of residual damage on device performance was evaluated via Schottky diode measurements. The GaAs wafers were etched under the following conditions:

- 300W (.32W/cm²), 90V dc self bias, 4 min., 4mTorr 20 sccm freon-12 discharge
 - 400W (.43W/cm²), 115V dc self bias, 4 min., 4 mTorr 20 sccm freon-12 discharge
 - 500W (.53W/cm²), 140V dc self bias, 4 min., 4 mTorr 20 sccm freon-12 discharge
- MIE samples were prepared for cross-sectional TEM analysis by mechanical thinning and ion milling. Microscopy was performed using a JEOL 2010 TEM operated at 200 KeV. Surface morphology micrographs were taken using multibeam bright-field imaging with seven beams included within the objective aperture. The samples were tilted such that the beam direction was parallel to the [110] zone axis. This reduced contrast effects at the surface, and optimized topography images. Weak beam dark-field images, using g_{220} ($S=g$) conditions, were used to identify the nature, density and depth of penetration of the surface defects.

The variations in power levels were reflected in both the structural and electrical properties of the etched GaAs. The surface morphology at the highest power density was 2.5 times rougher than that of the lowest power density (fig. 1 & 2). Specifically, the peak-to-valley distances were $\sim 90\text{\AA}$ for .53W/cm², 65\AA for .43W/cm² and 36\AA for .32W/cm². The full width at half maximum (FWHM) of the surface peaks were ~ 97 , 196 and 357 \AA respectively. Lattice damage consisted of small, $\sim 30\text{\AA}$ dislocation loops. The depth of residual damage was $\sim 700\text{\AA}$ at the higher power level with most of the defects concentrated in the upper 100\AA . The defect density was $10^{10}/\text{cm}^2$. The mid power level exhibited a defect penetration depth of $\sim 1100\text{\AA}$ with a density of $3.5 \times 10^9/\text{cm}^2$. At the lowest power level the defects extended deeper into the GaAs wafer (3000\AA) and were uniformly distributed with a defect density of $1.3 \times 10^9/\text{cm}^2$. These results suggest that the higher power level results in a higher defect density, however, the faster etch rate (accompanying the higher power level) results in a trade off between damage

accumulation (defect depth) and etch rate. Etch induced surface region defects, which affect device performance, are manifested in deviations of ideality factor (n) and Schottky barrier height (ϕ_B) values from an unetched control sample. The deviations of these parameters were 2% for the low and 6% for the high power level, with respect to the control sample. These deviations imply a degradation of electrical properties with increasing power conditions. Results of GaAs wafers RIE in CCl_2F_2 , using process parameters similar to those used in this study, were reported by Pearton et al.³ We compared our worse case MIE results ($.53\text{W}/\text{cm}^2$) to that of Pearton et al.³ Specifically, the RIE conditions were $.56\text{W}/\text{cm}^2$, 380V dc self-bias, 4 min. The surface morphology of the RIE GaAs was rougher than that of the MIE GaAs (fig. 1) by a factor of 20 (fig. 3). Peak to valley distances were $\sim 1900\text{\AA}$, and the FWHM of the surface peaks varied between 1000 and 1500\AA . Fig. 4 shows a band of defects, 100\AA dislocation loops, centered $\sim 400\text{\AA}$ beneath the surface. The density of the dislocation loops was $\sim \text{mid } 10^9/\text{cm}^2$. The deviations in Schottky barrier height and ideality factor, with respect to the unetched sample was $\sim 7\%$. Our results suggest that MIE of GaAs with freon-12 at the lower power levels yielded smoother surfaces, less damage and superior electrical properties vs. MIE at the higher power level. Furthermore, the material and electrical quality of MIE surfaces were superior to those etched via RIE at equivalent process parameters.

References

1. M.W. Cole et al., Scanning 14 (1992) 31.
2. M. Meyyappan et al., J. Vac. Sci. Technol. A 10 (1992) 1147.
3. S.J. Pearton et al., J. Appl. Phys. 65 (1989) 1281.

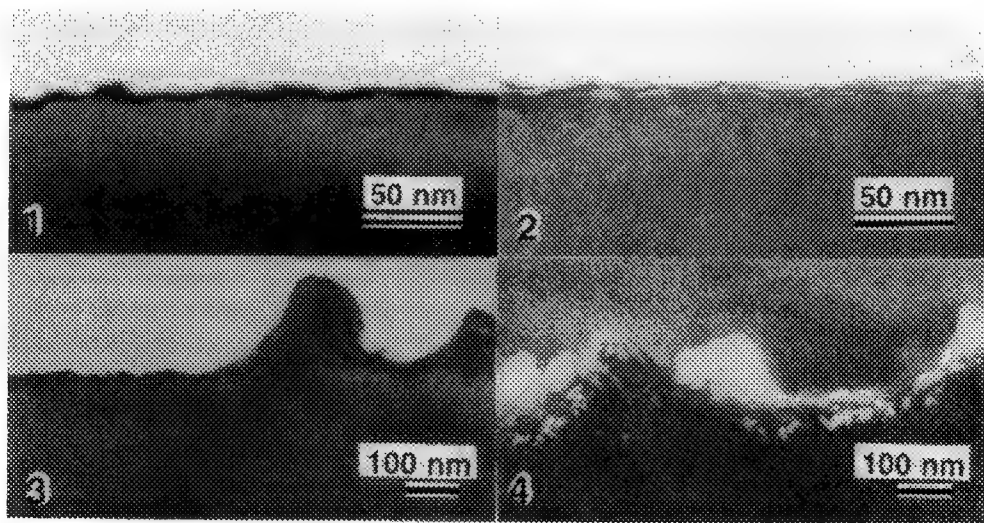


Fig. 1. BF TEM micrograph showing the high power level MIE surface morphology.
 Fig. 2. BF TEM micrograph showing the low power level MIE surface morphology.
 Fig. 3. BF TEM micrograph showing the RIE surface morphology.
 Fig. 4. DF TEM micrograph showing the RIE induced defects.

DIRECT OBSERVATION OF Fe-Al-Zn TERNARY INTERMETALLIC COMPOUND AND ITS TRANSFORMATION DURING THE EARLY STAGE OF HOT-DIP GALVANIZING

C. S. Lin, W. A. Chiou, and M. Meshii

Department of Materials Science and Engineering
Northwestern University, Evanston, IL 60208

The galvanized steel sheets have received ever increased attention because of their excellent post-painting corrosion resistance and good weldability. However, its powdering and flaking tendency during press forming processes strongly impairs its performance. In order to optimize the properties of galvanneal coatings, it is critical to control the reaction rate between solid iron and molten zinc.

In commercial galvannealing line, aluminum is added to zinc bath to retard the diffusion rate between iron and zinc by the formation of a thin layer of Al intermetallic compound on the surface of steel at initial hot-dip galvanizing. However, the form of this compound and its transformation are still speculated [1,2,3]. In this paper, we report the direct observations of this compound and its transformation.

The specimens were prepared in a hot-dip simulator in which the steel was galvanized in the zinc bath containing 0.14 wt% of Al at a temperature of 480 °C for 5 seconds and was quenched by liquid nitrogen. Cross sectional TEM specimens were prepared by a modified "sandwich" technique. The specimens were examined in Hitachi-700 TEM. Selected area diffraction patterns(SADP) were recorded using the same camera length. Chemical analysis was performed on Hitachi-2000 field emission AEM.

Several intermetallic phases in the coatings were observed in the TEM study. Fig.1 shows the bright-field image and SADP of FeAl₂ phase which is located about 1μm away from the coating and substrate interface. The δ phase was observed very near the interface between coating and substrate(Fig.2). Fig.3(a) and (b) show the bright-field image and the EDS spectrum from Fig.3(a). Another phase, either Fe-Al-Zn intermetallic compound or zinc-bearing Fe-Al intermetallic compound was observed(Fig.3(a)) as illustrated by the EDS spectrum(Fig.3(b)). SAD patterns(Fig.4) were taken from the same region shown in Fig.3. These two SADP can not be matched with the published structure of any Fe-Zn or Fe-Al binary compounds. It is therefore assigned as an Fe-Al-Zn ternary intermetallic compound. The interesting feature of these patterns is the faint parallel dot lines between fundamental spots as indicated by the arrows. Fig.5 shows the [1010] SADP of the δ phase. The high density of diffraction spots along [0001] direction is due to the large lattice constant (57Å). The faint parallel dot lines in Fig.4 are also probably due to the dense diffraction spots along [0001] direction. This suggests that the δ phase nucleates in the Fe-Al-Zn ternary compounds during hot-dip galvanizing process. This result is consistent with the Fe-Al-Zn phase diagram at 450 °C[2]. On the basis of above results, it appears that the so-called inhibition layer, Fe-Al-Zn ternary intermetallic compound, forms first and becomes a mixture of FeAl₂ and δ phases during a short period of hot-dip galvanizing [4].

References

1. M. Saito, Y. Uchida, T. Kittaka, Y. Hirose and Y. Hisamatsu, J. ISIJ, 77, (1991), 947.
2. M. Uredniek and J.S. Kirkaldy, Z. Met., 64, (1973), 899.
3. A.R.P. Ghuman and J.I. Goldstein, Met. Trans., 2, (1971), 2903.
4. This research is supported by AISI through the Northwestern University Steel Resource Center. The samples are provided by Inland Steel.

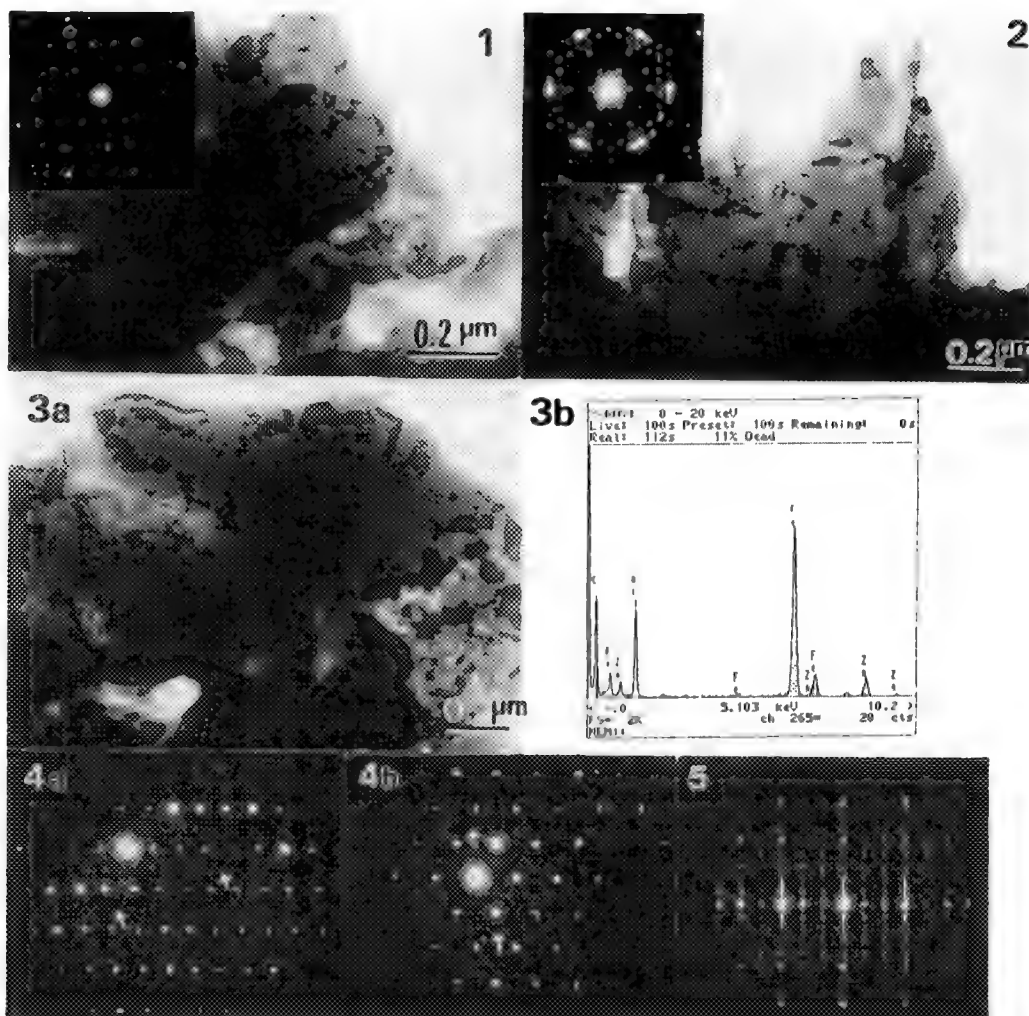


Fig.1 Bright-field image of FeAl_2 compound and its $[001]$ zone axis SADP.

Fig.2 Bright-field image of δ phase and its $[0001]$ zone axis SADP.

Fig.3 Bright-field image of Fe-Al-Zn ternary intermetallic compound and the EDS spectrum.

Fig.4 SADP from the same region shown in Fig.3.

Fig.5 SADP of δ phase in $[1010]$ zone axis.

TEM SAMPLE PREPARATION OF WEAR-TESTED ROOM-TEMPERATURE PULSED-LASER-DEPOSITED THIN FILMS OF MoS₂ BY ULTRAMICROTOMY

Pamela F. Lloyd and Scott D. Walck*

UES, Inc., 4401 Dayton-Xenia Rd., Dayton, OH 45432

*Materials Directorate, Wright Laboratory, WL/MLBT, Wright Patterson AFB, OH 45433-7750

Pulsed laser deposition (PLD) is a novel technique for the deposition of tribological thin films.¹ MoS₂ is the archetypical solid lubricant material for aerospace applications. It provides a low coefficient of friction from cryogenic temperatures to about 350°C and can be used in ultra high vacuum environments. The TEM is ideally suited for studying the microstructural and tribo-chemical changes that occur during wear. The normal cross sectional TEM sample preparation method does not work well because the material's lubricity causes the sandwich to separate. Walck et al. deposited MoS₂ through a mesh mask which gave suitable results for as-deposited films,² but the discontinuous nature of the film is unsuitable for wear-testing. To investigate wear-tested, room temperature (RT) PLD MoS₂ films, the sample preparation technique of Heuer and Howitt was adapted.³

Two 300 nm thick films were deposited on single crystal NaCl substrates. One was wear-tested on a ball-on-disk tribometer using a 30 gm load at 150 rpm for one minute, and subsequently coated with a heavy layer of evaporated gold. A 0.001 in. diameter gold wire was placed in the wear track as a marker as seen in Figure 1. A thick layer of carbon was evaporated on the as-deposited sample. The samples were embedded using Spurr's resin. An end mill was used to expose the NaCl which was dissolved using distilled water. After desiccating, the volume is filled with Spurr's resin again. The samples were microtomed using an AO/Reichert Ultracut with a Diatome 55° materials science diamond knife at a speed of 0.4-0.6 mm/sec producing films having thickness of 70-90 nm. They were collected on Athene 400 mesh thin bar copper grids. Prior to examination in the TEM, the samples were coated with a layer of carbon. This coating and the earlier surface coatings help prevent the resin from causing the near surface region of the MoS₂ film to separate from the rest of the sample when exposed to the electron beam. Figure 2 shows an SEM image of the prepared sample. Although the gold wire curls when cut, it is still useful as a marker. Figure 3 and 4 show the as-deposited and wear-tested films, respectively. The films are amorphous. The spherical particles are crystalline and are due to molten droplets being ejected from the target from laser-induced recoil pressure. Although the gold coating worked well in the wear-tested region of the sample, it separated from the untested areas of the film even before examination in the TEM. It appears that it separates cleanly from the MoS₂ surface because the areas of the gold coated samples not wear-tested are very similar in appearance to the film seen in Figure 3. Figure 5 is a montage of the as-deposited thin film which illustrates the quality and the amount of thin area which can be achieved with this sample preparation technique.

The arrows in Figure 4 indicate the near surface region which appear modified by wear. Previous Raman Spectroscopy results on wear-tested RT-PLD films showed that crystalline MoS₂ was produced.⁴ Electron diffraction results from the near-surface areas of the wear-tested samples did not show any crystallinity. It is possible that a small amount is present and the dark contrast of the gold is obscuring it in the image. It is also possible that the light load and short test period did not allow the crystallization of the MoS₂. Future applications of this technique will only use carbon coating.

REFERENCES

1. M. S. Donley et al., *Lecture Notes on Physics*, 389, New York, Springer-Verlag, (1991): 271.
2. S. D. Walck et al., submitted to *J. Mater. Res.*, 1992.
3. J. P. Heuer and D. G. Howitt, *J. Electron Microsc. Techn.*, (1990)14, 79.
4. N. T. McDevitt et al., *Wear*, in press, 1993.

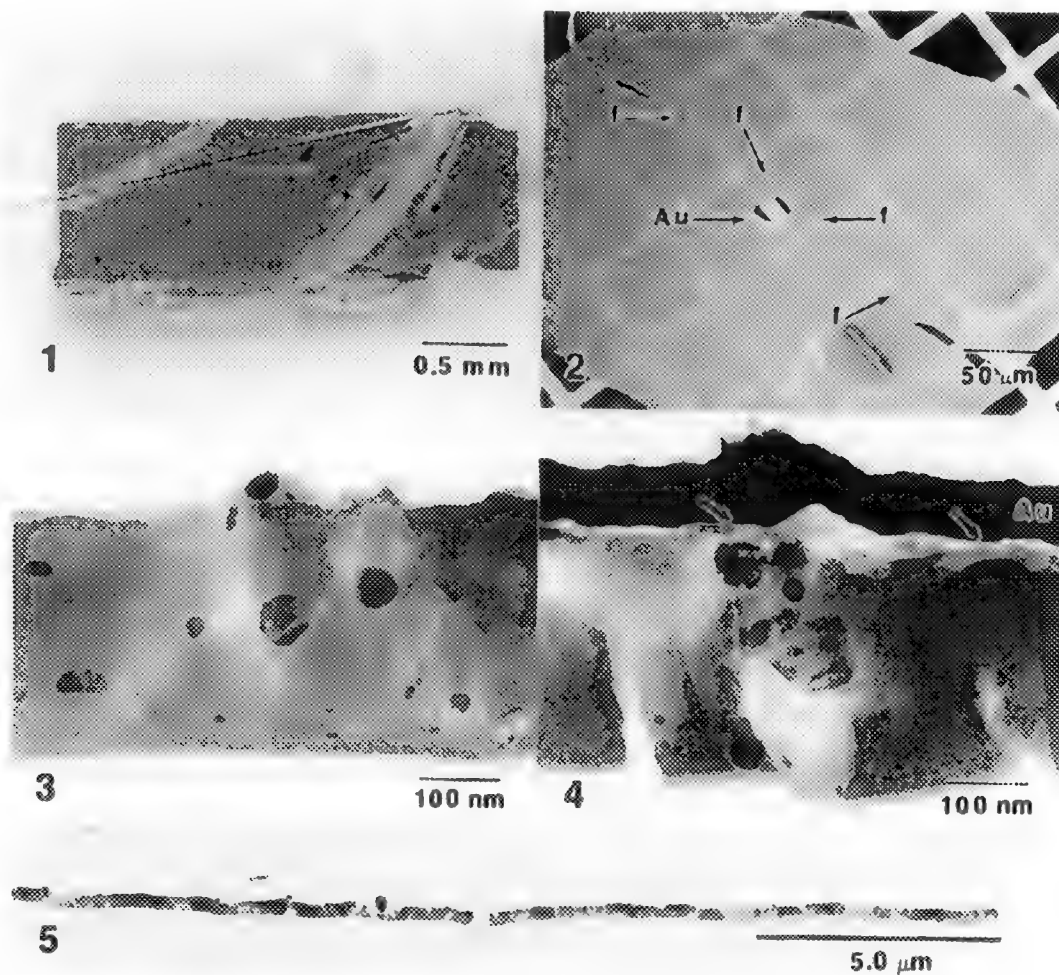


Fig. 1.--Photograph of wear-tested RT-PLD MoS_2 film with 0.001 in. diameter gold wire.
 Fig. 2.--SEM of microtomed TEM sample. Location of gold wire and film are indicated with arrows.
 Fig. 3.--TEM of as-deposited RT-PLD MoS_2 film.
 Fig. 4.--TEM of wear-tested RT-PLD MoS_2 film. Arrows indicate surface regions modified by wear.
 Fig. 5.--Low Magnification TEM of an as-deposited, RT-PLD MoS_2 prepared by microtoming.

CHARACTERIZATION OF NiO THIN FILMS ON α -Al₂O₃ BEFORE AND AFTER HEAT TREATMENT

Paul G. Kotula and C. Barry Carter

Department of Chemical Engineering and Materials Science, University of Minnesota,
421 Washington Avenue SE, Minneapolis, MN 55455-0132

The NiO- α -Al₂O₃ system is of interest as a model system for the study of phase boundaries and reaction kinetics in oxide ceramics. Such a system is of new importance when one of the constituents is a thin film because the reaction kinetics and its dependence on film microstructure is not well understood. Additionally, solid-state reactions between a thin film and single-crystal substrate can be used to produce buffer layers for heterojunctions.

In the present study, thin films of NiO have been grown on single-crystal α -Al₂O₃ substrates by pulsed-laser ablation (PLA). The PLA system used a KrF (248nm) excimer laser operating at 350 mJ per pulse with a pulse repetition rate of 10 Hz. The laser beam was focused to a spot 1x2mm on the surface of rotating NiO pellet. Films were grown at nominal substrate temperatures of 750°C and oxygen pressures of about 10 mTorr. Films were grown both on bulk substrates for which 6000 laser pulses was used to produce 1000Å films and electron-transparent substrates for which 500 laser pulses was used to produce 80Å films. Prior to deposition, the substrates were acid cleaned and then annealed at 1400°C for 8 hours in air in order to reconstruct the substrate surfaces into a series of low-index terraces (the substrate orientation quoted) separated by steps.¹ Films grown on TEM foils were observed without any further specimen preparation. Cross-section specimens for field-emission scanning electron microscopy (FESEM) were ground and polished until no scratches were visible across the interface and then coated with platinum. The same specimens were then used for cross-section TEM observations by polishing off the platinum, dimpling from the opposite side to about 15µm thick and then ion thinning to electron transparency at liquid-nitrogen temperatures in a variable-omega ion miller. All FESEM was performed with a Hitachi S-900 operated at 5kV in both secondary- and backscattered-electron imaging modes. All TEM was performed with a Philips CM-30 operated at 300kV.

The TEM-foil substrate geometry is particularly useful for observing the initial stages of oxide film growth.^{2,3} Figure 1a is a plan-view bright-field (BF) TEM image taken on the common (111)_{NiO} and (0001) _{α -Al₂O₃} poles of an 80Å-thick NiO film grown on an (0001) α -Al₂O₃ TEM foil. The growth rate was determined to be approximately 1.7Å/sec. The film is continuous as evidenced by the six sets of Moiré fringes which can be seen to cross the underlying substrate surface step as indicated by the arrow. The Moiré fringes result from interference between 220 and 3030 type reflections. Figure 1b is a BF TEM image, taken under the same diffraction conditions as above, which shows the film's microstructure and the underlying surface steps. The film is twinned on a very fine scale, consisting of two twin orientations. Such small twin grains have been observed in the 1000Å NiO films grown on (0001) α -Al₂O₃ substrates under the same conditions.⁴ From Figure 1b, it appears that these twins nucleate with equal probability on the substrates but the exact site of nucleation is a topic of current research. The microstructure of the thicker films grown under the same nominal conditions would indicate that the twins are generally larger and follow the original substrate surface steps.⁴

The reaction geometry of a thin film on a single-crystal substrate has previously been used to study the effect of substrate crystallography on the kinetics of the spinel phase transformation in the NiO- α -Al₂O₃ system using Rutherford backscattering spectrometry.⁵ This earlier study could not take into account the effect of the film's microstructure on the reaction kinetics. A new approach to the study of solid-state reactions has been developed which uses cross-section specimens and high-resolution backscattered-electron imaging in a FESEM. Figure 2a is a backscattered electron image of a film which had been reacted with the substrate in air for 6 hours at 1100°C. The α -Al₂O₃/NiAl₂O₄ boundary is smooth on this scale while the NiO/NiAl₂O₄ boundary is quite uneven. This interfacial roughness can

be explained with the aid of Figure 2b which is a cross-section dark-field TEM image, of the same sample as shown in Figure 2a, formed with the near-coincident $(\bar{1}\bar{1}1)_{\text{NiO}}$ and $(222)_{\text{NiAl}_2\text{O}_4}$. It is clear that the spinel has grown farther into the NiO where there is a grain boundary in the film. Using an approach as demonstrated here, it should be possible to subtract the effect of grain boundaries from the overall reaction kinetics provided the number of grain boundaries in the film is small.⁶

1. D. W. Susnitzky and C. B. Carter, *J. Am. Cer. Soc.* **75**, 2463 (1992)
2. M. G. Norton, S. R. Summerfelt, and C. B. Carter, *Appl. Phys. Lett.* **56**, 2246 (1990)
3. M. G. Norton and C. B. Carter, *Mat. Res. Soc. Symp. Proc.* **191**, 165 (1990)
4. P. G. Kotula and C. B. Carter, *Mat. Res. Soc. Symp. Proc.* **285** (1992)
5. Y. K. Simpson, E. G. Colgan, and C. B. Carter, *J. Am. Ceram. Soc.* **70**, C149-C151 (1987)
6. Research supported by the National Science Foundation under grant number DMR-8901218. Additional support was provided by the Center for Interfacial Engineering, an NSF Engineering Research Center. The authors wish to thank Prof. Stan Erlandsen for access to the Hitachi S-900 FESEM and Chris Frethem for technical assistance.

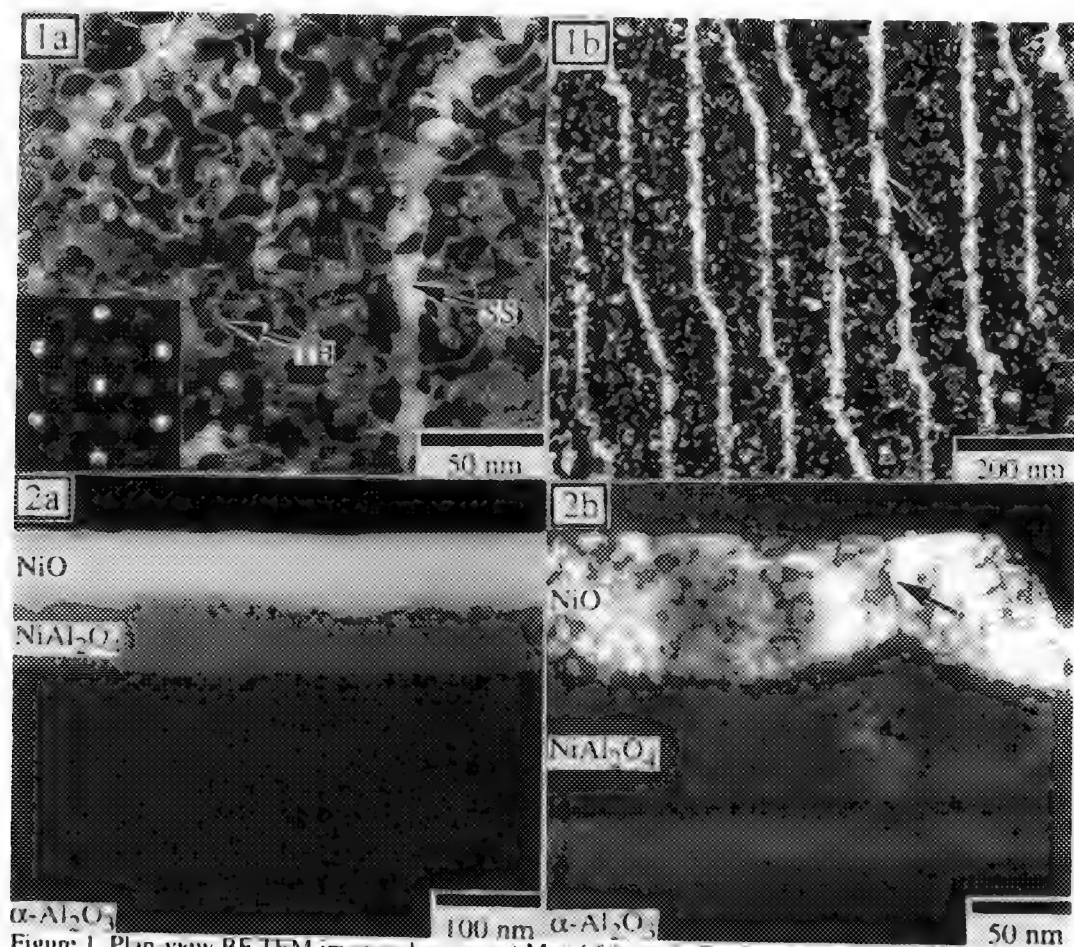


Figure 1. Plan-view BF TEM images showing: a) Moiré fringes indicating a continuous NiO film, arrows indicates a substrate surface step (SS) and a film twin-boundary (TB); b) Underlying substrate surface steps, arrow indicates a substrate surface step.
 Figure 2. a) Cross-section backscattered electron image of NiO film reacted 6 hours at 1100°C; b) Dark-field TEM image of the same specimen. Arrow indicates a grain boundary in the film.

Interfacial Study of Nanophase Pt or Pd Particles on the Surface of Nanophase WO₃ or TiO₂ Particles

Chi-Ming Hsu, Hong-Ming Lin, Chiun-Yen Tung, Teh-Yu Hsu and Chao-Cheng Yang[†]

Department of Materials Engineering, Tatung Institute of Technology, Taipei, Taiwan, R.O.C.
+Department of Humanity, Chemistry Division, National Yunlin Institute of Technology, Yulin County, Taiwan, R.O.C.

Nanocrystalline (NC) metals are a subdivision of the family of nanostructural materials. Nanostructural materials are single phase or multi-phase polycrystals, the crystal size of which is of the order of a few (typically 1-100) nanometers in at least one dimension [2]. Nanocrystalline materials have many interesting physical and chemical properties[3] which attract researchers. Particularly in catalyst's utility, it can provide a large specific surface area and active sites. Its size efficiency (Kubo efficiency[6]) may create different electron energy gap which permits us to do other functional designs[7]. Some phenomenons contribute to attractiveness of nanocrystalline material as catalysts or sensors. The interfacial study between NC metal and oxides became an important issue to evaluate the performance of the these applications.

Gas-condensation technique is used to produce the nanophase WO₃ or TiO₂ by evaporating the tungsten in 10 mbar O₂ atmosphere or pure titanium in (10 mbar O₂/90 mbar He) atmosphere, respectively. The nanophase oxides are collected by a rotating LN₂ cold trap. Before collection the oxides from the LN₂ cold trap, pure platinum(99.99%) or palladium(99.99%), are directly evaporated under 3 x 10⁻⁵ mbar He atmosphere onto the surface of nanophase WO₃ or TiO₂ particles to form NC Metal/NC Oxide interface. NC metal coated nanophase oxides will immerge in acetone solution and disperse on carbon film supported grid for TEM examination. Hitachi 800 STEM and JEOL 4000EX HRTEM are used to examine the nanophase particles and to analysis the interfacial properties of nanophase Pt or Pd particles on the surface of nanophase WO₃ or TiO₂ particles.

Figures 1 and 2 show the images of NC Pt and Pd coated nanophase WO₃, respectively. Several different shapes (rhombic, hexagonal or spherical) of particles have been observed in nanophase WO₃. The electron diffraction pattern indicates the structure of WO₃ is tetragonal. The size of nanophase WO₃ is in the range of 20 to 100 nm. The shape of nanophase TiO₂ is mostly spherical and the size is in the range of 20 to 90 nm. NC Pt and Pd coated nanophase TiO₂ are shown in Figures 3 and 4, respectively. The structure of nanophase TiO₂ is identified as a rutile. Nanophase Pt or Pd particles are homogeneously distributed on the WO₃ or TiO₂ surfaces and both are fcc structure. The size of NC Pt or Pd are less than 10 nm in diameter. HRTEM images in Figure 1(b)-4(b) show the well interfacial bonding between the NC Pt or Pd and nanophase WO₃ or TiO₂ can be achieved. The zone axis of atomic plane is indicated in each Figures. The results of this study demonstrate the possibility to synthesis the NC Metal/NC Oxide particles from the gas-condensation technique with good Metal/Oxide interfacial bonding.

REFERENCES

1. F. H. Froes and C. Suryanarayna, *JOM*, June, (1989)12.
2. Ryozi Uyeda, *Progress in Materials Science*, 35(1), (1991)1.
3. R. Kubo, *Japan J. of the Physical Society*, 17(6), (1962)975.
4. Kaoru Fujimoto, *Japan Surface*, 22(7), (1984)410.
5. Supported by NSC contract NSC-82-0405-E036-072 and Tatung Co. contract 80-17-0831.

Figure 1 : A. TEM and B. HRTEM images of nanophase Pt coated nanophase WO₃. Figure 2 : A. TEM and B. HRTEM images of nanophase Pd coated nanophase WO₃.

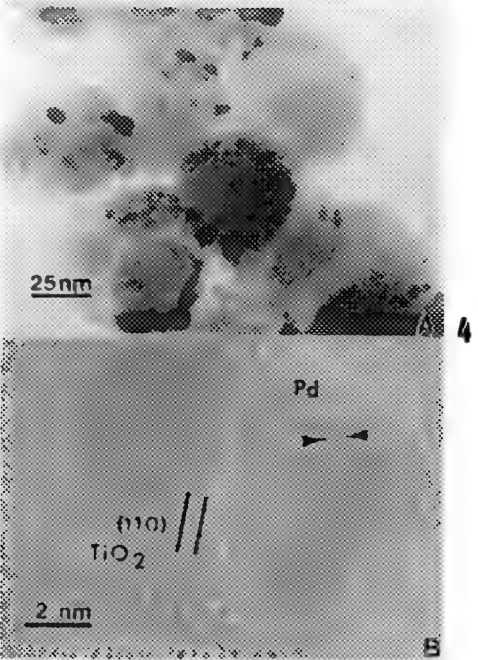
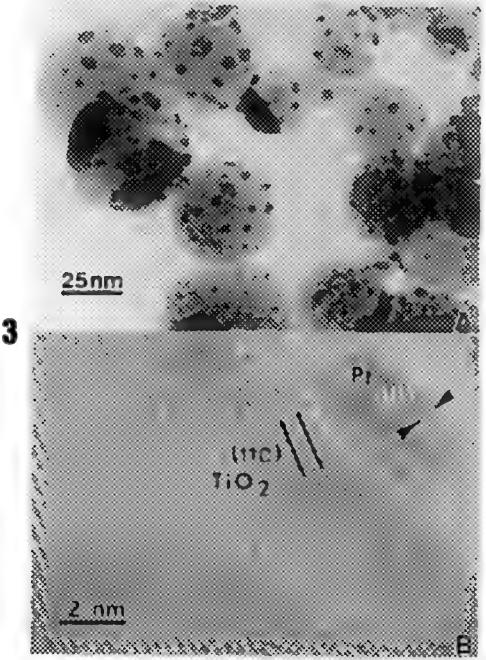
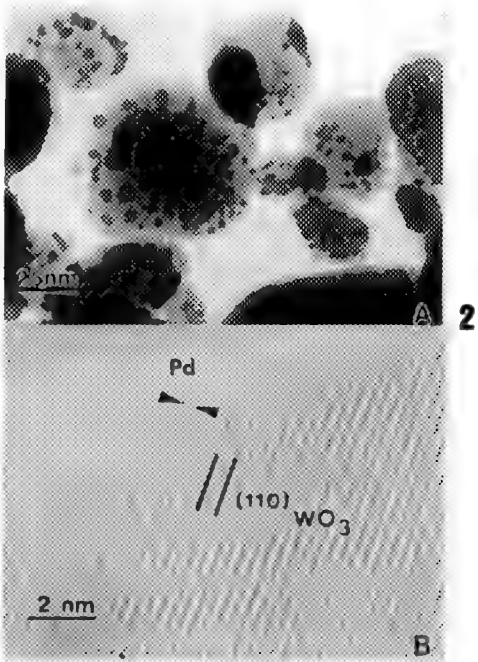
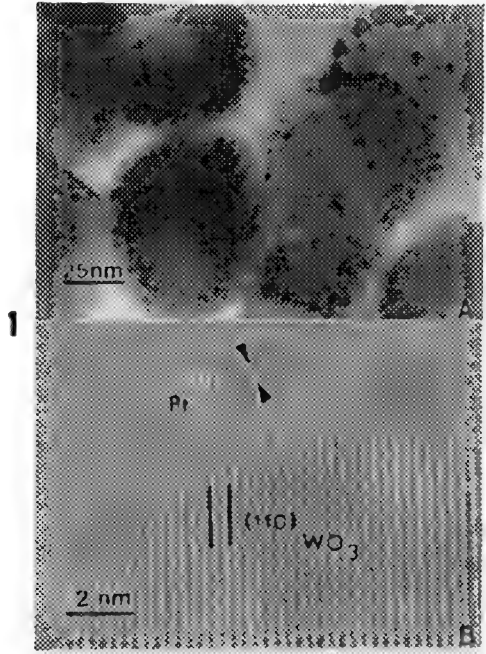


Figure 3 : A. TEM and B. HRTEM images of nanophase Pt coated nanophase TiO₂. Figure 4 : A. TEM and B. HRTEM images of nanophase Pd coated nanophase TiO₂.

ELEMENTAL ANALYSIS OF SINGLE ATMOSPHERIC PARTICLES INFLUENCING VISIBILITY AT THE GRAND CANYON

Barbara J. Turpin, Po-Fu Huang, Amy Roos, and Peter H. McMurry

Particle Technology Laboratory, Mechanical Engineering Department, University of Minnesota, Minneapolis, MN 55455

Collection and preservation strategies and a routine analysis procedure were developed for elemental analysis of individual atmospheric particles using a scanning-transmission electron microscope (STEM) equipped with a super ultra-thin window energy dispersive x-ray detector. These techniques were applied to airborne particles collected at Meadview, AZ, a remote site just downriver of the Grand Canyon. Collection, preservation and beam damage issues of concern in electron microscopic analysis of atmospheric particles will be discussed. Aerosol compositions are usually determined from bulk particle measurements, and it is assumed that compounds are either internally mixed (all present in each particle) or externally mixed (particles each contain a single compound). Insight into the microscopic mixing characteristics of atmospheric aerosols will ultimately further the understanding of atmospheric particle transformation, visibility degradation, and the fate of airborne pollutants.

Particles were collected in the summer of 1992 in three size fractions (1.0-0.5 μm , 0.5-0.26 μm , 0.26-0.12 μm in diameter) using a Hering Low Pressure Impactor and a 250 Å thick silver film substrate supported by a silver TEM grid. A silver substrate was chosen because the silver spectrum does not interfere with the spectra of the major elements present in typical aerosols in the Southwest (C, S, O, Al, Si, K, Ca, Fe). The substrates were prepared by first forming a thin film of nitrocellulose (about 250 Å) on the 200 mesh Pelco silver grids, and then depositing a silver film on the nitrocellulose in a Balzers' evaporator. The film thickness was measured using a quartz crystal detector. After coating the grids, they were baked in nitrogen (to prevent silver oxidation) in a tube oven for 15 minutes at 265-278 °C to remove the nitrocellulose. Spectra from these substrates exhibit low carbon and oxygen signals. Some of these particles contain considerable amounts of sulfate in the form of H_2SO_4 , $(\text{NH}_4)\text{HSO}_4$ and $(\text{NH}_4)_2\text{SO}_4$, and acidic sulfate particles have been found to be very unstable in the beam.^{2,3} For this reason, the samples were exposed to ammonia overnight and analyzed on the STEM at 300 kV rather than on the scanning electron microscope (SEM) at 20 kV to reduce sample heating. Samples were stored in N_2 until analysis to prevent substrate oxidation. Analysis of blanks stored in ambient air and blanks stored in nitrogen showed that in neither case did oxidation degrade the quality of the substrate over a storage period of 3 months.

The effect of ammonia exposure on sulfate losses due to electron beam damage was evaluated by collecting monodisperse H_2SO_4 particle samples of known loadings and exposing some samples to ammonia. Particles are generated with a Collison atomizer from a 0.1% by volume H_2SO_4 - H_2O solution. The resulting aerosol is dried in a silica gel diffusion drier and

a fraction of the aerosol is given a single charge using a PO-210 "neutralizer". The aerosol then flows in the annular region of a cylindrical differential mobility analyzer⁴, bounded by a sheath of particle-free air at the core. A high voltage rod at the centerline attracts the charged particles, and particles that reach the rod at a fixed location are separated from the remaining flow, forming a nearly monodisperse aerosol with known mean size. These particles were collected on a polished silver foil substrate in the Hering Low Pressure Impactor and imaged on the Jeol 840 SEM. For this experiment the rod voltage was set at 10,000 volts, yielding a monodisperse aerosol of 0.44 μm particles. Exposed and unexposed samples were compared with collected monodisperse particulate $(\text{NH}_4)_2\text{SO}_4$ samples. Large, instantaneous losses of unexposed H_2SO_4 particles were observed, and exposure to ammonia drastically reduced these losses.

Atmospheric particle samples collected at Meadview were imaged in transmission mode on a Philips CM30 STEM at 300 kV with the sample tilted 25% toward the detector. Spectra of about 300 particles per sample were collected using a super ultra-thin window EDAX detector, and peaks were integrated yielding counts and semi-quantitative particle compositions using an EDAX software package (PMTHIN). Dead time was held below 30% (roughly 3,000 counts/sec). A background subtraction protocol was constructed manually, stored and applied to all particles, subject to verification. Semi-quantitative compositions were calculated using the Cliff and Lorimer K factor method with theoretical constants suggested by Zaluzec.⁵ Absorption and fluorescence corrections were made when these corrections were greater than 10%. These corrections apply to films; corrections for submicron spheres are less severe.⁶ Therefore when corrections were necessary the true particle composition was bounded by the uncorrected and the corrected compositions. Once the protocol for the collection of spectra, identification of peaks, background subtraction, integration and quantitation was established, this routine was stored as a program file and run automatically when the beam was focussed on each subsequent particle. Because analyses took place over several months, the sensitivity of the EDAX detector to C, O, and N was monitored over the course of the analyses.

The successes and limitations of collection, stabilization and analysis methods and insights into microscopic mixing characteristics of particles affecting visibility at the Grand Canyon will be discussed.⁷

References

1. G. Mie, *Ann. Physik* (1908)25, 377.
2. W. A. Van Borm et al., *Atmos. Environ.* (1989)23, 1139.
3. J. E. Post and P. R. Buseck, *Environ. Sci. Technol.* (1984)18, 35.
4. B. Y. H. Liu et al., *J. Air Pollution Control Assoc.* (1974)24, 1067.
5. P. J. Sheridan, *J. Electr. Microsc.* (1989)11, 41.
6. N. A. Zreiba and T. F. Kelly, *X-Ray Spectrom.* (1988)17, 229.
7. This research was supported by the Electric Power Research Institute (RP2023-11) and the National Science Foundation (ATM-9217858).

TEM/HREM STUDY OF MECHANICAL ALLOYED Cu-Zr POWDERS

W. A. Chiou, C. S. Lin, and P. Liu

Department of Materials Science and Engineering, Northwestern University, Evanston, IL 60208

New technologies for the synthesis of materials with unique microstructures and properties have always been of great interest to materials scientists and engineers. It has recently been shown that the preparation of amorphous and nanocrystalline powders by mechanical alloying (MA) can be of great potential¹. While various mechanisms of amorphization have been proposed^{2,3}, the real process remains unclear. To understand the process/mechanism of amorphization and nanocrystalline formation, investigations of the interfacial regions between collided ball-milled elemental powders is essential. This paper presents an interfacial study of the agglomerated CuZr powders after ball milling.

Samples of commercially produced (AESAR) fine-grained (325 mesh, or 44 μm) Cu (99.3 %) and Zr (99%) powders were weighed to a weight ratio of 1 : 1 (atomic ratio 1.4 : 1) as the starting materials. These powders were mixed together in a steel vial and ball-milled in a SPEX mixer/mill machine. All the process of powder loading/unloading and ball milling were done in an argon gas chamber. To monitor the progress of mechanical alloying, a small portion of the powders was taken out and examined using X-ray diffraction and TEM analysis. However, agglomeration of CuZr particles with steel milling balls occurred after several hours of milling. The agglomerated powders were carefully cut, ground, polished, and ion milled in a liquid nitrogen stage for TEM observation.

TEM observation shows a range of grain size distribution from a few nm to submicron grains with a very high density of defects consisting mainly of dislocations (Figs.1 and 2). HREM study of very fine-grained area shows well-defined nanocrystalline grains as well as amorphous regions. The majority of nanocrystals appear to be polygonal. Three types of grain boundaries were observed: Sharp and straight interfaces found at the grain boundaries between large nanocrystals; (Arrows 1, Fig. 3); narrow and diffused interfaces often located between small nanocrystalline grains (Arrows 2, Fig. 3); and slightly diffused interfaces positioned in the immediate vicinity of dislocations in large crystals (Arrows 3, Fig. 3). The diffused interfaces associated with dislocations indicates polygonization, in which numerous subgrain structures are formed via the realignment of dislocations within the grain, may be responsible for the formation of nanocrystalline grains as opposed to direct fragmentation. The effect of ongoing amorphization is clearly shown in Fig. 4. Some regions of the grain boundaries have become so diffused that the resulting structure is indistinguishable from the amorphous phase. Microchemical analysis (using an electron beam of 1 - 2 nm) shows similar Cu-Zr compositions exist in many nanocrystal, interfacial and amorphous regions, indicating ongoing interdiffusion process between two elemental powders prior to amorphization (Fig.5).

The present study illustrates the formation of nanocrystalline grains precedes amorphization in the ball milling process. The interdiffusion between Cu and Zr has taken place in the early stage, and it may play an important role in the amorphization process. The study also suggests that polygonization, in addition to direct fragmentation, may have acted as the alternative mechanism for the formation of nanocrystalline grains structure.

References:

1. M. Arzt and L. Schultz, eds., *New Materials by Mechanical Alloying Techniques* (1989), Informations Gesellschaft, Verlag.
2. P. H. Shingu, ed., *Mechanical Alloying*, Materials Science Forum (Proc. Internat'l, Symp. Mech. Alloying) (1992). Trans Tech Publications.
3. H. Wiedersich and M. Meshii, eds., *Science of Advanced Materials* (1990), ASM International.
4. The authors would like to thank Prof. M. Meshii for his helpful discussion. This research was supported by the MRL program of the NSF, at the Material Research Center of Northwestern University, under award No. DMR-9120521.

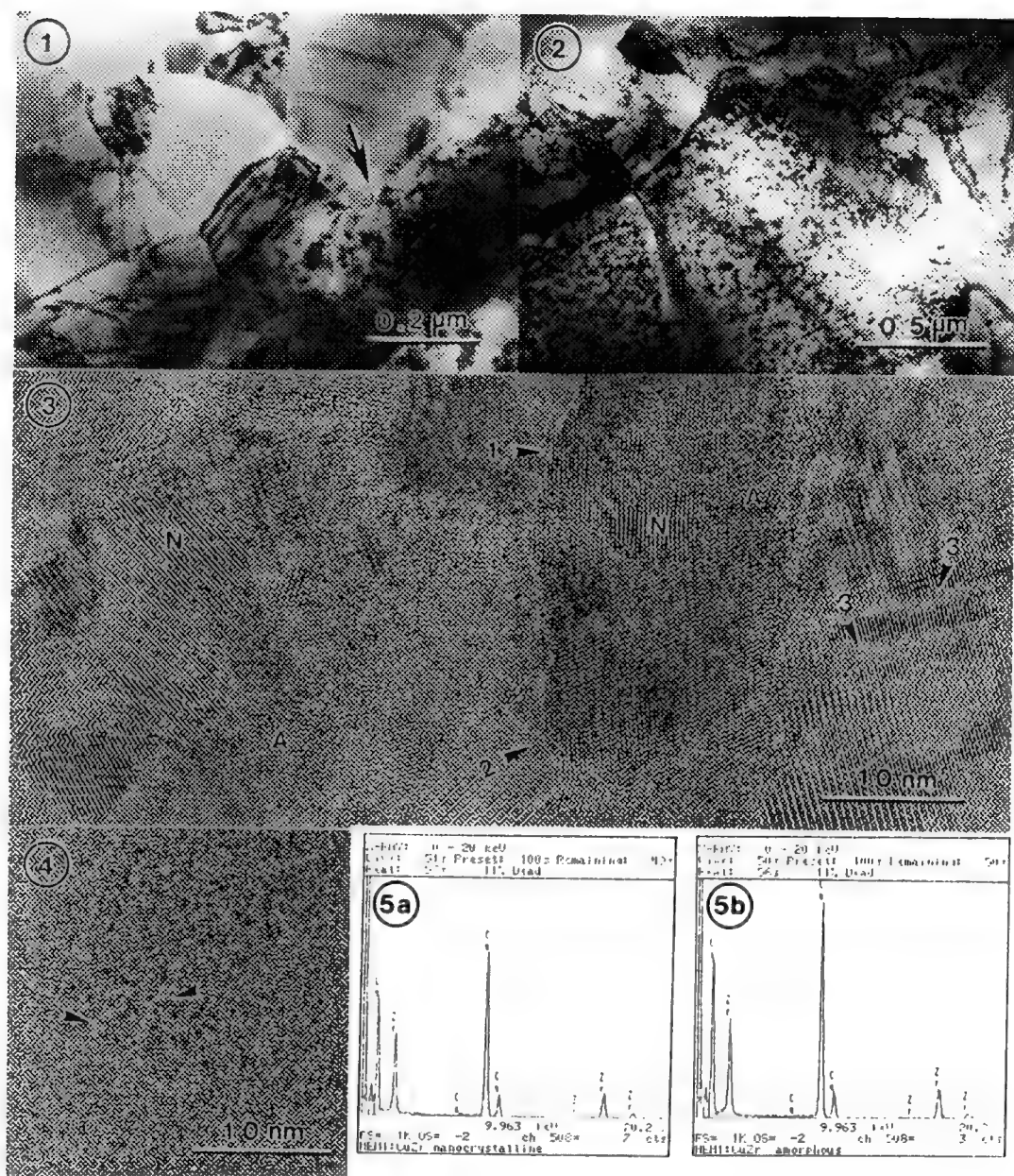


Fig.1 TEM micrograph showing nanocrystals (arrow) coexisted with defected submicron grains.
 Fig.2 TEM micrograph revealing high density of dislocations in larger grains.
 Fig.3 HREM image depicting nanocrystalline (N) and amorphous (A) phases. Note the clear and diffused grain boundaries indicated by arrows.
 Fig.4 HREM image illustrating the phase structure between diffused boundaries (arrow).
 Fig.5 EDS obtained from a nanocrystal (5a) and nearby amorphous phase region (5b).

ELECTONS' EYEVIEW OF BUCKYTUBES AND FRIENDS

Xiwei Lin, Yun-Yu Wang, X.K. Wang, A. Yee, Vinayak P. Dravid, R.P.H. Chang
and J.B. Ketterson*

Dept. of Mat. Science & Engineering, Northwestern University, Evanston, IL 60208,
*Dept. of Physics, Northwestern University, Evanston, IL 60208

Synthesis, characterization and properties of various all-carbon molecules, the fullerene family (buckyballs), have been on the research forefront since the large scale production scheme developed by Krätschmer et al.¹ Recently, Iijima and coworkers^{2,3} have reported TEM observations of hollow graphitic tubules of nanometer scale (buckytubes). In particular, the large scale buckytube synthesis method of Ebbesen and Ajayan⁴ has stirred considerable interest similar to that after the Krätschmer et al.¹ discovery of large scale buckyball synthesis.

We have synthesized gram-scale quantities of buckytubes and their derivatives based on an arc method similar to that of Ebbesen and Ajayan.⁴ The arc was formed between a 1" and a 1/2 " diameter graphite rods under 100 torr atmosphere of helium at a current of 180-200 Amps and a voltage of 20-30 V. The cross section of the resulting build-up rod consists of a gray core, followed by a black ring and another gray shell. The black ring in the middle consists of large number of buckytubes, many millimeters in length with a range of diameters. The transition region between the "black ring" and the outer shell consists of closed-shell particulate derivatives.

We report transmission electron microscopy (TEM) observations of graphite tubules (buckytubes) and their derivatives. We not only observe all the previously reported buckytube geometries, but also identify additional shapes of the buckytube derivatives (Figure 1). The detailed cross-sectional TEM images clearly reveal, for the first time, the cylindrical cross-section of buckytubes and the growth pattern of buckytubes as well as their derivatives⁵ (Figure 2). These first observations of frozen growth stages of buckytubes and derivatives suggest a helical growth mechanism³ analogous to that of crystal growth via screw dislocations. Nanodiffraction patterns from individual buckytubes are analyzed using computer simulations and helicity of individual tubes as a function of number of shells is determined. The anisotropy of electronic structure is revealed by momentum-transfer resolved electron energy loss spectrometry (EELS).⁵ The EELS spectra obtained along the tube direction are very much like those from graphite under similar geometry, while EELS spectra normal to the tube axis show considerable deviation from graphite (Figure 3). Based on the TEM observations, we propose that buckytubes act as precursors to closed shell fullerene (buckyballs) formation and the possible steps in buckyball formation are outlined.⁵ The proposed mechanism is indirectly confirmed with a set of critical arc evaporation experiments using residue-rod (containing various amount of buckytubes) as starting anode for fullerene production. A clear correlation was found between the amount of buckytubes in the rod and the fullerene yield.⁶

References:

1. W. Krätschmer et al., *Nature*, **347**, 354 (1990).
2. S. Iijima, *Nature*, **354**, 56 (1991).
3. S. Iijima et al., *Nature*, **356**, 776 (1992).
4. T.W. Ebbesen and P.M. Ajayan, *Nature*, **358**, 220 (1992).
5. V.P. Dravid et al., *Science*, in press (March 1993).
6. This research is partly supported by the MRL program of the NSF, at the MRC of Northwestern, under award no. DMR-9120521.

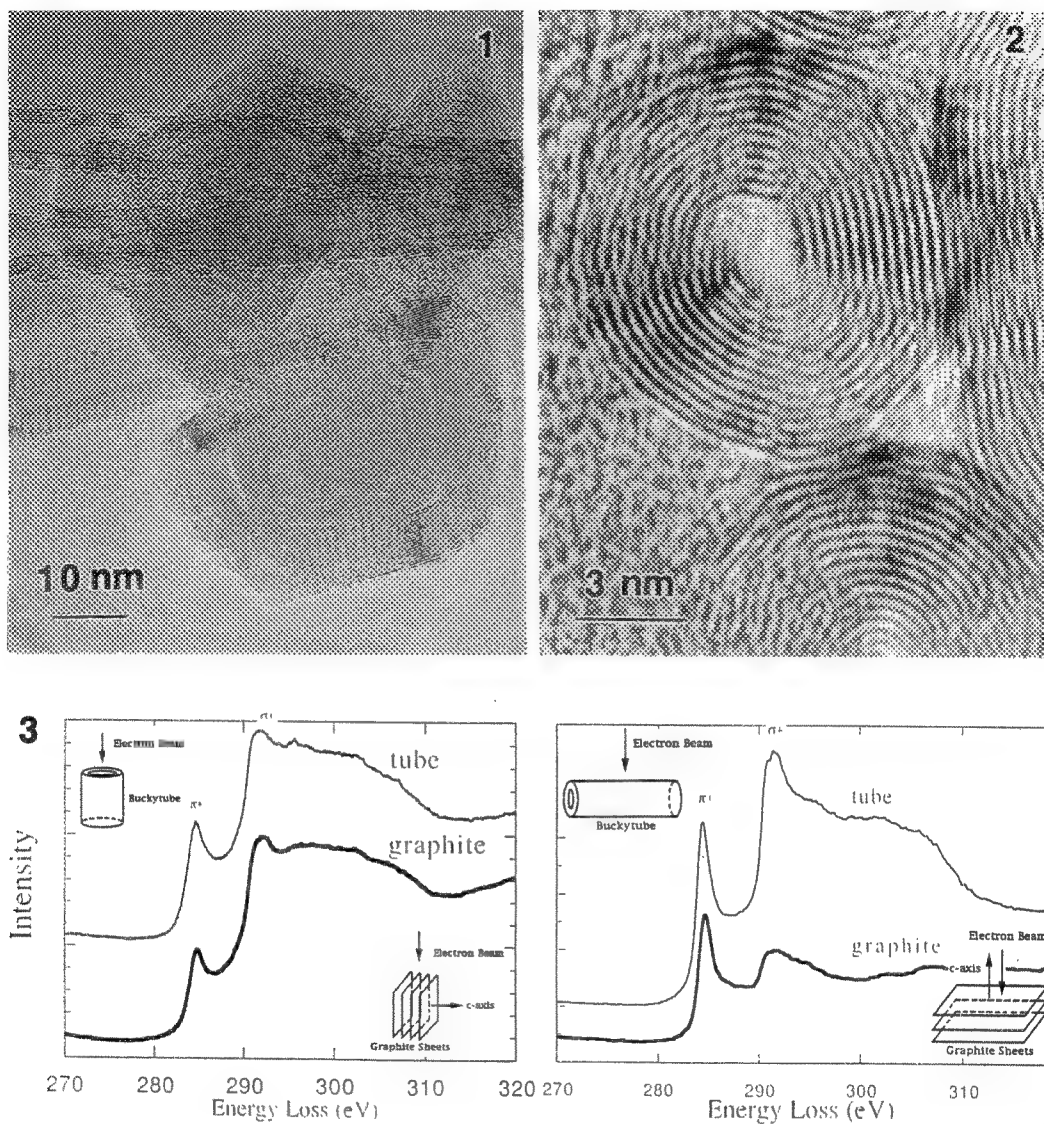


Figure 1: HRTEM images of buckytubes and derivatives. **Figure 2:** Cross-sectional HRTEM image of buckytubes. Cylindrical cross-section and helical growth pattern are clearly visible. **Figure 3:** Transmission EELS spectra from buckytubes along two different orientations, along with comparative spectra from graphite under similar geometry.

LOCATION OF ADATOMS ON Si(100) SURFACE USING THE ELECTRON CHANNELING EFFECT ON AUGER ELECTRON EMISSION

W. Qian, J.C.H. Spence and G.G. Hembree

Department of Physics, Arizona State University, Tempe, AZ 85287

Atomic-site location by channeling enhanced microanalysis (ALCHEMI) is a powerful technique for identifying both the atomic number and the location of impurity atoms in crystals¹. The principle of the technique is simple: electron intensities on particular crystallographic sites within unit cell oscillate with variation of the incident beam direction. The corresponding characteristic emission spectra from atoms at those atomic sites follow these oscillations if the inelastic scattering events are localized. By careful analyzing the spectra of the impurity species and those of the reference atoms on known sites at various tilting angles, the location of the impurity atoms can be obtained. However, most applications of this technique have used the channeling effect on characteristic x-ray emission or energy loss spectra for location of impurity atoms in bulk crystals²⁻⁴. Here we study the possibility of applying this technique for locating adatom positions on a crystal surface, using the channeling effect on characteristic Auger emissions.

Channeling effects on characteristic Auger electron emission were first been observed by Baines⁵ from the Al(111) surface, in the reflection geometry with near normal incident beams. Similar effects have been reported⁶ at the surface wave resonance conditions in RHEED from MgO and Si. This channeling effect shows promise for identifying adatom positions on crystal surfaces. We have studied theoretically the position of one monolayer of Ge atoms on Si(100) surface by monitoring the characteristic Auger electron emission from Si and those from Ge atoms at different incident beam directions in a transmission geometry (figure 1). Experiments are planned using the MIDAS, a STEM instrument with an Auger detector⁷. Auger detector and adatoms will be on the exit face of a transmission sample, since there is no channeling effect on the entrance side⁸. We first postulate two possible candidate sites for the Ge atoms: in site A, Ge atoms substitute Si atoms which form a (2x1) structure; in site B, the Ge atoms are in the projected positions of the regular Si atoms of the third layer in a unit cell. Simple 2-beam calculations were performed in order to find the best specimen thickness and to predict which orientations are likely to show strong channeling effects. The excitation of a particular beam g results in oscillation of the electron intensity at the exit face whose maximum and minimum are parallel to and have the spacing of the corresponding planes. It also results in the oscillation of the electron intensity along the beam direction. We found that incident beam directions near Si(220) Bragg conditions shows the strongest intensity oscillations, and specimen thickness of about 130nm is the best for these experiments.

Careful many beam dynamical calculations were also carried out in order to predict Auger electron emission from the two possible Ge sites, as well as from Si atoms, at different tilting angles near Si(220) Bragg condition. Figure 2 shows the crystal structure and the (2x1) super-cell used in the calculations. Multislice formalism was used with plane wave incidence near Si(100) zone axis. The sample we modeled is a perfect Si crystal except the last slice, where a mono-layer of Ge atoms located at either the (2x1) sites (site A) or at regular Si sites (site B). Several hundreds of beams were included for the total electron intensity distributions. Assuming that the inelastic scattering event which leads to Auger emission is localized, the intensity of Auger electrons emitted from Ge atoms is proportional to the electron intensity on those sites $I_{A,B}(T)$, the intensity of Auger electrons emitted from Si atoms is proportional to the thickness averaged electron intensities on Si sites

$$\sum_i I_{Si}(t_i) \exp(-\frac{t_i}{\lambda})$$

Here, t_i is the position of i th slice measured from the exit surface of the crystal, T (=131nm) is the crystal thickness and, λ is the mean free path of the Auger electrons emitted from Si atoms. The

calculation was carried out at different tilting angles around (220) Bragg conditions. Figure 3 is the result, which shows the Auger electron intensity variations from Ge atoms at site A and those from Si atoms. The variation of Auger electron intensity from Ge atoms at site B follows that from Si atoms. These two sites are thus easily distinguishable by taking Si as a reference site. Other possible Ge sites can be analyzed in the same fashion. The impact parameter $\langle b \rangle$ which determines the degree of localization of the corresponding inelastic scattering event can be estimated by the method of Bourdillon⁹. For Si-K shell excitation (Auger electron of 1601 eV), $\langle b \rangle \sim 0.034$ nm, about 1/6 of the Si {220} interplanar spacing. For Ge Auger electron emission at 1147 eV, the impact parameter is also small. We thus expect the delocalization correction is not necessary for qualitative studies. Work supported by NSF award DMR 9116362.

References

1. J.C.H. Spence and J. Taftø, *J. Microscopy* (1983) 130, 147.
2. J. Taftø, O.L. Krivanek, J.C.H. Spence and J.M. Honig, *Proc. Int. Conf. Elec. Microsc., 1982*, p.615.
3. C.J. Rossouw, P.S. Turner, T.J. White and A.J. O'Connor, *Phil. Mag. Lett.* (1989) 60, 225.
4. W. Qian, J.C.H. Spence, M. Kuwabara and R. Strychor, *Scripta Met. et Mat.* (1991) 25, 337.
5. M. Baines, A. Howie and S.K. Andersen, *Surface Science* (1975) 53, 546.
6. A. Ichimiya and Y. Takeuchi, *Surface Science* (1983) 128, 343; Y. Horio and A. Ichimiya, *Surface Science* (1985) 164, 589.
7. G.G. Hembree and J.A. Venables, *Ultramicroscopy* (1992) 47, 109.
8. J. Taftø and J.C.H. Spence, *Ultramicroscopy* (1982) 9, 243.
9. A.J. Bourdillon, *Phil. Mag.* (1984) A50, 839.

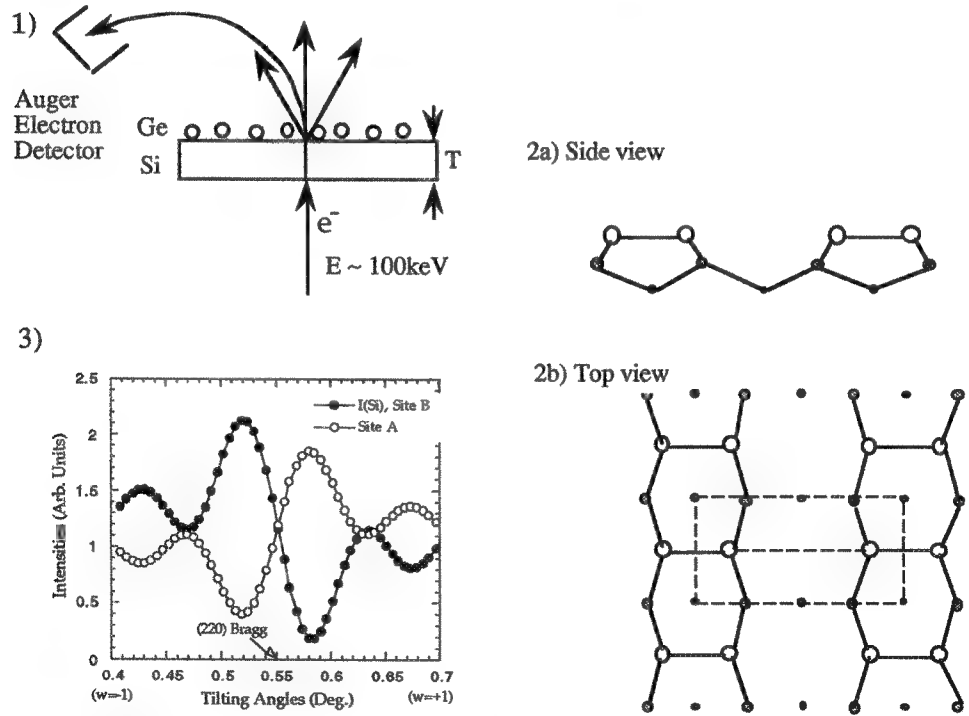


Fig. 1. The geometry of the channeling experiment.
 Fig. 2. The crystal structure and the (2×1) unit cell used.
 Fig. 3. The Auger electron intensity variations at different tilting angles.

A NOVEL UHV-REM AS APPLIED TO OBSERVATION OF RECONSTRUCTION OF Pt(100) SURFACE

Masaki Takeguchi, Tomoki Akita, Yoshizo Takai, Kichiro Shibata* and Ryuichi Shimizu

Department of Applied Physics, Faculty of Engineering,
Osaka University, Osaka 565, Japan
*Research Institute for Scientific Measurements,
Tohoku University, Sendai 980, Japan

Direct observation of surface reconstruction under reflection electron microscopy(REM) provides an intimate insight into basic processes on the surface, leading to more comprehensive understanding of surface physics in atomic scale. For this purpose we have developed a special UHV-specimen chamber, which allows various types of attachments, e.g., evaporator, ion gun, cooling facility, gas inlet and STM if necessary, to be mounted. This chamber was mounted in a 200kV transmission electron microscope(TEM), Hitachi H-700H, to construct a novel UHV-REM for surface study.

Fig.1 shows a schematic diagram of the UHV-TEM constructed in the present work. The specimen chamber is evacuated with turbomolecular pump and Ti sublimation pump to the vacuum pressure of $\sim 10^{-9}$ Torr. Some additional ports for, evaporator, gas-inlet, etc. are also attached around the specimen stage. Feedthrough metal bellows for driving system allows specimen holder to be translated in X- and Y-directions and to be tilted against electron beam without deterioration of vacuum pressure¹. In-situ observation of Si(111)1x1 \rightarrow 7x7 reconstruction shown in fig.2 has confirmed that the present UHV-TEM is a very powerful tool for study of surface reconstruction.

Pt(100) surface, which is reconstructed to hexagonal-5x20 by heating up to $\sim 150^\circ\text{C}$ and to rotated-hexagonal at more elevated temperature, $\sim 900^\circ\text{C}$, irreversibly², has not been investigated to our knowledge by REM in UHV condition so far. We have recently reported a simple method to produce a single-crystal droplet of Pt which has well-developed (100) facets³.

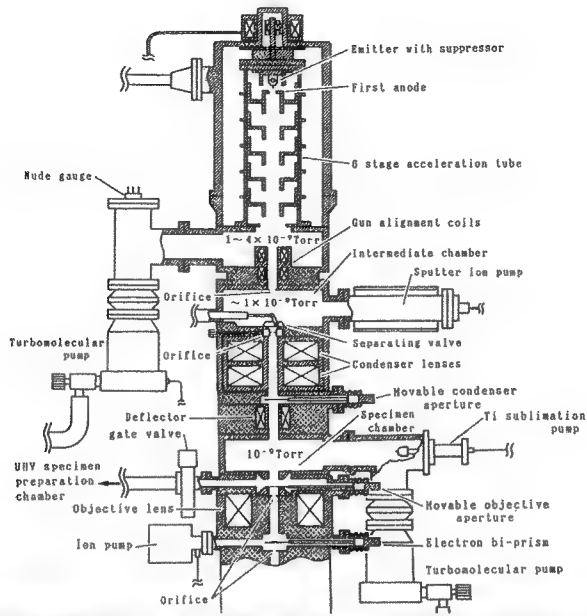
As a preliminary experiment, this sort of a droplet sample with Pt(100) was prepared in the UHV chamber and observed by REM with a conventional TEM, JEOL JEM-200CX. This REM observation has revealed reconstructed domains are with good reproducibility while the Pt sample was transferred through atmospheric pressure from the UHV chamber to TEM. Two kinds of superlattices have also been successfully observed in the domains as shown in fig.3.

Further observation of the Pt(100) reconstruction has been carried on in the UHV-REM and more detailed discussion on the reconstruction will be presented.

References

1. M.Takeguchi et al., Proc. 5th APEM Conf. p238
2. M.A.Van Hove et al., Surf.Sci. 103 (1981) 189
3. T.Akita et al., Submitted to Jpn.J.Appl.Phys.

1



3

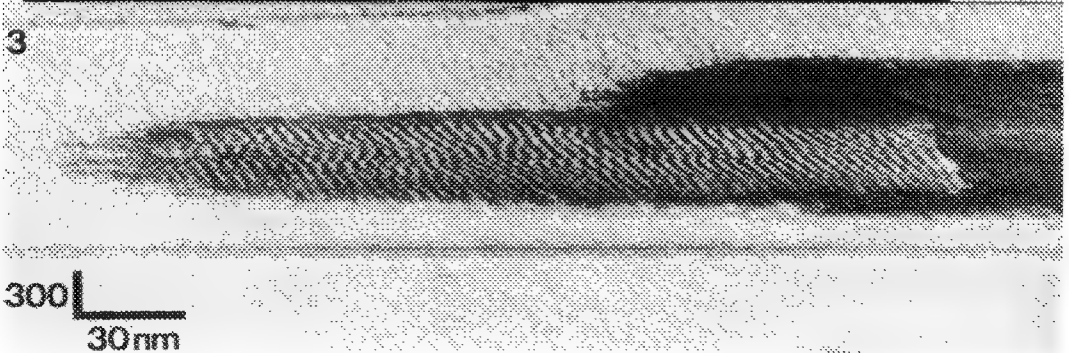


Fig.1---Schematic diagram of UHV-transmission electron microscope.
Fig.2---Si(111)1x1 \rightarrow 7x7 surface reconstruction in UHV-REM.
a)RHEED pattern and b)REM image.
Fig.3---REM image of reconstructed domains on Pt(100) surface.

TEM OBSERVATIONS OF SURFACE-STEP AND HOLE-EDGE FACETING IN ACID-ETCHED AND ANNEALED MgO THIN FOILS

Simon King and C. Barry Carter

Department of Chemical Engineering and Materials Science, Amundson Hall, 421 Washington Av SE,
University of Minnesota, Minneapolis, MN 55455

Surface-steps formed during the cleavage of MgO on {100} planes, the smaller steps of which may be of atomic height, have been observed in Reflection-Electron Microscopy investigations to be accurately aligned along $\langle 001 \rangle$ directions.¹ Steps of atomic height also have been identified on MgO smoke-particle platelets; these steps may be curved or straight, with the straight steps showing evidence for faceting along $\langle 001 \rangle$. Reference also is made to faceting along $\langle 011 \rangle$ and $\langle 012 \rangle$ directions.² Straight steps ~2 unit cells high, with edges along $\langle 100 \rangle$ also have been imaged by High-Resolution Profile-Imaging at the peripheries of MgO smoke microcubes.³ After etching in aqua-regia and annealing in air, however, high densities of "large" steps several unit cells high, as well as numerous holes, are formed.^{4,5} It is faceting in these foils that is reported here.

As can be seen in fig 1, obvious faceting of the surface-step traces is extremely rare in these foils, in marked contrast to substrates such as LaAlO_3 and SrTiO_3 , on which surface-step traces facet readily after a similar preparation treatment.⁴ For a region of the foil which is fairly flat, however, faceting of the surface-step traces sometimes does occur, such as for the two steps, labeled *B* and *T*, which lie on bottom and top surfaces, respectively. Here, a short section, where the step traces pass through an $\langle 011 \rangle$ orientation, has faceted along $\langle 011 \rangle$. As is evidenced by the narrowness of the contrast from these step traces when the $\{111\}$ plane is brought close to vertical (fig 1(a)), the step face here may be faceted on $\{111\}$.

The evidence for faceting is strongest at the peripheries of holes after annealing (Fig 2). In general for specimens exposed to aqua regia, the dominant facet is $\langle 001 \rangle$, however, faceting of the edge along the higher index directions $\langle 011 \rangle$ and $\langle 013 \rangle$ also is apparent.

The edge of a hole is shown at higher magnification in Fig.3. Here, faceting of the hole-edge faces may be seen as a constant separation of the extinction contours (arrowed) for a particular edge orientation. Notice that the observed fringe separation varies strongly with the hole-edge orientation, suggesting several different facet planes. In general, these planes appear steeply inclined, particularly for the $\langle 013 \rangle$ facet; however, whilst an estimate of the wedge angle at the hole-edge easily may be made, the identification of these facet planes is non-trivial in transmission geometry, since top and bottom surfaces may not be inclined at the same angle relative to the macroscopic (100) foil plane. Large angle tilting experiments, aimed at a more comprehensive determination of the orientation of these hole-edge facet planes, are also required.

As yet, after a considerable number of observations, no evidence for step trace faceting along $\langle 100 \rangle$ directions has been seen in these foils. The presence, or absence, of faceting along step traces and also the edge of the foil, will be sensitive to both the atomistic configurations of individual steps and the surface energy (which is related to the step-step interaction energy) of the vicinal facet-plane. Whilst there is, as yet, no detailed explanation of the lack of alignment of surface-steps along $\langle 001 \rangle$ directions, and their slight preference for $\langle 011 \rangle$ directions, possible avenues of exploration may be related to the step-edge geometry: The atomic species is constant along the length of $\langle 011 \rangle$ step edges (although calculations performed on $\langle 100 \rangle$ oriented atomic height steps do not currently suggest this to be an important factor),^{6,7} and a step-face, for a "large" step lying along $\langle 011 \rangle$, is geometrically able to facet on a $\{111\}$ plane, although this plane must be stabilized either by reconstruction and/or by the presence of surface adsorbates.^{8,9,10}

References:

- 1 Z.L. Wang et al; Surface Science, **273**, 88-108 (1992)
- 2 G. Lehmppfuhl, C.E. Warble; Ultramicroscopy, **19**, 135-146 (1986)
- 3 T. Tanji et al; Ultramicroscopy, **27**, 223-232 (1989)
- 4 M.G. Norton et al; Appl. Phys. Lett., **56**, 2246-2248 (1990)
- 5 S.L. King et al; Proc. Symposium B, M.R.S. Fall Meeting, Boston (1992) - in press.
- 6 P.W. Tasker and D.M. Duffy; Surface Science, **137**, 91-102 (1984)
- 7 E.A. Colbourn and W.C. Mackrodt; Solid State Ionics, **8**, 221-231 (1983)
- 8 M. Gajdardziska-Josifovska et al; Surf. Sci. Lett., **248**, L259-L264 (1991)
- 9 J.W. May; Advances in Catalysis, **21**, 151-280 (1970)
- 10 The authors acknowledge the support of the D.O.E. under grant number DE-FG02-92ER45465

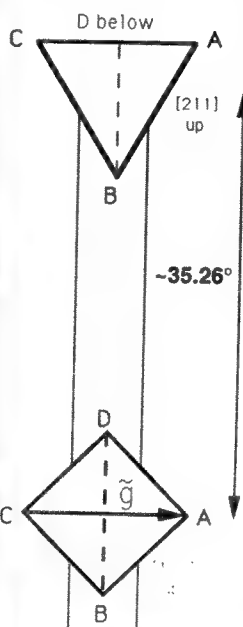
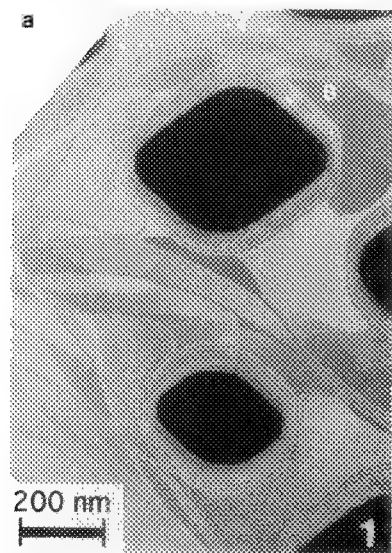
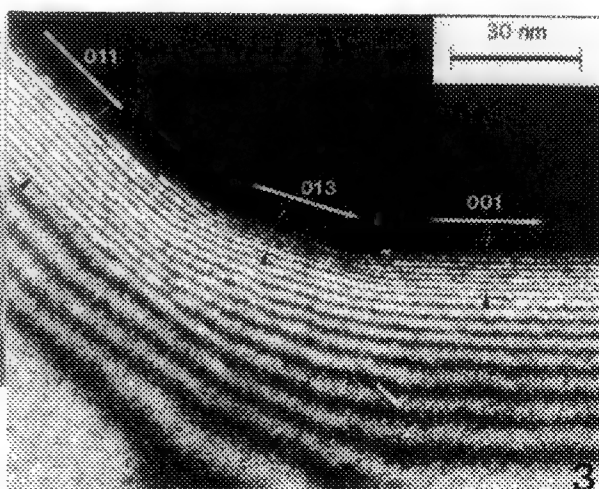
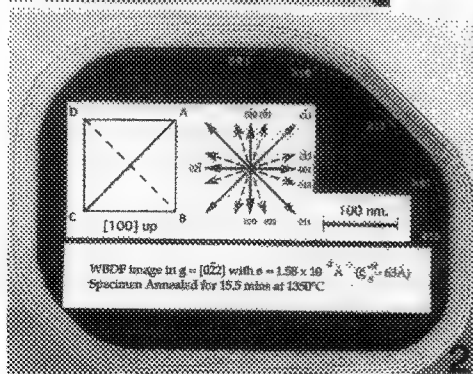


Fig.1: Near weak-beam DF images taken over a large angle of tilt. Foil orientations are indicated by the tetrahedra. MgO annealed for 15.5 min at 1350°C.

Fig.2: Faceting around the edge of a hole.

Fig.3: High magnification weak-beam DF image of a hole edge. Faceting is suggested by the constant separation of the extinction contours (arrowed).



CHARACTERIZATION OF MICROWAVE-SINTERED CERAMIC COMPOSITES

X. Zhang, Y. Pan, and T.T. Meek

Electron Microscope Facility and the Department of Materials Science and Engineering, The University of Tennessee, Knoxville, TN 37996

Industrial microwave heating technology has emerged as a new ceramic processing technique.¹ The unique advantages of fast sintering, high density, and improved materials properties makes it superior in certain respects to other processing methods. This work presents the structure characterization of a microwave sintered ceramic matrix composite.

Commercial α -alumina powder A-16 (Alcoa) is chosen as the matrix material. β -silicon carbide whiskers (Third Millennium Technologies, Inc.) are used as the reinforcing element. The green samples consisted of 90 vol% Al_2O_3 powder and 10 vol% ultrasonically-dispersed SiC whiskers. The powder mixture is blended together, and then uniaxially pressed into a cylindrical pellet under a pressure of 230 MPa, which yields a 52% green density. The sintering experiments are carried out using an industry microwave system (Gober, Model S6F) which generates microwave radiation at 2.45 GHz with a maximum output power of 6 kW. The composites are sintered at two different temperatures (1550°C and 1650°C) with various isothermal processing time intervals ranging from 10 to 20 min. The density of each sintered sample is carefully measured by an Archimedes method.² Fracture toughness of the composite is determined by an indentation method.³ Structural characterization of the composites is conducted using TEM, SEM, EDS, XPS, and XRD methods.

The test results indicate that the microwave sintered composite has an improvement in fracture toughness ($K_{Ic} = 4.5$ to $5.3 \text{ MPa} \cdot \text{m}^{1/2}$) over conventionally sintered monolithic alumina. Crack deflection along the whiskers is the major toughening mechanism operating in the composite (see Figure 1). Also, whisker bridging, whisker debonding, and whisker pullout all contribute to the improvement of fracture toughness of the composite.

TEM study shows that the interfacial bonding between the whiskers and the alumina matrix plays an important role in the composite materials. An amorphous interphase existed at the whisker-matrix interface (Figure 2). Strong interface interactions between the whiskers and the alumina matrix weakens the benefits of the whisker toughening effects. The samples sintered at 1650°C show higher toughness than those sintered at 1550°C where a strong interface interaction was obvious.

Ultra fine grain size is a characteristic of the microwave sintered composite (Figure 3), which is directly related to the microwave internal volumetric sintering mechanism. The investigation also shows that without using sintering aids there are amorphous layers formed on most of the alumina grain boundaries although the sintering temperature is 400 to 500°C lower than the melting temperature of the alumina (Figure 4). This observation provides direct evidence of the decrease of local melting temperature at the grain boundary area due to the effects of capillary and electromagnetic field.⁴⁻⁵

References

1. W.H. Sutton, Ceramic Bulletin, 68(1989)376
2. ASTM Standard C 693-84
3. G.R. Anstis et al., J. Am. Ceram. Soc., 64(1981)533
4. T.T. Meek, X. Zhang, and M. Rader, in D.A. Clark et al. Ed., Microwaves: Theory and Application in Materials Processing, Am. Ceram. Soc., Inc., Westerville, OH, (1990)81
5. The authors are grateful to Third Millennium Technologies, Inc. for providing the silicon carbide whiskers and to Aluminum Company of America for providing alumina powders.

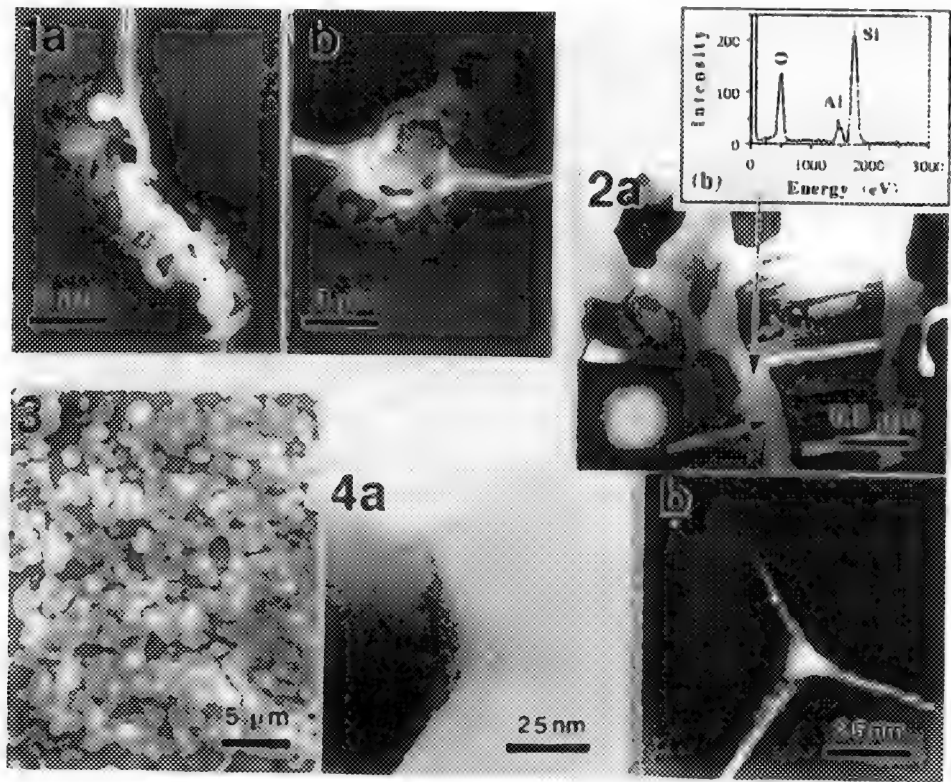


Figure 1. (a)Crack is deflected by about 40° along whisker lying on the polished surface, (b)crack is deflected along edge of whisker oriented perpendicular to polished surface.

Figure 2(a)TEM bright field image of SiC whisker bonded with alumina matrix through amorphous interphase. Inset shows SAD pattern of interphase region with typical amorphous diffraction, (b)EDS result of analysed area indicated by arrow.

Figure 3. SEM fractograph of specimen sintered at 1550°C for 30 min. Note that there is virtually no or very small grain growth under microwave sintering condition.

Figure 4. (a)TEM bright field image of alumina grains of composite sintered at 1650°C for 20 min, (b)corresponding TEM dark field image showing amorphous layers surrounding alumina grains.

STRUCTURAL DEFECTS INDUCED BY HEAVY-ION IRRADIATION IN SUPERCONDUCTING OXIDES

Yimei Zhu, H. Zhang,* Z.X. Cai, R.C.Budhani, D.O.Welch, and M.Suenaga
Division of Materials Science, Brookhaven National Laboratory, Upton, NY 11973
*Dept. of Mater. Sci. & Engng., Northwestern University, Evanston, IL 60208

We studied the the structure and properties of high Tc superconductors using heavy ions. While irradiation of $\text{YBa}_2\text{Cu}_3\text{O}_{7-\delta}$ (hereafter denoted as 123) with 300 MeV Au^{+24} and 276 MeV Ag^{+21} ions produces columns of amorphous tracks along the ion trajectories, such defects are only created occasionally during irradiation with 236 MeV Cu^{+18} , and are not induced with 182 MeV Si^{+13} . A comprehensive electron microscopy study of defect formation in $\text{Bi}_2\text{Sr}_2\text{Ca}_2\text{Cu}_3\text{O}_x$ and in oxygen-reduced and ozone-treated 123, shows that the degree of radiation damage (the size and the shape of the defect) by the heavy ions depends on: (a) the rate at which ions lose their energy in the target; (b) crystallographic orientations with respect to the incident ion-beam¹ (Fig.1); (c) thermal conductivity and chemical state (eg. oxygen concentration of 123) of the sample, and (d) the extent of pre-existing defects in the crystal. Calculation and simulation of the strain contrast surrounding the amorphous column using two-beam dynamical theory agree well with the observations and suggest that the reduced hole density observed in the crystal near the amorphous region is mainly due to lattice distortion. A thermal-spike model, based on ion-induced localized melting and anisotropic thermal conductivity of these materials, provided a qualitative basis for the formation of the amorphous tracks. Measurements of the superconducting properties of heavy-ion-irradiated thin films show an enhancement in critical current density when the density of the columnar defects is $\leq 5 \times 10^{10}/\text{cm}^2$ and their diameter is about the coherence length.

Furthermore, planar faults associated with the amorphous track were often observed in $\text{YBa}_2\text{Cu}_3\text{O}_{7-\delta}$ ($0.1 < \delta < 0.6$), especially when the ion-beam is parallel to the a-(or b-) axis. Fig.2 shows such faults; they are not pre-existing defects but were generated during the formation of the amorphous columns. The extension of the fault ranged from 3 to 5 times the radius of the amorphous column. Figure 3 shows examples of microchemical analysis of such faults with a 20Å probe (field emission source). We found that the predominant faults ($\sim 80\%$) are Cu-rich while the rest are either Cu-deficient or show no change in Cu concentration. Simulation of the HREM image of the planar defects with various structural model suggests that the Cu-rich faults are extrinsic stacking faults, consisting of one or two extra CuO planes inserted at the location of the original single CuO layer. The faults often start with a local 125 ($\text{YBa}_2\text{Cu}_5\text{O}_9$) structure near the amorphous column with a displacement $\mathbf{R}=1/6[302]$ (Fig.4), then change to a 124 ($\text{YBa}_2\text{Cu}_4\text{O}_8$) structure, and finally terminate in a 123 matrix. This finding supports our thermal-spike model and suggests that the diameter of the melting zone during heavy-ion irradiation is about the same as the width of the planar defect. Such planar defects are expected to have an additional beneficial effect on flux pinning in these superconducting materials.²

Reference

1. Y.Zhu, R.C.Budhani, Z.X.Cai, D.O.Welch, and M.Suenaga, *Philos. Mag. Lett.* **67** (1993) 125.
2. This research was supported by the U.S. Department of Energy, Division of Materials Sciences, Office of Basic Energy Sciences under Contract No. DE-AC02-76CH00016. The use of the H-9000 and HF-2000 microscopes in the Dept. of Mater. Sci. & Engng., Northwestern University is gratefully acknowledged.

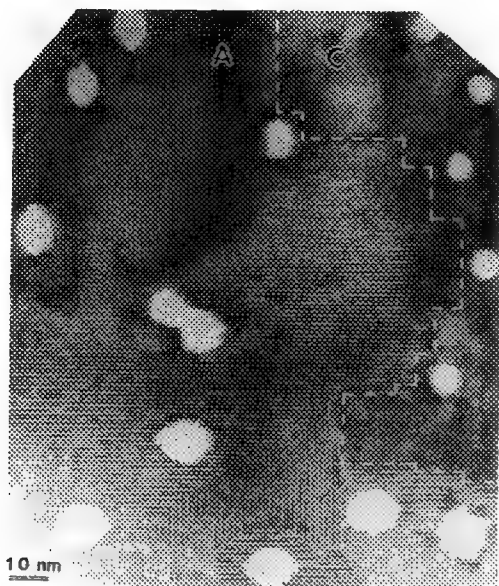


Fig.1 Lattice image of Au^{+24} -irradiated $\text{YBa}_2\text{Cu}_3\text{O}_7$ thin film. The amorphous regions appear large and elliptical when the incident-ion is parallel to the $[100]$ (or $[010]$) direction, but small and disk-shaped to the $[001]$ direction. A and C represent the a- (or b-), and c-axis parallel to the film normal, respectively.

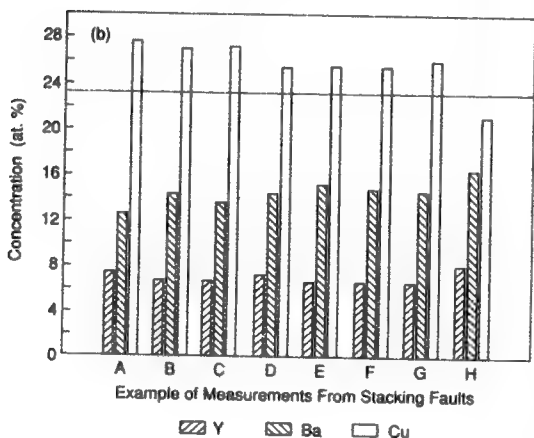


Fig.3 Examples of compositional measurements at the planar defects. The horizontal line indicates the average copper concentration measured in the crystal matrix.

Fig.2 Planar defects associated with the amorphous column of the ion tracks.

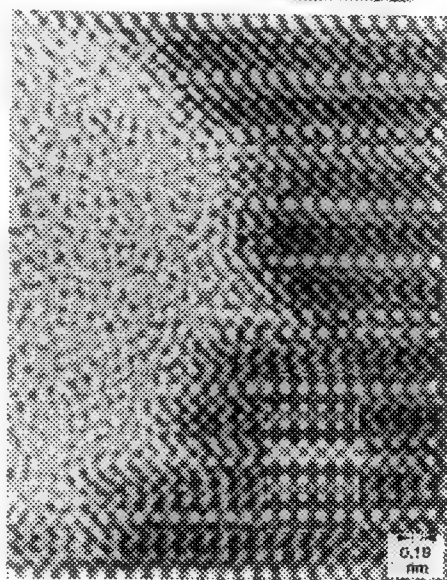
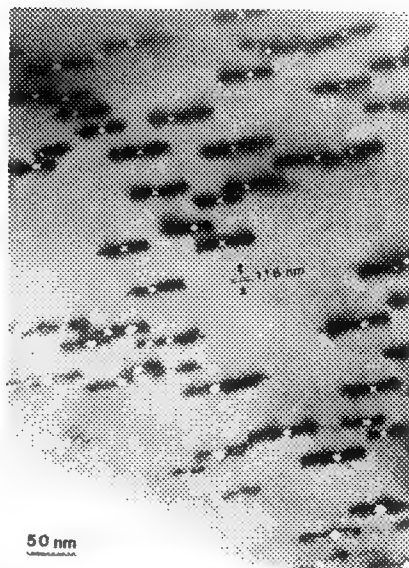


Fig.4 (100) projection of a HREM image of the amorphous column and the planar defects (extrinsic stacking faults, indicated by the pair-arrow). The calculated image of the planar defect is shown in the inset suggesting a local 125 structure with a plane normal $\mathbf{n}=[001]$ and a displacement vector $\mathbf{R}=1/6[302]$.

PHASE COMPOSITION AND LOCAL GRAIN ALIGNMENT AT THE Ag/SUPERCONDUCTOR INTERFACE IN Ag-SHEATHED Bi-Sr-Ca-Cu-O TAPES

Yi Feng, D.C. Larbalestier, S.E. Babcock, and J.B. VanderSande*

Applied Superconductivity Center, University of Wisconsin - Madison, Madison, WI 53706
*Department of Materials Science and Engineering, Massachusetts Institute of Technology, Cambridge, MA 02139

Texturing of the superconductor phase and proximity to a source of silver appear to be crucial to the development of high critical current density tapes of the Bi-Sr-Ca-Cu-O (BSCCO) high-temperature superconductors, yet relatively little is understood about the mechanism(s) by which the [001] texture develops and the complex role that the silver sheath material plays. We have studied the phase composition, alignment, and bonding at the Ag/BSCCO interface for silver-sheathed tapes of both the 2212 and 2223 phases that have been processed under fundamentally different conditions. High-resolution TEM imaging revealed details of the interface that give insight into these important questions.

Ag-sheathed BSCCO tapes with cation compositions $\text{Bi}_2\text{Sr}_2\text{CaCu}_2\text{O}_x$ (2212) and $\text{Bi}_{1.8}\text{Pb}_{0.4}\text{Sr}_{2.0}\text{Ca}_{2.2}\text{Cu}_3\text{O}_x$ (2223) were prepared by standard powder-in-tube methods. 2212 sample A was heat-treated at 920°C for 15 minutes to melt the superconductor core, then cooled at 240°C/h from 920°C to 840°C and annealed at 840°C for 70 hours. 2212 sample B was solid-state processed at 840°C for 70 hours; it did not undergo any melting. 2223 sample C was solid-state processed at 790°C for 72 hours. All heat treatments were done in air. Longitudinal cross-sectional TEM samples were prepared by mounting, mechanical grinding, and Ar-ion milling at 4.5kV in a liquid nitrogen-cooled stage. Phillips CM20 Ultratwin and Akashi 002B HRTEMs were used for imaging.

Fig. 1 shows a section of the Ag/BSCCO interface in melt-processed 2212 sample A. The interface was well-bonded and free of non-superconducting phases over its imaged length. As for all imaged segments of the interface, the (001) planes of the superconductor lie parallel to the polycrystalline Ag over most of the interfacial area and the superconductor phase terminates after the Bi-O double layer. Short facets of non-(001) BSCCO planes accommodate more macroscopic misalignment of the (001) planes away from the Ag interface. Careful inspection of the micrograph reveals a one-half-unit-cell-thick layer of the 2201 phase between the 2212 and the Ag that also terminates after the Bi-O double layer. This layer is also observed in sintered 2212 sample B (Fig. 2). The preference for formation of exactly one-half of a unit cell of 2201 is demonstrated dramatically at the step in the interface shown in Fig. 2. Here the step height equals one-half of the 2201 unit cell spacing and only the first half layer is 2201 on either side of the step. The 2201 layer that is in immediate contact with Ag on the left side of the step converts to the 2212 as the step is traversed from left to right and the layer is no longer immediately in contact with the Ag. In contrast, no evidence for 2201 or 2212 layers of any thickness is observed at the Ag/BSCCO interface in the sintered 2223 tape (Fig. 3). This was true of several different TEM samples corresponding to various stages of the growth of the 2223 phase. As for the 2212 case, the 2223/Ag interface is well-bonded, tends to lie parallel to the (001) planes of the superconductor, and is abutted by the double Bi-O planes of the 2223 phase. For example, sample C showed 2223 at the Ag/superconductor interface at an early stage in its processing when the overall ratio of 2223 to 2212 phase was only 1:9. Evidence for microstructural differences at the Ag/BSCCO interfaces in 2212 and 2223 tapes suggests that Ag may react differently with these two superconductor phases. The tendency of the 2201 one-half unit cell at the interface in 2212 tapes to mimic the

Ag/superconductor interface morphology suggests that it is stabilized by interface proximity. Together, these observations suggest that the 2201 half layer is a metastable equilibrium microstructure for this interface, perhaps due to a strain-minimization mechanism¹. In contrast to 2212, 2223 appears to be the stable phase at the Ag interface. Our results also suggest that Ag initiates the 2212 to 2223 conversion through 2223 formation at the Ag interface².

References

1. J.P. Hirth, J. Mater. Res. (in press).
2. Y.Feng, Y.E. High, D.C. Larbalestier, Y.S. Sung, E.E. Hellstrom, Appl. Phys. Lett. (in press).
3. This work was sponsored by DARPA (N00014-J-4115) and EPRI (RP8009-05). We thank R. Ray and E.E. Hellstrom for the 2212-BSCCO samples

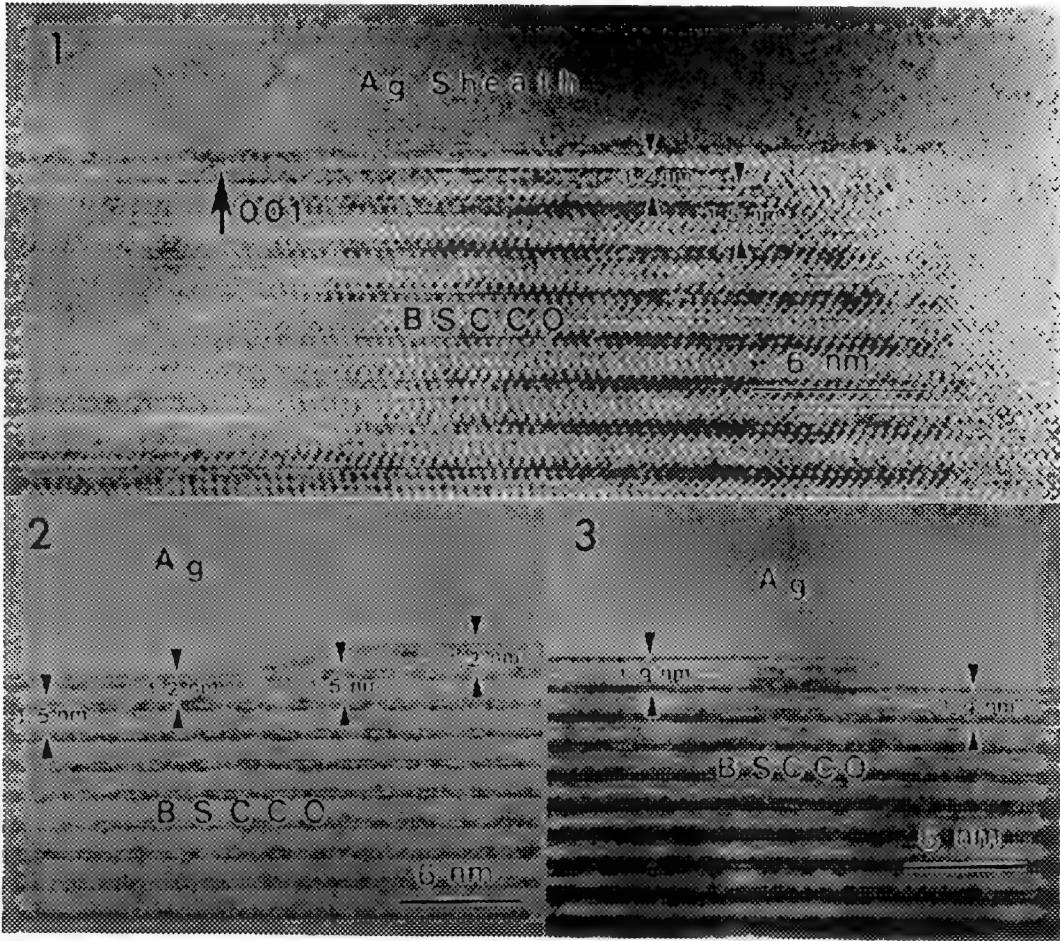


FIG. 1. A Ag-BSCCO interface in 2212 sample A. The one-half unit cell 2201 layer is observed at the interface.
 FIG. 2. A Ag-BSCCO interface in 2212 sample B. Notice a step with a height equal to one-half of the 2201 lattice spacing at the interface.
 FIG. 3 A Ag-BSCCO interface in 2223 sample C. No 2201 and 2212 were found at this interface.

TiO₂ ON MgO BY PLD: THE EFFECT OF THE SUBSTRATE TREATMENT

Simon King and C. Barry Carter

Department of Chemical Engineering and Materials Science, Amundson Hall, 421 Washington Av SE,
University of Minnesota, Minneapolis, MN 55455

The recent demonstration of the epitaxial growth of YBa₂Cu₃O_{7-x} (YBCO) onto (100) MgO passivated by a layer of the inverse spinel Mg₂TiO₄,¹ combined with the large number of possible reaction products of widely differing structure (normal spinel (Ti³⁺), inverse spinel, pseudo-brookite, perovskite) make the MgO-TiO₂ system one of the more interesting, and complex, currently under examination.²

Over the last few years, Hesse, Bethge and co-workers (see 1 for refs), have applied various microscopical techniques to the study of e-beam evaporated TiO₂ onto MgO. The present paper extends this investigation to pulsed-laser deposited (PLD) TiO₂ onto MgO. Unlike almost all previous studies of PLD films, pre-characterized "TEM-ready" substrates are used, a technique pioneered by Norton et al, thereby circumventing the possibility of affecting the film morphology during the thinning process.³ This technique also allows the imaging in the TEM of identical areas both before and after deposition.

Results from two specimens, both prepared according to the method of Norton et al (aqua-regia etch and annealing in air),⁴ are shown in this paper. These specimens have been annealed in air for 3.5 and 15.5 min, respectively. Identical depositions were performed on both specimens, at a substrate temperature of 500°C and employing the same rotating, compressed and sintered, rutile pellet of 98% theoretical density. The films are of thickness 50-55 nm after 2400 pulses. Full details of the deposition parameters will be given elsewhere.⁵

Fig.1 shows the 3.5-min annealed sample: Figs 1a and 1b are zone-axis bright-field (BF) micrographs before and after deposition, respectively. As can be seen in Fig 1b, a continuous, small-grained film has been formed. Individual grains, of sizes ~10-20 nm, are seen more clearly in defocused images (not shown), and Moiré fringes are in evidence at higher magnifications. An ostensibly similar film is shown on the 15.5-min sample (Fig 2). An even distribution of the grains over the substrate, apparently insensitive to the surface step positions, is seen when the image is defocused.

The (100) zone-axis diffraction patterns (DP) from the two samples, as shown in Fig 3, are quite different. The pattern from the 3.5-min sample indicates the formation of an anatase (A) film exhibiting a high degree of epitaxy.⁶ For the 15.5-min sample, however, the epitaxial relationship has nearly been lost. This is a very similar result to that achieved for the case of e-beam evaporation.⁵ The differences in the DP's become even more marked on tilting to a <112> pole (Fig 4). Evidence is now plainly visible in the DP from the 15.5-min annealed sample for a second phase, which has formed a perfect epitaxial relationship with the MgO substrate, and which has almost exactly double the lattice parameter of MgO. It is thought that this may represent the formation of a magnesium-titanate spinel (the inverse spinel Mg₂TiO₄ would seem the more likely). Imaging in one of these spots (arrowed in 4b), suggests that this second phase is distributed uniformly across terraces on the substrate, but apparently has not formed on the inclined step faces (Fig 2c). For the 3.5-min annealed sample, this area of the diffraction pattern (Fig. 4a) shows a weak, blurred reflection; imaging with this reflection gives no evidence for any significant amount of this second phase, in agreement with the diffraction data. The brightly visible crystallites are thought to be anatase, and arise from reflections near the edge of the 15μm objective aperture employed.

These specimens represent part of a larger study of the effect of substrate preparation on pulsed-laser deposited thin-films. Preliminary results indicate that the substrate preparation is a critical factor in governing the observed microstructure, as has been found for YBCO on MgO.⁷ Subject to further experimentation, the presence of the spinel phase, at very much lower temperatures than previously observed,¹ has profound implications for the fabrication of magnesium-titanate spinel films, and thence

for the production of superconducting tri-layered devices.⁸ Lastly, to our knowledge, this is the first time that the same area of a TEM foil has been imaged both before and after pulsed-laser deposition.⁹

References:

- ¹ D. Hesse et al, *Physica C* **202**, 277-288 (1992)
- ² e.g., J.F. Banfield and D.R. Veblen; *Amer. Mineralogist*, **77**, 545-557 (1992)
- ³ M.G. Norton et al; *Applied Phys. Lett.*, **55**, 2348-2350 (1989)
- ⁴ M.G. Norton et al; *Appl. Phys. Lett.*, **56**, 2246-2248 (1990)
- ⁵ S.L. King et al; *Appl. Phys. Lett.* - in preparation
- ⁶ D. Hesse; *J. Vac. Sci. Technol. A*, **5**, 1696-1702 (1986)
- ⁷ B.H. Moeckly et al; *Appl. Phys. Lett.*, **57**, 1687-1689 (1990)
- ⁸ H.P. Lang et al; *Physica C*, **202**, 289-297 (1992)
- ⁹ This research is supported by NSF under grant No. DMR-890128.

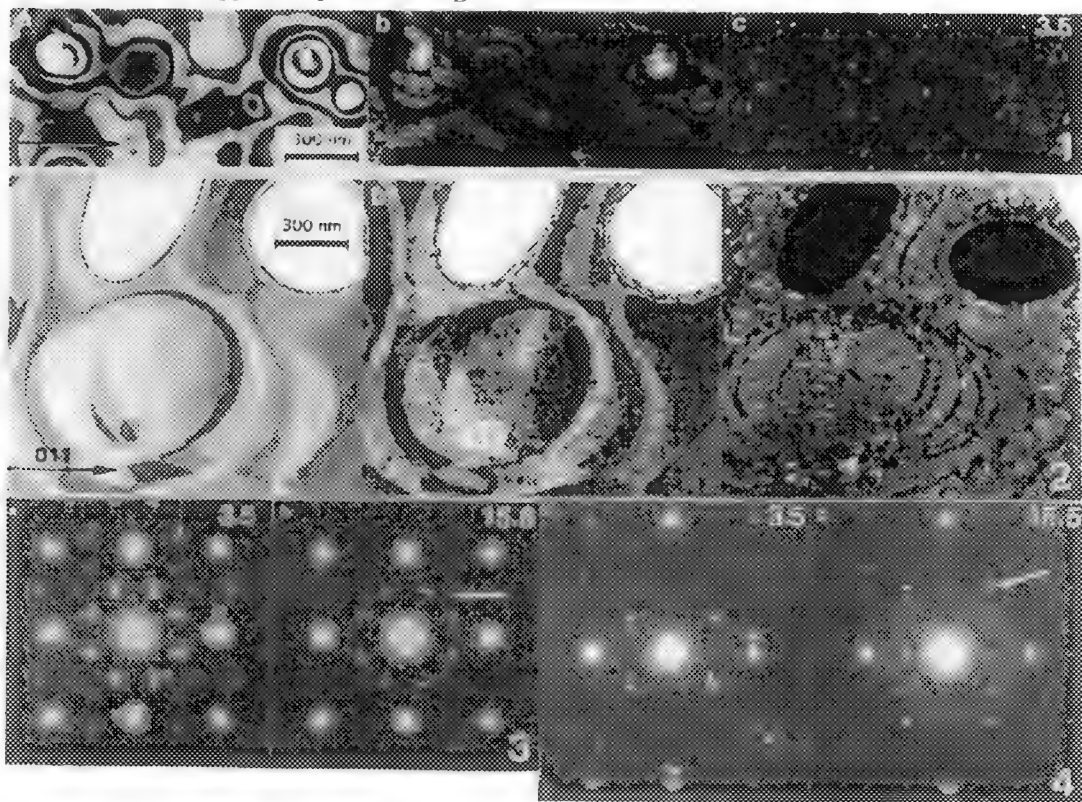


Fig.1: Titania deposited onto MgO (100) substrate which had been annealed for 3.5 min at 1350°C. (a) and (b) are (100) zone-axis BF micrographs taken before and after deposition, respectively. (c) DF micrograph taken using a spinel reflection.

Fig.2: MgO substrate annealed for 15.5 min at 1350°C. (a), (b) and (c) are BF and DF micrographs as for figure 1. Notice the contrast from the terraces when a spinel reflection is used to form the image.

Fig.3: (a) and (b) (100) zone-axis diffraction patterns from the 3.5 and 15.5-min samples, respectively. A spinel reflection is arrowed in figure 3(b).

Fig.4: (a) and (b) {112} zone-axis diffraction patterns from the 3.5 and 15.5-min samples, respectively. The spinel reflection used to form image 2(c) is arrowed.

IMAGING MICROSTRUCTURAL CONTACT DAMAGE IN SILICON

Jonathan C. Morris

Department of Mechanical Engineering and Materials Science, Rice University,
Houston, TX 77251

The indentation of single crystal silicon has been shown to produce a metal to semiconducting structural phase transformation [1-4]. This phase transformation dominates the effect of contact damage from both indentation and scratching at low loads and hence affects the results of related mechanical tests. We are examining the microstructure of contact damage in silicon in order to understand better the mechanisms which control its low-load mechanical and tribological behavior. Extensive transmission electron microscopy (TEM) as well as scanning electron microscopy (SEM) have been used to characterize both morphological and structural changes brought about by contact damage.

The plan-view bright field image in Figure 1 exhibits strong crystallographic contrast outside of the indented area. The indented area as well as the extrusions emanating from it are amorphous as evidenced by their lack of crystallographic contrast regardless of tilt as well as their diffuse illumination in dark field. Small bits of fragmented polycrystalline silicon are visible at the indentation borders as well as at the tip of one extrusion. No dislocation activity or any other defect structure is present save for the transformation. The plan-view scratch segment shown in Figure 2 shows many of the same characteristics as does the indentation, notably a transformed region, an absence of any significant dislocation activity, and extrusions of the transformed phase. This amorphitization from scratching is important to the field of tribology as well as to the understanding of brittle micromachining (diamond point turning of semiconductors).

Thin foils for TEM are made using essentially conventional methods albeit under carefully controlled conditions. Single crystal sections of electronic grade silicon wafers are first dimpled and polished to $< 10\ \mu\text{m}$ thick as indicated by red/orange light transmission. Indentations or scratches are then made on the polished dimpled surface with a microhardness tester fitted with a diamond indenter (Berkovich or Vickers). These samples are argon ion-milled at 5.5 kV and 0.4 mA from the opposite side at an angle of 12° for a short time (between 15 minutes and 45 minutes). Care is taken never to expose the side which has the contact damage to the ion beam in order to avoid possible amorphitization due to ion-milling damage.

References:

1. I.V. Gridneva, Yu. V. Milman, and V.I. Trefilov, *Phys. Status Solidi (a)* **14**, 177, (1972).
2. G.M. Pharr, W.C. Oliver, and D.R. Clarke, *Scripta Metall.* **23**, 1949, (1989).
3. D.R. Clarke, M.C. Kroll, P.D. Kirchner, R.F. Cook, and B.J. Hockey, *Phys. Rev. Lett.* **60**, 2156, (1988).
4. D.L. Callahan and J.C. Morris, *J. Mater. Res.* **7**, 1614, (1992).

Figure 1. (a & b) **0.5 μm**

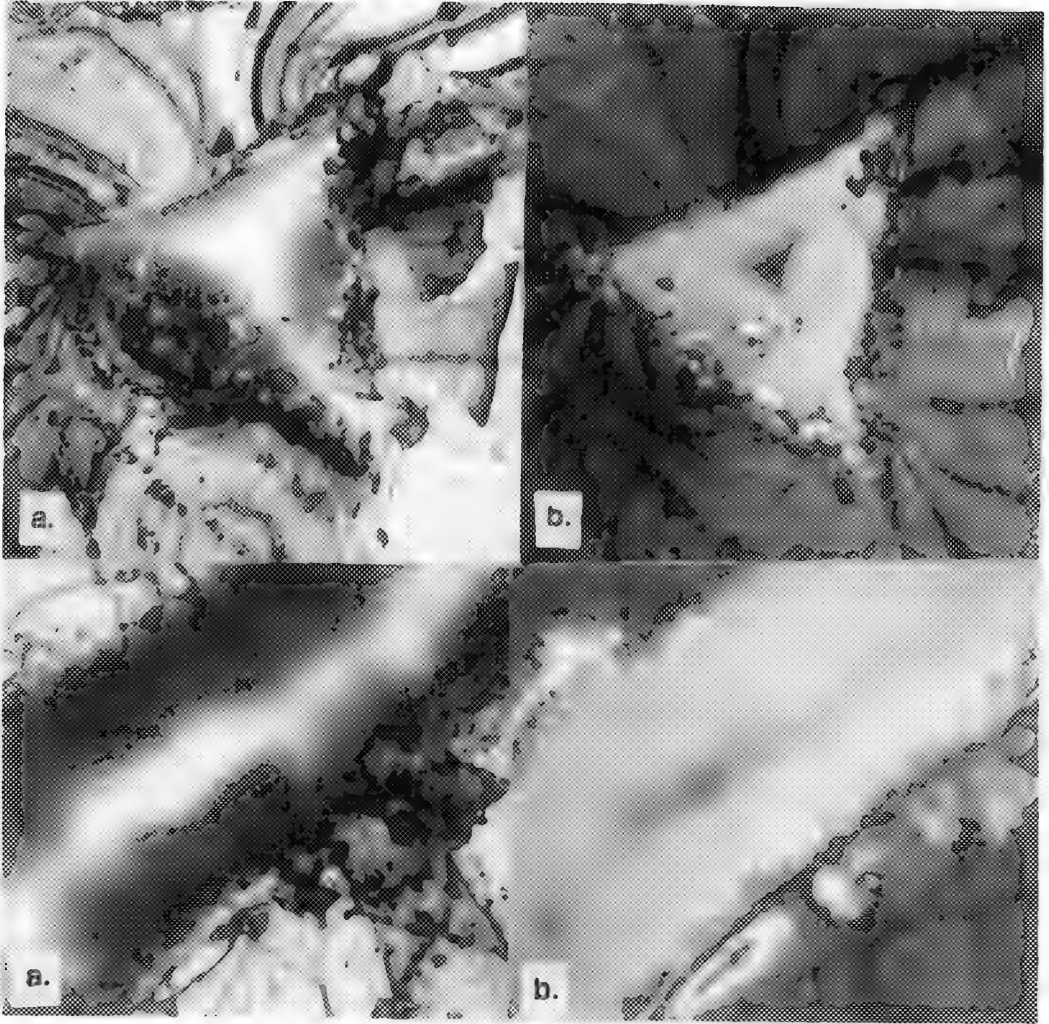


Figure 2. (a &b) **1 μm**

- Figure 1. (a) Bright field plan-view TEM image of a 1 gram Berkovich indentation in (100) Si
(b). Corresponding g220 dark field image
(from reference [4])
- Figure 2. (a). Bright field plan-view TEM image of a 2 gram Vickers scratch on (111) Si
(b). Corresponding diffuse dark field image

CHARACTERIZATION OF THE OXIDATION-SULFIDATION OF A PREOXIDIZED ODS FeCrAl ALLOY

B. A. Pint, B. M. Banks, J. C. Duncan, A. J. Garratt-Reed and L. W. Hobbs

H. H. Uhlig Corrosion Laboratory, Massachusetts Institute of Technology, Cambridge, MA 02139

Preoxidation is a common technique used to protect alloys from environmental degradation. A dense, adherent oxide is grown on an alloy before placing it into a more aggressive environment. Thus, under conditions such as the mixed O-S atmosphere found in coal gasification, the rapid formation of sulfide can be avoided.

While several studies have looked at the formation of protective alumina scales in mixed H_2 - H_2O - H_2S environments,^{1,2} none of these studies have considered the formation of less-protective, metastable aluminas on the oxidation behavior at temperatures less than 1000°C where θ - Al_2O_3 is commonly formed.³ This is especially important because in order to form an adherent alumina scale, an oxygen-active element such as Y, Ce, Hf or Zr is routinely added and these types of elements have been found to stabilize the lower-temperature alumina phases and inhibit the transformation to α - Al_2O_3 .⁴⁻⁵ Furthermore, the transformation from θ - to α - Al_2O_3 involves a 13% volume reduction and cracking through the scale which could compromise the protectiveness of the scale.⁶

In order to avoid these problems, preoxidations of a Y_2O_3 -dispersed Fe-20wt%Cr-4.5%Al-0.3%Ti alloy (Inco's MA956) were done in 1atm of dry, flowing O_2 for 2hr at 1000°C. These conditions had previously been shown to form a dense, adherent α - Al_2O_3 scale.⁷ The samples were then exposed to an H_2 - H_2O - H_2S atmosphere with $\log PO_2 = -20.6$ and $\log PS_2 = -7.6$ (gas mixture A) at 800°C for 20hr. Weight gains were measured during oxidation using a Cahn 1000 microbalance and after oxidation using a Mettler AE163 balance. An MA956 sample that was not preoxidized had a weight gain of $\approx 35\text{mg/cm}^2$ after 20hr at 800°C. The rate of weight gain was linear and the oxidation product was a complex mixture of Fe and Cr sulfides (using glancing angle x ray diffraction). Under the same conditions, the preoxidized MA956 sample had no detectable weight gain after 20hr. By increasing the sulfur content in the gas to $\log PS_2 = -6$ (gas mixture B) a weight gain of $\approx 0.2\text{mg/cm}^2$ was measured after 20hr.

SEM observations of the scale surface before and after exposure to the O-S environment indicated almost no change in the scale surface morphology. Large sulfides (100-200 μm) were observed in selected locations on the sample exposed to gas mixture B, which may account for much of the observed weight gain. Numerous small cracks were observed on the scale surface after preoxidation but very few cracks could be seen after exposure to the O-S environments. No oxide blades or whiskers indicative of θ - Al_2O_3 were observed on any sample. The oxide blades and increased oxidation rates observed in other studies^{2,10} may have been a result of the S in the gas mixture affecting the alumina phase transformation. By preoxidizing at 1000°C and forming an α - Al_2O_3 scale, the effect of S on the formation of the scale appears to have been avoided. However, this result does not address the possibility that the S could still penetrate the α - Al_2O_3 scale, eventually leading to scale breakdown.

To study the possible penetration of sulfur into the preoxidized scale by cracks or grain boundaries, TEM samples were made parallel to the sample surface near the oxide-gas interface and near the metal-oxide interface. The samples were analyzed in a FEG-STEM (VG Instruments HB5) equipped with XEDS. On the preoxidized sample exposed to gas mixture A, the α - Al_2O_3 grain size was very small ≈ 30 -60nm and a few small sulfides ($\approx 20\text{nm}$) were detected near the gas interface but no sulfur was detected near the metal interface. At both locations, Y and Ti were found segregated to the oxide grain boundaries but at the gas interface a small amount of S was also detected on the grain boundaries with an average apparent XEDS S/Al weight percentage ratio of 0.005. This is significantly less than the Y/Al ratio of 0.065 or the

Ti/Al ratio of 0.139. No evidence of scale cracking was observed in either sample. Further work, including transverse sections of the scale, will be conducted in order to further study the extent of S penetration in both gas mixtures A and B.¹¹

References

1. T. T. Huang, et al., J. Electrochem. Soc., 131 (1984) 2191.
2. Y.-K. Kim, et al., in D. Shores and G. Yurek ed., Proc. Electrochem. Soc. Fall Meeting, Electrochem. Soc., Pennington, NJ, (1986) 259.
3. G. C. Rybicki and J. L. Smialek, Oxid. Met., 31 (1989) 275.
4. P. Burtin, et al., App. Catalysis, 34 (1987) 225.
5. B. A. Pint, et al., MRS Symp. Proc., (1993) in press.
6. J. Doychak, et al., Met. Trans., 20A (1989) 499.
7. B. A. Pint, Ph.D. Thesis, Massachusetts Institute of Technology, Cambridge, MA, (1992).
8. L. W. Hobbs and T. E. Mitchell, in 'High Temperature Corrosion', R. Rapp ed., NACE, Houston, TX, (1983) 76.
9. K. Przybylski, et al., J. Electrochem Soc., 134 (1987) 3207.
10. T. T. Huang, et al., Met. Trans., 16A (1985) 2051.
11. The authors would like to thank the National Science Foundation for financial support; and Dr. W. Lipscomb at Inco for providing the alloy.

MICROSTRUCTURE OF FLY ASH CONTAINING CONCRETE, WITH EMPHASIS ON THE AGGREGATE-PASTE BOUNDARY

Marcelle A. Gillott*, Tarun R. Naik**, and Shiw S. Singh**

*Department of Biological Sciences,

**Center for By-Products Utilization, Department of Civil Engineering and Mechanics,
University of Wisconsin-Milwaukee

Concrete is a highly heterogeneous structural material that is subjected to complex stresses. It has been well established that concrete is weakest in the interfacial region between coarse aggregates and the hydrated cement paste. Although there have been several studies on the microstructure of fly ash containing cement pastes, relatively less is known about the effect of fly ash on the aggregate-paste boundary in concrete.¹

Air entrained plain portland cement concrete mixtures were prepared to produce a design strength of 6000 psi at the 28-day age. The air and H₂O-cementitious ratios were held approximately constant for both the control and fly ash containing preparations. ASTM Class C fly ash replaced 15% to 70% of the cement in various samples. Measurement of mechanical properties indicated compressive strength increased for concrete with up to 30% fly ash; only slight differences in tensile strength were observed among the control, 15% and 30% fly ash replacements. To facilitate the study of the microstructure at the aggregate-paste interface, small pieces were fractured and mounted side by side for examination in the SEM. In this manner, the lift-out scars formed when aggregates were pulled out of the concrete during fracture could be readily identified.

Fly ash particles were observed to be present at the paste-aggregate boundary as well as in the ribbons of cement paste between the aggregates. In both situations, the addition of fly ash particles favored the formation of thin hexagonal plates of calcium hydroxide (CH) over the massive euhedral CH crystals found in the no-fly ash control specimens (compare Figs 2-3). The ability of fly ash to reduce the amount of calcium hydroxide in plain cement paste has been documented previously.^{2,3}

Reaction between the fly ash particles and other cement components is evidenced by etching of the glassy surface of the fly ash. Varying degrees of etching have been observed, although a large number of observed fly ash particles appear to be unreacted. Some of the fly ash particles (Fig 4) are at least partially ensheathed by a duplex film.⁴ Examination of polished blocks of fly ash concrete reveals that some of the fly ash particles are partially or completely filled with elongated ettringite-like crystals (Fig 5). The crystals originate at the margins and grow inward from the shell, eventually filling the cavity.

References:

1. P.K. Mehta, ACI, Spec. Pub. 79(1983)1-40
2. Y Halse, *et al.*, Cem. & Con. Res. 14(1984)491-8
3. T. Naik and B.W. Rammee, ACI Mat. J. 86(1989)111-6
4. S. Diamond, *et al.*, Cem. & Con. Res. 10(1980)297-300

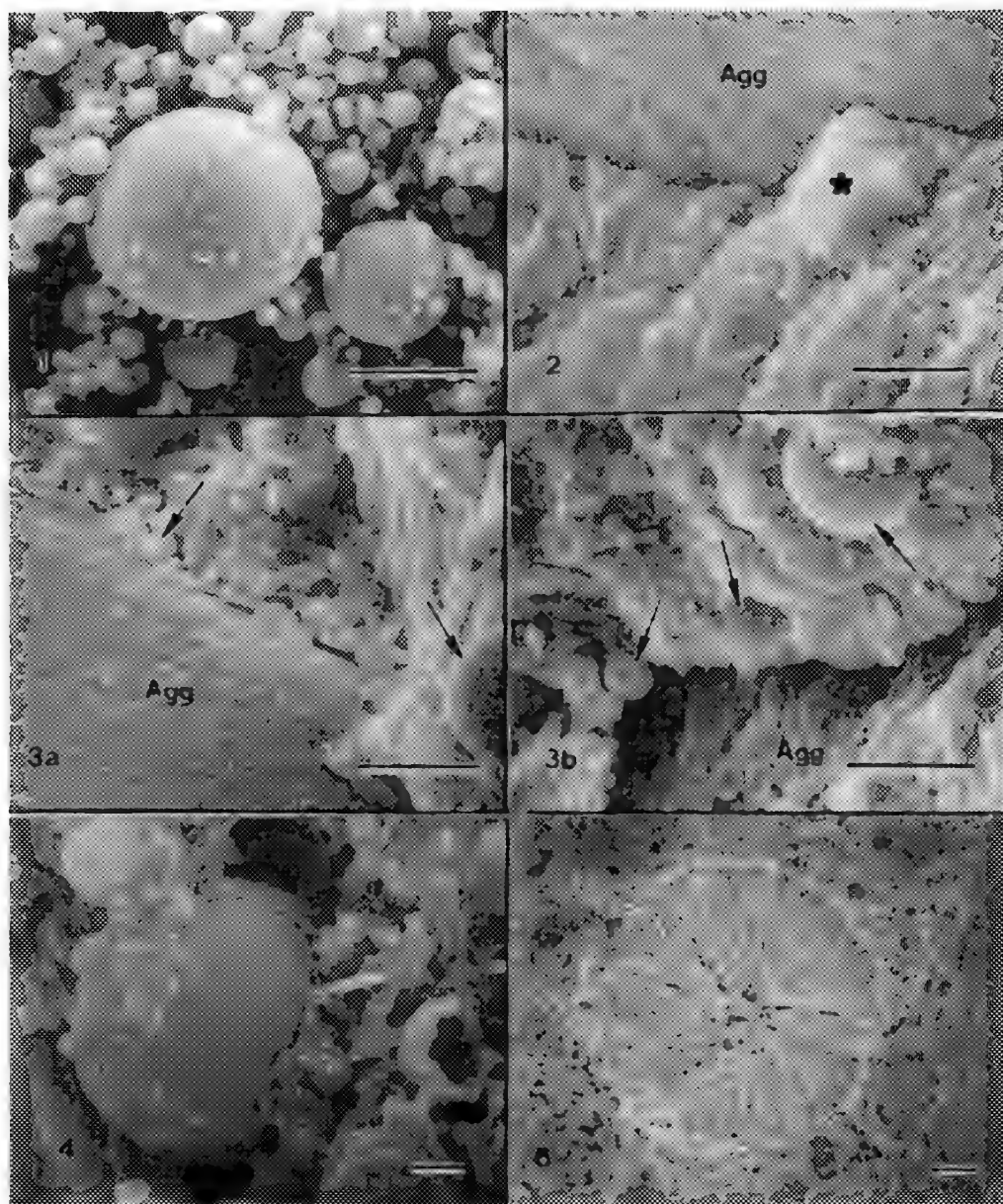


Fig 1. Type C fly ash used in this study. Scale = 10 μ m. Fig 2. Aggregate-paste boundary in control concrete showing large CH crystal (*) in interfacial area. Scale = 10 μ m. Fig 3. Fly ash particles (arrows) in the interfacial zone of in fly ash containing concrete. Fig 3a: 15% fly ash replacement; Fig 3b: 50% fly ash. Scale = 10 μ m. Fig 4. Duplex film partially surrounding fly ash particle. Scale = 1 μ m. Fig 5. Polished concrete specimen showing fly ash particle filled with ettringite-like crystals. Scale = 10 μ m.

A HIGH-RESOLUTION ELECTRON MICROSCOPY STUDY OF GRAIN BOUNDARIES IN Pr AND Co-DOPED ZnO CERAMICS

I.G. Solórzano, J.B. Vander Sande, K.K. Baek and H.L. Tuller

Center of Materials Science and Engineering, M.I.T., Cambridge, MA 02139

Metal oxide varistors are multijunction materials whose nonlinear current-voltage characteristics derive from the electrical activity of their grain boundary regions. The high degree of nonlinearity in polycrystalline ZnO has been attributed to the synergistic action of two types of cations added in sufficient concentrations: transition metals, such as Co and Mn which have ionic radii similar to that of the ZnO matrix, and dopants with large ionic radii, such as Bi and Pr which segregate at grain boundaries and usually form intergranular phases.^{1,2} The present investigation was undertaken with the objective to clarify the role of dopants in an electrically active Pr and Co doped ZnO ceramic by studying the structure and chemistry of individual grain boundaries through high-resolution electron microscopy (HREM) and analytical electron microscopy (AEM).

Bulk specimens containing 1 mol% Pr and 1 mol% Co were prepared by conventional sintering at 1400° C. Some samples followed an oxidative anneal at 650° C for 3 h to further enhance their electrical activity. Electron transparent samples were prepared by mechanical dimpling followed by argon ion beam milling under liquid nitrogen conditions. Low magnification and morphological observations in uncoated samples were possible with an environmental SEM. Conventional TEM observations were carried out with a JEOL 200CX microscope, while high resolution images of selected grain boundaries were obtained with a TOPCON microscope, both working at 200 kV. For analytical microscopy, a 100 kV field-emission-source STEM, VG HB5, was used.

The typical microstructure of an annealed sample shown in fig. 1, reveals a rather equiaxed porous material with average grain size around 50 μm . Significant precipitation is observed, mainly at grain boundaries, with an elongated particle shape. The majority of boundaries appear precipitate-free. Electron diffraction and dark field imaging shows that this phase is crystalline, corroborating our observation in this system conducted with samples prepared by an in-diffusion method³ and contrary to some observations in Bi-doped ZnO varistor⁴. A bright field/dark field pair of micrographs from a rather small intergranular precipitate is shown in fig. 2 where a precipitate pinning effect on the boundary can be inferred. Although no quantitative determination has been attempted, the EDS spectra from these intergranular precipitates reveals only Pr and O peaks in a constant ratio, suggesting that these precipitates constitute the Pr_2O_3 equilibrium phase as proposed by Mukae⁵. The same kind of stoichiometry has been found in precipitates at triple junctions such as shown in fig. 3.

The precipitate-free boundaries analysed exhibit Pr segregation while Co is homogeneously distributed in the ZnO matrix. This observation has been consistent in all boundaries analysed in this study independent of their degree of misorientation. The boundary arrowed in fig. 3 is an example of a low misorientation boundary, also shown in the HREM image of fig. 4. One can observe that the lattice plane fringes of the adjacent grain are continuous right up to the plane of the boundary. This observation, an observation made for all boundaries, implies the absence of

any amorphous layer at the boundary plane, and is therefore contrary to some conclusions drawn by investigators in Bi-doped ZnO varistors.⁴ The superimposed EDS spectra from the boundary of fig.4 and 60 nm away is shown in fig. 5. It is that there is significant Pr segregation at the boundary. Current work is underway to establish a correlation between the structure and composition of the grain boundaries, including precipitation/segregation effects, and the generation of interface traps and related electrical barriers.⁶

References

1. W.G. Morris, J. Vac. Technol. 13(1976)925.
2. D.R. Clark, J. Appl. Phys. 50(1979)6829.
3. I.G. Solórzano et al., Mat. Res. Soc. Symp. Proc. (1993), in press.
4. J. Wong et al., J. Appl. Phys. 46(1975)1827.
5. K. Mukae, Cer. Bull. 66(1987)1239.
6. The authors thank the Center of Materials Science and Engineering at M.I.T. for supporting this work under Contract NSF-MRI DMR-9022933.

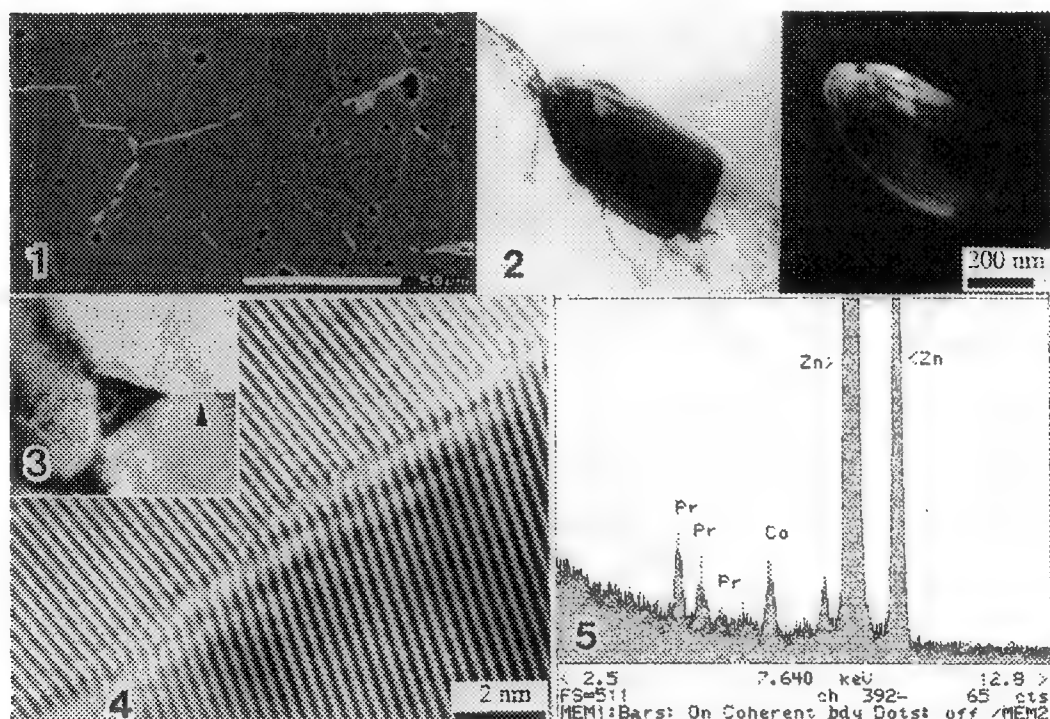


Fig. 1 - SEM micrograph of polycrystalline sample annealed at 650° C for 3 h.

Fig. 2 - TEM bright field/dark field set of typical grain boundary precipitate.

Fig. 3 - TEM bright field image of a triple junction precipitate.

Fig. 4 - HREM micrograph of a low misoriented boundary arrowed in fig. 3.

Fig. 5 - STEM EDS spectra from the grain boundary of fig. 4 (bars) and 60 nm away (dots).

CHARACTERIZATION OF COPPER OXIDE DEPOSITED ON α - Al_2O_3 BY PULSED-LASER ABLATION

M.W. Bench, K.B. Sartain, M.P. Mallamaci and C.B. Carter

Department of Chemical Engineering and Materials Science, University of Minnesota,
421 Washington Ave. SE, Minneapolis, MN 55455

The Cu-Al-O system is of considerable interest for electronic packaging, where thin copper wires are bonded to alumina substrates. In order to optimize the adhesion properties of Cu to alumina, it has been suggested that a ternary bonding environment is necessary at the interface.¹ In comparison to a model oxide system such as NiO/alumina, where NiO is the only stable oxide of Ni and only one phase forms during the reaction, the situation is more complex in the Cu-Al-O system. First, two oxides of copper can form with CuO stable at room temperature and Cu_2O stable above 1020°C in air. In addition, two copper aluminate reaction products (CuAl_2O_4 and CuAlO_2) can form in the Cu-Al-O system. In a previous study it was found that both form during reactions in air at 1100°C , with the relative positions of each dependent on the crystallographic orientation of the alumina substrate.²

In this investigation, pulsed-laser ablation has been used to deposit copper oxide onto single-crystal substrates of (0001) and (1102) α -(Al_2O_3), with the effect of substrate temperature being examined. The laser system used for the depositions was a Lambda Physik excimer laser (model 210i) operating with KrF ($\lambda = 248 \text{ nm}$) at a 10 Hz pulse repetition rate and at an energy of 200 mJ per pulse. The beam from the laser was focused into the deposition chamber and onto a rotating CuO target positioned at a 45° angle of incidence to the beam. The depositions were performed with the Al_2O_3 attached to a substrate heater positioned 6 cm from the target. During deposition and subsequent cool down, the chamber was maintained at an oxygen pressure 4-6 mTorr. Prior to deposition, the substrates were acid cleaned and then annealed in air for 8 hours at 1400°C , which produces a surface consisting of low index terraces separated by steps.³ The samples onto which depositions were performed consisted of both bulk and prethinned TEM specimens. After deposition, the samples were characterized using both SEM and TEM, utilizing a Hitachi S-900 field-emission SEM, a JEOL JSM-840 SEM, and a Philips CM30 TEM (operated at 300 kV).

An example of the result of a 500 pulse deposition on (0001) Al_2O_3 at a nominal substrate temperature of 800°C is shown in Figure 1. In this SEM micrograph it can be seen that copper oxide particles preferentially nucleate along the surface steps, although particles have also nucleated on the terraces. The structure of the particles is more clearly shown in the higher magnification micrograph of Figure 2, where it can be seen that many of the particles have a similar triangular shape and have the same orientation with respect to the substrate, thus suggesting an epitaxial relationship. Preferential orientations were also seen for the depositions on (1102) Al_2O_3 at 800°C . Figure 2 also illustrates that most of the particles show faceting regardless of their overall shape. In addition to these characteristics, many of the particles exhibit a contrast suggestive of a substructure consisting of a particle within a particle. When an otherwise identical deposition is performed on a (0001) Al_2O_3 substrate held at a nominal temperature of 600°C , the growth again occurs as particles but the preferential nucleation along surface steps is no longer seen, as is shown in Figure 3. In addition, the particle faceting and preferential orientations seen at 800°C are not present, with the individual particles exhibiting random shapes. A fraction of the particles do exhibit a similar particle-within-a-particle substructure as was seen after deposition at 800°C . The lack of any preferential orientation relationship is also the case for depositions on (1102) Al_2O_3 at 600°C . The growth of copper oxide as particles is in contrast to results seen for NiO depositions on (0001) Al_2O_3 , where a continuous film is observed for similar deposition conditions.⁴ Preliminary TEM analysis suggests that the depositions at the lower temperature produce CuO, and at the higher temperature a mixture of CuO and Cu_2O may be produced. A detailed analysis of the individual particle structures will be presented.⁵

1. J.E.E. Baglin et al., Nucl. Instrum. Methods **B19/20** (1987) 782.
2. D.W. Susnitzky and C.B. Carter, J. Mater. Res. **6** (1991) 1958.
3. D.W. Susnitzky and C.B. Carter, J. Am. Cer. Soc. **75** (1992) 2463.
4. P. G. Kotula and C.B. Carter, These proceedings.
5. Research supported by the National Science Foundation under grant number DMR-8901218 and by the Center for Interfacial Engineering at the University of Minnesota. The authors wish to thank Prof. Stan Erlandsen for access to the Hitachi S-900 and Paul Kotula for assistance with the laser ablation system.

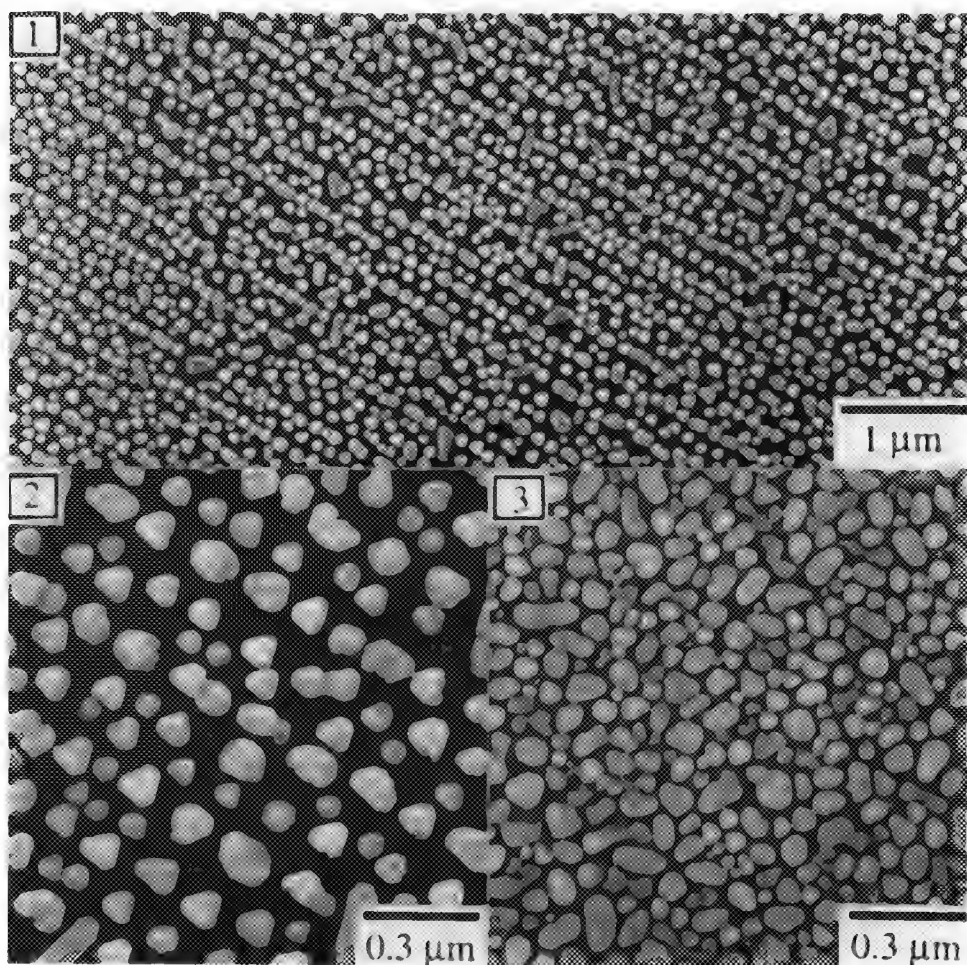


Figure 1. Secondary electron image of copper oxide particles on a (0001) α -(Al_2O_3) substrate from a deposition at a nominal substrate temperature of 800°C.

Figure 2. Higher magnification image of the same sample shown in Figure 1.

Figure 3. Secondary electron image of copper oxide particles on a (0001) α -(Al_2O_3) substrate from a deposition at a nominal substrate temperature of 600°C.

STUDY OF COBALT OXIDE FILMS DEPOSITED ON SINGLE-CRYSTAL YTTRIA-STABILIZED ZIRCONIA BY PULSED-LASER ABLATION

Sundar Ramamurthy, Stuart McKernan and C. Barry Carter

Department of Chemical Engineering and Materials Science, University of Minnesota,
421 Washington Avenue SE, Minneapolis, MN 55455-0132

One of the most common applications of pulsed-laser ablation (PLA) is the production of oxide films of almost any stoichiometry.¹ In this work, thin films of cobalt oxide were grown onto single-crystal yttria-stabilized zirconia (YSZ) substrates of (100) orientation. Film morphology during the early stages of growth has been studied.

Cobalt oxide films grown on suitable substrates have potential applications in electronic and magnetic devices. Like most transition metal oxides, cobalt oxide exists in more than one form, depending on the valence of the cations and their distribution. The transition from CoO to Co₃O₄ occurs at about 900°C in air, CoO being the high-temperature phase. However, by lowering the partial pressure of oxygen, the CoO stability region shifts down to much lower temperatures.²

The laser system used for the depositions was a Lambda Physik model 210i with KrF excimer laser ($\lambda=248$ nm) operating at an energy of 200 mJ per pulse. A Co₃O₄ pellet (96% dense) was fabricated as the target material. Films were grown onto specially prepared single crystal YSZ substrates. The substrate preparation procedure that was adopted is described elsewhere.³ This technique of growing thin-films onto single crystals of known orientation to understand the reaction kinetics has been previously studied for the NiO- α -Al₂O₃ system.^{4,5} Pulse repetition rate and substrate temperature were varied independently, and their effect on the growth morphology of the films was studied. The films were characterized by conventional transmission electron microscopy (TEM) and high-resolution TEM (HRTEM). Both plan-view and cross-section TEM samples were studied.

Films approximately 100 nm thick were grown at a substrate temperature of 700°C. A laser pulse repetition rate of 10 Hz was used in an atmosphere of 7 mTorr oxygen. TEM study of plan-view samples show interesting film morphology characterized by grain boundaries and Moiré fringes (Figures 1a and 1b). The film was found to grow epitaxially with the [111] direction of CoO and Co₃O₄ grains parallel to the [100] direction of the substrate. The microstructure revealed two distinct orientations of CoO. Multiple dark-field imaging in the TEM confirms the presence of two such orientations, while convergent-beam imaging from individual grains showed that the orientations were rotated by 90°. The average grain size of CoO grown under these conditions was found to be 2 μ m. HRTEM studies of the cross-section samples show a continuous film of Co₃O₄ at the substrate-film interface. The growth is found to be epitaxial with the (200) planes of YSZ parallel to the (222) planes of Co₃O₄ (Figure 2).⁷

1. See for example, papers in Mater. Res. Soc. Symp. Proc. **191** (1990)
2. R. Dieckmann, J. Phys. Chem. NF **107**, 189 (1977)
3. E. L. Fleischer et al, J. Mat. Res. **6**, No. 9, 1 (1991)
4. Y. K. Simpson et al, J. Am. Cer. Soc. **70**, C149-151 (1987)
5. P. G. Kotula and C. B. Carter, Mat. Res. Soc. Symp. Proc. **285** (1992)
6. S. McKernan, S. Ramamurthy and C. B. Carter, these proceedings
7. Research supported by NSF under grant No. DMR-8901218, and in part by the user program of the HTML Facility at Oak Ridge National Labs and by the DoE under contract DE-AC05-84OR21400 with Martin Marietta Energy Systems, Inc.

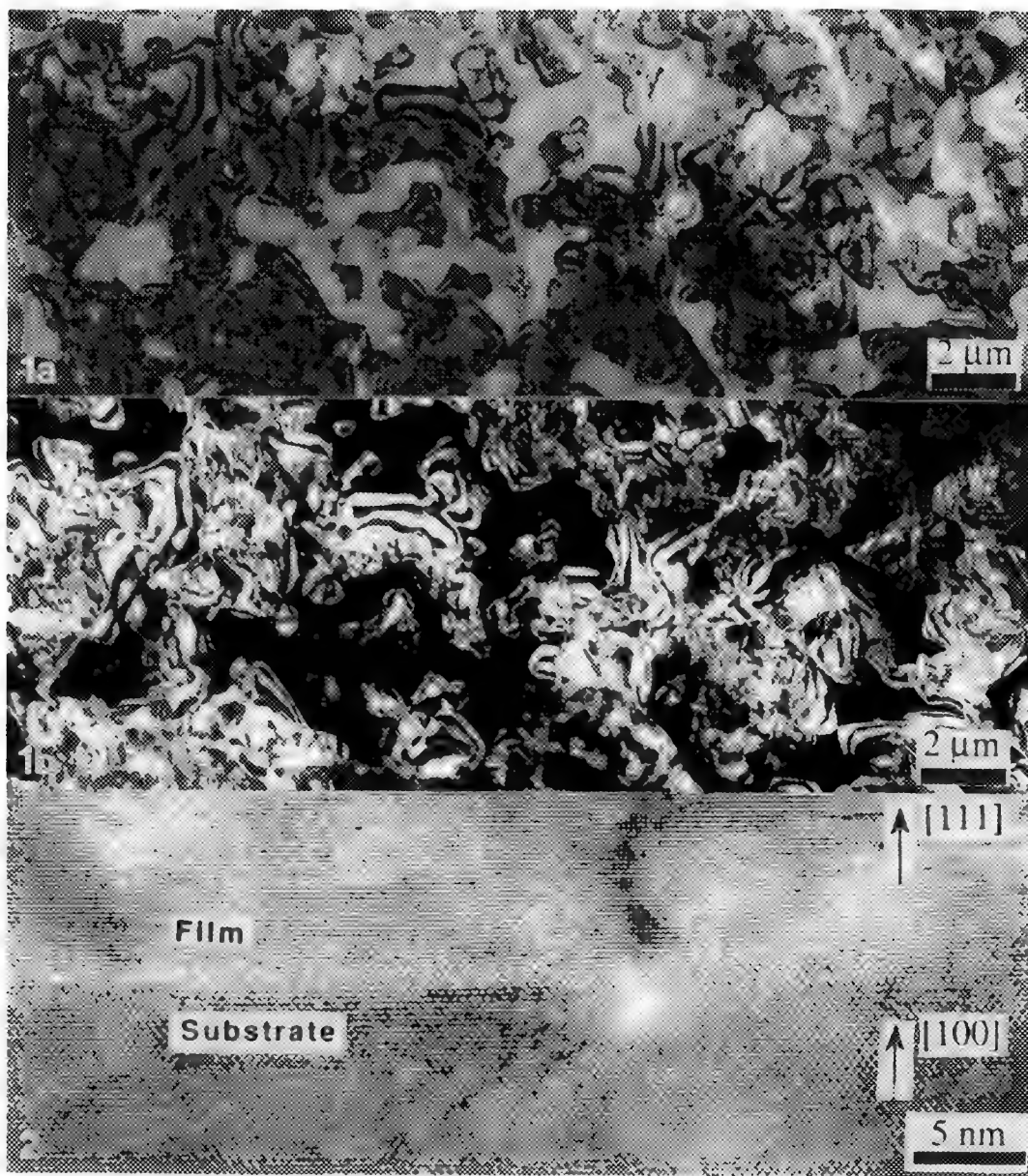


FIG. 1a. Bright-field TEM image of the plan-view sample.

FIG. 1b. Dark-field TEM image of the same area, imaged with the (220) reflection from CoO.

FIG. 2. High-resolution TEM image of a cross-section sample showing Co_3O_4 at the substrate-film interface.

A CROSS-SECTIONAL TEM STUDY OF ION-SPUTTERED HYDROXYAPATITE ON SILICON

K.V. Raghunathan, R.D. Griffin, E.D. Rigney, G.M. Janowski, and G. Petrik

Department of Materials Science and Engineering, The University of Alabama at Birmingham,
Birmingham, AL 35294-4461

Recent improvements in biomaterials have led to the development of coatings such as hydroxyapatite (HA), a calcium phosphate phase. One of the main reasons for the interest in HA as a coating material for titanium bone implants is that it is component of bone and teeth and would be expected to be biocompatible.

HA can be deposited by ion beam sputtering, which produces a thin, adherent coating which is initially amorphous¹. Studies of HA sputter deposited onto titanium have shown that the bond strength increases if the samples are heated-treated under vacuum and decreases if heat-treated in air (Figure 1). The present study will characterize the microstructural evolution of HA which was deposited on a model substrate, Si, after heat treatment.

Coatings of HA were ion beam sputter deposited onto single crystal [001] silicon wafers. The HA-coated silicon wafers were heat treated in air or vacuum at either 500 or 600°C for one hour. The silicon wafers were chosen as a model base material because it was discovered that electron beam transparent thin area could be produced in cross-sectional HA/silicon samples. Previous efforts to prepare cross-sectional HA/titanium samples were unsuccessful because of the large difference in the ion-milling rates of the two components. The cross-sectional samples were produced by the method outlined by Bravman and Sinclair² and ion-milling. They were examined at 200 kV using a liquid nitrogen cooled stage to prevent crystallization of the HA by the electron beam.

The microstructure of the HA samples was not a function of heat treatment atmosphere but was a function of heat treatment temperature. Columnar crystalline HA grains formed during heat treatment at 500 and 600°C. A typical image and selected area diffraction (SAD) pattern from HA are shown in Figure 2. Energy dispersive x-ray spectroscopy (EDS) did not show a compositional difference between the as-sputtered amorphous coating and the crystalline HA coating. There was also no evidence of the formation of any other calcium phosphate phases nor a trend in the lattice parameter of HA for all of the heat treatments. No interaction between the HA coating and the Si substrate occurred during the 600°C heat treatments. However, a Si-O-P amorphous layer between the silicon and the crystalline HA was observed in some areas after heat treatment at 500°C (Figure 3). Typical HA and Si-O-P EDS spectra are shown in Figure 4.

The microstructures of the model HA/Si samples offer no explanation for the observed differences in the bond strength of the heat treated HA/Ti samples. Crystalline HA was found in all of the heat treated samples regardless of temperature and heat treatment atmosphere. The interaction layer was only observed after heat treating at 500°C. Unfortunately, the differences between the oxidation behavior of Ti and Si and, likely, in the interfacial bond strengths make any extension of the HA/Si results to the HA/Ti system tenuous. However, it was demonstrated that the ion beam sputter deposited amorphous coatings crystallize into HA during 500 and 600°C heat treatments, as would also be expected in the Ti/HA system.

References

1. E.D. Rigney, Ph.D. Dissertation, Univ. of Alabama at Birmingham, 1989.
2. J.C. Bravman and R. Sinclair, J. Electr. Microsc. Tech., 1, pp. 53-61 (1984)

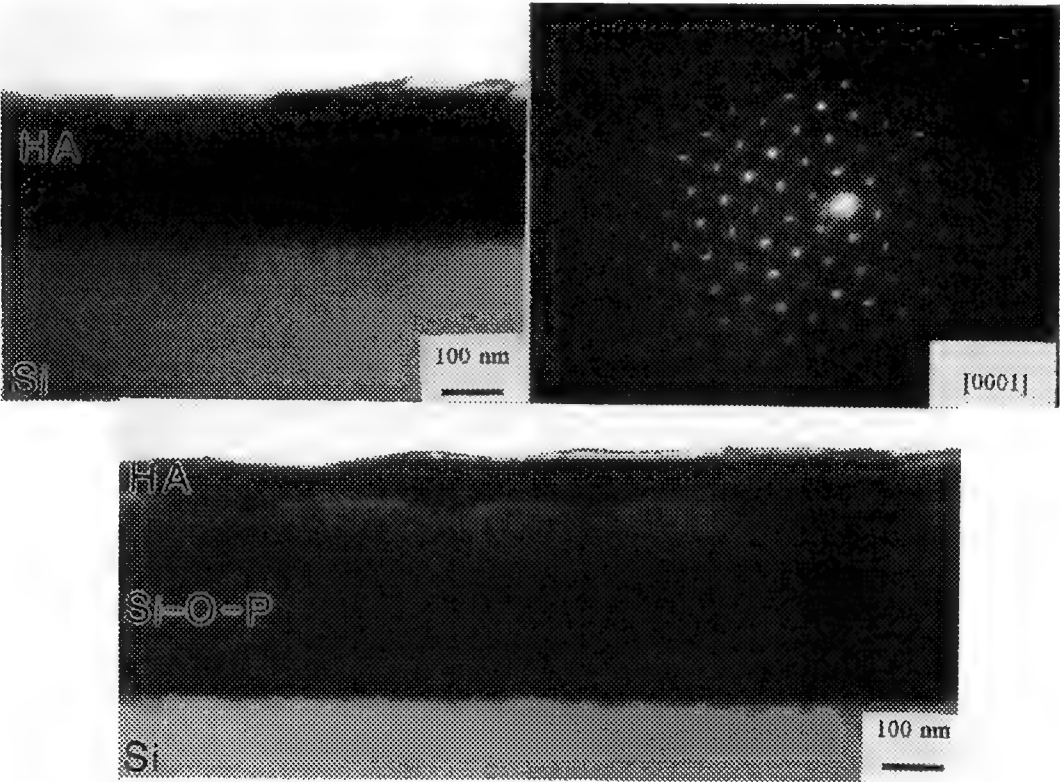
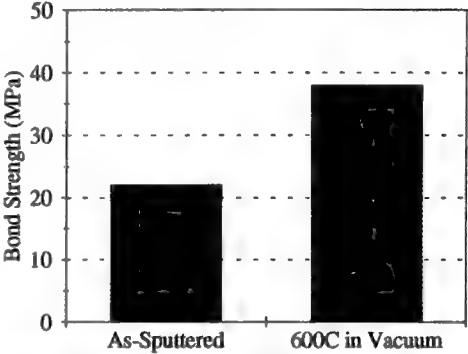
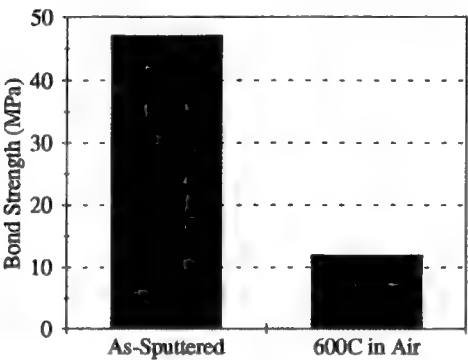


FIG. 1.--Bond strength data for two HA/Ti sample runs heat treated in a)air, b) vacuum.
FIG. 2.--A a) TEM-image and b) SAD of crystalline HA on silicon. These areas are typical for regions without the glassy interface layer (all 600°C samples and many areas of the 500°C samples).
FIG. 3.--A TEM image of the Si-O-P reaction layer which formed in some areas between the crystalline HA coating and the silicon substrate when heat treated at 500°C.

CBED DETERMINATIONS OF STEP-HEIGHTS ON ETCHED AND ANNEALED MgO (100) SURFACES

Simon King, Stuart McKernan and C. Barry Carter

Department of Chemical Engineering and Materials Science, Amundson Hall, 421 Washington Av SE, University of Minnesota, Minneapolis, MN 55455

The annealing in air of acid-etched (100)-oriented MgO substrates at 1350°C for 10 mins or more, has been shown to promote the formation of relatively large and well-defined surface steps.¹ It is the presence of these surface steps which are thought to result in the improvement in the super conducting properties of thin films, such as YBa₂Cu₃O_{7-x} (YBCO), deposited onto the surfaces of annealed, as oppose to unannealed, substrates.² YBCO, in particular, has been shown to exhibit grapho-epitaxy, in which steps on the surface promote the nucleation of islands and influence the subsequent growth into an interconnected film.³ The formation of this interconnected film may be influenced by the height of the steps on the substrate, whilst the height of the steps also may play a role in the island nucleation event itself. Therefore, an investigation of the step heights in the acid-etched and annealed substrates employed for the above studies is of paramount importance.

After experimentation with a number of different methods by which specimen thicknesses may be estimated, it was concluded that CBED gave the most accurate and reproducible results: An experimental technique, based on the "traditional" method of Kelly et al.,⁴ and Allen,⁵ was developed which accommodated the problems associated both with insulating, and progressively contaminating, samples, and with the application of the CBED technique specifically to the measurement of step heights, as oppose merely to the gathering of thickness information.⁶

Results acquired from a specimen annealed for 15.5 mins at 1350°C, and employing the above technique, are shown in Fig.1 (after reference 6). The areas from which individual spot patterns were taken are indicated in Fig.1(a) and strips cut parallel to the operating reflection ($g = \langle 220 \rangle$) from the diffracted disc at each position are shown in Fig.1(b). An analysis of this data, following refs. 5 and 6, is shown in figure 1(c) from which the thicknesses may be determined (see ref.6). The error bars, and errors quoted on thicknesses in table 1 of reference 6 are mean errors, propagated from measurement errors $\Delta\theta_i$ and $\Delta 2\theta_B$, as given by:

$$\Delta y_i = \pm \frac{2}{n_i^2} S_i^2 \left[\left(\frac{\Delta\theta_i}{\theta_i} \right)^2 + \left(\frac{\Delta(2\theta_B)}{2\theta_B} \right)^2 \right]^{1/2}; \Delta t = \pm \left| \frac{l^{-3/2}}{2} \Delta l \right|; \Delta l = \pm \left[\sum_{i=0}^{n_d} \left\{ (\Delta y_i)^2 \left(\frac{1}{n_d^2} + \left(\frac{\bar{x}(x_i - \bar{x})}{\sum (x_i - \bar{x})^2} \right)^2 \right) \right\} \right]^{1/2}$$

where, l is the intercept, t is the thickness, n_d is the number of data points, and other symbols have their usual meanings (see ref 4). The negligible percentage errors in accelerating voltage and lattice parameter are ignored, although it is a trivial matter to include them in the above equations.

Employing a conventional CM30, the minimum practical probe size in microprobe mode is given, nominally, as 5.6 nm. Theoretically, therefore, it should be possible to analyze small terraces (say, 10nm or less) and achieve satisfactory CBED discs (i.e., in which the maxima and minima appear as perfectly straight chords of the diffracted disc). In all of the above determinations, the position of the probe was checked both before and after photographing the diffraction pattern, and only data for which the probe had not moved during this process is analyzed.⁶ However, each individual determination may take a minute or so and problems with charging and specimen drift are unavoidable. For specimens such as is shown in figure 2, in which the morphology is on a much finer scale, this factor, as well as the fact that smaller steps are simply not visible under the 2-beam dynamical conditions necessary for CBED thickness determinations of this type, prohibits the use of a "step-by-step technique" such as this.

For these reasons, a new, faster, and potentially more accurate, technique for the determination of step heights currently is under development. Briefly, the specimen is translated, at as slow and constant a rate as possible, underneath the focused $\text{C}^{*}30$ probe (the electron beam path remains down the optic axis), and the image of the (220) CBED disc captured on videotape. This videotaped "CBED-trace" is then digitized and each frame is checked, via the comparison of parallel line traces taken from different parts of the diffracted disc, to ensure that a flat area lay under the probe. Frames/disc-images which are not from flat areas are discarded. The data from line traces across the remaining images is then processed in order to extract the positions of intensity extrema and calculate the specimen thickness based on the method of Allen⁵. Lastly, thicknesses from neighboring "good" frames are subtracted and step heights determined. A histogram is expected to be the most useful form for the final data. Preliminary results from an analysis of step heights employing this video method will be presented.⁷

References:

¹M.G.Norton et al; Appl. Phys. Lett., **56**, 2246-2248 (1990)
²B.H.Moeckly et al; Appl. Phys. Lett., **57**, 1687-1689 (1990)
³M.G.Norton and C.B.Carter; Scanning Microsc., **6**, 385-398 (1992)
⁴P.M.Kelly et al; phys. stat. sol. (a), **31**, 771-780 (1975)
⁵S.M.Allen, Phil. Mag. A, **43**, 325-335 (1981)
⁶S.L.King et al; Proc. Symposium B, M.R.S. Fall Meeting, Boston (1992) - in press
⁷The authors acknowledge the support of the D.O.E. under grant number DE-FG02-92ER45465

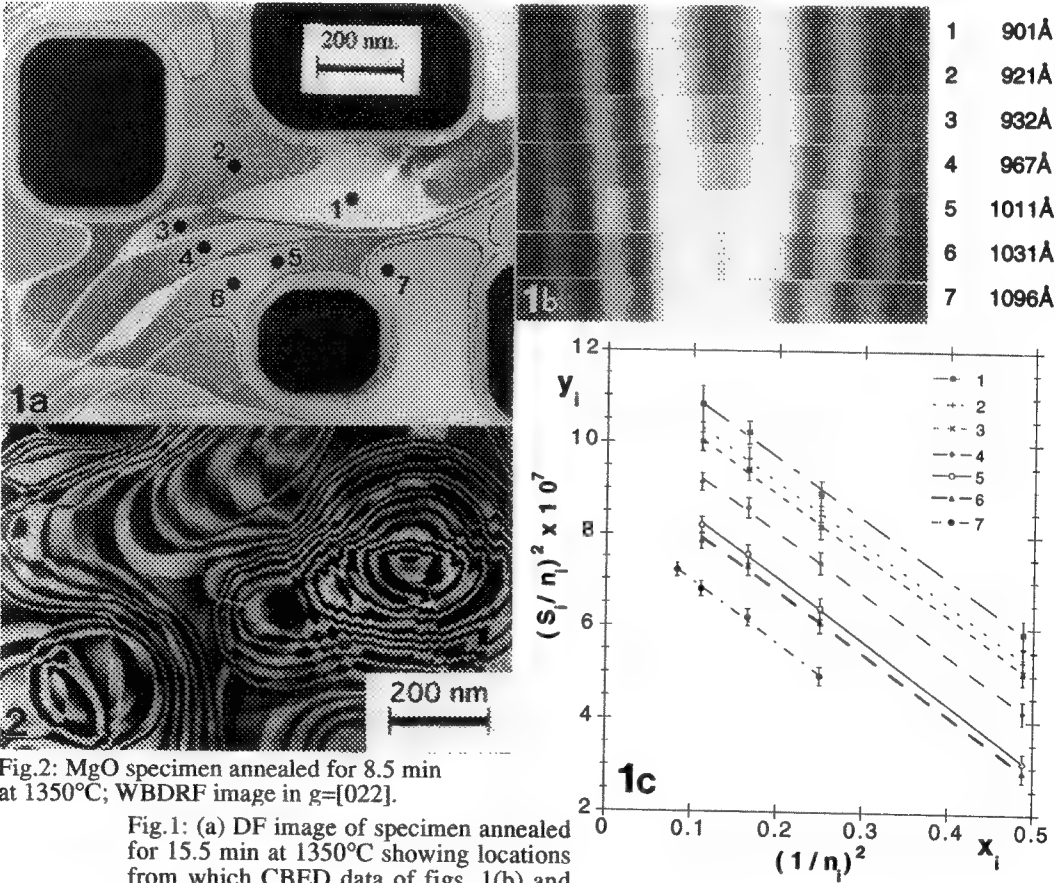


Fig.2: MgO specimen annealed for 8.5 min at 1350°C; WBDRF image in $g=[022]$.
 Fig.1: (a) DF image of specimen annealed for 15.5 min at 1350°C showing locations from which CBED data of figs. 1(b) and 1(c) are taken.

HRTEM Image of Twin Structure in Nanocrystalline Platinum

Hong-Ming Lin, Chi-Ming Hsu, Ching-Shung Huang, Ming-Shyong Lay and Pee-Yew Lee⁺

Department of Materials Engineering, Tatung Institute of Technology, Taipei, Taiwan, R.O.C.

⁺Marine Engineering Department, National Taiwan Ocean University, Keelung, Taiwan, R.O.C.

This paper presents recent result on the observation of microstructure of nanocrystalline platinum. Nanocrystalline powders of Pt are made by gas condensation method, and examined by using TEM and HRTEM. Twin structure is found first within the individual particle of as evaporated nanophase Pt particles which form twin during the nucleation and growth of particle. Twin also appears while neck growth take place during the sintering of as evaporated Pt with Al_2O_3 . The formation of these twins during sintering was due to the fact that the neck growth will induce a tensile stress which is high enough to pull the nanocrystalline powders to form twin structure. Twin plane of nanophase sintering Pt powder was identified by using the Fourier transformation as $\{111\}$ plane. It is the same as usually found in fcc bulk materials.

The pure nanocrystalline Pt particles with a diameter less than 100 nm had been produced by the gas evaporation in helium atmosphere. Starting materials are placed on the tungsten boat. The nanophase Pt particles are formed by evaporating the Pt under 100 mbar of He atmosphere and collected on the cold trap. As evaporated Pt powder is then mixed with 0.3 μm diameter of Al_2O_3 powder and sintered at 600°C. As evaporated nanophase Pt and sintering nanophase Pt are examined by using HITACHI-800 TEM and JEOL 4000EX HRTEM.

Figure 1 shows a HRTEM image of twin structure in as evaporated nanophase Pt particle. Image analysis of the twin plane is identified as $(1\bar{1}1)$ indicated in Figure 2. Sintering of nanophase Pt with Al_2O_3 also produces twin structure which is shown in Figure 3. The formation of the sintering twin is due to the neck growth of two particles. This neck growth will induce a capillary forces which is relating to the surface tension. According to the Laplace's equation the induced stress is calculated about 8000 psi, therefore, it is not surprised to see the twin structure during the sintering. This kind of twin can be classified as deformation twin. Through the Fourier transformation of lattice image, the diffraction pattern in Figure 3 shows that the sintering twin plane is (111) too. The observations of the formation of sintering twin plane in nanophase particles shows in Figure 4. Figure 4 indicates an electron beam induced sintering of nanophase Ni particles. The twin planes of nanophase Ni particles are formed by increasing the electron radiation time. It is evident that twin structure happens in two processes. One is the twin formation during nucleation and growth of Pt metal vapor in the gas condensation chamber. The other process is necking and growth during the sintering between particles and corresponds to the formation of sintering twin. Sintering will induce tensile stress which is proportional inversely to the curvature of radius of neck. This induced stress pulls the edge of particle and hence produces the twin structure. The observation of twin plane of nanophase Pt particles in this study is the same as that of the bulk Platinum. Twin plane is $\{111\}$ in fcc structure both for the nanophase and bulk platinum.

REFERENCES

1. A Karlen and A Tholenm, *Proceedings of Electron Microscopy Society of America*, (1985)382.
2. S. Tehuacanero, R. Herrera, M. Avalos and M. Jose Yacaman, *Acta Metall.*, **40**(7), (1992)1663.
3. W. Wunderlich, Y. Ishida, R. Maurer, *Scripta Metallurgica*, **24**(2), (1990)403.
4. Chihiro Kaito, Kazuo Fujita and Hatsuiro Hashimoto, *Japan J. of Applied Physics*, **12**(4), (1973)489.
5. Supported by NSC contract NSC-82-0405-E036-032.

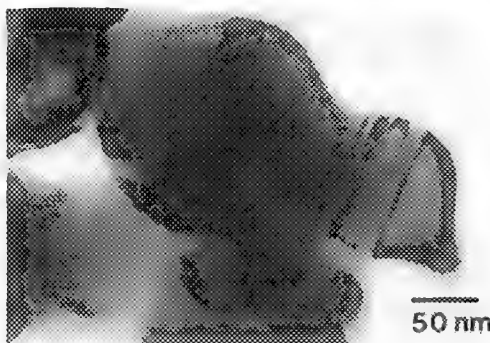
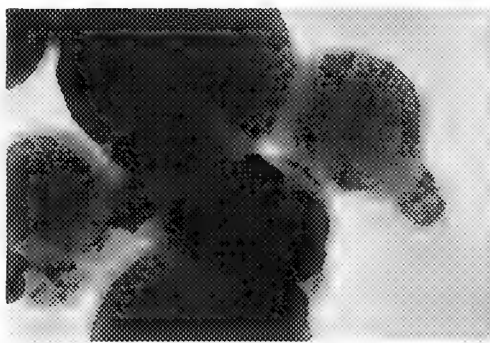
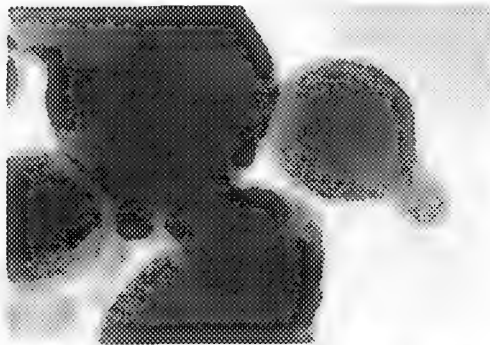
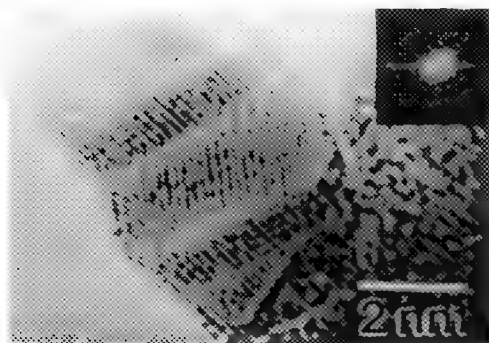
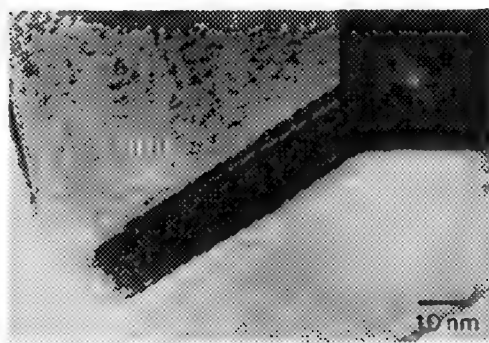


Figure 1 : HRTEM image of twin structure in as evaporated nanophase Pt.

Figure 2 : The image analysis indicated the twin plane of nanophase Pt is (111).

Figure 3 : HRTEM observation of the sintering twin plane of nanophase Pt on Al_2O_3 surface. Twin plane is (111).

Figure 4 : TEM observations of the sintering twin formation in nanophase nickel. Images (a), (b) and (c) are taken at few minute interval. The sintering of nanophase Ni is induced by the electron beam of TEM.

ELECTRON MICROSCOPY STUDY OF SHOCK SYNTHESIS OF SILICIDES

Kenneth S. Vecchio

Dept. of Applied Mechanics and Engineering Sciences, MC-0411, UC-San Diego, LaJolla, CA 92093

Shock-induced reactions (or shock synthesis) have been studied since the 1960's but are still poorly understood, partly due to the fact that the reaction kinetics are very fast making experimental analysis of the reaction difficult. Shock synthesis is closely related to combustion synthesis, and occurs in the same systems that undergo exothermic gasless combustion reactions. The thermite reaction ($\text{Fe}_2\text{O}_3 + 2\text{Al} \rightarrow 2\text{Fe} + \text{Al}_2\text{O}_3$) is prototypical of this class of reactions. The effects of shock-wave passage through porous (powder) materials are complex, because intense and non-uniform plastic deformation is coupled with the shock-wave effects. Thus, the particle interiors experience primarily the effects of shock waves, while the surfaces undergo intense plastic deformation which can often result in interfacial melting. Shock synthesis of compounds from powders is triggered by the extraordinarily high energy deposition rate at the surfaces of the powders, forcing them in close contact, activating them by introducing defects, and heating them close to or even above their melting temperatures.

Niobium and molybdenum silicides were synthesized by the passage of high-amplitude shock waves through elemental powder mixtures. These shock waves were generated by planar parallel impact of explosively-accelerated flyer plates on momentum-trapped capsules containing the powders (see Ref. 1 for details). Impacts were conducted at two velocities (1.2 and 1.9 km/s) and two temperatures (~300 and ~773K). Recovery of the specimens revealed unreacted, partially-reacted, and fully-reacted regions, in accord with shock energy levels experienced by the powders. Electron microscopy was employed to characterize the partially- and fully-reacted regions for the Mo-Si and Nb-Si systems, and revealed only equilibrium phases (such as: Nb, Si, NbSi₂ and Nb₅Si₃ in the Nb-Si system and Mo, Si, and MoSi₂ in the Mo-Si system). Selected-area and convergent beam electron diffraction combined with x-ray microanalysis verified the crystal structure and compositions of the reacted products.

Figure 1 shows backscattered electron micrographs of unreacted, partially-reacted and fully-reacted regions of the Nb-Si capsules. Figure 2 shows a backscattered electron micrograph of the transition between unreacted and partially-reacted regions of the Mo-Si capsule. Figure 3 is a TEM micrograph of the partially-reacted region of the Nb-Si capsule showing the small NbSi₂ particles embedded in resolidified Si, as verified by the presence of annealing twins. In both capsules, the formation of the disilicide phase occurs via the same reaction mechanism characterized by the small nodules forming along the metal-silicon interface. Diffusion couples between Nb and Si bulk materials were fabricated for the purpose of measuring static diffusion rates and determining the phases produced under non-shock condition. Comparison of these non-shock diffusion results with the shock synthesis results indicates that a new mechanism is responsible for the production of the NbSi₂ and MoSi₂ phases under shock compression. The rate of silicide formation under shock synthesis was approximately 10⁸ times faster than under non-shock conditions. In the Nb-Si system under shock compression, the reaction can be rationalized at the local level, through the production of a liquid-phase reaction product (NbSi₂) at the Nb-particle/Si-liquid interface, the formation of spherical nodules (~2 μm diameter) of this product through interfacial tension, and their subsequent solidification. The heat generated by the reaction is sufficient to melt niobium along the interface which facilitates both the expulsion of the NbSi₂ nodules into the liquid Si, and the generation of fresh Nb interface for further reaction. A similar reaction mechanism can also be rationalized for the Mo-Si system examined here.

References

1. M. A. Meyers, L.-H. Yu, and K. S. Vecchio, in *Shock Compression of Condensed Matter, 1991*, S. C. Schmidt et al., eds., Elsevier Science Publishers B. V., 1992.

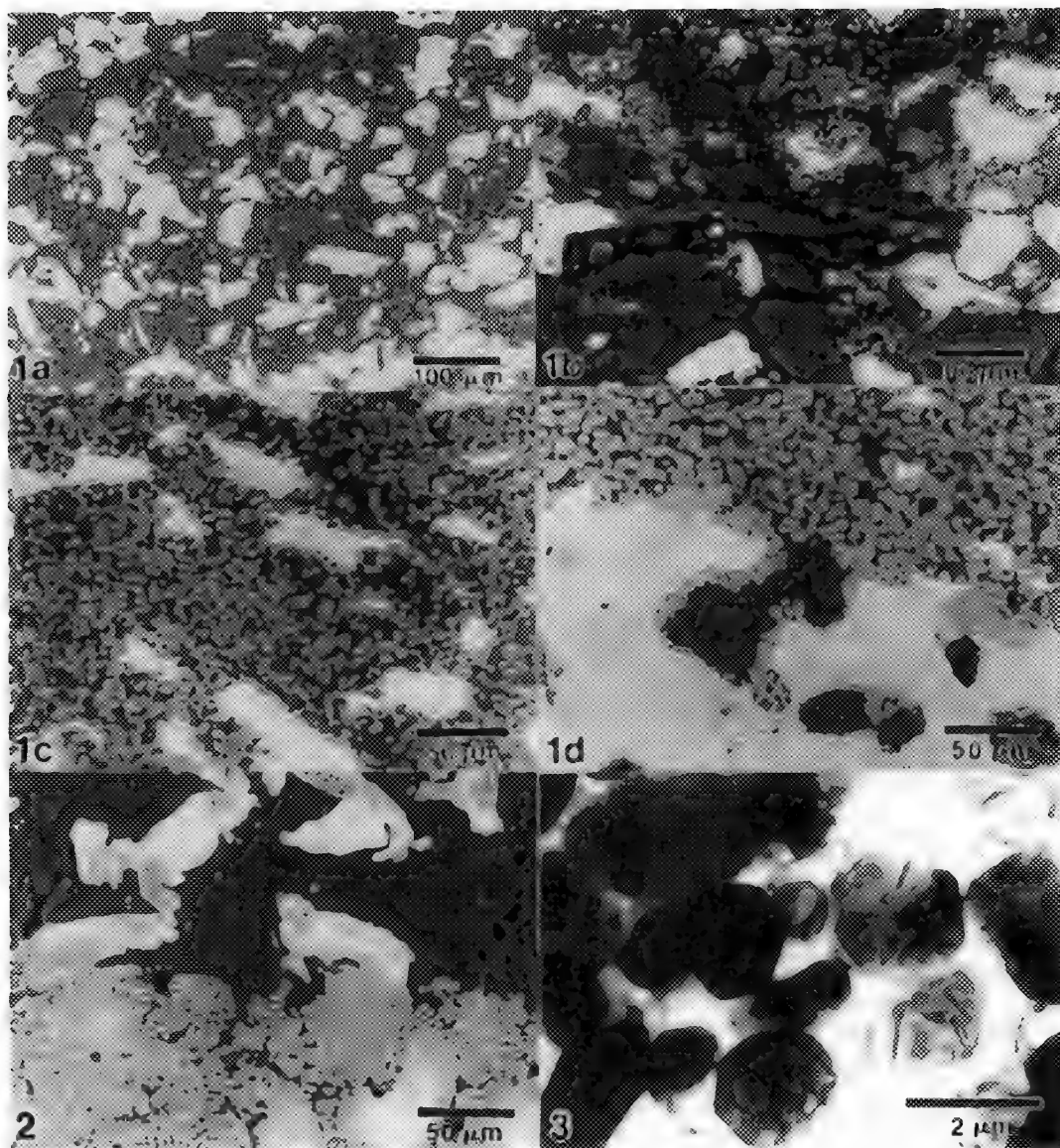


FIG. 1.--Backscattered electron micrographs of (a) the unreacted but compacted region taken from near the top of the capsule, (b) the transition region between unreacted and partially-reacted material, with the reacted material being the small gray nodules identified as NbSi_2 , (c) the partially-reacted region which makes up the majority of the sample and consists of Nb particles surrounded by a reaction layer of NbSi_2 nodules and embedded within a two-phase matrix of NbSi_2 nodules and silicon, (d) the transition region from the partially-reacted to fully-reacted material located near the bottom of the capsule.

FIG. 2.--Backscattered electron micrograph of the transition between unreacted and partially-reacted regions of the Mo-Si capsule.

FIG. 3.--TEM micrograph of the partially-reacted region of the Nb-Si capsule showing the small NbSi_2 particles embedded in resolidified Si, as verified by the presence of annealing twins.

ELECTRON MICROSCOPY STUDY OF CARBON CONTENT EFFECTS ON CARBIDE PRECIPITATION AND CHROMIUM DEPLETION IN TYPE 304 STAINLESS STEELS

E.A. Trillo, A.H. Advani, L.E. Murr and W.W. Fisher

Department of Metallurgical and Materials Engineering and Materials Research Institute
University of Texas at El Paso, El Paso, TX 79968

Carbon content is the most critical compositional variable in carbide precipitation and sensitization development in stainless steels (SS). Quantitative electrochemical test methods have conclusively demonstrated that an increase in carbon content enhances the susceptibility of SS to sensitization development.¹⁻³ The increase in sensitization has been considered to be caused by the influence of carbon on the thermodynamics of the precipitation-depletion process. This has been supported by limited TEM work.^{2,3} In this research, we are using electron microscopy to quantify the effects of carbon content on carbide precipitation and chromium-depletion development in SS. Initial observations that compare precipitation characteristics and depletion profiles in 0.011% C, 0.025% C, 0.051% C, and 0.07% C-containing, 304 SS heat treated at 775°C for 0.1-500 h are presented in this paper, and will be enhanced by a statistical analysis of carbon content effects on precipitate sizes, densities, and depletion profiles, to provide a valuable insight into the precipitation-depletion phenomena. Experimental methods used to study carbide precipitation and measure depletion profiles have been documented in previous work.⁴

Carbon content was observed to have a dramatic effect on grain boundary carbide precipitation in 304 SS. The critical effects of carbon on carbide precipitation in the four SS alloys are illustrated in Figure 1, which shows a systematic increase in carbide sizes and densities with increasing carbon content, for a 775°-10 h heat treatment. The 0.011% C sample was observed to contain essentially no carbides, while isolated to semi-continuous carbide formation was seen on grain boundaries in the 0.025% C alloy. Beyond 0.051% C, the carbide precipitation was observed to be continuous on most boundaries, though the carbides were noted to be significantly larger in the 0.07% C versus 0.051% C material. The systematic influence of the amount of carbon on carbide precipitation observed in this work is the cause for the increased sensitization susceptibility of SS observed with carbon content by previous researchers.¹⁻³

A comparison of chromium-depletion profiles, measured on the four alloys, illustrates the effects of carbon content on the thermodynamics and kinetics of sensitization development in SS (Figure 2). The minimum chromium level seen on the grain boundary reflects the thermodynamic equilibrium produced by the carbide nucleation reaction. The sharp decrease in the minimum value from the matrix level to 13% is caused by an increase in the activity of carbon with increasing carbon level from 0.011% to 0.07% C. A simultaneous change in the width of the depletion profiles is also produced with an increase in carbon content. The profile for the 0.011% C sample is essentially flat (i.e. there is no depletion), and the width of the profile then increases to 400 nm with an increase in the amount of carbon. The width represents a kinetic effect of carbon content on sensitization, and may be caused by an early onset of sensitization in high versus low carbon materials.¹ Clearly, carbon content is key to the precipitation-depletion process in SS, and we will focus on a statistical enhancement of our electron microscopy results to develop a fundamental understanding and model for the influence of carbon on sensitization development in SS.

1. S.M. Bruemmer, *Corrosion*, v. 42 (1), 1986, pp. 27-35.
2. C.L. Briant, R.A. Mulford, and E.L. Hall, *Corrosion*, v. 38 (9), 1982, pp. 468-477.
3. R. Pascali, A. Benvenuti, and D. Wenger, *Corrosion*, v. 40 (1), 1984, pp. 21-32.
4. A.H. Advani et al, *Scripta Metallurgica et Materialia*, v. 27, 1992, pp. 1759-1764.
5. The work was supported by NSF (RIMI) Grant HRD 9105065, and GSA Grant PF90-018 administered by the Materials Research Institute.

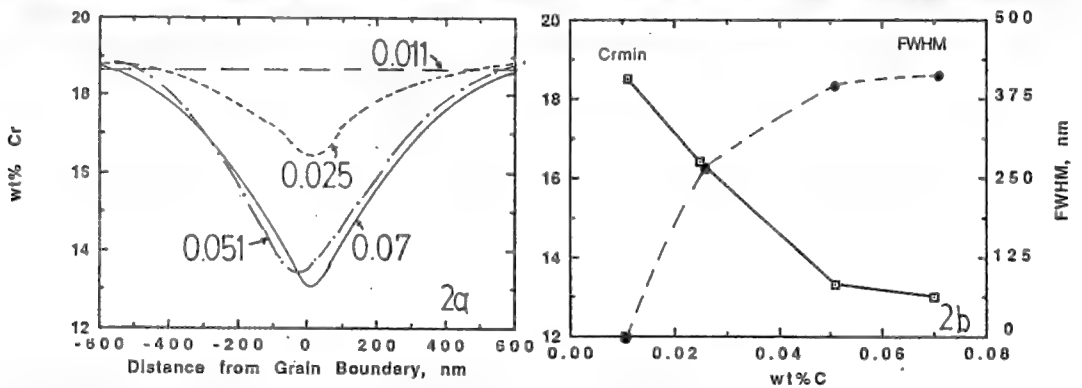
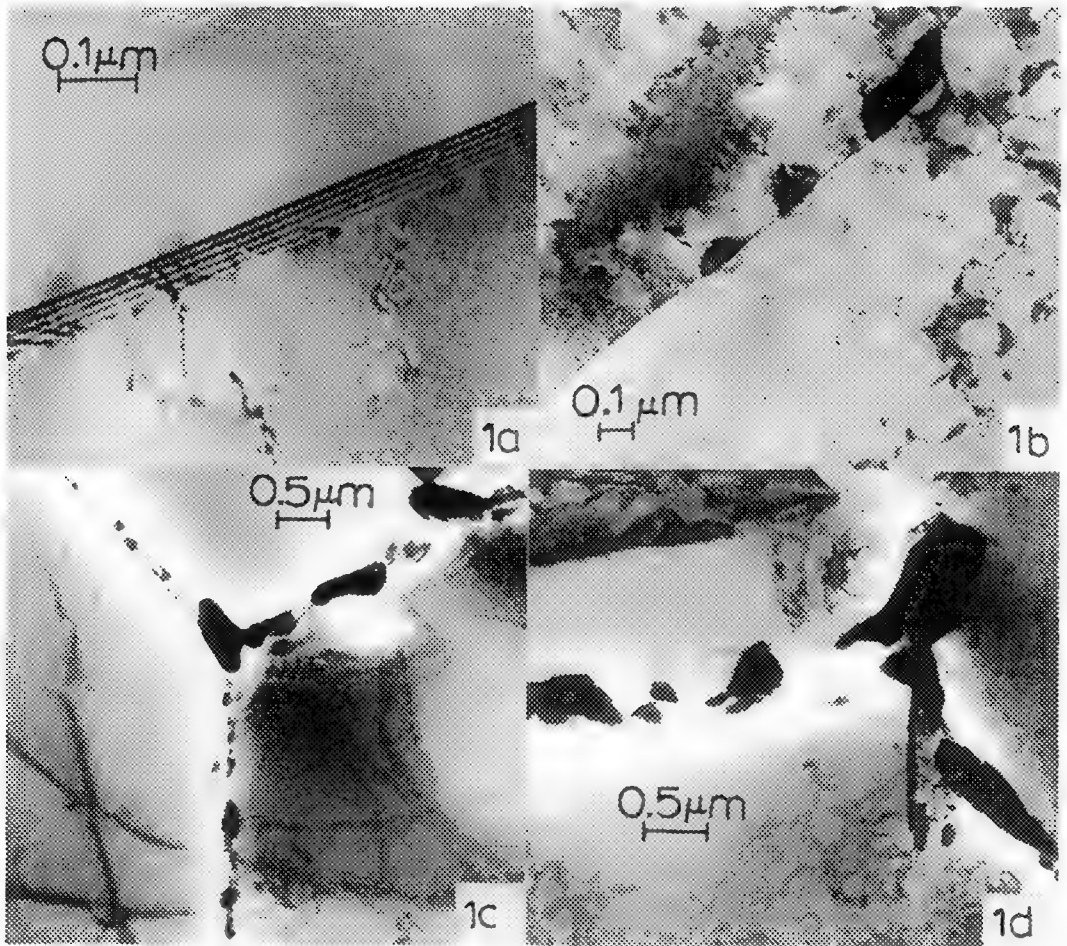


Figure 1. Illustration of carbon content effects on carbide precipitation in 0.011% C (a), 0.025% C (b), 0.051% C (c) and 0.07% C (d), Type 304 SS heat treated at 775°C for 10 h.

Figure 2. Comparison of chromium-depletion profiles (a), and chromium-minimums and full-width at half maximum (FWHM) values (b) measured as a function of carbon content in 775°C-10 h, Type 304 SS.

SOME COMPARATIVE OBSERVATIONS OF CARBIDE PRECIPITATION MORPHOLOGY RELATED TO COHERENT TWIN BOUNDARIES AND HIGH-ENERGY GRAIN BOUNDARIES IN STAINLESS STEELS

R. J. Romero, E. A. Trillo, A. H. Advani, L. E. Murr, and W. W. Fisher

Department of Metallurgical and Materials Engineering and Materials Research Institute, The University of Texas at El Paso, El Paso, Texas 79968 USA

Stickler and Vinckier¹ showed more than three decades ago that there is a very consistent relationship between the boundaries upon which carbides ($M_{23}C_6$) precipitate in 300 series stainless steels (having carbon contents ranging from 0.02 to 0.08 wt%). For example, carbides first appear on regular (high-energy) grain boundaries, then non-coherent boundaries and steps on annealing twins, and finally on coherent twin boundaries at a constant temperature above about 600° C, and at aging times which, correspondingly, change by orders of magnitude (1, 10, 100 hrs. respectively at 675°C for 304 stainless steel). We have examined a wide range of precipitation features on these various boundaries in 316 and 304 stainless steels which have not been described previously because there have been limited observations comparing carbide morphologies in the transmission electron microscope (TEM) for high-energy grain boundaries ($\gamma_{gb} \sim 800 \text{ mJ/m}^2$), non-coherent steps on twin boundaries ($\gamma_{TB} \sim 200 \text{ mJ/m}^2$), and coherent twin boundaries ($\gamma_{tb} \sim 20 \text{ mJ/m}^2$) for 316 and 304 stainless steels.^{2,3}

In this investigation we have observed some very interesting and consistent carbide morphologies associated with these three interfacial regimes, and we illustrate these observations in Figures 1-3. Figure 1 shows some optical microscope views of the three different boundary features (types) outlined above prior to sensitization and aging experiments to form carbide precipitates. Figure 2 shows carbides forming on each of these boundary types. Figure 2 illustrates the dramatic effect that deformation (strain) has on sensitization and carbide formation. While Figure 2 (a) and (b) show the delayed precipitation on coherent (annealing) twin boundaries, there is insufficient resolution to make any morphological distinctions. However as illustrated in the comparative TEM views in Figure 3, very distinct morphologies occur especially when comparing grain boundary precipitates and precipitates on coherent twin boundaries, particularly non-coherent steps on the boundaries. In each case, the precipitates grow prominently along coherent $\{111\}$ trace directions and are often fully coincident with $\{111\}$. These coherent precipitate interfaces produce facets or simple planar geometries (plates with aspect ratios related to ratios of the corresponding interfacial free energies). In these arrangements, illustrated in Figure 3, plates of carbides nucleate prominently at higher energy steps and grow parallel to the coherent $\{111\}$ planes. By comparison, plates or similar faceted morphologies grow out of small steps and ledges on grain boundaries along $\{111\}$ plane trace directions. These are rather classical phenomena which are quite consistent with fundamental nucleation and growth phenomena.^{2,3} Indeed, precipitation of carbides has been described by cuboidal and related morphologies in the matrix which arise through coincidence with $\{111\}$ planes in the fcc stainless steel matrix,² as discussed previously for growth from non-coherent twin boundaries.³

This research was supported in part by a National Science Foundation (RIMI) Grant HRD 9105065 and EPA Cooperative Agreement CR-81 8296-01-0 through the Southwest Center for Environmental Research and Policy. This work was also funded by GSA Grant PF 90-018 administered by the Materials Research Institute at the University of Texas at El Paso.

1. R. Stickler and A. Vinckier, Trans. ASM (1961) 54, 362.
2. L. E. Murr, Interfacial Phenomena in Metals and Alloys, Addison-Wesley, N.Y., 1975, Reprinted by Tech Books, Inc., Fairfax, VA, 1990.
3. N. Terao and B. Sasmal, Metallography (1980) 13, 117.

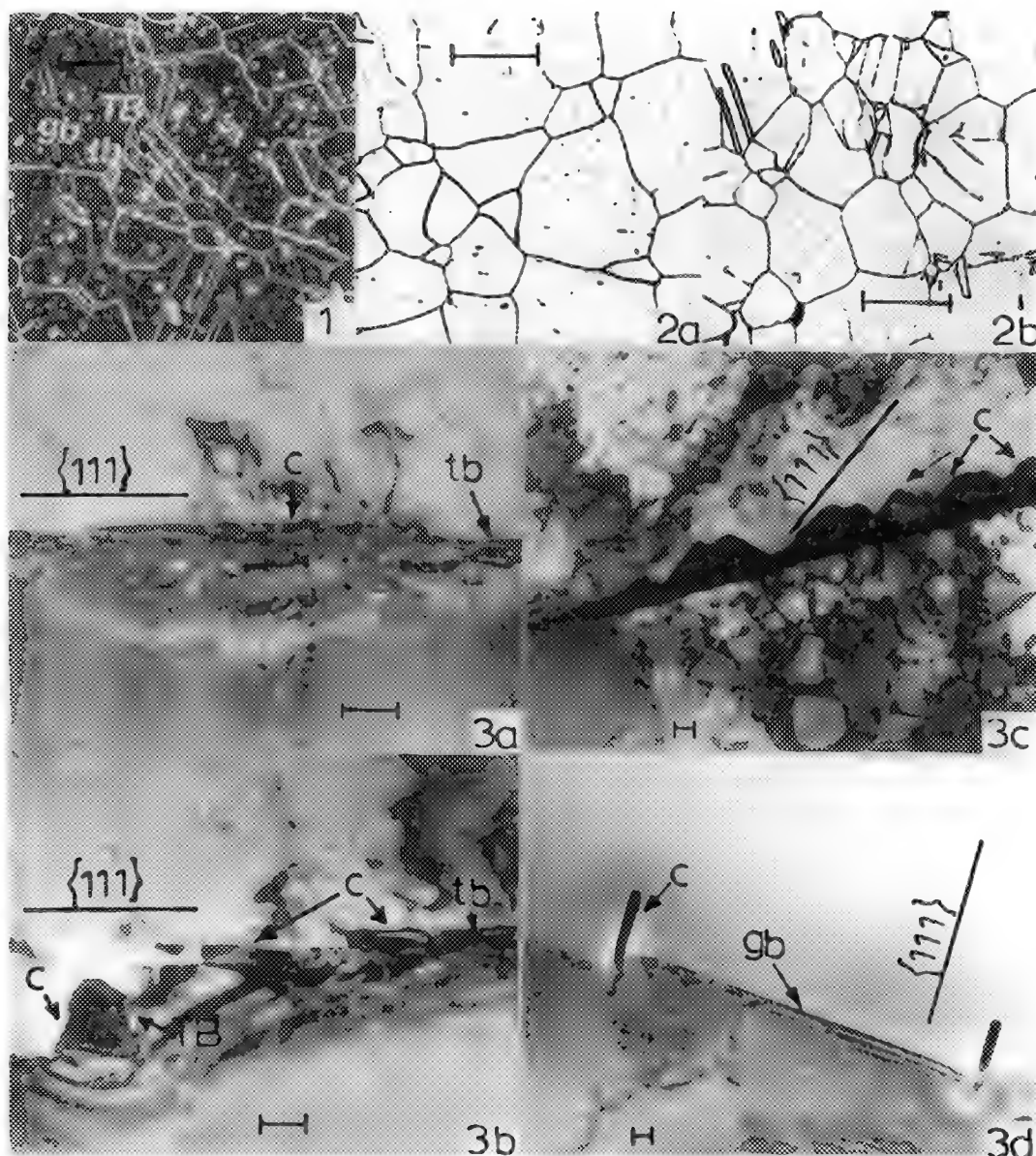


FIG. 1: Polarized light micrograph showing grain boundaries (gb) and coherent twin boundaries (tb) with non-coherent steps (TB) in 304 stainless steel. Bar = 0.1 mm.

FIG. 2: (a) Light micrograph showing etched (sensitized) grain boundaries in 316 stainless steel aged at 625°C for 100 h. (b) Light micrograph showing etched grain and twin boundaries in 316 stainless steel uniaxially strained 12% and aged at 625°C for 26 h. Bars = 0.1 mm.

FIG. 3: (a) and (b) show TEM images of carbides ($M_{23}C_6$) along coherent twin boundary in 304 stainless steel (0.07% C) aged at 775°C for 10 h. (c) TEM image of $M_{23}C_6$ carbides precipitating on a grain boundary in 304 stainless steel (0.025% C) aged at 775°C for 1 hr. (d) TEM image of $M_{23}C_6$ carbides growing from grain boundary steps in 304 stainless steel (0.05% C) aged at 775°C for 10 h. Carbides are denoted c. Bars = 0.1 μ m.

MECHANISMS OF TRANSGRANULAR CARBIDE PRECIPITATION IN DEFORMED 304 STAINLESS STEELS

A. H. Advani, L.E. Murr and W.W. Fisher

Department of Metallurgical and Materials Engineering and Materials Research Institute
University of Texas at El Paso, El Paso, TX 79968

Transgranular (TG) carbides form in thermomechanically processed austenitic stainless steels (SS) when the material is plastically deformed to high strain levels, typically above 20%, and for heat treatments that lie within the 500-850°C sensitization range of the SS. In recent work, we have shown that the TG carbide precipitation is site-specific, and favors deformation-induced sites created during the straining process.^{1,2} Specifically, twin-faults and their intersections, and dislocation intersections have been indicated to be preferred sites for TG carbide formation in 304 and 316 SS,^{1,2} while clustered regions containing a mix of fine-austenite and lath martensite were also observed to be critical sites for the TG precipitation in 304 SS.² In this paper, we present lattice image observations of carbide precipitates in the TG fine-austenite/lath martensite regions of 40% deformed, 670°C/0.1-10h heat treated, 0.051%C 304 SS, as a means to understand the mechanisms of TG carbide precipitation in the SS.

A low magnification view which illustrates the formation of TG carbides within the fine-austenite/lath martensite regions of deformed SS is shown in Figure 1. The carbides are seen to form on the interfaces created by the fine-austenite and lath martensite phases, which is similar to that on regular grain boundaries in SS. Lattice images of TG carbides which highlight the mechanisms of carbide precipitation are shown in Figures 2(a-e). The micrograph of Figure 2(a) indicates the location of a carbide precipitate with respect to a fine-austenite "grain." A higher magnification view (Figure 2(b)) shows carbide lattice fringes within the precipitate, and also documents the presence of a differently oriented set of carbide fringes within the fine-austenite region, close to the "grain boundary." A similar observation of a change in carbide lattice orientation across an interface is also illustrated in Figure 2(c). Other selected TG carbides showing undistorted lattices, and interfacial dislocations, are shown in Figures 2(d) and 2(e). The carbide lattice images described above are similar to those reported by Yong-Hua et al during precipitation of $M_{23}C_6$ in a superalloy.³

The observed lattice images of TG carbides indicate key mechanisms of interfacial carbide precipitation in SS. The undistorted carbide lattice images are indicative of a coherent relationship between the carbide and matrix. While the coherency requirement may be due to the lattice spacing of the carbide being approximately three times that of austenite,³ we cannot conclusively make the observation because of the intermix of lath martensite and fine-austenite present within the TG regions. The observed changes in lattice orientation across interfaces may be caused by the carbide nucleating separately on either side of the interface of highly misoriented "grains," so as to maintain coherency with the grain in which it grows.³ The dislocations seen on the carbide-austenite interface are due to the carbide trying to minimize the free energy of transformation by maintaining a semi-coherent interface with the matrix, in which the disregistry is taken up by misfit dislocations at the interface.⁴ Thus, there are a range of classical mechanisms by which the TG carbide forms and grows in 304 SS, and we believe that the preferred mechanism will be specific to each precipitate, so as to minimize the free energy of the system.

1. A.H. Advani et al, Corrosion, v. 47(12), 1991, pp. 939-947
2. A.H. Advani et al, accepted for publication in Acta Metallurgica et Materialia, Oct (1992).
3. R. Yong-Hua, G. Yong-Xiang and H.G. Xiang, Metallography, v. 22, 1989, pp. 47-55.
4. D.A. Porter and K.E. Easterling, Phase Transformations in Metals and Alloys, Chapman and Hall, University and Professional Division, New York, 1981, pp. 142-147.
4. The work was supported by NSF (RIMI) Grant HRD 9105065, and GSA Grant PF90-018 administered by the Materials Research Institute.

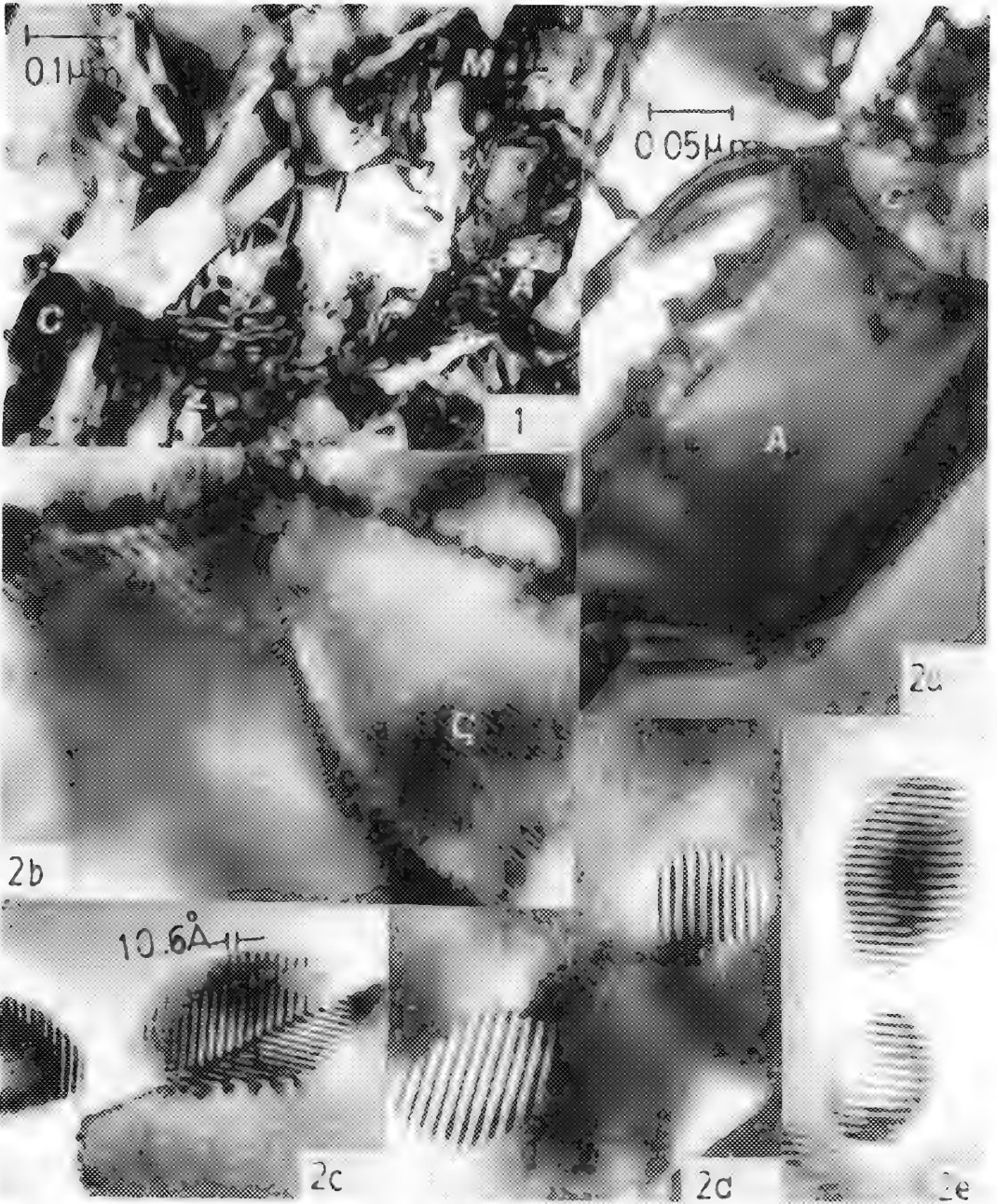


Figure 1. Illustration of TG carbide (C) formation within a fine-austenite (A)/lath martensite (M) region.
Figure 2. Lattice images documenting mechanisms of TG carbide precipitation in SS. The micrographs illustrate low (a) and high (b) magnification views of a carbide precipitate (C) in the vicinity of a fine-austenite "grain" (A), a change in carbide lattice orientation across an interface (c), undistorted carbide lattices (d), and interfacial dislocations seen within carbides (e).

TEM STUDY ON THE THERMOSTABILITY OF HAFNIUM CARBIDE DISPERSOIDS IN TUNGSTEN AT ULTRAHIGH TEMPERATURES

Mingqi Liu and John M. Cowley

Department of Physics and Astronomy, Arizona State University, Tempe, AZ 85287-1504

Tungsten dispersed by hafnium carbide (HfC) particles has been found to be the strongest metallic material at temperatures above 2000 K¹. The strength of W-HfC alloy is directly related to the thermostability of HfC particles at ultrahigh temperatures. In the present study, the growth behavior and growth mechanism of HfC particles from 2200 to 3000 K are examined with transmission electron microscopy (TEM) and a correlation between the particle size and alloy strength is established.

The examined material was a tungsten-3.6 wt%rhenium-0.35 wt%HfC alloy. The solid solution element rhenium was to improve the fabricability of tungsten at room temperature. Specimens were heated to a temperature between 2200 and 3000 K for two hours and then deformed in tension. After a 5% elongation, the specimens were rapidly cooled down to room temperature at a cooling rate greater than 200 K/s in order to maintain the high temperature substructures which were examined with a JEM-2000FX high resolution TEM.

Figures 1 to 3 show the TEM images of specimens at 2200, 2600, and 3000 K, respectively. The near-spherical HfC particles are located either along dislocation lines or in dislocation networks. From 2200 to 2600 K, HfC dispersoids are relatively stable with a radial growth rate less than 0.012 nm/K. The particle size obeys a statistical distribution and bulk diffusion is the main growth mechanism. Significantly coarsening of particles occurs at 2800 and 3000 K with a radial growth rate greater than 0.4 nm/K, causing a rapid decrease of alloy strength. The growth process above 2600 K is inhomogeneous, characterized by extremely large HfC particles surrounded by numerous small ones. The selective particle growth is attributed to the diffusion along dislocation "pipes" and grain boundaries. By using the cubic equation for particle growth², the activation energy for HfC growth is determined to be 50.2 ± 1.0 kcal/mol. A comparison between the diffusivities of hafnium and carbon in tungsten at ultrahigh temperatures suggests that diffusion of hafnium is the rate controlling process in HfC growth. The electron microdiffraction patterns obtained from HfC particles (Fig. 4) show that the lattice parameter of grown particles is smaller than that of pure HfC. Because the lattice parameter of HfC decreases with excess hafnium³, the present study hence concludes that the grown particles are hafnium-rich particles. The growth behavior of HfC particles is also correlated to the strength property of dispersion hardened tungsten. It has been shown that the hardening of tungsten by HfC is due to the departure side pinning and delocalization pinning (diffusional relaxation) of dislocations at dispersoids⁴. In the present study, the HfC particle diameter and interparticle spacing are determined from TEM images at each individual test temperature. By using a strengthening model of dislocation pinning, the strength of HfC dispersed tungsten is calculated as a function of temperature. The results have a good agreement with the the strengths determined in tension tests (Table 1). The small underestimation of the calculated values is because the calculation has not counted the contribution from the dislocation-dislocation interactions, as can be seen in Figs. 1 and 3.

References

1. K.S. Shin, et al., J. Metals, (1990)42, 12.
2. I.M. Lifshitz and V.V. Slyozov, J. Phys. Chem. Solids, (1961)19, 35.
3. P.G. Cotter and J.A. Kohn, J. Amer. Ceram. Soc., (1954)37, 415.
4. M. Liu and J. Cowley, Scripta Metall., (1993)28, 307.
5. This work was supported by National Science Foundations (NSF) grant DMR 90-14975 and made use of the TEM in the Materials Science and Engineering Laboratory at ASU. The authors are grateful to Dr. A. Luo and Dr. D. Jacobson for performing the mechanical tests.

Table 1.--Comparison of resolved shear stress increment $\Delta\tau$ calculated based upon TEM images with experimental value $\Delta\tau'$ over temperature region of 2200 to 3000 K.

Temperature (K)	Particle Diameter (nm)	$\Delta\tau$ (MPa)	$\Delta\tau'$ (MPa)	Deviation (%)
2200	42	156.1	61.8	-9.2
2400	47	49.5	52.7	-6.1
2600	52	44.0	45.4	-3.1
2800	156	17.3	19.2	-9.9
3000	207	12.9	13.1	-1.4

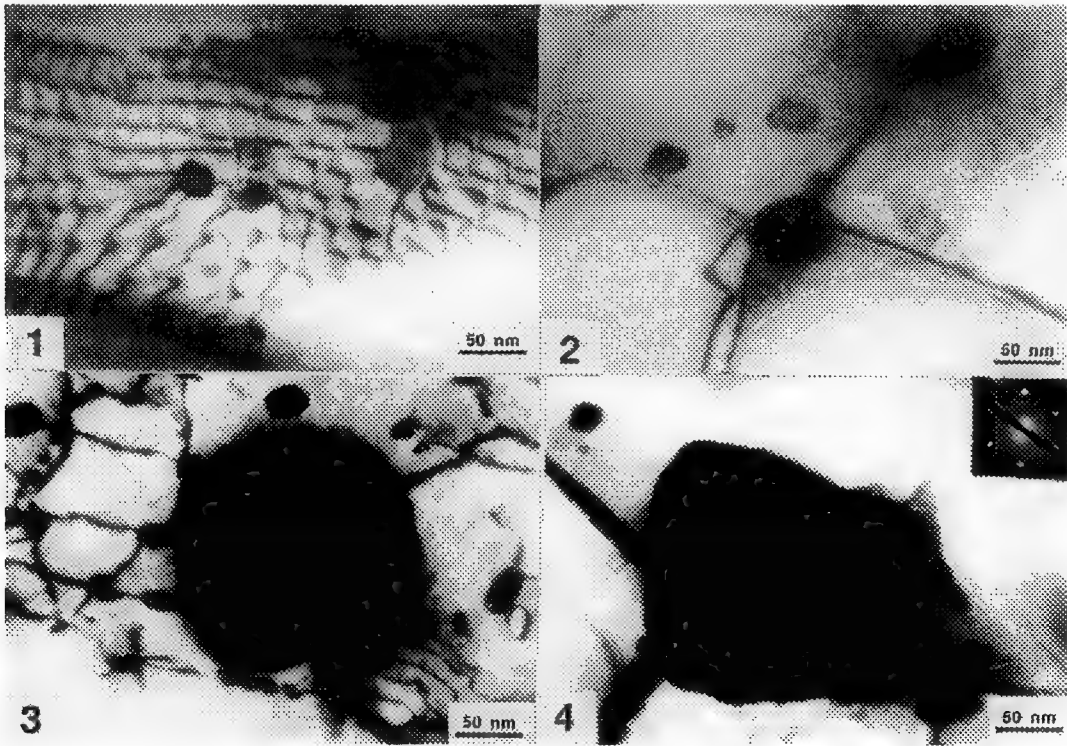


Fig. 1.--HfC particles in dislocation network in specimen tested at 2200 K.
Fig. 2.--Substructure of HfC dispersed tungsten at 2600 K. Slow particle growth is observed.
Fig. 3.--Substructure of specimen heated to 3000 K, showing selective particle coarsening.
Fig. 4.--Electron microdiffraction of a grown HfC particle that has a Hf-rich composition.

GROWTH KINETICS OF Al_2Cu IN AN Al-1.5Cu THIN FILM BY IN SITU TEM

M. Park, S.J. Krause, and S.R. Wilson*

Department of Chemical, Bio, and Materials Engineering, Arizona State University, Tempe, AZ 85287

*Core Technologies, Motorola Semiconductor Products Sector, Mesa, AZ 85202

Cu alloying in Al interconnection lines on semiconductor chips improves their resistance to electromigration¹ and hillock growth². Excess Cu in Al can result in the formation of Cu-rich Al_2Cu (θ) precipitates. These precipitates can significantly increase corrosion susceptibility due to the galvanic action between the θ -phase and the adjacent Cu-depleted matrix.³ The size and distribution of the θ -phase are also closely related to the film susceptibility to electromigration voiding.⁴ Thus, an important issue is the precipitation phenomena which occur during thermal device processing steps. In bulk alloys, it was found that the θ precipitates can grow via the grain boundary "collector plate mechanism" at rates far greater than allowed by volume diffusion.⁵ In a thin film, however, one might expect that the growth rate of a θ precipitate might be altered by interfacial diffusion. In this work, we report on the growth (lengthening) kinetics of the θ -phase in Al-Cu thin films as examined by in-situ isothermal aging in transmission electron microscopy (TEM).

Films with a composition of Al-1.5Cu (wt. %) were sputter-deposited at 325°C to a thickness of 0.75 μm on top of a Ti-W film. The plan-view TEM specimens of the as-deposited Al-1.5Cu films underwent in-situ isothermal annealing experiments in a Philips 400T TEM at 100 keV equipped with a heating stage. The time dependence of lengthening of the θ -phase was determined by measurements of half-lengths (R_I) of plate-like θ precipitates which were reacted at successively increasing times for aging temperatures of 250, 275, and 300°C. The specimens were solution annealed at 450°C for 15 min, cooled down to each annealing temperature, and then held for 40 seconds. The specimens were then cooled down to room temperature at a rate of $\sim 9^\circ\text{C}/\text{sec}$. At this stage, a fine θ precipitate at the grain boundaries was found and located in the viewing screen in TEM for further in-situ isothermal aging. The specimens were then ramp heated and isothermally annealed for up to 40 min at 250 and 275°C, and for up to 18 min at 300°C. Three individual θ precipitates were aged at each annealing temperature. A total of nine precipitates were separately analyzed.

The lengthening data (R_I vs. time (t)) for aging at 250, 275, and 300°C are shown in Figures 1a-c. The data points in each figure represent an individual θ precipitate varying in size, R_I with time (t) during aging. The data are plotted in log-log form. Table 1 shows time dependence of the growth (lengthening) of θ -phase in the Al-1.5Cu films aged at 250, 275, and 300°C. The actual time law, $R_I = At^n$ for the initial period of growth (up to ~ 20 min at 250 and 275°C; up to 10 min at 300°C), has n varying from 0.16 to 0.38 (Table 1). The average at shorter aging times is $n = 0.24$. After the initial period of growth, the actual time law, n decreases as the growth rate slows down significantly. Figures 2a through 2c show the growth morphologies of θ -phase, aged at (a) 250, (b) 275, and (c) 300°C, respectively.

In bulk Al-Cu alloys, the "collector plate mechanism"⁵ is reasonably well understood, based on the fact that the Cu solute migrates to the grain boundaries by volume diffusion, and then swiftly diffuses along the boundaries to the edges of the θ precipitate. However, in Al-Cu films, there is a "bamboo-like" grain structure, in which the θ -phase precipitates are located at the grain boundaries and the interfaces of the free surface and/or the sublayer. The collector plate model used for calculating the time law $R_I = At^n$ in bulk alloy can also be utilized in thin films for shorter aging times. This is because the mass flow of Cu to each collector plate in a thin film, which is the interface of surface and grain boundary, is converted into the volume amount of θ -phase, as was explained for the collector plate mechanism in bulk alloy. The lengthening of θ precipitate in an Al-4 wt.% Cu bulk alloy will vary as $t^{1/4}$, as found by Aaron and Aaronson. In this work on thin film, the average value (0.24) of n is in reasonable agreement with the theory ($t^{1/4}$ time law) for the bulk alloy, although considerable scatter was encountered in the experimental measurements. However, the lengthening of θ -phase at longer reaction times cannot fit the $t^{1/4}$ time law since the growth rate significantly slows down after initial period of growth. This is due to the fact that the Cu content in the untransformed Al matrix decreases continuously at long reaction times as the distance of Cu volume diffusion exceeds one half of the foil thickness (0.2–0.4 μm) for our samples which consisted of plan-view TEM specimens (e.g., the distances of Cu volume diffusion at 250°C for 20 min is 0.13 μm)⁶.

In summary, the lengthening rate of θ precipitate in Al-1.5Cu films was examined by in-situ annealing in TEM at 250, 275, and 300°C. The analysis of the results showed that the lengthening of θ precipitates in thin films varies as $t^{0.24}$ for the initial period of growth up to 10 to 20 min aging at the temperatures between 250 and 300°C. This is in very good agreement with the theory, the $t^{1/4}$ time law, of the collector plate mechanism for bulk alloys. However, the theory does not fit for longer annealing times because the distances of Cu volume diffusion exceed the film half thickness.

References

1. F.M. d'Heurle, Metall. Trans., A2, 683 (1971).
2. D.S. Herman, M.A. Schuster, and R.M. Gerber, J. Vac. Sci. Technol. 9, 515 (1971).
3. D. Weston, S.R. Wilson, and M. Kottke, J. Vac. Sci. Technol., A8, 2025 (1990).
4. C. Kim and J.W. Morris, Jr., J. Appl. Phys., 72, 1837 (1992).
5. H.B. Aaron and H.I. Aaronson, Acta Metall., 16, 789 (1968).
6. M.S. Anand, S.P. Murarka, and R.P. Agarwala, J. Appl. Phys., 36, 3860 (1967).
7. Authors acknowledge a support of the research from the Motorola-University Partnership in Research program. This work is based upon the research conducted at the Center for High Resolution Electron Microscopy, which is supported by the National Science Foundation under grant No. DMR-9115680.

Table 1. Summary of Al₂Cu (θ) Precipitate Lengthening by Interface-Aided Volume Diffusion. Curves were fitted to the data points plotted for the initial period of growth (up to 20 min at 250 and 275°C; up to 10 min at 300°C).

*The actual time law: $R_I = At^n$, (Average $n = 0.24$)

Aging Temp. (°C)	n		
250	0.26	0.20	0.38
275	0.16	0.17	0.20
300	0.23	0.32	0.25

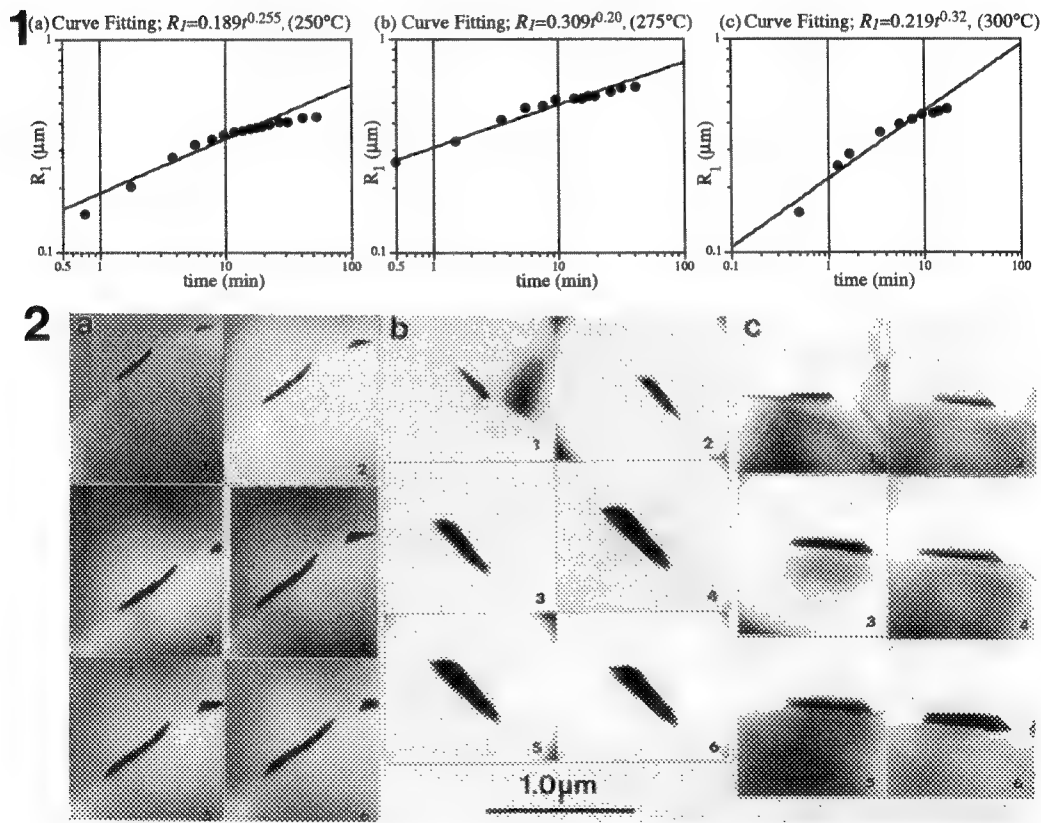


FIG. 1.--Variation of lengths (R_I) of θ precipitates with time at (a) 250, (b) 275 and (c) 300°C. Figures (a), (b) and (c) correspond to each individual Al₂Cu precipitate.

FIG. 2.--Plan-view TEM micrographs showing growth morphologies of the Al₂Cu (θ) precipitates reacted at successively increasing times for aging at (a) 250 (20 min max.), (b) 275 (20 min max.), and (c) 300°C (10 min max.).

COHERENCY-INDUCED MORPHOLOGICAL INSTABILITY IN NiAl-TYPE PRECIPITATE

G. Ghosh, G. B. Olson and M. E. Fine

Department of Materials Science and Engineering, Robert R. McCormick School of Engineering and Applied Science, Northwestern University, Evanston, IL 60208-3108

In many commercial alloys, phase transformation involves nucleation and growth of coherent precipitates. The elastic strain fields around individual coherent precipitates and the overlap of such strain fields constitute an "elastically constrained system" in which the precipitates exhibit shape transition and anomalous coarsening behavior. Results of classical γ - γ' system shows that an individual precipitate may split into two parallel plates (or doublet)^{1, 2} or eight smaller cuboids (or octet) with their faces parallel to the {100} directions²⁻⁴. Theoretical modeling of such shape transitions imply that the process is governed by the competition between interfacial and elastic energies⁵⁻⁷. Here, we report the shape transitions observed in an elastically constrained system involving bcc structures.

Polycrystalline specimens of Fe-6.42Al-14.8Ni (alloy#1) and Fe-8.08Al-12.2Cr-18.2Ni (alloy#2) were studied. Alloy#1 was solution treated at 1100°C followed by continuous cooling at 0.01°C/s to 950°C and subsequently helium quenched. Similarly, alloy#2 was solution treated at 1200°C and continuously cooled at 0.01875°C/s to 1065°C and helium quenched to room temperature. The continuous cooling experiments were done in a quenching dilatometer. Thin foils for transmission electron microscopy were prepared by standard procedures. The foils were examined near [100] zone axis.

In the above alloys NiAl-type (B2) precipitates nucleate and grow coherently and having cube-on-cube orientation relationship in α -Fe (A2) matrix. A wide variety of precipitate morphologies, as shown in Figures 1-2 (alloy#1) and 3-6 (alloy#2), were developed during continuous cooling experiments. Figure 1 suggests that only one quadrant of the cuboid has been shed from the rest of the particle which in turn has split into two (or doublet). Figure 2 also represents similar scenario, but for non-cuboidal morphologies. Figures 3-6 depict the most likely sequential process leading to splitting of a cuboid into an octet. Figure 3 shows an individual particle having convex (inward) edges. Figure 4 shows the instabilities which tend grow along [100] directions. The growth of the matrix phase into a cuboidal particle is shown in Figure 5. Both Figures 4 and 5 represent an early stage of splitting. Figure 6 shows the overlap of two cuboids. The particle on top has already split into an octet while the bottom one is undergoing fissioning. In Figures 1-6, the smaller precipitates form during second quench to room temperature. To the best of our knowledge this is the first report regarding the shape transitions involving bcc structures. The details and complexities of such splitting process, and the other experimental conditions under which splitting phenomena was (and was not) observed will be presented. The similarities and the differences between the present results and those reported on classical γ - γ' systems will also be discussed⁸.

REFERENCES

1. T. Miyazaki, H. Imamura and T. Kozaki, *Mater. Sci. Eng.* (1982), 54, 9.
2. M. J. Kaufman, P. W. Voorhees, W. C. Johnson and F. S. Biancaniello, *Metall. Trans. A* (1989), 20A, 2172.
3. J. H. Westbrook, *Z. Kristallogr.* (1958), 110, 21.
4. M. Doi, T. Miyazaki and T. Wakatsuki, *Mater. Sci. Eng.* (1982), 54, 9.
5. W. C. Johnson and J. W. Cahn, *Acta Metall.* (1984), 32, 32.
6. T. Miyazaki, K. Seki, M. Doi and T. Kozakai, *Mater. Sci. Eng.* (1986), 125, 77.
7. Y. Wang, L.-Q. Chen and A. Khachaturyan, *Acta Metall.* (1993), 279, 41.
8. This research was supported by Electric Power Research Institute.

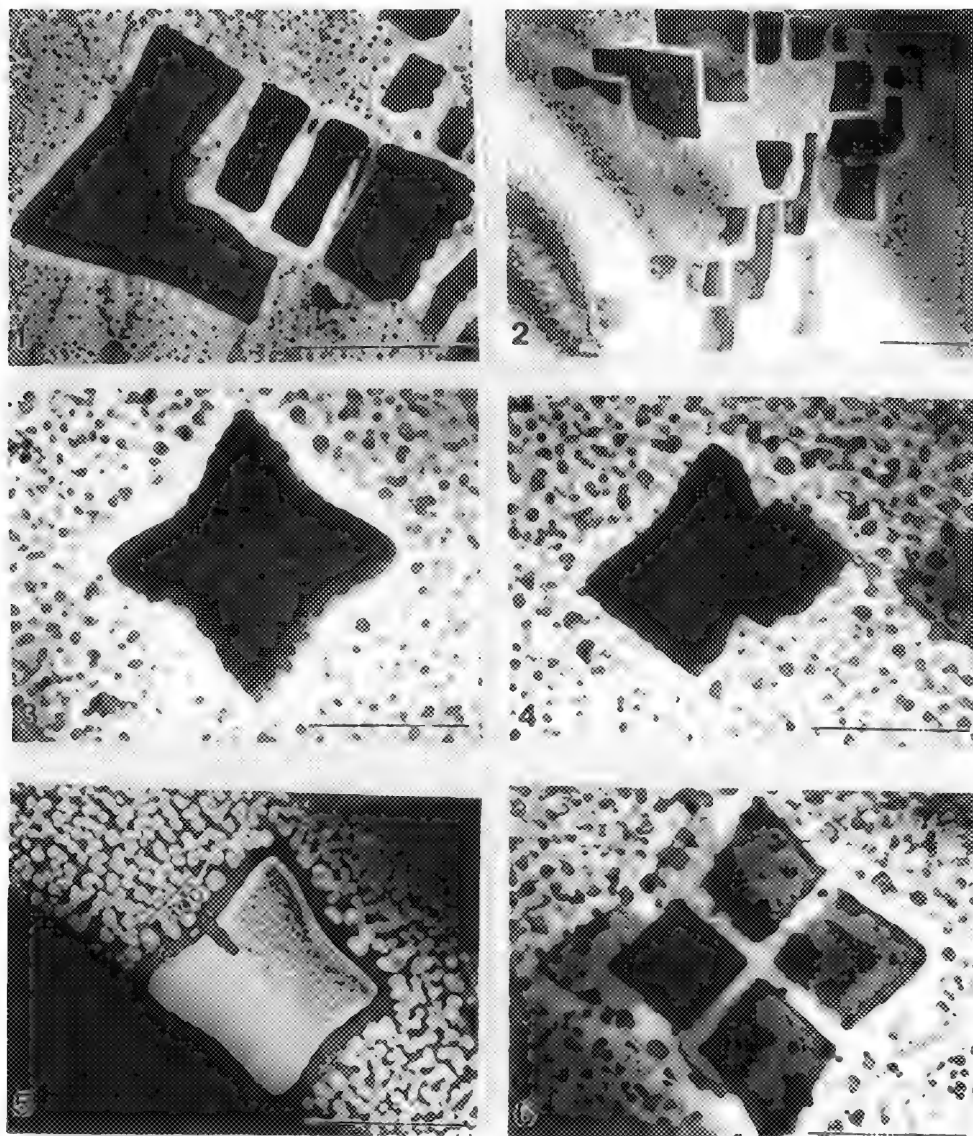


FIG. 1.--Bright-field TEM micrograph of alloy#1: shedding of one quadrant of the particle. Bar = 1 μm .
 FIG. 2.--Bright-field TEM micrograph of alloy#1: complex morphology after splitting. Bar = 1 μm .
 FIG. 3.-- Bright-field TEM micrograph of alloy#2: convex (inward) interface. Bar = 1 μm .
 FIG. 4.--Bright-field TEM micrograph of alloy#2: early stage of growth of instability. Bar = 1 μm .
 FIG. 5.--Dark-field TEM micrograph of alloy#2: growth of matrix phase into the particle. Bar = 1 μm .
 FIG. 6.-- Bright-field TEM micrograph of alloy#2: completion of fissioning into octet. Bar = 1 μm .

MICROSTRUCTURAL CHARACTERIZATION OF A CAST RENi_5 -BASED ALLOY

G. M. Michal* and L. Zhang**

*Department of Materials Science & Engr., Case Western Reserve University, Cleveland, Ohio 44106

**Technology Laboratory, EVEREADY Battery Company, Inc., Westlake, Ohio 44145

RENi_5 (RE: rare earth) based alloys have been extensively evaluated for use as an electrode material for nickel-metal hydride batteries.^{1,2} A variety of alloys have been developed from the prototype intermetallic compound LaNi_5 . The use of mischmetal as a source of rare earth combined with transition metal and Al substitutions for Ni has caused the evolution of the alloy from a binary compound to one containing eight or more elements.² This study evaluated the microstructural features of a complex commercial RENi_5 based alloy using scanning and transmission electron microscopy.

The alloy was evaluated in the as-cast condition. Its chemistry in at. pct. determined by bulk techniques was 12.1 La, 3.2 Ce, 1.5 Pr, 4.9 Nd, 50.2 Ni, 10.4 Co, 5.3 Mn and 2.0 Al. The as-cast material was of low strength, very brittle and contained a multitude of internal cracks. TEM foils could only be prepared by first embedding pieces of the alloy in epoxy. After sectioning, discs of the embedded alloy were dimpled, then ion beam milled to electron transparency. TEM analyses were performed with a Philips CM20 equipped with a windowless Ge detector.

Powder x-ray diffraction analysis indicated within the sensitivity of the technique that the alloy was a single hexagonal phase consistent with the $\text{La}(\text{Ni}, \text{Al})_5$ and $\text{La}(\text{Ni}, \text{Mn})_5$ structures found in the ICPDS-ICDD. Its lattice parameters were $a = 0.5015$ nm and $c = 0.4051$ nm. Because of its complex chemistry the phase will be referred to as REM_5 (M: transition metal plus aluminum). SEM analysis revealed that the alloy was not a single phase as can be seen in Figure 1. The image indicates some porosity and a second phase that appears to be sandwiched between the columnar as-cast grains of the REM_5 phase.

More detailed analysis of the second phase was undertaken using TEM. Figure 2 contains a BF image of the second phase surrounded by the REM_5 phase. EDS spectra from the second phase and the REM_5 matrix phase are shown in Figures 3a and b, respectively. The second phase was found to be enriched in rare earth and Co compared to the REM_5 phase. Using the REM_5 phase as an internal calibration, the ratio of total RE to M in the second phase was determined to be between 1:2 to 2:3. Forming a phase with such an enrichment in rare earth was surprising since the nominal RE to M ratio of the alloy was greater than 1:5. Figure 4 contains SAD patterns from the matrix and second phase shown in Figure 2. The matrix phase SAD pattern was indexed as the hexagonal REM_5 phase, and was used as an internal calibration for analyzing the d-spacings of the second phase SAD pattern. Consistent with the BF image, the SAD pattern from the second phase contains streaking indicative of a high density of stacking faults. A schematic representation of the second phase SAD pattern is shown in Figure 4c. The phase has spacings that are similar to the LaNi_2 phase found in the binary system.³ Combining the EDS result with the measured d-spacings provides reasonable evidence that the second phase found in this alloy is a complex Laves (AB_2 type) phase. Figures 4b and c also show that the second phase is twinned on the 0.728 nm d-spacing plane. Fine scale twinning and a resulting high density of stacking faults are commonly observed in Laves phase microstructures.^{4,5}

References

1. M. A. Fetcenko et al., Proceedings Hydrogen Storage Materials, Batteries and Electrochemistry 92-5 (1992) 141.
2. T. Sakai et al., Proceedings Hydrogen Storage Materials, Batteries and Electrochemistry 92-5 (1992) 51.
3. A. V. Klimyenko et al., J. of Less Common Metals, 144 (1988) 133.
4. Y. Liu et al., Met. Trans., 23A (1992) 3303.
5. Specimen preparation and TEM operation by Stuart Maloy and permission to publish this work by the EVEREADY Battery Company are both gratefully acknowledged.

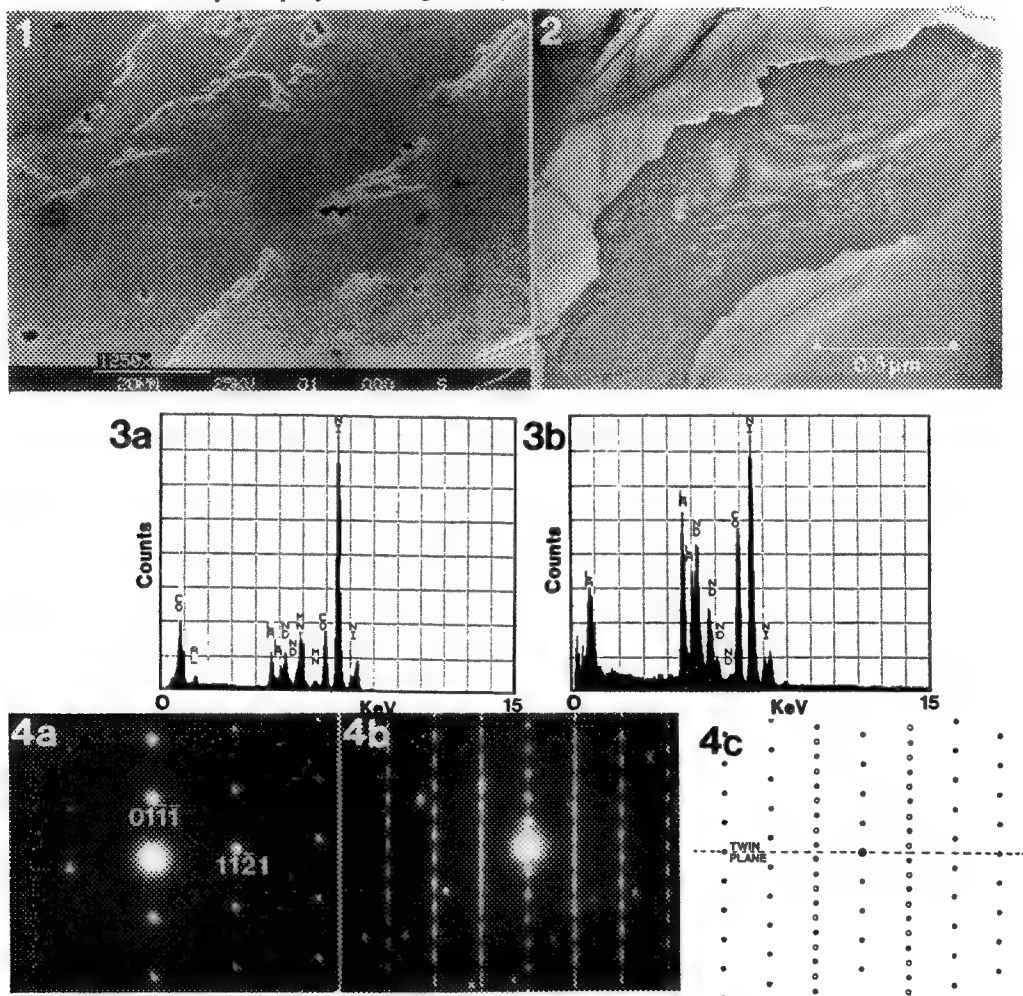


FIG. 1.--SEM image showing distribution of second phase in REM₅ matrix.

FIG. 2.--TEM BF image showing a region containing second phase.

FIG. 3.--EDS spectra from the region shown in Fig. 2 a.) REM₅ matrix 8,192 counts FS and b.) second phase 2,048 counts FS.

FIG. 4.--SAD patterns from the region shown in Fig. 2 a.) $[\bar{5}413]$ zone of REM₅ phase, b.) twinned second phase and c.) schematic of twinned second phase pattern.

δ' (Al₃Li) DISSOLUTION AS A THERMAL PROBE IN SHEAR-BANDING STUDIES

Roa Wen Chen and Kenneth S. Vecchio

Dept. of Applied Mechanics and Engineering Sciences, MC-0411, UC San Diego, LaJolla, CA 92093

The Al-Li alloy system can provide a unique opportunity to study the thermal history of shear-band formation by following the thermal dissolution of the precipitate phase δ' (Al₃Li) as a function of Li concentration and δ' solvus temperature. The Al-Li system was chosen primarily for the rather rapid precipitation and dissolution kinetics resulting from the high diffusivity of Li in the Al lattice. δ' is a spherical, coherent and metastable precipitate which is the main strengthening phase in dilute Al-Li alloys. Although δ' is metastable, the location of the δ' solvus in the Al-Li phase diagram has been well documented for dilute Li additions (<5 wt.% Li).^{e.g.1} The metastable δ' solvus increases in temperature with increasing Li concentration. As such, the dissolution of δ' within the shear bands, as a function of Li alloy concentration, can provide an internal temperature probe to study the thermal history of the shear band. For example, if the δ' solvus temperature for a 2 wt.% Li alloys is 235°C, and δ' is dissolved within the shear band during its formation, then it can be assumed that the temperature within the shear band exceeded 235°C. When an alloy composition is found in which the δ' is not dissolved during shear band formation, then a small window around the actual shear band temperature can be determined.

Four different Al-Li alloys were produced ranging in composition from approximately 2 wt.% Li to 4 wt.% Li. The heat treatment of each alloys was chosen to achieve the same size δ' distributed throughout the matrix. A special hat-shaped specimen was used to produce shear bands at a predetermined location within the specimen². Shear bands were generated in these specimens at both low strain rates and very high strain rates. At high strain rate, the formation of the shear band can be assumed to be adiabatic since the deformation occurred in a time frame significantly shorter than that required for cooling of the shear band region. A significant degree of heating occurs in the shear band as a result of the intense localized deformation. TEM specimen were sectioned from these shear band regions, and thin foils were prepared such that the electron transparent area contained the shear band.

Figure 1a shows an optical micrograph of a shear band in a 2.6 wt.% Li alloy. The starting matrix microstructure of this alloy is shown in Figure 1b, and consists of spherical δ' approximately 70nm in diameter. Figure 2a shows a TEM micrograph through a grain-scale shear band within a larger macroscopic shear band such as that shown in Figure 1a. The shear band region has undergone dynamic recrystallization producing a microcrystalline region as shown by the ring pattern of the insert (Figure 2b). Figures 3a and 3c are microdiffraction patterns obtained from either side of the shear band showing the superlattice reflections indicative of the δ' phase present surrounding the shear band. Figure 3b is a microdiffraction pattern taken from one of the small grains within the shear band, with superlattice reflections absent as a result of δ' being dissolved by the heating of the shear band region. Every grains analyzed within this shear band was devoid of any δ' as evident by the lack of superlattice reflections and an inability to image any precipitates. Similar analysis of higher Li alloys revealed recrystallized grains within the shear band, however in these cases the grains still contained δ' precipitates as revealed by both superlattice reflections and precipitate images. The occurrence of recrystallization within each shear band can be expected since the recrystallization temperature is approximately 200°C for Al. More interesting is the fact that the recrystallization occurred in higher Li alloys without disturbing the precipitate structure or the precipitate/matrix orientation relation.

References

1. D. B. Williams and J. W. Edington, 1975, *Acta Metall.*, **35**, 529.
2. L. Meyer, in "Shock-Wave and High-Strain-Rate Phenomenon in Materials", eds. M.A. Meyers, L. E. Murr, and K. P. Staudhammer, Marcel Dekker Inc., (1992) 49.

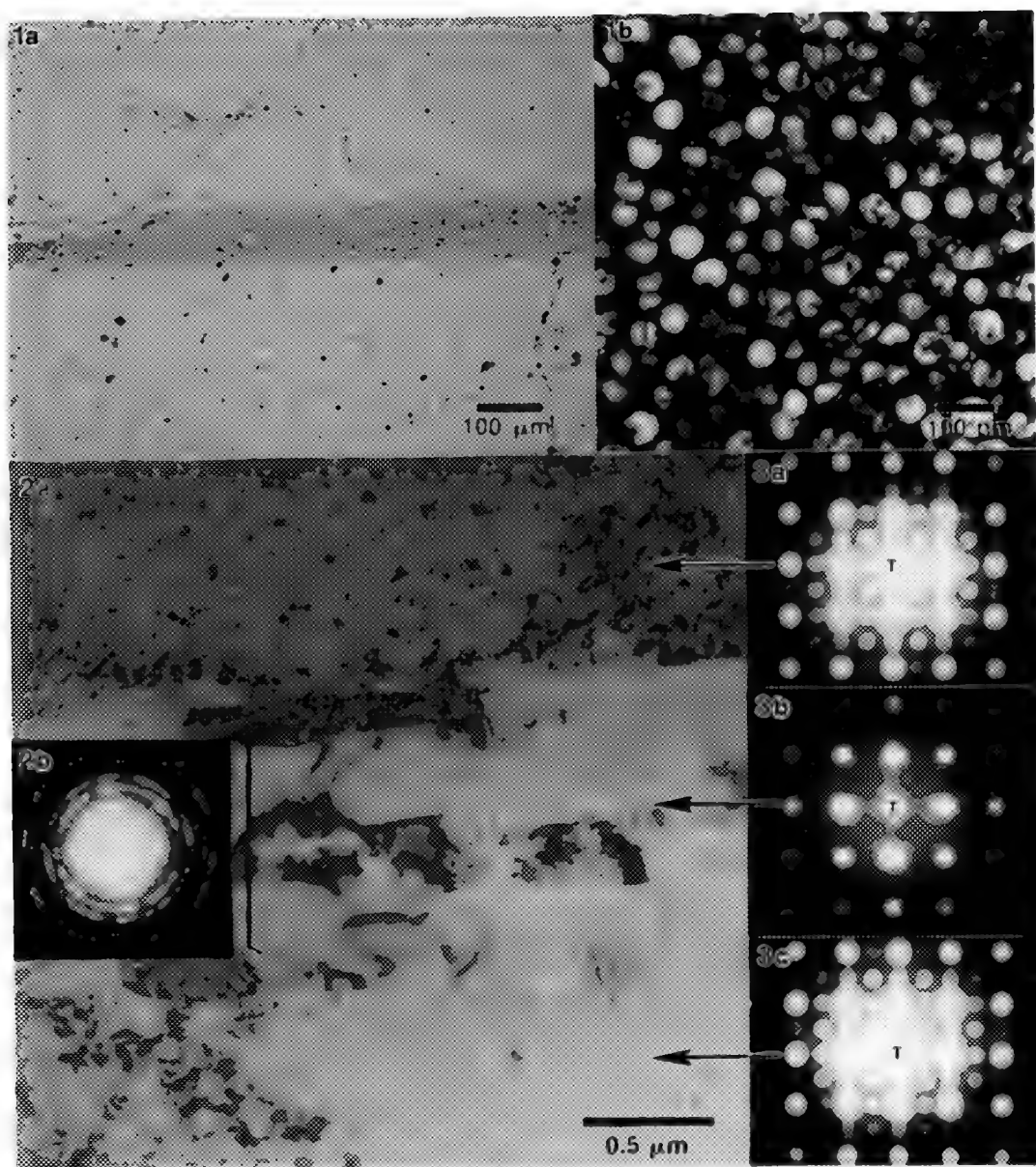


FIG. 1.--(a) Optical micrograph showing macroscopic shear band generated in 3 wt.% Li alloy, (b) Dark field TEM image using the δ' reflection showing the precipitate size and distribution in this alloy
 FIG. 2.--(a) TEM micrograph showing a grain-scale shear band(GSSB) within the macroscopic shear band. The GSSB region has undergone dynamic recrystallization during its formation resulting in microcrystalline structure as demonstrated by the insert (2b).
 FIG. 3.--Microdiffraction patterns obtained from either side of the GSSB (a) and (c), and within the small grains of the GSSB (b). The absence of superlattice reflection indicates that δ' was dissolved.

SHORT-RANGE ORDER TO LONG-RANGE ORDER TRANSITION IN A Cu-Ti ALLOY

J.S. Lee,* R.W. Carpenter,* H. Lim** and W.K. Choo**

*Center for Solid State Science, Arizona State University, Tempe, AZ 85287-1704

**Department of Electronic Materials Science and Engineering, KAIST, Taejon, Korea

Cu-Ti alloys have received attention due to their excellent age-hardenability. The age hardening phenomenon of Cu-Ti alloys is closely related to the early stage transformation involving short-range order (SRO), spinodal decomposition, and long-range order (LRO). Despite many researches, the transition from SRO to LRO state in this alloy system is still not understood. Woychik et al. have found $\{1\ 1/2\ 0\}$ SRO reflections in an electron diffraction pattern of an as-rapidly solidified (RS) Cu-15at.%Ti alloy (All indices are referred with respect to the fcc structure in this paper.).¹ With aging, the SRO reflections were replaced by the $4/5\{1\ 1/2\ 0\}$ LRO ($D1_a$) reflections. Recently, Yoo found the $\{1/2\ 1/2\ 0\}$ spots as well as the $\{1\ 1/2\ 0\}$ spots in an electron diffraction pattern of an as-RS Cu-15at.%Ti alloy.² This result may show that some other metastable phases can be present before the formation of the LRO phase. In the present paper, the initial stages of ordering process will be described.

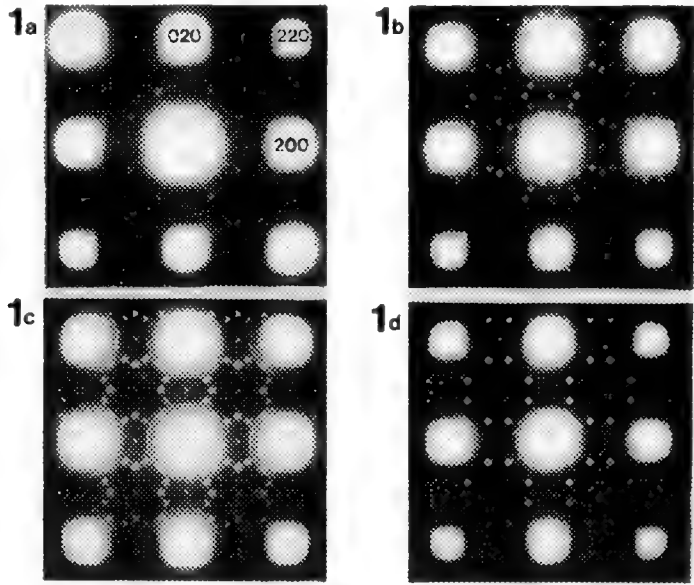
Because the decomposition rate of Cu-Ti alloys is very fast, we prepared an alloy of composition of Cu-12.3at.%Ti by the rapid solidification process. Long ribbons of 50 to 70 μm thickness and 5 to 10 mm width were obtained using the one-roll melt spinning apparatus. Heat treatments were done at a relatively low temperature (723K) to study the early stage transformation. Samples for TEM observations were thinned by mechanical grinding, dimpling, and ion-milling. A cold-stage specimen holder was used for ion-milling. HREM and electron diffraction experiments were done either in a JEM-4000EX operating at 400 kV or in an ISI-002B operating at 200 kV.

In the as-RS state, different diffraction patterns were obtained with respect to ribbon thickness change. Fig. 1(a) is a $[001]$ pattern from a 50 μm thick as-RS specimen and Fig. 1(b) is from a 70 μm thick as-RS specimen. For the 50 μm thick as-RS specimen, both the $\{1\ 1/2\ 0\}$ and the $\{1/2\ 1/2\ 0\}$ superlattice spots are found. The $\{1\ 0\ 0\}$ and the $4/5\{1\ 1/2\ 0\}$ spots are also found together with the $\{1\ 1/2\ 0\}$ and the $\{1/2\ 1/2\ 0\}$ spots for the 70 μm thick as-RS specimen. These differences apparently arose from the cooling rate difference between those two samples. Kulkarni and Banerjee have demonstrated that the short-range ordered alloy exhibiting the $\{1\ 1/2\ 0\}$ intensity maxima can lower its internal energy either by a secondary $\langle 1\ 1/2\ 0 \rangle^*$ ordering in a direction perpendicular to the original $\langle 1\ 1/2\ 0 \rangle^*$ k-vector or by an introduction of $\langle 1\ 0\ 0 \rangle^*$ ordering wave.³ The former produces the so-called N_3M structure^{3,4} which gives rise to the $\{1\ 1/2\ 0\}$ and the $\{1/2\ 1/2\ 0\}$ spots, and the latter produces the DO_{22} structure which gives rise to the $\{1\ 1/2\ 0\}$ and the $\{1\ 0\ 0\}$ spots. The higher intensity of the $\{1\ 1/2\ 0\}$ spots over that of the $\{1/2\ 1/2\ 0\}$ spots in Fig. 1(a) seems to indicate that the SRO phase coexists with the N_3M phase. And the appearance of the $\{1\ 0\ 0\}$ spots in Fig. 1(b) shows that the DO_{22} phase is formed after the N_3M phase occurs. The presence of the $4/5\{1\ 1/2\ 0\}$ LRO spots from the 70 μm thick as-RS specimen shows that the occurrence of the LRO phase is fairly fast in our alloy. Fig. 1(c) and Fig. 1(d) are $[001]$ electron diffraction patterns of 10 min and 1 hr aged specimens at 723K, respectively. After 1 hr aging, only the LRO reflections are found. Fig. 2 is a HREM image of the 70 μm thick as-RS specimen. Because four kinds of superlattices ($\{1\ 1/2\ 0\}$, $\{1/2\ 1/2\ 0\}$, $\{1\ 0\ 0\}$, and $4/5\{1\ 1/2\ 0\}$) are found from the same specimen, microdomains of different types coexist in this image. From the experimental observations, we can say that the formation of the LRO phase from the SRO state in Cu-Ti alloys occurs through a variety of intermediate states. The above results and a detailed analysis will be reported.⁵

References

1. C.G. Woychik et al., Metall. Trans. A, 16A (1985) 1353.
2. J.Y. Yoo, Ph. D. Thesis at KAIST (1989).
3. U.D. Kulkarni and S. Banerjee, Acta Metall., 36 (1988) 413.

4. U.D. Kulkarni and K. Madangopal, Scripta Metall., 23 (1989) 811.
5. This research was supported by grant from NSF, Division of Materials Research 89-01841, and performed at ASU/NSF HREM Facility. One of the authors (J.S.L.) expresses appreciation for the financial support provided by Korea Science and Engineering Foundation.



2



FIG. 1-- Selected area diffraction patterns of the Cu-12.3at.%Ti alloy : (a) as-RS (50 μm thick), (b) as-RS (70 μm thick), (c) 10 min aged at 723K, and (d) 1 hr aged at 723K, respectively.

FIG. 2-- HREM image of the 70 μm thick as-RS Cu-12.3at.%Ti alloy.

STUDY OF FACTORS AFFECTING CORROSION OF ALUMINUM AUTOMOTIVE WHEELS

H. K. Plummer, Jr., R. N. Simmons, R. W. Ocobock, T. A. Honey and M. C. Paputa Peck

Ford Motor Company, The American Road, Dearborn, MI 48121-2053, Mail Drop 3061/SRL

Aluminum automotive wheels, which have been used since the mid 1970's, have proven to be very rugged, but early wheels discolored with time. Since 1976 the machined "bright" exterior surfaces, have been coated with a chromium based "conversion" pretreatment^{1,2}, and painted with a "clearcoat" of polyester or acrylic to preserve appearance. These coated wheels can exhibit "filiform" corrosion between the Al surface and the clearcoat (Fig. 1). The corrosion is filamentous and closely follows aluminum grain boundaries. Corrosion results from oxidation of the aluminum (anode) in the presence of water and oxygen at a break (cathode) which intrudes through the clearcoat and conversion coat into the aluminum (Fig. 2). Current specifications require ≤ 1.6 mm filiform corrosion from a scratch after 400 h of accelerated corrosion testing. This paper correlates accelerated corrosion with the composition of the clearcoat paint, the UV absorbance of the paint and the microstructure of the Al / Cr conversion coat / clearcoat interface to learn the necessary parameters to produce Al wheels with enhanced protection. Production Al wheels, from a variety of sources, wheels prepared to our specifications and a design of experiments (DOE) wheel series prepared in our laboratories were examined.

The accelerated corrosion test exposes the test piece to UV weathering (400 h) with four water spray cycles every 23 h. After UV exposure the surface is scratched through the surface layers into the Al metal with a carbide scribe, followed by exposure to HCl vapor (1 h). The test piece is kept in a temperature (100°F) and humidity (80%) controlled chamber and filiform corrosion from the scratch is measured every 24 h. The presence of UV absorber in the clearcoat was detected from a 1 in. square piece of the wheel by diffuse reflectance UV spectroscopy⁴. Although several techniques exist to measure the thickness of the Cr conversion coat^{3,5} none mentioned, other than possibly Rutherford backscatter, could measure thickness ≤ 0.5 μm . Many papers, including some from this laboratory⁶⁻⁸, have reported using transmission electron microscopy (TEM) of ultramicrotomed thin sections to study surface layers on Al. Energy dispersive x-ray analysis in the TEM confirmed the conversion coating and its qualitative composition.

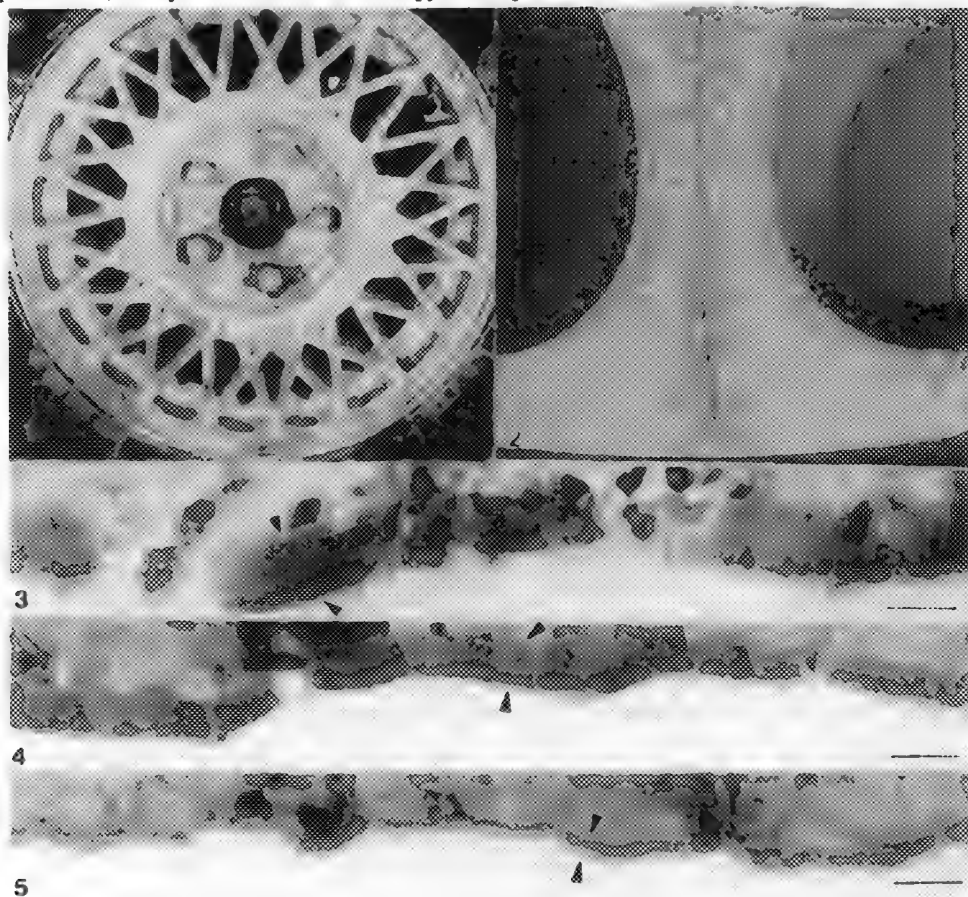
Figures 3-5 show the base Al, the Cr conversion coat and polyester paint layer from wheels exhibiting different corrosion results. Figure 3 shows a thick Cr conversion coat with no UV absorbing species in the paint and exhibits medium low corrosion (i.e. 2.4 mm @1008 h). Figure 4 shows a second sample with a thinner Cr conversion coat, with UV absorbing species in the paint, which exhibits low corrosion (i.e. 0.8 mm @1008 h). A third sample (Fig. 5) shows a very thin Cr conversion coat with no UV absorbing species in the paint, which exhibits high corrosion (i.e. 6.0 mm @600 h).

Conclusions drawn from this study are: The Cr conversion coating, applied by either a spray or a dip process, must be carefully controlled. The conversion coating should be dried near 170°F for a short time and must exceed 30 nm thickness. UV exposure of the conversion coat before clearcoating does not affect corrosion (DOE). The clearcoat layer must contain a UV absorbing species, and the results at this time suggest an acrylic formulation to be superior. Because of the results of this study a new testing specification now requires ≤ 1.6 mm filiform corrosion @ 1000 h.

REFERENCES

1. Wernick, S. et al., "Chemical Conversion Coatings" ASM Int. 5th Ed, "The Surface Treatment and Finishing of Aluminum and its Alloys" Vol.1, 1987, Ch 5

2. Eppensteiner, F.W. and Jenkins, M.R., "Chromate Conversion Coatings", Metal Finishing Guidebook and Directory, Metals and Plastics Publications Inc., 1991, p 418-31
3. Sajdera, N. "Thickness Testing", Ibid. p 549-673.
4. Springtencn, A. "A Guide to Reflectance Spectroscopy" Labsphere Inc, North Sutton, NH, 1993
5. Wernick, S. et al., "Properties and Tests of Anodic Coatings" ASM Int. 5th Ed, "The Surface Treatment and Finishing of Aluminum and its Alloys" Vol. 2, 1987, Ch 12
6. Bomback, J.L. and Musket, R.G., "Alpha Particle Induced X-Ray Analysis of Aluminum Oxide Film Thickness", Microbeam Analysis, 1980 p 187-91
7. McCune, R.C. and Plummer, Jr., H.K., "Transmission Electron Microscopy of Ultramicrotomed Barrier Anodic Films on Aluminum", Surface and Interface Analysis, Vol 4, No. 6, 1982, p 257-60
8. Plummer, Jr., H.K. et al., "Microstructural Evaluation of Aluminum Nitride Formation by Ion Implantation", Analytical Electron Microscopy, 1987, p 49-52



- Fig. 1.--Highly corroded Al wheel from accelerated vehicle testing. The wheel is 15 in. in diameter
- Fig. 2.--Al wheel section exhibiting filiform corrosion from a scratch (vertical line) and paint edges after 400 h accelerated testing. Magnification is approximately unity.
- Fig. 3.--TEM of thick ≤ 100 nm Cr conversion coating also containing Zr, S and Ca. Bar = 100 nm
- Fig. 4.--TEM of Cr conversion coating ≤ 62 nm also containing Zr and S. Bar = 100 nm
- Fig. 5.--TEM of Cr conversion coating ≤ 21 nm also containing Zr and S. Bar = 100 nm

CHARACTERIZATION OF LASER-IRRADIATED C₆₀ SOLUTION AND CELL DAMAGE BY SCANNING AND TRANSMISSION ELECTRON, AND ATOMIC-FORCE MICROSCOPY

Donna M. Brandelik, Richard L. Sutherland*, Hao Jiang**, Pamela Lloyd***, W. Wade Adams ****

*Science Applications International Corporation, Dayton, Ohio 45431

**Lawrence Associates Inc., Dayton, Ohio 45431

***UES, Inc., Dayton, Ohio 45432

****Wright Laboratory, Materials Directorate, WPAFB, Ohio 45433-7702

Investigation of laser irradiated purple C₆₀/toluene solutions revealed a photochemical change of the solution at high incident laser fluences. The initial purple solution turned pink and a black precipitate formed which was insoluble in toluene. Interaction at the cell surface was indicated as cell damage occurred before the solution changes were seen. Subsequent chemical analysis by Mass Spectroscopy showed that the pink solution contained C₆₀ and adducts. The black precipitate was found to contain no C₆₀, but instead contained only adducts and lower fullerenes. NMR on the pink solution revealed a SiCH_x peak as evidence of glass etching¹.

Scanning electron microscopy revealed needle crystals from a pure C₆₀ sample, in figure 1. Figure 2 shows the crystals from the pink solution. The black precipitate appears to have a porous, very grainy texture and lacks the crystalline structure of the other samples (figure 3). All three samples were deposited on carbon coated grids. The pyrex glass cell was damaged by the laser and showed an etching pattern (figure 4). This is very different from typical laser damage on glass which resembles a glass fracture pattern (figure 5). All samples were coated with 10 to 15 angstroms of Tungsten to decrease charging, and were examined on a Hitachi S-900 SEM at a 40+ degree tilt angle with a 1 to 2 Kev beam.

Transmission electron microscopy (JEOL 100CX) electron diffraction was performed on C₆₀ and the byproduct, and the TEM patterns for C₆₀ is shown in figure 6. The black precipitate gave a ring pattern. Analysis of the diffraction patterns for lattice d spacings is in progress and will be presented with the poster.

The pyrex cell was damaged by chemical etching in the 1.8 J/cm², 532 nm - wavelength laser beam. A silica quartz cell was also tested for comparison. The results show that the quartz cell was also chemically etched. Additional study of the cell damage by Atomic Force Microscopy is being performed and will be presented with the poster.

1. D.M. Brandelik, M.C. Brant, D.G. McLean, R L. Sutherland "Laser Induced Photochemical Degradation of C₆₀ Solutions.", presented at ACS national meeting, Denver, CO., March 28-April2, 1993.

2. This work was supported by WL/MLPJ, WPAFB, Ohio.

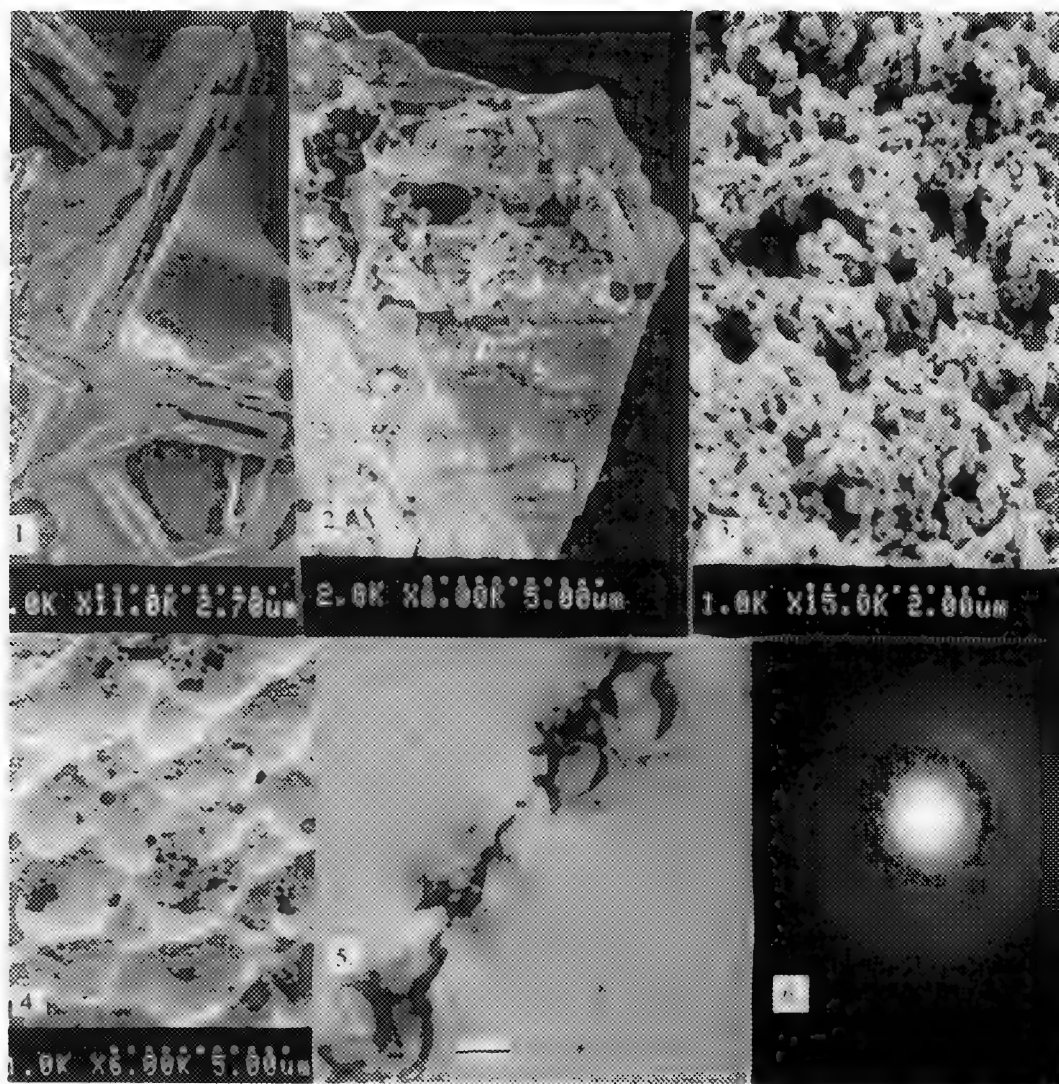


FIG. 1. -- SEM of pure C₆₀ needles. Bar = 2.7 μ

FIG. 2. -- SEM of pink solution crystals. Bar = 5.0 μ

FIG. 3. -- SEM of black ppt. Bar = 2.0 μ

FIG. 4. -- SEM of etched pyrex cell. Bar = 5.0 μ

FIG. 5. -- Optical microscope of typical laser pyrex cell fracture. Bar= 20 μ

FIG. 6. -- C₆₀ electron diffraction pattern.

ELECTRON MICROPROBE AND ELECTRON DIFFRACTION STUDY OF A NEW FERRIC IRON SANIDINE FROM THE LEUCITE HILLS, WYOMING

Kuehner*, S.M. and Joswiak, D.J.**

*Department of Geological Sciences, University of Washington, Seattle, WA 98195

**Department of Astronomy, University of Washington, Seattle, WA 98195

The group of minerals classified as feldspars are among the most common rock-forming minerals in the earth's crust. The majority of feldspar compositions fall within the ternary system $\text{NaAlSi}_3\text{O}_8$ - KAlSi_3O_8 - $\text{CaAl}_2\text{Si}_2\text{O}_8$, though substitution of other elements, usually in minor amounts, is common. Described here is a naturally occurring ferric iron sanidine feldspar composition in which up to ~70 mole% of the KAlSi_3O_8 molecule is replaced by $\text{KFe}^{3+}\text{Si}_3\text{O}_8$. It thus constitutes a new end-member feldspar composition and the data have been submitted to the Commission on New Mineral Names for evaluation.

The ferric iron sanidine is found in the 1.1ma volcanic rocks of the Leucite Hills, Wyo. The composition of these lavas and plugs is unusually rich in K and Fe^{3+} , and depleted in Al compared to typical basaltic rocks. Sanidine grains are among the last phase to crystallize in the groundmass of the rocks classified as orendites, and rarely exceed 150µm in length. Nearly all sanidine grains display a outward increase in Fe; the sanidine cores may have as little as 2.5 wt% Fe_2O_3 (16.5 wt% Al_2O_3) while the sanidine rims may reach 19.6 wt% Fe_2O_3 (2.7 wt% Al_2O_3). However, only those grains adjacent to quenched glass have the visually pronounced Fe-rich rims (Fig. 1). The Fe-rich rims are relatively narrow on (010) crystal faces compared with (001) faces, probably reflecting faster- (001) and slower- (010) growing crystallographic surfaces.

In order to document the compositional core-rim zoning profiles of these small grains without causing beam induced element mobility, a 3µm beam diameter and 5nA beam current was used during analysis with a JEOL 733 microprobe. The WDS system was configured such that x rays from Si, Al, K, and Fe were all acquired within the first 40 seconds of beam exposure to the sample. Concentrations of Sr, Ti, Ca, Na, Mg and Ba were also determined. In addition to the broad range of Fe_2O_3 ($\text{Fe}^{\text{tot}}=\text{Fe}^{3+}$), these sanidine grains are also atypical in having extremely high concentrations of TiO_2 (0.2-1.1 wt%) and MgO (0.1-0.7 wt%). These unusual compositions have been confirmed with TEM-EDS analyses and thus cannot be the result of beam overlap onto adjacent phases. Our data show that the ideal exchange $\text{Fe}^{3+}=\text{Al}_1$ results in a progressive tetrahedral site deficiency with increasing concentrations of Fe^{3+} . Assuming that feldspar stoichiometry (R_5O_8) must be maintained in the substitution, a near perfect correlation ($R^2=0.999$) is obtained by including Ti, Mg and excess Si ($\text{Si}-3.00$) with Fe^{3+} in the substitution for tetrahedral Al. Charge-balance considerations indicate that there is insufficient concentrations of R^{2+} cations to balance the high Mg through a $\text{R}^{2+}+\text{Mg}^{2+}=(\text{R}^{1+}+\text{R}^{3+})_{-1}$ substitution. This implies the rare substitution $\text{Mg}^{2+}+\text{Si}^{4+}=(2\text{Al}^{3+})_{-1}$ in $2\text{KAlSi}_3\text{O}_8$. Such a substitution couple has been found in synthetic leucite and kalsilite.^{1,2}

To provide evidence that the Fe-rich rims on the sanidine grains have monoclinic sanidine structure and are not a phase which fortuitously gives feldspar stoichiometry when all iron is assumed to be ferric, electron diffraction patterns from the sanidine rims were recorded on film with a JEOL 1200EX TEM operating at 120kV. Microdiffraction techniques employing both STEM (5% error) and conventional TEM (2% error) were used with a tilt/rotation holder. Evaporated carbon on the TEM grid was used for an internal standard. Eleven diffraction patterns giving 26 distinct d-spacings were measured. Using the unit cell parameters of ref. 3, each pattern produced internal consistency between measured angles for all combinations of indexed (hkl) planes. Very good agreement exists between our determinations and x-ray diffraction measurements from synthetic Fe-sanidine³ (Table 1) leading us to conclude that the Fe-rich rims are monoclinic Fe-sanidine feldspar.⁴

References

1. E.W. Rodder, American Journal of Science, 249(1951).
2. J.F. Schairer, Geological Society of America Bulletin, 56(1948)1349.
3. D.R. Wones and D.E. Appleman, U. S. Geological Survey Prof. Paper, 424C(1961)C309-C310.
4. Special thanks to J.P. Bradley for the microtome sample preparation. TEM data were collected in the interplanetary dust lab of D.E. Brownlee.

Table 1: Measured d-spacings from this study and Wones & Appleman (1961) compared with calculated values. Relative errors 2% except those with asterisk 5%.

Measured	W & A	Calculated	hkl
(Å)	(Å)	(Å)	
6.59		6.70	110
6.51	6.5	6.56	020
4.56*		4.64	021
3.90		3.90	200
3.81*	3.99	3.99	111
3.77	3.81	3.81	130
3.62		3.65	131
3.28*	3.35	3.35	220
3.21*		3.28	040
3.02	3.02	3.02	131
2.97*	2.978	2.976	222
2.95	2.934	2.935	041
2.74*		2.825	311
2.89*	2.803	2.806	132
2.75		2.85	201
2.61*	2.653	2.642	312
2.59		2.614	221
2.54		2.551	310
2.40	2.411	2.413	331
2.29	2.183	2.187	060
2.26*	2.289	2.296	332
2.24*		2.34	242
2.21*		2.26	132
2.17*		2.268	223
2.03*		2.145	401
1.89*	1.823	1.823	170

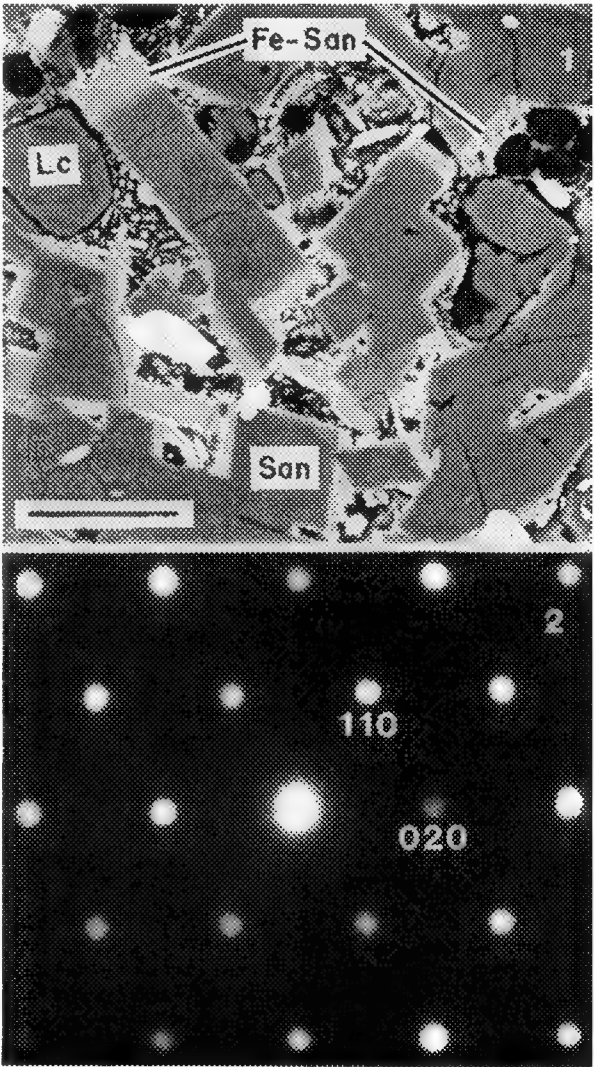


FIG. 1. BSE image showing Al-rich sanidine (medium grey) with bright, Fe-sanidine rims in quenched glass. Elliptical grains are leucite (grey) or analcime (dark). Large bright grains are apatite. Bar = 50um
FIG. 2. Electron diffraction pattern from an Fe-rich sanidine rim along [001].

ELECTRON ENERGY LOSS SPECTROSCOPY AND STOPPING-POWER CALCULATION OF THE SUPERCONDUCTOR $\text{Bi}_{1.8}\text{Pb}_{0.3}\text{Sr}_2\text{Ca}_2\text{Cu}_3\text{O}_{10}$

J. R. Dunlap, S. Luo, D. C. Joy*, D. C. Chakoumakos*, S. Zhu* and Y. Sun*

EM Facility, University of Tennessee, Knoxville, TN 37996-0810,

*Oak Ridge National Laboratory, Oak Ridge, TN 37831

Several studies have been undertaken to investigate the fine structure and superconductive properties of high temperature superconductors.^{1,2,3,4} Yuan et al.⁴ utilized electron energy loss spectroscopy (EELS) to determine the dielectric function of the superconductor $\text{Ba}_2\text{YCu}_3\text{O}_{7-x}$. In this study we performed EELS on the superconductor $\text{Bi}_{1.8}\text{Pb}_{0.3}\text{Sr}_2\text{Ca}_2\text{Cu}_3\text{O}_{10}$ at both room temperature and below the transition temperature and calculated such properties as the dielectric function, the inelastic mean free path and the stopping power for this material.

Powdered $\text{Bi}_{1.8}\text{Pb}_{0.3}\text{Sr}_2\text{Ca}_2\text{Cu}_3\text{O}_{10}$ was dispersed by sonication in a 0.2% (wt/v) solution of poly-(N-vinylpyrrolidone) in isopropanol. Individual crystals were allowed to settle and dry on a lacey carbon film. Figure 1 shows a typical individual crystal and Fig.2 shows a typical diffraction pattern. Electron energy loss spectra were recorded from single crystals which extended into holes in the film. The EEL spectra were recorded at room temperature and at 95°K which is below the transition temperature of 105°K. Samples were examined and electron energy loss data collected on an Hitachi H-800 operating in the TEM mode at 200 KeV. A collection semiangle of 5.3 mrad and a FWHM spectral resolution of 6 eV were used for all studies. A Gatan cryo-holder was used for the low temperature studies.

The results from the experimental EEL spectral data are represented in Fig.3. At both room temperature and below the transition temperature, i.e. under superconductive conditions, the EEL spectra show a double plasmon with one peak center at 21 eV and a second at 37 eV. The average t/λ value was found to be 0.15

An FFT deconvolution procedure was used to get the single scattering profile from the EEL spectral data. From our calculations the average crystal thickness, under superconductive conditions was determined to be ca. 10 nm, therefore the spectra represent the single scattering distributions. The dielectric energy loss function $\text{Im}(-1/\epsilon)$ was obtained from the single scattering distribution and the absolute scale was determined by the sum rule. Kramers-Kronig analyses were carried out to obtain ϵ_r and ϵ_i . The total inelastic mean free path was calculated to be about 90nm. The stopping power dE/dS was calculated from Eq.(1)⁵

$$-\frac{dE}{dS} = \frac{2\pi e^4 n N_{\text{eff}}(E)}{E} \ln\left(\frac{1.166E}{I_{\text{eff}}(E)}\right) \quad (1)$$

where E is the instantaneous energy of the electron, n the number of unit cells per unit volume, A the atomic weight and N_{eff} and I_{eff} are the effective electron number and mean ionization potential respectively. N_{eff} and I_{eff} were calculated by sum rule. Figure 4 shows the stopping power for $\text{Bi}_{1.8}\text{Pb}_{0.3}\text{Sr}_2\text{Ca}_2\text{Cu}_3\text{O}_{10}$ at 95°K. According to our calculations the main contribution to stopping power and inelastic mean free path are from valence electrons, i.e. interband transitions and plasmon excitations. Therefore the calculated mean ionization potential of 45 eV is much lower than the 363eV value calculated from the general formula.

A comparison of the experimental data indicates that there is no obvious change in the EEL spectra when going from room temperature to below the transition temperature. We conclude therefore, that the superconductive condition does not influence the fast electron energy loss mechanism.

References

1. D. P. Beesabathina et al., Proceedings of the 49th annual Meeting of the Electron Microscopy Society of America (1991), 1090.
2. N.J. Zaluzec et al., Proceedings of the 46 th annual Meeting of the Electron Microscopy Society of America (1988), 872.
3. H.-J. Ou and J.M. Cowley,, Proceedings of the 46 th annual Meeting of the Electron Microscopy Society of America (1988), 882.
4. J. Yuan et al., J. Phys. C: Solid State Phys. (1988) 21, 517.
5. S. Luo et al., Radiation Effects and Defects in Solid (1991)117, 235.

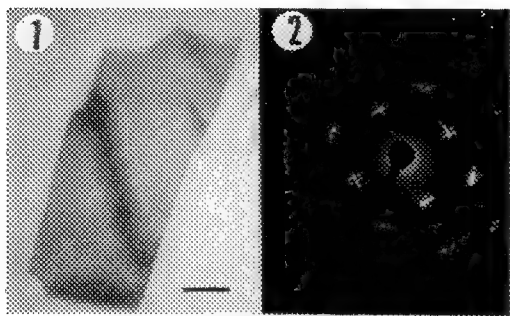


Fig.1 Single crystal of $\text{Bi}_{1.8}\text{Pb}_{0.3}\text{Sr}_2\text{Ca}_2\text{Cu}_3\text{O}_{10}$
Bar = 50 nm
Fig.2 Diffraction pattern from crystal.

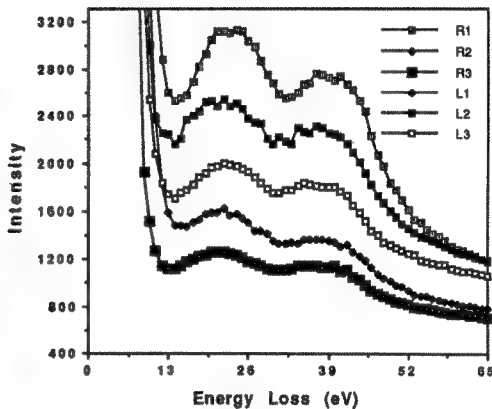


Fig.3 Comparison of EEL spectra between the room temperature and below the transition temperature. R1,R2 and R3 for room temperature.

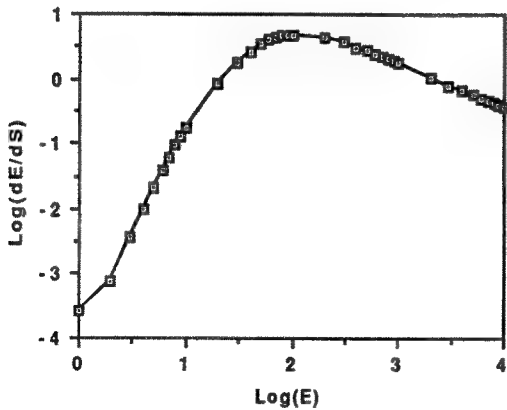


Fig.4 Calculated Stopping power for superconductor $\text{Bi}_{1.8}\text{Pb}_{0.3}\text{Sr}_2\text{Ca}_2\text{Cu}_3\text{O}_{10}$ at 95°K.

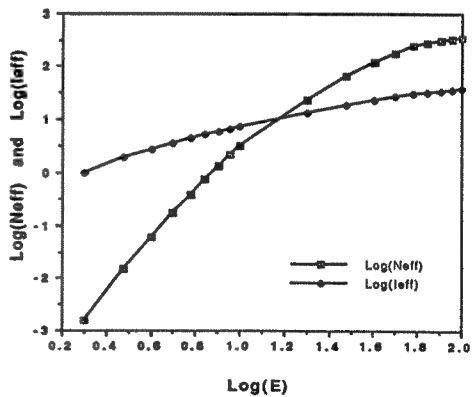


Fig.5 Calculated N_{eff} and I_{eff} for superconductor $\text{Bi}_{1.8}\text{Pb}_{0.3}\text{Sr}_2\text{Ca}_2\text{Cu}_3\text{O}_{10}$ at 95°K.

MICROSTRUCTURE OF SUPERCONDUCTING $\text{Y}_1\text{Ba}_2\text{Cu}_3\text{O}_{7-x}/\text{Nd}_{1.85}\text{Ce}_{0.15}\text{CuO}_{4-y}$ BILAYER FILMS

D. Prasad Beesabathina, L. Salamanca-Riba, S. N. Mao, X. X. Xi, T. Venkatesan

Center for Superconductivity Research, University of Maryland, College Park, MD 20742

Superconducting bilayers of $\text{Y}_1\text{Ba}_2\text{Cu}_3\text{O}_{7-x}$ (YBCO) and $\text{Nd}_{1.85}\text{Ce}_{0.15}\text{CuO}_{4-y}$ (NCCO) are of particular interest for the study of the interaction between p-type superconductors (YBCO) and n-type superconductors for possible device applications. The microstructural study is crucial since the crystallinity and interface quality of the bilayers effect the characteristics of heterojunctions. In this report, we present details of the microstructure of superconducting NCCO/YBCO bilayers.

NCCO/YBCO bilayers were deposited on three different single crystal substrates of (001) LaAlO_3 , (001) SrTiO_3 , and (001) Y-ZrO_2 (YSZ) using pulsed laser deposition. The details of the deposition and superconducting properties are reported elsewhere.¹ The samples reported in this report have typical YBCO thickness of 2000 Å and NCCO thickness of 4000 Å.

Figure 1(a) shows a bright field image of a NCCO/YBCO bilayer grown on YSZ and exhibits a Moire' fringe pattern in some regions of the NCCO film. The Moire' fringes have a spacing of $\sim 31.01\text{Å}$. The calculated fringe spacing originating from overlap of (004) lattice planes of NCCO and (004) lattice planes of cubic $\text{Ce}_{0.5}\text{Nd}_{0.5}\text{O}_{1.75}$ (CNO) is $\sim 30.51\text{Å}$. This value is in close agreement with the measured value, indicating that the parallel Moire' fringes result from the overlap of NCCO phase and CNO phase along the electron beam direction. In earlier studies,² we reported detailed studies of the cubic CNO phase present in NCCO films. A [110] zone axis electron diffraction pattern taken from the YSZ-NCCO interface is shown as inset to Fig. 1. The orientation relationship was determined to be: $[001]_{\text{YSZ}}//[001]_{\text{NCCO}}$ and $[010]_{\text{YSZ}}//[110]_{\text{NCCO}}$. A columnar grain structure was observed in NCCO film grown on YSZ (see Fig. 1). Films deposited on the (100) SrTiO_3 and (100) LaAlO_3 yielded a similar columnar grain structure of the NCCO film, indicating that the grain structure is not the result of the misfit between the substrate and the NCCO film. We believe that the columnar grain structure is mostly due to roughness of the surface that is caused by the occurrence of cubic CNO grains. We also observed grain boundaries starting from the CNO phase inside the NCCO film (marked by arrow in Fig. 1). Figure 2 shows a [110] high resolution lattice image of the NCCO-YBCO interface. The interface is free of intermediate phases. The [110] zone axis electron diffraction pattern is shown as inset. In this case, the epitaxial relationship was determined to be: $[001]_{\text{NCCO}}//[001]_{\text{YBCO}}$ and $[110]_{\text{NCCO}}//[110]_{\text{YBCO}}$. Stacking defects were also observed in the YBCO film. In general, the NCCO-YBCO interfaces are wavy and are not as sharp as the substrate-NCCO interfaces. The wavy nature of the NCCO-YBCO interface is attributed to a rough NCCO surface.

In summary, the growth morphology of superconducting NCCO/YBCO bilayers grown on three different substrates was investigated by transmission electron microscopy. The NCCO/YBCO bilayers are predominantly c-axis-oriented. The sharpness of the NCCO-YBCO interface is limited by the occurrence of cubic CNO phase in the NCCO film which in turn, we believe, is effecting the surface roughness of the NCCO film. Studies are in progress to completely eliminate the cubic CNO phase in the NCCO film.

This work was supported by the National Science Foundation contract No. DMR-9020304

1. S. N. Mao, X. X. Xi, Qi. Li, Takeuchi, S. Bhattacharya, C. Kwon, C. Doughty, A. Walkenhorst, T. Venkatesan, C. B. Whan, J. L. Peng, and R. L. Green (submitted to Appl. Phys. Lett.).

2. D. Prasad Beesabathina, L. Salamanca-Riba, S. N. Mao, X. X. Xi, and T. venkatesan (submitted to Appl. Phys. Lett.).

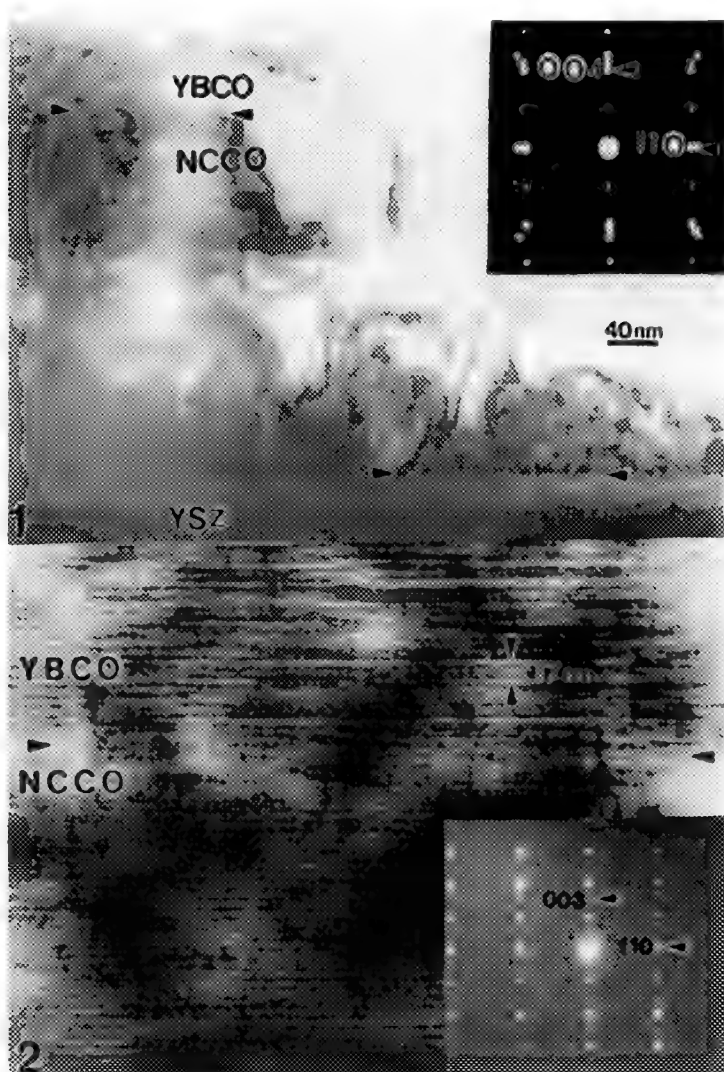


Fig. 1. Bright field image of NCCO/YBCO bilayer sample grown on YSZ, exhibiting parallel Moire' fringes in NCCO film..

Fig. 2. [110] high resolution lattice image of NCCO/YBCO interface of the sample grown on YSZ, showing the interface structure.

Analytical Electron Microscopy of a Ag-Y-Ba-Cu Superconductor Precursor Material

A. J. Strutt, M. T. Simnad, E. Lavernia * and K. S. Vecchio

Department of AMES, Mail code 0411, University of California-San Diego, La Jolla, CA 92093

* 616 Materials Science and Engineering, Department of Mechanical & Aerospace, University of California-Irvine, Irvine CA 92717

Analytical electron microscopy (AEM) has been used to characterize a Ag-rich superconductor precursor material whose composition (before oxidation) was based on 10 wt.% of a YBa_2Cu_3 alloy and 90 wt.% Ag, and the same material after an oxidation heat treatment of 690°C for 24 hours. The material had been produced by a melt spinning process as a metallic alloy to permit deformation of the material (in the metallic state) prior to subsequent oxidation to form the ceramic superconducting Y-Ba-Cu oxide phase.

The microstructure was characterized using a Philips CM30 AEM, at 300 kV, using specimens thinned to electron transparency by ion-milling. Energy dispersive X-ray spectroscopy (EDX) was performed using the same instrument, with a Link Analytical solid-state X-ray detector with an ultra-thin window.

In the as-formed condition, the Y-Ba-Cu alloy phase exists as discrete particles at the triple points of the relatively fine (approx. 250 nm.) Ag-rich grains (Fig.1) and is of a granular morphology, whereas after oxidation and the associated grain growth (figs. 2, 5 and 6), the Y-Ba-Cu-oxide phase appears lighter, with more uniform contrast. Such changes are probably due to the lower average atomic weight of the oxidized Y-Ba-Cu alloy, which leads to a greater ion beam thinning rate during specimen preparation, and which would also permit greater electron beam penetration upon subsequent examination.

The Ag-rich grains are frequently twinned and also contain a fine dispersion of coherent, apparently plate-like precipitates which coarsen as a result of the oxidation heat treatment (cf. figs. 1 and 2). The EDX spectra of the Ag-rich grain (Fig.3) and oxide particle (Fig.4) show the significant enrichment of barium in the oxide phase, but also show that Ba is present (to a lesser extent) in the Ag-rich grains. Since the solubility of barium in silver is negligible, the Ba-peaks in Fig.3 are probably caused by the fine coherent precipitates which may be of the Ag_5Ba phase.¹

Fig. 6, which shows a dark-field micrograph of Y-Ba-Cu oxide particles in a Ag-rich matrix, was formed from one of the low intensity low angle reflections in the selected area diffraction pattern (inset) and clearly indicates an orientation relationship between the two phases.

The microstructure of the oxidized material (as shown by TEM) confirms the results of previous thermogravimetric analysis which suggested that a higher oxidation temperature may be necessary to form an interconnected superconducting oxide phase.² Results of the current work also suggest that barium may form a coherent phase with silver, with a potential deleterious effect on ductility.³

References

1. G. Bruzzone, *et al.*, J. Less Common Metals (1987) 128, 259.
2. E. A. Early, *et al.*, J. Appl. Phys. (1992) 71, 1327.
3. This work was funded by the U.S. Department of Energy under grant no. DE-FG03-86ER45230.

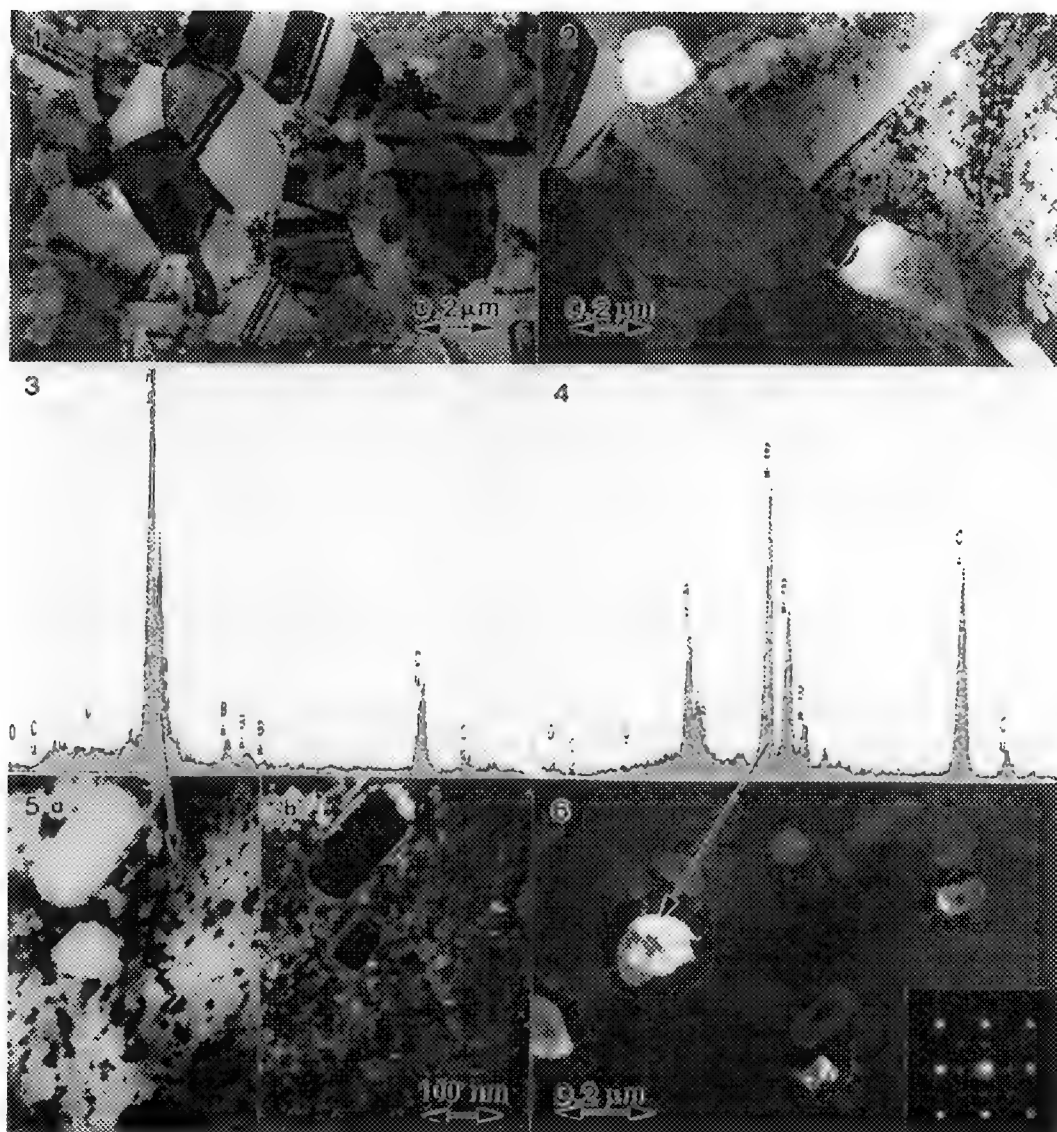


Fig.1 General microstructure of the precursor material.

Fig.2 As Fig.1, after oxidation at 690°C for 24 hours.

Fig.3 EDX spectrum from a Ag-rich grain of the oxidized material.

Fig.4 As Fig.3, but from a particle of the Y-Ba-Cu oxide phase.

Fig.5 (a) Bright and (b) dark field micrographs showing large, internally nucleated Y-Ba-Cu oxide particles together with fine coherent precipitates of a Ag-Ba intermetallic phase in a Ag-rich matrix.

Fig.6 Dark field image of Y-Ba-Cu oxide phase particles, as in Fig.5, with (inset) the corresponding SAD pattern which shows the low intensity, low angle reflections of the type used to from the main image.

A TEM AND EDS STUDY ON THE EFFECT OF BACK MELTING ON DIRECTIONALLY SOLIDIFIED HgZnTe

H.J. Zuo, R.D. Griffin, R.A. Andrews, and G.M. Janowski

Department of Materials Science and Engineering, University of Alabama at Birmingham, Birmingham, AL 35294-4461

Bulk growth of II-VI semiconductors such as HgZnTe (MZT) is difficult because of the gravity-induced convection that occurs during solidification. This convection can lead to crystal defects (primarily dislocations and subgrain boundaries) and composition inhomogeneities which may limit device performance. Crystals grown in the low-gravity environment of space should have fewer of these defects. However, the limited duration of space shuttle experiments and the need for uniform composition make it imperative that the initial composition transient that occurs in directionally solidified alloys be eliminated. One proposed solution to this problem is back-melting. In the first stage of this process, a section of the specimen is directionally solidified and the remainder is quenched. The quenched portion is then remelted and directionally solidified. In the flight experiment, the remelting and second directional solidification step will be carried out in space.

The present report will discuss the results of an earth-based study to determine the effect of back-melting on the dislocation Burgers vector and chemical homogeneity of a directionally solidified MZT crystal. A previous scanning electron microscopy (SEM) study of this same sample showed an increase in the zinc content at the back-melted interface without changes in crystallographic orientation across the interface.¹

Transmission electron microscopy (TEM) samples were cut from longitudinal sections of the back-melted crystal on both sides of the back-melted interface and away from the interface. The disks were mechanically polished through 0.25 μm diamond paste and then chemically polished with a 2% bromine-methanol solution using a single jet polisher.² The samples were examined at 200 kV in a JEOL 2000FX TEM. A liquid nitrogen cooled stage was used to prevent the volatilization of mercury during examination.

A TEM image of the back-melted interface is shown in Figure 1. The area near the back-melted interface contained triangular and hexagonal pits that may have been precipitates that were selectively dissolved during sample preparation (Figure 2). There was no evidence of a difference in composition between the pits and the surrounding material, although this observation may be a result of total dissolution of the precipitate and some of the surrounding matrix. Convergent Beam Electron Diffraction (CBD) patterns from both sides of the interface (Figure 3) showed no change in orientation. Energy dispersive x-ray spectra (EDS) from both the back-melted interface and samples taken away from the interface showed an increased Zn content. This result is in agreement with the previous SEM study. Analysis of dislocations in both the pre- and post-back-melted region showed no differences. All dislocations examined showed contrast consistent with the direction of $\mathbf{b} = \langle 110 \rangle$.

This TEM examination of the back-melted interface in an MZT sample showed excellent agreement with previous SEM results. The composition inhomogeneity and crystallographic continuity across the interface were confirmed. Additionally, there was some evidence that precipitates may have formed near the interface. It was also found that no difference in dislocation character was found on either side of the interface.

References

1. H.J. Zuo, M.W. Price, R.D. Griffin, R.A. Andrews, and G.M. Janowski, Proc. EMSA Fiftieth Annual Meeting (1992), 1696.
2. Private communication with H. Schaake, Texas Instruments, Dallas, TX.

3. This work was supported under NASA Contract NAS8-38672. The MZT sample was grown at the Space Science Laboratory at NASA/Marshall Space Flight Center, Huntsville, AL.

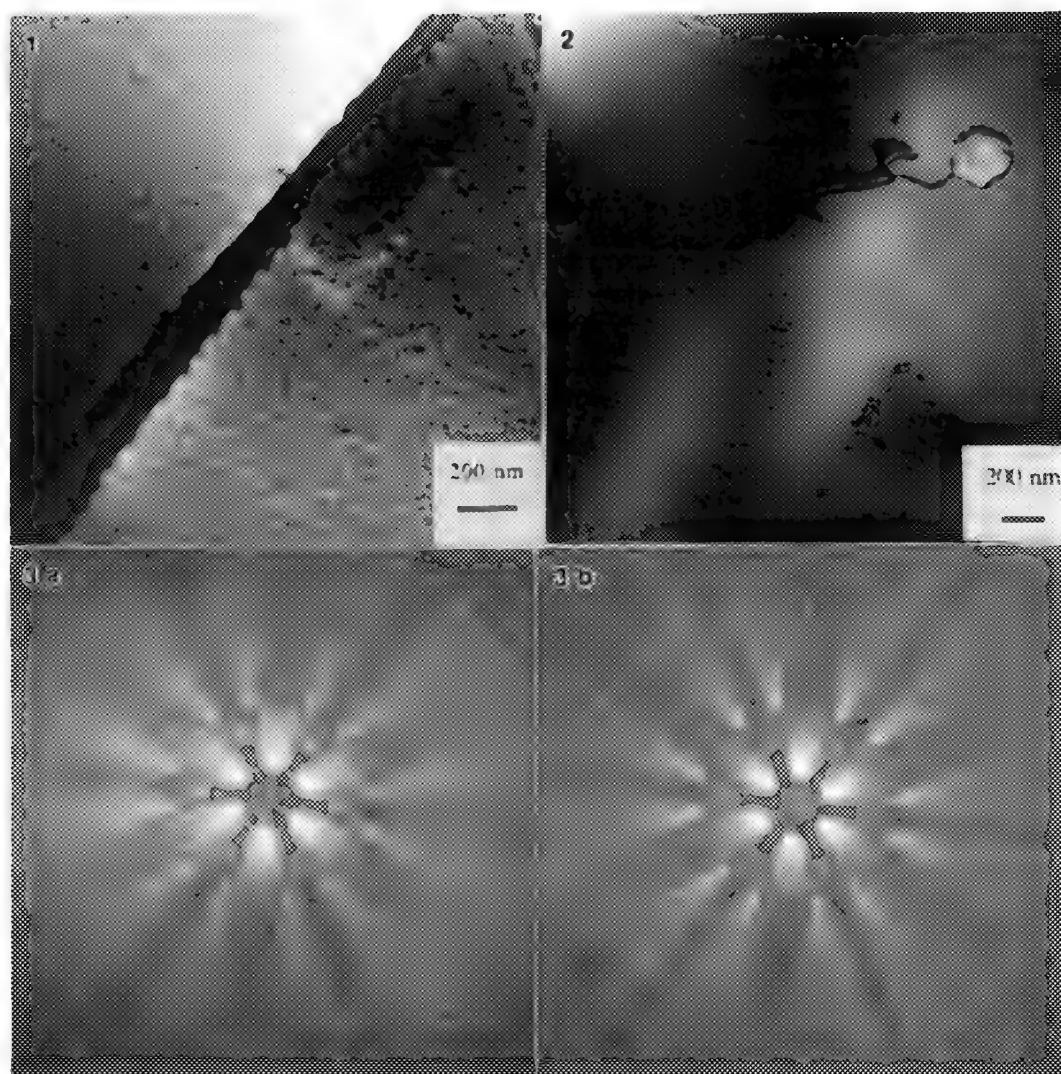


FIG. 1.--TEM image of the back-melted interface.

FIG. 2.--TEM image of the pits found near the back-melted interface.

FIG. 3.--CBD patterns taken from both sides of the back-melted interface. No shift in the orientation was found.

ELECTRON MICROSCOPY OF NATURAL AND EPITAXIAL DIAMOND

J.B. Posthill*, T. George**, D.P. Malta*, T.P. Humphreys***, R.A. Rudder*, G.C. Hudson*,
R.E. Thomas*, and R.J. Markunas*

* Research Triangle Institute, Research Triangle Park, NC 27709-2194

** Center for Space Microelectronics Tech., JPL, Calif. Inst. of Tech., Pasadena, CA 91109

*** Department of Physics, North Carolina State University, Raleigh, NC 27695-8202

Semiconducting diamond films have the potential for use as a material in which to build active electronic devices capable of operating at high temperatures or in high radiation environments. Ultimately, it is preferable to use low-defect-density single crystal diamond for device fabrication. We have previously investigated polycrystalline diamond films with transmission electron microscopy (TEM) and scanning electron microscopy (SEM)^{e.g.1}, and homoepitaxial films with SEM-based techniques^{e.g.2}. This contribution describes some of our most recent observations of the microstructure of natural diamond single crystals and homoepitaxial diamond thin films using TEM.

We are developing techniques to thin diamonds to electron transparency in the region of interest; particularly as diamond is difficult to mechanically thin. One simple (but time consuming) approach for the fabrication of plan-view diamond TEM samples is to thin only by ion milling. Figs. 1 and 2 show TEM micrographs taken from a (100) natural type IIb (semiconducting) diamond crystal and a (100) natural type Ia diamond that have been ion milled to electron transparency. The mottled background contrast observed in both images is believed to be an artifact due to ion milling. An average dislocation density of $\sim 5 \times 10^7 \text{ cm}^{-2}$ was observed in the type IIb material, and the dislocation distribution was found to be nonuniform. Dislocations were not observed via TEM in the type Ia diamond (dislocation density $< 10^5 \text{ cm}^{-2}$), but nitrogen-containing platelets that lie on {100} planes, characteristic of type Ia diamond, were observed. A technique for more rapid thinning for plan-view TEM sample preparation was achieved by laser ablation (Fig. 3), which is described in more detail elsewhere³. Although it is recognized that defect densities will vary from stone to stone for natural diamond, type Ia has consistently been found to show lower dislocation densities.

Homoepitaxial diamond films were grown on (100) type Ia diamond substrates using water/methanol mixtures in an rf-driven plasma-enhanced chemical vapor deposition (PECVD) reactor. The growth conditions were comparable to that described elsewhere⁴. They were then ion milled from the back-side for plan-view TEM examination. Figs. 4 and 5 respectively show the featureless topography recorded by a field emission gun SEM and dislocations observed by TEM in a film grown for 50 minutes. The average dislocation density was found to be $\sim 5 \times 10^6 \text{ cm}^{-2}$, and no other types of defects were observed. This dislocation density would be considered high by single crystal Si standards, but it does represent the current benchmark for diamond epitaxy. We are certain we are observing the epilayer because of the absence of nitrogen-containing platelets. Note also that the micro-Raman spectrum of the diamond epitaxial layer showed the characteristic LO phonon peak with a FWHM of 2.4 cm^{-1} , comparable to that of the substrate. These results show that growth of homoepitaxial diamond can be achieved on natural type Ia diamond to a reasonable standard. In other words, the presence of the nitrogen-containing platelets in the substrate does not result in catastrophic dislocation densities in the diamond epilayer.⁵

References

1. J.B. Posthill, et al., Proc. 47th Ann. Meet. Electron Microsc. Soc. of America, 592 (1989).
2. D.P. Malta, et al., Proc. 49th Ann. Meet. Electron Microsc. Soc. of America, 880 (1991).
3. T. George, et al., Appl. Phys. Lett., in press.
4. R.A. Rudder, et al., Appl. Phys. Lett., 60 329 (1992).
5. The authors gratefully acknowledge support for this program from SDIO/IST through ONR (Contract No. N00014-92-C-0081).

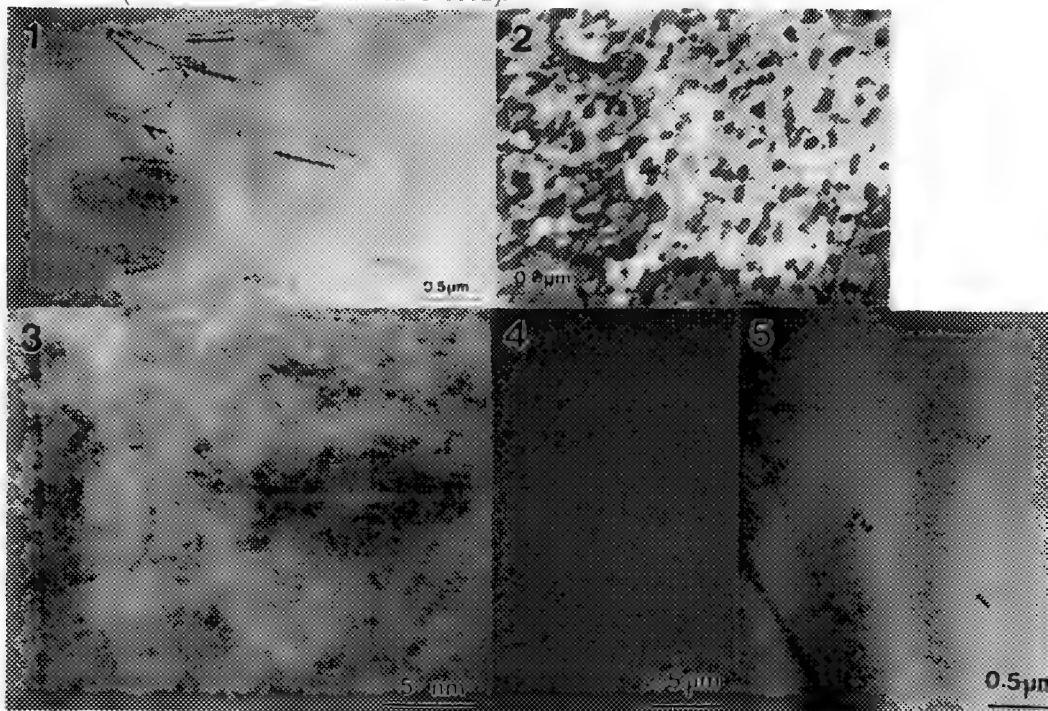


FIG. 1.--TEM of single crystal C(100) [type IIb]. Note high dislocation density. Sample prepared by ion milling.

FIG. 2.--TEM of single crystal C(100) [type Ia]. Note the presence of {100} nitrogen platelets (shown inclined in this [110] orientation) characteristic of natural type Ia diamond. Sample prepared by ion milling.

FIG. 3.--Higher magnification TEM of single crystal C(100) [type Ia] in [100] orientation. Sample prepared by laser ablation.

FIG. 4.--SEM topographical image of diamond homoepitaxial film grown using water/methanol mixture. The surface is featureless.

FIG. 5.--TEM plan-view of diamond homoepitaxial film grown using water/methanol mixture. Sample prepared by ion milling.

CRYOMICROSCOPY OF LOW- T_g LATEX PARTICLES VIA FREEZE DRYING

J. R. Reffner

Analytical Research Department, Rohm and Haas Co., Spring House, PA 19477

Transmission Electron Microscopy (TEM) is a powerful tool for investigating the structure of latex particles. However, examining low T_g (glass transition, $T_g < \text{room temperature}$) latex particles requires special techniques due to the significant deformation which occurs if the particles are dispersed onto a substrate at room temperature. Here a freeze drying (FD) technique is presented which permits individual emulsion particles, including stained particles, to be examined in a manner that minimizes deformation by maintaining the particles at temperatures below T_g .

Typically, particle morphology is determined from images of individual latex particles dispersed onto a supporting ultra-thin substrate or from images of ultra-microtomed sections of films cast from the latex. Examining particles dispersed onto a substrate is often advantageous, allowing direct determination of particle shape and characterization of the morphology prior to the film formation process. Although low T_g materials can be examined using this technique, information about the size, shape and morphology of phase separated domains can be obscured by the deformation which occurs when the particles are examined at room temperature. Freeze Fracture (FF)^{1,2} and Cryomicroscopy of frozen or vitrified aqueous dispersions²⁻⁴ have been used to examine low T_g latex particles. FF has several limitations since a replica of the fracture surface is imaged, rather than the particles. Cryomicroscopy of frozen or vitrified aqueous dispersions permits the particles to be directly examined. Although a very useful technique, acrylic latex particles in an icy or vitreous aqueous matrix typically cavitate after exposure to electron irradiation which significantly alters the morphology of the particles.^{4,5} The cavitation has been used to infer particle morphology based on distinguishing acrylic domains, which cavitate, from polystyrene domains, which do not cavitate when exposed to electron irradiation.⁴

Freeze dried samples were prepared by nebulizing a dilute latex (0.001 wt% solids) onto a carbon coated support film on a TEM grid. The TEM grid, attached to an aluminum block, is cooled in liquid nitrogen prior to the nebulizing step, and removed from the liquid nitrogen bath for only a few seconds during the nebulizing step. The samples were then transferred under liquid nitrogen into a Gatan cold stage. The cold stage was then inserted into the prechamber of the TEM (a JEOL 1200EX) and warmed to -85°C causing the water to sublime. The samples were subsequently imaged at 120 KeV while maintained at -85°C . Samples were stained with RuO₄ (known to stain polystyrene⁶) by addition of 0.1 ml of 0.5% RuO₄ solution (obtained from Polysciences®) to 5 ml of the diluted emulsion 2-4 hours prior to nebulizing.

Figures 1 and 2 are images of a mixture of polystyrene latex (Polysciences® 140 nm monodisperse particles, $T_g \sim 105^\circ\text{C}$) and an acrylic latex (80% butyl acrylate/ 20% methyl methacrylate, $T_g \sim 10^\circ\text{C}$). In Figure 1 the sample was prepared by dispersing the particles onto a substrate using the FD technique. The acrylic particles appear circular when examined at normal incidence (electron beam perpendicular to the substrate) and when the sample is tilted 45° (Figures 1a and 1b respectively), indicating that the particles are essentially spherical. In Figure 2 the particles were dispersed at room temperature. While the acrylic particles appear round at normal incidence (Figure 2a) they appear oval when tilted 45° (Figure 2b), indicating that the particles have deformed onto the substrate. This is confirmed by the lower contrast and larger diameter of the particles relative to that observed in Figure 1.

Figure 3 is an image of a mixture of polystyrene latices (Polysciences® 350 and 140 nm monodisperse particles) and the acrylic latex imaged in Figures 1 and 2. The sample was stained with RuO₄ and prepared using the FD technique. The higher contrast of the 350 nm polystyrene particle relative to the acrylic particle, which are indistinguishable in unstained samples, is due to RuO₄ staining of the polystyrene. This demonstrates that this staining procedure is compatible with the FD technique.

FD provides a means of examining individual low T_g acrylic particles, including stained particles, without the deformation which occurs when examined at room temperature or the cavitation typical with cryomicroscopy of the aqueous dispersions. This permits particle shape and phase separated morphologies to be characterized in minimally deformed particles. The likelihood that other common staining reagents can be used in a similar manner suggests additional applications of the FD technique.⁷

References

1. Wang, Y., Kats, A., Juhue, D., Winnik, M., *Langmuir*, 8, 1435-1442, (1992).
2. Shaffer, O. L., et al., *Proc. 49th Ann. Mtg. EMSA*, 1160-61 (1991).
3. Talmon, Y., *Proc. 45th Ann. Mtg. EMSA*, 496-499 (1987).
4. Silverstein, M., Talmon, Y., Narkis, M., *Polymer*, 30, 416-424, (1989).
5. Talmon, Y., *J. Electron Microscopy Tech.*, 2, 589-596, (1985).
6. Trent, J., Scheinbeim, J., Couchmon, P., *Macromolecules*, 16, 589-598, (1983).
7. The author wishes to thank Dr. Patricia Lesko for synthesizing the acrylic emulsion and Dr. Andrea Kirk and Dr. Barrett Bobsein for helpful input.

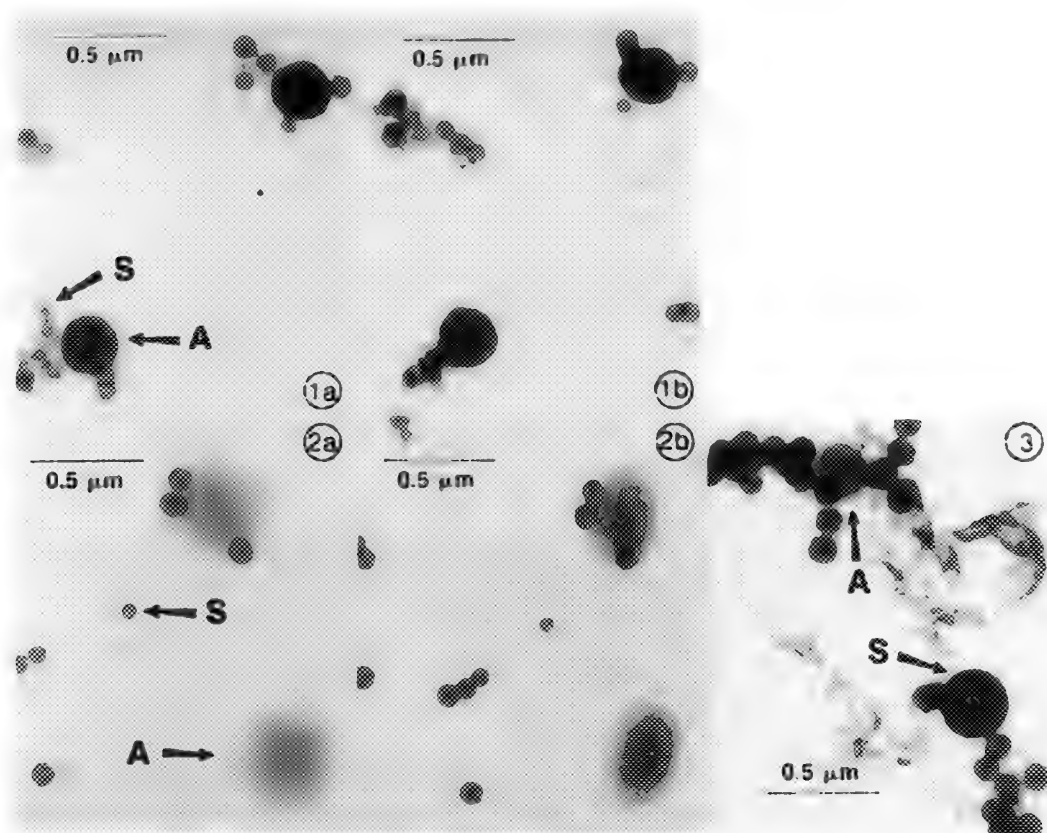


FIG. 1. Mixture of low T_g ($T_g \approx -10^\circ \text{C}$) acrylic particles (A) with 140 nm polystyrene particles (S) dispersed by freeze drying and examined at -85°C ; a) 0° tilt, b) 45° tilt about a vertical axis.

FIG. 2. Same particles as in Figure 1 dispersed and examined at room temperature; a) 0° tilt, b) 45° tilt about a vertical axis.

FIG. 3. Same particles as in Figure 1 mixed with 350 nm polystyrene particles (S) stained with RuO_4 .

MORPHOLOGICAL BEHAVIOR OF COMPATIBILIZED TERNARY BLENDS PREPARED BY MECHANICAL MIXING

S.D. Smith,* R.J. Spontak,† D.H. Melik,* S.M. Buehler,* K.M. Kerr,* and R.-J. Roe‡

*Corporate Research Division, The Procter & Gamble Company, Cincinnati, OH 45239

†Department of Materials Science & Engineering, North Carolina State University, Raleigh, NC 27695

‡Department of Materials Science & Engineering, University of Cincinnati, Cincinnati, OH 45221

When blended together, homopolymers A and B will normally macrophase-separate into relatively large ($>>1\ \mu\text{m}$) A-rich and B-rich phases, between which exists poor interfacial adhesion, due to a low entropy of mixing. The size scale of phase separation in such a blend can be reduced, and the extent of interfacial A-B contact and entanglement enhanced, via addition of an emulsifying agent such as an AB diblock copolymer. Diblock copolymers consist of a long sequence of A monomers covalently bonded to a long sequence of B monomers. These materials are surface-active and decrease interfacial tension between immiscible phases much in the same way as do small-molecule surfactants. Previous studies¹⁻⁴ have clearly demonstrated the utility of block copolymers in compatibilizing homopolymer blends and enhancing blend properties such as fracture toughness. It is now recognized that optimization of emulsified ternary blends relies upon design considerations such as sufficient block penetration into a macrophase (to avoid block slip) and prevention of a copolymer multilayer at the A-B interface (to avoid intralayer failure).⁵ In this work, the morphologies of several ternary blends compatibilized with various quantities of symmetric diblock copolymers differing in chain length are investigated.

All of the blends presented here are composed of polystyrene (S) and polybutadiene (B) homopolymers possessing molecular weights (M) of 40 kDa each. These homopolymers, along with a series of symmetric (50/50 wt%/wt%) poly(styrene-*b*-butadiene) (SB) diblock copolymers, were synthesized via living anionic polymerization in cyclohexane at 60° C. The initiator was sec-butyllithium. Each ternary blend was prepared by mixing the two homopolymers and a block copolymer in a HBI System 90 torque rheometer attached to a Rheomix 600 mixer-sensor equipped with roller-style rotors. During mixing at 200 rpm and 140° C, the torque (and, hence, blend viscosity) was monitored as a function of time for 10 min. Specimens for transmission electron microscopy (TEM) were produced by taking a small portion of each blend and quenching it in liquid nitrogen. A smaller specimen piece was fractured under these conditions and immediately placed in either a Reichert-Jung FC-4E or Ultracut-S cryoultramicrotome maintained at -125° C. Sections measuring about 70 nm thick were produced with a 35° Diatome cryodiamond knife and were immediately subjected to OsO₄ vapor, which preferentially stained the B-rich phases and prevented them from flowing on 1000 mesh Cu grids. Micrographs were obtained with both Zeiss EM902 and ISI 002B electron microscopes.

Figure 1 is a series of electron micrographs showing the effect of copolymer M on blend morphology. Each blend presented here is emulsified with 10 wt% added copolymer. In Fig. 1a, the copolymer possesses M=20 kDa, and the blend consists of irregularly shaped S domains. This blend does not easily flow but does retain its shape upon deformation. Note that B-rich dispersions measuring up to $\approx 90\ \text{nm}$ across reside within the S domains. The copolymer M is increased to 60 kDa in Fig. 1b, and many of the S domains are observed in circular cross-section, which is expected as the domains adopt a spherical morphology. The small B-rich aggregates are again visible here. In Fig. 1c, the copolymer M is increased to 120 kDa. In this case, most of the S domains appear circular in projection. A specimen of the blend shown in Fig. 1b, fractured and replicated with Pt/C at cryogenic temperatures, is provided in Fig. 2 for comparison. Note the uniform dispersion of cross-fractured spherical S domains residing within a matrix of B. Shown in Fig. 3 are torque profiles which follow the evolution of mixing in the three blends displayed in Fig. 1. The steady-state torque response is seen to increase noticeably with the M of the added copolymer. Additional blends containing different copolymer compositions will be presented to illustrate some of the practical compatibilization attributes of diblock copolymers.

References

1. D.-W. Park and R.-J. Roe, *Macromolecules* (1991)24, 5324.
2. H. Tanaka et al., *Macromolecules* (1991)24, 240.
3. T. Inoue et al., *Macromolecules* (1970)3, 87.
4. S. Anastasiadis et al., *Macromolecules* (1989)22, 1449.
5. C. Creton et al., *Macromolecules* (1992)25, 3075.
6. We thank J.L. Burns for her assistance in fracturing the blend at cryogenic temperatures.

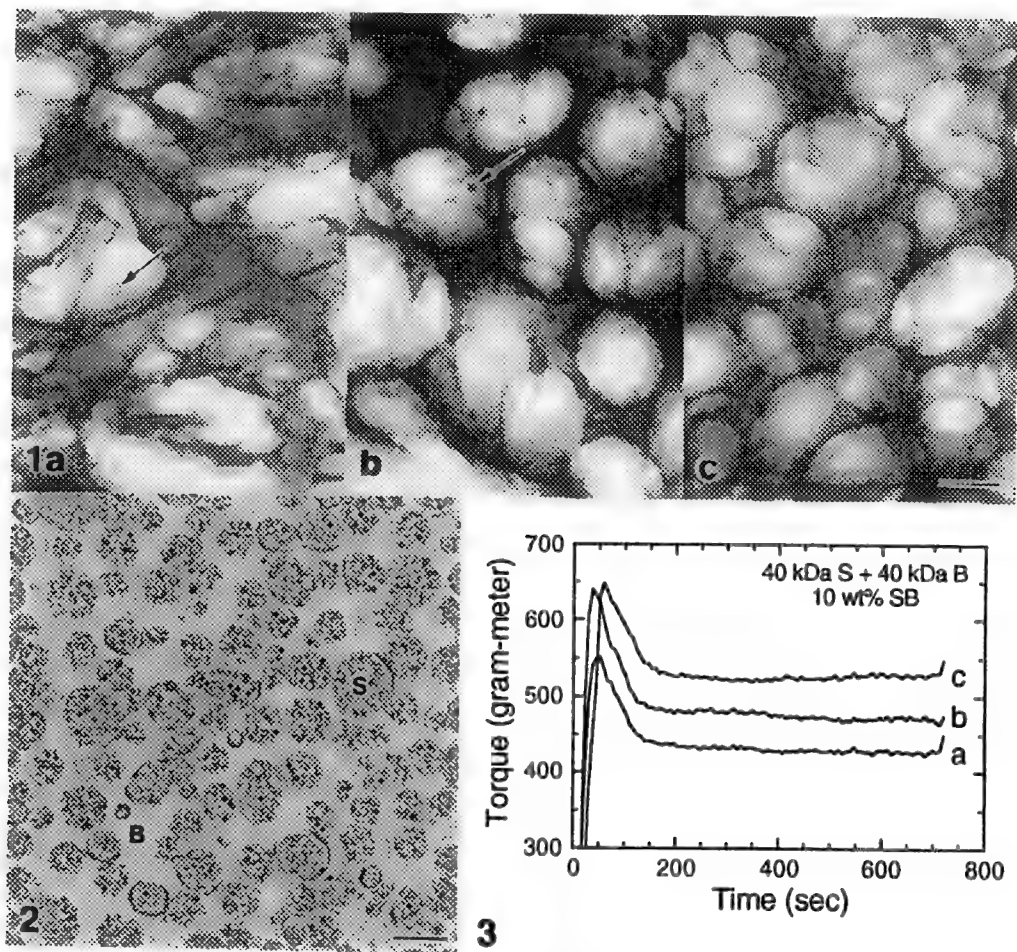


FIG. 1.--Electron micrographs of ternary blends compatibilized with diblock copolymers of different molecular weights: (a) 20 kDa, (b) 60 kDa, and (c) 120 kDa. Each blend consists of 10 wt% added copolymer. Note stained B-rich aggregates residing in S-domains (arrows). Bar = 250 nm.

FIG. 2.--Replicated fracture surface of ternary blend containing 60 kDa diblock copolymer. Spherical S-rich domains possess rough texture, while B-rich matrix appears relatively smooth, upon fracture at ca. -170°C. Bar = 500 nm.

FIG. 3.--Time response of torque to mixing in 50/50 S/B ternary blends with 10 wt% added SB diblock copolymer. Copolymer M follows legend in Fig. 1 caption. Blends were mixed at 140°C for 10 min.

DIRAC-FOCK CALCULATIONS OF SCATTERING FACTORS AND MEAN INNER POTENTIALS FOR NEUTRAL AND IONISED ATOMS

David Rez and Peter Rez*

Pennine House, Pennine Drive, London NW2 1PA, England

* Center for Solid State Science and Physics Dept, Arizona State University, Tempe, AZ 85287

Tables of X-ray and electron scattering factors are essential for programs that calculate diffraction intensities or simulate images. These tables are calculated from atomic charge densities derived from Hartree Fock programs for atoms. The most frequently used results are those due to Doyle and Turner¹ who used Coulthard's relativistic Hartree Fock program. They did not calculate scattering factors for all elements and other results using different programs were used to complete the tables given in the International Tables for Crystallography. As microscopy and diffraction become more quantitative it has become important to reexamine the calculation of atomic scattering factors using more recent Hartree Fock codes to quantify more precisely differences due to solid state effects. We also feel it is desirable to calculate all naturally occurring elements, and their common ionised states, using the same program.

The charge densities were calculated using the Multi-Configuration Dirac-Fock code of Grant et al². In this program the Dirac equation is solved for all configurations of the unfilled shells. Full details of the methods are given in the paper by Grant et al. The X-ray scattering factors can be calculated from the radial charge density using

$$f_x(s) = 4\pi \int_0^\infty r^2 \rho(r) \frac{\sin(4\pi sr)}{(4\pi sr)} dr$$

where $s = \sin\theta/\lambda$. We have tabulated the results on a grid up to $s=6.0\text{\AA}^{-1}$ following Doyle and Turner. The differences are less than 0.1 % for all elements over the full range of s . For the negative ions we used the Watson sphere technique. We have also parameterised the atomic X-ray scattering factors by a sum of four Gaussians

$$f_x(s) = \sum_j a_j \exp(-b_j s^2)$$

using the Levenberg-Marquadt procedure as given in Numerical Recipes³. The range of parameterisation and the accuracy of the fit can vary significantly among the elements. We have therefore decided to quote a range of s over which the parameterisation is valid, as well as a χ^2 value and the sum of a_j which should be equal to the atomic number - charge. In our experience this is a very sensitive test of convergence and we feel that parameterisations should be rejected if there is a discrepancy of more than 2-3%. Not only is a constant value of $f_x(\infty)$ unphysical, it is also indicative of a convergence problems in the minimisation procedure. Furthermore in many cases the minimisation procedure does not converge to a unique result due to the many closely spaced local minima. For these reasons we recommend interpolating from table as a function of s , rather than using parameterisations. A complete table in ASCII need only use 200Kbytes which is negligible for computer systems today. The electron scattering factors can always be calculated from the X-ray factors using the Mott formula which goes to the Rutherford scattering factor as s increases.

$$f_{el}(s) = \frac{me^2}{2h^2} \frac{(Z - f_x(s))}{s^2}$$

Due to recent developments in holography there has been much interest in the mean inner potential, which can be calculated from the X-ray scattering factors by taking a limit as s tends to zero in the Mott formula. We have calculated mean inner potentials from our values of $f_{el}(0)$, those given by Doyle and Turner, and results of calculations using the Hermann-Skillman program. There is an uncertainty for the ionised calculations of $\pm 0.4\text{V}$ due to freedom in choosing the Watson sphere radius for the O^{2-} ion. The results

are very sensitive to ionisation state as can be seen in the Table for SiO₂ and MgO, assuming neutral and ionised atoms. This implies phase shifts measurements from holography can detect fractional changes in ionicity. The changes in the other scattering factors are much less. As an example the difference between the X-ray structure factors assuming ionised and neutral atoms in MgO is 8.6% for 111, 2.6% for 311 and negligible for all others.

1. P.A. Doyle and P. Turner, Acta Cryst, (1968), A24, 390.
2. I.P. Grant, B.J. McKenzie, P.H. Norrington, D.F. Mayers, N.C. Pyper, Comput. Phys. Comm., (1980), 21,207.
3. W.H. Press,B.P. Flannery,J.A. Teulolsky,W.T. Vetterling, Numerical Recipes, (1989) (Cambridge)

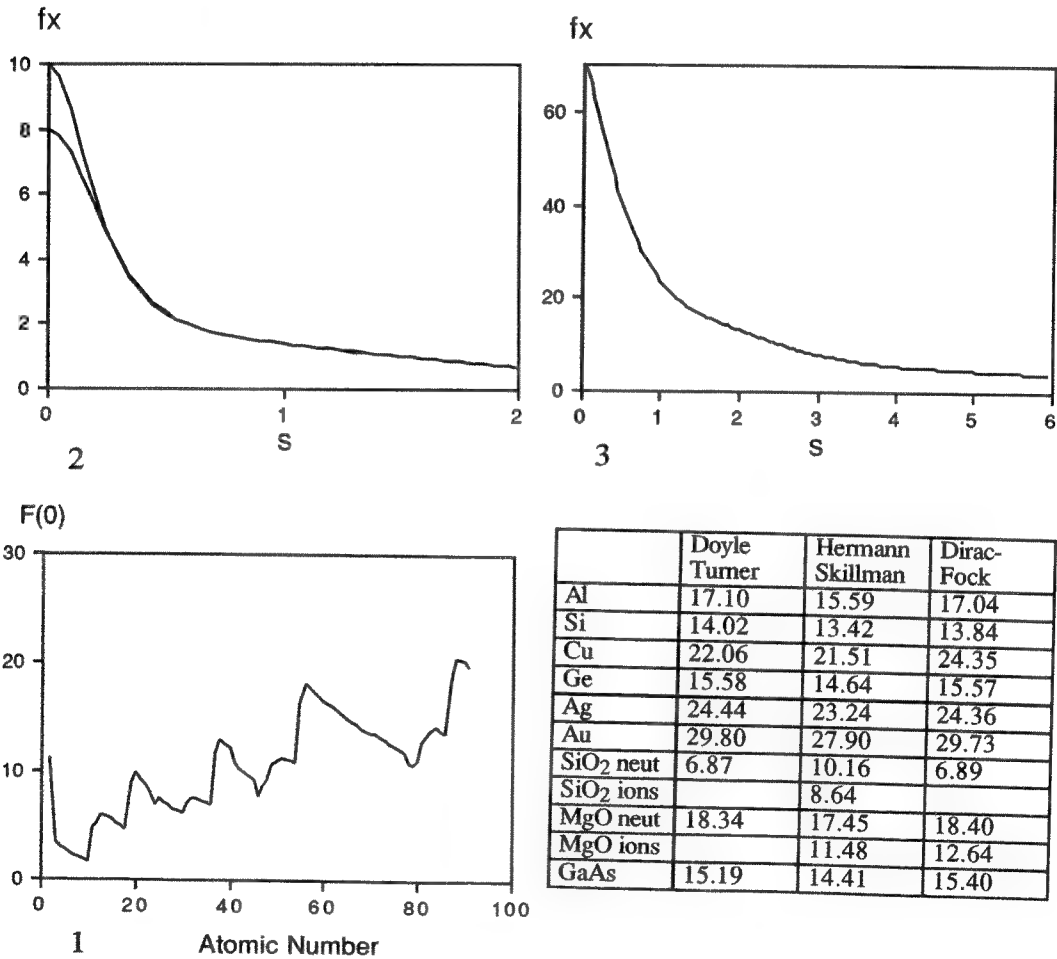


Table -- Mean inner potentials in Volts calculated using Doyle-Turner electron scattering factors, Hermann-Skillman Hartree-Slater program and the Grant et al Dirac-Fock program.
 Fig. 1. -- Variation of neutral atom electron scattering factor with atomic number.
 Fig. 2. -- Atomic X-ray scattering factor for oxygen. The higher line is for O²⁻.
 Fig. 3. -- Atomic X-ray scattering factor for Yb.

STRUCTURE DETERMINATION OF INORGANIC STRUCTURES BY HREM, CIP, AND ELECTRON DIFFRACTION

Xiaodong Zou¹, V.G. Zubkov², Gunnar Svensson³ and Sven Hovmöller¹

Structural¹ and Inorganic³ Chemistry, Stockholm University, S-106 91 Stockholm, Sweden
Russian Academy of Sciences, Institute of Solid State Chemistry, Pervomayskaya 91, 620219 Ekaterineburg, GSP-145, Russia²

High resolution electron microscopy (HREM) combined with crystallographic image processing (CIP) is becoming a powerful technique for solving inorganic structures. With the image processing systems CRISP¹ and ELD², running on a personal computer, this technique can be easily established in other laboratories. HREM images and electron diffraction patterns are digitized by a CCD camera and transferred into a PC. Phases and amplitudes are extracted from the Fourier transform of the HREM images. For thin crystals of metal oxides, the phases obtained by HREM and CIP inside the Scherzer resolution of the microscope are identical to the x-ray structure factor phases.

Electron diffraction extends to much higher resolution than EM images (beyond 1 Å). The quality of the amplitudes is also higher than that from images, since ED data is not affected by the contrast transfer function (CTF). Amplitudes extracted by ELD are close to x-ray diffraction amplitudes (within 30%).

The [001] projection of Ba₃Nb₁₆O₂₃ (space group Cmmm, a=20.930, b=12.478, c= 4.162 Å) was studied. Various HREM images, taken with a JEOL 200CX microscope, were processed.^{1,2} Not only those images^{1a} from which the structure projection can be easily seen contain correct phase information; even one image^{1b} with severe crystal tilt had correct phases. All the 31 independent reflections up to 1.9 Å resolution were equal to those calculated from the model obtained by x-ray crystallography. From the lattice averaged (p1) map very little structure information can be seen.^{3a} When the symmetry cmm is imposed, a much better map is obtained with all metal atoms appearing at their correct positions.^{3b}

Although phases were correct up to 1.9 resolution, amplitudes were damped very much for the high resolution reflections. The cmm map does not give much information beyond 2.4 Å resolution. When electron diffraction amplitudes^{2a} were used instead of those from the Fourier transform, all the metal atoms were resolved and even some oxygen atoms were visible.^{3c} The atomic co-ordinates obtained from the projected potential map were close (within 0.05 Å) to those of the structure model obtained from the x-ray powder diffraction³.

Kinematic ED amplitudes were calculated from the model refined from x-ray powder diffraction to an R-value of 5.11%.^{2c} They are close to the experimental ED amplitudes, which means ED amplitudes are not always terribly affected by multiple scattering. Thus, ED amplitudes can possibly be used even for refining atomic co-ordinates, including those of the smaller atoms such as oxygen.

References

1. S. Hovmöller, *Ultramicroscopy* (1992) **41**, 121.
2. X.D. Zou, Y. Sukharev, and S. Hovmöller, *Ultramicroscopy* (1993) **49**, in press.
3. V.G. Zubkov et al. to be published.

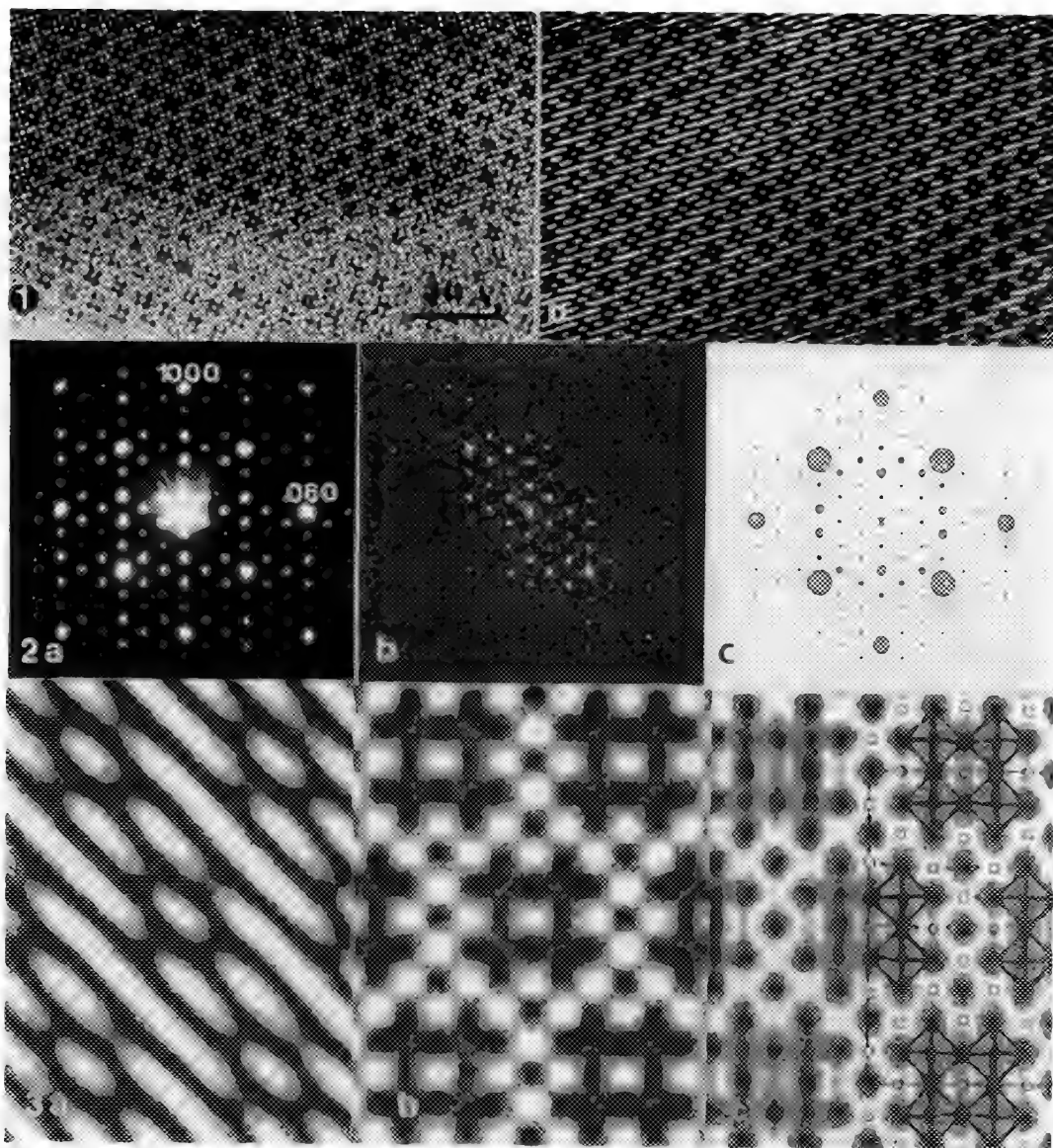


Fig 1 HREM images of $\text{Ba}_3\text{Nb}_{16}\text{O}_{23}$. a) well aligned and b) severely tilted

Fig 2 a) ED pattern of $\text{Ba}_3\text{Nb}_{16}\text{O}_{23}$ b) FT of the tilted crystal in Fig 1b c) Calculated ED pattern based on the structure model refined by X-ray diffraction.

Fig 3 a) Projected potential map of $\text{Ba}_3\text{Nb}_{16}\text{O}_{23}$. a) before and b) after imposing the cmm symmetry Phases and amplitudes from the FT (Fig 2b) of the HREM image c) Same as b, but now the amplitudes are those obtained by ELD from the ED pattern in Fig 2a The x-ray model is superimposed Dark rings correspond to Ba or Nb atoms, empty circles to oxygen atoms

ADVANTAGES OF FE-TEM FOR CONVERGENT-BEAM ELECTRON DIFFRACTION

T. Kaneyama, T. Tomita, Y. Ishida and M. Kersker*

JEOL Ltd., 1-2, Musashino 3-chome, Akishima, Tokyo, 196 JAPAN
* JEOL (U.S.A.) Inc., 11 Dearborn Road, Peabody, MA 01960

Many electron microscopes equipped with a field-emission gun (FE-TEMs) are now used for the purpose of improving the spatial and the energy resolution in energy dispersive x-ray spectroscopy and electron energy loss spectroscopy. For the convergent-beam electron diffraction techniques, FE-TEMs have greater advantages than conventional electron microscopes with a thermal LaB₆ cathode. We discussed these advantages using JEM2010F and JEM2010, which have equivalent specifications except for the electron source and the condenser lens system.

High spatial resolution

The brightness of an FE-gun ($\sim 5 \times 10^8 \text{ A cm}^{-2} \text{ sr}^{-1}$) is about 100 times that a conventional LaB₆ cathode. The gun can obtain enough current for taking CBED patterns in an exposure time of a few seconds even with an electron probe less than 1 nm in diameter (FIG. 1). Steep wedge shapes and rapid bends within the illuminated area deteriorate the accuracy of quantitative CBED analysis. Improvement of the spatial resolution by a small probe reduces these inevitable averaging effects.

High angular resolution

Lattice parameter changes or strain fields around interfaces can be determined by Higher Order Laue Zone (HOLZ) line patterns. HOLZ lines with a larger Bragg angle or at higher accelerating voltage increases the measurement accuracy. These lines are, however, hard to recognize because of the low contrast and narrow width.¹ Improvement of the angular resolution in CBED patterns by using a small electron source makes faint HOLZ lines visible (FIG. 1). This improvement is most effective in the Large Angle CBED² (LACBED) and Convergent Beam Imaging³ (CBIM) techniques.

High coherency

When a highly coherent electron probe is used, contrast due to interference appears at the overlapping region of CBED disks. If an electron probe has a smaller diameter than the lattice parameter and is defocused to illuminate a few projected unit cells, the interference is observed as parallel sets of fringes like a lattice image (FIG. 2).⁴ The positions of these fringes are connected directly to the relative phase of the projected crystal structure factor. Interference fringes of 0.27 nm lattice spacing have been obtained with an electron probe demagnified by the strongly excited condenser-objective lens system.⁵ It is expected that this technique, called Coherent CBED, will be applied to the determination of crystal structures and the study of crystal lattice defects.

References

1. P. M. Jones et al., Proc. R. Soc. Lond. A. (1977)354, 197.
2. M. Tanaka et al., J. Electron Microsc. (1980)20, 408.
3. C.J.Humphreys et al., Phil. Mag. (1989)A58, 787.
4. W. J. Vine et al., Ultramicroscopy (1992)41, 423.
5. M. Terauchi et al., Proceedings of IUCr 16 Beijing (1993).

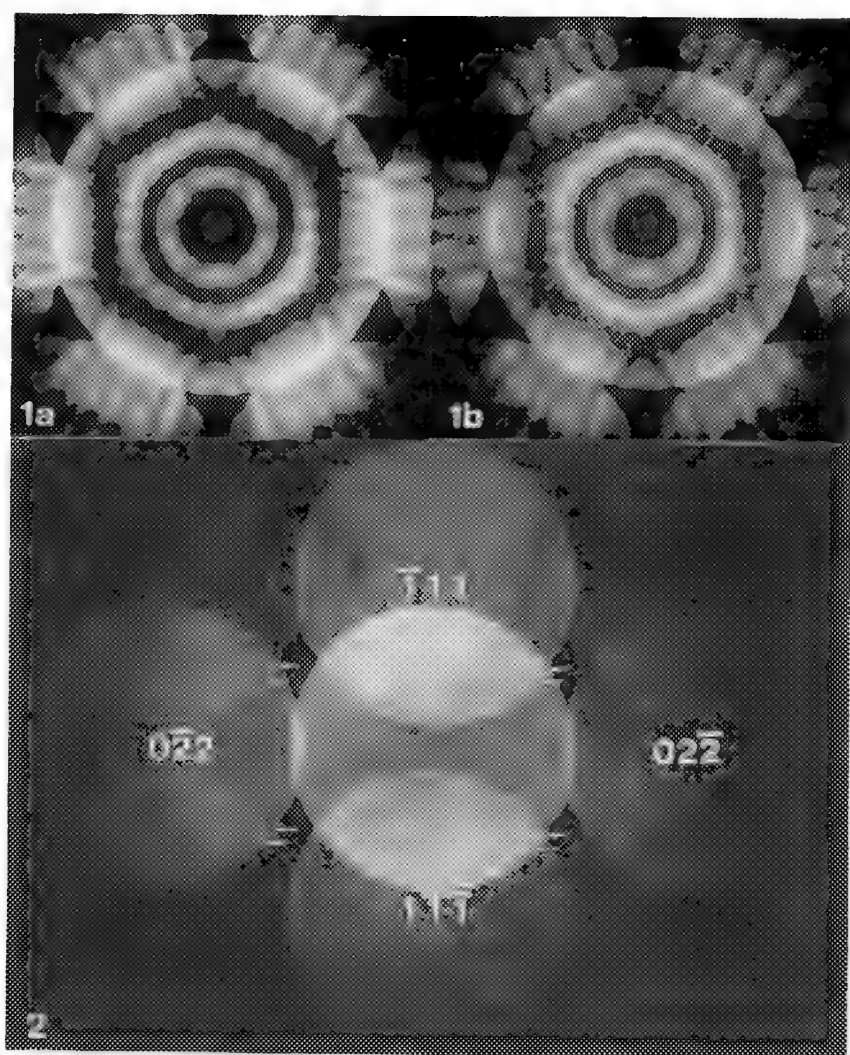


FIG. 1. CBED patterns of Si in $[111]$ incidence at 200kV, recorded with 0.5 nm diameter FEG probe and 4 sec exposure (1a), with 1 nm diameter LaB_6 probe and 60 sec exposure (1b).
 FIG. 2. Coherent CBED pattern of Si in $[211]$ incidence at 200kV. Arrowed fringes are produced by the interference of 111 systematic reflection.

QUANTITATIVE ANALYSIS OF CONVERGENT-BEAM ELECTRON DIFFRACTION PATTERNS

Xiwei Lin, Jing Zhu* and Vinayak P. Dravid

Dept. of Materials Science & Engineering, Northwestern University, Evanston, IL 60208

*Central Iron & Steel Research Institute, Beijing, P.R. China

In recent years, there have been great advances in electron crystallography by quantitative convergent beam electron diffraction (QCBED). From the distribution of dynamical diffraction intensities, QCBED can determine the Fourier components of the crystal potential accurately and completely, enabling direct measurement of phases of crystal structure factors¹. Given the combination of small probe size in CBED and the high accuracy of the quantitative analysis (e.g. determination of bonding charge distributions² in covalent crystals), QCBED is a powerful experimental methods for detection of a small change in the crystal potential of a few nanometer structure (e.g. near grain boundaries/defects).

More recently, interest has shifted towards the possibility of the automated matching of experimental and theoretical CBED patterns by optimization for speed and even higher accuracy^{3,4}. In this work, the combined variable matrix algorithm is used to automate the least-squares refinement. The program was tested by calculated intensities randomized with Gaussian distribution as experimental data. The path of optimization to the minimum is showed in Fig.1. It was found that the minimization time scales linearly with the number of variable parameters and the refinement error decreases with increasing thickness, at a thickness of about 3 extinction distance, the error is 0.1% if the intensity is in 10^5 . The program is quite reliable within a range that becomes smaller as specimen thickness increase. The range for the thickness of 3 extinction distance is about 10% of starting values.

The renormalized eigenvector method⁵ is used for calculations of dynamical intensities. For the efficiency in the refinement and the optimum choice of experimental conditions, the analytic gradients of diffraction intensity with respect to the parameters that are varied are calculated based on the differential matrix method⁶ that was developed to include the effects of all HOLZ reflections. Fig.2 is a collection of simulations of Ni_3Al (8 1 $\bar{1}$) CBED patterns and their gradient map with respect to the structure factor U_{011} . It was found that the (000) disc is more sensitive to the change of U_{011} than diffracted discs and most sensitive areas are in the intensity transition band. Fig.3 shows the intensity and the gradients varying as functions of specimen thickness. The gradients reach their maxima at the slope of intensity surge, so the optimum thickness for the refinement of structure factor would be in the range of the slope, i.e the area with quite high intensity and maximum gradients.⁷

References:

- (1) Spence, J.C.H and Zuo, J.M (1992) Electron Microdiffraction, Plenum Press, New York.
- (2) Zuo, J.M., Spence, J.C.H. and O'Keeffe (1988), Phys. Rev Lett. 61, pp. 353-356.
- (3) Zuo, J.M. and Spence, J.C.H. (1991), Ultramicroscopy, 35, pp.185-196.
- (4) Bird, D.M. and Saunders, M. (1992). Acta Cryst. A48, pp.555-562.
- (5) Zuo, J.M., Gjonnas, K. and Spence, J.C.H. (1989) J. Elect. Micro. Tech. 12, pp29-55.
- (6) Speer, S., Spence, J.C.H. and Ihrig, E. (1990). Acta Cryst. A46, pp.763-772.
- (7) This research is partially supported by NSF-DMR 9203722 & DoE DE-FG02-92ER45475.

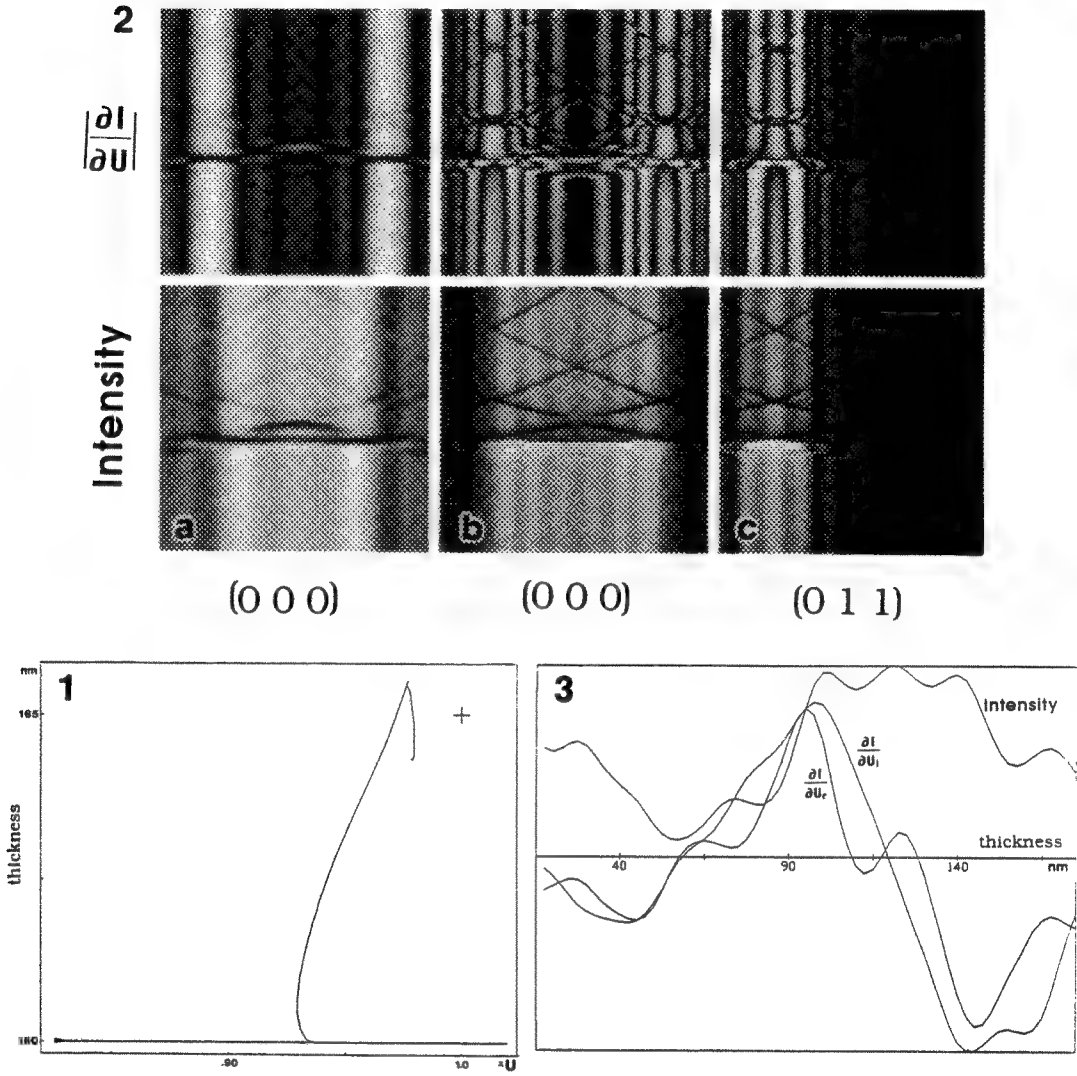


Fig.1 The path in the refinement of U_{011} and thickness, the arrow indicates the start point and the cross marks the "true" values in the intensity calculation. **Fig.2** A collection of simulations of Ni_3Al (8 1 $\bar{1}$) CBED patterns and their gradient map with respect to U_{011} at 200 kV, with thicknesses of 100 nm (a) and 300 nm (b,c) respectively. **Fig.3** The intensity and the gradients as functions of specimen thickness at a point of (0 0 0) disc.

SIMULATING ELECTRON MICROSCOPE DIFFRACTION MODE WITH A MACINTOSH-BASED PROGRAM

J. M. Zuo, H. R. Zhu* and Andrew Spence*

Dept. of Physics, Arizona State University, Tempe, AZ 85287

*16203 S. 26th Pl, Phoenix, AZ 85044

With the recent trend towards to the quantification of electron diffraction patterns, there is an increasing need for simulating the geometry of convergent beam electron diffraction patterns, and especially the high order Laue zone (HOLZ) lines in such patterns. The simulation program is useful in the way that the simulated and the experimental pattern can be compared, and then the important diffraction parameters such as reflection indices, beam directions and lattice constant could be found and used. Here we describe a Macintosh based program, which simulates electron diffraction pattern in the same way as the operation of electron microscope diffraction mode. The program has a control panel with the 'scroll bar' control devices for x and y tilt of specimen stage, x and y deflection of diffraction pattern and camera length (see figure 1). The user can change the simulated diffraction pattern by changing the 'control devices' with a pointing device such as a mouse. Thus the program can be used with the same set of controls existing on the modern electron microscope. This has the distinctive advantage over the existing programs for simulation of diffraction patterns and HOLZ lines^{1,2}. Most of these programs require the input of specific beam direction, zone axis and other parameters by the user. It is often to repeat the simulation several times before the simulated diffraction pattern can match the experimental one. Such procedure can become very time consuming. Thus it is highly desirable to have a program, which has the minimum input parameters and behave just like microscope.

The program requires an input of crystal unit cell parameters, atomic positions and composition. These parameter can either be read from a file or enter through keyboard in a data window as shown in figure 1. The program use the structure data to calculate the kinematic intensity of each reflection and scale them in the logarithmic scale. There are two separate exposure parameters to control the level of intensity to be shown in the simulate CBED pattern. One is for the elastic intensity which controls the disks and HOLZ lines, and the other is for the inelastic intensity which controls the Kikuchi lines. In this way, the usual problem of overcrowding simulated pattern with all possible lines can be avoided and more realistic looking simulated pattern can be obtained. The HOLZ lines and Kikuchi lines are simulated according to the equation ²

$$K_y = -g_x K_x / g_y + g_z K_z / g_y - g^2 / 2g_y \quad 1$$

where x,y and z denote the component of wavevector in a Cartesian microscope coordinate, which is fixed. The beam direction of the center of zero disk always travel along the negative z axis direction. The program also use a crystal coordinate (x',y',z'), which is fixed to the crystal. This crystal coordinate initially coincides the microscope coordinate for the staring zone axis. The subsequent crystal tilt will rotate the crystal coordinate away from the microscope coordinate. The relation between the crystal and the microscope coordinates for a crystal x tilt α and y tilt β is given by

$$\begin{pmatrix} x' \\ y' \\ z' \end{pmatrix} = \begin{pmatrix} \cos\beta & \sin\alpha\sin\beta & -\cos\alpha\sin\beta \\ 0 & \cos\alpha & \sin\alpha \\ \sin\beta & -\sin\alpha\cos\beta & \cos\alpha\cos\beta \end{pmatrix} \begin{pmatrix} x \\ y \\ z \end{pmatrix} \quad 2$$

For a given tilt, the program finds the closest zone axis, reflections close the Ewald sphere of center of the zero disk, and calculates positions of each reflection and HOLZ lines. The results are plotted in a separate window (see figure 1).

The possible applications of this program include: indexing diffraction patterns, beam direction measurement (texture analysis), lattice parameter measurement and teaching electron diffraction.

Reference

- 1. J. A. Eades, S. More, T. Pfullmann and Jon Hangan, Ultramicroscopy, 1992
- 2. J. C. H. Spence and J. M. Zuo, Electron Microdiffraction, 1992, Plenum Press, New York

Figure 1. Layout of program EMLab on Macintosh® desktop.

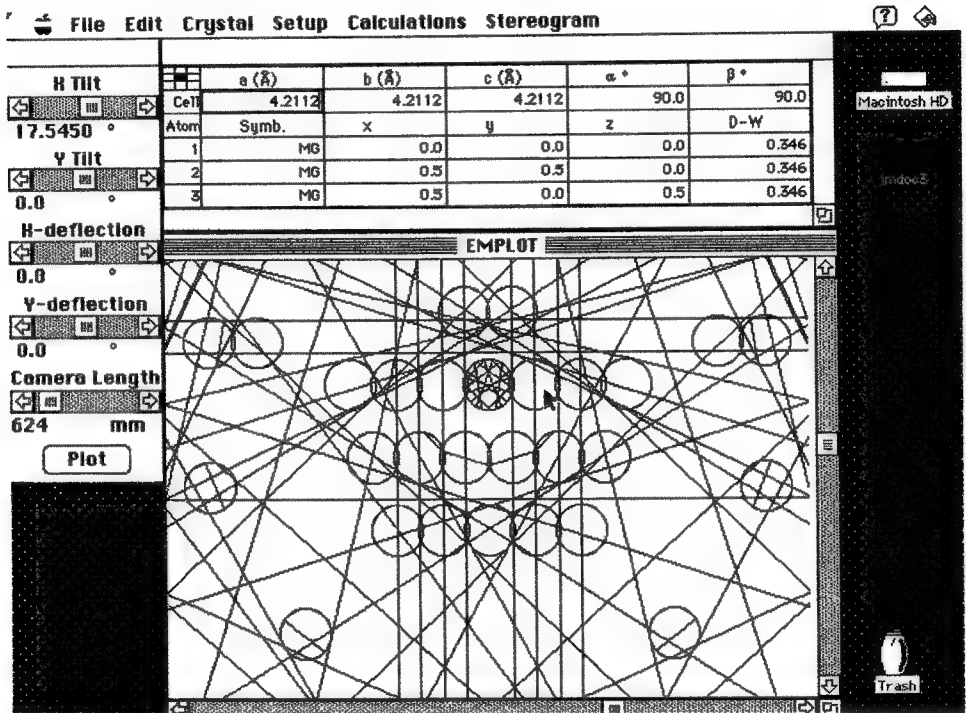
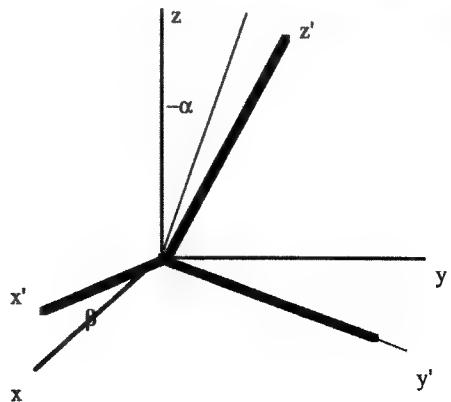


Figure 2. Relation between microscope coordinate (x,y,z) and crystal coordinate (x',y',z') for x-tilt α and y-tilt β .



COMMENTS ON THE USE OF THE RELATIVISTIC SCHRÖDINGER EQUATION IN HIGH-ENERGY ELECTRON DIFFRACTION

by Marc Op de Beeck

University of Antwerp (RUCA), Groenenborgerlaan 171, B-2020 Antwerp, Belgium

1. Introduction

In high energy electron diffraction the electrons are accelerated to a velocity which becomes comparable to the velocity of light. It is therefore obvious that in principle the Relativistic Dirac Equation (RDE) [1] should be used to describe the diffraction process. However, in 1961, Fujiwara [2,3] published his famous paper in which he derived that the transition probabilities calculated with the RDE agreed, up to a very good approximation, with these of the Schrödinger equation, provided the relativistic corrections to the values for the electron mass and wavelength are taken into account. As this Relativistic Schrödinger Equation (RSE) is much easier to handle, it became the fundament of all theoretical developments in electron microscopy and of all commercially available simulation packages.

It is our believe however that the results of Fujiwara have been misinterpreted. The correct interpretation will lead to a correction of more than 15% on the kinetic energy of the electron.

2. Theory

In order to prove the validity of the RSE, Fujiwara proved that, in the presence of a crystal potential, the transition probability between different eigenstates of the free electron Hamiltonian, agreed, up to a very good approximation with the results of the RDE. For both theories, the eigenstates for the free electron case can be written as plane waves. The relativistic description of a free electron in the RDE involves :

$$H = i\hbar \alpha \cdot \nabla + \beta m_0 c^2 = i\hbar d/dt \quad (1a)$$

$$E(k) = \pm (\hbar^2 c^2 k^2 + m_0^2 c^4)^{1/2} \quad (1b)$$

$$|k, s\rangle = u(k, s) \exp(i2\pi [k \cdot r - E(k)t/\hbar]) \quad (1c)$$

Where α en β are the well known Dirac matrices, k is the wave vector, s is the spin state and m_0 is the electron rest mass and u is the amplitude which is a four-vector quantity and takes different forms for the different eigenstates ($\pm 1/2$, spin up/down) [1]. The Fujiwara proposal for the RSE of a free electron yields :

$$H = -\hbar^2/2m \Delta \quad (2a)$$

$$E(k) = \hbar^2 k^2/2m \quad (2b)$$

$$|k, s\rangle = u \exp(i2\pi [k \cdot r - E(k)t/\hbar]) \quad (2c)$$

where the amplitude u is independent of the electron spin and the wave vector. In order to investigate the equivalence of both theories for electron diffraction, the probability is calculated for a transition between two free electron eigenstates $|k_0, s_0\rangle$ and $|k, s\rangle$ due to multiple scattering at the crystal potential $V(r)$, yielding :

$$\begin{aligned} |\langle k, s | V | k_0, s_0 \rangle|^2 &= |\delta(E_{k_0} - E_k) \sum_{n=1}^{\infty} \frac{1}{n!} \sum_{c_1} \sum_{c_2} \dots \sum_{c_{n-1}} x \\ &\times \frac{\langle k, s | V | c_1 \rangle \langle c_1 | V | c_2 \rangle \dots \langle c_{n-1} | V | k_0, s_0 \rangle}{(E_1 - E_2 + i\epsilon) \dots (E_{n-1} - E_k + i\epsilon)}|^2 \end{aligned} \quad (3)$$

where the delta function represent the energy conservation for elastic scattering between the initial and final eigenstates. The summations over the $|c_i\rangle$ involve all intermediate 'virtual' states. It should be noted

that for these virtual states no strict energy conservation is required as can be seen from the Heisenberg principle. Calculating (3) Fujiwara found, apart from a small relativistic spin correction, equivalent results for both Hamiltonians (1a,2a) which proved the validity of the RSE.

It can however easily be verified that the proposed form for the RSE cannot describe a relativistic free electron as both Hamiltonians have different energy eigenvalues. But as only energy differences are relevant in equation (3), this incompatibility can easily be solved by addition of a constant term to the Hamiltonian. The new Hamiltonian

$$H = -\hbar^2/2m \Delta + [(m^2 + m_0^2)c^2] / 2m \quad (4)$$

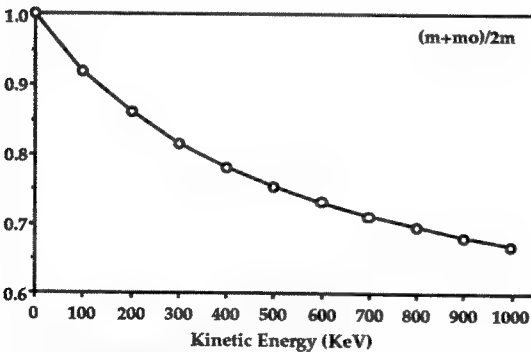
can be shown to have the same eigenvalues and -functions as the RDE, and will lead to the same transition matrix elements as the original RSE.

The addition of the constant term however implies a redefinition of the electron wave length. Currently the wave vector is calculated using " $\hbar^2 k^2 = 2mE_{kin}$ ". The new wavevector has a magnitude " $\hbar^2 k^2 = (m+m_0)E_{kin}$ " which yields the correct value for a relativistic theory. The correction factor " $(m+m_0)/2m$ " for the kinetic energy is shown in the figure below. For medium energies, a relative error of 20% is found. This implies e.g. that all simulations currently done for 400 KeV, actually are correct for an accelerating potential of 310 KeV.

Using the high energy equation [4] with k the uncorrected wave vector,

$$i4\pi (\hbar^2/2m) k_z \sqrt{(m+m_0)/2m} d\Psi(r)/dz = -(\hbar^2/2m) \Delta_r \Psi(r) + V(r) \Psi(r) \quad (5)$$

the influence of this error on image calculations can be evaluated more easily. If the projection approximation for the potential is used, the correction on the kinetic energy can equally be described by a scaling of the thickness parameter of the crystal. As the thickness of the crystal is virtually unknown, no basic interpretation errors are made. However, as soon as Higher Order Laue Zones are relevant (e.g. in CBED), the scaling of the kinetic energy should really be accounted for. As far as the imaging part is concerned, this scaling will also imply a redefinition of the spherical aberration coefficient and the defocus calibration due to their coupling with the wave-length. It is our believe however that, in the past, these coupled parameters ($C_s \lambda^3$ and $\Delta f \lambda$) have been determined consistently so that no errors are introduced in this part of the image simulation.



3. Acknowledgment.

The author is indebted to the Belgian I.W.O.N.L. for financial support.

4. References.

- [1] Sakurai, "Advanced Quantum Mechanics", publ. Addison-Wesley Publishing Company (1967)
- [2] Fujiwara, J. Phys. Soc. of Japan, Vol. 14, No 11, pp 1513-1524 (1959)
- [3] Fujiwara, J. Phys. Soc. of Japan, Vol. 16, No 11, pp 2226-2238 (1961)
- [4] e.g. Van Dyck, Advances in Electronics and Electron Physics, Vol. 65, pp. 295-355. (1985)

A PARAMETRIZATION OF INELASTIC SCATTERING FACTORS FOR HIGH-ENERGY ELECTRON DIFFRACTION

D. J. Seale and S. S. Sheinin

Department of Physics, University of Alberta, Edmonton, Alberta, Canada T6G 2J1

Theoretical images of model structures play a vital role in the analysis of both diffraction and phase contrast electron microscope images. In the theoretical calculations required to produce these images it is important to take absorption, due to inelastic scattering, into account. This is done by including an imaginary part in the Fourier coefficients of the lattice potential, V' . These coefficients have been presented in a variety of ways. Radi¹ has calculated the absorptive potentials for a number of crystals. He found that the most important contribution to these potentials is due to thermal diffuse scattering (TDS), except for the V'_0 term, which does not affect image contrast. The Einstein model, in which all atoms are assumed to vibrate independently of one another, is normally used in calculating the contribution of TDS to the absorption process. This approximation allows one to calculate the absorption potential as a sum of contributions due to the different atoms in the crystal.

Bird and King² have calculated the contribution of TDS to the inelastic scattering factors for all neutral atoms with atomic number less than 99. These factors allow the imaginary part of the Fourier coefficients to be calculated for any crystal, regardless of its complexity. However, since the scattering factors depend on the Debye parameter, $B = 8\pi^2 \langle u^2 \rangle$, these values are difficult to parametrize in the usual way. Instead, Bird and King calculated the values for each atom at ten different values of the scattering vector, s , and six different values of B . They then provided a subroutine to interpolate between these values for other values of s and B . Weickenmeier and Kohl³ have derived a formula for the calculation of the form factors for any value of B or s , which is based on a parametrization of elastic scattering factors. However, this formula is very complicated and is not easily incorporated into the computer programs used to calculate image contrast. It is the purpose of this paper to present a simple parametrization of the data given by Bird and King which allows the inelastic scattering factors to be calculated simply, and with a minimum of data. Also, the parametrization has been applied to a number of ions, which were constituents of the compound crystals covered by Radi.

In order to keep the parametrization as simple as possible, only one exponential term was used to represent the variation of inelastic scattering factor with s for a given atom and Debye parameter:

$$f'(s, B) = A(B) \exp [b(B) s^n(B)] \quad (1)$$

The three values, A , b and n , were then fit to the following set of formulas to give their variation with B :

$$\begin{aligned} A(B) &= A_A (B + b_A)^{n_A} + C_A \\ b(B) &= A_b B^{n_b} + C_b \\ n(B) &= A_n \exp (b_n \sqrt{B}) + C_n \end{aligned} \quad (2)$$

Therefore, there is a total of 10 parameters required for each atom. These parameters will be given in a paper by the authors⁴ for all 98 neutral atoms covered by Bird and King and also for all ions covered by Radi. It should be noted that the Debye-Waller factor is included in (1).

Figure 1 shows the agreement obtained between the neutral atom data calculated by Bird and King and the values given by (1) using the parameters given in reference 4. It should be noted that only values actually calculated by Bird and King are shown, i.e. interpolated values obtained by using their subroutine were not used. Fig. 1a shows the data for 5 different atoms with atomic numbers ranging from 10 to 40. In Fig. 1b, the data shown is for one atomic species but for three Debye parameters, 0.15, 0.7, and 2.0. Figures 2a,b show a comparison of the values obtained from (1) with the absorption potentials given by Radi for KF and KCl respectively. The two crystals have different Debye

parameters, 1.08 and 1.93 respectively. The upper and lower curves represent the reflections with all even and all odd indices, respectively. In each case, the two curves were fit as accurately as possible. The average of the two curves then gave the data for K, while the average difference between the curves provided the data for the anions. The continuous line represents the values given by the parametrization for the ions involved using (1).

In conclusion, the results shown in figs. 1 and 2 demonstrate that the parametrization method presented in this paper gives excellent agreement with previously published data.^{1,2} In the case of ionic crystals, the agreement is not quite as good as for crystals consisting of neutral atoms, but is still considerably better than that which can be achieved by using neutral atom data to describe ionic crystals.⁵

References

1. G. Radi, Acta Cryst. (1970)A26, 41.
2. D. M. Bird and Q. A. King, Acta Cryst. (1990)A46, 202.
3. A. Weickenmeier and H. Kohl, Acta. Cryst. (1991)A47, 590.
4. D. J. Seale and S. S. Sheinin, to be published.
5. This research was funded by the Natural Sciences and Engineering Research Council of Canada.

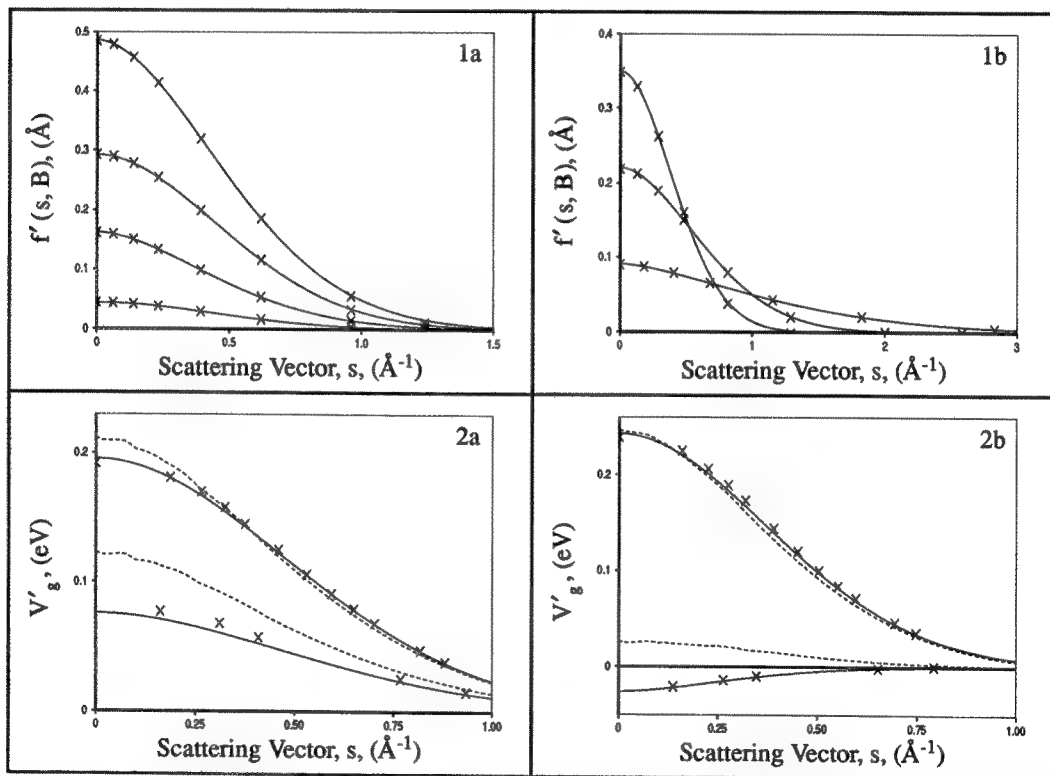


Fig. 1. -- Neutral atom absorptive form factors from Bird and King² (x's) and values calculated from parametrization (continuous line). (a) Atoms ranging in atomic number from 10 to 30 for a Debye parameter of $B = 1.3$. (b) Debye parameters of 0.15, 0.7 and 2.0 for Zn ($Z = 30$).

Fig. 2. -- Imaginary part of Fourier coefficient for ionic crystals with different Debye parameters. X's are calculated values are from Radi¹, continuous line is from the parametrization of ion data using (1), and dashed line is from neutral atom values of Bird and King². (a) KF ($B = 1.08$), (b) KCl ($B = 1.93$).

A PSEUDO THREEFOLD HELICAL STRUCTURE FOUND IN SILK LANGMUIR-BLODGETT FILMS BY ELECTRON DIFFRACTION

Weiping Zhang*, Samuel P. Gido*, Wayne S. Muller**, Stephen A. Fossey** and David L. Kaplan**

*Department of Polymer Science and Engineering, University of Massachusetts, Amherst, MA 01003

**Biotechnology Division, US Army Research, Development & Engineering Center, Natick, MA 01760

The high performance tensile properties of silkworm (*Bombyx mori*) silk fiber has resulted in a long standing interest in the semicrystalline morphology of this material. The properties of silk fiber depend not only on the chemical composition (primary protein structure) but also on the fiber spinning conditions present in the silk gland which induce the formation of a β -sheet based crystalline morphology (secondary protein structure). Knowledge of the silk structure is essential for understanding how the natural spinning processes results in such excellent material properties, but surprisingly few experimental results are available concerning the detailed structures of silk proteins. Two β -sheet based silk fibroin crystalline structures (e.g. silk I ¹ and silk II ²) have been studied by many authors, but the silk I structure remains largely uncharacterized. Here we report results from thin silk films prepared by the Langmuir-Blodgett (LB) technique which display a new silk fibroin structure with a threefold helical chain conformation.

The preparation of silk LB films for TEM observation is described in detail elsewhere ³. Silk fibroin obtained from dried silk fiber was solubilized in aqueous solution by LiBr salts. Once the silk was in solution the LiBr was removed by dialysis and the solubilized silk was spread on the surface of a LB trough with a water subphase. The aqueous subphase in the trough had a neutral pH and a temperature of 10°C. For TEM observation, the silk film was collected by dipping nickel T1000 grids at a surface pressure of 16.7 mN/m. The grids were dipped only once to give single layer films which were studied by SAED at 200 KeV using a JEOL JEM-2000FX TEM.

Although our silk films were produced by the LB technique there is evidence for crystallite rather than monolayer formation. Atomic force microscopy ⁴ indicates hard crystallite regions in the LB films with length scales on the order of 20 to 40 nm. Thus we suspect that small crystallites form on the water surface in the trough. This conclusion is supported by electron diffraction observation of the films which indicates a polycrystalline structure. Two typical SAED patterns are shown in Fig. 1 and 2. The very small thickness of the film, light atoms involved and the electron beam sensitivity of the proteins result in a strong transmission spot and weak reflections in the diffraction patterns. Thus multiple exposures were used in printing both figures to make the interesting reflections easily visible. The six inner reflections in Fig. 1 appear to have a three or six fold symmetry with a lattice parameter of 4.17 Å, from which $a = 4.82$ Å can be derived. Fig. 2 is a pattern produced by many small crystallites with different orientations. The marked inner and outer rings correspond to lattice spacings of 3.14 and 1.57 Å, respectively. This LB silk structure does not match reported d-spacings and symmetries for β -sheet structures like silk I or the orthorhombic silk II.

A trigonal structure of polyglycine II with unit cell parameters of $a = 4.8$ Å and $c = 9.3$ Å and a space group of P3₁ has been reported ^{5,6}. In this structure, all the polypeptide chains are parallel and each one has a threefold screw axis (3₁ helical chain conformation). Three amino acid residues are contained within each turn of this helix. The helical chains are packed in a hexagonal array, each chain being hydrogen-bonded to each of its six neighbors. Resulting from the threefold screw, for 00 l reflections, only those with $l = 3$ can appear in diffraction patterns, e.g. 003 (3.1 Å) and 006 (1.55 Å) reflections. Comparing our LB silk diffraction patterns with the polyglycine II data, the marked rings in Fig. 2 can be indexed as {003} and {006}. Our diffraction patterns closely match the published polyglycine II spacings and intensity features. Thus, a trigonal unit cell with $a = 4.82$ and $c = 9.42$ Å for a helical silk

structure can be established. The close lattice spacing correspondence between the helical silk and the polyglycine II indicates that the silk helices also contain three residues per turn. However, these residues can be Gly, Ala or Ser. Apparently, the small volume differences between Gly, Ala and Ser do not disrupt the general 3_1 structural motif or significantly perturb lattice spacings. However, larger residues such as Tyr and Leu, which are also present in the silk fibroin protein, would not be able to fit into the helical structure or the unit cell. This is consistent with previous investigations of β -sheet based structures in which these larger amino acids were also suspected to only occur in the non-crystalline regions. We refer to the new silk structure as a pseudo helix for the following reason: The repeat sequence of the crystallizable portions of the silk fibroin ⁷ chain is $(\text{Gly-X})_n$ where X can be either Ala or Ser, a true screw structure like polyglycine II requires all the amino acid residues in the helix to be identical.

Using electron diffraction we have discovered that a new pseudo helical silk structure is induced by aqueous LB processing.

References

1. O. Kratky, E. Schauenstein and A. Sekora, *Nature* (1950)165, 319.
2. R.E. Marsh, R.B. Corey and L. Pauling, *Biochim. Biophys. Acta* (1955), 16, 1.
3. W.S. Muller, L.A. Samuelson, S.A. Fossey and D.L. Kaplan, submitted to *Langmuir*.
4. S. P. Gido *et al.* Unpublished data.
5. F.H.C. Crick and A. Rich, *Nature* (1955)176, 780.
6. F.J. Padden, Jr., and H.D. Keith, *J. Appl. Phys.* (1965)36, 2987.
7. D.J. Strydom, T. Haylett and R.H. Stead, *Biochem. Biophys. Res. Comm.* (1977)79, 932.

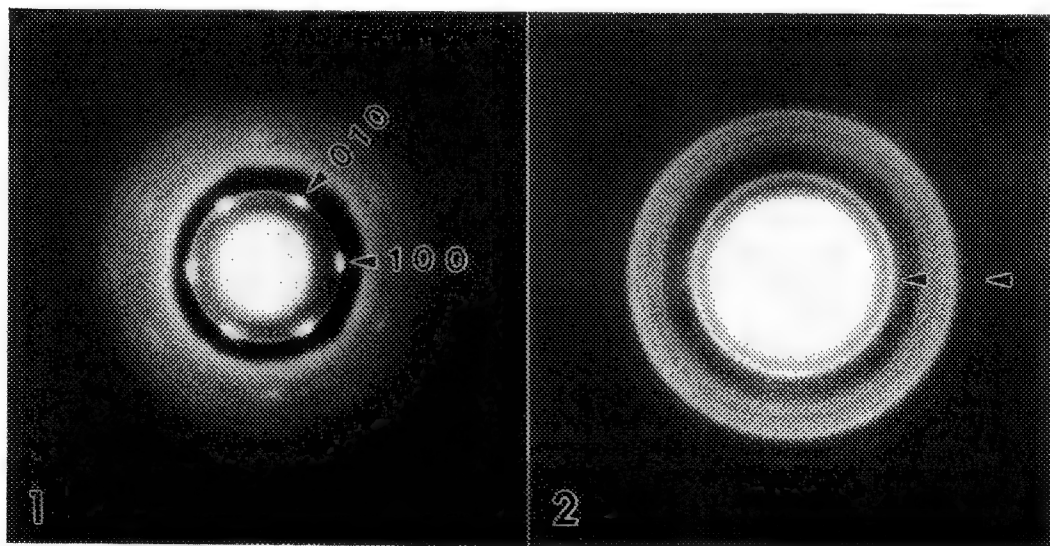


Fig. 1 SAED pattern of the silk film along the $[001]$ direction of a threefold screw structure.
 Fig.2 SAED pattern of many small crystallites with different orientations in the silk film. The marked rings are the $\{003\}$ and $\{006\}$ reflections of the threefold screw structure.

ELECTRON MICROSCOPY AND DIFFRACTION OF CRYSTALLINE DENDRIMERS AND MACROCYCLES

C. J. Buchko, P. M. Wilson, Z. Xu, J. Zhang, S. Lee, J. S. Moore, and D. C. Martin

Departments of Materials Science and Engineering, Chemistry, and the Macromolecular Science and Engineering Center,
The University of Michigan, Ann Arbor, MI 48109-2136

The synthesis of well-defined organic molecules with unique geometries opens new opportunities for understanding and controlling the organization of condensed matter. Here, we study dendrimers and macrocycles which are synthesized from rigid phenyl-acetylene spacer units [1]. Both units are solubilized by the presence of tertiary butyl groups located at the periphery of the molecule. These hydrocarbon materials form crystalline and liquid crystalline phases which have been studied by differential scanning calorimetry, hot stage optical microscopy, and wide-angle x-ray scattering (WAXS).

The precisely defined architecture of these molecules makes it possible to investigate systematic variations in chemical architecture on the nature of microstructural organization. Here we report on the transmission electron microscopy (TEM), selected area electron diffraction (SAED), and high resolution electron microscopy (HREM) studies of crystalline thin films formed by deposition of these materials onto carbon substrates from dilute solution. Electron microscopy is very attractive for gaining structural information on new molecules due to the scarcity of material to grow single crystals suitable for conventional crystallography. For this work we used a JEOL 4000 EX operating at 400 kV and a Philips EM420 operating at 120 kV. Since the molecules are sensitive to electron beam damage, novel low dose techniques were used to dynamically capture images and diffraction patterns with a YAG crystal, image intensifier, and video camera [2].

Samples have characteristic spacings that change with arm generation (dendrimers) and substitution on the ring (macrocycles), showing systematic variations in crystal packing. WAXS indicates that the disorder of PAM (phenyl-acetylene macrocycle) and PAD (phenyl-acetylene dendrimer) increases with larger group substitution on the ring and higher arm generations, respectively. This is confirmed by SAED. Total end point dose (TEPD) [3] of the PAM series ranges from 4.5×10^{-2} C/cm² to 8.6×10^{-3} C/cm². PAD-4 and PAD-10 have TEPDs of 1.3×10^{-2} C/cm² and 1.2×10^{-3} C/cm², respectively. TEPD increases as a function of crystallinity, and therefore decreases with generation and size of the molecule.

High resolution micrographs display conspicuous defects, such as edge dislocations and grain boundaries, and the lattice lines assume curved configurations. The SAED patterns show broadening of the peaks and increased crystal misorientation with increasing side group length. As the size increases, the number of conformations available to the molecule also increases, making it more difficult to pack the molecules with fewer defects.

Figure 1 shows a SAED of the base PAM, with an inset of the molecular schematic. Spacings are 0.38 and 1.09 nm. These molecules have a cyclic structure of benzene rings connected by acetylene spacers. The 0.38 spacing corresponds to the face to face packing of the molecules. This has been determined by scanning tunneling microscopy (STM) of the crystal surface and molecular modeling.

Figure 2 shows the SAED of the base PAD-4, and an inset of the molecule [1]. Spacings are 0.64 and 2.05 nm. Current work includes matching WAXS, SAXS, and SAED data with molecular modeling using Polygraf™ and Cerius™ [4] to determine a possible crystal structure.

Figure 3 is a TEM micrograph of PAM-ET, with a schematic inset of the molecule. This crystal exhibits the characteristic symmetry of the molecule.

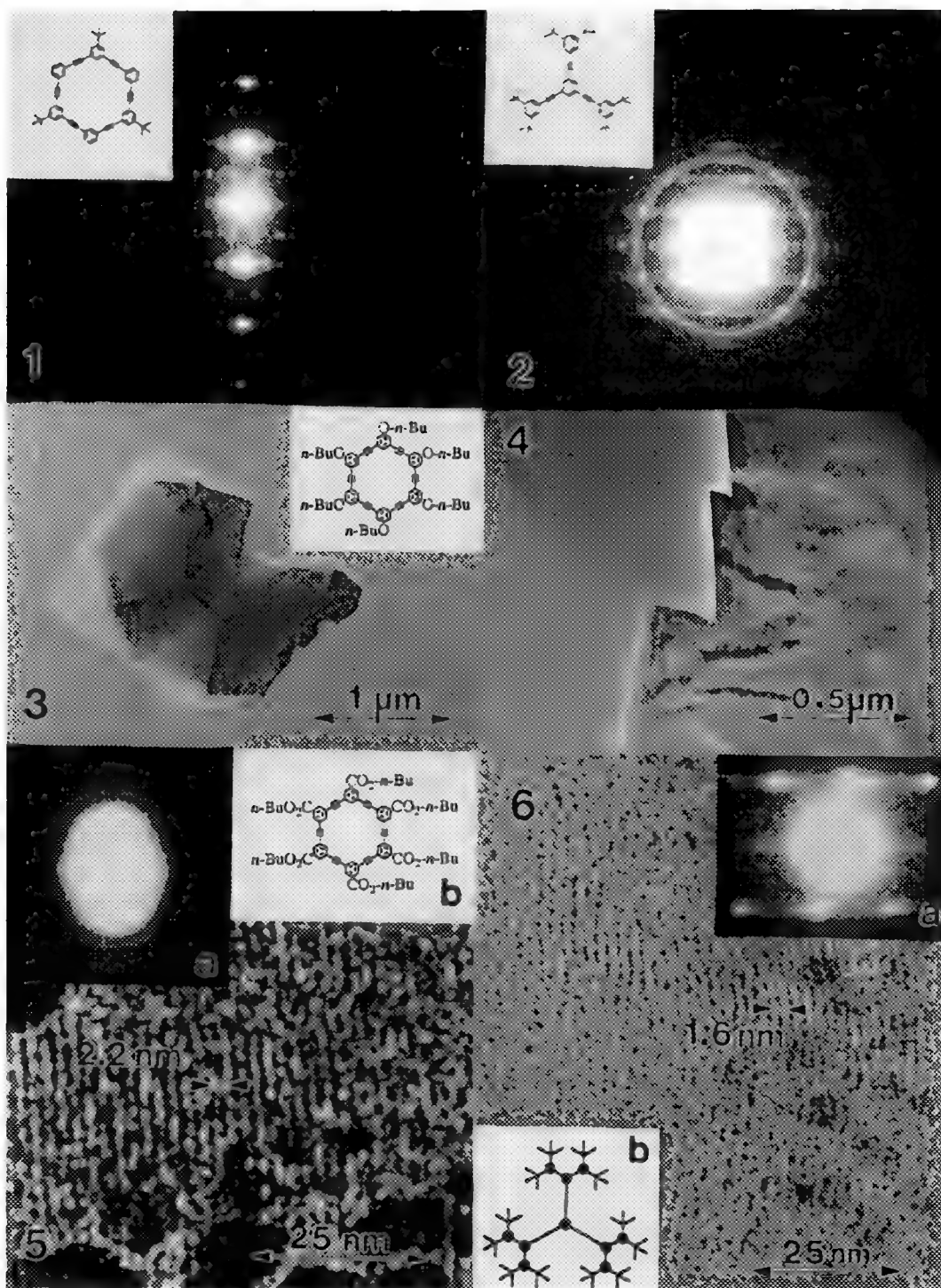
Figure 4 is a TEM micrograph of the base PAD. The 0.64 nm spacing is in the long direction of the crystal, which is consistent with molecular modeling of layers of tilted stacks of PAD-4. Aspect ratios of 40:1 have been observed.

Figure 5 is a HREM image of PAM-B, revealing 2.2 ± 0.2 nm fringes which correspond to the side to side packing of stacks of PAM-B molecules. The SAED in inset A shows the misorientation of crystallite that are present in the HREM images. Inset B is a molecular schematic of PAM-B.

Figure 6 is a HREM image of PAD-10, the first generation dendrimer. Lattice fringes of 1.6 ± 0.2 nm are labeled. Note the curvature of the fringes. Inset A is the corresponding SAED, with layer line spacing of ~ 0.62 nm, and inset B is a diagram of the molecule using a shorthand notation.

References

1. Z. Xu, PhD. Dissertation, University of Michigan, 1992
2. J. Liao and D. C. Martin, Science (in press)
3. D. C. Martin, P. M. Wilson, J. Liao, Polymer Preprints, 1992
4. Molecular Simulations Inc., Burlington, MA., 1993



IMPROVEMENT OF AMPLITUDE-DIVIDED ELECTRON HOLOGRAPHY

Q. Ru, J. Endo and A. Tonomura

Electron Wavefront Project, JRDC, P.O. Box 5, Hatoyama, Saitama 350-03, JAPAN

Compared with the wavefront-divided electron holography obtained by an electron biprism,¹⁻² the amplitude-divided one proposed by Matteucci *et al.*³ has some essential advantages: less necessary coherency, wide interference area and available to most of transmission electron microscopes. In order to confirm and achieve these advantages in practical use, we introduce some improvements in both hologram formation and reconstruction steps. Two electron-optical setups and experimental results are presented for small objects ($<1\ \mu\text{m}$) and much large objects ($>1\ \mu\text{m}$), respectively.

The electron-optics for taking the holograms of small objects is illustrated in Figure 1. A single crystal thin film (gold film of 0.2nm lattice spacing is used in our experiment) is placed on the objects (latex particles of 120 nm on a thin carbon film are used here) with a certain gap. In fact, the gap is spontaneously made by the microgrids of the specimen film and the crystal film. The lenses are adjusted to image the crystal film, so that two images of the object carried by the 0-order and 1-order diffraction beams are formed separately in different positions. The two beams are selected by the objective aperture, and form a curved lattice fringe pattern, i.e. off-axis electron hologram in the screen. Because the object is largely defocused and the hologram consists of as many as about 2000 lattice fringes, we use at first an optical reconstruction system to correct the defocusing and reduce the carrier fringes, and then use the digital method⁴ to separate the amplitude and phase distributions from the optically reconstructed in-focus image. Furthermore, a null-hologram (without object) under the same lens condition is also recorded and reconstructed for eliminating the system errors due to the electron and optical lens aberrations. The experimental results obtained from an HF-2000 transmission electron microscope are shown in Figures 2-3.

An equivalent electron-optics for observing much large objects has early been proposed by Matteucci *et al.*. In this case, the object is placed on the select-area-aperture plane. Because the lattice fringes are enlarged nearly 100 times in this object plane, 2000 fringes of 0.2nm gold lattice can cover as wide area as 20 μm of the object plane. Such wide interference area has never been achieved by an electron biprism system. In their paper, however, the defocusing was so small that the images carried by the 0-order and 1-order beams overlapped together and that the in-focus image could not be reconstructed. Here we introduce a large gap between the object plane and the crystal image plane under the objective lens to separate these twin images, and then correct the defocusing in optical reconstruction step. In our experiment, a 10 μm long fiber-glass tip charged externally, is hung up a conducting wire and placed in the select-area-aperture plane of the microscope. Therefore, the electrical field distribution around the charged tip can be observed from the reconstructed contour phase map, as shown in Figure 4.

Since the amplitude-divided method does not require high coherency, bright holograms can be recorded. All of our holograms were exposed within 5 seconds on Kodak-4489 photographic films. High contrast fringes can also be observed in real time through a TV camera.

References

1. G.Mollenstedt and H.Duker, Z. Physik 145(1956)377.
2. A.Tonomura, Rev. Mod. Phys. 59(1987)637.
3. G.Matteucci *et al.*, Ultramicroscopy 6(1981)109.
4. M.Takeda and Q.Ru, Appl. Opt. 24(1985)3068.

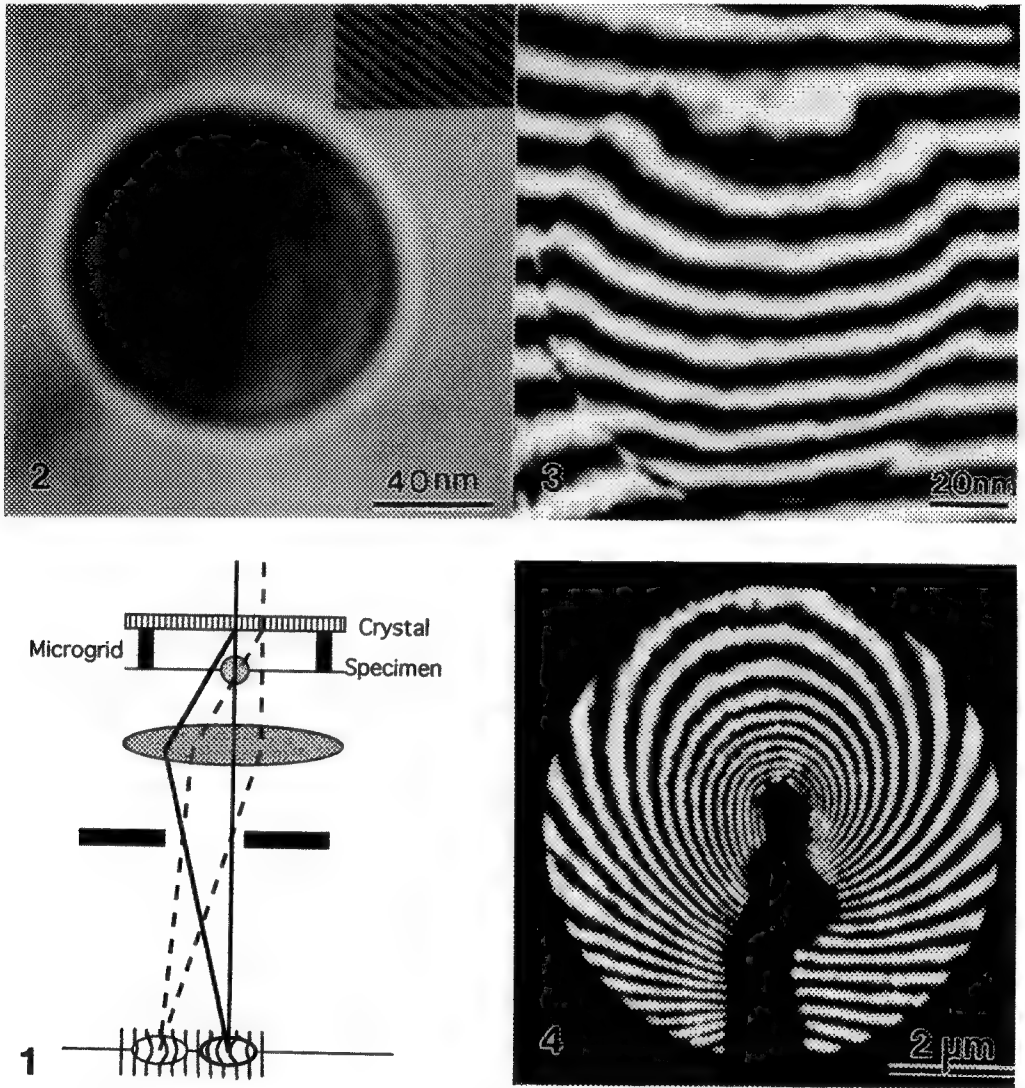


Fig.1. Electron-optical setup of amplitude-divided electron holography by using single crystal as beam splitter. Intermediate lenses are omitted from figure.

Fig.2. Hologram of defocused latex particle. Part of enlarged fringes is shown in top-right region.

Fig.3. Reconstructed contour phase map of latex particle.

Fig.4. Reconstructed contour phase map around top of charged tip.

A HIGH-RESOLUTION FRAUNHOFER IN-LINE ELECTRON HOLOGRAPHY

Takao Matsumoto, Takayoshi Tanji, and Akira Tonomura

Tonomura Electron Wavefront Project, ERATO, JRDC
P.O. Box 5, Hatoyama, Saitama 350-03, Japan

In-line holography is advantageous in terms of contrast in imaging weak phase objects.¹ However, most of the recent articles on electron holography² had an off-axis configuration employing an electron biprism and were applied successfully only to objects with a rather strong phase shift such as magnetic flux and thin crystals. When it comes to the observation of considerably weak phase object, the off-axis method fails. We applied Fraunhofer in-line electron holography to observe an undecagold cluster³, the core of which has a diameter of 0.82 nm, and obtained a high resolution image with high contrast that has been obtained neither by off-axis electron holography nor by conventional transmission electron microscopy.

A Hitachi HF-2000 electron microscope equipped with a 200-kV cold field emission gun was used during the experiment. The specimen, Monoamino-Undecagold (NanoProbes, Inc., Stony Brook, N.Y.), was prepared in a highly dispersive form on a thin carbon film supported by a thick holey carbon film. We recorded holograms in a Fraunhofer condition to reduce the so called twin image problem.⁴ Holograms recorded with the electron microscope were photographically reversed to amplify the low contrast in the originals. The reversing process enhances the contrast of the hologram and hence the reconstructed phase. Holograms were reconstructed numerically using our image processing facilities based on the Apollo DN10000.

The Fraunhofer in-line holograms (Fig. 1a, 1b) show the interference fringes between the weak scattering wave and the strong background wave, though undecagold was not recognized in a focused electron micrograph. The hexagonal shape in the interference fringes is apparent even in Fig. 1a, and it is more evident in a far Fraunhofer hologram shown in Fig. 1b. The reconstructed phase (Fig. 2) shows that there are two isolated, a twin, and an array of molecules within a field. The contrast of the interference fringes from one and two molecules is weak, especially in the original holograms, but these molecules are nevertheless reconstructed as isolated molecules with high contrast. One of the benefits of electron holography is the possibility to build images at any desired electron optical conditions from the reconstructed phase. An example is shown in Fig. 3. A defocused image of undecagold (defocusing is about 1 μ m) shows a hexagonal projection with a diameter of about 2 nm, as suggested by the hexagonal interference fringes in holograms. The structure of undecagold is described by a centred icosahedron from which a hexagonal or a pentagonal perspective view is possible.⁵ A pentagonal projection was observed in a high-resolution STEM image.⁶

A high-resolution Fraunhofer in-line electron holography was employed to directly visualize the isolated undecagold cluster. The high contrast and high resolution of the method is especially useful for the observation of isolated weak phase objects such as isolated biological molecules.

References

1. J. Munch, *Optik* (1975)**43**, 79.
2. A. Tonomura, *Rev. Mod. Phys.* (1987)**59**, 639.
3. P.A. Bartlett, *et al.*, *J. Am. Chem. Soc.* (1978)**100**, 5085.
4. B.J. Thompson, *et al.*, *Appl. Opt.* (1967)**6**, 519.
5. P. Bellon, *et al.*, *J. Chem. Soc., Dalton Trans.* (1972)1481.
6. A.V. Crewe, in: *Proc. 9th International Congress on Electron Microscopy*, 1978: Vol. 3, p.197.

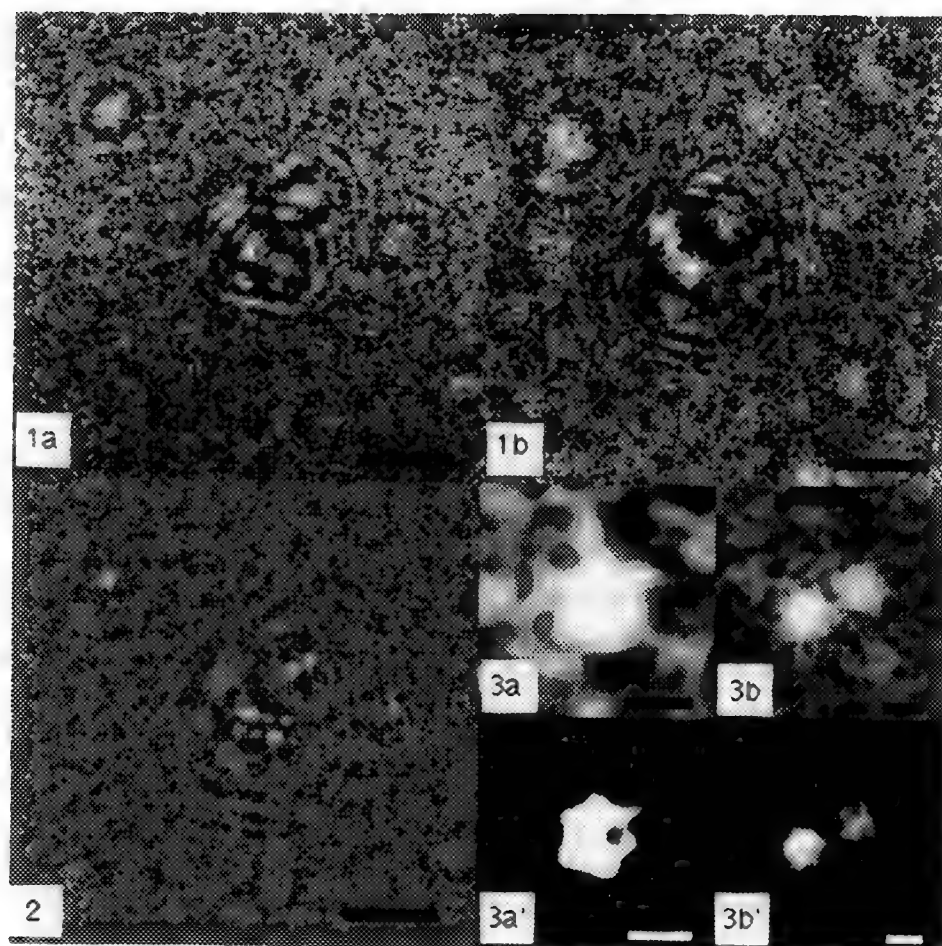


FIG. 1: Fraunhofer in-line electron holograms of undecagold. Defocusings were estimated as $13.6\ \mu\text{m}$ for 1a and $30.0\ \mu\text{m}$ for 1b, respectively. Bars represent 20 nm.

FIG. 2: Reconstructed phase from an in-line hologram, as shown in Fig. 1a. An array of several clusters and isolated clusters were reconstructed. Most of the bright spots are of the same size except a few in the array at the center of the field. These are aggregates of two clusters. Bar represents 20 nm.

FIG. 3: Defocused (about $1\ \mu\text{m}$) images built from the reconstructed phase (3a and 3b). In 3a' and 3b', cut-off levels are adjusted to make the hexagonal projection clear. The isolated molecule at the top left in Fig. 2 corresponds to 3a and 3a', while 3b and 3b' correspond to the twin molecules near the center. Hexagonal projections with 2 nm diameter can be seen, that are related to the centred icosahedral structure of undecagold. Hexagonal projections are also suggested by the hexagonal interference fringes shown in Fig. 1b. All bars represent 2 nm.

THE EFFECT OF CORE SIZE ON THE HOLOGRAPHIC INTERFERENCE IMAGES OF SUPERCONDUCTING FLUXONS IN TILTED SPECIMENS

G. Pozzi, J.E. Bonevich* and A. Tonomura*

Department of Materials Science, University of Lecce, via Arnesano, 73100 Lecce, Italia

*Advanced Research Laboratory, Hitachi Ltd., Hatoyama, Saitama 350-03, Japan

Recently, observations of quantized flux lines in thin superconducting specimens have been successfully carried out in transmission electron microscopy by means of standard methods of Lorentz microscopy¹ and also by electron holography.² The breakthrough with respect to the previous unsuccessful attempts is represented by the fact that the specimen is observed tilted with respect both to the electron beam and the ancillary magnetic field that is used to introduce and stabilize the fluxons in the specimen.

Although a reduction of the phase difference with respect to the optimum situation of fluxons perpendicular to the beam is expected in this set-up, it has nonetheless been possible to ascertain by means of a simple model that this reduction is not below the detectability limit that can be reached by the most advanced phase sensitive methods available today in electron optics, such as electron holography. However calculations have been carried out so far either for the single fluxon case, taking into account also its core structure,³ or for an array of 25 flux tubes (i.e. fluxons with negligible core size) arranged in a triangular lattice.⁴

The aim of this work is to extend the above calculations to the case of an array of fluxons having a finite core size described by the London model, and to show how the phase difference and its overall topography depend on the ratio of the specimen thickness to the London penetration depth L , which is directly related to the core size.

Owing to computing time, we have considered the case of an array of 9 fluxons arranged in a regular triangular lattice of side $0.5 \mu\text{m}$, distorted in order to account for the specimen tilt of 45° . Calculations have been done for a constant specimen thickness of 120 nm and for two values of L , 30 and 60 nm.

The results of the calculations are presented in the form of n -times amplified contour density maps, that, in addition to presenting vividly the information on the phase difference values and topography, have the advantage that they can be directly compared with those obtainable by means of holographic phase amplification techniques.

Fig.1 (a) reports the expected contour level map ($n=8$) for the central part of the triangular fluxon lattice for the case of negligible core size, whereas (b) and (c) have been calculated for the finite core size, corresponding to L equal to 30 and 60 nm respectively. It can be seen that the fringes become narrower in the proximity of the cores and wider in the regions between them but apart from the flux tube case (a), no relevant differences are present between the different patterns.

In order to emphasize the differences due to the finite core size, it has been found convenient to subtract a linear phase, corresponding to the constant deflection due to the mean magnetic field, so that the phase on both sides of the fluxon cores is nearly constant. The $16\times$ amplified contour density maps after this linear phase subtraction are presented in figure 2 for the case of flux tube $L=0$ (a) and the two values of L , $L=30$ nm (b) and $L=60$ nm (c).

These patterns show immediately that the trend of the contour fringes across the fluxon cores is very sensitive to its topography, so that it is expected that this important information will be obtained from the analysis of amplified holographic maps recorded at a resolution inferior to the expected value of the core size.

References

1. K. Harada, et al., *Nature* (1992) 360, 51.
2. J.E. Bonevich, et al., *these proceedings*.
3. A. Migliori, G. Pozzi and A. Tonomura, *Ultramicroscopy* (1993) 49, 87.
4. G. Pozzi and A. Tonomura, *Proc. 10th Eur. Cong. on Electr. Microsc.* 2 (1992) 47.

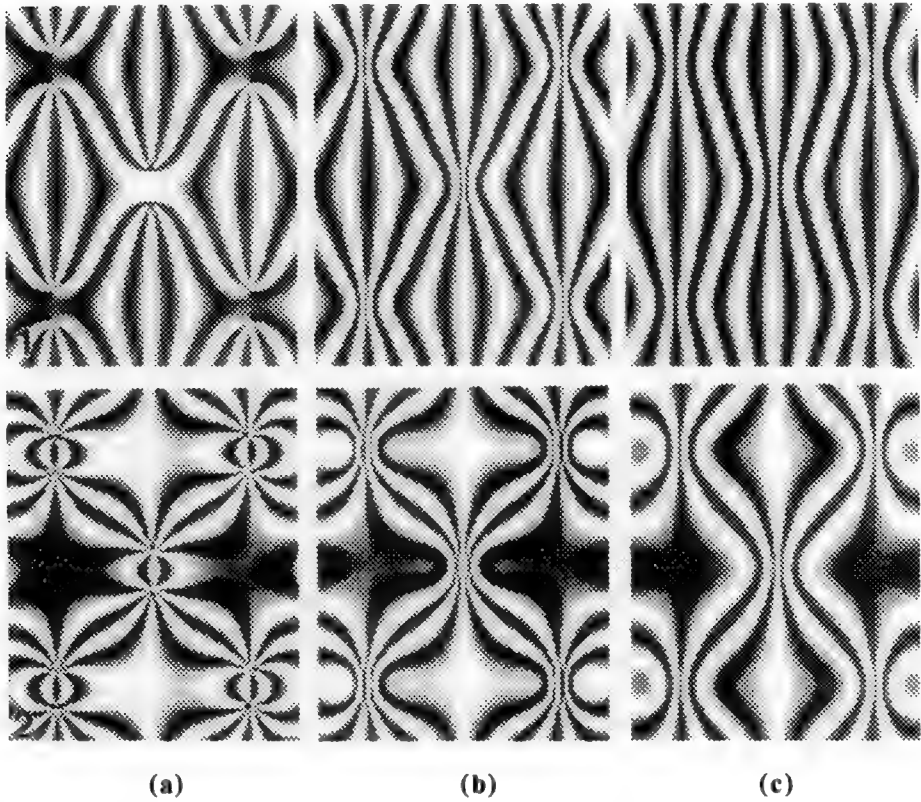


FIG. 1. 8 \times amplified contour map of the phase of the central part of a triangular array of fluxons having different core sizes. (a) $L=0$; (b) $L=30$ nm; (c) $L=60$ nm.

FIG. 2. 16 \times amplified contour map of the phase of the central part of a triangular array of fluxons having different core sizes after subtraction of a linear bias. (a) $L=0$; (b) $L=30$ nm; (c) $L=60$ nm.

AUTHOR INDEX

A

Abel, F. L., 362
 Acharya, R., 158
 Ackland, D. W., 250
 Adams, W. W., 866, 868, 1184
 Ade, H., 636, 648, 650, 902
 Advani, A. H., 1164, 1166, 1168
 Agard, D. A., 74, 150, 182, 204,
 436, 448, 554, 558, 888
 Agarwal, M., 170
 Aggarwal, S. K., 406
 Ahn, C. C., 634
 Aida, K., 356
 Aihara, K., 356
 Akin, D. E., 138
 Akita, T., 1132
 Akpunonu, B. E., 338
 Aksay, I. A., 500
 Al-Ghoul, K. J., 200
 Al-Jassim, M. M., 440, 812
 Alani, R., 718
 Albrecht, R. M., 230
 Alexander, B. D., 726
 Alexander, R. W., 792
 Allard, L. F., 592, 936, 1066,
 1076, 1092
 Amos, W. B., 156
 Ancin, H., 160, 268, 562
 Anderson, D. M., 884
 Anderson, E., 636, 650
 Anderson, J. R., 742
 Anderson, R., 708, 838
 Ando, A., 256
 Andrews, R. A., 1194
 Andrews, S. B., 568
 Angelides, K. J., 34
 Apkarian, R. P., 608, 610
 Armbruster, B., 224, 528, 530
 Arrhenius, G., 168
 Asano, G., 308, 356, 360, 430,
 432, 470
 Ashraf, M., 356
 Asselbergs, P. E. S. J., 258
 Auchterlonie, G. J., 442
 Avinash, G. B., 206
 Ayers, J. D., 1026

B

Babcock, S. E., 1140
 Bachmann, K. J., 818

Badger, A. M., 398
 Baek, K. K., 1150
 Bailey, B., 88
 Bains, H. K., 324, 334
 Balczon, R., 342
 Balhorn, R., 646
 Ball, T. B., 216
 Bando, Y., 1080
 Banks, B. M., 1146
 Barker, W. W., 52
 Barmak, K., 842
 Barry, J. C., 442, 730
 Bartlett, M. S., 26
 Bass, J., 1098
 Bast, T., 392
 Batson, P. E., 574, 816, 858
 Baumbach, G., 426
 Bawa, R., 324, 334
 Bawa, S. R., 324, 334
 Bearden, A., 84
 Becich, M. J., 32, 484
 Becker, D. E., 160
 Bellare, J. R., 240, 284
 Bench, M. W., 800, 1152
 Benedict, J., 708
 Bennett, B. R., 826
 Bennett, M. H., 778
 Bentley, J., 438, 446, 592,
 904, 928, 962, 1006
 Berg, R. H., 110
 Bergles, D. W., 100
 Bernas, H., 808
 Berns, M. W., 10
 Berta, Y., 930
 Bertero, G. A., 1038
 Besmann, T. M., 918
 Betzig, E., 8
 Beven, A., 146
 Bhadriraju, K., 284
 Bhattacharjya, A. K., 160
 Bhattacharyya, S., 276, 564
 Bickar, D., 126
 Bielat, K., 302
 Bingham, I., 382
 Bingham, L., 382
 Bird, D., 688
 Birkmire, R. W., 440
 Birnbaum, H. K., 804, 806
 Bisher, M. E., 748
 Bishop, G. A., 288

Bishop, K., 136
 Black, D. R., 504
 Blackham, R. T., 232
 Blackson, J., 582
 Blechschmidt, B., 330
 Bloom, B. R., 358
 Boissy, R. E., 402
 Boissy, Y. L., 402
 Bonevich, J. E., 1050, 1096, 1
 Bonnell, D. A., 966
 Boraas, M., 420
 Borg, T. K., 362, 364
 Borisy, G. G., 120
 Bormans, B., 1030
 Boublik, M., 330
 Bourett, T. M., 114, 282
 Bow, J. S., 714, 810, 832, 914
 Boyce, S. T., 400
 Bradley, G. F., 870
 Bradshaw, A. M., 998
 Braig, K., 330
 Brandelik, D. M., 1184
 Branton, D., 56
 Braue, W., 920
 Braunfeld, M. B., 204, 436
 Brelje, T. C., 156
 Bright, D. S., 220, 538
 Brink, J., 686
 Brown, R. S., 472
 Browning, N. D., 576
 Bruley, J., 596
 Brun, N., 836
 Brynestad, J., 598
 Buchanan, J., 100
 Buchanan, R. A., 568
 Buchheit, R. G., 850, 860
 Buchko, C. J., 1218
 Buckett, M. I., 982
 Budhani, R. C., 1138
 Buehler, S. M., 1200
 Bugelski, P. J., 398
 Buggy, J., 362
 Bunn, R. D., 550
 Burgess, G., 688
 Burgess, M. L., 362
 Burke, M. G., 232, 854, 862
 Burmester, C., 666
 Burnett, J. C., Jr., 316, 388
 Burns, J. L., 50
 Burry, R. W., 288

AUTHOR INDEX

Buseck, P. R., 742
 Bustamante, C., 86
 Butler, J. H., 870

C

Caccamo, D. V., 404
 Cafaro, A., Jr., 312
 Cafaro, J., 312
 Cai, Z. X., 1138
 Cairncross, A., 716
 Callahan, D. A., 132
 Callahan, D. L., 872, 904
 Calomeni, E. P., 244
 Cameron, S., 902
 Carbone, K., 330
 Garcia, P. F., 1040
 Cardell, E. L., 218, 300
 Cardell, R. R., 218, 298, 300,
 390, 394
 Carlino, V., 460
 Carlton, R. D., 278
 Carpenter, D. A., 270
 Carpenter, D. O., 162
 Carpenter, G. C., 586
 Carpenter, R. W., 714, 810, 832,
 914, 920, 1180
 Carragher, B. O., 96, 496
 Carrington, W. A., 148, 164
 Carter, C. B., 438, 760, 800, 926,
 928, 934, 948, 964, 1120,
 1134, 1142, 1152, 1154, 1158
 Caspar, D. L. D., 672
 Celotta, R. J., 1032
 Cesefias, L. A., 418
 Chabala, J. M., 604
 Chakoumakos, D. C., 1188
 Chamberlin, R. V., 1026
 Chan, H. M., 946
 Chang, R. P. H., 1128
 Chapman, H. N., 646
 Chapman, J. N., 1030
 Chen, A., 424
 Chen, H., 448
 Chen, J. K., 314
 Chen, R. W., 1178
 Chen, Y., 44, 120
 Cheng, P. C., 158, 654
 Chernoff, D. A., 518, 526
 Chernoff, E. A. G., 518
 Chestnut, M. H., 50

Cheung, W. W. K., 28
 Chien, K., 242
 Chiou, W. A., 1116, 1126
 Chiruvolu, S., 880
 Chisholm, M. F., 576, 802
 Chiu, W., 686
 Choi-Feng, C., 726
 Choo, W. K., 1180
 Christensen, K. N., 818
 Christie, B., 226
 Chue, C., 78
 Cieslinski, R. C., 892
 Clarke, J., 58
 Clausing, R. E., 1006
 Cleary, A., 130
 Clyborne, W., 448
 Cochener, B., 10
 Coene, W. M. J., 1036, 1070
 Cohen, A. R., 160
 Cohen, K. L., 248
 Cole, M. W., 1114
 Cole, R. W., 80, 180
 Conway, J. F., 570
 Conway, W. S., 320
 Cooper, J. A., 276
 Cosandey, F., 834, 836
 Costello, M. J., 200, 492
 Costello, S., 902
 Cowley, J. M., 752, 960, 968,
 1004, 1026, 1082, 1170
 Crang, R. F. E., 348
 Crewe, A. V., 2
 Crimp, M. A., 1098
 Crooks, K., 192
 Crozier, P. A., 670, 724
 Cullis, A. G., 814
 Cunningham, B., 796, 1094
 Czamota, G. J., 194

D

Dahmen, U., 458
 Dailey, M. E., 100
 Damlama, M., 94
 Danilatos, G. D., 786
 Das Chowdhury, K., 920
 Datye, A. K., 782
 Daugherty, C., 106
 Davidson, A. D., 474
 Davilla, S. D., 220
 Davis, J. L., 826

Davis, R. F., 832
 Davis-Cox, M., 162
 DeArdo, A. J., 744
 Deerinck, T. J., 96, 98, 634
 DeHoff, R. T., 486, 540
 de Jong, M. J. C., 258
 Demczyk, B. G., 1046
 den Broeder, F. J. A., 1036
 Denehy, G., 412
 Deng, X. F., 1054
 DeRosier, D. J., 672
 de Ruijter, W. J., 262, 546, 1062
 Desimoni, J., 808
 De Veirman, A. E. M., 1036
 Diaz, R., 672
 Diaz G., M., 336
 Dillin, A. G., 274
 Dillman, R., 64
 Dimonie, V. L., 882
 DiSalvo, F. J., 820
 Dixon, A., 156
 Donley, M. S., 852
 Dorset, D. L., 660, 684
 Downing, K. H., 668
 Downs, M. B., 310
 Drake, R. L., 390, 394
 Dravid, V. P., 702, 944, 1088,
 1128, 1208
 Drewien, C. A., 850, 860
 Driscoll, C., 382
 Drucker, J. S., 766
 Dudley, M. A., 42
 Dufner, D. C., 700
 Duncan, J. C., 1146
 Duncombe, P. R., 948
 Dunlap, J. R., 444, 454, 1188
 Dunny, G., 44
 Dvorak, A. M., 712

E

Eades, J. A., 214, 676, 1008
 Earnshaw, W. C., 78
 Echlin, P., 142
 Eckley, D. M., 78
 Edelman, H. S., 940
 Edmiston, C. E., 374
 Egerton, R. F., 220
 Ehrman, J. M., 700
 Ekman, J., 420
 El-Aasser, M. S., 882

AUTHOR INDEX

Elliot, R. L., 198
 Ellis, E. A., 318
 Ellisman, M. H., 96, 98, 634, 642
 Endo, J., 1220
 Engel, A., 628
 Engel, W., 998
 Ennis, M., 292
 Eppell, S. J., 230
 Erbe, E. F., 46, 70, 122
 Eriksson, L., 658
 Erlandsen, S. L., 36, 44, 370, 460
 Evans, B. A., 484
 Evans, D., 192
 Evans, N. D., 446, 958

F

Fagan, P. J., 754
 Fairbairn, D. W., 272
 Fan, G. Y., 168, 634, 642
 Farkas, D. L., 88
 Fassel, T. A., 294, 374
 Fay, F. S., 164
 Fay-Guthrie, D., 64
 Fei, L., 522, 524, 994
 Fejtl, M., 162
 Feng, Y., 940, 1140
 Ferrier, R. P., 1030
 Fields, S. D., 134
 Fincher, J., 48
 Fine, M. E., 1174
 Fisher, A. T., 446
 Fisher, K. A., 58, 508
 Fisher, R. M., 464
 Fisher, W. W., 1164, 1166, 1168
 Fitzgerald, E. A., 614
 Flaherty, D. M., 716
 Flyvbjerg, A., 428
 Fonda, R. W., 984, 988
 Fortin, D., 414
 Fossey, S. A., 1216
 Fouriaris, G., 1048
 Frank, J., 548
 Fraser, H. L., 662
 Fraser, S. E., 90
 Fratkin, J. D., 22
 Fraundorf, P., 224, 524, 528, 530,
 532, 534, 994
 Frethem, C., 460
 Freudenrich, C. C., 12
 Frey, J. K., 424

Frickes, M., 192
 Friedman, D. J., 812
 Friedmann, T. A., 732
 Fujimaki, N., 344
 Fukushima, K., 254
 Fuller, E. R., Jr., 490
 Fung, J. C., 182
 Furcinitti, P. S., 184, 452
 Furuya, F. R., 330
 Futamoto, M., 1012

G

Gai, P. L., 924
 Gajdardziska-Josifovska, M., 828,
 1090
 Gallegos de L., G., 336
 Galvin, M. E., 896
 Gao, K., 300
 Garancis, J., 312
 Garcia, C. I., 744
 Garcia, J. H., 404
 Gard, D. L., 176
 Gardner, J. S., 366, 382
 Garnaes, J., 510
 Garratt-Reed, A. J., 600, 950, 1146
 Gavin, M., 370
 Geary, S., 382
 Geipel, T., 992
 Gelber, T. A., 10
 George, T., 1196
 Gerthoffer, W. T., 24
 Ghoneim, S., 426
 Ghosh, G., 746, 1174
 Ghosn, C. R., 10
 Giammara, B. L., 248
 Gibson, J. M., 640, 844
 Gido, S. P., 1216
 Giffin, B. F., 300, 394
 Gilbert, C. S., 280
 Gilerovitch, H. G., 288
 Gilliland, K., 12
 Gilloteaux, J., 196, 354
 Gillott, M. A., 420, 1148
 Givargizov, E. I., 818
 Gladman, T., 1048
 Godleski, J. J., 286, 602
 Goehner, R. P., 772
 Goheen, M. P., 26
 Goldstein, J. I., 250, 848
 Gómez G., L., 336

Goodhew, P. J., 706
 Gourdie, R. G., 266
 Goyal, A., 936
 Goynes, W. R., 352
 Grant, M. B., 318
 Gray, R. T., 368, 378
 Greaser, M. L., 294
 Green, C. R., 266
 Green, L. M., 726
 Greene, J. E., 804, 806
 Greene, W. B., 102
 Gregory, M. A., 384
 Gribelyuk, M. A., 674, 1082
 Griffin, R. D., 1156, 1194
 Griffiths, D. P., 246
 Gronskey, R., 798
 Gross, D. J., 606
 Gross, L. J., 556
 Gruenstein, E., 620
 Grundke-Iqbal, I., 190
 Gubbens, A. J., 204, 586
 Gundersen, H. J. G., 480
 Gunning, W. T., 244, 338
 Gustafsson, M. G. L., 58
 Guthrie, P. B., 64

H

Hagege, S., 836
 Haider, M., 624
 Hainfeld, J. F., 330
 Hakkens, F. J. G., 1036
 Hall, J. B., 726
 Hall, R. H., 368
 Hamilton, T. A., 322
 Hamkalo, B. A., 72
 Hammond, E. C., 794
 Han, B.-G., 680
 Han, K. F., 204, 558
 Hanker, J. S., 248
 Hanna, L. G., 924
 Hansen, B., 382
 Hanyu, Y., 104
 Harada, K., 1050, 1096
 Harb, J. M., 20
 Harlan, D. M., 306
 Harmer, M. P., 946
 Harrach, H. S. von, 250, 996
 Harrick, R. W., 532
 Harriger, M. D., 400
 Harris, K. M., 92

AUTHOR INDEX

Harry, M., 420
 Hart, T. K., 398
 Hashimoto, T., 252
 Hasslen, S. R., 36
 Hastings, C. L., 278
 Hatch, V., 286, 602
 Hattori, Y., 430, 432
 Haugh, J. J., 232
 Hawes, C., 128, 192
 Haydon, P., 512
 Head, J. F., 198
 Heathcote, R. D., 424
 Heatherly, L., 1006
 Heckman, C. A., 222
 Heckman, J. W., 1098
 Heckmann, R. A., 366
 Heeschen, W. A., 894
 Hembree, G. G., 1130
 Henderson, E., 512
 Henderson, J., 192
 Heng, Y. M., 482
 Hepler, P. K., 132
 Herring, R. A., 1056, 1086
 Hesketh, P. J., 516
 Hess, W. M., 216, 380
 Heuer, A. H., 170, 954
 Heusser, R. C., 242
 Hicks, B., 34
 Highett, M., 146
 Hills, C. R., 850
 Hillyard, S., 820, 976
 Hirayama, T., 1028
 Hirose, K., 252
 Ho, K. L., 404
 Ho, R., 434, 566
 Hobbs, L. W., 210, 788, 906, 950, 1146
 Hockett, D., 12
 Hoffpauir, J. M., 14
 Høier, R., 682
 Hoines, L., 1098
 Holdren, D. N., 248
 Holen, D., 420
 Hollingshead, J., 382
 Holmberg, D. L., 350
 Holmes, T. J., 152, 268, 276
 Holmestad, R., 682, 692, 698
 Honda, T., 202, 254
 Honda, Y., 1012
 Honey, T. A., 1182

Hoover, M. L., 14
 Horita, Z., 698
 Hombostel, M., 820
 Horton, L. L., 1006
 Horwich, A. L., 330
 Hosokawa, F., 202, 254
 Hossler, F. E., 238
 Hovmöller, S., 658, 1204
 Howard, R. J., 114, 282
 Howard, T. A., 32, 484
 Howell, D. A., 1098
 Howell, K. E., 184
 Howells, M., 638
 Howland, R. S., 516
 Hren, J. J., 818
 Hsiao, B., 902
 Hsu, C.-M., 1122, 1160
 Hsu, T.-Y., 1122
 Hua, M., 744
 Huang, B. M., 824
 Huang, C.-S., 1160
 Huang, P.-F., 1124
 Hudson, G. C., 614, 1196
 Huggins, B. J., 726
 Hughes, C. W., 232
 Hukee, M., 316, 388
 Hulbert, S., 650
 Humphreys, T. P., 1196
 Hung, M., 1110
 Hunziker, E. B., 108
 Hurley, J. P., 740
 Hurst, V. J., 52
 Hutchins, G. A., 900
 Hütten, A., 1018

I

Ichihashi, M., 252
 Ichikawa, M., 104
 Igarachi, M., 1050
 Ikuta, T., 970
 Imamura, G. M., 462
 Inaba, N., 1012
 Ingber, B. F., 352
 Ingram, P., 12, 220, 588
 Ip, W., 270
 Iqbal, K., 190
 Ishida, Y., 202, 1080, 1206
 Ishihara, A., 188
 Ishikawa, H., 344
 Ishiwata, T., 360, 470

Ishizaki, M., 386
 Ishizuka, K., 1084

J

Jackson, A. G., 264
 Jacobs, R. E., 90
 Jacobsen, C., 636, 638, 648
 Jacobson, A. J., 748
 Jacobson, K., 188
 Jahn, W., 118
 James, W. J., 524
 Jamison, J. M., 196
 Janowski, G. M., 1156, 1194
 Janssen, A. J. E. M., 1070
 Januszewski, T. C., 20
 Janzen, E. G., 392
 Jarnot, B. M., 396
 Jayaram, G., 1002
 Jesson, D. E., 802, 978, 996
 Jiang, H., 1184
 Jiang, M., 292
 Jiang, S. S., 960
 Jiang, X. G., 644
 Jiao, J., 750, 756, 758
 Jin, X., 988
 Jobe, R., 226
 Joens, S., 260
 Johnson, E., 650
 Johnson, J. E., Jr., 190
 Johnson, R. H., 652
 Jondle, D., 512
 Jones, G. P., 362
 Jones, I. P., 662
 Jones, K. M., 440
 Jones, M. H., 332
 Jones, M. L., 242
 Jones, S. N., 776
 Josephs, R., 116, 556
 Joslin, D. L., 958
 Joswiak, D. J., 1186
 Joy, D. C., 454, 550, 582, 764, 870, 1092, 1094, 1188
 Judkins, R. F., 338
 Jung, P. S., 228

K

Kaduk, J. A., 726
 Kamino, T., 252
 Kan, F. W. K., 62
 Kaneyama, T., 254, 1206

AUTHOR INDEX

- Kang, Y.-H., 306
 Kao, C. H., 314
 Kao, W.-Y., 386
 Kaplan, D. L., 1216
 Karkare, S., 354
 Karr, T., 74
 Kasai, H., 1050, 1096
 Kashiwado, I., 430, 432
 Katler, M., 286, 602
 Katrinak, K. A., 740, 742
 Kawabe, U., 1050
 Keery, W. J., 776
 Keller, R., 172
 Kelley, M. H., 1032
 Kelly, J. F., 490
 Kelly, T. R., 354
 Kenik, E. A., 592, 854, 1106
 Kern, D., 636, 650
 Kerr, K. M., 1200
 Kersker, M., 202, 254, 1080, 1206
 Ketterson, J. B., 1128
 Khan, S., 54
 Khan, S. A., 270
 Kilaas, R., 458, 542
 Kim, H., 654
 Kim, H. S., 450
 Kim, M. J., 236, 714, 810, 832, 914
 Kim, S. G., 236
 Kim, S. J., 874
 Kim, Y. J., 932
 King, A. H., 942
 King, J. S., 288
 King, S., 964, 1134, 1142, 1158
 Kircher, C. H., 398
 Kirk, B., 12
 Kirkland, E. J., 220
 Kirz, J., 636, 648, 650
 Kitami, Y., 1080
 Kjoller, K., 518
 Klabunde, U., 716
 Klepeis, S. J., 708
 Knapp, H. F., 628
 Ko, C.-H., 650
 Koehler, J. K., 332
 Komorowski, R. A., 20
 Kömüves, L. G., 30, 42
 Kondo, S., 1050
 Kondo, Y., 202
 Konno, T. J., 830
 Kontra, R., 936
 Kopf, D. A., 588
 Kordesch, M. E., 506
 Koster, A. J., 204, 436, 448
 Kotula, P. G., 760, 1120
 Krause, S. J., 866, 1108, 1172
 Kremer, J. R., 184, 452
 Kress, Y., 358
 Krishna Murthy, G. G., 602
 Krishnamurthi, V., 152
 Krivanek, O. L., 262, 546, 586, 972, 1062
 Kriven, W. M., 932, 952, 956
 Kroeger, D. M., 598, 936
 Kryder, M. H., 1010
 Kuboki, K., 260
 Kuehner, S. M., 1186
 Kundmann, M. K., 586
 Kuo, J. S., 314
 Kuwabara, M., 1020
- ### L
- Ladinsky, M. S., 184
 Lakis, R. E., 722
 Lamont, S., 96
 Landh, T., 884
 Lane, C. W., 200
 Lanni, F., 88
 Larabell, C. A., 66
 Larbalestier, D. C., 940, 1140
 Lavernia, E., 1192
 Lay, M.-S., 1160
 Leapman, R. D., 568, 594, 686
 Leber, M. L., 546, 972
 LeClair, S., 264
 Lee, C.-H., 306
 Lee, J., 188
 Lee, J. D., 1108
 Lee, J. S., 1180
 Lee, P.-Y., 1160
 Lee, S., 1218
 Lee, S. K., 236
 LeFurgey, A., 12, 588
 Lenz, P. H., 340
 Leonard, M., 188
 Levi-Setti, R., 604
 Lewis, M. E., 210
 Lewis, M. R., 556
 Li, D., 726
 Li, L., 116
 Li, L. S., 886
 Li, Z. G., 754, 1040
 Liang, L., 754
 Liang, Y., 966
 Liao, J., 890
 Liaw, L.-H. L., 10
 Lichte, H., 1074
 Lightfoot, F. G., 278, 296
 Liliental-Weber, Z., 808
 Lim, H., 1180
 Lin, B., 330
 Lin, C. S., 846, 1116, 1126
 Lin, H.-M., 1122, 1160
 Lin, P. S.-D., 630
 Lin, T. H., 654
 Lin, W., 268
 Lin, X., 1128, 1208
 Lin, X. W., 808
 Lin, Z., 878
 Lindaas, S., 636, 638, 648
 Lindley, V., 422
 Linton, R. W., 498
 Liu, Jiang, 818
 Liu, Jingyue, 580, 720, 784, 968, 1058, 1060
 Liu, M., 752, 1170
 Liu, P., 1126
 Liu, W., 554
 Liu, W.-L., 290
 Liu, Y.-H., 152
 Lloyd, P. F., 1118, 1184
 Lo, W., 1060
 Loew, L. M., 164
 Login, G. R., 712
 Long, J. C., 790
 Longo, F. J., 40
 Lordi, S., 214, 1000, 1008
 Lou, J. C., 798
 Lowden, R. A., 918, 922
 Lu, P., 834, 836
 Luna, J., 620
 Luna, J., 620
 Lundgren, K., 72
 Luo, S., 454, 582, 1188
 Luzarraga, M. B., 794
 Luzzi, D. E., 984, 988
 Lyman, C. E., 220, 250, 838

AUTHOR INDEX

M

- Ma, Y., 214, 1008
 McAfee, G. H., 780
 McCandless, B. E., 440
 McCartney, M. R., 724
 McCarty, K. F., 732
 McCourt, M. P., 660, 684
 McCoy, K. L., 274
 McCracken, A. A., 274
 McCrone, W. C., 908
 McDonald, K., 112
 McDonough, K. A., 358
 McEwen, B. F., 494
 McFadyen, I. R., 612, 1022
 McGibbon, M. M., 576
 McGregor, C. G. A., 316, 388
 McHargue, C. J., 958
 McIntosh, J. R., 112, 184, 452
 Mackay, A. M., 78
 Mackenzie, J. M., 246
 McKernan, S., 760, 910, 926, 1154, 1158
 Mackin, R. W., 160
 McLane, G. F., 1114
 MacLay, G. J., 516
 McMahan, G., 710
 McMullan, D., 762
 McMurry, P. H., 1124
 McWilliams, T. S., 794
 Maher, D. M., 662
 Mahoney, M. G., 606
 Mahoney, T. M., 484
 Malecki, M., 186
 Maleeff, B. E., 398
 Malis, T., 710, 838, 840
 Mallamaci, M. P., 438, 928, 948, 1152
 Malm, J.-O., 974
 Maloy, S. A., 912
 Malta, D. P., 614, 1196
 Mankos, M., 1026
 Mansfield, J., 688
 Manstein, D., 118
 Mantl, S., 802
 Mao, S. N., 1190
 Maracas, G. N., 810
 Marchant, R. E., 230
 Marchese-Ragona, S. P., 226
 Markunas, R. J., 614, 1196
 Mars, M., 384
 Marsh, T., 512
 Marshall, M. T., 640
 Marthinsen, K., 682
 Martin, D. C., 890, 1218
 Martoglio, P. A., 616
 Martone, M. E., 96, 98
 Masters, B. R., 166
 Matsuda, T., 1050, 1096
 Matsuda, Y., 1012
 Matsumoto, G., 104
 Matsumoto, T., 1222
 Matsunami, T., 386
 Matsushima, H., 260
 Medford, R. M., 792
 Medlin, D. L., 732
 Meek, T. T., 1136
 Melanson, L. A., 672
 Melik, D. H., 1200
 Menger, F. M., 608
 Merkle, K. L., 982
 Meshii, M., 1116
 Meyer, C. E., 546
 Mia, A. J., 474
 Michael, J. R., 590, 772
 Michaels, J. E., 298
 Michal, G. M., 1176
 Mikami, S., 256
 Miliotis, M. D., 368
 Miller, C. A., 304
 Miller, F. J., 178
 Miller, G. A., 946
 Miller, M., 408
 Miller, M. K., 862
 Miller, T. J., 800
 Millette, J. R., 472
 Mills, K. R., 322
 Mills, M. J., 732
 Milroy, A. M., 328
 Minter, J. R., 728
 Mirkarimi, P. B., 732
 Miroslavov, Y. A., 348
 Mis, J. D., 796
 Misra, M., 570
 Mitchell, G., 902
 Mitchell, M. W., 84
 Mitchell, T. E., 912, 916
 Mohamad, M., 390
 Mohan, A., 1094
 Mojzsis, S., 168
 Moninger, T., 466, 468
 Monson, F. C., 238
 Mooney, C. B., 520
 Mooney, P. E., 262, 1062
 Moore, J. S., 1218
 Moore, K. C., 476
 Moore, S., 426
 Morar, J. F., 816
 More, K. L., 918, 922
 Moreland, J., 1034
 Morgan, D. G., 672
 Morita, M., 64
 Moriyama, K., 256
 Morphey, M. K., 112
 Morris, J. C., 1144
 Morris, R. E., 300, 394
 Morrison, W. H., III, 138
 Mrosko, B., 642
 Mueller, D. M. J., 790
 Mueller, W. F., 22
 Mülleijans, H., 596
 Muller, D. A., 626, 1100
 Müller, M., 124
 Müller, T., 106
 Muller, W. S., 1216
 Murphy, R. F., 304
 Murr, L. E., 1164, 1166, 1168
 Murray, D. J., 892

N

- Naik, T. R., 1148
 Nakagami, Y., 308
 Nakamura, O., 256
 Nakamura, S.-I., 308
 Namimatsu, S., 308
 Napier, R., 192
 Nathan, M. I., 800
 Neil, T. E., 860
 Nelson, R. D., 36
 Newbury, D. E., 502, 594, 856
 Newkirk, J., 524
 Nicholls, A. W., 250
 Nichols, B. L., 42
 Nichols, D. H., 304
 Niu, L., 512
 Nolan, T. A., 1076, 1092
 Nolan, T. P., 1016
 Norton, M. G., 934
 Nowroozi-Esfahani, R., 516
 Nyengaard, J. R., 428, 478

AUTHOR INDEX

O

Oakford, L. X., 474
 Ocobock, R. W., 1182
 Oehler, V., 648
 Ofengand, J., 330
 Oguro, T., 308, 356
 Oho, E., 212
 O'Keefe, M. A., 208, 458, 974, 980
 Oldenbourg, R., 82
 Oldham, W. G., 798
 Olesen, J. B., 222
 Oliver, T. N., 188, 200
 Olmsted, S., 44
 Olson, G. B., 746, 1174
 Olson, J. M., 812
 O'Neill, K. L., 272
 O'Neill, M. P., 84
 Oot, D. F., 516
 Op de Beeck, M., 1068, 1070, 1212
 Orlow, S. J., 402
 Osborne, L. C., 84
 Osheroff, N., 74
 O'Toole, E., 452
 Otten, M. T., 258, 1072
 Owen, C., 672
 Owens, D. W., 760

P

Paciornik, S., 208, 458
 Palazzo, R. E., 180
 Pan, M., 670, 1058
 Pan, Y., 1136
 Panessa-Warren, B. J., 38
 Paputa Peck, M. C., 1182
 Paredy, D. R., 158
 Park, J., 264
 Park, J. C., 1108
 Park, M., 1172
 Parker, M. A., 1014
 Parnley, R. T., 280
 Parseghian, M. H., 72
 Parthasarathy, M. V., 106
 Patil, R., 874
 Paweletz, N., 342
 Pawley, J. B., 44, 156, 630
 Peachey, L. D., 344
 Pedraza, D. F., 1106
 Pennycook, S. J., 576, 802, 978, 996
 Perdigao, J., 410, 462

Peters, K.-R., 212
 Peters, N. S., 266
 Petrali, J. P., 322
 Petrik, G., 1156
 Petrovic, J. J., 912, 916
 Pfeiler, E., 422
 Phillips, D. A., 954
 Phillips, H. M., 872, 904
 Pierce, D. T., 1032
 Pike, S., 100
 Pike, W. T., 690
 Pint, B. A., 950, 1146
 Pirouz, P., 992
 Piston, D. W., 154
 Pixley, S. K., 408
 Plass, R., 1088
 Platz, C. C., 332
 Plummer, H. K., Jr., 1182
 Pohland, O., 844
 Polizzotto, L., 552
 Pooley, C. D., 320
 Popoola, O. O., 956
 Porter, L. M., 832
 Postek, M. T., 768, 776
 Posthill, J. B., 614, 1196
 Pozzi, G., 1050, 1056, 1096, 1224
 Prasad Beesabathina, D., 1190
 Price, J., 634
 Price, R. L., 362, 364
 Pringle, O. A., 524
 Putnam, W. S., 864

Q

Qian, M., 578, 584, 632, 696, 1060, 1130
 Qiao, Y., 430, 432
 Qin, L. C., 210, 1102
 Quella, S. E., 306
 Qui, N., 1052

R

Radic, M. Z., 72
 Radmilovic, V., 980, 990
 Radzinski, Z. J., 544
 Raghunathan, K. V., 1156
 Rajesh, R., 810
 Ramamurthy, S., 926, 948, 1154
 Ramirez B., E., 336, 418
 Ranjan, R., 1016
 Rank, J.-L., 672

Rasch, R., 428
 Rash, J. E., 64
 Rastomjee, C. S., 998
 Rau, W. D., 1064
 Rauch, J., 62
 Rausenberger, B., 998
 Ravikumar, V., 986, 1088
 Rawlins, D., 146
 Ray, R., 322
 Reagan, W. J., 726
 Reffner, J. A., 616
 Reffner, J. R., 1198
 Reid, P. D., 126
 Reilly, M., 416
 Reine, B. A., 140, 464
 Reinhardt, J. W., 462
 Reinke, L. A., 392
 Reneker, D. H., 874
 Revel, J.-P., 704
 Rez, D., 1202
 Rez, P., 220, 416, 1202
 Rieder, C. L., 80, 180
 Ries, A. L., 32
 Rigney, E. D., 1156
 Rigsby, L. L., 138
 Ris, H., 186
 Rizvi, T. A., 292
 Robertson, I. M., 804, 806
 Robins, A., 122
 Robinson, J. M., 326
 Robinson, K. A., 608, 792
 Robinson, K. E., 618
 Rodriguez, C., 160
 Rodriguez, J., 466, 468
 Roe, R.-J., 1200
 Roeder, A. D., 176
 Roitman, P., 1108
 Romero, R. J., 1166
 Romig, A. D., Jr., 590
 Roos, A., 1124
 Rothery, S., 266
 Roy, S., 320
 Roysam, B., 160, 268
 Ru, Q., 1028, 1220
 Ruben, G. C., 190
 Rudder, R. A., 614, 1196
 Rühle, M., 674
 Ruiz, T., 672
 Russ, J. C., 488, 536
 Russell, P. E., 246, 520

AUTHOR INDEX

Russell, S. D., 134
 Ryan, F. J., 350

S

Safer, D., 330
 Saghbini, M., 72
 Saiga, T., 386
 Salamanca-Riba, L., 1190
 Saltzberg, M. A., 924
 Samarabandu, J. K., 158
 Sanders, K. M., 24
 Sanger, J. R., 374
 Sarikaya, M., 500, 578, 584
 Sartain, K. B., 1152
 Satiat-Jeunemaitre, B., 128, 192
 Sato, Y., 252
 Sauerbrey, R., 872, 904
 Saunders, M., 688
 Scalettar, B. A., 150, 182
 Schabert, F. A., 628
 Schatten, H., 342
 Scheinfein, M. R., 4, 632, 766, 1026
 Scherer, B., 12
 Schippert, M., 630
 Schröder, R. R., 118, 666
 Schroeder, M. M., 176
 Schwach, T., 372
 Schwartz, D. K., 510
 Seale, D. J., 1214
 Sedat, J. W., 74, 150, 182, 204, 436, 448, 554, 558
 Segall, I., 882
 Segovia, F., 418
 Seraphin, S., 756, 758
 Severs, N. J., 60, 266
 Shaapur, F., 234, 236, 714
 Shaffer, O. L., 882
 Shah, D. B., 378
 Shain, W., 162
 Shaiu, W.-L., 512
 Shanabrook, B. V., 826
 Shao, Z., 434, 566
 Shattuck, M. B., 58
 Shaw, P., 146
 Shaw, T. M., 948
 Sheinin, S. S., 450, 1214
 Shen, C., 532, 534
 Sheppard, C. J. R., 144
 Sheth, S. R., 240

Shi, S.-L., 568
 Shibata, K., 1132
 Shimizu, R., 970, 1132
 Shinozaki, D. M., 654
 Shipley, M. T., 290, 292
 Shiota, K., 256
 Sidles, J. A., 6
 Siew, S., 22
 Silberman, J., 412
 Silcox, J., 626, 820, 858, 976
 Silvis, H. C., 892
 Simmons, R. N., 1182
 Simmons, S. R., 230
 Simnad, M. T., 1192
 Simon, M., 330
 Simpliciano, V. M., 98
 Simpson, D. G., 364
 Sinclair, R., 830, 1016, 1038
 Singh, B., 18
 Singh, S. S., 1148
 Siriwardane, H., 524
 Skornick, W., 602
 Slakey, L. L., 606
 Slinkman, J. A., 822
 Sluder, G., 178
 Smith, D. D., 304
 Smith, D. J., 736, 782
 Smith, J. W., 26
 Smith, S. B., 86
 Smith, S. D., 888, 1200
 Smith, S. J., 100
 Smolik, S., 604
 Solórzano, I. G., 1150
 Somlyo, A. P., 434, 566
 Son, U. T., 818
 Soto, G. E., 96
 Spellward, P., 1054
 Spence, A., 1210
 Spence, J. C. H., 632, 692, 696, 698, 1060, 1130
 Speyer, R. F., 930
 Spinnler, G. E., 784, 1058
 Spontak, R. J., 50, 888, 1200
 Sprinzl, M., 330
 Spudich, J. A., 118
 Sreeram, A. N., 210
 Standing, M. D., 272, 380
 Stanley, E., 512
 Statham, P. J., 250
 Stearns, R. C., 286

Stearns, R., 602
 Steeds, J. W., 664, 1054
 Steele, E., 220
 Stepanova, A. N., 818
 Stern, E. A., 578, 584
 Stern, M. E., 10
 Steven, A. C., 570
 Strobel, G. A., 380
 Strout, G. W., 134
 Strutt, A. J., 1192
 Studer, D., 108
 Stupp, S. I., 886
 Su, S.-C., 456
 Suematsu, H., 916
 Suenaga, M., 938, 942, 1138
 Summers, J. L., 196
 Summers, P., 310
 Sun, S. Q., 568
 Sun, Y. R., 598, 1188
 Sundaram, S. K., 930
 Surrent, A. D., 922
 Sutherland, R. L., 1184
 Sutliff, J. A., 774
 Suzuki, M., 1012
 Svensson, G., 658, 1204
 Swaminathan, S., 662
 Swann, P. R., 718
 Swedlow, J. R., 74, 150
 Swiech, W., 998
 Szarowski, D. H., 162, 268

T

Tafto, J., 938
 Takai, Y., 970, 1132
 Takeguchi, M., 1132
 Takizawa, T., 326
 Tall, B. D., 368, 378
 Talmon, Y., 876
 Tam, G., 1112
 Tamburro, C. H., 14
 Taniguchi, Y., 970
 Tanji, T., 1028, 1056, 1084, 1086, 1222
 Tanner, J., 382
 Taylor, C. A., 396
 Taylor, D. L., 88
 Taylor, R. W., 346
 Tentschert, J., 528
 Tepper, J. M., 94
 Terracio, L., 362, 364

AUTHOR INDEX

Terracio, M., 364
 Thaer, A. A., 166
 Theodore, N. D., 1110, 1112
 Theurkauf, W., 174
 Thibodeaux, D. P., 352
 Thomas, E. L., 868
 Thomas, G., 990, 1018
 Thomas, R. E., 1196
 Thompson, J. R., 598
 Thompson, R. P., 266
 Thornton, J. T., 520
 Tivol, W. F., 660
 Tomita, T., 1080, 1206
 Tong, X., 640, 844
 Tonomura, A., 1024, 1028,
 1050, 1056, 1078, 1096,
 1220, 1222, 1224
 Torihashi, S., 24
 Tortora, G. T., 38
 Touryan, L. A., 788
 Towner, R. A., 392
 Treacy, M. M. J., 748
 Treadwell, H., 346
 Trillo, E. A., 1164, 1166
 Tritsch, G., 302
 Trus, D. L., 570
 Tryka, A. F., 278
 Tsai, F., 960, 1004
 Tsu, R., 806
 Tsukruk, V., 874
 Tsuno, H., 254
 Tuft, R. A., 164
 Tuller, H. L., 1150
 Tung, C.-Y., 1122
 Turner, J. H., 208
 Turner, J. N., 162, 268, 276, 660
 Turpin, B. J., 1124
 Twigg, M. E., 826

U

Ueda, K., 260
 Ueki, Y., 252
 Ujiie, M., 366
 Umezawa, A., 940
 Unguris, J., 1032

V

Vaisberg, E., 180
 Van de Velde, R. L., 242
 Vander Sande, J. B., 1140, 1150

Vander Wood, T. B., 738
 Van Dyck, D., 1068, 1070
 van Kavelaar, M., 754
 Van Zwet, 1070
 Vargas, M., 412
 Vassilyev, A. E., 348
 Vecchio, K. S., 1162, 1178, 1192
 Velu, E. M. T., 520
 Venables, D., 1108
 Venezia, R., 312
 Venkatesan, T., 1190
 Verkhovsky, A. B., 120
 Vesenska, J., 512
 Větvicka, V., 14
 Vezie, D. L., 868
 Vincent, R., 664, 1054
 Viney, C., 864
 Visokay, M. R., 1020, 1042
 Viswanathan, R., 510, 514
 Vladar, A. E., 768, 776
 Voigt-Martin, I. G., 656
 Völkl, E., 1066, 1076

W

Waddell, W., 332
 Wagner, J., 108
 Wagner, R. J., 826
 Wagner, J. B., Jr., 960
 Wakamatsu, K., 386
 Walck, S. D., 852, 1118
 Waldschmidt, T., 426
 Walne, P. L., 444
 Walther, P., 44
 Waltz, K., 10
 Wang, F., 198
 Wang, G., 654
 Wang, J.-Y., 942
 Wang, L., 968
 Wang, L. M., 1104
 Wang, X. K., 1128
 Wang, Y.-Y., 434, 944, 1128
 Wang, Z. L., 598, 694, 936, 1006
 Wargovich, T. J., 318
 Warren, J. B., 38
 Washburn, J., 808
 Watada, A. E., 320
 Waterman, J. R., 826

Waters, J., 80
 Weatherby, T. M., 340
 Weaver, J. H., 760
 Weber, W. J., 1104
 Wei, C.-M., 316, 388
 Wei, S. J., 136
 Weickenmeier, A. L., 692, 698
 Weiss, J. K., 766
 Welch, D. O., 1138
 Wells, O. C., 770
 Wells, C. L., 44, 370, 460
 Weng-Sieh, Z. S. H., 798
 Wergin, W. P., 46, 70, 122, 320
 Whalen, L. R., 64
 Wilbrink, J., 546
 Williams, D. B., 250
 Williams, G., 840
 Williams, R., 306
 Williams, R. K., 598
 Williams, S., 636, 648
 Wilson, P. M., 1218
 Wilson, S. R., 1172
 Winchester, S. C., 924
 Winey, K. I., 896
 Winter, K., 12, 16
 Winters, M. K., 272
 Wirick, S., 636, 648
 Withrow, S. P., 1106
 Wittig, J. E., 1044, 1052
 Wodnicka, M., 200
 Wodnicki, P., 200
 Wong, K., 572, 858
 Wong, T. L., 84
 Wood, B. A., 898
 Wood, D., 264
 Woodward, J. T., 68
 Woodward, T. H., 246
 Wordeman, L., 76

X

Xi, X. X., 1190
 Xiao, H. Z., 804, 806
 Xiao, S. Q., 170, 954
 Ximen, J., 630
 Xu, S.-J., 292
 Xu, Z., 1218
 Xue, G., 804

Y

Yamada, M., 260

AUTHOR INDEX

Yamanaka, N., 386
Yamasaki, Y., 608
Yamashiro, S., 392
Yamashita, T., 1016
Yanaka, T., 256
Yang, C.-C., 1122
Yang, V. C., 314
Yao, M.-H., 734, 736, 782
Yee, A., 1128
Yoder, E., 426
Yokoyama, M., 360, 470
Yorio, T., 474
Yoshida, T., 1050, 1096
Young, S. J., 96, 634
Yuge, K., 432

Z

Zabinski, J. S., 852
Zaluzec, N. J., 220, 622,
662, 688
Zandbergen, H. W., 1070
Zasadzinski, J. A. N., 68, 510
Zavadil, K. R., 860
Zeitler, E., 998
Zhang, H., 944, 1138
Zhang, J., 1218
Zhang, L., 1176
Zhang, W., 1216
Zhang, X., 636, 648, 1092,
1094, 1136
Zhang, Y., 98
Zhao, L., 434
Zhou, D., 756, 758
Zhou, Z. H., 560
Zhu, H. R., 1210
Zhu, J., 1208
Zhu, J. G., 812
Zhu, S., 1188
Zhu, Y., 938, 942, 1138
Ziesmer, D. N., 32
Zottola, E. A., 372
Zou, X., 658, 1204
Zubkov, V. G., 1204
Zuo, H. J., 1194
Zuo, J. M., 678, 692, 698, 1210